SKOPJE

EUROCK 15-19 SEPT 2026

RISK MANAGEMENT IN ROCK ENGINEERING

Risk Management in Rock Engineering

ISRM Regional Symposium

Proceedings Vol. 1



ISRM

ДГМ
МАГ

ДРУШТВО ЗА ГЕОТЕХНИКА НА МАКЕДОНИЈА
MACEDONIAN ASSOCIATION FOR GEOTECHNICS

RISK MANAGEMENT IN ROCK ENGINEERING

PROCEEDINGS OF THE REGIONAL SYMPOSIUM OF THE INTERNATIONAL SOCIETY FOR ROCK MECHANICS, EUROCK 2026, SKOPJE, 15-19 SEPTEMBER

Risk Management In Rock Engineering

Eurock 2026

Editors:

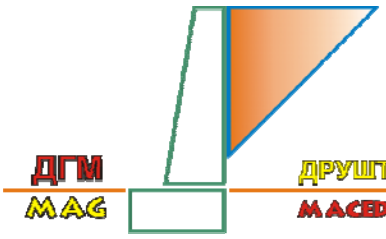
Milorad Jovanovski

Igor Peshevski

Skopje, 2026



ISRM



ДРУШТВО ЗА ГЕОТЕХНИКА НА МАКЕДОНИЈА
MACEDONIAN ASSOCIATION FOR GEOTECHNICS

© Macedonian Association for Geotechnics, Skopje R.N. Macedonia

All rights reserved. No part of this publication or the information contained herein may be reproduced, stored in retrieval system, or transmitted in any form or by means, electronic, mechanical, by photocopying, recording otherwise, without written prior permission from the publishers.

Published by: Macedonian association for geotechnics

Print by: Studentski servis DOO Skopje

Copies: 50

CIP - Каталогизација во публикација
Национална и универзитетска библиотека "Св. Климент Охридски", Скопје

624.12:[005.52:005.334](062)

REGIONAL symposium of the International society for rock mechanics, Eurock 2026 (6 ; 2026 ; Skopje)
Risk management in rock engineering : Eurock 2026 : Proceedings of the Regional symposium of the International society for rock mechanics, Eurock 2026, Skopje, 15-19 September / editors Milorad Jovanovski, Igor Peshevski. - Skopje : Macedonian association for geotechnics, 2026. - 2 св. (850 ; 782 стр.) : илустр. ; 30 см

Библиографија кон трудовите

ISBN 978-9989-2053-6-1 (Vol. 1)
ISBN 978-9989-2053-7-8 (Vol. 2)

а) Механика на карпи -- Инженерство -- Управување со ризик -- Собири

COBISS.MK-ID 69435397

Table of contents

Preface xviii
Welcome Message from the ISRM President xix
Organization xx
Committees xxi

Volume 1

Keynote lectures

Time-based hydro-mechanical modelling of tunnelling in weathered granite 3-15
Lidija Zdravkovic; D. M. Potts; J. H. Shin

Planetary Rock Mechanics and Future Prospects 17-32
Ömer Aydan

NMT-NATM hybrid method for sustainability and risk reduction 33-45
Nicholas Barton

CO_2 Sequestration and Mineralization in Basalts in Eastern China: Prospects, Constraints and Challenges 47-60
Fengshou Zhang

Impact of climatic variations on rock slope stability 61-70
Muriel Gasc-Barbier

Understanding failure mechanisms to design and manage risks for surface and underground excavations 71-95
Neil Bar

The importance of rock engineering for deep open pit slopes: Some considerations 97-130
Reşat Ulusay

Risk assessment methods

The principle of rock bridges uncertainty 133-138
Davide Elmo; Giulia Torsello; Luca Zorzi

Permeability and acoustic emission response characteristics during injection-induced fault slip 139-144
Ke Zhang; Qiang Li; Yueqiang Ma; Sida Jia; Jinsen Li; Quan Gan; Derek Elsworth

Application of DeepLabV3+ Model in Metro Tunnel Lining Crack Detection 145-150
Zhutian Pan; Xuepeng Zhang; Yujing Jiang

Weathering impact on the long-term stability of weak rocks 151-156
Bojan Janevski; Milorad Jovanovski

Risk management and Flexible Foundation Design for the electricity tower construction in the Swiss Alps 157-162
Natalia Maca; Yasir Husain

Reliability Limits of Rock Mass Classifications and a Zonal Approach for Reducing Design Risk 163-168
Milan Tumara; Milutin Petrović

Advanced InSAR Monitoring of Ground Deformation in the Polog Valley 169-174
Tome Gegovski; Zlatko Bogdanovski; Zlatko Srbinoski; Filip Kasapovski; Filip Petrovski

A probabilistic fragmentation-based rockfall model for open-pit and natural slopes 175-180
Maddalena Marchelli; Marco Paganone

From nominal energy to capacity curves: a probabilistic framework for reliability-based design of flexible rockfall barriers 181-186
Valerio De Biagi; Maddalena Marchelli; Francesco Pimpinella

Geotechnical risk ranking matrices 187-193
Justin Dixon; Trevor G. Carter; Phil J.H. deGraaf; Hazim Abu-Taleb

A methodology for fall of ground hazard assessment in underground mines 195-200
Amoussou Adoko; Amoussou Coffi Adoko; Richard Masethe

Optimal Stoping Limits, Stability, and Dip Pillars for Seismicity: SA Gold Mine 201-212
Richard Masethe; Onke Vetman; Thuthukani Sibiya

Towards a reliability-based monitoring system for uplift under concrete buttress dams 213-218
Johanna Dyberg Thonée; Maryam Zamzami; Johan Spross; Marie Westberg Wilde; Fredrik Johansson

Phase-field fracture simulation of the strain rate effect on fracture propagation 219-224
Armin Chehreh; Lucas Conrad Witte; Mandy Duda; Tobias Backers

Geotechnical and operational risk management planning for a long ore pass 225-230
Jeanne Walls

Integrating rigid body methods with rockfall simulation to evaluate instability along Tegalrejo road, Gunung Kidul, Indonesia 231-236
Adi Satria Nugraha; Hasan Tri Atmojo; Prosida Rhapsody; M. Rizqi Ikhwan Firman Maulana

Fall of Ground Risk Assessment in Underground Excavations Using a Fuzzy Cognitive Rock Engineering System 237-242
Assiya Tursanova; Rashid Afshar; Amoussou Adoko

Reliability-based design of the rock slope support considering the planar failure of multiple blocks 243-248
Renato Pereira; José Muralha; Luís Lamas

Risk-Informed Foundation Optioneering in Karst Terrain: From Geotechnical Risk to Sustainable Development 249-254
Mohamed Mahmoud; Omar Hamza

Disaster Risk Assessment for the City of Pirot: Potential Hazards of Rockfalls, Landslides and Erosion 255-263
Nikola Romić; Elefterija Zlatanović; Zoran Bonić; Nemanja Marinković; Branimir Stanković

Rock properties, testing methods and site characterization (incl. planetary rock mechanics)

Numerical investigation of fluid flow in intersecting fractures based on photogrammetry 267-272
Masoud Torkan; Sandaru Liyanarathna Vidanage; Lauri Uotinen; Mateusz Janiszewski; Mikael Rinne

Updated knowledge of inflatable rock bolts 273-278
Charlie Li

A model for estimating the penetration of hard rock tunnel boring machine in practice 279-284
Saffet Yagiz; Aitolkyn Yazitova; Jafar Hassanpour

Using Blanco Mera granite as standard reference and benchmark material 285-290
Manuel Alejandro González-Fernández; Mauro Muñiz-Menéndez; Ignacio Pérez-Rey

An adaptive data sampling strategy for in-situ stress characterization 291-296
Asieh Hamidi; John.P. Harrison; Diego Mas Ivars; Hossein A. Kasani; Abel Sánchez Juncal

Examples of cliff failures along the shores of Mediterranean Sea and the role of bioerosion 297-302
Sinem Ugur; Ömer Aydan; Halil Kumsar

Integrated Petrographic and Sorption Analysis of Pore Morphology in Sub-bituminous Coals 303-308
Ashutosh Tripathy; Madhurima Mazumder; T.N Singh

Uniaxial compressive strength and durability of sandstones and marls with varying moisture content 309-314
Sanja Dugonjić Jovančević; Martina Vivoda Prodan; Josip Peranić; Igor Ružić

Damage characteristics of thermally treated sandstone using the block punch index test 315-323
Sourav Das; Ratan Das; Debasish Mazumder

Exposure Time Dependency of Freeze and Thaw Damage on Hard Rocks 325-330
Ayten Ceyda Koseomur; Ahmet Gunes Yardimci

Slaking sensitivity of rocks – insights from a multi laboratory parameter study 331-336
Markus Kaspar; Christine Latal; Gerhard Pittino

Estimation of long-term behavior of rock from short-term creep tests 337-342
Kimihiro Hashiba; Katsunori Fukui

Research on ambient vibration-based quantitative assessment of tunnel lining defect using laser Doppler vibration measurement 343-348
Xuepeng Zhang; Ningbo Li; Yujing Jiang; Yao Wang; Guoshuai Wei

Numerical modelling of cracking in granite due to Joule heating and piezoelectric actuation 349-354
Timo Saksala

Physical Modeling of Rockfill Material for Construction of Specific Waste Disposals Using a Large-Scale Direct Shear Apparatus 355-360
Tamara Jovanovska; Eray Altıncı; Bahadır Başdemirci; Jovan Papić

Scale effects or statistical misinterpretation: a critical assessment of uniaxial compressive strength data 361-366
Risto Kiuru; Ignacio Pérez-Rey; Mauro Muñiz-Menéndez; James Woodman

The correlation between the compressive strength and dielectric constant for granites 367-372
Sair Kahraman; Ozge Yaman Harman; Selçuk Helhel

Full-scale impact test on a reinforced earth embankment with advanced monitoring for rockfall protection 373-378
Stefano Vigna; Maddalena Marchelli; Valerio De Biagi; Simone Saltarin; Matteo Nadalini; Alberto Grimod; Franz Demonte; Daniele Peila

Effect of rock matrix permeability on fluid-injection-induced hydro-mechanical coupled behaviour of rock discontinuities 379-384
Atsushi Sainoki; Daisuke Asahina; Naoki Iwata; Adam Schwartzkopff

Experimental Analysis of Flake Formation Under Roadheader's Pick Impact 385-390
Diego José Guerrero-Miguel; M, Inmaculada Álvarez-Fernández; M. Belén Prendes-Gero; Celestino González-Nicieza

Application of a Traction Tests Device in Rock Material Specimens 391-396
M, Inmaculada Álvarez-Fernández; Víctor Martínez-Ibáñez; Luis Álvarez-Gómez; Juan Carlos Peñas-Espinosa

Advances and Challenges in Multiple Failure State Triaxial Testing of Rocks – 50 years' experience 397-402
Samad Narimani; Morteza Davarpanah; Balazs Vasarhelyi

Microstructural analysis of granite tested under uniaxial compression conditions 403-408
Lucas Conrad Witte; Mandy Duda; Armin Chehreh; Simone Cornelia Pansa; Tobias Backers

Triaxial creep testing on argillaceous weak rock for DSGSD movement prediction 409-414
Francesco Campana; Marco Barla; Alessandra Insana

Physical and analytical modelling of sliding-toppling combined slope failures 415-420
Sifan Yuan; Patricia Carracelas Lamela; Ignacio Pérez-Rey; Leandro R. Alejano

Novel approaches for the evaluation of the roughness of discontinuities and failure surfaces in landslides and rock slopes 421-426
Chang Omar; Doug Stead; Davide Donati

Cyclic thermal treatment of a sandstone from the Upper Rhine Graben 427-433
Katharina Meta Neumann; Mandy Duda; Tobias Backers

Elastic Wave Velocity Response to Saturation in Rocks: Laboratory Characterization 435-440
Júlia Figueiredo; Danúbia Damaceno; Bárbara Souza; Inácio Carvalho; Cibele Cláuver

A step forward in the resilience of flexible rockfall protection systems 441-449
Roberto J. Luis-Fonseca; Werner Gerber; Remo Dudler; Helene Lanter; Vjekoslav Budimir

Development and application of experimental systems for the measurement of thermal properties in rocks using representative-size specimens 451-458
Miguel Herbón-Penabad; Yan Li; Andrea Muñoz-Ibáñez; Jordi Delgado-Martín; Ricardo Juncosa-Rivera; Adrià Perez-Carreras; Enric Ibañez-Martinez; Jose María Segura-Serra; Jacobo Canal-Vila; Jose Alvarellos-Iglesias

Mode I Fracture Toughness Tests of Limestone under High-Temperature Isothermal Condition 459-464
Jordi Delgado-Martín; Yan Li; Miguel Herbón-Penabad; Andrea Muñoz-Ibáñez

UAV-Based Geostructural Characterization of Discontinuities in a Rock Wall to Support Rockfall Stability Analyses 465-471
Alessandro Valletta; Salar Khaiiatali; Chimene Larissa Mbougoue Mabapgap

Artificial Fracture Generation and Surface Roughness Quantification in Brittle Rocks 473-478
Tégawendé Nikiema; Nicolas Gonze; Fanny Descamps; Jean-Pierre Tshibangu

A robust sampling strategy for UCS using wireline geophysics 479-484
Amirreza Shakib; Anton Kepic; Duy Thong Kieu; Mark Bunch; Nigel Cook; Maryam Parsajoo

Combined geophysical techniques to predict and map rock mechanics parameters 485-490
Anton Kepic; Duy Thong Kieu; Amirreza Shakib; Maryam Parsajoo

Proof-of-concept pipeline for digital rock mass analysis using an inexpensive 360° camera 491-496
Mateusz Janiszewski; Masoud Torkan; Sandaru Liyanarathna Vidanage; Panu Oikkonen; Adrián Riquelme; Jyri Liukko; Lauri Uotinen

Analysis of the Mechanical Behavior of Callovo-Oxfordian Claystone under Temperature: Contribution of 3D X-Ray Tomography 497-502
Bahaa Abou Chakra; Dragan Grgic; Audrey Bonnelye; Christophe De Lesquen

Laboratory evaluation of long-term behaviour of different natural and cementitious materials 503-510
Goran Baloević; Goran Vlastelica; Nikola Grgić; Mario Filipović; Saltanat Yesselbayeva; Gábor Somodi; Gyula Bögöly; Péter Görög

Assessing the unconfined compressive strength of limestones using indirect testing methods 511-515
Nino Salčin; Miloš Marjanović

Assessing rock mass properties for a hydropower project using deformability tests 517-522
Jigme Tshewang; Mahendra Singh

Thermal Cycling Effects on Granite Pore Structure at Moderate Temperatures 523-528
María Elvira Garrido; Carlos Valentin Cedeño; Víctor Martínez-Ibáñez; Carlos Hidalgo-Signes; Diego José Guerrero-Miguel

Effect of Biot–Willis Coefficient in Coupled Hydro-Mechanical Hydraulic Fracturing Analysis 529-534
Kiyoshi Kishida; Yuki Tatemura; Sho Ogata; Hideaki Yasuhara

Tensile fracturing in granite and gneiss investigated by DIC and thin sections 535-540
Lars Jacobsson; Linus Brander; Johan Sandström; Mathias Flansbjer

Comparison of porosity, permeability and hydraulic conductivity of sandstones from mercury intrusion porosimetry and laboratory tests 541-546
Leona Vavro; Martin Vavro; Daniela Řimnáčová

Characterizing Shear Strength of Rock Discontinuities under the Patton Failure Criterion 547-551
Mauricio Prudencio

Bonded Contact Calibration in DEM using Nano Indentation Test 553-560
Yogeshwar Murugesan; V B Maji

Stability Assessment of Block–Flexural Toppling Using Numerical and Deterministic Approaches 561-566
Hasan Atmojo; Antonina Martireni; Wira Cakrabuana; Khori Sugianti

Study on the Variation of Vibration Characteristics in Rock Tunnels Depending on Ground Conditions and Tunnel Structures Using Ambient Vibration Measurements 567-572
Kosuke Kawata; Natsumi Tamura; Nobuharu Isago

Permeability Estimation from 3D Digital Core Models Derived from X-Ray CT Imaging 573-579
Ha Jung Je; Kwang Yeom Kim

Safe Footing Distance for an Isolated Footing Adjacent to an Excavation Wall in Jointed Rock Masses 581-586
Argha Biswas; Mahendra Singh; Aditya Singh

The effect of confining pressure on the needle penetration index for three different pyroclastic rocks 587-592
Sair Kahraman; Anıl Kaya

Thermal Shock Sensitivity of Limestone Rock Under Rapid CO_2-Induced Cooling 593-598
Fawad Sheikh; Ákos Török

Replica-based experimental framework for characterizing fluid flow in a dislocated fracture 599-604
Sandaru Liyanarathna Vidanage; Masoud Torkan; Mateusz Janiszewski; Mikael Rinne; Lauri Uotinen

Validating Large-Diameter Bored Pile Design in Danian Limestone via Testing 605-610
Anna Wudzka; Adriana Hernandez-Guardado; Francesco Petrella

Development of a Rock-Type s Matrix for Using the Combined Compression and Shear Test System (C-CAST) for Design of Inclined Pillars 611-616
Doreen Kapiri; Fidelis T Suorineni

Plastic swelling and hardening mechanisms of in-situ heated Callovo-Oxfordian claystone 617-622
Junfeng Ren; Philipp Braun; Carlos Pula; Minh-Ngoc Vu; Siavash Ghabezloo

Comparison of Empirical Vs30 Modeling and Field Measurements in Kosova Using GIS-Based Spatial Analysis 623-628
Latif Hasi; Julijana Bojadjieva; Kemal Edip; Vlatko Sheshov; Irena Gjorgjeska; Toni Kitanovski; Dejan Ivanovski; Nazmi Hasi

A Large-Scale Shear Apparatus for Rock Discontinuities and Interfaces 629-634
Coffi Gbewade

Correlation between structural geological and geotechnical properties of the rock mass at the Lukovo Pole dam site 635-643
Ljupce Kulakov

Resolution-induced uncertainty in DEM-predicted brittle damage thresholds in sandstone 645-650
Jinci Chen; Elli-Maria Charalampidou; Ali Ozel; James Woodman; Audrey Ougier-Simonin

Application of Fiber - Reinforced Concrete in Tunnel Construction: Innovations and Challenges 651-657
Bojana Grujic

Physics-informed theory modelling of rock engineering features from TBM operational data 659-665
Hanan Samadi; Andrea Danzi

Status of Rock Slope Characterization Using Remote Sensing Techniques: A Bibliometric Analysis 667-672
Raymundo Ruiz Flores; Nelly Lucero Ramírez Serrato; Adrián J. Riquelme Guill; Fabiola Doracely Yépez Rincón; Rodrigo Gutiérrez Navarro; Javier Mancera Alejandrez

Non-destructive Determination of Building Stone Provenance 673-679
Karel Pavelka; Eva Matoušková; Kateřina Kovářová

Pre-Peak Nonlinearity of Granodiorite in Mohr–Coulomb and Hoek–Brown Models 681-686
A. Z. Ter-Martirosyan; G. O. Anzhelo; L. YU. Ermoshina; Viacheslav Lunin

Application of ARMR for rock slope design 687-692
Harry Saroglou; Neil Bar

Design methods and analysis (incl. EC 7)

A next-generation blast design via seismic intelligence 695-700
Guzin Gulsev Uyar Aksoy; Cemalettin Okay Aksoy; Ozan Savas; Hasan Eray Yaman; Vehbi Ozacar

Integrated Drone-Based Stope Geometry Reconciliation and Stability Assessment at the Dannemora Mine 701-706
Xander Gwynn; Sophie Wilson; Michael Meyer; Carlos Carranza-Torres

Sustainability in Rockfall Protection Works: State-of-the-Art and LCA-Based Approaches 707-712
Laura Turbessi; Isabella Bianco; Giovanni Andrea Blengini; Anna Maria Ferrero; Gessica Umili

A new design method for internal forces estimation in yielding tunnel linings 713-718
Lorenzo Batocchioni; Elena Turrini; Chiara Pandolfi; Salvatore Miliziano

Applicability of the Stability Graph Method for Designing Large Caverns in Rock 719-724
César Torrero; Luis Jordá; Salvador Senent

Numerical Modelling of a Secant Caisson Wall Shoring System in High-Stress Shallow Bedrock 725-730
Hamzeh AhmadiResketi

Design of reinforced sprayed concrete arches in rock tunnelling 731-738
Srđan Spasojević

Optimization of shear strength parameters of deposited clastic sediments via crack shape 739-744
Danijela Božić; Vladimir Čebašek; Veljko Rupar

Advancing Slope Stability Practice in New Zealand: The NZGS Guidelines and their application in Greywacke 745-750
Eleni Gkeli; Nick Peters; Alan Wightman; Doug Mason

Analysis of Underground Roadway Stability under Geomechanical Parameters Uncertainty using RS2 Finite Element Modelling 751-756
Martin Itoolwa Kulula; Piotr Małkowski

Transforming Element-Level Testing into Boundary-Value Experiments through Distributed Fibre Optic Sensing 757-762
Qazim Llabjani; Alessio Ferrari; Paul Marschall; Lyesse Laloui

Application of a nested modelling approach for the analysis of landslide-tunnel systems 763-768
Pietro Festi; Davide Donati; Angelo Ballaera; Gianluca Marcato; Lisa Borgatti

What are the representative values for the mechanical properties of a rock joint? 769-774
Johan Spross; Fredrik Johansson; Ignacio Pérez-Rey

Mobilisation of a fully grouted passive rock bolt along its length 775-780
Elise Le Guidec; Coffi Gbewade; Yannick Fargier; Marion Bost

Estimation of boundary stresses of high-pressure lined rock caverns using superposition of Inglis solutions 781-786
Lauri Uotinen; Mert Ali Aydoğmuş; Mateusz Janiszewski

Lessons from Full-and Partial-Face Excavation in Difficult Rock Conditions 787-792
Gianluca Bella; Matteo Falanesca; Davide Merlini; Filippo Gianelli; Roberto Schuerch; Miriam Piemontese

Assessing Caving Risk Related to Rockmass Bulking 793-799
Trevor G. Carter; Andre van As

Geotechnical Challenges and Adaptive Excavation Strategies: The Konovo Tunnel Case Study 801-806
Vojkan Jovičić; Boštjan Volk; Elvir Muhic

Construction Challenges of the Karavanke Tunnel's Eastern Tube in Water-Bearing Conditions 807-812
Jože Ratej; Boštjan Volk; Vojkan Jovičić

RMR based tunnel support 813-820
Ferenc Deák; Alex Lowson

A Hybrid FLAC3D-MPM Approach for Post-Failure Slope Behavior 821-826
Christian Cancino; Jim Hazzard; Corne Coetzee

Integrated Workflow for Bench-Berm Design Optimisation and Reconciliation 827-832
Felipe Sanz

Verification of underground excavation stability during tunnel construction 833-838
Hrvoje Antičević; Josip Peranić; Željko Arbanas

Application of Auxetic reinforced mortar elements for pressurized tunnels 839-844
Arsham Moayedi Far; Marlene Villeneuve; Giuseppe Loporcaro

Computer-Aided Selection of Pillar Geometry in Deep Room-and-Pillar Panels Using Calibrated Large-Scale 3D FEM 845-850
Krzysztof Fulawka; Piotr Mertuszka; Lech Stolecki; Mateusz Malesza; Radoslaw Wasilewski

Volume 2

Rock dynamics, crustal stress and earth/marsquakes

New Three-Dimensional Rock Stress Measurement Method in Vertically Downhole 853-858
Tatsuya Yokoyama; Kiyotoshi Sakaguchi; Takashi Danjo; Koji Ogawa

Unloading impact failure mechanisms and kinetic energy analysis of coal-rock composites in deep roadways 859-864
Dejian LI; Bo Hu; Tongjie Sun; Mingyuan Zhang

Landslide behavior interpretation based on inclinometer and surface displacements monitoring at cut & cover 6, Railway Corridor VIII (N. Macedonia) 865-870
M. Alper Sengul; Natasha Nedelkovska; Kostas Koukaliaroglou; Bojana Atanasova; Ibrahim Gurel

PROCEEDINGS OF THE REGIONAL SYMPOSIUM OF THE INTERNATIONAL SOCIETY FOR ROCK MECHANICS, EUROCK 2026, SKOPJE, 15-19 SEPTEMBER

Rock mechanics related to environmental and mining engineering

Rock Mechanics Aspects of Debar Crystal Cave – Macedonian Wonder of Nature 873-882
Milorad Jovanovski; Igor Peshevski; Todorka Samardzioska; Milica Jovanoska Mitreska; Sead Abazi; Filip Kasapovski; Todor Delovski; Velimir Petrovski

Friction-Angle Sensitivity of Open-Pit Slope Stability and Field Performance 883-888
Cemalettin Okay Aksoy; Guzin Gulsev Uyar Aksoy; Ozan Savas; Burak Gurel; Bilal Akyuz; Yavuz Aydemir; Ali Burak Aktaş

Design of a Controlled Blasting Operation for the Removal of an Unstable Rock Mass from a Rock Slope 889-894
Marilena Cardu; Carmine Todaro

Fractal Quantification of Crack Networks: Predicting Rock Damage in Thermally Exposed Rock Environments 895-900
Özge Dinç Göğüş; Ömer Ündül; Enes Zengin; Mehmet Korkut; Mehmet Mert Doğu

Risk assessment of seismic events by mine flooding 901-906
Michael Alber

Data analysis for the assessment of roadheader performance in carbonate rocks 907-913
Toluwase Daniel Olaiya; Saffet Yagiz; Zhan-ping Song; Zhilin Cao; De-Sai Guo

Predictive Block Stability Analysis by Integrating UAV-Based Photogrammetry and Back Analysis 915-920
Yalin Umur Dogan

Biomineralization using Enzyme-induced carbonate precipitation under vacuum environment for bio-rocks formation on lunar surface 921-927
Yuru Chen; Gyeongjo Min; Daisuke Fukuda; Satoru Kawasaki

Significance of Mobile Machine Damage on Resin-Grouted Bolts 929-934
Andreas Esterhuizen; Bryan Watson

Risk mitigation with measurements while constructing second tunnel adjacent to existing tunnel 935-940
Kazuo Sakai; Osamu Suzuki; Tetsuya Ikeda; Gentaro Aoki

What does nature know that engineers do not? Lessons from natural rock arches for rock mass classification and design 941-946
Giulia Torsello; Davide Elmo; Doug Stead

From Empirical to Reliability-Based Design: Enhancing ELOS Predictions in Open Stope Mining 947-952
Amoussou Adoko; Adil Bolegenov; Rashid Afshar; Gabit Sansyzbekov

Application of Fuzzy Inference Systems for Open Stope Design in Narrow Orebody Conditions 953-958
Amoussou Adoko; Adil Bolegenov; Masoomeh Mirrashid; Askar Imashev

Impact of elastic and strength anisotropy on seal integrity in energy storage 959-964
Daniel Bücken; Tobias Backers; Ki-Bok Min

Numerical study of an abandoned mine repurposed for CAES systems 965-970
Juliana Lopez Ochoa; Alessandra Insana; Marco Barla; Oscar Jaime Restrepo Baena

Stability Analysis and Support Design for the Deepening of the Main Shaft in the Trepça Mine, Kosovo 971-976
Gzim Ibishi; Melih Genis; Mahmut Yavuz; Arjanit Ademi

The rock mechanical background of the Praid salt mine disaster 977-982
Edina Bartakovics; Ákos Török; Balazs Vasarhelyi

Laboratory-Scale Assessment of 2D and 3D Bonded-Particle Models 983-988
Enes Zengin; Ömer Ündül; Özge Dinç Göğüş; Mehmet Mert Doğu

Rockfall Mechanisms at the Silivri Cliffs, Istanbul (Türkiye): Assessment and Mitigation 989-994
Mehmet Mert Doğu; Ömer Ündül

Influence of Freeze–Thaw Cycles on the Behaviour of Fibre-Reinforced Shotcrete 995-1000
M Naveen; Ankesh Kumar

Deterministic DFN Modelling and Analysis of Large Caverns at 1000 m Depth 1001-1008
Ali Rahnama; David Saiang

Deterministic and Probabilistic Assessment of Rock Slope Stability in Dolomite Quarries in Hungary 1009-1015
Ferenc Ferdinánd Füzesi; Gyula Bögöly

Numerical Assessment of Repository Stability Based on Preliminary Disposal Concept for High-Level Radioactive Waste in Korea 1017-1022
Dae-Sung Cheon; Min-Jun Kim; Jai-Yong Park; Hyung-Ju Yun

Assessment of mine stability during selective coal seam extraction with backfill into the mined-out space 1023-1031
Dmytro Malashkevych; Iryna Kovalevska; Maksym Snihur

Traffic-Light Framework for Early Liquefaction Assessment in Tailings Storage Facilities 1033-1039
Nikolay Y. Milev

Engineering geological parameters of sandstone hosting future highway tunnels, an example from Hungary 1041-1046
Edina Bartakovics; Ákos Török

Energy absorption capacity of cable bolts under impact loading for the stability of underground excavations 1047-1055
Adel Mottahedi; Naj Aziz; Alex Remennikov; Ali Mirzaghorbanali

Investigation of failure mechanisms around a cylindrical cavity in rock mass under true-triaxial loading 1057-1063
Ravindra Kumar Burnwal; Aditya Singh

Effect of Thermal-Shock Damage on Heat Extraction from Hot Dry Rock 1065-1071
Rugesh Kalanji; Ankesh Kumar; Jogender Singh

Progressive Reactivation of the Baliyanala Landslide: Geological Controls and 3D Numerical Assessment 1073-1080
Saurabh Prakash Aher; Sarada Prasad Pradhan; Vikram Vishal

Tailings Heterogeneity and Multi-Scenario Response of an Upstream Tailings Dam 1081-1087
Bo Huang; Qiang Guo; Yewei Tian; Qixian Jiao; Zian Li

Experimental investigation of undercut stratified rocks using base friction technique 1089-1094
Mohammad Hossein Khosravi; Amir Kheirabadi; Alireza Kargar; Gholamreza Saedi

Long-term monitoring of strain changes around a circular tunnel at the Grimsel Test Site 1095-1102
Alice Petrlíková; Lubomír Staš

Implications of climate change on rocks and rock engineering projects

Acid-Induced Physico-Mechanical Damage in Carbonate Rock 1105-1111
Azemeraw Wubalem; Chiara Caselle; Anna Maria Ferrero; Gessica Umili; Linda Pastero; Laurenz Schröer; Veerle Cnudde

Coastal vulnerability assessment in complex geological and changing climate conditions 1113-1118
Sanja Dugonjić Jovančević; Igor Ružić; Čedomir Benac

Rock mass instabilities in periglacial environments induced by climate change 1119-1124
Frederic Pellet; Xiaoqin Lei

Assessment of site suitability for lined rock caverns in repurposed mine drifts for underground hydrogen storage 1125-1132
Lena Bäcklund; Ping Zhang

Rockfall triggering mechanisms in soft rocks - climatic factors and suction changes effects 1133-1138
Natasa Stambuk Cvitanovic; Ana Duhovic

Geotechnical aspects of soft rocks and hard soils

Hydro-mechanical coupled behaviors of weakly cemented sandstones during two-phase fluids displacement: insights from a micro-continuum VOF-BPM method 1141-1148
Shihang Chen; Fengshou Zhang

Defining a graphical basis for developing roughness model of discontinuity 1149-1154
Miodrag Bujisic; Zvonko Tomanovic

Interpreting the Slaking Mechanism of Soft Rock Using a Coupled Hydraulic–Mechanical Model 1155-1160
Risa Komuro; Mamoru Kikumoto; Kiyoshi Kishida

Practical experiences from application of remedial measures for slopes in gypsum rock masses 1161-1166
Pero Cvetkovski; Viktor Popordanoski; Tomislav Stefoski

Back analysis of the original design predictions by using tunnel face mapping, in-situ measurements and numerical modelling - A1 Lugoj-Deva motorway tunnels 1167-1174
Ferenc Deák; Ákos Tóth; Răzvan Umbrărescu; Constantin Matanie; Tomas Marik

Field Observations and Numerical Back-Analysis of an Excavation in Marl Rock Supported by a Strut-Free Buttress Pile Wall 1175-1180
Timur Grubić; Adis Skejić; Mladen Kapor; Anis Balić

Failure Mechanism of Symbiotic Slope of Carbonaceous Phyllite and Graphite Schist 1181-1187
Xiang Guanya; Ning Nan; Chuanke Xu; Junyong Liu; Weiwei Su; Bo Wang

Geosynthetic-Reinforced Soil Systems for different Landslide Stabilization 1189-1194
Ehsan Bordbar; July Jaramillo; Thomas Hasslacher

Laboratory Assessment of Shear Strength Parameters of Carpathian Flysch 1195-1200
Andrzej Gluchowski; Wojciech Sas

Effect of Mn^{2+} and Ni^{2+} on Microbially Induced Carbonate Precipitation for Producing Bio-beachrock 1201-1206
Rahubadda Kankanamge Hiroshima Surangani; Anjula Buddhika Nayomi Dassanayake; Chulantha Lakmal Jayawardena; Niki Evelpidou; Satoru Kawasaki

Rock mechanics for cultural heritage

Geotechnical Assessment of Rock Slopes at the Medieval Fortification of Mileševac 1209-1216
Zoran Berisavljevic; Stefan Jovanović; Milovan Popović

Long-term performance of the rock-hewn structures in the Zelve Valley, Cappadocia, Türkiye 1217-1224
Nazlı Tunar Özcan; Reşat Ulusay; Ömer Aydan

Changes of geomechanical state around reconstructed underground roadways in the historical salt mine 1225-1230
Zbigniew Niedbalski; Piotr Małkowski; Łukasz Bednarek

A Preliminary Assessment of Stone Selection for Istanbul's Cultural Heritage Buildings 1231-1236
Enes Zengin; Ömer Ündül; Özge Dinç Göğüş; Mehmet Mert Doğu; Mehmet Korkut

Thermal effects on the strength of marine psammitic building stones 1237-1242
Marek Brabec; Lukáš Krmíček

Semi-destructive determination of compressive strength of building and decorative stone based on its drillability 1243-1248
Martin Vavro; Leona Vavro; Libor Žídek

Weathering properties of rock blocks and rock mass at natural heritage site Devils Town, Serbia 1249-1255
Miloš Marjanović; Ksenija Micić; Zoran Berisavljevic; Dragana Đurić; Dušan Berisavljević; Biljana Abolmasov

Physical – mechanical properties of the rocks from Kuklici natural heritage site 1257-1263
Miloš Marjanović; Ivica Milevski; Branislav Sretković; Aleksandra Nikolovska Atanasovska; Uroš Đurić; Igor Peshevski

Performance Evaluation of a Ventilated Stone Façade after 48 Years of Service Life 1265-1270
Alenka Mauko Pranjić; Peter Zapušek; Janez Sevšek; Ana Mladenovič; Primož Oprčkal; Sandi Čeferin

Assessment of the long-term performance of the underground tomb Amenophis 3rd Paraoh as an ancient rock engineering structure in Luxor, Egypt 1271-1276
Ömer Aydan; Hisataka Tano; Melih Genis; Mohammed Sakr

Determination of Abrasion Characteristics of Ancient Stone Architectural Elements by Field-based Measurements and Laboratory Testing 1277-1285
Murat Dirican; Ahmet Furkan Çalıkoğlu; Mustafa Erkayaoğlu; Tuna Kalaycı

Heritage stones from RN. Macedonia 1287-1292
Hristina Krsteska

Application of Information Technology for the Preservation of Architectural Monuments 1293-1301
N Shalobyta; T Shalobyta; Ž Cuckič; V Cuckič; Karel Pavelka

Artificial Intelligence and Machine Learning in Rock Mechanics and Rock Engineering

Application of Machine Learning techniques for estimating sinkhole parameters caused by underground mining 1305-1310
Alicja Szmigiel; Krzysztof Tajduś; Janusz Rusek

Intelligent rock mass classification for different TBM projects 1311-1316
Chenfeng Gao; Shaokang Hou; Songyu Yue; Chenyao Wei; Yaoru Liu

Study on time-dependent deformation surrogate model for Reservoir Bank Slope Considering Water Effects 1317-1322
Chenyao Wei; Chenfeng Gao; Songyu Yue; Denghui Yu; Zhiyong Pang; Yaoru Liu

Predicting fluid and mechanical response in 3D discrete fractures using graph neural network 1323-1328
Botong Du; Zhao Feng; Fengshou Zhang; Bicheng Yan

Early Warning of Ground Settlement and Sensitivity Analysis for Super-large Earth Pressure Balance Shield 1329-1334
Jie Wang; Yadong Xue; Wei Luo; Wei Wang; Shouzeng Jiao; Jie Tang

Uncertainty in AI-aided Engineering Geological Modelling 1335-1342
Trevor G. Carter; Giovanna Vessia; Antonio Dematteis; Wayne Barnett; Diego Di Curzio

Application of Machine Learning for Factor of Safety Assessment in a Dolomite Quarry Using Geotechnical and Seismic Inputs 1343-1348
Saltanat Yesselbayeva; Péter Görög

Feature extraction and classification of spatially varying rock mass around a circular tunnel using CNN 1349-1355
Pratishtha Mishra; Debarghya Chakraborty

Towards Predictive Tunnel Safety: Integrating a Wireless Monitoring System with Machine Learning for Real-Time Risk Assessment 1357-1362
Davorin Kolic

Verification of a Methodology for Structural Data Acquisition Using Smartphone-Based LiDAR 1363-1370
Igor Ivanovski; Natasha Nedelkovska; Gose Petrov; Milorad Jovanovski; Gorgi Dimov

A machine learning-based tool for calibrating UDEC-BBM parameters for modelling intact rocks 1371-1376
Fengchang Bu; Michel Jaboyedoff; Ruoshen Lin

Overbreak/underbreak prediction in drill-and-blast tunnelling using machine learning: automated feature selection from MWD data 1377-1382
Alla Sapronova; Thomas Marcher

Modeling of Carbon Dioxide Adsorption Capacity in Unconventional Reservoir using Machine Learning 1383-1388
Ashutosh Tripathy; Ashutosh Kumar; Madhurima Mazumder

Reproducible geotechnical metrics from AI-assisted core logging 1389-1394
Lucas Sun Lie Tan; Mikael Rinne; Mateusz Janiszewski; Ivan Avramov

Evidence-Linked Point Load Test Measurement Uncertainty via Human-Supervised AI 1395-1400
Dragan Dimitrievski; Ljupco Dimitrievski; Teodor Dimitrievski; Marija Jovancevska

Machine Learning-Based Prediction of Bearing Capacity of Shallow Foundations on Rock Masses 1401-1408
Taha Sadeghi Golshan; Amirmohammad Rahimi Lenji; Fateme Asgari Bashkani; Ahmad Fahimifar

Intelligent Landslide Early Warning Systems: Application on the Skopje-Veles Road Section 1409-1414
Zlatko Zafirovski; Stefani Gjorgjevska

Case histories

Satellite InSAR for Vegetated Landslide Analysis: Highway 4, Slovenia 1417-1422
Stefano Presezzi; Mckenzie Douglas; Chiara Giannico

InSAR Analysis for Dam Safety and Landslide Risk Management: the Drin Cascade - Albania 1423-1428
Stefano Presezzi; Mckenzie Douglas

Stability assessment of quarry slopes through laboratory tests and numerical modelling 1429-1434
Laura Turbessi; Chiara Caselle; Gessica Umili; Anna Maria Ferrero

Numerical Analysis of Cervo Cliff Stability Due to Basal Marine Erosion 1435-1440
Maria Lia Napoli; Monica Barbero; Diego Minuto; Alessandro Scarpati

Rapid Landslide Analysis in an Alpine Watershed: A Case Study of the Rio Fenils (NW Italy) 1441-1446
Anna Maria Ferrero; Laura Turbessi; Gessica Umili; Maria Migliazza; Luca Biamino; Sofia Fellini; Roberta Narcisi; Marta Sacco; Federico Vagnon

Risk mitigation in deep excavations affected by Lava-baked Paleosols 1447-1452
Tommaso Ragazzo; Tommaso Tassi; Pietro Zanetti

Geotechnical Risks of Foundation in Karst : A Case Study of Wind Power Plant Podveležje, BiH 1453-1460
Azra Špago; Amir Ačkar

Comparative assessment for prediction of settlements for piles in weak rocks: Case study 1461-1466
Sead Abazi; Spasen Gjorgjevski; Josif Josifovski; Bojan Susinov

Challenges in the construction tunnel in BIM rocks: Case Study for Farish tunnels 1467-1472
Hristijan Dimitrieski; Vesna Dimitrieska

Alarming and monitoring system on the Simplon Pass 1473-1478
Jonas Von Wartburg; Ólafur Stitelmann; Janine Wetter; Maxence Carrel

Rockfall alarm system in Vissoie, Val d'Anniviers 1479-1484
Jonas Von Wartburg; Janine Wetter; Ólafur Stitelmann; Maxence Carrel

Monitoring of the Kleines Nesthorn and the Birch Glacier during the rock avalanche in Blatten 1485-1490
Janine Wetter; Maxence Carrel; Ólafur Stitelmann; Jonas Von Wartburg

Ten Years of Digital Rockfall-Protection Net Operation at Ovella: Cost-Efficient Construction and Maintenance Through Continuous Monitoring and Alarming 1491-1495
Janine Wetter; Maxence Carrel; Stitelmann Ólafur; Jonas Von Wartburg

Engineering-Geological characteristics of the terrain along the regional road in N.Macedonia, section of v.Novo Konsko - Dam Konsko 1497-1502
Aleksandar Murdjovski; Rozeta Jankova; Saso Georgievski; Teodor Dimitrievski

Serviceability Assessment of a Mining Waste Dump for Photovoltaic Power Plant Installation 1503-1512
Bojan Susinov; Jovan Papić; Josif Josifovski; Sead Abazi

Coefficient of Restitution for Gypsum Rockfall Modeling: Insights from Field Tests and Numerical Simulations 1513-1518
Veselina Jovanoska; Despina Vojnoska; Mihaela Daniloska; Angela Naumcheska; Ace Trajanovski; Igor Pesevski

3D Rockfall Analyses of Marl Slopes in Brovinje, Croatia 1519-1524
Martina Vivoda Prodan; Sanja Dugonjić Jovančević; Josip Peranić; Igor Ružić

Research on Deformation Characteristics and Instability Mechanism of Retrogressive Landslide Under the Coupling of Engineering Disturbance and Rainfall 1525-1531
Yanhong Zhu; Jiansong Shi; Chuanke Xu; Shengyun Huang; Yang Yu

Slope stability of fossil landslide in Flysch sediments 1533-1538
Elena Angelova; Borislav Gjoshevski; Laste Ivanovski; Orce Petkovski

Consulting activities for geotechnical investigations for Express road A2 Rankovce – Kriva Palanka, Republic of N. Macedonia 1539-1544
Saso Georgievski; Dance Todorova; Ljupce Zrlev; Teodor Dimitrievski

Rock Mechanics education and training

Evert Hoek's legacy in Rock Mechanics and Rock Engineering 1547-1561
Ivan Vrkljan

MaStER_G – tracing environmental resilience to geohazards 1563-1568
Igor Petrovic; Davor Stanko; Dragoslav Rakic; Irena Basaric Ikodinovic; Jelka Lukic; Kemal Edip; Julijana Bojadjieva; Vlatko Sheshov; Jovan Br. Papic; Josif Josifovski; Igor Peshevski; Sandro Lemos Machado; Mehran Karimpour Fard

How To Be A Functional On-Site Geotechnical Engineer 1569-1574
Andy Beveridge; Benjamin Morin; Anthony de Veth

Rock Mechanics Education in European Universities: A Comparative Review of Academic Programs and Trends 1575-1579
Matej Dimitrievski

Rock Engineering and Dam Safety: Building Stronger Partnership 1581-1586
Arjan Jovani

Preface

On behalf of the Macedonian Association for Geotechnics (MAG), National Group in ISRM, it is our pleasure to welcome the international ISRM community to Skopje for EUROCK2026, the ISRM Regional Symposium on **Risk Management in Rock Engineering**.

This symposium continues the tradition of EUROCK events in providing a global forum for academics, researchers, consultants, and practitioners to exchange knowledge and present innovations. The central theme emphasizes the integration of safety, sustainability, and innovation in rock engineering, addressing challenges posed by complex ground conditions, urban development near critical infrastructure, and environmental concerns.

The program includes sessions on risk assessment, site characterization, rock dynamics, climate change impacts, cultural heritage preservation, and the application of Artificial Intelligence in rock engineering.

Case histories, education, and training will further enrich the discussions. Complementing the technical program are short courses, workshops, exhibitions, technical tours, and student competitions, alongside cultural and social events showcasing Skopje and our country.

We are proud to present more than 220 peer-reviewed papers in these proceedings, together with seven invited lectures delivered by distinguished experts. This rich body of work reflects the breadth and depth of current advances in rock mechanics and rock engineering.

EUROCK2026 is envisioned not only as a scientific symposium but also as a celebration of collaboration and cultural exchange.

We extend our gratitude to the ISRM family and the wider geotechnical community for their contributions to advancing rock mechanics and strengthening the bonds of our profession.

Prof. Milorad Jovanovski

Chair of EUROCK2026

Prof. Igor Peshevski

Co-Chair of EUROCK2026

President of MAG

Welcome Message from the ISRM President

Dear Colleagues,

On behalf of the International Society for Rock Mechanics and Rock Engineering, it is my great pleasure to welcome you to EUROCK 2026 in Skopje.

Since the first EUROCK Symposium was held in Chester, United Kingdom, in 1992 under the chairmanship of Professor John A. Hudson, the EUROCK series has, for more than three decades, played a distinguished role as the European Regional Symposium of ISRM and as a major forum for the international rock mechanics community. It has brought together researchers, engineers, practitioners, and young professionals from Europe and around the world, providing an important opportunity to share knowledge and experience and to build lasting professional relationships. Through these activities, EUROCK has contributed greatly to advances in rock mechanics and rock engineering and to the growth of the ISRM community.

I would like to express my appreciation to the ISRM National Groups and Organizing Committees that have sustained this valuable tradition over the years. The continuity and success of EUROCK also demonstrate the central role played by our National Groups in advancing the work of ISRM worldwide.

The theme of EUROCK 2026, “Risk Management in Rock Engineering”, is timely and important and will remain so in the years ahead. Uncertainty and risk are inherent in rock engineering, and their responsible management is essential to the safety, resilience, and sustainability of projects in mining, civil infrastructure, and energy development.

The scale and diversity of the EUROCK 2026 are particularly encouraging. More than 220 peer-reviewed papers are included in these Proceedings, demonstrating the strong international interest in EUROCK 2026 and the breadth and depth of current research and practice in our field. The wide-ranging program, including seven invited lectures, will make the symposium even more rewarding and engaging.

I hope this event will inspire new ideas, strengthen cooperation, and encourage young researchers, engineers, and first-time ISRM participants to become more actively involved in the international rock mechanics community.

I extend my sincere appreciation to the Macedonian Association for Geotechnics, Professors Milorad Jovanovski and Igor Peshevski, and all members of the Organizing Committee. I also thank the invited lecturers, speakers, authors, reviewers, sponsors, and everyone who has contributed to making EUROCK 2026 possible.

I wish all participants productive discussions, valuable professional exchanges, and an enjoyable stay in Skopje.

Seokwon Jeon

President

International Society for Rock Mechanics and Rock Engineering

Organization

MAG was established in 1998 and already in 2002 has organized its First national symposium, with a commitment to reunion on every four years: these were realized in 2006, 2010, 2014 and in 2022. Number of participants has been successively increasing, so most of them had international editorial boards. In the meantime, MAG organized a seminar for Eurocodes 7 and 8 in 2008 and the XVI Danube-European Conference with the International Society for Soil Mechanics and Geotechnical Engineering (ISSMGE), as well as a seminar on risks in tunnel construction, in collaboration with the International Tunneling and Underground Space Association (ITA) in 2018. Along with lecturers from fore mentioned organizations, MAG also hosted the boards of ISSMGE and ITA. In addition, with the support of ISRM, MAG organized the Fifth Symposium in 2022 in a form of an ISRM Specialized Conference. This event was a Second Conference of the regional geotechnical societies, and as such was also promoted by the ISSMGE. These conditions enabled to have there the presidents of both the ISRM and of ISSMGE. In June 2024, MAG hosted the 28th European Young Geotechnical Engineers Conference of the ISSMGE. Due to such dedication and other multilayered commitments, MAG was awarded as Best performing National group in ISRM for 2021-2023, as well as for Most active professional society in frame of the Macedonian Engineering Institution for 2024. Future significant scientific events in organization of MAG include the ReSyLAB 2027 - 7th Regional Symposium on Landslides in the Adriatic-Balkan Region and the co-organization of the 9th International Conference on Earthquake Geotechnical Engineering to be held in Šibenik on the Croatian Adriatic in May 2029 together with main organizer the Croatian Geotechnical Society, under the auspices of the ISSMGE's TC203 Earthquake.

Committees

ISRM International Advisory Committee

Seokwon Jeon	R. Korea	ISRM President
Jannie Maritz	South Africa	Vice President for Africa
Ki-Bok Min	R. Korea	Vice President for Asia
Qianbing Zhang	Australia	Vice President for Australasia
Muriel Gasc-Barbier	France	Vice President for Europe
Esteban Hormazábal	Chile	Vice President for Latin America
Martin Grenon	Canada	Vice President for North America
Milorad Jovanovski	R.N. Macedonia	Vice President at Large
Kiyoshi Kishida	Japan	Vice President at Large
Fengshou Zhang	China	Vice President at Large
Luís Lamas	Portugal	Secretary General

International Honorary Advisory Committee

Reşat Ulusay	Türkiye
Biljana Abolmasov	Serbia
Nick Barton	Norway
Mancao He	China
Ivan Vrkljan	Croatia
Sergio A. B. da Fontoura	Brasil
Vojkan Jovicic	Slovenia
Ahmet Sağlamer	Türkiye
Ömer Aydan	Japan
Sevda Dehkhoda	Australia
Laura Pyrak-Nolte	USA
Norikazu Shimizu	Japan
Charlie C. Li	Norway
José Félix Pavón	Paraguay
Philippe Vascou	France
Dietmar Adam	Austria
Mahendra Singh	India
Radomir Folić	Serbia
Naum Gapkovski	R.N. Macedonia
Kosta Talaganov*	R.N. Macedonia
Vlatko Seshov	R.N. Macedonia

Ljupco Dimitrievski	R.N. Macedonia
Spasen Gjorgevski	R.N. Macedonia
Ljubomir Tancev	R.N. Macedonia
Tihomir Nikolovski	R.N. Macedonia

International Scientific Committee

Amoussou Coffi Adoko	Kazakhstan
Rasit Altindag	Türkiye
Karrar Ali AlSaadi	Iraq
Neil Bar	Hungary
Monica Barbero	Italy
Altin Bidaj	Albania
Volodymyr Bondarenko	Ukraine
Vladimir Cebašek	Serbia
Nataša Štambuk Cvitanović	Croatia
Klaus Rieker	Germany
Kremena Dedelyanova	Bulgaria
Fanny Descamps	Belgium
Mustafa Erkayaoglu	Türkiye
Muriel Gasc-Barbier	France
Siavash Ghabezloo	France
Phill de Graph	Australia
Bojana Grujić	Bosnia and Herzegovina
Henri Robert G.K. Hack	Nederlands
Erika Prina Howald	Switzerland
Essaieb Hamdi	Tunisia
Lars Jacobsson	Sweden

Petr Konicek	Czech Republic
Risto Kiuru	Finland
Heinz Konietzky	Germany
Irina Kovalevska	Ukraine
Mahdi Karkush	Iraq
Janko Logar	Slovenia
Ivan Livinsky	Kazakhstan
Natalia Maca	Poland
Dmitro Malashkievich	Ukraine
Miloš Marjanović	Serbia
Alison McQuillan	Australia
Maria Rita Migliazza	Italy
Nikolay Milev	Bulgaria
Maria Lia Napoli	Italy
Leandro Alejano Monge	Spain
José Delgado Muralha	Portugal
Mauro Muñiz-Menéndez	Spain
Maddalena Marchelli	Italy
Dominique Ngan-Tillard	Nederlands
Vladimir Noskov	Russia
Henki Oedegaard	Norway

Ervin Paçi	Albania
Paulo Miguel Lopes Pinto	Portugal
Salma Souissi	Tunisia
Harry Saroglou	Greece
Dominique Ngan-Tillard	Nederlands
Jorge Terron	Norway
Jean-Pierre Katshidikaya Tshibangu	Belgium
Andrey Totsev	Bulgaria
Akos Torok	Hungary
Trushko Vladimir Leonidovich	Russia
Gessica Umili	Italy
Lauri Uotinen	Finland
Patrick Vidstrand	Sweden
Goran Vlastelica	Croatia
Saffet Yagiz	Kazakhstan
Sabid Zekan	Bosnia and Herzegovina
Bojan Žlender	Slovenia
Josif Josifovski	R.N. Macedonia
Jovan Papic	R.N. Macedonia
Sead Abazi	R.N. Macedonia
Stevco Mitovski	R.N. Macedonia

Bojan Susinov	R.N. Macedonia
Julijana Bojadzieva	R.N. Macedonia
Kemal Edip	R.N. Macedonia
Violeta Gesovska	R.N. Macedonia
Ljupco Petkovski	R.N. Macedonia
Darko Nakov	R.N. Macedonia
Goran Mijoski	R.N. Macedonia
Gjorgi Gjorgiev	R.N. Macedonia
Elena Angelova	R.N. Macedonia
Nataša Nedelkovska	R.N. Macedonia
Toni Kitanovski	R.N. Macedonia
Bojan Janevski	R.N. Macedonia
Todorka Samardzioska	R.N. Macedonia

Organizing Committee

Igor Pehevski
Milorad Jovanovski
Dragan Dimitrievski
Jovan Br. Papić
Nataša Nedelkovska
Bojan Susinov
Sead Abazi
Elena Angelova
Tamara Jovanovska
Josif Josifovski
Zlatko Ilijovski
Ljupco Dimitrievski
Kemal Edip
Julijana Bojadzieva
Bojan Janevski
Stevco Mitovski
Frosina Panovska
Teodor Dimitrievski
Dejan Ivanovski
Toni Kitanovski
Velimir Petrovski
Todor Delovski
Done Nikolovski
Husamedin Dželadin
Biljana Krsteska-Papić
Despina Vojnoska
Veselina Jovanoska
Mihaela Daniloska
Angela Naumcheska
Stefan Gacov
David Chaushevski
Stefan Tulovic
Miladin Krstanoski
Viktorija Velinska
Ivana Koceva
Tamara Dojoshevska
Leontina Ilievska
Andrijan Treneski
Ilijan Blazevski
Ana Petrova
Bojana Koleva
Dimitar Goshev
Agon Shinani
Lazar Bozhinovski
Borislav Gjoshevski
Vane Rujkov
Nikola Kocevski
Filip Stojanovski
Biljana Naceva

Keynote lectures

Time-based hydro-mechanical modelling of tunnelling in weathered granite

L. Zdravkovic & D. M. Potts
Imperial College London, London, UK
l.zdravkovic@imperial.ac.uk
0000-0003-3092-0628

J. H. Shin
Konkuk University, Seoul, South Korea

Abstract

This paper considers the construction practice of NATM tunnelling in a mixed face and water bearing ground profiles comprising different levels of rock degradation. The study is based on the geological conditions of the Seoul subway (South Korea), where the geology around the city comprises a large granite batholith. Deeply weathered granite in this area is frequently encountered in many civil engineering works, including subway construction.

One frequent challenge for tunnel construction is the geological profile which comprises decomposed granite above the tunnel spring-line and weathered granite below. The former is practically a soil while the latter is a transitional zone to the underlying rock, containing parts of residual soils and of partially weathered and/or fresh rock. Another challenge is the design of tunnel linings with the presence of pore water pressures and possible water infiltration into tunnels.

This paper develops a numerical model to investigate and quantify the pore-water pressure and its potential effects on the tunnel lining. It is shown that the development of pore-water pressure on the lining is dependent on the lining permeability and the deterioration of the drainage system, particularly for a tunnel with both a primary and a secondary lining. The magnitude of pore-water pressure on a NATM tunnel constructed in this ground conditions and the effect of tunnel shape are investigated. Design curves for estimating pore-water pressure loads on a secondary lining are proposed.

Keywords

Tunnelling, Weathered rock, Numerical modelling, Lining permeability.

1 Introduction

1.1 Hydraulic conditions

Tunnelling beneath the water table induces pore water pressure changes and alters the hydraulic regime in the ground. This can cause seepage into the tunnel and often produces a long-term interaction between the tunnel and the surrounding soil. According to Peck (1969), one of the requirements for a satisfactory tunnel design is to be capable of withstanding, during its lifetime, all the influences that it may experience. The most critical long-term influences caused by groundwater are leakage and external pore-water pressures on the lining. Water leakage could be particularly problematic for the efficient operation of the tunnel system, and it can lead to the deterioration of various components, especially in rail and highway tunnels. The pathways for water infiltration into the tunnel are usually shrinkage cracks in the concrete lining, construction joints, and cracks due to concrete deterioration or structural failure. The latter are the most dangerous and can cause overall tunnel failure (O'Rourke 1984; Parks et al. 1986).

The New Austrian Tunnelling Method (NATM) was preferred in the Seoul Subway construction, as it allows the excavation profile to cope effectively with the variable ground conditions. A wide range of tunnel shapes was used, from circular/elliptical to horse-shoe shapes. The cases of NATM tunnel failures, associated with pore-water pressures acting on the lining, were reported by Ferreira (1995) and Lee et al. (1996). The tunnels had both a primary and a secondary lining, and structural damage was observed only in the secondary linings. Shin et al. (2002) studied numerically the long-term variation of ground loading on 4 m diameter tunnels constructed 20 m beneath the ground surface. They indicated that the ground loading depended primarily on the nature of the soil and the hydraulic boundary conditions, such as lining and soil permeability. They also showed that the distribution of pore pressure corresponding to long-term seepage depended on the relative permeability of the lining and the surrounding soil/rock. Availability of field measurements of long-term ground and pore pressures is often limited to be able to support validations of numerical models. However, a significant case record was presented by Inokuma and Ishimura (1995), involving measured total soil and water pressures around a concrete segmental lining of a 5 m diameter and a 32 m dep tunnel, which was constructed with a slurry shield in loose clayey silty sands. The data in Fig. 1 show that most of the ground loading was from the pore-water pressure, the effective stress component from the soil itself being small.

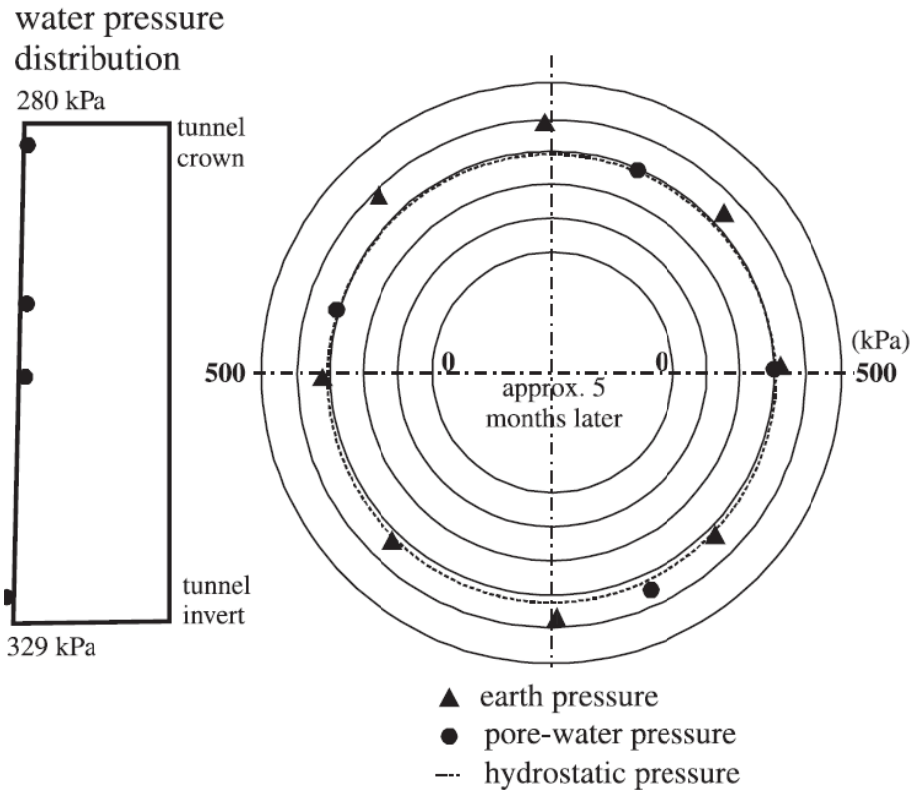
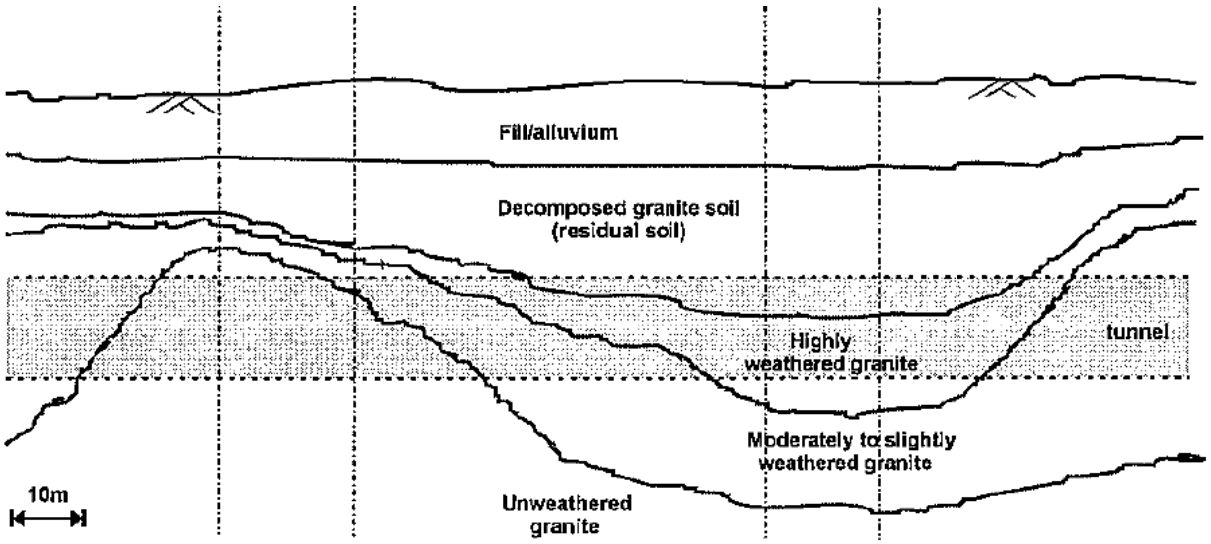


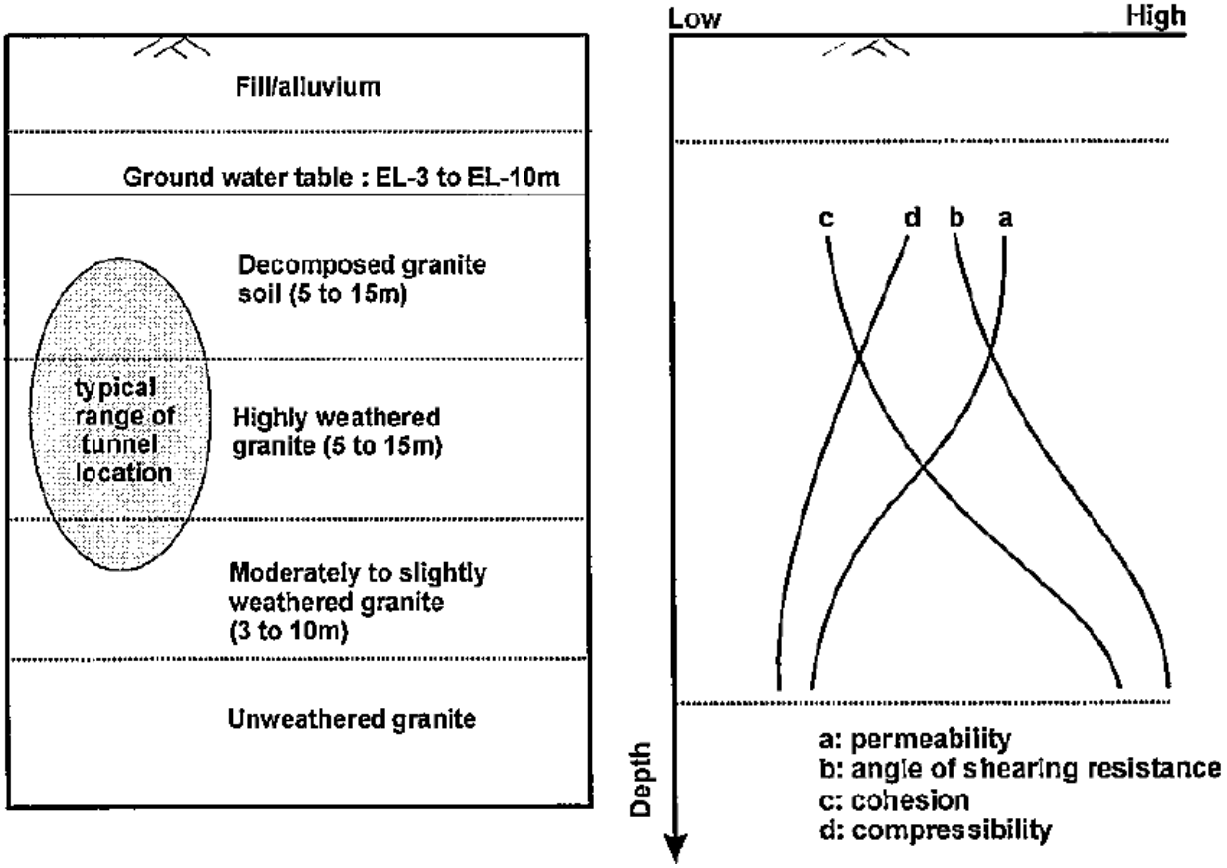
Fig.1 Field measurements of pore-water pressure on a tunnel in silty sand (modified from Inokuma and Ishihara 1995).

1.2 Ground profile

Fig. 2a shows a typical geological profile in the Seoul area, with a subway alignment from 15 to 30 m below the ground surface, therefore engaging different levels of granite weathering at the tunnel face. The weathering reduces with depth, without the development of core stones and the weathering profile is shown in Fig. 2b. The decomposed granite is formed from the in-situ decomposition of the parent rock and has the characteristics of soil. The weathered rock beneath it has the components of residual soils and partly weathered or fresh rock. The engineering properties of in-situ materials vary continuously, as depicted schematically in Fig. 2c.



(a) Soil profile and tunnel alignement



(b) Typical thicknesses of weathering profile, (c) Typical variation of soil properties

Fig. 2 Typical geological profile and tunnel location in the Seoul Subway construction.

2 Numerical model

2.1 Modelling of NATM construction

The key elements involved in the construction of the Seoul Subway are: tunnelling below the groundwater table; mixed-face ground conditions; a noncircular tunnel cross section; tunnels with drainage systems; and tunnels with both a primary and a secondary lining. Numerical modelling of this type of tunnel requires consideration of several geotechnical aspects such as three-dimensional behaviour at the tunnel heading and coupled behaviour between the soil and the groundwater.

The geological profile adopted in the numerical model is shown in Fig. 3. The NATM, using sprayed concrete lining (SCL) or shotcrete, was the main tunnelling method, due its flexibility to accommodate different tunnel shapes in mixed-face ground conditions. A circular and, a more typical, horseshoe shaped tunnel openings in Seoul Subway are investigated through the analyses presented in this paper.

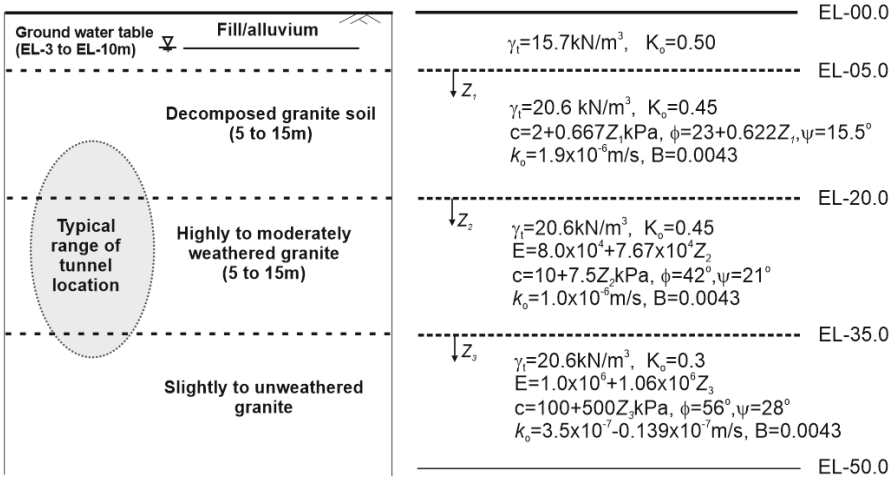


Fig. 3 Ground profile and material properties. γ_t – saturated bulk unit weight; c – cohesion; ϕ – angle of shearing resistance; ψ – angle of dilation.

A large part of the Seoul Subway incorporates design concept of primary and secondary lining. The primary lining includes not only shotcrete but also a wire mesh and steel support and is considered as the primary support system that resists and redistributes external loads. Secondary lining is constructed much later, hence its load-bearing capacity is considered negligible.

The typical excavation advance rate of the tunnel heading during Seoul Subway construction was approximately 2 m/day. Considering the 3D effects of real tunnel construction and that the time-related response of decomposed granite is reasonably fast (a few months) due to its higher permeability, as summarised in Fig. 3 (1.0E-6 to 1E-7 m/s), the implication is that the effect of ground water movement occurs concurrently with tunnel excavation. Based on Shin and Potts (2002), who developed a procedure for 2D modelling of the actual 3D tunnelling process, the 2D hydro-mechanically coupled analyses in the current study adopted the excavation time $T = 15$ days as equivalent of a 2.0 m/day tunnel advance rate. This results into the time for lining installation in the analysis of $t^* = 0.459T$.

Excavation in the analyses is simulated by removing the finite elements representing the soil within the tunnel. The software evaluates the stresses that these elements apply to thetunnel excavation boundary, converts them to equivalent nodal forces, and then applies these in the reverse direction over several increments (i.e., time steps) of the analysis, together with the actual removal of these elements from the mesh (see Potts and Zdravkovic 1999).

2.2 Modelling of lining permeability and drainage system

While it is a common assumption that most tunnels act as drains at some point in time (Ward and Pender 1981), the mechanics of water flow through a concrete lining is a complex phenomenon. Such a flow, strictly, involves seepage, diffusion and sorption. In this paper the main concern is seepage, hence only this aspect is considered. The flow around a tunnel depends on its lining permeability and any drainage system that defines the hydraulic boundary conditions. The approach for realistic modelling of flow through lining developed in this paper, combines beam elements with appropriate

structural stiffness to represent the structural primary lining, and thin solid elements around the lining that have pore pressure degree of freedom and are therefore permeable. The detail of this discretisation in a finite element (FE) mesh is shown in Fig. 4. The permeability of these elements at the start of analysis is equal to the permeability of the surrounding soil. After tunnel excavation and installation of the beam-element lining, this single layer of solid elements is assigned the permeability of the lining. The secondary lining is not considered in the analyses reported here, as its structural capacity is neglected.

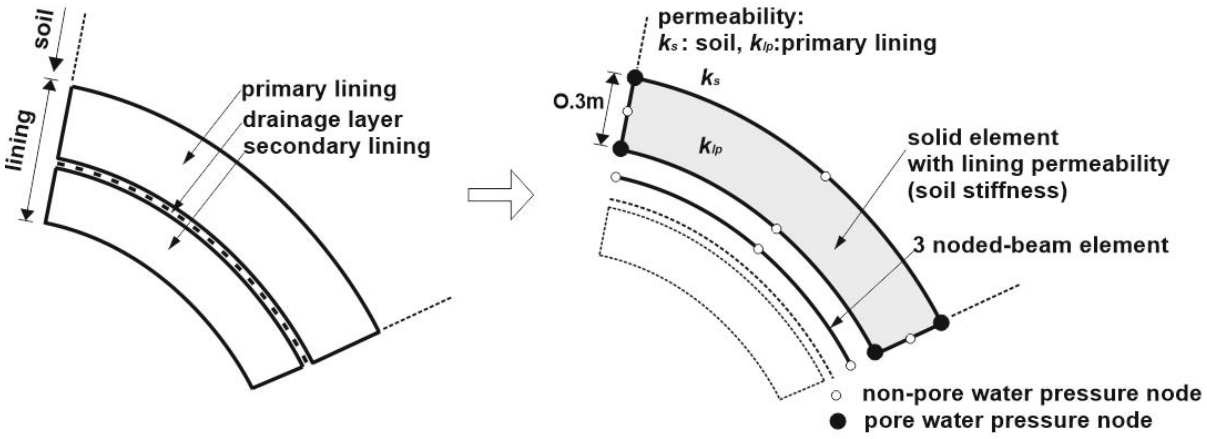


Fig. 4 Modelling of the NATM lining with a drainage system.

3 Finite element analysis

Hydro-mechanically coupled 2D finite elements analyses in the paper were performed with the Imperial College Finite Element Program (ICFEP, Potts and Zdravkovic 1999, 2001), adopting a modified Newton-Raphson scheme with an error-controlled sub-stepping stress-point algorithm as a nonlinear solver.

3.1 Ground profile and constitutive modelling

Fig. 5 shows close up details of FE meshes around analysed tunnel geometries. The soil domain was discretised with 8-noded isoparametric solid continuum elements and the tunnel lining with 3-noded beam elements, as discussed earlier. A 4m diameter circular tunnel represents a typical analysis to be compared against the same tunnel geometry in different ground conditions. The 8.2 m horse-shoe shaped tunnel is typical in Seoul Subway, while the equivalent 9.2m diameter circular tunnel is analysed for comparison of the two geometries.

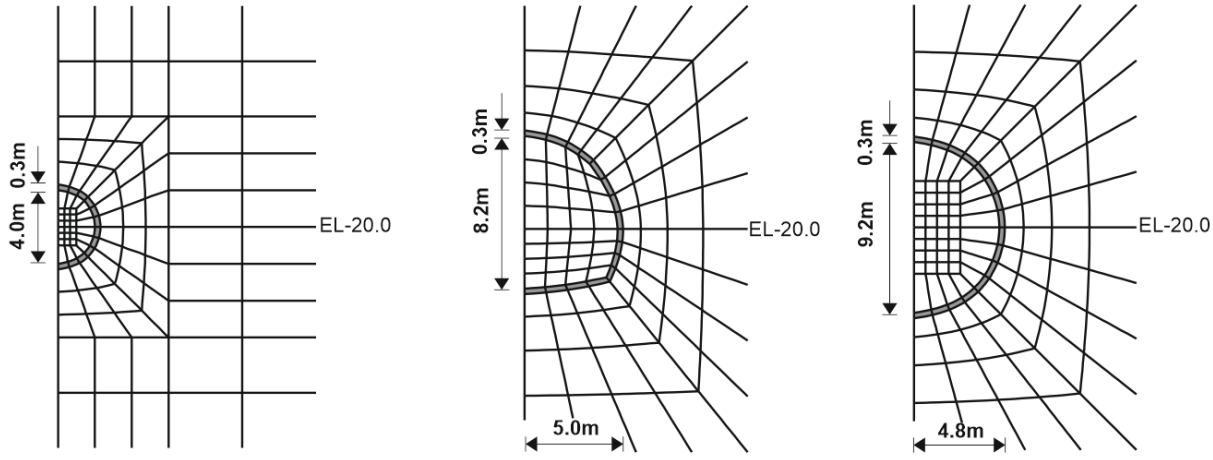


Fig. 5 Finite element models and dimension of analysed tunnels.

The spring-line elevation of all tunnel geometries is at 20.0 m depth. The soil layer above spring-line to the ground surface is the decomposed granite, while the layer below, to the bottom of the mesh, represents the moderately weathered granite. The ground water level was 2.5 m below the ground surface, as depicted in Fig. 3. The soil mechanical behaviour was simulated with a nonlinear Mohr-

Coulomb model, comprising the Mohr-Coulomb yield surface and a nonlinear small strain overlay model. The adopted soil properties from site investigation are summarised in Fig. 3. The NATM sprayed concrete lining was modelled as linear elastic.

3.2 Modelling of permeability

The permeability of the ground was modelled with the nonlinear permeability model proposed by Vaughan (1989), where permeability, k, varies with mean effective stress, $k = k_0 \exp(b \cdot p')$, $k_0$being the permeability at zero mean effective stress and b is a fitting parameter. The permeability model parameters are also summarised in Fig. 3. The permeability of sprayed concrete depends on the water-cement ratio (Neville 1995) and for the usual 0.3-0.55 range the permeability typically varies from 1.0×10^{-10} to 1.0×10^{-12} m/s. Similar to soils, this intact permeability is not usually relevant, as the bulk permeability is influenced by cracks and construction gaps, as more readily available paths for water ingress. Consequently, the evaluation of lining permeability is challenging. In practice, the rate of flow into a tunnel and pore-water pressure acting on the lining will be dependent on the relative permeability of the lining to the adjacent soil. Therefore, the relative permeability of the lining to the soil, k_l/k_s, where k_l is the coefficient of permeability of the lining and k_s is the coefficient of permeability of the soil at the level of the tunnel spring line (based on the initial mean effective stress p' before tunnel construction), could be more important than the absolute value of permeability itself.

3.3 Initial and boundary conditions

In terms of initial stresses, the pore water pressure was assumed hydrostatic with depth from the phreatic surface at 2.5 m below ground level, and zero above the phreatic surface. The initial vertical and horizontal effective stresses were determined from this pore pressure profile and the bulk unit weight and K_0 values given for each layer in Fig. 3.

The mechanical boundary conditions prescribed zero horizontal displacements on the vertical axis of symmetry and on the right hand side vertical boundary of the finite element mesh, while both the vertical and horizontal displacements were set to zero on the bottom boundary of the mesh. The appropriate hydraulic boundary conditions at the tunnel boundary were selected to reflect the desired flow conditions. A fully permeable boundary was modelled by prescribing the pore-water pressure on the excavation boundary as zero, while an impermeable boundary was modelled by prescribing the flow rate as zero. A partially permeable lining was represented by prescribing an appropriate lining permeability and the pore-water pressure on the excavation boundary as zero. The vertical axis of symmetry and the bottom boundary of the mesh were prescribed as no flow boundaries (impermeable), while on the right hand side vertical boundary the pore pressures were assumed not to change from their initial values.

3.4 Analysed cases

A 4m diameter tunnel (Fig. 5) was analysed with the objective of quantifying the pore water pressure contribution to ground loading against typical tunnel construction in London Clay, as a much less permeable soil. A horseshoe shaped tunnel of 8.2 m height and 10.6 m width was analysed as a typical shape on the Seoul Subway. To investigate the effect of tunnel shape, an equivalent 9.2 m diameter circular tunnel was also analysed, having the same cross-sectional area of 66.5 m^2.

4 Results and discussion

Results from the analyses are presented in terms of long-termpore-water pressures (i.e. after full equalisation). These are considered at the outer boundary of the tunnel lining, 0.3 m away from the excavated surface of the tunnel. The potential effects are considered in terms of ground loading and lining performance (i.e. hoop thrust and bending moment). Ground loadings are total normal stresses acting on the lining and consist of effective stress and pore water pressure components. Therefore, the relative contribution of pore water pressure to the ground loading is also considered. Figure 6 defines the ground loading and the pore water pressure and also defines the latter as percentages of the ground loading and of the overburden stress at tunnel axis level.

4.1 Typical analysis

Fig. 7 shows the development of pore water pressure on a tunnel lining in decomposed granite soil, for the 4 m diameter tunnel. Two extreme cases for the hydraulic boundary condition at the tunnel excavation boundary were considered: fully permeable and impermeable. Decomposed granite soil is

sufficiently permeable to give negligible unbalanced (or excess) pore-water pressure at the end of tunnel excavation. The long-term condition is reached reasonably fast. Fig.7 presents the long-term pore-water pressure distribution along a vertical line above the tunnel crown and along a horizontal line at the level of the tunnel spring line. As expected for the fully permeable lining, pore water pressure on the lining is zero, while for the impermeable lining the initial hydrostatic pore water pressure is maintained.

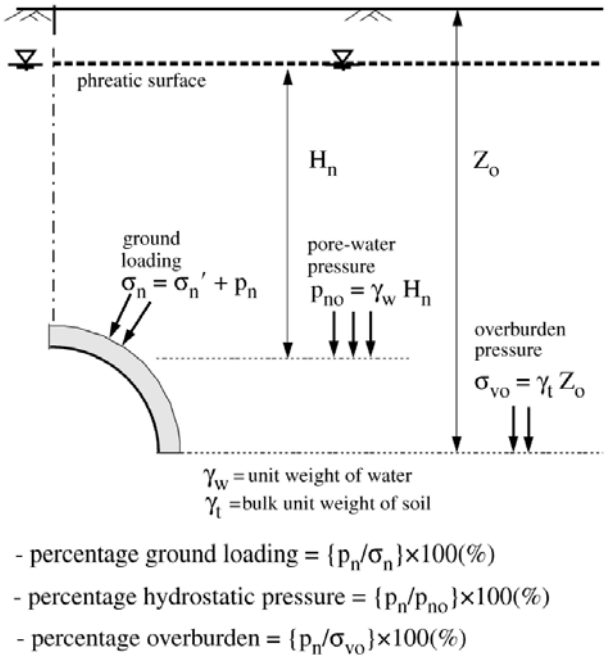


Fig. 6 Quantities used to define pressures on tunnel lining.

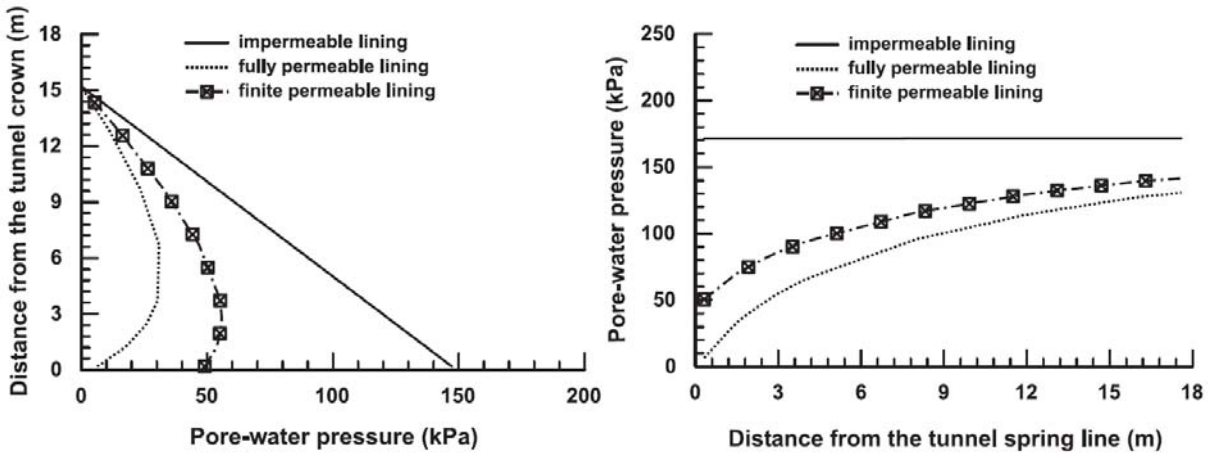


Fig. 7 Long-term pore water pressure: left – above the tunnel crow; right – horizontally along the spring line.

The above results are interpreted in terms of pressures acting on the tunnel lining and are depicted in polar diagrams in Fig. 8. The distribution of the pore water pressure (left) on a fully permeable lining shows zero lining load, while that on an impermeable lining is close to the ground load (as evaluated according to Fig. 6). Calculated as a percentage of the ground loading (Fig. 8 right), the pore pressure on an impermeable lining contributes at 90%.

The effect of finite lining permeability in this analysis is examined with a magnitude of lining permeability $k_l = 1.0 \times 10^{-7}$ m/s, assuming that it is 10 times lower than the permeability of the soil, i.e $k_l/k_s = 0.1$. The results in Fig. 7 and Fig. 8 plot in between the two extreme cases of lining permeability. A pore water pressure of approximately 50 kPa has developed on the lining around the tunnel, comprising around 30% of ground loading. Clearly, this distribution is dependent on the magnitude of the actual lining permeability, k_l.

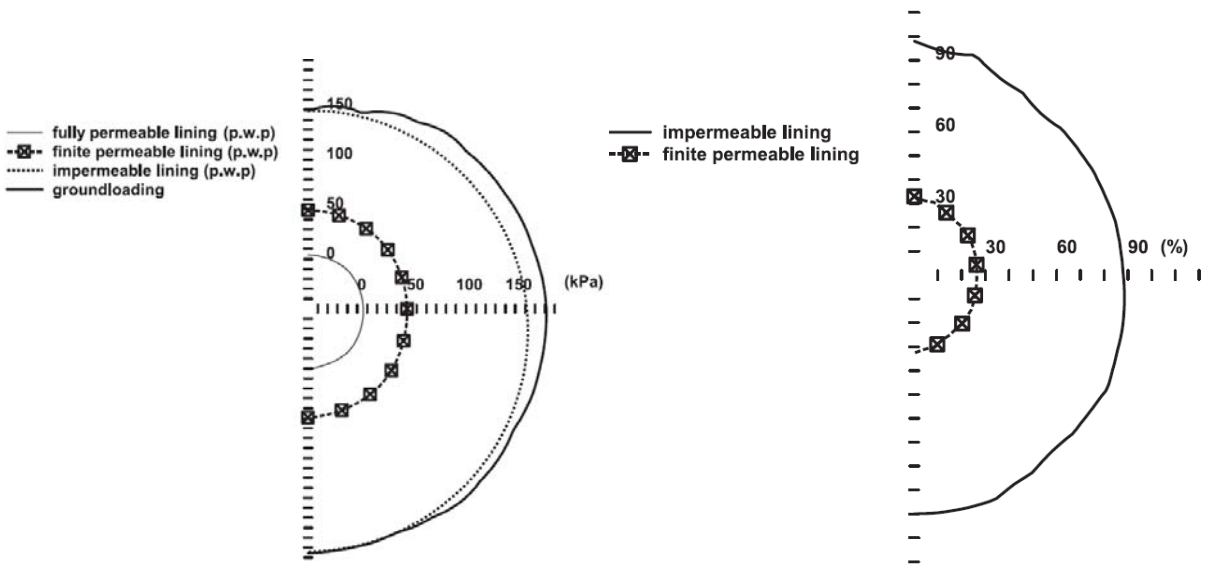


Fig. 8 Long-term loads on lining: left – pore water pressure; right – pore water pressure as percentage of ground loading.

4.2 Comparison with a low permeability soil

In this section, the above results obtained for permeable decomposed granite ground conditions are compared against those obtained from the analysis adopting London Clay ground conditions. This clay has a much lower permeability but higher stiffness due to its overconsolidated state. The analysis of Shin et al. (2002) adopted the same 4.0 m diameter and 20 m spring line depth tunnel geometry.

Only the case of a tunnel with an impermeable lining is considered here. Contrary to decomposed granite, significant pore pressure changes in London clay continue to occur in the long-term after tunnel construction, as depicted in Fig. 9. The long-term distribution of pore water pressures around the tunnel for both soils is the same (Fig. 10 left), however, the ground loading for London clay is larger. The reason for this is that under impermeable lining conditions, swelling takes place in the long term and increases the total stress acting on the lining. Fig.10-right presents the distribution of pore-water pressure as a percentage of ground loading, showing that in London clay, the proportion of pore-water pressure is about 70% of the ground loading at the tunnel spring line, whereas in the decomposed granite soil it is about 90% (similar to the field data shown in Fig. 1). Consequently, the percentage contribution of pore-water pressure to ground loading is dependent on soil type and increases with an increase in soil stiffness.

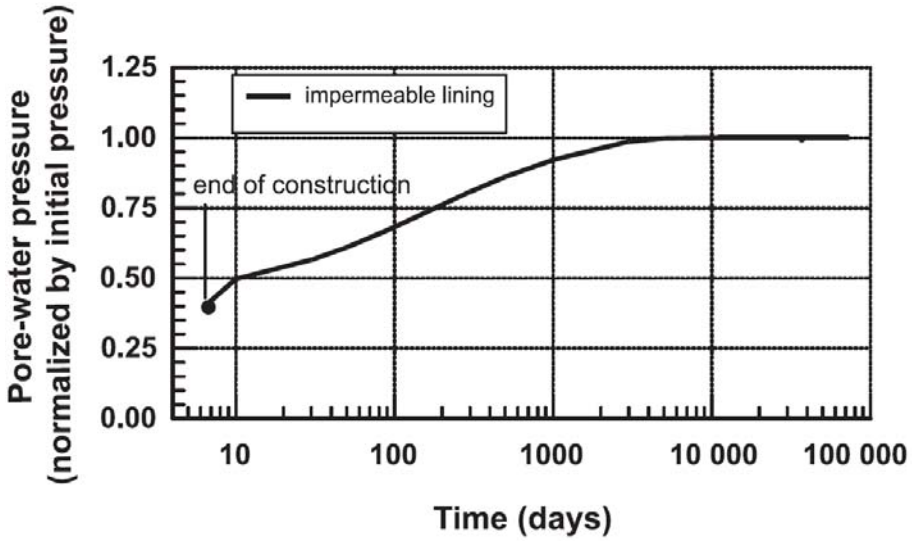


Fig. 9 Long-term evolution of pore water pressure in London clay at the tunnel crown.

4.3 Design considerations for a secondary lining

The implications of the drainage system operation in the primary lining have consequences on the pressures acting on the secondary lining. If blockage of seepage routes in the primary lining happens

in the long term, it has the effect of reducing the permeability of the lining, therefore pore water pressures will develop and act on the lining. In addition, clogging of the drainage filter system would result in the development of water pressures also acting on the secondary lining (Poscher and John 1993).

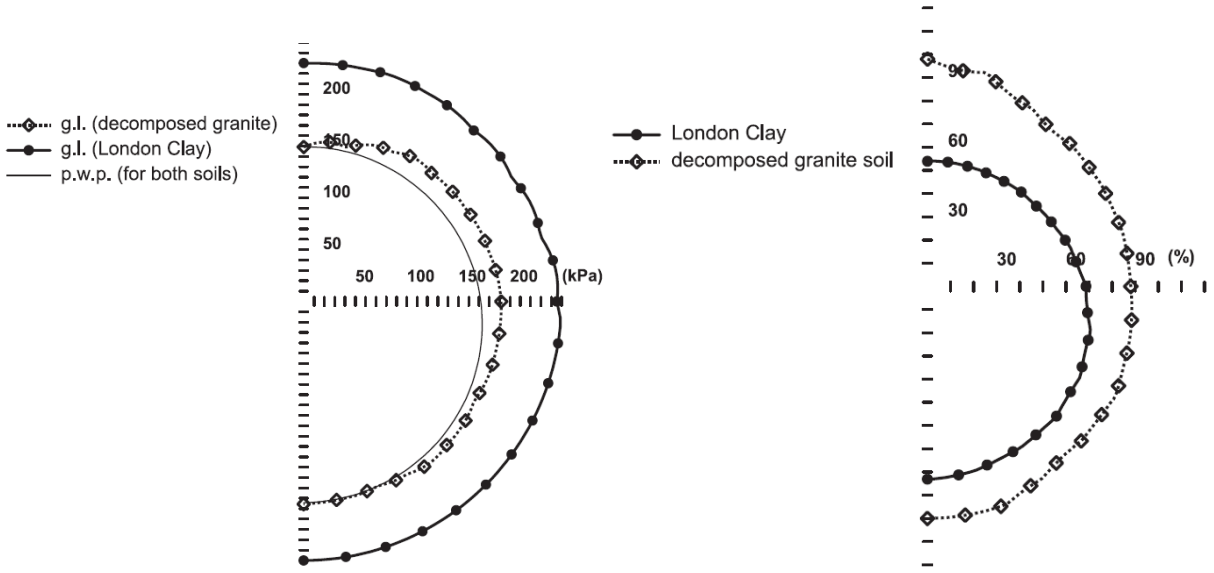


Fig. 10 Comparison of different soil types: left – pore water pressure; right – ground loading.

Not many references in the literature are concerned with loadings on secondary linings. However, as reported insome failure cases (Ferreira 1995; Lee et al. 1996), the most obvious source of loads on the secondary lining would bethe build-up of pore water pressures. In the continuation of this numerical study, the deterioration of the drainage system is achieved by reducing the lining permeability, with assumptions depicted in Fig. 11. The relative permeability between the soil and the drainage system (filter) is considered, as pore-water pressure development is influenced by the relative permeability. Analyses were performed for the tunnel in decomposed granite soil with permeability ratios k_f/k_s varying from 1 to 0.001, where k_f is the permeability of the drainage system (filter), and k_s is the permeability of the soil at the level of the tunnel spring line. It is assumed that the permeability of the primary lining is the same as that of the adjacent soil ($k_s = 1.9 \times 10^{-6}$ m/s).

Figure 14*a* presents the resulting pore-water pressure.

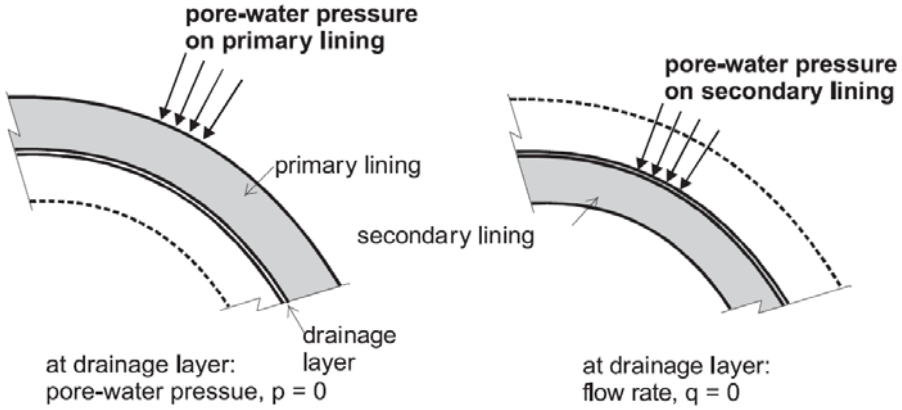


Fig. 11 Potential effect of water pressure: left – drainage system working properly; right – blocking of drainage system.

To quantify the magnitude of pore-water pressure generated due to a decrease in filter permeability, the long-term pore water pressures, p_n, on the lining are normalised by the initial hydrostatic pore-water pressure, p_{no}, (see Fig. 6) and plotted against the permeability ratio k_f/k_s. A single representative curve is obtained from interpretations at several points around the tunnel and is shown in Fig. 12. It is worth noting that the pore pressure increase is significant. Up to 80% of the initial pore water pressure builds up on the secondary lining if filter permeability reduces from $k_f/k_s = 1.0$ to $k_f/k_s = 0.001$. Figure 12 can be used to evaluate the magnitude of pore water pressure evolution on

the secondary lining, if the magnitude of the reduction in filter permeability can be appropriately estimated.

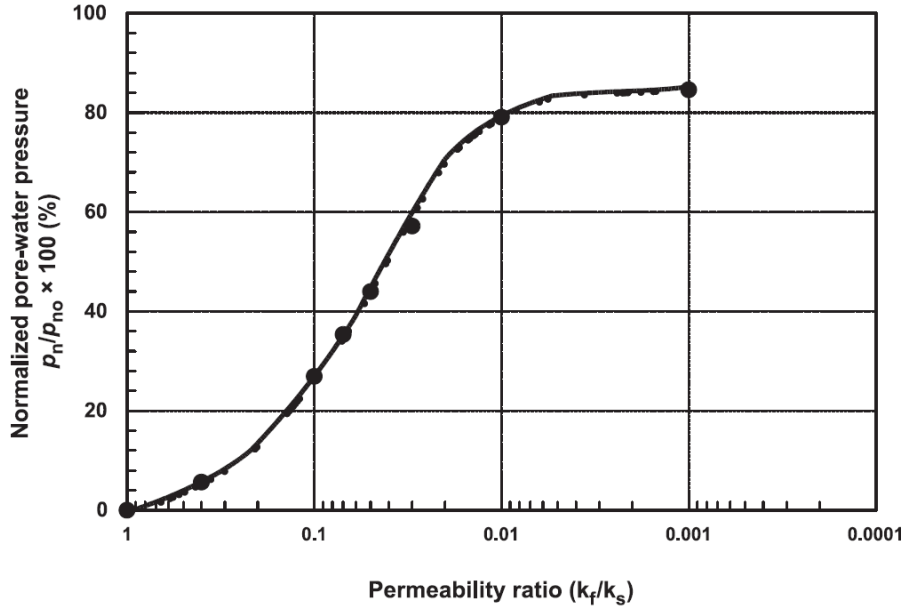


Fig. 12 Variation of pore water pressure loads on secondary lining vs. permeability of the drainage system.

5 Impact on non-circular NATM tunnels

The study on a circular tunnel presented so far indicated that although the magnitude of pore water pressure on tunnel lining can be high, there was little possibility of tensile stresses developing in the lining. However, NATM tunnels in the Seoul Subway are predominantly horseshoe shaped and can therefore be susceptible to high bending moments and associated tensile stresses. The numerical analyses presented in this section are performed on one such cross-section, 8.2 m high and 10.6 m wide, in the same ground conditions as the above analyses of a circular tunnel.

Four scenarios were considered for the hydraulic boundary condition at the tunnel: fully permeable, finite permeability ($k_l/k_s = 0.1$ and 0.01); and impermeable lining. Fig. 13 shows distributions of ground loading and pore pressure on the lining. The peak value of ground loading occurs at the location of the corner of the horseshoe cross-section, where $\theta = -30^o$, and it increases from 400 kPa for a fully permeable lining to 440 kPa for an impermeable lining. The location of the peak value moves upward with the decrease in lining permeability. The contribution of the pore water pressure to the ground loading varies significantly with location around the lining and increases with the decrease in lining permeability, as shown in Fig. 14.

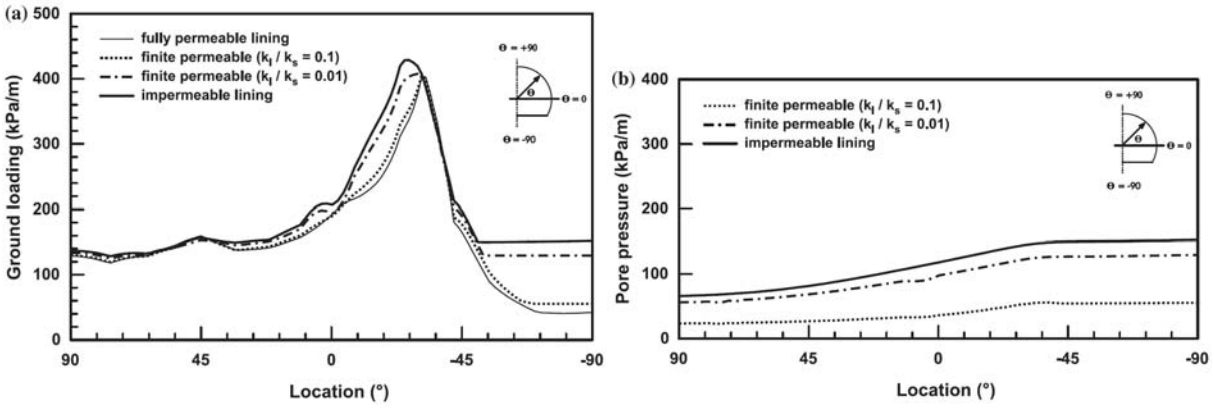


Fig. 13 Pressures on primary horseshoe shape lining: left – ground loading; right – pore pressure.

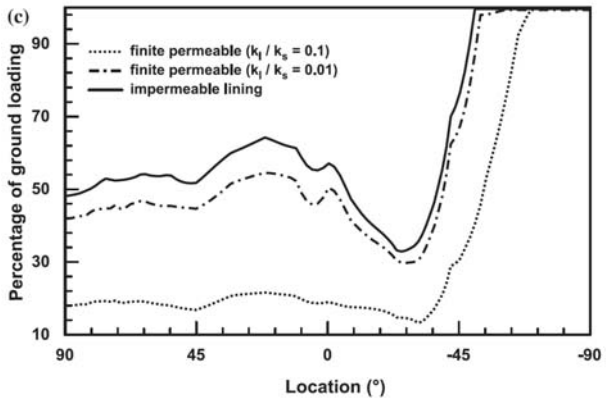


Fig. 14 Pore pressure as percentage of ground loading on a primary horseshoe shaped lining.

The effect of pore-water pressure on lining performance was also investigated. Although the differences in ground loadings, as indicated in Fig. 13, do not appear to be large, significant changes in hoop thrust and bending moment were induced in the tunnel wall and invert, as shown in Fig. 15. A decrease in lining permeability results in a significant increase in the hoop thrust and in the bending moment below the tunnel spring line. The maximum hoop thrust and bending moment occurred in the impermeable lining. A thrust of 900 kN/m occurred at around the spring line, and abending moment of 300 kN·m/m occurred at the corner ofthe lining, at $\theta = -30^{o}$. This maximum bending moment is approximately 100% larger than that obtained for the permeable lining.

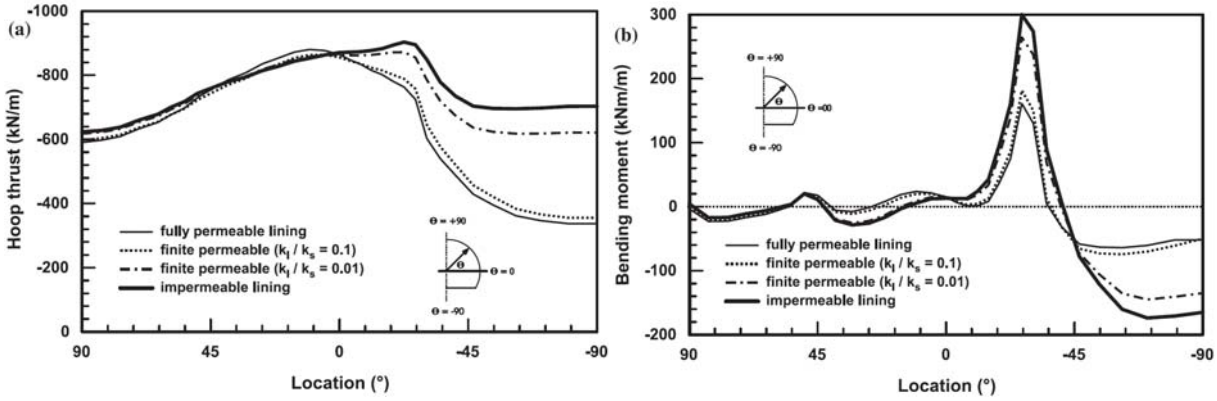


Fig. 15 Response of a primary horseshoe shaped lining: left – hoop thrust; right – bending moment.

If clogging occurs in the drainage layer between the primary and the secondary lining, the pore pressures shown in Fig. 13 would act on the secondary lining. The performance of the secondary lining due to such pore-water pressures is presented in Fig. 16, which shows the distribution of maximum principal stress (tension positive), predicted to occur between the tunnel spring line and the corner. As expected, the magnitude of tensile stress increases as the permeability of the drainage layer reduces and demonstrates that excessive bending distortion, as a direct result of degradation of the drainage layer, in a horseshoe-shaped tunnel could lead to unacceptable tensile stresses in the secondary lining.

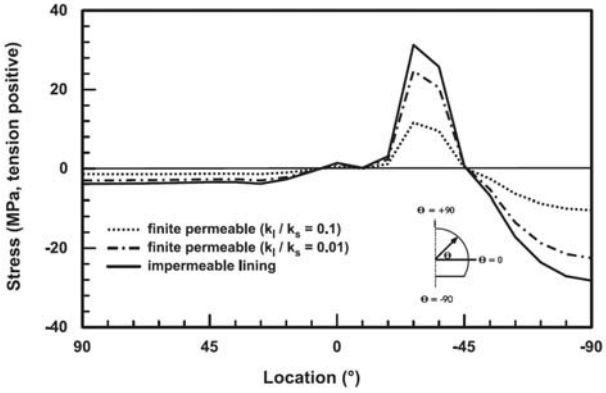


Fig. 16 Maximum principal stress in a secondary lining due to pore water pressure (tension +ve).

Shin et al. (2005) examined these predictions against some known failure cases, notably the failure of the secondary lining on the Seoul Subway (Lee et al. 1996) and a similar failure in the Carvalho Pinto Road tunnel in Brazil (HSE 1996). In both cases only the secondary lining was affected, developing long cracks parallel to the tunnel axis between the spring line and the corner (θ from 0^o to -30^o), due to the pore pressure loading. Those observations were in the location of the tensile stress predicted in Fig. 16.

In the construction of the Seoul Subway, the majority of the ground conditions warranted the use of a horseshoe shaped tunnel. Shin and Potts (2002) highlighted that in decomposed granite, due to its significant increase of stiffness with depth, a horseshoe-shaped tunnel was structurally more beneficial than a circular tunnel. However, this benefit would reduce if the lining loads from pore-water pressure were considerable, particularly for the secondary lining. To quantify the effect of tunnel shape, an analysis was performed of a circular tunnel with a secondary lining and with the same cross-section area of the horseshoe shape tunnel, and the results compared. Geological conditions, tunnel depth and modelling details were the same for the two tunnels. Fig. 17 compares the distribution of ground loading and pore pressure for the case of $k_l/k_s = 0.1$. Although the predicted pore pressures on a circular lining are higher than on the horseshoe shaped lining in the upper part of the tunnel, the pore pressure contribution to ground loading varies between 30 and 40% for the former lining and between 15 and 100% for the latter. Regarding the behaviour of the secondary lining due to pore water pressure loading on the circular tunnel, the effect is negligible as the maximum principal stress is everywhere compressive. The lower part of the horseshoe shaped tunnel, however, develops tensile stress. This indicates that the time dependency of the permeability due to degradation of the drainage system should be considered when designing non-circular tunnels.

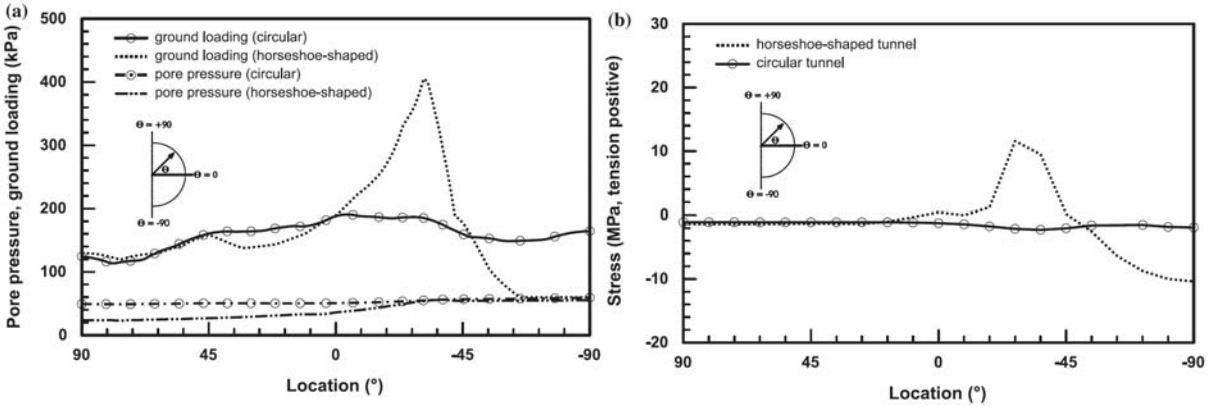


Fig. 17 The effect of tunnel shape: left-pore pressure and ground loading; right-secondary lining performance.

6 Conclusions

The study presented in this paper reveals the complexity of NATM tunnelling below the ground water level, in mixed ground conditions of a weathering rock. Through the robust numerical model, which was shown to predict reliably the field observations, the following are identified as key outputs:

- The majority of the ground loading on a tunnel in a weathered rock arises from pore water pressure, if the lining is impermeable;
- Changes in lining permeability change the contribution of the pore water pressure to ground loading, without changing the magnitude of ground loading;
- The magnitude of the pore water pressure on the lining is dependent on the relative permeability of soil to lining, k_l/k_s; as this ratio decreases, the pore pressure increases.

It was also highlighted that tunnel shape has a strong impact on the lining stresses resulting from external water pressure. Numerical analysis of a non-circular NATM tunnel revealed that the development of residual pore-water pressures could cause significant detrimental effects on a secondary lining in the long term. Excessive bending distortion in a noncircular tunnel could lead to unacceptable cracking in the lining and ultimate lining failure.

It is recommended that the time dependency of lining permeability due to the deterioration of the drainage system should be considered as a critical factor in lining design, particularly for a secondary

lining, which is usually not designed to cope with pore-water pressure loading. By performing a parametric study for a tunnel with different lining permeabilities, a design curve is proposed to help evaluate the likely pore-water pressure loads on a secondary lining in decomposed granite ground conditions.

References

Ferreira AA (1995) Cracks and repairing of the Carvalho PintoRoad Tunnel (Brazil). Exchange of correspondence with Healthand Safety Executive, UK (in 1996).

Hajra MG, Reddi LN, Glasgow LA, Xiao M, Lee IM(2002) Effects of ionic strength on fine particle clogging of soilfilters. Journal of Geotechnical and Geoenvironmental Engineering,**128**(8): 631–639.

HSE (1996) Safety of new Austrian tunnelling method (NATM)tunnels, a review of sprayed concrete lined tunnels with particularreference to London Clay. Health and Safety Executive(HSE) UK.

Inokuma A, Ishimura T(1995) Earth pressure acting on shield driven tunnels in soft ground. *In p*roceedings of the InternationalConference on Underground Construction in SoftGround, New Delhi, India, A.A. Balkema, Rotterdam, TheNetherlands, pp. 221–224.

Lee YN, Byun HK, Shin OJ (1996) Cracking of subwaytunnel concrete lining and its repair. *In* Proceedings of the NorthAmerican Conference Nat '96 and 22nd General Assembly InternationalTunnelling Association, Washington, D.C., 21–24A.A. Balkema, Rotterdam, The Netherlands,pp. 325–329.

Neville AM (1995) Properties of concrete, 4th ed., LongmanGroup Limited, Malaysia.

O'Rourke TD (1984). Guidelines for tunnel lining design. AmericanSociety of Civil Engineers, Reston, Va.

Parks P, Francis J, Gorlov A, Gorlova E, Guertin JD (1986) Water intrusion problems in transit tunnels. Final Report (UMTA-MA-06-0156-86-1) to US Department of Transportation,UMTA Technical Assistance Program

Peck RB (1969) Deep excavations and tunnelling in soft ground –state of the art. *In* Proceedings of the 7th International Conferenceon Soil Mechanics and Foundation Engineering, State ofthe Art Volume, pp. 225–290.

Poscher G, John M (1993) Experiences gained with measuresdesigned to reduce shotcrete eluations in the tunnels of theVerbingsdungskurveNantenbach. *In* Proceedings of the International Symposiumon Sprayed Concrete, Oslo, pp. 401–415.

Potts DM, Zdravkovic L 2(1999)Finite element analysis in geotechnical engineering: theory; Thomas Telford Publishing, London, UK.

Shin JH, Potts DM (2002) Time-based two dimensionalmodelling of NATM tunnelling. Canadian Geotechnical Journal,**39**: 710–724.

Shin JH, Addenbrooke TI, Potts DM (2002) A numericalstudy of the effect of groundwater movement on long-term tunnelbehaviour. Géotechnique, **52**(6): 391–403.

Shin JH, Potts DM, Zdravkovic L (2005) The effect of pore-water pressure on NATM tunnel linings in decomposed granite soil. Canadian Geotechnical Journal 42, pp 1585-1599,

Vaughan PR (1989)Non-linearity in seepage problems — theoryand field observation. De Mello Volume, Edgard Blucher Ltd.,Sao Paulo, Brazil. pp. 501–516.

Ward WH, Pender MJ (1981) Tunnelling in soft ground–general report. *In* Proceedings of the 10th International Conferenceof Soil Mechanics and Foundation Engineering, Stockholm,Sweden, A.A. Balkema, Rotterdam,The Netherlands. Vol. 4, pp 261–275.

Planetary Rock Mechanics and Future Prospects

Ö. Aydan
University of the Ryukyus, Nishihara, Okinawa, Japan
aydan@cs.u-ryukyu.ac.jp
0000-0002-7304-6486

Abstract

There is recently an increasing interest to explore the ways to find out the characteristics of other planets and possibility of exploiting their mineral resources. Images from Mars particularly show the striking similarities between rocks on Earth and those of Mars. One can easily notice layered rock masses, jointing, weathering effects and some slope stability issues such as plane and wedge sliding, block and flexural toppling type failures.

The dynamics issues in Mars, Moon and Venus and other planetary objects remain to be the similar to those on Earth. Although mankind has no direct access to Mars yet, the exploration rovers, Mars Reconnaissance Orbiter and InSight Lander provided very valuable data so that some dynamics issues should be recognized.

Low gravity planetary bodies such as comets and asteroids have been great interest to mankind since early times. Attempts to bring materials from several asteroids were recently successful and they may provide important information on the characteristics and how to mine the asteroids. Furthermore, some familiar phenomena of slope failures, sinkholes, debris flow and boulder toppling under low gravitational environment are observed at these low gravity bodies.

This keynote lecture covers thoughts of the author on the aspects of planetary rock mechanics and rock engineering deducted from the images sent to the earth from Mars, Moon and Venus by exploration rovers and from comets and asteroids from spacecrafts. Particularly the images from Mars are spectacular to imagine and infer many aspects planetary rock mechanics and resemblances of rocks and their weathering, discontinuity formations, slope stability problems and natural caves lead to mankind contemplate possible mechanics and material behavior of rocks and their related scientific and engineering aspects.

Keywords

Planetary mechanics, Exploitation, Rock slopes, Sinkholes, Quakes.

1 Introduction

USA and Russia (formerlyUnion of Soviet Socialist Republic (USSR)) initiated space programs and sent several spacecrafts to Moon, Venus and Mars and some of them landed on Moon, Venus and Mars to find out the characteristics of other planets and possibility of exploiting their mineral resources. Some of most impressive images from the Apollo Program of NASA were the man from Earth

standing next to lunar rock mass and a geologist from Earth is hitting lunar rock by a geologist hammer. USA and Russia (former Union of Soviet Socialist Republic (USSR)) initiated space programs and sent several spacecrafts to Moon, Venus and Mars and some of them landed on Moon, Venus and Mars to find out the characteristics of other planets and possibility of exploiting their mineral resources. Some of most impressive images from the Apollo Program of NASA were the man from Earth standing next to lunar rock mass and a geologist from Earth is hitting lunar rock by a geologist hammer. The images from recent Mars exploration rovers such as Opportunity, Spirit, Curiosity and Perseverance (NASA 2019b, 2022) showed striking similarities between rocks on Earth and those of Mars. One can easily notice layered rock masses, jointing, weathering effects and some toppling type rock slope stability problems as well as sinkholes (skylights) related to the collapse of underground openings.

Mankind has been exploring space objects since very old times. For example, Sumerians, who established a great civilization in the Mesopotamia during a period between 4000 to 2000 BC, laid out the foundations of the modern astronomy. Indian, Chinese, Persian, Arabian and Turkish astronomers fundamentally are similar to those of Sumers. Figure 1 shows the symbols of universe according to Sumerians and Oz Tamga (symbol) of proto-Turks on basaltic rock surface at Saymalıtaş (Kyrgyzstan) (e.g., E. Herzfeld, 1930; Cığ, 2020; Somuncoğlu, 2010, 2011).



(a) Sumerian bowl symbolizing universe (4000BC)

(b) Oz Tamga (Symbol) (Saymalıtaş, older than 5000 BC, likely to be 10000 BC).

Fig. 1 Some artifacts symbolizing universe from Sumers and proto-Turks.

The author felt the necessity to teach about the Planetary Rock Mechanics during his Rock Mechanics Classes at Tokai University since 2010 and the University of the Ryukyus since 2014. Since then, the author has been actively doing research in the topic and published many articles about Mechanics and Engineering of rocks of planetary bodies together with emphasis on those from Earth as a planetary body and discussed the future directions of studies and implications.

In this article, some thoughts of the author on the aspects of planetary rock mechanics and rock engineering deducted from the images sent to the earth from Mars, Moon, Mercury and Venus by exploration rovers and from comets and asteroids from spacecrafts are described. Particularly the images from Mars and Moon are spectacular to contemplate and infer many aspects planetary rock mechanics and resemblances of rocks and their weathering, discontinuity formations, slope stability problems and natural caves lead to mankind contemplate possible mechanics and material behaviour of rocks and their related scientific and engineering aspects.

2 Solar System and Terrestrial Planetary Bodies

As well-known, the solar system consists of eight planets, namely, Mercury, Venus, Earth, Mars, Saturn, Jupiter, Uranus, Neptune. On the basis of computations, the existence of a planet between Mars and Jupiter was estimated. However, at the estimated location, an asteroid belt exists. This asteroid belt might have corresponded to the missing planet. Initially, Pluto was found in 1930 and it was considered to be the 9th planet until 2006. On the basis of definition of planets of our solar system, it was not assumed to be the 9th planet any more. The density of planets differs as a function of distance from the Sun and it decreases as the distance increases. Terrestrial planets such as Mercury, Venus, Earth and Mars (Figure 2) are considered to be quite similar to each other in many

aspects while they are different from each other in terms of size and geology. Mercury and Venus have no natural satellites while the Earth has Moon as a natural satellite. Mars has two natural satellites called as Deimos and Phobos.

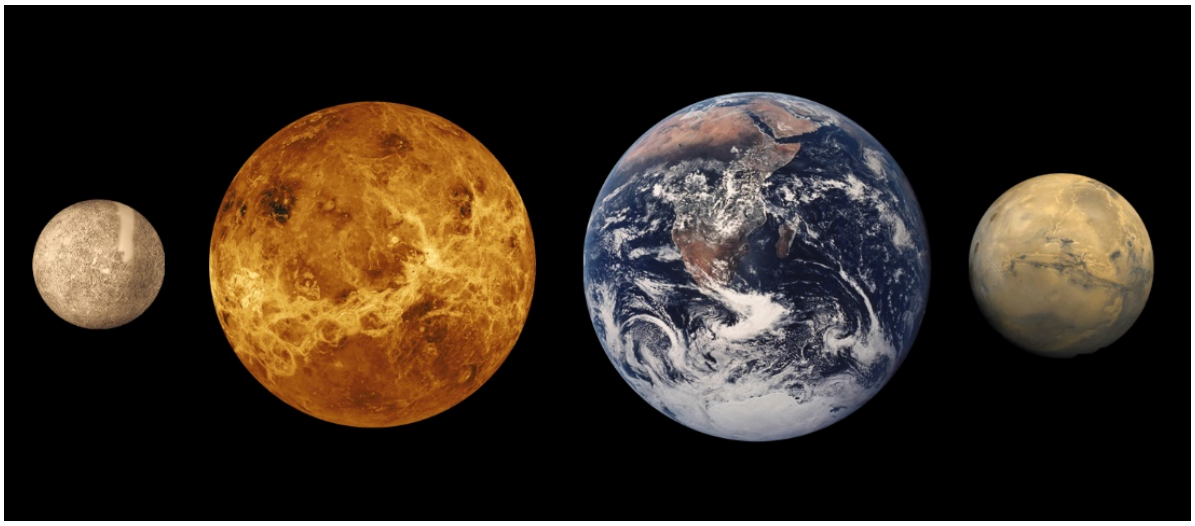


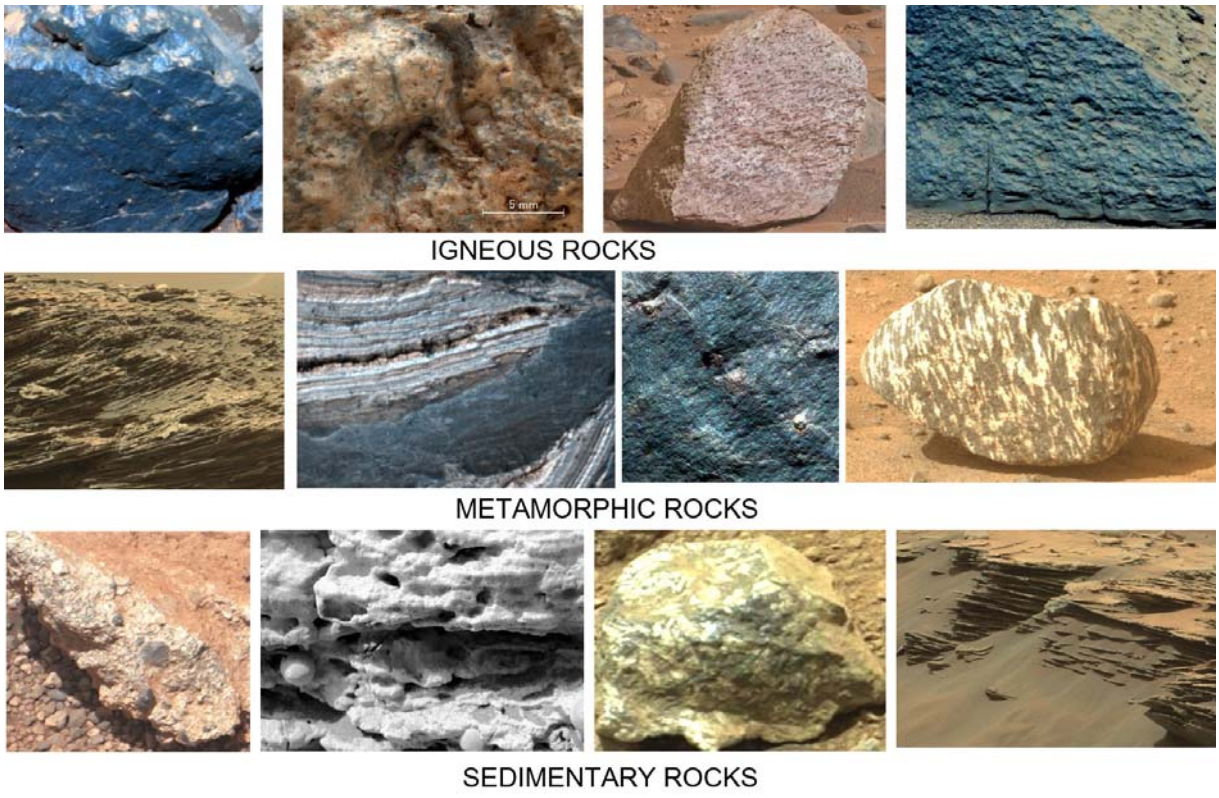
Fig. 2 Planetary bodies: Mercury, Venus, Earth and Mars (from NASA).

3 Rocks, Discontinuities and Weathering of Planetary Bodies

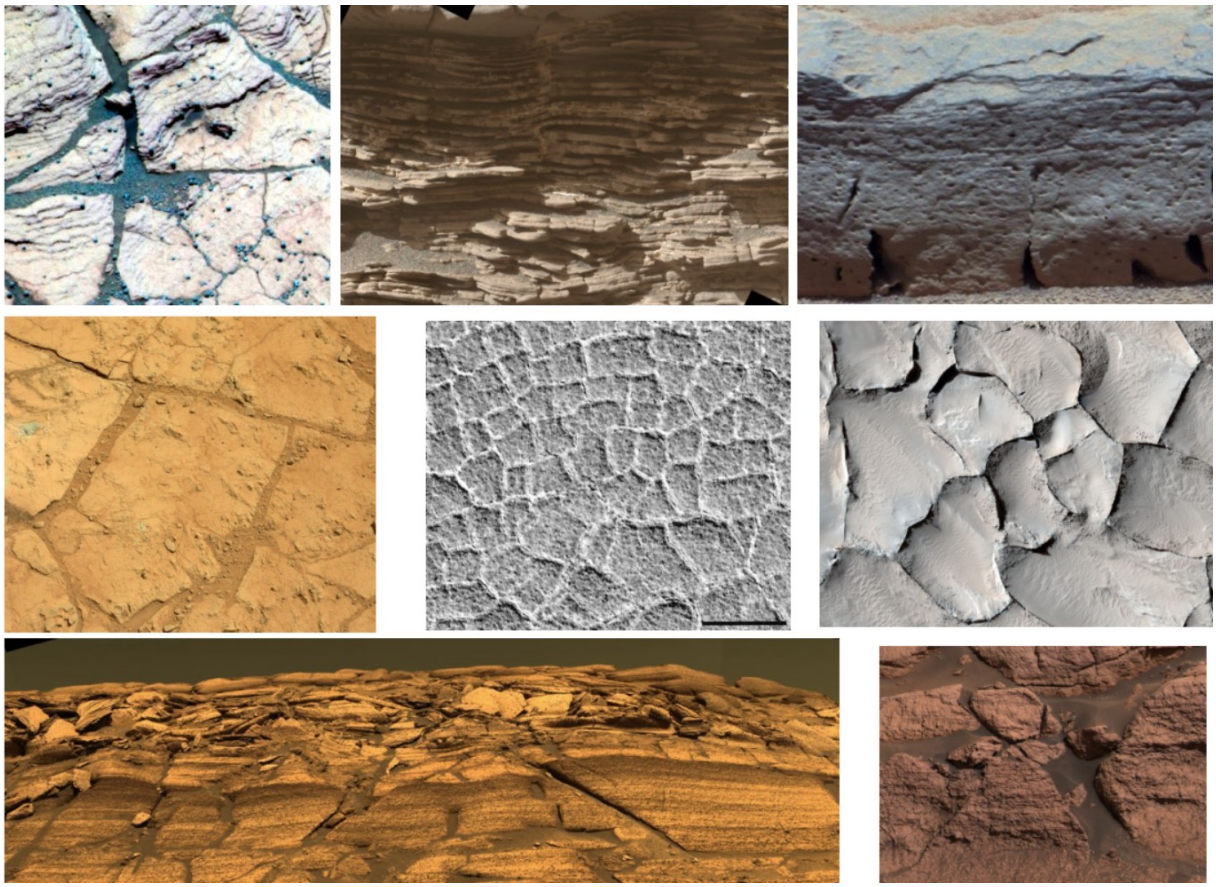
The information on the rocks of other planetary bodies besides those of the Earth are available from meteorites fallen on Earth, explorations using the unmanned and manned explorers on Moon, Mars and Venus as well as optical and electro-magnetic exploration rovers. In addition, some, unmanned space probes sent to several asteroids provided additional information on their constituting substances. It is very likely that the rocks of planetary bodies would be quite close to those of Earth. For examples, the classification of rocks is igneous, metamorphic and sedimentary on the bases of the images, drilling, cores and their chemical analyses performed on various sites on Mars as well as on Moon. Although it still needs some clarifications whether rocks seen in Earth fully exist on Mars. However, the sedimentary rocks (such as conglomerate, sandstone, siltstone, mudstone, sulphate deposits), metamorphic rocks such as phyllite, shale and serpentine and extrusive rocks (basalt, andesite-like (silicate bearing basalt), breccia) of Mars clearly similar to those of Earth (Figure 3a,b).

Flow planes, bedding planes and schistosity planes, which are intrinsic to each rock class, are distinctly observed. In addition, some discordant sedimentation of sandstone layers was also distinctly observed. There are various causes for the formation of discontinuities in rocks. The causes can be grouped into a) tension discontinuities due to cooling, drying, freezing, bending, flexural slip, uplifting, faulting, and stress relaxation associated with erosion or retreating glacier, b) Shear discontinuities due to folding, and faulting, c) Discontinuities due to intrinsic properties of rocks (sedimentation, metamorphism, magma flow). Without any exception, discontinuities in rocks/rock masses of Mars are fundamentally similar to those observed in Earth as seen in Figure 4.

The surface morphology and filling situations rock discontinuities are quite similar to those seen in Earth. Although the striation of shear discontinuities could not be confirmed from the images taken by the Mars Exploration Rovers, they should be quite similar to those observed on Earth. The chemical analyses of the filling material so far showed that they are generally consisted of calcium sulphate (anhydrite) or calcium carbonate (calcite). Sometimes they included boron minerals, which are probably associated with dissolved substances when the planet was wet environment in the past.



(a)



(b)

Fig. 3 Views of (a) of rocks, (b) discontinuities observed in Mars (images from NASA).

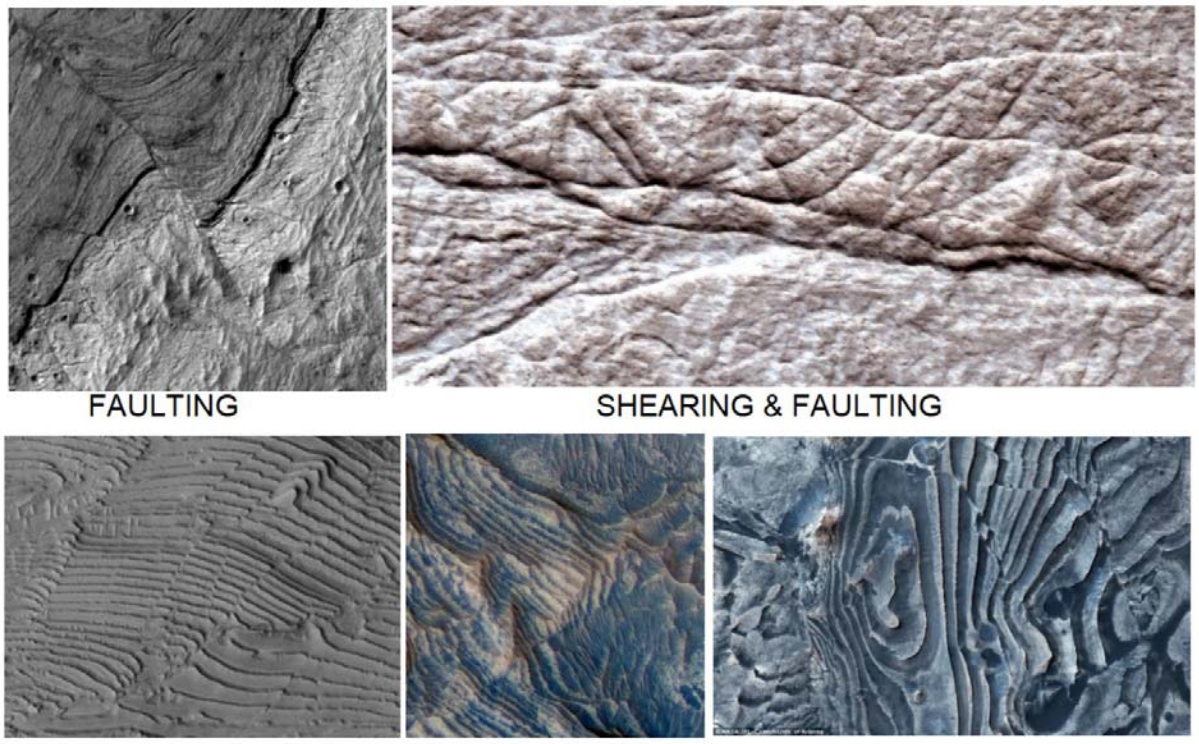


Fig. 4 Views of large scalediscontinuities observed in Mars.

4 Stress Sates of Planetary Bodies

Stress state is one of the most important items when rock mechanics and rock engineering to be utilized in moon and other planets. Particularly, the engineering design requires data on in-situ stress state as well as quake related topics. Figure 5 shows the density, gravity and hydrostatic pressure distributions with depth in Venus and Mars together with those of Earth.

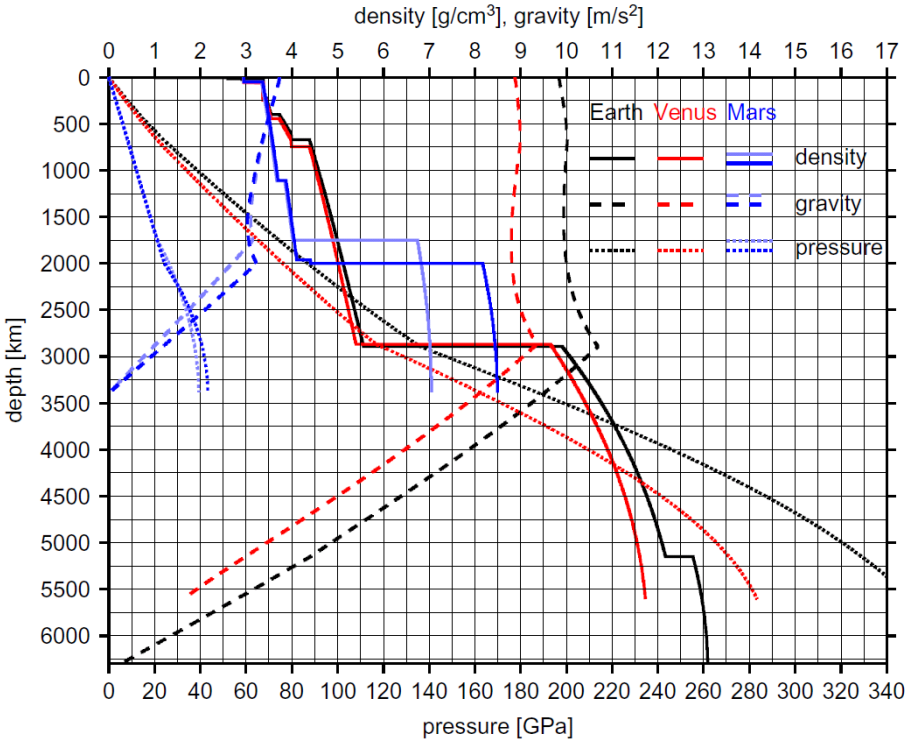


Fig. 5 Comparison of the density, gravity and hydrostatic pressure distributions with depth in Venus and Mars together with those of Earth (from Steinberger, 2010).

The author analysed the stress state of Moon, Mercury, Venus as well as Earth by considering the following cases:

CASE 1: Planetary bodies are in liquid state (hydrostatic)

CASE 2: the crust and mantle are elastic solids and the core is in liquid state (non-hydrostatic)

CASE 3: the crust and mantle are elasto-plastic solids and the core is in liquid state (isothermic: room temperature)

CASE 4: the crust and mantle are thermo-elasto-plastic solids and the core is in liquid state (non-isothermic)

Parameters b_1, b_2, S_o, S_∞ of the yield criterion were chosen as 0.2 GPa^{-1}, 0.0014 $^oC^{-1}$, 0 MPa, 5GPa, respectively.

Figure6 shows the distributions of radial and tangential stresses in the lithosphere for each case. The elasto-plastic analyses showed that the whole crust and mantle became plastic. Large tangential stresses seen in CASE 2 were dissipated when the plastic behaviour of the crust and mantle was considered. The tangential stresses dissipated in the mantle increased both radial and tangential stresses in the core. The consideration of the thermo-elasto plastic behaviour of the mantle and the crust of the earth further decreased the deviatoric stresses in the mantle and in the crust.

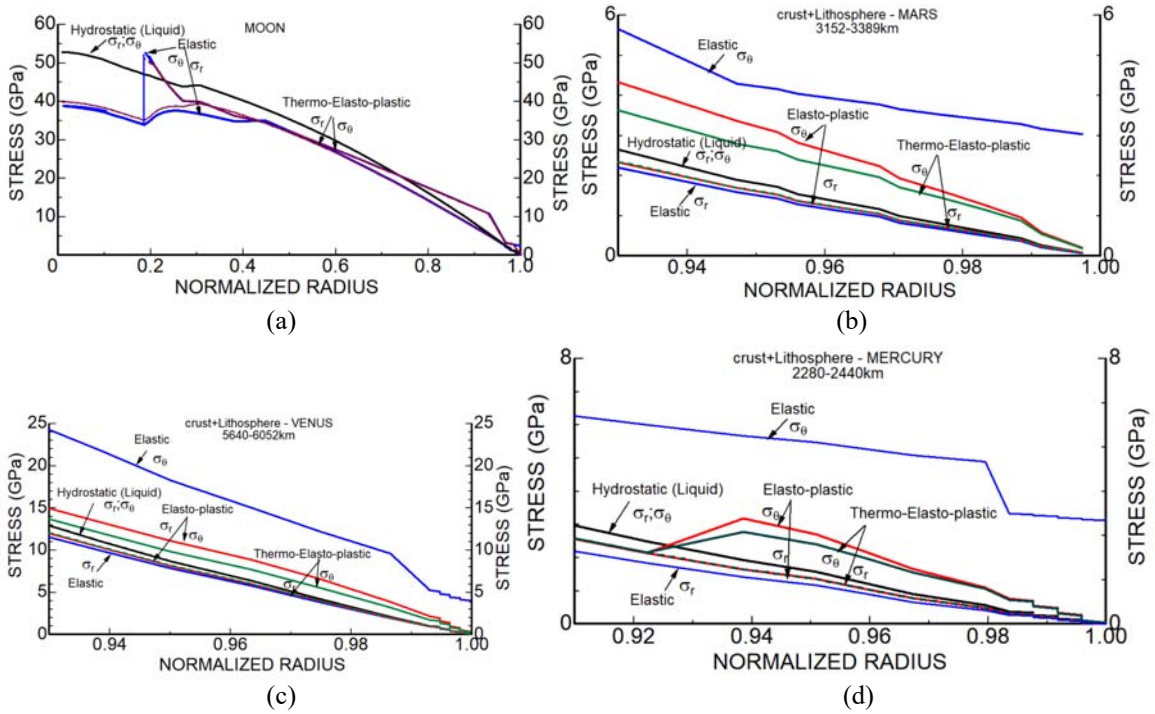


Fig.6 Distribution of stresses (a) throughout Moon, and lithosphere of (b) Mars, (c) Venus and (d) Mercury.

5 Rock Slopes

The images and drilling operations performed by Mars Exploration Rovers (Opportunity, Sprit, Curiosity, Perseverance) on some selected rocks and rock blocks indicated that rocks are quite similar to those of the earth. It still needs some clarifications whether rocks seen in Earth fully exist on Mars. However, the sedimentary rocks (such as conglomerate, sandstone, siltstone, mudstone, sulfate deposits), metamorphic rocks such as phyllite, shale and serpentine and extrusive rocks (basalt, andesite-like (silicate bearing basalt), breccia) of Mars clearly similar to those of Earth. Although the present climatic conditions such as none existence of rainfall and groundwater and large difference of daily temperature, the failures due to gravitation and seismic forces, impacts, differential weathering are likely to occur. Furthermore, it is well understood that the circumstances in the past were quite similar to those of Earth and many paleo rock slope failures should be very similar to those observed on Earth. In this section, rock slope failures in Mars on the bases of the images provided by Mars Rovers of NASA are summarized with the consideration of the following conditions:

a) Slope Failures in Layered Rock Mass

b) Slope Failures in Jointed Rock Mass

c) Actual or Potential Slope Failures in Discontinuous Rock Mass

d) Steep or Overhanging Cliffs in Layered Rock Mass
e) Failures of Overhanging Cliffs in Discontinuous Rock Mass
f) Stability of Precarious Rock Blocks
g) Impact and Vibration Induced Mass Movements.

Aydan (1989) categorized rock slope failures on Earth. Fundamentally rock slope failures involve three categories, specifically, intact rock or rock mass, discontinuities and intact rock and discontinuities. They may be named as shearing or bending failure, combined shearing and sliding, buckling, flexural toppling, planar and/or wedge sliding and columnar toppling. Figure 7 shows some examples of rock slope failures in Mars.

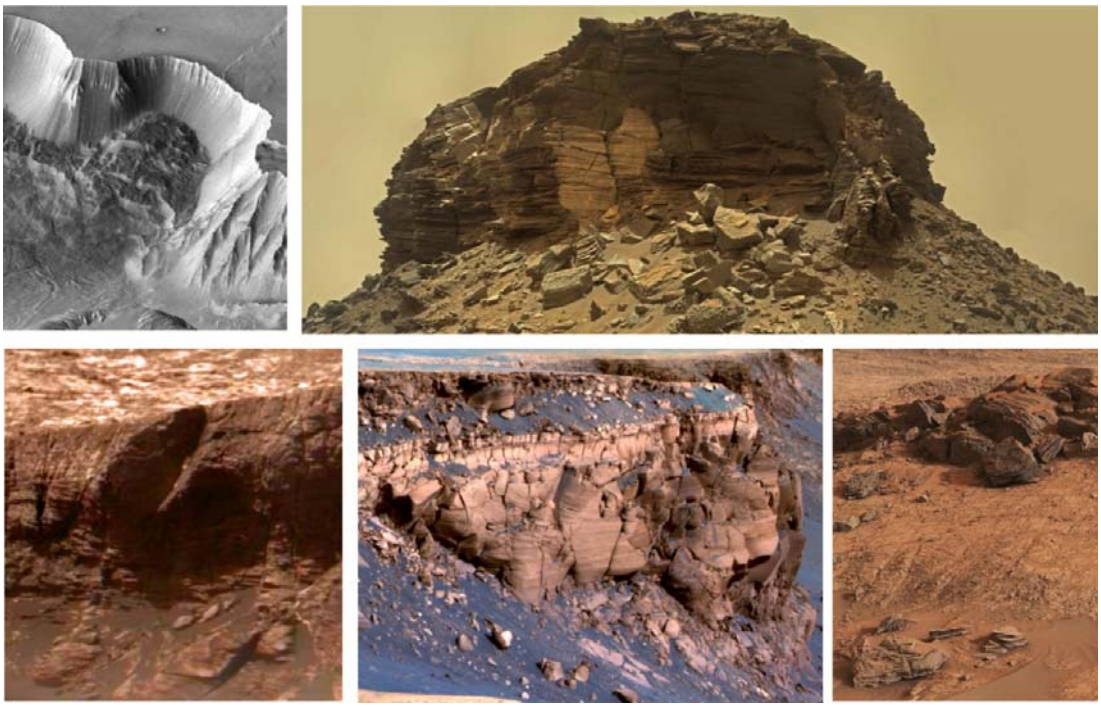


Fig.7 Views of slope failures observed in Mars.

Figure 8 shows an application of the integrated slope stability assessment proposed by Aydan et al. (1991) to rock slopes of Mars. Lines in the figure represent the relations between the bedding plane and lower slope angle for stability of rock slopes for jointed rock mass. The friction angles used in this graph are for those of basaltic rock joints on Earth.

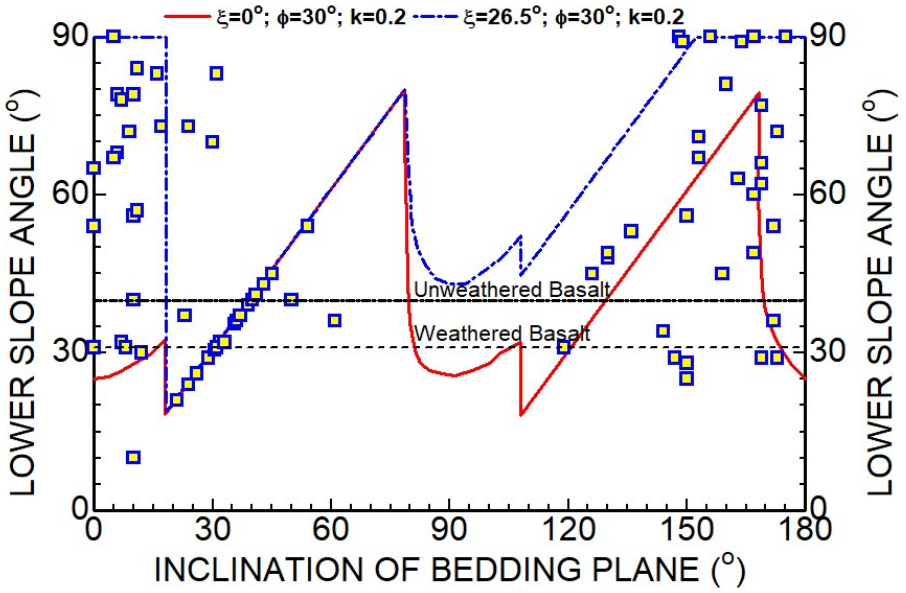


Fig.8 The relation between inclination of bedding plane and lower slope angle for rock slopes on Mars.

6 Underground Openings

The stability issues of underground cavities and sinkhole issues on Earth and other terrestrialbodies. Sinkholes are a severe problem on Earth. This problem has been often observed in karstic terrains, evaporitic formations and volcanic regions on Earth. The images as seen in Figure 9 clearly showed that sinkholes also formed in Mars. These sinkholes have been found in basaltic flow areas. Some of sinkholes may also be formed by impacts of meteorites and/or rifting induced by tectonic movements.

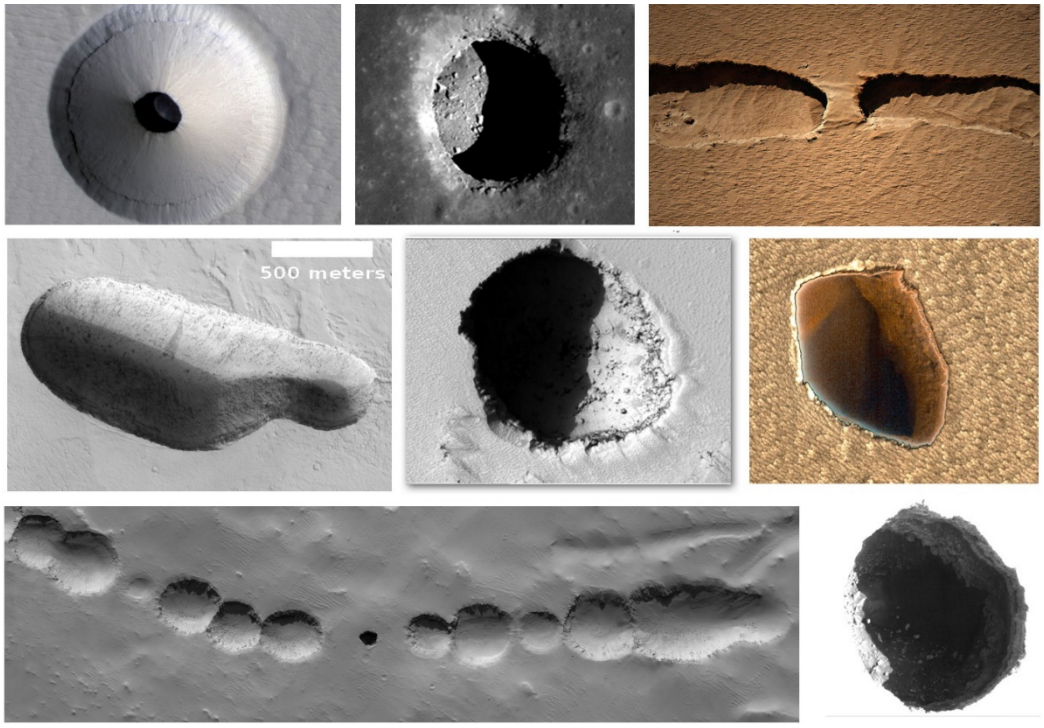


Fig.9 Images of sinkholes in Mars (compiled from the images released by NASA).

As noted from the figure, basalts of Mars are quite porous, which may be called vesicular basalt. It is very likely that the porous structure may lead heavy weathering as well as a decrease of mechanical properties. As there is no experimental data on Martian basalt, the drilling and grinding operations by the rovers on rocks of Mars may be utilized to infer their mechanical properties. As reported by Aydan (2022), the tensile and uniaxial strength of vesicular basalt decreases as a function of porosity (Figure 10). As the basalts of Mars resemble to those of Earth. Therefore, the mechanical properties of the vesicular basalt of Earth may be utilized to evaluate the mechanical properties of Martian vesicular basalts.

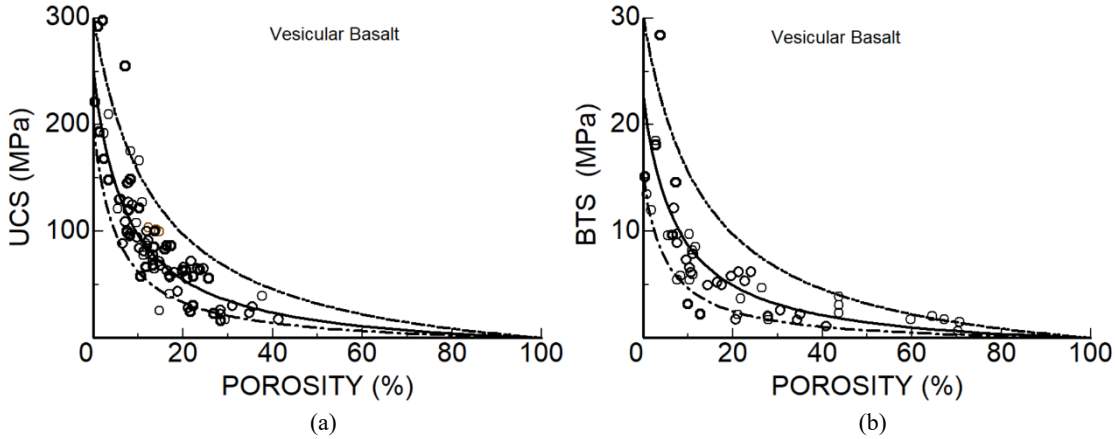
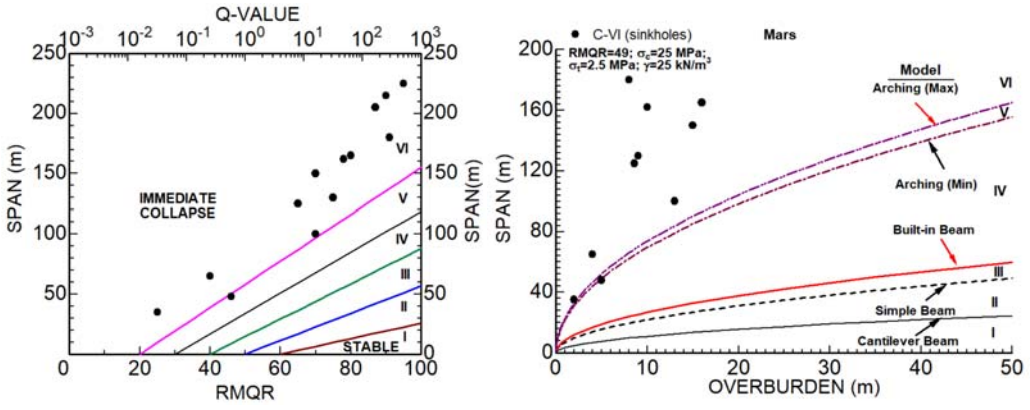


Fig.10 Variation of (a) uniaxial compressive strength and (b) Brazilian tensile strength of basalt from Türkiye and Japan with porosity.

In this sub-section, the applicability of some stability assessment techniques to the sinkholes in Mars are presented. Fundamentally, empirical, analytical and numerical methods can be used described. The methods are not presented herein and the interested readers can consult some publications (e.g.,

Kawamoto and Aydan 1999; Kawamoto et al. 1991; Aydan et al. 1996; Aydan and Tokashiki 2011; Lang 1994). Specifically, empirical and analytical methods are utilized described.

Some attempts have been done to evaluate these two parameters from images on the bases of knowledge available from sinkholes of Earth. Furthermore, that the strength of vesicular basalt is estimated to be about 25 MPa in view of its porosity. As the gravity coefficient of Mars and Moon is 0.387 times that of Earth, the stress induced by the Mars gravity is assumed to be 0.387 times that on Earth, respectively. By considering these facts, the empirical and analytical methods have been used to assess the sinkholes occurrence for Mars. The estimations from empirical and analytical methods are shown and compared with observational data in Figure 11. The overall trend is quite promising despite many data are based on some inferences for similar situations on Earth. Once again it is noted that the analytical methods yield also the bounds to be on the safe side. When observational data is compared with empirical estimations, the overall trends are quite similar and the empirical estimation is on the safe side.



(a) (b)

Fig. 11 Comparison of (a) empirical and (b) analytical stability charts with observation data on Mars.

7 Seismicity and Quakes

It is shown that quakes also occur in planetary bodies and named as Marsquakes and Moonquakes. Furthermore, the possibilities of Venusquakes and Mercuryquakes are contemplated. This issue may be quite important regarding the settlement and exploitations of the planetary bodies by mankind.

Aydan (2017c, 2022a,b, 2023b) stated that possible causes of quakes in planetary bodies are as follow:

a) Impacts by Meteorites

b) Thermal Contraction & Expansion

c) Volcanic Activity

d) Large Scale Mass Movements

e) Plate-tectonic Type Movements

f) Daily Rotation and Annual Solar Motion

It should be noted Earth is well-instrumented while there is very limited instrumentation on Moon and Mars for seismic events. In this chapter, quakes on Earth (e.g. Aydan 2023a, 2017b, 2002, 2003, 2006, 2007, 2009, 2012a; Aydan et al. 2005a,b, 2007a,b; Ulusay et al. 2001, 2003a,b) are considered and available knowledge and information are extended to other terrestrial bodies.

The seismometers installed in Moon recorded moonquakes, which were initially unexpected (Figure 12). The records from the moonquakes revealed inner structure of the moon like that of Earth. It was found that the earthquakes were categorized as deep earthquakes resulting from the tidal force interaction between Earth and Moon, shallow earthquakes due to tectonic forces and thermal stress variations and other earthquakes due the meteorite and lunar module impacts. The magnitude of the shallow earthquakes could be up to 5.5 while the magnitude of the deep earthquakes was much smaller and generally less than 2. The shallow earthquakes may pose a hazard to a lunar habitat and they may last for more than 10 minutes. The deep earthquakes occur at depths of 700 to 1000 km and it occurs periodically at 14 and 206 days, implying the causes of the events are terrestrial and related to solar

tidal forces. It was found that the vibrations caused by impacts can last for more than 1 hour while deeper earthquakes last only 10-20 minutes. The reason for such a long seismic vibration is considered to be due to the existence of a thick elastic crust. As the viscosity of the crust small, the vibrations last longer for surface impacts.

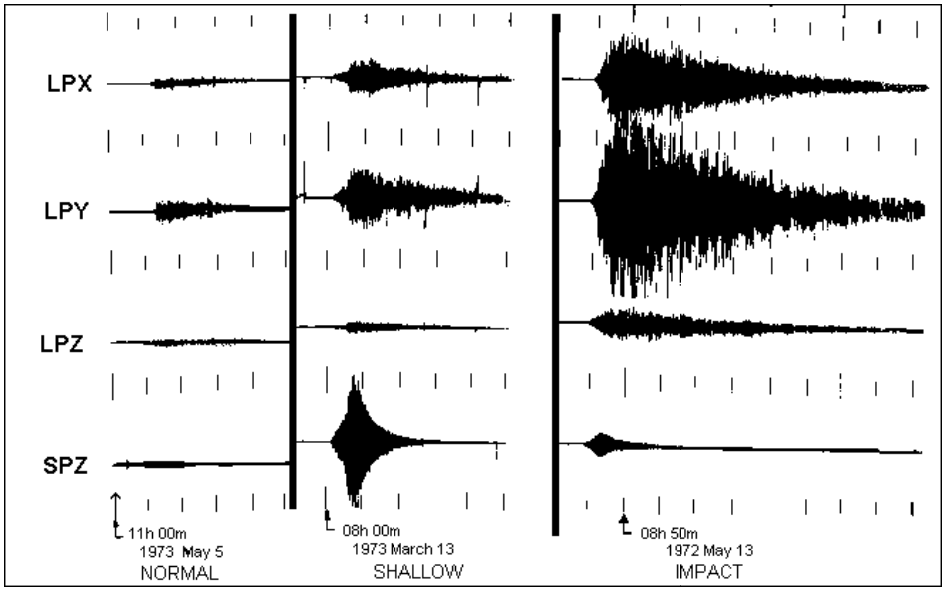


Fig.12 Records of moonquakes and lunar impacts (time marks 10 minutes) (from NASA)

The first seismic observation station, named as InSight Lander was installed on Mars very recently in 2018.The InSight Lander touched down on Mars on November 27, 2018. Until the record of a seismic event on April 6, 2019, the occurrence of Mars quakes was a speculative issue. The first seismic event on April 6, 2019 confirmed the existence of quakes of Mars (Figure 13). The first vibration record obtained from a marsquake by the InSight Lander was quite longer than those observed on Earth and shorter than those on Moon as seen in Figure 12. The seismic monitoring would improve the understanding of the seismicity and the interior structure of Mars and provide essential data on the necessity of quakeproof design of structures to be built in Mars or similar planetary objects.

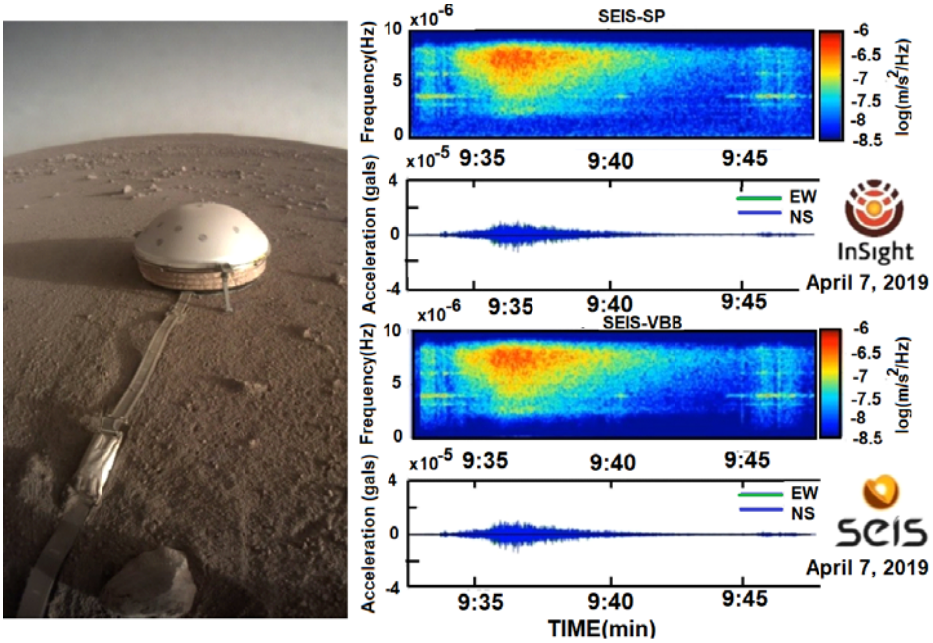


Fig.13 A seismic record by the seismometer of the INSIGHT Mars module of a marsquake occurred on April 24, 2019 (arranged from NASA).

There is no doubt that quakes do occur in Venus in view of volcanic activities and the existence of large-scale fracture zones. The possibility of installing seismometers on the surface of Venus is extremely difficult due to thick clouds and greenhouse effect, surface temperatures of Venus approach 462 °C causing water vaporization. Recently NASA has been exploring to utilize the same technique to monitor the earthquakes in California. Compared to conventional seismographs, there are some

technical issues with balloon equipped with air-pressure sensors for determining the location, magnitude of earthquakes and its focal mechanism, it is probably the only technique available so far.

Mercury is likely to have seismic activities, which may be referred as "mercuryquakes". These quakes are thought to be primarily caused by the shrinkage of the planet. The existence of large fault scarps (up to 1000 km long) suggests significant tectonic activity and potentially strong "quakes" on Mercury. NASA detected smaller scale thrust faults with a length ranging from 1 to 7 km. For such fault lengths, the estimated moment magnitude of earthquakes could range between 4.2 and 5.6 using the empirical relations proposed by Aydan (2012).

8 Characteristics of Planetary Bodies

8.1. Properties of rocks and discontinuities

As discussed in previous sections, rocks from moon and Mars are quite similar to those of Earth. In rock mechanics and rock engineering, numerous experiments on rock, rock discontinuities and rock masses have been carried out and many mechanical and engineering properties have been determined. Nevertheless, it is needless to say that we need to carry out similar experiments for extraterrestrial rocks probably in their environment. During the Apollo program, more than 300 kg rock sample have been brought to Earth. However, no mechanical experiments have been carried out yet. The Mars rovers provided many images of rocks, rock masses and discontinuities. Back analyses of many images may provide some information on the mechanical analyses. Furthermore, the back analyses of failed rock slopes and rock cliffs may further provide on strength properties of rock masses. Some of such analyses are reported by several researchers (e.g. Luccitta (1979); Schultz, 2002; Neuffer & Schultz, 2006). The force and rate of advance during drilling operations by the MERs such as Curiosity may also provide another data on mechanical properties of intact rocks.

8.1.1 Inference of Properties from Rocks broken by MERs

As shown in Figure 14a, a platy rock piece was broken due to bending stress under the weight of the MER through its metallic wheel. This type breakage can be utilized to infer bending (tensile) strength of terrestrial planetary bodies. The bending theory for beams on elastic foundations may be utilized for such purpose. If the loading is somewhat complicated, numerical analyses may be used. The simple technique might be the utilization frame type analyses capable of considering ground reaction.



(a) (b)

Fig.14 (a) Broken or fracture platy rock fragments due to weight of MERs and (b) Views of drilling tailings in Mars and laboratory on Earth.

8.1.2 Inference of Properties from Drilling and Grinding Operations by MERs

The force and rate of advance during drilling operations by the MERs such as Curiosity, Perseverance may also provide another data set on mechanical properties of intact rocks (Aydan 2022b 2023b). Particularly, the utilization of drilling performance and drill-hole tailings shown in Figure 14b and drilling performance may yield additional data on the physico-mechanical properties of rocks. Besides

empirical techniques, numerical methods may be utilized to evaluate drilling performance and back analyses the physico-mechanical properties.

8.2 Utilization of Index Test Techniques

Many index test techniques have been developed in the field of Rock Mechanics and Rock Engineering. Although the utilization of proper testing techniques is always necessary, it is almost impossible to implement them during explorations of rocks and discontinuities in other terrestrial planetary bodies. Therefore, this section addresses this issue and describes some index methods for assessing the physico-mechanical properties of rocks, available in the field of Rock Mechanics and Rock Engineering (e.g., Aydan 2012b; Aydan et al. 2014a; Ulusay et al. 2015, 2025; Aydan and Ulusay 2024), which may be utilized in the next generation exploration rovers. In addition, numerical studies require the evaluation of parameters of constitutive laws and some available techniques for such a purpose have been introduced in this sub-section.

8.2.1 Elastic Wave Velocity

When rocks are assumed to be isotropic, p-wave and s-wave velocities of samples are measured in a single direction. However, they should be measuredperpendicular to bedding (schistosity) and two mutual directions parallel to the bedding plane (schistosity) if the anisotropy is dominant. Such examples are described in literature (e.g., Aydan and Ulusay 2003, 2013; Aydan et al. 1993, 1996b; Sezaki et al. 1990, 1994; Seiki and Aydan 2003)and there are many empirical relations to establish the relations among wave velocities and strength and deformability characteristics. These type measurements may also be done by equipping the explorers with appropriate devices. If mankind gets access the exploration sites, similar devices can also be used in such explorations of the terrestrial planetary bodies.

8.2.2 Schmidt Rebound Number

Schmidt hammer, which is initially developed for concrete of civil and architectural structures, are used in Rock Mechanics and Rock Engineering applications with some modification of the devices (Seiki and Aydan 2003; Aydan and Ulusay 2024). Schmidth hammer can also be used as an index testing device in planetary explorations. Therefore, the present exploration rovers may be equipped with such devices. However, major issue would be the interrelations between the rebound value and strength and deformability properties as the gravitation fields in planetary bodies are different. When this index method is utilized, some consideration on the existence of inclusions in rock matrix should be also given as the rebound values will be different for soft/hard matrix and hard/soft inclusions. In addition, the direction of measurement must be also taken into account.

8.2.3 Needle Penetration Index Tests

The needle penetration device is developed by MARUTO Co. of Japan (Maruto Co., 1999). The device can measure the applied load up to 100 N and the penetration depth is up to 10 mm. The diameter of the needle is 0.82 mm (Ulusay et al., 2014; Aydan, 2012b; Aydan et al., 2014a). The ratio of applied load to penetration depth is called needle penetration index (NPI). The original motivation to develop this device was to assess the properties of squeezing rocks (soft rocks with UCS up to 30 MPa) in tunneling and soft rocks beneath large bridge foundations, as it is often difficult to sample rocks and to test them in laboratory. The damage caused to rock by the needle penetration is also quite negligible and the device can also be effectively used in assessing the state and properties of rocks in archeological remains excavated in/on rock mass, particularly.

Another penetration test device utilizing a low-capacity loading device and a special rod-like loading platen with a flat-end was developed by Aydan et al. (2008). The device is presently used in laboratory conditions. However, it can be easily used in field explorations. The diameter of rod-like platen ranges between 1 to 3 mm. However, experimental results indicates that there are some undesired stress concentrations when the diameter is less than 1mm and the rod-like platen may buckle when high strength rock is tested. For the interpretation of the experimental results, the nominal strain is defined in terms of penetration displacement divided by rod diameter. Furthermore, the applied stress is defined by dividing the applied load by the area of the flat-end. The device is equipped with a load cell and a displacement transducer to record load-displacement responses. In addition, an AE sensor is attached to the sample to monitor the cracking phenomenon. This device has also big potential to be utilized in explorations in terrestrial planetary bodies.

8.2.4 Equotip or Leeb Hardness (Rebound) Tests

Equotip hardness (rebound) test device was originally developed for evaluating the hardness of metals However, since 1990's it is also widely on rocks (e.g. Aydan and Ulusay 2024; Ulusay et al. 2025). The device measures the ratio of a rebound height of a small hardened steel sphere to the original drop height and the ratio is multiplied by 1000. As the test area is very small, it can be utilized in many places and it is very likely to measure also the state of matrix and inclusions in some rocks. It is probably one of suitable techniques for terrestrial explorations as it is small device and data storage should be quite easy with some small technical modifications. It should be noted that some slight damage definitely occurs beneath the impact locations always even in many hard rock samples, and, the Equotip hardness (rebound number) differs even on the same surface and the surface conditions.

8.2.5 Inference of Parameters of Elasto-plastic Constitutive Law

The analytical and numerical methods require the parameters of constitutive laws, which are not strength parameter only. In other words, some researchers mistakenly consider the constitutive laws to be only strength criteria. The determination of fundamental parameters of constitutive laws for rocks constituting terrestrial planetary bodies is almost impossible without actual rock samples. In this sub-section, the procedure for determining some important parameters based on uniaxial compression strength (UCS) is introduced.

The details of the parameters and their utilization have been described in the publications of Aydan et al. (1993, 1996b), which were initially developed for rocks of tunnels subjected to squeezing phenomenon and it was extended to high strength rocks subjected to rockburst conditions. These parameters were utilized to assess the deformation responses of various rock structures on Earth. It is also common not to find many parameters used in analytical and numerical analyses. Even for such cases, simple parameters such as uniaxial compressive strength and/or elastic wave velocity can be utilized. Sometime, elastic-wave velocity is more easily found. The procedure for determining some important parameters based on uniaxial compression strength (UCS) is introduced. Figure 15 shows the idealized strain-stress relations during deformation together with internal fracturing of rocks. As shown in Figure 16, Aydan et al. (1993, 1996b) defined some plastic deformation parameters using the strain levels for post-yielding behaviour.

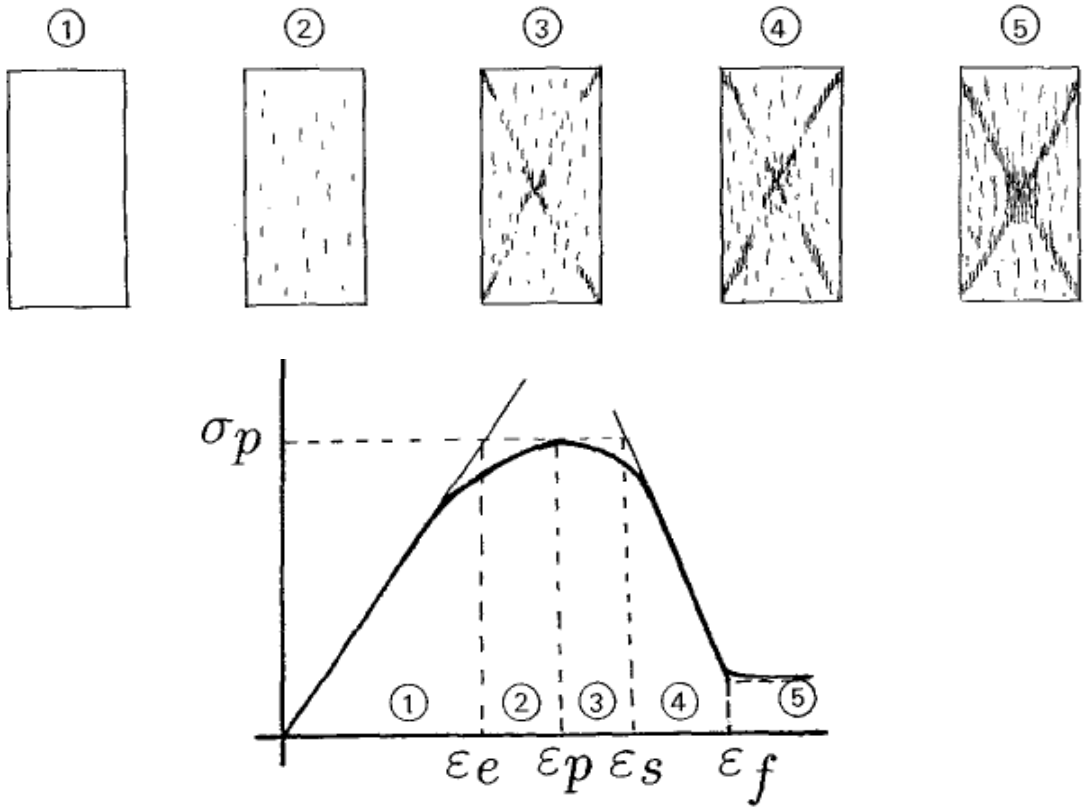


Fig. 15 The idealized strain-stress relations during deformation together with internal fracturing.

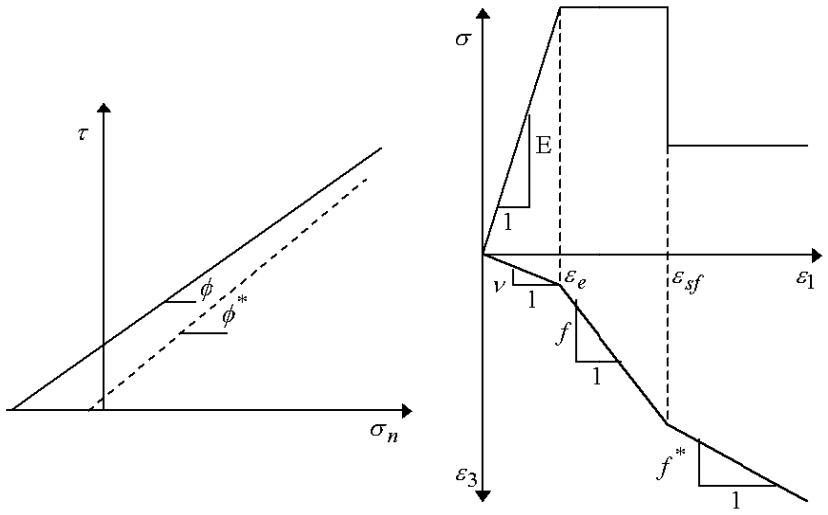


Fig. 16 Illustration of definition of plastic deformation parameters using the strain levels for post-yielding behaviour.

Therefore, the interrelation between elastic wave velocity and uniaxial compressive strength shown in Figure 17 may be utilized if there is no data on uniaxial compressive strength (UCS). However, if the uniaxial compressive strength (UCS) data is available, some of the direct relations established by Aydan et al. (1993, 1996b) and extended to high strength rocks (Aydan et al. 2001; Aydan, 2018a) shown in Figure 18, can be utilized to evaluate the parameters of post-yielding of rocks to assess the response of rock structures in other terrestrial planetary bodies using the analytical and numerical analyses. The same methodology may also be extended to evaluate the visco-elasto-plastic parameters of rock in other planetary bodies using the knowledge gained from rocks of Earth.

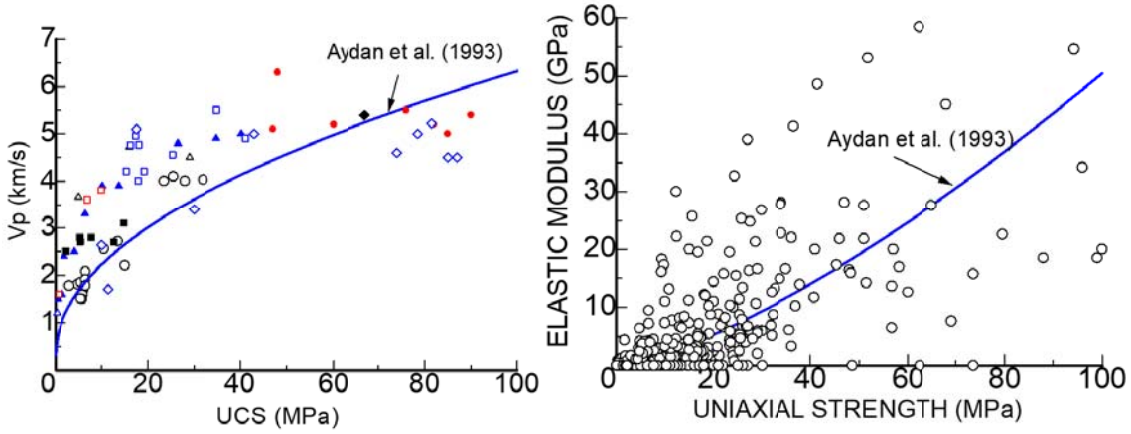


Fig. 17 Interrelations uniaxial compressive strength (UCS) among p-wave velocity and elastic modulus.

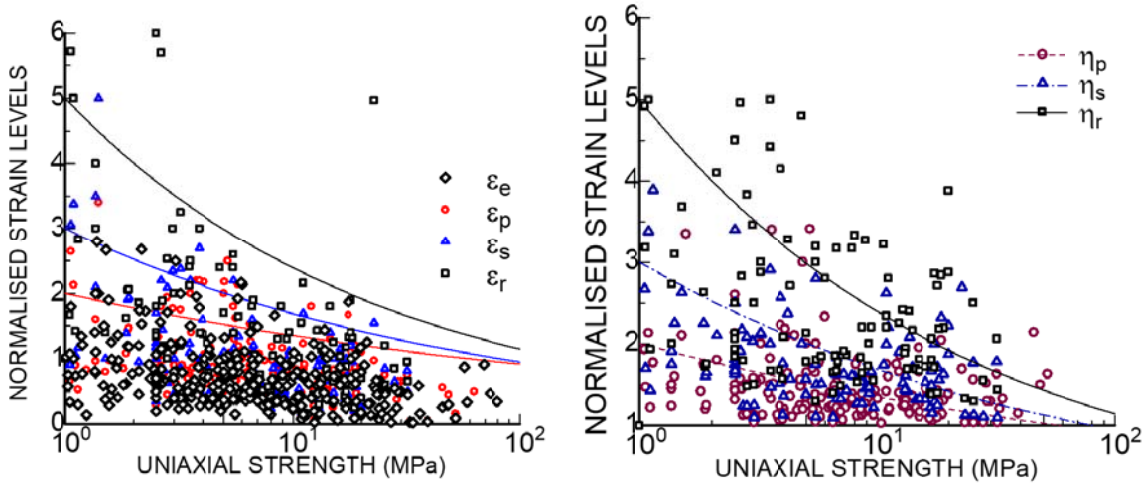


Fig. 18 Interrelations uniaxial compressive strength (UCS) among plastic behaviour parameters.

9 Conclusions

The rock mechanics aspects of Mars are quite similar to those of the Earth. The differences result from gravitational acceleration, climatic conditions (temperature, humidity, winds), thickness of atmosphere and none or limited amount of ground water. The knowledge on the behaviour of rocks, discontinuities and rock masses acquired on the Earth can be easily used in Mars with the consideration of the differences resulting from gravitation acceleration, climatic conditions and fluid in rock masses.

The knowledge on the behaviour of rocks, discontinuities and rock masses acquired on the Earth can be adopted in Mars with the consideration of the differences resulting from gravitation acceleration, climatic conditions and fluids in rock masses. On the basis of knowledge gained from rocks of Earth, the stress state of Mars is studied using an thermo-elasto-plastic behaviour constitutive model and spherical symmetric finite element method four different conditions. Although these results are preliminary, they are expected to provide some bases for future studies. The computational results clearly explain why mountains are higher in Mars compared with those on Earth and why tectonics is less pronounced in Mars.

This study is summarized the techniques to evaluate the stability of natural underground structures and sinkhole formation in Mars on the bases of some information, data and inferences obtained from the natural underground structures in volcanic areas on Earth. The available techniques and mechanical data were utilized by considering the gravitational conditions in Mars. Despite some ambiguities on material properties as well as rock mass conditions in Mars, these preliminary analyses provide some insight view of sinkholes on Mars and their possible stability situations. Undoubtedly more data and more detailed analyses utilizing numerical techniques would provide better information about the stability of caves and conditions of sinkhole formation in Mars. In addition to the conditions considered in this study, the dynamic loading conditions due to marsquakes and impacts by the meteorites will be necessary in future studies.

Acknowledgements

The author gratefully acknowledges NASA and the people involved in the development and operation of Mars exploration programs, Mars rovers, namely, Opportunity, Sprit and Curiosity and earlier rovers, and processing and releasing their images on related web-sites. Thoughts of the author are based on Images of Mars Rovers and mostly obtained from the following web-site: https://mars.nasa.gov/mer/gallery/images.html

References

Anderson, D. L., Miller, W. F., Latham, G. V., Nakamura, Y., Toksöz, M. N., Dainty, A. M., Duennebier, F.K., Lazarewicz, A.R., Kovach, R.L.,Knight, T. C. D.(1977). Seismology on Mars. Journal of Geophysical Research, 82(28), 4524-4546.

Aydan, Ö. (1993). A consideration on the stress state of the earth due to the gravitational pull. The 7th Annual Symposium on Computational Mechanics, Tokyo, 243-252.

Aydan, Ö. (1995). The stress state of the earth and the earth's crust due to the gravitational pull. The 35th US Rock Mechanics Symposium, Lake Tahoe, 237-243.

Aydan, Ö. (2000a). A stress inference method based on structural geological features for the full-stress components in the earth's crust, Yerbilimleri, No. 22, 223-236.

Aydan, Ö. (2012): Ground motions and deformations associated with earthquake faulting and their effects on the safety of engineering structures. Encyclopaedia of Sustainability Science and Technology, Springer, R. Meyers (Ed.), 3233-3253.

Aydan, Ö. (2016): An integrated approach for the evaluation of measurements and inferences of in-situ stresses. RS2016 Symposium, 7th Int. Symp. on In-situ Rock Stress, Tampere, 38-57.

Aydan, Ö. 2017. Some Thoughts About Rock Mechanics Aspects of Mars. UNSW, 3rd Off Earth Mining Forum - 2017OEMF.

Aydan, Ö. 2023. Earthquake Science and Engineering, Taylor and Francis. 494p.

Aydan, Ö., Y. Ichikawa, Y. Shimizu, and K. Murata (1991). An integrated system for the stability of rock slopes. The 5th Int. Conf. on Computer Methods and Advances in Geomechanics, Cairns, 1, 469-465.

Johnston, D.H., Toksöz, M.N., 1977. Internal structure and properties of Mars. Icarus 32, 73-84.

Latham, G., Ewing, M., Press, F., Sutton, G., Dorman, J., Nakamura, Y., Lammlein, D., Duennebier, F., and Toksöz, N. : 1971, Science 174, 687-692.

Lucchitta, B.K., 1979. Landslides in Vallis Marineris, Mars. J. Geophys. Res. 84, 8097–8113.

Nakamura, Y. (2003), New identification of deep moonquakes in the Apollo lunar seismic data. Phys. Earth Planet. Inter., 139, 197–205.
NASA 2008. Exploration: NASA's plans to explore the moon, mars and beyond. http://www.nasa.gov/
NASA 2019: Images. https://mars.nasa.gov/mer/gallery/images.html
Neuffer, P.D., Schultz, R.A., 2006. Mechanisms of slope failure in Valles Marineris, Mars. Q. J. Eng. Geol. Hydrogeol. 39 (3), 227–240.
Schultz, R.A., 2002. Stability of rock slopes in Valles Marineris, Mars. Geophys. Res. Lett. 29, 1932.
Sohl, F., Spohn, T., 1997. The interior structure of Mars: Implications from SNC meteorites. J. Geophys. Res. Planets 102 (E1), 1613–1635.
Steinberger, B., Werner, S.C., Torsvik, T.H. (2010). Deep versus shallow origin of gravity anomalies, topography and volcanism on Earth, Venus and Mars. Icarus, 207, 564–577.
Toksöz, M.N., Hsui, A.T., 1978. Thermal history and evolution of Mars. Icarus 34 (3), 537–547.
Watters, T.R. 1995. Planets: A Smithsonian Guide. MacMillan, USA, 256p.

NMT-NATM hybrid method for sustainability and risk reduction

Nick Barton,
Nick Barton & Associates, Oslo
nickrbarton@hotmail.com
0000-0002-1269-8755

Abstract

In 1992 a group of authors from Norwegian companies proposed the name NMT (the Norwegian Method of Tunnelling) as a distinctive alternative to the well-known NATM of Austria. In a nut-shell one can call NMT 'single-shell' while NATM can be called 'double-shell'. NMT is most appropriate for tunnel and cavern construction in medium to hard jointed rock. Support and reinforcement are guided by Q-system application. NATM with its final cast concrete lining can be considered most appropriate for lower quality, weathered and faulted rock.

Temporary support and reinforcement methods: shotcrete with mesh or fibre reinforcement, bolting and lattice girders (LG) are typically associated with NATM, prior to the drainage fleece, membrane and cast concrete. In the case of NMT the permanent bolting and shotcrete are deliberately chosen to be of high quality and corrosion protected and are both applied up to the tunnel face, with the final layer of shotcrete perhaps making a total thickness of 10cm also applied only a round or two behind the face. In case of poor rock conditions such as faulted rock, a more robust alternative to LG is used in NMT, called RRS (rib-reinforced shotcrete arches).These consist of systematically bolted arches of reinforcing bars typically 6 x 16mm diameter, welded to cross-bars and sprayed into the form of a thick local arch that may be repeated at 1.5 to 3m intervals. NMT may also have a final concrete lining ifthe rock mass quality is very poor such as $Q < 0.01$. In such cases cost and time involved will have approached that of NATM. Systematic high-pressure pre-injection is a frequent first stage of NMT. This radically reduces risk and actually also reduces support and reinforcement needs.

In this article a tentative NATM-NMT-NATM hybrid approach is suggested for a 'typical hard rock tunnel through a weathered hillside' as so frequently encountered for motorways in tropically weathered regions. Both ends of the tunnel would be NATM while a longer central NMT construction would save cost and time overall. Two case records will be described in which, due to unaccounted conditions, the NATM portions were over-loaded and LG folded due to high vertical loads. Risk reduction measures will be suggested. Due to overbreak effects on concrete volumes in NATM, greater lengths of NMT means greater sustainability as overbreak is not filled in the case of NMT.

Keywords

Tunnelling, NMT, NATM, Lattice girders, Overbreak, RRS.

1 Introduction

1.1 NMT and the Gjøvik cavern connection

The six-companies and seven-authors article that suggested the letters 'NMT' in 1992, was based on synthesising what was increasingly being used in tunnels in Norway following 1974 Q-system development and later acceptance by our road and rail authorities in Norway. It was a two-part publication: Barton, N., Grimstad, E., Aas, G., Opsahl, O.A., Bakken, A., Pedersen, L. & Johansen, E.D. 1992. Norwegian Method of Tunnelling. WT Focus on Norway, World Tunnelling. The Norwegian companies involved were NGI, Selmer A/S, A/S Veidekke, Entreprenørservice A/S, NoTeBy and Statkraft. Some in Norway who were left out complained about NMT and Q for several more years. In fact the prominent contractors and designers of the ongoing Gjøvik cavern were our co-authors. The 62m span cavern is shown in Figure 1 in two contexts.

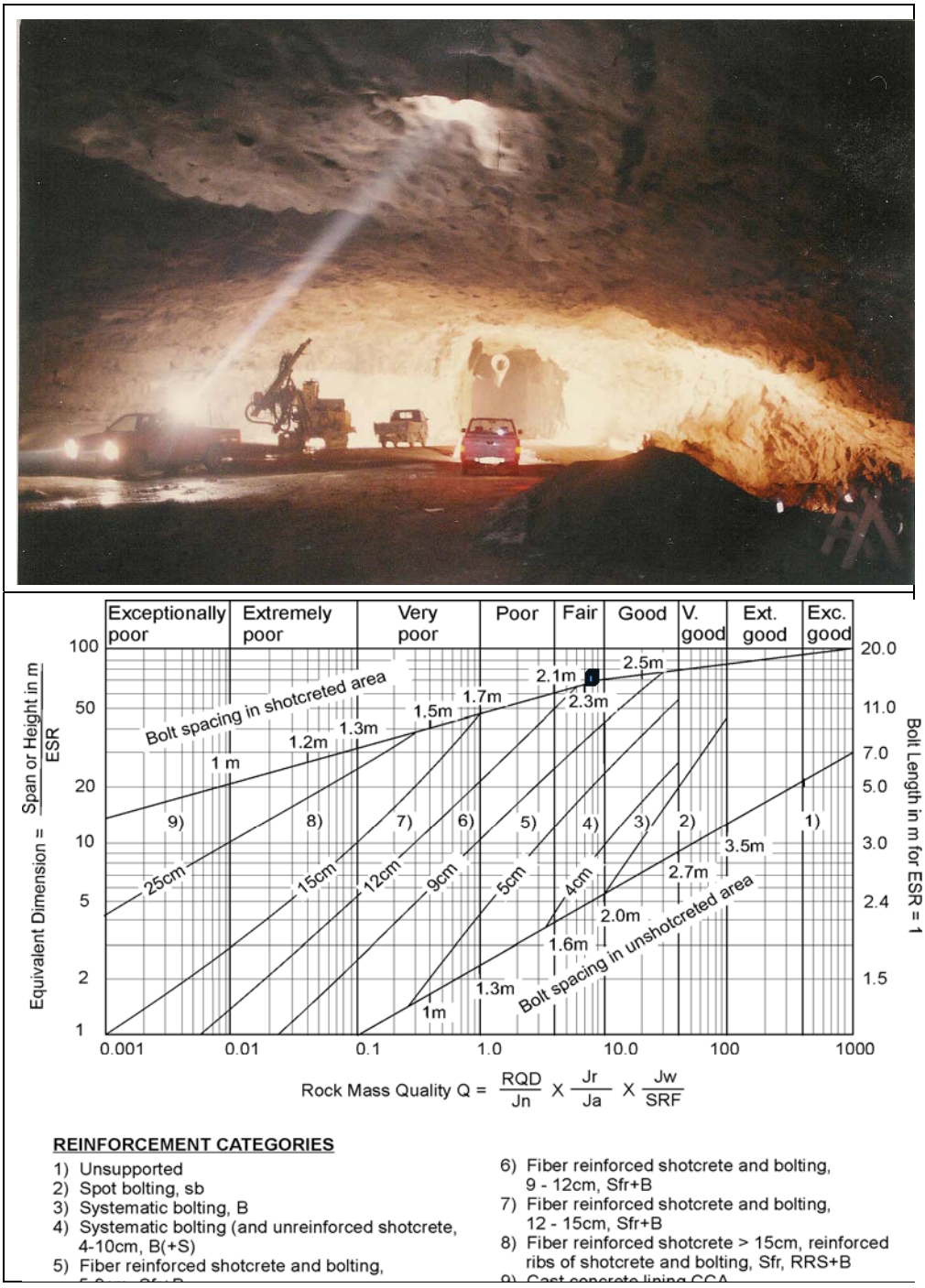


Fig. 1. The top-heading of the 62m span Gjøvik cavern with a mean Q-value of approx. 10, range 2 to 30. The dog-leg kink in the Grimstad and Barton (1993) Q-based support diagram was due to Gjøvik and its extreme span in rock of fair to good quality.

2 NMT components B plus S(fr) plus RRS

The components of NMT can be most conveniently illustrated by photographs and diagrams, as in Figure 2. On the left: S(fr), S(mr) – not favoured, and CT-bolts. RRS examples are shown on the right.

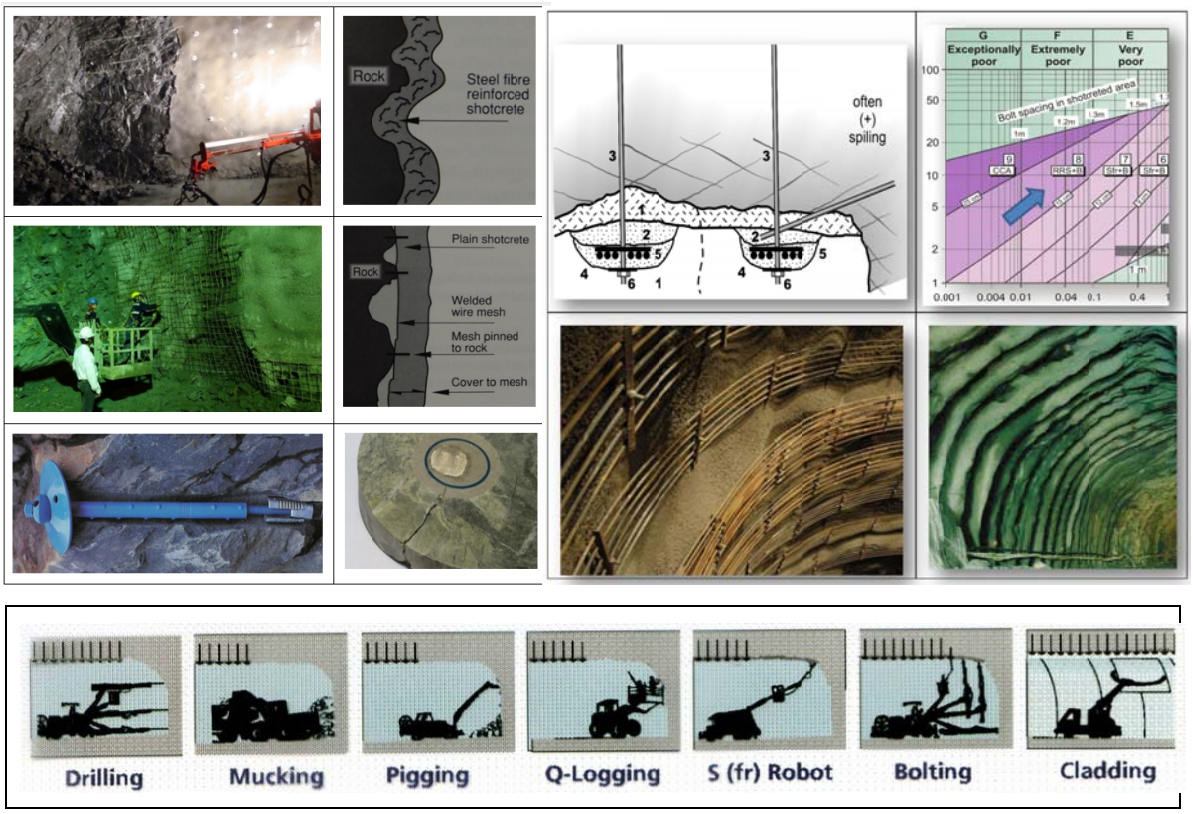


Fig.2 In the NMT method the clear preference since about 1980 has been S(fr) rather than S(mr) as this increases longevity. The graphic drawings of S(fr) and S(mr) (mid-left) are from Vandevall (1990). The longevity argument also applies to the CT-bolt, with the short blue demo photographed bottom-left. In the right-hand panels RRS is illustrated. Their design is detailed in Figure 3. Note the bending for architectural reasons. (National Theatre Station, Oslo). This 28m station cavern was constructed beneath a deep clay-filled depression. For convenience no overbreak is shown. In reality if there had been overbreak both bolting and shotcrete would follow the overbreak, which is not filled.

The PVC-sleeved CT-bolts are typically 3m up to 6m length. They have four layers of corrosion protection even after joint deformation: galvanizing, epoxy paint, outer annulus of grout (may be cracked due to joint deformation during the next tunnel advance), PVC sleeve, inner annulus of grout. The drilling, mucking, scaling, followed by Q-logging ('the owner's half hour'), S(fr) application by robot, and CT-bolting are illustrated in the lower diagram.

In the case of roads with heavy traffic PC-element cladding with outer membrane may be used. One may then be looking at a total of 10cm of shotcrete and 25cm of concrete, compared with obviously more in the case of NATM. This is because with NMT overbreak is not filled. The permanent reinforcement effect of bolting (CT-type) in NMT means that cast concrete lining is only used in exceptionally poor conditions (e.g. $Q < 0.01$).

In a later section of this paper the security of systematically bolted RRS arches in bad rock driven by NMT principles will be compared with the obviously faster application of lattice girders in NATM. The convenience of LG is appreciated but they are not recommended in the case of NMT for reasons that will become clear when considering their relative deformability. NMT principles are based on early application of permanent support and therefore small deformations. Only in major cavern construction will deformation monitoring be considered necessary. There were 7 pre-installed MPBX in the case of the Gjøvik cavern, and three shorter MBX installed in the top-heading.

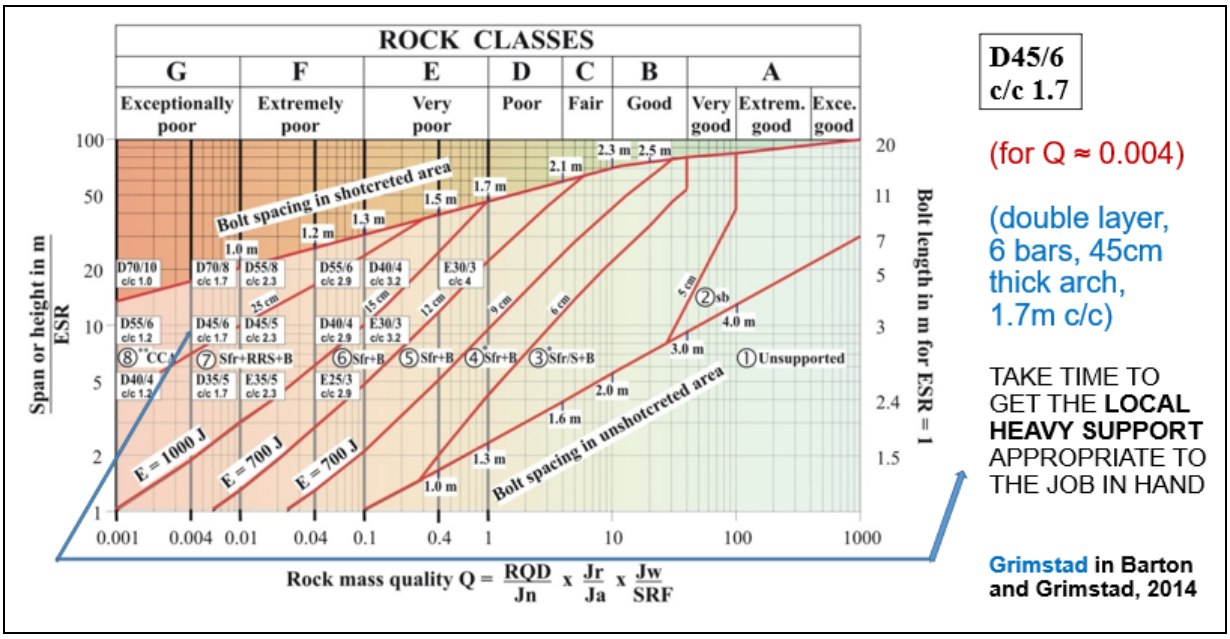


Fig. 3 The Q-system based design chart details, especially of RRS, from Grimstad.

3 NATM components

Figure 4 illustrates the various stages of NATM tunnel construction, with typically a top-heading and benching approach. It may be sequential split face in the case of soil-like conditions.

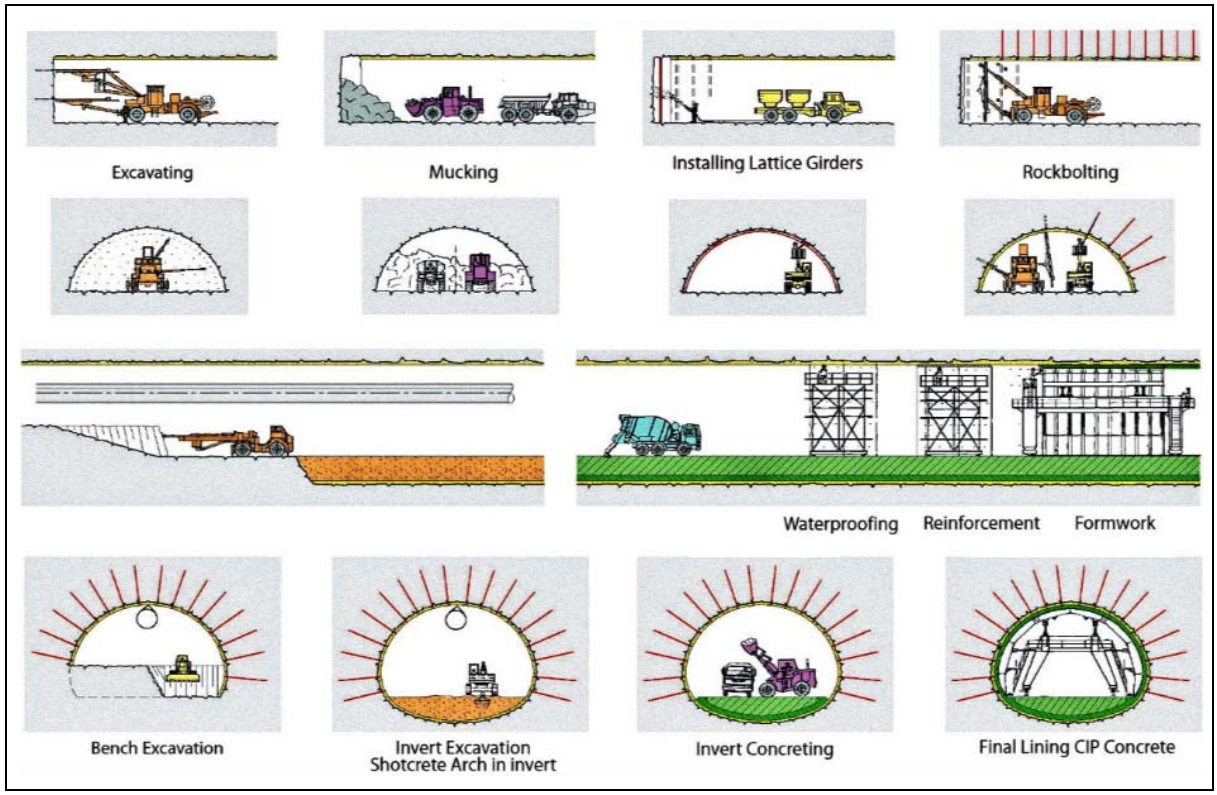


Fig. 4 Eight of the activities occurring with NATM tunnel construction when top-heading followed by benching are utilized. This is a coloured version of the official ASG (2010) report. Note no overbreak.

Note that overbreak has been ignored in the drawings but may severely affect shotcrete and concrete volumes in practice. In Figure 5, potential major overbreak has been sketched, and actual overbreak photographed. Readers may assume it has been exaggerated. However, 0.5m, 1m, 2m and even 3m are occasionally experienced in jointed rock. It depends on the ratio of Jn/Jr from the Q-system (Fig. 6).

4 Overbreak challenges

As with all tunnelling in jointed rock there is the problem of overbreak, and as will be clear from Figure 5 this is a minor problem with NMT as overbreak does not need to be filled, while for NATM it results in a potentially large volume of 'extra' shotcrete and concrete as the over-break has to be filled. Overbreak is also problematic for LG contact with the rock and may also present a '3D' challenge for drainage fleece and membrane installation prior to the concrete lining.

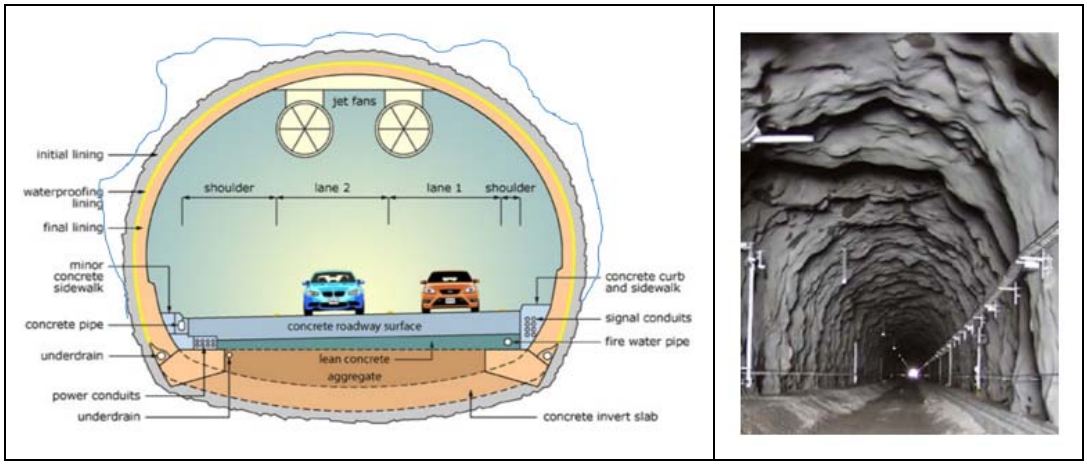


Fig. 5 A perhaps exaggerated addition of overbreak to an NATM tunnel (left), while overbreak >1m is clearly accepted in this Swedish rail tunnel where Q + S(fr) + B (= 'NMT' in practice) was used.

Figure 6 illustrates by means of a drawing (top-left), by means of joint roughness profiles (top-right) and by means of two photographs of significant overbreak with ratings for Jn/Jr = 9/1.5 why overbreak occurs when sufficient numbers of joint sets and sufficiently planar-surfaced jointing are present.

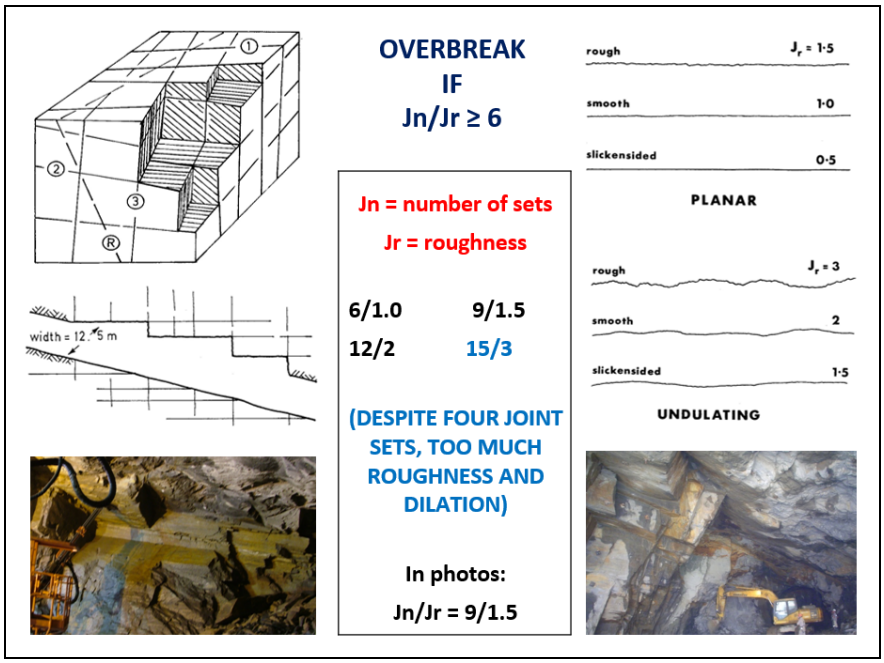


Fig. 6 A simple criterium for the likelihood of overbreak occurring in tunnelling. This influences cost (more shotcrete in NMT, more concrete in NATM) and therefore sustainability. The black ratios of Jn/Jr will be likely to suffer overbreak, but not the blue example as < 6.

In the case of mining, overbreak will affect drift and roadway stability with possible increases of shotcrete support, and in the context of underground stoping perhaps the threat of not only increased dilution but also blockage of draw-points. Figure 7 illustrates Q-histogram logging at the Kiruna Oscar project where long-hole drilling drifts were severely affected by overbreak and near failure as sketched in the central panel.

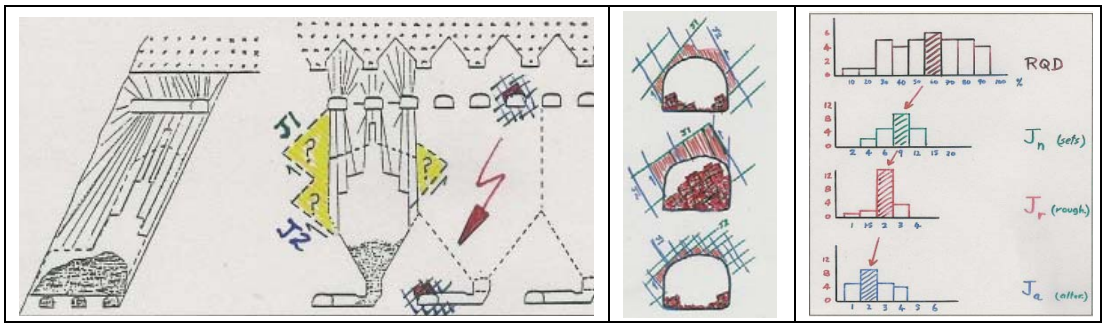


Fig. 7 Overbreak effects at Kiruna LKAB Oscar long-hole drilling Project. On this occasion in 1987 the author used Q-parameter histogram logging to characterize the likelihood of overbreak or stability problems. Most-frequent ratings for RQD, Jn, Jr and Ja of 60, 9, 2 and 2 did not explain the strong overbreak. However, with extreme values like Jn = 12 and Jr = 1 or 1.5, also assisted by Ja = 3 or 4, excessive over-break and near drift collapse in some cases was explained in a logical manner.

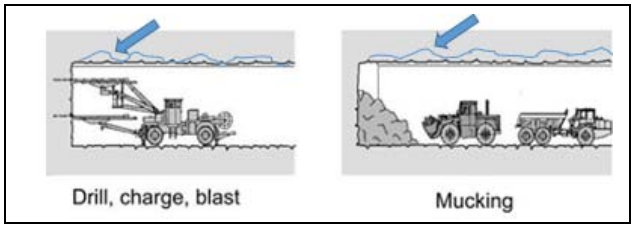


Fig.8. Overbreak affects NMT and NATM in different ways due to the final concrete of NATM.

5 Shear strength determines tunnel reinforcement and support needs

The ratio Jr/Ja seen in Figure 9 is remarkably close to being a friction coefficient. It is obviously also a potential parameter for indicating the increased (or decreased) likelihood of overbreak and increased (or decreased) amounts of shotcrete in NMT (periphery length increased, or not) and of increased volumes of concrete (or not) in the case of NATM. Jr/Ja therefore also affects sustainability.

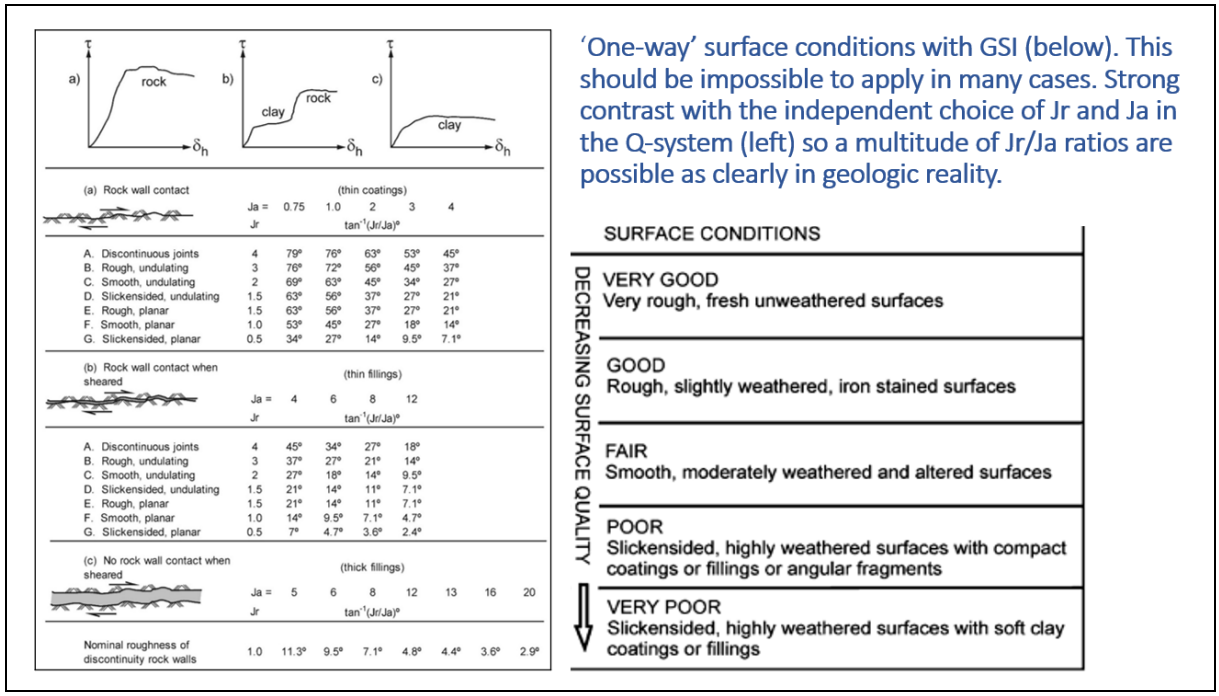


Fig. 9 The Q-parameter pair Jr and Ja are also important indicators of overbreak potential as well as the ratio of Jn/Jr. Note that the 'joint condition' ratio in Q is in another class of reality compared to the 'x-axis' in the GSI diagram of Hoek (or Hoek and Marinos). As seen on the right rough joints cannot be clay filled or be in weathered rock while smooth-planar joints have to be in weathered rock and also be clay filled. It is not clear to the author how users of GSI get around this severe limitation (basically an elimination of much of engineering geology) in practice.

Readers may be aware that the formula for the Q-value can be generalized by normalizing Q with UCS/100. Q_C is defined as Q x σ_c/100 with compression strength expressed in MPa. It was found (Barton, 1995 and Barton, 2006) that Qc correlated much better than Q with P-wave velocity and with the stress or depth-dependent deformation modulus. The seven-parameter equation forQc = RQD/Jn x Jr/Ja x Jw/SRFxσ_c/100 can be 'cut in half' and appears to approximately lly represent the cohesive component (CC) and the frictional component (FC) of rock masses as suggested in Table 1 and Figure 10.

Table 1. Left: The Qc-based equation 'cut in half' to represent the cohesive and frictional strength of rock masses, contrasted with the Hoek-Brown equations for the supposed 'c' and 'ϕ' of rock masses. Right: These three supporting equations mean that GSI is repeated 16x and 12x in the H-B equation of shear strength. However if two further supporting equations (e.g. for σ'_{3n}) are included, we see a remarkable 78x repetition of GSI, which is already a limited descriptor of rock mass quality.

Expression	Origin
$\varphi \approx \tan^{-1}\left(\frac{J_r}{J_a}\times\frac{J_w}{1}\right)$	FC from Q
$\varphi' = a\sin\left[\frac{6am_b(s+m_b\sigma'_{3n})^{a-1}}{2(1+a)(2+a)+6am_b(s+m_b\sigma'_{3n})^{a-1}}\right]$	From GSI
$c \approx \left(\frac{RQD}{J_n}\times\frac{1}{SRF}\times\frac{\sigma_c}{100}\right)$	CC from Q
$c' = \frac{\sigma_{ci}\left[(1+2a)s+(1-a)m_b\sigma'_{3n}\right](s+m_b\sigma'_{3n})^{a-1}}{(1+u)(2+a)\sqrt{1+[6am_b(s+m_b\sigma'_{3n})^{a-1}]/[(1+a)(2+a)]}}$	From GSI

$$c' = \frac{\sigma_{ci}\left[(1+2a)s+(1-a)m_b\sigma'_{3n}\right](s+m_b\sigma'_{3n})^{a-1}}{(1+a)(2+a)\sqrt{1+(6am_b(s+m_b\sigma'_{3n})^{a-1})/(1+a)(2+a)}}$$

$$\phi' = \sin^{-1}\left[\frac{6am_b(s+m_b\sigma'_{3n})^{a-1}}{2(1+a)(2+a)+6am_b(s+m_b\sigma'_{3n})^{a-1}}\right]$$

$$m_b = m_i\exp\left(\frac{GSI-100}{28-14D}\right) \quad s = \exp\left(\frac{GSI-100}{9-3D}\right) \quad a = \frac{1}{2}+\frac{1}{6}\left(e^{-\frac{GSI}{15}}-e^{-\frac{20}{3}}\right)$$

Figure 10 shows four potential rock masses with successively decreasing rock mass quality and rock strength due to strongly decreasing Qc. The suggested equations for FC and CC are evaluated and given tentative units of degrees ° and MPa. It is interesting to note that the classic Mohr-Coulomb equation of 'c + σ_n tan ϕ' (which actually fails to describe the strength of rock masses as cohesion has to be broken before friction can be mobilized) is in the case of Qc replaced by 'CC x tan FC' – so the potential cohesive strength is modified (reduced, or sometimes increased) by the frictional strength – a not illogical criterium. The components 'c' and σ_n tan 'ϕ' are not added as in M-C and H-B.

RQD	J_n	J_r	J_a	J_w	SRF	Q	σ_c	Q_c	FC°	CC MPa	V_p km/s	E_{mass} GPa
100	2	2	1	1	1	100	100	100	63°	50	5.5	46
90	9	1	1	1	1	10	100	10	45°	10	4.5	22
60	12	1.5	2	0.66	1	2.5	50	1.2	26°	2.5	3.6	10.7
30	15	1	4	0.66	2.5	0.13	33	0.04	9°	0.26	2.1	3.5

Four rock masses with successively reducing character: more joints, more weathering, lower UCS, more clay.

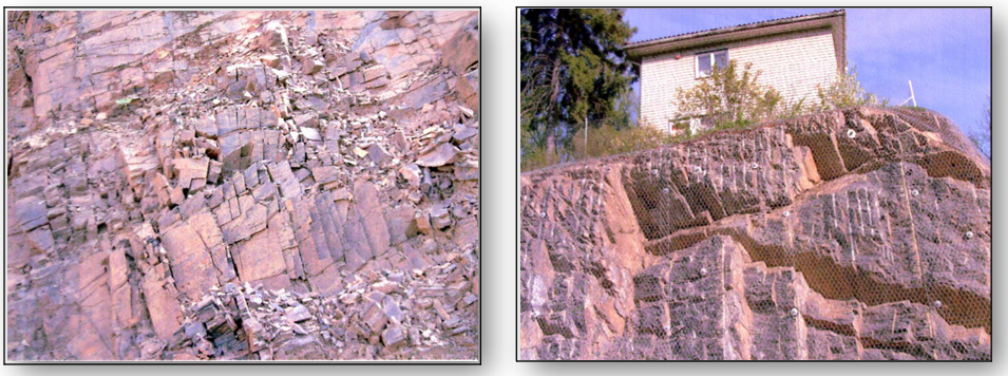


Fig. 11 Top: Four example rock masses with decreasing quality and decreasing rock strength and the apparent realism of the FC and CC estimates of frictional and cohesive strength. Rock masses with low CC need relatively more S(fr) (such as urgently needed for the shale in the left photograph) and rock masses with low FC need relatively more bolting (such asthe massive limestone in the right photograph which has only bolting).The FC and CC components of Qc correspond closely to the original 'conditional factors' for choosing more or less shotcrete and more or less bolting in the original Barton et al. 1974 Q-system tunnel support tables.

6 Choice of tunneling depth as potentially serious consequences

Some years ago the author presented a paper in Hong Kong with the title: '*The Shallow Metro Syndrome'*. This was in response to several years following a new metro line in São Paulo, Brazil: Linha 4-Amarela on behalf of the contractor consortium. Despite warnings by several other experts, the designers and owners had apparently prioritized 'short escalators' perhaps having concern for passengers' experiences and future maintenance costs. They apparently failed to understand the time and cost consequences of mixed-face tunnelling through saprolite, clay, granite or gneiss, choosing the adverse elevation/shallow depth where each could be met in the same tunnel face. The project suffered years of delays and cost overruns. In London, long escalators are needed to reach London clay, the cheapest and most stable tunnelling medium. The long escalator rides are entertaining due to adverts.

One of the São Paulo Linha 4 station caverns in granite suffered 2 to 4m over-break (Figure 12). The other end of the station was in clay. The shallow location of the tunnels and stations had enormous consequences on cost and delay and indirectly cost seven lives at the next station about 1km away. Lattice girders and shotcrete were overcome by the vertical loading from an unanticipated 10m high ridge of 'differentially *less-weathered*' gneiss. It was not discovered despite five nearby boreholes on either side of the planned station cavern, and one even on the axis of the future cavern. In retrospect cross-hole seismic tomography should have been attempted. Refraction seismic failed due the very noisy 24/7 environment next to five lanes of traffic. Figures 13 and 14 show the tragic consequences.



Fig. 12 Shallow metro consequences: mixedface, overbreak, potential collapse through to the surface.

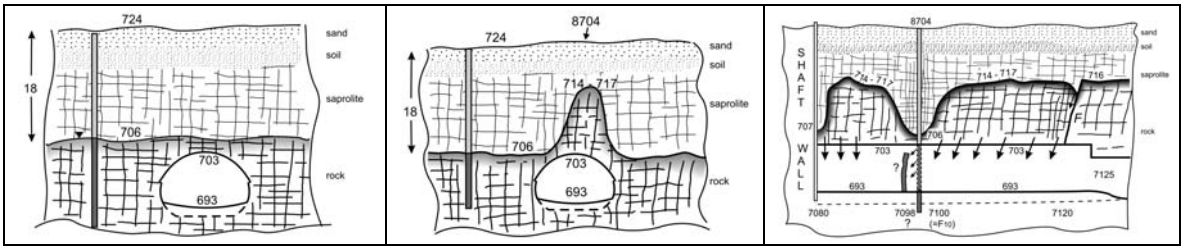


Fig. 13 a, b, c. Five boreholes surrounding or within the planned station cavern failed to reveal the presence of a ridge-of-rock, which had a 'fatal' fracture zone along its axis. All five boreholes suggested just 3m of rock cover. The undiscovered 10m high ridge-of-rock was the result of differential weathering. 'Robust' LG of 32mm x 25mm x 25mm embedded in 30-40cm of S(fr) suddenly folded, allowing the less weathered ridge-of-rock to fall 10m.

The massive collapse seen in Figure 14 caused five people driving in a minibus to be sucked into the sudden failure. Their vehicle was not found for 12 days as it had been sucked to a lower level than most of the surrounding sand and clay. The falling ridge-of-rock had a piston-like effect. A tunnel worker was blown over some distance from the sudden cavern collapse. Two pedestrians were also sucked into the collapse.



Fig. 14 The collapse of the Pinheiros Station cavern during construction. The fatalities occurred along the small road (Rua Capri) seen on the right. Five boreholes had failed to detect the 10m high ridge of less weathered rock that was hidden beneath the cavern axis drawn on the left photograph.

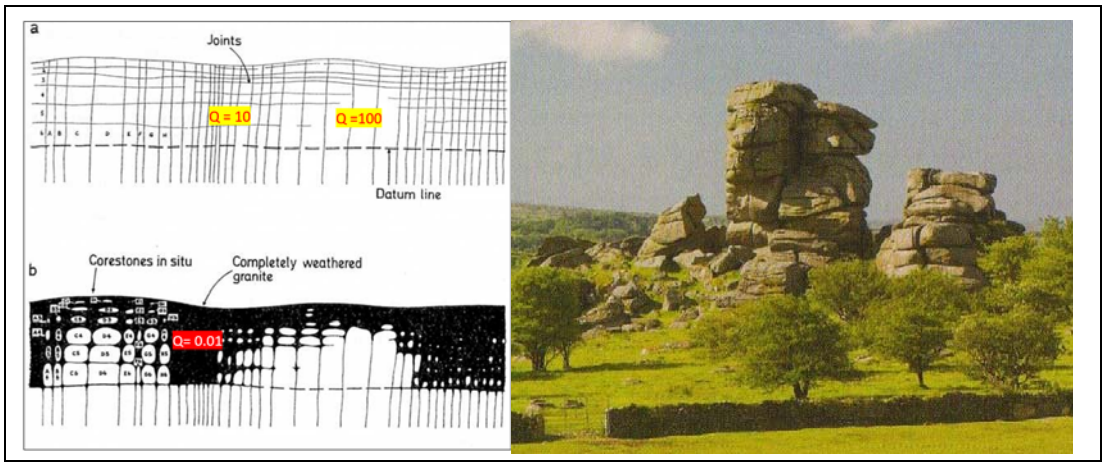


Fig. 15 Two drawings from 'The problem of tors' by Linton (1955) have been given possible Q-values to demonstrate the possible morphological progression to core stones, in this case to dangerous ridges of less weathered rock that can load tunnel or cavern support if too shallow excavations are planned. The tor photograph from S.W. England with a chance 'central' fracture is a potential model for the tragically missed ridge-of-rock (Figure 13c).



Fig. 16 This shows the top of the loosened 'ridge-of-rock' *after* it had fallen 10m to the cavern floor.



Fig. 17 Before and after. The same lattice girders of 32mm x 25mm x 25mm dimensions appear to have limited strength when confronted with a large concentrated vertical load. Designers are usually assuming a rare evenly distributed load. In this case a very high vertical loading was experienced due to an extreme 'ridge-of-rock' core stone phenomenon. This was not discovered in the police-led investigations.

On another occasion contractors tunneling for a motorway city bypass through presumed jointed granites had to tackle deeply weathered (saprolitic) materials at each end. So in principle NATM solutions were chosen for the first 150-200m at each end of the tunnel, and NMT-style Q-based B + S(fr) in the central hard rock kilometers in jointed granite. The unfortunately over-simplified design for the 'NATM' sections is illustrated in Figure 18. Regrettably both the sloping ground and vertically oriented phyllite and a dike (neither were discovered) were not modelled. Approximately 140m of the right tube collapsed on a Saturday afternoon when all the tunnelers were at a God-given barbeque so a tragedy was avoided. Three months later 140m of the parallel tunnel also collapsed. There were no casualties as the site was closed pending a hearing. The more realistic UDEC model by Bandis is illustrated in Figure 19.

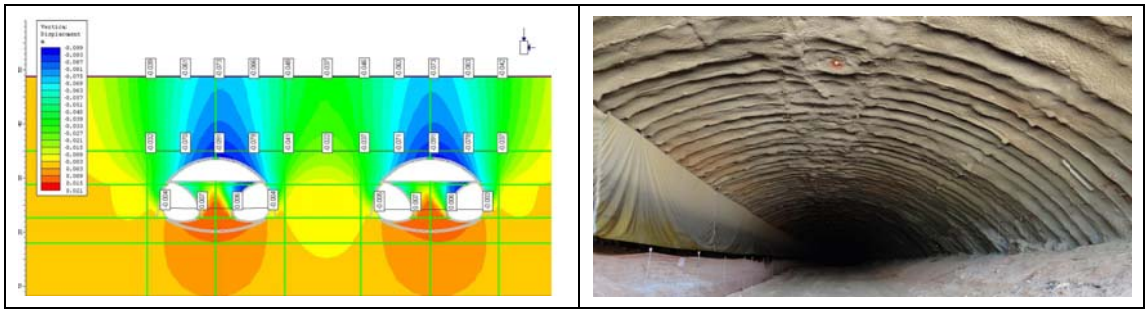


Fig. 18 Optimistic symmetric design, when actually sloping ground. Light lattice girders. No bolts due to saprolite. Much more than specified shotcrete thickness due to 30 to 80cm of over-break. This is the second tube. 140m collapsed three months after the 1st 140m collapse. Again, lattice girders folded.

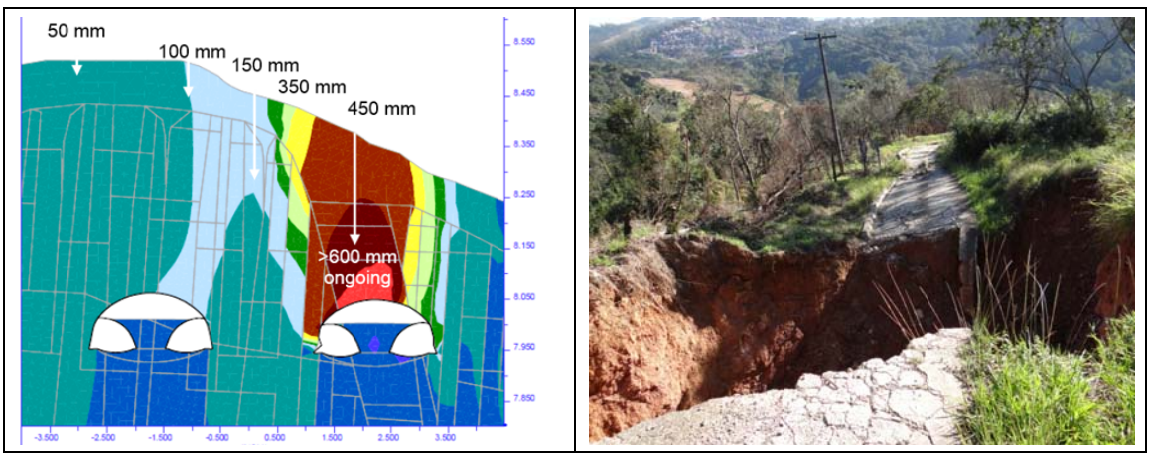


Fig. 19 When the vertical structure (and sloping ground) was modelled the imminent failure is understood. The photograph is after the 2nd tube collapse. UDEC modelling by Bandis.

7 Steel sets and lattice girders invite and need deformation to function

Why lattice girders may allow significant deformation is suggested in the instrumented tunnel results from Ward et al. 1983 shown in the left diagram of Figure 20. Firstly, reinforcing any rock mass with systematic bolting and holding it in place with shotcrete (solving the frictional strength/weakness and cohesive strength/weakness) is obviously positive, as proved by the top experimental results of 2-3mm.The circular steel ribs result show how poorly steel sets are working. Rockmass deformation and loosening and potentially reduced rock mass strength is needed before the tangential strain builds in the LG so that it can finally resist radially. Elephant feet must also resist the axial load in the LG.

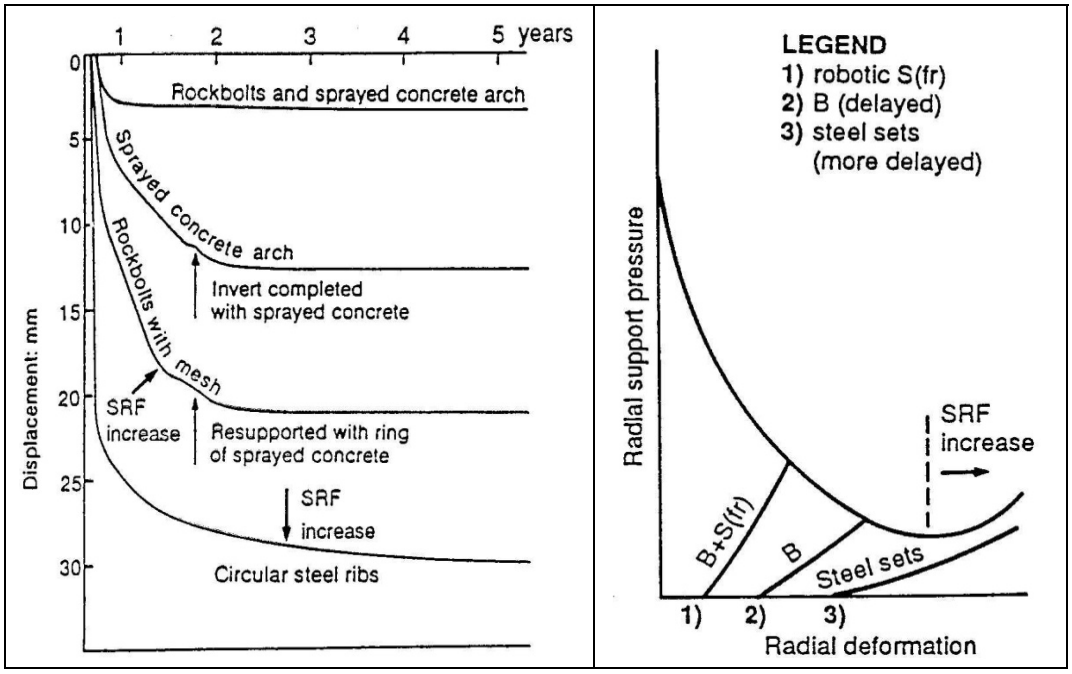


Fig. 20*Left:* Avoidance of steel sets (or lattice girders) remains an important advisory for NMT Q-system users. The instrumented experimental tunnel was driven in mudstones. Figure from Ward et al. 1983. *Right:* Steel sets and lattice girders allow and even require loosening of the rock mass to make better contact, i.e. an increase of SRF in the Q-value. Barton and Grimstad, 1994. The use of steel sets with constant spacing so not allowing for faulted rock, i.e. increased loading, can cause tragic collapses as seen in Figure 21.



Fig. 21 Collapse in partly completed down-stream surge chamber arch in Bhutan. Tragically, six workers were caught in the collapse. First collapse ≈ 35,000 m^3. There was an attempt to remove fallen rock (approx. 15,000 m^3 was removed). Note the extra destruction of steel sets in the 'left' arch due to the fault. A larger collapse subsequently occurred.

The total volume of collapsed rock mass finally reached approx. 70,000m^3, basically initiated due to constant steel set spacing despite changed conditions. As a point of difference when using NMT there is a specific 'owner's half-hour' when engineering geologists representing both sides (owner and contractor) map conditions together and try to agree on the Q-based 'support class'. This occurs after every blast.

In this section a potential source of weakness of NATM has been identified by means of the exceptional design challenges illustrated. It surely must be assumed that lattice girders leave some room for improvement as they do not seem to be stiff enough. Most frequently a 'triangular' format with e.g. 32, 25, 25 mm bars, or a much lighter version: 20, 16, 16mm bars are supposed to add

stability to the shotcrete they reinforce once sprayed in. Figures 17 and 18 show initial deficiencies here with presently insufficient shotcrete. An obviously delaying but much more robust solution is to use a 'rectangular' bundle of four equal bars or 2 + 2 of different diameter *and bolt them into the arch.*

The key structural change would be the ease of mounting / welding a cross-piece with a central bolt hole. In other words bolting the unconventional 4-bar LG in a similar way to RRS (Figure 2: mid-right). This would take longer but would be 'an order of magnitude' safer. The bolting would be an integral part of the bolt reinforcement of the tunnel or cavern arch, as it is in the case of the RRS which is used with NMT if rock mass conditions are very unstable, for instance due to faulting.

8An example of failed NMT due to water velocity

On occasion there are of course collapses with NMT.A Canadian tunnelling consultant recently suggested that Norwegians should not consult outside Norway. In 'reply' it was suggested that he should stay in Canada also. (Barton, Grimstad and Panthi, 2024). Collapses have been experienced in major fault zones where failure to recognize the greatly reduced quality has been the cause. Even failure to identify clay in discontinuities in a sub-sea tunnel. There have also been cases where the design company has not understood the functions of SRF, resulting in multiple collapses of a 'so-called' NMT. An Australian author once criticised Q/NMT because of a cavern collapse, most likely due to the fact that the bolts were ungrouted. Ungrouted bolts and failure to recognise swelling clay resulted in major collapses on another continent. In several projects where asked to give independent opinions, 'painting with shotcrete' (1mm to 5mm?) has been the obvious cause of local collapses. This is a very serious corner-cutting operation made by occasional sub-contractors in several countries.

The case to be described here is due to failure of the designer to recognise that diversion tunnel water velocities as high as 10m/s and even 12m/s are far too high without at least invert erosion protection. Insult was added to injury by the 'design' (or poorly-considered drawing) of a sharp bend in the tunnel close to a fault zone. Obviously water in a 12 x 14m diversion tunnel will exert a huge force on the walls when travelling at 36-40km/hr and forced round a sharp bend. The original Q-system case records from hydropower projects were generally based on 1.5 to 2.5m/s headrace tunnel velocities and no sharp bends. The low velocity is to prevent debris transport, so no 'rock in the turbines'!



Fig. 22 A cascade of tunnel failures occurred at Hidroituango, Colombia, starting with the conical feature and ending in flow of rock debris through the powerhouse and transformer hall. A 2.5 billion dollar claim and 4 years delay were the final result of the simple design error. Note sharp bend.

9 Conclusions

1. Single-shell NMT and double-shell NATM can provide valid solutions to the three principal parts of a typical tunnelling project: the two portal areas in weathered rock and the usually much longer central section of a tunnel that is generally in higher quality rock.

2. By its very nature NATM is more expensive and less sustainable in terms of the volume of concrete needed in the portal areas. This is because overbreak needs to be filled in the case of NATM but not in the case of NMT.

3. Lattice girders are considered to be deformation enhancing because radial support pressure is not immediately developed. Stiff footings (elephant feet) are needed, contact with the rock arch is necessary through diligent shotcreting, followed by build-up of tangential strain along the structure and finally the desired radial but mostly passive support.

4. The design of lattice girders can be improved if a rectangular 4-bars system is used with a welded plate and bolt hole. Systematic bolting of lattice girders would be 'a delaying factor' as it is with RRS in the case of NMT, but the support and reinforcement effects would be enormously improved, and the effects of non-uniform loading much reduced.

References

Austrian Society for Geomechanics (2010) NATM: The Austrian Practice of Conventional Tunneling.

Barton, N., Lien, R. & Lunde, J. (1974) Engineering classification of rock masses for the design of tunnel support. Rock Mechanics. 6: 4: 189-236.

Barton, N., Grimstad, E., Aas, G., Opsahl, O.A., Bakken, A., Pedersen, L. & Johansen, E.D. (1992) Norwegian Method of Tunnelling. WT Focus on Norway, World Tunnelling, June: 6p. August: 5p. 1992.

Barton, N. & Grimstad, E. (1994) The Q-system following twenty years of application in NMT support selection. 43rd Geomechanic Colloquy, Salzburg. Felsbau, 6/94, 428-436.

Barton, N. (1995) The influence of joint properties in modelling jointed rock masses. Keynote Lecture, 8th ISRM Congress, Tokyo, 3: 1023-1032, Balkema, Rotterdam.

Barton, N. (2006) *Rock Quality, Seismic Velocity, Attenuation and Anisotropy.* Taylor & Francis, UK & Netherlands, 729 p.

Barton, N. and E. Grimstad. (2014) Q-system - an illustrated guide following forty years in tunnelling. Web site www.nickbarton.com 43p.

Barton, N., E. Grimstad, and K. Panthi, 2024. Viewpoint - response to Brox opinion on foreign application of Norwegian Tunnelling Method. (Response to article: 'Key principles for hydropower tunnel design, construction and operation' by D. Brox, published in H&D Issue 4, 2024. H&D Issue 5, 2024.

Grimstad, E. & Barton, N. (1993) Updating of the Q-System for NMT. Proceedings of the International Symposium on Sprayed Concrete - Modern Use of Wet Mix Sprayed Concrete for Underground Support, Fagernes, 1993, (Eds Kompen, Opsahl and Berg. Norwegian Concrete Association, Oslo, 46-66.

Linton, D. L. (1955) The problem of tors. Geographical Journal, 121, 470-487.

Vandevall, M. (1990) *Dramix - Tunnelling the World*. NV Bækert S.A.

Ward, W. H., Tedd, P., & Berry, N. S. M. (1983) The Kielder experimental tunnel: final results. Géotechnique, 33(3), 275–291

CO_2 Sequestration and Mineralization in Basalts in Eastern China: Prospects, Constraints and Challenges

Fengshou Zhang
Tongji University, Shanghai, China
fengshou.zhang@tongji.edu.cn
0000-0002-4998-6259

Abstract

Basalt-hosted CO_2 mineralization has emerged as a promising geological storage pathway due to its high storage permanence and low long-term leakage risk. In eastern China, widespread Cenozoic basalt formations are located close to major industrial emission clusters, providing favorable source-sink matching for near-source carbon storage. This study presents an integrated assessment of the prospects, constraints, and challenges of CO_2 sequestration and mineralization in eastern China basalts, with a site-specific investigation of the Bailonggang-Sanjiagang basalt system in the Shanghai coastal region. Geological characterization reveals strong vertical heterogeneity in lithofacies, mineralogical composition, and porosity-permeability properties, which fundamentally control reservoir accessibility and storage performance. Batch reaction experiments on representative basalt samples from Shanghai and Zhanjiang confirm effective CO_2 mineralization through carbonate precipitation, demonstrating strong mineralization potential in buried basalt reservoirs. Site-scale storage assessment under dissolved CO_2 injection indicates a realizable storage capacity of 75.10 Mt, while showing that practical storage capacity is governed primarily by effective pore accessibility and injectivity rather than by reactive mineral availability alone. Coupled reactive transport analysis further reveals dynamic porosity evolution during injection, characterized by an initial dissolution-enhanced stage followed by precipitation-induced self-sealing, which directly affects injectivity sustainability and mineral trapping efficiency. The results highlight that reservoir heterogeneity, reactive transport evolution, and mineralization-induced geomechanical responses represent critical constraints on field-scale deployment. Future development of basalt-hosted CO_2 mineralization in eastern China requires improved multi-scale THMC coupling, reliable upscaling from laboratory characterization to field deployment, and adaptive data-informed injection management to improve long-term storage efficiency and operational safety.

Keywords

CO_2mineralization, Basalt reservoirs, Geological carbon storage, Reactive transport.

1 Introduction

Geological carbon storage has been widely recognized as an essential pathway for mitigating anthropogenic carbon dioxide (CO_2) emissions and achieving carbon neutrality targets (IPCC, 2005). Among the various storage mechanisms, mineral trapping has attracted increasing attention because it offers the highest degree of storage permanence by converting injected CO_2into thermodynamically

stable carbonate minerals (Matter et al., 2016; Kelemen et al., 2019). Compared with conventional structural trapping in sedimentary reservoirs, where CO_2remains in mobile gaseous or supercritical phases and long-term containment depends strongly on caprock integrity, mineralization storage in mafic rocks provides an intrinsically safer alternative by immobilizing CO_2 through water-rock reactions (Gislason et al., 2010; Snæbjörnsdóttir et al., 2020). In particular, basalt formations are considered highly favorable for carbon mineralization because they are rich in Ca-, Mg-, and Fe-bearing silicate minerals, which can rapidly dissolve under CO_2-rich aqueous conditions and precipitate stable carbonate phases, thereby enhancing storage security and reducing long-term leakage risks.

Field-scale demonstrations have provided compelling evidence for the feasibility of basalt-based CO_2 mineralization storage. The CarbFix Project in Iceland showed that more than 95% of injected CO_2 could be mineralized within two years under favorable hydrogeochemical conditions (Matter et al., 2016), while pilot-scale injection tests at Wallula Basalt Pilot Project further demonstrated the operational viability of sustained injection and in situ carbonation (White et al., 2020).These successful cases have significantly advanced global interest in basalt-hosted CO_2 storage. In China, extensive Cenozoic basalt formations are distributed across the eastern coastal region, particularly within the Lower Yangtze and adjacent intraplate volcanic provinces (Zhang et al., 2023). Unlike the major sedimentary basins in northwestern China, which are geographically distant from major industrial emission sources, these eastern coastal basalt formations are located within densely industrialized and high-emission regions such as the Yangtze River Delta. This favorable source-sink spatial matching offers a strategic advantage for near-source CO_2 storage by reducing transportation distance, infrastructure requirements, and overall deployment costs (Zentou et al., 2025).

Despite these advantages, the deployment of CO_2 mineralization storage in eastern China basalts still faces several critical scientific and engineering challenges. First, basalt reservoirs are inherently heterogeneous, with strong vertical and lateral variations in lithofacies, pore-fracture connectivity, and permeability, which directly control injectivity and fluid accessibility. Second, CO_2 mineralization is governed by coupled reactive transport processes, in which mineral dissolution and carbonate precipitation continuously modify pore structures and permeability evolution (Ouyang et al., 2025). Third, mineralization-induced pore structure evolution and pressure perturbations may alter reservoir mechanical behavior and affect storage integrity (Xin et al., 2024). These coupled interactions form a strongly nonlinear thermo-hydro-chemo-mechanical (THMC) system, whose behavior remains insufficiently constrained under realistic geological conditions. In this paper, we provide an integrated assessment of CO_2 sequestration and mineralization in basalts in eastern China by combining regional geological analysis, site-specific characterization of the Bailonggang-Sanjiagang basalt system, experimental mineralization evidence, and coupled process-based interpretation. The paper focuses on three key questions: (1) what are the geological prospects for basalt-hosted CO_2 mineralization in eastern China; (2) what are the major constraints controlling storage efficiency and injectivity; and (3) what are the key scientific and engineering challenges toward future field-scale deployment?

2 Prospects for CO_2 Mineralization in Basalts in Eastern China

2.1 Geological distribution and reservoir characteristics of Cenozoic basalts

The distribution of Cenozoic basalts in eastern China is primarily controlled by the tectonic interaction between the Eurasian and Pacific plates, particularly along the circum-Pacific structural belt and major fault systems such as the Tan-Lu fault zone. Under this extensional geodynamic setting, widespread intraplate volcanism formed discontinuously distributed basaltic successions across Shandong, Jiangsu, Zhejiang, and the Shanghai coastal region (see Fig. 1). These basalt formations constitute one of the most important geological resources for CO_2 mineralization storage in China.

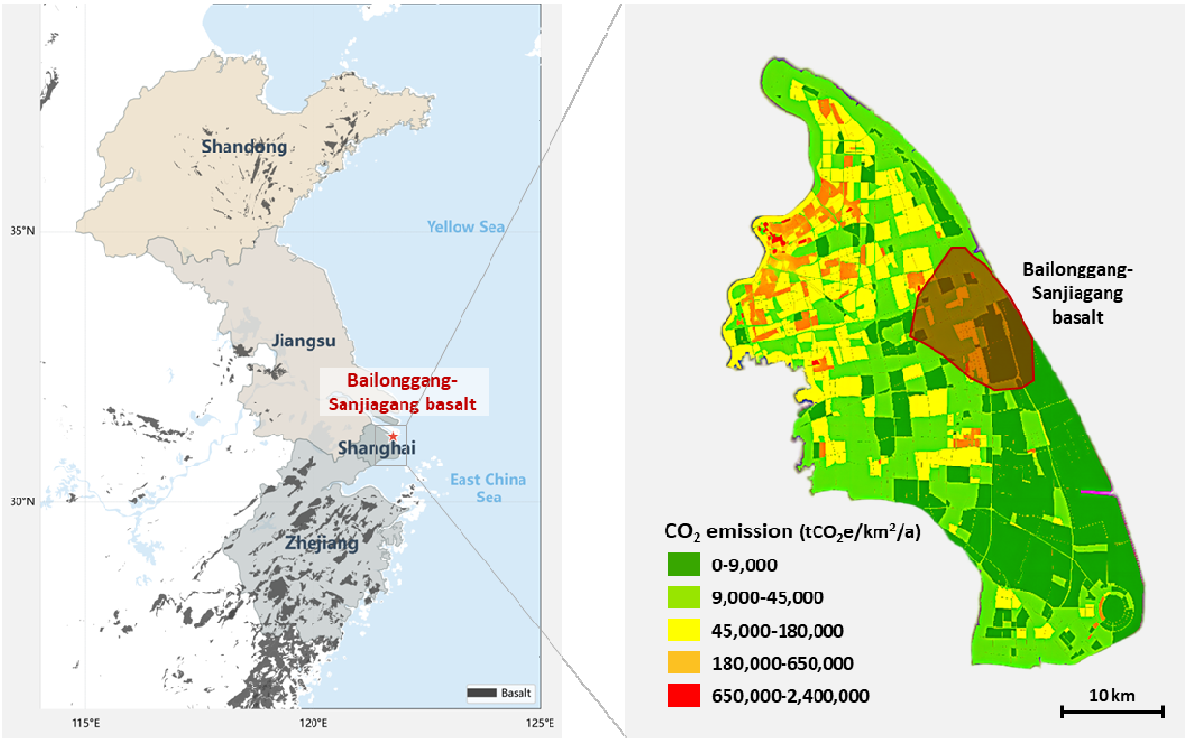


Fig. 1 Basalt reservoirs in Eastern China and Shanghai region.

Basalt reservoirs exhibit several favorable characteristics for CO_2 mineralization storage. They are rich in reactive Ca-, Mg-, and Fe-bearing silicate minerals, including plagioclase, pyroxene, and olivine, which provide essential cations for carbonate precipitation (Gislason et al., 2010; Matter et al., 2016). In addition, volcanic processes generate multi-scale pore-fracture systems, including vesicles, amygdales, cooling joints, and tectonic fractures, providing storage space and fluid migration pathways.

However, basalt reservoirs in eastern China also exhibit strong heterogeneity in thickness, pore structure, permeability, and alteration degree. Secondary mineral infilling and structural compartmentalization may significantly reduce effective pore connectivity, indicating that storage potential is controlled not only by mineral abundance but also by injectivity and fluid accessibility.

2.2 CO_2 mineralization mechanismsin basalt systems

The long-term security of CO_2 storage in basalt formations relies on in situ mineralization, where injected CO_2 is converted into stable carbonate minerals. Compared with conventional structural trapping, mineralization storage offers higher permanence and lower leakage risk (Snæbjörnsdóttir et al., 2020).

After injection, CO_2 dissolves into formation water and forms carbonic acid, initiating the acidification of the fluid system:

$$CO_2 + H_2O \rightleftharpoons H_2CO_3 \rightleftharpoons HCO_3^- + H^+ \rightleftharpoons CO_3^{2-} + 2H^+ \#(1)$$

The decrease in pH promotes the dissolution of primary silicate minerals and basaltic glass, which constitutes the rate-limiting step in mineral carbonation. Representative dissolution reactions include:

$$Mg_2SiO_4 + 4H^+ \rightarrow 2Mg^{2+} + 2H_2O + SiO_{2(aq)} \#(2a)$$

$$CaAl_2Si_2O_8 + 8H^+ \rightarrow Ca^{2+} + 2Al^{3+} + 4H_2O + 2SiO_{2(aq)} \#(2b)$$

These reactions release divalent cations into solution while simultaneously consuming protons, thereby buffering the fluid acidity and sustaining further dissolution. The relatively fast dissolution kinetics of mafic minerals compared to more silica-rich phases make basalt particularly favorable for this process.

As cation concentrations increase, carbonate precipitation occurs through reactions such as:

$$(Me^{2+}) + CO_2 + H_2O \rightarrow MeCO_3 + 2H^+ \quad (Me = Ca, Mg, Fe) \#(3)$$

This process forms a dynamic feedback between mineral dissolution and carbonate precipitation. Dissolution enhances porosity and fluid accessibility, whereas precipitation progressively reduces pore space and permeability. The competition between these two processes controls injectivity, mineralization efficiency, and long-term storage performance (Ouyang et al., 2025).

2.3 Source-sink matching and deployment advantages in coastal eastern China

Eastern China is one of the largest industrial and CO_2-emitting regions in China, particularly the Yangtze River Delta, where fossil-fuel-intensive industries are highly concentrated (Liu et al., 2022). Developing near-source geological storage is therefore critical for regional decarbonization.Unlike conventional sedimentary storage targets in northwestern China, which are far from major emission sources, eastern coastal basalt formations are located close to industrial clusters. This favorable source-sink matching can significantly reduce transportation distance, infrastructure requirements, and deployment costs (Zhang et al., 2022; Zentou et al., 2025).

The Bailonggang-Sanjiagang basalt system (see Fig. 1) in Shanghai represents a typical near-source storage target, combining favorable geological conditions for mineralization with direct proximity to major emission sources. This makes it an ideal pilot-scale site for evaluating the feasibility of basalt-hosted CO_2 mineralization in eastern China.Overall, eastern China basalts provide a promising pathway for CO_2 mineralization storage due to their favorable mineral reactivity, reservoir distribution, and source-sink matching. However, their actual storage performance remains constrained by reservoir heterogeneity, injectivity limitations, and coupled reactive transport processes, which require site-specific assessment in the following section.

3 Site-Specific Assessment: The Bailonggang-Sanjiagang Basalt System

3.1 Geological architecture and reservoir stratification

The Bailonggang-Sanjiagang basalt system, located in the eastern Shanghai coastal region, represents a typical buried Cenozoic mafic reservoir in eastern China and serves as a representative pilot-scale site for evaluating CO_2 mineralization storage potential. Geologically, the reservoir is situated at the eastern termination of the Jiang-Shao fault zone within the Lower Yangtze tectonic domain, where the basement has experienced multiple stages of tectonic superposition associated with compression-extension transitions since the Mesozoic. This tectonic evolution controlled the emplacement, preservation, and subsequent structural modification of the Neogene basalt succession, resulting in a structurally complex and heterogeneous volcanic reservoir architecture(Li et al., 2016; Wang et al., 2014; Yang et al., 2016).

As shown in Fig. 2, the target reservoir corresponds to the Neogene Bailonggang-Sanjiagang basalt formation, which is widely distributed beneath Quaternary sedimentary cover in the eastern Shanghai coastal area. Based on regional geological mapping and borehole interpretation, the effective areal extent of the basalt reservoir is estimated to be approximately 86 km², forming one of the largest buried mafic reservoirs in the Shanghai region. Its location within the Yangtze River Delta industrial cluster provides a favorable near-source geological sink for CO_2 storage, where captured CO_2 can be transported over relatively short distances from major emission sources.

From an engineering perspective, the study site is strategically located between a volcanic center and an existing geothermal exploration well, providing valuable constraints on subsurface thermal-hydrological conditions and reservoir continuity. The proximity to the volcanic vent (~0.8 km) suggests relatively well-developed basalt thickness and eruptive facies preservation, while nearby geothermal exploration (~2.6 km away) provides additional hydrogeological constraints on reservoir temperature and fluid conditions.

To characterize the reservoir geometry and internal architecture, integrated geophysical surveys and deep borehole drilling were conducted. Surface-wave dispersion inversion reveals a distinct shear-wave velocity contrast at depths of approximately 350-400 m, corresponding to the top of the basalt formation. Localized velocity anomalies indicate structural discontinuities, likely associated with fault development, which may significantly influence reservoir compartmentalization and fluid migration pathways.

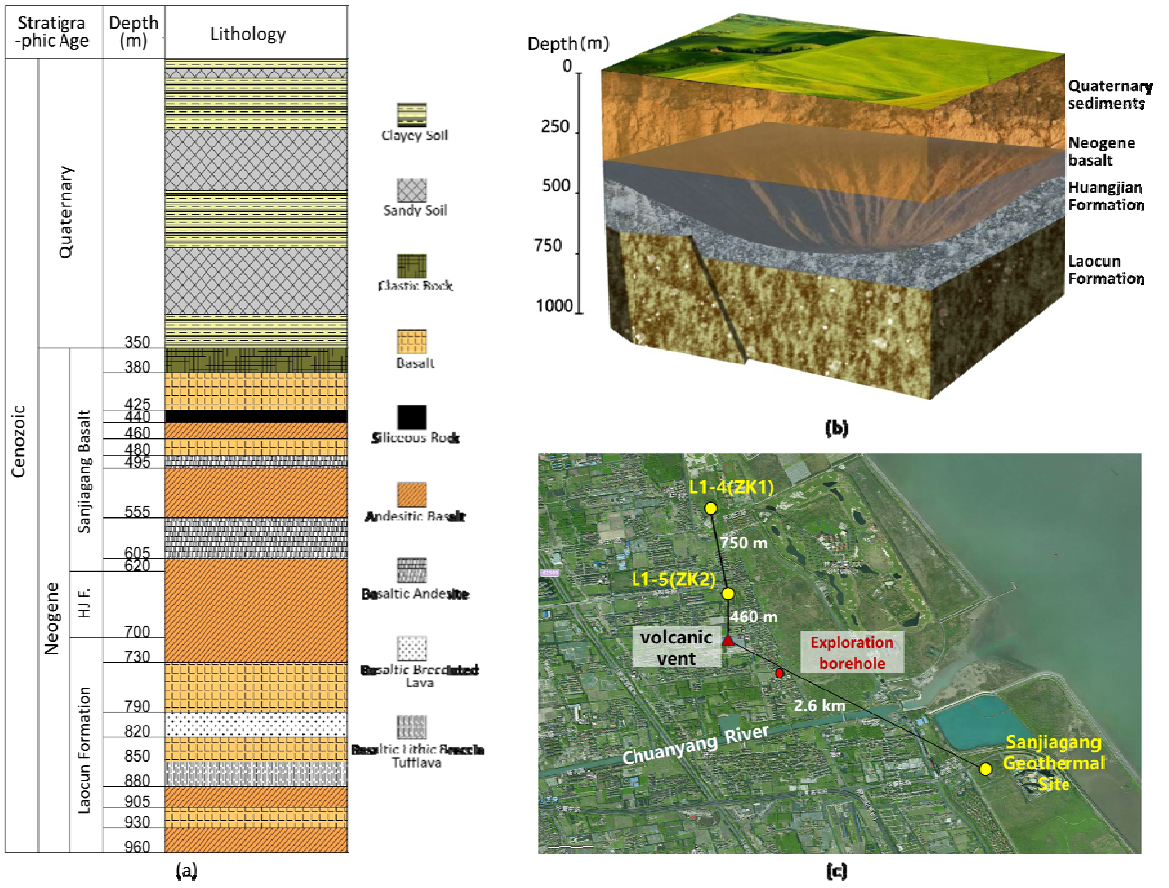


Fig. 2(a) Stratigraphy in theBailonggang-Sanjiagang basalt region, (b) Schematic diagram of the 3D stratigraphic distribution, and (c) Plan view of field borehole core sampling in the Shanghai region.

A deep exploration borehole (~970 m) further constrained the vertical architecture of the basalt reservoir. Core observations and integrated geological interpretation reveal pronounced vertical stratification and thickness variability, with the basalt formation generally thickening toward the volcanic center and thinning laterally. Based on lithological observations and petrographic characteristics, the reservoir can be subdivided into three major stratified intervals: a shallow interval (350-490 m), a middle interval (490-650 m), and a deep interval (650-960 m).

The shallow interval is dominated by vesicular and amygdaloidal basalt, characterized by well-preserved primary eruptive pore structures and locally developed fractures, providing favorable storage space and injectivity conditions. The middle interval is relatively denser and more structurally continuous, consisting mainly of basaltic andesite interlayered with localized pore-bearing facies, representing a relatively stable reservoir unit. In contrast, the deep interval exhibits stronger alteration and structural complexity, characterized by altered amygdaloidal basalt, brecciated lava, and extensive secondary mineral infilling, reflecting prolonged fluid-rock interaction and tectonic overprinting.

This vertically stratified architecture reflects the combined effects of primary volcanic facies distribution and secondary post-emplacement alteration, forming a strongly heterogeneous reservoir system. Such heterogeneity fundamentally controls the distribution of pore space, permeability, mineral accessibility, and fluid migration behavior, and therefore directly governs CO_2 injectivity and mineralization efficiency. The Bailonggang-Sanjiagang basalt system thus provides an ideal natural laboratory for evaluating the coupled geological constraints on CO_2 mineralization storage in eastern China.

3.2 Vertical heterogeneity in lithofacies and petrophysical properties

Core characterization, including petrographic observations, XRD/XRF analysis, and porosity-permeability measurements, reveals pronounced vertical heterogeneity in the Bailonggang-Sanjiagang basalt reservoir, reflecting the combined effects of primary volcanic emplacement and subsequent alteration.

As shown in Fig. 3, the reservoir can be divided into three vertically stratified intervals with distinct lithofacies characteristics. The shallow interval (350-490 m) is dominated by vesicular and amygdaloidal basalt, with abundant primary pore spaces and locally developed fractures, indicating favorable storage accessibility. The middle interval (490-650 m) is relatively denser and more structurally continuous, consisting mainly of basaltic andesite interlayered with localized pore-bearing facies. In contrast, the deep interval (650-960 m) exhibits stronger alteration and structural complexity, characterized by altered amygdaloidal basalt, brecciated lava, and extensive secondary mineral infilling.

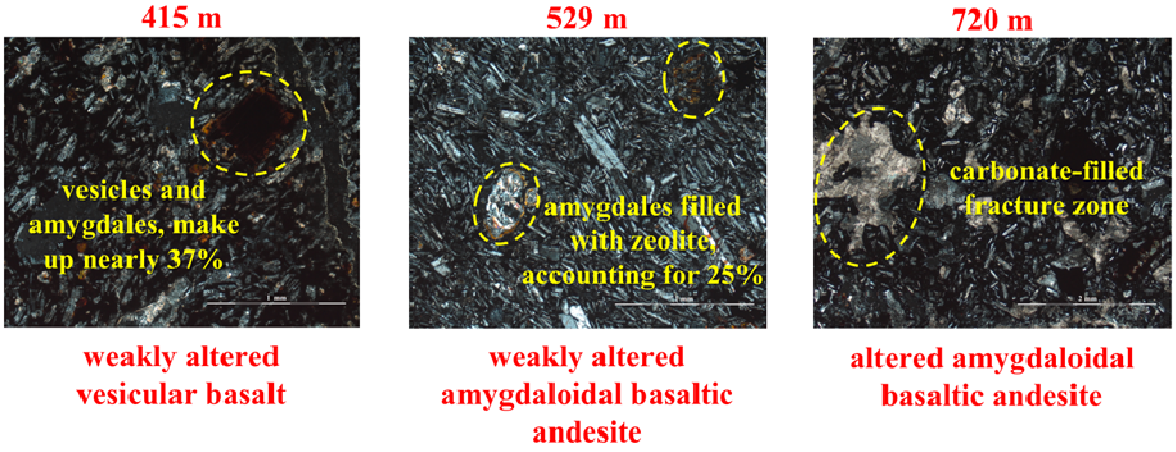


Fig. 3 Representative petrographic characteristics of the shallow, middle, and deep intervals of the Bailonggang-Sanjiagang basalt reservoir.

Mineralogical analysis (Fig. 4) further confirms clear vertical variation. The shallow and middle intervals are dominated by plagioclase and pyroxene, providing favorable reactive mineral sources for CO_2 mineralization. With increasing depth, pyroxene content decreases progressively and alteration minerals such as chlorite and montmorillonite become increasingly abundant, indicating stronger water-rock interaction and reduced reactive mineral preservation.

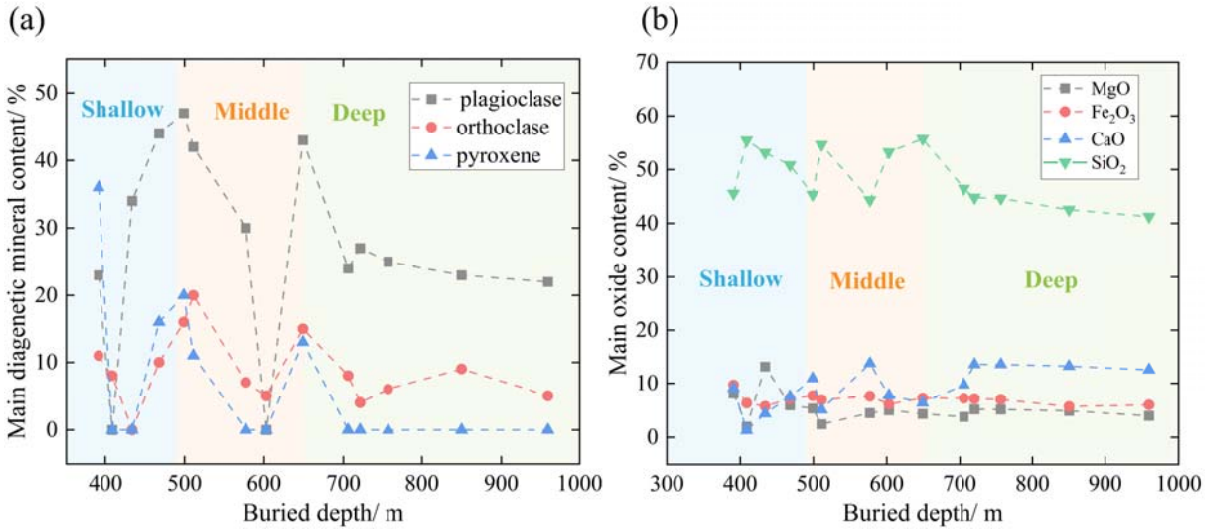


Fig. 4 Vertical variations in mineralogical and geochemical compositions of the Bailonggang–Sanjiagang basalt reservoir: (a) major mineral assemblages; (b) major oxide compositions.

The porosity-permeability measurements (Fig. 5) show strong depth-dependent variation. Porosity ranges from 1.894% to 25.464%, while permeability ranges from 0.671 to 33.437 mD. The shallow interval generally exhibits higher porosity and permeability, reflecting better preservation of primary pore structures and fracture networks. The middle interval shows relatively lower but more stable transport properties, suggesting better structural continuity and more predictable fluid migration behavior. In the deep interval, although some pore space remains locally preserved, permeability decreases significantly due to extensive secondary mineral infilling and reduced pore-throat connectivity.

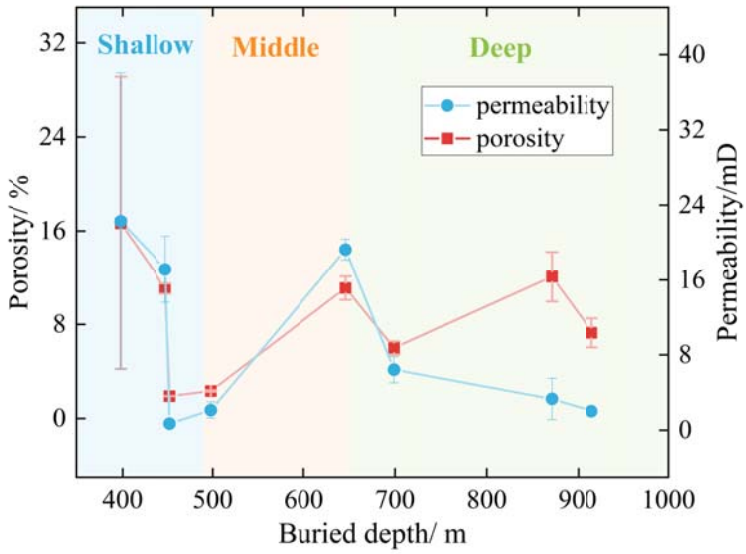


Fig. 5 Vertical distribution of porosity and permeability in the Bailonggang-Sanjiagang basalt reservoir.

These results demonstrate that the vertical heterogeneity of the basalt reservoir fundamentally controls CO_2 injectivity, fluid accessibility, and mineralization efficiency. The shallow interval offers favorable injectivity but stronger heterogeneity, the middle interval provides a relatively balanced reservoir condition, and the deep interval possesses large storage volume but stronger transport limitations. This heterogeneity forms the geological basis for evaluating mineralization potential and storage performance in the following sections.

3.3 Experimental evidence of mineralization potential

To evaluate the mineralization reactivity of the Bailonggang–Sanjiagang basalt reservoir toward CO_2 storage, a series of batch reaction experiments were conducted under simulated reservoir conditions using representative subsurface basalt samples from the Shanghai coastal basalt system. Core samples were collected from depths of approximately 396 m and 450 m (denoted as SH-396 and SH-450), corresponding to the middle reservoir interval. For comparison, basalt samples from Zhanjiang, including an outcrop sample (ZJ-O) and a subsurface sample at 450 m depth (ZJ-450), were also tested to provide additional constraints on mineralization behavior under different geological conditions.

All samples were crushed into powder to enhance reactive surface area and reacted under controlled conditions (60 °C, CO_2 pressure of 10 MPa, and water-rock ratio of 20) for 56 days. The objective was to assess mineral carbonation potential, reaction efficiency, and the influence of initial mineralogical states on CO_2 mineralization.Mineralogical analyses before and after reaction provide direct evidence of CO_2 mineralization. The Shanghai basalt samples are dominated by reactive silicate minerals, primarily plagioclase and pyroxene, together with varying amounts of clay minerals, indicating different degrees of pre-existing alteration. After reaction, newly formed carbonate minerals, particularly magnesite, were identified in the reacted samples, confirming effective mineral trapping through water-rock interaction (Fig. 6).

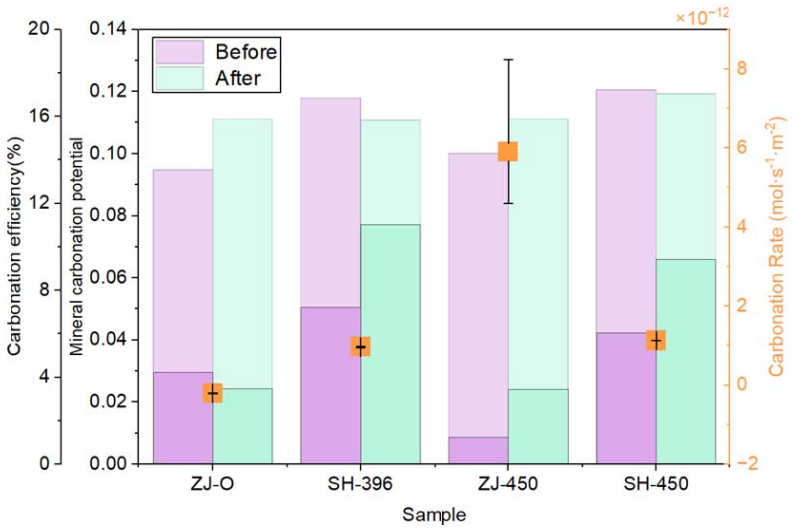


Fig. 6 Experimental evidence of CO_2 mineralization in representative basalt samples: mineralogical changes and carbonation efficiency before and after reaction.

Quantitative carbon analysis further confirms mineral carbonation by showing a clear increase in carbon content after reaction in all subsurface samples. Based on the measured carbon uptake, both carbonation extent and reaction rate were estimated. The results show that subsurface basalt samples exhibit significantly higher carbonation efficiency than the outcrop sample, indicating that buried basalt systems provide more favorable mineralization conditions than weathered surface-exposed basalts.

Notably, the Shanghai subsurface basalt samples (SH-396 and SH-450) consistently exhibit strong carbonation performance, demonstrating high reactivity under reservoir-relevant conditions. Although variations in carbonation rate are observed among the Shanghai and Zhanjiang samples, these differences are primarily related to variations in mineralogical composition and initial alteration states, rather than fundamental differences in mineralization mechanisms.

These experimental results provide direct evidence that buried basalt reservoirs in eastern China possess strong CO_2 mineralization potential. More importantly, the comparison between the Shanghai and Zhanjiang samples demonstrates that mineralization efficiency is highly sensitive to the initial reservoir conditions, including mineral preservation state and reactive surface accessibility. This experimental evidence supports the feasibility of basalt-hosted CO_2 mineralization in eastern China and provides important constraints for the site-scale storage assessment in the following section.

3.4 Storage potential assessment under dissolved CO_2 injection

To evaluate the practical storage potential of the Bailonggang-Sanjiagang basalt reservoir, a site-scale assessment framework was established under a dissolved CO_2 injection scenario, where CO_2 is injected in carbonated water rather than as a separate supercritical phase. This strategy can reduce buoyancy-driven migration and minimize the risk of caprock disturbance, while promoting direct water-rock interaction and accelerating in situ mineralization.

The storage assessment integrates two capacity limits: (1) the dissolution-based storage capacity constrained by effective pore volume and fluid transport accessibility, and (2) the mineralization-based storage capacity constrained by the availability of reactive Ca- and Mg-bearing minerals. To account for the strong vertical heterogeneity of the reservoir, the shallow, middle, and deep intervals were evaluated separately using representative petrophysical and mineralogical parameters.

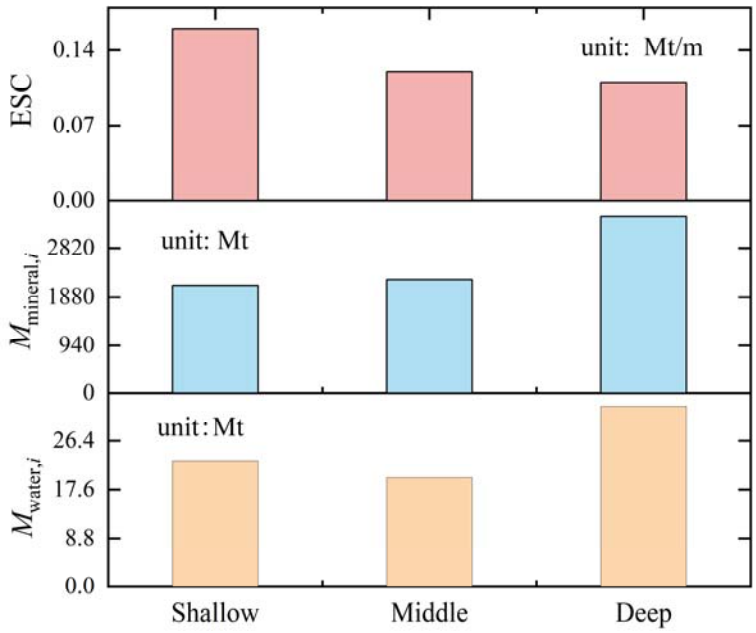


Fig. 7 Site-scale assessment of CO_2 mineralization storage potential in the Bailonggang-Sanjiagang basalt reservoir: dissolution-based capacity and mineralization-based capacity for different stratified intervals.

The results show that the dissolution-based storage capacities of the shallow, middle, and deep intervals are estimated at 22.76 Mt, 19.77 Mt, and 32.57 Mt, respectively, yielding a total realizable storage capacity of 75.10 Mt (Fig. 7). In contrast, the corresponding mineral reaction capacities are significantly higher in all three intervals, indicating that reactive mineral availability is not the limiting factor for storage.

The deep interval contributes the largest absolute storage capacity due to its greater thickness and higher CO_2 solubility under elevated pressure conditions. However, its lower permeability and stronger secondary alteration impose significant injectivity constraints. In contrast, the shallow interval exhibits the highest effective storage contribution per unit thickness, benefiting from better pore preservation and higher injectivity accessibility, although it also shows stronger local heterogeneity. The middle interval provides relatively balanced storage performance, combining moderate storage capacity, better structural continuity, and more stable transport properties.

These results indicate that the effective storage potential of basalt reservoirs is governed primarily by pore accessibility, fluid transport capacity, and injectivity, rather than by mineral reaction capacity alone. From an engineering perspective, the shallow and middle intervals represent the most favorable target horizons for pilot-scale CO_2 mineralization storage, while the deep interval may serve as a secondary storage target with larger capacity but stronger operational constraints.

4 Coupled Constraints on CO_2 Mineralization in Basalts

4.1 Reactive transport and porosity evolution

Reactive transport processes fundamentally control reservoir evolution during CO_2 mineralization in basalt systems. During injection, mineral dissolution and carbonate precipitation occur simultaneously, continuously modifying pore structures and fluid flow pathways, and thereby directly controlling injectivity and mineralization efficiency.

At the early stage of injection, CO_2-rich acidic fluids promote the dissolution of primary silicate minerals, leading to local pore enlargement and increased porosity. This dissolution-enhanced stage improves fluid accessibility and facilitates further water-rock interaction. As the reaction progresses, dissolved cations accumulate and carbonate precipitation gradually intensifies, progressively occupying pore space and reducing effective porosity.

As shown in Fig. 8, the coupled reactive transport simulations capture both the spatial distribution of carbonate precipitation and the associated porosity evolution during CO_2 injection. The results show that carbonate precipitation is concentrated near the injection zone and progressively expands outward,

while the surrounding reservoir undergoes heterogeneous pore structure changes. The reservoir near the injection well initially experiences pore expansion dominated by dissolution, followed by localized pore reduction associated with carbonate precipitation. This transition reflects the evolution from a self-enhancing regime to a self-sealing regime, which fundamentally controls the sustainability of fluid injection and mineral trapping.

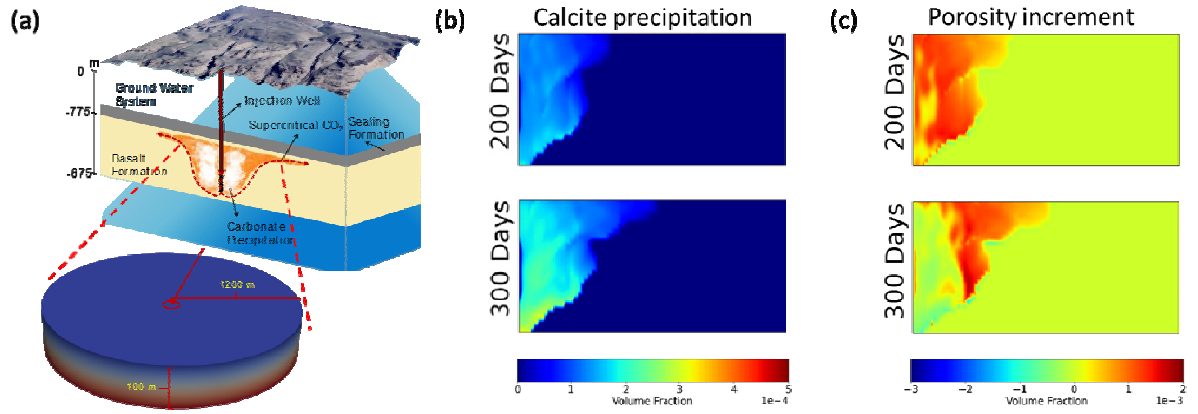


Fig. 8 Reactive transport evolution during CO_2 mineralization in basalt reservoirs: (a) conceptual and numerical model; (b) spatial distribution of calcite precipitation; (c) spatial evolution of porosity showing the transition from dissolution-enhanced pore development to precipitation-induced self-sealing.

Such dynamic porosity evolution represents a key constraint on basalt-hosted CO_2 mineralization. While dissolution improves injectivity and reaction accessibility, excessive precipitation may reduce effective pore connectivity and restrict fluid migration. Therefore, successful mineralization storage requires balancing reaction efficiency and long-term transport sustainability.

4.2 Reservoir accessibility and injectivity constraints

Although basalt reservoirs contain abundant reactive minerals for CO_2 mineralization, their effective storage performance is fundamentally constrained by reservoir accessibility and injectivity. As demonstrated in the site-scale storage assessment, the theoretical mineral reaction capacity of all stratified intervals significantly exceeds the dissolution-based storage capacity, indicating that reactive mineral availability is not the primary limiting factor for mineralization storage. As shown in Fig. 7, the large discrepancy between the mineralization-based capacity and the dissolution-based capacity directly reflects the practical limitation imposed by effective pore accessibility and fluid transport capacity.Instead, the practical storage capacity is governed by the effective pore volume and the ability of CO_2-rich fluids to access and circulate within the reservoir.

Reservoir accessibility is strongly controlled by pore connectivity, permeability distribution, and structural continuity. In heterogeneous basalt systems, effective fluid migration pathways are often highly localized due to the coexistence of vesicular zones, dense lava interiors, fracture networks, and secondary mineral infilling. Even in intervals with relatively high porosity, poor pore-throat connectivity may significantly restrict fluid transport and reduce effective mineral accessibility.

Injectivity constraints become increasingly important during long-term operation. As discussed in Section 4.1, reactive transport continuously modifies pore structures through the competing effects of dissolution and precipitation. Although early-stage dissolution may improve injectivity locally, progressive carbonate precipitation near the injection well may reduce effective permeability and restrict fluid penetration into the broader reservoir volume. This localized self-sealing effect may significantly reduce storage efficiency by limiting the effective sweep volume of reactive fluids.

The vertical heterogeneity of the Bailonggang-Sanjiagang basalt reservoir further amplifies these constraints. The shallow interval provides favorable injectivity due to better preserved pore-fracture systems, while the middle interval offers relatively stable transport conditions with improved structural continuity. In contrast, the deep interval possesses larger storage volume but is more strongly constrained by permeability reduction and alteration-induced pore isolation. These differences indicate that reservoir selection for CO_2 mineralization storage must balance storage capacity and injectivity accessibility.

Therefore, improving storage accessibility and maintaining sustainable injectivity represent critical engineering challenges for basalt-hosted CO_2 mineralization. Effective injection design, interval selection, and operational control are essential to maximize fluid-rock contact and enhance the realizable storage potential.

4.3 Injection strategy impacts on mineralization efficiency and storage security

Injection strategy plays a critical role in controlling both mineralization efficiency and storage security in basalt-hosted CO_2 sequestration. In heterogeneous basalt reservoirs, variations in injection location and injection rate directly affect fluid accessibility, reaction distribution, and pressure evolution, thereby influencing the overall storage performance.

Table 1Effects of injection rate and location on porosity and CO_2 sequestration efficiency.

Scenario	Injection Location	Injection Rate	Porosity Changes Near Wellbore	Sequestration Efficiency
1	Bottom	3 kg/s	-6.4×10^{-4}	10.3%
2	Bottom	5 kg/s	-5.4×10^{-4}	9.6%
3	Top	5 kg/s	-1.5×10^{-4}	8.4%

As summarized in Table 1, both injection location and injection rate significantly affect porosity evolution near the wellbore and final sequestration efficiency. Under the bottom injection condition, increasing the injection rate from 3 kg/s to 5 kg/s results in less porosity reduction near the wellbore, but also slightly decreases the final mineralization efficiency. In contrast, top injection at the same rate further reduces porosity reduction near the injection zone, indicating improved injectivity preservation, although the final sequestration efficiency becomes lower.

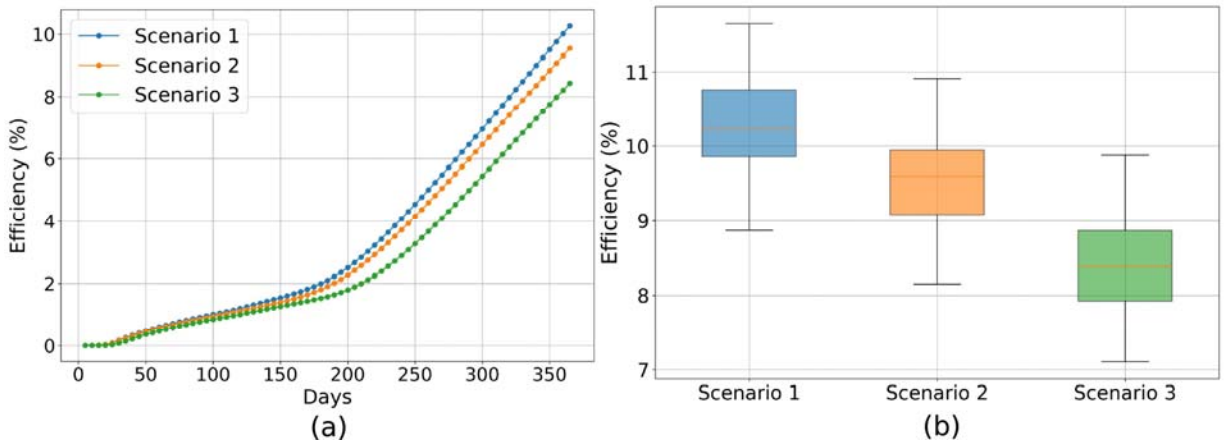


Fig. 9 Temporal evolution of CO_2 mineralization efficiency under different injection strategies.

The temporal evolution of sequestration efficiency shown in Fig. 9 further illustrates the dynamic effects of injection strategy on mineralization performance. In all scenarios, sequestration efficiency increases progressively with time, reflecting the gradual development of mineralization reactions. A clear acceleration of mineral trapping is observed after approximately 150 days, coinciding with significant magnesite precipitation, indicating that the availability of dissolved cations has reached a critical threshold for large-scale carbonate formation.

These results indicate an important operational trade-off. Bottom injection tends to achieve higher mineralization efficiency due to longer fluid-rock interaction pathways and stronger fluid retention, but may also induce stronger local porosity reduction and potential injectivity loss. In contrast, top injection may better preserve injectivity and fluid accessibility, but may reduce effective mineral trapping efficiency.

Therefore, effective injection strategies for basalt-hosted CO_2 mineralization should balance mineralization efficiency, injectivity sustainability, and storage security. Adaptive injection design, including interval selection and injection rate control, is essential for improving long-term storage performance while minimizing operational risks.

5 Challenges and Future Directions

5.1 Multi-scale THMC coupling and uncertainty

One of the most critical challenges for basalt-hosted CO_2 mineralization is the strong thermo-hydro-mechanical-chemical (THMC) coupling that governs reservoir evolution during injection. Unlike conventional geological storage, mineralization storage involves continuous interactions among fluid flow, heat transfer, geochemical reactions, and mechanical responses, forming a highly nonlinear coupled system.

At the pore scale, mineral dissolution and carbonate precipitation dynamically modify pore geometry and reactive surface accessibility, directly affecting local transport properties and reaction kinetics. At the reservoir scale, these local changes may progressively alter permeability distribution, fluid migration pathways, and pressure evolution. Meanwhile, mineralization-induced pore structure evolution may further affect rock stiffness, deformation behavior, and fracture stability, creating feedback between geochemical evolution and geomechanical responses.

A major challenge lies in bridging these coupled processes across scales. Laboratory experiments provide direct constraints on reaction kinetics and mineralization behavior, but their representativeness at reservoir scale remains limited. Conversely, field-scale simulations often rely on simplified assumptions regarding reaction kinetics, permeability evolution, and mechanical property changes, introducing substantial uncertainty into long-term storage predictions.

Reducing these uncertainties requires improved multi-scale THMC coupling frameworks that integrate laboratory observations, site-specific characterization, and field-scale reactive transport modeling. Developing robust predictive models for coupled reservoir evolution will be essential for improving storage performance evaluation and operational risk assessment in future basalt-hosted CO_2 mineralization projects.

5.2 Upscaling from laboratory characterization to field deployment

Bridging the gap between laboratory characterization and field-scale deployment remains a major challenge for basalt-hosted CO_2 mineralization. Laboratory experiments provide direct evidence of mineral carbonation potential and reaction pathways under controlled conditions, but their results are often obtained under simplified physical and chemical environments that differ significantly from in situ reservoir conditions.

At laboratory scale, crushed rock samples and controlled reaction conditions can greatly enhance fluid-rock contact and reaction efficiency, often leading to accelerated mineralization rates compared with natural reservoir systems. In contrast, field-scale reservoirs are characterized by strong lithological heterogeneity, variable pore-fracture connectivity, and complex fluid transport pathways, which may substantially limit effective mineral accessibility and reaction extent.

The site-specific assessment of the Bailonggang-Sanjiagang basalt system demonstrates that effective storage capacity is governed primarily by reservoir accessibility and injectivity rather than by reactive mineral abundance alone. This highlights the importance of integrating laboratory observations with realistic reservoir characterization and field-scale transport constraints when evaluating practical storage performance.

Future field deployment requires improved upscaling strategies that link laboratory-derived reaction kinetics, reservoir-scale heterogeneity, and operational conditions. Pilot-scale injection tests, integrated monitoring, and continuous model calibration will be essential for reducing scale-dependent uncertainty and improving the reliability of field-scale mineralization storage assessment.

5.3 Toward adaptive and data-informed injection management

The strong heterogeneity and dynamic reservoir evolution of basalt-hosted CO_2 mineralization require more adaptive injection management strategies than conventional geological storage operations. Because injectivity, fluid accessibility, and mineralization efficiency may evolve continuously during injection, static operational designs may become suboptimal or even increase storage risks over time.

Adaptive injection management aims to adjust operational parameters, such as injection interval, injection rate, and injection duration, based on the evolving reservoir responses. Continuous

monitoring of pressure evolution, fluid migration, and geochemical changes can provide important constraints on reservoir behavior and help identify early signs of injectivity reduction, localized self-sealing, or abnormal pressure buildup.

The integration of site monitoring data with predictive reservoir models offers a promising pathway toward data-informed operational control. By continuously updating reservoir conditions and reducing model uncertainty, adaptive strategies can improve fluid-rock contact efficiency, maintain sustainable injectivity, and reduce geomechanical risks.

Future basalt-hosted CO_2 mineralization projects will increasingly rely on integrated monitoring, dynamic model updating, and adaptive operational decision-making. Such data-informed injection management will be essential for improving long-term storage efficiency, operational safety, and field-scale deployment reliability.

6 Conclusions

Eastern China basalts represent a promising pathway for CO_2 mineralization storage due to their favorable mineralogical reactivity, widespread regional distribution, and advantageous source-sink matching with major industrial emission clusters. Compared with conventional sedimentary storage systems, basalt-hosted mineralization provides enhanced long-term storage security through permanent carbonate trapping, offering important opportunities for regional carbon mitigation.

The site-specific assessment of the Bailonggang-Sanjiagang basalt system demonstrates strong storage feasibility and mineralization potential. Integrated geological characterization, mineralogical analysis, petrophysical measurements, and batch reaction experiments confirm that buried basalt reservoirs in eastern China possess favorable reactive mineral assemblages and effective carbonation capacity. The site-scale storage assessment under dissolved CO_2 injection further indicates a realizable storage capacity of 75.10 Mt.

However, the effective performance of basalt-hosted CO_2 mineralization is fundamentally constrained by reservoir accessibility, injectivity sustainability, and coupled reactive transport evolution. The results show that practical storage capacity is controlled primarily by effective pore accessibility and fluid transport capacity rather than by reactive mineral availability alone. In addition, mineralization-induced porosity evolution and geomechanical responses introduce further uncertainty in long-term reservoir performance and storage security.

Future development of basalt-hosted CO_2 mineralization in eastern China requires improved multi-scale THMC coupling, more reliable upscaling from laboratory characterization to field deployment, and adaptive data-informed injection management. Integrating site-specific characterization, coupled process modeling, and dynamic operational control will be essential for advancing pilot-scale demonstration and future industrial-scale deployment of CO_2 mineralization storage in basalt systems.

References

Metz B, Davidson O, De Coninck HC, Loos M, Meyer L (2005) IPCC special report on carbon dioxide capture and storage. Cambridge: Cambridge University Press.

Matter JM, Stute M, Snæbjörnsdottir SÓ, Oelkers EH, Gislason SR, et al. (2016) Rapid carbon mineralization for permanent disposal of anthropogenic carbon dioxide emissions. Science, 352(6291), 1312-1314.

Kelemen P, Benson SM, Pilorgé H, Psarras P, Wilcox J (2019) An overview of the status and challenges of CO_2 storage in minerals and geological formations. Frontiers in Climate, 1(9), 1-20.

Gislason SR, Wolff-Boenisch D, Stefansson A, Oelkers EH, Gunnlaugsson E, et al. (2010) Mineral sequestration of carbon dioxide in basalt: A pre-injection overview of the CarbFix project. International Journal of Greenhouse Gas Control, 4(3), 537-545.

Snæbjörnsdóttir SÓ, Sigfússon B, Marieni C, GoldbergD, Gislason SR, Oelkers EH (2020) Carbon dioxide storage through mineral carbonation. Nature Reviews Earth & Environment, 1(2), 90-102.

White SK, Spane FA, Schaef HT, Miller QRS, White MD, Horner JA, McGrail BP (2020) Quantification of CO_2 Mineralization at the Wallula Basalt Pilot Project. Environmental Science & Technology, 54(22), 14609-14616.

Zhang L, Wen R, Li F, Li C, Sun Y, Yang H (2023) Assessment of CO_2 mineral storage potential in the terrestrial basalts of China. Fuel, 348, 128602.

Zentou H, AlZahrani AA, Behar O, Tayeb AM, Abdelnaby MM (2025) Progress in Large-Scale Carbon Capture Deployment: Status, Challenges, and Prospects. Advanced Sustainable Systems, 2400626.

Ouyang W, Feng Z, Zhang F, Xia Z, Shen X (2025) CO_2 sequestration and mineralization in basalts: Insights from a deep learning-based surrogate model. Engineering Geology, 354, 108173.

Xin Y, Yoo H, Min KB, Rutqvist J (2024) Coupled geomechanical analysis of irreversible compaction impact on CO_2 storage in a depleted reservoir. International Journal of Greenhouse Gas Control, 135, 104158.

Liu Z, Deng Z, He G, Wang H, Zhang X, Lin J, Qi Y, Liang X (2022) Challenges and opportunities for carbon neutrality in China. Nature Reviews Earth & Environment, 3(2), 141-155.

Zhang J, Wang Z, Kang J, Song X, Xu D (2022)Several key issues for CCUS development in China targeting carbon neutrality. Carbon Neutrality, 1(1), 17.

Li S, Li X, Zhao S, Yang Z, Liu X, Guo L, Wang Y, HaoY, Zhang J, Hu M (2016). Global Early Paleozoic Orogens (III): Intracontinental Orogen in South China. Journal of Jilin University (Earth Science Edition), 46(4), 1005-1025.

Wang D, Zhan X, Wang J (2014) Evidence of fission Track data for thermotectonic evolution history of the Lower Yangtze area. Offshore oil, 34(3), 55-60.

Yang H, Tian X, Bai Z, Zhang Z (2016) Discussion on the relationship between pan Pacific plate movement and Mesozoic geological evolution of eastern Chinese continent. Journal of Jilin University (Earth Science Edition), 46(3), 781-797.

Impact of climatic variation on rock slope stability

M. Gasc-Barbier
GéoCoD, Cerema, Aix-en-Provence, France
muriel.gasc@cerema.fr
0000-0001-9192-9816

Abstract

Climate significantly impacts the stability of rock masses and associated engineering structures, primarily through altered water regimes, thermal variations, and shifts in the 0°C isotherm. The IPCC (2019) highlights increased global temperatures, extreme weather events, intensified precipitation, droughts, and rising sea levels, all of which affect the physical and mechanical properties of rock masses. While water-related factors like rainfall and snowmelt are major triggers for rock instabilities, some rockfall events seems to be linked to other climatic factors, such as thermal cycles and freeze-thaw processes or may have combined triggering factors.

This paper briefly reviews the key processes influencing rock mass evolution, including the impact of atmospheric water (saturation, joint lubrication, and karstification), positive thermal cycles (thermal shock and fatigue), and changes in the 0°C isotherm (permafrost thaw, cryoclasty, and freeze-thaw cycles). Field observations and laboratory experiments demonstrate that these processes degrade mechanical properties, reduce strength, and increase instability risks. However, their integration into constitutive laws remains challenging. Understanding these complex interactions is crucial for assessing and mitigating climate change impacts on rock mass stability.

Keywords

Climate, Hydric variation, Freeze-thaw cycles, Thermal fatigue, Rock slope stability.

1 Introduction

If the reality of climate change is less and less questioned, taking into account its impact on rock masses or engineering structures is much more complicated. A very synthetic summary of the latest IPCC (2019) report provides:

- average rise in global surface temperatures, but very important local changes, some areas will see their average temperature cool while others will increase,
- increase in the number of extreme weather events (storms, droughts, heat domes or, on the contrary, cold drops),
- intensification of precipitation (same amount of water annually but concentrated in a smaller number of days),
- increase in the frequency of drought periods,
- increase in catastrophic weather events (hurricanes, storms, floods),
- melting glaciers and frozen soils,
- increase in the salinity of groundwater near the coast due to rising sea levels.

These events will have a major impact on the physical and mechanical characteristics of rock masses and consequently on their mechanical stability and associated structures (underground structures, rock embankments, open-air quarries, sea cliffs, etc.). But before evaluating the effect of climate change, it is important to better describe the effect of the climate. When considering the effect of climatic variations on rock instabilities, the first thought is destabilisation following heavy rain. But water variations should not be the only ones to be considered. Indeed, Delonca et al (2014) analysed the database of rock falls that reached La Réunion principal highway and showed that while rain is the main trigger, more than 50% of events are linked to other factors. Eisbacher and Clague (1984) showed that 66% of landslides in the Alps were due exclusively to precipitation or snowmelt and 25% to anthropogenic activities or earthquakes. Ravanel et al. (2017) also in the Alps, showed an increase in rock fall events during hot summers, with this increase being related to ice melting.

Having outlined the main factors to be considered in the evolution of the rock mass, we will review the description of climate factors in terms of processes, following the work presented by the CFMR (French Rock Mechanic NG) working group on climate change (Conil et al., 2024), that is: impact of atmospheric water, positive thermal cycles, changes in the 0°C isotherm.

2 Key-factors in the evolution of the rock mass

The natural rock mass evolution over time is weathering. Its speed will depend both on the intrinsic characteristics of the rock masses and on various external factors. A summary diagram of these factors and characteristics is provided in Fig 1.

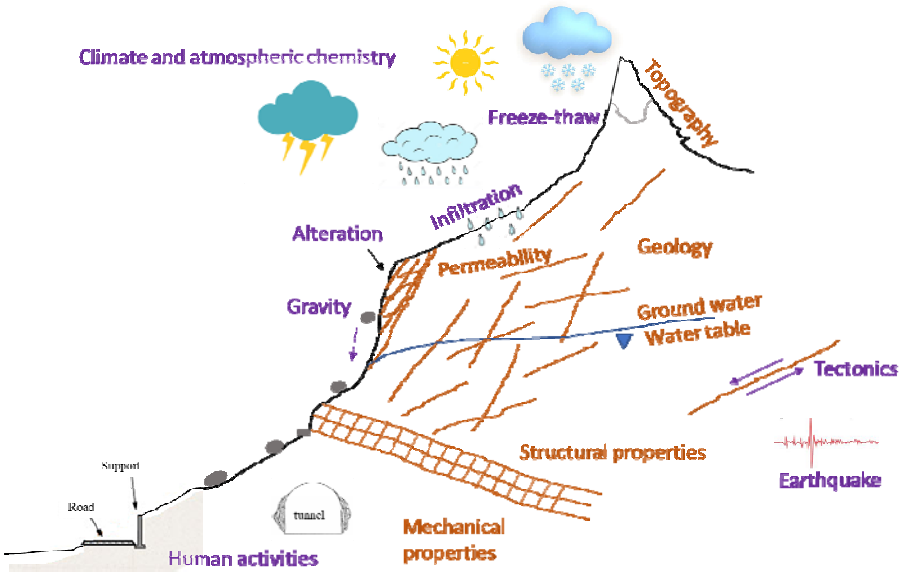


Fig. 1 Intrinsic characteristics of rock masses (brown) and main external factors (purple).

The intrinsic characteristics of the rock site under consideration, shown in brown in Fig 1, include:

- Geological and mineralogical nature of the rock as well as hydrogeological and structural conditions,
- Geomorphological conditions: localisation, morphology, topography of the site (height of the slopes, their inclination exposure(s), etc...),
- Regional tectonic conditions, which will have an influence on the initial state of stress of the massif,
- "Physical" condition of the rock mass (depth of alteration, *in situ* stress, presence or absence and type of vegetation),
- Fracturing conditions of the rock mass (identification of discontinuities families, persistence and extension, fracturing density, opening and/or filling of discontinuities, etc.),
- Hydraulic conditions (permeability, drainage, etc.)
- Mechanical characteristics of the rock mass at the appropriate REV (Representative Elemental Volume) scale, i.e., constitutive laws for both the rock matrix and the joints or, if homogenisation, the properties (strength and modulus) of the homogenised rock mass.

External factors correspond to everything that will disturb the "balance" of the rock massif and will therefore influence its weathering as well as the creation of potential instabilities. They are shown in purple in Fig 1. These are mainly:

- Local climatic conditions (rain, snowmelt, freeze-thaw, sun exposure, daily and seasonal temperature ranges),
- Factors related to the water cycle (climate, precipitation, evapotranspiration or effective rainfall distribution parameters, etc.),
- Presence or absence of rivers or sea at the foot of the cliff, which will lead to mechanical erosion up to under-caving,
- Permafrost local conditions (if any),
- Seismicity and regional tectonic activity,
- Human activities.

3 Impact of water variations on rock masses

As briefly described in the introduction, climate change is already imposing, and will continue to modify the water regime in various parts of the world (IPCC (2019). We will not detail here these evolutions but we will focus on their impact on the rock mass and the rock discontinuities.

3.1 Increased of water content

Numerous studies (Zhou et al., 2016; Althaus et al., 1994 among others) have shown that when the saturation of the rock increase, its strength decrease. Pan et al.(2020) studied the influence of saturation on UCS and Young's modulus of several rock types (Fig 2). Gombert et al. (2013) and Lafrance (2016) have shown that for clayey limestones or porous rocks such as chalk, the deterioration in mechanical properties could result in a loss of up to 70% in UCS compared with the dry state.

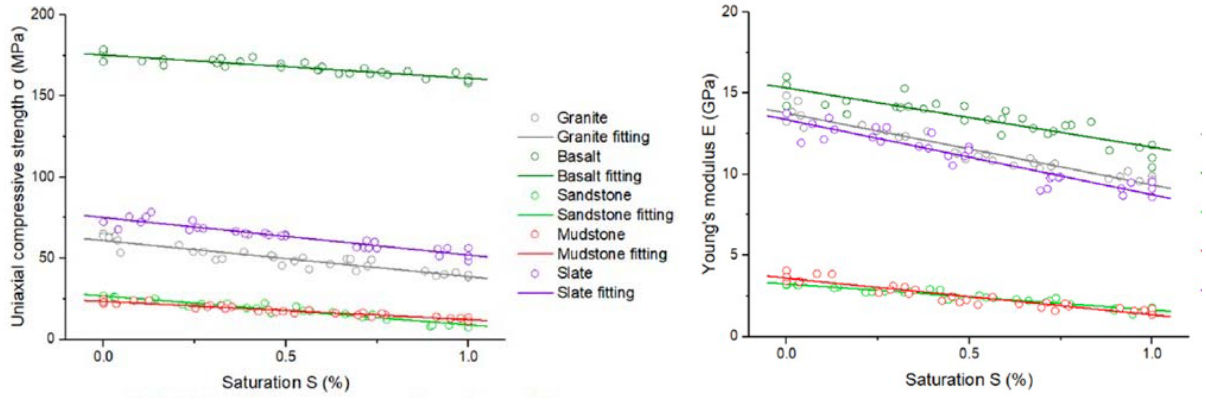


Fig. 2 Decrease in the mechanical properties of several types of rock as a function of saturation. a-simple compressive strength, b-Young's modulus after Pan et al.(2020).

3.2 Joint Lubrication or leaching

Heavy rainfall can lead to leaching of fractures, which in turn can lead to a decrease in the cohesion of discontinuities and therefore an increase in instabilities. Moreover, water has a lubricating effect on the stratification joints and fracture planes. This lubricating effect contributes to lowering the friction coefficient of discontinuities and consequently to a decrease in the strength of the rock mass (Al Heib et al., 2023; Paquette 2014). Pan et al. (2020) have for example shown that slates with a dry state friction angle between 35.5° and 44.5° have a saturated state friction angle of 30° to 36.9°.

3.3 Covering land loading

Over the main predisposing and/or triggering factors for widespread collapses of underground quarries, water and more particularly floods, very heavy rains and leaching, are in a good place (Al Heib et al. 2023). The stability of underground excavations, particularly in soft rock (limestone, calcarenite, gypsum, etc.), is significantly affected by climatic and hydrological factors such as heavy rainfall, drought (Castellanza et al., 2018).

The effects of hydraulic loading are relatively complex: rapid changes in water levels in abandoned underground caves can have opposing effects, particularly when the caves are located below the water table. If submersion occurs, as noted above, there is a decrease in the mechanical properties of sensitive rocks (unconfined compressive strength, modulus, etc.) and/or in the shear strength of submerged discontinuities, as well as an increase in pore pressure within porous rocks. Nevertheless, these effects can be mitigated by confining the pillars through hydrostatic pressure and by relieving pressure on the overlying strata.

3.4 Correlation of rainfall – slope instabilities?

The influence of rainwater infiltration on slope stability has been extensively under study in recent years (Bernardie et al., 2014; Brooks et al., 2004; Iverson, 2000; Song et al., 2020). Wang et al. (2003) pointed out that it is now proven that water is a major factor in triggering slope instabilities, with preferential circulation in rock discontinuities rather than in the rock mass. Furthermore; discontinuities often act as channels for groundwater in rock masses (Cascini et al., 2010; Djerbal & Melbouci, 2012; Raj & Sengupta, 2014; Terajima et al., 2013; Uwihirwe et al., 2020; X. Zhao et al., 2018, among others). In these cases, the water pressure depends on the density of fracture and of the joint properties such as their alteration and filling with fine materials such as clay and gouge.

However, the correlation between rainfall and landslide is not so obvious: Sandersen et al. (1997) observed that the influence of a large water supply in the last 24 hours is minimal on most rockfall events, while the water supply acting over a longer period seems to be of greater importance. However, no direct link has been established between the increase in water quantity and the movements recorded in the massif. Delonca, et al (2014) highlighted several statistical correlations between rock falls and meteorological factors, such as precipitation (daily precipitation interval, frequency of the interval) as a function of the geology and climate of the sites studied (Réunion, Burgundy, Auvergne). They confirm the link between precipitation and boulder falls in some regions, but not in others where more than 50% of events are linked to other factors (Fig 3).

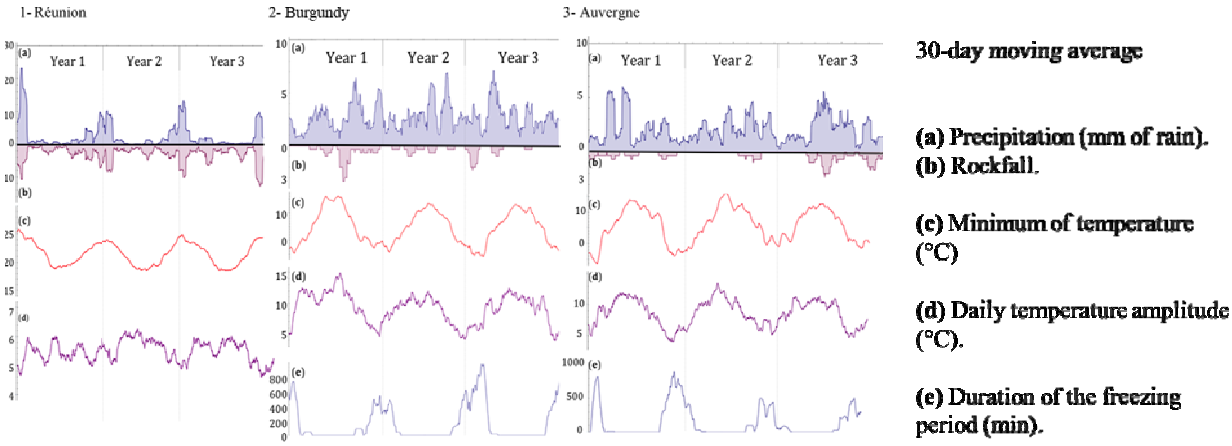


Fig. 3 Correlation between rockfalls and climatic factors, reworked from Delonca et al. (2014).

3.5 Modification of the calc-carbonic balance in the karstification process

A rather less intuitive aspect of the water table variations linked to climate change, is the changes to calc-carbonic balance in the karstification process. This phenomenon will be all the more important as the rocks are more soluble (gypsum, anhydrite).

Fig 4, inspired by Gombert (1994) shows the different stages of the karstification process. Binet et al. (2019) showed that the increase in global temperature will lead to an increase in the dissolved CO_2 content and thus modify the aggressiveness of seepage water. Similarly, increased temperatures and humidity will lead to an increase in the production of pedogenetic CO_2 which will make seepage water more aggressive and therefore disturb the calc-carbonic balance. It seems that climate change affects both hydrology, dissolution rates and mass movements, thus modifying karst patterns.

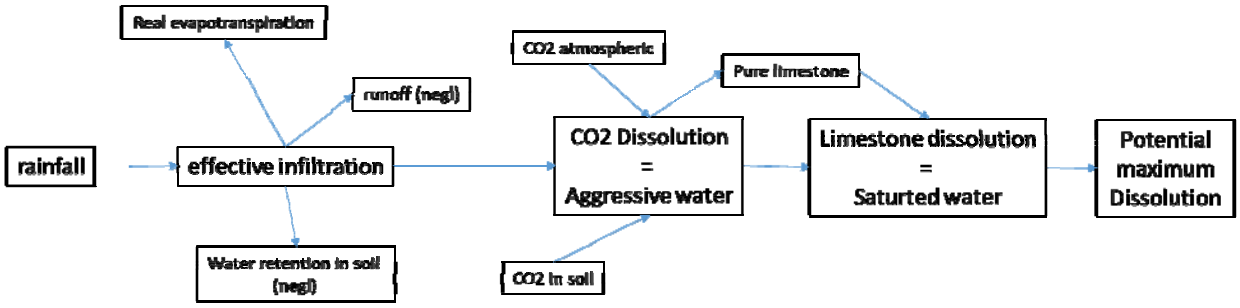


Fig. 4 The karstification process, inspired by Gombert (1994).

4 Impact of positive thermal variations on rock masses

4.1 Thermal shock

It is well known that thermal loading by temperature variation of the rock can induce inter- and intragranular micro-cracks related to the differential expansion of minerals (e.g., Fortin et al., 2018). But most of the studies carried out on this subject have been realized for temperatures well above 100°C which is not particularly relevant here. Nevertheless, they identify the phenomenon of thermal shock, which causes damage or even cracking of the rock under the influence of a sudden, large-amplitude temperature change. Hall (1999) proposes a critical thermal loading rate associated with thermal shock of approximately 2°C/min. The physical phenomenon is that related to quenching (Fortin et al., 2018), with an amplitude that will depend on the temperature variation. Classical quenching involves rapidly immersing a sample that has been heated up to 300°C in water at 20°C. The core of the sample is still hot and tends to contract, while the edges are already cold. In this case, the stresses at the edges of the sample can cause microcracks to form, extending from the edge of the sample toward its core. In the context of climatic variations, and considering the 2° threshold, it is reasonable to question whether such phenomena occur locally when (very) cold rain fall on a still-warm rock massif or in the case of wildfires fuelled by droughts.

4.2 Thermal fatigue

Beyond the effect of the punctual variation in temperature, thermal fatigue which results from repeated thermal cycles also plays an important role in the evolution of the rock mass. The oldest study found on the subject is from Grigg (1936). In recent years, more and more studies are proposing *in-situ* observations and measurements of the phenomenon (Bakun-Mazor et al., 2013; Breytenbach, 2022; Cloutier et al., 2015; Collins and Stock, 2016; Grøneng et al., 2011; Gunzburger et al., 2005; Vargas et al., 2004; Vlcko et al., 2009 among others). Merrien-Soukatchoff and Gasc-Barbier (2023) presented an up-to-date review of the measurement methods and in situ tools. Depending on the site, recording periods range from a few hours to more than a decade, and all types of rock are affected. The most commonly used measurement method involves installing crackmeters to observe the opening and closing of cracks with temperature. Fig 5 shows 2 examples for 4 days and 10 years.

Although observations and *in-situ* measurements are becoming more frequent, we still have very few experimental works to describe the corresponding mechanical behaviour (Aires-Barros, 1977; Gasc-Barbier et al., 2014; Gómez-Heras et al., 2006). Thermal fatigue significantly degrades the elastic moduli, tensile strength and uniaxial compressive strength of rocks (Villarraga et al., 2018) as well as tensile and shear parameters (Alzo'ubi and Alneasan, 2025). This damage is in fact a process of micro-

cracking caused by the combined action of differential expansion of rock constituents and local thermal gradients, both of which can give rise to high-intensity internal stresses (Hall and Thorn, 2014). Thus, while small temperature fluctuations may be considered an elastic phenomenon on a macroscopic scale, their repetition over time leads to fatigue damage, the formation or propagation of cracks, which can result in instability.

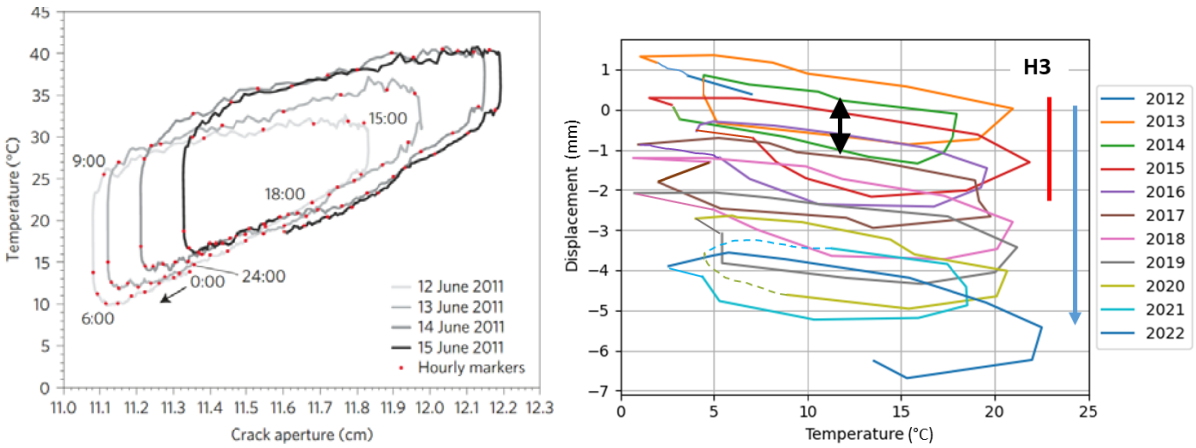


Fig. 5 Fracture openings/closures as a function of temperature. a- 4 days (Collins and Stock, 2016), b- 10 years (Gasc-Barbier et al. 2024).

5 Impact of changes in the 0°C isotherm

5.1 General concepts - definitions

Permafrost is a layer of ground (soil or rock) that remains frozen continuously for at least two consecutive years. It can occur both at the surface and at depth, sometimes extending hundreds of meters below the surface. This frozen ground typically contains ice, sediments, gases, and ancient organic matter. Permafrost is characteristic of polar and subpolar regions, but it also exists in high mountain areas. In Europe, it is found mainly around the Arctic Circle and in the Alps, and to a lesser extent in the Sierra Nevada and the Pyrenees.

Cryosuccion is a phenomenon in which liquid water is drawn, by capillary forces, toward the freezing zone within the rock in order to restore the water film that forms between the ice surface and the pore wall: when a rock cools below 0°C, the water contained in its pores or cracks freezes, but a thin layer of water always remains between the pore wall and the frozen water. As the volume of ice increases, this layer of water shrinks compared to what it would be on a free surface. Cryosuccion refers to the transport of liquid water toward the freezing front. If the increase in pressure caused by cryosuccion exceed the rock tensile strength, it can induce fracturing of the rock mass.

Cryoclasty is the process by which rock is fractured as a result of repeated freeze-thaw cycles.

In a given area, the depth of frost depends on both internal factors (water content, temperature, thermal conductivity, etc.) and external factors (outside temperatures, variations, ranges, frequencies, and snowpack thickness), which strongly influence the geological and climatic dynamics of cold environments. Climate change is leading to a decrease in the number of days with freezing temperatures, which will profoundly alter soil thermal conditions. The average increase in the 0 °C isotherm will reduce the cumulative period during which materials remain frozen. At the same time, this rise in the isotherm may lead to an increase in the number of freeze-thaw cycles that the ground will undergo, since areas that were initially frozen throughout the winter may be subjected to multiple cycles over the same period. This phenomenon is particularly significant in mountainous and polar regions.The change in thermal rhythm is accentuated by a faster melting of the snowpack, which exposes the ground to longer temperature variations. These transformations have several major consequences on the landscape. On the one hand, increased cryoclasty intensifies rock fragmentation, weakening slopes and cliffs (Fig 6). On the other hand, the gradual degradation of permafrost disrupts soil stability, contributing to landslides, subsidence, and the release of trapped gases. Finally, the accelerated melting and retreat of glaciers are profoundly transforming mountain environments, altering hydrology, ecosystems, and natural hazards.



Fig. 6 Photos illustrating slope destabilization related to Permafrost thawing. a. https://thenarwhal.ca; b. Photo K Orlinsky

5.2 Thawing of land that was initially permanently frozen

To understand the issue of ground thawing, it is important to recall the stabilizing role that ice plays in frozen ground: fissural ice acting as a very rigid cement, increases the cohesion and shear strength of rock fractures. Furthermore, it causes the ground to become artificially impermeable, since the water is frozen and cannot flow. Thus, the melting of ice trapped in rock fissures has significant consequences for the stability of rock masses. The temperature increase destabilizes the rock mass through three main mechanisms: increased ice plasticity, loss of adhesion between the ice and the rock, and increased hydraulic pressure within the rock mass due to meltwater. This process is particularly evident in high-mountain areas, where the degradation of permafrost leads to an increase in rockfalls and landslides (Ravanel et al. 2020). During thawing, the melting of ice affects not only the mechanical properties of the bedrock but also its waterproofing function, thereby accelerating cryogenic erosion of surface layers, particularly in the case of weathered rocks (see fig 6a).

Other erosive processes related to ice degradation must be taken into account, particularly paraglacial processes, such as glacial decompression: as glaciers retreat, the release of stress exerted by the ice on rock faces can lead to their destabilization. Ice shelves, which form a band of ice along the coastlines of cold regions, play a dual role. On the one hand, they protect these coastlines from mechanical marine forces, such as waves and currents, thereby slowing erosion. On the other hand, they play an erosive role by promoting abrasion on outcrops, particularly in soft rocks, and by contributing to cryoclasty.

5.3 Impact of freeze/thaw cycles

The impact of freeze-thaw (FT) cycles on rocks is probably the most widely studied climate-related phenomenon both on site and in laboratories. For instance, D'Amato et al. (2014) showed that the frequency of boulder fall on the St Eynard cliff was multiplied by 7 during freeze-thaw episodes.

In laboratories, it is observed that as the number of FT cycle increase, UCS, Elastic Young Modulus, elastic waves velocities and shear properties decrease (Aral et al., 2021; Deprez et al., 2020; Gasc-Barbier and Merrien-Soukatchoff, 2022; Liping et al., 2019; Liu et al., 2020; Ma et al., 2020; Martınez-Martinez et al., 2008; Yavuz, 2011; Zhou et al., 2020 among other)and depending on the experimental conditions, with a sufficient number of cycles, the sample can reach macroscopic failure, which is the illustration of cryoclasty. The physical process behind it lies in the fact that water expands by approximately 9% when it freezes. However, this increase in volume alone cannot explain the damage caused to rocks by freezing. Taber (1930) demonstrated that even when water in soils is replaced by an interstitial fluid that tends to contract, the ground surface still heaves up following freezing. This ‘heaving’ is linked to the cryosuccion described above and has a direct impact on the hydromechanical behaviour of the rock. It leads to the formation of segregation ice (ice lenses) that forms at the freezing front, causing a local increase in volume and a water deficit at depth, which can then result in desiccation fractures. When the ice melts, ice lenses gradually disappear, and in weak or highly fractured rock, this melting causes the rock to deform gradually. This phenomenon is called gelifluxion and macroscopically it looks like creep.

6 Conclusion and outlook

The impact of climate on the stability of rock masses is a complex subject that requires consideration across multiple temporal and spatial scales. In this paper, we have examined three different processes, impact of atmospheric water, positive thermal cycles, changes in the 0°C isotherm, which we have sought to illustrate briefly by describing both field observations and laboratory experiments. Although most of them are clearly identified on field, they are still often poorly described, particularly in terms of constitutive laws. A lot of work remains to be done to be able to accurately model the impact of climate on the rock mass, and even more so if we wish to anticipate the effects of climate change.

7 Acknowledgements

The author would like to express her gratitude to the Carnot Clim'adapt Institute of Cerema for its support.

References

Aires-Barros, L., 1977. Experiments on thermal fatigue of non-igneous rocks. Engineering Geology 11, 227–238.

Al Heib, M., Conil, N., Gombert, P., 2023. Influence of geology and topography on the occurrence of mine massive collapse—back-analysis of a historical collapse of chalk mine (France). Bull EngGeol 82, 230. 10.1007/s10064-023-03234-z

Althaus, E., Friz-T Pfer, A., Lempp, C., Natau, O., 1994. Effects of water on strength and failure mode of coarse-grained granites at 300 C. Rock Mech Rock Eng., 1994, 1994- 01-01; 27(1):1–21.

Alzo'ubi, A.K., Alneasan, M., 2025. The impact of moderate thermal fluctuations on dolomite: From strength enhancement to microstructural sensitivity. Results in Eng. 28, 107679. 10.1016/j.rineng.2025.107679

Aral, İ.F., Boy, R., Dinçer, A.R., 2021. Effects of freeze-thawing cycles on the physical and mechanical properties of basaltic and dolomitic rocks evaluated with a decay function model. Bulletin of Engineering Geology and the Environment 80, 2955–2962. 10.1007/s10064-021-02132-6

Bakun-Mazor, D., Hatzor, Y.H., Glaser, S.D., Carlos Santamarina, J., 2013. Thermally vs. seismically induced block displacements in Masada rock slopes. International Journal of Rock Mechanics and Mining Sciences 61, 196–211. 10.1016/j.ijrmms.2013.03.005

Bernardie, S., Desramaut, N., Malet, J.-P., Maxime, G., Grandjean, G., 2014. Prediction of changes in landslide rates induced by rainfall. Landslides 12. 10.1007/s10346-014-0495-8

Binet, S. et al. 2020. Global warming and acid atmospheric deposition impact on carbonate dissolution and CO2 fluxes in French karst hydrosystems: Evidence from hydrochemical monitoring in recent decades, Geochimica et Cosmochimica Acta, 270, pp. 184–200. 10.1016/J.GCA.2019.11.021.

Breytenbach, I.J., 2022. Seasonal bedrock temperature oscillations and inversions as a function of depth and the implications for thermal fatigue. Physical Geography 43, 401–418. 10.1080/02723646.2020.1847242

Brooks, S.M., Crozier, M.J., Glade, T.W., Anderson, M.G., 2004. Towards Establishing Climatic Thresholds for Slope Instability: Use of a Physically-based Combined Soil Hydrology-slope Stability Model. Pure and applied geophysics 161, 881–905. 10.1007/s00024-003-2477-y

Cascini, L., Cuomo, S., Pastor, M., Sorbino, G., 2010. Modeling of Rainfall-Induced Shallow Landslides of the Flow-Type. journal of geotechnical and geoenvironmental engineering - ASCE 85–98. 10.1061/(ASCE)GT.1943-5606.0000182

Castellanza, R., Lollino, P., Ciantia, M., 2018. A methodological approach to assess the hazard of underground cavities subjected to environmental weathering. Tunnelling and Underground Space Technology 82, 278–292. 10.1016/j.tust.2018.08.041

Cloutier, C., Locat, J., Charbonneau, F., Couture, R., 2015. Understanding the kinematic behavior of the active Gascons rockslide from *in-situ* and satellite monitoring data. Engineering Geology 195, 1–15. 10.1016/j.enggeo.2015.05.017

Collins, B.D., Stock, G.M., 2016. Rockfall triggering by cyclic thermal stressing of exfoliation fractures. Nature Geoscience 9, 395–400. 10.1038/ngeo2686

Conil N., Cosenza P., Defortis S., Do D.P., Gasc M., Jung S., Adi-Aad E. Climate Change and Rock Mechanics – Some Reflections. JNGG 2024. Poitiers, France. June 25-27, 2024.

D'Amato, J., Hantz, D., Guerin, A., Jaboyedoff, M., Baillet, L., Mariscal, A., 2016. Influence of meteorological factors on rockfall occurrence in a middle mountain limestone cliff. Nat. Hazards Earth Syst. Sci. 16, 719–735. 10.5194/nhess-16-719-2016

Delonca, A., Günzburger, Y., Verdel, T., 2014. Statistical correlation between meteorological and rockfall databases. Nat. Hazards Earth Syst. Sci. 14, 1953–1964. 10.5194/nhess-14-1953-2014

Deprez, M., De Kock, T., De Schutter, G., Cnudde, V., 2020. A review on freeze-thaw action and weathering of rocks. Earth-Science Reviews 203, 103143. 10.1016/j.earscirev.2020.103143

Djerbal, L., Melbouci, B., 2012. The Ain El Hammam landslide (Algeria): causes and evolution. Bulletin of Engineering Geology and the Environment 71. 10.1007/s10064-012-0423-x

Eisbacher G. Clague J. 1984. Destructive mass movements in high mountains: hazard and management, Geological Survey of Canada Paper 84-16, Ottawa, Ont. 1984. 230 p. https://publications.gc.ca/site/eng/9.852678/publication.html

Fortin, J., Gasc-barbier, M., Merrien-soukatchoff, V., 2018. Behaviour of rocks in temperature, in: Gasc-Barbier, M., Merrien-Soukatchoff, V., Berest, P. (eds.), Thermomécanique des roches. Presses des Mines, Paris.

Fei, L., Jaboyedoff, M., Derron, M.-H., Choanji, T., Sun, C., 2025. Multiscale observations of diurnal thermal effects on rock failure and crack dynamics in soft marl layers (La Cornalle molasse rock wall, Switzerland). Engineering Geology 354, 108159. https://doi.org/10.1016/j.enggeo.2025.108159

Gasc-Barbier, M., Girma, G., Gendre, V., 2014. Laboratory analysis of thermal fatigue in limestone, in: Rock Engineering and Rock Mechanics: Structures in and on Rock Masses - Proceedings of EUROCK 2014, 10.1201/b16955-46

Gasc-Barbier, M., Merrien-Soukatchoff, V., 2022. Effect of Freezing-Thawing Cycles on the Elastic Waves' Properties of Rocks. Geosciences 12, 103. 10.3390/geosciences12030103

Gasc-Barbier, M., Merrien-Soukatchoff, V., Krzewinski, V., Azemard, P., Genois, J.-L., 2024. Assessment of the influence of natural thermal cycles on dolomitic limestone rock columns: A 10-year monitoring study. Geomorphology 464, 109353. https://doi.org/10.1016/j.geomorph.2024.109353

Gombert, P., 1994. Simplified theoretical approach to karst dissolution. Karst 24:41–51.10.3406/karst.1994.2341

Gombert P, Auvray C, Al Heib M (2013) *In-situ* and laboratory tests to evaluate the impact of water table fluctuations on stability of underground chalk mines. Procedia Earth and Planetary Science 7:304–308

Ghoreychi, M. 1983 Stability of partial workings with pillars in a post-failure state: application to the case of underground chalk quarries. Ph.D. thesis in Vandoeuvre-les-Nancy, INPL 1983

Gómez-Heras, M., Smith, B.J., Fort, R., 2006. Surface temperature differences between minerals in crystalline rocks: Implications for granular disaggregation of granites through thermal fatigue. Geomorphology 78, 236–249. 10.1016/j.geomorph.2005.12.013

Griggs, D.T., 1936. the factor of fatigue in rock exfoliation. The Journal of Geology 44 (7):783-796

Grøneng, G., Christiansen, H., Nilsen, B., Blikra, L, 2011. Meteorological effects on seasonal displacements of the Åknes rockslide, western Norway. Landslides 8, 1–15. 10.1007/s10346-010-0224-x

Gunzburger, Y., Merrien-Soukatchoff, V., Guglielmi, Y., 2005. Influence of daily surface temperature fluctuations on rock slope stability: Case study of the Rochers de Valabres slope (France). Inter J. of Rock Mech. and Min Sc. 42, 331–349. 10.1016/j.ijrmms.2004.11.003

Hall, K., 1999. The role of thermal stress fatigue in the breakdown of rock in cold regions. Geomorphology 31, 47–63. 10.1016/S0169-555X(99)00072-0

Hall, K., Thorn, C.E., 2014. Thermal fatigue and thermal shock in bedrock: An attempt to unravel the geomorphic processes and products. Geomorphology 206, 1–13. 10.1016/j.geomorph.2013.09.022

IPCC, 2019. Global Warming of 1.5°C IPCC Special Report on the Impacts of Global Warming of 1.5°C Above Pre-Industrial Levels and the Associated Global Greenhouse Gas Emission Trajectories in the Context of the Climate.

Iverson, R.M., 2000. Landslide triggering by rain infiltration. Water Resources Research 36, 1897–1910.

Korsnes, R.I., Madland, M.V., Austad, T., Haver, S., Røsland, G., 2008. The effects of temperature on the water weakening of chalk by seawater. Journal of Petroleum Science and Engineering 60, 183–193. 10.1016/j.petrol.2007.06.001

Lafrance N, Souley M, Auvray C, Favreau O, Labiouse V (2014) Aging of chalk rocks in an underground quarry. Rock engineering and rock mechanics: structures in and on rock masses: proceedings of the international symposium EUROCK 2014b: 445–450. Leiden: CRC Press

Liping, W., Ning, L., Jilin, Q., Yanzhe, T., Shuanhai, X., 2019. A study on the physical index change and triaxial compression test of intact hard rock subjected to freeze-thaw cycles. Cold Regions Science and Technology 160, 39–47. 10.1016/j.coldregions.2019.01.001

Liu, T., Zhang, C., Cao, P., Zhou, K., 2020. Freeze-thaw damage evolution of fractured rock mass using nuclear magnetic resonance technology. Cold Regions Science and Technology 170, 102951. 10.1016/j.coldregions.2019.102951

Ma, W., Gao, W., Guo, S., Zhao, Y., Wu, Z., Yang, C., 2020. Evaluation and improvement on the freeze-thaw durability performance of the polyurethane stabilized Pisha sandstone for water and soil conservation. Cold Regions Science and Technology 177, 103065. 10.1016/j.coldregions.2020.103065

Martınez-Martinez, J., Benavente, D., Ordonez, S., Garcıa-del-Cura, M.A., 2008. Multivariate statistical techniques for evaluating the effects of brecciated rock fabric on ultrasonic wave propagation.

International Journal of Rock Mechanics and Mining Sciences 45, 609–620. 10.1016/j.ijrmms.2007.07.021

Merrien-Soukatchoff, V., Gasc-Barbier, M., 2023. The Effect of Natural Thermal Cycles on Rock Outcrops: Knowledge and Prospect. Rock Mechanics and Rock Engineering 56, 6797–6822. 10.1007/s00603-023-03420-1

Ollier, C.D., 1963. Sunstroke weathering; examples from central Australia. American Journal of Science 261, 376–381. 10.2475/ajs.261.4.376

Pan, Y., Wu, G., Zhao, Z., He, L., 2020. Analysis of rock slope stability under rainfall conditions considering the water-induced weakening of rock. Computers and Geotechnics 128, 103806.10.1016/j.compgeo.2020.103806

Paquette Y. 2014. Behaviour of the land above partial workings, diagnosis of stability and organisation of the monitoring of abandoned partial workings. The case of the quarries of the Nord-Pas-de-Calais region 42. HAL Id: ineris-00972119. https://ineris.hal.science/ineris-00972119.

Raj, M., Sengupta, A., 2014. Rain-triggered slope failure of the railway embankment at Malda , India Rain-triggered slope failure of the railway embankment at Malda , India. Acta Geotechnica 9, 789–798. 10.1007/s11440-014-0345-9

Ravanel, L., Magnin, F., Deline, P., 2017. Impacts of the 2003 and 2015 summer heatwaves on permafrost-affected rock-walls in the Mont Blanc massif. Science of the Total Environment 609, 132–143. 10.1016/j.scitotenv.2017.07.055

Ravanel L., Magnin F., Gallach X., Deline P. 2020. Évolution des parois rocheuses gelées de haute montagne sous forçage climatique. La Météorologie, 2020, 111, pp.34-40. ff10.37053/lameteorologie-2020-0090ff. ffhal-03028348v2f

Sandersen, F. &Bakkehøi, Steinar&Hestnes, Erik & Lied, K. 1997. The influence of meteorological factors on the initiation of debris flows, rockfalls, rockslides and rockmass stability. Publikasjon - NorgesGeotekniskeInstitutt. 201. 97-114.

Song, Z., Li, X., Lizárraga, J.J., Zhao, L., Buscarnera, G., 2020. Spatially distributed landslide triggering analyses accounting for coupled infiltration and volume change. Landslides v. 10.1007/s10346-020-01451-1

Taber, S., 1930. The Mechanics of Frost Heaving. The Journal of Geology 38, 303–317. https://doi.org/10.1086/623720

Terajima, T., Miyahira, E., Miyajima, H., Ochiai, H., Hattori, K., 2013. How hydrological factors initiate instability in a model sandy slope. Hydrological Processes 28, 5711–5724. 10.1002/hyp.10048

Uwihirwe, J., Hrachowitz, M., Bogaard, T.A., 2020. Landslide precipitation thresholds in Rwanda. Landslides 17, 2469–2481. 10.1007/s10346-020-01457-9

Vargas, E.A., Castro, J.T., Amaral, C., Figueiredo, R.P., 2004. On mechanisms for failures of some rock slopes in Rio de Janeiro, Brazil: thermal fatigue?, *in*: Landslides: Evaluation and Stabilization/Gliss de Terrain: Evaluation et Stabilisation, Set of 2 Volumes. pp. 1007–1011.

Villarraga, C.J., Gasc-Barbier, M., Vaunat, J., Darrozes, J., 2018. The effect of thermal cycles on limestone mechanical degradation. International Journal of Rock Mechanics and Mining Sciences 109. 10.1016/j.ijrmms.2018.06.017

Vlcko, J., Greif, V., Grof, V., Jezny, M., Petro, L., Brcek, M., 2009. Rock displacement and thermal expansion study at historic heritage sites in Slovakia. Circa Geol 58, 1727–1740. 10.1007/s00254-008-1672-7

Wang, J.G., Ichikawa, Y., Leung, C.F., 2003. A constitutive model for rock interfaces and joints. International Journal of Rock Mechanics and Mining Sciences 40, 41–53. 10.1016/S1365-1609(02)00113-2

Yatsu, E., 1988. the nature of weathering: an introduction, Sozosha. ed. Overseas distributor Maruzen Co., Tokyo

Yavuz, H., 2011. Effect of freeze-thaw and thermal shock weathering on the physical and mechanical properties of an andesite stone. Bulletin of Engineering Geology and the Environment 70, 187–192. 10.1007/s10064-010-0302-2

Zhao, X., Sun, Y., Feng, Q., Baharuddin, M.F.T., Hazreek, Z.A.M., Azman, A.A., Hsiao, D.H., Hsieh, C.S., Yeh, L.C., Lin, D.Y., Phan, V.T.-A., 2018. A study on an instability slope in Taiwan subjected to rainfalls. IOP Conf. Series: Earth and Environmental Science 143, 12018. 10.1088/1755-315/143/1/012018

Zhou, X.P., Li, C.Q., Zhou, L.S., 2020. The effect of microstructural evolution on the permeability of sandstone under freeze-thaw cycles. Cold Regions Science and Technology 177, 103119. 10.1016/j.coldregions.2020.103119

Zhou, Z., Cai, X., Cao, W., Li, X., Xiong, C., 2016. Influence of water content on mechanical properties of rock in both saturation and drying processes. Rock Mech Rock Eng 49 (8), 3009–3025.

Understanding failure mechanisms to design and manage risks for surface and underground excavations

N. Bar
Gecko Geotechnics, Kingstown, Saint Vincent and the Grenadines
neil@geckogeotech.com
0000-0001-7948-2468

Abstract

Ground failures are a common aspect of rock slope and underground excavation design. Some ground failures are accepted and even economically attractive provided they are managed so that no personnel are at unacceptable risk. Too many failures impact on productivity and project costs. Larger scale ground failures are less tolerable due to their economic impacts, schedule delays and negative publicity, irrespective of how well they were managed. Poorly managed ground failures have been the cause of numerous fatalities in mining, tunnelling and construction industries.

Failure mechanisms in surface and underground excavations are becoming more and more understood. With improvements in numerical modelling since the 2000s, it has become possible to replicate almost all complex failure mechanisms in numerical simulations. However, more often than not, this level of detail occurs only after a ground failure event has happened. Much of the predictive stability modelling that is undertaken during the design of a rock slope or underground excavation contains significant geological uncertainty, includes simplification when simulating potential geotechnical problems and does not consider all plausible failure mechanisms. For many projects, this design is static, and is not revisited after excavations commence and more engineering geological information becomes available.

This paper focuses on the need for understanding failure mechanisms to effectively design surface and underground excavations and manage residual risks through a combination of a continuous improvement framework and critical control measures.

Keywords

Failure mechanisms, Rock slopes, Underground excavations, Continuum, Discontinuum.

1 Introduction

Collapses or failures of rock slopes or underground excavations present various forms of risk to people, equipment, infrastructure and the environment.

Rock slope failures on man-made and natural slopes include slope instability, rock falls and landslides, as well as debris flows and shallow slips in weathered rock. Similarly, for underground excavations, collapses may involve excavation-scale instability, rock (or block) falls, squeezing, rockburst and inrushes in some conditions.

1.1 Socioeconomic impacts of ground failure events

The socioeconomic consequences of rock slope and underground excavation failures have direct costs such as removing the failed rock debris and stabilizing the excavation. There is also a wide range of indirect costs which include, but are not limited to:

- Potential losses of life;
- Damage to vehicles and injury to passengers on highways, railways and tunnels or damage to equipment and injury to personnel in mining;
- Damage to buildings and infrastructure in urban areas in the event of near surface tunnel collapses;
- Traffic and goods transport delays;
- Business disruptions, loss of revenue or reduced productivity;
- Decreased land values and associated loss of tax revenue;
- Flooding and/or disruption of water supplies where rivers are blocked by landslides;
- Impairment or sterilization of mineral resources;
- Legal costs, social costs, reputational damage to designers, construction and mining companies with potential for company closure.

In the twelve-year period between 2004 and 2016, almost 56,000 fatalities were recorded globally (i.e. average of 4,666 per annum) from non-seismic slope failures including landslides (Froude and Petley, 2018). The majority of these slope failures involved human activity such as mining, construction and hill cutting and many were initiated by rainfall. As illustrated in Figure 1, more recent research indicates the frequency of fatal landslide events has increased considerably in 2024 and 2025 and included 4,933 and 5,091 fatalities, respectively (Petley, 2025; 2026).

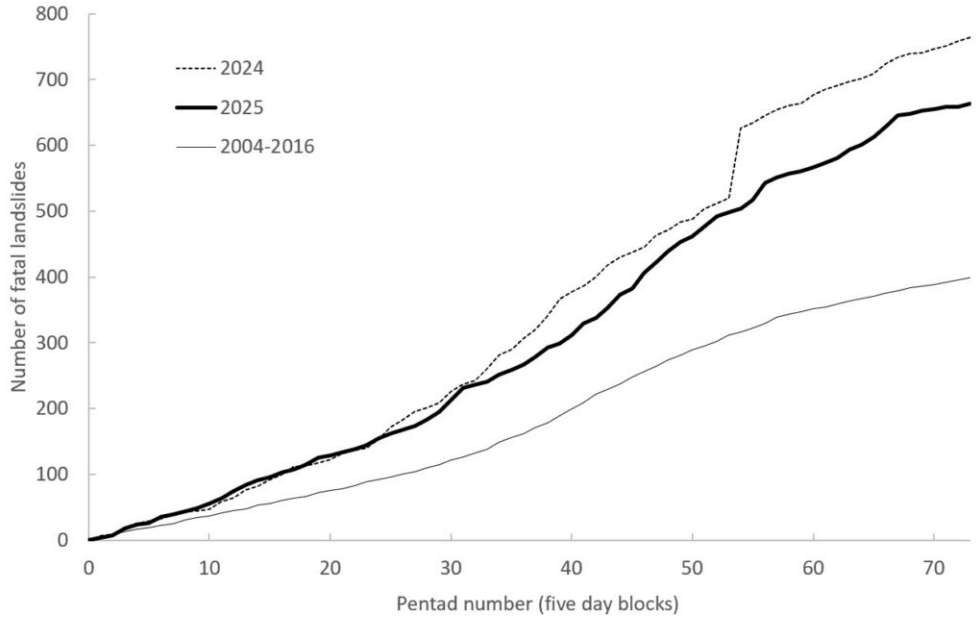


Fig. 1 Global fatal landslides in 2025 plotted using pentads (five-day blocks) with the 2004-2016 long term average and the exceptional year of 2024 are included for reference (Petley, 2026).

Documented examples of socioeconomic consequences of rock slope failures include:

- The Manefay Slide at the Bingham Canyon copper mine in 2013 was approximately 50 million cubic metres in volume (Ross, 2017). It was estimated to cost over $1 billion to clean

up. In Salt Lake County, Utah, sales-tax revenues reduced by 3.4% by the end of 2013 and were attributed to the slope failure (Ward, 2015);

- Several fatal landslide events have occurred in recent years in the mining industry and resulted in 200 fatalities in 2026 at Rubaya Coltan mine, Democratic Republic of the Congo (RFI, 2026) and 53 fatalities in 2023 at Xinjing coal mine, China (Li et al. 2025);
- In Medellin, Colombia, where bedrock is highly weathered and intense rainfall events occur, 74% of deaths resulting from natural hazards are due to slope failures. A single slope failure in 1974 resulted in over 770 fatalities (Carvajal et al. 2012).

The consequences of rock failure in underground excavations were the source of significant research and technological improvement throughout the 20th century; including improved rock mass classification and empirical design, the use of improved ground support such as shotcrete and systematic bolting to replace steel arches as well as the use of tunnel boring machines (TBM).In the 21st century, further advancements included the use of numerical simulations of stability, monitoring, and an enhanced 'safety first' culture. By way of comparison, the construction of the Gotthard tunnels in Switzerland had significantly less rock failure related fatalities in the 20thand 21stcenturies as excavation methods and ground support technology improved (Idris et al. 2004):

- 1872-1882: 177 fatalities during railway tunnel construction;
- 1969-1980: 12 fatalities during road tunnel construction;
- 1999-2016: 2 fatalities during Gotthard Base Tunnel construction (Wikipedia, 2026).

For similar reasons to those in tunnelling, underground mining has also observed dramatic reductions in fatalities in many countries. By way of example in Figure 2, fatalities from roof failures in underground coal mines in the United States (US) have reduced significantly. Mark (2024) indicated that more than 50,000 fatalities from roof falls were recorded in the 20th century. This has dramatically reduced in the first part of the 21st century with zero fatalities from roof falls being recorded in 2016, 2018, 2019 and 2020 (Mark, 2024). However, further improvement remains possible with 46 fatalities and 33 permanent disabilities recorded from roof falls in coal and non-metal mines in the US between 2010 and 2019 (Rashed et al. 2022).

Higher levels of improvement were observed in the Western Australian mining industry where rock falls were ranked the number one cause of fatalities in the 1980s and 1990s (DMP, 2014). Between 2000 to 2012, only three fatalities were recorded in underground mines related to working below unsupported ground and two from pit slope failures.

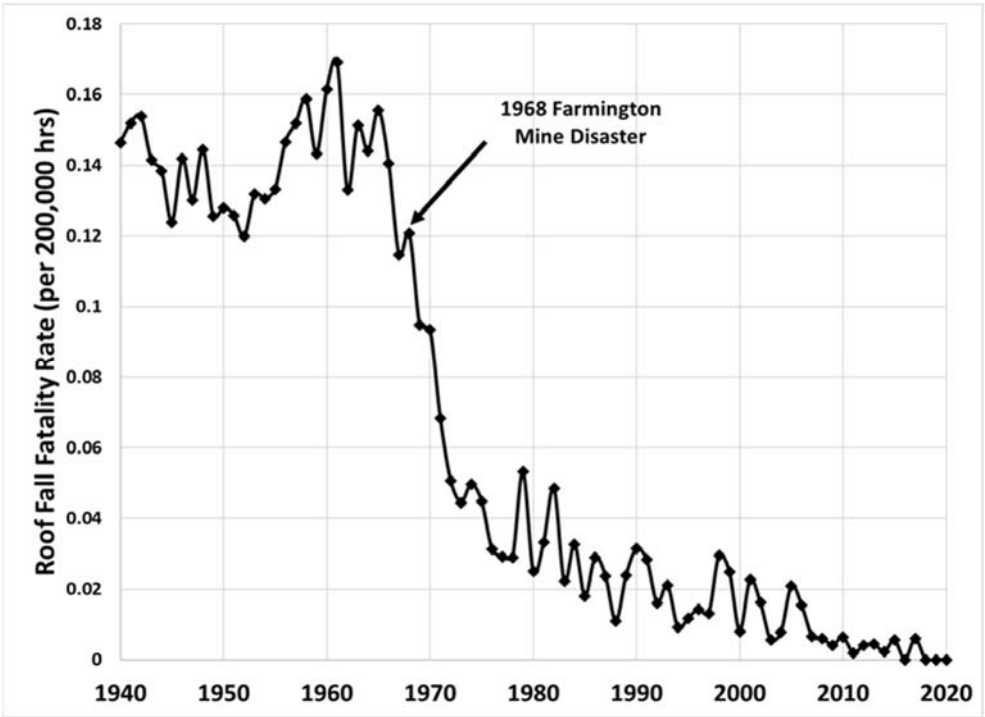


Fig. 2 Roof fall fatality in US underground coal mining, 1940-2020 (Mark, 2024).

Rock failures can also initiate secondary hazards. A rock slope failure into a body of water can trigger a seiche (tsunami in a closed body of water). Examples can be found in nature and civil and mining engineering projects, including:

- Rock slides from Ramnefjell mountain into Lake Lovatnet caused enormous waves that washed up to 74 m above the lake's water level in Norway during the first part of the 20th century and caused more than 60 fatalities (Grimstad, 2005; Waldmann et al. 2021);
- The Vajont slide in Italy in 1963 inundated a reservoir, sending a wave over the crest of the dam that destroyed the town of Longarone and resulted in over 2000 fatalities (Kiersch, 1965; Ghirotti et al. 2013);
- A pit wall failure into a flooded pit at Katanga copper mine in the Democratic Republic of the Congo resulted in seven fatalities (Jamasmie, 2016). Days later, a similar event at Ok Tedi copper-gold mine in Papua New Guinea caused another fatality (Tlozek, 2016).

A voluminous failure underground can cause an airblast or a sudden and often dangerous displacement of a massive volume of air; for example, a pillar collapse during block caving caused an air blast that killed four miners at North Parkes mine in Australia in 1999 (Bailey, 2003).

Smaller sized rock falls or failures in operating railway tunnels can be the cause of derailment as had occurred in the Vierzy railway tunnel in 1972, which resulted in 108 deaths (Arnould, 2010).

1.2 Geological (inherent) uncertainty

In both civil and mining engineering projects, it is practically impossible to assess the stability of rock slope cuttings and benches, tunnel advance or underground mine development in real-time, using analytical approaches such as kinematics, limit equilibrium or numerical modelling. The rate of excavation advance is usually too fast for this (Bar, 2024). Empirical methods using rock mass classification systems such as RMR (rock mass rating) and Q for underground excavations and SMR (slope mass rating) and Q-slope offer near real-time approaches for assessing stability and support requirements. However, rock mass classification systems often may not be able to address all the issues at stake. The trigger for the instability of a design may depend on minor details such as the occurrence, the precise orientation or the persistence of a geological structure (joint, fault, etc) in a particular position in the rock mass in relation to the excavation, the larger or smaller extent of an altered zone or the length and quality of a reinforcement element (Alejano, 2025).

Since rock slopes, tunnels and mines are excavated in natural geological formations (which usually have limitations with respect to site investigations), significant uncertainty and variability inevitably exists in the estimation or calculation of resting forces. Uncertainty in slope and underground excavation design primarily stems from the inherent natural variability of ground conditions; i.e. geological and engineering geological uncertainty and anomalies (Hoek and Diederichs, 2006).Figure 3 describes rock slope design uncertainty associated with the geotechnical components and is based on a similar concept for tunnelling scenarios by Paraskevopoulou and Boutsis (2020).

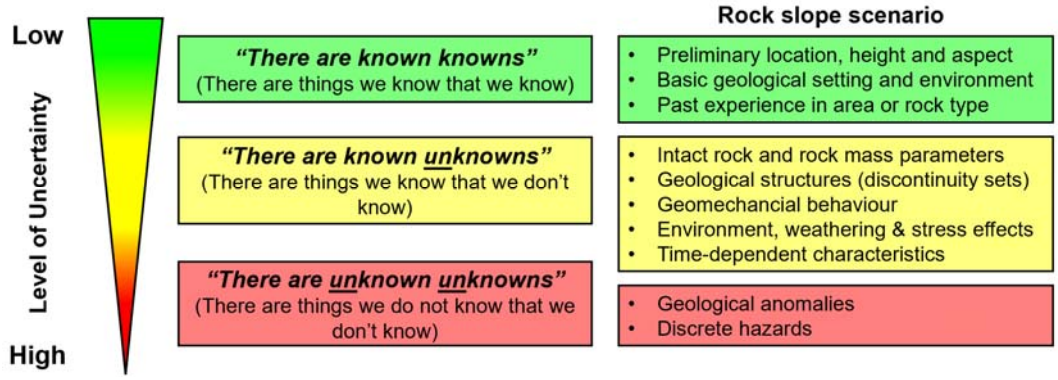


Fig. 3 Design uncertainty in association with the geotechnical engineering components for a rock slope scenario (Bar, 2024).

1.3 Design frameworks and processes

Rock slope design has been considered an iterative process in civil and mining engineering projects for 50 years since Hoek and Londe (1974) developed the closed-loop framework shown in Figure 4. This flow chart has a robust initial design process, which is followed by monitoring and observing

slope performance during excavation, and feeding back observations, lessons learned and new data into improving the design.

Similar frameworks for the design of rock slopes have been adopted in civil and mining engineering with guidance provided by Wyllie and Mah (2004) and for ground support design of underground excavations (Hoek et al. 2000).

In the late 2000's, divergence occurred between rock slope design in civil and mining engineering applications with the development of guidelines for open pit slope design (Read and Stacey, 2009) as part of the mining industry funded Large Open Pit (LOP)project. This was followed by an update to rock slope engineering guidance for civil engineering applications by Wyllie (2018). The resultant slope design process in Figure 4 for open pits by Read and Stacey (2009) includes an iterative process for considering mine planning and risk evaluation prior to excavation. However, unlike its predecessors, it does not have a clear feedback loop for improving and optimizing the design based on monitoring, new data, slope performance, etc.

It is understood that the next update of the LOP project (circa 2027) will include a closed-loop framework following the general principles of Hoek and Londe (1974) with consideration for modern slope and underground monitoring systems and their capability in identifying emerging hazards or threats (Nicoll et al. 2017; Lynch et al. 2018; Bar and Dixon, 2021).

Hoek et al (2000) and ÖGG (2010) provide similar schematic procedures for the geotechnical design of underground excavations. Many consulting firms and mining companies prescribe internal procedures for rock slope and underground excavation design for the purpose of standardization (Haile et al. 2020). In many instances, such processes may deviate significantly from the general principles by Hoek and Londe (1974) and Hoek et al (2000) and focus on achieving standardized outputs without investigating failure mechanisms in sufficient detail.

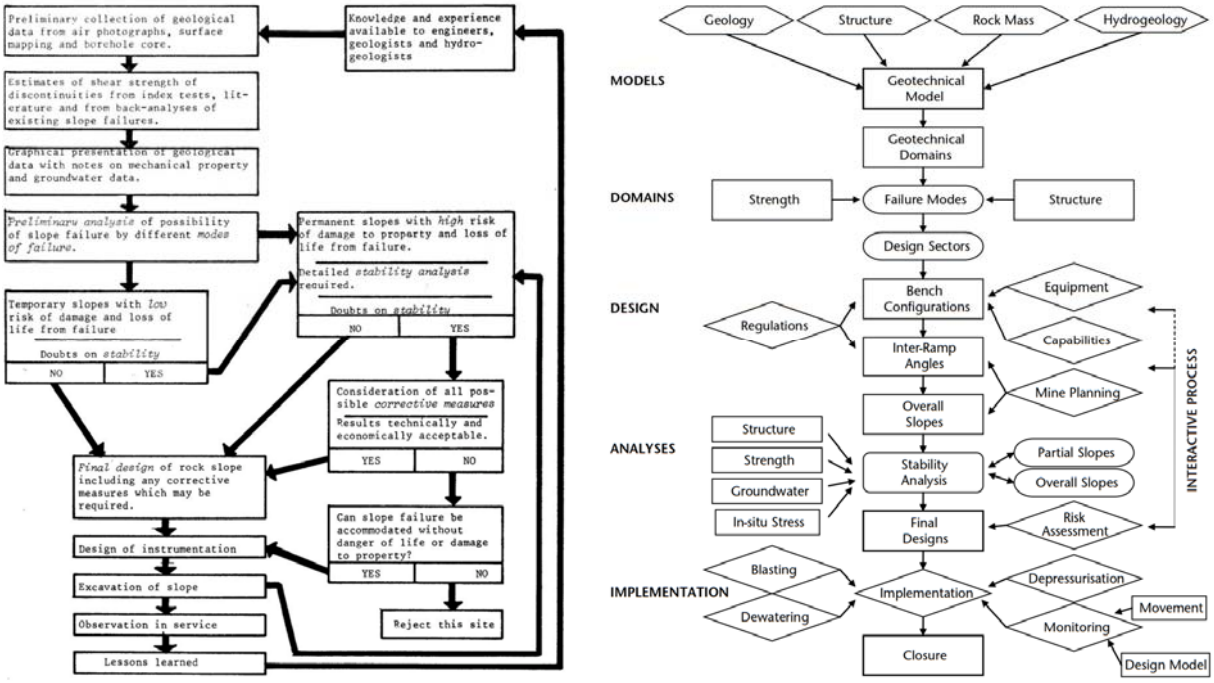


Fig. 4 Left: Closed-loop rock slope design flow chart (Hoek and Londe, 1974). Right: Linear open pit slope design process (Read and Stacey, 2009).

Rock excavation design and management in civil and mining engineering applications are quite different in terms of:

- The design life of a civil engineering slope, tunnel or cavern could be in excess of 100 years, whilst a slope, development or stope in a mine could range from a few weeks or months (individual benches, stopes and production developments), to a few years (inter-ramp slopes and capital development),or several years (overall slopes, shafts, etc).
- Risk exposure in civil engineering excavations involves the public (e.g. several thousands of people or more per day on roads, highways and railways) with very little or no access control

and without routine monitoring instrumentation. On the contrary, in mining, access is strictly controlled (e.g. typically less than 200 mine workers per day) with several options for additional control measures; including monitoring instrumentation.

- Prior to design, site investigations for civil engineering excavations may be limited to outcrop mapping and limited drilling for understanding subsurface conditions. On the contrary, mineral deposits are extensively drilled to understand the economic feasibility of deposit extraction. Arguably there should be a lower level of uncertainty in a mining engineering project than in civil engineering; however, geological and geotechnical conditions around a mining project are often significantly more complex.

Despite the abovementioned differences, uncertainty related risks described in Figure 3 affect the design and management of rock slopes and underground excavations in civil and mining engineering projects in a similar manner.

By adopting the framework for slope and underground excavation design and management in Figure 5, uncertainty and risk can be reduced and proactively managed through a continuous improvement process. Such a process would assist in managing safety and has capacity to add economic value by enabling slope optimization as well as underground excavation size and support optimization.



Fig. 5 Continuous Improvement Framework for Safe and Economic Rock Excavation Design and Management.

The continuous improvement framework in Figure 5 can be incorporated into a Ground Control Management Plan (GCMP) or Slope Management Plan (SMP) with detailed processes for each component. By way of example, various elements of the 'Geotechnical Model and Understanding Failure Modes' could be described in further detail, as could the process for their development and their limitations:

- Geological model (lithology, weathering and alteration);
- Structural model (major, medium and minor);
- Rock mass model;
- Stress model;
- Groundwater model;
- Potential failure modes.

Understanding the limitations of a geotechnical model and potential failure modes can be used to define the risks from which appropriate control measures can be developed including the selection of suitable modelling and monitoring methods.

2 Understanding failure mechanisms

Understanding failure mechanisms that can occur for a specific rock slope or underground excavation is a key step for selecting appropriate stability analyses to develop a suitable design. Such a design may consider slope angles and heights, underground excavation spans and shapes, ground support requirements, depressurization (e.g. pore pressure reduction) requirements, etc.

2.1 Rock slopes

Real world rock slope failures are rarely circular, spherical or ellipsoidal. In a recent review of over 500 rock slope failures in open pit mines, rock mass and circular failure modes accounted for only 10% and 8% of the database, respectively (McQuillan and Bar, 2024). The vast majority and remaining 82% were structurally-driven failures such as planar, wedge, toppling or step-path mechanisms. Similarly, in a database of over 600 rock slopes assessed as part of the development of the Q-slope method for rock slope engineering, Bar and Barton (2024) identified that circular failure accounted for only 3% of cases.

Since most failure modes in rock slopes are structurally-driven and may involve one or more geological faults or other persistent singularities, which are almost certainly oblique (i.e. not perfectly parallel) to the slope, stability should be assessed in three dimensions (3D). Rock slope failure modes should be assessed using 3D analysis method in a geotechnical design review process in the case of any of the following conditions (McQuillan and Bar, 2023):

- Non-linear slope geometry;
- Spatially or laterally varying geological and hydrogeological conditions;
- Spatially varying material strengths, including anisotropic material behaviour in the same unit;
- Singularities and persistent geological structures, striking and intersecting up to 50° from the slope orientation;
- Highly variable 2D results within close spatial proximity to each other.

Many rock mechanics and geotechnical engineering textbooks describe the four simple failure mechanisms for rock slopes shown in Figure 6 (Wyllie and Mah, 2004):

a. Plane failure, i.e. planar sliding along one persistent discontinuity which is dipping out of the face. Planar failures generally occur when the discontinuity is sub-parallel (±20°) to the strike of the slope;
b. Wedge failure, i.e. sliding along the intersection of two discontinuities. The plunge of the line of intersection between the two joint planes must be flatter than the dip of the slope face;
c. Toppling failure occurs in strong rock containing discontinuities dipping steeply into the face. Two types of toppling exist: block (*e*) and flexural (*f*) per Figure 7;
d. Circular failure in rock fill, very weak rock or closely fractured rock with randomly oriented discontinuities (Wyllie and Mah, 2004). However, the textbook definition of circular failures is seldom applicable to rock slopes. Although in many instances, failure mechanisms visually appear circular or ellipsoidal in jointed rock masses, they are usually step-path mechanisms involving some dominant discontinuity sets. As such, the term ‘circular failure’ is often interchanged with the terms ‘rock mass failure’ or ‘step-path failure’ when dealing with rock slopes. In rare cases, circular failures occur in extremely weak, homogeneous rock masses that display soil-like properties (e.g. saprolites).

Goodman and Shi (1985) and Poisel and Preh (2004) discuss failure mechanisms for rock slopes in greater detail as shown in Figure 7:

e. Block toppling involving the forward rotation of column or slab-shaped blocks, similar to dominos. These mainly occur in high strength rocks with low discontinuity strengths (Goodman and Bray, 1976);
f. Flexural toppling caused by bending of column or slab-shaped rock blocks like a cantilevered beam (Hittinger and Goodman, 1978);
g. Rock slumping involving the backward rotation of rock blocks (Kieffer, 1998);
h. Slab translation, rotation or tower descent can occur where high strength rocks overlay an incompetent base – “hard on soft” (Poisel and Eppensteiner, 1988);
i. Column buckling of slab-shaped blocks can occur where the slab thickness is significantly less than the slope height (Cavers, 1981);
j. Kink band slumping involves an ‘S’ shaped deformation in laminated rock due to slope creep (Kieffer, 1998);

k. Active-passive blocks (or wedges) involve the sliding of multiple rock blocks on a polygonal sliding plane, which is usually 'activated' by the upper block(s) and resisted to a degree by the lower block(s) (Gußmann, 1981);
l. Translational creep involves continuous downslope deformation and is mainly associated with low strength rocks such as shales and phyllites (Zienkiewicz et al. 1975);
m. Block falls, also termed rock falls or falling of loose blocks (Goodman and Shi, 1985);
n. Single block rotation on a discontinuity (Wittke, 1990);
o. Complex failure mechanisms formed by a combination of components of failure mechanisms described in *a* to *n*. Geological conditions are often complex such that failure mechanisms often involve a combination of the simple modes of failure (i.e. a combination of plane, wedge, toppling and circular) to form a 'complex' (or composite) failure mechanism. Often, this is also referred to as 'step-path failure' and this category of failure involves various combinations of shearing on discontinuities and fracturing of intact rock bridges (McMahon, 1971; Baczynski, 2000; Baczynski and Bar, 2019).

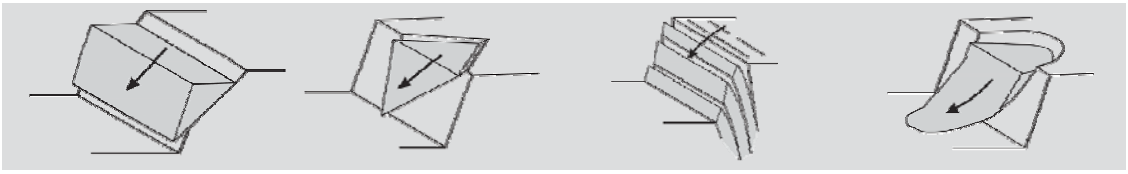


Fig. 6 Illustrations of simple rock slope failure mechanisms (Wyllie and Mah, 2004).

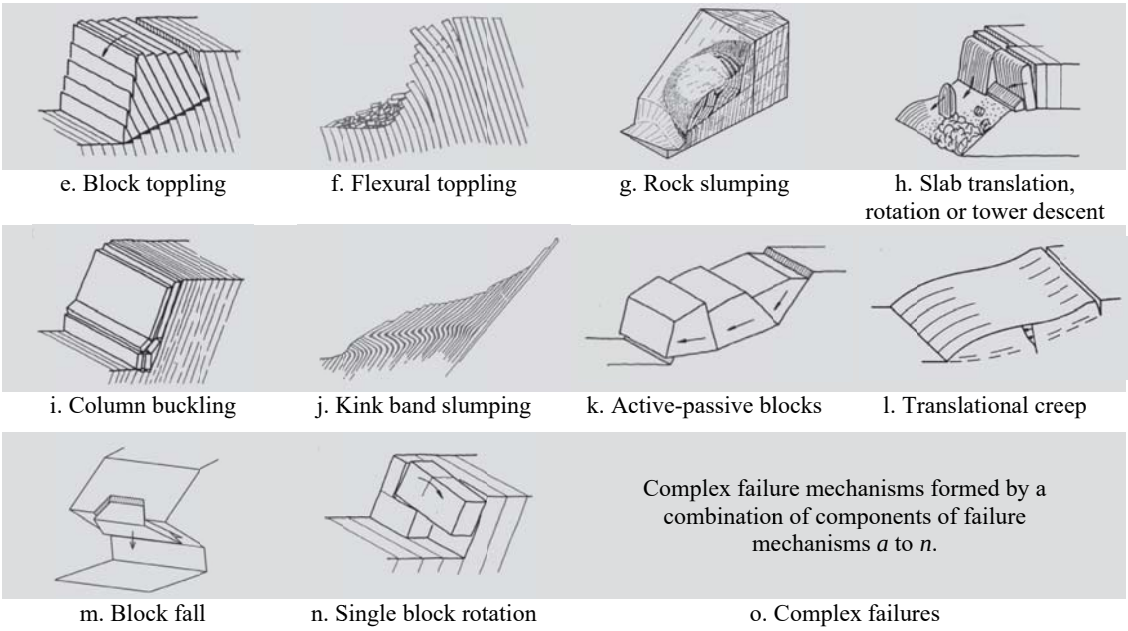


Fig. 7 Illustrations of additional rock slope failure mechanisms (Poisel & Preh, 2004).

Yuan et al. (2026) describe several combined failure mechanisms in rock slopes (e.g. active-passive blocks comprising a planar slide in the active block causing toppling in the passive block below).

Slope stability in weak and complex rock masses is a practical problem where anisotropy, weathering, and heterogeneity must be incorporated adequately in geotechnical models for stability analyses (Jovanovski et al. 2024).

For the design of rock slopes, it is critical to ensure that reasonable failure modes are investigated based on the geotechnical model. Quite simply, assessing for rotational (circular or near-circular) failure modes is considered inadequate in the context of real world, physical outcomes (Bar, 2024).

McQuillan et al. (2020) undertook a survey of the Australian coal mining industry enquiring what types of slope stability analyses were routinely applied. The results indicated over 90% of engineers applied 2D Limit Equilibrium Method (LEM) and over 80% undertook kinematic analysis using stereographic projections. Kinematic analysis is able to assess the potential for simple failure modes such as planar and wedge sliding and toppling. 2D LEM is able to calculate the Factor of Safety of

slopes with potential for planar sliding and circular or near-circular rotational failure mechanisms. Neither of the abovementioned commonly used methods can assess the Factor of Safety of slopes with potential wedges, toppling, active-passive blocks, complex or combined failure modes, or slopes with complex geometry or the inclusion of one or more faults or anisotropy that are not perfectly perpendicular to the 2D cross-section. Remarkably, less than 15% of survey responses indicated the use of 3D numerical methods; which are able to assess complex failure mechanisms which may be structurally-driven.

For the purpose of calculating a Factor of Safety, 2D and 3D LEM can only be used for failure mechanisms *a*, *b*, and *d* from Figures 6 and 7, and only when discontinuities are not steeply dipping (i.e. generally with a dip ≤70°). The remaining failure mechanisms require numerical simulations (i.e. finite element, finite difference, discrete element or hybrid methods).

2.2 Underground excavations

As part of a general underground excavation design procedure (Figure 9), three key steps are usually followed (Schubert et al. 2003):

- Determining rock mass types (i.e. assessing engineering geological conditions and geotechnically relevant key parameters for each ground type);
- Determining actual rock mass behaviour types (i.e. observing excavations for signs of excessive stress, deformation patterns and failure mechanisms);
- Determining excavation and ground support criteria and verifying system behaviour.

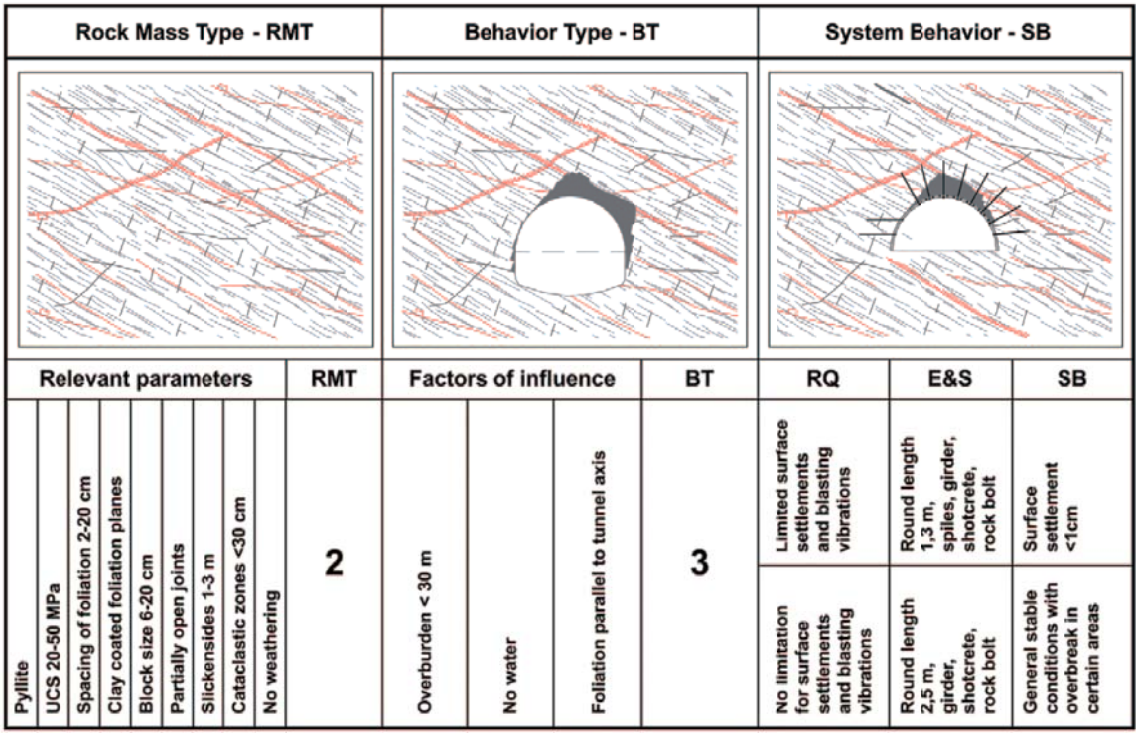


Fig. 8 Example of the underground excavation design procedure (Schubert et al. 2003).

When determining behaviour types for each rock mass, consideration must be given to local influencing factors including the relative orientation of discontinuities to the excavation, groundwater conditions, stress situation, etc. The behaviour of underground excavations should be evaluated for the full excavation without considering any excavation method or sequence and support or other auxiliary stabilization measures. Figure 9 summarizes eleven general categories that most-commonly occur:

1. Stable ground with the potential of small, local, gravity-induced falling or sliding of blocks;
2. Voluminous discontinuity-controlled, gravity-induced fall and sliding of blocks (or wedge failures) with the occasional local shear failure on discontinuities. Stability is controlled by the geometrical and mechanical characteristics of the discontinuities;
3. Shallow stress-induced failure in combination with discontinuity- and gravity-controlled failure;
4. Stress-induced failure involving large ground volumes and large deformation (i.e. squeezing ground);

5. Rockburst: a sudden and violent failure of the rock mass, caused by highly stressed, brittle rocks, and the sudden release of accumulated strain energy. Brittle failure and rock bursting typically occurs at depth;
6. Buckling and anisotropic strain of rocks with a narrowly-spaced discontinuity set, frequently associated with shear failure;
7. Voluminous overbreak in the crown with progressive shear failure (also termed chimney type failure);
8. Ravelling of dry or moist, intensely fractured, poorly interlocked rocks or soil with low cohesion;
9. Flow of intensely fractured, poorly interlocked rocks or soil with high water content;
10. Swelling ground involves a time dependent volume increase of the ground caused by physical-chemical reaction of the ground and water in combination with stress relief;
11. Complex failures may involve a combination of several behaviours with strong local variations of stresses and deformations over long sections due to heterogeneous ground (e.g. in heterogeneous fault zones; block-in-matrix rock, tectonic melanges, etc).

The aforementioned failure mechanisms can be conceptualized using sketches as shown in Figure 8, and later evaluated using numerical methods, which can then form the basis for determining excavation requirements and ground support systems. 3D LEM is only applicable to behaviour type 2 (discontinuity-controlled block fall).

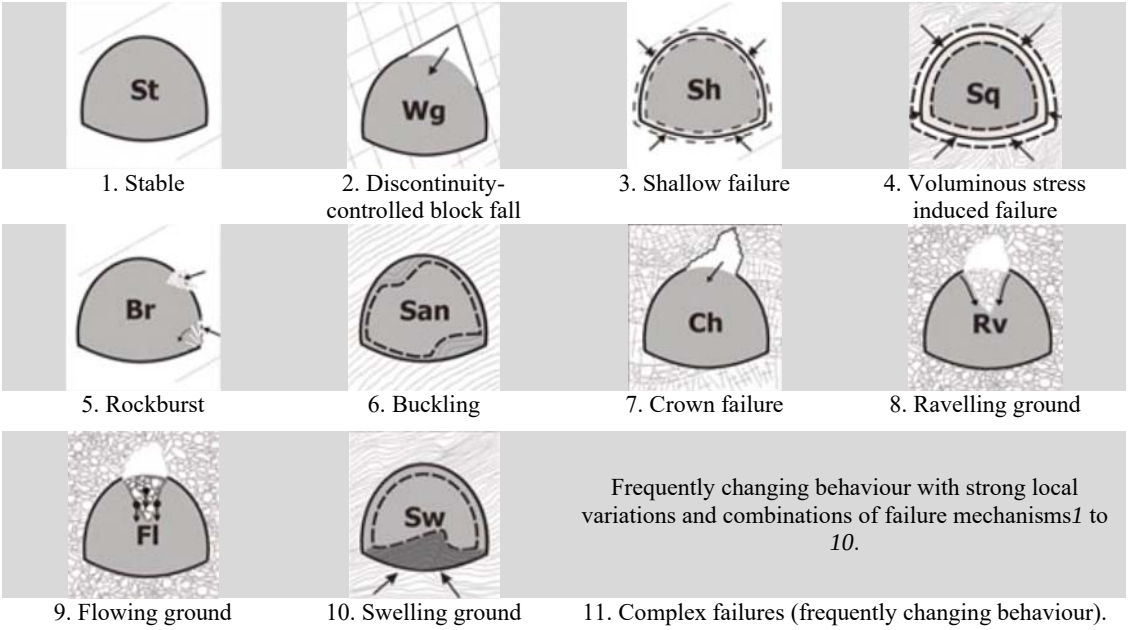


Fig. 9 Underground Excavation Behaviours and Potential Failure Mechanisms (after Schubert et al. 2003; Oke et al. 2013)

Hoek & Brown (1980) presented concepts, which have been developed over 45+ years to relate intact rock strength (UCS or σ_c) and the maximum principal stress (σ_1) using the stress versus strength ratio and GSI (formerly RMR_{76}) to indicate potential failure modes of underground excavations (Figure 10).

Barton et al. (1974; 2024) provide similar stress versus strength ratios (Stress Reduction Factor B, SRF_b) to provide insights into potential stress-related rock mass damage.

The continued use of rock mass classifications including RMR or the Q-system for assessing excavation stability and ground support requirements remains invaluable. Conceptual and empirical approaches are particularly useful for validating the appropriateness of numerical modelling outputs prior to the commencement of excavations and during excavation as part of a reconciliation or validation process. However, on their own, empirical approaches are generally unable identify the plausible failure mechanisms without significant engineering geological judgement.

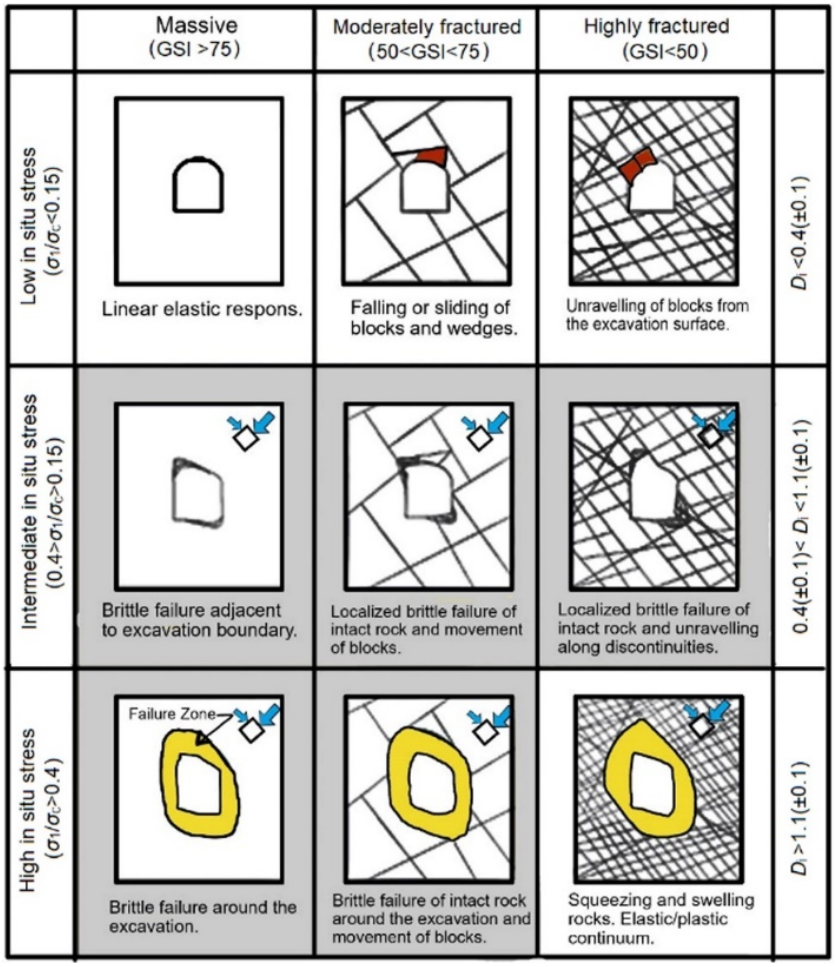


Fig. 10 Potential Failure Modes based on the Ratio of In-Situ Stress and Intact Rock Strength and GSI (after Askaripour et al. 2002; Castro et al. 2012; Hoek & Brown, 1980; Martin et al. 1998).

3 Simplification risks when simulating geomechanical problems

Fifty years ago and beyond, rules-of-thumb and empirical methods formed the basis of underground excavation and ground support design. Empirically-derived rock mass classification systems such as Rock Mass Rating, RMR (Bieniawski, 1973; 1989) and the Q-system (Barton et al. 1974; 2024), were developed to assess rock mass quality from drill core and face mapping for predicting or updating support requirements for underground excavations.

Erharter et al (2025) undertook a global study on the use of 37 (empirical) rock mass classification systems and identified that the most used systems for tunnels, caverns and underground mines were the Q-system, RMR and Geological Strength Index, GSI (Hoek & Brown, 1997; Marinos, 2019). Similarly for rock slopes, the most used systems were GSI, Q-slope and RMR.

By commonly applying rules-of-thumb and empirical approaches, significant simplifications were made from understanding ground behaviour to developing a solution for excavation stability based on available case records.

3.1 Levels of simplification in numerical models

Numerical simulations or models can be used to overcome limitations of kinematic and limit equilibrium analyses. Numerical simulations can be completed in 2D or 3D and have the capability to calculate stresses, deformation (strain) and pore pressure using a variety of constitutive relationships, which include (in order of increasing complexity) linear-elastic, multi-linear elastic, elastic (hyperbolic), elasto-plastic and elasto-visco-plastic.

Numerical models divide the rock mass into finite or discrete elements. Each element is assigned an idealized stress-strain relation and properties that describe how each material behaves. These elements are connected in a continuum model (e.g. boundary element, finite element or finite difference elements), separated by discontinuities in a discontinuum model (discrete elements or discrete fracture

networks), or hybrid models (e.g. combined finite-discrete elements). Jing (2003) and Stead & Coggan (2012) provide detailed descriptions of continuum and discontinuum methods.

Discontinuum models represent the rock mass as an assemblage of discrete blocks, and discontinuities are treated as boundary conditions between blocks (Gigli et al. 2012). The discrete blocks can be rigid or deformable. A termination criterion is required to stipulate whether a discontinuity terminates in the rock mass or against other discontinuities and is fundamental for providing the rock mass with strength derived from intact rock bridges. However, it is practically impossible to represent every discontinuity within a rock mass, so simplifications are required. Holistically, in a practical problem, site investigations and geological uncertainty are a key limitation in precisely representing the geometry and geomechanical characteristics of individual intact rock blocks and discontinuities.

Continuum models assume materials behave isotropically as a continuous body, which are often described using the Mohr-Coulomb or Hoek-Brown failure criteria (Hoek & Brown, 1980). Large discontinuities such as faults are explicitly modelled as interfaces; however, persistent joints, bedding or foliation and other smaller scale discontinuities are implicitly modelled by user defined ubiquitous joint models or directional shear strengths. In continuum models, no actual failure surface is formed; however, an estimation of slip surface location and shape can be predicted by the concentration of shear strain in the model (Sjöberg, 1999). Deformation (strain) in a continuum model is represented as a continuous displacement field, which may not be realistic for large slope deformations.

Numerical simulations require increased computational time and computing power compared with limit equilibrium; and 3D numerical simulations require significantly more time and power than 2D.Irrespective of the modelling method applied, several simplifications are necessary (Sjöberg, 1999) and include but are not limited to the mechanics of the predicted failure mechanism, slope geometry, loads acting on the slope, geology, complexity of geological structure and groundwater. Model calibration is required to ensure that numerical simulations, including many or all of the aforementioned simplifications, produce results that represent actual ground behaviour.

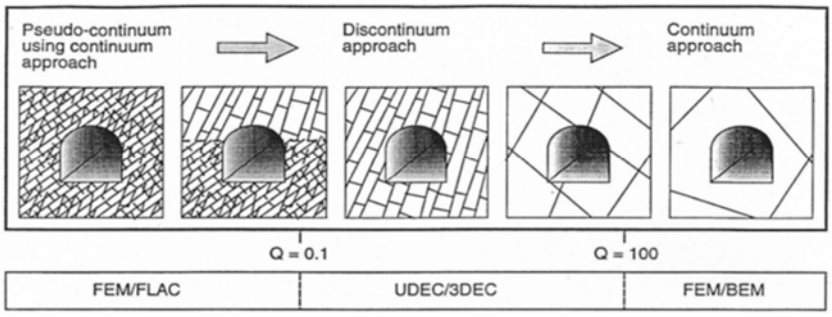


Fig. 11 Conceptual Rock Masses separated by broadly appropriate modelling techniques for underground excavations, approximately 90% of which are likely to require discontinuum treatment (Barton, 2025).

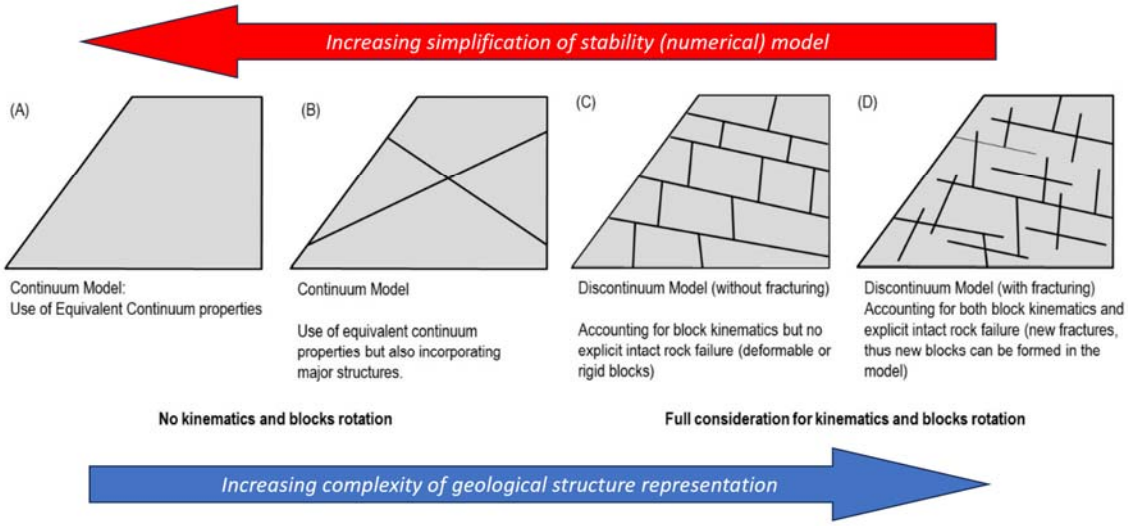


Fig. 12 Example of how continuum modelling trades structural complexity (C and D) for geometrical simplicity (A and B) in rock slopes (Shapka-Fels & Elmo, 2022). Level of simplification required generally increases with slope size (height).

Figures 11 and 12 present examples of typical underground and rock slope excavations modelling with various modelling techniques and levels of simplification. As excavation (or slope) sizes increase, and/or, when discontinuity spacing or fracture frequency increase, so does the need for simplification and use of continuum approaches.

By way of example, GSI, which is a key component of the Hoek-Brown Failure Criterion (Hoek & Brown, 1980; 2019), is commonly used for estimating rock mass strength and stiffness characterization in LEM and various (continuum) numerical models. The Hoek-Brown failure criterion for intact rock is based on a strong set of empirical data. GSI offers an intuitive classification of rock mass quality that uses nomographs (or can be derived from RMR and Q) to downgrade intact rock properties (strength and stiffness) to equivalent rock mass properties in a continuum model, which reduces the need for modelling all discontinuities explicitly (i.e. a simplification of the assemblage of intact rock pieces and discontinuities to a homogeneous and isotropic mass). Limitations of GSI and the Hoek-Brown Failure Criterion include, but are not limited to:

- The Hoek-Brown failure criterion requires that the rock mass behave isotropically, and that failure does not follow a preferred direction imposed by the orientation of a specific discontinuity or a combination of two or three discontinuities. In these cases, the use of GSI is meaningless as the failure is governed by the shear strength of these discontinuities and not of the rock mass (Marinos et al. 2005);
- The GSI system should not be applied to those rock masses in which there is a clearly defined dominant structural orientation (Marinos et al. 2005);
- It is inappropriate to assign GSI values to excavated faces in strong hard rock with a few discontinuities spaced at distances of similar magnitude to the dimensions of the tunnel (Marinos et al. 2005);
- The GSI system assumes that, because the rock mass is made up of a sufficiently large number of joint sets and randomly oriented discontinuities, it can be treated as a homogeneous and isotropic mass of interlocking blocks (Hoek & Brown, 2019).

3.2 Conceptual consequences of oversimplification

Failure mechanisms modelled for a rock slope can be significantly dependent upon the input parameters and modelling assumptions that are used. By way of example, the blocky limestone rock mass shown in Figure 13 has been used to conceptually model the failure mechanisms from Figure 6 (i.e. planar, toppling and circular), which are identified depending on the inputs and assumptions that are used.

The blocky limestone is moderately strong with continuous bedding and perpendicular, discontinuous, orthogonal cross-joints as shown in Figure 13. For simplicity, the rock mass has been shown using a 2D cross-section and one of the cross-joints is therefore not considered.

Material properties for the rock mass are shown in Table 1. These consider a continuum approach in which GSI is used to downgrade rock mass strength with the inherent assumption of homogeneous and isotropic conditions (GSI=55); and a discontinuum approach which considers intact blocks (GSI=90) are separated by discrete bedding planes and cross-jointing with different orientations.

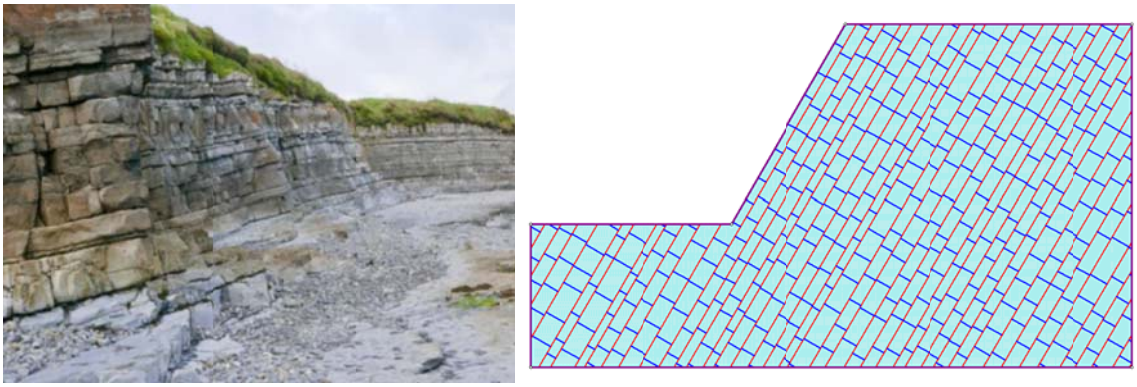


Fig. 13 Blocky limestone rock mass. Left: photograph of rock outcrop; Right: discontinuum model representation of rock mass (note: bedding dip angle different to photograph).

Table 1Material properties for blocky limestone rock mass

Parameter	**Continuum** (Homogeneous, Isotropic)	**Discontinuum** (Heterogeneous, Anisotropic)
Limestone UCS [MPa]	50	50
Hoek-Brown material constant, m_i	9	9
Limestone Geological Strength Index, GSI	55	90 ^
Damage Factor, D	0	0
Limestone Young's Modulus, E_m [GPa]*	14	80
Limestone Poisson's Ratio	0.3	0.3
Bedding Orientation	-	Variable (refer Fig. 14)
Bedding Persistence	-	Continuous
Bedding Cohesion, c' [kPa]	-	20
Bedding Friction Angle, φ [°]	-	35
Cross-Joint Orientation	-	Perpendicular to bedding
Cross-Joint Persistence	-	Discontinuous
Cross-Joint Cohesion, c' [kPa]	-	0
Cross-Joint Friction Angle, φ [°]	-	40
Bedding/Cross-Joint Normal Stiffness, k_n [MPa/m]	-	100,000
Bedding/Cross-Joint Shear Stiffness, k_s [MPa/m]	-	10,000
Fault Zone Cohesion, c' [kPa]	0	0
Fault Zone Friction Angle, φ [°]	20	20
Fault Zone Young's Modulus, E_m [GPa]	1	1
Fault Zone Poisson's Ratio	0.3	0.3

^ *Assumes intact rock (massive) with possibility of random joints.*
** Based on simplified approach by Hoek & Diederichs (2006).*
Note: daylighting fault zone only applied in Figure 15 (shown in pink).

2D Finite Element Method (FEM) analysis was performed in RS2 software (Rocscience Inc) on the continuum model and three discontinuum models each with different bedding and cross-jointing orientations to demonstrate different failure mechanisms. As illustrated in Figure 14, the four models attained vastly different results:

- Failure mechanisms included circular failure when a continuum approach was used, to daylighting and non-daylighting planar sliding and toppling mechanisms depending on the bedding (anisotropy) orientation.
- Factors of Safety (Critical SRF) ranged from 1.3 for a daylighting to 8.3 for a non-daylighting planar failure mechanism. Circular failure attained a Factor of Safety of 3.5.
- Variation in terms of Factor of Safety from the continuum model was -31% to 137% depending on the failure mechanism that was modelled.

The ability to model vastly different failure mechanisms and attain variation in Factors of Safety for a relatively simple rock mass should immediately highlight the need for engineering geological judgement and critical thought when considering model inputs and interpreting the validity of modelling results.

The model results in Figure 14 also highlight that both planar failure (daylighting) and toppling mechanisms have lower Factors of Safety than those attained by continuum modelling for circular failure, i.e. continuum approaches may *not* be conservative depending on the engineering geological conditions encountered.

In Figure 15, an adversely oriented (daylighting) fault zones was included in the same four models initially shown in Figure 14. With the inclusion of a major structure (fault zone), the models identified:

- Planar failure with sliding through the fault zone.
- Factors of Safety (Critical SRF) ranged from 0.55 to 0.74, i.e. all unstable.
- Variation in terms of Factor of Safety from the continuum model was only -26% to 22%. Further refinement through improved meshing and larger lateral model extents would likely reduce the variation in this model further.

The models in Figures 14 and 15 demonstrate that in instances where adversely oriented, major geological structures greatly influence stability, the simplification of smaller discontinuities such as bedding planes and joints to a continuum approach has a limited effect on global stability. However, in

cases where major structures are not the key influencer of stability, the smaller discontinuities and their orientations have a significant impact upon results, and simplification to a continuum approach can have a significant impact on the model outputs.

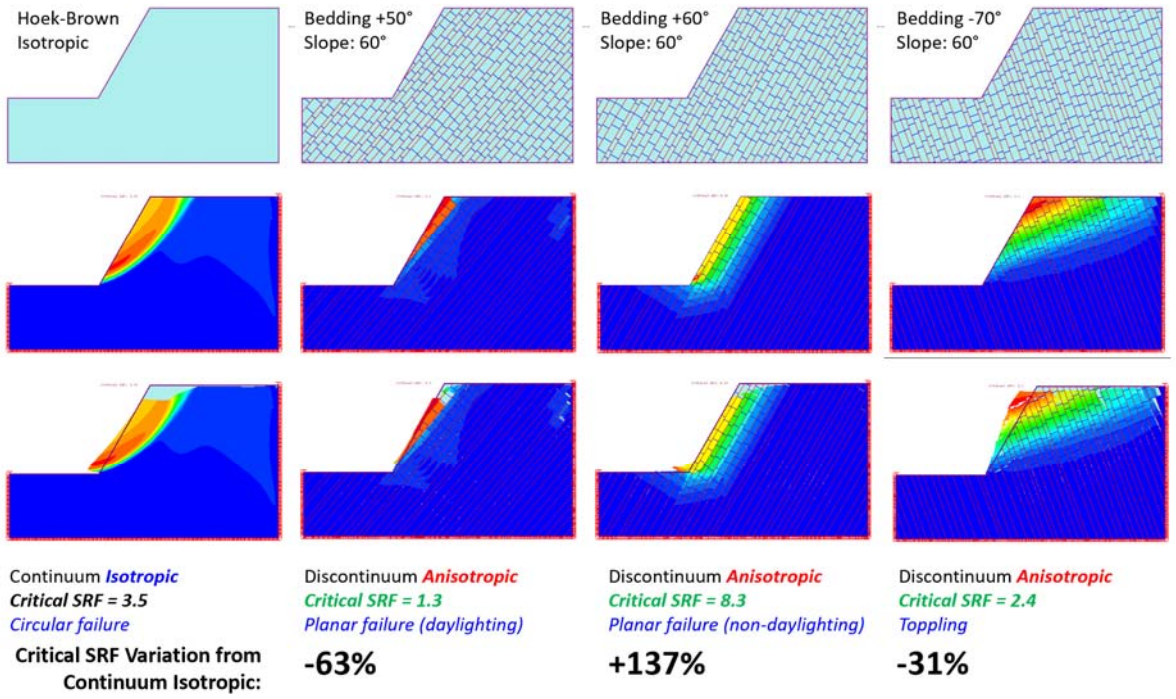


Fig. 14 Comparison of 2D FEM modelling results for a 60°,70 m high slope in a blocky limestone rock mass depending on the assumed engineering geological conditions, different levels of simplification, subsequent failure mechanisms and Factors of Safety (Critical SRF). From left to right: isotropic conditions modelling circular failure (similar to 'A' in Fig. 12); anisotropic conditions modelling daylighting planar failure; anisotropic conditions modelling non-daylighting planar failure; anisotropic conditions modelling toppling (similar to 'D' in Fig. 12 although simplified in terms of constitutive models).

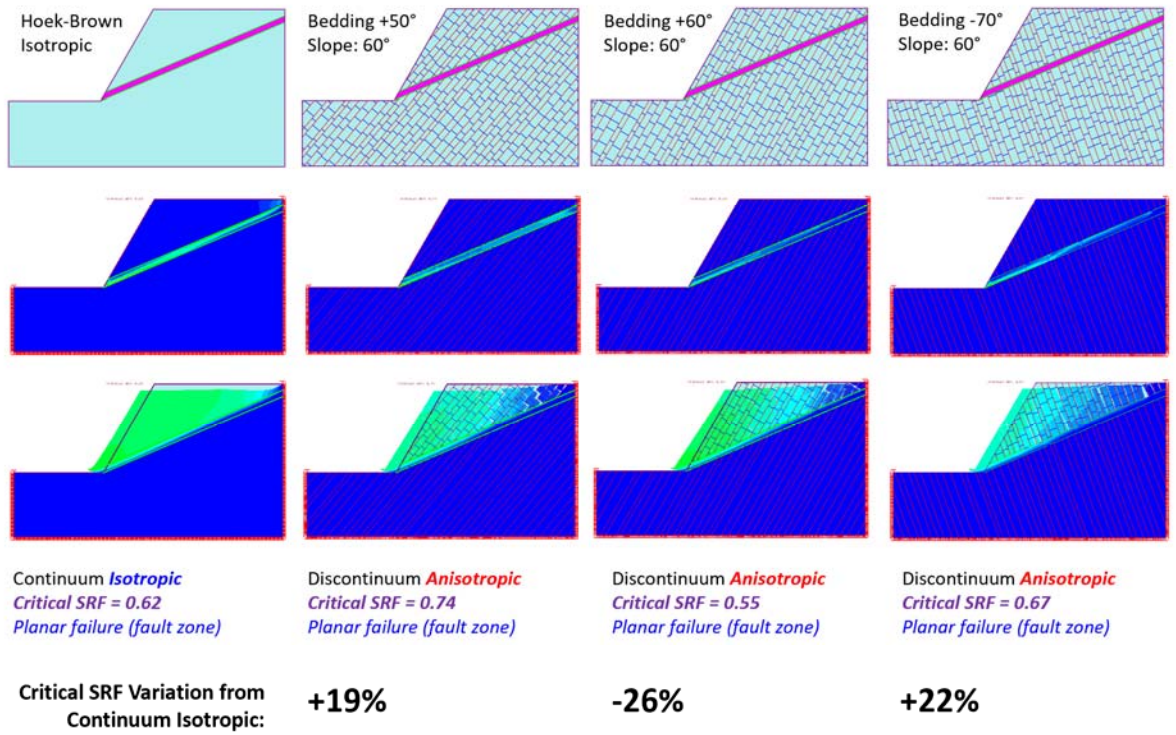


Fig. 15 Comparison of 2D FEM modelling results for a 60°, 70 m high slope in a blocky limestone rock mass undercut by a daylighting geological fault zone (pink) with assumed engineering geological conditions, different levels of simplification, and Factor of Safety (Critical SRF). From left to right: isotropic (similar to 'B' in Fig. 12) and anisotropic (similar to 'D' in Fig. 12) conditions all predicting planar failure along fault zone.

The same principles can be applied to modelling underground excavations to understand failure mechanisms, predict displacements and the appropriateness of ground support.

By way of example, Figure 16 shows modelled displacements for Gjøvik Cavern in Norwayusing continuum and discontinuum approaches. The results showed:

- Continuum model with a large zone of displacement and potential for a voluminous stress induced failure (failure mechanism #4 in Figure 9). Maximum displacement of 8.8 mm.
- Discontinuum model with localized zones of displacement in the roof and potential for discontinuity-controlled block falls (failure mechanism #2 in Figure 9). Maximum displacement of 4.2 mm.

Continuum predicted twice the maximum displacement of discontinuum. The discontinuum approach attained similar results to historicdiscrete element method modelling in UDEC software (Itasca) by Barton et al. (1994), which was validated by monitored displacements from borehole extensometers after construction.

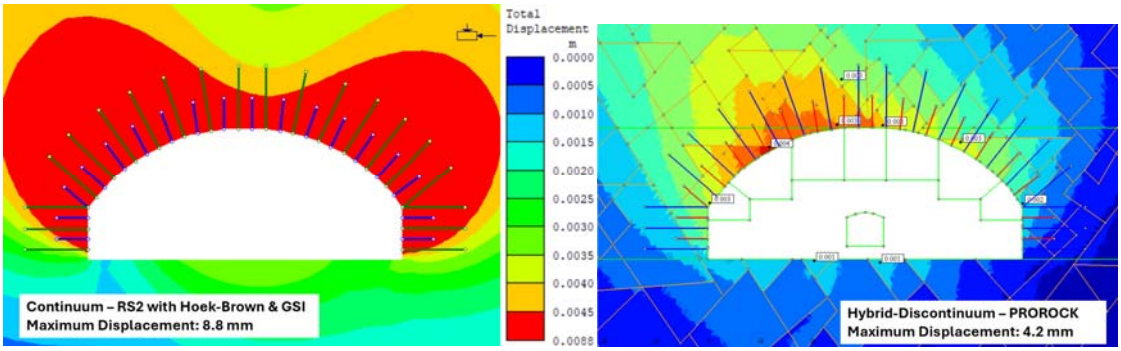


Fig. 16 Comparison of Gjøvik Cavern (62m Span) modelling results showing predicted displacements. Left: 2D FEM continuum, homogeneous and isotropic in RS2 software). Right: 2D Finite-Discrete Element Method (FDEM: hybrid discontinuum approach in PROROCK software by Scientia) Continuum modelling predicts double the maximum displacements and a substantially larger zone of displacement than the discontinuum approach (Bar, 2025).

A key limitation of the examples shown in Figures 14 to 16 is that only 2D analysis was performed (i.e. simplification into two dimensions). Inclusion of 3D analysis could identify more complex failure mechanisms in three-dimensions, which could be more critical than those identified in 2D.

It should also be noted that the number of material properties required to undertake discontinuum analysis is considerably more than for continuum (as shown in Table 1). As such, more effort is required in site investigations and characterization.

3.3 Real world consequences of oversimplification

In the 2020s, modelling circular failure mechanisms for rock slopes appears to be increasingly popular, despite the rarity of circular failures in the real world (i.e. 3 to 10% of rock slope failures).

By way of example, Figure 17 shows recent academia and software developments that have focused on modelling circular failure for large rock slopes. All examples assume homogenous and isotropic ground conditions and simplify the rock mass to a continuum (A in Figure 12) and aim to attain similar FoS outputs precise to two decimal places. These include using LEM and FDM to develop and validate slope design charts (e.g. slope height versus angle by Styles & Vakili, 2020) and spreadsheet tools (for predicting FoS by Carranza-Torres, 2021), which only consider circular failure mechanisms. It also includes software developments to enable manipulation of the damage factor (D) in the Hoek-Brown failure criterion to model shallower circular slip surfaces in 2D LEM (Ma et al. 2022).

Notwithstanding the abovementioned tools' usefulness for assessing the potential of circular failure, their popularity is disproportional to their relevance in terms of real world rock slope behaviour.

The same applies for underground excavations where simplification of a rock mass to continuum approach for modelling is common practice.These simplifications, in many instances, may have significant consequences for real world applications as is demonstrated through the following cases studies.

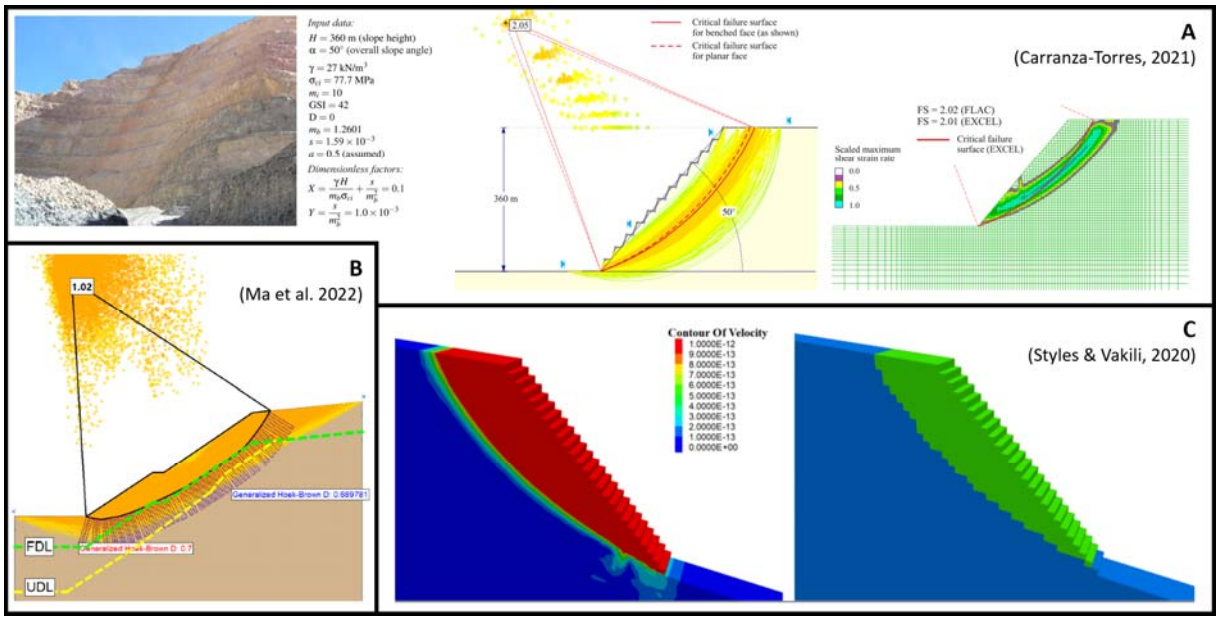


Fig. 17 Recent popularity of modelling circular failure mechanisms for rock slopes despite their rarity in the real world (only 3 to 10% of rock slope failures are 'circular' in previously mentioned databases). A: 200m high rock slope (UCS = 77 MPa) with high FoS modelled in 2D LEM (Slide2) and 2D FDM (FLAC) by Carranza-Torres (2021). B: Circular failure modelled in 2D LEM (Slide2) despite the use of gradational damage factor (D) manipulation with depth to attain FoS of approx. 1.00 (Ma et al. 2022). C: Circular failure modelled for 200m high rock slope using 3D FDM (FLAC3D with SlopeX plug-in) by Styles & Vakili (2020).

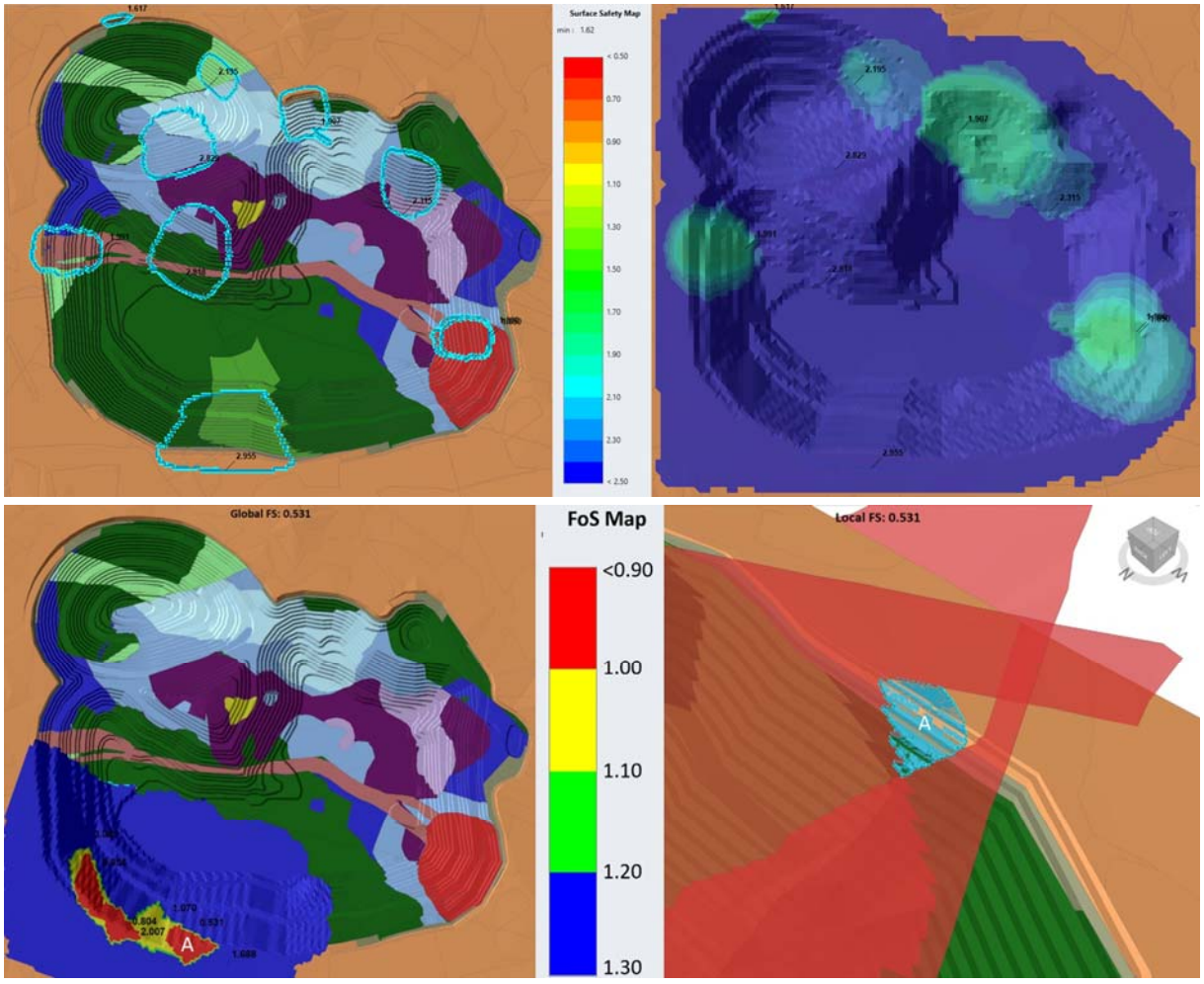


Fig. 18 3D LEM analysis of Aktogay Open Pit Copper Mine (Bar & Zlobin, 2024). Top: Faults omitted from analysis: Factor of Safety exceeds 1.50 for all slope sectors. Bottom: Faults included in south-west quadrant for detailed analysis: Factor of Safety is less than 1.00 for three individual wedges and approximately 1.07 for a fourth, larger wedge.

3.3.1 Pit slope stability modelling with and without faults

Failing to assess the potential for a large range of failure mechanisms, including complex ones can result in inappropriate stability analyses being undertaken and resulting in inappropriate designs. By way of example, Figure 18 presents the results of two sets of three-dimensional (3D) LEM analyses for a proposed design of Aktogay copper mine, with and without the inclusion of geological faults (Bar and Zlobin, 2024).

The geological faults are oblique to the slope in the south-west quadrant and form low Factor of Safety (FoS) wedges; which are expected to be unstable. Without the inclusion of faults, the analyses only check for circular and ellipsoidal rotational failure mechanisms through the (isotropic) rock mass and indicate a high FoS (overestimated by up to 50%) with apparent (but non-existent) potential for slope steepening.

If 2D LEM were to be undertaken, as appears to be most commonly practiced according to McQuillan et al. (2020), the modelled failure mechanism would have been planar sliding instead of wedges; which is intrinsically incorrect and would have different stability modelling results yet again.

3.3.2 Heap leach pad stability modelling using LEM and FEM

For rock fill structures, such as a waste rock dump or heap leach pad, assessment of failure mechanisms and the selection of appropriate stability analysis techniques is critical. In the author's industry experience, 2D LEM is most commonly used for modelling heap leach pad stability.

Figure 19 illustrates how 2D and 3D LEM analyses attained high FoS while modelling sliding along a constructed liner and shearing through the Heap Leach (HL) fill material (Bar et al. 2025). In comparison, 2D and 3D Finite Element Method (FEM) was able to identify active-passive block sliding along the liner. In this case, 2D LEM analysis results overestimated FoS by over 35% compared to the 3D FEM results.

As mentioned earlier, LEM is unable to model active-passive blocks. Such profound differences in FoS should be considered very consequential, particularly in light of the recent heap leach failures in Türkiye and Canada.

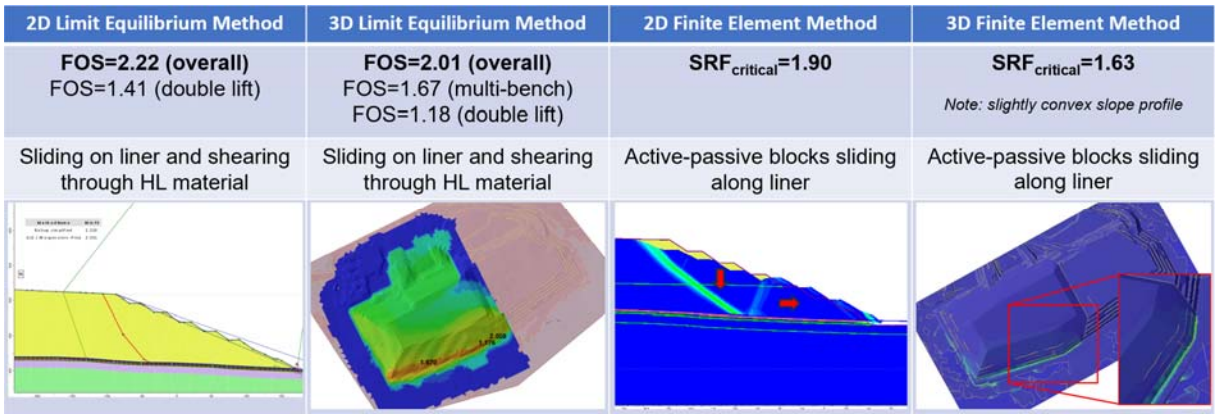


Fig. 19 2D and 3D LEM and FEM analysis of Aktogay Heap Leach Pad (Bar et al. 2025). From left to right: decreasing modelled Factor of Safety and differences in identified failure mechanism.

In the examples shown in Figures 18 and 19, not considering the potential failure mechanisms based and undertaking appropriate stability analyses would have resulted in overestimation of Factors of Safety and could have provided an unachievable and unsafe design.

3.3.3 Drainage tunnel modelling: continuum versus discontinuum

A drainage tunnel in Papua New Guinea was proposed in a blocky to very blocky siltstone rock mass (Bar & Baczynski, 2018). As shown in Figure 20, the siltstone has sub-horizontal bedding with two to three sets of sub-perpendicular joints. Bedding and joint conditions are generally fair with smooth and slightly altered joint walls.

Q values range from 1 to 4, and GSI typically ranges from 40 to 55.In-situ stresses are low with the tunnel depth not exceeding 300 m ($\sigma_1/\sigma_c<0.12$), and intact rock strength, σ_c, is in the order of 70 MPa.



Fig. 20 Very blocky siltstone. Left: fresh siltstone in existing exploration tunnel (3 m wide x 3.5 m high). Right: Slightly weathered siltstone outcrop (approx. 2m high in photograph).

Table 2 Material properties for very blocky siltstone rock mass

Parameter	**Continuum** (Homogeneous, Isotropic)	**Discontinuum** (Heterogeneous, Anisotropic)
Siltstone UCS [MPa]	70	70
Hoek-Brown material constant, m_i	10	10
Siltstone Geological Strength Index, GSI	45	100 ^
Damage Factor, D	0	0
Siltstone Young's Modulus, E_m [GPa] *	9	40
Siltstone Poisson's Ratio	0.26	0.26
Bedding/Joint Normal Stiffness, k_n [MPa/m]	-	100,000
Bedding/Joint Shear Stiffness, k_s [MPa/m]	-	10,000

^ *Assumes intact rock (massive).*
* *Based on simplified approach by Hoek & Diederichs (2006).*

Numerical methods were used to assess drainage tunnel behaviour using two approaches with 2D FEM (RS2 software). Table 2 summarizes the material properties used for elastic analysis to understand potential failure mechanisms for an unsupported tunnel. Figure 21 shows modelled displacements for the drainage tunnel using continuum and discontinuum approaches, which indicate:

- Continuum model with a relatively large zone of displacement and potential for a shallow failure (failure mechanism #3 in Figure 9). Displacements exceed 20 mm up to a depth of approximately 1 m behind the side walls and below the floor.
- Discontinuum model (intact blocks separated by discontinuities) with localized zones of displacement in the roof and potential for discontinuity-controlled block falls (failure mechanism #2 in Figure 9). Maximum displacement of 3 mm at a depth of approximately 1 m behind side walls and roof.

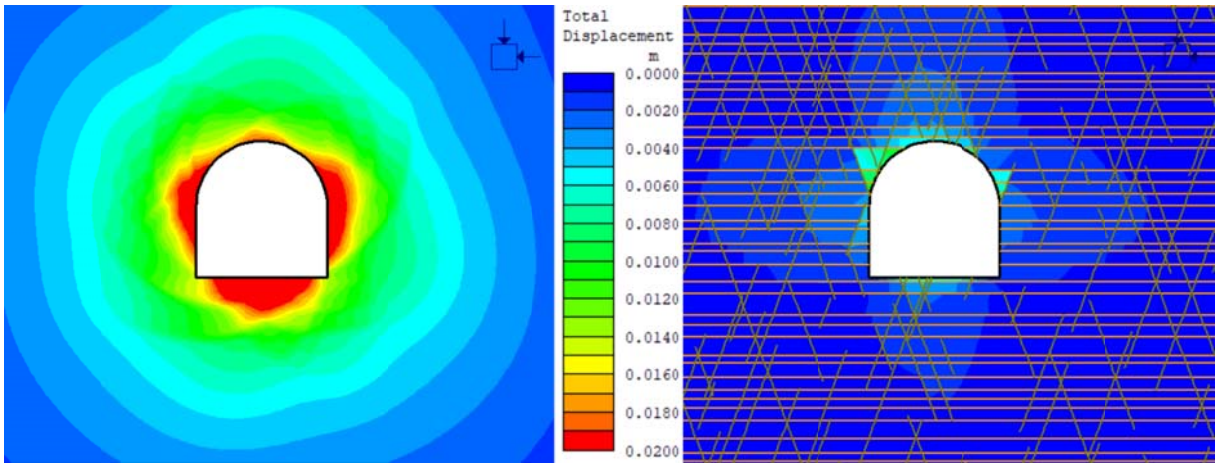


Fig. 21 Unsupported Drainage Tunnel (5 m wide x 5.5 m high) 2D FEM Elastic Model Results in RS2 software showing Total Displacement (Bar, 2025). Left: Continuum, homogeneous & isotropic model outputs showing potential for shallow failure with over 20 mm displacements up to a depth of approx. 1 m behind side walls and below floor. Right: hybrid discontinuum model outputs showing potential for discontinuity-controlled block falls and less than 3 mm displacements at a depth of approx. 1 m behind side walls and roof.

Ground support requirements based on the continuum model (combination of shotcrete, mesh and bolting) would be significantly higher than predicted by the hybrid discontinuum model, which indicates only a need for spot bolting and mesh for small block fall protection. Based on the observed excavation performance in the existing exploration tunnel (Fig. 20), the hybrid-discontinuum model outputs are significantly more realistic than the continuum model.

4 Residual risk management

As a result of the inherent geological uncertainty in rock masses and the simplification that occurs when modelling geomechanical problems, residual risks remain present when excavations commence with the potential for socioeconomic impacts of ground failure events.

Residual risks need to be managed through the use of a continuous improvement framework (e.g. Figure 5) and critical control measures that are developed and implemented during study phases and during and after excavation.

Critical control measures are the equipment, systems, procedures, and policies that an organization uses to prevent injuries and death (Ross, 2017). Critical control measures can also be used for minimizing other socioeconomic impacts of rock slope and underground excavation failures such as damage to equipment, infrastructure, business disruptions, and the impairment or sterilization of mineral resources.Figure 22 presents a framework of five critical control measures are often used for managing ground failure risks (Bar et al. 2022).

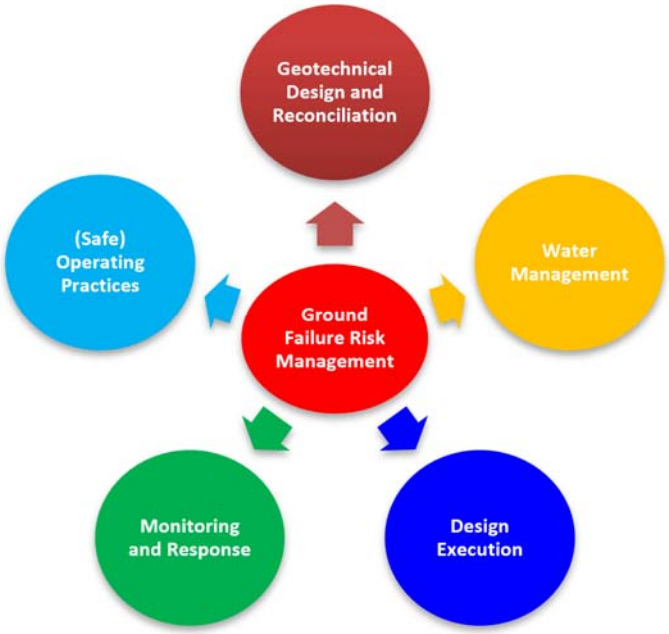


Fig. 22 Ground Failure Risk Management Critical Control Measures.

Geotechnical design involves the use of geological, rock mass, structural and hydrogeological data to develop a geotechnical model. This geotechnical model forms the basis of stability analyses, which are used to design a pit slope with acceptable factors of safety or probabilities of failure. Geotechnical models are often developed from limited data and inherently contain various degrees of uncertainty and risk.The reconciliation aspect of this control measure requires ongoing validation of the geotechnical model as the excavations advance to check whether geotechnical model assumptions remain valid and whether uncertainties pose a risk or provide economic opportunity. Elements of geotechnical reconciliation include the validation of excavation geometries (e.g. bench width capacity for rock fall risk management or overbreak and underground excavation spans), local geology, intact rock strengths, rock mass classifications, discontinuity orientations and conditions, presence and condition of major geological structures, pore pressures and displacement monitoring results.Geotechnical design and reconciliation is an engineering control measure that is particularly effective for managing larger failure mechanisms. It also assists in mitigating risks associated with smaller rock falls.

Water management involves a combination of groundwater extraction through pumping and surface water management to minimize water ingress to facilitate safe and productive operations (drilling, blasting and excavation). For slopes, dewatering also assists in depressurization (i.e. reducing pore pressure in the slopes), which is further achieved through the installation of horizontal drains on each pushback. Water management is an engineering control measure that is particularly effective for managing slope failures. It has a limited effect on mitigating risks associated with smaller rock falls.

Design execution focuses on achieving the correct geometric design, installing water drainage and minimizing damage to the rock mass from blasting. Operating practices focus on ensuring all personnel working on the project are aware of geotechnical hazards, how to work safely during normal operating conditions (e.g. never working under unsupported ground in underground excavations; a minimum safe distance of 15 meters away from slopes without a job hazard analysis or JHA). Design execution and operating practices are a combination of engineering and administrative control measures, respectively. They are primarily effective for managing risks associated with rock falls and smaller scale failure mechanisms. This control measure alone is not considered effective for large scale failure mechanisms (e.g. overall slope failure, crown pillar failure in an underground mine).

Monitoring and response may use an array of instrumentation to identify changes in ground displacements, pore pressure and excavation induced seismicity. This instrumentation and visual observations may be used to identify potential hazards. Trigger-action-response-plans (TARPs) can be developed to respond to potential hazards and may include temporary evacuations of the at-risk area. Although highly sophisticated instrumentation is used to identify emerging threats, this control measure remains administrative as it relies on personnel to identify the threat, respond and communicate it to the personnel, who are then required to act accordingly. Monitoring and response has been used for primarily for managing safety risks associated with slope failure and rockburst.

5 Discussion and conclusions

Many excavations in rock (slopes and underground) are not designed in detail; some are not designed at all and are merely excavated under the guidance of a project supervisor or equipment operator. Many excavations that appear to have a detailed design, may have significant geological uncertainty or include excessive simplification in stability predictions and may not assess failure mechanisms appropriately.

Current industry practitioners, academia and software developer trends relating to stability modelling appear to focus on attaining a precise Factor of Safety value. In the case of rock slopes, more often than not, stability models assume circular or quasi-circular failure modes in the analysis, rather than attempting to understand and model actual or more realistic failure mechanisms where FoS may be substantially different since circular failures account for less than 10% of real world rock slope failures. In many such instances, the model outputs and subsequent designs would largely be wrong since the plausible failure mechanisms were not investigated.

Alejano (2025) reviewed the application of rock mass classification systems, including their misuse. A similar review of case studies and published articles on the misuse rock slope and underground excavation stability modelling, including over-simplification and incorrect failure mechanism appraisal is warranted and strongly encouraged by the author. Such an undertaking should include academics and practitioners from various institutions around the world.

With inherent geological uncertainty, it is possible, even probable that geological anomalies such as faults were not identified prior to excavation. By adopting a continuous improvement framework and updating models throughout the design and excavation process, it is more likely that the anomalies would be identified and associated ground failure risks could be managed than if the models were completely static. It may perhaps be beneficial to start from the viewpoint that *'all models are wrong, but some are useful'*; planning for contingency and then focusing efforts to validate the models to determine the most appropriate or applicable results.

Rock engineers should be encouraged to think critically and assess potential failure modes more deeply rather than merely following a design workflow from point A to point Z. '*It is better to be approximately right than precisely wrong*'. The use of probabilistic analysis is often beneficial, yet the ability to include a statistically-derived location and orientation of a geological anomaly (e.g.

unfavourably oriented fault) remains out of reach. As such, the use of plausible sensitivity analyses is strongly encouraged.

The number of experienced rock engineers appears to be decreasing over the last decade with a significant drop in university graduates from the discipline. The demand for rock engineering projects requiring numerical methods is increasing, which means less experienced engineers with more projects around the world. At the same time, access to easy-to-use numerical modelling software has become ever more abundant, i.e. more engineers are applying numerical methods, and often they have less experience than their predecessors. Many engineers using numerical modelling methods have little or no field experience observing real world ground behaviour. Less experienced engineers, higher demand for stability modelling, and increased project throughput using prescribed design workflows will likely lead to incorrect assessments of failure mechanisms.

In order to minimize the risk and consequence of ground failure events relating to rock slopes and underground excavations, realistic failure mechanisms need to be well understood. By focusing to understand them in different engineering geological settings and simplifying problems only as much as is reasonable, future designs of rock slope and underground excavations may become safer and more economically attractive.

Lastly, for real world projects there are always time and budget constraints. Significant effort should be made by rock engineers during all project phases from initial designs to excavation and asset operation, to explain in economic terms (as well as safety), to project managers, directors and investors; the risks and consequences of inadequate design of rock slopes and underground excavations and the geological uncertainty that remains present if a continuous improvement framework and critical control measures for managing ground failure risks are not implemented.

Acknowledgements

The author sincerely thanks Dr Alison McQuillan and Prof Milorad Jovanovski for their peer review of this paper.

References

Alejano LR (2025) Rock Mass Classification Systems: A Useful Rock Mechanics Tool, Often Misused. Rock Mechanics and Rock Engineering. 58: 11147-11167.

Arnould M (2010) Tunnel ferroviaire de Vierzy : vieillissement, altération des maçonneries calcaires - Causes de l'effondrement catastrophique du 16 juin 1972. Revue Française de Géotechnique. 131-132: 93-99.

Askaripour M, Saeidi A, Rouleau A, Mercier-Langevin P (2002) Rockburst in underground excavations: A review of mechanism, classification, and prediction methods. Underground Space. 7: 577-607.

Bailey J (2003) Findings and recommendations RE: Inquest into the deaths of R. Bodkin; M. House; S. Osman and C. Lloyd-Jones: on the 24th of November, 1999 at the E26 Lift 1 Mine North Parkes Mines, Parkes, NSW. Coroners Court of New South Wales, Australia.

Baczynski NRP (2000). Stepsim4 "Step-Path" Method For Slope Risks. GeoEng 2000: International Conference on Geotechnical and Geological Engineering. Lancaster, 2: 86-92.

Baczynski NRP, Bar N (2019) Slope Failure Risks by Engineering Geological Logic and the Simplified Step Path Method. 13th Australia New Zealand Conference on Geomechanics. Sydney, Australia: 511-515.

Bar N (2024) Digital Twin Concept for the Safe and Economic Design and Management of Rock Slopes. 6th Regional Symposium on Landslides in the Adriatic-Balkan Region, Belgrade, Serbia, 15–18 May 2024.

Bar N (2025) On the use of numerical methods to assess underground excavation stability: continuum versus discontinuum and hybrid approaches. Southeastern Europe Tunnelling Conference, Belgrade, Serbia, 1-3 October 2025: 243-253.

Bar N, Baczynski NRP (2018) Ground Characterization and Design of a Drainage Gallery Tunnel Network for a Large Open Pit Mine in a High Rainfall Environment. 10th Asian Rock Mechanics Symposium, Singapore, 29 October – 3 November 2018, 12p.

Bar N, Barton NR (2025) Q-Slope: Rock Slope Engineering 10 Years on. Rock Mechanics and Rock Engineering. 58: 11453-11474.

Bar N, Cobián JC, Bautista M, Mojica B, Coli N, Preston C, Ribeiro R, Bueno G, Lopes L, (2022) Brittle and Ductile Slope Failure Management. Slope Stability 2022, Tucson, USA, 17-21 October 2022.

Bar N, Dixon RA (2021) Unveiling unknowns: Practical application of InSAR for slope performance monitoring and risk management across multiple surface mines. Engineering Geology. 293: 106326.

Bar N, McQuillan A, Zlobin G, Meloni F (2025) Criticality of 3D Numerical Modeling for Assessing Heap Leach Pad Stability and Integration with Monitoring Data, Including InSAR. Heap Leach Solutions 2025, Sparks, USA: 19-21 October 2025.

Bar N, Zlobin G (2024) Геотехническое проектирование откосов карьера «Актогай» (Казахстан) и управление рисками. Gornyi Zhurnal. 2024(1): 89-94.

Barton N (2025) Twenty Strange Years in the World of Rock Mechanics and Engineering Geology. Current Trends in Civil & Structural Engineering 11(4): 13p.

Barton N, By TL, Chryssanthakis P, Tunbridge L, Kristiansen J, Løset F, Bhasin RK, Westerdahl H, Vik G (1994) Predicted and Measured Performance of the 62m Span Norwegian Olympic Ice Hockey Cavern at Gjøvik. Int. Journal of Rock Mechanics, Mining Science & Geomechanics Abstracts. 31(6): 617-641.

Barton N, Grimstad E, Abrahão R, Bar N (2024). Q-based developments during the last 50 years. Fjellsprengningskonferansen 2024: 24.1-24.34.

Barton N, Lien R, Lunde J (1974). Engineering classification of rock masses for the design of tunnel support. Rock Mechanics. 6(4): 189-236.

Bieniawski ZT (1973) Engineering Classification of Jointed Rock Masses. Transactions of the South African Institution of Civil Engineering. 15(12): 335-344.

Bieniawski ZT (1989) Engineering rock mass classifications. United States, John Wiley & Sons: 251p.

Carvajal HEM, Restrepo PAI, Azevedo GF (2012) Landslide risk management in Medellin, Colombia. *In* Extreme Rainfall Induced Landslides an International Perspective. Oficina de Textos,São Paulo.

Carranza-Torres C (2021) Computational tools for the analysis of circular failure of rock slopes. Eurock 2021, Torino, Italy, 21-24 September 2021: 43p.

Castro LAM, Bewick RP, Carter T (2012) An overview of numerical modelling applied to deep mining. *In* Innovative Numerical Modelling in Geomechanics, CRC Press: 22p.

Cavers DS (1981) Simple methods to analyse buckling of rock slopes. Rock Mechanics. 14: 87-104.

DMP (2014) Fatal accidents in the Western Australian mining industry 2000-2012: what lessons can we learn? East Perth, Department of Mines and Petroleum, 24p.

Erharter GH, Bar N, Hansen TF, Jain S, Marcher T (2025) International Distribution and Development of Rock Mass Classification: A Review. Rock Mechanics and Rock Engineering. 58: 11169-11180.

Froude MJ, Petley DN (2018) Global fatal landslide occurrence from 2004 to 2016. Natural Hazards and Earth System Sciences. 18(8): 2161-2181.

Ghirotti M, Masetti D, Massironi M, Oddone E, Sapigni M, Zampieri D, Wolter A (2013) The 1963 Vajont Landslide (Northeast Alps, Italy). Italian Journal of Engineering Geology and Environment. 6: 635-646.

Gigli G, Frodella W, Mugnai F, Tapete D, Cigna F, Fanti R, Intrieri E, Lombardi L (2012) Instability mechanisms affecting the cultural heritage sites in the Maltese Archipelago. Natural Hazards and Earth System Sciences. 12(6): 1883-1903.

Goodman RE, Bray JW (1976) Toppling of rock slopes. Rock Engineering for Foundations and Slopes. 2: 201-234.

Goodman RE, Shi GH (1985) Block theory and its application to rock engineering. New Jersey, Prentice Hall.

Grimstad E (2005) The Loen Rock Slide – An Analysis of the Stability. 11th International Conference and Field Trip on Landslides (ICFL), Trondheim to Geiranger, Norway, 1-10 September 2005.

Gußmann P (1988) KEM (Kinematical Element Method) in geomechanics. 6thInternational Conference on Numerical Methods in Geomechanics, Innsbruck: 823-828.

Hittinger M, GoodmanRE (1978) JTROCK, a computer program for stress analysis of two dimensional, discontinuous rock masses. Report No. UCB/GT/78-04. The University of California, Berkley.

Haile A, Ross D, Maldonado A, Neyaz A, Rajbhandari C (2020) BHP Western Australia Iron Ore geotechnical open cut slope design system: a simple pragmatic process for slope risk decisions. Slope Stability 2020, Perth, Australia, 12-14 May 2020: 415-426.

Hoek E, Brown ET (1980). Empirical Strength Criterion for Rock Masses. Journal of the Geotechnical Engineering Division. ASCE 106 (GT9): 1013-1035.

Hoek E, BrownET (2019) The Hoek-Brown failure criterion and GSI - 2018 edition. Journal of Rock Mechanics and Geotechnical Engineering. 11: 445-463.

Hoek E, Diederichs MS (2006) Empirical estimation of rock mass modulus. International Journal of Rock Mechanics and Mining Sciences. 43(2): 203-215.

Hoek E, Kaiser PK, Bawden WF (2000) Support of Underground Excavations in Hard Rock, London, CRC Press: 228p.

Hoek E, Londe P (1974) The design of Rock Slopes and Foundations. General Report for the Third Congress of the International Society for Rock Mechanics, Denver, United States of America, 78p.

Idris J, Al Heib M, Verdel T (2004) Feedback from a database created for reporting accidents in tunnels and galleries. *In* Urban Transport X, Boston, WIT Press: 41-50.

Jamasmie C (2016) Glencore says all seven workers dead after Katanga mine accident in Congo. https://www.mining.com/glencore-says-all-seven-workers-dead-after-katanga-mine-accident-in-congo/. Accessed at 10 May 2026.

Jing L (2003) A review of techniques, advances and outstanding issues in numerical modelling for rock mechanics and rock engineering. Int. Journal of Rock Mechanics & Mining Sciences. 40: 283-353.

Jovanovski M, Janevski B, Peshevski I (2024) Integral approach in stability analyses for weak anisotropic rocks. 6th Regional Symposium on Landslides in the Adriatic-Balkan Region, Belgrade, 15–18 May 2024.

Kieffer DS (1998). Rock slumping: A compound failure mode of jointed hard rock slopes. PhD Thesis. The University of California, Berkley.

Kiersch GA (1965) The Vaiont Reservoir Disaster. Mineral Information Service. 18(7): 129-138.

Li J, Yang T, Deng W, Du S, Zhang Z, Ma H, Wang H, Guo J, Liu L (2025) Evaluating failure mechanisms of excavation-induced large-scale landslides in Xinjing open-pit coal mine through integrated UAV imagery and 3D simulation. Landslides. 22: 2021-2036.

Ma T, Cami B, Javankhoshdel S, Yacoub T, Corkum B, Curran J (2022) Effect of Disturbance Factor Distribution Function on Stability of an Open Pit Mine. 56th US Rock Mechanics / Geomechanics Symposium, Santa Fe, USA, 26-29 June 2022: 7p.

Lynch R, Meyer S, Lötter E, Lett J (2018). Tracking cave shape development with microseismic data. Caving 2018, Caving 2018, Vancouver, Canada, 15-17 October 2018: 555-564.

Mark C (2024) The Road to Zero: The 50-Year Effort to Eliminate Roof Fall Fatalities from US Underground Coal Mines. Mining, Metallurgy & Exploration. 41: 727-741.

Marinos V, Marinos P, Hoek E (2005) The geological strength index: applications and limitations. Bulletin of Engineering Geology and the Environment. 64: 55-65.

Martin CD, Kaiser PK, McCreath DR (1998) Empirical estimation of rock mass modulus. International Journal of Rock Mechanics & Mining Sciences. 43: 203-215.

McMahon BK (1971) Statistical methods for the design of rock slopes.First Australia-New Zealand Conference on Geomechanics. 1: 314-321.

McQuillan A, Bar N (2023) The necessity of 3D analysis for open-pit rock slope stability studies: Theory and practice. Journal of the Southern African Institute of Mining and Metallurgy. 123(2): 63-70.

McQuillan A, Bar N (2024) Forecasting Open Pit Slope Failure Runout Distances. Journal of the Southern African Institute of Mining and Metallurgy. 124(6): 355-360.

McQuillan A, Canbulat I, Oh J (2020) Methods applied in Australian industry to evaluate coal mine slope stability. International Journal of Mining Science and Technology. 30(2): 151-155.

Nicoll S, Bar N, Du Plessis P (2017) Managing Risks on an Active Haul Road Adjacent to a Propagating Subsidence Zone at Telfer Gold Mine. Procedia Engineering. 191: 172-178.

ÖGG (2010) Guideline for the Geotechnical Design of Underground Structures with Conventional Excavation. Version 2.1. Salzburg, Austrian Society for Geomechanics: 42p.

Oke J, Vlachopoulos N, Marinos V (2013) Umbrella Arch Nomenclature and Selection Methodology for Temporary Support Systems for the Design and Construction of Tunnels. Geotechnical and Geological Engineering. 32(1): 97-130.

Paraskevopoulou C, Boutsis G (2020) Cost Overruns in Tunnelling Projects: Investigating the Impact of Geological and Geotechnical Uncertainty Using Case Studies. Infrastructures. 5(9): 73.

Petley DN (2020) The deadly landslide at the Carmen Copper Mine in the Philippines. https://blogs.agu.org/landslideblog/2020/12/24/carmen-copper-mine-1/. Accessed at 10 May 2026.

Petley DN (2025) Global fatal landslides in 2024. https://eos.org/thelandslideblog/fatal-landslides-in-2024. Accessed at 10 May 2026.

Petley DN (2026) Global fatal landslides in 2025. https://eos.org/thelandslideblog/global-fatal-landslides-in-2025. Accessed at 10 May 2026.

Poisel R, Eppensteiner W (1988) A contribution to the systematics of rock mass movements. 5thInternational Symposium on Landslides, Lausanne. 2: 1353-1357.

Poisel R, Preh A,(2004) Rock Slope Initial Failure Mechanisms & their Mechanical Models. Felsbau. 2: 40-45.

Rashed G, Xue Y, Khademian Z, Sears M (2022) Ground-Fall Accident Trends in Mining: 2010 to 2019. 41st International Conference on Ground Control in Mining, Canonsburg, United States, 26-28 July 2022.

Read JRL, Stacey PF (2009) Guidelines for Open Pit Slope Design. Collingwood, CSIRO Publishing: 511p.

Ross B (2017) Rise to the Occasion – Lessons from the Bingham Canyon Manefay Slide. Englewood, Society for Mining, Metallurgy & Exploration: 246p.

RFI (2026) Landslide at DR Congo coltan mine kills more than 200, including children. https://www.rfi.fr/en/africa/20260305-landslide-at-eastern-dr-congo-coltan-mine-kills-200-children-rubaya. Accessed at 10 May 2026.

Schubert W, Goricki A, Riedmüller G (2003) The Guideline for the Geomechanical Design of Underground Structures with Conventional Excavation. Felsbau. 21(4): 13-18.

Shapka-Fels T, Elmo D (2022) Numerical Modelling Challenges in Rock Engineering with Special Consideration of Open Pit to Underground Mine Interaction. Geosciences. 12(5): 23p.

Sjöberg J (1999) Analysis of Large Scale Rock Slopes. PhD Thesis. Luleå University of Technology: 788p.

Stead D, Coggan J (2012). Numerical modeling of rock-slope instability. Landslides: Types, Mechanisms and Modeling. Cambridge, Cambridge University Press.

Styles TD, Vakili A (2020) Slope angle versus slope height - the basis of an empirical tool for slope design within fractured rock masses using IUCM. Eurock 2020, Trondheim, Norway, 14-19 June 2020: 8p.

Tlozek E (2016) Rock fall at Papua New Guinea mine claims life of Ok Tedi worker. https://www.abc.net.au/news/2016-03-11/man-dies-after-rockfall-at-reopened-ok-tedi-mine/7239652. Accessed at 10 May 2026.

Waldmann N, Vasskog K, Simpson G, Chapron E, Støren EWN, Hansen L, Loizeau J-L, Nesje A, Ariztegui D (2021) Anatomy of a Catastrophe: Reconstructing the 1936 Rock Fall and Tsunami Event in Lake Lovatnet, Western Norway. Frontiers in Earth Sciences. 9: 18p.

Ward JT (2015) Bingham Canyon Landslide: Analysis and Mitigation. BSc Thesis, University of Nevada: 150p.

Wikipedia (2026) Gotthard Base Tunnel. https://en.wikipedia.org/wiki/Gotthard_Base_Tunnel. Accessed at 10 May 2026.

Wittke W (1990) Rock Mechanics. Berlin, Springer.

Wyllie DC (2018) Rock Slope Engineering Civil Applications, Boca Raton, CRC Press: 620p.

WyllieDC, Mah CW (2004) Rock Slope Engineering Civil and Mining, London, Spon Press: 456p.

Yuan S, Ding B, Guan K, Pérez-Rey I, Li T, Alejano LR (2026) Analysis of a rock slope instability mechanism combining wedge and circular failure in a soft rock mass. Int. Journal of Coal Science & Tech. 13(49).

Zienkiewicz OC, Humpheson C, Lewis RW (1975) Associated and non-associated visco-plasticity and plasticity in soil mechanics. Geotechnique. 25: 671-689.

The importance of rock engineering for deep open pit slopes: Some considerations

R. Ulusay
Hacettepe Univ., Dept.of Geological Engg., Ankara, Türkiye
resat@hacettepe.edu.tr
0000-0003-1930-7611

Abstract

When compared to underground mining, open pit mining is a more cost-effective mining method allowing high grade of mechanization and large production volumes. Much more need due to the exponential growth in the world population with easily accessible mineral resources becoming more scarce, increasing commodity prices, and improved production capabilities, leaded to much deeper and larger open pit slopes than have previously been considered and implemented. Therefore, particularly in the last few decades, depths of open pits approached and exceeded 1000 m. At these increased depths the risk of slope failure becomes greater, dependent upon the imposed design, and makes engineers question whether the analytical assumptions previously used on lesser slope heights are still valid. Formation of slope damage features, such as brittle fracture, rock mass dilation and bulging, are the main factors causing deformation of deep open pits and high natural rock slopes. In addition, strength of slope forming rock masses and discontinuities is reduced by the progressive accumulation of slope damage and cause a decrease in slope stability. In this keynote differences and similarities between the stability of "deep-large" and "classical (shallower)" open pit slopes are discussed in terms of the main factors controlling slope stability such as rock type, discontinuities, effect of degradation, rock damage, hydrogeological conditions, rock mass strength, geotechnical model, effects of in-situ stresses and earthquakes, and importance of movement monitoring based on the recent practice and using some examples selected from practice.

Keywords

Deep open pit, Slope stability, Failure mechanism, Slope monitoring, Rock damage.

1 Introduction

Slope design, regardless of the dimensions of the slope, is an integral part of open-pit mining engineering. The slope angle is also a key component that determines whether a proposed or existing project can remain economically viable. The first studies concerning the geotechnical design of open-pit slopes were carried out in the late 1960s and early 1970s. Initially, slope design was conducted according to the principles of soil mechanics and other branches of materials engineering. At that time, only a few open pits had slope heights slightly exceeding 300 m, and pit designs were commonly based on the rule of thumb "take the overall slope angle as 45° and then observe" (Stacey 2009). This approach often led to widespread slope instabilities in open pits, resulting in injuries and/or fatalities as well as severe economic losses and long-term interruptions in ore production.

By the late 1980s, parallel to the increase in global population and the growing demand for ore production, deposits that had previously been considered uneconomical for open-pit mining due to their low grades and deep occurrence began to be exploited. Furthermore, several existing open pits weredeepened. A plot showing the historical record of open pit slope height and overall slope angle, including data from Sjöberg (1999) (orange circles, representing open pits up to 1999) together with more recent data compiled by the author from the various sources (blue triangles), is presented in Fig. 1.This plot indicates that, except for a few pits, the depth of the majority of open pits was between 300 and 400 m until the early 2000s. However, after 2000, mining operations began to be carried out in open pits exceeding 500 m in depth, with some reaching depths of up to 1350 m. Open-pit slopes excavated to depths of several hundred meters were regarded as "deep slopes". However, it is important that these operations are conducted in a safe and economic manner. This means that competent designs and techniques should be adopted to support the ever growing mining capacities. However, the attainment of depths exceeding 500 m in some modern open pits (Figs. 1 and 2) has resulted in the occurrence of ground stresses that are high even by underground mining standards, along with highly complex slope behaviours and instability mechanisms (e.g. Sjöberg 1999, 2013; Stacey et al. 2003; Elmo et al. 2007, 2022; Lorig 2009; Tuckey et al. 2013; Cambio et al. 2019; Donati et al. 2020). Compared with soil-like materials, rock masses are discontinuous in nature due to the presence of joints and other discontinuities. As in-situ stresses increase with depth, rock material failure within the slope-forming rock units becomes more pronounced, leading to damage accumulation and a reduction in strength.Although the slope design process described in many publications is generally similar for all mine slopes, the prediction of ground performance in deep open pit slopes exceeding 500 m in height involves relatively greater uncertainty due to the factors such as high stress, intact rock breakage and time-dependent behaviour, and therefore, such open pits are considered as deep/ultra-deep open pits (Robotham 2011).

The complexity of slope failures due to increase in depth of slopes makes it increasingly difficult to answer key questions in slope design, such as: (a) what types of slope instabilities could affect the pit? (b) what is the likelihood of a major instability developing? (c) what could be the potential consequences of such failures? and (d) can the operation withstand these consequences? (Karzulovic 2004). Therefore, compared to shallow open pits, the design of deep and large open-pit slopes inherently involves a significantly higher degree of uncertainty. Moreover, when compared to classical open pits, limited experience gained from deep open-pit designs, together with the inherent knowledge gaps and limitations of conventional analytical methods, further affect the process of assessing the stability of deep slopes. Therefore, this requires a better understanding of catastrophic and expensive slope failures in deep open pits.

In this keynote, differences between "deep-large" and "classical (shallower)" open pits are discussed in terms of the main factors affecting the stability of open pit slopes, such as rock type, degradation and discontinuities, formation and effect of damage in rock slopes due to in-situ stresses, hydrogeological conditions, and strength of rock masses and discontinuities. Then the role of geotechnical model, influence of earthquakes and in-situ stresses, slope movement monitoring, which are particularly more important for deep open pits, are also highlighted with some examples selected from practice. The methods of analysis, such as kinematic, limit equilibrium and numerical methods used in slope stability assessments for deep and conventional open-pit mines have not been included within the scope of this keynote, since these methods constitutes a separate topic in their own right.

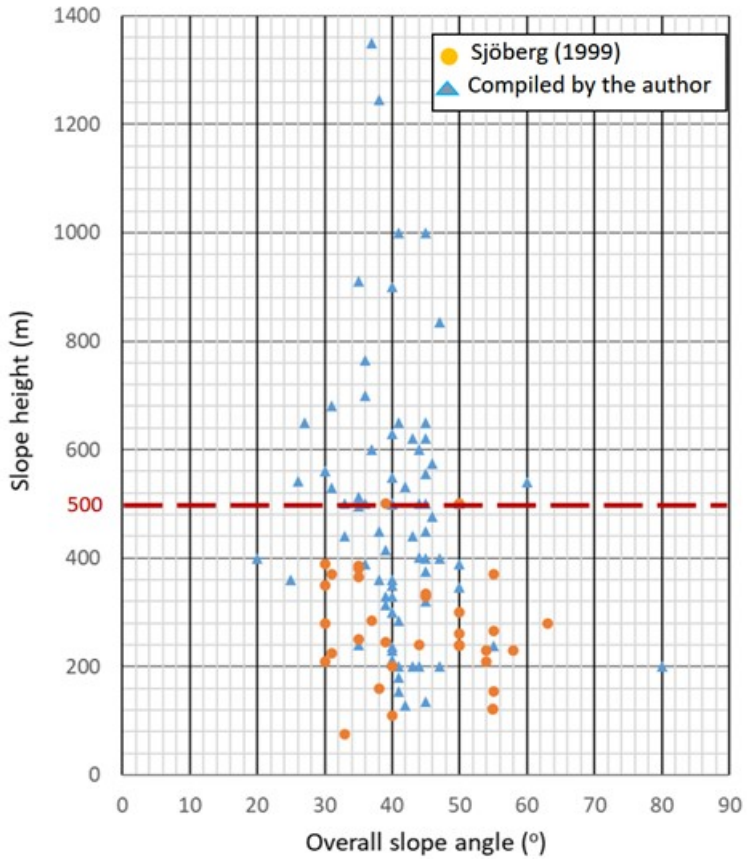


Fig. 1.Plot showing the increase of the open pit slopes based on the data on overall slope angle and slope height compiled from open pits in different countries (drawn using the data from Sjöberg (1999) and most recent data provided from different sources by the author).

(a)



(b)



Fig. 2. Examples of deep/ultra-deep open pits: (a) Bingham Canyon Copper Mine, USA (current depth: 1350 m; Photo courtesy of Rio Tinto Kennecott ROV &Survey Teams, Ergun (2026)), (b) Chuquicamata Mine, Chile (current depth:1000 m) (from Contreras et al. 2019).

2 Effects of main inputs on slope stability

2.1 Effect of rock type

Because of their different origins and nature, rocks possess distinct intrinsic geological properties. For example, in soft and weak rocks such as schists and shales, the principal factor controlling slope stability is the lithology of the rock itself. In contrast, in hard rocks such as granite and limestone, stability is mainly governed by the dominant sets of discontinuities.The mineralogical composition of rockscontrols the mechanical properties and the behavior of the rock mass andalso determine the strength of the rock mass.

Another important rock slope instability is experienced in **B**lock-**I**n-**M**atrix **ROCK**s (Bimrock), which are complex geological mixtures such as mélanges, conglomerates, faulted and sheared rocks, where blocks of varying rock types and origins are embedded in a finer-grained matrix (e.g. Medley, 1994, 2012; Figs. 3a.1-a.3)). Bimrock behaviour is particularly common in open pits excavated within the following geological environments, such as ophiolite belts, subduction melanges, serpentinite-mixed rock zones, tectonic breccia zones, large-scale fault zones and porphyry copper deposits containing volcanic breccia and agglomerate. In such materials, the types of slope instabilities, as well as the shape and location of potential failure surfaces, depend on the frequency, size, and orientation of the blocks (Fig. 3b). Due to the significant spatial, lithological, and mechanical variability of these materials, the accurate geological and geotechnical characterization of bimrocks is essential to avoid unforeseen and costly surprises during slope excavation. In a hypothetical example given in Fig. 3c for the problem related to mischaracterization of a bimrock in a slope case, the geotechnical investigation for a main road the exploration borings were teminated about 2 m into sandstone bedrock. The engineer concluded that the instability was shallow and composed of clay and boulder colluviums sliding on the contact with the underlying sandstone bedrock (Fig. 3c.1). After the excavation started, it was seen that the instability was actually a deep-seated earth flow in pervasively sheared melange, rather than a shallow soil mass sliding on top of the bedrock (Fig. 3c.2). Although some works have been conducted and some approaches have been recommended, there is still no general consensus on the approaches and guidelines for site characterization of bimrockss, and therefore, further studies and combination of their results with existing experiences are necessary.

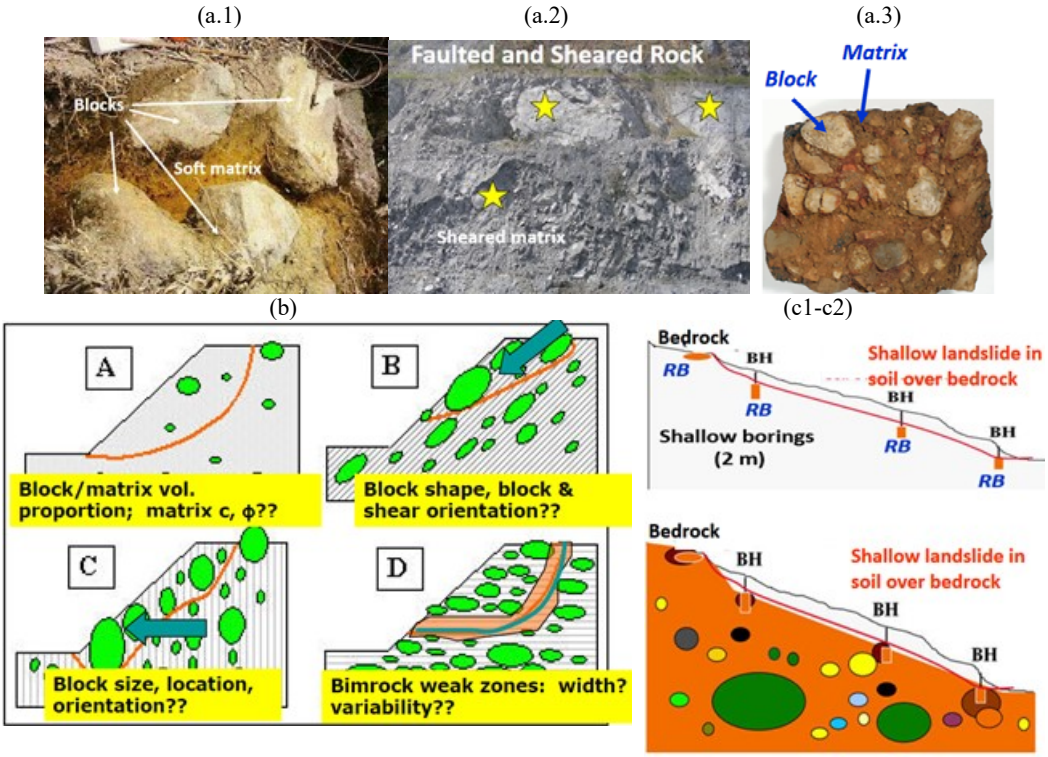


Fig. 3.(a) Views from three typical bimrocks (a.1. coarse blocks in soft matrix, a.2. faulted and sheared rock, a.3. conglomerate; Medley 2012), (b) effects of block proportion and orientation on slopes and failure surfaces excavated in bimrocks: (A) very low block proportion-analysis similar to that for soil slopes, (B) failure surface influenced by the orientation and nature of matrix shearing,(C) large blocks which influence tortuous failure surface that negotiate around blocks and strength to matrix, (D) block-poor zones within generally block-rich are weaker and more likely to fail (Medley 2012), (c) a hyphothetical example on mischaracterization of bimrocks (c.1. before and c.2. after borings) (Medley 2008).

2.2 Effect of degradation

Rocks may undergo degradation when they are exposed to atmospheric conditions and/or hydrothermal fluids through rock mass. The degradation process is commonly known as deterioration in the forms of weathering and alteration depending upon the physical and chemical process involved. Weathering transforms hard rocks into soft rocks which maintain the structure of the intact rocks, but are characterized by higher void ratios and reduced bond strengths. Soft rocks are transformed into thick granular soil mantles generally called residual soils. The degradation process also influences the joint spacing and discontinuity filling material in the form of clay and results in drastic changes in strength and deformability characteristics of the slope forming rock mass.

Significant progressive deterioration of rock slopes may occur in engineering time, often giving rise to the need for unplanned maintenance and constituting safety hazard, and the physical and chemical weathering effects can be predominant in controlling the modes of rock slope failure. For example, open sheet/exfoliation joints, which are formed by stress relief as a result of erosion of igneous plutons, tend to run sub-parallel to the rock head with a tendency to daylight in the cut slopes resulting in a structurally controlled instability such as planar failure (Fig. 4a). If the slope forming rock mass has transformed into a soil due to intense chemical weathering (grades V or VI) or alteration, the slope will fail in the form of circular sliding as commonly observed in soil slopes and this kind of failure can be more dangerous for deep open pits as seen in Fig. 4b. Differential weathering, which is a common source of rock slope instability particularly along steep slopes, generally occurs in cases where slopes consist of inter-layered hard (e.g. sandstone, limestone) and soft rock (e.g. shale, claystone, tuff and mudstone) units. As differential weathering of softer rocks progresses, undercutting can lead to loss of support and collapse (falls or topples) of the overlying material. Large-scale, sub-vertical discontinuities and over-break fractures may promote failure by intersecting undercut surfaces and/or reducing block size within the rock mass (Fig. 4c) (e.g. Neiman 2009, Admassu et al. 2012). Deterioration, however, is rarely given much attention at the design stage; emphasis is on the avoidance of deep-seated failure.

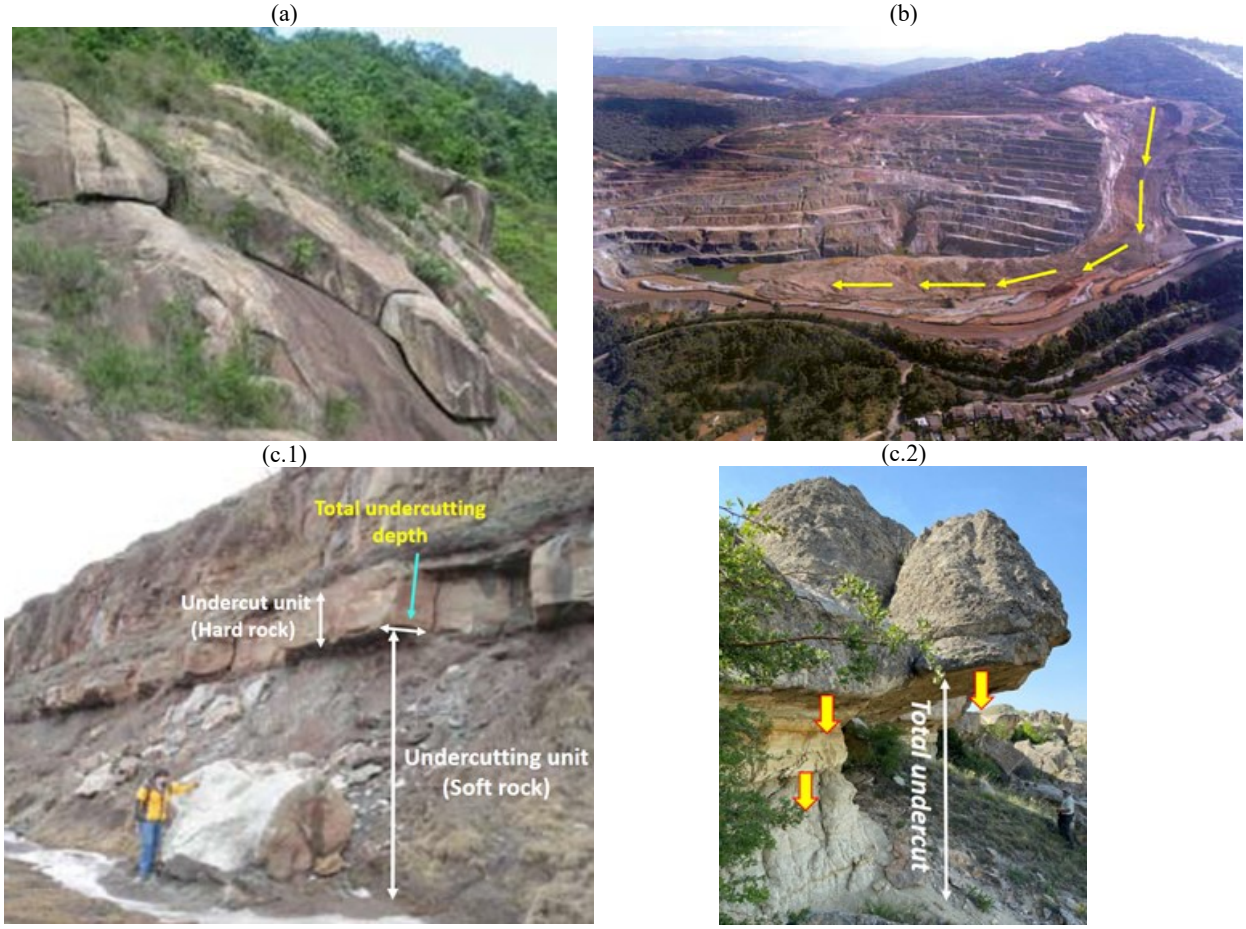


Fig. 4. (a) Partial movement and dilation of sheeting slabs typical of early stage of failure in Hong Kong (Hencher et al. 2011), (b) failure of weathered zone material in an open pit (Martin and Stacey 2013), (c.1-c.2) examples for undercutting-induced rockfalls due to differential weathering in USA (Admassu et al. 2012) and in Cappadocia, Türkiye (Photo: R. Ulusay), respectively.

2.3 Effect of structural features and scale

In rock masses divided by discontinuities, the most significant factor controlling slope instability is different types of discontinuities such as bedding planes, joints, faults, and schistosity. The adverse interaction between discontinuities and the slope orientation plays a major role in the development of slope instabilities. Depending on the degree of structural control exerted by discontinuities, four main types of instability models are generally recognized. The first group includes failures that develop along discontinuities or their lines of intersection, such as “planar”, “wedge” and “multi-planar” failures, and those occurring along columnar structures dipping opposite to the slope direction called “toppling failure” (Fig. 5a–d). Multi-planar failure is a type of structurally controlled instability in which sliding occurs along two or more intersecting discontinuity planesand unlike simple planar failure, movement is governed by a combination of planes that together form a kinematically feasible sliding surface. Structurally-controlled failures are commonly observed both in shallow and deep open pit mine slopes and multi-planar failures can involve large rock volumes and may develop progressively. The second group represents circular (rotational) failures, which are partly passes through the rock material and partly along discontinuities, without structural control, similar to those observed in soil slopes, where the rock mass is highly fractured by closely spaced discontinuities (Fig. 5e.1), or extremely weak or highly weathered or altered (Fig. 5e.2). Rotation and translation of individual blocks in the rock mass would help to create a failure surface. Mapping of natural discontinuities can be conducted according to sampling methods suggested by ISRM (1981, 2007), independently of whether the discontinuity parameters are collected using direct physical mapping or indirect data collection by means of remote sensing techniques, such as digital photogrammetry and laser scanning techniques.

As emphsized by a number of researchers (e.g. Sjöberg 1999; Lorig 2009), the traditional assumption of low-stress conditions in slopes implies that structurally conrolled failures mentioned above dominate in rock slopes, while this may be true for slopes with large scale structural features, it does not necessarily apply to a rock mass with many, but smaller, discontinuities. For a high slope, the rock mass will appear to be very fractured, as the length of individual discontinuties is small compared to the dimensions of the slope. This effect of scale is shown in Fig. 6a-c. for 30 m, 90 m and 500 m high bench slope, interramp slope and overall slope with angles of 70^o, 30^o and 50^o, respectively. In these figures, a 2-D cross-section of the slope is shown with two hyphotetichal joint sets with the following characteristics: Joint A (length. 10±1 m; rock bridge: 3±1 m, spacing: 3 m) and Joint B (length. 8±2 m; rock bridge: 5±2 m, spacing: 3 m; spacing: 7 m). Fig. 6 suggests that a rock mass can thus be described as being a closely jointed when the joint spacing is small in relation to the scale of the entire slope. From this it is evident that the failure mode of a large scale slope can differ significantly from that of a small scale slope (Sjöberg 1999). As shown in Fig. 6d, a rock mass than might appear “blocky” for an underground opening could appear “disintegrated” for a large and deep slope (Lorig 2009) and these examples higlight the importance of scale effect in rock slopes, particularly for deep open pits.

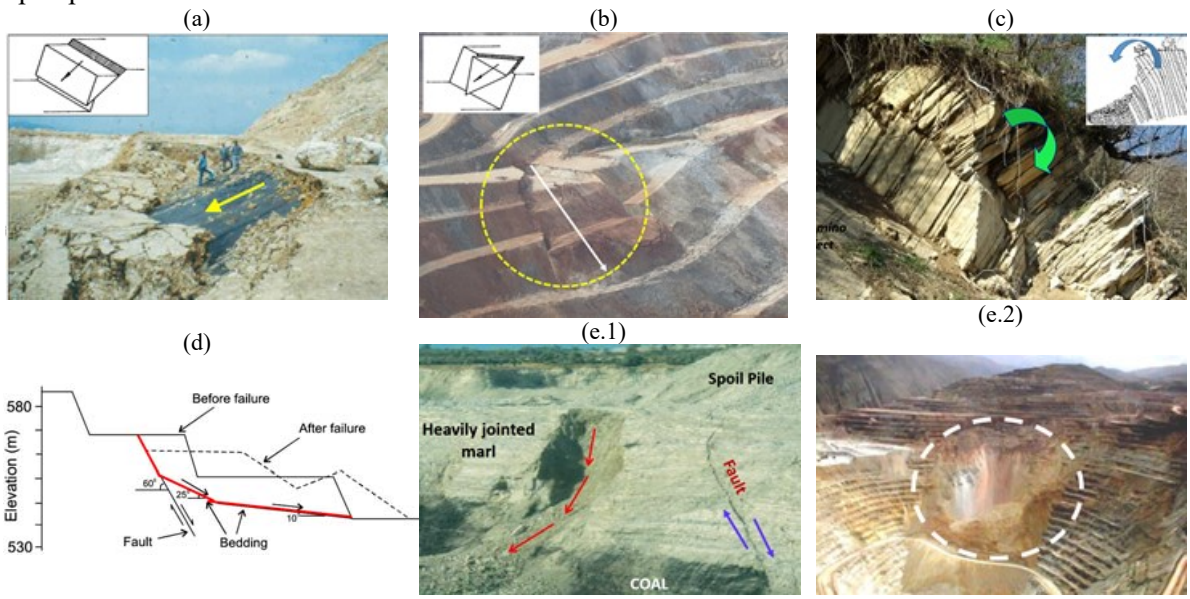


Fig. 5**.** Five main structurally-controlled failure modes occurring in rock slopes: (a) planar, (b) wedge, (c) toppling and (d) multi-planar failure, and circular failure in (e.1) a heavily jointed rock mass (a, d, e.1- Ulusay 1991; b, c - Photo: R. Ulusay) and (e.2)failure in a highly weathered east wall slope at Cuajone open pit in 1999 (Peru) (Hormazabal et al. 2013)

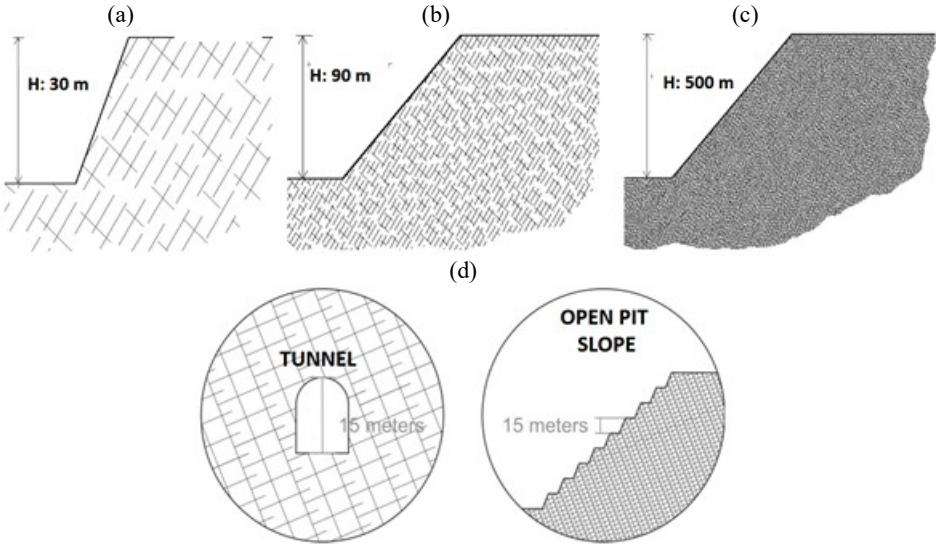


Fig. 6.Discontinuity patterns for (a) bench, (b) inter-ramp and c) large scale overall rock slopes with different slope angles of 70^o, 50^o and 50^o and two different pre-existing joint sets (slightly rearranged from Sjöberg 1999), (d) illustration of how the same rock mass could appear differently for an underground excavation and a rock slope (Lorig 2009).

2.4 Rock damage in deep open pits

Today, slopes of deep open pit mines can reach depths in excess of 1 km and as a result of this progress, they are subjected to deformations which are inevitably associated with the formation of slope damage features, such as rock mass dilation and bulging, brittle fracture and rock falls. The progressive accumulation of slope damage, in turn, causes strength degradation, and consequently the risk of instability increases. Due to a combination of geological units with different characteristics, the intersection of a greater number of structural elements, higher magnitudes of in-situ stresses, and increased deformation with depth, more complex (composite) instability mechanisms are often encountered in deep/ultra-deep open pits (>500 m). This is the most distinctive difference between deep and conventional (shallower) open-pit mine slopes. Based on the evidence from the past cases supported some form of extensional mechanics occurring with yield and failure of deeper open pit slopes.Some researches and practitioners (e.g. Hoek et al. 2000; Stacey and Xanbin 2004) considered that in addition to structurally controlled failures, deep open pit slopes may also involve composite defect failure mechanism.

Long- and short-term deformation of rock slopes is associated with the formation of slope damage features, and consequently, the instability models in deep open pits are strongly dependent on the scale of the slope. Based on the findings from Ok Tedi Mine in New Papua Guinea, Little (1999) and Baczynski (2000) proposed a model for deep and large slope instabilities with complex failure surfaces covering interaction of five possible zones of different strength that can act in the development of some instability at an inter-ramp or global scale.As schematically illustrated in Fig. 7a, in deep and ultra-deep open-pit slopes, sliding may occur not only along unfavourably oriented discontinuity planes, but also through shear failure within the intact rock bridges (intervals of intact rocks between the tips of adjacent and non-persistent discontinuities), and by the dilation of step-like arrangements of steep and sub-horizontal joint systems within the rock mass and increase in rock falls. In this conceptual illustration, Donati et al. (2020) emphasized that such damage induced fracture connectivity on secondary permeability, pore water pressure and shear strength along failure surfaces is critical. An example showing how the presence of rock bridges could manifest even within a rock mass characterized apparently fully continuous and interconnected fractures is given in Fig. 7b. The prism failure mechanism proposed byPrandtl (1923) stability analysis of the curved or irregular surface geometry by Mencl (1966) first time. In this method, the stiffness of the sliding mass influences the development of kinematic freedom and the transfer of driving force from an upper active block, through a Prandtl transition wedge and into a lower passive block (Fig. 7c). Eberhardt et al. (2004) and Fisher and Eberhardt (2007) found that a Prandtl zone of yielded rock mass developed at the base of the sliding surface and propagated towards the upper active wedge and it provides an accurate description for the development of kinematic freedom, respectively. Based on the analyses, considering “volumetric rock bridges” and using distinct element code UDEC for the assessment of stability of model slopes Tuckey et al. (2013) concluded that it may be especially applicable in the case of highly fractured rock masses, or in very large open pit slopes, where jointing can be considered effectively homogenous.

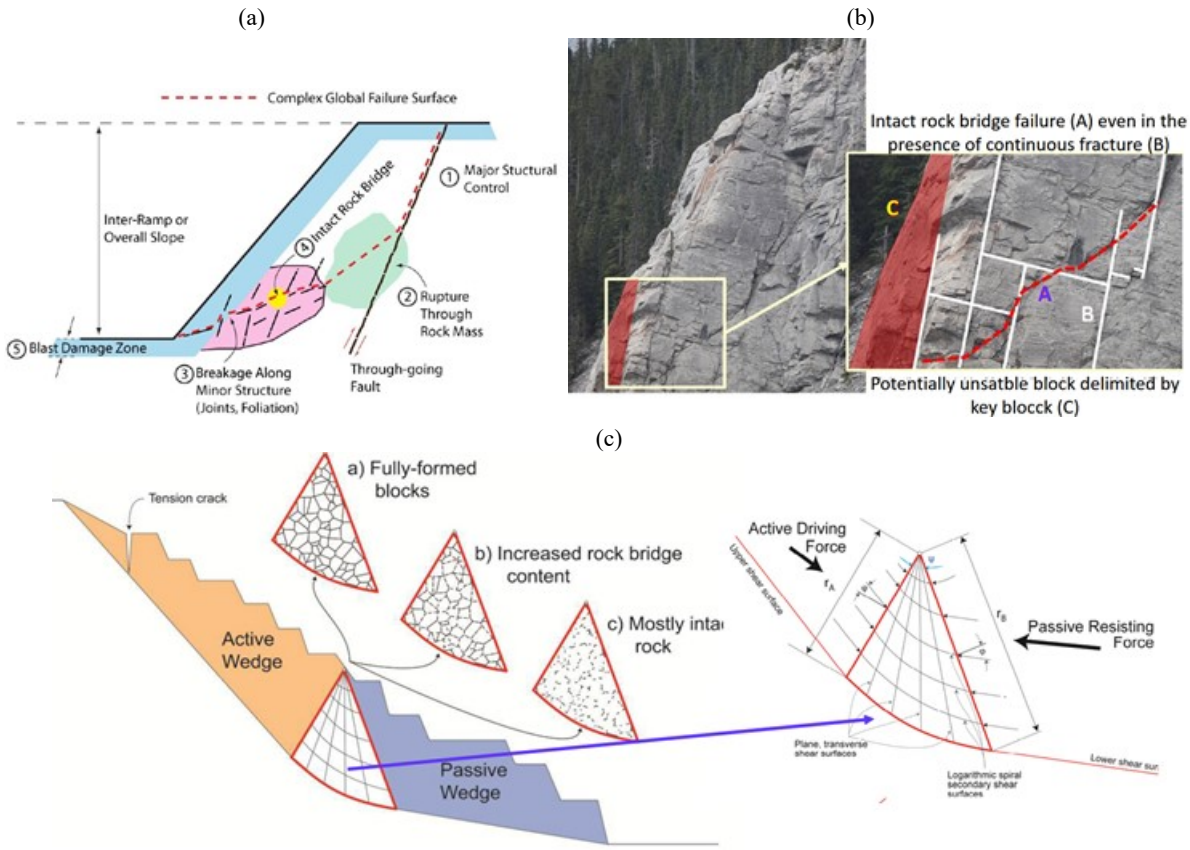


Fig. 7. (a) Conceptual illustration of a composite failure through a deep pit slope (modified by Tuckey et al. (2013) from Little (1999) and Baczynski (2000)), (b) example showing how ongoing intact rock bridge failure may occur even in the presence of apparently continuous fractures (modified from Elmo et al. (2018) by Elmo et al. (2022)) (c) Prandtl wedge applied to bi-linear slope failure; the Prandtl Prism functions as a transition zone, where the direction of driving stresses from the active upper block are transferred to the lower passive block (Tuckey 2008).

The Bingham Canyon Mine, located in the Utah State of USA (see Fig. 2a), is a major producer of copper, gold, silver and molybdenum since 1906 and is currently the deepest (1350 m) open pit mine in the world. A huge slope instability, called Manefay Slide, occurred in the upper northeast wall of this pit on April 10, 2013 which was a largely unconfined nose-shaped geometry (Ross 2017)(Fig. 8). Williams et al. (2021), who evaluated theManefaySlide after it occurred using modern InSARtechniques, mentioned that the mechanism of this slide has been studied, reviewed and back-analysed with numerical models by experts, however, there has only been a single publication by Ross (2017) released with first-hand knowledge of the mechanics and it established a consensus that the failure is a complex, active-passive failure.



Fig. 8 Views from the Manefay Slide occurred in Bingham Canyon Mine, Utah, USA (Sources: http://www.mining.com; Williams et al. (2021))

The geology of the mine is complex and varied and includes sedimentary rocks folded, faulted, intruded by igneous materials and subjected to alteration (Porter et al. 2012). Although previously a number of much smaller and simpler wedge and circular failures have developed in this mine, Ross (2017) mentioned that due to its complexity the Manefay slide which was different than any of the previous wedge and circular failures developed in this pit, it could not be identified with standard 2D analyses. In summary, the mechanism of this slide is explained by Ross (2017) as given below.
(i) when the movement started it caused a reduction in strength between the beds of sandstone and siltstone additional movement became easier,
(ii) in addition to reduced cohesion, clayey contacts called gouge with low permeability created perched water table and resulted in a saturated zone,
(iii) the active block was moving down the dip of Manefay bed and this movement was being resisted by the massive wall west of the active block, which was solid rock and had no place to move (Fig. 9a)
(iv) the strength of the active block was exceeded by the weight and stresses of the active block, the passive block failed in a catastrophic manner and was ejected from between the immovable wall to the west (Fig. 9b),
(v) the 1st block moving changed the area of the mass tend to fail and created a new active block (gray colored area in Fig. 9c). But much of the 2nd active block included old mining waste from earlier decades. The stress on the 2nd passive block became critical and 40 minutes after the 1st failure the stress broke the intact rock along the estimated failure plane as shown in Fig 9d. In his book, Ross (2017) emphasizes that the ManefaySlide was a complex failure at a mine with intricate geology and geologic structures and it was also true for all deep and large open pit mines that should consider the possibility of a large-scale active/passive failure mechanism as a part of the geotechnical analyses and highwall designs.

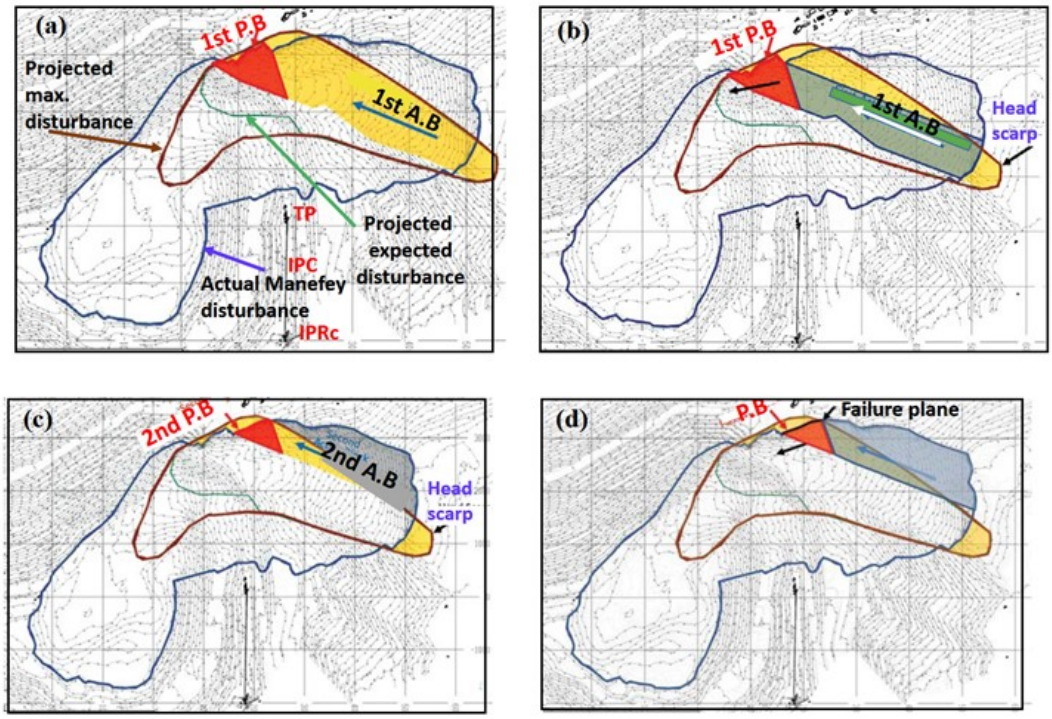


Fig. 9 (a) Manefay Slide general layout and active block (A.B) and psssive block (P.B) - pre-failure, (b) 1stfailure, (c) 2nd active block, (d) 2nd failure (slighty rearranged from Ross (2017))

Quantificaton of discontinuity persistence and intact rock bridges within rock slopes is a critical component of rock slope stability assessments and requires both the use of new data collection techniques and rigorous data interpretation through fracture network analysis (Elmo et al. 2007). Jennings (1970) is the first researcher who documented the importance of intact rock bridge fracturing for slope stability assesments. More recently, the Discrete Fracture Network (DFN) approach using the probability density functions to represent discontinuity orientation, spacing and persistence has been developed and was shown as a useful numerical tool for the use of synthesizing fracture network models obtained from digitally and conventionally mapped data and its use increased particularly in the last decade (e.g. Elmo et al. 2007, 2014, 2015, 2018, 2022; Stead and Eberhardt 2013; Tuckey and Stead 2016; Rogers et al. 2009, 2014; Dershowitz et al. 2017; Donati et al. 2020; Montiel et al. 2020; Ojeda et al. 2023; Ambah et al. 2025).

The DFN approach is based on the characterization of each discontinuity set within a structural domain using statistical distributions of fracture properties mainly orientation, length (persistance), intensity, termination percentage and spatial variation. Since direct investigation of rock structures in rock masses in 3D is not possible, discontinuity data sampled from mapping of exposures in variably oriented outcrops (2D) and boreholes (1D) are used in DFN approach to generate shotcastic discontinuity model which shares statistics of the samples and allows for the incorporation of deterministic discontinuities such as faults or highly persistent joints (Elmo et al. 2013). Natural discontinuity mapping can be conducted using the traditional outcrop mapping (scan-line survey/linear mapping), rectangular window mapping (ISRM 1981, 2007). In addition, indirect data collection with the use of more advanced remote sensing techniques such as terrestrial digital photogrammetry and laser scanning techniques (LiDAR), and also unmanned aerial vehicles (UAV) to characterize the rock masses in open pits considerably increased (e.g. Elmo et al. 2013; Stead et al. 2012, 2019). Such 3D models are also employed to map and characterize slope damage features, such as tension cracks (Stead et al. 2019; Donati 2019), brittle fractures (Sampaleanu et al. 2017; de Vilder et al. 2017); and characteristics of blast damage and intensity, and seepage intensity (Lupogo 2017; Tuckey and Stead 2016; Vivas et al. 2015). An example of DFN fracture model and DFN stereogram for the Los Pleambres open pit (Chile) are given in Fig. 10. In literature (e.g. Sjöberg 1999; Donati et al. 2020), it is recommended that since at bench scale the modes of failure in open pits are generally structurally controlled (without combination of the rock mass with discontinuities), unless the rock mass has low quality, DFN approach is used for inter-ramp and overall slope scales.

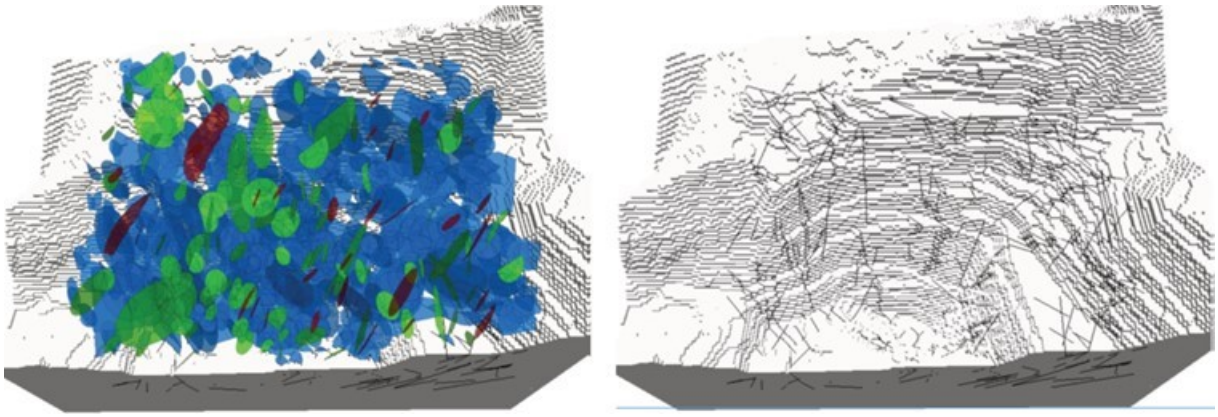


Fig. 10 An example of DFN model for an open pit mine (Montiel et al. 2020).

2.5 Selection of shear strength for discontinuities and rock masses

2.5.1 Shear strength of discontinuities

Accurate determination of the geomechanical parameters of discontinuities and rock masses which are the key inputs for slope stability analyses, is essential for correctly evaluating the stability of rock slopes. The use of empirically suggested parameter values based solely on lithology, discontinuity surface characteristics, or rock mass classifications is no longer considered suitable approaches, and therefore, experimental methods are preferred.

Sjöberg (1999) have highlighted the importance of scale on the strength of the rock mass in open-pit slopes and it is schematically shown in Fig. 11a. The reduction in strength with increasing scale (i.e., when the slope includes more benches) results from the greater number of discontinuities within the rock mass. Therefore, the strength of discontinuities is of primary importance in structurally-controlled slope failures. The degree of roughness must be considered when selecting the appropriate failure criterion for determining the shear strength of discontinuity surfaces. For planar and smooth discontinuity surfaces and discontinuities with thick filling (shearing only of the filling), the "Mohr–Coulomb failure criterion" (Fig. 11b) is the most widely used linear criterion independent of normal stress. It has two components: peak and residual strengths. Hence, a design decision must be made regarding which set of values to use. Although using residual shear strength parameters (c_r, ϕ_r) ensures a conservative (safer) design, it may also lead to uneconomical results. Therefore, it is a common practice to use residual shear strength parameters for fault surfaces that have undergone shearing during their formation. Another approach is to use residual strength values in the analyses for discontinuities that show a rapid reduction in shear strength toward residual levels after very small displacements in shear stress–shear displacement curves. In addition, results of back-analyses of failed rock slopes can be compared with laboratory-determined shear strength parameters obtained from

samples representing the actual failure surfaces. Discontinuities with rough and/or undulating surfaces behave differently under shear loading: initially, asperities are sheared off, and once the surfaces become smoother, shear movement continues at lower strength levels. Hence, the Mohr–Coulomb criterion is not applicable to such discontinuities; their failure envelopes are curved and depend on normal stress (σ_n). For such discontinuities, the "Barton's (1976) criterion" is used to determine their shear strength (Fig. 11b). In slope stability analyses, it is necessary to calculate equivalent cohesion and friction angle from the curved failure envelope.

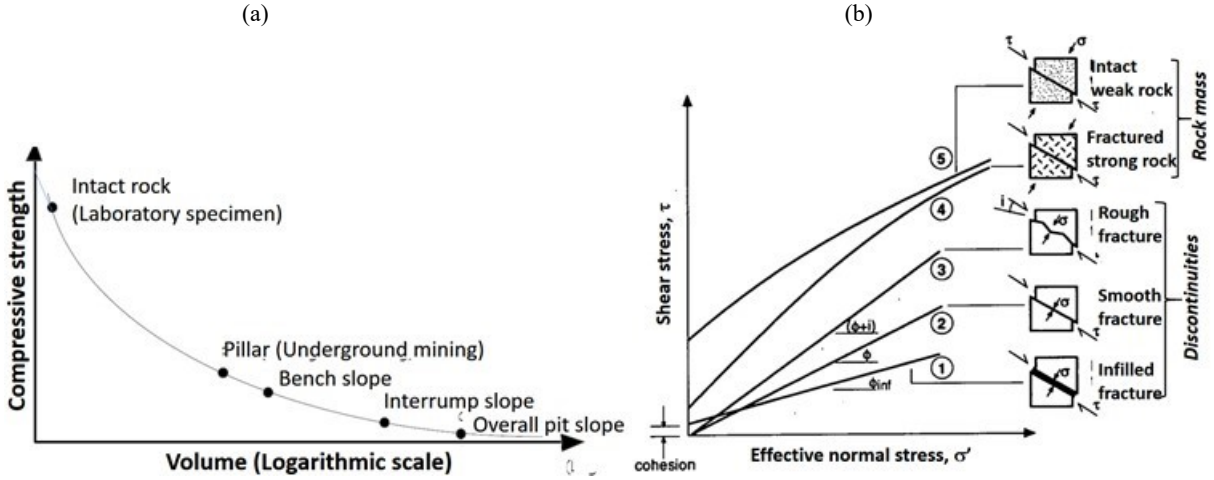


Fig. 11 (a) Scale effect on rock mass compressive strength in terms of rock slopes (Sjöberg 1999), (b) relationships between normal and shear stresses for different discontinuity surfaces and the corresponding failure criteria (Transportation Research Board 1996)

2.5.2Shear strength of rock masses

In rock masses, divided by multiple discontinuity sets with different orientations, the overall behaviour is controlled by both the discontinuities and the intact rock material. Therefore, strength and deformability properties of rock masses should ideally be determined using samples that include both the intact material and discontinuities. However, obtaining meter-sized samples from such environments and preparing them for laboratory testing is generally impossible, and suitable large-scale testing equipment is not available. Laboratory tests on core samples are not representative of rock mass, in-situ testing on rock mass cannot be practical and economic for all cases. On the other hand, even representative values of large scale rock strength can be obtained from the back-analyses of failed slopes, this can only be possible for slopes failed through rock masses. As emphasized by Renani and Cai (2022), since rock masses represent highly variable and complex systems of intact rocks and discontinuities of varying mechanical properties and geometric configurations, which have been subjected to different in-situ stress regimes and geological processes, determination of their mechanical characteristics is a difficult issue.

In response to the lack of suitable failure criterion for rock masses, Hoek and Brown (1980a, b) suggested an empirical nonlinear rock mass failure criterion to estimate the strength of rock masses to be used in analysis and design of rock engineering structures, such as tunnels, slopes and others. The Hoek-Brown (H-B) criterion is based on the following assumptions: (i) rock mass exhibits an isotropic behaviour, (ii) intermediate principal stress has a negligible effect on strength of rock, and (iii) strength of jointed rock masses is not sensitive to the rate of loading (Hoek and Brown 1980a). The originators of this criterion also suggested that it can be used for determining the strength of rock masses consisting of intact rock blocks separated by intersecting discontinuities in low confinement environments where the behaviour is controlled by block sliding and rotation without significant degree of intact rock failure. The criterion has been commonly used for the above purposes over the past forty-five years and repeated revisions were also made to the criterion (mainly Hoek and Brown (1988) - Updated criterion; Hoek et al. (1992) - Modified criterion; Hoek and Brown (1997) - Generalized criterion). Since the original criterion is too optimistic for slope design, the generalized criterion was updated in its 2002 and 2018 editions (Hoek et al. 2002; Hoek and Brown, 2019) and the concept of undisturbed and disturbed to provide a method for downgrading near surface rock masses and RMR to estimate H-B parameters were introduced in the updated criterion. The "*a"* parameter was introduced in the modified criterion (Hoek et al. 1992) to produce a criterion with zero tensile strength. In the generalized criterion (Hoek and Brown 1997), Geological Strength Index (GSI)

replaced to RMR of Bieniawski (1989) as a geological data input and the linear regression method for estimating the equivalent Mohr-Coulomb cohesion and friction angle was introduced. In the 2002 edition of the criterion, new derivations of relations between the parameters m_b(reduced value of material constant m_i),s and a (material constants) and GSI were provided and the disturbance factor (D) was introduced to account for blast damage and stress relaxation in slopes. The guidelines given in the 2002 update of the criterion mostly remained same in its 2018 update (Hoek and Brown 2019).

Although it is widely used in practice, repeated updates to this criterion have led to insufficient awareness among practitioners of certain issues, such as "the criterion is only based on tri-axial test data on Panguna andesite from an open pit in Papua New Guinea (Hoek and Brown 1980a, b) and no additional test data on rock mass strength was used for supporting its updates", "its origin, scope and evolution", "uncertainty and influence of parameters", and "scale effect". The main limitations and/or difficulties of the failure criterion are briefly discussed in the following paragraphs.

Until the publication of the 2002 update of the criterion, the switch at GSI=25 was arbitrarily and validity of this boundary value has not been confirmed by case studies. Although the parameters s and a are sensitive to the GSI value, according to Hoek and Brown (1997), the exact location of this switch has negligible practical importance. Based on the stability analysis of a hypothetical drained slope consisting of rock masses with the GSI values between 20 and 30 using the generalized H-B criterion, Sönmez and Ulusay (2002) indicated that a strength gap appears between the failure envelopes of rock masses with GSI values of 25 and 26 (Fig. 12a), suggesting that this situation probably arises from the equations employed for the estimation of a and s at GSI<25 and GSI>25. In addition, the strength envelopes of the rock masses with GSI values smaller and greater than 25 intersect each other at certain normal stress levels (Fig.12b) . In other words, this situation suggests that a weaker rock mass may possess higher strength than that of a stronger one when the normal stresses corresponding to the intersections are exceeded. To overcome these difficulties in the generalized H-B criterion, some approaches and improvements to the estimates of rock mass parameters have been suggested by Sönmez and Ulusay (2002) and the validity of the proposed improvements has been checked by their application to different rock masses and to hypothetical and real slope cases.Their analyses showed that s should be estimated from the suggested equation which considers the effect of rock mass disturbance and GSI values between 5 and 100, regardless of any switch value for the GSI. In addition, it was also validated that the boundary of GSI < 25 suggested by the criterion should be replaced by GSI < 30 to overcome the difficulties related to the estimation of the parameter a (for GSI > 30 a = 0.5; for GSI < 30 a= 0.65 - (GSI / 200)).

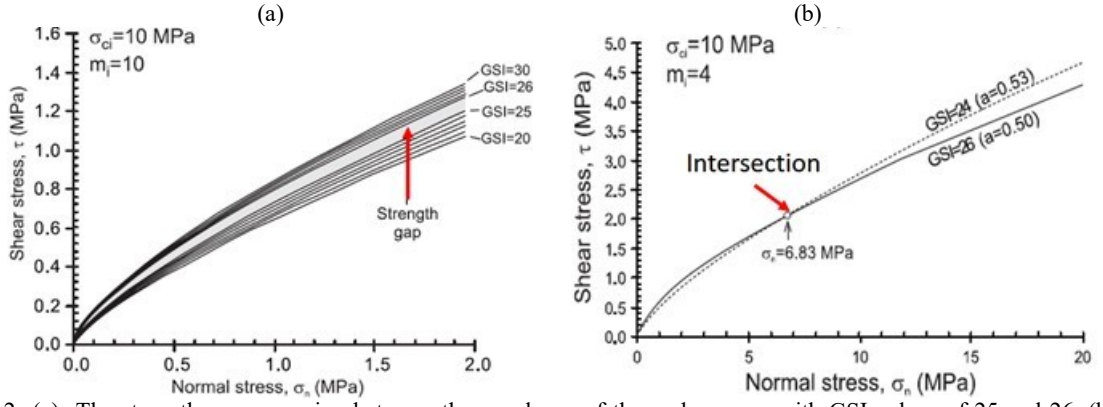


Fig. 12 (a) The strength gap appearing between the envelopes of the rock masses with GSI values of 25 and 26, (b)) an example illustrating the effect of m_i on intersection of the failure envelopes of a rock masses when the generalized H-B criterion is used (Sönmez and Ulusay 2002)

The guideline for estimating the disturbance factor, which shows some similarities with that proposed by Sönmez and Ulusay (1999, 2002), was proposed by Hoek et al (2002) who left decision on the severity of disturbance to the users. However, when compared to the guidelines for the disturbance factor (D) suggested by Hoek et al. (2002). the disturbance factor (d_f) suggested by Sönmez and Ulusay (1999) provides various degrees of disturbance severity (considering the type of excavation, such as mechanic excavation, blasting) based on the disturbance effects described by Kendorksi et al. (1983).

The original qualitative GSI chart (Hoek 1994; Hoek et al. 1995) was later modified by Hoek and Brown (1997), who added GSI contours to the chart without meaningful numerical axes to determine a basis for positioning on the chart. Then the categories of "laminated and sheared weak rocks" and "intact-massive rock" were included in the GSI chart by Hoek et al. (1998), Hoek (1999) and Hoek

and Marinos (2000), respectively. Due to the qualitative nature of the GSI charts suggested in the updates of the criterion, there are some subjectivity and uncertainty in their application. In other words, it is possible to estimate different GSI values from the charts for the same rock mass by different persons depending on their personal experience. Therefore, some researchers have provided approaches to the quantification of GSI chart with numerical axes and these chronologically include Sönmez and Ulusay (1999, 2002), Cai et al. (2004), Russo (2009) and Renani et al. (2019). Due to lack of the parameters with related interval limits to describe discontinuity surface conditions of the discontinuities and the rock mass structure in the GSI System, two terms namely, "structure rating (SR)".based on volumetric joint count (Jv) and "surface condition rating (SCR)" estimated from the parameters such as roughness, weathering and infill, were suggested by Sönmez and Ulusay (1999, 2002) in the quatititative GSI chart they recommended. The surface conditions given on the X-axis of the GSI chart recommended by the originators of the H-B criterion are only based on descriptions which can cause incorrect assessments. For example, slickendisiding (in "very poor" surface condition) should be "highly weathered and with clay filling". But this description does not consider that rougher discontinuity surfaces may have clay filling and be weathered (Barton 2025).Therefore, the quantitative GSI charts based on separate rating values selected for each dicontinuity surface condition provide estimation of more representative GSI values.

A quantitative GSI chart using RQD and R (adopted from RMR rock mass classification system of Bieniawski (1989) was recommended by Hoek et al. (2013) and they mentioned that this quantitative chart is applicable to tunnels with spans of 10 m and slopes with a maximum height of 20 m and lower GSI values should be selected for larger scales. This suggestion also causes an uncertainty for practitioners. Based on the two case studies where it has been possible to compare the results of the available quantification schemes with back-analysed strength from large scale open pit instability, Duran (2016) reported that the quantitative GSI charts of Sönmez and Ulusay (2002) and Russo (2009) have provided the values of GSI to those provided by assessing RMR_{89} and utilizing the equivalance suggested by Hoek et al. (1995). Duran (2016)also recommended that review of further case studies to allow refinement of the quantification schemes and to assess their applicability to large scale open pit slopes are needed. Hoek et al. (1998) also proposed a new rock mass category to accomodate thinly foliated or laminated, folded and predominantly sheared weak rocks of non-blocky structure. But previously Hoek (1994) emphsized that the H-B criterion is applicable to "intact rock" or to "heavily jointed rock masses" which can be considered homogeneous and isotropic. Since the strength and deformability characteristics of such rock masses are governed by the displacements along numereous very thinly spaced pre-sheared and slickensided foliation planes, introducing of this new category into the GSI chart seems not to be realistic. Therefore, this category was not included into the quantitative GSI charts proposed by Sönmez and Ulusay (1999, 2002). But this rock mass category was used by the H-B failure criterion until 2013 when its originators acknowledged that the failure of such rock masses should not be included within its applicability range, and they therefore, excluded both this category and the category of massive (intact) rock masses from the GSI chart.(Hoek et al. 2013). In addition, Marinos and Hoek (2000) proposed a GSI chart for heterogeneous and tectonically deformed sedimentary rocks and its extended version was published by Marinos and Carter (2018). On the other hand, GSI charts for ophiolites (Marinos et al., 2005) and tectonically undisturbed molassic rocks (Hoek et al., 2005) were also proposed to including tunelling projects in northern Greece. In the GSI system, very poor rocks are generally defined by GSI value below 27 (Morales et al. 2004) or 25 (Hoek and Brown 1997). In order to better characterize the poor rock masses without disregarding its original concept, the modified GSI chart, which can be used for poor and very poor rock masses with GSI ranging between 6 and 27 and is integrated with existing GSI chart, was also recommended by Osgui et al. (2010) as an assistant tool for GSI estimation for such rocks.

The H-B constant m_i, which defines the non-linear strength envelope of rock material, depends on the frictional characteristics of the minerals involved by rock material. Therefore, its accurate determination is a great influence in the estimation of strength of brittle rock materials. Hoek and Brown (1980a-b, 1997) suggested regression analysis of results obtained from the numereous tri-axial tests at least five sets of tests under different $\sigma_3$values. Heok and Brown (1980a) also proposed a guideline to estimate m_i as a range only based on rock type and its latest version with a more detailed lithological classification was proposed by Hoek (2007). Since the m_i values are given in a range in this guideline, it is difficult to select exact m_i values. In the absence of tri-axial tests, there are different methods, such as R-index (the ratio between σ_c and σ_iHoek and Brown 1980a,b; Mostyn and Douglas

2000; Richards and Read 2011; Mehrishal et al. 2015), crack stress initiation model, which is a special form of R-index (Cai 2010), UCS-based model (Shen and Karakus 2014; Vasarhelyi et al. 2016), tensile strength (TS) model (Wang and Shen 2017) and combination (UCS-TS) method (Arshadnejat and Nick 2016) are available to estimate m_i. However, some of these prediction methods are based on limited data and limited rock types. Recently, Karakul and Ulusay (2022) developedϕ-based method using three σ_1 and σ_3 data pairs from tri-axial tests and Davaranpah et al. (2022) statistically analysed a database and introduced new material constants for igneous, sedimentary and metamorphic rocks. Both studies revealed that the ranges of calculated and predicted m_{ii}values are much larger than those of the m_i ranges in the m_i table proposed by the originators of the failure criterion and it is generally still inappropriate. These two recent studies on m_i given above indicated that R-index approach with new material constants provides the best fit for all studied rocks and is not influenced by rock type (Davaranpah et al. 2022), and the ϕ-based method proposed by Karakul and Ulusay (2022) gives the best estimation for m_i and only 2 out of 121 sets of data fall out of the lines between m_i(±calculated) /± 10°.Readers are also encouraged to consult other sources concerning evaluations of the H-B failure criterion (e.g. Renani and Cai, 2022; Barton, 2023, 2025; Aydan et al., 2012).

In his paper on mechanical properties of rock masses, as one of the two originators of the H-B failure criterion, Brown (2008) strongly recommends the following issues when using this criterion: (i) it is not intended to replaced and depend for its successful application on, careful thought, detailed appraisals of site geology, carefully conducted site characterization and laboratory test programs, and a detailed evaluation of mechanics of the engineering problem being addressed, (ii) both the criterion and its derivatives should not be used as "black box" or "cook book" approaches, (iii) as done in some cases, $m_i$values should not be taken from tables in final design, instead it should be determined from required tests, and care should be paid to the selection of parameters, such as disturbance factor (D). The author of this paper considers that the above comments by Brown (2008) are very useful and important.

2.5.3 Shear strength of bimrocks

Main factors affecting the overall mechanical properties of BIMROCKs are: (a)mechanical properties of matrix, (b) Volumetric Block Proportion (VBP), (c) shape and size distribution of blocks,and (d) orientation of blocks relative to failuresurfaces. Due to the great spatial, lithological and mechanical variability of bimrocks, neglecting the contributions of blocks, choosing instead the strength and deformability of the weak matrix may result in too conservative and expansive for many bimrocks in terms of slope design (e.g. Medley 1994, Lindqusit 1994, Kim et al. 2004, Wakabayashi and Medley 2004, Medley and Zekkos 2011).But Lindquist (1994) showed that the strength of bimrocks depends on volumetric block proportion (VBP) and when VBP ≤ 25% it is considered that the material is soil or weak rock, and when VBP > 75% there is little further addition in strengthbecause blocks start to touch each other (Fig.13a). Based on the experimental studies on artificial bimrocks, some authors(e.g. Lindquist 1994, Sönmez et al. 2006, Kalender et al. 2014) proposed empirical strength criteria assuming that bimrocks are homogeneous and isotropic rock masses with equivalent mechanical properties which can be defined according to their block proportions and strength parameters of matrix. One of these empirical criteria is given in Fig. 13b as an example.

In order to overcome the size limitation of laboratory specimens, in-situ shear box tests (BIM Test) on shale-limestone caotic complex Bimrock from an open pit in Italy was also conducted by Coli et al. (2011). The in-situ testing apparatus cosists of a flat frontal steel plate with two horizontal bottom and of two side plates, and all the plates are 80 cm wide, 50 cm high and 1.5 cm thick and is connetced to a hydraulic jack (Fig. 14a). A constant displacement of 0.05 mm/sec was applied during the test. In general, the failure surfaces show tortuous paths, characterised by a step profile and by abrupt local slope variations due to the presence of protruded calcareous blocks (Fig. 14b). Due to unknown saturation and pore pressure, the upper sliding area was divided into slices in order to calculate the shear strength parameters, and a pair of c and ϕ parameters was calculated for each test specimen with the aid of limit equilibrium method of analysis performed on each cross-section of the sliding surfaces, and using the results VPB-ϕ and VPB-$c$graphs were drawn (Fig. 14c.1-c.2). As seen from these graphs, ϕ increases with the increase in VBP with a high coefficient of determination (R^2= 0.85) (Fig. 14c.1), while cohesion shows a strong decrease from test P2 to test P1. This sudden drop in cohesion is observed at the VBP threshold of 20-25% which represents the threshold value between a matrix-controlled and a block controlled behaviour according to previous studies (e.g. Lindquist 1994, Kim et al. 2004, Sönmez et al. 2006). However, Coli et al. (2011) remarked that the bimrock's shear

parameters obtained through the in-situ shear tests are not effective but operative parameters under natural conditions, and very likely, partially drained conditions; therefore, the proposed comparison has the only purpose of giving an indication about the respective magnitudes.Napoli et al. (2021) aimed statistically to investigate and compare the stability of theoretical slopes in the most widespread bimrocks and used model bimrocks obtaining blocks with variable shapes, dimensions, arrangements and contents. Their results based on fifteen configurations indicate that block shapes and orientations significantly affect the stability of slopes in bimrocks only when the block contents are greater than 40%, and the blocks inclined 0°to the horizontal provide the most tortuous and irregular failure surfaces and, consequently, the highest safety factors.

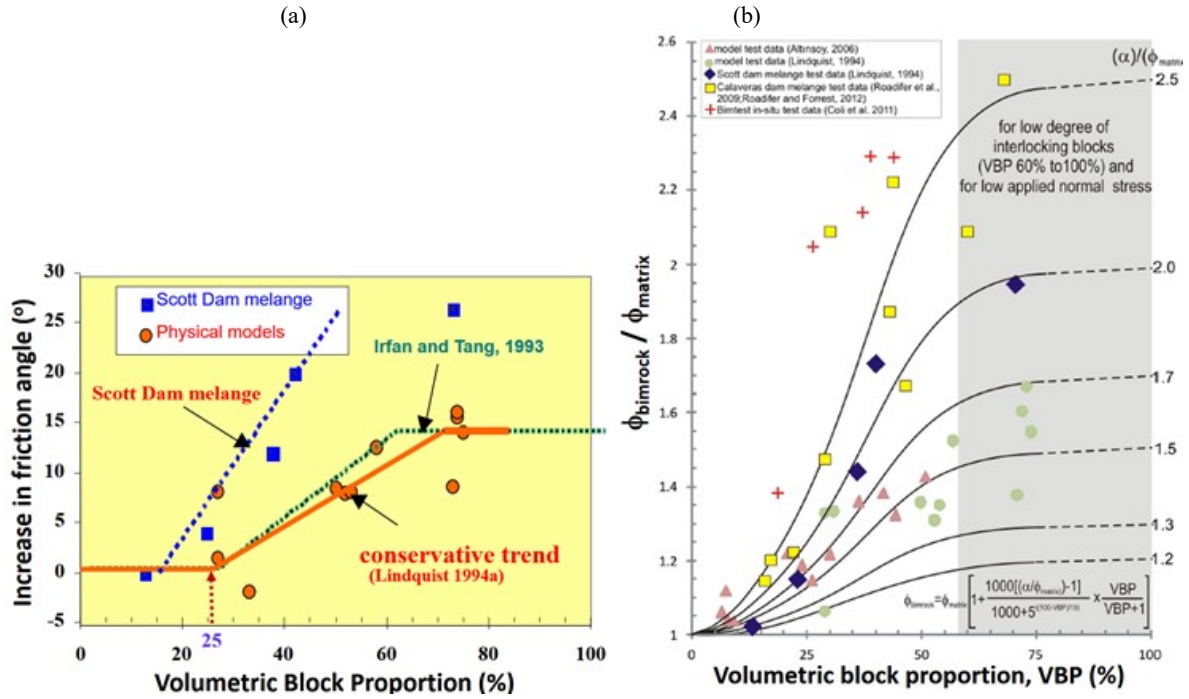


Fig. 13 (a) Strength of bimrocks increases with volumetric block proportion (Lindquist 1994), (b) the graphical presentation of the empirical approach for predicting $\phi_{bimrock}$ (Kalender et al. 2014)

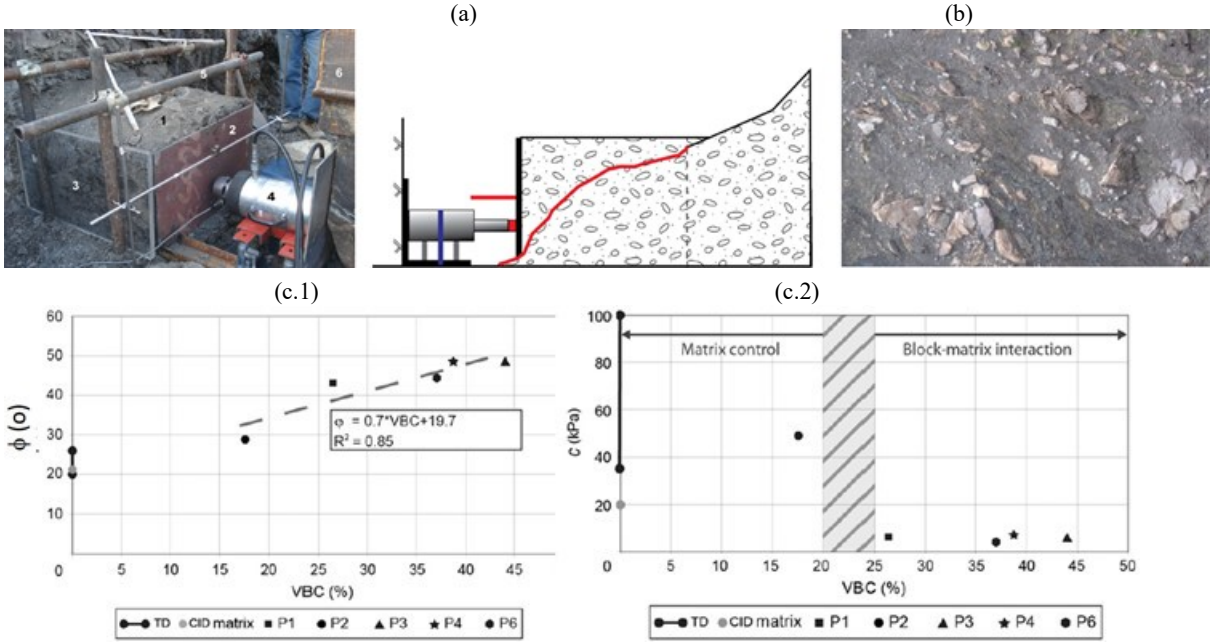


Fig. 14 (a) In-situ shear test apparatus used for a bimrock and schematic representation of the test and failure surface, (b) shale–limestone chaotic complex bimrock. and (c.1) correlations between friction angle and VBP, and (c.2) cohesion and VBP (Coli et al. 2011)

By considering that there is still no general concensus on the approaches/methods for the site characterization and determination of geomechanical properties of bimrocks, the author of this keynote recommends the followings for future studies on bimrocks: (i) laboratory tests on larger sized specimens should also be conducted, (ii)in case of huge blocks greater than the size of the test device, the dimesion of the in-situ BİM shear test cannot be a practical way in all cases, (iii) since real

bimrocks generally contain non-spherical blocks, assumption of block sphericity has limitation, therefore, future studies on other block shapes (such as elipsoids etc.) are neccessary,(iv) influence of structural features in bimrocks should also be investigated, (v) in laboratory experiments and numerical solutions, matrix is considered as a homogeneous rock mas, however, when it is anisotropic (such as laminated shale or slate)matrix anisotropy should not be ignored, (vi)since there existonlya few study addressing the behaviour of bimrocks under seismic loading (their dynamic properties), this issue also needs further studies.

2.6 Hydrogeological conditions and conceptual hydrogeological model

Pore water pressures acting within discontinuities reduce the effective stress, which in turn decreases the shear strength of discontinuities and/or the rock mass, adversely affects slope stability. Therefore, the hydrogeological conceptual model, which complements thegeotechnical model of a rock slope, can be critical to the slope design. By considering this, a clear understanding of the water pressure distribution and reducing any pressure is an essential controlling factor and should not be overlooked especially in the design of large and deep slopes. This model is essential for clearly understanding the distribution of pore water pressure and for determining appropriate measures to reduce it. The importance of hydrogeology has rapidly gained momentum particularly 2000s to meet the requirements of deeper and larger open pit mining projects. The advent of new monitoring systems, and particularly the use of grouted-in vibrating wire piezometers (VWP) has contributed to a practical understanding of the factors that control the behaviour of water pressure in the pit slopes (Read and Stacey 2009).

Mining can cause changes to the hydraulic properties of the slope forming materials due to: (a) changes induced by blasting, creating an over-break zone (5-40 m thick) and fluid-to-solid hydro-mechanical changes at deeper elevations; (b) litho-static unloading by removal of the overburden may result in an expansion of the fracture aperture and pore space and depending on these pore pressure reduces. However, reduction of high pressure seldom occurs in fractured rock because transient flow of water occurs towards depressurized area to equalize the pressure drop; (c) deformation resulted from drainage and reduction of pore pressure; (d) changes the hydraulic properties of the slope forming materials due to slope failure (Beale 2013). Except for rocks with hydraulic conductivity coefficients of 10^{-8} m/s or greater, the traditional practice of simply drawing a phreatic surface in slope cross-sections and assuming hydrostatic pore pressures below it is now considered an incorrect approach for deep and large open pits (Read and Stacey 2009). In addition, the research by the Large Open Pit (LOP) project indicated that effect of deformation in pore pressure in fractured rocks became important in zones where the permeability is less than 10^{-8} m/s (Read and Stacey 2009; Galera et al. 2009). As illustrated in Fig. 15a, depending on the depth of the pit, particularly in deep open pits, pore pressures may vary, and partially saturated zones may exist. If the geology is characterized weak points in a slope, they may create future instability and should be identified early in the investigation program, so that hydrogeology can be focused on these areas, instrumentation can be installed to measure pore pressure and geotechnical parameters at the same interval in the same drill hole (Fig. 15b). Therefore, the hydrogeological conditions cannot be represented by a single, uniform groundwater level. For this reason, the involvement of mining hydrogeology experts is of great importance in assessing the stability of open pit slopes.

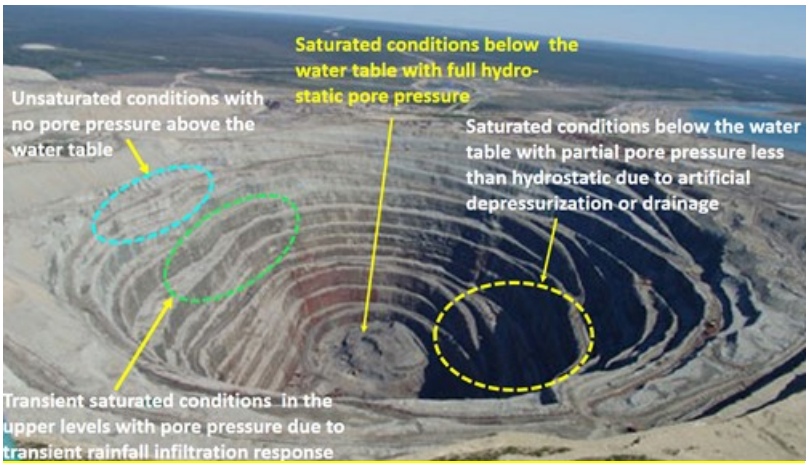
For the geotechnical models, the development of a good groundwater conceptual model is an important part of the rational design of deep and large open pits. A conceptual groundwater model is a realistic, defensible, albeit simplified representation of the hydrogeological system (Beale et al. 2013). By collecting and evaluating data obtained through modern hydrogeological measurement and monitoring techniques, a hydrogeological conceptual model can be developed and integrated with the geotechnical model. Based on regional and mine scales, the conceptual hydrogeological model considers the three regimes given below (Beale et al. 2013): (a) geology (stratigraphical units and their variations, locations and interactions, geological structures), (b) hydrology (natural and artificial recharge to the groundwater system, natural discharge from the groundwater system, groundwater-surface water interaction), (c) hydraulics (hydraulics of the main geological units, groundwater flow paths).Such a model should also be used for designing appropriate drainage solutions. Two examples of hydrogeological conceptual model are given in Fig.16.

The following types of groundwater control are commonly used in open pit slopes:

(i) Dewatering (pumping) wells: They are used general mine dewatering and slope depressurization. When a general lowering of the groundwater level in permeable slope forming material is needed vertical pumps are used outside the crest or within the pit area.

(ii) Horizontal and steep angle (or vertical) drains: They are commonly used to relieve groundwater pressure behind the pit slope. Sub-horizontal drain holes can be considerably effective in hard rock slopes if they are long enough to reach the rocks mass in the vicinity of potential failure surfaces. In large slopes, in order to achieve this goal, drain holes with a length of 200 to 300 m may be required. Vertical or angled drains can be used where a large hydraulic gradient is developed within the slope.
(iii) Drainage tunnel: They are constructed behind the slope or underneath the pit and their use particularly increased in large open pits. Their construction and operation without interfering mining and their construction earlier in a mine and providing active depressurization are the main advantages of this control method.
(iv) Cut-off system (slurry wall, grouting of permeable fracture systems): They are used to reduce the amount of water reaching the pit with the aid of reducing the permeability of a particular rock unit or a zone along the flow path.
(v) Removal of the water using in pit-sumps: It can be applied when the rock mass in the pit slope has relatively low permeability.

(a)



(b)

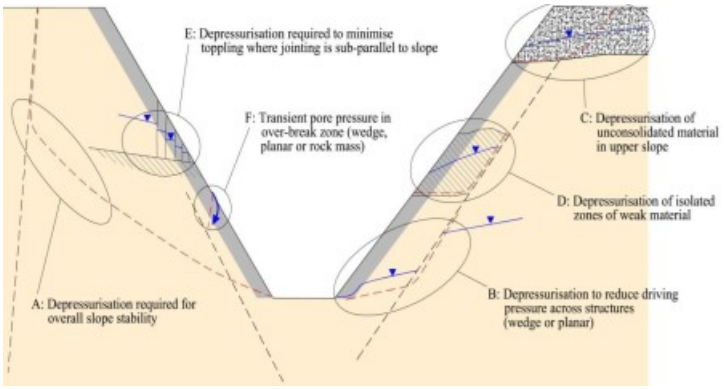
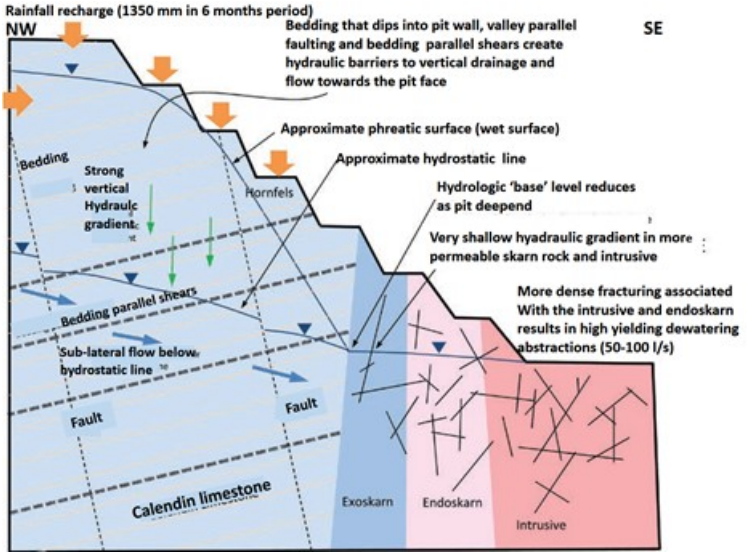


Fig. 15(a) Possible hydrogeological conditions at different depths of a deep open-pit slope (different groundwater conditions are shown on photo of an open pit (*mining-technology.com*)), and (b) focusing the hydrogeology program on potential failure modes (source: LOP project; Beale 2013).

In most large open pits, a combination of the above measures is used in different sectors or at different stages of the mine life. A brief information for the groundwater control conducted at Kışladağ gold open pit (most recently 440 m deep) in Türkiye (Furtana et al. 2023) is given in this paragraph as an example. Although the east side of the pit shows good drainage towards the pit sump, the west side shows slow drainage due to orientation of the joint sets and the youngest intrusion with lowest hydraulic conductivity. Two flight submersible pumps (250 m^3/h maximum pumping capacity of 150 m head) are used in the sump (Fig.17a). In 2012, three pumping wells were drilled, and yield of water was between0.2- 5 lt/s, and five test wells were drilled in 2020 for the assessment of hydraulic conductivity of various parts of the pit. Trial advance pumping wells at the pit bottom were drilled to help dewatering at the pit floor and three of them were converted to monitoring wells. After the implementation of the monitoring and test results, long horizontal drains with length of longer than 250 m were drilled (Fig. 17b) in the southwest of the pit to increase the drawdown rate and to improve the pit slope stability and the current monitoring methodology using four VWPs sensors inside the pit worked well (Fig. 17c). The drains exceeded expectations in the SW of the pit and maximum

drawdown of 50 m was observed in monitoring wells (Fig.17d). The results of this dewatering application revealed that there is no pore pressure on production levels of the Phase 4pit until the 650L which improved the stability of the Phase 3 pitwalls.

(a)



(b)

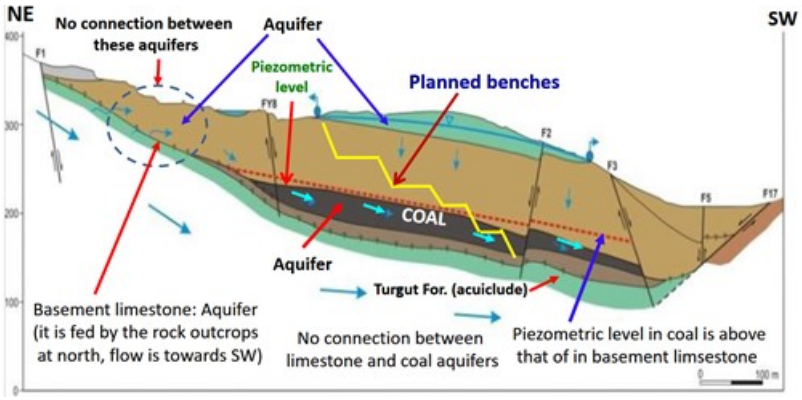
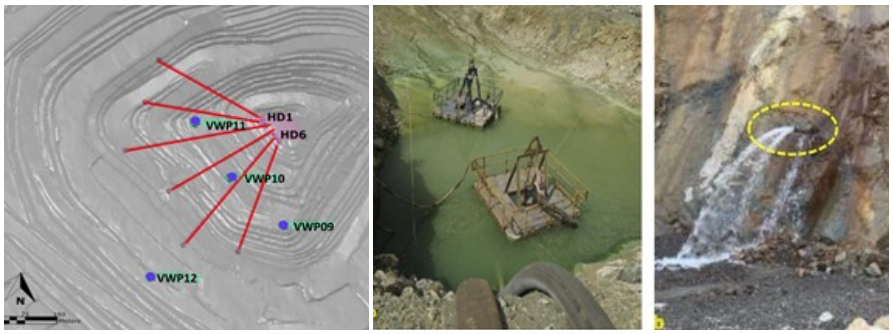


Fig. 16 Hydrogeological conceptual models prepared for (a) the Antamina pit in Peru (Pottie et al. 2013) and (b) a lignite open pit in Türkiye (arranged from Ulusay et al. 2013)

(a) (b) (c)



d)

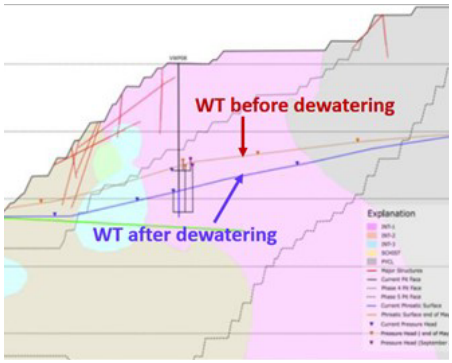


Fig. 17 (a) Wells (VWP) and drainnholes (HD) , (b) location of pumps at 650L,(b) groundwater flow from the horizontal drain HD-08, (d) vertical cross-section of HD02 showing water tables before and after dewatering (Furtana et al. 2023)

3 Geotechnical model and geotechnical domains

The objective of open pit slope design takes into consideration an analysis of the overall slope stability of open pit wall, inter-ramp angle and height, and bench design, and provides an optimal excavation design that leads to the steepest possible slopes while ensuring safety, ore recovery and financial returns are maximized. The formalized geotechnical model has been largely developed about over the past 50 years and is the basis for all open pit slope design and consists of following four sub-models (components) (Stacey 2009): (i) geological model, (ii) structural model, (iii) rock mass model (properties of materials and discontinuities), and (iv) hydrogeological model (Fig. 18).

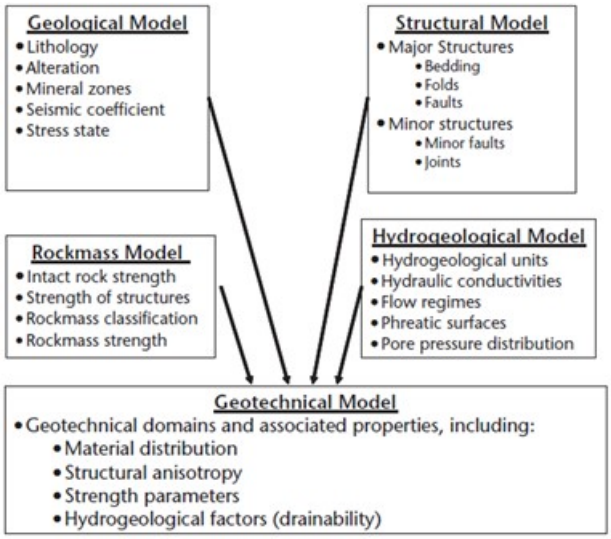


Fig. 18 Component information and output from the geotechnical model (Read and Stacey 2009)

The *geological model*provides presentation of a 3D distribution of the types of the lithologies forming the pit walls and the degree and type of weathering and alteration which can affect material properties. Core logging is also emphasized as a critical source of data for subsurface model support and logging process is also recommended. This model also helps better understanding of the regional geological setting and the genesis of the mineralization and is generally prepared by the mine geologists who primarly focus on the mineralizaton and may have a somewhat different view of the slope forming geological units.For example; waste is of little interest to the mine geologistand hence rock types may be poorly differntiated even their mechanical properties, structure and fabric may vary. In addition, although a small amount of highly altered feldspars may be of significance to the ore genesis, alteration does not necessarily weaken the rock, silicification can increase the rock strength. Therefore, the slope designer should be fully aware of the basis and terminologyused in the geological model and discuss it with the mine geologist when necessary.

The *strucural model*is divided into two sub-models, the major structures (faults, folds and shear zones at the inter-ramp to overall pit scale) and structural fabrics or discontinuites (joints, bench scale faultsgenerally at bench scale). Major structures should be continuous both along strike, down dip and persist over multiple benches. Since structural fabric has limited persistence but close spacing, attention should also be paid in design at bench scale and inter-ramp stacks. Major structures should be characterized in terms of size, nature and infillings by structural geologists. However, structural fabric is generally investigated by rock engineer and/or engineering geologist, and coordination between both professions is necessary during the construction of the major structural model.

The purpose of the *rock mass model*is to determine the engineering properties of the rock mass, structures and intact rock to be used in the stability analyses for the pit design. The most commonly used rock material properties are index properties (such as point load strength index, porosity, unit weight, P- and S-wave velocities) and mechanical properties (uniaxial and 3-axial compressive strengths, tensile strength, Young's modulus and Poisson's ratio). In open pit slope stability assessments, determination of shear strength of structural defects (faults, joints, beddings etc.)by both laboratory and field shear tests. In addition, thestiffness of structural defects for numerical modeling purposes are also determined.Rock mass classification for the slope forming materials is also considered in this model. Although the laboratory methods for testing small scale samples are well defined and standardized, the extension of the results to deep slopes several hundred meters high

needed some advances. The empirical H-B criterion of which limitations are discussed in section 2.5.2,became a tool to assess the strength of large rock masses both for slopes and underground openings. The two rock Laubscher criteria, “rock mass strength” and “design rock mass strength”, were proposed for use in only underground mining (Laubscher and Jacubec 2001). However, as a part of Large Open Pit (LOP) project, which is an international research and technology transfer project on the stability of rock slopes in open pit mines (lopproject.com), some advances have been made in development of more rigorous approach to the determination of rock mass strength DFN and Syntetic Rock Mass (SRM) (Potyondy and Cundall 2004) models. Most recently, as an alternative to methods based on RMR assessments, CNI (Call & Nicholas Inc.) (Cylwik et al 2022) proposed a new empirical rock mass failure criteria related to the strength of the rock mass directly to the degree of fracturing in the rock mass through a combination of the intact rock strength and the natural fracture strength as afunction of RQD. However, due to some data limitations, this criterion couldn’t find a wider application yet. It is also noted that back-analysis of open pit slope failures and even of stable slopes can be usefuul in the determination of material properties.Building the *geotechnical model* recommended by Read and Stacey (2009) is a step-by-step process of bringing successive layers of individual or combination of datasets into a 3D solid model using a modelling system.

A *geotechnical domain* is a volume of rock that shares similar geological, geomechanical and hydrogeological characteristics. Instead of the entire open pit as a single block, design engineers divide it into the domains to apply specific design parameters and account for structural controls to ensure pit slopes remainsstable while maximizing ore recovery. A geotechnical model showing the geotechnical domains at an open pit in Africa is given in Fig. 19a as an example.In addition, the importance of the geotechnical model is illustrated by a hypothetical example shown in Figure 19b. In this example, weathered dacite occurs at the upper levels, underlain by fresh and intact dacite, and a fault dipping in the same direction as the slope is present at the rear. In addition, a weak chloritic zone intersecting the fault exists at the base. The shear strength parameters of these units and weakness planes are characterized by the relations:$c_1 >> c_2 \approx c_3$ and $\phi_1 >> \phi_2 \approx \phi_3$.When only the weathered daciteis considered, the slope, behaving like a soil mass, may exhibit a circular-type failure within this material. However, it is also possible that the rear fault connects with the weak chloritic zone dipping toward the excavation, forming a multi-surface sliding mechanism. This is because the shear strength of both weakness zones is lower than that of the weathered dacite.In such a case, it would be appropriate to analyse both possible instability types separately and to decide based on the analysis results which failure mechanism is the most critical. The stabilization measures should then be designed accordingly.

(a) (b)

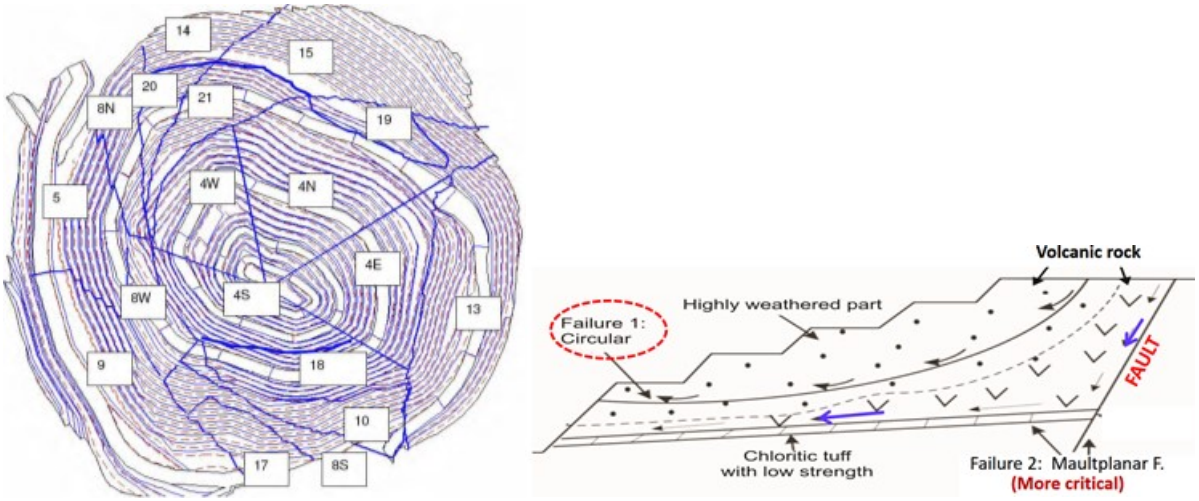


Fig. 19 (a) Geotechnical design domains in relation to the final pit shell of the Cadia Hill Open Pit (Pothitos and Webster (2006), after Franz (2009)), (b) a hypothetical cross-section forming the basis of a geotechnical model for an open-pit slope drawn by the author.

4 Influence of in-situ stresses on deep open pits

In-situ stress is the stress prior to any excavation, results from the weight of the overburden and tectonic stresses in the region, and all rocks are subjected to in-situ stresses. Open pit excavations cause changes in the existing stress field due to stress relief, and these changes can have significant

consequences for the behaviour of rock masses. In rock slopes, while pit walls generally become distressed close to the slope face, stress concentrations develop at the toe of the slope. In general, the following assumptions are made for open pit slopes: (a) the slope-forming rock mass is influenced only by gravity-induced stresses, and (b) these stresses are not large enough to exceed the strength of the rock mass and cause failure (Read and Stacey 2009).Therefore, it is thought that in-situ stresses are small and not measured. In addition, all analysis methods of limit equilibrium are based on gravitational loading and lateral stresses are not included in the analyses. Although neglecting pre-mining in-situ stresses may be acceptable for shallow open pits, it has been shown to be invalid for deep open pits in hard rocks. But the main difference between shallow and deep open-pit slopes is that rock mass damage due to in-situ stresses develops much more extensively in deep open pits. As excavation proceeds, stress redistribution occurs and the rock mass is subjected to successive stress variations. Therefore, in increasingly deepening open pits, measurement of in-situ stresses became important, particularly where the stresses at the bottom of the pit are likely higher than the strength of the rock.

The Palabora mine, where open pit operations began in 1966, is an example of a slope failure resulted from change in stress conditions (Fig. 20a). The development of block cave operation was decided in 1996. While the slopes of this open pit mine has been completely stable during the open pit mining to a depth of 800 m, a large failure with dimensions of 800 m high and by 300 m long behind the NW wall of the pit occurred during the transitioning of the open pit to underground mine (Fig. 20b). The caving caused a change in the stress environment which resulted in development of a major failure. Based on the study by Moss et al. (2006), there has been interaction between the open pit and the cave, initially the impact of the open pit on the cave was to concentrate stress within the ground between pit floor and cave, and increase stress level resulted in cave propagation by causing existing fractures to extend and formation of new fractures.

(a) (b)

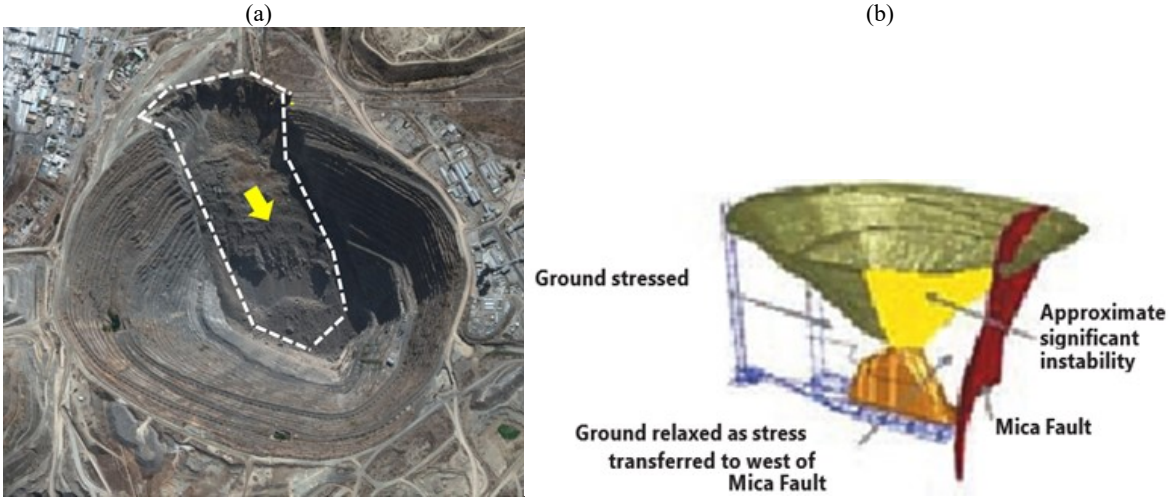


Fig. 20 (a) Quickbird image of the NW wall failure at Palabora mine, S. Africa (Woo et al. 2012), (b) zone of slope instability in this pit (Moss et al. 2006)developed during the transitioning from open pit to underground mass mining.

In very deep and ultra-deep open pits, the stress state around the excavation becomes increasingly complex, with zones of both very high and very low stresses occurring within the rock mass. Measurement of vertical stress is generally estimated by the equation "$\sigma_v = \gamma z$" where γ is the unit weight of the rock, and z is the depth from the surface. Measurements of vertical stresstaken from mining and civil engineering projects around the world generally confirm the validity of this equation (Hoek et al. 2009). however, as shown in Fig. 21a, significant scatter is observed in these measurements. Determination of horizontal stresses ($\sigma_h = k\sigma_v$; k is the ratio of the average horizontal stress to the vertical stress) is much more difficult than that of vertical stress. Measurements from different parts of the world have shown that the coefficient k tends to be high at shallow depths and generally increases with depth (Hoek and Brown, 1980a, b). Sheorey (1994) proposed an elasto-static thermal stress model for estimating k values globally, as given in Eq.1 which is used only as a preliminary approximation. Sheorey's model is a simplified one, and it should be noted that the tectonic history of a site plays a significant role in determining in-situ stress conditions.

$$k = 0.25 + 7E_h\,(0.001 + (1/z)) \qquad (1)$$

Where z depth (m)
E_h average deformation modulus of the upper crust (GPa)

Stress changes induced by successive excavation stages can lead to tensile failure of the rock, rock mass damage, and crack development, all of which negatively affect the strength of the rock. Results of simple numerical analyses performed for a deep (500 m), 40° homogeneous rock slope with two different σ_h/σ_v ratios (0.5 and 1.0) (Fig. 21b) have shown that, as the stress magnitude increases, fracture development parallel to the pit boundary also increases, and these fractures occur within the rock material between natural discontinuities.

Seismic data confirms that the deeper a slope is, the more stressed and therefore the more it fractures. Today, in very deep open pits, where high stresses are present, micro-seismic activity monitoring is used to evaluate the damage processes affecting pit slopes. Excavation-induced fracturing and crack propagation in the rock mass generate high-frequency seismic waves, which can be recorded by accelerometers and geophones. The micro-seismic monitoring performed by Lynch and Malovichko (2006) at Navachab gold mine in Namibia during period of unloading and resultant high micro seismic events to monitor a possibly problematic shear zone lying roughly sub-parallel to the slope showed that fracturing and most of the events occurred beneath the level of the pit floor (Fig. 21c). This combined with any absence of surface movements, indicates relative stability of the shear zone.

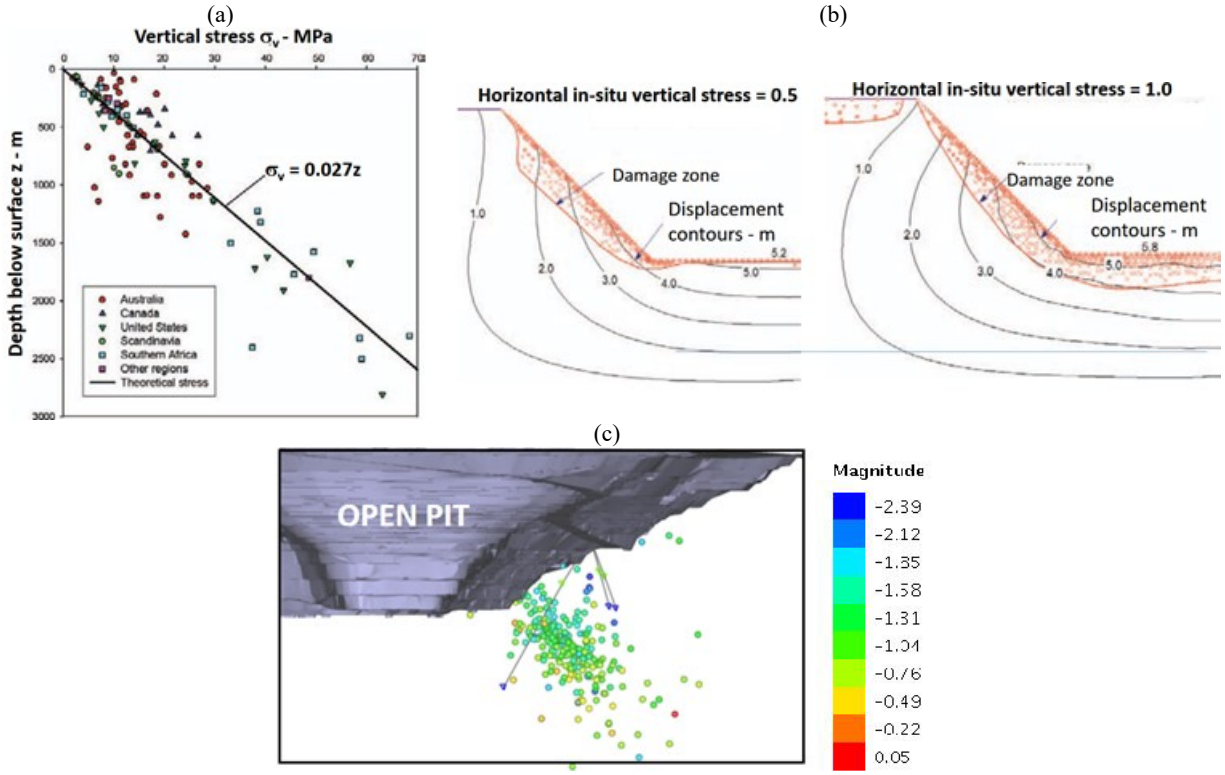


Fig. 21 (a) Measured vertical stresses from various parts of the world (Hoek and Brown 1980b), (b) predicted damage zones and displacements for slopes with *k* values of 0.5 and 1.0, respectively, in a 500 m deep and 45° homogeneous rock slope (Hoek et al. 2009), (c) seismic activity induced by overburden removal at an open pit (Lynch and Malovichko 2006).

The main direct methods for measurement of in-situ stresses are overcoring, hydraulic fracturing and, flatjack techniques, drillhole deformation gauge and CSIRO-type cell. Detailed descriptions of these tests are given in ISRM Suggested Methods (ISRM 2007) and also in Amadei and Stephansson (1997). In addition, the use of Acoustic Emission (AE) test to monitor when core is loaded to the point where new damage occurs (Villeascusa et al. 2002) increased in 2000s.It is also noted that numerical modelling has become the preferred tool for rock mechanics analysis in almost it's all fields of application today. These techniques, both 2D and 3D, also found an area of application for the assessment of stress effect on open pit slopes (e.g. Lorig 1999, Stacey et al. 2003, Sjöberg 2013). Hoek et al. (2009) discussed that the uncertainty of other parameters, such as geology, rock mass strength and groundwater conditions, has a larger influence on slope behaviour than variations in stress. However, these investigators recommend that careful consideration is required for cases with high horizontal stresses, where underground excavations are located close to a pit and for deep open pits. But based on the literature, due to the very limited number of in-situ stress measurements in open pit mines (e.g. Obara et al. 2000, Wang et al. 2025) validation studies are considerably limited, and therefore, in-situ stress measurements for deep open pits should be conducted and will be useful for the safety of these mines and for validation studies.

5 Influence of earthquakes on deep open pits

Earthquakes cause stress changes in slopes. Combination of static stresses with the dynamic stresses resulted from earthquakes may exceed available strength along a potential sliding surface and cause failures in the form of slides and rockfalls. Read and Stacey (2009) mentioned that there are no recorded cases of large scale earthquake-induced open pit slope failures which disrupted mining operations. However, more recently there have been some earthquake-induced damages were reported in open pitsin China (2008, M7.9), Chile (2010 M8.8; 2015, M8.3) and Papua New Guinea (2018, M7.5) and, except some mining infrastructure damage in the first three earthquakes and natural slope failures in the last one, none of those were significant to be recorded as causing injuries, pit slope failures and interruptions in production (Estrada and Weir 2023a). In addition, there are anecdotal reports, not officially published, of earthquake-induced open pit slope failures (Estrada and Weir 2023b; Ross 2017) in Chuquicamata Mine (Chile) prompting the adoption of advance monitoring and mitigation measure and Bingham Canyon Mine (USA) where ground movement and slope instabilities occurred and caused seismic activity. Based on te study by Azhari and Özbay (2017), who developed a database for investigating the circumstances under which dynamic loading if earthquakes cause slope failures in deep open pit mines with a long lifetime, it was concluded that open pit mines may strill experience reportable if struck by earthquakes with local depth of less than 40 km, epicentral distance less than 100 km and magnitude gretar than 6.0. In addition, their results also showed that even though the valley shape geometry and absence of top weathered layer make open pit mines less prone to earthquake-induced failures, excessive pressure in the pit slopes still carries risk of earthquake-triggered failures in open pit slopes. Factors affecting pit slope performance under earthquake loads and their consequences are summarized in Table 1.

Table 1 Factors affecting pit slope performance under earthquake load (arranged from Estrada and Weir (2023b)

Factor	Impact on slope	Consequence
Topography	Topographical amplification increased in topographical amplification at the surface and particularly slope crest and man-made topographical alterations (i.e. deep/large pits) amplifies ground motion at the crest.	Amplifies ground motion and may be detrimental if mine infrastructure is located close or at pit crest.
Slope geometry	Slope geometry (concave or convex) has a significant impact on amplifying the ground shaking of slope ridges. For improving seismic performance, natural terrain curvature of open pit is modified.	Pit slope geometry may scatter seismic waves reducing the impact of the earthquake shaking.
Rock material & mass properties	Pit slopes with contrasting lithologies or weathered material may experience increase earthquake shaking at be more risk of instability.	Slopes with stiffness contrast or inweak rock may subject to amplification
Water	Pore pressure may increase the probability of failure on a pre-existed failure surface. Dewatering in mining makes open pits less prone to failure.	Water management (pore pressure and surface water control, dewatering) may make the pits less prone to failures.
Open pit design	Typically open pit slopes are designed with a FOS ≥1.2 which may accommodate some level of earthquake loading.	FOS for static design may ccommodate some level of shaking

Based on the results from some generic analyses carried out by Toh (2010), the peak ground acceleration (PGA) at the pit crest could be amplified up to 17% from the “flat ground” PGA, with greater amplifications (over 35%) of spectral accelerations at other periods greater than zero seconds. Fig. 22 shows an example of accelerations within a 300 m high slope, where accelerations within a slip surface extending from crest to ¼ slope depth relatively constant, but average acceleration within a slip surface over the entire slope height is much lower than the maximum acceleration at the crest.

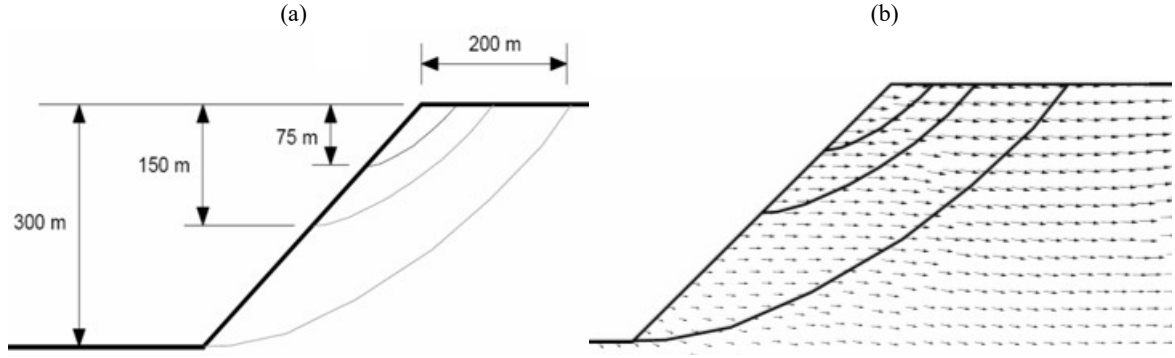


Fig. 22 (a) Potential slip surfaces for which topographical and scale effects were investigated, (b) acceleration magnitude vectors at the instant of maximum crest acceleration (Toh 2010).

In practice, in addition to pseudo-static approach (Seed 1979), numerical dynamic calculations are employed for slope stability evaluation of open pits by using different softwares such as Plaxis, ANSYS, Slope/W, UDEC, 3DEC, and Newmark's deformational method (Newmark 1965).The pseudo-static approach is the most commonly used method for open-pit slopes and provides the factor of safety (FOS) as an indication of whether a slope may fail during an earthquake. But it involves some limitations and assumptions, which are not discussed in this paper. For example, in this approach, the applied horizontal force (as a proportion of gravitational force) is assumed to be constant throughout entire slip mass, both with depth and laterally. Toh (2010) mentions that this assumption could not be considered appropriate for ovearall slopes of open pits, particularly deep/large open pit slopes, and maximum average accelaration that is experienced by a mine slope will be different from the PGA. Although more inputs, such as earthquake ground motion characteristics and dynamic material properties, are necessary for dynamic analysis, they can overcome the limitations of the limit equilibrium analysis for deep/large hard rock slopes. However, Toh et al. (2013) emphasize that many inputs used for dynamic analysis are not well understood for deep hard rock slopes. It is well known that amplification caused by earthquakes at the cliff sides due to topographical effects and lateral movements play an important role on damages to mining facilities and other structures located very close to the slope crest, particularly on those of the constructed on soil like materials and soft and weak rocks. Aydan (2015) recommends that probably, slope angle reduction would be the most desirable measure, and the fundamental concept should be such that the overall stability of the slope must be attained by the self-resistance of ground (Fig. 23a). When there are some occasions, that is, it is impossible to reduce slope angle due to slope-cut height and the construction next to slopes is allowed, there should be a safety zone between the slope crest and allowable construction boundary as illustrated in Fig. 23b.

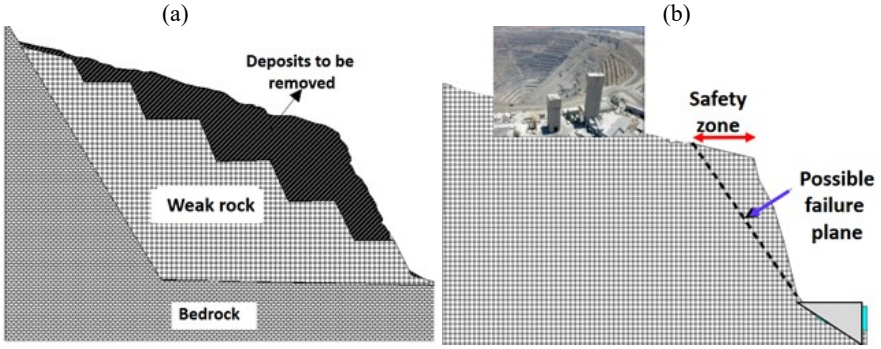


Fig. 23 (a) Slope angle reduction, (b) implementation of safety zone concept for the minşig facilities close to the slope crest (slightly modified from Aydan 2015)

There is limited available information and details of mine damages or slope failures during earthquakes. Mining operations in a few countries located at highly active seismic regions, such as Chile, Peru and Mexico, where deep/large open pit mines also exist, open pit mines are required to be designed with appropriate earthquake loads that depend on their site specific seismic hazard assessments. The necessity of accounting for seismic loading in slope stability analysis, particularly for those of deep/large open pit mines located in earthquake prone regions, increases. In other words, it would be beneficial to place greater emphasis on considering earthquake effects and the use of relevant analysis methods in the design of rock engineering structures, including deep/large open-pit mines.

6 Importance of monitoring for deep open pit slopes

Slope stability analyses and stabilization techniques are highly sensitive to data obtained from laboratory tests, the geometry of the sliding mass and failure surface, and time-dependent changes in the mechanical properties of both the discontinuities and the rock masses. Moreover, determining the ultimate stability of very deep open-pit slopes, especially during the design stage, is quite difficult using the currently available investigation data and analytical techniques. To eliminate or at least minimize the uncertainties arising from these factors, conducting intensive monitoring programs for all open pits has become an essential for management of safety and production consequences of slope failures. With increasing depths, the problems associated with rock deformation, their intensity and frequency also increased and slope failures became as one of the major concern for planning deep open pits. With the advent of many deep opencast mines, slope monitoring systems has become a vital component in planning deeper mines and to aid in mitigating hazards due to pit slope failures.

The main objectives of slope movement monitoring are:(a) ensuring safe operational conditions for personnel and equipment, (b) identifying potentially unstable zones and minimizing slope displacements, (c) determining the mechanisms of developing instabilities and providing data for remedial measures, and(d) assessing the performance of the implemented slope design. Considering that open-pit mines are becoming progressively deeper, it is now common practice to employ *multiple monitoring methods* simultaneously. The movement monitoring techniques used in open-pit slopes can be grouped into three categories: (a) *conventional method* (visual inspection-used as a means of monitoring slopes which are characterized by lower level of danger), (b) *real-time surface-based methods* which detects visible signs of instability and quantifies surface level deformations and displacements, and (c) *subsurface methods*which measures deep within the slope forming materials of the pit. Conventional techniques include visual inspection and mapping of tension crack along the slope face. Mapping and monitoring of tension cracks formed along the slopes is a traditional and a reliable tool for identification of major failures.

6.1 Surface monitoring methods

Because open-pit mining involves a dynamic excavation process and continuous slope advancement, *real-time surface-based monitoring methods*, which are also called *Advanced Monitoring Techniques*, are generally preferred. Among these, the two most commonly used techniques are slope stability radar and robotic total station. The *slope stability radar* (SSR) allows real-time monitoring of slope movements with sub-millimetre accuracy and is independent of atmospheric conditions. It continuously scans the slope face to detect surface deformations (Fig. 24a)from a stationary platform without the need for reflectors or prisms. The system scans a region of the slope and divides the area of interest into pixels. The amount of movement is measured for each pixel and compared with the amount of movement from the previous scan. When the alarm thresholds defined by the user are exceeded, the radar automatically sends e-mail or text alerts to responsible personnel. However, since the system cannot provide three-dimensional data, it does not give information on the direction or geometry of the movement and is therefore often used in combination with 3D geodetic monitoring systems, such as robotic total station.Fukuzono (1985) found that the time accelerating creep failure under gravity loading was inversely proportional to the deformation velocity. Time-of-failure (TOF) can be estimated from the inverse velocity versus time plot by extrapolating the trend to the x-axis. Rose and Hungr (2007) successfully applied this method for predicting time of slope failure in three hard-rock open pit mines. Fig. 24b shows an example about inverse velocity graph. SSR may also be for checking the performance of remedial measures against slope movement. As seen from the example given in Fig. 24c, horizontal drains were installed on the slope monitored by SSR. The upper radar imageshows slope movement (red area) due to water pressure in the slope, while the lower image represents the situation after the drains were installed indicating that movement stopped. Fig. 24d shows a typical SSR image.

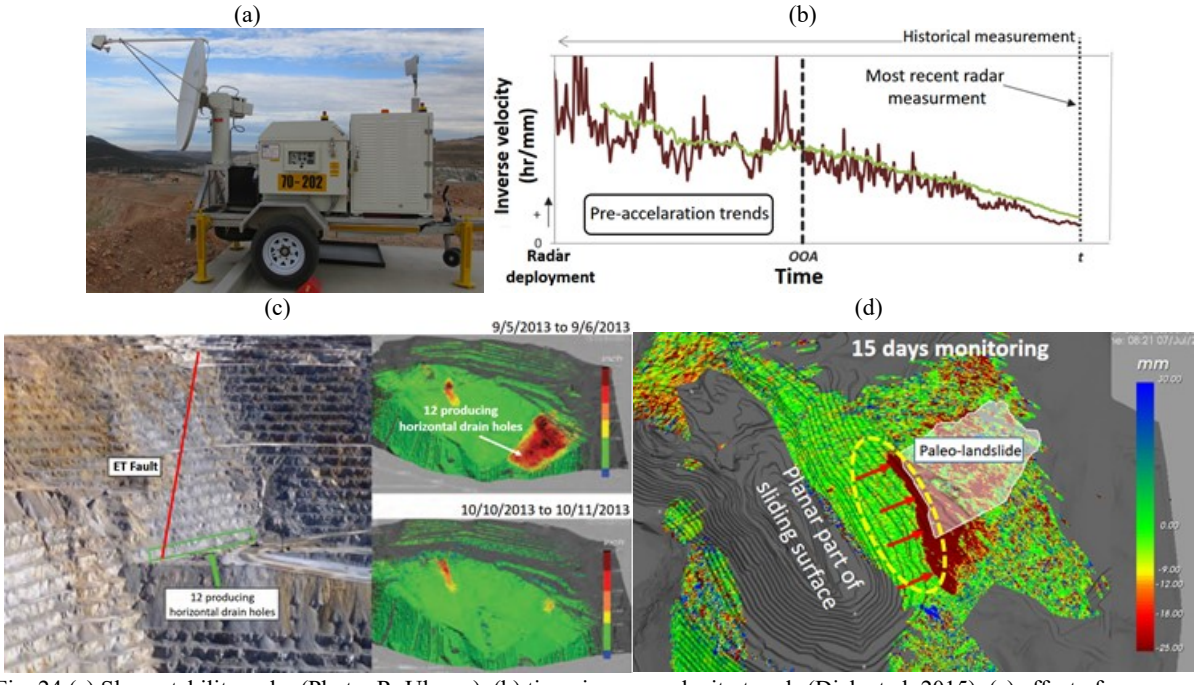


Fig. 24 (a) Slope stability radar (Photo: R. Ulusay), (b) time–inverse-velocity trends (Dick et al. 2015). (c) effect of horizontal drain holes monitored by SSR at an open pit mine (Beale 2018), (d) an SSR image from a coal open pit in Türkiye (Ulusay and Çağlan 2022)

The *robotic total station* (RTS) (Fig. 25a) measures displacements at prisms installed on various parts of the pit slopes, allowing the calculation of three-dimensional displacement, velocity, and direction of movement (Fig. 25b). Warning levels set in the system are transmitted to the mine engineers, enabling real-time assessment of slope conditions and providing an early warning function. RTS provided with GNSS receivers are increasingly being used for automated, accurate, efficient and cost effective survey for monitoring slope in deep and large open pits (Brown et al. 2007). The total station can be fixed at point for continuous monitoring of the slope at the preset interval timings or it can be shifted from one point to other point manually for monitoring the fixed prisms movement.

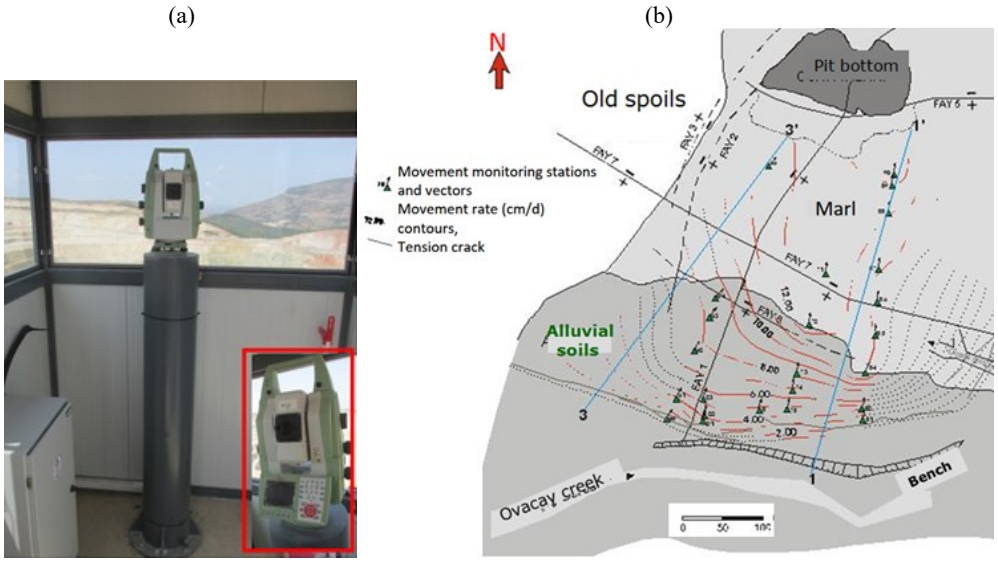


Fig. 25 (a) Robotic total station (RTS) (Photo: R. Ulusay), (b) a pit plan showing movement vectors (black arrows) based on monitoring data from TS, movement rate and tenison cracks at a lignte open pit in Türkiye (Tuncay and Ulusay 2001)

Non - Reflective LiDAR (**Li**ght **D**etection **A**nd **R**anging) *Scanning* utilizes a beam of laser lights, targeted towards the area of monitoring which returns the pictorial / digital representation of the critical area of the slope and their relative movements using the travel time of the reflected radiations (Abellan et al. 2014). They provide virtual copies of slope in minutes, like photographic images highlighting critical areas. Laser scanners are active self-contained measurement technology that generates its own light for measurement process. Though, the application of laser scanners is well proved in monitoring landslides, the method has found lesser application in monitoring open pit slopes. The application of LiDAR on mine surveying is simple, high economic benefit with rapid time saving thus providing successful slope monitoring, but restricted to weather conditions and terrain humidity, and recently automated LiDAR systems with precision as high as 1-5 mm have become available (Eberhardt et al. 2020).

Satellite radar, also known as *InSAR* (**In**terferometric **S**ynthetic **A**perture **R**adar), is a technology widely used in mining for geotechnical monitoring, applied to open-pits, waste dumps, dams, industrial slopes, and underground mines (subsidence). This method detects slow deformations, covering over a large area. With this, InSAR enables strategic monitoring, with the detection of deformationprocesses in their premature state. Datasets provide 1-2 mm resolution coverage of ground movement for most of the earth and the method has large-area application and no ground instruments or site work is needed and can detect movements where risk was not previously suspected. As the limitations of this method; its measurement frequency is limited by satellite passing from 2 to 12 days and it serves as a supplement to, rather than a replacement for, local monitoring methods such as prisms and SSR.

Digital photogrammetry is a simple remote sensing technique to monitor slope movements. Its objective is to identify wide displacement behavior of a target inferred by the comparison of photographed images using digital camera. Using such digital photographs, it is also possible to estimate the geometric properties of the objects such as shape and position, the progress, extent and cause of slope deformation (Ohnishi et al. 2006). Recent developments in the method have provisions for the generation of 3D models from the terrestrial photographs and the method is extensively applied for monitoring large scale structures with a greater accuracy. The method provides to survey the inaccessible areas and highrock faces in rapid time providing remote characterization tool for rock slope practitioners.

As a remote sensing method, *Infrared Thermography* (IRT), is used to detect areas of instability in open-pit slopes by analyzingthermal radiation patterns.IRT measures the infrared radiation emitted by surfaces, allowing for the generationof heat maps that visualize temperature variations which often manifest as negative temperature anomalies, can serve as indicators ofprecursory slope failure. One of the main limitations of this method is signal attenuation due to atmospheric conditions, which can causesignal degradation over long measurement ranges (Le Roux et al. 2025).

6.2 Sub-surface monitoring methods

Due to their ability to measure localized angular deformation and detect subsurface displacements, *borehole inclinometers* are widely used for slope stability monitoring to collect information on the locations of deep-seated failure surfaces. This equipment uses sensors and probes to detect differential movements in real time with sub-millimeter accuracy. In open pit slope monitoring, the probe inclinometer is the most commonly used type of inclinometer in which the probe travels along guide grooves in a plastic tube grouted to the drill hole. As a more recently developed monitoring device, *Time Domain Reflectometer* (TDR) is also used for the same purpose of inclinometer and detects the location of shearing across a grouted borehole, but not the magnitude of deformation. TDR uses the working principle of transmission lines to detect localized strain and deformation by measuring the reflection of electromagnetic pulses sent along a coaxial or fiber optic cable embedded within a borehole in a slope (Le Roux et al. 2025). The method provides high resolution and real time slope stability monitoring. TDR cables are gaining popularity due to its advantages over inclinometers, such as less installation costs, deeper hole depths, rapidly and remote monitoring and possibility of immediate deformation and complex installation.

Evident indicators of slope failure, such as tension cracks, can be monitored using *wireline extensometers*, which measure the dilation of cracks by detecting changes in displacement of a wire anchored to the unstable part of ground. Changes in the length of the wire are measured manually, however, development of modern sensors, such as vibrating wire displacement transducers, has digitized this process, allowing for remote and continuous slope monitoring (Osasan and Afeni 2010).

The groundwater monitoring for open pits is conducted using boreholes and piezometers which measure the total groundwater head at any given location. Types of the piezometers are standpipe piezometers, horizontal piezometers andvibrating wire piezometers (VWP) (single or multi-level). Most commonly used piezometers in open pit mines are standpipe piezometer and VWP. Widespread adoption and standard use of VWPs for monitoring pore pressure in open pit mine slopes and deep groundwater management gained momentum in the 1990s and accelerated rapidly in the early 2000s.

In modern deep and ultra-deep open pit operations, *integrated use of different monitoring systems*has proven effective in reducing risk levels and numbers of fatalities. Two typical examples on this issueare given from the Bingham Canyon Copper Mine (Utah, USA), which has recently reached a depth of approximately 1.4 km. The first major failure, called Manefay Slide that occurred on April 10, 2013 (see Fig. 8), was identified by a multi-sensor monitoring (ground-based system) network consisting of GPS, SSR, RTS, InSAR, LiDAR and wirelineextensometers without no injuries or fatalities. Only some equipment damage was reported, as the run-out distance of the sliding material had been slightly underestimated (Williams et al. 2021). The consensus is that its failure mechanism is a complex failure being along the faulted and clay-filled Manefay beds(Ross 2017). Similarly, another failure, called Leo Failure, occurred onMay 312021 and affected 457 m high southeast portion of the same open pit. This failure, movement was also detected by multiple slope monitoring methods including SSR, RTS, GPS, thermal camera and InSAR, and there were again no injuries or losseswith the aid of slope monitoring studies (Ergun et al. 2023).

7 Conclusions

Evaluation of rock slope stability requires the combined use of a geotechnical model, which includes rock type, discontinuities, weathering characteristics, hydrogeological conditions, material behaviour, and rock engineering methods**.**

At present, knowledge of instability mechanisms in deep and large rock slopes excavated in hard, brittle, and jointed rock masses remains limited. As open pits continue to deepen and complex instability mechanisms involving combined failure surfaces become more common, the current trend is to combine conventional and numerical analysis methods with advanced monitoring techniques**,** while also making use of back-analysis results from pit slopes that have already experienced

instability. In particular, compiling the strength parameters of rock masses derived from completed and future back-analyses of deep and large-scale slope failures into a database would be valuable for assessing deepening slopes that have not yet failed.

Rock masses are rarely homogeneous and isotropic and modes of failure are not always circular or semi-circular. Therefore, all potential modes of failure should be identified to be able to estimate the most suitable rock mass strength parameters and to pursue the most appropriate method of stability analysis.In open pit slope stability investigations, particularly for deepening large open pits, prime attentions should be paid to the evaluation of slope damage.

The integration of different slope stability analysis techniques could represent a major advancement. Within this framework, the development of more powerful numerical programs capable of realistically modellingcombined failures along discontinuities and through intact rocks. Further research is also needed to improve the characterisation,modelling and strength estimation of bimrocksin slopes.

In terms of earthquakes, attention to seismic-induced rock slope instabilities remains limited. Therefore, it would be beneficial to focus more on earthquake inducedslope failures and to incorporate dynamic effects into slope stability analyses.Attention should also be paid the amplification effect due to earthquakes on mine facilities located very close to the crest of the open pit slopes.

Particularly in modern deep and ultra-deep open pit operations, it should be remembered that integrated use of different monitoringsystemsis more effective in reducing risk levels and numbers of fatalities. In addition, Artificial Intelligence (AI) and machine learning can analyse large datasets, identifying early warning signs of instability.

Acknowledgements

The author would like to express his sincere gratitude to Esteban Hormazabal (Chile), Suseno Kramadibrata (Indonesia), Rui Kong (China), Gökhan Furtana (Türkiye), and Serdar Ergün (USA) for providing additional information on the current overall slope angles and heights of some open-pit mines.

References

Abellan A, Oppikofer T, Jaboyedoff M, Rosser NJ, Lim M, Lato MJ (2014). Terrestrial laser scanning of rock slope instabilities. Earth Surface Processes and Landforms 39: 80-97, doi.org/10.1002/esp.3493 .

Admassu Y, Shakoor A, Wells NA (2012) Evaluating selected factors affecting the depth of undercutting in rocks subject to differential weathering. Engineering Geology 124: 1-11, doi.org/10.1016/j.enggeo.2011.09.007.

Amadei B, Stephansson O (1997). Rock Stress and its Measurement. Chapman & Hall, London.

Ambah E, Elmo D, Zhang Y (2025) Fracture undulation modelling in discontinuum analysis: Implications for rock- mass strength assessment. Geoetchnics 5: 1-19, doi.org/10.3390/geotechnics5030058.

Arshadnejad S, Nick N (2016) Empirical models to evaluate of ‘‘m_i’’ as an intact rock constant in the Hoek–Brown rock failure criterion. Proceedings of 19th Southeast Asian Geotechnical Conference & 2nd AGSSEA Conference (19SEAGC & 2AGSSEA) Kuala Lumpur, 943–948.

Aydan Ö (2015) Lessons from the recent great earthquakes on the performance of buildings under different geotechnical environments. In: 2nd International Sustainable Buildings Symposium, Ankara, Türkiye (Keynote).

Aydan Ö, Tokashiki N, Geniş M (2012) Some considerations on yield (failure) criteria in rock mechanics. In: Proceedings of 46thUS Rock Mechanics / Geomechanics Symposium (ARMA Symposium), Chicago IL, USA; Paper No. 12-640.

Azhari A, Ozbay U (2017) Investigating the effect of earthquakes on open pit mine slopes. International Journal of Rock Mechanics and Mining Sciences 100: 218-228, doi.org/10.1016/j.ijrmms.2017.10.005.

Baczynski NRP (2000) STEPSIM4 Step-path method for slope risks. GeoEng 2000, Proceedings of the International Conference on Geotechnical and Geological Engineering, Melbourne, Australia, 1-6.

Barton N (1976) The shear strength of rock and rock joints. International Journal of Rock Mechanics and Mining Sciences 13: 255-279, doi.org/10.1016/0148-9062(76)90003-6.

Barton N (2023) GSI or JRC –continuum or discontinuum modelling–some suggestionsand some critique. 15thISRM Congress 2023& 72nd Geomechanics Colloquium. W. Schubert and A. Kluckner (eds.).

Barton N (2025) Reflections on an unrealistic continuum branch of rock mechanics – discontinuous behavior comparisons. Nick Barton and Associates Rock Engineering, Norway, 30 p.

Beale G (2013) Water and slope stability – the application of a new science. Slope Stability 2013, PM Dight (ed.), Australian Centre for Geomechanics, Perth, Brisbane, Australia, 43-55.

Beale G (2018) The role of water in slope design for weak rocks. In: Guidelines for Open Pit Slope Design in Weak Rocks- Part 4, G. Beale and J. Read (eds.), CSIRO, Australia,

Beale G, Milmo P, Raynor M, Price M, Donze F (2013) Preparing conceptual hydrogeological model - Part 3. In: Guidelines for Evaluating Water in Slope Stability, G. Beale and J. Read (eds.), 153-213.

Bieniawski ZT (1989) Engineering Rock Mass Classifications. John Wiley and Sons, New York.

Brown ET (2008) Estimating the mechanical properties of rock masses. SHIRMS 2008 – Y. Potvin, J. Carter, A. Dyskin, R. Jeffrey (eds.), Australian Centre for Geomechanics, Perth, Australia, 3-21.

Brown N. Kaloustian S, Roeckle M (2007). Monitoring of open pit mines using GNSS satellite receivers and robotic total stations. Slope Stability 2007, Y. Potvin (ed.), Australian Centre for Geomechanics, Perth, Australia, 417-429.

Cai M, Kaiser PK, Uno H, Tasaka Y, Minami M (2004) Estimation of rock mass strength and deformation modulus of jointed hard rock masses using the GSI system. International Journal of Riock Mechanics and Mining Sciences 41:3–19, doi:10.1016/S1365-1609(03)00025-X.

Cambio D, Hicks DD, Moffitt K, Yetisir M, Carvalho JL (2019) Back-analysis of the Bingham Canyon South Wall: A quasi-static complex slope movement mechanism. Rock Mechanics and Rock Engineering 52: 4953-4977, doi.org/10.1007/s00603-019-01958-7.

Coli N, Berry P, Boldini D (2011) In situ non-conventional shear tests for the mechanical characterization of a bimrock. International Journal of Rock Mechanics and Mining Sciences 48: 95-102, doi: 10.1016/j.ijrmms.2010.09.012.

Contreras LF, Hormazabal E, Ledezma R, Arellano M (2019) Geotechnical risk analysis for the closure alternatives of the Chuquicamata open pit. In: Mining Geomechanical Risk 2019, J Wesseloo (ed.), Australian Centre for Geomechanics, Perth, 373-388.

Cylwik SD, Killian JR, Cicchini PF (2022) A practical strength criterion for rock masses based on quantitative input parameters. Proceedings of Slope Stability 2022, Tucson, USA.

Davarpanah SM, Sharghi M, Vasarhelyi B, Török A (2022) Characterization of Hoek–Brown constant $m_i$of quasi-isotropic intact rock using rigidity index approach. ActaGeotechnica 17: 877–902,doi.org/10.1007/s11440-021-01229-2.

de Vilder SJ, Rosser NJ, Brain MJ (2017) Forensic analysis of rockfall scars', Geomorphology, 295: 202–214, doi.org/10.1016/j.geomorph.2017.07.005

Dershowitz WS, Finnila A, Rogers S, Hamdi P (2017). Step path rock Bridge percentage for analysis of slope stability. Proceedings of Symposium of American Rock Mechanics Association, Paper-17-1045, 1-9.

Dick GJ, Eberhardt E, Cabrejo-Liévano AG, Stead D, Nick D. Rose ND (2015) Development of an early-warning time-of-failure analysis methodology for open-pit mine slopes utilizing ground-based slope stability radar monitoring data. Canadian Geotechnical Journal. 52: 515–529, doi.org/10.1139/cgj-2014-0028.

Donati D (2019) The characterization of slope damage using an integrated remote sensing-numerical modelling approach. PhD Thesis, Simon Fraser University, Burnaby, Canada.

Donati D, Stead D, Elmo D, Onsel E (2020) New techniques for characterizing damage in rock slopes: implications for engineered slopes and open pit mines. Slope Stability 2020, PM Dight (ed.), Australian Centre for Geomechanics, Perth, Australia, 129-144.

Duran A (2016) Rock mass assessment - what goes wrong? APSSIM 2016 – PM Dight (ed.), Australian Centre for Geomechanics, Perth, Brisbane, Australia, 493-596.

Eberhardt E. Stead D, Coggan JS (2004) Numerical analysis of initiation and progressive failure in natural rock slopes-the 1991 Randa rockslide, International Journal of Rock Mechanics and Mining Sciences 41: 69–87, doi.org/10.1016/S1365-1609(03)00076-5.

Eberhardt E, Ness M, Noon D, Schwarz E, Stacey P (2020) Overview of slope monitoring. In: Guidelines for Slope Performance Monitoring, Chapter 2, R. Sharon and E. Eberhardt (eds.) CSRIO Publishing and CRC Press, 7-16.

Elmo D, Yan M, Stead D, Rogers SF (2007) The importance of intact rock bridges in the stability of high rock slopes -Towards a quantitative investigation using an integrated numerical modelling; Discrete fracture network approach. Slope Stability 2007. Y. Potvin (ed), Australian Centre for Geomechanics, Perth, Australia, 253-266.

Elmo D, Stead D, Eberhardt E, Vyazmensky A (2013). Applications of finite/discrete element modelling to rock engineering problems. International Journal of Geomechanics 13(5): 565-580, doi: 0.1061/(ASCE)GM.1943-5622.0000238.

Elmo D, Stead D, Rogers S. (2015). Guidelines for the quantitative description of discontinuities for use in Discrete Fracture Network Engineering. Proc. of the 13th ISRM Congress. Montreal, Canada. Paper 587.

Elmo D, Donati D, Stead D (2018)Challenges in the characterization of intact rock bridges in rock slopes. Engineering Geology 245:81–96, doi.org/10.1016/j.enggeo.2018.06.014.

Elmo D, Stead D, Yang B, Marcato G, Borgatti L (2022) A New Approach to characterize the impact of rock bridges in stability analysis. Rock Mechanics and Rock Engineering 55: 2551–2569, doi.org/10.1007/s00603-021-02488-x.

Ergun S (2026) Bingham Canyon Mine, Utah, USA – An example of large scale open pit. Engineering and Mining Journal April 2026 issue: 32-37.

Ergun S, Cambio D, Williams CP, Gaida, M, Lawrence K, Katsaga T, Lorig, L, Weigel J, Gibbs J, Chapin G, Peik B, Sankhaneel S (2023) Back-analysis of the Bingham Canyon Mine southeast wall: a complex slope failure mechanism called Leo. PM Dight (ed.), SSIM 2023: Third International Slope Stability in Mining Conference, Australian Centre for Geomechanics, Perth, pp. 559-576, doi.org/10.36487/ACGrepo/2335_37.

Estrada BE, Weir FM (2023a) Open pits, earthquake damage and seismic design: an overview. SSIM 2023, PM Dight (ed.), Australian Centre for Geomechanics, Perth, Australia, 675-684.

Estrada BE, Weir FM (2023b) Should earthquake loading be considered for open pit slope design in Australia? AUSIMM Bulletin, October 2023 issue, https://www.ausimm.com/bulletin/bulletin-articles-all/.15 January 2026.

Fisher BR, Eberhardt E (2007) Numerical modeling and shear strength estimates of bi-planar dip slope failures. Proceedings of the 11th Congress of the International Society for Rock Mechanics, Lisbon, R. Sousa, Olalla, N. Grossmann (eds.), Vol. 1, Taylor & Francis, London, 629-632.

Franz J (2009)An investigation of combined failure mechanisms in large scale open pit slopes. PhD Thesis, University of New South Wales, Sydney, Australia.

Fukuzono T (1985) A new method for predicting the failure time of a slope. In: Proceedings of the 4th International Conference and Field Workshop on Landslides, Tokyo, Japan. Japan Landslide Society, pp. 145–150.

Furtana G, Özkan E, Sak A (2023) Open pit slope depressurization using horizontal drains at Kışladağ gold mine, Turkey: a case study. 28th International Mining Congress and Exhibition of Türkiye (IMCET), Antalya, Türkiye (on CD).

Galera JM, Montero J, Perez C, Montego L., Varona P (2009) Coupled hydromechanical analysis of Cobre Las Cruces open pit. Proceedings of International Symposium on Rock Slope Stability in Open Pit Mining and Civil Engineering (Slope Stability 2009), Santiago, Chile, on CD-rom.

Hencher SR, Lee SG, Carter TG, Richards LR (2011) Sheeting joints: Characterization, shear strength and engineering. Rock Mechanics and Rock Engineering 44: 1–22, doi.10.1007/s00603-010-0100-y.

Hoek E (1994) Strength of rock and rock masses. ISRM News Journal 2: 4-16.

Hoek E (1999) Putting numbers to geology-an engineer's viewport. Quarterly Journal of Engineering Geology 32 (1): 1-19, doi.org/10.1144/GSL.QJEG.1999.032.P1.01.

Hoek E, Brown ET (1980a) Empirical strength criterion for rock masses. J GeotechEngDiv, ASCE 106:1013–1035, doi.org/10.1061/AJGEB6.0001029.

Hoek E, Brown ET (1980b) Underground excavations in rock. Inst. of Mining and Metallurgy, London, UK.

Hoek E, Brown ET (1988) The Hoek–Brown failure criterion—a 1988 update. In: Curran JH (ed.) Proc. 15th Canadian Rock Mechanics Symposium, Toronto, 31–38.

Hoek E, Brown, ET (1997) Practical estimates of rock mass strength. International Journal of Rock Mechanics and Mining Sciences, 34 (8): 1165-1186, doi.org/10.1016/S1365-1609(97)80069-X.

Hoek E, Marinos P (2000) Predicting tunnel squeezing problems in weak heterogeneous rock masses. Tunnels and Tunneling International 132: 45–51.

Hoek E, Brown ET (2019) The Hoek-Brown failure criterion and GSI 2018 edition. Journal of Rock Mechanics and Geotechnical Engineering 11: 445-463, doi.org/10.1016/j.jrmge.2018.08.001.

Hoek E. Wood D. Shah S (1992) A modified Hoek-Brown criterion for jointed rock masses. ISRM Symposium: Eurock'92-Rock Characterization, J. A. Hudson (ed.), Thomas Telford, pp. 209-213.

Hoek E, Kaiser PK, Bawden WF (1995) Support of Underground Excavations in Hard Rock. Balkema, Rotterdam.

Hoek E, Marinos P, Benissi M (1998). Applicability of the geological strength index (GSI) classification for very weak and sheared rock masses: the case of the Athens schist formation. Bulletin of Engineering Geology and Environment 57. 151-160, doi10.1007/s100640050031.

Hoek E, Read J, Karzulovic A, Chen ZY (2000). Rock slopes in civil and mining engineering. Proceedings of GeoEng2000 Conference, MC Erwin (ed.), Melbourne, Australia, Vol. 1, 643–658.

Hoek E, Carranza-Torres CT, Corkum B (2002) Hoek-Brown failure criterion-2002 edition. Proceedings of the 5th North American Rock Mechanics Symposium, Toronto, Canada, Vol 1, 267-273.

Heok E, Marinos P, Marinos P (2005) Characterization and engineering properties of tectonically undisturbed but lithologyically varied sedimentary rock masses. International Journal of Rock Mechanics and Mining Sciences 42 (2): 277-285, doi:10.1016/j.ijrmms.2004.09.015.

Hoek E, Hutchinson J, Kalenchuk K, Diederichs M (2009) Influence of in situ stresses on open pit design. In: Guidelines for Open Pit Slope Design, J. Read and P. Stacey (eds.), App. 3, CSIRO, Australia, 437-445.

Hoek E, Carter TG, Diederichs MS (2013) Quantification of the Geological Strength Index Chart. Proceedings of the 47th US Rock Mechanics/Geomechanics Symposium, San Francisco, Paper No. ARMA13- 672.

Hormazabal E, Veramendi R, Barrios J, Zuñiga G, Gonzalez F (2013) Slope design at Cuajone Pit, Peru. Proceedings of Slope Stability 2013, P.M. Dight (ed), Australian Centre for Geomechanics, Perth, Australia, 528-539.

Irfan TY, Tang KY (1993) Effect of the coarse fraction on the shear strength of colluvium in Hong Kong. Hong Kong Geotechnical Engineering Office, TN 4/92, 128 p.

ISRM (1981) Rock characterization, testing and monitoring. ISRM Suggested Methods. T. Brown (ed.), Pergamon Press, Oxford, UK.

ISRM (2007) The complete ISRM suggested methods for rock characterization, testing and monitoring: 1974–2006. In: R. Ulusay, JA Hudson (eds), Suggested methods prepared by the ISRM Commission on Testing Methods. Compilation arranged by the ISRM Turkish National Group, Kozan Ofset, Ankara, Türkiye.

Jennings JE (1970) A mathematical theory for the calculation of the stability of slopes in open cast mines. Proc. of Planning of Open Pit Mines, Johannesburg, S. Africa, 87-102.

Kalender A, Sönmez H, Medley E. Tunusluoglu C, Kasapoğlu KE (2009) An approach to predicting the overall strengths of unweldedbimrocks and bimsoils. Engineering Geology 183: 65-79, doi.org/10.1016/j.enggeo.2014. 10.007.

Karakul H, Ulusay R (2022) A new internal friction angle–based approach for estimating Hoek–Brown constant *mi* and its comparison with those estimated from some current methods. Bulletin of Engineering Geology and the Environment (2022) 81:316, doi.org/10.1007/s10064-022-02820-x.

Karzulovic, A. (2004) The importance of rock slope engineering in open pit mining business optimization, Proc. 9th Int. Symp. Landslides: Landslides; Evaluation & Stabilization, Rio de Janeiro, Brazil, W. Lacerda, M. Ehrlich, S. Fontoura and A. Sayao (eds.), Balkema, New York, Vol. 1, 443-456.

Kendorski FS, Cummings RA, Bieniawski ZT, Skinner EH (1983) Rock mass classification for block caving mine drift support. Proceedings of the 5th International Congress on Rock Mechanics, ISRM, Melbourne, B51-B63.

Kim C, Snell C, Medley E (2004)Shear strength of Franciscan complex melange as calculated from back-analysis of a landslide. Proceedings of 5th International Conference on Case Histories in Geotechnical Engineering, New York, 1-8.

Laubscher DH, Jakobe J (2001). The MRMR rock mass classification for jointed rock masses. Underground Mining Methods: Engineering Fundamentals and International Case Studies, (eds WA Hustrulid and R Bullock (eds.)), Society of Mining Engineers, AIME, New York. pp. 474–481.

Le Roux R, Sepehri M, Khaksar Murray SI (2025) Slope stability monitoring methods and technologies for open-pit mining: A systematic review. Mining 5: 1-35, doi.org/10.3390/mining5020032.

Lindquist ES (1994). Strength and deformation properties of melange. PhD Thesis, University of California at Berkeley, USA.

Little T (1999) The reliability of blast damaged slopes, Proceedings of AusIMMEXPLO'99, C. Workman-Davies (ed.), Kalgoorlie, Australia, Australasian Institute of Mining and Metallurgy, Carlton. 1-9.

Lorig L (2009) Challenges in current slope stability analysis methods. Proceedings of Slope Stability, Santiago, Chile,1-21.

Lupogo K (2017) Characterization of blast damage in rock slopes: an integrated field-numerical modelling approach. PhD Thesis, Simon Fraser University, Burnaby, Canada.

Lynch RA, Malovichko DA (2006) Seismology and slope stability in open pit mines. The South African Institute of Mining and Metallurgy, International Symposium on Stability of Rock Slopes in Open Pit Mining and Civil Engineering, Cape Town, S. Africa, 375-389.

Marinos P, Hoek E (2000) GSI—a geologically friendly tool for rock mass strength. In: Proceedings of GeoEng 2000 International Conference on Geotechnical and Geological Engineering, Melbourne, Australia, 1422–1440.

Marinos V, Carter TG (2018) Maintaining geological reality in application of GSI for design of engineering structures in rock. Engineering Geology 239: 282-297, doi.org/10.1016/j.enggeo.2018.03.022.

Marinos V, Marinos P, Hoek E (2005) The geological strength index: Applications and limitations. Bulletin of Engineering Geology and the Environment 64: 55-64, doi.org/10.1007/S10064-004-0270-5.

Martin CD, Stacey PF (2013) Pit slopes in weathered and weak rocks. Slope Stability 2013, P.M. Dight (ed), Australian Centre for Geomechanics, Brisbane, Australia, 3-29.

Medley EW (1994) The engineering characterization of melanges and smilar block-in-matrix rocks (bimrocks). PhD dissertation, Department of Civil Engineering, University of California at Berkeley, California.

Medley EW (2008) Engineering the geological chaos of Franciscan and other Bimrocks. 12th US Rock Mech. Symp. and 2nd Canada Rock Mech. Symp., S. Francisco, USA.

Medley EW (2012) Simple concepts useful for characterizing complex Bimrocks underlying slopes. ASCE-AEG Landslide and Slope Stability Short Course, California, USA.

Medley EW, Zekkos D (2011). Geo-practitioner approaches to working with antisocial mélanges. Invited paper. Mélanges: Processes of Formation and Societal Significance, The Geological Society of America Special Paper 480, J. Wakabayashi Y, Dilek Y (eds.), 261-277, doi:10.1130/2011.2480(13).

Mehrishal A, Sharifzadeh M, Shahryar K (2015) Estimating of Hoek– Brown mi using internal friction angle. Proceedings of the 24th International Mining Congress of Türkiye, IMCET 2015, 488–493.

Mencl V (1966) Mechanics of landslides with non-circular slip surfaces with special reference to the Vaiont slide, Géotechnique16 (4): 329–337, doi.org/10.1680/geot.1966.16.4.329.

Montiel E,Varona P, Fernandez C, Espinoza Z (2020) Use of discrete fracture networks in 3D numerical modelling for stability analysis in open pitsSlope Stability 2020, PM Dight (ed.), Australian Centre for Geomechanics, Perth, Australia, 913-926.

Morales T, Uribe-Etxebarria G, Uriarte JA, Valderrama IF (2005) Geomechanical characterization of rock masses in Alpine regions: The Basque Arc (Basque-Cantabrian basin, Northern Spain). Engineering Geology 71: 343–362, doi:10.1016/S0013-7952(03)00160-.

Moss A, Diachenko S, Townsend P (2006) Interaction between the block cave and the pit slopes at Palabora mine. Journal of South African Institute of Mining and Metallurgy 16: 479-484.

Mostyn G, Douglas K (2000) Strength of intact rock and rock masses. Proceedings of International Conference on Geotechnical and Geological Engineering, Vol 1. Techonomic Publishing, Lancaster, UK, 1389–1421.

Napoli ML, Barbero M, Scavia C (2021) Effects of block shape and inclination on the stability of mélange bimrocks. Bulletin of Engineering Geology and the Environment 80: 7457–7466, doi.org/10.1007/s10064-021-02419-8.

Neiman WL (2009) Lessons learned from rates of mudrock undercutting measured over two time periods. Environmental and Engineering Geoscience XV (3): 117–131, doi:10.2113/gseegeosci.15.3.117.

Newmark NM. (1965) Effects of earthquakes on dams and embankments. Géotechnique 15 (2): 39-160, doi.org/10.1680/geot.1965.15.2.139.

Obara Y, Nakamura N, Kang SS, Kaneko K (2000) Measurement of local stress and estimation of regional stress associated with stability assessment of an open-pit rock slope. International Journal of Rock Mechanics & Mining Sciences 37: 1211-1221, doi.org/10.1016/S1365-1609(00)00054-X.

Ohnishi Y, Nishiyama S, Yano T, Matsuyama H, Amano K (2006). A study of the application of digital photogrammetry to slope monitoring systems, International Journal of Rock Mechanics and Mining Sciences 43 (5): 756–766, doi.org/10.1016/j.ijrmms.2005.12.002

Ojeda P, Elmo D, Rogers S, Brzovic A (2023) Discrete Fracture Network (DFN) analysis to quantify the reliability of borehole-derived volumetric fracture intensity. Geosceience 13: 1-22, doi.org/10.3390/geosciences13060187.

Osasan KS, Afeni TB (2010) Review of surface mine slope monitoring techniques. Journal of Mining Science 46 (2): 177-186, doi:10.1007/s10913-010-0023-8.

Osgoui RR, Ulusay R, Ünal E (2010) An assistant tool for the Geological Strength Index to better characterize poor and very poor rock masses.International Journal of Rock Mechanics and Mining Sciences 47: 690–697, doi: 10.1016/j.ijrmms.2010.04.001.

Pothitos F, Webster S (2006). Cadia Hill Pit Geotechnical Report.Internal Comp. Report, Newcrest Minin Ltd.

Pottie J, Sanchez A, Gilbert D, Beale G (2013) Antamina west wall. In: Guidelines for Evaluating Water in Slope Stability, Appendix 4, G. Beale and J. Read (eds.), CSIRO, Australia, 507-512.

Porter J, Schroeder K, Austin G (2012) Geology of the Bingham Canyon Porphyry Cu-Mo-Au deposit, Utah. In: Special Publication 16, J. Hedenquist, M. Harris, F. Camus. CO Littleton (eds.), Society of Economic Geologists, 127–146.

Potyondy DO, Cundall PA (2004) A bonded-particle model for rock. International Journal of Rock Mechanics and Mining Science &Geomechanics Abstracts41 (8): 1329–1364, doi.org/10.1016/j.ijrmms.2004.09.01

Prandtl L (1923) AnwendungsbeispielezueinemhenckyschenSatzüber das plastischeGleichgweicht. Berlin *Z.* Angew. Math. 3: 401-406.

Read J, Stacey P (2009) Guidelines for open pit slope design. CSIRO, Australia.

Renani HR, Cai M (2022) Forty-year review of the Hoek–Brown failure criterion for jointed rock masses. Rock Mechanics and Rock Engineering 55: 439–461, doi.org/10.1007/s00603-021-02661-2.

Renani HR, Martin CD, Cai M (2019) An analytical model for strength of jointed rock masses. Tunneling and Underground Space Technology 94:103159, doi. org/ 10. 1016/j. tust. 2019. 103159.

Richards L, Read SAL (2011) A comparison of methods for determining m_i, the Hoek-Brown parameter for intact rock material. Proceedings of 45th US Rock Mechanics/Geomechanics Symposium, American Rock Mechanics Association, San Francisco, Paper No. ARMA 11-246.

Robotham MF (2011) Slope design in large open pit mines.Slope Stability 2011: International Symposium on Rock Slope Stability in Open Pit Mining and Civil Engineering, Vancouver, Canada.

Rogers S, Elmo D, Beddoes R, Dershowitz B (2009) Mine scale DFN modelling and rapid upscaling in geomechanical simulations of large open pits. In: International Symposium on Rock Slope Stability in Open Pit Mining and Civil Engineering, Santiago, Chile.

Rogers S, Elmo D, Webb G, Catalan A (2014) Volumetric fracture intensity measurement for improved rock masscharacterization and fragmenatation assessment in block caving operations. Rock Mechanics and Rock Engineering 48: 633-649, doi:10.1007/s00603-014-0592-y.

Rose ND, Hungr O (2007) Forecasting potential rock slope failure in open pit mines using the inverse-velocity method. International Journal of Rock Mechanics & Mining Sciences 44 (2007) 308–320, doi: 10.1016/j.ijrmms.2006.07.014.

Ross B (2017) Rise to the occasion: Lessons learned from the Bingham Canyon Manefay Slide. Society for Mining, Metallurgy and Exploration Inc. (SME), Colorado, USA.

Russo G (2009) A new rational method for calculating the GSI. Tunneling and Underground Space Technology 24: 103–111, doi.org/10.1016/J.TUST.2008.03.002.

Sampaleanu C, Stead D, Donati D, Griffiths C, D'Ambra S, LeBreton R (2017) Characterizing brittle fracture induced rockfall in an open sub-level retreat excavation. Proceedings of the 51st US Rock Mechanics/Geomechanics Symposium, American Rock Mechanics Association, Alexandria, Paper Number: ARMA-2017-0236.

Seed HB (1979) Considerations in the earthquake-resistant design of earth and rockfill dams. Géotechnique 29 (3): 215-263, doi.org/10.1680/geot.1979.29.3.215.

Shen J, Karakus M (2014) Simplified method for estimating the Hoek- Brown constant for intact rocks. Journal of Geotechnical and Geoenvironmental Engineering 140 (1): doi:10.1061/(ASCE)GT.1943-5606.0001116.

Sheorey PR (1994). A theory for in situ stresses in isotropic and transversely isotropic rock. International Journal of Rock Mechanics and Mining Sciences &Geomechanics31(1): 23–34, doi.org/10.1016/0148-9062(94) 92312-4.

Sjöberg J (1999). Analysis of large scale rock slopes. PhD thesis, Lulea University of Technology, Lulea, Sweden.

Sjöberg, J (2013) Numerical analysis, slope design and in situ stress. Slope Stability 2013, P.M. Dight (ed.), Australian Centre for Geomechanics, Brisbane, Australia, 29-43.

Sönmez H, Ulusay R (1999) Modifications to the geological strength index (GSI) and their applicability to stability of slopes. International Journal of Rock Mechanics and Mining Sciences 36 (6):743–760, doi.org/10.1016/S0148-9062(99)00043-1.

Sönmez H, Ulusay R (2002) A discussion on the Hoek-Brown failure criterion and suggested modifications to the criterion verified by slope stability case studies. Yerbilimleri, 26: 77-99, (Link: www.yerbilimleri.hacettepe.edu.tr).

Sonmez H, Gökçeoğlu C, Medley EW, Tuncay, E, Nefeslioglu HA (2006) Estimating the uniaxial compressive strength of a volcanic "bimrock". International Journal of Rock Mechanics and Mining Sciences 43: 554–561, doi.org/10.1016/j.ijrmms.2016.03.022.

Stacey PF (2009) Pit slope design process. Proceedings of Slope Stability, Santiago, Chile, 1-15.

Stacey TR, Xianbin Y (2004). Extension in large open pit slopes and possible consequences. Proceedings of MassMin 2004, A Karzulovic and M. Alfaro (eds.). Chilean Engineering Institute, Santiago, Chile

Stacey TR, Xianbin Y, Armstrong R, Keyter GJ (2003) New slope stability considerations for deep open pit mines. Journal of the South African Institute of Mining and Metallurgy 103 (6): 373-389.

Stead D, Eberhardt E (2013) Understanding the mechanics of large landslides. Italian Journal of Engineering Geology and Environment, Book Series (6): 85-108, doi.org/10.4408/IJEGE.2013-06.B-07.

Stead D, Jaboyedoff M, Coggan JS (2012) Rock slope characterization and geomechanical modelling. Proceedings of Landslides and Engineered Slopes: Protecting Society through Improved Understanding, E. Eberhardt, C. Froese, K. Turner, S. Leroueil(eds.), Taylor & Francis Group, London, 83-100.

Stead D, Donati D, Wolter A, Sturzenegger M (2019) Application of remote sensing to the investigation of rock slopes: experience gained and lessons learned. ISPRS International Journal of Geo-Information 8 (7): 1-24, doi:10.3390/ijgi8070296.

Toh, JCW (2010) Seismic analysis for open pit mines. Australian Geomechanics Society, Sydney Chapter Symposium, 13 October 2010, Sydney, Australia, 91-108.

Toh JCW, Green DKE, Swarbrick GE, Fowler MJ, Estrada BE (2013) Earthquake stability assessment for open pit mine slopes. Slope Stability 2013, PM Dight (ed.), Australian Centre for Geomechanics, Perth, Brisbane, Australia, 1187-1202.

Transportation Research Board (1996) Rock strength properties and their measurement. In: Landslides Investigation and Mitigation, Chp. 14, Special Report No. 247, AK Turner and LR Schuster (eds.), National Academy Press, Washington D.C., 372-390.

Tuckey Z (2008) An integrated field mapping-numerical modelling approach to characterizing discontinuity persistence and intact rock bridges in large open pit slopes. MSc Thesis, Simon Fraser University, Fac. of Sciences, Dept. of Earth Sciences, Burnaby BC, Canada.

Tuckey Z, Stead D (2016) Improvements to field and remote sensing methods for mapping discontinuity persistence and intact rock bridges in rock slopes. Engineering Geology 208: doi:10.1016/j.enggeo.2016.05.001.

Tuckey *Z,* Stead D, Eberhardt E (2013) Combining field methods and numerical modelling to address challenges in characterizing discontinuity persistence and intact rock bridges in large open pit slopes. Slope Stability 2013, PM Dight (ed), Australian Centre for Geomechanics, Perth, Australia, 189-204.

Tuncay E, Ulusay R (2001) Deterministic and probabilistic treatments of multi-planar failures at Himmetoğlu (Turkey) coal mine. Canadian Geotechnical Journal 38 (4): 828-849.

Ulusay R (1991) Geotechnical evaluations and deterministic design considerations for pitwall slopes at Eskihisar (Yatağan-Muğla) strip coal mine. PhD Thesis, Middle East Technical University, Department of Geological Engineering, Ankara, Türkiye, 340 p (in English).

Ulusay R, Çağlan D (2022) Investigation on the east highwall of the DivriğiTaşlıtepe open pit subjected to instability and assessment of its slope stability. Unpublished Report for Demir Export, Ankara, Türkiye, 213 p (in Turkish)

Ulusay R, Ekmekçi M, Tuncay E, Hasançebi N (2013) Slope optimization and design based on geotechnical and hydrogeological assessments for a new coal mine. Proceedings of ISRM Symposium EUROCK2013, Rock Mechanics for Resources, Energy and Environment, M. Kwasniewski and D. Lydzba (eds.), Wroclaw, Poland, 703-708.

Vasarhelyi B, Kovacs L, Torök A (2016) Analyzing the modified Hoek- Brown failure criteria using Hungarian granitic rocks. Geomechanics and Geophysics for Geo-Energy and Geo-Resources 2: 131–136, doi:10.1007/s40948-016-0021-7.

Villaescusa E, Li J, Baird G (2002). Stress measurement for oriented core. International Journal of Rock Mechanics and Mining Sciences 39: 603-615, doi.org/10.1016/S1365-1609(02)00059-X.

Vivas, J, Stead, D, Elmo, D, Hunt C (2015) Simulating the interaction between groundwater and brittle failure in open pit slopes. International Journal of Geological and Environmental Engineering, 9 (12): 295–1303, doi:10.36487/ACG_repo/2025_03.

Wakabayashi J, Medley EW (2004) Geological characterization of melanges for practitioners. Felsbau 22: 10-18.

Wang W, Shen J (2017) Comparison of existing methods and a new tensile strength based model in estimating the Hoek-Brown constant m_i, for intact rocks. Engineering Geology 224: 87–96, doi:10.1016/j.enggeo.2017.05.008.

Wang M, Cai M, Maloney S, Dun M (2025) Determination of mine –wide stress using numerical back analysis: a case study of Juwaneng mine. International Journal of Rock Mechanics and Mining Sciences 194: 1-16, doi.org/10.1016/j.ijrmms.2025.106235.

Williams C, Ross B, Zebker M, Leighton J, Gaida M, Morkeh J, Robotham M (2021) Assessment of the available historic RADARSAT-2 synthetic aperture radar data prior to the Manefay slide at the Bingham Canyon Mine using modern InSAR techniques. Rock Mechanics and Rock Engineering 54 (1), 1-21, doi.org/10.1007/s00603-021-02483-2.

Woo K-S, Eberhardt E, Rabus B, Stead D, Vyazmensky A (2012) Integration of field characterization, mine production and InSAR monitoring data to constrain and calibrate 3-D numerical modelling of block caving-induced subsidence. International Journal of Rock Mechanics and Mining Sciences 53: 166-178, doi.org/10.1016/j.ijrmms.2012.05.008.

Risk assessment methods

The principle of rock bridges uncertainty

D. Elmo & G. Torsello
University of British Columbia, Vancouver, Canada
davide.elmo@ubc.ca
0000-0001-5095-4425, 0000-0002-9442-8854

L. Zorzi
WSP, Vancouver, Canada

Abstract

Rock engineering practice has long relied on rock bridge percentage as a measurable design parameter. Yet, this reliance rests on an assumption that a geometric property of a post-failure system can be meaningfully assigned to a pre-failure rock mass. This paper argues that it cannot. Observation is never theory-neutral, and the conceptual framework we bring to rock bridge characterisation shapes and distorts what we claim to measure. We introduce the principle of rock bridge uncertainty: the conditions required to identify and measure a rock bridge are the same conditions that confirm the rock mass has already failed or is in the process of failing. Through a series of mechanistic and geometric paradoxes, we demonstrate that rock bridges are not pre-existing features of the rock mass; they are products of the failure process itself. This distinction has direct consequences for failure forecasting methods, including the inverse velocity method, whose applicability to brittle failure is constrained by the very uncertainty that the principle describes. In place of deterministic rock bridge percentage, we propose the concept of rock bridge potential, a probabilistic characterisation of the strength of a fractured rock mass. The implications extend beyond technical methodology to engineering practice: by embracing uncertainty rather than ignoring it, we can make better-informed decisions about slope stability, excavation design, and risk management in fractured rock masses.

Keywords

Rock bridges, Uncertainty, Rock bridge potential, Failure mechanisms.

1 Introduction

Newton famously refused to speculate about the cause of gravity. *Hypotheses non fingo* (I frame no hypotheses), as he declared. His law of gravity does not refer to an underlying physical mechanism; it requires no unobservable quantities, only measurable ones. This is precisely why it worked. But Newton's discipline is harder to maintain than it appears. When attempting to understand rock mass behaviour, we often assume our process is equally straightforward: collect data, make observations, and synthesize an interpretation. This assumes we approach the rock mass without preconceptions. In reality, unless we have some a priori framework for what we expect to find, how do we decide which observations matter and which data to collect? Observation is never theory-neutral. We always bring

conceptual frameworks that guide what we look for and how we interpret what we find. Rock bridges exemplify this problem perfectly. Can we say, as Newton did, that the equations we use to characterize rock bridge strength require no unobservable quantities?

Consider Jennings (1970, 1971), who proposed Equations 1 and 2 to derive the shear strength parameters of a discontinuity equivalent to a set of co-planar rock bridges and joints (Figure 1). The equation contains a parameter, k, which must be measured.

$$c_{eq} = (1-k)c + kc_j \quad (1)$$

$$Tan\phi_{eq} = (1-k)Tan\phi + kTan\phi_j \quad (2)$$

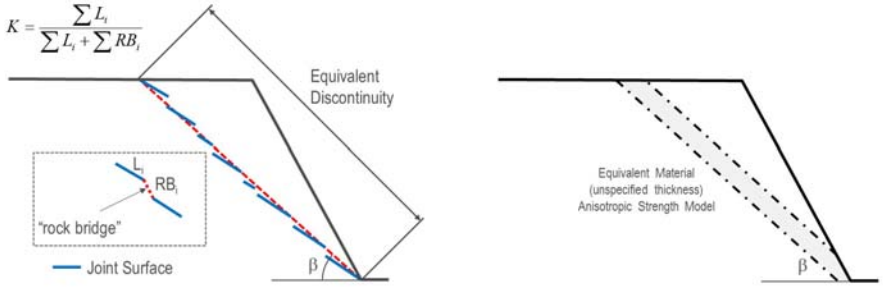


Fig. 1 Conventional representation of rock bridges according to Jennings (1970, 1971). Note that this approach is used to either specify the shear strength of a continuous (discrete) discontinuity surface or to define anisotropic rock mass properties in limit equilibrium and continuum modelling.

Before failure, the spatial distribution and geometry of rock bridges could, in principle, be described probabilistically, as there is no way to measure the number, size and location of the rock bridges. However, unlike Newton's gravitational constant, k is not an observable property of the pre-failure system; it is a post-failure interpretation retroactively imposed on a reality that no longer exists in its original state. By assuming a failure surface along which to measure k, we are, in effect, framing a hypothesis and then treating it as a measurement. Note that this approach neglects the tensile strength of rock bridges. This is not a matter of conservatism. The failure mechanism implicit in Equations 1 and 2 is one of pure shear, which excludes tensile resistance by assumption rather than by choice. This leads to the important question of whether the geometrical representation of rock bridges shown in Figure 1 is a faithful description of physical reality, or just a convenient construct that the literature has collectively normalized. We speak confidently about measuring the rock bridge percentage (the percentage of RBi relative to the total of RBi and Li) without questioning what rock bridges actually represent mechanically. The danger is circularity: we define rock bridges geometrically, design methods to measure them, and then treat the resulting numbers as physical evidence, without ever questioning whether the original geometric definition captures what actually governs failure.

This is not merely a practical limitation that better instrumentation might one day overcome. It is an epistemological constraint since identifying a rock bridge requires evidence of failure. This paper examines the implications of that constraint. It proposes a design framework for characterizing potential failure mechanisms that is consistent with what we can and cannot actually know about a rock mass before it fails.

2 Mechanistic uncertainty and geometric paradoxes

Consider the problem illustrated in Figure 2, which shows a block partially fractured through its half-section. If we were to complete the fracture by fully separating the block into two pieces, would we be proving that a rock bridge existed before failure, or merely witnessing the outcome of a failure mechanism? The distinction matters. The same block can be split by applying either a tensile or a shear force, and although the results appear identical, the failure surface would likely differ between the two cases. If the failure surface defines and measures the rock bridge, then the same pre-failure geometry yields different rock bridge measurements depending on how failure is induced. The rock bridge, in this view, is not a pre-existing geometric feature waiting to be measured, but a product of the failure process itself.

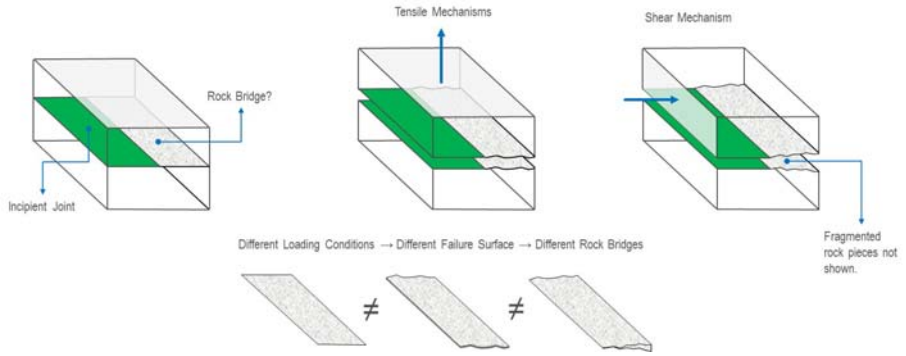


Fig. 2 A block partially fractured through half its cross-section. Completing the fracture by applying either a tensile or shear force produces the same result but different failure surfaces, raising the question of whether the rock bridge was a pre-existing geometric feature or a product of the failure mechanism itself.

This reframes the problem fundamentally. If rock bridges are a manifestation of a failure mechanism rather than an independently measurable property of the intact rock mass, then measuring them a priori is not merely difficult; it is conceptually incoherent. Equations 1 and 2 are used in a failure criterion that encodes an assumption about which failure mechanism occurred. It does not describe the rock mass before failure; rather, it presents a particular interpretation of the rock mass after failure and works backwards from there.

Consider the following three geometric tests of the assumptions current methods make about rock bridges.

1. If we removed all the joints from the slope problem illustrated in Figure 3a, would the rock bridges still exist? When rock bridges are defined as the intact rock material between the endpoints of existing joints, their existence is conditional; they exist only relative to the joints that bound them. Remove the joints, and the rock bridges appear to disappear with them. Did the rock bridges truly disappear, or did they grow to the point where they exist everywhere at once in the now-intact rock mass?
2. Conversely, consider equivalent slope problems sharing the same rock bridge percentage but very different geometries (Figure 3b). According to Jennings's equations, the equivalent cohesion is identical whether the failure surface contains one, two or even fifteen rock bridges. Any attempt to scale cohesion to the specific length of individual gaps implicitly assumes a universal scaling law for rock strength (an assumption recent work has called into question; see Bewick and Elmo 2025) and complete knowledge of the failure surface geometry before failure. The consequences of this become clear when examined numerically. For a slope of height (H) of 30.5m with a failure plane inclined at 33 degrees, a problem with 10,000 rock bridges would consist of a series of 5.6mm joints separated by gaps of just 1μm (10^{-3} mm). To the naked eye, this would be indistinguishable from a single continuous joint surface. And yet Jennings's equations would assign it the same equivalent cohesion as a slope with a single rock bridge spanning the entire failure surface.
3. Now consider an intact rock slope, without joints, loaded by a surcharge along the crest (Figure 4). As loading increases, new cracks will eventually appear and propagate. Those cracks play the role of the joints in Figure 1, and the intact intervals between them are, by definition, rock bridges. Using Jennings's framework, we have created rock bridges. And yet we could not have known their locations without predicting exactly where the new cracks would form. This paradox reveals that we cannot treat rock bridges as a property of the rock mass in its current state. They are a property of a future failure state that does not yet exist.

These geometrical paradoxes further highlight the challenge of defining rock bridges relative to a failure surface that has yet to form, and they are central to the concept of rock bridge potential introduced in Section 4.

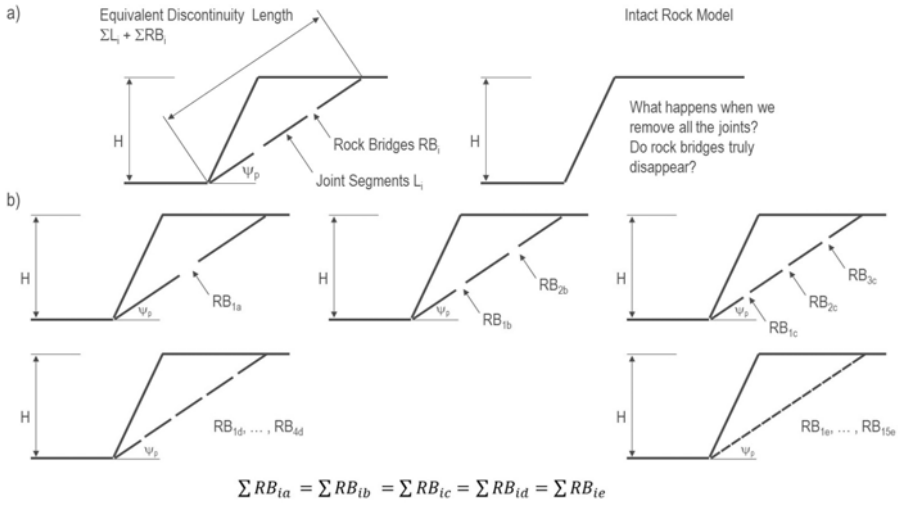


Fig. 3 Illustration of the geometric paradoxes arising from the classical approach to rock bridge characterization in rock engineering design. (a) Do rock bridges truly disappear if we remove the joints? (b) How can 5 different slope geometries be assigned the same equivalent cohesion as defined in Equation 1?

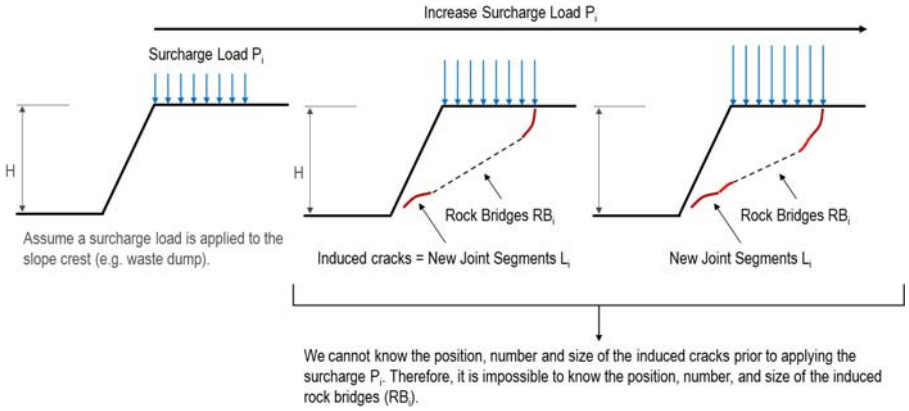


Fig. 4 Illustration of how an initially intact rock mass develops new cracks under increasing load. These cracks define rock bridges retrospectively. Their locations could not have been known without predicting exactly where fractures would form, confirming that rock bridges are a property of a future failure state, not of the current rock mass.

3 The principle of rock bridge uncertainty

Once the position and size of a rock bridge are known, this knowledge manifests in measurable deformation, indicating that the rock mass has already begun to respond to loading. But by that point, it may be too late to accommodate the deformation in design. This creates a fundamental dilemma. Designing against failure requires anticipating the deformations we wish to prevent, which means knowing where the rock bridges are and how large they are. This is precisely the information that becomes available only after failure processes are already underway.

We term this the principle of rock bridge uncertainty: the conditions required to identify and measure a rock bridge are the same conditions that confirm the rock mass has already failed or is in the process of failing.

The principle has a direct analogue in quantum mechanics, where the act of measurement disturbs the system being measured. Here, the disturbance is irreversible, since once the rock mass has failed, the pre-failure configuration cannot be recovered; it can only be inferred. And it is that inference, dressed in the language of measurement, that current methods present as a design parameter. The practical consequence is that any design approach based on a deterministic value of rock bridge percentage is, at best, an assumption about which failure mechanism will occur and where. At worst, it is a false precision that ignores the very uncertainty it should quantify and may lead to non-conservative strength estimates (Elmo 2023). Acknowledging this does not make the engineering problem unsolvable,but it reframes what a solution can legitimately claim.

The principle of rock bridge uncertainty is clearly expressed in the application of the inverse velocity method to brittle failure. As discussed by Beingessner (2026), the past two decades have seen

significant advances in slope monitoring technology, accompanied by a growing reliance on phenomenological approaches to failure forecasting. However, the inapplicability of the inverse velocity method to certain brittle failure cases, such as the Libby Dam in Montana (Rose and Hungr, 2007), illustrates the risk of overreliance on monitoring data. Slope monitoring technologies are capable of detecting brittle failure precursors, but only when the underlying failure mechanism is sufficiently understood, and it is precisely that understanding which current approaches to rock bridge characterisation fail to provide. In fractured rock masses, rock bridges must rupture to create the very failure surface that the inverse velocity method assumes exists from the outset. Indeed, in Fukuzono's (1985) experiments, a failure surface exists from the outset; therefore, the method presupposes what the rock mass has not yet produced.

Progressive rock bridge degradation occurs through brittle fracturing and the coalescence of discontinuities, generating episodic acceleration that reflects discrete bridge failures, periods of apparent stability that mask internal crack propagation, and sudden transitions when critical connectivity thresholds are exceeded. Field observations confirm that inverse velocity trends become interpretable only after sufficient bridges have failed, approximating a through-going failure surface. Before this transition, inverse velocity patterns are erratic (Beingessner 2026). This is a direct expression of the pre-failure uncertainty we have described. The method becomes readable precisely when the rock bridge problem has already resolved itself. This reframes inverse velocity analysis not as a prediction tool but as a state-dependent indicator whose validity depends on how far along the failure surface has progressed. Paradoxically, while the method cannot predict failure timing during the rock bridge rupture phase, monitoring inverse velocity patterns can serve as an indirect indicator of approaching criticality, specifically, of the transition from failure surface creation to acceleration along established discontinuities. A rigorous application, therefore, requires identifying when sufficient failure has occurred to enable viable failure mechanisms and integrating connectivity metrics with traditional displacement monitoring to better constrain uncertainty in rock-bridge-controlled systems.

4 Rock bridge potential as a mechanistic correct alternative to the rock bridge percentage

The arguments developed in the preceding sections converge on a single conclusion: rock bridges cannot be treated as measurable geometric features of a pre-failure rock mass. But if rock bridges cannot be measured, how should they be characterized? We propose that the answer lies in reframing the problem entirely, from one of measurement to one of potential. The distinction is not merely semantic. A measurable quantity describes something that exists in a determinate state prior to observation. A potential describes the capacity of a system to produce a particular outcome under particular conditions. Rock bridges, we argue, belong to the second category. They do not exist as fixed geometric entities waiting to be measured; they emerge as the rock mass transitions from a stable to a failed state. Before that transition, we can speak only of the potential for rock bridges to develop along a future failure surface that does not yet exist.

This interpretation (referred to as the Bologna Interpretation in Elmo 2023) draws an instructive analogy from quantum mechanics. A spinning coin has no definable face until it stops; the outcome (heads or tails) is not hidden from us but genuinely undetermined until the spin resolves. In the same way, a stable rock mass contains no definable rock bridges. It contains the potential for rock bridges to form and break simultaneously with the initiation and propagation of rock mass failure. To insist on measuring rock bridges before failure is to insist on reading the face of a coin that has not yet stopped spinning.

This concept is referred to as the rock bridge potential (Figure 5). Elmo (2023) provides several quantitative examples of rock bridge potential. Rather than seeking a deterministic rock bridge percentage value, the rock bridge potential characterises the strength capacity of a fractured rock mass through a combination of parameters: intact rock strength, loading conditions (both magnitude and direction), the connectivity of the existing discontinuity network, and the degree of block interlocking within the rock mass (Elmo 2023). Each of these governs not only whether rock bridges will form, but where, how many, and of what size. Quantifying rock bridge potential in practice requires the explicit modelling of intact rock fracturing, simulating the initiation, propagation, and coalescence of cracks within a represented discontinuity network, rather than prescribing failure surface geometry in advance.

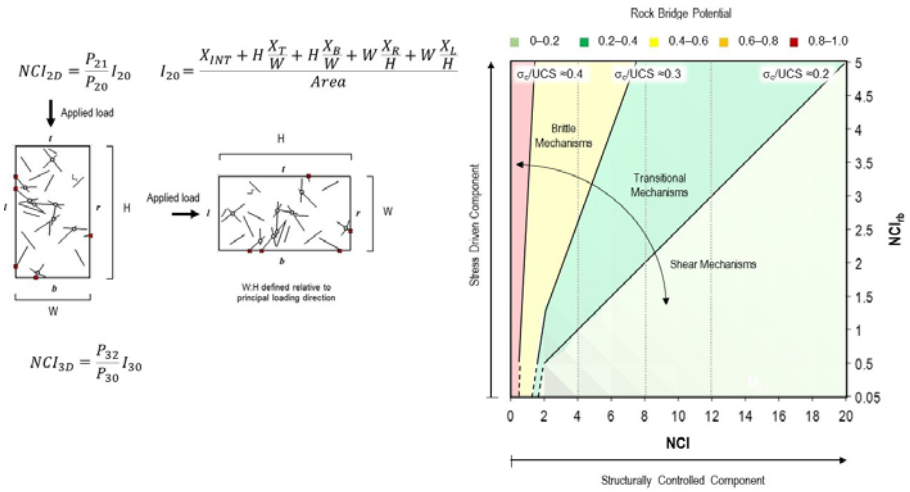


Fig. 5 Concept of rock bridge potential and formulae for 2D and 3D analysis, modified from Elmo 2023 and Bewick and Elmo (2025). NCI represents a measure of natural fracture connectivity prior to failure. NCI_{rb} is a measure of the net connectivity associated with the formation of new cracks.

5 Conclusions

Before we can ask how to measure rock bridges, we must first ask whether the measurement we are attempting is coherent. The principle of rock bridge uncertainty presented in this paper says it is not. The conditions that allow us to identify and measure a rock bridge are the same conditions that tell us the rock mass has already failed. This does not mean the engineering problem is unsolvable. It means that the solution must be reframed. The question is not what the rock bridge percentage is along a potential failure surface, but what the probability is that a kinematically viable failure surface will develop under anticipated loading conditions. Answering that question requires models that explicitly represent the discontinuity network and simulate intact rock fracturing, so that rock bridges emerge and fail as they do in reality, rather than being prescribed as fixed geometric inputs. This is not a higher standard of modelling sophistication, but the minimum condition for consistency with what rock bridges actually represent.

Jennings' framework represented a necessary and valuable step in the development of rock engineering, but continuing to rely on it while ignoring its fundamental limitations is no longer defensible. This is not a question of practical convenience versus model complexity. It is a matter of professional ethics. We owe it to the discipline and to those who depend on our designs to work with frameworks that acknowledge what we can and cannot know.

References

Beingessner T (2026) Slope damage and acceleration of slope failures. MASc Thesis. University of British Columbia.

Bewick RP, Elmo D (2025) Size Effect and Rock Mass Strength. Canadian Geotechnical Journal. 62: 1-18. https://doi.org/10.1139/cgj-2024-0531.

Elmo D (2023) The Bologna interpretation of rock bridges. Geosciences, Vol. 13(2), 33 https://doi.org/10.3390/geosciences13020033.

Fukuzono T (1985)A method to predict the time of slope failure caused by rainfall using the inverse number of velocity of surface displacement. Journal of the Japan Landslide Society (Landslides), 22(2), 8–13.

Jennings, JE (1970) A mathematical theory for the calculation of the stability of slopes in open cast mines. In Planning Open Pit Mines,Proceedings, Johannesburg; Van Rensburg, P.W.J., Ed.; A.A. Balkema: Cape Town, South Africa, 1970; pp. 87–102.

Jennings, JE (1971) An approach to the stability of rock slopes based on the theory of limiting equilibrium with a material exhibiting anisotropic shear strength. Stability of rock slopes. In Proceedings of the 13th US Symposium on Rock Mechanics, Urbana, IL, USA, 30 August–1 September 1971.

Rose ND, Hungr O (2007) Forecasting potential rock slope failure in open pit mines using the inverse-velocity method,International Journal of Rock Mechanics and Mining Sciences,Volume 44, Issue 2,Pages 308-320,https://doi.org/10.1016/j.ijrmms.2006.07.014.

Permeability and acoustic emission response characteristics during injection-induced fault slip

Ke Zhang[1,2], Qiang Li[1,2], Yueqiang Ma[1,2], Sida Jia[1,2], Jinsen Li[1,2] Quan Gan[1,2], Derek Elsworth[3]

[1]*State Key Laboratory of Coal Mine Disaster Dynamics and Control, Chongqing University, Chongqing, China*
[2]*School of Resources and Safety Engineering, Chongqing University, Chongqing, China*
[3]*Department of Energy and Mineral Engineering, EMS Energy Institute and G3 Center, Pennsylvania State University, University Park, PA, USA*

quan.gan@cqu.edu.cn
0000-0001-5201-8817

Abstract

Here we performed fluid injection experiments on granite samples containing smooth faults under varying initial critical stress states. Results demonstrate that the initial critical stress state exerts first-order control on seismic activity, with critically stressed faults exhibiting stronger seismic responses during activation. During injection, the pressure rapidly increases and then stabilizes at a constant level. Under different critical stress conditions, injection-induced reactivation of faults will result in a different acoustic emission response. Slip events occur abruptly, highlighting the sudden and destructive nature of injection-induced unstable slip. We found that faults closer to critical instability exhibited shorter failure durations, manifested as AE signals concentrated within a narrower time window. This work elucidates how initial fault stress governs the co-evolution of permeability and acoustic emission response, advancing understanding of injection-induced seismicity physics.

Keywords

Injection-induced seismicity, Stress state, Permeability, Acoustic emission.

1 Introduction

Injection-induced seismicity has become a globally pervasive geophysical phenomenon that poses significant challenges for subsurface engineering applications, especially enhanced geothermal systems (EGS), shale gas wastewater reinjection, and CO_2 sequestration projects (Ellsworth 2013). The current mechanistic understanding of injection-induced seismicity includes multiple coupled processes, pore pressure diffusion, thermal-water-mechanical interactions, seismic wave triggering, and aseismic slip transients (Guglielmi et al. 2015). Of these, pore pressure diffusion through fault zones is widely recognized as the predominant triggering mechanism (Shapiro et al. 2011), with elevated fluid pressures lowering the effective normal stress and facilitating fault reactivation (Elsworth et al. 2016). The dynamic interplay between permeability evolution and induced seismicity during high-pressure fluid injection is particularly important for optimizing EGS reservoir performance, ensuring the integrity of the nuclear waste repository, and advancing physics-based seismic hazard assessment (Woo et al. 2019). Field observations and laboratory experiments have consistently demonstrated that injection-induced sliding events exhibit complex magnitude-frequency distributions modulated by coupled hydrodynamic processes (Passelègue et al. 2018).

The initial stress state of the fault is a key factor controlling the seismic activity by injection induced (McGarr 2014). The traditional theory, based on the assumption of moderate stress state, has established a fundamental theoretical framework between the release of seismic moments and the injected volume (Galis et al. 2017). Field observations and experimental studies have shown that stress states of many faults are closer to the critical instability conditions, which makes the classical model based on the assumption of moderate stress have obvious limitations in predicting actual seismic activities (Li et al. 2021). Faults under different initial stress states exhibit distinct response to fluid injection. This is not only reflected in the scale of seismic moment release but also affects the suddenness of instability and the mode of rupture propagation.

The evolution of fault permeability also plays a critical role in injection-induced seismicity. As a key parameter governing pore pressure diffusion and fluid migration pathways, dynamic changes in permeability directly influence the redistribution of effective stress and the destabilization process of faults. Seismic events exert multifaceted control over hydrogeological systems by affecting dynamic permeability; seismic waves generated by seismic activity led to either increased or decreased permeability. The magnitude-frequency distribution provides a fundamental framework for the statistical patterns of seismic activity, typically described by the Gutenberg-Richter law (Gutenberg and Richter 1944). According to this law, a negative correlation exists between earthquake magnitude and occurrence frequency, corresponding to a low frequency for large magnitudes and a high frequency for small magnitudes (Tormann et al. 2015).

We conducted fluid injection tests on granite samples containing smooth artificial faults, with pre-loaded strengths at 80%, 84%, 88%, and 92% of peak shear strength. Faults closer to the critical instability state exhibited greater stress drop and higher peak slip rates.

2 Materials and Methods

Fluid injection experiments were conducted on fractured granite samples. The granite primarily consists of quartz (33%), feldspar (62%), and mica (5%), with an average grain size of approximately 2 mm. The granite exhibits a porosity of about 0.6% and macroscopically uniform texture. Experimental results measured using the pressure pulse decay method indicate an intrinsic permeability of 1.3 μD for the granite matrix. Granite samples with a diameter of 50 mm and height of 100 mm were cut at a 30° angle to the core axis, ensuring each sample contained a smooth fault inclined at 30° to the axial direction. Two drill holes with a nominal diameter of 2.5 mm were drilled in parallel along the vertical direction near the fault surface at the end of the sample, to allow fluid flow from the core holder inlet into the fracture and subsequently to the exit hole, which was 5 mm from the edge of the sample. The samples were fixed within the core holder using two layers of polytetrafluoroethylene and separated from the surrounding oil.

The fluid-driven fault reactivation experiment was carried out by using a high-temperature and high-pressure triaxial fault shear permeability test system at ambient temperature (20°C), and using silicone oil and distilled water as the enclosing fluid and injection fluid, respectively. The normal stress (σ_n) and shear stress (τ) of the fracture are calculated as:

$$\sigma_n = \sigma_3 + (\sigma_1 - \sigma_3)cos^2\psi \quad (1)$$

$$\tau = (\sigma_1 - \sigma_3)\sin\psi\cos\psi \quad (2)$$

where σ_1 is the axial stress, σ_3 is the confining stress, and the sampling frequency is 10 Hz; σ_1-σ_3 are the deviatoric stresses measured directly by the pressure measuring element in the vessel; ψ is the inclination angle of the fracture relative to the core axis. Since the pore pressure interacts with the positive stress on the fracture surface, the effective normal stress is calculated as:

$$\sigma_{eff} = \sigma_n - P_{pore} \quad (3)$$

During fluid injection, the normal and shear stresses on the fracture are maintained by controlling the axial and peripheral pressures through a servo system. The shear displacement along the fracture (d_{slip}) is calculated as:

$$d_{slip} = \frac{d_l}{\cos\psi} \quad (4)$$

where d_l is the load point displacement, measured in a triaxial fault shear permeability test equipment vessel. The evolution of permeability (k) at rock fractures was calculated based on the cubic law:

$$k = \frac{e_h^2}{12} \quad (5)$$

where e_h is the fracture aperture (m) at the fracture surface. In this study, it is considered that the fluid flows only at the fracture surface thus leading to induced shear slip, and the fracture aperture is calculated as:

$$e_h = \left[-\frac{12\eta LQ}{w(P_{in} - P_{out})}\right]^{\frac{1}{3}} \quad (6)$$

where Q is the steady-state flow rate (m^3/s), P_{in}-P_{out} (ΔP) is the pressure difference, and η is the fluid viscosity (1.002×10^{-3} Pa-sec for distilled water at 20°C).

3 Results

3.1 Injection-induced slip behaviour is controlled by vary initial critical stress state of the fault

The initial stress state of faults governs the pattern and intensity of injection-induced fault reactivation. Under constant confining pressure σ_3=11 MPa and injection pressure p=1 MPa, granite specimens containing smooth interfaces inclined at 30° relative to the core axis were subjected to axial loading. This led to a progressive increase in resolved shear stress with slip until it reached 92%/88%/84%/80% of the peak shear strength τss. In the second stage, we maintained a fixed axial piston position to ensure zero displacement conditions at both ends of the granite specimens. Fluid injection then commenced at a rate of 1 MPa/min, increasing from 1 MPa to 10 MPa. Due to the high permeability of the fracture surfaces, fluid pressure rapidly reached millisecond-scale equilibrium within the specimens. During fluid injection, both representative sample sets exhibited distinct dynamic slip events throughout the pressure ramp, characterized by rapid shear stress decline and abrupt displacement increase.

The dependence of injection-induced seismicity on the initial stress state of faults is summarized visually in Fig.1. The stress drop decreases from 1.38 MPa at 92% critical stress to 0.84 MPa at 80% critical stress. The injection pressure required to induce instability is inversely proportional to the fault's initial stress state. Faults with a critical stress of 92% slip when injection pressure to 4.1~4.7 MPa, whereas faults with an initial stress state of 80% require a greater injection value to slip.

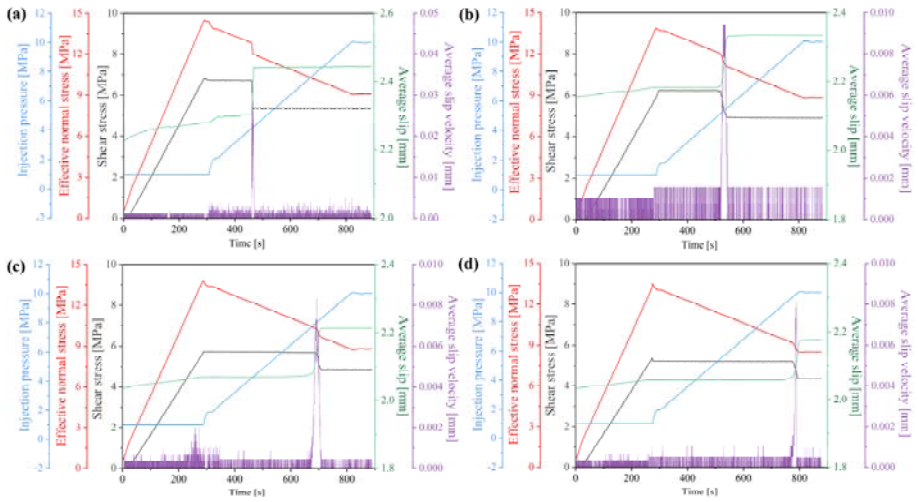


Fig. 1 Mechanical behavior of injection - induced fault slip under vary critical stress states. (a), (b), (c), (d) shows the mechanical behavior across 92% / 88% / 84% / 80% critical stress states.

To sum up, our results jointly depict the continuous spectrum of the fault slip mode controlled by the initial stress state. There is a common trend that faults closer to the critical instability state exhibit more intense seismic slip instability, characterized by greater stress drop, faster sliding speed, earlier instability occurrence time and lower trigger pressure. In contrast, faults preloaded to lower stress levels exhibit progressive quasi-static sliding responses.

3.2 Characteristics of injection-induced failure mode

Fig.2 illustrates the AE response characteristics of injection-induced fault slip. Results indicate that the AE response intensifies as the initial stress state of smooth faults approaches critical instability (e.g., 92% τ_{ss}). For smooth faults, the maximum AE energy increased significantly from 109.25 mV*ms to 139.83 mV*ms as the initial stress rose from 80% to 92%, while the ring-down counts (RDC) also increased from 28 to 39. This systematic increase in AE energy reveals that fault reactivation under higher stress states generates higher-energy microfracture activity, indicating a more violent brittle failure process. Furthermore, the initial stress state significantly influences the temporal characteristics of instability events. We found that faults closer to critical instability exhibited shorter failure durations, manifested as AE signals concentrated within a narrower time window. This indicates that fault instability under high stress states exhibits greater suddenness and faster fracture propagation speeds.

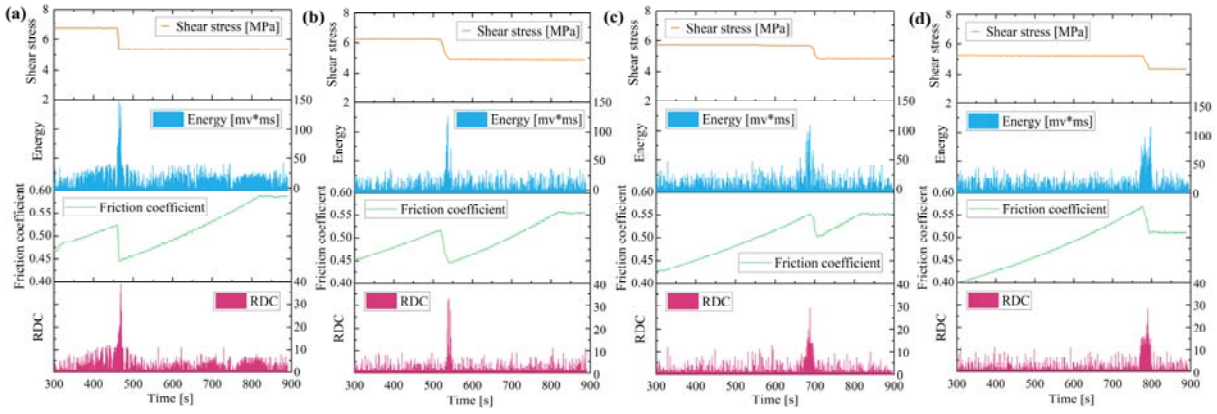


Fig. 2 AE characteristics of injection-induced fault slip process. (a), (b), (c), (d) shows the mechanical behavior across 92% / 88% / 84% / 80% critical stress states

The most direct mechanism for injection-induced fault slip is the reduction in closure pressure due to increased pore pressure. Once reactivated, the fault's frictional response may lead to stable slip or unstable slip. In this study, smooth faults exhibited dynamic slip during injection-induced failure, with the friction coefficient abruptly decreasing from the static to kinetic value.

4 Discussion

When fault instability occurs, permeability exhibits rapid growth (Fig.3). Sustained diffusion under high pore pressure reactivates faults previously at critical stress states. Dynamic slip events cause rock fracture expansion, facilitating fluid flow through fracture pathways and thereby increasing permeability. We estimated the *b*-value during the experiment using the maximum likelihood method and calculated its standard error σ(*b*). The data shows the temporal trend of *b*-value during the experiment, with black error bars representing the standard error. The abrupt decrease in b-value corresponds to a sudden increase in permeability, dropping from 1.42±0.1 during background events to 0.78±0.1 during slip events. Notably, the continuous decline in the b-value exhibited precursor characteristics earlier than the abrupt change in permeability. This advance time systematically increased with decreasing initial critical stress state, extending from 4 seconds at 92% critical stress to 15 seconds at 80% critical stress. Furthermore, faults closer to failure exhibited greater increases in permeability during slip events. Following slip events, the experimental system entered a new stable state where permeability stabilized. Cracks reached a new equilibrium post-slip, and the stabilization of flow pathways eliminated severe permeability fluctuations.

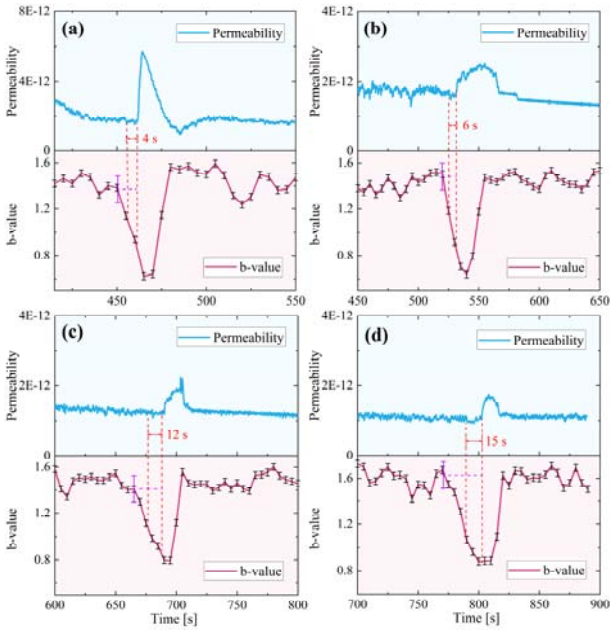


Fig. 3 Permeability and *b*-value characteristics of injection-induced fault slip process. (a), (b), (c), (d) shows the mechanical behavior across 92% / 88% / 84% / 80% critical stress states.

Through meticulous experimental design, we systematically monitored the dynamic changes of permeability and b value during the microseismic activity stage. The experimental results reveal the connection between fluid injection and fault slip behavior under vary stress states. With the continuous injection of fluid, the fluid seeps through the fissures and eventually enters the slip zone, inducing the slip of the fault.

5 Conclusions

We conducted triaxial shear permeability tests on smooth-jointed granite samples to understand the mechanism of injection-induced seismicity under different initial stress states of faults. We reveal that the initial critical stress state of faults exerts primary control over seismic activity. During injection operations, the injection pressure rapidly increases before stabilizing at a constant level for fluid injection. Slip events occur abruptly, reflecting the sudden and destructive nature of injection-induced unstable slip. We found that faults closer to critical instability exhibited shorter failure durations, manifested as AE signals concentrated within a narrower time window. Concurrently, shear stress variations demonstrate fluid injection's impact on fault stability, with pore pressure increases initially causing a slight decrease in shear stress and a rapid drop during slip events.

References

Ellsworth, W.L. (2013). Injection-induced earthquakes. Science 341 (6142), 1225942.

Guglielmi, Y., Cappa, F., Avouac, J.-P., Henry, P., Elsworth, D. (2015). Seismicity triggered by fluid injection–induced aseismic slip. Science 348 (6240), 1224–1226.

Shapiro, S.A., Krüger, O.S., Dinske, C., Langenbruch, C. (2011). Magnitudes of induced earthquakes and geometric scales of fluid-stimulated rock volumes. Geophysics 76 (6), WC55–WC63.

Elsworth, D., Spiers, C.J., Niemeijer, A.R. (2016). Understanding induced seismicity. Science 354 (6318), 1380–1381.

Woo, J.U., Kim, M., Sheen, D.H., Kang, T.S., Rhie, J., Grigoli, F., Ellsworth, W.L., Giardini, D. (2019). An in-depth seismological analysis revealing a causal link between the 2017 Mw 5.5 Pohang earthquake and EGS project. J. Geophys. Res. 124, 13060–13078.

Passelègue, F. X., Brantut, N. & Mitchell, T. M. (2018). Fault reactivation by fluid injection: controls from stress state and injection rate. Geophys. Res. Lett. 45, 837–846.

McGarr, A. (2014). Maximum magnitude earthquakes induced by fluid injection. J. Geophys. Res.: Solid Earth 119, 1008–1019.

Galis, M., Ampuero, J.P., Mai, P.M., Cappa, F. (2017). Induced seismicity provides insight into why earthquake ruptures stop. Sci. Adv. 3 (12), eaap7528.

Li, Z., Elsworth, D., Wang, C. et al. 2021. Constraining maximum event magnitude during injection-triggered seismicity. Nat Commun 12, 1528. https://doi.org/10.1038/s41467-020-20700-4.

Gutenberg B, Richter C F. (1944). Frequency of earthquakes in California. Bulletin of the Seismological Society of America, 34(4): 185-188.

Tormann, T. et al. (2015). Randomness of megathrust earthquakes implied by rapid stress recovery after the Japan earthquake. Nat. Geosci. 8, 152–158.

Application of DeepLabV3+ Model in Metro Tunnel Lining Crack Detection

Z.T. Pan,
College of Safety and Environmental Engineering, Shandong University of Science and Technology, Qingdao, China
PanZT1001@163.com

X.P. Zhang
State Key Laboratory of Disaster Prevention and Ecology Protection in Open-pit Coal Mines, Shandong University of Science and Technology, Qingdao, China

Y.J. Jiang
School of Engineering, Nagasaki University, 1-14 Bunkyo-machi, Nagasaki, Japan

Abstract

Detection of tunnel lining defects is an important part of tunnel maintenance. Manual inspection methods for tunnels are often inefficient and difficult to adapt to large-scale inspection tasks within limited maintenance time. In response to the aforementioned limitations, an automatic detection method tailored for metro tunnel linings and grounded in deep learning is developed. The Metro Tunnel Defect Detection System (MTDDS) developed in this study can capture high-resolution lining surface images with a resolution of 0.2 mm/pixel, and its maximum detection speed reaches 20 km/h. Furthermore, this paper presents the EDeepLab model to realize the detection and segmentation of defect images. Experimental comparisons conducted on the self-constructed dataset demonstrate that the model achieves a mean intersection over union (mIoU) of 84.77%, a class mean pixel accuracy (mPA) of 94.96%, and a frames per second (FPS) of 18.52. Field tests based on the proposed method confirm that the algorithm delivers more stable segmentation results for tunnel lining defect detection. This study provides a high-efficiency, high-precision automatic solution for tunnel lining defect detection; the MTDDS and EDeepLab model outperform traditional manual inspection in both speed and accuracy, offering reliable technical support for intelligent tunnel maintenance and structural safety assessment in engineering practice.

Keywords

Tunnel lining, Deep learning, Surface crack, DeepLabV3+.

1 Introduction

Infrastructure construction, including tunnels and underground engineering, has undergone rapid progress worldwide. As a result, the importance of tunnel maintenance has gained significant prominence (Song et al., 2024). Various issues can arise in tunnel linings due to complex environmental conditions such as geological variations, surrounding rock pressure, differential settlement, hydrological conditions, and temperature changes (Deng et al., 2022; Shim, 2024). Crack disease is one of the preconditions to facilitate other diseases, so detecting crack disease is the primary step for providing a precise assessment of the tunnel lining damage status.

Conventional manual visual inspection remains the predominant approach for detecting structural deterioration in tunnels (Zhou et al., 2023). However, those methods are often subjective with low accuracy, resulting in significant discrepancies in inspection quality among different inspectors, especially given the limited timeframe. These limitations underscore the need for developing automatic inspection systems. Consequently, numerous mobile tunnel inspection systems (MTISs) have come into existence, incorporating cameras, lasers, sonar, and ground-penetrating radar into mechanical, electronic, and/or robotic platforms (Huang et al., 2024).

Classical image processing algorithms, such as the threshold algorithm, filtering algorithm, mathematical morphology image processing algorithm, and region growing algorithm, have been used for image segmentation (Gong et al., 2021). However, these algorithms are limited by noise and the complexity of disease images, making it challenging to achieve clear segmentation of the affected areas. In recent years, deep convolutional neural networks (DCNNs) (Rafiei & Adeli, 2016; Rafiei & Adeli, 2018; Wang et al., 2020) as a deep learning method for computer vision have emerged as a core research focus in computer vision due to their powerful feature extraction capabilities. Unlike traditional algorithms, DCNNs employ an end-to-end feature learning approach without the need for manual pre-defined feature operators. They autonomously handle parameters through the network and effectively process complex information (Bang et al., 2019; Yu et al., 2023; Ronneberger et al., 2015). DCNNs can perform multi-level image processing, converting low-dimensional data into high-dimensional data, and achieving pixel-level segmentation through decoders or classifiers by utilizing deeper networks.

Aiming at the above deficiencies, this study puts forward a high-precision segmentation model. First, a deep learning-based framework named EDeepLab is introduced based DeepLabV3+ to segment cracks on tunnel lining surfaces. Then, a lighter structure optimizing the original feature extraction network is adopted to solve the problem of data redundancy and to reduce the memory space of the model. Meanwhile, multiple attention mechanisms are introduced to enhance the model's sensitivity to areas with tiny cracks and cracks interfered by noise, leading to better performance of defect detection and segmentation. At last, ablation experiments, effectiveness experiments and generalization experiments on the constructed surface crack datasets are conducted to verify the validity of the EDeepLab model.

2 Overall methodology

2.1 Framework of inspection methodology

Figure 1 presents a comprehensive overview of the automated metro tunnel defect detection methodology, which is comprised of three distinct stages. First, the MTDDS captures images of the tunnel lining surface. Then, a CNN-based classifier filters the collected data to isolate crack images, thereby constructing a defect dataset. Finally, a U-shaped convolutional network, DSC_CrackU, which incorporates DSConv, is employed to achieve semantic segmentation of the identified defects.

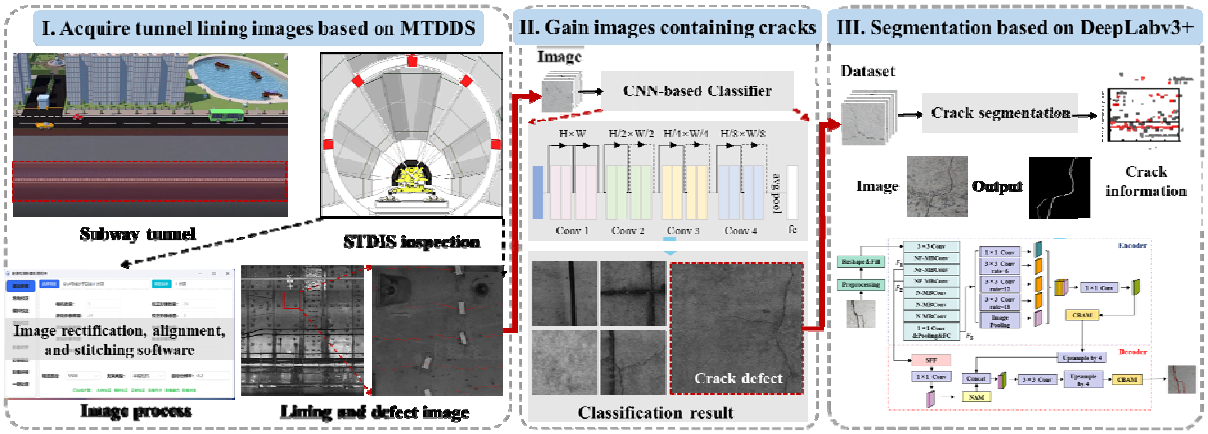


Fig. 1 Framework of automatic metro tunnel crack inspection methodology.

2.2 Metro tunnel disease detection equipment

The MTDDS developed here uses modular assembly with a total weight of about 100 kg. It possesses several main modules, including the CCD camera, light source, mobile detection vehicle and control platform. The CCD camera module is composed of packaged CCD cameras, which can be controlled by remote access to the internal industrial computer. The image captured by the 8K high-frequency color linear array camera acquires distinct details, which can help realize the color restoration of the tunnel surface under dynamic operation. The cameras can capture images with a resolution of 0.2 mm/pixel at speeds of up to 20 km/h. High-quality images captured with CCD cameras require precise lighting. To meet these requirements, the MTDDS incorporates LED light sources into the camera module, providing the necessary illumination for tunnel environments. At a distance of 4,000 mm, the lighting achieves an intensity of up to 17,300 Lux, with a spot size of 2,800 mm×100 mm. The vehicle platform weighs 47 kg and can support additional loads of approximately 55 kg. Operators can monitor essential operational conditions via a control panel and manage the operations, including starting, navigating, and shutting down, within a 30m rang using a remote control. MTDDS structure. Table 1 compares the main parameters of MTDDS with those of previous detection devices.

Table 1. Key parameters of various equipment compared to MTDDS.

System	Cramera	Power supply	Portability	Precision (mm)	Movement speed (km/h)
Tunnelings	Laser	Truck	Part	1	30
Ukai	Line scan	Truck	No	0.8	10 (Max 30)
tCrack	CCD	Trailer	Part	0.3	2.5
MTI-100	CCD	Lithium battery	Modularity	0.3	5 (Max 8.4)
MTDDS*	CCD	Lithium battery	Modularity	0.2	5 (Max 20)

3 Proposed crack extraction method DeepLabV3+

This section will introduce the details of the EDeepLab model. Figure 2 shows the structure of EDeepLab.

Resize the preprocessed image to a size of 512×512, and then feed it into the optimized EfficientNetV2 for feature extraction. Three feature layers, F_1, F_2 and F_3 with different depth information are output at the front, middle, and back respectively, and their sizes are 128×128×48, 64×64×64, and 32×32×272. The shallower feature layers F_1 and F_2 are transmitted to the decoder, while the feature layer F_3 is input into ASPP for feature extraction at different scales.

In the decoding part, first, the feature layers F_1 and F_2 are fused using the SFF (Shallow Feature Fusion) module. Then, the NAM (Normalization-based Attention Module) is used to extract local details of crack diseases from the feature layer fused by SFF, and CBAM (Convolutional Block Attention Module) is used to extract the global semantic information of cracks from the feature layer processed by ASPP. At the end of the model, CBAM is added to adjust and enhance the semantic information of cracks and reduce the interference of background noise.

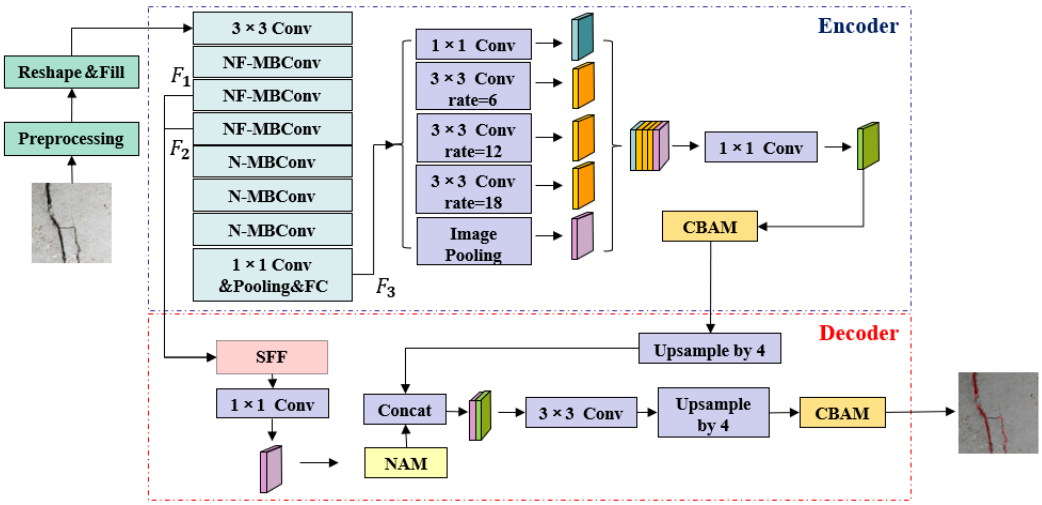


Fig. 2 Structure of EDeepLab.

Efficient NetV2 has made a series of improvements to address the main issues in V1, such as the slow computation speed caused by the use of Depthwise convolutions in shallow networks. Firstly, on the basis of MBConv, it introduces Fused-MBConv, replacing the original 1×1 convolution and depthwise convolution with a single 3×3 convolution. This solves the problem of slow speed when using depthwise convolution in shallow networks. Additionally, it adopts the training-aware neural architecture search (training-aware NAS) technology to obtain the optimal network structure algorithm, and adjusts to get the optimal Fused-MBConv and MBConv structures.

First, the input image undergoes 3×3 standard convolution to obtain a feature map F. After feature map F is processed by 3×3 convolution, it is fed into the NAM module for the extraction of sensitive information from shallow features. After extraction, the resulting feature map goes through 1×1 convolution and a Dropout layer, and then is added to the original feature map F to obtain the output map F_out. This entire process constitutes NF-MBConv. After repeating this operation three times, three rounds of N-MBConv are performed sequentially. Finally, 1×1 convolution, pooling, and fully connected operations are carried out.

4 Experiment and results

4.1 Environment configuration

To assess the accuracy of the lining crack segmentation algorithm, the current study primarily focuses on training EDeepLab model. The improved model is then compared with the original DeepLabV3+, U-Net, ResNet, and FCN models. The experimental algorithm is implemented using Python 3.8 programming language on the PyCharm platform. The experimental system used is Windows 11, equipped with an 11th Gen Intel(R) Core (TM) i7-11700 processor, 64 GB of running memory, and an NVIDIA RTX A4000 GPU.

4.2 Metro-Tunnel Crack dataset

To create a high-resolution Metro-Tunnel Crack dataset with ample samples and comprehensive data on tunnel lining surface diseases, the current study primarily focuses on metro shield tunnels. After collecting images, they were carefully examined and combined, resulting in a total of 580 lining crack images. These images have a pixel size of 512×512 and possess diverse backgrounds. The backgrounds include variations in lighting, water stains, pipelines, spalling, scratches, and other forms of noise interference. This assortment of images accurately represents real-life tunnel scenarios and guarantees the robustness of the trained model.

4.3 Effective experiment for EdeepLab

EDeepLab is trained and compared with four classical models: FCN, ResNet, U-Net, and the original DeeplabV3+, using the Metro-tunnel Crack dataset to evaluate its effectiveness. Result illustrates the convergence of each model, which occurs after 300 training epochs. The final losses for each model are as follows: EDeepLab (0.10), DeepLabV3+ (0.15), U-Net (0.12), ResNet (0.16), and FCN (0.18). Notably, EDeepLab demonstrates a superior convergence effect and velocity.

Table 2 presents the segmentation performance of the different models. EDeepLab achieves the highest F1 score of 0.89. The mIoU of the proposed model surpasses those of U-Net and the original DeeplabV3+ by 1.46%, and 2.50% respectively. Additionally, the mPA of the proposed model exceeds those of U-Net and the original DeeplabV3+ by 1.31%, and 1.22% respectively. The FPS of the proposed model is 18.52f/s, which is 7.12f/s higher than that of the original DeeplabV3+. In terms of model size, FCN has 72.45M Parameters, which is 27.35M less than EDeepLab. However, its accuracy is significantly lower than those of other models. Therefore, it can be concluded that EDeepLab outperforms other models in all aspects of performance. It enables lightweight and efficient disease feature extraction for tiny cracks on the lining surface of subway tunnels.

Table 2. Segmentation performance of different models on Metro-tunnel Crack dataset (the symbol of '↓&↑' is the contrast between EDeepLab and original DeepLabV3+)

Test No.	Model	F_1	mIoU(%)	mPA(%)	FPS(f/s)	Parameters(M)
1	FCN	0.76	73.25	86.22	13.14	72.45
2	ResNet	0.85	81.93	91.93	13.71	167.59
3	U-Net	0.87	83.31	93.65	8.41	119.72
4	DeepLabv3+	0.86	82.27	93.74	11.40	144.45
5	EDeepLab	0.89↑0.03	84.77↑2.50	94.96↑1.22	18.52↑7.12	99.80↓44.65

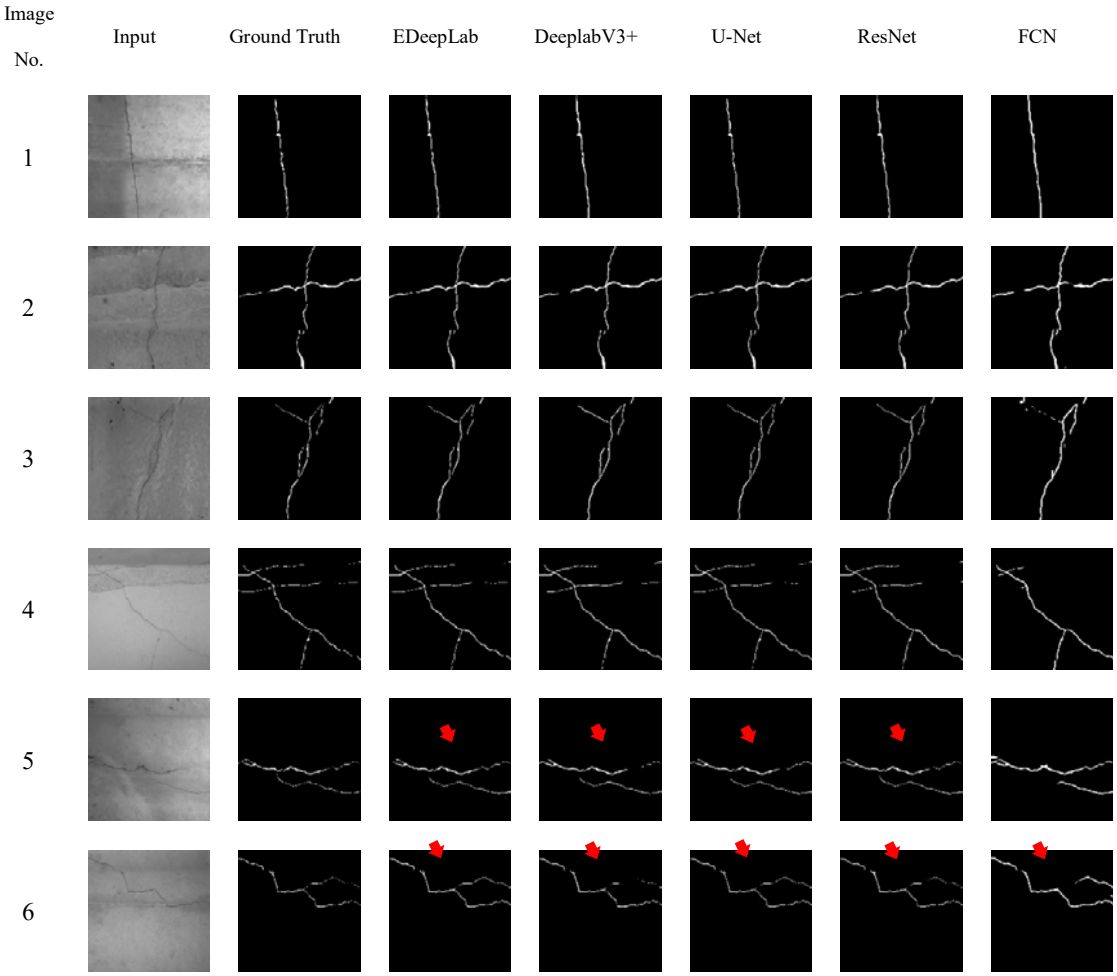


Fig. 3 Detection results of Metro-tunnel Crack dataset (the area marked by arrows is a small lining crack).

For quantitatively illustrating the fine performance of tiny cracks of the proposed model, cracks with an average width of less than 5 pixels and length for maximum crack width of greater than 8 pixels or less than 10% of the whole crack length are regarded as tiny cracks. There are 6 pieces of tiny crack images without noise interference, which are representative images selected from the Metro-tunnel Crack dataset. The average width is less than 4 pixels, and more than 95% crack width of each crack is less than 8 pixels, which fits the pre-defined criteria for a tiny crack. Figure 3 presents the segmentation results of different models, providing a more intuitive insight into their respective

segmentation performance. For images containing identifiable target cracks, each model is generally able to segment the crack images. However, in Image No.5 and Image No.6 of Figure 3, where it is challenging to distinguish the crack, EDeepLab also shows a better performance. This is attributed to the SSF and multiple attention mechanisms employed by EDeepLab during training, which enhance the extraction of tiny targets.

5 Conclusion

Over time, tunnel linings are prone to deterioration due to the formation of cracks and other distresses. The purpose of this study is to address the limitations of current tunnel defect detection methods by developing a comprehensive detection system that includes front-end image acquisition, crack segmentation, and identification. This contributes to the effective maintenance and reinforcement of tunnel systems. The innovations of this study are as follows:

MTDDS is designed to improve the efficiency of lining crack detection. The maximum detection speed of this device is 20 km/h, with an image resolution of 0.2 mm/pixel. It adopts a modular assembly method, which enables easy setup and operation; its total weight is approximately 100 kg, ensuring high portability on the track.

Based on the original DeeplabV3+ model, the EDeepLab model achieves model lightweighting by replacing the backbone network and enhances segmentation accuracy by adding multiple attention mechanisms. When tested on the constructed Metro-tunnels Cracks dataset, the EDeepLab model achieves an mIoU of 84.77%, an mPA of 94.96%, and an FPS of 18.52 f/s.

References

Bang, S. Park, S. Kim, H. & Kim, H. (2019)Encoder‒decoder network for pixel‐level road crack detection in black‐box images. Computer‐Aided Civil and Infrastructure Engineering 34(8), 713-727.

Deng, J. Singh, A. Zhou, Y. Lu, Y. & Lee, V. C. S. 2022. Review on computer vision-based crack detection and quantification methodologies for civil structures. Construction and Building Materials 356, 129238.

Gong, Q. Zhu, L. Wang, Y. & Yu, Z. (2021) Automatic subway tunnel crack detection system based on line scan camera. Structural Control and Health Monitoring 28(8), e2776.

Huang, J. Yang, X. Zhou, F. Li, X. Zhou, B. Lu, S. & Slob, E. (2024) A deep learning framework based on improved self‐supervised learning for ground‐penetrating radar tunnel lining inspection. Computer‐Aided Civil and Infrastructure Engineering 39(6), 814-833.

Rafiei, M. H. & Adeli, H. (2016) A novel machine learning model for estimation of sale prices of real estate units. Journal of Construction Engineering and Management 142(2), 04015066.

Rafiei, M. H. & Adeli, H. (2018) Novel machine learning model for construction cost estimation taking into account economic variables and indices. Journal of Construction Engineering and Management 144(12), 04018106.

Ronneberger, O. Fischer, P. & Brox, T. (2015) October. U-net: Convolutional networks for biomedical image segmentation. In International Conference on Medical image computing and computer-assisted intervention pp. 234-241. Cham: Springer international publishing.

Shim, S. (2024) Self‐training approach for crack detection using synthesized crack images based on conditional generative adversarial network. Computer‐Aided Civil and Infrastructure Engineering 39(7), 1019-1041.

Song, G. Huang, Y. Wang, Z. Feng, Q. Jia, F. & Wang, S. (2024) Review of Railway Operation Tunnel Inspection System and Condition Assessment Method. Acta PolytechnicaHungarica 21(1), 259-279.

Wang, Q. Wu, B. Zhu, P. Li, P. Zuo, W. & Hu, Q. (2020) ECA-Net: Efficient channel attention for deep convolutional neural networks. In Proceedings of the IEEE/CVF conference on computer vision and pattern recognition pp. 11534-11542.

Yu, H. Sun, H. Tao, J. Qin, C. Xiao, D. Jin, Y. & Liu, C. (2023) A multi-stage data augmentation and AD-ResNet-based method for EPB utilization factor prediction. Automation in Construction 147, 104734.

Zhou, Z. Zhang, J. & Gong, C. (2023) Hybrid semantic segmentation for tunnel lining cracks based on Swin Transformer and convolutional neural network. Computer‐Aided Civil and Infrastructure Engineering, 38(17), 2491-2510.

Weathering impact on the long-term stability of weak rocks

B. Janevski
Civil Engineering Institute "Macedonia", Skopje, Macedonia
bojan.janevski@gim.mk
0000-0002-3767-5840

M. Jovanovski
University Ss. Cyril and Methodius, Skopje, Macedonia

Abstract

Weathering processes and prolonged atmospheric exposure significantly impact the mechanical properties of weak metamorphic rocks, notably compromising their structural integrity and increasing the risk of slope failure. This comprehensive study examines the impact of weathering on schists and phyllites along the A2 motorway in Macedonia. Methodologically, the research integrates detailed field surveys and slope stability assessments to quantify changes in key geotechnical parameters, including uniaxial compressive strength, the geological strength index, and the material constant, as functions of exposure duration.

The results demonstrate significant deterioration in strength characteristics attributable to progressive mineral decomposition, fissuring, and disintegration driven by climatic factors. Empirical data indicate that slopes subjected to prolonged weathering exhibit a higher incidence of shallow landslides and surface instabilities, which strongly correlate with reductions in strength parameters. Graphical models illustrate the temporal progression of strength degradation, providing valuable insights for predictive stability assessments.

The findings underscore the need to incorporate weathering effects into geotechnical design, especially for infrastructure projects with long service lives on weak rock foundations. An empirical relationship between exposure time and strength degradation is proposed. Recommendations include continuous monitoring and the integration of degradation factors into slope stability analyses to effectively mitigate geohazard risks.

Keywords

Long-term Stability, Slope Stability, Strength Degradation, Weak Rocks, Weathering.

1 Introduction

The stability of slopes in rock masses, especially in low-quality rock masses, is directly related to weathering, which has a negative impact through reduction in shear strength, acceleration of decomposition (especially in surface zones), and the creation of tension cracks. The intensity of rock weathering and its geochemical alteration influence shallow landslide occurrence in weak metamorphic rocks, establishing a link between weathering degree and slope failure susceptibility (Silwal et al. 2024). Weathering has been demonstrated to weaken rock mass structure and decrease slope safety factors in long-term stability analyses. Although weathering effects play a crucial role in determining slope stability, few researchers have investigated the effects of weathering, and the traditional analysis methods either overlook these factors or oversimplify them (Liu et al. 2024). Therefore, the alteration, i.e., the decomposition of the rock masses over time, as a result of the negative atmospheric influence, in the surface zones of the slopes, in the zone of the joint walls, but also generally at the level of the massif, should be taken into account, especially in weak rock masses, which are susceptible to these unfavourable processes.

There have been a number of studies related to weathering and slope stability. Berisavljevic et al. 2018 investigate the weathering-induced failures of the heterogeneous fissile rock mass consisting of sandstone and shale and propose a model aimed at addressing the delayed failure of cuts. Recent research has specifically addressed the degradation of schist rock masses due to climatic weathering cycles. Experimental evidence shows that dry–wet and freeze–thaw cycles significantly reduce the mechanical strength and alter the microstructure of schists, leading to increased porosity and reduced bearing capacity, which directly impacts the long-term stability of rock slopes under environmental loading (Jin et al. 2025). Similarly, investigations into combined weathering cycles demonstrate that these processes accelerate deterioration and strength losses in schist, emphasising the need to incorporate weathering effects into predictive slope stability models (Gao et al. 2025). Zhang et al. 2025 emphasise that weathering coupled with rainfall infiltration in weak interlayer rock slopes alters failure mechanisms and expands instability zones, highlighting the need for comprehensive stability assessment and mitigation planning.

Based on the above considerations, several excavated slopes are selected to evaluate the long-term stability through stability analyses. The findings indicate that slopes subjected to prolonged weathering show higher incidences of shallow landslides and surface instabilities, which correlate strongly with reductions in UCS and GSI values. Graphical models were developed to illustrate the temporal trends of strength degradation, providing valuable insights for predictive assessments.

The study underscores the importance of incorporating weathering effects into geotechnical design, especially for long-term infrastructure projects situated on weak rock masses. Recommendations emphasise the necessity for ongoing monitoring, proactive stabilisation measures, and the integration of degradation factors into slope stability analyses to mitigate potential geohazards effectively.

2 General characteristics of the analysed slopes

The study area encompasses a part of the A2 highway, specifically the Kicevo–Ohrid section (Fig. 1), currently under construction. The geological composition predominantly includes low-metamorphic Palaeozoic rocks, with phyllite as the dominant lithology, along with graphitic schists and quartz-sericite schists.

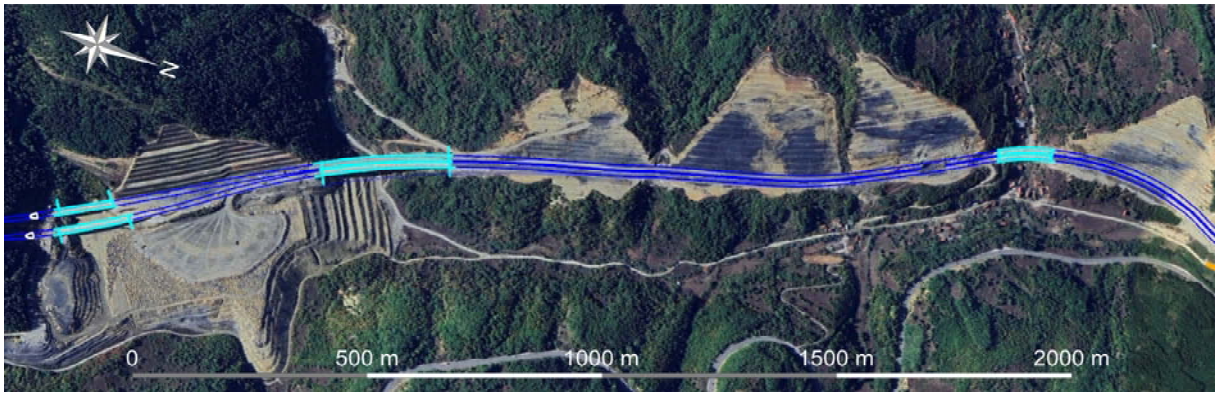


Fig. 1 Aerial view of a part of the A2 highway route, Section Kichevo–Ohrid.

The terrain is characterized by mountainous topography, which has historically experienced instability during construction phases. The rock masses are tectonically disturbed and susceptible to local instability, especially during prolonged or intense rainfall. During excavation, these rock masses are relatively solid, but after a certain time of exposure to atmospheric influence, they significantly lose their properties and soften, especially in the surface zones. Therefore, the assessment of slope stability must incorporate the progressive effects of weathering, especially in weak rock masses, to ensure long-term safety and performance. Given these site conditions, the methodology used to assess the slope stability is briefly explained.

3 Methodology

In this research, several cut slopes were selected (Fig. 2) which, after several months, processes of local instability started to appear with signs of intensification over time.



Fig. 2 Illustration of the selected slopes, demonstrating shallow failures primarily in surface zones attributable to weathering.

For each slope shown in Fig. 2asafety factor (Fs = 1,31–1,53) was calculated in the design phase, but after a certain period, instabilities and landslide processes were observed. Subsequent observations revealed progressive instability, attributed to reductions in shear strength and deformability due to atmospheric exposure.

The material properties adopted in the initial design stage correspond to moderately weathered rock-mass conditions identified during excavation. Laboratory testing and field rock mass classification were performed during the construction stage, before the development of significant atmospheric weathering effects on exposed slope surfaces. The rock masses were modelled using the generalized Hoek-Brown failure criterion. The Geological Strength Index (GSI) classification incorporated discontinuity conditions, blockiness, and surface conditions observed at the time of excavation. However, it did not explicitly account for long-term degradation caused by progressive weathering processes. Similarly, the laboratory uniaxial compressive strength (UCS) values were obtained from samples representing the intact-rock condition at the time of sampling, without accelerated-weathering treatment or durability testing. Therefore, the subsequent parameter reductions applied in the long-term stability analyses were intended to simulate the progressive deterioration of the exposed rock mass due to weathering effects occurring after excavation and prolonged atmospheric exposure. Namely, the UCS, GSI, and the material constant (m_i) are reduced to obtain the labile limit equilibrium at failure, i.e., Fs = 1,0. For simplification purposes and due to the limited availability of long-term degradation data, UCS, GSI, and m_i were reduced using the same proportional reduction factor to simulate progressive weathering-induced deterioration. This approach was adopted to evaluate the overall sensitivity of slope stability to weathering-induced degradation rather than to reproduce the exact deterioration mechanism of each parameter. The analysis incorporated the time elapsed since excavation, with the main parameters summarized inTable 1.

Table 1. Main characteristics of the analysed slopes and computed safety factors.

Slope ID	UCS [MPa]	GSI	m_i	Exposure to weathering	Sliding depth	Fs	Reduction to Fs = 1,0 [%]
a	5	17	5	12 months	2,5 m	1,34	17,9
b	10	23	6	22 months	3,0 m	1,43	21,8
c	4	17	5	14 months	3,0 m	1,31	17,5
d	12	27	6	17 months	5,5 m	1,46	20,1
e	15	30	7	8 months	2,5 m	1,34	14,7
f	10	25	6	11 months	3,5 m	1,31	17,1
g	8	23	6	5 months	4,5 m	1,33	15,2
h	3,5	15	5	26 months	2,0 m	1,53	23,2

The results indicate that in susceptible rock masses, strength parameters decrease progressively with increased exposure duration, leading to a corresponding decline in safety factors. Slopes with longer exposure times, such as slopes “b” and “h,” exhibited higher initial safety factors but also experienced greater percentage reductions, highlighting the significant weakening due to weathering.

These results indicate significant weakening of the slopes over time due to weathering. This is consistent with studies showing that weathering processes reduce rock strength and lower slope stability. These findings underscore the necessity of considering time-dependent strength degradation in long-term slope stability assessments, especially in weak, weathering-prone rocks.

4 Results

The graphical display of the dependence between the value of the safety factor and the exposure time of the slopes to atmospheric influences is shown in Fig. 3, and the dependence between the percentage reduction of the UCS, GSI, and m_i, concerning the exposure time, is shown in Fig. 4.Fig. 3 depicts the relationship between safety factor and exposure time, illustrating a clear downward trend as exposure increases. Fig. 4 presents the percentage reduction of key parameters (UCS, GSI, mi) as functions of exposure duration, highlighting the progressive weakening of rock masses due to weathering. The trend lines suggest that the strength degradation can be approximated by empirical equations, facilitating predictive modeling of long-term stability. It should be emphasized that the adopted reduction factors represent post-excavation degradation effects and are therefore additional to the initial geotechnical characterization performed during the design stage.

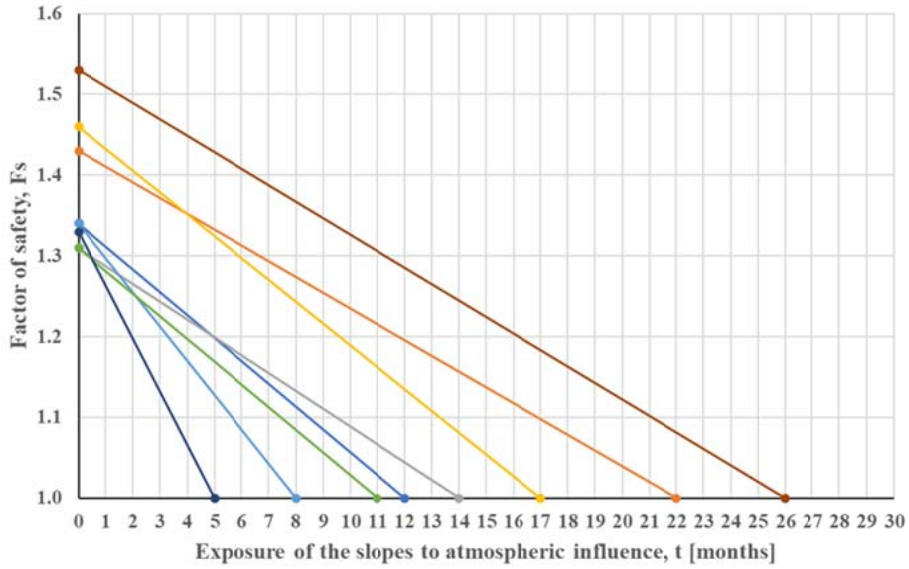


Fig. 3 Graphical dependence between the safety factor and the exposure time of the analysed cuts.

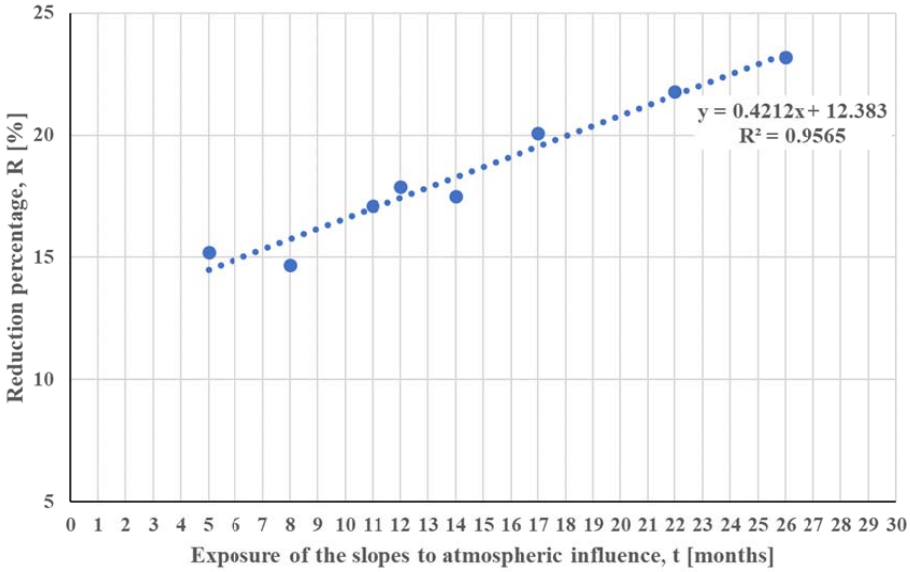


Fig. 4 Graphical dependence between the exposure time and the reduction percentage of the parameters (UCS, GSI, and m_i).

Based on these empirical trends, an equation (see Eq. 1) is obtained by linear regression of the empirical data shown in Fig. 4 to estimate the reduction factor (R) as a function of exposure time in months (t), providing a practical tool for long-term stability assessments and design considerations.

$$R = 0.4t + 12.4 \quad (1)$$

5 Conclusions

Prolonged weathering significantly diminishes the shear strength of weak rock slopes, accelerating surface degradation and increasing the likelihood of shallow failures. The rate of strength reduction correlates strongly with exposure duration, emphasizing the importance of long-term monitoring and adaptive design strategies. Analyses indicate that safety factors decrease over time under constant geometrical conditions, necessitating the incorporation of time-dependent weakening models into slope stability evaluations. The use of conservative strength parameters or empirical reduction equations is recommended to ensure long-term safety. The findings advocate for the revision of geotechnical design standards to explicitly account for aging and weathering effects. Future research should focus on advanced monitoring techniques and the development of predictive weathering models to improve the reliability of long-term slope stability assessments in weak rock environments.

References

Berisavljevic Z, Berisavljevic D, Rakic D, Radic Z (2018) Application of geological strength index for characterization of weathering-induced failures. Građevinar, 70 (2018) 10: 891-903. https://doi.org/10.14256/JCE.1876.2016

Gao J, Jin J, Wang D, Lei S, Lu J, Xiao H, Li J, Li H (2025) Mechanical and microstructural properties of schist exposed to freeze-thaw cycles, dry-wet cycles, and alternating actions. International Journal of Mining Science and Technology 35 (2025) 783-800. https://doi.org/10.1016/j.ijmst.2025.04.003

HasanMFR, Frastika MY, Agung PAM, Susilo A, Suryo EA, Zaika Y, Juwono AM, Zulaikah S (2024) Influence of rock weathering and saturation on compressive strength and slope stability: A uniaxial test analysis. International Journal of Safety and Security Engineering. Vol. 14, No. 1, pp. 145-153. https://doi.org/10.18280/ijsse.140114

Liu W, Sheng G, Kang X, Yang M, Li D, Wu S (2024) Slope Stability Analysis of Open-Pit Mine Considering Weathering Effects. Applied Sciences 2024, 14, 8449. https://doi.org/10.3390/app14188449

Janevski B (2025) Integral methodology for slope instability risk assessment in weak rock masses. Dissertation at Ss. Cyril and Methodius University, Skopje, Macedonia.

Jin J, Wang D, Lu J, Yin L, Xiao H, Li J (2025) Effects of dry-wet and freeze-thaw cycles on the mechanical properties and microstructure of quartz schist. Results in Engineering 27 (2025) 105770. https://doi.org/10.1016/j.rineng.2025.105770

Psarropoulos PN, Makrakis N, Tsompanakis Y (2024) Climate Change Impact on the Stability of Soil Slopes from a Hydrological and Geotechnical Perspective. GeoHazards 2024, 5(4), pp. 1190-1206.https://doi.org/10.3390/geohazards5040056

Silwal BR, Gyawali BR, Yoshida K (2024) Geochemical and mineralogical analysis of low-grade metamorphic rocks and their response to shallow landslide occurrence in Central Nepal. Geoenvironmental Disasters (2024) 11:37. https://doi.org/10.1186/s40677-024-00301-9

Zhang S, Zhu G, Xu C, Ma J, Sun Z (2025) Stability influence of weak interlayer rock slope under rainfall. Frontiers in Earth Science. 13:1564077. https://doi.org/10.3389/feart.2025.1564077

Risk management and Flexible Foundation Design for electricity tower construction in the Swiss Alps

N. Maca
Ischebeck Titan Polska, Kraków, Poland,
natalia.maca@titan.com.pl
0009-0001-2792-0830

Y. Husain
Friedr. Ischebeck GmbH, Ennepetal, Germany
0009-0000-7953-1610

Abstract

Electricity tower construction for a new 380 kV transmission line was proposed in Valais, Switzerland. The line followed steep elevations in the Alps where most of the towers were located. The project posed critical risks that needed to be actively addressed: 1) a constrained construction window in the summer months (May to September) 2) aggressive sulphate rich ground which necessitated the highest possible corrosion protection 3) non-uniform ground conditions and elevations across the line 4) logistics limited by the available transportation methods of machines. The paper describes an active and early risk management regimen adopted jointly by the Contractor, Designer & Supplier which resulted in a successful project construction plan.

The risk management measures included: designing the foundations with additional safety factors in accordance with SIA (Swiss codes); having a unique design for each tower taking into account the loadings, ground conditions and elevations; using TITAN INOX grouted micropiles which are corrosion protection applicable in any condition; planning logistics with packaging machines and materials intended to be transported via helicopters. These measures resulted in a durable solution for the entire design life of the structures ensuring that the electricity supply to Switzerland would be uninterrupted by avoiding any future corrosion related failures.

Keywords

Risk management, Micropiles, Electricity tower foundations, Difficult access, High corrosive aggressivity, Stainless steel, INOX.

1 Historical Context and Introduction

Following the Fukushima nuclear accident in 2011 in Japan, many countries took note and rethought their energy and power policies internally. Switzerland, already having an inherent advantage in producing hydroelectric power due to experiencing high precipitation and the presence of Alps which cover 58% of the country's landmass, was amongst those countries which decided to wean off their existing nuclear sources of power and increase their production and supply of hydroelectric power. Five years later in 2016, this led to the creation of the Swiss Energy Strategy 2050 (Swiss Federal Assembly, 2016). The aim of the Strategy is to restructure the national energy system to achieve climate neutrality by 2050 and to increase the overall electricity production levels without disrupting existing supply routes.

To implement this strategy, significant new infrastructure and upgrading of dated power infrastructures was required. Many different programs were launched and one amongst these was Swissgrid's Strategic Grid 2025 (Swissgrid Ltd, 2015). One of the objectives of the Swissgrid Strategic Grid was to upgrade the existing 87km long electric corridor between Metteln and Ulrichen from 220 kV to 380 kV. This required the construction and installation of new higher capacity electricity transmission towers. While most of the construction along the entire 87 km line was carried out using conventional methods, a specific 8.8 km section between Mörel and Ernen (Fig. 1) characterized by helicopter-only access and highly aggressive ground conditions is the focus of this paper.

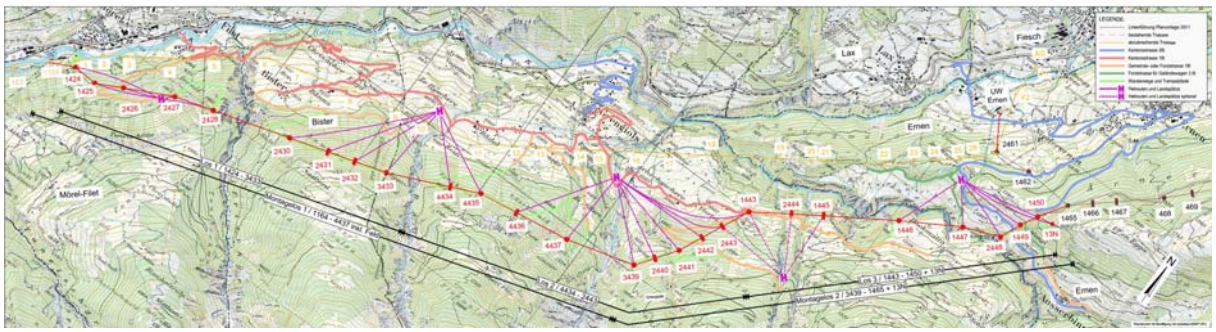


Fig. 1 Overview of the Mörel–Ernen 8.8 km line section with mast locations (Swissgrid Ltd, 2020).

In this context, risk management became a key driver for foundation design, requiring systematic identification and mitigation of geotechnical, environmental, and logistical uncertainties to ensure constructability and long-term performance in alpine conditions. The paper presents a case study of the design, construction and risk management system approach adopted for these foundations in a constrained environment.

2 Project Description and Site Conditions

The proposed construction comprised 27 new380kV transmission towers of various types(Swissgrid Ltd, 2020).Three of these masts, 2448, 1443 and 3439, were designed as extended Type A4 dead-end structures, carried the highest loads and underwent several redesign iterations during the project. Each tower consists of four legs, with each foundation leg designed to resist compression loads in the range of 800 to 4500 kN, tension loads up to 4500 kN, moments up to 3200kNm in both directions accompanied with varying lateral loads.

The principal design engineer was AFRY Schweiz AG (formerly Pöyry), Baden, responsible for both tower structural analysis and foundation design under project number 4590 with preliminary foundations designs especially concerning micropiles being prepared by Friedr. Ischebeck GmbH.

The elevations of these proposed towers ranged from around 900 to 1200m above sea level up on extremely remote access locations. The south-facing slope above the RhôneValley introduced geometrical challenges for the foundation construction, as even within a single mast all four legs were positioned at different elevations and founded in varying ground conditions. Fig. 2 shows an example of differing elevations of the legs of a single tower.

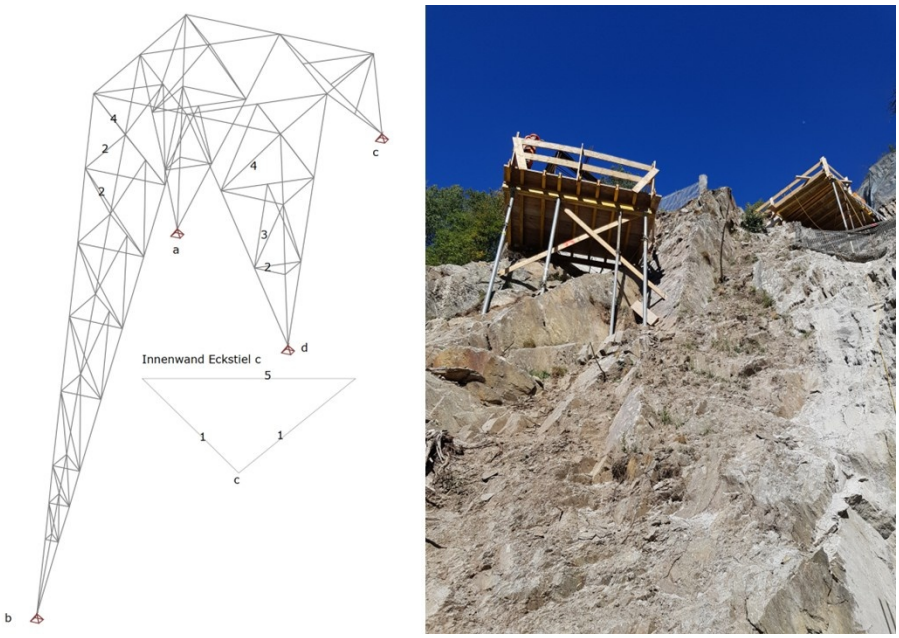


Fig. 2 An example of differing elevations of the legs of a single tower.

The general geological profile along the proposed construction corridor was of loose, weathered moraine and colluvial material overlying competent crystalline bedrock predominantly gneisses and related metamorphic rocks. However, the depth of the weathered rock from the surface varied significantly. The line was divided into 3 sections. In the lower sections (Construction Scopes 1 & 2) the loose strata presence is significant with a depthof up to a few metres. In contrast, in Construction Scope 3 which is the upper section, hard rock was encountered at or immediately below the surface. These highly variable geological conditions posed significant challenges for foundation pile construction, requiring adaptable installation methods.

Furthermore, soil chemical investigations carried out confirmed the presence of high amounts of sulphates in the groundwhich confirmed the exceptionally high corrosion risk for the foundation design acc. to SIA 267(SIA, 2013).

3 Foundation Design and Durability

The foundation design process for this project was highly iterative, with multiple revisions made to address risks that successively emerged during the design and construction phases, while maintaining high utilisation ratios and resulting in an efficient final design.

The engineering office stated that a sulphate attack on the foundation could occur which together with the required service life in accordance with SIA 267led to the classification of corrosion potential asLevel 3b, corresponding to very high corrosion exposure and the need for enhanced durability measures. In addition,challenging construction conditions limited the possible corrosion protection systems. For instance, it could not be ensured that fully prefabricated grout bodies with plastic-sheathed (DCP) micropiles would be transported into the Alps without damage. Additionally, solid bar with DCP systems with couplings (instead of fully prefabricated micropiles) do not comply with the Swiss requirements for double corrosion protection. Under these constraints, stainless steel hollow bars qualified as the only acceptable solution.

Consequently, the designer specified that the micropiles had to be manufactured from stainless steel, leading to the selection of TITAN 40/16 ($R_k = 530\ kN$) INOX, which satisfied both the durability requirements and the construction and schedule constraints. This became the standard micropile type for all foundations within the project scope. All designs were therefore based on this micropile type, with the number and arrangement of piles in each foundation cap determined so that the internal forces from the tower leg reactions remained within their resistance.

The design process made it essential to design each tower leg separately, since the 27 towers exhibited significant variation in loadings, overall ground elevations, individual leg elevations and ground conditions. Initiallythe loads from each tower leg were transferred into a selected micropile

configuration within the given pile cap footprint, and several combinations of vertical and inclined micropiles were proposed to optimize the solution. These calculations were performed in ENSOFT GROUP software with the pile caps modelled as rigid elements and the micropiles having a pinned connection to the pile caps which allow for rotation and displacement in all directions. The design verification was carried out in accordance with the Swiss geotechnical design standard SIA 267:2013 and across the different foundations, the minimal configuration required 6 micropiles per leg, while the maximal required 22 micropiles per leg.

However, this initial approach proved insufficient once the three-dimensional mountain geometry was considered.When the preliminary micropile layouts were superimposed on the actual terrain, it became evident that some of the piles would protrude outof the slope face and therefore could not be constructed in their proposed positions. Fig. 3 shows the initial micropiles arrangement proposal for a given tower location, with two micropiles marked with red circles protruding beyond the slope face. The terrain thus directly constrained the feasible pile orientations and necessitated further redesign to adjust the micropile layout so that all piles remained fully embedded within the mountain slope.

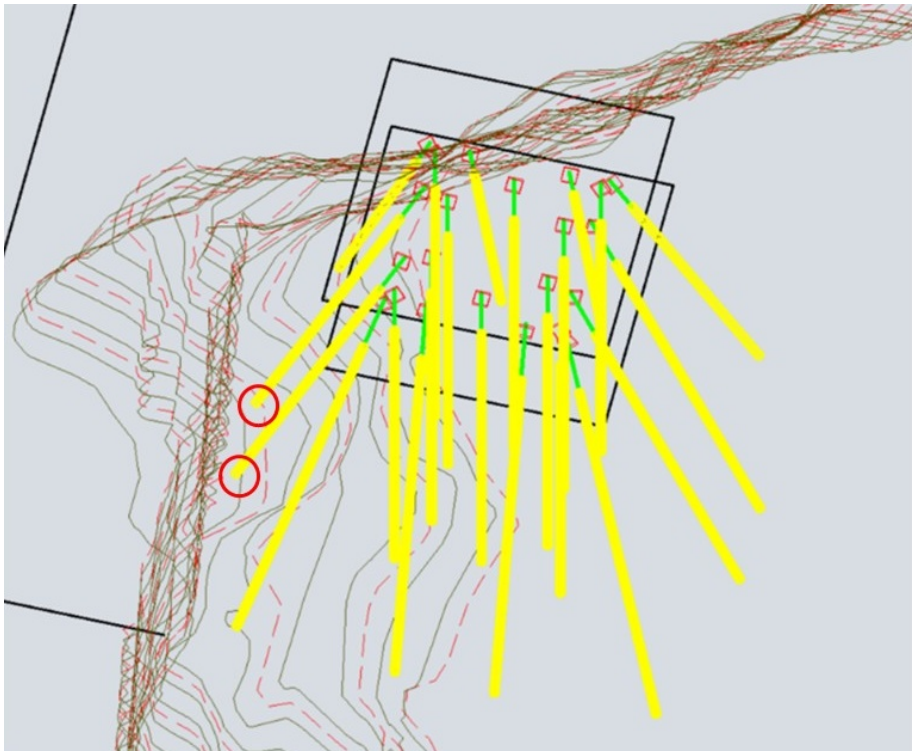


Fig. 3 Installed micropiles at one tower location prior to pile cap concreting.

4 Construction and Logistics

Construction issues governed several of the design choices of the project. The tight construction window meant that the principal designer could not afford to lose any time after mobilization and therefore required bulletproof forecasting of potential problems.

To manage the construction activities, the towers were first divided into 3 scopes: Construction Scope 1, 2 and 3. Construction Scopes 1 and 2 were on the lower elevations while Construction Scope 3 was situated on the higher scope. As access by road or cableway was not possible, all materials and equipment had to be transported exclusively by helicopter. Accordingly, threehelicopter landing spots were chosen, ensuring that the helicopters could be safely landed. Fig. 4 shows the location of one of the proposed masts along with the helicopter landing location.



Fig. 4 The construction site access by helicopter and installed micropiles at one tower location prior to pile cap concreting.

This logistical constraint also dictated the choice of the micropile system, as discussed previously. In addition, reliable and short delivery times for all materials were essential, further favouring the chosen micropile system over alternatives with significantly longer lead times. To mobilize effectively with helicopters, all materials and machineries were packed into max packing weights of 950 kg for the helicopter to be able to transport these without posing any safety concerns. In this context, INOX hollow-bar micropiles were selected over other DCP systems because their modular, segmental form and lower individual component weights were compatible with helicopter transport to the remote alpine sites.

There were also some modifications made to standard procedures: although TITAN INOX 40/16 is typically used as a self-drilled system, for this project the installation method was changed to installation in pre-bored holes to achieve higher efficiency in hard rock conditions, with the bars installed as central reinforcement. After installation, the micropiles were then grouted using pre-installed grouting hoses. The static tension load tests performed on the executed micropiles confirmed the quality of workmanship and demonstrated that the required design resistance was achieved. Fig. 4. shows the installed micropiles at one of the locations prior to pile cap concreting and Fig. 5 presents the assembly of steel lattice tower.



Fig. 5 Assembly of a one of lattice mast supported on micropile foundation in the Mörel–Ernen section.

5 Risk Identification and Risk Management

The project illustrates early, proactive risk identification and clear communication between all the parties involved in the construction, enabling the successful management of the risks outlined in the previous sections. It also demonstrates a high degree of flexibility in both foundation design and construction techniques, allowing the team to adapt to changing conditions and constraints as the project progressed. Building on this framework, the key risks and the corresponding mitigation measures adopted for weather, durability, design, logistics, and geological/installation aspects are summarised in Table 1.

Table 1. Overview of key project risks and mitigation measures.

Theme	Risk	Consequence	Measure
Weather	Limited construction period in summer months due to harsh weather during winters	Postponement of entire project for 6 – 9 months if not completed within the summer months	Early procurement & mobilization at site. The design and construction activities for various masts and areas were performed concurrently
Durability	High sulfate concentration in ground	Reducing durability and increasing the chance of corrosion of the installed micropile foundations	Stainless steel micropiles were chosen over other possible solutions which couldnot fulfil the logistical constraints ortechnicalrequirements
Design	Variation in loadings, ground elevations and geometry	Either unsafe or overdesigned micropile numbers and lengths	Customized, specific foundation design for all individual legs of all towers / masts
Geology / Installation	Hard crystalline rock at or near surface	Better drilling progress with down the hole hammerin the limited construction period	Adapt pre-bored holes with TITAN INOX 40/16 as central reinforcement
Logistics	No access	No possibility to reach the site and mobilize plant & equipment	Arrangements were made to fly all equipment via helicopters. The maximum weight of all packing units was restricted to 950 kg

6 Conclusion

The project demonstrated that early and systematic risk management, combined with flexible foundation design and construction, enabled the successful design and construction of critical energy infrastructures in highly constrained alpine conditions. Adapting both the micropile concept and the construction methods to logistics, geology and durability requirements proved essential for maintaining safety, constructability and schedule. In particular, the use of INOX hollow-bar micropiles provided a robust corrosionprotected solution that could be transported by helicopter and efficiently installed in hard rock, while still achieving the required design performance. The experience from the Mörel–Ernen section underlines the value of close collaboration between designer, contractor and supplier, and shows that such stainless-steel micropile systems can effectively address combined challenges of difficult access, variable ground and high corrosive aggressivity.

References

SIA (2013) *SIA 267:2013 – Geotechnik (Geotechnical Design)*. Zürich: SIA.

Swiss Federal Assembly (2016) *Federal Energy Act (Energiegesetz, EnG) of 30 September 2016*. Bern: Swiss Confederation. Online access: www.fedlex.admin.ch/eli/cc/2017/762/de.

Swissgrid Ltd (2015) *Grid 2025*. Laufenbur: Swissgrid. Online access: www.swissgrid.ch.

Swissgrid Ltd (2020) *Ulrichen - Eren- Mörel 380 kV Line – Foundation Design and Construction Documentation*. Internal project documentation. Swissgrid Ltd.

Reliability Limits of Rock Mass Classifications and a Zonal Approach for Reducing Design Risk

M. Tumara
Energoprojekt-Hidroinženjering, Belgrade, Serbia
milan.tumara@gmail.com
0009-0003-9488-1952

M. Petrović
Hidroenergo MVB, Belgrade, Serbia
petrovic.m.milutin@gmail.com

Abstract

Rock mass classification systems such as RMR, Q, and GSI have become indispensable tools in rock mechanics yet their empirical correlations are often applied with more confidence than warranted. These systems were developed for different purposes and rely on distinct input parameters, making value conversions between them frequently inadequate, as they fail to fully capture the complexity of actual geological conditions—especially in heterogeneous or tectonized rock masses.

This paper addresses the reliability limits of such approaches and introduces a practical method for reducing interpretative uncertainty through zoning of the rock mass based on the comparative application of multiple classification systems. The method compares classification results across intervals, identifies zones of agreement and divergence, and defines geotechnical domains through rule-based zoning.

This approach enables the identification and delineation of quasi-homogeneous geotechnical domains with similar engineering-geological and geotechnical characteristics, providing a more reliable basis for the assessment of deformability across different parts of a structure.

The method supports subsequent zoning tailored to excavation and support design and contributes to improved decision-making in complex geological environments such as deep mine shafts and dams.

Keywords

Rock mass classification, Rock Mass Zoning, Deformability Assessment, Risk Management.

1 Introduction

Rock mass zoning represents an important step in the site investigation phase for dams and underground structures. Through zoning, geotechnical domains are defined, for which deformability and strength parameters are assigned, forming the basis for the selection of support systems, numerical analyses, and stability assessment.

For this purpose, engineering practice relies on rock mass characterization, i.e., the assessment of rock mass quality, most commonly based on classification systems. Developed over different periods in accordance with the technological and scientific advancements of their time, numerous classification systems such as RMR, Q, and MRMR (Bieniawski 1989; Barton et al. 1974;Laubscher 1990)utilize partly similar and partly different input parameters. They evaluate rock mass properties, discontinuities, and the influence of groundwater in different ways, and they differ in scoring resolution and number of classes. Consequently, different systems applied to the same dataset may yield partially consistent or divergent results, reflecting their conceptual foundations and intended applications.

The authors of these classification systems aim to achieve a balance between simplicity for practical use and sufficient accuracy for reliable interpretation (Bieniawski 1992). The development of classification systems has primarily focused on improving evaluation criteria, adapting them to various geological and engineering conditions, and establishing empirical correlations for design purposes. However, in practice, empirical correlations between different classification systems are often applied based on individual engineering experience, and sometimes without full consideration of their limitations (Serafim and Pereira 1983; Hoek and Diederichs 2006).

Furthermore, reliance on a single classification system (often due to time constraints in data processing) may be insufficient. Likewise, converting results from one system to another may eliminate valuable information contained in their differences, thereby increasing interpretative uncertainty. The reliability of such approaches depends on the geological context, the degree of rock mass homogeneity, and the quality of input data. The use of conversions is particularly problematic in heterogeneous or tectonized rock masses, where differences between classification results tend to be more pronounced (Špago et al. 2015).Regional deviations between empirical correlations have also been reported by Jovanovski (2005).

2 Interpretative Uncertainty

The idea of using multiple classification systems is not new and has often been recommended. Each classification system aims to provide sufficiently reliable results for its intended application. By defining a structured approach for integrating the results of multiple classification systems, interpretative uncertainty can be reduced, thereby contributing to improved design quality and reduced engineering risk. Several factors influencing uncertainty should be distinguished: natural variability of geological and geotechnical characteristics of the rock mass, uncertainty related to the extent and quality of available data (data acquisition and processing), interpretative uncertainty arising from the manner in which classification results are interpreted (Baecher and Christian 2003).

Interpretative uncertainty represents the degree of indeterminacy in defining the boundaries and classes of geotechnical domains, resulting from methodological limitations, differences between applied classification systems, and the type, quality, and completeness of input data.

Differences in the results of individual classification systems may represent additional information about the structural and mechanical complexity of the rock mass. Different systems emphasize different controlling factors, such as discontinuity characteristics, intact rock strength, stress conditions, or groundwater influence (Marinos and Hoek 2000). Their parallel application to the same rock mass interval may therefore reveal changes that would remain unrecognized if only a single classification system were used. Comparative analysis of multiple classification results represents a form of internal cross-validation of classifications. Intervals of agreement increase confidence in the classification, while intervals of divergence indicate zones that require additional geological–geotechnical interpretation and may represent boundaries of geotechnical domains.

3 Methodological Framework

The application of the proposed framework requires adequately planned site investigations and the collection of data of sufficient diversity, detail, and reliability, as the outcome of zoning directly depends on the quality of the input dataset. Within such an approach, data acquisition and interpretation represent a key phase preceding analysis and design.

The methodological framework proposed in this study is based on the following steps:

1. *Collection and compilation* of a dataset that enables the application of multiple classification systems.
2. *Independent application of two or more classification systems* to the same intervals within the dataset.
3. *Verification of the correct application of each classification system (QA/QC)* – first control.
4. *Comparative interpretation of results* obtained from different classification systems.
5. *Identification of intervals of agreement and intervals of divergence*.
6. *Analysis of the causes of divergence* – second control and interpretation of differences.
7. *Definition and application of logical zoning criteria*.
8. *Definition of geotechnical domains* through the fulfilment of all established logical criteria.

Within the parallel application, classifications related to the hydrogeological behaviour of the rock mass may also be incorporated, particularly in dam projects, where permeability represents a dominant zoning criterion.

3.1 Intervals of Agreement and Divergence

Intervals of agreement represent sections of the profile in which different classification systems indicate the same or similar rock mass class. Intervals of divergence represent sections of the profile in which classification systems yield different class ratings (e.g., good rock versus poor rock). Divergence may result from differences in how individual classification systems account for the influence of groundwater, discontinuities, stress conditions, or scoring resolution.

3.2 Zoning Logic

Zoning is performed following the interpretative synthesis of results obtained from multiple classification systems.

In this process, predefined rules are applied, such as:

- minimum domain length in relation to the project scale,
- prioritization of fault and fractured zones, depending on the type and function of the designed structure,
- constraints imposed by lithology,
- selection of a representative class in cases of differing classifications across systems.

The definition of a minimum domain length is necessary to avoid excessive zoning detail that lacks practical significance. Faulted and highly fractured zones, as well as intervals with pronounced rock mass jointing, must be prioritized, as they represent zones of weakness and may significantly influence excavation stability. Zoning should be carried out within the framework of the corresponding lithological type of rock mass.

In cases where different classification systems assign different categories to the same interval, the selection of a representative class is based on predefined decision principles. Depending on the project, the following approaches may be adopted:

- *conservative principle* (adoption of the less favourable category – on the side of safety),
- *hierarchical principle* (e.g., priority given to a system that incorporates stress conditions),
- *project-dependent principle* (e.g., for dams, priority is given to a classification that better reflects permeability).

When three or more classification systems are applied, a “rule of the apparently more favourable category” may be defined. In such cases, if two or more classifications indicate a less favourable category, the less favourable value is adopted as representative. Clearly defined decision-making principles enable, where necessary, formalization of the procedure and its application to large datasets, thereby improving the efficiency of the analysis.

A geological–geotechnical domain defined in this manner represents a quasi-homogeneous zone within which the variability of classification results remains within defined ranges that generally correspond to the same rock mass category. Such defined geotechnical domains form the basis for further, more detailed zoning in relation to excavation and support design, enabling more rational dimensioning and reduction of design-related risk. Following the completion of the zoning process, representative rock mass parameters (e.g., deformability, strength parameters, or GSI) can be assigned to each geotechnical zone, derived from the statistical range of classification results within that zone using commonly applied engineering procedures. Proposed methodological framework is presented in Fig. 1.

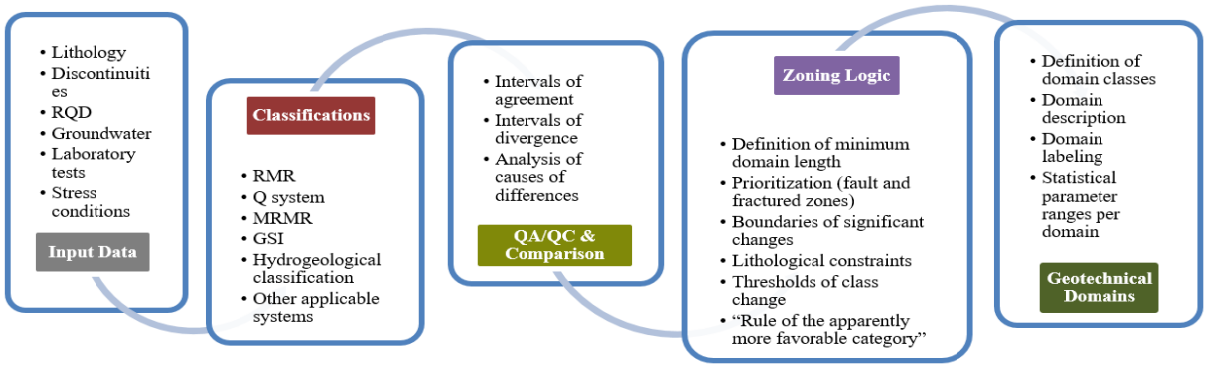


Fig. 1 Proposed methodological framework for rock mass zoning based on the comparative application of classification systems.

4 Case studies

The applied classifications and their comparison are adapted to the specific engineering context of the analysed structure. For the mining shaft, three classification systems were applied to assess ground conditions and support requirements, while for the dam cross-section case, two classification systems were used. In both cases, geometry and the zone of influence play an important role. For the dam, the interpretation covers the entire dam profile, whereas for the shaft excavation, the zone of influence is more limited. The same interval-based evaluation methodology was applied in both cases, in accordance with borehole intervals and laboratory testing results of core samples, followed by rock mass zoning along the borehole profile.

4.1 Example 1 – Mining Shaft

An interval-based zoning approach is demonstrated using data for a mining shaft exceeding 1500 m in depth (Fig. 2), provided by Hidroenergo MVB, Belgrade. The investigation borehole was drilled continuously along the axis of the planned shaft, and the results were extrapolated to the surrounding rock mass within the shaft influence zone. The following classification systems were applied: Rock Mass Rating (RMR), Mining Rock Mass Rating (MRMR), and Q-system (Bieniawski 1989; Laubscher 1990; Barton et al. 1974). The classification was first performed for individual drilling intervals and subsequently aggregated by grouping intervals of the same class, resulting in the left part of the table shown in Fig. 2.

Geotechnical units were then defined in accordance with the described methodology, and corresponding GSI value ranges were assigned as reference values for subsequent parameter assignment to geotechnical domains. Geotechnical domains were then delineated, representing the zoned shaft alignment in accordance with indicative excavation and support conditions.

Figure 2 clearly demonstrates that divergences between classification systems do not represent random variation, but rather form spatially organized intervals corresponding to changes in engineering geological conditions. These intervals represent natural boundaries of geotechnical domains and enable more reliable rock mass zoning compared to the use of individual classification systems alone. Subsequently, by assigning appropriate parameters to the geotechnical domains based on investigation results, more detailed geotechnical modelling can be performed. This directly supports support design selection and risk control in deep excavations.

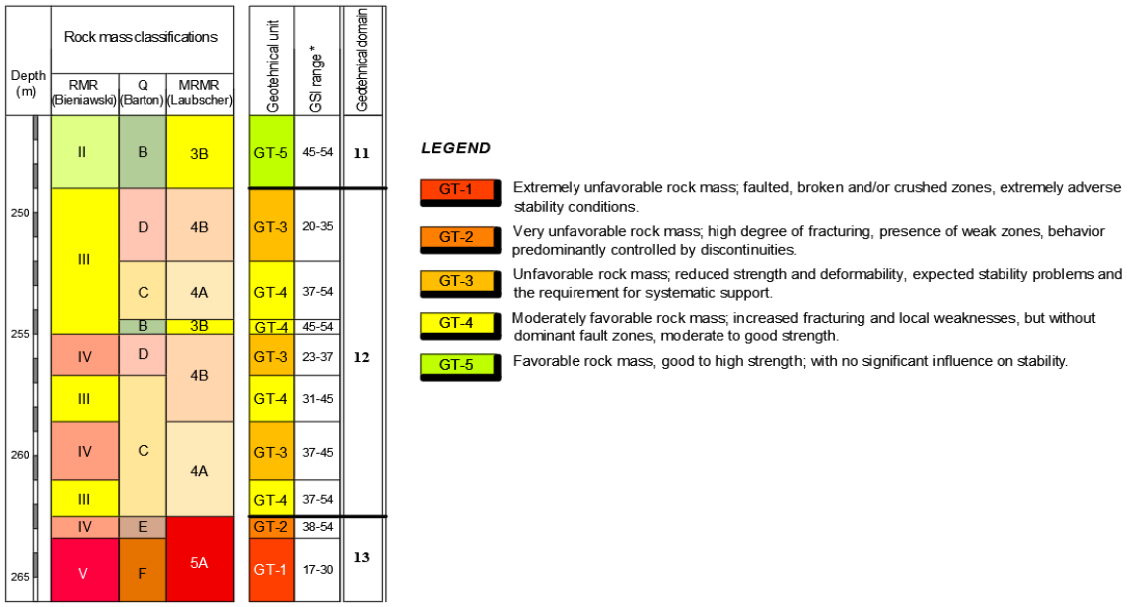


Fig. 2 Comparative rock mass classification results (RMR, Q and MRMR) and derived geotechnical domains (11–13) along the shaft profile (depth 246–266 m), with indicative GSI ranges associated with geotechnical units and corresponding engineering behaviour.

4.2 Example 2 – Dam Cross-Section "Pambukovica"

The cross-section of the planned Pambukovica dam for flood protection is located upstream of Ub in Serbia (investigation and design carried out by Energoprojekt-Hidroinženjering, Belgrade). The assessment of rock mass quality directly influences the selection of dam type, as well as the technical design of the dam and associated structures.A total of seven investigation boreholes were drilled along the axis of the planned dam. Data interpolation was performed between the boreholes, with extrapolation applied at the ends of the dam profile. Two classification systems were applied: RMR and Q.

In the presented example (Fig. 3), spatial differences between interpretative boundaries defined based on the RMR and Q classifications indicate zones of increased interpretative uncertainty. Given that only two classification systems were applied and that the structure represents a high-risk hydraulic facility, a conservative boundary may be adopted for the purpose of rock mass zoning.

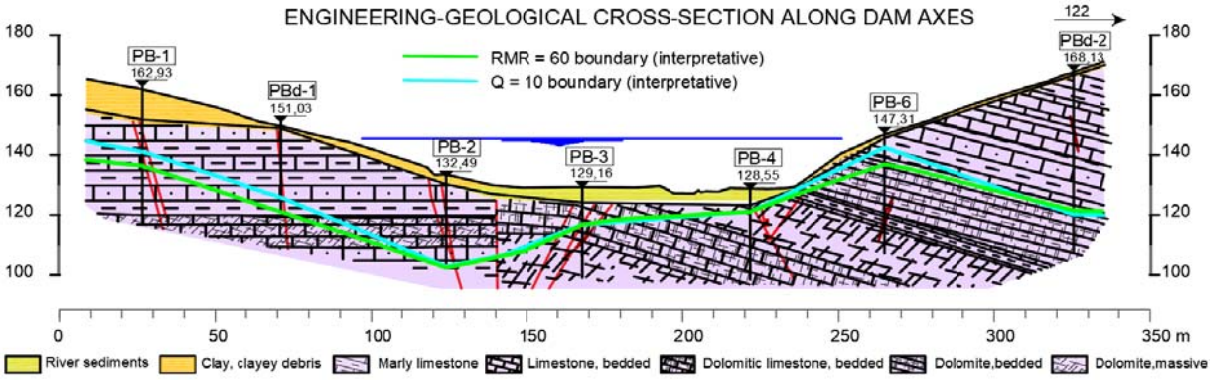


Fig. 3 Engineering-geological crossection along Dam axes with interpretative boundaries of RMR=60 and Q=10.

In cases of more pronounced differences, the application of a third classification system may be considered. In such cases, domains would first be defined at each borehole using the same methodology as for the shaft example, followed by interpretation along the engineering-geological cross-section. In all cases, these boundaries should, as far as possible, be evaluated in relation to other relevant data, such as seismic refraction surveys and similar investigations, in order to achieve a final interpretation. This is particularly important for permeability control and dam safety assessment.

5 Discussion

In complex geological conditions, individual classification systems often do not provide a sufficient interpretative model for design purposes. Their isolated application may lead to an oversimplified representation of the rock mass and the neglect of important aspects of its behaviour. As demonstrated in the examples shown in Fig. 2 and Fig. 3, intervals of divergence between classification systems are clearly delineated along the borehole profile and the dam site, representing zones of increased interpretative uncertainty. Divergences in the results of different classification systems, when properly applied, do not represent errors, but rather reflect the differing sensitivity of individual systems to structural characteristics, groundwater conditions, and stress state. In this sense, differences between classification results can be regarded as an additional source of information on the complexity of the rock mass. The comparative analysis of multiple classification systems enables the identification of intervals of agreement and divergence, providing a basis for more reliable rock mass zoning. This approach is consistent with the concept of defining geotechnical domains based on classification results (Savić et al. 2021). The application of clearly defined logical and engineering rules in this process reduces interpretative risk and improves the reliability of input parameters for geotechnical modelling. However, the method remains dependent on the quality and representativeness of input data.

6 Conclusion

Empirical rock mass classification systems are of great importance and represent a fundamental tool for assessing rock mass quality and engineering behaviour. If, after verification of correct application and elimination of potential procedural errors, differences between classification results still persist, these should not be regarded as shortcomings, but rather as an additional source of information which, when properly interpreted, enables more reliable definition of geotechnical domains. Divergences between classification results often indicate zones of increased structural complexity and potentially unfavorable rock mass behaviour. The proposed zoning framework, based on the comparative analysis of classification systems and the application of logical decision rules, represents a practical approach for reducing interpretative uncertainty and improving the reliability of geotechnical ground models. Conceptually, the method is universal and can be applied under various engineering conditions, using different classification systems, including future developments. This approach reduces interpretative uncertainty, improves input reliability, and directly contributes to safer and more robust engineering design.

References

Baecher GB, Christian JT (2003) Reliability and statistics in geotechnical engineering. Wiley

Bieniawski ZT (1989) Engineering rock mass classifications. Wiley, New York

Bieniawski ZT (1992) Design methodology in rock engineering. Balkema, Rotterdam

Barton N, Lien R, Lunde J (1974) Engineering classification of rock masses for the design of tunnel support. Rock Mechanics 6(4): 189–236

Hoek E, Diederichs MS (2006) Empirical estimation of rock mass modulus. International Journal of Rock Mechanics and Mining Sciences 43(2): 203–215

Jovanovski M (2005) Some data about rock mass rating for the rock masses from the Republic of Macedonia

Laubscher DH (1990) A geomechanics classification system for the rating of rock mass in mine design. Journal of the South African Institute of Mining and Metallurgy 90(10): 257–273

Marinos P, Hoek E (2000) GSI – a geologically friendly tool for rock mass strength. Proceedings of GeoEng 2000 International Conference on Geotechnical and Geological Engineering, Melbourne, pp. 1422–1440

Savić D, Tumara M, Petrović M (2021) Importance of geotechnical investigation for design and construction of shafts over 1000 m deep. World Journal of Engineering and Technology 9: 250–267. https://doi.org/10.4236/wjet.2021.92018

Serafim JL, Pereira JP (1983) Considerations on the geomechanical classification of Bieniawski. Proceedings of the International Symposium on Engineering Geology and Underground Construction, Lisbon

Špago A et al. (2015) Correlation dependency between rock mass quality and mechanical properties in carbonate rock masses

Advanced InSAR Monitoring of Ground Deformation in the Polog Valley

T. Gegovski, Z. Bogdanovski, Z. Srbinoski, F. Kasapovski, F. Petrovski
University Ss. Cyril and Methodius, Skopje, N. Macedonia
gegovski@gf.ukim.edu.mk

Abstract

Understanding ground deformation across valley floors and mountain slopes is essential for assessing terrain stability and enabling the timely detection of landslides. Satellite radar interferometry provides an effective means for high-precision, wide-area deformation mapping, allowing early identification of zones prone to slope instability.

This study focuses on the Polog Valley in northwestern North Macedonia and its surrounding slopes, forming a broad intermontane basin bordered by the Shar Planina, Zheden, and Bistra mountains. The objective is to identify and quantify deformation patterns across the valley and adjacent slopes using advanced InSAR techniques. A multi-temporal analysis of Sentinel-1 SAR data (2014–2025) was performed by combining ascending and descending orbits and applying the PSInSAR and QPSInSAR techniques. To obtain physically meaningful motion estimates, line-of-sight (LOS) displacements from both geometries were decomposed into dominant east–west and vertical components.

The results indicate that the central plain of the Polog Valley remains stable, with mean LOS deformation rates within ±1 mm/year. In contrast, three active deformation zones were identified near the villages of Gjermo, Selce, and Rakovec. In the northern part of Gjermo, mean cumulative east-oriented displacements are around 35 cm, with about 11 cm mean vertical subsidence, while at the entrance to Selce, mean west-oriented displacements exceed 20 cm with similar mean subsidence. In the southern part of Rakovec, mean east-oriented displacements reach about 12 cm together with roughly 5 cm of mean vertical subsidence. These deformation patterns are consistent with the local slope morphology, with east-inclined slopes at Gjermo and Rakovec and west-inclined terrain at Selce.

The findings confirm the effectiveness of advanced InSAR time-series techniques for detecting and characterizing localized slope instabilities. For the identified deformation zones, integrating satellite-based observations with geodetic and geotechnical monitoring is recommended to support long-term stability assessment and timely detection of landslides in the Polog Valley.

Keywords

PSInSAR, QPSInSAR, Polog Valley, Ground deformation, Monitoring.

1 Introduction

Slope instabilities are among the most significant natural hazards, posing risks to settlements, infrastructure, and human safety. Effective hazard assessment requires accurate and continuous monitoring of ground deformation at regional or global scales. Traditional geodetic methods, such as leveling and GNSS, are limited by sparse spatial coverage and discrete temporal sampling, which motivates the use of satellite-based interferometry techniques. Advanced InSAR techniques have been widely applied to monitor slope deformation across diverse environments. For instance, InSAR has been used to map regional-scale displacement in the Po Valley, northern Italy (Antonielli et al., 2016), to detect slow-moving landslides in steep and mountainous terrains in Nepal (Bekaert et al., 2020), and to characterize slope deformation in the hilly and mountainous region of Umbria, central Italy (Ponziani et al., 2023). These studies demonstrate the capability of InSAR to provide detailed and comprehensive deformation information that complements conventional monitoring approaches.

The Polog Valley represents an interesting case study for ground deformation analysis, as several studies have focused on assessing its slope stability. Among the recent works (Jovanoskiet al.,2021) applied both innovative and conventional methods for landslide detection, including the use of DInSAR techniques to map and monitor slope movements. Building upon these studies, the present research provides, for the first time, a 10-year comprehensive analysis of ground deformation in the Polog Valley using advanced InSAR techniques, specifically PSInSAR and QPSInSAR. For the unstable zones in Gjermo, Selce, and Rakovec, LOS displacement was decomposed into east–west and vertical components, enabling a robust long-term characterization of slope dynamics.The analysis presented in this study focuses on the geometric representation of the detected ground movements, without addressing the underlying causes of such displacements.

2 Study area

The study focuses on the Polog Valley, located in the northwestern part of the Republic of North Macedonia. The Polog Valley represents an intermontane basin surrounded by mountain massifs that bound it on all sides. The valley is oriented in a north–south direction, with an average elevation between 400 and 600 m a.s.l., while the surrounding hills and mountains rise above 1500-2000 m a.s.l., including the Shar Planina, Bistra, and Zheden mountain ranges.

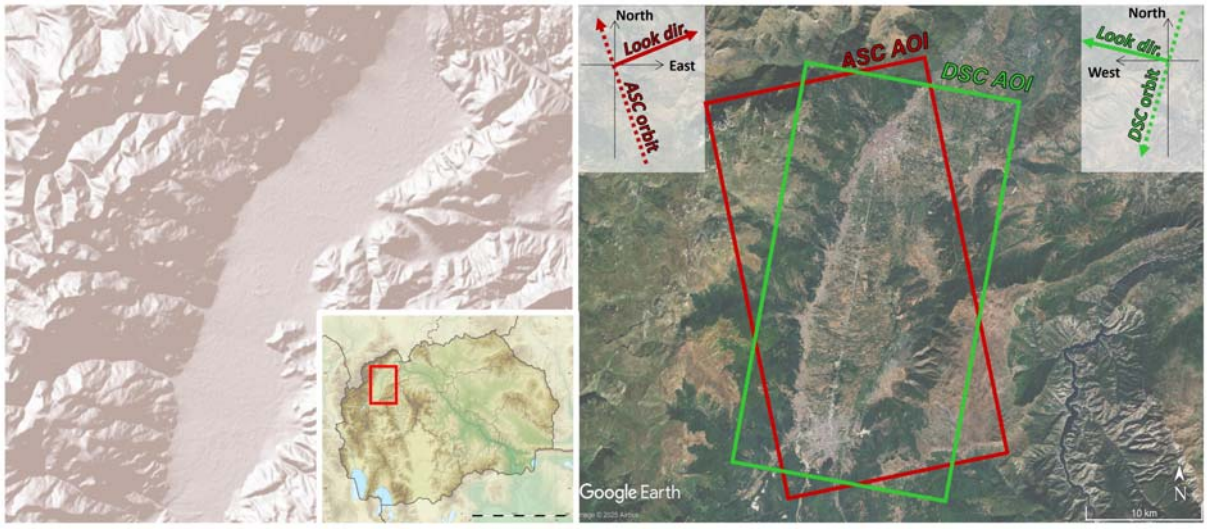


Fig. 1 Topographic view (left) and satellite view (right) of the Polog Valley, showing the areas analysed with Sentinel-1 in ascending and descending orbits.

From a geological perspective, the Polog Valley is a neotectonic depression filled with Quaternary alluvial, colluvial, and proluvial deposits. These sediments rest on older Paleozoic and Mesozoic rocks that form the bedrock and surrounding hilly–mountainous areas. In the higher parts, sedimentary, metamorphic, and locally volcanic rocks dominate, reflecting a complex geological evolution and tectonic activity in the region (Ćulumoska-Gjorgjievska et al.,2015).

3 Methodology

3.1 Utilized Advanced InSAR Techniques

InSAR is a remote sensing technique used to measure ground displacements by analysing phase differences between repeated radar acquisitions. Conventional differential InSAR (DInSAR) is often limited by temporal and geometrical decorrelation, as well as atmospheric effects, which has led to the development of advanced multi-temporal InSAR approaches.In this study, PSInSAR and QPSInSAR techniques were applied to investigate slope instability in the Polog Valley and surrounding mountainous areas. PSInSAR identifies stable radar targets (permanent scatterers) to estimate ground deformation with millimetre accuracy over long time periods (Ferretti et al., 2001). QPSInSAR extends this approach to partially coherent targets (Quazi PS), improving deformation monitoring in areas with lower target density, such as mountainous terrains (Perissin & Wang, 2012).

3.2 Overview of the SAR Dataset Used for Polog Valley Monitoring

To implement the PSInSAR and QPSInSAR techniques, a comprehensive multi-temporal Sentinel-1 (C-band) SAR dataset was compiled for the Polog Valley. The dataset provides consistent temporal coverage, with an initial revisit interval of 12 days that was shortened to 6 days following the launch of Sentinel-1B and maintained at 6 days with the recent operational deployment of Sentinel-1C. Both ascending and descending orbit acquisitions were considered, covering the period from October 2014 to June 2025. The specifications of the SAR acquisitions utilized for this study are summarized in Table 1, while the analysed area in both orbits is shown in Fig. 1 (right).

Table 1. Specifications of the Sentinel-1 SAR dataset used in this study.

Satellite Orbit	***Ascending***	***Descending***
Number of SLC images	*485*	*467*
Polarization	*VV*	*VV*
TOPS Sub swath	*2*	*1*
Orbit path	*175*	*153*
Incidence angle (θ)	*39.4°*	*33.8°*
Heading angle (α)	*-170°*	*-11°*

3.3 Processing Workflow of Advanced InSAR Approaches

The PSInSAR technique, due to its high processing efficiency, was employed to analyse ground displacements across the entire Polog Valley.The SAR dataset, summarized in Table 1, was processed by generating interferograms with respect to a single reference acquisition, covering the full observation period and without applying spatial filtering. All processing was performed using SARPROZ software, and a simplified workflow is presented in Fig. 2.

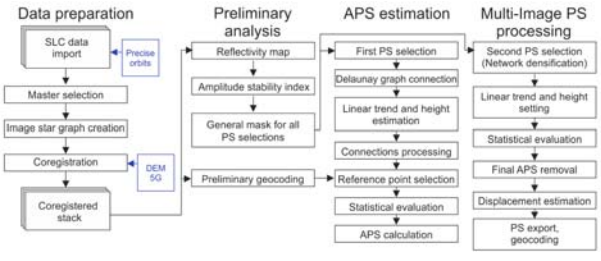


Fig.2 Simplified workflow of PSI Processing in SARPROZ.

The QPSInSAR approach was applied as a complementary method to the unstable areas previously identified by PSInSAR due to its higher computational cost. By exploiting multiple interferograms and applying spatial filtering, it enabled a more detailed analysis of ground displacements in the villages of Gjermo, Selce, and Rakovec, providing refined information on localized slope instabilities.

InSAR measures displacements along the viewing geometry (LOS direction), which do not always provide an intuitive representation of ground motion, so the displacements derived from ascending and descending orbits were integrated and decomposed into vertical and east–west components to better reflect actual ground movement.

4 Results and Discussion

4.1 PSInSAR and QPSInSAR Resultsfor the Polog Valley

The PSInSAR analysis of the entire Polog Valley, based on ascending orbit data, identified 22,507 PS points with coherence values ranging from 0.70 to 0.97 (average 0.85), indicating high reliability. For the three unstable locations in the villages of Gjermo, Selce, and Rakovec, detailed QPSInSAR analyses were subsequently performed, and the results of both are shown in Fig. 3.

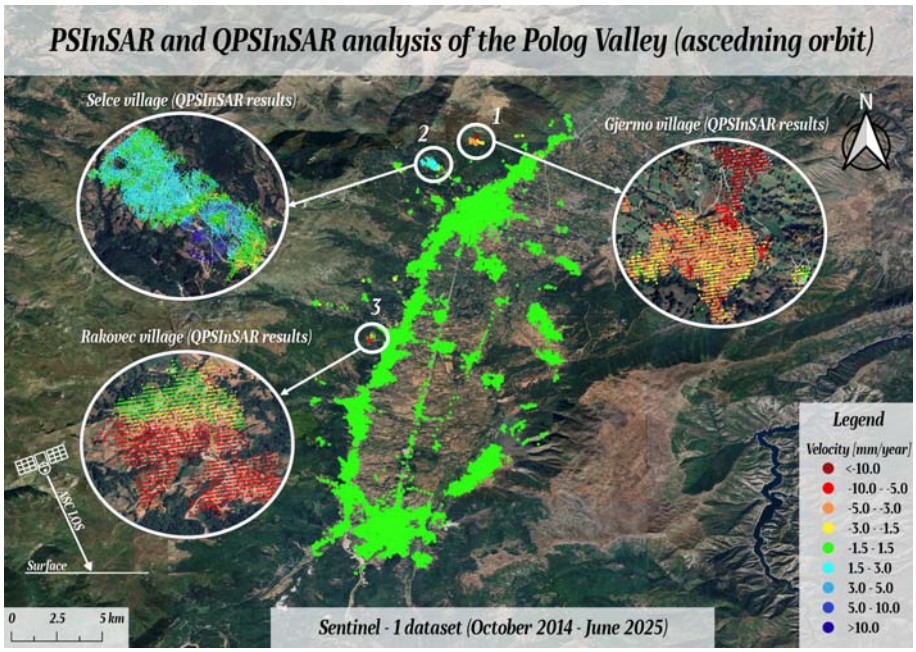


Fig. 3 PSInSAR and QPSInSAR displacement velocity map over the Polog Valley (ascending dataset).

From Fig. 3, it can be observed that most PS points across the basin are green, indicating negligible displacements. Three localized zones are highlighted and further detailed with QPSInSAR analysis: subsidence in Gjermo with a maximum cumulative displacement of -45 cm and an average of -36 cm in the northern part, uplift in Selce with a maximum cumulative displacement of 20 cm and an average of 10 cm in the south-eastern part, and subsidence near Rakovec with a maximum cumulative displacement of -19 cm and an average of -11 cm in the southern part, all over the analysed period and detected in the LOS of the ascending orbit.

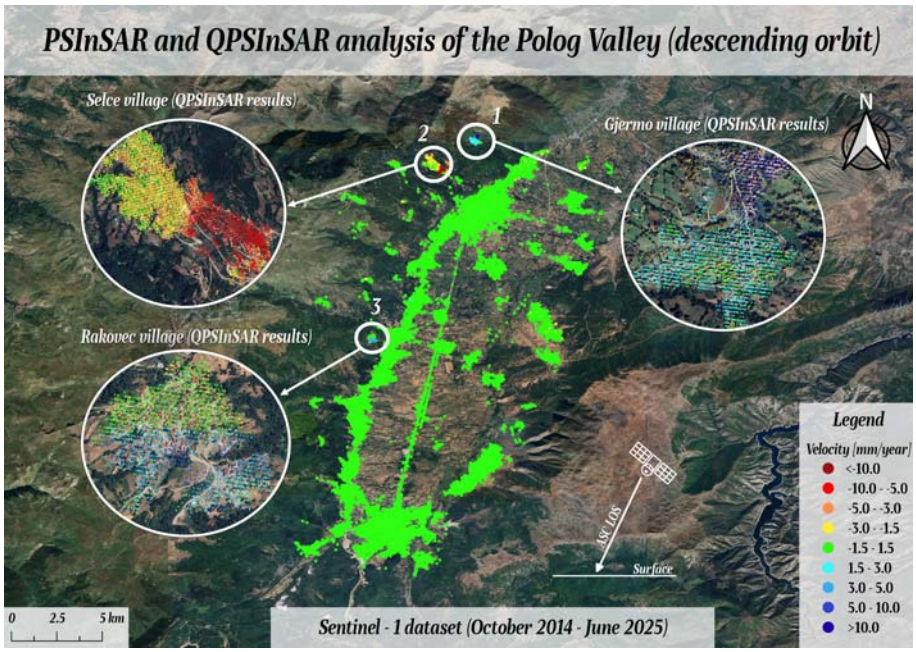


Fig. 4 PSInSAR and QPSInSAR displacement velocity map over the Polog Valley (descending dataset).

A complementary PSInSAR analysis based on descending orbit data identified 24,283 PS points with minimum temporal coherence values ranging from 0.70 to 0.95, with an average coherence of 0.84, confirming reliable results. From Fig. 4, an identical pattern is observed across the Polog Valley, consistent with the ascending orbit results. In the three detected unstable zones, opposite LOS displacements are noted in the descending orbit: uplifting in Gjermo with a maximum of +28 cm and an average of +15 cm in the northern part, subsidence in Selce with a maximum of -35 cm and an average of -20 cm in the south-eastern part, and uplifting near Rakovec with a maximum of +7 cm and an average of +5 cm in the southern part, all over the analysed period. The opposite LOS displacement patterns observed from the two viewing geometries suggest a strong contribution of horizontal ground movements in these areas.

4.2 LOS Displacement Decomposition Results

LOS displacement decomposition is applied to better constrain the direction of ground movements. Using results from ascending and descending orbits, LOS displacements can be mathematically transformed into two components of the three-dimensional Cartesian system, most commonly the East–West and Vertical directions. Due to the different viewing geometries of the two acquisition modes, the definition of a Region of Uniform Motion (RUM) is required to ensure a consistent and reliable decomposition.

The decomposition of LOS displacements for Gjermo village is shown in Fig. 5. East–west movements are *eastward* oriented, with maximum cumulative displacements of 58 cm and an average of 35 cm in the northern part over the analysed period. Vertical cumulative *subsidence* reaches up to 20 cm, with an average of approximately 11 cm over the analysed period.

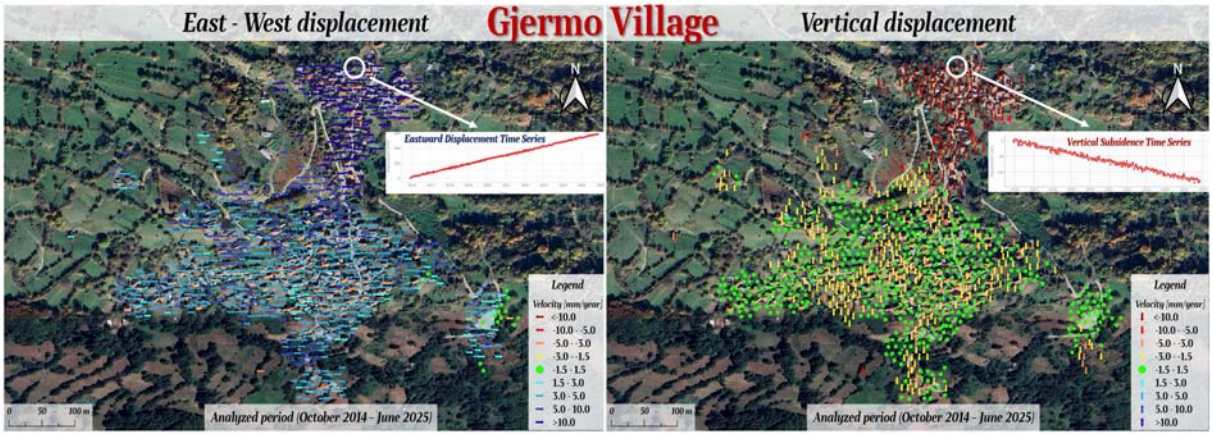


Fig. 5 Decomposed East – West (left) and Vertical (right) displacement in Village of Gjermo.

The decomposition of LOS displacements for Selce village is shown in Fig. 6. East–west movements are *westward* oriented in the southeastpart of the village, with maximum cumulative displacements of 30 cm and an average of 20 cm over the analysed period. Vertical displacements show *subsidence*, reaching up to 25 cm, with an average of 20 cm, over the analysed period.

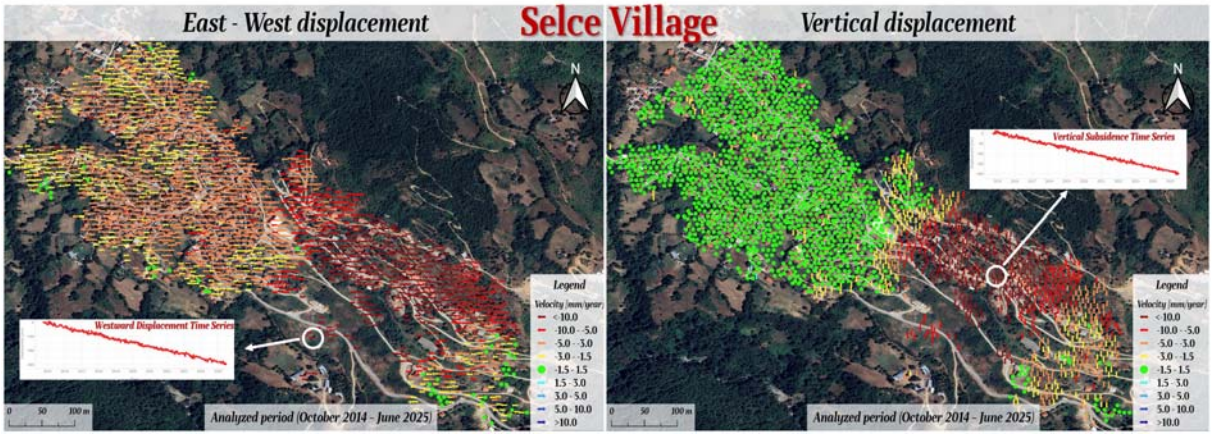


Fig. 6 Decomposed East – West (left) and Vertical (right) displacement in Village of Selce.

The decomposition of LOS displacements for Rakovec village is shown in Fig. 7. East–west movements are predominantly *eastward* in the southern part, with maximum cumulative displacements of 23 cm and an average of 12 cm. Vertical displacements are more stable, with maximum *subsidence* of 10 cm and an average of 5 cm in the southern area over the analysed period.

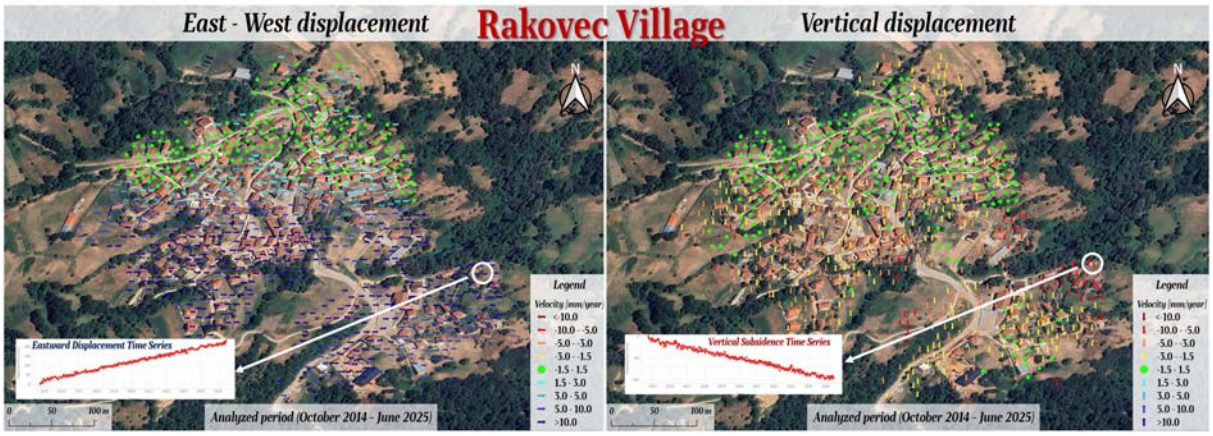


Fig. 7 Decomposed East – West (left) and Vertical (right) displacement in Village of Rakovec.

4.3 Discussion of the Results

The Polog Valley is largely stable, with localized displacements at Gjermo, Selce, and Rakovec, consistent with terrain morphology. Due to the limitations of C-band InSAR in vegetated areas, PS and QPS points are sparse but sufficient to represent ground displacement across the valley and surrounding terrain. A second limitation is the lack of detailed field investigations. Geodetic and geotechnical monitoring of the detected critical zones, together with continuous advanced InSAR analysis, are recommended to confirm and further validate these observations.

5 Conclusion

Advanced InSAR analysis provides an effective tool for detecting and monitoring ground deformation over large areas such as the Polog Valley. The results indicate generally stable conditions, with localized displacements at Gjermo, Selce, and Rakovec. However, these findings would be more reliable if supported by additional detailed geodetic and geotechnical monitoring of the unstable zones, which is the main recommendation of this study, to verify and characterize the observed deformation.

References

Antonielli B, Monserrat O, Bonini M, Cenni N, Devanthéry N, Righini G, Sani F (2016) Persistent Scatterer Interferometry analysis of ground deformation in the Po Plain (Piacenza–Reggio Emilia sector, Northern Italy): seismo-tectonic implications. Geophysical Journal International 206(2): 1440–1455. https://doi.org/10.1093/gji/ggw227

Bekaert D, Handwerger A, Agram P, Kirschbaum DB (2020) InSAR-based detection method for mapping and monitoring slow-moving landslides in remote regions with steep and mountainous terrain: an application to Nepal. Remote Sensing of Environment 249: 111983. https://doi.org/10.1016/j.rse.2020.111983

Ferretti A, Prati C, Rocca F (2000) Nonlinear Subsidence Rate Estimation Using Permanent Scatterers in Differential SAR Interferometry. IEEE Transactions on Geoscience and Remote Sensing 38(5): 2202–2212. https://doi.org/10.1109/36.868878

Jovanovski M, Peshevski I, Gjorgiev G, Nedelkovska N, Nicodemo G, Reale D, Fornaro G, Peduto D (2021) Landslide characterization in the Polog Region (R.N. Macedonia) by innovative and conventional methods. Mediterranean Symposium on Landslides – MSL2021, June 2021. https://doi.org/10.13140/RG.2.2.15994.62406

Perissin D, Wang T (2012) Repeat-pass SAR interferometry with partially coherent targets. IEEE Transactions on Geoscience and Remote Sensing 50(1): 271–280. https://doi.org/10.1109/TGRS.2011.2160644

Ponziani F, Ciuffi P, Bayer B, Berni N, Franceschini S, Simoni A (2023) Regional-scale InSAR investigation and landslide early warning thresholds in Umbria, Italy. Engineering Geology 327: 107352. https://doi.org/10.1016/j.enggeo.2023.107352

Ćulumoska-Gjorgjievska A, Stafilov T, Šajn R (2015) Spatial distribution of chemical elements in soils in the Polog Region, Republic of Macedonia. Geologica Macedonica 29(2): 155–166

A probabilistic fragmentation-based rockfall model for open-pit and natural slopes

M. Marchelli
Politecnico di Torino, Turin, Italy
maddalena.marchelli@polito.it
0000-0002-9919-2916

M. Paganone
Department of Planning, Water Resources and Land Use, Autonomous Region of Valle d'Aosta, Aosta, Italy

Abstract

Accurate prediction of rockfall propagation is critical for designing safe slopes in open-pit mines as well as in other engineered or natural environments. Fragmentation during impact significantly alters runout distances, energy dissipation, and the hazard footprint, yet most trajectory models neglect this phenomenon or treat it empirically. This study applies RockFRAG, a novel probabilistic 2D lumped-mass model, developed by the author and implemented in a code, that explicitly incorporates fragmentation processes informed by laboratory experiments accounting for impact energy, block shape and rock-mass structure through probabilistic fragment trajectories.

Applied to synthetic open-pit bench profiles, fragmentation-aware and intact-block simulations are compared across different bench configurations, showing that neglecting fragmentation is not inherently conservative: depending on face angle and bench geometry, breakage can either extend runout and increase pit-floor arrival probability, or promote earlier arrest through fracture-energy dissipation. These geometry-dependent, non-monotonic effects cannot be captured by non-fragmenting assumptions and lead to significant differences in runout envelopes and impact conditions. These findings underscore the need to account for fragmentation in runout-based design checks and bench performance evaluation. A probabilistic treatment is essential to cover uncertainty in fragment behaviour and slope interaction, enabling risk-informed design beyond deterministic assumptions, with implications extending to mountainous environments where impact-induced breakage commonly influences runout variability and the performance of protective measures.

Keywords

Fragmentation, Trajectory analysis, Rockfall, Open pit, Hazard assessment.

1 Introduction

Rockfall is a major safety concern in both engineered and natural slopes, with significant operational implications in open-pit mines and mountainous terrain (Macciotta et al., 2021). Blasting, evolving bench geometries and rock-mass variability drive event frequency in mines, while lithological contrasts and discontinuity networks govern instability on natural slopes (Ferrari et al., 2016).

Trajectory models range from lumped-mass formulations, which treat the block as a point mass, to rigid-body approaches that resolve shape-dependent dynamics (Li and Lan, 2015). Lumped-mass models are computationally efficient and well suited for probabilistic analyses where block shape or release conditions are poorly constrained, as is common in open-pit mines and on natural cliffs with diffuse source areas (McNabb et al., 2025). Their ability to accommodate parameter variability makes them widely used in probabilistic hazard studies. Accurate prediction of rockfall propagation requires an adequate representation of slope geometry and block–slope interaction parameters, as both strongly control impact conditions and mobility. In open-pit mines, operational modifications such as crest loss and debris accumulation frequently produce deviations from ideal geometries (Darling, 2011), and comparable complexity characterises natural slopes. These geometric and material uncertainties, together with variability in impact conditions, have motivated probabilistic approaches capable of yielding distribution-based estimates of runout and velocities (Wang et al., 2014).

Synthetic bench profiles have been widely used to derive design charts for pit-slope layouts and protective measures (Alejano et al. 2007; Marchelli et al. 2023), yet impact-induced fragmentation, a key control on mobility, energy dissipation and trajectory patterns (Ruiz-Carulla et al., 2020; Gili et al., 2022), is rarely included. Breakage redistributes energy among multiple fragments and can either increase or reduce runout depending on the impact configuration, making explicit probabilistic treatment of fragmentation essential. This work applies RockFRAG (Marchelli, 2026), a new lumped-mass model with an energy-based fragmentation module calibrated on laboratory drop tests (Marchelli et al., 2025), to idealised open-pit geometries to quantify how fragmentation alone alters runout distributions and impact velocities, with implications for both engineered and natural slopes.

2 Methodology

The study focuses on variability introduced by impact-induced fragmentation. To isolate the effect of fragmentation, eight three-bench synthetic geometries representative of typical open-pit environments are analysed, combining two bench heights h_b (15 m, 20 m), two bench widths w_b(7 m, 10 m) and two face angles β (55°, 85°), consistent with previous parametric studies (Alejano et al., 2007; Marchelli et al., 2023). Such idealised layouts provide a controlled and reproducible basis for assessing slope-scale kinematics and retention capacity. For each geometry, non-fragmenting (N.F.) and fragmenting (F) simulations are compared, the latter governed by the probabilistic energy-based module described in Section 2.1.

For each geometry, 1000 realisations are run from the upper bench crest for both N.F. and F. conditions. Classical lumped-mass block–slope interaction parameters, i.e. normal and tangential restitution coefficients (COR_n, COR_t) and friction angle (φ)are sampled from Gaussian distributions consistent with values calibrated for lumped-mass rockfall models under open-pit conditions. These parameters reflect impacts on rocky faces and debris-covered treads and reproduce typical block–slope interactions reported in mining environments (Alejano et al., 2007; Marchelli et al., 2023). A deliberately low friction angle is adopted to account for rolling behaviour, which is not explicitly represented in the lumped-mass formulation, and a small surface-roughness variation is included to mimic local topographic irregularities. To limit uncertainty sources and input complexity, in this stage, the block is modelled as a spherical element (≈1 m³), with mechanical properties consistent with those of the rock-face material and no internal structural features. Input parameters for the geometric configurations and block–slope interaction are summarised in Table 1, together with the fragmentation-related parameters used in the analyses (as detailed in Sec. 2.1).

Table 1. Input parameters for the geometric configurations and block–slope interaction.

Parameter	Value
Bench height heights h_b (m)	15, 20
Bench height width w_b (m)	7, 10
Bench face angle β (°)	55, 85
N° of benches (-)	3
Block diameter (m)	0.62±0.06
Tensile strength σ_t(MPa)	7±0.7
Block density (kg/m^3)	2700
Block shape factor $k_{s,E_{th}}$ (-)	1

Parameter	Value	
	Face	Bench
COR_n (-)	0.4±0.03	0.35±0.03
COR_t (-)	0.85±0.03	0.8±0.03
ϕ (°)	8±1	8±1
Young modulus (GPa)	50±5	20±2
Poisson ratio (-)	0.2	0.2
Surface roughness (°)	±1	±1

2.1 Trajectory model

Fragmentation is evaluated at every impact using an energy-based criterion applied to the normal component of the pre-impact kinetic energy $E_{k,n}^{b}$. Breakage occurs when the ratio $\epsilon = E_{k,n}^{b}/E_{\text{th}}$ exceeds unity, where the threshold E_{th} depends on the effective tensile strength $\tilde{\sigma}_t$, the contact modulus Y_{eq}, an equivalent diameter d_{eq}, and a shape factor $k_{s,E_{th}}$ that lowers the threshold for non-spherical blocks (details in Marchelli, 2026). Structural effects are introduced by assigning $\tilde{\sigma}_t$according to rock-mass class (intact, moderately fractured, highly fractured) and, for the moderately fractured class, by sampling joint orientation θ and applying an orientation-dependent reduction consistent with drop-test evidence (Marchelli et al., 2025; Marchelli et al., 2026). Once $\epsilon > 1$, resulting fragment masses are sampled via Monte Carlo from a bilinear complementary cumulative distribution fitted to laboratory drop tests on intact and pre-fractured samples, with the slopes and breakpoint of the distribution depending on ϵ and on rock-mass class. Mass conservation is enforced, and a minimum fragment mass prevents excessive multiplicity. The remaining kinetic energy after fracture is distributed among fragments proportionally to their mass, consistent with observations of energy partitioning. Post-impact fragments velocities (v_f^a) are assigned through an energy-balanced rebound rule that accounts for deformation and fracture-energy loss via an effective normal restitution $COR^* = \psi\, COR_n$, where ψ scales calibration values to the target substrate. The post-impact velocity vector due to normal impact is $\tilde{v}_f^a = v_n^b\, COR^*$, while directions are sampled from ejection-angle ranges that depend on rock-mass class, joint orientation and ϵ. Tangential components inherit the parent term $v_t^b COR_t$. Each fragment then propagates as a new body within the same lumped-mass framework, inheriting the parent's rock-mass and shape class. The current implementation is two-dimensional for computational efficiency; a 3D extension including lateral dispersion is planned. RockFRAG has been validated against laboratory drop tests on specimens with controlled discontinuities (Marchelli et al., 2025), large-scale field fragmentation experiments, and full-scale propagation tests (Bourrier et al., 2021; Gili et al., 2022); full details are reported in Marchelli (2026). As a representative example, Table 2 compares simulated and observed fragment runout statistics at Vallirana Site 4 (Barcelona, Spain; Gili et al., 2022; Matas et al., 2020), where 24 limestone blocks were released and 22 fragmented producing 1241 fragments. Restitution parameters were calibrated independently on the fragmentation-free Site 1 and transferred without adjustment to Site 4, isolating the fragmentation module performance. Errors remain below 10% across the maximm runout and the 50% cumulative-mass distance, confirming field-scale physical reliability.

Table 2. Observed vs. simulated fragment runout distances at Vallirana Site 4 (data from Matas et al., 2020).

Statistic	Observed (m)	Numerical (m)	Error (%)
Runout at 50% cumulative mass	≈13.5	14.6	8.1
Maximum runout	35.2	33.6	4.4

3 Results and Discussion

The simulations are performed using a tailored script implementing the trajectory model (RockFRAG) in Matlab (R2023b). All the kinematic parameters and block-reaching probability (p_r)are recorded along the slope and at the pit floor, where block or fragment arrivals are most critical for operational safety and for the preliminary definition of mitigation measures. As pit-retention capacity is a key aspect of open-pit slope design, the results can be analysed in light of the acceptance criteria of Read and Stacey (2009): at the bench scale, acceptable failure probabilities range between 10–20 % (80–90 % reliability), while at the overall slope scale a reliability requirement of up to 90-95 % may be appropriate. For the purpose of designing protection structures, the 95th-percentile values of the main kinematic quantities (trajectory h_{95}, velocity v_{95} and kinetic energy E_{95}) are evaluated.

Across the eight synthetic geometries, the comparison between non-fragmenting (N.F.) and fragmenting (F.) simulations highlights two fundamentally different behavioural regimes, controlled primarily by the bench-face angle and secondarily by bench width and height. A first regime, typically associated with shallow face angles (β = 55°), shows that fragmentation increases the runout distance and leads to a higher proportion of trajectories reaching lower benches or the pit floor. In these cases, fragmentation generates a large number of small fragments, characterised by low individual masses, that travel efficiently across bench treads. At the same time, the breakage process occasionally produces rare but dynamically significant high-energy fragments, as reflected in the upper-tail values of the 95th-percentile velocity and kinetic energy profiles. These isolated events extend the extreme

runout envelope well beyond the intact-block prediction, demonstrating that the assumption of a single non-fragmenting block does not safely bound the runout in shallow-slope geometries. The h_b =15 m-w_b =10 m β = 55° geometry (Fig. 1.a) offer clear examples of this behaviour: substantial portions of F case trajectories exceed the 10 % reliability threshold at both intermediate benches and at the pit floor, even when the corresponding N.F. simulations indicate limited mobility.

A contrasting regime emerges for steep face angles (β = 85°). In these configurations, fragmentation predominantly enhances retention rather than mobility. The steep geometry promotes near-normal impacts on the upper bench, resulting in substantial fracture-energy dissipation during breakage. The post-impact velocities of the resulting fragments are generally lower than those of the intact block, producing reduced flight heights and shorter downslope travel distances. As a result, the F curves lie consistently to the left of the N.F. curves, indicating improved bench effectiveness. For wide benches (w_b= 10 m), the fragmenting simulations often eliminate pit-floor arrivals entirely, whereas the N.F. runs may still include a small number of exceedances. The h_b =20 m-w_b =10 m β = 85° geometry (Fig. 1.b) exemplifies this effect, where the fragmentation model yields $p_r$values well below the acceptance thresholds across all slope sectors.

The variability observed in the full dataset is summarised in Table 1, reporting, for each geometry, p_r, h_{95}, v_{95}, and E_{95} at the end of bench 1, end of bench 2 and the beginning of the pit floor. Reaching probabilities below 5% are reported for completeness but do not affect reliability assessment. Considering a 95% reliability target (p_r, ≤ 5%), only two configurations ($\beta = 85°, h_b = 10$m) satisfy the criterion regardless of fragmentation; while twofurther geometries meet it in the non-fragmenting case only, confirming that intact-block assumptions can be non-conservative. Two systematic trends emerge. First, in shallow-angle geometries, fragmentation raises $p_r$across all slope sectors and increases both h_{95}, and v_{95}, at the pit floor, confirming that neglecting fragmentation is non-conservative when the slope promotes shallow impacts and long bench-tread traversal. Second, in steep-angle geometries, fragmentation reduces $p_r$and maintaining similar h_{95} and v_{95}, at each bench, indicating improved retention and demonstrating that fracture-energy dissipation can dominate over the mobility-enhancing effects of small fragment generation. Across all configurations, the N.F. case consistently exhibits the highest E_{95} as the very small masses generated by fragmentation inherently limit the energy carried by single fragments. This aspect is fundamental for assessing bench performance and the expected loading on pit-floor protection measures.

Table 3. Probability of reaching each slope sector (p_r), and 95th-percentile trajectory heigh (h_{95}), velocity (v_{95}) and kinetic energy (E_{95}) at the end of bench 1, end of bench 2, and at the beginning of the pit floor. n.a.=no arrivals. Values of p_r <5%, (underlined) are reported for completeness but are not relevant for reliability assessment.

h_b-w_b-β	1st bench				2nd bench				Pit-floor			
N.F – F.	p_r (%)	h_{95} (m)	v_{95} (m/s)	E_{95} (kJ)	p_r (%)	h_{95} (m)	v_{95} (m/s)	E_{95} (kJ)	p_r (%)	h_{95} (m)	v_{95} (m/s))	E_{95} (kJ)
15-7-55	93-86	0.0-0.2	3.8-5.2	19.8-2.7	23-54	0.0-0.15	2.7-9.4	10.2-0.8	23-54	0.2-4.6	7.4-16.5	326.6-4.9
15-10-55	19-53	0.0-0.0	2.5-3.7	8.9-0.7	<0.1-17	0.0-0.1	3.5-7.9	22.3-0.7	<0.1-16	0.1-2.3	10.2-15.4	250.2-0.6
20-7-55	100-99	0.9-0.9	5.7-8.0	35.4-3.2	40-63	0.0-0.7	2.9-11.6	10.9-0.8	40-63	0.0-11.6	18.8-19.9	502-1.7
20-10-55	21-20	0.0-0.0	3.7-5.1	18.2-0.8	15-34	0.0-0.1	2.6-10.1	10.5-0.4	15-34	0.0-9.4	18.8-19.7	504-1.1
15-7-85	35-3	0.0-0.0	1.9-2.2	10.3-0.4	5-<0.1	5.2-5.1	6.6-7.4	57.3-0.6	5-<0.1	14.9-14.9	14.7-10.4	270-1.2
15-10-85	<0.1-n.a.	5.5-n.a	10.4-n.a	147.0-n.a	n.a.-n.a				n.a.-n.a			
20-7-85	66-27	6.6-6.6	10.1-10.2	30.0-1.2	42-16	9.3-6.7	10.7-9.0	210-0.9	42-15	19.2-17.3	15.6-12.3	310-2.6
20-10-85	20-<0.1	2.8-2.8	4.4-3.6	25-0.4	<0.1-<0.1	4.5-2.5	6.6-4.8	59.4-0.0	<0.1-<0.1	20-17.4	18.8-11.1	260.2-0.4

Overall, the results show that fragmentation produces geometry-dependent, non-monotonic changes in mobility that intact-block assumptions cannot capture. Breakage spreads energy among many low-mass fragments with limited rebound, yet it can still generate rare high-energy trajectories that drive long-runout extremes. Shallow faces enhance the mobility of small fragments, whereas steep faces favour energy dissipation and improve capture. These outcomes underline the need to include fragmentation in probabilistic analyses and runout-based reliability checks for open-pit slope design.

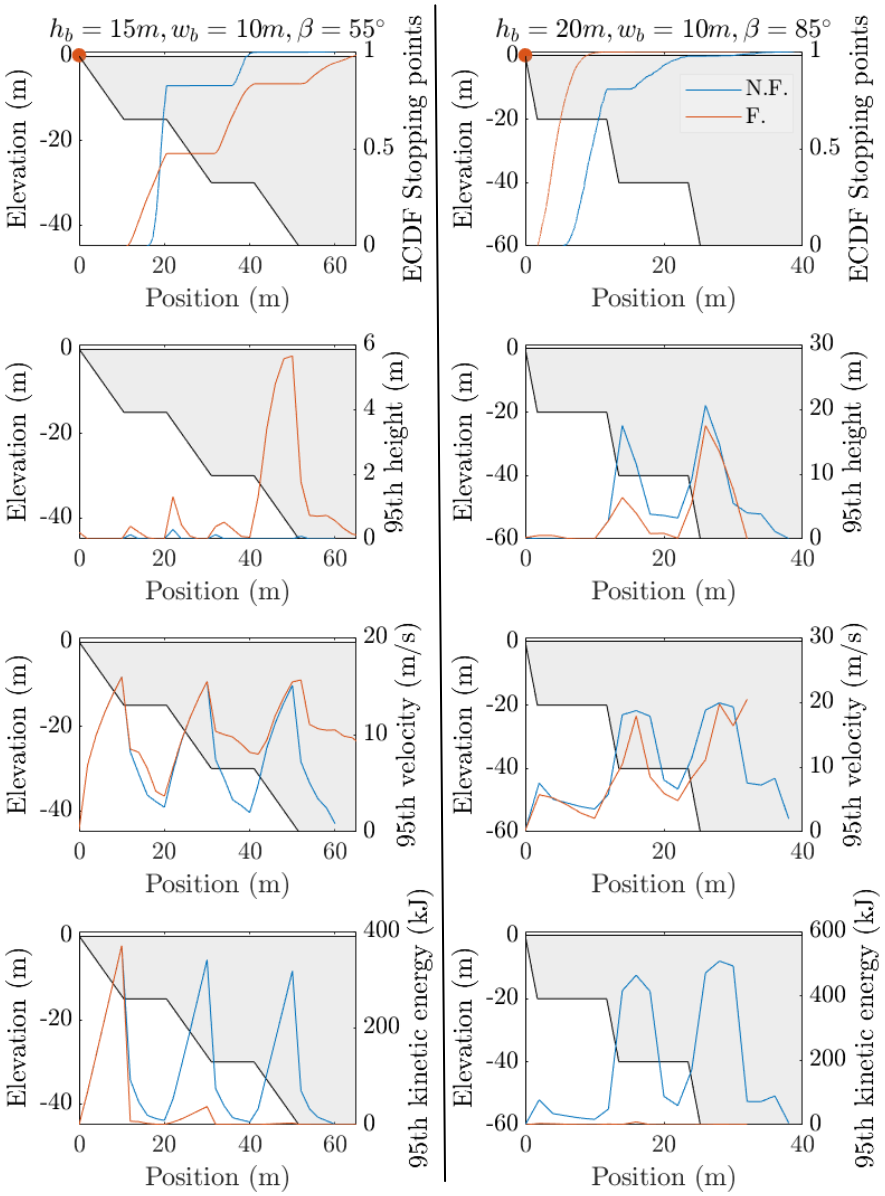


Fig. 1 Comparison between N.F. and F. simulations for:(a) h_b= *15 m,* w_b = *10 m,* β = *55°* and (b) h_b = *20 m,* w_b= *10 m,* β = *85°*. Panels showstopping-point profiles (empirical cumulative density function ECDF), 95th-percentile height, velocities, and kinetic energies along the slope. Red dots represent the source area.

4 Conclusions

The analyses performed on ideal synthetic bench geometries demonstrate that fragmentation exerts a systematic and geometry-dependent influence on rockfall propagation and pit-floor hazard. For shallower faces, fragmentation markedly increases run-out distances, arrival probabilities and upper-tail impact velocities, indicating that neglecting breakage can result in non-conservative design assessments. Conversely, for steep faces, fragmentation may have a limited effect or even improve retention when benches are sufficiently wide, as fracture-energy dissipation promotes earlier stopping, although some very high-velocity trajectories may still arise.

These findings underscore the need to account for fragmentation in runout-based design checks and in evaluating bench performance. Fragmentation can alter conclusions on catch-bench effectiveness and

the loading conditions for protective measures, as its effects on mobility are geometry-dependent. In contexts with uncertain inputs or structural conditions, analysing both fragmenting and non-fragmenting scenarios provides a more robust basis for design, ensuring that the full range of plausible runout and impact conditions is captured.

References

Alejano LR, Pons B, Bastante F, Alonso E, Stockhausen H (2007) Slope geometry design as a means for controlling rockfalls in quarries. International Journal of Rock Mechanics and Mining Sciences 44(6):903–921. 10.1016/j.ijrmms.2007.02.001

Bourrier F, Toe D, Garcia B, Baroth J, Lambert S (2021) Experimental investigations on complex block propagation for the assessment of propagation models quality. Landslides 18(2):639–654. 10.1007/s10346-020-01517-6

Darling P (Ed.) (2011)SME mining engineering handbook (Vol. 1), 3rd edn. Society for Mining, Metallurgy, and Exploration, Englewood, Colorado.

Ferrari F, Thoeni K, Giacomini A, Lambert C (2016) A rapid approach to estimate the rockfall energies and distances at the base of rock cliffs. Georisk 10(3):179–199. 10.1080/17499518.2016.1139729

Gili JA, Ruiz-Carulla R, Matas G, Moya J, Prades A, Corominas J, ... &Mavrouli O (2022). Rockfalls: analysis of the block fragmentation through field experiments. Landslides, 19(5), 1009-1029. 10.1007/s10346-021-01837-9

Li L, & Lan H (2015). Probabilistic modeling of rockfall trajectories: a review. Bulletin of Engineering Geology and the Environment, 74(4), 1163-1176. 10.1007/s10064-015-0718-9

Macciotta R, Altamirano F, Gibbins L, Espezua M, Fernández R, &Maguiña J (2021). Rock fall hazard analysis for in-pit operations potentially impacting external sensitive areas. Mining, 1(2), 135-154. 10.3390/mining1020009

Matas G, Lantada N, Corominas J, Gili JA, Ruiz-Carulla R, Prades A (2020) Simulation of full-scale rockfall tests with a fragmentation model. Geosciences 10(5):168. 10.3390/geosciences10050168

Marchelli M, Peila D, Giacomini A (2023) Rockfall in open pit mines: management of the pit geometry and protection measures design. International Journal of Rock Mechanics and Mining Sciences 170:105551. 10.1016/j.ijrmms.2023.105551

Marchelli M, Guccione DE, Giacomini A, Buzzi O (2025) Fragmentation patterns and trajectories during rockfall: influence of discontinuities and impact conditions through drop tests. Rock Mechanics and Rock Engineering: 1–33. 10.1007/s00603-025-04937-3

Marchelli M (2026). A new probabilistic rockfall trajectory model incorporating fragmentation, rock mass quality and block shape variability. International Journal of Rock Mechanics and Mining Sciences, 206, 106624

McNabb JC, Potter JJ, Restrepo JA, Warren SN, Ryan TM, &Luxbacher KD (2025, June). Quantifying Topographic Influences on Rockfall Trajectories in Open Pit Mines Using Stochastic Rockfall Modeling. In ARMA US Rock Mechanics/Geomechanics Symposium (p. D021S002R006)

Read J, Stacey P (2009) Guidelines for open pit slope design. CSIRO Publishing, Clayton.

Ruiz-Carulla R, Corominas J, Gili JA, Matas G, Lantada N, Moya J, ... & Puig C (2020). Analysis of fragmentation of rock blocks from real-scale tests. Geosciences, 10(8), 308. 10.3390/geosciences10080308

Wang X, Frattini P, Crosta GB, Zhang L, Agliardi F, Lari S, Yang, Z. (2014). Uncertainty assessment in quantitative rockfall risk assessment. Landslides, 11(4), 711-722. 10.1007/s10346-013-0447-8

From nominal energy to capacity curves: a probabilistic framework for reliability-based design of flexible rockfall barriers

V. De Biagi, M. Marchelli, F. Pimpinella
Politecnico di Torino, Turin, Italy
valerio.debiagi@polito.it
0000-0003-1866-9362

Abstract

Politecnico di Torino, Italy

Flexible rockfall barriers are widely adopted passive protection systems in mountainous regions, yet their design still relies on deterministic criteria based on Maximum Energy Level (MEL) and Service Energy Level (SEL) tests. These standardized procedures provide a single nominal energy value, which does not reflect the variability of real impact scenarios nor the stochastic nature of barrier performance. This limitation hinders the integration of reliability-based principles into design, a cornerstone of modern structural engineering.

This work merges a probabilistic framework to estimate the mechanical performance of flexible rockfall barriers under a wide range of impact scenarios into the RockStop software, integrating the resulting capacity curve within the software and enabling its practical use in design workflows. The framework derives capacity curves for flexible rockfall barriers and is built upon a generalized multi-component analytical model, developed by the authors, that simulates barrier response under arbitrary impact conditions by assembling analytical representations of each component (net, wire ropes, posts, energy dissipators). A Monte Carlo simulation scheme propagates uncertainties in geometry, mechanical properties, impact position, and component variability, generating a probabilistic description of the barrier's energy absorption capacity. Results show that highly eccentric impacts can significantly alter the nominal capacity. The integration of trajectory outputs, combined with the barrier capacity curve, in RockStop enables site-specific assessment of all possible actions and their frequency, allowing the calculation of failure probability for both newly installed and existing barriers.

This framework marks a major advancement toward risk-informed design by enabling the integration of reliability-based safety formats for rockfall barriers, supporting comprehensive lifecycle performance assessment, and providing a robust basis for quantifying residual risk after mitigation.

Keywords

Reliability-based analysis, Risk mitigation, Rockfall, Software.

1 Introduction

Flexible rockfall barriers are among the most widely implemented passive protection systems for mitigating rockfall hazard in mountainous terrain (Peila and Ronco, 2009). Their mechanical

characterization and certification rely on two standardized full-scale impact tests: the Service Energy Level (SEL) and the Maximum Energy Level (MEL), as prescribed in EAD 340059-00-0106 (EOTA 2018). These tests provide a unique nominal energy capacity for each barrier type, obtained under strictly controlled impact conditions: central impact, fixed block geometry, prescribed velocity, and a specific three-module configuration. While this procedure ensures comparability across products, it also embeds a fundamental limitation: real impact scenarios rarely correspond to the standardized test configuration. In practice, block size, velocity, trajectory height, impact angle and, crucially, impact position, vary widely, leading to markedly different load-transfer mechanisms and structural responses (Yu et al., 2021). Full-scale tests, analytical formulations and numerical simulations consistently show that such variations may induce significant variation in actual barrier capacity compared to the nominal MEL value (Coulibaly et al., 2019).

A second major limitation arises on the action side of the design format. Current national guidelines (e.g., UNI 11211-4:2018; ONR 24810:2021) prescribe the use of single characteristic values derived from trajectory simulations (typically the 95th percentile of block velocity and impact height), assuming a representative block volume, to represent all possible rockfall events. This simplification overlooks the inherently stochastic nature of block mass, kinematics and trajectory height distributions, which may span orders of magnitude depending on site-specific geological and geomorphological conditions. Consequently, the design action is treated as a fixed quantity, although the underlying variability is large and well documented (Bourrier et al., 2016; Macciotta, 2019).

Taken together, these two simplifications (a unique deterministic resistance from MEL testing and a unique characteristic action from trajectory percentiles) make it impossible to quantify the true probability of failure of flexible barriers. Recent reliability-based studies illustrate that the actual failure probability of flexible barriers may vary by orders of magnitude depending on the event frequency, block size distribution, kinematic variability, barrier installation configuration and performances (De Biagi et al, 2020; Marchelli et al., 2020, Marchelli et al., 2021). Neglecting the intrinsic variability of both resisting and acting quantities may therefore lead to designs that are either overly conservative or insufficiently safe. To address these limitations, a dedicated software, RockStop (De Biagi and Marchelli, 2025), has been developed to implement a time-independent reliability-based design framework, allowing designers to compute the failure probability of rockfall barriers by integrating site-specific probabilistic descriptions of impact velocity and trajectory height, derived from trajectory analyses, together with the block mass frequency distribution. In its original formulation, however, RockStop assumes a deterministic resistance, represented by the nominal MEL value, thereby inheriting the limitations of current design practice.

In this work, we enhance the RockStop framework by replacing the deterministic MEL-based resistance with a probabilistic capacity curve, constructed from thousands of simulated impact scenarios. The capacity curve is derived by repeatedly evaluating the barrier's mechanical response under randomized impact conditions, including variations in impact position, block size, geometric tolerances, and component mechanical properties. These simulations are performed using a generalized multi-component analytical model, developed by the Authors (Pimpinella et al., 2025; Pimpinella et al., under review), which captures the full load-transfer mechanism of the system and explicitly accounts for the effects of eccentricity and component-level variability on energy dissipation. By integrating the resulting capacity curve into RockStop, the software transitions from a single-value representation of resistance to a distribution-based description of barrier capacity, ensuring that both actions and resistances are treated consistently within a reliability-based design framework. This upgraded approach enables a truly operational, site-specific assessment of failure probability, grounded in the actual variability of impact scenarios and system response. An illustrative application on an RXI-100 barrier is presented to demonstrate the construction of the capacity curve and its implications for reliability-based design.

2 Methodology

2.1 Generalized Multi-Component Analytical Model (GMCM)

The construction of the capacity curve requires a mechanical model capable of reproducing the behaviour of a flexible rockfall barrier under arbitrary impact conditions while maintaining computational efficiency sufficient to allow thousands of simulations. For this purpose, a Generalized

Multi-Component Analytical Model (GMCM) developed by the Authors is employed (Pimpinella et al., 2025). The model represents the barrier as the assembly of its fundamental mechanical subsystems, namely the intercepting structure, wire ropes, energy dissipating devices, posts, and foundations, each described by analytical relations derived from experimental evidence and numerical modelling. Within the GMCM, the intercepting structure is discretized into sets of equivalent fibres whose axial response reproduces the stiffness and strength of the underlying ring-net or wire-mesh arrangement. The impactor is assumed to interact with the net along a localized region, and the net–rope system transmits the load to the longitudinal and panel ropes. Energy dissipators, arranged along selected rope lines, activate once their characteristic force threshold is reached, contributing to the majority of the energy absorption through controlled plastic deformation. Posts and boundary elements redirect the load through bending and axial mechanisms, with their behaviour included in the model through calibrated force–displacement relations.To account for the possibility of direct impacts on the posts, an *ad-hoc* metamodel, specifically developed to reproduce their behaviour under direct impact, is incorporated to capture the additional energy dissipation mechanisms and deformation patterns observed in full-scale tests and detailed numerical simulations (Pimpinella et al., 2024).

The GMCM adopts an incremental quasi-static formulation, applying the impact load in increasing steps and solving sequentially for the displacements and internal forces within each subsystem. At each increment, the model verifies compatibility of deformation and equilibrium of forces among components, identifying the sequence of activations, yielding, stiffening or softening that characterizes the load path. Mechanical and geometric properties, as well as impact coordinates, enter the analysis as input parameters. When these are varied stochastically within a Monte Carlo scheme, the GMCM computes the absorbed energy for each realization as the work performed along the force–displacement path up to the failure displacement of the system. For each impact scenario, the capacity of the barrier is:

$$C_d = \int_0^{w_u} F(w)\, dw \qquad (1)$$

where $w_u$is the displacement corresponding to the onset of failure in any subsystem. Repeating this procedure over thousands of random impact scenarios produces a distribution of dissipated energies, from which the capacity curve is derived (Pimpinella et al., under review). The GMCM therefore provides the mechanical backbone for quantifying the variability of the resisting side of the reliability problem, explicitly capturing the influence of impact eccentricity, block radius, component dispersion and geometric tolerances on the barrier's energy absorption capacity.

2.2 RockStop module for reliability-based design

To operationalise the probabilistic mechanical characterisation provided by the GMCM, the resulting capacity curve is integrated into RockStop, a software tool originally developed by the Authors (De Biagi and Marchelli, 2025) to implement time-independent reliability-based design of rockfall barriers. From previous releases, RockStop now combines the distributions of block mass, velocity and trajectory height from runout analyses with the event frequency along the slope, with a full probabilistic capacity distribution obtained from the GMCM-based Monte Carlo simulations.

In the reliability formulation adopted by RockStop, the failure probability can be associated with two distinct modes: excessive energy, occurring when the block's kinetic energy exceeds the barrier's energy absorption capacity, and excessive height, arising when the block's trajectory height surpasses the nominal height of the barrier. Assuming a lumped-mass trajectory model the failure probability associated with excessive energy over a timeτ is expressed as:

$$F_k(\tau) = 1 - \exp\left[-\lambda\tau \int_0^{\infty} p_f(\mu)\, f_{mk}(\mu)\, d\mu\right] \qquad (2)$$

where λ is the mean annual frequency of rockfall events, $f_{mk}(\mu)$ is the probability density of block mass (derived from deposit surveys or volume–frequency laws), and $p_f(\mu)$ is the conditional probability of failure given a block of mean mass μ. In the original formulation, $p_f(\mu)$ was evaluated as the probability that the kinetic energy exceeded the deterministic barrier capacity. With the introduction of a capacity curve to assess barrier kinetic energy retention capacity, $p_f(\mu)$ becomes:

$$p_f(\mu) = P(E_d < E_i(\mu, v)) \quad (3)$$

meaning that the probability of failure is obtained by comparing the incoming kinetic energy $E_i = \frac{1}{2}mv^2$ with the full distribution of dissipated energy E_d obtained from the values of C_d. Thus, the resisting term is now treated probabilistically, consistent with the action term.With an expression analogous to Eq. (2), the probability of failure due to excessive trajectory height can be computed. Assuming independence between energy-driven and height-driven failure modes, the total annual failure probability is obtained by summing the two corresponding annual failure probabilities. This value represents the primary output of RockStop when assessing an existing barrier, or the target parameter to be achieved in the design of a new installation.

With the integration of the capacity curve, RockStop now treats both actions and resistances as random variables, enabling reliability-based design in two modes. In "design mode", the user specifies a target annual failure probability, and RockStop identifies the minimum capacity curve (and corresponding barrier product) satisfying this target. In "assessment mode", the software computes the annual failure probability for an existing installation. In both cases, the adoption of the probabilistic capacity curve ensures that the design reflects the true variability of barrier performance across impact locations and component states, rather than a single nominal test result.

3 Example of application

To demonstrate the operational capabilities of the proposed probabilistic framework and its integration within RockStop, an application is carried out for a site located in the North-Western Italian Alps, where recurrent rockfall activity has been documented along a steep granitic slope overlooking a secondary mountain road. Historical records and field evidence indicate the presence of frequent small-to-medium rockfall events, associated with freeze-thaw cycles and differential weathering of jointed rock masses. A preliminary geomorphological survey identified a source area extending between 1050 and 1000a.s.l., with an estimated annual frequency of events equal to λ=0.5 yr^{-1}.

Trajectory simulations were performed using a lumped-mass runout model on the reconstructed slope profile. A total of 5000 trajectories were generated, sampling initial block positions, restitution parameters and rolling conditions within ranges obtained from field observations. At the barrier location, selected at an elevation of 870a.s.l. to maximise interception efficiency, the distribution of impact velocities exhibited a right-skewed shape with a mean of 13.1 m/s and a 95th percentile of 16.2 m/s. Trajectory heights measured at the centre of mass of the blocks showed a 95th percentile of 3.0 m, with sporadic impacts exceeding 3.4 m. Block sizes in the deposition area were surveyed following a four-square homogenisation procedure (Marchelli and De Biagi, 2019), yielding a minimum volume of 0.2 m^3 Pareto-Type I shape parameter equal to 1.9, confirming the dominance of small blocks in the frequency distribution.

Given the expected impact energies and the spatial constraints imposed by the slope, an RXI-100 flexible barrier was selected as a representative protective system. Its nominal MEL is 1000 kJ, and its nominal height is 4.0 m. For the present analysis, the barrier geometry, net characteristics, rope arrangement and dissipator properties were defined according to manufacturer data and previous analytical studies conducted on the same technology. The barrier layout was then introduced into the GMCM-based simulation framework.

A Latin Hypercube sampling was carried out by performing 205 simulations, each representing a distinct impact position. Exploiting the symmetry of the barrier configuration and impact mechanics, impacts were simulated over one quarter of a single module only, with results subsequently extended to the full module. Impact scenarios were defined through random sampling of longitudinal and transverse eccentricities, which were found to be the relevant parameters in barrier's capacity.

For each realisation, the GMCM computed the dissipated energy up to system failure, allowing the construction of the site-specific capacity distribution for the RXI-100 barrier. The dissipated energy was normalised with respect to MEL value E_{MEL}. Fig. 1a illustrates the spatial distribution of the normalised dissipated energy E_d/E_{nom} as a function of impact eccentricity within the analysed quarter-module. The results highlight a pronounced spatial dependency of barrier performance: highly unfavourable eccentric impacts are associated with dissipated energies close to 300 kJ, whereas

configurations characterised by quasi-central impacts and symmetric activation of the longitudinal dissipators may exceed 1500 kJ. Overall, only 19 % of simulated impacts resulted in a dissipated energy exceeding the nominal MEL, confirming the strong sensitivity of barrier capacity to impact location, consistently with previous probabilistic investigations.

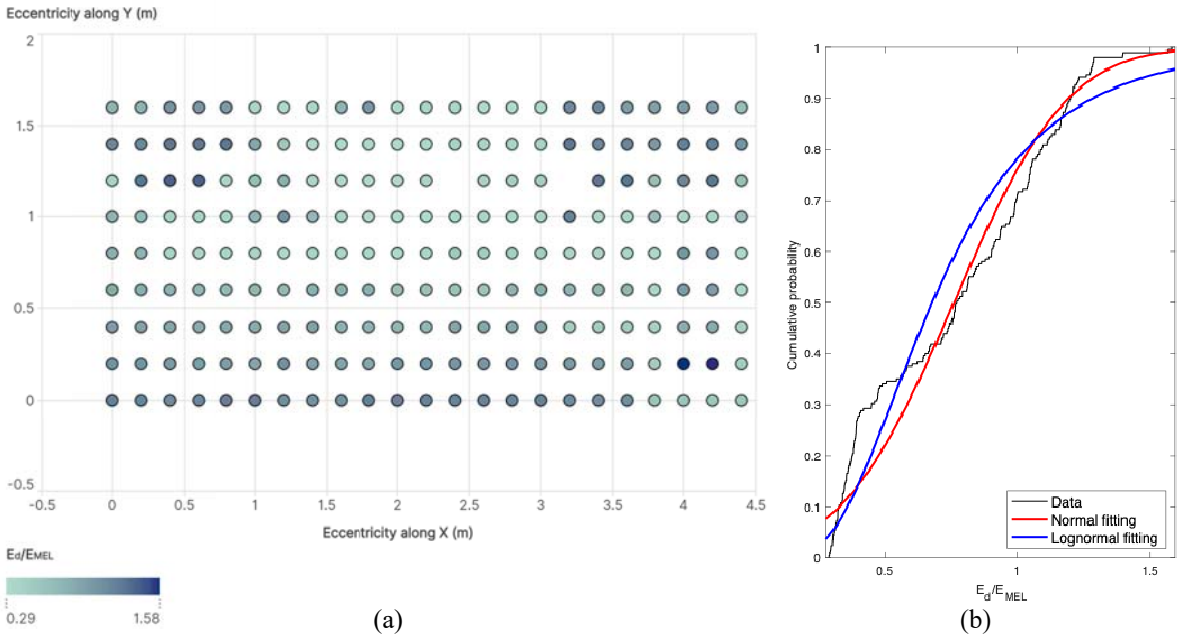


Fig. 1 (a) Spatial distribution of the normalised dissipated energy E_d/E_{MEL} as a function of longitudinal (X) and vertical (Y) impact eccentricity, obtained from LH simulations performed on one quarter of a barrier module. In (b), the empirical cumulative distribution and its normal and lognormal fittings are reported.

By aggregating all simulated impact scenarios, the empirical cumulative distribution of the normalized capacity E_d/E_{MEL} was derived. A statistical fitting procedure showed that this cumulative distribution is best approximated by a normal distribution (red curve in Fig. 1b, with mean and CoV equal to 0.76 and CoV equal to 0.4435), providing a compact probabilistic representation of the barrier capacity. This probabilistic capacity curve was subsequently implemented in RockStop together site-specific distributions of block mass, trajectory height and impact velocity at the barrier location. The conditional failure probability for each potential impact event was evaluated by comparing the incoming kinetic energy with the probabilistic resisting energy, and the total annual failure probability was computed within the time-independent reliability framework. For the RXI-100 barrier at the considered site, the resulting annual failure probability was equal to 1.0×10^{-2}, with energy-driven failures providing the dominant contribution due to the relatively high proportion of impacts characterized by unfavourable eccentricities. Recalculating the risk after installation of the barrier yields a residual risk for the protected road of the order of 10^{-5}, consistent with the individual life safety tolerability thresholds specified in UNI 11211-2 (2021).

4 Conclusions

This work presented a probabilistic framework for the mechanical and reliability-based assessment of flexible rockfall barriers, overcoming the limitations of conventional MEL-based deterministic design. By coupling a generalised multi-component analytical model with Monte Carlo simulations, the variability of barrier performance under arbitrary impact conditions was quantified and synthesised into a capacity curve that more realistically represents the resisting behaviour of the system. Integration of this probabilistic resistance model into RockStop enables a consistent treatment of actions and resistances as random variables within a time-independent reliability framework. Application to an RXI-100 barrier in a representative Alpine setting demonstrated that impact eccentriccity and component-level variability have a strong influence on system capacity and failure probability, with the resulting annual failure probability shown to be compatible with acceptable thresholds for individual risk when appropriately calibrated. Overall, the proposed framework supports transparent, site-specific and performance-based design of flexible rockfall barriers, providing a robust tool for the assessment and optimisation of both new and existing installations. Future developments may extend the methodology to account for ageing effects and component degradation during time.

References

Bourrier F, Baroth J, Lambert S (2016) Accounting for the variability of rock detachment conditions in designing rockfall protection structures. Natural Hazards 81(1):365–385. https://doi.org/10.1007/s11069-015-2084-0

Coulibaly JB, Chanut MA, Lambert S, Nicot F (2019) Toward a generic computational approach for flexible rockfall barrier modeling. Rock Mechanics and Rock Engineering 52(11):4475–4496. https://doi.org/10.1007/s00603-019-01878-6

De Biagi V, Marchelli M, Peila D (2020) Reliability analysis and partial safety factors approach for rockfall protection structures. Engineering Structures 213:100553. https://doi.org/10.1016/j.engstruct.2020.110553

De Biagi V, Marchelli M (2025) A new tool to quantify the failure probability of rockfall net fences. In: Rocscience International Conference 2025 (RIC 2025), 451–459. Atlantis Press. https://doi.org/10.2991/978-94-6463-402-5_45

EOTA (2018) EAD 340059 00 0106 Falling Rock Protection Kits. European Organisation for Technical Assessment, Brussels

Macciotta R (2019) Review and latest insights into rock fall temporal variability associated with weather. Proceedings of the Institution of Civil Engineers – Geotechnical Engineering 172(6):556–568. https://doi.org/10.1680/jgeen.18.00224

Marchelli M, De Biagi V (2019) Optimization methods for the evaluation of the parameters of a rockfall fractal fragmentation model. Landslides, 16(7), 1385-1396. https://doi.org/10.1007/s10346-019-01182-y

Marchelli M, De Biagi V, Peila D (2020) Reliability based design of protection net fences: Influence of rockfall uncertainties through a statistical analysis. Geosciences 10:280. https://doi.org/10.3390/geosciences10070280

Marchelli M, De Biagi V, Peila D (2021) Reliability based design of rockfall passive systems height. International Journal of Rock Mechanics and Mining Sciences 139:104664. https://doi.org/10.1016/j.ijrmms.2021.104664

ONR (2021) ONR 24810 Technical protection against rockfall. Austrian Standards Institute, Vienna

Peila D, Ronco C (2009) Design of rockfall net fences and the new ETAG 027 European guideline. Natural Hazards and Earth System Sciences, 9(4), 1291-1298. https://doi.org/10.5194/nhess-9-1291-2009

Pimpinella, F., Marchelli, M., Lanter, A., & De Biagi, V. (2024). Numerical back-analysis of impacted rockfall barriers steel posts: discussion on the effectiveness of the system. In 14th International Symposium on Landslides 2024, Chambery, 8-12 July 2024

Pimpinella F, Marchelli M, De Biagi V (2025) A generalized multi component analytical method to study the performance of a rockfall barrier under a generic impact condition. Computers and Geotechnics 188:107602. https://doi.org/10.1016/j.compgeo.2025.107602

Pimpinella F, Marchelli M, De Biagi V (2025) Towards a probabilistic description of the mechanical performance of rockfall retaining systems. Engineering Structures (submitted)

UNI (2018) UNI 11211 4: Rockfall protective measures – Part 4: Definitive and executive design. UNI, Milano

UNI (2021) UNI 11211 2: Rockfall protective measures – Part 2: Preliminary intervention programme. UNI, Milano

Yu Z, Luo L, Liu C, Guo L, Qi X, Zhao L (2021) Dynamic response of flexible rockfall barriers with different block shapes. Landslides 18(7):2621–2637. https://doi.org/10.1007/s10346-021-01658-w

Geotechnical Risk Ranking Matrices

J. Dixon
Fortescue, Perth, Australia

T. G. Carter
TGC-GeoSolutions, Oakville, Ontario, Canada
tcarter@tgcgeosolutions.com
0000-0001-6746-959X

P. J. H. deGraaf
Giraffe Mining Consultants, Perth, Australia

H. Abu-Taleb
Fortescue, Perth, Australia

Abstract

Risk assessments for evaluating geotechnical hazards on major mining and civil projects have become increasingly popular over the last several decades. Trends in international tunnel contracts to require Risk Registers and Geotechnical Baseline Reports has spurred much of this interest in the Civil sector. Environmental and Social risks along with public perception issues have driven development in the Mining industry, but still there remains a challenge assessing and effectively communicating geotechnical risk. While quantitative assessment has become more sophisticated, inevitably synthesis is needed, still demonstrating credibility. Risk evaluation is just another tool to help aid improved understanding and support better informed business decisions. Simplification, based on well-reasoned argument, is required for decision making, but still with quantitative back-up.

Classically, even the most complex QRA's have needed to be boiled down to plot on a "likelihood versus consequence" matrix for communication to management and stakeholders. Mostly these are formulated with rankings for financial, project, operational, environment, social or health and safety risk. Incorporating risk due to geotechnical ground conditions is often complex. The recently introduced 5x5x5 3D matrix diagram developed for open pit closure (Hawley et al., 2024, Carter et al., 2022), based on similar approaches in other industries (Bao et al., 2022, Watson 2004, Cram, 2004) provides an approach for ranking geotechnical risk in an equal way as other drivers. In the 3D matrix, one axis is the ground condition hazard rating, which can be stability PoF/FoS for infrastructure components (foundations, tunnel linings etc.,) or mechanisms (hydrofracture, overstress) or any other aspect of geotechnical significance. This scale, together with the design confidence axis (design uncertainty, data sparsity or imprecision), form one side of the block diagram representing the likelihood component that is classically used in standard 5x5 matrices. The consequence axis, forms the last component of the 3D diagram. The overall diagram and approach outlined in this paper has been formulated tohelp improve understanding and communication of key risk scenarios, so as to allow better decision-making when undertaking risk assessments for geotechnically impacted projects.

Keywords

Risk Assessment, Matrices, Uncertainty, Decision Analysis, Failure Modes.

1 Introduction

Risk Assessments have become commonplace in almost all engineering projects, but often more focused on institutional, financial, operational, organizational, environmental or social risk, than on geotechnical hazards, such as adverse ground conditions that present geotechnical risk. Not infrequently geotechnical risk is assessed only as a component of these other risk considerations. This is despite geotechnical hazards being central to some of the largest major project construction claims, the cause of (or sometimes just blamed for) delays and cost overruns and often cited as the prime reason for major financial, operational and/or closure risks in mining projects.

Over the last several decades, trends in international tunnel contracts to require Risk Registers and Geotechnical Baseline Reports (GBRs) has spurred interest, and more rigid requirements for, quantitative risk assessments (QRAs) to be applied for examining problematic geotechnical aspects. Environmental and social risks have driven similar trends in the Mining industry, but still there remains a challenge assessing geotechnical risk. While quantitative assessment has become more sophisticated, inevitably synthesis is still needed for in-depth understanding, yet still demonstrating credibility. Application of AI into risk analysis has the potential to facilitate more informed assessment, but if used incorrectly can equally easily lead to misleading conclusions. AI has potential to improve data synthesis and support risk assessments, but engineering judgement remains essential because many geotechnical uncertainties cannot be fully quantified. Effective risk management therefore requires both quantitative analysis and simplified communication of key uncertainties. The dilemma of diverging trends to more sophistication in QRAs, yet an overwhelming need for simplification to help understanding, is leading to advocation of well-reasoned argument as providing a better path forward for decision making, but still with quantitative back-up.

2 Background – Risk Ranking Methodology Development

In a mining context, with a need to rationalize well-reasoned argument (Miller, 2019), and still quantitatively assess, for example, remnant slope instability risk for open pit closure, a rigorous, yet relatively simple, probabilistic risk assessment approach was developed in 2022 to allow: (a) end of mining potential slope stability hazard levels to be categorized, (b) design confidence in stability evaluations to be ascertained, (c) remnant potential closure risks to be identified, (d) target stability reliability goals to be established and (e) potential mitigation options for remediation to be examined as measures to reduce long-term stability risks to less than target levels (Carter et. al, 2022, Hawley et al., 2024). The recommended workflow developed to apply the methodology is illustrated in Figure 1.

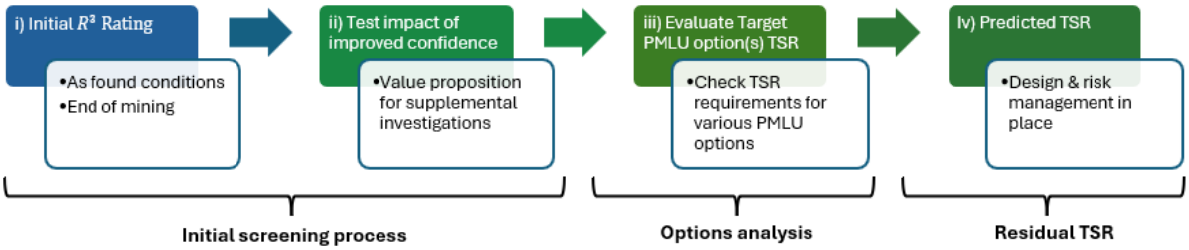


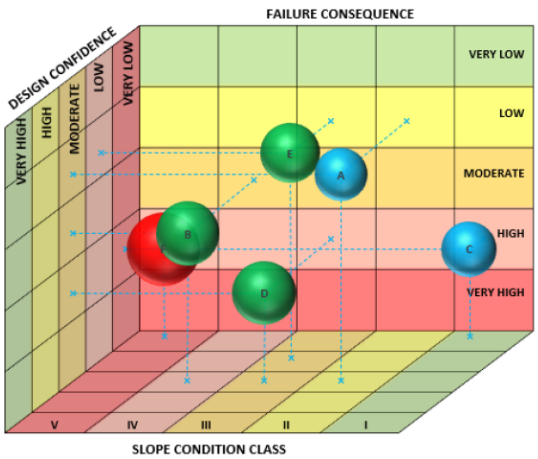
Fig. 1Recommended Residual Risk Rating ($R^{3)}$ Screening and Target Stability Rating (TSR) Risk Evaluation Process Workflow for various Post Mining Land Use (PMLU) options (updated from Carter et al., 2022).

This approach concentrates on assessing geotechnical risk through instability evaluation. One major inherent problem though, is that geotechnical, and even more so, geological risks are generally invisible to untrained stakeholders, many of whom may be external to the operation or project, but are seriously concerned with long term impacts. Trends today, towards ever increasing use of sophisticated and visibly impressive 3D numerical geomechanics and Building Information Modelling (BIM) approaches for analysis and information transfer to designers and stakeholders (often based on limited or non-existent site investigation data) have the potential to obscure real geotechnical risks, even to knowledgeable observers. The proposed risk screening and hazard ranking approach outlined in 2022 therefore utilizes failure mechanisms as the lead guideline for assessing hazard type and probability of occurrence (likelihood), whether it be for slope instability concerns, the initial procedure application, or for tunneling or underground works, dams, foundations, bridges or for any other structure of concern. This allows the suggested procedure to be applied at any project state, but it helps particularly in early project stages, as the Residual Risk Ranking (R^3) provides useful insight for evaluating design options.

3 Risk Reliability Matrix

Matrix methods, as commonly employed in many health and safety styles of risk assessment because of their apparent simplicity, allow ready ranking of Risk = Likelihood x Consequence. Such 2D matrices have significant limitations though, when applied to assessing geotechnical instability likelihood.

For geotechnical conditions the complexity of the ground must be totally understood if anything close to high reliability can be placed on any analytical or numerical assessment, (Carter, 1992, 2018). Total understanding of prevailing geotechnical conditions must extend to full appreciation of all potential active and passive mechanisms and must also achieve high reliability in understanding all credible failure modes. Achieving certainty in geotechnical or geological engineering is however impossible. Natural ground condition variability and lack of understanding of the actual in situ ground conditions influencing the failure, due to inadequate site investigation data are just two of the many significant uncertainties that impact reliability of any Probability of Failure (PoF) estimate. Analytical or numerical tools cannot completely replicate real failure mechanisms, thus introducing additional uncertainty. Inexactitude in understanding hydrogeological conditions and magnitudes and/or involvement of other mechanisms influencing stability add further uncertainty, let alone vagaries due to variability in competence of those executing the analyses. An uncertainty measure must therefore be accumulated along with PoF estimates in order to rank confidence in understanding that computed PoFs are correct. The mining industry, for instance, typically embraces risk management at an operational level, with developments in geotechnical Design Acceptance Criteria (DAC) focusing on managing design risk through application of confidence-consequence based DAC (Macciotta et al., 2022) along with robust operational safety controls. However, it is acknowledged that in some cases DAC selection is mandated by regulatory codes and standards (e.g. in civil construction), legal exposure and industry precedent.



INITIAL CONDITION RANKINGS			
Slope Condition Class Rating	Design Confidence Rating	Failure Consequence Rating	ESR R^3 Score
V = 5	VL = 4	VH = 5	80-100
IV = 4	L = 4	H = 4	60-80
III = 3	M = 3	M = 3	40-60
II = 2	H = 2	L = 2	20-40
I = 1	VH = 1	VL = 1	<20

SLOPE SECTOR	Slope Condition Class Rating	Design Confidence Rating	Failure Consequence Rating	Initial R^3 Score
A	II	M	L	12
B	IV	M	M	36
C	I	VL	H	16
D	III	M	H	36
E	III	L	L	24
F	V	VL	H	80

Fig. 2 Three-dimensional Risk-Reliability Matrix and example Initial Expected Stability R^3 Ranking for guiding selection of closure Target Stability Rating (TSR) for Open Pit slopes (de Graaf, Beale and Carter, 2025).

To resolve these difficulties in ascribing credibility to the assessed likelihood of failure (expressed as PoF) and to help quantify all these various uncertainties, a third, "Design Confidence" ranking axis is introduced to the classic two-dimensional "hazard likelihood" = PoF, versus "consequence impact" matrix. Adding this third axis, as shown in Figure 2, is a powerful improvement in allowing scaling of degree of understanding of uncertainty achieved in the analyses. Consideration of adequacy (or otherwise) of degree of determination of geotechnical variability as a result of site investigation data acquisition and coverage now becomes possible, along with assessment of all other related uncertainties.

This third axis, (focused towards a subjective judgmental relative ranking of degree of design understanding / confidence) gives a credibility check on the estimated likelihood of failure (as defined quantitatively with PoF numbers from analytical or numerical assessments of stability (of whatever is of concern – tunnel face/portal, cavern, slope, foundation, retaining structure, dam, wharf/pier) when set alongside, the again, more qualitative and subjective judgmental assessments, for the consequence axis.

The diagram in Figure 2 shows application of the 3D Risk-Reliability matrix as initially developed for assessing slope instability risk for open pit mine closure, but is equally applicable to any other geological/geotechnical engineering design situation, with risk sections delineated appropriately for

the expected ground conditions and failure mechanisms. The axes in the diagram respectively rank (1) PoF scenarios for all credible expected failure mechanisms for the anticipated Ground Conditions (in this case ranking slope stability), (2) Design Confidence, meaning degree of uncertainty in data/understanding/analysis methods etc in assessing the PoF, and (3) Failure Consequence – ranking the potential impact in financial/institutional/physical or reputational risk terms if failure were to occur.

Each scale is divided into five classes, with appropriate numerical scales to aggregate to a total 100 score for worst case conditions. For the six example slope zones considered in the lower right-hand table alongside the 3D matrix diagram in Figure 2, their R^3 scores are reflected in the colour coding and size of each plotted sphere in the 3D diagram, each scaled in accordance with perceived risk, with Table 1 providing guidance on recommended Target Stability Reliability (TSR) criteria actions for improving/mitigating or otherwise dealing with the defined conditions, (in this case potential slope instability examined from the viewpoint of longevity of stability, post mine closure).

Table 1. Recommended Target Stability Reliability (TSR) criteria actions based on initial R^3 scores; in this case focused on remnant instability issues in a pit closure context(from de Graaf,Beale and Carter, 2025, updated from Carter, 2022.)

R^3 Score	R^3 Score	Suggested TSR Static FoS*,**	Recommended Actions
R3 > 80	Extreme	FoS > 2.0 PoF < 0.5%	Comprehensive and rigorous analysis required to develop deep understanding of failure mechanisms and behaviour to support implementation of very robust controls. Detailed numerical crest breakback and/or runout analyses to establish permanence exclusion zones. Likely requires detailed supplementary field and laboratory investigations. Detailed evaluation of feasibility of alternatives/trade-off studies to reduce R^3 achieve ALARP objective. Very high design reliability required. FoS>2 is needed unless Quantitative Risk Assessment (QRA) undertaken.
60≤ R3≤80	Very High	1.8≤FoS≤2.0 PoF <0.75%	
40≤ R3≤60	High	1.5≤FoS≤1.8 PoF <1%	Rigorous analysis is necessary, so that thorough understanding of mechanisms is obtained and robust controls can be implemented. Detailed numerical runout analyses to establish permanent exclusion zones. May require supplementary field and laboratory investigations. Trade-off studies to assess feasibility of reducing R^3 score and achieving ALARP objectives. High design reliability required. FoS>1.5
20≤ R3≤40	Moderate	1.3≤FoS≤1.5 PoF <1.5%	Moderate level of reliability of all critical inputs required to support stability analysis. Standard analysis and/or empirical approaches sufficient. Good understanding is needed of scenario so that appropriate controls can be implemented. Empirical breakback and/or runout analyses to establish permanent exclusion zones. May require supplementary field and laboratory investigations. Confirm alignment with ALARP objective. Good design reliability required. FoS>1.3
R3<20	Low	1.2≤FoS≤1.3 PoF <3%	Evaluate reliability of all critical inputs to support stability analysis. Apply good practice, guidance, and hierarchy of controls. May require targeted investigations to address areas where knowledge is lacking or unreliable. Confirm alignment with ALARP objective. Fair design reliability required FoS >1.2

*For relinquishment and passive closure objectives; one class lower for active closure or ongoing 'care and maintenance' objectives (FoS 1.2 minimum). **For seismic design follow risk-based decision tree approach.

4 Application Experience

While this 3D matrix approach has received wide acceptance as a step forward, several challenges have arisen in the application of the developed approach. Mostly these concerns have revolved around (i) the confidence axis and the implied assumption that the rankings assigned to this confidence scale could be directly multiplied against the consequence scores to define risk, and (ii) definition of credible failure modes and mechanisms, so that the ground stability axis can be appropriately scaled.

4.1 Likelihood

The assumption inbuilt into the logic of the R^3 derivation is that real "Likelihood" of a hazard actually occurring can only be assessed by the product of the two left hand axes in Figure 2 – Ground Conditions (ie., stability state) and Design Confidence (ie., understanding). Rigorous stability analysis can define Probability of Failure (PoF), but that probability evaluation result may not be completely definitive due to many uncertainties, which affect the accuracy of that analysis. The definition of the ground stability class, based on the assumed or calculated stability state, can be affected by inadequate

understanding of failure mechanism, and rockmass, structural, hydrogeological, or seismicity conditions. Additionally, in a situation where mitigation measures are being considered (such as slope regrading, reinforcement, buttressing etc), the degree of uncertainty in the analysis further increases due to inexactitude of understanding of the effectiveness of the proposed remediation measure. These uncertainties need to be considered when ranking the Design Confidence with factors that are most relevant to the failure mode dictating the final rating.

While the Design Confidence axis should be considered the *defacto* measure of degree of understanding to rank the reliability of the stability assessment to ensure that it reflects the ground behaviour accurately, it is important to not consider this axis in isolation. Revising rankings on the confidence axis to reflect increases in analysis reliability, due to, for example, gathering more site investigation data to better define the failure mechanism, may also result in possible changes needing to be made to the ground stability rankings because of the analysis improvements. Changes in both axis rankings must therefore always be considered together, as both axes need to be properly linked to correctly define real hazard likelihood of occurrence.

In addition, care must be taken to only utilize the matrix for decision ranking. It is recognized, for instance, that in examining potential improvements in confidence that can be achieved with better analysis and better understanding for cases at the adverse end of the two linked axis scales (4's and 5's), simple multiplication of the rankings for design confidence and ground stability state will plateau at some level lower than what intuitively might be a more appropriate number. This is not seen as a complication for use of the matrix, as this idiosyncrasy of the 5x5x5 matrix algebra is not an issue for good condition rankings with scores lower than 3, consistent with the aim being to always move towards resolution of such problems by de-risking a more hazardous situation through careful design application.

4.2 Credible Failure Modes

The discussion above touched on uncertainty in definition of appropriate failure mechanisms, and that some of this uncertainty needs to be reflected in both the design confidence and the ground stability axes rankings. Definition of credible failure modes and accuracy of modelling and/or analytics inherent in the involved mechanism calculations is also always an issue in ensuring precision and reliability of any analysis, particularly if mechanisms are complex. This is often the case for high rock slopes, where both shear and tensional processes may interact and where both intact and discontinuity behaviour could be equally important. There is however a case to be made that design consequence aspects also need such consideration, which may sound counter intuitive; but, given certain impact scenarios, there is an argument to be made that consequence should not be defined by a single threshold (ie., not just PoF<1%, FoS >1.5, as for example listed in Table 1), but should also be risk based.

4.2.1 Definitions

The Global Industry Standard on Tailings Management GISTM publication defines a credible failure mode (scenario) as a technically feasible way a tailings facility could fail, given its materials and foundation, configuration, drainage and surface-water controls across its lifecycle. Which modes are credible can change as conditions change. Importantly, the term is "not associated with a probability of this event occurring", and the guide notes that having credible failure modes does not, by itself, indicate the facility is unsafe, (Global Tailings Review, 2020). Much industry discussion has thus subsequently resulted in terms of how to define credibility, with two main interpretations existing, one being related to the failure mode being physically possible/technically feasible and the other focused on negligibility. These debates continue, highlighting the complexity associated with any decision on credibility.

In the context of utilizing the R^3 approach for mine closure, and also for more general engineering application, the following five guiding principles are thus considered prudent to apply, with each aligned with both the GISTM recommendations and those included within the Guidelines for Open Pit and Waste Dump Closure (de Graaf, Beale and Carter,2025), viz:

1. Potential failure modes should not be dismissed early in the evaluation process and each must be supported by appropriate technical information, with confidence commensurate with the likely risk the mode presents;
2. Credible failure modes require a technically feasible mechanism, initiating event and failure

process;

3. A failure mode is considered credible if it is physically possible and its likelihood is not so remote as to be clearly negligible;
4. Frequency-based arguments (qualitative or quantitative) and structured expert judgement can be used to support analysis assessment, but any numerical threshold must be consequence- and context-dependent; and
5. Credibility should be periodically reviewed as conditions and knowledge evolve.

4.2.2 Application of the 3D-Matrix

In terms of the general application of the R^3 matrix the following further guiding principles are provided for practitioners:

- The evaluation must be based on credible failure modes that have been given due consideration based on the knowledge base and the failure mode initiation and progression, with each properly and clearly described in language that all stakeholders can understand;
- The stability assessment measure (FoS/PoF) is relevant at the point of exposure where the consequence impact will occur, as illustrated in Figure 3; and
- The confidence rating is not an "average". It must be based on the confidence in the factors that influence the credible failure mode.

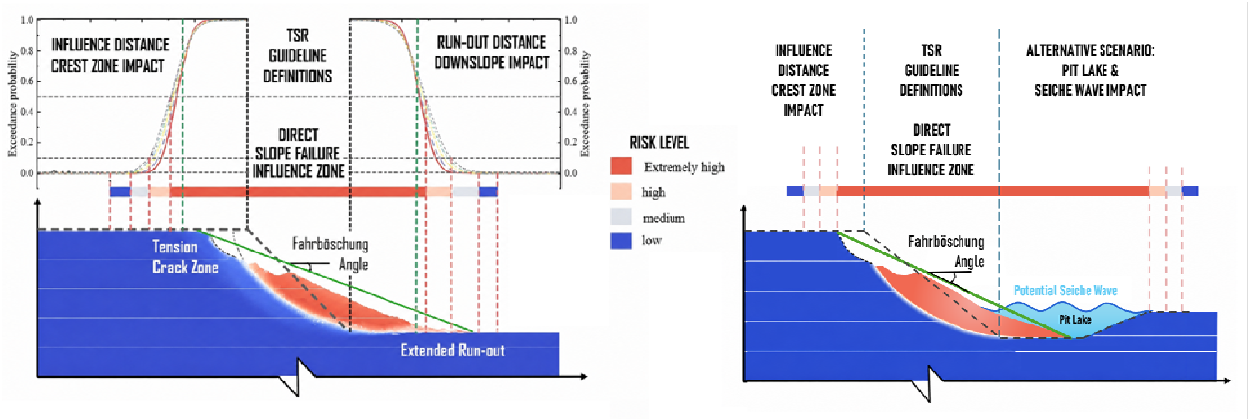


Fig. 3 R^3 consequence impact examples: crest zone impact and downslope run-out (left), seiche wave impact (right).

In addition, the R^3 approach is intended to be dynamic. For many purposes, the matrix can be readily utilized for assessing "what if" scenarios. For developing remediation measures, for instance, there is clear merit in applying the R^3 matrix approach iteratively, utilizing the initial slope condition rating (SCCR) as a seed, based on the calculated PoF. This PoF also generates a target TSR, that needs to be achieved for acceptability. This linkage allows multiple option scenarios to be explored; in the case shown in Table 2, for improving the slope from Class IV to a Class I or Class II condition.

Table 2. Example multiple option scenario assessment.

Calculated PoF (Analysis)	R^3 Assessment				Suggested TSR		Target SCCR (Based on TSR PoF)	SCCR PoF Range
	SCCR	DCR	FCR	Score	TSR FoS	TSF PoF		
7.50%	IV	L	VH	80	>2	<0.5%	I	<0.5
0.40%	I	L	VH	20	>1.3	<1.5%	II	0.5-1.5
1.40%	II	L	VH	60	>1.8	<0.75%	II	0.5-1.5

5 Conclusions/Recommendations

Geotechnical risk assessment increasingly demands a balance between analytical sophistication and the practical need to communicate credible, decision-useful summaries to diverse stakeholders. In its simplest form, risk management is a process to identify, analyse, assess, mitigate, monitor, and report on risks. The goal most often is to inform and improve business decisions. Notwithstanding Lord Kelvin's 1889 mantra "that if it can't be measured, we don't really understand it", many real-world risk settings can't be modelled, measured, or reduced to tidy probabilities-too many unknowns sit outside the data. When numbers fail, we need judgement and adaptability instead. The 3D matrix is intended to help in this regard. It can best be thought of as a semi-quantitative screening and

communication tool, rather than providing a means for making absolute calculations of "total risk". Its value is in making explicit estimates based on: (i) a likelihood proxy linked to ground condition and instability propensity, (ii) consequence to receptors, and (iii) the confidence/uncertainty underpinning the assessment. By separating these elements, the approach supports transparent discussion of what is known, what is uncertain, and where further work or controls are most impactful.

It would be expected that in most situations the outcome of R^3screening would be carried forward into an ALARP demonstration supported by Well-Reasoned Argument (WRA) (Miller, 2019). In such situations ALARP must not be considered a numerical threshold; it is a structured decision process that requires deep understanding of reasonably foreseeable hazards and risk pathways, and documented risk-reduction options defining how the intended controls can be made both robust and effective.

A practical workflow for applying the 3D matrix for geotechnical projects is:

- Stage 1: Clearly set out objectives and frame the perceived risks – define design objectives with measurable success criteria and determine the associated R^3 and target TSR values;
- Stage 2: Iteratively undertake appropriate stability analyses and options evaluations– assess credible mechanisms with analysis commensurate with risk, and iterate, applying feasible controls/remediation options considering efficacy, reliability, practicality, and cost.
- Stage 3: Test stakeholders risk acceptance and aversion levels – engage stakeholders to agree the final design and provide evidence that further measures are not reasonably practicable.

Utilizing the 3D matrix helps in achieving such acceptance by providing a consistent bridge between detailed geotechnical assessment and the simplified formats typically needed for management and stakeholder decision-making. It can also provide a clear structure for integrating AI-enabled synthesis (where appropriate) while still retaining necessary transparency and credibility, allowing defensible engineering judgement.

References

Bao, C., Li, J., Wu, D. (2022). *Three-Dimensional Risk Matrix: Theoretical Basis and Construction.* In: Risk Matrix. Innovation in Risk Analysis. Springer, Singapore. https://doi.org/10.1007/978-981-19-1480-5_8

Carter T.G. (1992). *Prediction and Uncertainties in Geological Engineering andRock Mass Characterization Assessment*. In: Proceedings of the 4th Italian RockMechanics Conference, Torino, pp 1.1–1.22

Carter, T.G.: (2018) *Suggested standards for improving structural geological definition for open pit slope design.* In: Proceedings of Slope Stability 2018, Sevilla, Paper #102, 26 pp.

Carter, T.G., de Graaf, P.J.H.; Dixon, J.; Creighton, A.; Macciotta, R.; Silva-Tulla, F. and Stacey, P. (2022). *Transitioning from Mine Operations to Closure – the Dilemma of differing geotechnical Design Acceptance Criteria perspectives*, Proc. 15th Int. Conf. on Mine Closure, Oct. 2022, Brisbane, Australia.

Cram, Robert S. (2000) *3D Model for Qualitative Risk Assessment*. Paper presented at the SPE International Conference on Health, Safety, and Environment in Oil and Gas Exploration and Production, Calgary, Alberta, Canada, March 2000

de Graaf, P. J. H., Beale, G., & Carter, T.G., (Eds.). (2025). *Guidelines for Open Pit and Waste Dump Closure*. CSIRO Publishing, 400pp

Global Tailings Review. (2020). *Global industry standard on tailings management*. United Nations Environment Programme. https://globaltailingsreview.org/global-industry-standard/

Hawley, M., Carter, T. G., Dixon, J., & de Graaf, P. J. H. (2024). *Risk based design targets for closure of waste rock dumps*. Paper presented at the International Symposium on Slope Stability 2024, Brazilian Mining Association, Brazil

Macciotta R, Creighton A, Martin CD (2022) *Reliability Based Design Acceptance Criteria for inter-ramp and overall pit slopes—fundamental considerations and mathematical background*. In: Slope 2022, proceedings of the slope stability conference in civil and mining 2022, Tucson, AZ, US October 17–20.

Miller, K (2019), 'Constructing a legally sound demonstration of ALARP', *Proceedings of Hazards 29*, Symposium Series No. 166,Institution of Chemical Engineers, Birmingham.

Watson, C. C. (2004). *Risk assessment using the three dimensions of probability (likelihood), severity, and level of control*. Proceedings of the 22nd International System Safety Conference. International System Safety Society.

A Methodology for Fall of Ground Hazard Assessment in Underground Mines

A. Tursanova & A. Adoko
School of Mining and Geosciences, Nazarbayev University, Astana, Kazakhstan
amoussou.adoko@nu.edu.kz
0000-0003-1396-7811

R. Masethe
University of KwaZulu Natal, Durban, South Africa

Abstract

In this study, the FoG index, a dimensionless indicator, is introduced to quantify the FoG hazard and its influencing factors using the Rock Engineering Systems (RES) and Artificial Neural Network (ANN) approaches. The RES is applied as a practical tool for determining complex and highly nonlinear correlations among the input parameters via an interaction matrix, while ANN is implemented to objectively assign weights to the input parameters of the FoG index. The East Sary-Oba mine, located in Kazakhstan, is used as a case study. The mine, characterized by complex geological formations including faults and shear zones, faces persistent FoG hazards that challenge existing risk mitigation strategies. A FoG database with over 150 documented FoG cases, consisting of parameters such as the rock mass parameters, the excavation geometry, the excavation support conditions, and the FoG size, was employed to construct the RES interaction matrix and to derive the FoG index. The proposed index was compared with observed FoG size and the results showed excellent agreement. It was concluded that the results of this study could be used to elaborate guidelines for FoG hazard assessment in underground mines.

Keywords

Fall of Ground, Rock engineering system, ANN, Quantitative hazard assessment

1 Introduction

Fall of Ground (FoG) is a major geotechnical hazard in underground mining and remains a significant contributor to accidents, injuries, and operational disruptions (Mark, 2021). FoG incidents occur within a wide range of conditions in the form of roof fall, rib spilling, and fallouts as a result of stress concentration or structurally controlled failure or both. Industry statistics and safety reports consistently identify ground falls as one of the leading sources of risk in underground operations, despite the recent technological advances in ground control (Małkowski & Juszyński, 2021; Adoko & Kaisa, 2023). This highlights the critical importance of FoG hazard assessment for effective ground control and mine safety management. FoG is inherently a multi-factor problem governed by the interaction of numerous parameters, including rock mass quality, excavation geometry, support systems, groundwater conditions, stress relaxation, mining-induced stress changes, and presence of

adverse geological features (Wu et al., 2018; Adoko et al., 2020; Hekmatnejad et al., 2021; Zuo et al., 2024). One of the main reasons FoG incidents remain difficult to prevent is the inherent variability in rock mass properties and geological structures surrounding underground excavations (Adoko et al., 2019). In addition, relevant geological data may not always be readily available. Therefore, quantifying FoG behaviour as the mechanical response of the surrounding rock masses due to mining is essential in ground control.

Recent developments in rock engineering have introduced system-based and data-driven methods to address this task. For example, the Rock Engineering Systems (RES) approach introduced by Hudson (1992) provides a structured device for analysing complex geotechnical problems by representing the interactions among influencing parameters through an interaction matrix (Shin et al., 2009; Zhang et al., 2024; Salmi et al., 2025). However, the assignment of parameter weights in RES often relies on expert judgment, which introduces subjectivity into the analysis (Adoko et al., 2019; Zhang et al., 2024). To address that issue,this study proposes an ANN-based RES approach to objectively determine the FoG system weightsas suggested by several studies (Li et al., 2019).

2 Methods

2.1 FoG data description

The East-Sary Oba underground mine, located in Central Kazakhstan is used as a case study. It operates room-and-pillar mining systems. The mine has experienced several significant FoG incidents in recent years. Each case includes field observations and design parameters such as the excavation dimensions, rock mass condition, support, geology, groundwater, and the FoG size. The mine is characterized by structurally complex rock mass conditions, including faults, shear zones, variable lithological contacts, and calcite-filled fracture networks (Kazakhmys Corporation LLC, 2019). Ground support systems used in the mine consist mainly of steel and polymer anchor bolts and shotcrete (Shaposhnik, 2022). The ground water conditions vary, ranging from dry to localized inflow with the maximum inflow of 3.85 L/s (Issayeva et al., 2025). The selected variables employed for the FoG hazard assessment encompass 13 parameters namely, excavation type (P1), excavation span (P2), excavation height (P3), excavation depth (P4), fault presence (P5), shear zone (P6), groundwater condition (P7), support category (P8), fracture rating (P9), uniaxial compressive strength (P10), friction angle (P11) and geological conditions (P12). The dependent parameter is FoG (P13). Fig. 1 shows the correlations between parameters.

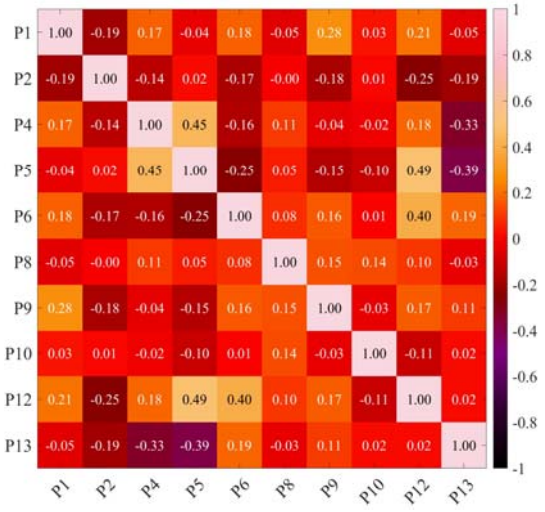


Fig. 1 Heatmap showing the correlations between the FoG and its controlling factors.

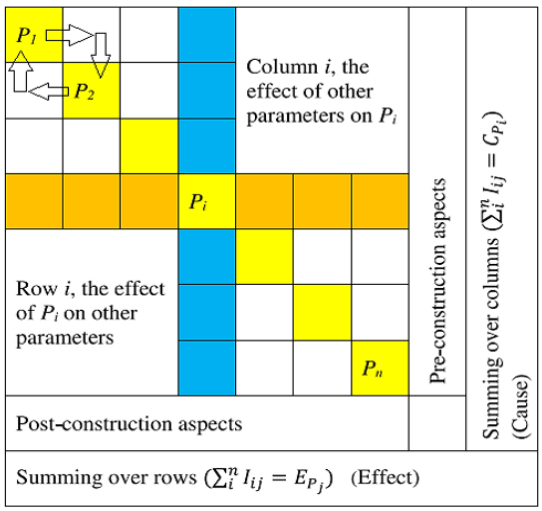


Fig.2 Illustration of the working principle of the Rock Engineering System.

2.2 Rock Engineering System (RES)

2.2.1 Basic overview of the RES

The working principle of RES is illustrated in Fig.2 and uses a cause-effect mechanism that relates every factor influencing the problem at hand (e.g. FoG) to every other factor with different weights according to their influence. An interaction matrix (IM) is constructed by positioning diagonally each

influencing parameter, P_i and P_j. Then, using a clockwise convention, their interactions are represented in the off-diagonal boxes.For a multiple-dimensional interaction matrix containing *n* input parameters P_n, a $n \times n$ matrix (i.e. n rows by n columns) is obtained. Next, the interactions (off-diagonal components $I_{ij}, (i \neq j)$) are typically rated using a semi-quantitative scale ranging from 1 to 4(Hudson, 1992), depending on the strength of the interaction. This step is known as IM encoding. The resulting ratings constitute the interaction matrix. After the matrix has been coded, the cause-effect interactions can be quantified. The sum of the row values for each parameter is called cause value and denoted as C_i, and the sum of the column values is the effect value E_i. The cause C_i, and effect E_i associated with the *ith* parameter P_i for the *ith* row and the *jth* column can be computed as (Hudson, 1992):

$$C_i = \sum_{j=1}^{n} I_{ij}; \; E_j = \sum_{i=1}^{n} I_{ij} \tag{1}$$

where I_{ij} represents the interaction components of the IM; C_i is calculated over jth column while E_j is obtained over ith row. Then, the weights assigned to each parameter influencing the FoGbehaviour can be expressed as the percentage of the sum of the system's cause and effect for such parameters according to the following equation:

$$W_i = \frac{C_i + E_i}{\sum C_i + \sum E_i} \times 100 \tag{2}$$

The FoG index describing the FoG behaviour is computed as:

$$FoG\ index = \sum W_i \times V_i \tag{3}$$

In Eq. 3 V_i denotes the rating values (Adoko et al., 2017) assigned to each the parameter P_i of FoG system. The values of FoG index can range from 0 to 100. The higher the index value, the greater the FoG risk.

2.2.2 RES weighs as the first order partial derivatives of a trained ANN

To obtain the components of the interaction matrix without using a semi-qualitative rating method, a first-order partial derivatives of a trained ANN model can be used (Li et al., 2019). The interaction components are computed using the first partial derivatives of the network output with respect to each input parameter:

$$IM_{ij} = \frac{\partial o_i}{\partial o_j} \tag{4}$$

Where o_i represents the output associated with parameter P_i, o_j represents the input corresponding to parameter P_j. These derivatives capture the sensitivity of the system response to changes in individual parameters and inherently account for nonlinear relationships learned by the ANN.

3 Results

3.1 Derivation of the RES Interaction Matrix

The FoG database described in Section 2.1 was used to train a Back Propagation Neural Network (BPNN) in order to quantify the interactions among the selected parameters. MATLAB is used for the training. The input parameters consist of the 12 selected parameters while the target variable was the FoG size. The network was configured with the *feed forward net* function. The network architecture (Fig. 3) consisted of an input layer (12 nodes), an output layer (12 nodes) and two hidden layers (10 neurons each) as suggested by recent works (Adoko et al., 2017). This configuration allows the calculation of first-order partial derivatives once the training is completed. The traditional Levenberg-Marquardt back propagation algorithm was used; the datasets were randomly divided into training, validation and testing datasets. The testing results indicated a prediction accuracy of 0.95. Fig. 4 shows the best validation performance given by the mean square error (MSE); the best validation performance was 0.00053 at epoch 37, which was considered satisfactory for this study. Table 1 presents the components of the interaction matrix after training, according to Eq. 4. As can be seen the interactions along the diagonal are almost equal to 1 highlighting an adequate training of the network.

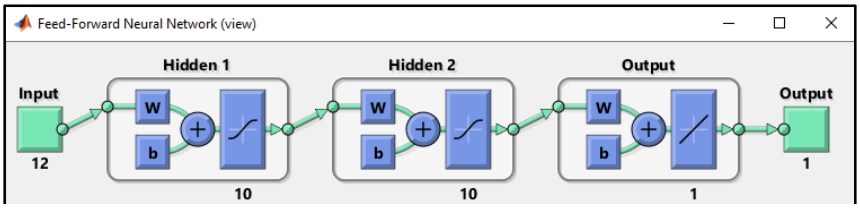


Fig. 3 ANN configuration for the FoG index.

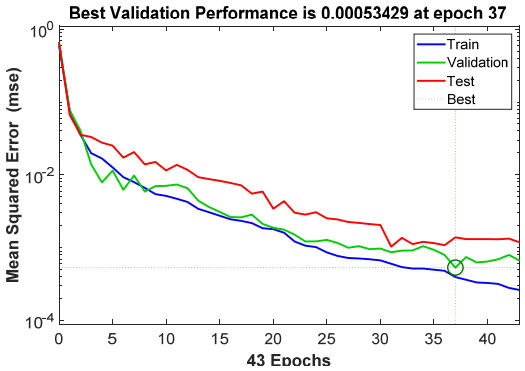


Fig. 4 Network performance.

Table 1 ANN-based interaction matrix

0.995	0.751	0.888	0.001	0.130	0.020	0.150	0.599	0.362	0.160	0.180	0.175
0.544	**0.899**	0.555	0.003	0.100	0.070	0.333	0.801	0.000	0.050	0.100	0.775
0.262	0.650	**1.001**	0.000	0.000	0.000	0.210	0.485	0.000	0.090	0.001	0.362
0.231	0.451	0.355	**0.998**	0.958	0.997	0.205	0.629	0.555	0.025	0.090	0.666
0.501	0.821	0.821	0.431	**1.000**	0.562	0.172	0.762	0.751	0.578	0.752	0.558
0.362	0.548	0.613	0.000	0.000	**1.002**	0.376	0.862	0.058	0.354	0.689	0.850
0.274	0.175	0.150	0.000	0.188	0.000	**0.998**	0.362	1.000	0.004	0.012	0.650
0.001	0.001	0.000	0.000	0.000	0.000	0.000	**1.000**	0.362	0.062	0.080	0.362
0.000	0.492	0.410	0.000	0.200	0.151	0.051	0.755	**0.971**	0.256	0.090	0.405
0.003	0.007	0.003	0.018	0.003	0.009	0.250	0.010	0.024	**1.005**	0.120	0.758
0.020	0.004	0.020	0.003	0.180	0.010	0.003	0.003	0.003	0.457	**1.001**	0.845
0.301	0.333	0.444	0.050	0.008	0.013	0.020	0.690	0.604	0.019	0.002	**1.003**

3.2 Parameter weight, intensity and dominance

The weights of the FoG system are computed according to Eqs. 1-2 and the obtained interaction matrices. The results are presented in Table 2. It can be seen that the most important parameters are P2, P5, P8 and P12 while the least important include P4, P10 and P11.

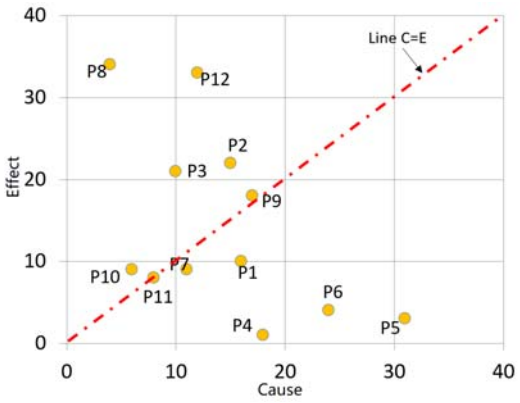


Fig. 5 Cause vs Effet plot.

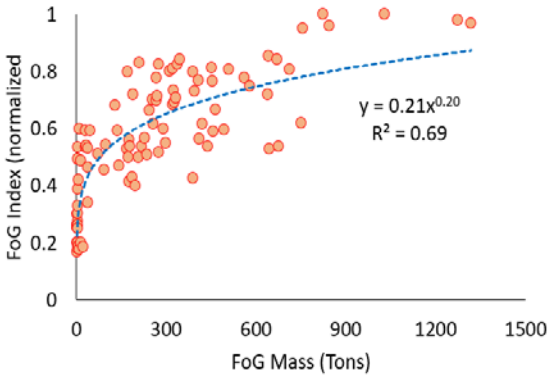


Fig. 6 Comparison between normalized FoG index and Actual Fog.

Table 2. FoG parameter weights.

	P1	**P2**	**P3**	**P4**	**P5**	**P6**	**P7**	**P8**	**P9**	**P10**	**P11**	**P12**
RES	7.6	10.8	9.0	5.5	9.9	8.1	5.8	11.0	10.2	4.4	4.7	13.1
ANN-RES	8.0	10.2	8.5	7.7	11.5	8.8	6.2	9.2	8.8	4.4	4.9	12.0

Fig.5 shows the cause-effect plot illustrating the different interactions among parameters in the FoG system. The most intense parameters include P12, P2 and P8; the most dominant parameters were P5 and P8. However, P8 influences the system more by its effect while P5 more with its cause. Meanwhile P7, P9, P10, and P11 seem to have equal cause and effect in the system. These parameters exert comparatively limited influence on FoG occurrence.

3.3 Fog index

Finally, the FoG index was calculated for the whole dataset according to Eq. 3. In order to validate the results, the FoG index values were compared with observed FoG size. The results are provided in Fig. 8. As it can be seen, a power function was used to fit the data. A coefficient of correlation of R = 0.83 (R^2 = 0.69) was obtained, indicating a strong correlation between the proposed index and the actual FoG.The index was scaled into [0,1] for convenience. Based on its definition (see Eq. 3), it integrated the 12 parameters to describe the FoG size. The FoG size can be estimated using the following empirical relationship:

$$FoG\ index_norm = 0.21 FoG^{0.20} \quad (6)$$

4 Discussions

The results indicate that fracture rating, shear zones, support category, excavation span, fault presence, and geo-engineering rating were the most influential parameters controlling the FoG Index. These findings are consistent with the dominant FoG mechanisms observed at the East Sary-Oba mine, including roof subsidence, wedge failures in shear zones, bedding-plane failures, and structurally controlled failures in faulted areas (Shaposhnik, 2022). Conversely, parameters such as intact rock UCS, friction angle, groundwater condition, excavation depth, height, and excavation type exhibited comparatively lower influence, suggesting that their influence is secondary under the geo-engineering conditions of the East Sary-Oba mine. Similar trends have been reported in recent FoG-related studies (Małkowski & Juszyński, 2021). The results further demonstrate that the integration of ANN and RES provides a robust framework for FoG hazard assessment. The ANN-based weighting process reduces the subjectivity associated with expert-driven approaches while preserving the interpretability of the RES methodology. However, the ANN architecture and hyperparameters were selected through iterative trial-and-error procedures, and the current database remains limited for broader generalization. Future studies should therefore focus on expanding the dataset, incorporating additional parameters such as blasting effect on the excavations (Imashev et al., 2024) and accounting for uncertainties in parameter properties (Adoko et al., 2011), and implementing advanced optimization techniques to improve model robustness and transferability.

5 Conclusions

This study proposed a novel FoG Index based on the integration of Rock Engineering System and ANN to quantify FoG hazards in underground excavations. Using over 100 FoG cases from the East Sary-Oba mine, the results showed that excavation span (P2), fault presence (P5), support category (P8), fracture rating (P9), and geo-engineering rating (P12) were the most influential parameters controlling FoG occurrence. Among them, P5 and P8 were identified as the dominant factors. An empirical relationship between the FoG Index and observed FoG conditions yielded a strong correlation coefficient (R= 0.83), demonstrating good agreement with field observations. The results suggest that the FoG Index can serve as apractical tool for FoG hazard assessment, ground control design, and geotechnical risk management. However, the ANN training relied on trial-and-error optimization, and the dataset remains limited for broader generalization. Future work should extend the database to additional mining sites and incorporate advanced optimization and reliability analysis techniques.

Acknowledgment

This research was funded by the Science Committee of the Ministry of Science and Higher Education of the Republic of Kazakhstan (Grant No. AP26199097). The authors also wish to acknowledge the support of Kazakhmys Company for providing an internship to the first author and for facilitating data collection at the Zhylandy Mine.

References

Adoko, A. C. & Kaisa, N. B. 2023. Development of an Expert System for Unplanned Fall of Ground Assessment in Coal Mine Excavation Intersections. In *the Proccedings of 57th U.S. Rock Mechanics/Geomechanics Symposium*. ARMA-2023-0585.

Adoko, A. C., Phumaphi, P. T. & Zvarivadza, T. 2017. Quantifying Rock Mass Behavior around Underground Excavations In *the Proccedings of The 51st US Rock Mechanics / Geomechanics Symposium, 25-28 June, San Francisco, California* ARMA.

Adoko, A. C., Vallejos, J. & Trueman, R. 2020. Stability assessment of underground mine stopes subjected to stress relaxation. *Mining Technology: Transactions of the Institute of Mining and Metallurgy*.

Adoko, A. C., Zhalel, M. & Phumaphi, P. T. 2019. Fall of ground characterization: A case study of BCL Mine, Botswana. In *the Proccedings of 53rd U.S. Rock Mechanics/Geomechanics Symposium*.

Adoko, A. C., Zuo, Q.-J. & Wu, L. 2011. A Fuzzy Model for High-Speed Railway Tunnel Convergence Prediction in Weak Rock. *Electronic Journal of Geotechnical Engineering*. 16(Q): 1275-1295.

Hekmatnejad, A., Crespin, B., Vallejos, J. A., Opazo, A. & Adoko, A. C. 2021. A hybrid predictive model of unstable rock blocks around a tunnel based on estimated volumetric fracture intensity and circular variance from borehole data sets. *Tunnelling and Underground Space Technology*. 111.

Hudson, J. A. 1992. *Rock engineering systems: theory and practice*. Chichester: Ellis Horwood.

Imashev, A., Mussin, A. & Adoko, A. C. 2024. Investigating an Enhanced Contour Blasting Technique Considering Rock Mass Structural Properties. *Applied Sciences*. 14(23): 11461.

Issayeva, L., Istekova, S., Tolybaeva, D., Togizov, K., Saurykov, Z. & Issagaliyeva, A. 2025. Petrophysical Characteristics of Geological Formations of the Zhezkazgan Ore District (Kazakhstan) and Their Relationship with Mineralization. *Minerals*. 15(11): 1106.

Kazakhmys Corporation LLC (2019). Mining plan for underground mining of the Eastern Saryoba and Western Saryoba deposits of the Zhilandy group of deposits, Head Design Institute of Kazakhmys Corporation LLC. **5.1-PZ**

Li, N., Zare Naghadehi, M. & Jimenez, R. 2019. Evaluating short-term rock burst damage in underground mines using a systems approach. *International Journal of Mining, Reclamation and Environment*: 1-31.

Małkowski, P. & Juszyński, D. 2021. Roof fall hazard assessment with the use of artificial neural network. *International Journal of Rock Mechanics and Mining Sciences*. 143: 104701.

Mark, C. 2021. An updated empirical model for ground control in U.S. multiseam coal mines. *International Journal of Mining Science and Technology*. 31(2): 163-174.

Salmi, E. F., Sellers, E. J. & Hamman, E. 2025. Rock Engineering Systems for Quantifying Risks and Controls for the Resilient Design and Optimisation of Long and Ultra-long Ore Passes. *Rock Mechanics and Rock Engineering*. 58(11): 12359-12418.

Shaposhnik, Y. N. (2022). Development of resource-saving technology for supporting mine development workings in the geomechanical conditions of the Zhilandy deposit: Intermediate stage I. Internal Expert PRO LLP report: unpublished.

Shin, H.-S., Kwon, Y.-C., Jung, Y.-S., Bae, G.-J. & Kim, Y.-G. 2009. Methodology for quantitative hazard assessment for tunnel collapses based on case histories in Korea. *International Journal of Rock Mechanics and Mining Sciences*. 46(6): 1072-1087.

Wu, L., Adoko, A. C. & Li, B. 2018. An Illustration of Determining Quantitatively the Rock Mass Quality Parameters of the Hoek–Brown Failure Criterion. *Rock Mechanics and Rock Engineering*. 51(4): 1063-1076.

Zhang, Z., Hosseini, S., Monjezi, M. & Yari, M. 2024. Extension of reliability information of Z-numbers and fuzzy cognitive map: Development of causality-weighted rock engineering system to predict and risk assessment of blast-induced rock size distribution. *International Journal of Rock Mechanics and Mining Sciences*. 178: 105779.

Zuo, Q., Li, X., Li, P., Deng, M. & Adoko, A. C. 2024. Surrounding rock instability mechanism for fault-crossing tunnels in water-rich soft rock. *Bulletin of Engineering Geology and the Environment*. 83(6).

Optimal Stoping Limits, Stability, and Dip Pillars for Seismicity: SA Gold Mine

R. T. Masethe; O. Vetman & T. Sibiya
College of Agriculture, Engineering and Science, University of KwaZulu-Natal, Durban, South Africa
masetheR@ukzn.ac.za
0000-0002-4420-7885

Abstract

This study integrates two critical geotechnical investigations conducted at a shallow gold mine in South Africa, focusing on optimal stoping limits, ground stability, and the effectiveness of stabilizing dip pillars within broader seismicity management strategies. The first component evaluates the optimal stoping limit for the 202 N S1 Raise Line to minimise abutment stress on the underlying 202 N Returned Air Way (RAW). Geological complexities, including major faults dipping at 65° and 85° south, minor discontinuities, and an over-excavated section measuring 4.4–4.8 m, necessitated a rigorous assessment of ground stability. Numerical modelling using IMS Vantage tested stoping spans of 5 m, 10 m, and 15 m to determine their impact on the Rock Condition Factor (RCF). Although a 15 m span produced the most favourable stability conditions, it was economically unviable. The 10 m stoping limit emerged as the optimal compromise, with localised instability addressed through a combination of resin-grouted bolts, mesh, lacing, and shotcrete to mitigate Fall of Ground (FOG) risks. The second component investigates the performance of 15 m stabilizing dip pillars, introduced in 2020 to manage seismicity, which nevertheless continued to escalate by 2023 with increasing seismic events of large magnitude ($M_L \geq 2.0$). These seismic events produced damaging rockbursts that threatened safety and disrupted production. Analysis revealed limitations in the dip pillar design and inconsistent adherence to seismicity management principles, including bracket pillar placement and lead-lag formation. Comparative assessments of Average Pillar Stress (APS), face stress, closure rates, and seismic response between compliant and non-compliant mining areas highlighted the need for improved pillar configurations. Overall, the research underscores the importance of optimised stoping spans, robust support strategies, and strict compliance with seismicity management principles to enhance ground stability, reduce seismic hazards, and sustain safe, efficient production at a shallow gold mine.

Keywords

Average Pillar Stress, Moment Tensor, Field stresses, Rock Condition Factor.

1 Introduction

1.1 Background of the study area

The geology of the Witwatersrand Basin has been widely studied (Beach & Smith, 2007; Fletcher, 2009; Viljoen, 2009; Dankert & Hein, 2010). The basin formed between about 3.07 and 2.71 billion years ago as a result of tectonic interactions between the Zimbabwe and Kaapvaal cratons (Armstrong et al., 1991; Robb & Meyer, 1995). These interactions created a foreland basin in which several stratigraphic units were deposited above a granite–greenstone basement. The earliest deposits were the volcano-sedimentary rocks of the Dominion Group, which were later overlain by the Witwatersrand Supergroup. This supergroup is divided into the lower West Rand Group (WRG), composed mainly of quartzites and ferruginous shales deposited in shallow marine environments, and the upper Central Rand Group (CRG), which is dominated by quartzites and gold-bearing conglomerates (McCarthy, 2006; Dankert & Hein, 2010). Sedimentation began in shallow marine conditions and gradually shifted to more continental environments as the basin filled and regressed (Tucker et al., 2016). The basin, located in South Africa, developed over roughly 360 million years and is recognised as the world's largest gold-producing basin (see Fig. 1)

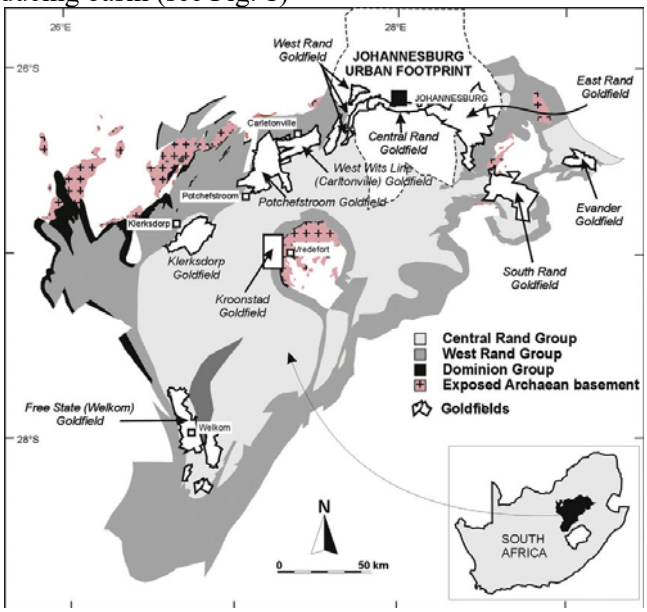


Fig. 1 A diagrammatic representation of the study area from the Witwatersrand Basin (modified from Dankert and Hein, 2010).

The West Rand Group forms the lower portion of the Witwatersrand Supergroup and averages about 4,500 m in thickness (Tainton & Meyer, 1990). It is mainly composed of quartzites and shales in roughly equal proportions, representing shallow-marine shelf sand bodies and finer sediment deposits (Pretorius, 1979; Eriksson et al., 1979; Beukes & Nelson, 1995). Magnetite-bearing shale layers within the group serve as important magnetic markers for deep basin exploration (Tucker et al., 2016). The WRG developed in response to mechanical subsidence within a pull-apart basin formed under trans-tensional rifting conditions (Maynard & Klein, 1995) and is subdivided into the Hospital Hill, Government, and Jeppestown subgroups (Johnson et al., 2006). These subgroups record varying depositional settings, ranging from shallow-marine quartzites and outer-shelf shales in the Hospital Hill Subgroup to lithologically diverse sequences in the Government Subgroup that include conglomerates, iron formations, and diamictites. The Jeppestown Subgroup contains a range of rock types and records a transgressive sequence marked by upward-fining quartzites that grade into shales and iron formations.

The Central Rand Group overlies the West Rand Group and differs significantly in composition and depositional environment. It contains a higher proportion of quartzites and conglomerates, with a quartzite-to-shale ratio of approximately 12:6 (Pretorius, 1976), and the quartzites are typically feldspar-poor (Law et al., 1990). This group represents the upper part of the Witwatersrand Supergroup and hosts most of the basin's gold deposits, particularly within conglomeratic reef horizons (Sanders et al., 1994). The CRG is subdivided into the Johannesburg and Turffontein subgroups. The Johannesburg Subgroup consists mainly of quartzites deposited in fluvial braid-plain environments, while the Turffontein Subgroup represents the final stage of sedimentation in the basin, characterised by prograding braid-plain deposits and conglomeratic units associated with placer gold mineralisation, such as the Kimberley Reef (Johnson et al., 2006; McCarthy et al., 1990). The

geological history of the basin was later modified by major events including tectonic deformation, the Vredefort meteorite impact, and the emplacement of the Bushveld Complex, all of which contributed to metamorphism and partial remobilisation of gold mineralisation (SACS, 1980; Tucker et al., 2016).

1.2 Locality of the area of study, mining methods, and the effects of geological structures

The study area is located within the Witwatersrand Basin in Gauteng, approximately 30–40 km west of Johannesburg. The mining operations occur along the northern margin of the basin and target the South Reef, which forms part of the Central Rand Goldfields. Stratigraphically, the South Reef occurs about 80 m above the Main Reef Leader and is characterised by several pebble bands associated with gold mineralisation (Viljoen et al., 2016; Viljoen, 2009). The reef has historically been regarded as one of the major gold-producing horizons in the Central Rand and is considered the stratigraphic equivalent of the Nigel Reef in the East Rand Goldfields (Viljoen et al., 2016). Lithologically, the South Reef typically ranges from about 1 to 1.5 m in thickness and consists of a basal pebble lag containing a gold-rich bitumen seam overlain by conglomerates interbedded with quartzites (Johnson et al., 2006).

Mining operations in the study area exploit this reef at intermediate depths ranging between approximately 1,650 and 2,000 m below surface, where the orebody occurs as a thin, carbonaceous, and friable seam that is economically viable for extraction (Stacey, 1989). The reef is gently inclined at about 10° towards the southeast and lies approximately 900 m below the Kimberley Reef. Although the South Reef is relatively thin, in some areas measuring only a few centimetres in thickness, it contains a high proportion of free gold, with mineralisation reaching roughly 70%, making it highly attractive for underground mining despite the associated technical challenges (Grave, 2009). Structurally, the orebody is bounded and segmented by several major geological features, including the Roodepoort Fault, the Witpoortjie Horst, and local fault systems such as the Saxon Faults, which divide the reef into large structural blocks and influence ground stability during mining (Stacey, 1989).

Deep-level gold mining within the Witwatersrand Basin occurs at depths commonly exceeding 1,500 m below surface, where high in-situ stresses significantly influence excavation stability. Under these conditions, mining-induced seismicity and rock mass deformation represent major geotechnical challenges. Stress levels in such environments can exceed 100 MPa, creating conditions that increase the likelihood of seismic events, rockbursts, and hanging-wall instability. Consequently, the design of underground excavations requires careful evaluation of stope geometry, extraction sequences, and support systems to ensure safe and efficient operations in South African gold mines

1.2.1 Mining methods

Mining methods in deep-level underground operations are designed to maximise ore extraction while maintaining ground stability and minimising geotechnical hazards. In South African gold mines, particularly those exploiting the Ventersdorp Contact Reef (VCR), Sequential Grid Mining (SGM) has become an important mining strategy for managing the high-stress conditions associated with deep mining. SGM was developed at Kusasalethu Mine in the late 1980s as an alternative to longwall and scattered mining methods, which were associated with significant stress concentrations and frequent rockburst occurrences (Handley et al., 2000). The method involves the systematic extraction of ore through a grid of raises and crosscuts, typically spaced approximately 200 m apart, creating mining panels supported by dip stabilising pillars (see Fig. 2). These pillars, commonly around 30 m wide, provide regional support and regulate stress redistribution within the rock mass, thereby controlling the Energy Release Rate (ERR) and improving ground stability during mining (Handley et al., 2000). This design enables extraction efficiencies of approximately 85%, although pillar size and spacing are adjusted according to mining depth and stress conditions.

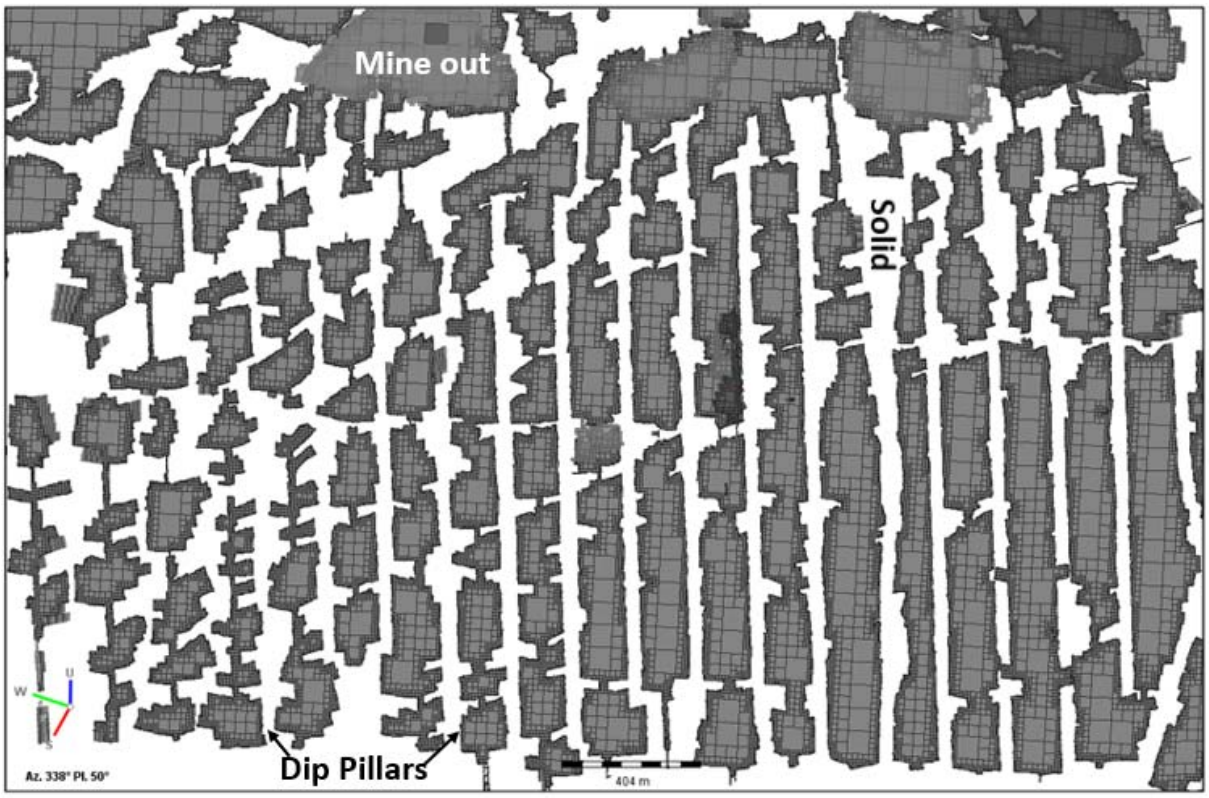


Fig. 2 Sequential grid mining layout (SGM) in the Witwatersrand basin.

The SGM layout typically maintains a V-shaped mining configuration down-dip, which promotes more uniform stress distribution as mining progresses (Jooste & Malan, 2015). This configuration also allows geological structures to be bracketed within stabilising pillars, which reduces the risk of seismic events associated with structural reactivation. Additional advantages of the method include reduced off-reef development and improved selectivity in areas where ore grades are erratic or geological conditions are complex (Jooste & Malan, 2015). However, the strict sequencing requirements of SGM can limit production flexibility and may result in slower production rates and higher upfront development costs. To address these challenges, modified approaches such as multi-raise mining methods have been introduced while retaining the key safety and stability benefits of the original SGM concept.

1.2.2 The effects of geological structures

The performance and safety of underground mining methods are strongly influenced by the presence of geological structures such as faults, joints, and dykes. These structures significantly affect rock mass behaviour, stress redistribution, and the stability of underground excavations. Faults are particularly critical in deep mining environments because they can be reactivated by mining-induced stress changes. When a slip occurs along a pre-existing fault plane between the hanging wall and footwall, sudden dynamic loading may be generated, which can trigger seismic events or rockbursts that threaten worker safety and disrupt production activities (Li et al., 2008; Chen et al., 2012). Faults can also displace the ore body, complicating mining layouts and reducing the stability of surrounding rock masses (Zhou et al., 2023). In many cases, sudden slips along faults during mining can cause large-scale instability within the surrounding rock mass, resulting in dynamic failures such as seismic events or rockbursts (Zhou et al., 2023). As a result, fault zones are considered critical features in mine planning and must be carefully incorporated into mining layouts and support designs.

Joints and other discontinuities also play a major role in the mechanical behaviour of rock masses in underground mining environments. These planes of weakness reduce the shear strength of rock masses and influence the distribution of stresses around excavations, which can increase deformation and the likelihood of failure (Chen et al., 2023). The orientation and continuity of joints are particularly important, as certain joint angles relative to the stress field, commonly between 30° and 45°,can significantly reduce rock mass strength and increase displacement around underground openings (Liu et al., 2021). Depending on their distribution and orientation, joints may lead to different failure

mechanisms, including rockbursts, block rotation, or sliding failures (Qie et al., 2023). Consequently, accurate joint mapping and probabilistic rock mass analyses are essential for predicting rockfall hazards and designing appropriate support systems (Zhou et al., 2023).

Dykes represent another important geological feature that influences mining operations and rock mass behaviour. These igneous intrusions typically form along pre-existing fractures such as faults and joints and often possess mechanical properties that differ significantly from those of the surrounding host rock (Bell, 1983; Keneti & Sainsbury, 2020). The contrast in stiffness and strength between dyke material and surrounding rock can result in stress concentration zones that increase the likelihood of sudden rock failure. Studies have shown that the risk of strain bursts is often higher near dyke contacts due to these stress concentrations (Duan et al., 2022). In the South African mining industry, dolerite dykes are particularly common and are known for their high strength and brittle behaviour under tectonic stress conditions (Wagner & Schumann, 1991; Demenkov & Basalaeva, 2025). Their presence can therefore significantly influence mine design, support requirements, and extraction sequences.

In underground mining operations, the stope and access layout are two critical components that must be optimised during the design phase. These elements cannot be considered independently because ore extracted from stopes must be transported to the surface through the access network (Hou et al., 2019). Optimal stoping limits, therefore, play a fundamental role in balancing ore recovery with ground stability (Jager & Ryder, 1999). The design of underground excavations must consider several geotechnical parameters, including rock strength, in-situ stress conditions, and the geometry of the orebody (Jager & Ryder, 1999). Ground stability analysis is essential for evaluating rock mass behaviour under stress and identifying potential hazards such as subsidence, rockfall, and seismic instability (Ryder & Jager, 2002). Appropriate ground support systems must then be designed based on these analyses to mitigate risks and maintain excavation stability, while continuous monitoring during mining operations allows for adjustments as conditions evolve (Potvin et al., 2019).
To mitigate seismic risk and ensure geotechnical stability in deep-level mining environments, dip pillars with a width of approximately 75 m are frequently integrated into the mining layout. These structures act as regional support elements, separating mining panels (approximately 175 m in span) to effectively regulate the redistribution of mining-induced stresses (Jager & Ryder, 1999). By limiting the extent of extraction and stabilising geological structures such as faults and joints, dip and bracket pillars reduce the likelihood of large seismic events triggered by mining activities. However, as mining progresses deeper and extraction ratios increase, the long-term effectiveness of these pillars requires ongoing evaluation to ensure that they continue to provide adequate support and control seismicity. Numerical modelling has become an essential tool for evaluating underground excavation stability and optimising stope design. These modelling techniques allow geotechnical engineers to predict deformation patterns, assess stress redistribution, and estimate support loads using integrated geological and geotechnical data (Coulthard, 1999). In addition, numerical models serve as investigative tools for assessing uncertainties and evaluating potential risks associated with underground mining (Fels & Elmo, 2022). Within these analyses, parameters such as the Rock Condition Factor (RCF) are used to quantify rock mass quality and its response to mining-induced stresses, thereby guiding the design of reinforcement systems and determining appropriate stope dimensions (Hoek & Brown, 1980). Through such approaches, optimal stoping limits, stability conditions, and dip pillar configurations can be established to minimise seismic hazards while maintaining productive mining operations in South African gold mines.

2 Optimal Stoping Limits

The 202 N S1 Raise represents a relatively short excavation, approximately 70 m in length, but it is situated within a geologically complex and structurally constrained environment. The raise is intersected and influenced by several significant geological discontinuities, of which two major fault structures play a dominant role in controlling both the mining layout and the achievable extraction span. The first structure is a fault dipping at 65° to the south, with an estimated displacement of ±31 m. This fault effectively separates the N1 RAWand N1 S1 Raise Lines, acting as a key structural boundary within the mining area. The second fault, positioned toward the upper extent of the raise line, is steeper, dipping at approximately 85°, with a larger displacement of ±68 m. Importantly, the

202 N S1 Raise the focus of this study is located on the structurally weaker side of this latter fault, which has direct implications for stability and stoping design.

As illustrated in Fig.3, these two faults define the structural framework within which the raise exists. The highlighted zones show their spatial relationship to the raise line and surrounding excavations. However, several critical aspects influencing the case study are not explicitly visible in the image. Most notably, the figure does not depict the presence of a middling of approximately 14 m between the base of the raise and the N1 RAW. This middling introduces a significant design concern, as abutment stresses generated during stoping operations at the base of the raise are likely to transfer upward and accumulate above the N1 RAW. This stress interaction is a key factor in determining safe and optimal stoping limits.

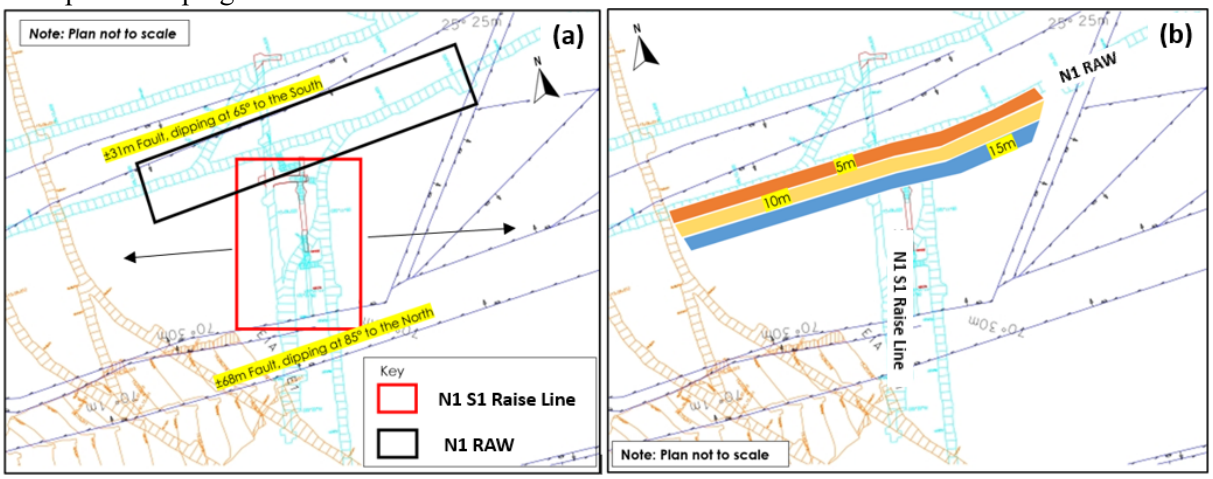


Fig. 3 (a) The mining Plan illustrates the N1 RAW, N1 S1Raise line, and two major faults, and the arrows indicate mining direction. (b) Plan showing the modelled scenarios (5, 10, 15 m) away from the N1 RAW.

Additionally, the historical mining practices that have affected the current excavation geometry are not shown. During early development, the upper section of the raise was mined off-reef, leaving the footwall in place due to poor mining practices. Subsequent footwall ripping was later conducted to expose the orebody. This resulted in an oversized excavation, with a maximum height reaching approximately ±4.8 m. Figure 3(b) does not capture the overbreak or the irregular excavation profile, both of which are critical to understanding the current stability conditions.

The underground assessment focused on evaluating the physical condition of the raise line and its associated infrastructure. The N1 RAW was equipped with primary support consisting of shepherd's crook tenders; however, no secondary support had been installed. The crosscut (X/cut) was supported using end-anchored Kat-bars in conjunction with welded mesh, and no adverse ground conditions were observed in this area. Overall, ground conditions along the raise line were generally satisfactory, with only minor localised concerns observed in both the N1 RAW and the raise line. Despite these largely stable conditions, the reduced middling thickness between the raise base and the N1 RAW introduces a potential risk of progressive abutment stress transfer.

To assess and mitigate this risk, IMS Vantage numerical modelling software was utilised. The primary objective of the analysis was to determine the optimal stoping limit at the base of the raise line. This was achieved by evaluating variations in the Rock Condition Factor (RCF) across three proposed stoping scenarios, located 5 m, 10 m, and 15 m from the RAW, as defined in the mining plan (See Fig. 4b).

The Rock Condition Factor (RCF), developed by Wiseman (1979) of the Chamber of Mines, South Africa, is a practical measure used to assess tunnel stability by relating induced stress at the excavation boundary to the strength of the rock mass. It is expressed as (see Eq. 1).

$$RCF = \frac{3\sigma_1 - \sigma_3}{F\sigma_c} \qquad (1)$$

where σ_1 and σ_3 represent the maximum and minimum field stress components in the plane of the excavation cross-section, σ_c is the uniaxial compressive strength of the intact rock, and F represents a reduction parameter that accounts for the weakening effect of geological discontinuities on rock mass strength. In competent, relatively intact rock, F is close to 1, whereas in highly jointed or bedded rock masseswith discontinuities spaced less than about 0.1 m, F is typically reduced to approximately 0.5. For larger excavations (e.g., 6 × 6 m compared to standard 3 × 3 m tunnels), F is further reduced by about 20% to reflect the additional weakening associated with excavation size. This simplified approach, which integrates both analytical and numerical considerations, provides a practical and efficient design tool requiring limited input parameters (Jager & Ryder, 1999).

At the mine, the Rock Condition Factor (RCF) is used as a primary indicator for assessing ground conditions and guiding support design. RCF values below 0.7 indicate stable ground requiring minimal support, values between 0.7 and 1.4 represent intermediate conditions needing moderate support, and values equal to or greater than 1.4 indicate unstable ground that requires specialised support systems. The influence of jointing is directly incorporated through the factor F, where F = 1 corresponds to intact rock and F = 0.5 represents highly jointed rock masses

The Rock Condition Factor was applied to evaluate model sensitivity and determine optimal stoping limits of 5 m, 10 m, and 15 m. The aim was to improve production efficiency while minimizing stress-induced damage to the rock at the working (RAW) face through optimized layout design and appropriate support systems. These simulations provide insight into the relationships among mining geometry, stress distribution, and ground support performance, thereby informing safer and more productive underground excavation strategies. For the N1 RAW, Fig. 4(a) shows that at a 5 m stoping limit (measured from the bottom of the N1 S1 raise line), RCF values exceed 1.12, corresponding to average ground conditions as defined by Wiseman (1979). This suggests that mining up to 5 m would generally yield average stability along the full strike span of over 150 m, with additional support required throughout the RAW.

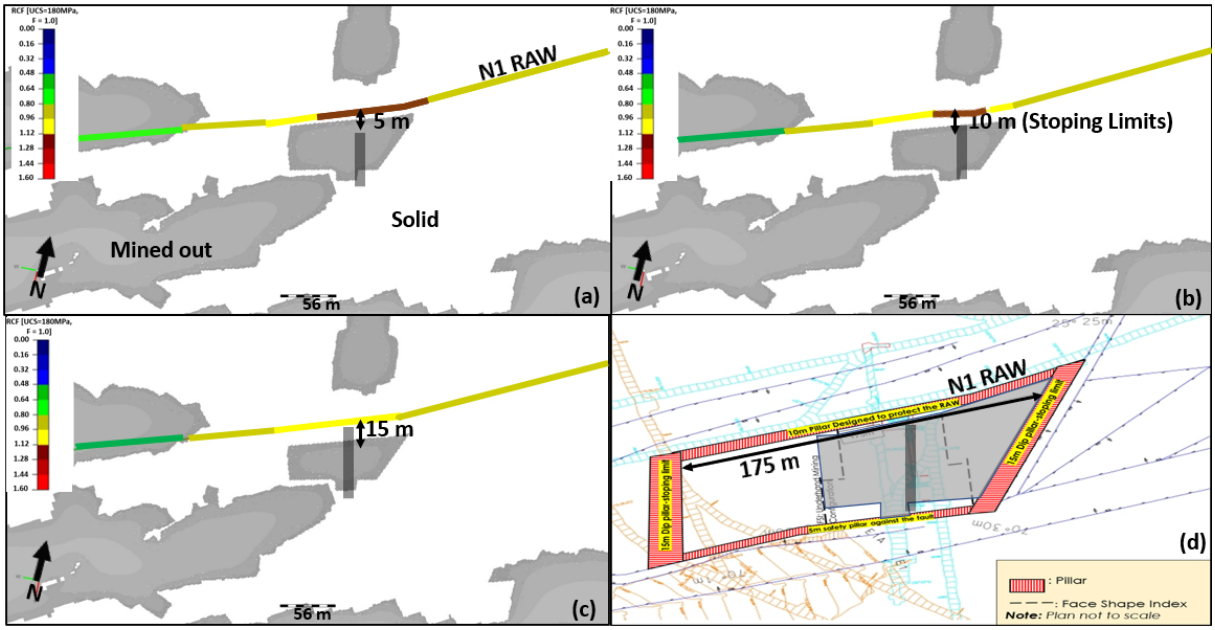


Fig. 4 (a) Rock Condition Factor (RCF) of 5 m stoping limit, (b) RCF of 10 m Stoping limit, (c) RCF of 15 m Stoping limit, and (d) 202 N S1 Raise Line overall mining layout.

At increased stoping limits, ground conditions show progressive improvement. Fig. 4(b) indicates that at a 10 m stoping limit, RCF values remain above 1.12, still reflecting average conditions, but the extent of concern is reduced compared to the 5 m case. Instability is expected to be localized primarily around the intersection of the N1 RAW and the N1 S1 crosscut, suggesting the benefit of a wider pillar. However, secondary support would still be required in this zone. Fig. 4(c) further demonstrates that at a 15 m stoping limit, RCF values range between 0.96 and 1.12, indicating improved and more stable average ground conditions relative to the other scenarios. This reflects a notable enhancement in stability, with the 15 m pillar showing strong potential to mitigate instability in the N1 RAW and reduce the need for extensive support. However, further analysis may still be warranted.

Considering the relatively short length of the N1 S1 Raise Line (approximately 70 m), a 5 m stoping limit is not recommended due to the highly unstable ground conditions in the N1 RAW, which would necessitate technically demanding and costly specialized support systems such as yielding props, cable anchors in the tunnels, or backfilling in the operating stopes. Conversely, a 15 m stoping limit is also unsuitable; although the rock mass under this scenario demonstrates good stability with only minimal reinforcement required (e.g., rockbolts or mesh), the increased mining span reduces the extractable area, thereby limiting ore recovery and negatively affecting production efficiency and profitability. A 10 m stoping limit between the Raise Line and the RAW is therefore recommended, as it achieves an optimal balance between ore extraction, rock stability, and cost-effective support requirements, maximizing the available mining block while minimizing the risk of stress-induced fracturing or overstoping. As illustrated in Figure 4(d), the overall mining layout shows that the blank spaces represent remaining extractable ore panels, underscoring the economic advantage of adopting the 10 m limit to ensure both safety and sustainable production.

3 Stability, Dip Pillar Layout

The mine continues to experience persistently high seismic activity despite the introduction of 15 m-wide stabilizing dip pillars in April 2020, posing ongoing safety and operational challenges. By 2023, mining-induced seismic events ($M_L \geq 2.0$) had increased, elevating the risk of rockbursts that threaten worker safety, damage infrastructure, and disrupt production. This trend indicates that the current pillar design may not be effectively mitigating seismic hazards, highlighting the need to reassess the use of 15 m dip pillars. The existing conceptual framework, based on a grid of dip and bracket pillars, aims to control Energy Release Rates (ERR), maintain Average Pillar Stress (APS) within safe limits (~ 27–30 MPa), and incorporate geological structures such as dykes through planned mining sequences; however, its effectiveness under current conditions remains uncertain.

The Sequential Grid Mining model was originally developed to enable safe, high extraction in deep-level mining while maintaining ERR below 20 MJ/m², but its implementation, along with seismic management strategies such as lead-lag configurations and bracket pillars, has not been fully evaluated at this mine. In addition, limited data on time-dependent pillar (creep) behaviour and seismic indicators, such as pillar strain, restricts a comprehensive understanding of the problem. Time-dependent behaviour involves gradual deformation, delayed fracturing, and stress redistribution within pillars under sustained loads, often exacerbated by the growth of fractures over time. This process can lead to scaling, effectively reducing pillar width, increasing stress concentrations, and ultimately raising the likelihood of pillar failure, thereby contributing to the observed seismicity.

This section aims to evaluate the effectiveness of the 15 m-wide stabilizing dip pillars implemented at this Shaft and assess their compliance with seismicity management principles in mitigating seismic activity. It examines their performance in the context of the continued increase in seismic events (ML ≥ 2.0) observed by 2023, while also assessing alignment with key practices such as lead-lag configurations and bracket pillars. The study further compares closure rates, face stress, Average Pillar Strength (APS), and seismic response between compliant and non-compliant areas to understand how adherence influences seismic risk. It also highlights limitations in the current pillar design, particularly the lack of data on time-dependent pillar behaviour, and proposes improvements to enhance safety and operational efficiency. The following input parameters were used in the numerical model: Young's Modulus (E) - 70GPa, Poisson's Ratio (v) - 0.2, Depth - 1793m, Vertical stress (σ_{zz}) – 0.02750 MPa/m, Stress on x-direction (σ_{xx}) - 0.013750 MPa/m, Stress on y-direction (σ_{yy}) – 0.013750 MPa/m, Static friction angle – 25^o, Dynamic friction angle –20 °, Cohesion – 0 MPa.

Figures 5(a) and (b) present the Average Pillar Stress (APS) model for raise line S (polygons 1D–5D) and raise line N (polygons 1B and 2B). The results show that, irrespective of compliance with pillar sizes and stoping limits, one pillar in raise line S (polygon 4D) is subjected to elevated stress levels of 350–375 MPa, likely due to scaling or time-dependent (age-related) behaviour. In contrast, another pillar within the same polygon experiences lower stresses of 275–300 MPa, with this variation attributed to excessive mining spans, underscoring the importance of adhering to design limits in controlling APS. Similarly, isolated pillars in polygons 2D and 1D of raise line S exhibit elevated stress levels (325–350 MPa), as they are more susceptible to overloading due to uneven stress distribution when mining spans are exceeded. This observation supports findings by Jager and Ryder (1999; 2002) that poor design and excessive spans increase the likelihood of instability and pillar

failure. Notably, one 15 m-wide dip pillar in polygon 4D performs adequately, with a stress of 275 MPa, below the maximum allowable limit of 325 MPa.

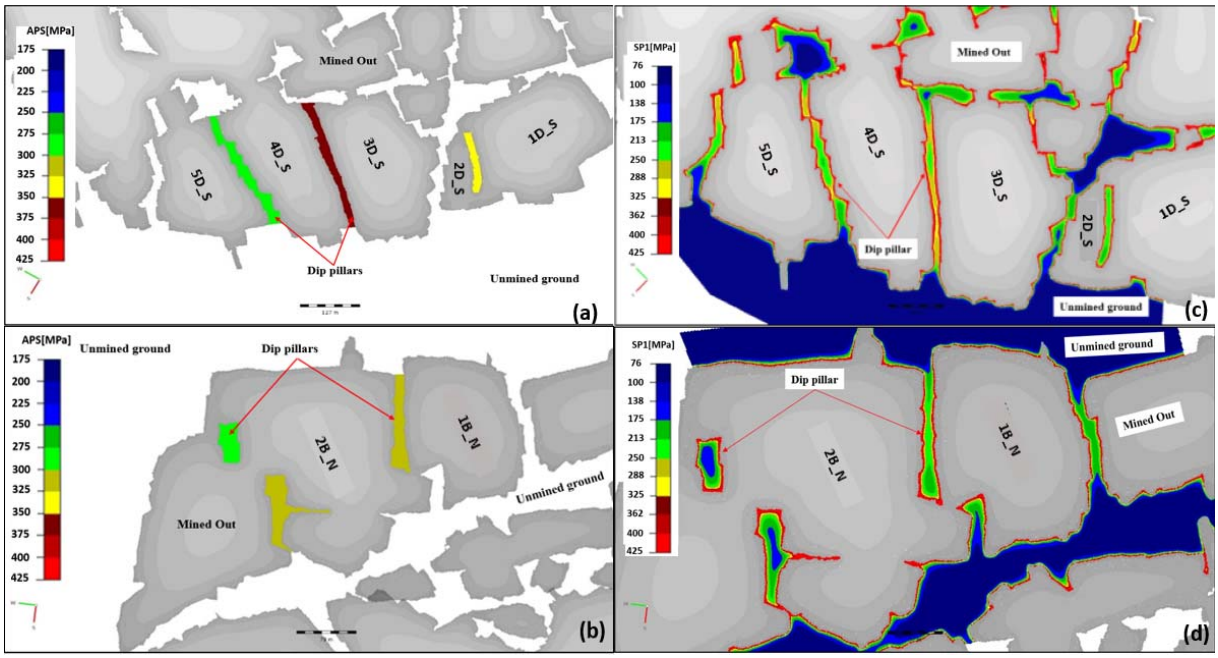


Fig. 5(a) Average Pillar Stress (APS) model for the raise line S in polygon 1D-5D (b) APS model for the raise line N for polygons1B and 2B. (c) Face Stress Model (FSM) for the raise line S in polygon 1D-5D and (d) FSM in B and 2B.

A similar trend is observed in raise line N (polygon 2B), where pillars experience elevated stresses ranging from 275 to 325 MPa, as shown in the APS model. These conditions are attributed to poor compliance with lead-lag sequencing, the presence of isolated pillars, and excessive mining spans, all of which contribute to uneven stress distribution and increased seismic risk. Isolated pillars, in particular, are more vulnerable to overloading as they bear disproportionate loads in expanding mining environments, leading to instability. However, as in raise line S, one dip pillar in polygon 2B performs well, maintaining stress levels below 300 MPa. Overall, the findings indicate that practices such as partial or complete mining of stabilizing dip pillars, leaving remnant or undersized pillars, and inadequate spacing contribute to elevated stress concentrations, increasing the risk of pillar failure and associated seismic activity.

Face stress represents the maximum principal stress acting normal to the advancing mining face and is a critical factor influencing rock fracturing, rockbursts, and overall working conditions. Elevated face stresses, particularly in high-extraction environments, are widely recognized as a major contributor to increased seismic hazard potential. Fig. 5(c) and (d) demonstrate the relationship between face stress, mining span, and dip pillar positioning, showing that as mining spans increase and panels advance toward dip pillars, stress levels rise in both raise lines S and N. The model results indicate that face stresses exceed the permissible threshold of 300 MPa, primarily due to excessive mining spans, non-compliance with dip pillar design and spacing, and panel holing near raise lines.
These elevated stresses, especially those associated with panel holing and poor adherence to seismicity management principles, are linked to an increased likelihood of larger seismic events, reinforcing findings from previous studies that emphasize the importance of pillar stability in controlling rock mass failure (Jager and Ryder, 1999). The results further show that inadequate dip pillar spacing, remnant and isolated pillars, and uncontrolled panel advancement contribute to stress concentrations beyond safe limits, leading to instability and heightened seismic activity. Effective face stress management can therefore be achieved through controlled panel advancement, optimized pillar design, and strict adherence to dip pillar spacing and mining span guidelines, all of which are essential for mitigating seismic risks and ensuring long-term excavation stability.

4 Closure and Numerical Modelling

The closure model provides insight into how elevated stress levels from overlying strata cause convergence between the hanging wall and footwall in underground mines. Fig. 6 shows that 15 m-

wide stabilizing dip pillars can effectively reduce closure when properly implemented, as seen in polygons 5D and 4D of raise line S. However, excessive closure of 0.30–0.35 m is observed in polygons 1D_S and 3D_S, significantly reducing centre gully height and creating unsafe working conditions, particularly for post-mining activities such as infrastructure reclamation. These poor conditions are linked to non-compliance with dip pillar design, excessive mining spans, and older workings where dip pillars were not installed.

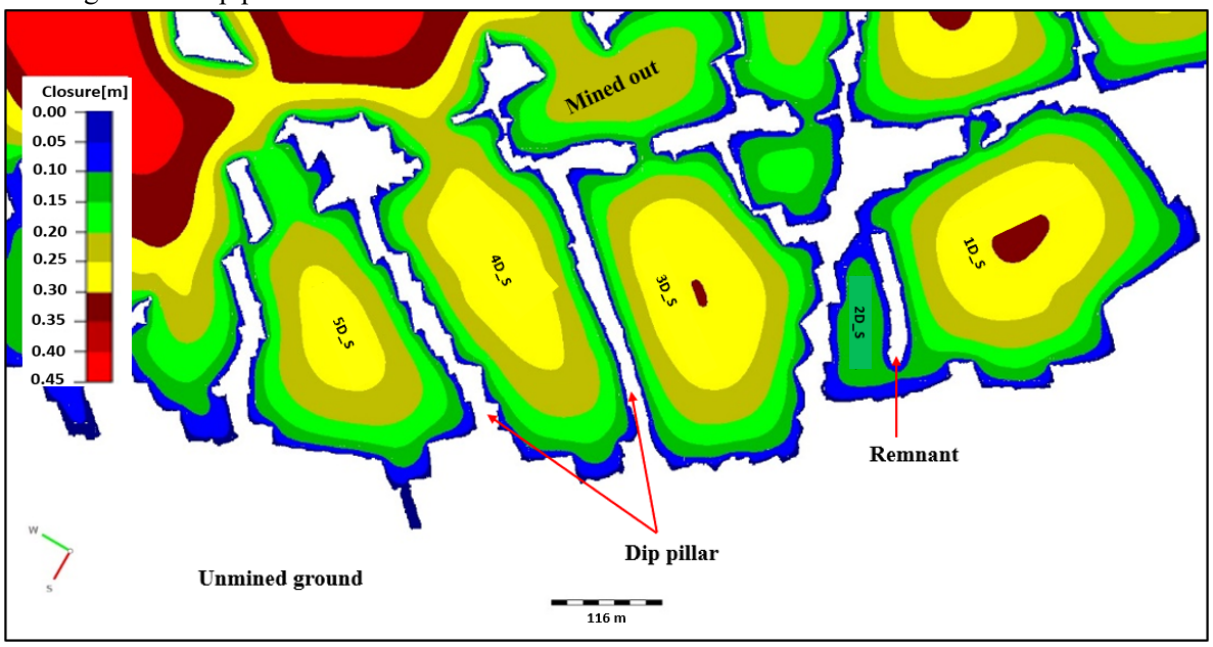


Fig. 6 Closure model for the raise line S for polygons (e.g.,5D, 4D, 3D, 2D, and 1D).

Closure monitoring through loggers, manual measurements, and calculations using rock properties remains essential for assessing these risks. Overall, the results highlight that proper adherence to dip pillar design and controlled mining spans is critical in reducing closure, maintaining excavation stability, and ensuring safer underground working conditions.

5 Conclusion

Optimum Stoping Width: Numerical modelling confirms that a 10 m stoping limit provides the best balance between ground stability and production efficiency. While a 5 m limit results in widespread unstable conditions requiring costly support, and a 15 m limit improves stability but reduces ore recovery, the 10 m span effectively localises instability to the RAW crosscut intersection and minimises risks such as stress-induced fracturing and overstoping. To manage these localised high-stress zones, a combination of active (grouted rock bolts) and passive (mesh and shotcrete) support is recommended to enhance rock mass integrity, reduce fall-of-ground risks, and ensure long-term excavation stability.

Seismicity and Pillar Design: The study further shows that the effectiveness of 15 m-wide stabilizing dip pillars is highly dependent on strict compliance with design and seismicity management principles. Where correctly implemented, pillars reduced stress, closure, and seismic risk, improving safety and productivity; however, poor adherence, such as incorrect support spacing, excessive mining spans, and panel holing, led to elevated stress levels, instability, and increased seismic events, including production disruptions. Overall, maintaining proper pillar design, spacing, and mining practices is essential to control seismicity, reduce closure, and ensure safe, sustainable mining operations.

References

Armstrong RA, Compston W, Retief EA, Williams IS, Welke HJ (1991) Zircon ion microprobe studies bearing on the age and evolution of the Witwatersrand Basin. Precambrian Research 53(3–4): 243–266. https://doi.org/10.1016/0301-9268(91)90074-K.

Beach DA, Smith ND (2007) Geological evolution of the Witwatersrand Basin and its sedimentary environments. Journal of African Earth Sciences 48(2): 123–145.

Bell FG (1983) Engineering properties of rocks. Butterworths, London.

Beukes NJ, Nelson DR (1995) Depositional environments of the West Rand Group. Journal of African Earth Sciences 21(3): 345–360.

Chen Z, Li X, He M (2012) Rockburst mechanisms and prediction in deep mining. Rock Mechanics and Rock Engineering 45(6): 1023–1035.

Coulthard MA (1999) Numerical modelling in geomechanics. Report Series. Institution, Location.

Dankert BT, Hein KAA (2010) Geology and gold mineralisation of the Witwatersrand Basin. Ore Geology Reviews 36(1–3): 1–15.

Demenkov PS, Basalaeva EM (2025) Mechanical behaviour of dolerite under stress conditions. Rock Mechanics and Rock Engineering 58(1): 45–60.

Duan K, Li X, Zhou J (2022) Strain burst mechanisms near geological discontinuities. Rock Mechanics and Rock Engineering 55(3): 1501–1515.

Eriksson KA, Truswell JF, Eriksson PG (1979) Sedimentology of the Witwatersrand Basin. Precambrian Research 9(1–2): 1–27.

Fels L, Elmo D (2022). Numerical modelling for underground excavation design. International Journal of Rock Mechanics and Mining Sciences 152: 105050. https://doi.org/10.1016/j.ijrmms.2022.105050.

Fletcher CJN (2009) Sedimentology and stratigraphy of the Witwatersrand Supergroup. South African Journal of Geology 112(3): 201–220.

Grave EJ (2009) Gold mineralisation characteristics of the South Reef. Dissertation at the University of the Witwatersrand.

Handley MF, Stacey TR, Malan DF (2000) Sequential grid mining in deep-level gold mines. Journal of the South African Institute of Mining and Metallurgy 100(1): 25–32.

Hoek E, Brown ET (1980) Empirical strength criterion for rock masses. Journal of the Geotechnical Engineering Division 106(9): 1013–1035.

Hou Z, Xie H, Zhang R (2019) Optimization of underground mining layouts. International Journal of Mining Science and Technology 29(3): 345–352. https://doi.org/10.1016/j.ijmst.2019.03.003.

Jager AJ, Ryder JA (1999) A Handbook on Rock Engineering Practice for Tabular Hard Rock Mines. Safety in Mines Research Advisory Committee, Johannesburg.

Johnson MR, Anhaeusser CR, Thomas RJ (2006) The Geology of South Africa. Geological Society of South Africa, Johannesburg.

Jooste Y, Malan DF (2015) The application of sequential grid mining in South African gold mines. Journal of the Southern African Institute of Mining and Metallurgy 115(2): 123–132.

Keneti A, Sainsbury BA (2020) The influence of dykes on rock mass behaviour in underground mining. International Journal of Rock Mechanics and Mining Sciences 128: 104267 https://doi.org/10.1016/j.ijrmms.2020.104267.

Law JD, Phillips GN, Groves DI (1990) Geochemistry of Witwatersrand quartzites. Journal of Geochemical Exploration 36(1–3): 123–145.

Li X, Chen Z, Zhou J (2008) Dynamic loading and seismic response in underground excavations. International Journal of Rock Mechanics and Mining Sciences 45(6): 1003–1012.

Liu Q, Jiang Q, Feng X (2021) Jointed rock mass behaviour and failure mechanisms. International Journal of Rock Mechanics and Mining Sciences 140: 104700. https://doi.org/10.1016/j.ijrmms.2021.104700.

Maynard JB, Klein C (1995) Sedimentary and tectonic evolution of the Witwatersrand Basin. Geological Society of America Bulletin 107(6): 689–701.

Masethe, R. T., Durrheim, R. J., & Manzi, M. S. D. (2019). The seismic response to mining during the extraction of the Thuthukani shaft pillar, Kloof Operations, South Africa. In *Deep Mining 2019: Proceedings of the Ninth International Conference on Deep and High Stress Mining* (pp. 71-86). The Southern African Institute of Mining and Metallurgy.

Masethe, R. T., & Zvarivadza, T. (2025). The Impact of Scattered Mining on Gold Recovery: A Case Study in the Deep Level Gold Mine, South Africa. In *ARMA US Rock Mechanics/Geomechanics Symposium* (p. D021S002R003). ARMA.

McCarthy TS (2006) The Witwatersrand Supergroup. In: Johnson MR et al. (eds) The Geology of South Africa. Geological Society of South Africa, Johannesburg.

McCarthy TS, Stanistreet IG, Robb LJ (1990) Provenance and depositional environment of the Central Rand Group. South African Journal of Geology 93(2): 223–236.

Potvin Y, Hadjigeorgiou J, Stacey TR (2019) Ground support in mining and underground construction. CRC Press, Boca Raton.

Pretorius DA (1976) Gold distribution in the Central Rand Group. Economic Geology 71(6): 1087–1108.

Pretorius DA (1979) The depositional environment of the Witwatersrand Supergroup. Economic Geology 74(3): 460–476.

Qie L, Zhao J, Li X (2023) Failure mechanisms in fractured rock masses. Rock Mechanics and Rock Engineering 56(4): 2101–2115.

Robb LJ, Meyer FM (1995) The Witwatersrand Basin, South Africa: geological framework and mineralization processes. Ore Geology Reviews 10(1–2): 67–94.

Ryder JA, Jager AJ (2002) A textbook on rock mechanics for tabular hard rock mines. Safety in Mines Research Advisory Committee, Johannesburg.

SACS (1980) Stratigraphy of South Africa Part 1: Lithostratigraphy of the Republic of South Africa. Geological Survey of South Africa, Pretoria.

Sanders JV, Robb LJ, Groves DI (1994) Gold-bearing conglomerates of the Witwatersrand Basin. Economic Geology 89(3): 507–526.

Stacey TR (1989) Rock engineering design in deep-level gold mines. Journal of the South African Institute of Mining and Metallurgy 89(6): 183–195.

Tainton KM, Meyer FM (1990) Stratigraphy of the West Rand Group. South African Journal of Geology 93(3): 300–312.

Tucker RF, Viljoen RP, Anhaeusser CR (2016) Sedimentation and tectonic evolution of the Witwatersrand Basin. South African Journal of Geology 119(1): 1–16.

Viljoen RP (2009) An introduction to the Witwatersrand Basin geology. South African Journal of Geology 112(3–4): 211–230.

Viljoen RP, Viljoen MJ, Pearton TN (2016) The South Reef and its correlation across the Witwatersrand Basin. South African Journal of Geology 119(2): 345–360.

Wagner H, Schumann EH (1991) Rockburst control in South African gold mines. Journal of the South African Institute of Mining and Metallurgy 91(7): 209–217.

Wienand, G., Masethe, R. T., &Mgiba, C. (2024). High horizontal stress at depth incorporating reverse faults in Ya Rona Shaft, South Africa. In *New Challenges in Rock Mechanics and Rock Engineering* (pp. 965-970). CRC Press.

Zhou H, Zhang C, Li S (2023). Fault influence on underground excavation stability. Engineering Geology 310: 106900. https://doi.org/10.1016/j.enggeo.2022.106900

Towards a reliability-based monitoring system for uplift under concrete buttress dams

J. Dyberg Thonée, M. Zamzami, J. Spross
KTH Royal Institute of Technology, Stockholm, Sweden
jdy@kth.se
0009-0000-7988-2939, 0009-0003-9547-6529, 0000-0001-5372-7519

M. Westberg Wilde
KTH Royal Institute of Technology, Stockholm, Sweden&AFRY, Solna, Sweden
0000-0003-2584-1183

F. Johansson
KTH Royal Institute of Technology, Stockholm, Sweden
0000-0002-8152-6092

Abstract

Uplift is one of the major forces acting on concrete dams and is inherently difficult to predict. In dam safety guidelines, uplift is typically evaluated deterministically, assuming simplified pressure distributions along the concrete–rock interface. For buttress dams, the concrete–rock contact area is smaller than that of gravity dams, but in the presence of persistent fracture planes in the rock foundation, the effective area over which uplift can act can be substantially larger. Due to the low self-weight of buttress dams, this poses a significant safety concern, as sliding stability has been shown to be sensitive to variations in uplift.To address these safety concerns, pore pressure monitoring with alarm thresholds and predefined countermeasures has been proposed in dam safety guidelines. However, there is limited guidance on how such alarm thresholds should be defined or implemented in practice.In this paper, we introduce a reliability-based framework in which alarm thresholds are derived from target probabilities of failure. The methodology is demonstrated for a concrete buttress monolith with characteristics similar to those of an existing dam in northern Sweden, where the probability of sliding failure is evaluated with uplift pressure represented by a random variable. The proposed framework enables the upper tail of the pore pressure distribution to be truncated at the alarm threshold, allowing stability requirements to be satisfied in re-evaluations of existing dams without structural measures while maintaining the required level of safety. Practical considerations when defining alarm thresholds are discussed, including how exceedance of an alarm threshold may reflect long-term changes in hydraulic behaviour caused by deterioration processes in the rock foundation and how to provide sufficient lead time for pre-defined countermeasures.

Keywords

Uplift pressure, Alarm thresholds, Monitoring, Probability of failure, Dam safety.

1 Introduction

Concrete buttress dams are commonly used for hydropower purposes as a material-efficient alternative to gravity dams. The reduced self-weight due to their slender design is compensated by mobilisation of vertical hydrostatic load through the inclined upstream front plate and by the limited concrete–rock interface beneath the buttress. However, in the presence of sub-horizontal fracture planes, uplift pressure may act along a larger fracture interface and increase the resulting load (Goodman et al. 1983). Such fracture planes are relatively common in Nordic rock masses due to stress relief associated with post-glacial rebound and are, during dam safety evaluations of existing structures, sometimes identified in the rock foundation under monoliths where they were previously unknown. Uplift pressure is also inherently variable and depends strongly on local geological conditions (Hanna et al. 1993; Hu and Ma 2016). Therefore, the description of uplift pressure is subject to uncertainties arising from spatial variability beneath the monolith, fluctuations in reservoir water level, potential clogging of the drainage system, and possible degradation of the grout curtain (Ruggeri 2004). Consequently, uplift pressure is expected to vary spatially and over time, and as the exact nature of this variation is uncertain, it may be represented as a random variable in stability analyses. Despite this, existing design guidelines for stability evaluations do not explicitly address uplift pressure along fracture planes beneath buttress dams, nor do they account for the variability of uplift pressure (e.g. FERC 2016a; Swedenergy 2020).

Monitoring of uplift pressure with piezometric measurements can support dam safety assessments by providing continuous information on hydraulic conditions in the foundation. For a monitoring system to be effective, the monitored parameters must be representative of the processes governing stability, and alarm thresholds must be linked to structural performance limits and predefined countermeasures (ICOLD 2000). Existing guidelines emphasises the need for alarm thresholds (e.g. FERC 2016b) but provides limited guidance on how these should be defined. For an existing structure, lead time must be carefully estimated, to not create an overly conservative or excessively sensitive system (Pate-Cornell and Benito-Claudio 1987). This requires identifying the processes influencing the monitored behaviour and evaluating plausible scenarios and their lead times for countermeasures (Dunnicliff 1993).

Piezometric measurements from operating buttress dams in northern Sweden have shown that uplift pressures beneath some monoliths equipped with drilled drainage holes can be significantly lower than those assumed in current design guidelines. In this study, it is demonstrated how dam stability evaluations can be improved using a reliability-based framework in which uplift pressure is represented by a random variable. By defining alarm thresholds for pore pressure, less conservative uplift pressure assumptions can be used compared to those suggested in deterministic design guidelines, while still ensuring an adequate level of safety. The proposed methodology is demonstrated through an example evaluating the probability of sliding failure for a single buttress monolith. Practical aspects related to defining pore pressure alarm thresholds are also discussed, including processes that may lead to increased uplift pressure over time.

2 Methodology

2.1 Evaluated scenarios

Two scenarios were considered to illustrate how a measurement-based evaluation of uplift, combined with a monitoring system with alarm thresholds, can improve the evaluated safety of a monolith in a buttress dam. In both scenarios, the probability of sliding failure was evaluated using probabilistic calculations, where the friction coefficient of the rock joint (δ_{F}), and the unit weights of rock (γ_{r}) and concrete (γ_{c}), were treated as random variables. Although ice load (I) is likely associated with considerable variability (Westberg Wilde and Johansson 2016), it is for simplicity assumed constant in this analysis, and the associated uncertainty is therefore not included within the scope of the study. In Scenario A, uplift was assumed deterministic in accordance with the Swedish dam safety guidelines RIDAS (Swedenergy 2020). In Scenario B, the pore pressure at the measurement point (u) was treated as a random variable and controlled through a monitoring system in which the alarm threshold was defined to meet the target probability of failure. The methodology is illustrated through a calculation example for a buttress monolith based on an existing dam equipped with drainage and previously strengthened with pre-stressed anchor cables (Fig. 1). The sub-horizontal fracture acting as a potential

sliding plane was assumed based on observed geological conditions at the site, where similar fractures have been identified.

2.2 Limit state function and input data

The sliding plane was assumed to have an inclination of 10° from the horizontal (α) as illustrated in Fig. 1.The uplift force (U) was assumed to act along the fracture constituting the potential sliding plane under the dam. The hydrostatic load (H) was defined by the water pressure resulting from the head difference (h_{RWL}) between the reservoir water level (RWL) and the sliding plane. The ice load (I) was assumed to act at the RWL. All these forces (U, H and I) were assumed to act along the full width of the monolith (w_{fp}). The force from the pre-stressed anchor cables (T) was calculated considering an installation inclination (θ) of 50° relative to the sliding plane. The total vertical force from self-weight (W_{tot}) was calculated as the sum of the weights of the concrete monolith, the rock mass above the sliding plane, and the vertical force from the water acting on the front plate.

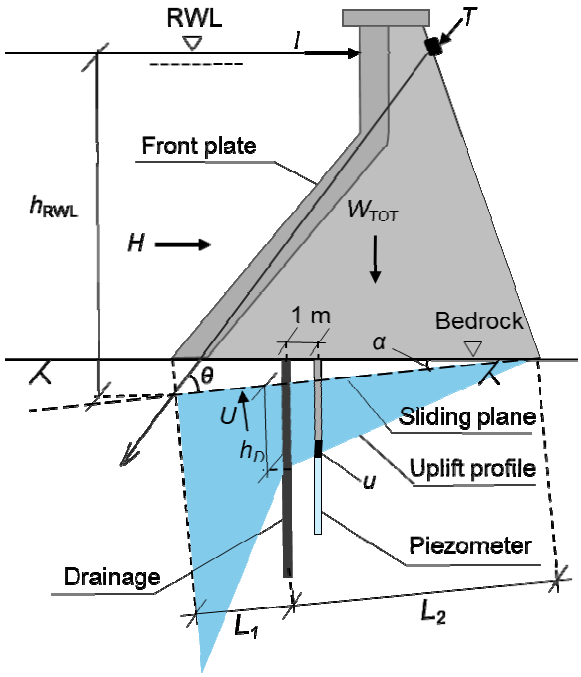


Fig.1 Cross-section of the buttress monolith and the forces acting on the potential sub-horizontal sliding plane in the rock foundation. Arrows indicate considered forces.

The limit state function for sliding failure along a sliding plane can then be derived from the Mohr-Coulomb failure theory and expressed as the shearing forces acting along the sliding plane:

$$G = [W_{\mathrm{tot}} \cos\alpha + T \sin\theta + (H + I) \sin\alpha - U]\delta_{\mathrm{F}} - [(H + I) \cos\alpha - (W_{\mathrm{tot}} \sin\alpha + T \cos\theta)]. \quad (1)$$

For Scenario A, U was calculated with uplift defined by h_{RWL} at the dam heel and decreasing linearly toward the dam toe, with the pressure at the drainage location reduced by 50% according to the Swedish dam safety guidelines, RIDAS (Swedenergy 2020). For Scenario B, U was calculated as a function of u given by

$$U = [L_1 h_{\mathrm{D}} + L_1(h_{\mathrm{RWL}} - h_{\mathrm{D}})/2 + L_2 h_{\mathrm{D}}/2\,] w_{\mathrm{fp}} \gamma_w, \quad (2)$$

where h_{D} is the pressure head at the drainage location, scaled from the measured u at the piezometer location distanced 1 m from the drainage via

$$h_{\mathrm{D}} = u/\gamma_w \times L_2/(L_2 - 1), \quad (3)$$

With γ_w denoting the unit weight of water, and L_1 and L_2 the distances indicated in Fig. 1. The coefficient of variation (COV) for u was assumed to reflect both spatial variability beneath the monolith and temporal variations in uplift pressure, guided by indications of pore pressure variability in fractured rock foundations as reported by Pereira et al. (2021) and by the COV proposed for the total uplift force U by Westberg Wilde and Johansson (2016). The parameters in Eqs. 1-3 are defined in Table 1.

Table 1. Input data.

Description	Symbol	Distribution	Value
Distance from dam heelto drainage	L_1	Constant	6 m
Distance from drainage to dam toe	L_2	Constant	26 m
Distance from RWL to sliding plane	h_{RWL}	Constant	38 m
Monolith width	w_{fp}	Constant	8 m
Ice load	I	Constant	1600 kN
Tension force in anchor cables	T	Constant	3000 kN
Volume of concrete	V_{c}	Constant	1450 m^3
Volume of rock	V_{r}	Constant	700 m^3
Volume of water above front plate	V_{w}	Constant	2650 m^3
Measured pore pressure	u	Normal	μ = 51 kPa COV = 20%
Friction coefficient of rock joint[1]	δ_{F}	Normal	μ = tan(42º) COV = 7%
Unit weight of concrete[2]	γ_{c}	Lognormal	μ = 24 kN/ m^3 COV = 3%
Unit weight of rock[3]	γ_{r}	Lognormal	μ = 26.5 kN/ m^3 COV = 2 %

[1] (Johansson et al. 2010, Ríos-Bayona et al. 2021).
[2] (JCSS 2001)
[3] Mean value and standard deviation from investigations at Forsmark (SKB 2005) presented by Westberg Wilde & Johansson (2016).

2.3 Reliability analysis

In reliability calculations the probability of violating a limit state, G, is defined as $p_{\mathrm{f}} = P(G \leq 0)$. A safety requirement is set as $p_{\mathrm{f}} \leq p_{\mathrm{T}}$, where p_{T} is the target failure probability. The level of safety is commonly expressed by the reliability index β, where $\beta = -\Phi^{-1}(p_{\mathrm{f}})$ and Φ is the standard normal distribution function. The calculated β is then compared with a target value β_{T}. For a large-consequence dam, β_{T} = 5.2 (Westberg Wilde and Johansson 2016). If the target is not met, one possibility is to implement alarm thresholds on a monitored random variable (Spross and Johansson 2017), such as the pore pressure (u). The alarm threshold value required to satisfy p_{T} is found by considering the threshold as a truncation of u, and solving the following equation for u_{alarm}:

$$P(G \leq 0 | u \leq u_{\mathrm{alarm}}) = p_{\mathrm{T}}. \tag{4}$$

For the investigated scenarios, the probability of sliding failure was calculated using Monte Carlo simulation (5 billion simulations performed in MATLAB), with a relative error of approximately 9% at the 95% confidence level, which was considered acceptable while maintaining a reasonable computation time.

3 Results

The results from the two scenarios illustrate the importance of how uplift is evaluated in the stability analysis. For Scenario A, where U was evaluated in accordance with the guidelines, the uplift pressure at the piezometer location was calculated to 148 kPa (deterministic value), resulting in a reliability index of $\beta = 3.4$, which does not satisfy the requirement β_{T} = 5.2. However, for Scenario B, where U was evaluated as a function of the measured u following Eq. 2 (μ=51 kPa, COV= 20%), it was found that the target reliability could be satisfied by introducing an alarm threshold at 70 kPa (Eq. 4). Thus, the different outcomes of the two scenarios demonstrate how the safety requirements for this monolith can be met using a monitoring system, where uplift is evaluated from piezometric measurements and controlled through alarm thresholds, rather than by performing structural measures.

4 Discussion

4.1 Monitoring system as an alternative to structural measures

Comparison of Scenarios A and B highlights the sensitivity of sliding reliability to the assumed uplift representation. In Scenario B, the uplift force is expressed as a function of pore pressure at the piezometer location, where pore pressure is modelled as a random variable and the upper tail of its

distribution is truncated at the alarm threshold. Although no structural modifications are made to the dam, sufficient safety can still be ensured as long as the continuously monitored pore pressure does not exceed the alarm threshold. This monitoring-based approach better reflects the actual hydraulic conditions beneath the dam and can potentially reduce unnecessary conservatism. However, at the same time, it increases sensitivity to deviations from the assumed behaviour. As noted by Spross et. al. (2014), an issue with using piezometric measurements in stability evaluations lies in ensuring that exceptional uplift loads are controlled, as measurements primarily reflect normal operating conditions and may therefore not capture such behaviour. In the proposed monitoring framework, this limitation is addressed through continuous pore pressure monitoring combined with defined alarm thresholds, where exceedance triggers predefined countermeasures.

4.2 Uncertainty considerations when defining alarm thresholds

The main advantage of measurement-based uplift evaluation is the reduction of epistemic uncertainty through site-specific observations. However, it is important to recognise which sources of uncertainty are represented in the assumed variability. A major uncertainty that should be reflected in the uplift variability is model uncertainty arising from the derivation of uplift based on measurements from a single piezometer, together with the assumption of linearity along the uplift profile. Another important component is the inherent variability, both spatially and over time. In addition, as dams operate for many decades in natural environments where conditions cannot be fully controlled, temporal variability arising from long-term deterioration processes must also be considered in the evaluation of uplift variability, and thus in the design of the monitoring system.

In practice, operational alarm thresholds should allow sufficient lead time to identify the cause of increased pore pressure and implement appropriate countermeasures. Establishing such limits therefore requires identifying processes that may increase uplift over longer time periods and estimating the rate at which they may develop. For dams equipped with drainage, a probable cause of increased uplift pressure over time is clogging of drains. As drainage significantly reduces uplift, clogging of drains may lead to a gradual increase in uplift pressure (Ruggeri 2004). The conditions for clogging are highly site dependent (da Silva 2015), and reported rates vary substantially. Swedish case studies indicate gradual deterioration corresponding to approximately 10% clogging over 30 years (Johansson et al. 2017), although more rapid clogging of up to 50% within 10 years has been documented (Farinha et al. 2005). For dams equipped with grout curtains, another possible cause of increased uplift is degradation of the grout curtain (Ruggeri 2004). This process might be driven by chemical leaching, with calcium leaching widely recognised as a durability concern (Yu and Zhang 2017). As the grout deteriorates, the seepage in existing fractures beneath the dam may increase, leading to increased uplift pressure (Yue et al. 2022). Although chemical degradation of grout curtains has not been widely studied for Swedish dams, long-term increases in uplift of approximately 40–50% have been reported as the anti-seepage function of grout curtains deteriorates (Zhang et al. 2021; Yue et al. 2022). However, both the magnitude and timescale are strongly site dependent.

Both clogging of drainage systems and degradation of grout curtains are typically slow processes, which enables the use of alarm thresholds while still allowing sufficient time to analyse the situation and implement countermeasures. Such measures, including cleaning or re-drilling drainage holes and re-grouting the grout curtain, can be operationally demanding and may also cause unexpected changes in the foundation conditions, as observed by Spross et al. (2016) during re-grouting which caused washout of fractures. However, alarm thresholds should not be applied if achieving the target reliability requires them to be set excessively low, as this would imply a high probability of interventions becoming unavoidable.

5 Conclusions

In this paper, a methodology is outlined for monitoring the stability of existing dams through piezometric measurements of pore pressure with alarm thresholds defined within a reliability-based framework. The approach demonstrates how piezometric measurements can be used to represent uplift pressure in stability evaluations when combined with a monitoring system with defined alarm thresholds. Such an approach may allow existing monoliths to fulfil safety requirements without structural measures, provided a monitoring system capable of detecting changes in uplift behaviour and alarm thresholds that allow sufficient lead time for predefined countermeasures. Further research is needed to better understand uplift variability, including identifying and quantifying the different components of uncertainty associated with uplift pressure and with how uplift pressure is modelled.

Acknowledgements

This study is part of a PhD project supported by the Swedish Centre for Sustainable Hydropower (SVC), grant no. 32018 and VKU32014. Piezometric measurement data were provided by Uniper.

References

da Silva, J. F. (2015) Clogging of drains and its influence on the stability of concrete dams. Proceedings of the ARMA US Rock Mechanics/Geomechanics Symposium:ARMA-2015-140.

Dunnicliff, J.(1993). Geotechnical instrumentation for monitoring field performance: John Wiley & Sons.

Farinha, F., E. Portela, C. Domingues, and L. Sousa (2005) Knowledge-based systems in civil engineering: Three case studies. Advances in engineering software 36 (11-12):729-39.

FERC (Federal Energy Regulatory Commission) (2016a) Engineering Guidelines for the Evaluation of Hydropower Projects: Chapter III Gravity Dams, Washington, DC

FERC (Federal Energy Regulatory Commission) (2016b) Risk-informed decision making (RIDM)-risk guidelines for dam safety (Interim Guidance).

Goodman, R. E., B. Amadei, and N. Sitar (1983) Uplift pressure in crack below dam. Journal of energy engineering 109 (4):207-21.

Hanna, A. W. , H. D. Plewes, R. Wong, and W. C. Seyers (1993) Investigations of high uplift pressures beneath a concrete dam. Canadian Geotechnical Journal 30 (6):974-90.

Hu, J., and F. Ma (2016) Comprehensive investigation method for sudden increases of uplift pressures beneath gravity dams: Case study. Journal of Performance of Constructed Facilities 30 (5):04016023.

ICOLD (International Commission on Large Dams) (2000) Automated dam monitoring systems: Guidelines and cae histories, Bulletin 118 Paris, France

Johansson, F., A. Krounis, and M. Westberg Wilde (2017) Igensättning av dränage under betongdammar– Orsaker, övervakning och åtgärder: Energiforskrapport 2017: 369.

Pate-Cornell, M. E., and C. P. Benito-Claudio (1987) Warning systems: Response models and optimization. Uncertainty in risk assessment, risk management, and decision making:457-68.

Pereira, R., A. L. Batista, L. C. Neves, and J. M. Casaca (2021) A priori uplift pressure model for concrete dam foundations based on piezometric monitoring data. Structure and Infrastructure Engineering 17 (11):1523-34.

Ruggeri, G. (2004) Working Group on Uplift Pressures under Concrete Dams, Final Report. ICOLD (International Commission on Large Dams), Italy

Spross, J., and F. Johansson (2017) When is the observational method in geotechnical engineering favourable? Structural safety 66:17-26.

Spross, J., F. Johansson, and S. Larsson (2014) On the use of pore pressure measurements in safety reassessments of concrete dams founded on rock. Georisk: Assessment and Management of Risk for Engineered Systems and Geohazards 8 (2):117-28.

Spross, J., F. Johansson, L. K. T. Uotinen, and J. Y. Rafi (2016) Using observational method to manage safety aspects of remedial grouting of concrete dam foundations. Geotechnical and Geological Engineering 34 (5):1613-30.

Swedenergy (2020) Betongdammar [Concrete dams]. Energiföretagens riktlinjer för dammsäkerhet (RIDAS) [Swedish Hydropower Companies' Guidlines for Dam Safety]. Swedenergy, Stockholm

Westberg Wilde, M., and F. Johansson (2016) Probabilistic model code for concrete dams. Energiforsk AB, Stockholm, Sweden

Yu, Y., and Y. X. Zhang (2017) Coupling of chemical kinetics and thermodynamics for simulations of leaching of cement paste in ammonium nitrate solution. Cement and Concrete Research 95:95-107.

Yue, J., Z. Shen, L. Xu, and K. Zhang (2022) Numerical analysis the calcium leaching effect in concrete and concrete-rock interface on concrete gravity dam anti-sliding stability. Case studies in construction materials 17:e01158.

Zhang, K., L. Xu, L. Qiu, J. Tan, C. Yang, and K. Zhang (2021) Numerical analysis of concrete gravity dam seepage characteristics evolution considering the calcium leaching effect. Advances in Civil Engineering 2021 (1):9042863.

Phase-field fracture simulation for strain rate effect on fracture propagation

A. Chehreh, LC. Witte, M. Duda & T. Backers
Ruhr University Bochum, Bochum, Germany
hossein.asgharichehreh@ruhr-uni-bochum.de

Abstract

For the spatial and temporal upscaling of results from uniaxial compressive strength tests on rocks, numerical methods are necessary to predict rock behaviour under complex geomechanical conditions, as in foundation, slope stability, underground space, and reservoir studies. Correctly estimating the impact of time and scale on parameters can lead to reduced design risk. Previous studies on phase-field modelling of rocks often employed a single open flaw to simulate fracture initiation, and two to four open flaws to represent fracture propagation and failure. These flaws were generally arranged in a geometrically ordered pattern. However, in natural rock formations, microfractures are predominantly closed and exhibit a random distribution depending on texture.

This study used a phase-field approach to simulate brittle fracturing in granite containing multiple randomly distributed, closed pre-existing microcracks, employing the principal stress criterion as the driving force in the phase-field evolution equation. This study focuses on analysing the sensitivity of the model to crack density and phase-field parameters. The effect of strain rate was investigated, and phase-field parameters were calibrated accordingly.

To demonstrate the accuracy of the presented approach, numerical simulations are compared with experimentally obtained results, showing that the approach is capable of temporal and spatial upscaling when microstructural features are considered.

Keywords

Phase-field fracture, Strain rate, UCS test, Stress perturbation, Micro Cracks analysis.

1 Introduction

Predicting the failure of materials and structures due to crack nucleation and propagation is crucial for many engineering applications. As a result, several numerical frameworks have been developed to capture complex fracture phenomena. Finite element methods (FEM) are often employed in conjunction with models based on linear elastic fracture mechanics. In contrast to methods that represent cracks as discrete curves or surfaces of discontinuity, the phase-field approach (PFM) models cracks with a spatially diffuse fracture zone using an additional continuous field variable, referred to as the phase-field coefficient. This coefficient is used to degrade the material's elastic stiffness and stress-carrying capacity. The phase-field fracture approach naturally captures the emergence of complex crack patterns and behaviour, including crack nucleation, turning, branching, and intersecting in both two and three dimensions without requiring any additional constitutive assumptions. Due to this feature, phase field models have been extensively utilised to simulate an array of brittle fracture problems (Bourdin 2007), and crack growth in rock and rock-like materials (Zhao et al. 2023).

In this study, we propose a phase-field model for simulating brittle fractures developing at different externally applied strain rates in granite containing pre-existing (micro-) cracks. We applied the principal stress criterion as driving force in the evolution equation of the conventional phase-field model (CPFM) presented by Miehe (2010a) and simulated the fracture process in COMSOL Multiphysics. The terms ‘fracture’ and ‘crack’ are used synonymously.

1.1 Phase field formulation

We consider an elastic body $\Omega \subset R^d$ with $d \in \{1,2,3\}$ representing the spatial dimensions as illustrated in Fig. 2c. The external boundary and the internal discontinuity set of this elastic body are denoted as $\delta\Omega$ and Γ, respectively. The phase-field method is typically employed by integrating a variational approach, which necessitates the fracture energy ψ_f to be derived from the stored elastic energy ψ_ε (Miehe et al. 2010a). Fracture propagation can be conceptualised as a process that minimises the energy functional $\psi_{(u,\Gamma)}$ according to

$$\psi_{(u,\Gamma)} = \underbrace{\int_\Omega \psi_{(\varepsilon(\boldsymbol{u}),\varphi)}\, d\Omega}_{\psi_\varepsilon} + \underbrace{\int_\Gamma G_c\, d\Gamma}_{\psi_f} - \underbrace{\int_\Omega B_{(x,t)}.\boldsymbol{u} d\Omega - \int_{\partial\Omega_t} T_{(x,t)}.\boldsymbol{u}\, d\,\partial\Omega_t}_{W_{ext}}, \quad (1)$$

where $\boldsymbol{u}$, G_c, W_{ext}, B, T, and φ represent the displacement field, the critical strain energy release rate, the external work, the body force, the surface traction, and an auxiliary field, $\varphi(x,t) \in [0,1]$ (with x being a position vector), known as the phase field. This phase field is employed to diffuse the crack surface over the domain Ω as depicted in Fig. 2d. Consequently, in the regularised model, the phase field φ assists in smoothing out discontinuities, facilitating the numerical treatment of fractures according to

$$\varphi = \begin{cases} 0 & \text{if material is intact} \\ 1 & \text{if material is fully cracked} \end{cases}. \quad (2)$$

Then, by combining equations (1) and (2), and by substituting W_{ext} with the external crack driving stress σ_{ext}, and ψ_f with critical stress σ_c, the phase-field fracture driving force relies on the principal stress criterion concept D,

$$D = \xi \left\langle \left(\frac{\sigma_{ext}}{\sigma_c}\right)^2 - 1 \right\rangle, \quad (3)$$

where $\langle \mp \rangle$ is the Macaulay bracket, and ξ is the material factor, a dimensionless parameter greater than zero that triggers the activation of damage due to the elasto-plastic contribution and governs the post-nucleation behaviour of cracks.

1.2 Effect of phase-field parameters on simulation results

To evaluate the effects of different phase-field parameters on simulation results we performed a set of numerical simulations of uniaxial deformation experiments in a medium with two pre-existing flaws (Fig.1).

1.2.1 Critical stress $\boldsymbol{\sigma_c}$

An increase in external stress is accompanied by a gradual increase in stress at crack tips (Fig. 1a); Therefore, at a certain point, a critical stress level, $\boldsymbol{\sigma_c}$, is reached, beyond which the driving force, D,

becomes equal to 1. By decreasing the critical stress, the fracture propagation starts earlier (Fig. 1b).The critical stress $\boldsymbol{\sigma}_c$ can be determined by calibrating the crack initiation threshold ($\boldsymbol{\sigma}_{ci}$) that is assumed to be proportional to experimentally determined fracture toughness.

1.2.2 Material factor $\boldsymbol{\xi}$

With a further increase in external stress by following a particular slope, $\boldsymbol{\xi}$, according to Equation (3), the crack propagates. The high rate of fracture propagation exhibits a rapid increase for high values of $\boldsymbol{\xi}$, whereas low propagation rates are observed for small values of $\boldsymbol{\xi}$ and therefore, $\boldsymbol{\xi}$ controls the brittleness. Considering that $\boldsymbol{\xi}$ governs the behaviour of the phase field fracture following thecritical crack initiation point,σ_{ci}, it can be stated that in samples containing two or more joints (Fig. 1c), $\boldsymbol{\xi}$ can be defined by calibrating the slope of the stress-strain diagram in stable crack growth or the crack initiation stress to crack coalescence stress ratio, σ_{cd}.

1.2.3 Length scale $\boldsymbol{l_c}$

Although Miehe et al. (2010a) noted that the response of equation (3) is independent of the internal length scale, $\boldsymbol{l_c}$, determining its correct value affects the mechanical behavior of fractures by controlling the size of the regularisation zone (Fig. 1d), and the modelling cost by adjusting the finite elements mesh size (Molnar et al. 2020). According to Miehe et al. (2010b), $\boldsymbol{l_c}$ is a function of the finite element mesh size and previous studies have calculated the length scale according to the set mesh size, h_{mesh}, through $l_c \geq 2h_{\text{mesh}}$.

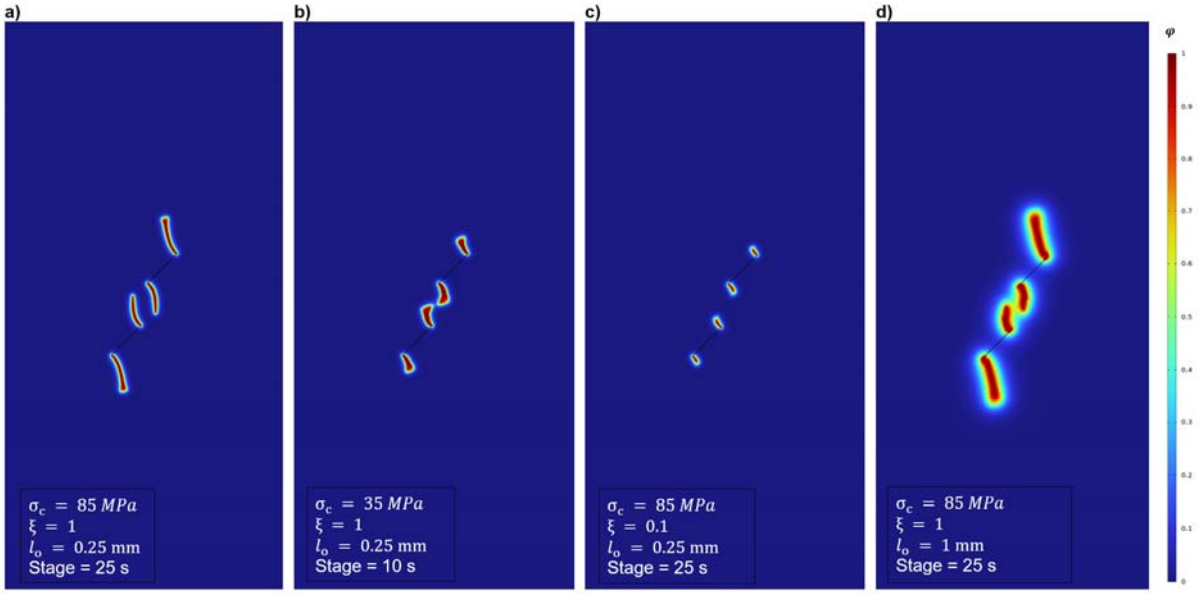


Fig. 1 Effect of phase-field coefficients on fracture propagation applying the CPFM in a numerical simulation of a uniaxial deformation experiment of a medium with two flaws with 45° inclination: (a) reference simulation, (b) effect of critical stress, (c) effect of material factor,(d) effect of length scale.

2 Material, model configuration and calibration

Numerical models were developed to replicate the laboratory experiments performed on granite specimens (samples from Padang quarry, China; Witte et al. 2025) within this study. The cylindrical specimen has an idealised dimension of 40 mm in diameter and 80 mm in length (Fig. 2a). For the time-dependent study used in CPFM, loading was applied with a controlled strain rate ranging from $1{\cdot}10^{-3}$ to $1{\cdot}10^{-6}$ s^{-1}, corresponding to a displacement rate of $0.08{\cdot}10^{-3}$ to $0.08{\cdot}10^{-6}$ mm s^{-1}. The geometric configuration of the models as well as the boundary conditions and microcracks are illustrated in Fig. 2a. Monitoring points were evenly distributed to capture a comprehensive view of the axial stress distribution. The average of these recorded values served as a representative measure of axial and lateral stress and displacement. The purpose of the calibration of the CPFM was to align its key parameters, i.e., uniaxial compressive strength (UCS) and Young's modulus, with the laboratory results. The micro-parameters of the model can be categorised into three groups, including those associated with crack geometry, i.e., crack length, L (1 mm), and crack density ($5cm^{-2}$), elastic properties of minerals, i.e., Young's modulus (55 GPa), Poisson`s ratio (0.3) and bulk density (2650 kg m^{-3}), and phase field damage parameters, i.e., critical fracture stress, σ_c (MPa), material

factor, ξ, and internal length scale, l_c (0.2 mm). The external stress, σ_{ext} (MPa), was calculated from the maximum stress at macroscopic failure. Fig. 2c shows the calibration procedure flow chart for CPFM parameters. The basic model (with a strain rate of $1 \cdot 10^{-5}$ s^{-1}) was calibrated first using the experimentally obtained micro-parameters for further modelling with different strain rates and under different boundary conditions. The results of the parameter calibration are summarised in 0.

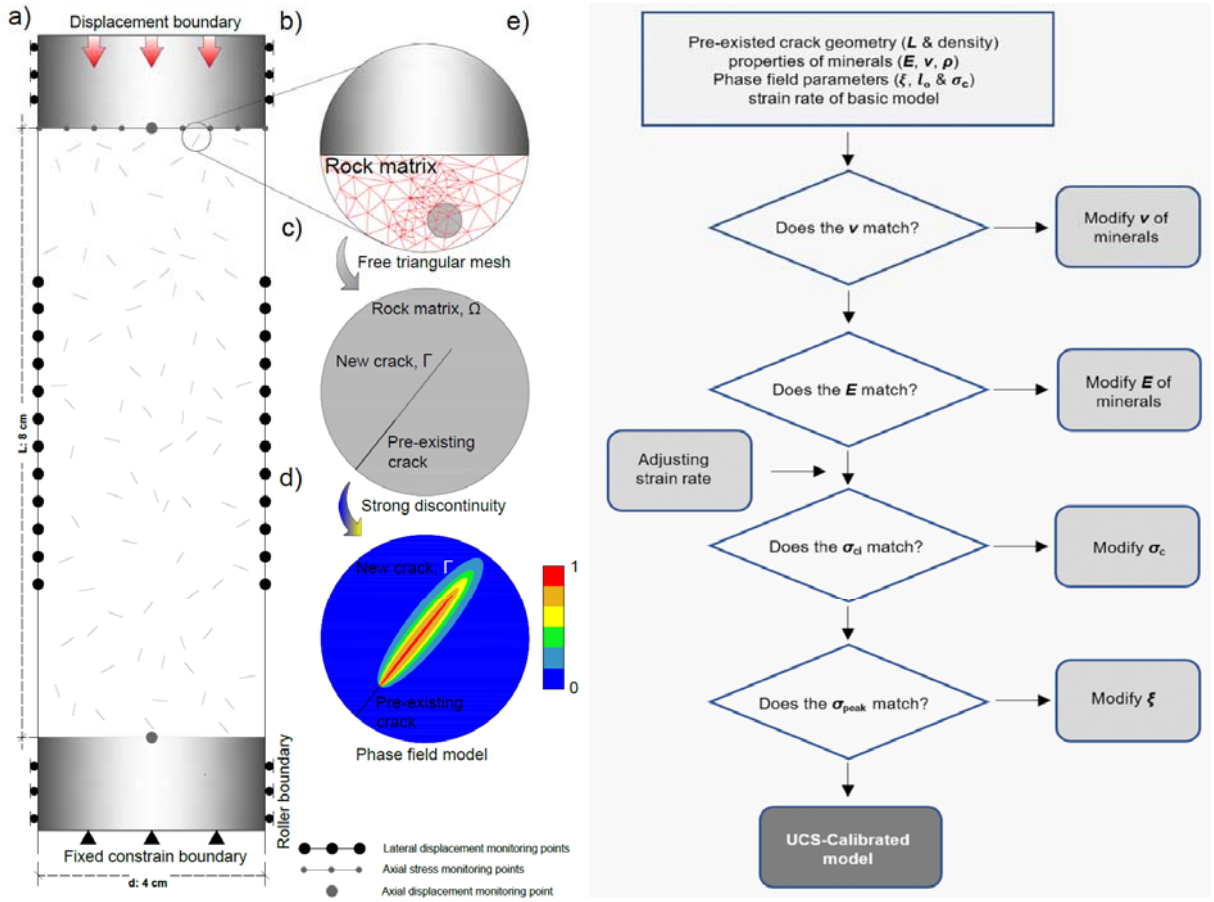


Fig. 2 (a) uniaxial compressive strength test model, (b) free triangular mesh, (c) pre-existing and new cracks in displacement field, (d) new existing crack in the phase field model, (e) flow chart of CPFM parameter calibration.

3 Simulation results

The results of the UCS basic model are depicted in Fig. 3. The CPFM effectively represents various stages of the fracturing process (c.f. Bieniawski 1967). These phases include the linear elastic response, initiation of cracks, stable crack propagation, coalescence and unstable crack propagation, and eventually macroscopic failure. However, certain aspects observed in laboratory experiments, such as crack closure and post-peak behaviour, could not be simulated. For calibration, all parameters were adapted from the basic model, with adjustments made only to the critical stress σ_c and the material factor ξ. As shown in Fig. 4 and 0, the yield stress and the number of fractures increase with increasing strain rate, while the total fracture length decreases.

Table 1. Comparison of numerical and experimental results for UCS tests at difference strain rates.

Strain rate (s^{-1})	Calibration results		Simulation results (MPa)	Experimental results (MPa)	Accuracy (%)
	Critical stress, σ_c (MPa)	Material factor, ξ (-)			
$1 \cdot 10^{-6}$	77	0.1	216	213 ± 20	98
$1 \cdot 10^{-5}$	80	0.13	227	225 ± 17	99
$1 \cdot 10^{-4}$	85	0.21	242	243 ± 18	99
$1 \cdot 10^{-3}$	100	1.8	258	259 ± 18	99

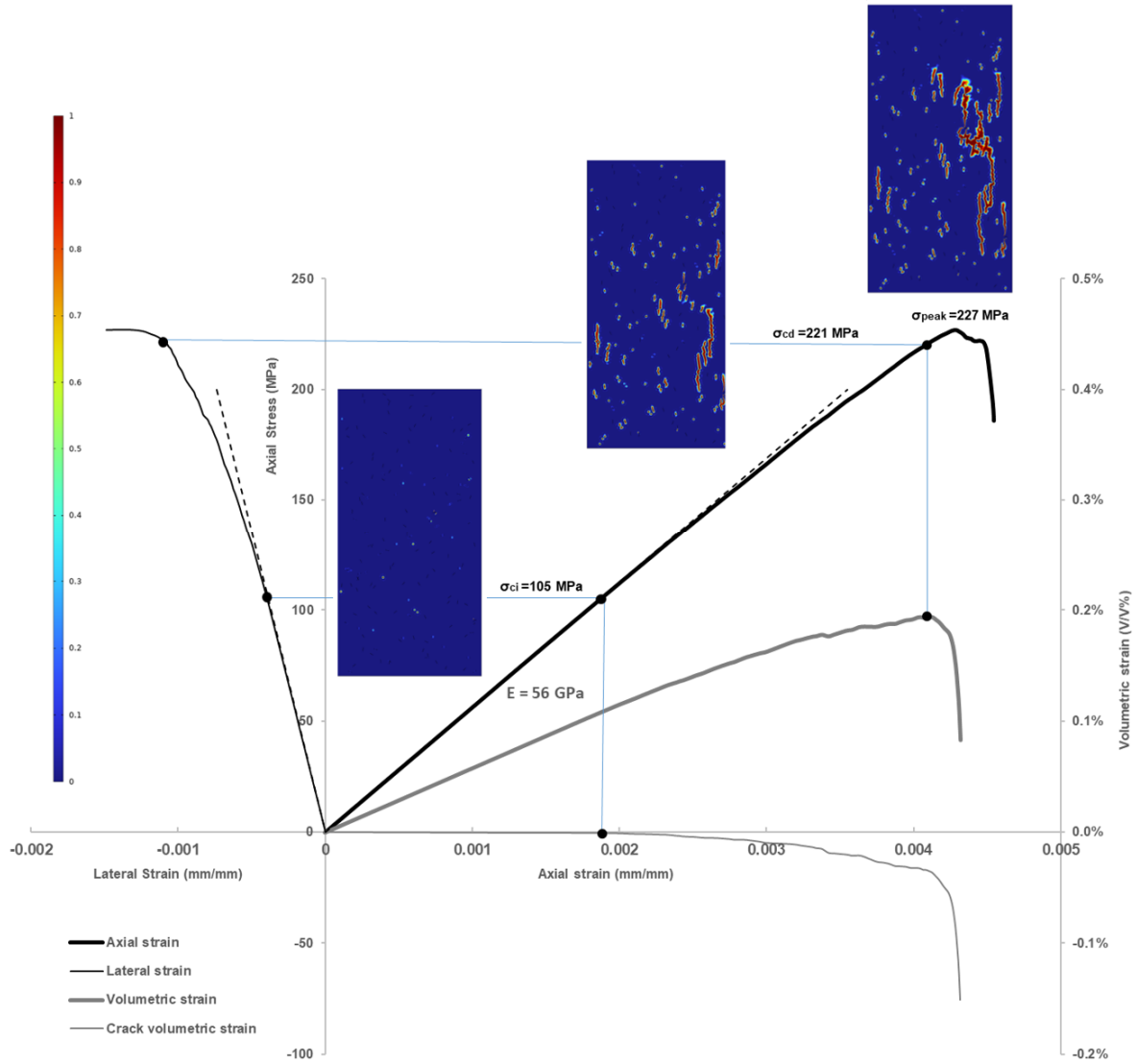


Fig. 3 Stress-strain curves of basic model of CPFMincluding crack initiation, macroscopic failure and post failure.

4 Discussion

Two key aspects are aimed at in simulating rock mechanics experiments in this study: (1) achieving numerical results that closely match experimental findings, and (2) capturing accurately the fracture pattern, fracture growth, and coalescence that represents the correct stress distribution within the model. The first objective is achieved through parameter calibration, the second by modelling the microstructure. 0 compares the simulation results with experimental data, demonstrating that the first objective has been successfully met. In line with the second objective, Fig. 4 illustrates the effect of strain rate on the tensile-to-shear stress ratio in the numerical uniaxial test. As the strain rate increases, this ratio rises, leading to a larger region governed by the tensile stress mechanism. This behaviour aligns with experimental observations, where tensile fractures occur. While the simulated overall fracture pattern compares well with the microstructural observations, some quantitative microstructural properties of uniaxially deformed granite specimens do not closely agree with the numerical simulation results. We formulate the thesis that part of the discrepancy may be due to the free lateral motion in uniaxial experiments. Further investigations, in particular under triaxial deformation conditions, should complement the present results and test the formulated thesis.

5 Conclusion

This study explored the effect of time scale on the mechanical behaviour of Padang granite through conventional phase-field fracture modelling (CPFM) using COMSOL Multiphysics. CPFM enables precise simulations and analysis of rock mechanical behaviour by considering the response of multiple pre-existing cracks in rock specimens and investigating the relation between rock mechanical parameters and phase-field numerical parameters. This study emphasises the importance of

incorporating microstructural features to simulate strain rate effects in numerical simulations for a more comprehensive understanding of rock mechanics and failure mechanisms. These insights can enhance the design and interpretation of mechanical tests in geomechanical applications and help to develop temporal and spatial upscaling approaches.

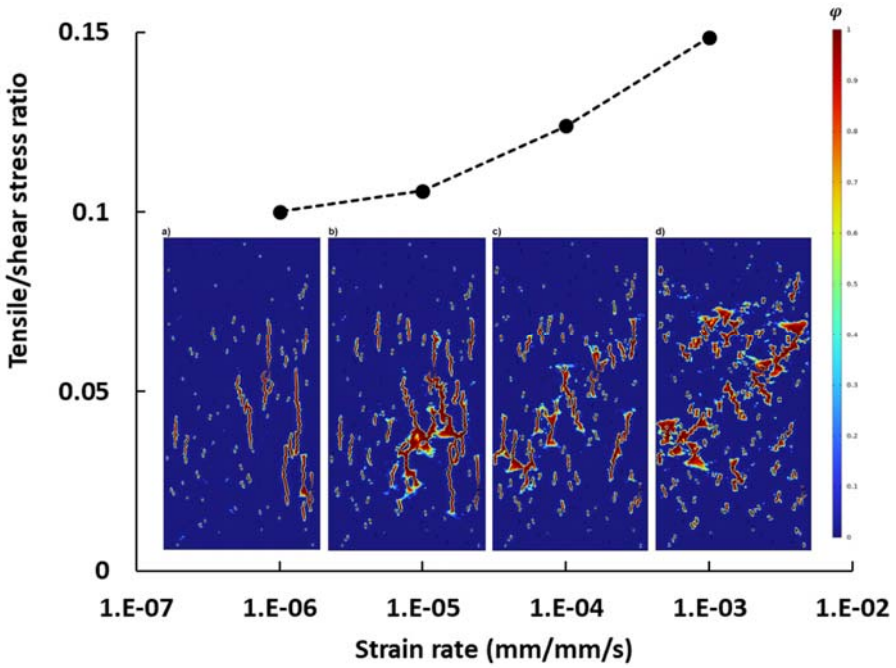


Fig. 4 Tensile to shear elements ratio after macroscopic failure in UCS tests at different strain rates and snapshots of the macroscopic failure pattern in numerical UCS tests at different strain rates: (a) strain rate $1 \cdot 10^{-6}$ s^{-1}, (b) strain rate $1 \cdot 10^{-5}$ s^{-1}, (c) strain rate $1 \cdot 10^{-4}$ s^{-1}, (d) strain rate $1 \cdot 10^{-3}$ s^{-1}.

Aspects of this work have been performed within the projects BeNuQuA (funding by SSM, Sweden) and AGENS (funded by the German Federal Ministry for Economic Affairs and Energy). We would like to thank for supporting our research.

References

Witte LC, Parvin S, Aydin M, Duda M, Backers T, Chehreh A (2025) Predictive capability of coupled rock behaviour – development of an experimentally based benchmark for numerical quality assurance (BeNuQuA). Ruhr University Bochum doi: 10.60517/F1881N35N.

Bieniawski Z (1967) Mechanism of brittle fracture of rock: part I - theory of the fracture process. International Journal of Rock Mechanics and Mining Sciences & Geomechanics Abstracts 4 (4): 405-406.

Bourdin B (2007) Numerical implementation of the variational formulation for quasi-static brittle fracture. Interfaces Free Bound 9 (3): 411–430.

Griffith AA (1921) The phenomena of rupture and flow in solids. Philosophical Transactions of the Royal Society 221: 163-197.

Miehe C, Hofacker M, Schaenzei LM, Aldakheel F (2015) Phase field modeling of fracture in multi-physics problems. Part II. Coupled brittle to ductile failure criteria and crack propagation in thermo-elastic-plastic solids. Computational Methods in Applied and Mechanical Engineering 294: 486-522.

Miehe C,Welschinger F,Hofacker M (2010a) Thermodynamically consistent phase-field models of fracture: variational principles and multi-field FE implementations, International Journal for Numerical Methods in Engineering 83 (10): 1273-1311.

Miehe C, Hofacker M,Welschinger F (2010b) A phase field model for rate-independent crack propagation: Robust algorithmic implementation based on operator splits. Computational Methods in Applied and Mechanical Engineering 199 (45): 2765-2778.

Molnar G, Doitrand A, Esteves R, Gravouil A (2020) Toughness or strength? Regularization in phase-field fracture explained by the coupled criterion, Theoretical and Applied Fracture Mechanics 109: 102736.

Zhao D, Yin B, Storm J, Kaliske M (2023) A phase-field formulation incorporating mode-dependent fracture toughness for fracture modeling in rock-like materials. Engineering Fracture Mechanics 289: 109345.

Geotechnical and operational risk management planning for a long ore pass

J Walls
AMC Mining Consultants (Pty) Ltd
jwalls@amcconsultants.com

Abstract

The use of long ore passes for ore handling presents an appealing alternative to offset the energy burden and safety risks associated with trucking solutions for underground extraction. In particular, where orebody shape and infrastructure arrangement presents an opportunity to place and utilise a long ore pass, inclusion of a geotechnical and operational risk assessment during the planning stage becomes imperative to eliminate potential fatal flaws or severe impediments to the operation.

Several recent studies have been concluded within the broader industry to review and benchmark geotechnical and operational risk management issues associated with the use of long (300-500 m) and ultra long (>500 m) ore passes; however, knowledge and data in the public domain specific to geotechnical and operational risk assessment for long ore passes remains limited. Specific questions that remain unanswered include the cumulative risk effect of known hazards – both geotechnical and operational – as a function of ore pass length, and strategies to successfully manage a long ore pass.

This paper presents a single case study in which a detailed, albeit qualitative, risk management assessment was carried out to determine the feasibility for utilising a long ore pass in a caving operation. As an outcome of the risk assessment, decisions were enabled regarding planned risk mitigation interventions, ore pass maintenance and replacement strategy, and ore handling solutions required to ensure a feasible and sustainable operation. These included planned placement ofa replacement pass, column height monitoring, the use of continuous column feed, water management, access points for hangup release, and a split pass system. Results of this case study may assist in expanding the current knowledge base, and solution management for similar industry challenges.

Keywords

Long ore pass, Risk management, Geotechnical, Operational, Planning.

1 Introduction

In a caving operation, the target orebody shape and orientation frequently lends itself to options where macro infrastructure layouts can be designed, meaning widely separated infrastructure connected through long drives or shafts. In a case where “top of mine” and “bottom of mine” infrastructure separated 300-400 m vertically, for establishment of sublevel caving extraction levels, and materials handling infrastructure, this presented an attractive potential to benefit from direct materials transfer

through a series of single long drop pass systems (Fig. 1). In this case, the planning of an ultra-long ore passes transfer system was employed to optimise on development and production throughput.

However, while the operational case was strategically self-evident, input from multidisciplinary stakeholders was required to ensure against the potential for system failure that may result in severe consequential rehabilitation requirements (Hadjigeorgiou 2013). Dependencies for successful operability of such an ultra-long pass system are a function of several contributing conditions, accounting for, amongst many others, the prevention of, and controlled release of hangups, ore pass stability and longevity, safety, and reliable throughput (Stacey 2005), discussed further herein. Careful consideration must therefore be given to assess critical infrastructure vulnerability, the consequence to operational sustainability, ensuring against potential failure, suspension of production, either temporarily or more long term, and serious safety risks.

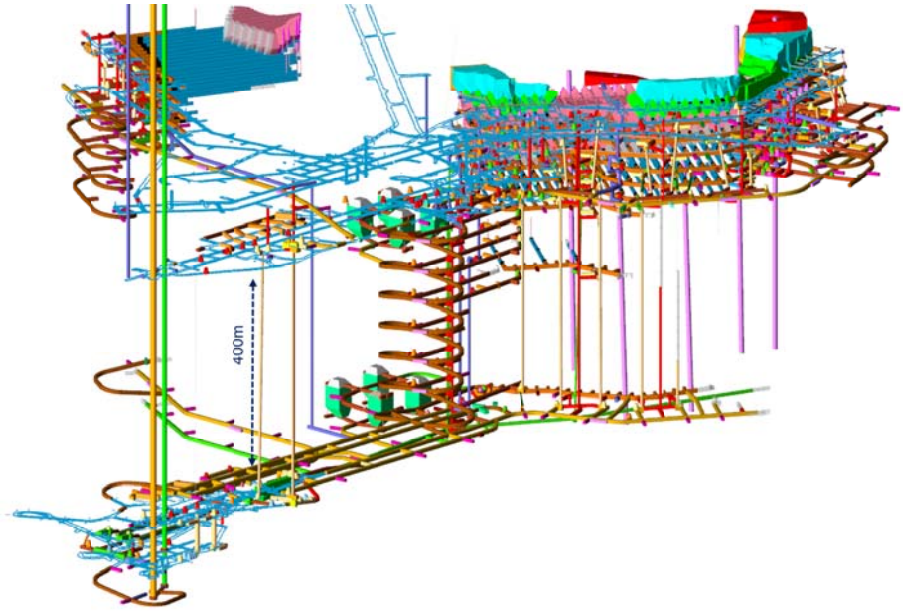


Fig. 1 Macro infrastructure layout for a sublevel cave operation showing ultra long ore pass location (400 m).

A case in point is discussed herein where a detailed, albeit largely qualitative, risk assessment and risk management strategy were carried out through the collective and engaged input of multidisciplinary stakeholders, to determine conditions under which the ultra-long pass system might be feasible for the duration of the mine's production needs.

2 Industry references

A key challenge to assess the likelihood for success or failure of an ultra-long pass system, aside from the obvious rock-wall stability, muck flow and handling constraints, is obtaining examples of similar cases against which to benchmark. In the case under consideration, successful boring of the raise was ruled out as major risk on the basis of proximal passes and geotechnical analysis for shaft construction already completed in the same host environment – i.e. siting in terms of rock mass conditions and local stress state was not a principal concern (Walls 2019, McCracken and Stacey 1989). However, the probable longevity of the pass, and sustainable operability was more difficult to define given the nature of muck that would pass through the shaft (Bartlett 2020, Bartlett 2022, Bunker et al 2015), and uncertainties in operability for the length of the ore pass system (Salmi 2024).

Recent work (Salmi 2024) presents an effort to compile and compare known cases of rock passes > 300 m previously implemented in the industry (Table 1). These cases highlight dominant problems encountered, however while the cases include significantly long ore passes up to 500 m and longer, information to relate the problems to the length of the passes is less clear. For example a dominant problem described as "hang ups due to feeding wet muck" may be encountered in any length of ore pass when poor or incorrect operational conditions are exercised. Additionally, consequences of associated components such as the host rock conditions, duration of pass operation, and column control are not clearly related to the length of the pass, but merely cases where long ore passes have encountered difficulties. The relationship of air blast risk increase as a function of ore pass length is acknowledged (Salmi 2024), with numerical assessments to evaluate impact from uncontrolled release

of hangups having found that discharge height is a major contributor to safe ore pass management (Wang 2021); however, each of these findings affirm the requirement to consider the effect of ore pass length on the risk management requirements to ensure feasible operability as a function of ore pass length.

Table 1. Industry examples of ultra-long passes > 300 m (Salmi 2024).

Operation	**Location**	**Maximum ore pass length (m)**	**Method of excavation**	**Dominant problem**
Rio Blanco Division, Adina, Codelco	Chile	516	-	Hang-ups due to feeding wet muck
Brunswick	Canada	325	Raise-boring	Structural failure, Stress-induced failure
Grasberg	Indonesia	500 to 650	-	Severe air blast/back blast, dust mitigation issue and serious wear which resulted in significant widening of some passes in the system
Henderson	Colorado, USA	Currently 200 in full length. Mine may use passes with lengths beyond 300 in the future	Raise-boring	Flow dynamic issues and preferential draw in the ore passes' system, significant piston effect, and dust propagation in the system
Kiirunavaara	Sweden	Around 350	Raise-boring	Significant wear and deterioration, stress and structural induced failures, issues with oversized fragments blocking ore passes
Finsch Mine Petra Diamonds	South Africa	350	Conventional drill and blast methods	Extensive wear and deterioration, resulting from prolonged scaling, rendered one of the long ore passes irreparable and necessitated its abandonment

The intuitive recognition of cumulative potential for failure as a function of increasing ore pass length one may consider to be self-evident. By contrast, quantification of this cumulative increase is yet to be explicitly defined and did not form part of the case under consideration.

Additionally, while there is a clear thread throughout the available source material to account for the influence of multidisciplinary components, from geotechnical through to construction, operational, maintenance and monitoring (Salmi 2024, Hadjigeorgiou 2013, Bunker et al 2015, Bartlett 2020, Bartlett 2022), a particular practical consideration was encountered as a challenge for the case in this paper, which was ultimately overcome through considerable leveraging of geotechnical risk reporting to gather a multidisciplinary stakeholder engagement and carry out a risk review for the ore pass plan. The outcomes of the risk review, albeit largely qualified rather than quantified, enabled a considered approach, the outcome of which was to define alternative arrangements, and minimum ore pass management protocols.

3 Geotechnical conditions

Specific to the case in question, the departure point to motivate for a risk review arose through geotechnical assessment of the probable ore pass longevity based on rock conditions hosting the planned ore pass system. As indicated, reasonable confidence for overall wall stability was determined through rock mass characterisation (Roberts 2011, Peck and Lee 2008), and scanning of an adjacent completed ventilation raise (operational data). However, three vulnerable locations were identified where the pass intersected dolerite intrusions (Fig. 2, Fig. 3, Fig. 4), and where initial unravelling had the potential to exacerbate with wear. Stress-induced failure was ruled out as a potential contributor, based on the scanned images, and rock mass analysis. While the potential unravelling against dolerite presented a concern, the regional persistence of the dolerite intrusions precluded alternative siting. As a result, the likelihood for increased wear in these locations was accounted for in the risk review, together with the cumulative effect of decreased lifespan for the ore pass system as a function of the ore pass length, and vulnerability to critical failure for the infrastructure design.

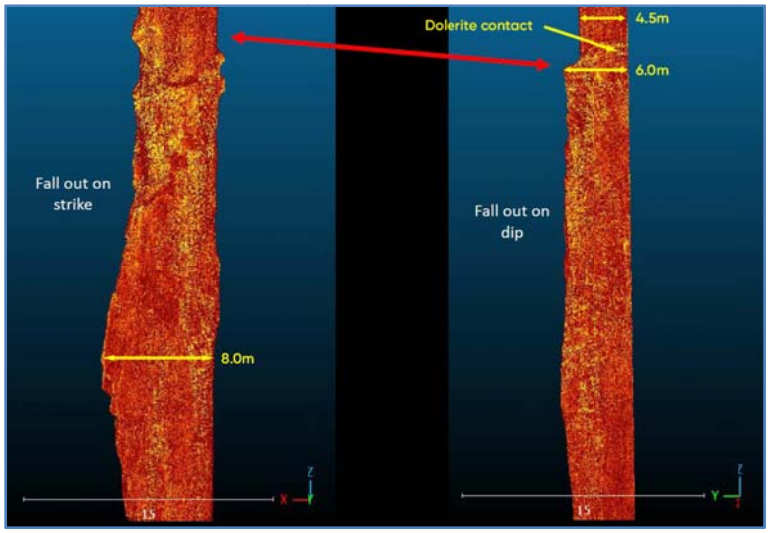


Fig. 2 Scanned adjacent ventilation pass perimeter (operational data).

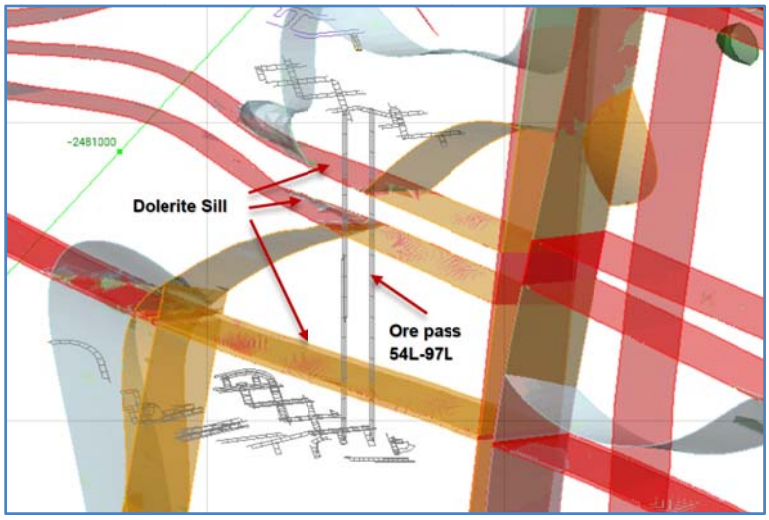


Fig. 3 Lithological section showing dolerite intersection through ore pass system.

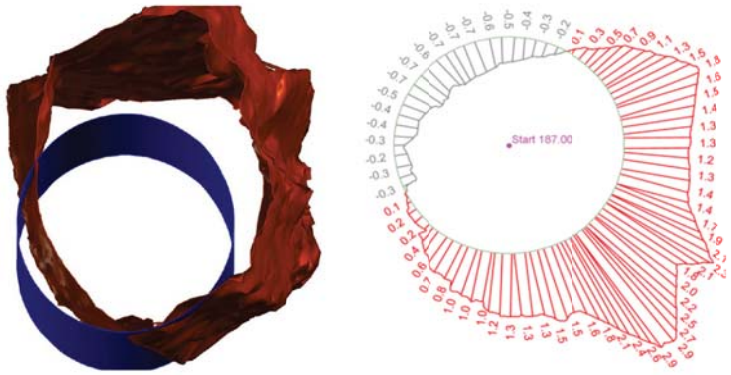


Fig. 4 Cross section showing diameter and perimeter change through dolerite intersection.

4 Mining risk management

To ensure a sustainable ore pass utilisation plan, a multi factor analysis was undertaken with input from multiple disciplinary stakeholders, including mining, safety, engineering and operators (Table 2). Consideration was given to:

- Air blast risk potential as a function of hangup height
- Potential severity of consequence as a function of hangup height release
- Practicalities for hangup release
- Increased complexity of hangup release requirements as a function of pass length, and therefore hangup height

- Potential for increased wear from bombing for hangups
- Potential for uncontrolled release, and severity as a function of hangup height
- Practicalities of column height monitoring
- Practicalities and dependencies of ore pass functionality through sustained continuous ore flow
- Critical production dependencies
- Water ingress management

A series of six alternative arrangements was compiled, with consideration for schedule impact on construction, practicalities for execution, maintenance, replacement strategies and safe throughput management. The completion of a quantified decision matrix provided a significant breakthrough for planning a replacement system and a mid level transfer, which previously had been regarded as superfluous. In the short term, the planned 400 m ore pass system was agreed and elected as the most pragmatic early startup approach, simultaneous to the establishment of mitigation measures including the mid level and replacement passes.

Table 2 Multi-factor analysis applied to determine ore pass design and operation risk management constraints for ultra long pass arrangement.

Option	Features	Longevity	Operability	Hangup management	Constructivity	Scheule	Contingency/Mitigation	Safety	Opex	Capex	Score
	Weighting %	10%	15%	20%	5%	10%	10%	15%	5%	10%	100%
Option 1 – Base case mid level transfer with LHD loading	54L crusher chamber 54L ore pass 3500mm 74L loading area with LHD 94L-97L transfer pass 97L bulkhead with apron feeder and CNV belt	5	7	8	8	5	5	5	2	3	5.7
Option 1a – 54L mid level transfer with apron feeder	54L plug 3500mm 54L-74L ore pass 3500mm 74L transfer feeder 74L-94L ore pass 4500mm 94L-97L transfer pass	5	6	6	4	2	2	6	5	4	4.8
Option 1b – mid level transfer with Hagg loader	54L - ring beam 3500mm (20m) 54L-74L ore pass 3500mm 74L Haggloader feeder 74L flexible conveyor train (FCT) 74L-94L ore pass 4500mm 94L-97L transfer pass	5	3	7	7	5	5	5	4	2	5.0
Option 1c – mid level transfer gravity feed	54L – ring beam 3500mm (20m) 54L-74L ore pass 3500mm 74L transfer pass 74L-94L ore pass 4500mm 94L-97L transfer pass	2	1	4	1	5	5	4	8	6	3.8
Option 2a – mid level transfer gravity feed with finger passes	54L – ring beam 3500mm (20m) 54L-74L ore pass 3500mm 74L transfer pass 74L plug on main ore pass 94L ore pass 450mm	2	7	4	1	5	5	4	6	6	4.6
Option 2b – single 400m vertical pass	Single 400m ore pass from 54L OPA to 94L dead box, with mid-level access for identification and unblocking hang ups	2	8	6	10	7	5	3	7	8	5.9

5 Conclusions

A key outcome for this case study was the pragmatic approach of multidisciplinary stakeholder engagement to determine a resolution for the ultra long ore pass system that would enable short term efficiency, while ensuring long term mitigation strategies. The engagement of multidisciplinary input

for ultra long ore pass risk management is well understood within the realms of industry experience. However, the practicalities of bringing together the professionals for collective engagement require additional effort. It is considered a significant achievement of this case that the collective risk review was accomplished, with the outcomes for significant planning and design adaptations, while still utilising the benefit of ultra long ore pass development in the early stage of the operation.

Ultra-long passes have great economic benefit potential and as such will continue to be planned within mine designs wherever possible. However, an additional finding while conducting this case study was that the cumulative increase in risk management requirements associated with an increase in pass length is intuitively and qualitatively self-evident, whereas there remains the need to provide quantitative relationships between risk elements as a function of ore pass length. As described, for example, if the rock walls are situated in good ground, the "spot" likelihood for stability is similar to that for a shorter pass. However, the length of the pass increases the number of locations at which poorer zones will occur, and therefore cumulatively increases the likelihood for failure somewhere within the pass. As such the frequency for rehabilitation, release of hangups, and more severe events including air blasts continue to render a long pass system vulnerable.

Commensurate risk mitigation and management must therefore be explicitly built into the design and management plan to mitigate against potential failure, which is likely to occur sooner rather than later. To achieve the required risk mitigation measures, collective engagement must be driven, usually as an outcome of geotechnical assessment, to bring together the multidisciplinary stakeholders in the ultimate risk management decision making outcomes for a successful ultra long ore pass operation.

References

Bartlett P. (2020) Lessons learned in designing ore handling systems for kimberlite ore (internal report).

Bartlett P. (2022) Mining in Kimberlite (internal report).

Bunker KA, Campbell AD, O'Toole, D, Penney, A (2015) Guidelines for ore pass design in a sublevel cave mine. *Design Methods in Underground Mining 2015.* Perth: Australian Centre for Geomechanics.

Hadjigeorgiou JS (2013) The absence of strategy in ore pass planning, *The Journal of The Southern African Institute of Mining and Metallurgy*, vol 113, pp 795-801.

McCracken AS, Stacey TR (1989) Geotechnical Risk Assessment of Large Diameter Raise-bored Shafts. *Shaft Engineering Conference* (pp. 309-316). IMM.

Peck WA, Lee, MF (2008) Stability of Raise Bored Shafts in Australian Mines. *13th Australian Tunneling Conference.* Melbourne.

Roberts MN (2011). Shaft Barrel and Station Support for the 10 m Diameter Service Shaft and the 7 m Diameter Production Shaft.TWP - De Beers.

Salmi EF, Phan T, Sellers EJ, Stacey TR (2024) A review on the geotechnical design and optimisation of ultra-long ore passes for deep mass mining. *Journal of Environmental Earth Sciences, 83:301-*

Stacey TR (2005). Setting the scene: rockpass accident statistics and general guidelines for the design of rockpasses. *South African Institute of Mining and Metallurgy*, vol 105, no 11, pp 745-752.

Walls EJ. (2019). Geotechnical data analysis to select a feasible method for development of a long axis, large diameter vertical ventilation shaft. *Journal of the South African Institute of Mining and Metallurgy*, 377-384

Wang J, Cuifeng D, YaPeng W (2021) Research on the Influencing Factors and Prediction Model of Impact Airflow in the Process of Unloading of an Ore Pass Based on a Coupled Computational Fluid Dynamics and Discrete Element Method. ACS Omega. 2021 Aug 31;6(36):23100-23109.

Integrating rigid body methods with rockfall simulation to evaluate instability along Tegalrejo road, Gunung Kidul, Indonesia

Adi Satria Nugraha
Universitas Pembangunan Nasional "Veteran", Yogyakarta, Indonesia
adinugraha42228@gmail.com
0009-0004-2824-7811

Hasan Tri Atmojo
Lecturer, Sleman, Indonesia

Prosida Rhapsody
Geobrugg Indonesia

M. Rizqi Ikhwan Firman Maulana
Universitas Pembangunan Nasional "Veteran", Yogyakarta, Indonesia

Abstract

Rockfall along transportation corridors is strongly controlled by slope geometry, discontinuity conditions, block size, surface material properties, and impact energy loss. This study integrates rock mass characterization, RMi-based block volume estimation, restitution coefficient calibration, and rigid body rockfall simulation to evaluate slope instability along Tegalrejo Road, Gunung Kidul, Indonesia. Field mapping, scanline measurements, and laboratory data were used to characterize interbedded tuffaceous sandstone and siltstone slopes. Rock Mass Rating (RMR) values range from 41 to 63, while Geological Strength Index (GSI) values range from 36 to 58, indicating fair to good rock mass quality. Potential block volumes estimated using RMi range from 0.000265 to 0.0588 m^3 and were used as rigid body inputs in RocFall3. The calibrated normal restitution coefficients are 0.315 for sandstone and 0.28 for siltstone, producing rebound heights of 4.96 cm and 3.92 cm from an initial drop height of 0.50 m. These values indicate low rebound behavior on weathered and rough slope surfaces. The unprotected simulation shows that several trajectories may reach the road corridor, with maximum kinetic energy, translational velocity, and total runout distance reaching 28.58 kJ, 31.17 m/s, and 332.05 m, respectively. A 6 m flexible rockfall barrier with an energy capacity of 111 kJ is proposed to reduce rockfall propagation toward the road.

Keywords

Rockfall simulation, Rigid body, RMi, RocFall3, Road slope mitigation.

1 Introduction

Rockfall is a common hazard on steep slopes and rock cuts, where detached blocks move downslope through free fall, bouncing, and rolling, potentially threatening roads and nearby infrastructure. Along Tegalrejo Road, Gunung Kidul, several rockfall and landslide events have disrupted traffic, including the 2023 incident that temporarily closed the road (Kompas.com, 2023). These events are closely related to the local geological setting, where the Kebobutak Formation, composed of breccia interbedded with sandstone and siltstone, is affected by structural controls associated with the Opak and Tegalrejo fault systems (Munandar et al., 2017; Surono, 2009).

Rock mass quality was evaluated using Rock Mass Rating (RMR) and Geological Strength Index (GSI) to characterize the general condition of the slope, while Rock Mass Index (RMi) was applied to estimate potential block volumes. The integration of RMR, GSI, and RMi provides representative geological and geometrical inputs for the rockfall simulation, particularly in defining rock mass condition, discontinuity-controlled instability, and potential rigid body block size (Hoek, 2007; Palmström, 1995).

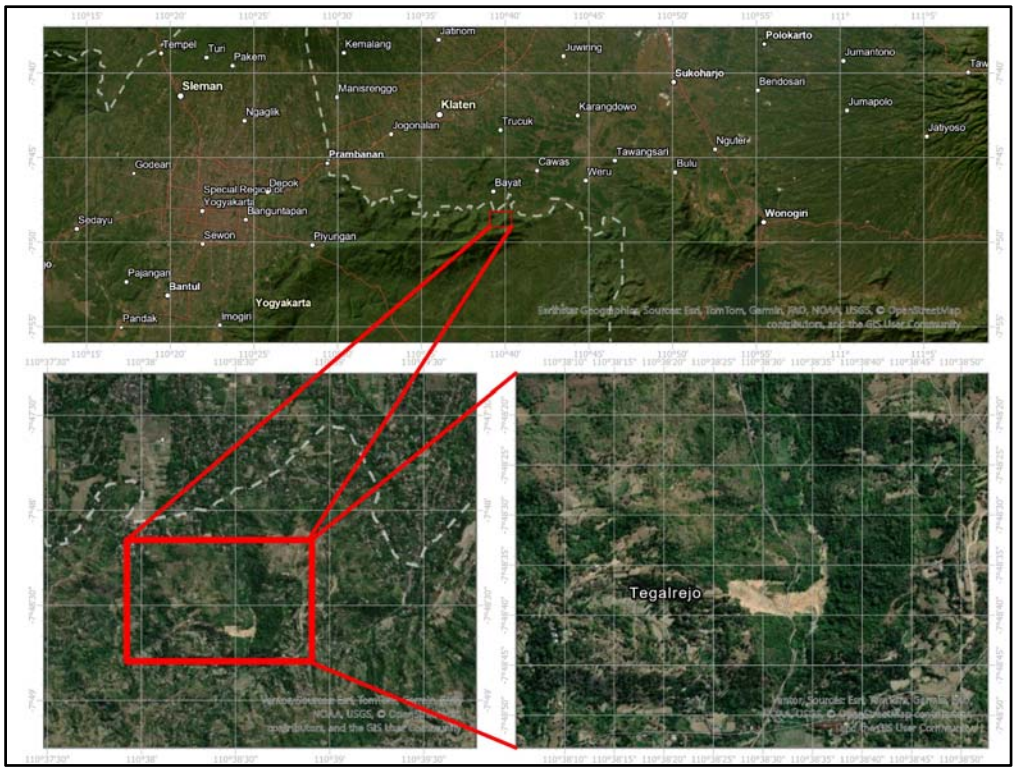


Fig. 1 Site Location of The Rockfall Along Tegalrejo Road (Google Earth Pro, 2026).

Identifying potential rockfall sources remains a primary challenge in hazard assessment because block movement is controlled by slope geometry, discontinuities, block size, and surface conditions. In this study, detached blocks are represented using a rigid body approach, where the blocks are treated as non-deformable objects with defined geometry, mass, and contact behavior. This approach allows the evaluation of rockfall trajectories, kinetic energy, velocity, bounce height, and runout distance. Therefore, this study combines rigid body methods with rockfall simulation to support hazard evaluation and mitigation planning along Tegalrejo Road.

2 Geological Setting and Rock Mass Characterization

The study area is located within the Southern Mountains Zone of Java and regionally belongs to the Kebobutak Formation (Surono, 2009). The rock mass consists predominantly of interbedded tuffaceous sandstone and siltstone with moderate to intense weathering conditions.

Geomorphologically, the area is characterized by structural hills and steep valley slopes with slope inclinations locally exceeding 70%.

Field observations identified several structural discontinuities, including paired joints, shear fractures, and minor strike-slip faults trending northwest–southeast. These discontinuities form weak zones that control potential block detachment and slope instability.

Rock mass characterization was conducted using scanline surveys and laboratory testing. Rock Mass Rating (RMR) values range between 41–63, indicating fair to good rock mass quality. Geological Strength Index (GSI) values range from 36–58, reflecting moderately fractured sedimentary rock masses. RMi analysis indicates potential block volumes ranging from 0.000265 m³ to 0.0588 m³.

The combination of moderate rock quality and highly developed discontinuities indicates that structurally controlled rockfall mechanisms dominate the study area.

Table 1. Summary of rock mass characterization.

Parameter	**Result**
Dominant lithology	Interbedded tuffaceous sandstone and siltstone
Main discontinuities	Bedding planes, joints, shear fractures, minor faults
RMR value	41–63
RMR class	Fair to good
GSI value	36–58
Estimated block volume	0.000265–0.0588 m³
Main rockfall control	Discontinuity, weathering, and steep slope geometry

3 Methods

This study combined field mapping, scanline measurements, rock mass characterization, RMi-based block volume estimation, and three-dimensional rockfall simulation. Field data were used to identify lithology, slope geometry, discontinuity conditions, groundwater, and evidence of previous rockfall activity. Rock mass quality was evaluated using RMR and GSI, while potential block volumes were estimated using RMi and used as representative rigid body inputs.

Rockfall modelling was performed in RocFall3 using simplified square and rectangular rigid blocks derived from field-based block dimensions. Seven release sources were selected from critical slope sections identified through field observation and hazard zonation. The model inputs included block volume, block shape, slope geometry, surface material type, normal and tangential restitution coefficients, and dynamic friction. Block deformation and fragmentation were not explicitly simulated, as the modelling focused on trajectory behavior, kinetic energy, velocity, bounce height, and runout distance.

The normal restitution coefficient was estimated using the rebound-height relationship:

$$R_n = \sqrt{\frac{h_2}{h_1}} \tag{1}$$

Where:

a. R_n : Normal coefficient of restitution

b. h_1 : Effective fall height of the rock before impact,

c. h_2 : Rebound height of the rock after impact

Simulation outputs were evaluated using kinetic energy, translational velocity, bounce height, and total runout distance. Only valid trajectories with “Stopped” status were used in the interpretation to avoid overestimating results from numerical errors. A flexible rockfall barrier was then placed at the critical section where the main trajectories intersect the road alignment, and protected and unprotected scenarios were compared to assess barrier effectiveness.

4 Result and Discussion

4.1 Rockfall Simulation

The rockfall hazard assessment along Tegalrejo Road shows spatial variation from low to high hazard levels. The variation is mainly controlled by slope geometry, lithological contrast, weathering degree, discontinuity condition, and previous rockfall evidence. The RHRS analysis indicates that moderate-risk zones dominate the study area, particularly on slopes composed of interbedded tuffaceous sandstone and siltstone with moderate weathering. These zones are characterized by fractured rock masses and slope segments that are sufficiently steep to promote block detachment.

Locally, high-risk zones occur on steep road-side slopes where discontinuities are well developed and previous rockfall activity has been observed. These zones are critical because detached blocks may directly reach the road corridor. Therefore, the RHRS map is used as the initial basis for identifying critical slope sections requiring further rockfall trajectory simulation.

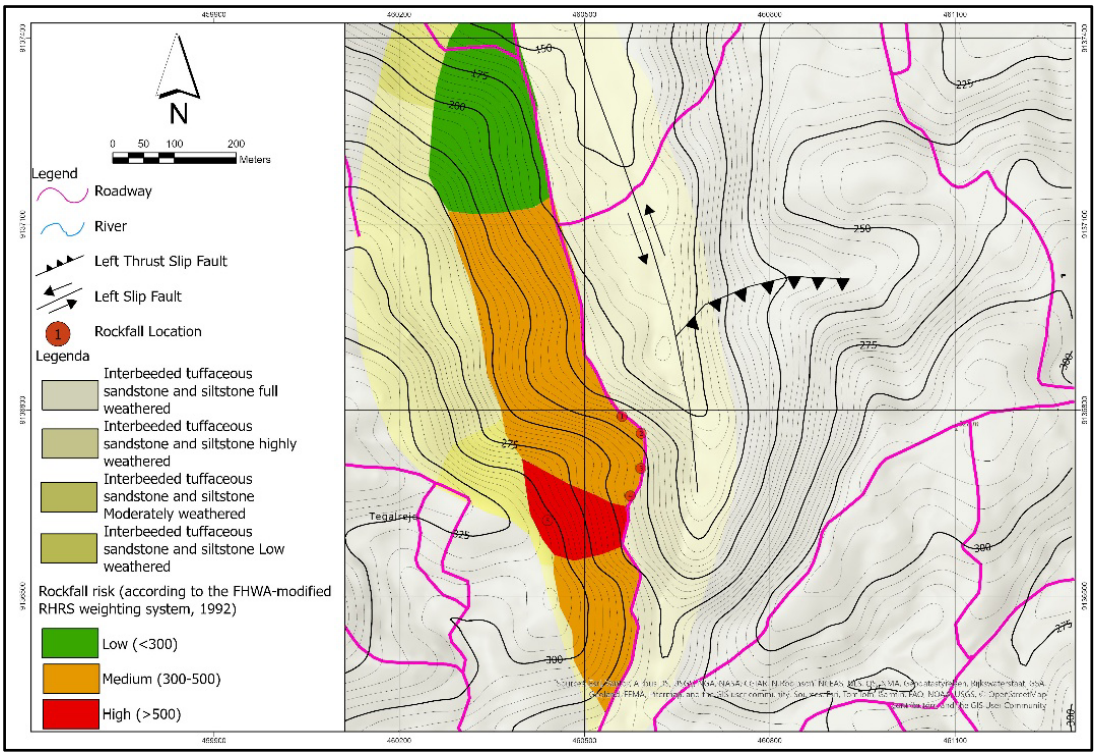


Fig. 2 Rockfall hazard zonation based on RHRS analysis along Tegalrejo Road.

4.2 Rockfall Simulation without Barrier

The unprotected rockfall simulation was carried out to evaluate the natural propagation behavior of detached blocks before the application of any mitigation structure. The simulation considered several release sources distributed along the critical slope sections, with different rigid block shapes representing field-based block geometry. The input parameters, including block volume, surface material properties, restitution coefficient, and dynamic friction, were calibrated using field evidence such as observed rockfall deposits, slope morphology, and impact traces along the road corridor.The restitution coefficient calculation indicates that sandstone and siltstone have relatively low rebound behavior. Using an initial drop height of 0.50 m, sandstone with Rn = 0.315 produced a rebound height of 0.0496 m, or 4.96 cm, while siltstone with Rn = 0.28 produced a rebound height of 0.0392 m, or 3.92 cm. These low rebound heights reflect significant energy loss during impact, which is consistent with the weathered and rough slope surface conditions observed in the field. Therefore, the calibrated restitution values support the simulated movement pattern, which is dominated by rolling, local sliding, and limited bouncing along several slope sections.

The results show that the rockfall trajectories vary significantly among the release sources. This variation is mainly controlled by the source location, slope inclination, local changes in slope geometry, and block shape. In the unprotected condition, several trajectories are able to reach the road corridor and continue downslope, indicating that the existing road section is located within the potential rockfall runout zone. The simulated movement is generally characterized by a combination of bouncing, rolling, and local sliding mechanisms.

To provide a clearer interpretation of the simulation outputs, the rockfall paths were statistically summarized for each seeder. Only valid trajectories with a "Stopped" status were used in the statistical analysis, while paths terminated by numerical error or maximum computation steps were excluded. The summary of the main simulation outputs is presented in Table 2.

Table 2. Summary of rockfall simulation outputs under the unprotected condition.

Seeder	Max duration [s]	Max kinetic energy mean/max [kJ]	Max translational velocity mean/max [m/s]	Total runout distance mean/max [m]	Design implication
Point Seeder 1	35.31	4.25 / 12.55	15.49 / 27.37	144.37 / 332.05	Long runout-dominant source
Point Seeder 2	39.29	1.62 / 22.48	7.90 / 20.60	51.94 / 294.41	High-energy and long-runout source
Point Seeder 3	27.36	1.32 / 28.58	4.11 / 21.44	19.91 / 183.06	Governing impact-energy source
Point Seeder 4	34.36	1.95 / 12.29	11.46 / 18.14	50.55 / 198.45	Moderate energy and runout
Point Seeder 5	14.91	0.21 / 0.99	4.71 / 14.43	12.23 / 66.77	Low-energy source
Point Seeder 6	0.77	0.12 / 0.69	2.14 / 3.39	0.30 / 0.68	Limited propagation
Point Seeder 7	29.68	3.38 / 8.20	15.41 / 31.17	123.42 / 322.49	Highest velocity and long-runout source

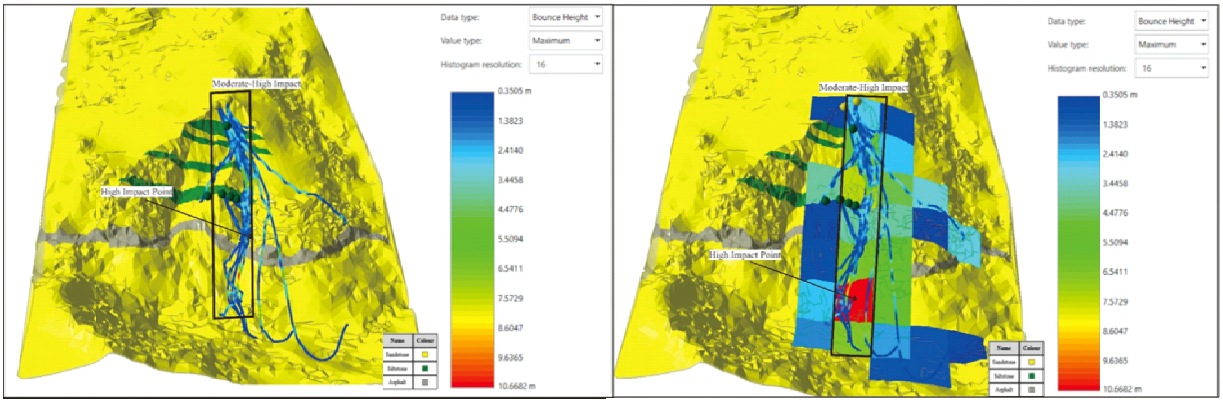


Fig. 3 Rockfall simulation without barrier: (a) trajectory path and (b) bounce height distribution.

4.3 Rockfall Simulation with Barrier and Mitigation

The simulation with a rockfall barrier shows a significant reduction in rockfall propagation toward the road corridor. The barrier acts as a passive protection system that intercepts falling blocks before they reach the road. Compared with the existing-condition model, the protected scenario shows a more controlled trajectory distribution and reduced bounce height beyond the barrier position.

The selected barrier model is based on a flexible rockfall protection system with an energy capacity of 111 kJ and a height of 6 m. The barrier is placed above the road alignment to intercept rock blocks before they enter the transportation corridor. This position is considered effective because it directly cuts the main rockfall paths identified in the unprotected simulation.

The simulation results indicate that barrier installation reduces the exposure of the road to falling blocks. However, barrier installation should be combined with other mitigation measures, including scaling of loose blocks, local rock netting on highly fractured slope faces, drainage improvement, and periodic monitoring. These additional measures are important because the slope instability is structurally controlled by discontinuities and affected by differential weathering between sandstone and siltstone layers.

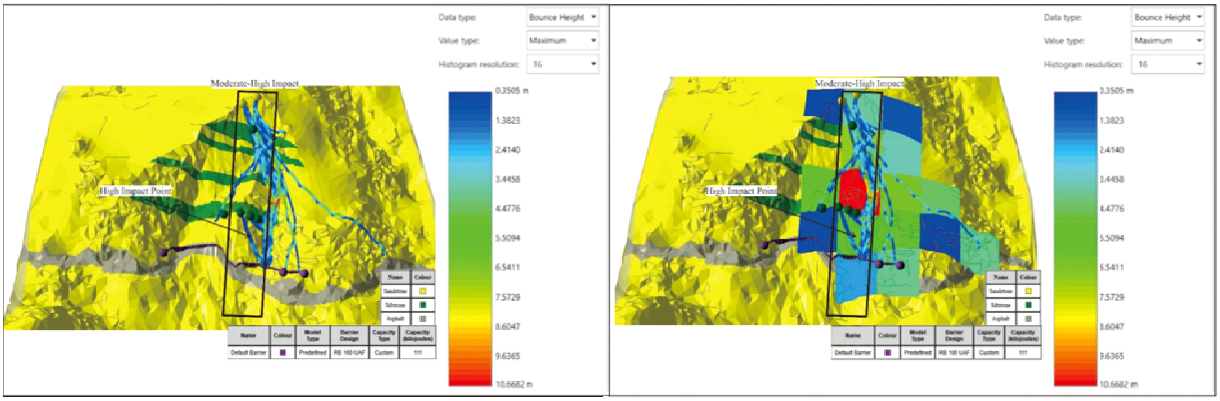


Fig. 4 Rockfall simulation with barrier: (a) trajectory path and (b) reduced bounce height distribution after barrier installation.

5 Discussion

The integrated results show that rockfall susceptibility along Tegalrejo Road is mainly controlled by steep slope geometry, interbedded tuffaceous sandstone–siltstone, weathering, and discontinuity networks. Although the RMR and GSI values indicate fair to good rock mass quality, bedding planes, joints, shear fractures, and minor faults form potential release surfaces for block detachment. The RMi-based block volume estimation provides representative rigid body inputs, while the low calculated rebound heights of sandstone and siltstone indicate significant energy loss during impact on weathered and rough slope surfaces. The unprotected simulation confirms that several trajectories can reach the road corridor, indicating that the road lies within the potential runout zone. The critical source varies depending on the evaluated parameter, with maximum kinetic energy, translational velocity, and total runout distance reaching 28.58 kJ, 31.17 m/s, and 332.05 m, respectively. Therefore, mitigation planning should consider not only kinetic energy, but also velocity, bounce height, and runout distance. The protected scenario indicates that a 6 m flexible rockfall barrier with an energy capacity of 111 kJ can reduce rockfall propagation toward the road by intercepting the main trajectories before they reach the exposed area. Because the instability is structurally controlled and affected by weathering, the barrier should be supported by scaling of loose blocks, local rock netting, drainage improvement, and periodic monitoring.

6 Acknowledgement

The author gratefully acknowledges PT Lenusa Consulting for their support as a research partner in providing geological modelling using Leapfrog Geo. Their contribution greatly assisted the development of the geological model used to support the interpretation of slope conditions and rockfall source areas in this study.

The author also expresses sincere appreciation to PT ASABA for facilitating the use of SLAM scanning technology during the field survey. The scan data provided valuable support for identifying slope discontinuities and improving the reliability of field-based rock mass characterization.

References

Hoek E (2007) Practical rock engineering. Rocscience, Toronto.

Kompas.com. (2023). Longsor beberapa bulan yang lalu, akses jalan warga Gedangsari Gunungkidul. Kompas. https://yogyakarta.kompas.com/image/2023/06/22/110917278/longsor-beberapa-bulan-yang-lalu-akses-jalan-warga-gedangsari-gunungkidul?page=1 Accessed 30 April 2026.

Munandar A, Prasetyadi C, and others (2017) Geological structure analysis of the Southern Mountains, Gunung Kidul area. Geological Journal of Indonesia 12(1):33–45.

Palmström A (1995) RMi – a rock mass characterization system for rock engineering purposes. Rock Mechanics and Rock Engineering 28(1):49–66.

Samodra G, Sartohadi J, Chen G, Kasama K (2014) Automated landform classification in a rockfall-prone area, Gunung Kelir, Java. Earth Surface Dynamics 2:339–348.

Surono (2009) Litostratigrafi Pegunungan Selatan bagian timur Daerah Istimewa Yogyakarta dan Jawa Tengah. Jurnal Sumber Daya Geologi 19(3):209–221.

Fall of Ground Risk Assessment in Underground Excavations Using a Fuzzy Cognitive Rock Engineering System

A. Tursanova, R. Afshar & A. Adoko
School of Mining and Geosciences, Nazarbayev University, Astana, Kazakhstan
amoussou.adoko@nu.edu.kz
0000-0003-1396-7811

Abstract

Fall of Ground (FoG) incidents remain among the most critical safety and operational hazards in underground mining. This study introduces a causality-based Rock Engineering System (RES) for the risk assessment of FoG hazards in underground excavations. A FoG risk index is proposed to systematically quantify the hazard level and evaluate the influence of contributing factors. The RES is weighted using a fuzzy cognitive map (FCM) to reduce subjectivity in determining the interaction matrix of the FoG system. A dataset of over 100 FoG cases from a local underground mine was compiled to develop and validate the FoG risk index. The results indicated that ground support conditions, excavation geometry, and rock fracturing are among the most important parameters controlling FoG occurrence in the mine. The proposed index was compared with the observed FoG size, and the results showed a good correlation (R = 0.78). It is concluded that the proposed index can be effectively used to assess FoG risk in underground excavations.

Keywords

Fall of Ground (FoG), Rock Engineering System (RES), Fuzzy Cognitive Map (FCM), Underground Mining.

1 Introduction

The stability of underground openings remains a critical concern in mining operations. Fall of Ground (FoG) refers to a gravity-driven mining hazard characterized by the detachment of loose rock from excavation surfaces (Peng, 2022). FoG may result from either structural or stress-induced failure and can occur even in supported excavations, posing serious risks to safety, productivity, and profitability of underground mining operations worldwide (Wang et al., 2022). Consequently, effective FoG management requires a comprehensive understanding of the factors controlling the failure mechanisms of the surrounding rock mass.

To improve mine safety and mitigate FoG hazards, numerous assessment approaches have been developed over the past decades, including numerical modelling, empirical methods, expert systems, machine learning, probabilistic techniques, and decision-matrix approaches (Adoko et al., 2019; Isleyen et al., 2021; Małkowski and Juszyński, 2021). Although these methods have significantly enhanced FoG prediction and understanding, many of them still struggle to objectively capture the

complex interactions among the controlling factors. This challenge arises because FoG is inherently a multifactorial problem governed by the interaction of parameters such as rock mass quality, excavation geometry, support systems, groundwater conditions, stress redistribution, and adverse geological structures (Wu et al., 2018; Adoko et al., 2020; Hekmatnejad et al., 2021; Zuo et al., 2024).

Recent advances in rock engineering have therefore emphasized system-based and data-driven approaches for addressing such complexity. Among these, the Rock Engineering Systems (RES) approach provides a structured methodology for analysing complex geotechnical systems through interaction matrices representing relationships among influencing parameters (Hudson, 1992; Salmi et al., 2025). Recent studies suggest that the predictive capability of RES can be further enhanced through integration with intelligent techniques such as Fuzzy Cognitive Maps (FCMs), which enable a more objective quantification of parameter interactions and system weights based on expert knowledge (Zhang et al., 2024). FCMs combine fuzzy logic and neural-network concepts to represent causal reasoning in complex systems (Cosma et al., 2017). Accordingly, this study develops a causality-based RES framework in which FCMs are employed to establish the interaction matrix for FoG hazard assessment in underground excavations.

2 Methodology

2.1 An overview of the RES-FCM

The RES utilizes an interaction matrix to represent causal relationships among parameters controlling a rock engineering problem such as FoG occurrence. The matrix is square, with main factors P_i located along the leading diagonal, while off-diagonal cells encode pairwise interactions I_{ij}. These interactions are conventionally quantified using the Expert Semi-Quantitative (ESQ) coding scheme, which assigns values between 0 (no interaction) and 4 (critical interaction). As shown in Fig. 1a, each row corresponds to the Cause (C_{pi}) of factor P_i, representing its influence on other parameters, while each column corresponds to the Effect (E_{pj}), representing the influence of other parameters on P_i. The cause and effect values are computed as:

$$C_{pi} = \sum_{j=1}^{n} I_{ij}, n \qquad E_{pj} = \sum_{i=1}^{n} I_{ij}, n \tag{1}$$

whereC_{pi} and E_{pj} are the number of columns and rows, respectively.

Once the cause and effect values are obtained, the parameter interaction intensity (PII), calculated as (C+E)/√2, and the parameter dominance (PD), calculated as (C-E)/√2, are employed to characterize the degree and nature of interaction among the parameters.

The overall importance of each factor (weight) is determined by the normalized sum of cause and effect as follows:

$$a_i = \frac{(C_i + E_i)}{(\sum_i C_i + \sum_i E_i)} \times 100 \tag{3}$$

This weighting ensures that both causal and effect contributions are incorporated into the system analysis. The FoG index describing the FoG behaviour is computed as:

$$FoG\ Risk_{index} = \sum a_i V_i \tag{4}$$

In Eq. 4 $V_i$denotes the rating values assigned to each the parameter P_i of FoG system. The values of FoG index can range from 0 to 100. The higher the index value, the greater the FoG risk.

The RES matrix can be used to initialize and then train a Fuzzy Cognitive Map (FCM) topology (see Fig. 1b). In this diagram, nodes (C1,C2,…,Cn) represent the FoG parameters are known as concepts, while directed edges (W_{ij}) denote causal relationships. The FCM update rule is:

$$A_i^t = f\left(A_i^{t-1} + \sum_{j\neq i}^{N} A_j^{t-1} \times W_{ij}\right) \tag{5}$$

whereA^t is the fuzzy value of a concept at iteration t, A^{t-1} is its value in the previous iteration, W_{ij} is connection weight linking concept C_j to concept C_i. This iterative process continues until convergence, allowing dynamic simulation of parameter interactions. After convergence an FCM interaction matrix is obtained.

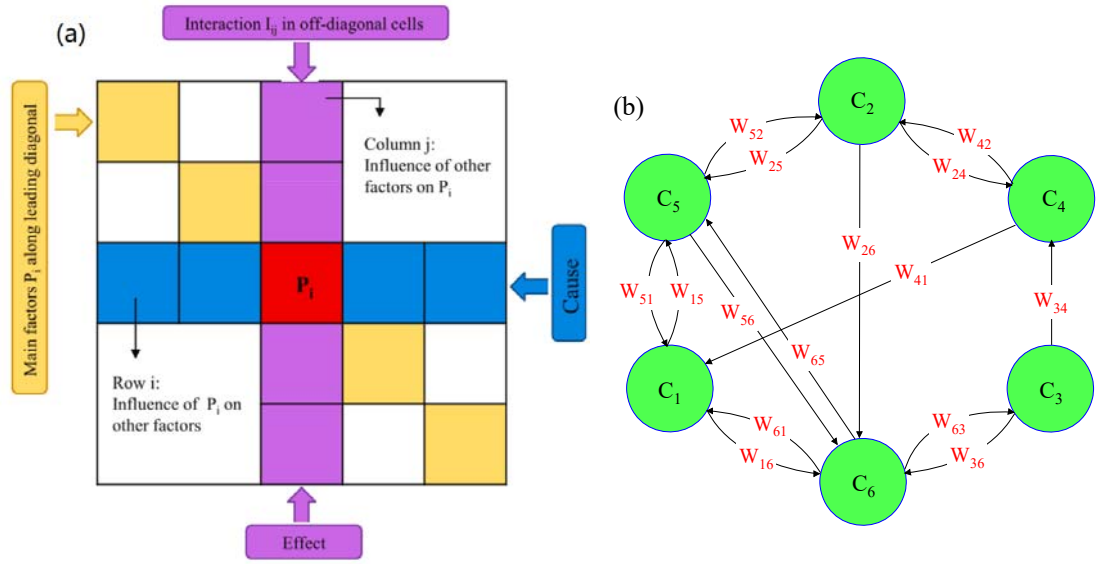


Fig. 1 (a) RES working principle and (b) Graphical representation of FCM topology.

2.2 Data description

In this study, 100 FoG cases from a local underground mine was compiled to develop and validate the FoG risk index model. The dataset contains 13 parameters namely, excavation type (P1), excavation span (P2), excavation height (P3), excavation depth (P4), fault presence (P5), shear zone (P6), groundwater condition (P7), support category (P8), fracture rating (P9), uniaxial compressive strength (P10), friction angle (P11) and geological conditions (P12). The dependent parameter is FoG (P13). A sample of the dataset is shown in Table 1.

Table 1. FoG data sample.

P1	P2	P3	P4	P5	P6	P7	P8	P9	P10	P11	P12	FoG (Tons)
3	5.22	5.15	292.49	0	0	2	2	3	184.7	53.8	1	712.85
2	4.74	4.88	252.09	0	0	0	2	2	184.7	53.8	0	15.9
2	11	6	130	0	0	2	1	2	149.3	59.8	3	195.52
3	17.34	9.89	194.4	1	0	2	3	2	184.7	53.8	4	129.85
3	5.94	5	112	0	1	0	1	2	149.3	59.8	4	388.96
3	10.3	4.76	131	0	0	2	2	2	206.3	60	0	266.22
3	5.3	5.06	337	1	0	3	2	2	184.7	53.8	4	3.38
2	11.3	8.92	204	1	0	0	2	2	184.7	53.8	4	88.4
3	7	5.7	94	0	0	1	1	1	184.7	53.8	1	177.55
3	4.96	4.76	259	0	0	2	3	3	184.7	53.8	3	408.1

3 Results and discussions

First, the interaction matrix based on semi-qualitative encoding was established (Table 2). The interactive intensity, dominance, and cause–effect relationships among the twelve excavation-related parameters are presented in Fig. 2a and Fig. 2b. The results indicate that P8 and P9 exhibit the highest interaction intensities, highlighting their strong influence on excavation stability and fragmentation. In contrast, P1 and P4 show relatively low interaction intensities, suggesting a weaker direct influence within the system.

Regarding dominance, P5 and P6 emerge as the most influential parameters, exerting strong and positive causal effects on other factors, whereas P8 indicates the largest negative dominance. P8 and P9 are more subordinate and largely influenced by external parameters as shown in the cause–effect diagram in Fig. 2b. Parameters located below the equality line (C = E), including P1, P4, P5, P6, and P7, are dominant factors driving FoG occurrence. In contrast, P2, P3, P8, P9, and P12 lie above the line, indicating subordinate behavior and greater dependence on other parameters. Parameters P10 and P11, located near the equality line, exhibit balanced cause–effect relationships and comparatively limited influence within the system. Overall, the analysis demonstrates that structural and geomechanical parameters and support conditions control most the FoG behavior, which is consistent

with FoG mechanism. Subordinate parameters such as support category, groundwater condition, and fracture rating play secondary roles, primarily influenced by dominant factors rather than driving system behaviour.

Table 2. RES matrix used in this study.

P1	**4**	**4**	**0**	**0**	**0**	**0**	**3**	**2**	**0**	**0**	**0**
0	P2	2	0	0	0	1	3	2	0	0	0
0	3	P3	0	0	0	1	2	2	0	0	0
1	2	2	P4	0	0	1	3	3	2	1	1
2	3	3	1	P5	1	2	4	4	2	2	4
2	3	3	0	0	P6	2	4	4	4	4	4
0	1	1	0	0	0	P7	4	4	4	4	4
0	0	0	0	0	0	0	P8	2	0	0	0
1	2	2	0	0	0	2	4	P9	0	0	2
1	1	1	0	0	0	0	4	3	P10	3	3
0	1	1	0	0	0	0	4	4	4	P11	3
1	1	1	0	0	0	0	3	0	0	0	P12

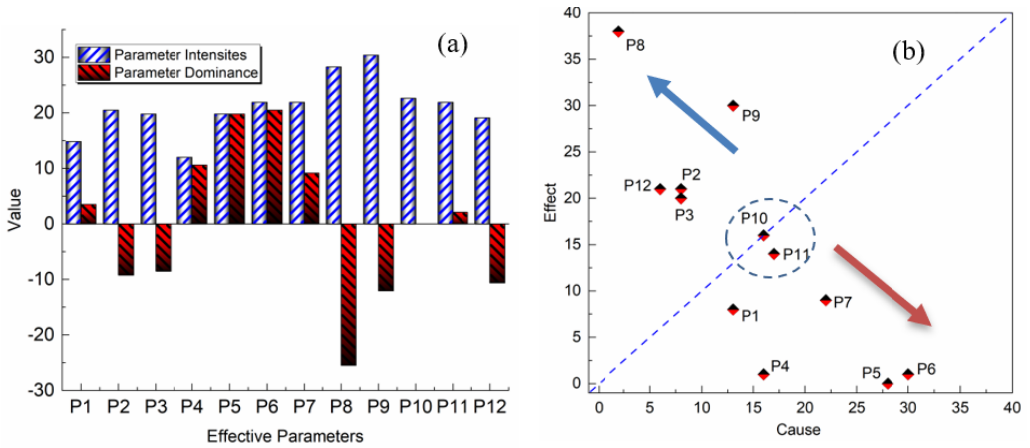


Fig. 2(a) Parameter intensity and dominance; (b) Cause-effect plot for the FoG risk index.

3.1 FCM training

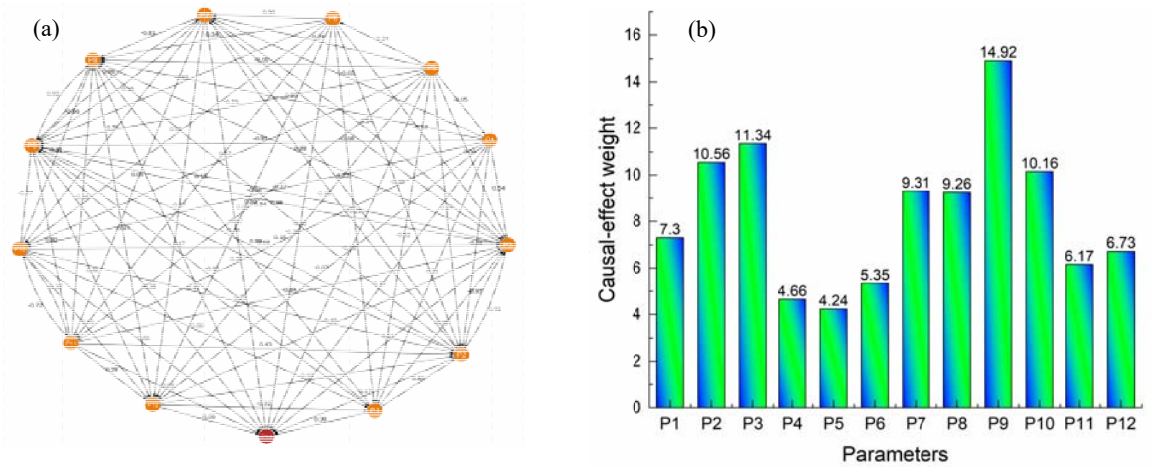


Fig. 3 (a) the structured topology of the map and (b) the resulting final weights of those parameters.

The designed FCM network is shown in Fig. 3(a), while the parameter interaction weights are presented in Fig. 3(b). These weights were obtained through the FCM updating process applied to the initial RES interaction matrix, and the resulting matrix is provided in Table 3. The results indicate that P9 emerges as the most influential parameter, highlighting its critical role in FoG occurrence. Other dominant parameters include P2, P3, and P10, all of which exhibit relatively high cause–effect weights. In contrast, P5 and P6 were found to be less dominant within the FoG system.

The integrated analysis suggests that fracture rating, compressive strength, excavation span, excavation height, groundwater conditions and, support conditions are the primary factors controlling FoG risk in the study area. Conversely, geological structures such as fault zones and shear zones exhibited comparatively lower influence on FoG occurrence.

These findings are somewhat inconsistent with the observed site conditions and therefore constitute a limitation of the present study. Actually, the dominant FoG mechanisms observed at the Mine, included roof subsidence, wedge failures in shear zones, bedding-plane failures, and structurally controlled failures in faulted areas. This discrepancy may be attributed to the use of a training algorithm within the FCM framework combined with the limited size of the available dataset. Future research should therefore focus on expanding the database, incorporating additional influencing factors such as blasting effects on excavations (Imashev et al., 2024), and also accounting for uncertainties in parameter properties (Adoko et al., 2011). Nonetheless, the current results are in agreement with FoG occurrence modes as suggested by previous studies (Małkowski and Juszyński, 2021).

Table 3. Interaction matrix used to initiate the FCM.

P1	**0.599**	**0.250**	**0.000**	**0.000**	**0.000**	**0.000**	**0.358**	**0.469**	**0.000**	**0.000**	**0.000**
0.000	P2	0.966	0.000	0.000	0.000	0.176	0.846	0.203	0.000	0.000	0.000
0.000	0.910	P3	0.000	0.000	0.000	0.951	0.881	0.341	0.000	0.000	0.000
0.208	0.977	0.543	P4	0.000	0.000	0.031	0.205	0.805	0.355	0.156	0.068
0.523	0.235	0.082	0.047	P5	0.243	0.239	0.060	0.229	0.668	0.505	0.259
0.212	0.377	0.118	0.000	0.000	P6	0.898	0.343	0.878	0.556	0.181	0.089
0.000	0.225	0.535	0.000	0.000	0.000	P7	0.807	0.485	0.755	0.054	0.669
0.000	0.000	0.000	0.000	0.000	0.000	0.000	P8	0.988	0.000	0.000	0.000
0.903	0.895	0.766	0.000	0.000	0.000	0.953	0.917	P9	0.000	0.000	0.459
0.862	0.754	0.678	0.000	0.000	0.000	0.000	0.210	0.775	P10	0.374	0.686
0.000	0.428	0.838	0.000	0.000	0.000	0.000	0.157	0.797	0.722	P11	0.277
0.927	0.099	0.395	0.000	0.000	0.000	0.000	0.968	0.000	0.000	0.000	P12

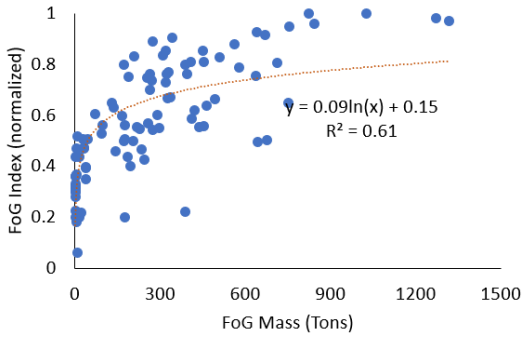


Fig. 4 Comparison between normalized FoG risk index and Observed FoG size.

3.2 Fog index

Finally, the FoG index was calculated for the whole dataset according to Eq. 4. In order to validate the results, the FoG index values were compared with observed FoG size. The results are provided in Fig. 8. As it can be seen, a power function was used to fit the data. A coefficient of correlation of **R = 0.78** (R^2 = 0.61) was obtained, indicating a strong correlation between the proposed index and the actual FoG. The index was scaled into [0,1] for convenience. The FoG size can be estimated using the following empirical relationship:

$$FoG\ Risk_{index} = 0.09 ln FoG + 0.15 \quad (6)$$

4 Conclusion

This study investigated the feasibility of implementing of Rock Engineering System and Fuzzy Cognitive Map methodology to establish a novel index to quantify FoG risk in underground mine excavations. The results showed that fracture rating, compressive strength, excavation span,

excavation height, groundwater conditions and, support conditions are the primary factors controlling FoG risk in the study area. Conversely, geological structures such as fault zones and shear zones exhibited comparatively lower influence on FoG occurrence. In addition, an empirical relationship between the FoG Risk Index and observed FoG conditions yielded a strong correlation coefficient (R= 0.78), demonstrating good agreement with field observations. The results suggest that the FoG Index can serve as a practical tool for FoG hazard assessment, ground control design, and geotechnical risk management. However, the dataset remains limited for broader generalization. Future work should extend the database to additional mining sites and incorporate more parameters.

Acknowledgment

This research was funded by the Science Committee of the Ministry of Science and Higher Education of the Republic of Kazakhstan (Grant No. AP26199097). The authors also wish to acknowledge the valuable contributions of the anonymous reviewers.

References

Adoko, A. C., J. Vallejos and R. Trueman. 2020. Stability assessment of underground mine stopes subjected to stress relaxation. Mining Technology: Transactions of the Institute of Mining and Metallurgy.

Adoko, A. C., M. Zhalel and P. T. Phumaphi. 2019. Fall of ground characterization: A case study of BCL Mine, Botswana. In the Procedings of 53rd U.S. Rock Mechanics/Geomechanics Symposium.

Adoko, A. C., Q.-J. Zuo and L. Wu. 2011. A Fuzzy Model for High-Speed Railway Tunnel Convergence Prediction in Weak Rock. Electronic Journal of Geotechnical Engineering. 16(Q): 1275-1295.

Cosma, G., D. Brown, M. Archer, M. Khan and A. Graham Pockley. 2017. A survey on computational intelligence approaches for predictive modeling in prostate cancer. Expert Systems with Applications. 70: 1-19.

Hekmatnejad, A., B. Crespin, J. A. Vallejos, A. Opazo and A. C. Adoko. 2021. A hybrid predictive model of unstable rock blocks around a tunnel based on estimated volumetric fracture intensity and circular variance from borehole data sets. Tunnelling and Underground Space Technology. 111.

Hudson, J. A. 1992. Rock engineering systems: theory and practice. Chichester, Ellis Horwood.

Imashev, A., A. Mussin and A. C. Adoko. 2024. Investigating an Enhanced Contour Blasting Technique Considering Rock Mass Structural Properties. Applied Sciences. 14(23): 11461.

Isleyen, E., S. Duzgun and R. McKell Carter. 2021. Interpretable deep learning for roof fall hazard detection in underground mines. Journal of Rock Mechanics and Geotechnical Engineering. 13(6): 1246-1255.

Małkowski, P. and D. Juszyński. 2021. Roof fall hazard assessment with the use of artificial neural network. International Journal of Rock Mechanics and Mining Sciences. 143: 104701.

Peng, S. 2022. Roof bolting and underground roof falls. Geohazard Mechanics.

Salmi, E. F., E. J. Sellers and E. Hamman. 2025. Rock Engineering Systems for Quantifying Risks and Controls for the Resilient Design and Optimisation of Long and Ultra-long Ore Passes. Rock Mechanics and Rock Engineering. 58(11): 12359-12418.

Wang, Y. J., L. S. Zhao and Y. S. Xu. 2022. Analysis of Characteristics of Roof Fall Collapse of Coal Mine in Qinghai Province, China. Applied Sciences (Switzerland). 12(3).

Wu, L., A. C. Adoko and B. Li. 2018. An Illustration of Determining Quantitatively the Rock Mass Quality Parameters of the Hoek–Brown Failure Criterion. Rock Mechanics and Rock Engineering. 51(4): 1063-1076.

Zhang, Z., S. Hosseini, M. Monjezi and M. Yari. 2024. Extension of reliability information of Z-numbers and fuzzy cognitive map: Development of causality-weighted rock engineering system to predict and risk assessment of blast-induced rock size distribution. International Journal of Rock Mechanics and Mining Sciences. 178: 105779.

Zuo, Q., X. Li, P. Li, M. Deng and A. C. Adoko. 2024. Surrounding rock instability mechanism for fault-crossing tunnels in water-rich soft rock. Bulletin of Engineering Geology and the Environment. 83(6).

Reliability-based design of the rock slope support considering the planar failure of multiple blocks

R. Pereira, J. Muralha & L. Lamas
Laboratório Nacional de Engenharia Civil, Lisbon, Portugal
rpereira@lnec.pt
0000-0002-3580-520X

Abstract

The assessment of rock slope stability is inherently complex due to the discontinuous nature of rock masses, where failure mechanisms are primarily governed by the geometric and mechanical properties of discontinuities. Traditionally, engineers have relied on deterministic methods based on the concept of factor of safety. However, these approaches often fail to explicitly quantify the uncertainties associated with rock mass properties and geometry. This paper investigates the stability of a multiple-block planar sliding using an analytical system-component formulation. By reducing the potential failure modes of an N-block system to N primary failure modes, the study compares the traditional deterministic design with a reliability-based design approach aligned with the Eurocodes.

The research specifically addresses the influence of geometric uncertainties, considering the dip angle of the sliding surface as a random variable. A comparative analysis was conducted for a slope with six blocks, evaluating the support force required to achieve target reliability indices versus the typical values of the factor of safety. Results indicate that traditional deterministic approaches often overestimate the required support force, serving as an upper bound. Conversely, the equivalent factors of safety derived from the reliability-based design approach vary with the mean dip angle but on average align with the partial factors for the shear strength suggested in Eurocode 7.

Furthermore, the study demonstrates that while multi-block interactions significantly impact stability at lower dip angles, the system tends to behave as a single monolithic volume as the dip angle increases. These findings suggest the adequacy of semi-probabilistic partial factors for idealized rock slope problems while highlighting the benefits of reliability-based methods for design optimization.

Keywords

Rock slope support, Reliability-based design, Planar sliding, Multiple-block system.

1 Introduction

Stability analysis is a fundamental problem in geotechnical engineering, with significant implications for the safety of natural and excavated slopes. While a wide range of analytical and numerical tools is available, the assessment of rock slope stability remains particularly challenging due to the inherently discontinuous nature of rock masses. Unlike in soils, rock mass behaviour is governed by discontinuities, whose geometric and mechanical properties control the kinematics and mechanisms of failure (Hoek and Bray 1981, Goodman 1989).

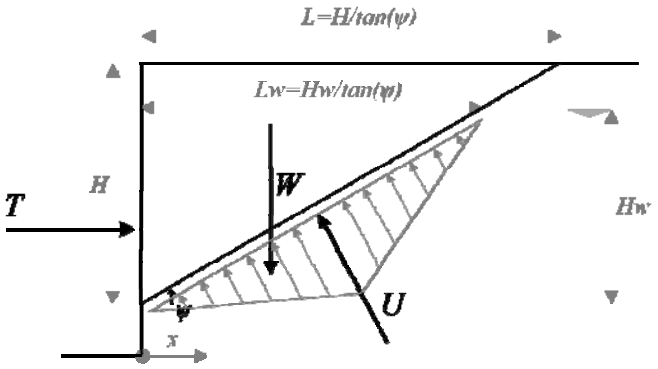
Traditionally, rock slope stability has been evaluated using deterministic approaches based on the factor of safety (*FoS*), in which input parameters are considered as fixed values. Although widely used in practice, this approach does not explicitly account for the uncertainty inherent in rock mass properties. As a result, probabilistic methods have gained interest mostly at the regulation level with a push to include rock mechanics in the scope of Eurocodes (Lamas *et al* 2023). However, the partial factor method, the main approach for limit state verification in the Eurocodes, is complex to be applied to structures so sensitive to geometric properties. In this regard, reliability-based methods have been appointed as potential alternatives given their ability to seek economic optimization under uncertain conditions (Bozorgzadeh and Harrison 2019).

The case of planar sliding of multiple blocks is a sub-problem that given the ability to describe failure mechanisms with analytical formulations, is interesting to be analysed. In this case, the interaction between blocks and the kinetics of the problem can be accounted for in a simpler manner by developing a system-component formulation. This issue was already studied by the authors (Pereira *et al* 2026), and this paper intends to compare the results of this approach with the traditional one and investigate the adequacy of the partial factors in idealized problems, so its application is still possible.

2 Multiple-block planar sliding analysis

Stability analysis regarding planar sliding in rock slopes can easily be carried out considering the limit equilibrium method. Its assumptions are that rock blocks behave as rigid-bodies and the sliding surface is planar and persistent. Fig.1 illustrates the loads acting on a rock block prone to planar sliding due to a set of discontinuities parallel to the slope face outcropping at it. In these conditions, safety is traditionally quantified by the *FoS* given by the ratio between the sliding resistance and the driving actions, i.e.

$$FoS = \frac{(W \cdot \cos\psi - U + T \cdot \sin\psi) \cdot \tan\phi}{W \cdot \sin\psi + T \cdot \cos\psi} \tag{1}$$



Legend:

- H and L are the height and the length of the block.
- H_w and L_w are the height and the length of the portion of the block submersed.
- ψ is the slope dip angle.
- W, U and T are the net forces from the block self-weight, the water pressure and the support, respectively.

Fig. 1 Illustration of the loads acting on a rock block prone to planar sliding.

However, when this potentially unstable volume of rock is divided into several blocks (see Fig. 2), the interaction between those blocks makes the safety quantification more complex, especially in the presence of groundwater, allowing this volume to split apart and only a set of blocks losing stability.

In this case, which may be caused by the presence of another set of discontinuities subvertical and parallel to the slope face, each block presents its own equilibrium state, loading the set of blocks to its left (towards the slope face) if it is unstable or not if it is stable. Such complex loading state is usually analysed using numerical models, with less efficiency. However, in idealized conditions, assuming

uniformity of the shear strength along the sliding surface and rigid-body behaviour of the blocks, physical restraints allow for analytical methodologies for stability analysis to still be carried out.

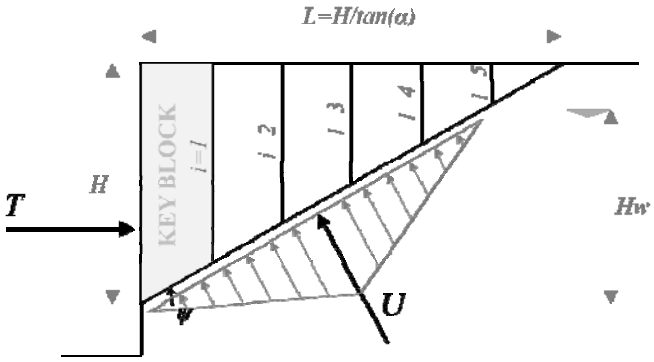


Fig. 2 Illustrative model of a volume of 6 blocks prone to planar sliding.

As mentioned, each block may be itself stable or unstable depending on the loads acting on it and transmitted to it by the block on its right. Considering that the slope instability requires the instability of the key block (the block at the slope free face), there are 2^{N-1} combinations of the stable state of the remaining N-1 blocks, being N the total number of blocks. However, in practice, each block can only become unstable if all the blocks to its left are themselves unstable. Thus, each one of the N-1 discontinuities intersecting the rock volume may divide it into two sets of blocks: a block set A, necessarily unstable, and a block set B, either unstable, loading the former, or stable, reducing the failure modes to (N-1)×2. Furthermore, the situation when block sets A and B slide together is independent of the discontinuity dividing the rock volume. Therefore, the total number of failure modes is reduced to N, corresponding to the instability of *j* blocks at the left, with *j=1,..., N*.In such situation, the representative *FoS* may be the smallest value computed for each failure mode *j*.

In deterministic design of the slope support, the *FoS* is considered a safety indicator, and the intention is to quantify the force needed for the *FoS* to achieve a target value. The solution of this problem can be obtained directly since *FoS* has an analytical expression given in terms of the design variables, in this case the force applied by the support, given by:

$$T = \frac{W \cdot (FoS \cdot \sin\psi - \cos\psi \cdot \tan\phi) + U \cdot \tan\phi}{(FoS \cdot \cos\psi - \sin\psi \cdot \tan\phi)} \tag{2}$$

In reliability-based design, the reliability index β (or the associated probability of failure) is the safety indicator and its target value is often defined in regulations, such as the Eurocodes (EN1990-1 2023). The solution of the problem is obtained through probability theory, expressing the probability of occurrence of failure mode *j* as:

$$P\left[FoS_j < 1\right] \tag{3}$$

Since there are several failure modes involved, due to the existence of several blocks, the rock volume to be analysed is described as a system of blocks and the reliability problem is formulated at the system level. The system fails whenever a failure mode occurs. For each failure mode to occur the stability conditions of sets A and B must be fulfilled. A fully description of this formulation is presented in Pereira *et al* (2026). To calculate the probability of failure of the system a simulation routine was prepared, where each failure mode is checked in turn, incorporating adaptive sampling techniques to speed up the process.

3 Geometric uncertainties

Rock slope stability assessment must account for the inherent uncertainties involved, mostly associated with material properties, resistances, loads and geometric properties. The latter are especially relevant given the sensitivity of the rock mass behaviour to its discontinuous nature (Einstein and Baecher, 1983). In stability assessment of moderately weathered rock masses, failure mechanisms often develop through discontinuities, so its geometric discretization is crucial.

In planar failure of rock slopes, the orientation (dip angle) of the sliding surface is the key factor. The uncertainty on its definition, mostly due to limited site information, must not be ignored. In

probabilistic approaches this uncertainty can be accounted for directly by considering the dip angle as a random variable to which a probabilistic model, such as the von Mises distribution (Fisher, 1953), is assigned. On the other hand, in traditional deterministic approaches a range of plausible values of the dip angle may be established, based on available data, geological context and professional judgement, from which the worst-case scenario is adopted for stability calculations. A hypothetical link between the two may be set by matching the range of plausible values to a confidence interval with a high confidence level.

The selection of the worst-case scenario regarding the dip angle follows a risk-averse behaviour of the rock engineer, who seeks for the most demanding situation with respect to the support needed. For planar sliding, this worst-case scenario is dependent on the external loading. For blocks solely loaded with water pressures, besides their dead weight, it can be showed that the dip angle of the sliding surface that maximizes the support needed (here denoted critical dip angle ψ_c) depends on the targeted *FoS*, being given by:

$$\tan\psi_c = \frac{\tan\phi + \sqrt{\tan^2\phi + FoS^2}}{FoS} \tag{4}$$

where ϕ is the friction angle of the sliding surface. In this loading case, a rock engineer would select the dip angle within the pre-defined range closer to the critical value.

4 Deterministic versus reliability-based design of the support

The design of the slope support follows the definition of a conceptual design model of the ground and the identification of kinematically admissible failure mechanisms. In a context of a rock slope with multiple blocks potentially unstable due to planar sliding, the failure modes were derived in section 2. In this section, a comparison between the traditional deterministic approach based on global factors of safety and the reliability-based approach is intended.

The problem to be tested is described as the stability analysis of a volume of rock, defined by a discontinuity parallel to the slope face and outcropping H=10 meters below the crest, prone to planar sliding (see Fig. 2). Suppose that this volume is intersected by another set of equally spaced vertical discontinuities, parallel to the slope face, forming a system of N=6 blocks. In this situation there are N=6 failure modes associated with the possible instability of larger portions of the rock volume, such as explained before. For simplicity, the water level is fixed at the slope crest and a Mohr-Coulomb envelope with no cohesion is considered for the shear strength of the sliding surface.

To compare the deterministic and reliability-based approaches, some considerations must be made. Firstly, the tangent of the friction angle of the sliding surface is considered as a random variable following a lognormal distribution with mean value of 1 (corresponding to an angle of 45°) and a coefficient of variation of 10%, such as indicated in EN1997-1 (2024). The corresponding characteristic (5^{th} percentile) value of the friction angle, considered in deterministic calculations, is 40.2°. The dip angle is also considered as a random variable following a von Mises distribution with a concentration parameter κ=350 so that the interval ±5° around the mean angle ψ_m corresponds to a 90% confidence interval. In the deterministic approach, for the sake of comparison, this confidence interval is taken as the range of plausible values of the dip angle and the value considered in the calculations is, as mentioned, the one within this interval closer to the critical dip angle. For generalization purposes, the analysis was repeated for mean dip angle ψ_m ranging from 15° to 75°.

For the reliability-based approach, the target reliability indices considered are those indicated in the Eurocodes (EN1990-1 2023), namely 3.3, 3.8 and 4.3 for structures of consequence classes CC1, CC2 and CC3, respectively. With this respect, a direct comparison to the deterministic approach is not possible since there are no settled criteria that establish the target factor of safety. In fact, this factor, which intends to include several sources of uncertainty, is set subjectively by the designer, although the range from 1.3 to 1.5 is often seen as a “rule of thumb” (Wyllie and Mah 2005).The reliability-based design is performed iteratively using the Monte Carlo simulation with adaptive sampling and the deterministic design is computed directly from equation (2) for each failure mode and then assume the larger value of the support as the design value. Fig. 3 shows the results, where the grey-shadowed area corresponds to the solution of the deterministic design (DD), considering the range of *FoS* from 1.3 to

1.5, and the three coloured lines correspond to the solution of the reliability-based design (RBD) for consequence classes CC1, CC2 and CC3.

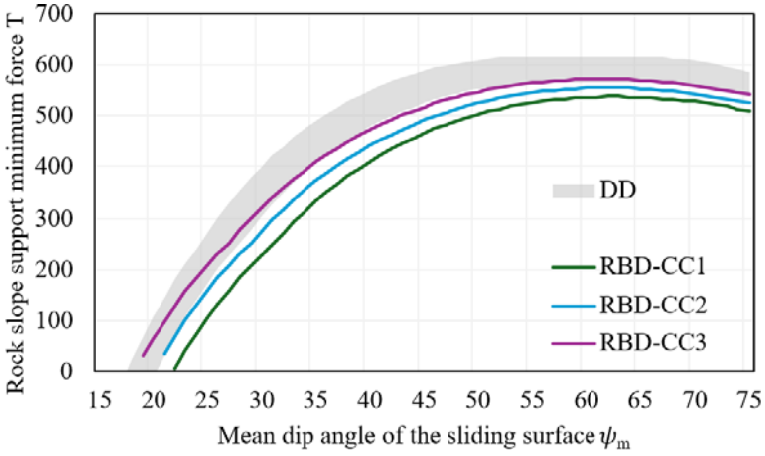


Fig. 3 Rock slope support minimum force obtained following the deterministic and the reliability-based approach.

The range of values of the *FoS* tend to overestimate the minimum force of the rock slope support, indicating that 1.3 to 1.5 are an upper bound for possible values to be adopted as partial factors in the semi-probabilistic approach. In this respect, Fig. 4 shows the equivalent *FoS* that would be obtained by considering the values of the support force computed following the reliability-based design approach. These values were calculated after an inverse analysis, solving Eq. (1) using the support force obtained in the reliability-based design.

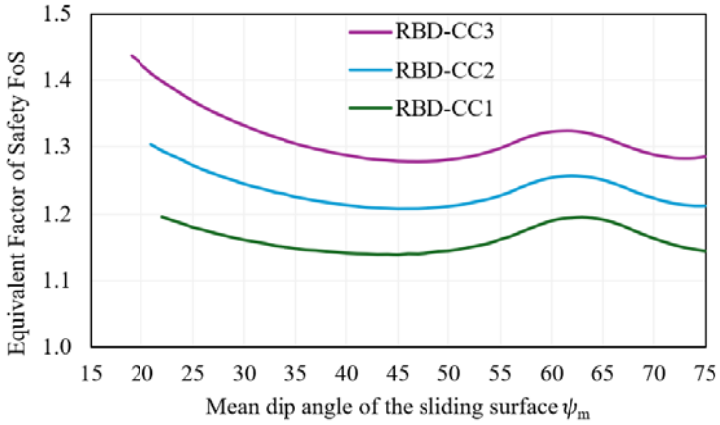


Fig. 4 Factor of safety computed considering the support force obtained in the reliability-based design.

Although the strategy implemented in deterministic calculations to account for the uncertainty of the dip angle can control the variation of the safety level (it inflects for dip angles greater than the critical dip angle ψ_c, roughly between60° and 65°), the equivalent *FoS* still varies with the mean dip angle of the sliding surface. However, the partial factors for the shear strength suggested in Eurocode 7 (EN1997-3 2025), of 1.125, 1.25 and 1.375 for structures of consequence classes CC1, CC2 and CC3, respectively, grossly matches an average value of the equivalent *FoS* determined, suggesting its adequacy. It should however be noted that other situations regarding the loading conditions of the slope, namely external loading and variable water levels, may put this conclusion in question.

Another aspect addressed was the effect of considering a more complex design model, accounting for a set of discontinuities intersecting the volume of rock and generating several blocks. A comparison of the support force determined for the multi-block model with the one obtained in the simpler case that only accounts for the instability of the whole volume can be found in Fig. 5. In fact, differences are only perceived for lower values of the mean dip angle. In fact, as the dip angle increases the possibility for the volume of rock to split apart and some blocks (set A) lose stability while others (set B) remain stable becomes unlikely. The water pressures installed in the vertical joints between the two block sets is less capable of withstanding the weight of block set B, which more easily slides together with block set A.

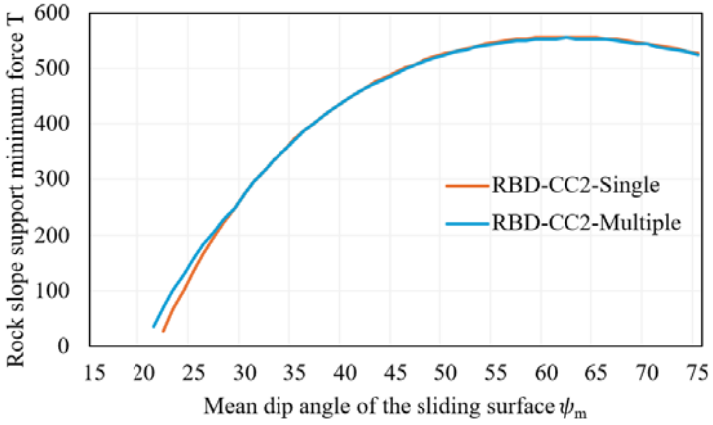


Fig. 5 Rock slope support minimum force for a multi-block and single block models.

5 Conclusions

This study demonstrates that rock slope stability analysis significantly benefits by changing from deterministic to reliability-based design. By modelling the rock mass as a system of multiple interacting blocks, this research captures complex failure modes that traditional single-block models overlook, particularly at lower dip angles. The comparison reveals that the conventional factor of safety range of 1.3 to 1.5 often leads to conservative and consequently uneconomical support designs. Conversely, the partial factors suggested in Eurocode 7 (1.125 to 1.375) were found to be adequate, as they closely match the average equivalent factor of safety derived from probabilistic analyses, validating their adequacy for idealized planar sliding scenarios. Ultimately, incorporating geometric and material uncertainties through probabilistic methods provides an optimized approach to geotechnical safety.

References

Bozorgzadeh N, Harrison JP (2019) Reliability-based design in rock engineering: Application of Bayesian regression methods to rock strength data. Journal of Rock Mechanics and Geotechnical Engineering 11(3): 491–504. doi:10.1016/j.jrmge.2019.02.002

Einstein HH, Baecher GB (1983) Probabilistic and statistical methods in engineering geology. Rock Mechanics and Rock Engineering 16: 39-72. doi: 10.1007/BF01030217

EN 1990-1 (2023) Eurocode: Basis of structural and geotechnical design. European Committee for Standardization, Brussels

EN 1997-1 (2024) Eurocode 7: Geotechnical design – Part 1: General rules. European Committee for Standardization, Brussels

EN 1997-3 (2025) Eurocode 7: Geotechnical design – Part 3: Geotechnical structures. European Committee for Standardization, Brussels

Fisher RA (1953) Dispersion on a sphere. Proceedings of the Royal Society. A: Mathematical, Physical and Engineering Sciences 217 (1130): 295–305. doi:10.1098/rspa.1953.0064

Goodman RE (1989) Introduction to rock mechanics. 2nd edn, John Wiley & Sons Ltd., New York

Hoek E, Bray JW (1981) Rock slope engineering. 3rd edn. The Institution of Mining and Metallurgy, London

Lamas L, Burbaum U, Estaire J, Harrison J, Nuijten G, Pereira R (2023) Rock engineering design in tomorrow's geotechnical toolbox: Eurocode and the basis of structural and geotechnical design (the second generation of EN 1990 and EN 1997). Geomechanics and Tunnelling 16, 469-490. doi: 10.1002/geot.202300021

Pereira R, Muralha J, Lamas L (2026)Application of reliability analysis and probabilistic design of the reinforcement of rock slopes (in Portuguese). Geotecnia 166:3-22. doi: 10.14195/2184-8394_166_1

Wyllie DC, Mah C (2004) Rock slope engineering – Civil and mining. 4thedn. Spon Press, New York

Risk-Informed Foundation Optioneering in Karst Terrain: From Geotechnical Risk to Sustainable Development

Mohamed H. Mahmoud[a,b] & Omar Hamza[b]
a. WSP, Dubai, United Arab Emirates
b. University of Derby, Derby, United Kingdom
m.hassan31@unimail.derby.ac.uk
0000-0001-6970-4290

Abstract

This study shows that risk-informed geotechnical decision-making provides a clear and reliable foundation for demonstrating sustainability outcomes in karst-affected construction projects across the Middle East. Karst terrain is common in the region and creates significant uncertainty that, if not addressed early, can transfer risks related to safety, project schedule, high material consumption, and elevated carbon emissions to the construction phase. Current practices often respond to this uncertainty with conservative, material-heavy solutions that increase these risks during construction, extend timelines, and increase cost and embodied-carbon consumption.

To tackle these issues, the study introduces a design-stage framework in which the Sustainable Development Goals are not used as fixed design rules. Instead, SDGs 3, 8, 12, and 13 naturally arise as outcomes of managing project-specific risks related to safety, project schedule, material usage efficiency, and embodied carbon. Applying this methodology to a high-load building on karstic limestone in Saudi Arabia demonstrates its practical benefits. Comparative analysis shows that a piled foundation better localises and manages karst risks compared to a raft foundation with probing and grouting. This results in lower construction risk exposure (SDG 3), a more predictable project schedule and procurement (SDG 8), reduced material use (SDG 12), and significantly lower embodied carbon in the design stage (SDG 13). Carbon impacts are presented as comparative indicators that reflect uncertainties in regional emissions.

These findings illustrate that sustainable outcomes in rock engineering can be advanced by integrating SDG evidence generation into standard risk-based design processes. Further case studies across different geological formations, foundation types, and load classes are needed before the approach can be considered generally applicable.

Keywords

Karst risk management, Foundation optioneering, Risk-informed geotechnical design, Sustainable development goals (SDGs), Embodied carbon in ground engineering.

1 Introduction

In 2015, all United Nations (UN) member countries, including those in the Middle East, pledged to achieve the 17 Sustainable Development Goals (SDGs) by 2030 (UNDESA 2015). Four SDGs are directly relevant to construction: SDG 3 (health and safety risk management), SDG 8 (decent work, labour productivity, and schedule certainty), SDG 12 (efficient use of raw materials), and SDG 13 (reduced greenhouse gas emissions). The Middle East is undergoing rapid development through initiatives such as Saudi Arabia's Vision 2030 (Saudi Vision 2023), creating significant pressure to deliver projects sustainably. However, achieving SDGs 3 and 8, for example, is hindered by limited awareness of Safety in Design (SiD) among regional practitioners. A survey of 29 geotechnical professionals found that only 30% were "very knowledgeable" in SiD, consistent with findings from Hassanain et al. (2022), and both studies emphasise the need for earlier design-stage integration of safety principles. Regarding SDGs 12 and 13, designers often favour conservative approaches, such as geotechnical engineers addressing cavity risks. Karst formations are widespread across the Arabian Gulf, including the Jubaila Limestone in Saudi Arabia and the Simsima Limestone in Qatar (Mansour et al. 2024; Nawaz et al. 2020). Cavities, fractured zones, and highly weathered rock create geotechnical uncertainties that commonly drive engineers toward conservative, material-intensive solutions (Waltham 2005). This is compounded by the late availability of geotechnical data and tight project schedules, resulting in excess material consumption, elevated embodied carbon, higher costs, and increased construction safety risks. Carbon quantification is further complicated by reliance on Western benchmarks that may not reflect regional manufacturing conditions (Rasha et al. 2022).

This study aims to establish a systematic method for managing risks associated with achieving SDGs 3, 8, 12, and 13 in construction projects across the Middle East. Through a case study from the Arabian Peninsula, this paper illustrates how geotechnical engineers can apply a risk-informed decision framework to aid in foundation selection in karst terrains, thereby advancing the four SDGs.

2 Methodology

This study adopts a structured, risk-informed design methodology for foundation selection in karst terrain. In this framework, SDGs 3, 8, 12, and 13 are treated as derived outcomes of engineering decisions taken to manage project-specific geotechnical risks, rather than as fixed design targets. The methodology integrates hazard identification, risk assessment, option development, and risk control within Stages 1–3 of the RIBA Plan of Work 2020 (RIBA 2020), where design interventions have the greatest influence on safety, programme, material demand, and embodied carbon (Pantelidou et al. 2012). The four SDGs are operationalised through specific sub-targets relevant to construction practice: SDG 3 via sub-target 3.9 (reduction of deaths and illnesses from hazardous conditions); SDG 8 via sub-target 8.8 (protection of labour rights and promotion of safe working environments); SDG 12 via sub-target 12.2 (sustainable management and efficient use of natural resources); and SDG 13 via sub-target 13.2 (integration of climate change measures into policy and planning). This mapping is an adaptation for geotechnical design practice; the indicators used are proxies for these sub-targets rather than direct measures of UN reporting metrics (UNDESA 2015).Fig. 1 summarises the workflow.

2.1 RIBA Stage 1: hazard identification and objective definition

The process begins with the identification of karst-related hazards using available geological and geotechnical evidence, including historical records, geological mapping, borehole data, and geophysical survey outputs. Indicators such as core loss, drilling anomalies, and variable ground response are used to define the presence and spatial variability of potential cavities and fractured zones. In parallel, project objectives are established through Value Engineering (VE) function analysis (SAVE 2007 and Mahmoud and Deab 2021), which translates design drivers into explicit engineering criteria, including structural performance, constructability, and carbon management in accordance with PAS 2080.

2.2 RIBA Stage 2: risk assessment and option development

Identified hazards are translated into project risks through a structured assessment aligned with ISO (2018a), based on the evaluation of likelihood and consequence under geotechnical uncertainty. The output is a risk profile describing the likely effects of ground conditions on construction safety (SDG 3), programme reliability and procurement (SDG 8), material demand (SDG 12), and embodied carbon (SDG 13). This risk profile provides the basis for option development.

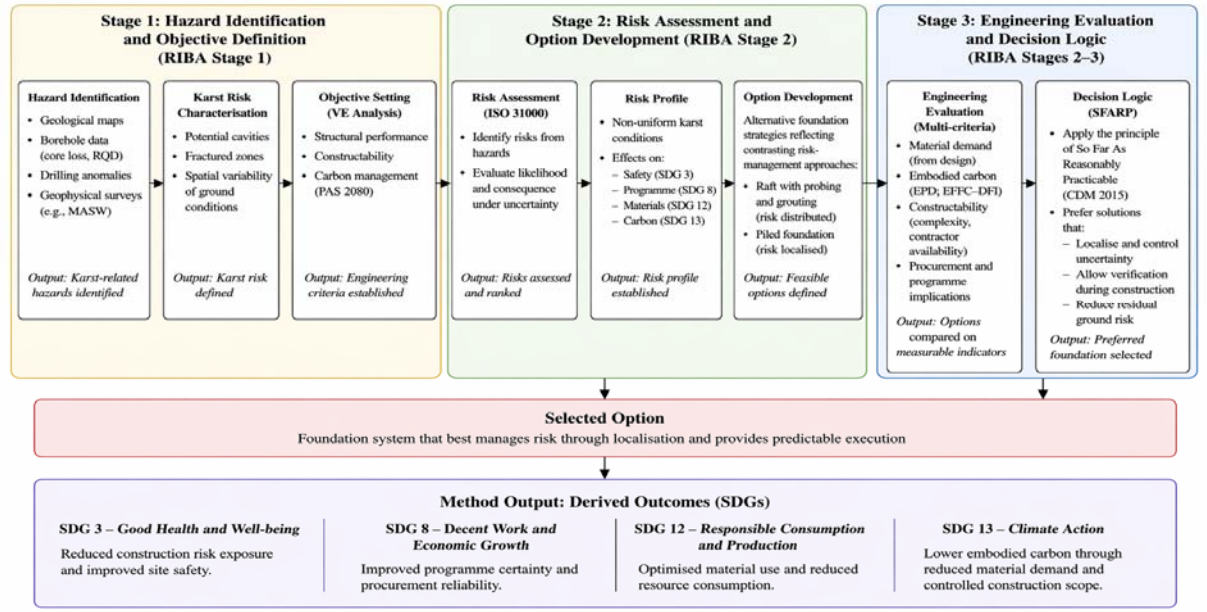


Fig. 1 Risk-informed geotechnical optioneering workflow across RIBA Stages 1–3.

2.3 RIBA Stages 2-3: engineering evaluation and decision logic

As part of the value engineering process, each option is evaluated through a multi-criteria engineering assessment comprising: (i) material demand estimated from the proposed design, (ii) embodied carbon assessed using the EFFC–DFI methodology (EFFC and DFI 2013), (iii) constructability, including execution complexity and contractor availability, and (iv) procurement and programme implications. This converts qualitative differences between options into measurable engineering indicators for direct comparison. Foundation selection is then undertaken using engineering judgement guided by the principle of reducing risks to a level that is So Far as Reasonably Practicable (SFARP), consistent with CDM 2015 (HSE 2015). Preference is given to solutions that control uncertainty through risk localisation, allow verification during construction, and reduce exposure to residual ground risk, rather than to options that depend on extensive area-wide treatment. The selected solution must perform at least as well as all alternatives across the four SDG-linked indicators. When full dominance is not achieved, the option that performs better on most criteria is preferred, and the rationale is documented in the risk register to ensure transparency and traceability.

2.4 Method output

The output of the methodology is a traceable evidence framework linking ground conditions, engineering decisions, and project outcomes. Improved safety, programme certainty, material efficiency, and lower embodied carbon are therefore interpreted as consequences of effective geotechnical risk management within the design process, rather than as independent sustainability checks.

3 Results and Discussion

This section validates the framework defined in Section 2 by demonstrating its step-by-step application to the foundation design of an iconic building in Radiyah, KSA, under an average net bearing pressure of approximately 500 kPa at foundation level. Each sub-section corresponds to a framework step and shows the inputs used, the decisions taken, and the SDG-relevant outcomes produced.

3.1 Preparation and Brief Stage

The building rests on the Jubaila Limestone Formation, which features thick layers of moderately strong aphanitic and calcarenitic limestone. Near the ground surface, this formation is usually highly weathered and fractured, but it becomes more intact a few meters below the surface (SGS, 1991). The initial geotechnical investigation (GI), part of a larger district development project, involved nine boreholes within the building site and probing records beneath proposed isolated footings. The data review showed Unconfined Compressive Strength (UCS) values ranging from 5.25 MPa to 48.5 MPa, with an average around 20 MPa. Borehole core recovery data were classified in accordance with EN ISO 14689 (ISO 2018b). Using this classification and recovery data, Jubaila Limestone (JL) can be divided into three sub-layers: Highly Weathered Jubaila Limestone (HWJL), Moderately Weathered

Jubaila Limestone (MWJL), and Slightly Weathered/Fresh Jubaila Limestone (FJL). Overall, the rock formation is primarily classified as FJL, with some areas of MWJL and HWJL. Twenty-eight probing points indicated the presence of cavity potential, mostly concentrated on the western side of the plot. The boreholes suggest a low risk of cavities, but the probing data raise concerns about possible karst features. This uncertainty is a key geotechnical risk that affects construction safety (SDG 3), project schedule (SDG 8), and material efficiency (SDG 12).

The project aims to consider constructability, local contractor availability, and sustainability as key project objectives. The Client did not set specific carbon targets, which aligns with PAS 2080:2023 (BSI 2023) guidelines. In such cases, the Designer should collaborate with the asset owner or manager to establish these targets. Since this project supports KSA's Vision 2030 for environmental sustainability, the team agreed to prioritise designs that reduce the carbon footprint, aiming to cut it by half as per UNFCCC (2023). Function analysis was conducted using the value engineering methodology, which confirmed that the foundation's primary function is to safely support the superstructure loads. The design objectives and all functions were identified. Because the project falls under Category 3 (GC3) per Eurocode 7 (BSI 2013) due to its complex ground conditions, an extensive Geotechnical Investigation program was planned. This included drilling 37 rotary-cored boreholes to depths of up to 40 meters in accordance with the Saudi Building Code (SBCNC 2018). It also involved performing a MASW geophysical survey over the entire site, spanning 7.2 kilometres on a 5 m by 5 m grid.

3.2 Concept Design and Spatial Coordination Stages

Phase 2 GI findings included multiple drill-bit drops, core loss between 0.5 m and 1.55 m, and drilling-fluid losses in more than half of the boreholes. MASW profiles indicated shear-wave velocities of 500 m/s to 3,500 m/s, suggesting fractured or vuggy horizons but no extensive open cavities. Two technically viable foundation solutions were developed: a raft foundation incorporating probing and grouting, and a piled foundation with pile caps. Each proposed design solution should be evaluated to confirm that risks are managed to the extent of So Far as Reasonably Practicable (SFARP) in accordance with the CDM 2015 regulations (HSE 2015). The raft option involves uncertainty in scope, programme, and cost due to the varying sizes of subsurface cavities. Risk is spread across the entire raft area and necessitates expert grouting contractors, rigorous quality checks, and extra verification boreholes. Conversely, piling provides greater predictability of scope and performance, with risks confined to specific pile locations assessed during drilling. The karst risk assessment indicates that the proposed foundation systems do not sufficiently mitigate this risk during the design phase, given the residual risk associated with karstic formation. Therefore, this residual risk was transferred to the construction stage. A qualified contractor should be appointed to oversee risk management during construction. From a procurement perspective, raft foundations require specialist, qualified subcontractors that may not be readily available in KSA. Piling is a common technique in the country, facilitating easier procurement and execution. This analysis indicates that piling offers better risk management than raft foundations. For such projects, an Early Contractor Involvement (ECI) procurement strategy, introduced in KSA law (MOF 2019), was recommended to enhance risk management.

The piling method involves installing bored piles beneath pile caps. The estimated concrete volume for this method is about 26% of the volume required for a raft, excluding grouting quantities. Designers can use tools such as the EFF CDFI carbon calculator or an equivalent to estimate the carbon emissions of each design. The Author has received funding from WSP to develop the first carbon calculator for geotechnical applications in the Middle East. The collected environmental product declaration (EPD) reveals a notable difference in emissions compared to the EFFC–DFI data. For example, the steel emissions factor from EFFC–DFI is 1597.7 kg CO2e per unit, whereas local EPDs range from 1120 to 2413 kg CO2e per unit. This variability is likely due to differences in the manufacturing technology of steel reinforcement. Mahmoud et al. (2021) showed that cement and steel are the main contributors to total embodied carbon emissions, so contributions from water and aggregate were considered negligible. The piling option uses 592 tonnes of cement and 313 tonnes of steel, resulting in 1,176 tonnes of embodied carbon emissions. In contrast, the raft foundation requires 950 tonnes of cement and 1,311 tonnes of steel, resulting in a total of 3,609 tonnes of emissions. This indicates that the piling method reduces embodied carbon emissions by roughly 67% compared to the raft foundation, excluding any grout quantities associated with the raft foundation. Grouting quantities were excluded because no defined treatment scope was available at the design stage as a direct consequence of residual karst uncertainty.

Raft foundations can have widely varying costs because of subsurface cavity networks, making it difficult to accurately forecast budgets. In contrast, pile foundations offer more predictable costs, as they are based on a specific design and can be verified during pile installation and load testing. From an economic perspective, piling is more cost-effective, with an estimated cost of 6 million Saudi Riyals (SAR) compared to nearly 10 million SAR for raft foundations, excluding grouting. No dedicated Phase 2 GI programme was commissioned for this project; the detailed design was therefore completed using only Phase 1 data. Residual risk was managed through conservative pile specification and communicated to the contractor via the CDM 2015 health and safety file. The carbon estimates should therefore be interpreted as indicative comparative values subject to this uncertainty.

3.3 Discussion

The options were assessed through a risk-informed optioneering process that considers construction safety exposure (SDG 3), constructability, procurement and project schedule reliability (SDG 8), material usage (SDG 12), and indicative embodied carbon (SDG 13). In comparing raft foundations (with probing and grouting) to piling, the latter demonstrates superior performance in health, safety, and environmental impact, as demonstrated in the preceding analysis. Raft construction involves a two-stage process, probing and grouting, followed by raft placement. There is uncertainty regarding timelines due to variable ground conditions. Piling also consists of two stages, pile installation and pile cap casting, but offers greater project schedule predictability. Quality control for raft foundations depends on grouting records and additional borehole investigations, whereas piling benefits from standardised testing methods. This comparison indicates that the piling method more effectively meets the design objectives and consistently outperforms the raft foundation alternative across all functional criteria. This assessment aligns well with the recommendations of Wagener and Von (1984), who recommended using piles for high loads in karst and rafts for light- to medium-load conditions. Table 1 presents a risk-informed comparison of foundation options and the associated evidence supporting SDGs 3, 8, 12, and 13.

Table 1. Risk-informed comparison of foundation options and associated evidence supporting SDGs 3, 8, 12, and 13.

SDG #	Risk Indicator	Piling	Raft after Probing and Grouting
3	Health and safety during construction	Risk exposure largely confined to pile locations. Lower material quantities indicate reduced worker exposure to activities such as material handling, dust exposure, and plant operations.	Risk exposure distributed across the full foundation footprint. Higher material quantities indicate increased worker exposure related to probing, grouting, and associated construction activities.
8	Project schedule reliability and specialist procurement	Lower programme and delivery risk supported by a well-established piling practice in KSA. Indicative cost is around six million SAR.	Potential project prolongation and programme risk due to reliance on specialist grouting subcontractors and uncertainty in treatment extent. Indicative cost is about ten million SAR (excluding grouting).
12	Material inefficiency	Reduced material demand: 592 t cement and 313 t steel.	Increased material demand: 950 t cement, 1,311 t steel, with additional grouting materials.
13	Embodied carbon	Indicative embodied carbon is around 1,176 t CO_2e (design stage comparative estimate).	Indicative embodied carbon is around 3,609 t CO_2e (design stage comparative estimate).

4 Summary and Conclusions

This study explores how risk-informed foundation optioneering in karst terrain can provide evidence during the design phase to support Sustainable Development Goals (SDGs) 3, 8, 12, and 13. By conducting comprehensive geotechnical risk management, the study compares two foundation alternatives for a high-load building in Saudi Arabia. Analysis results show that early design choices strongly influence construction safety, project schedule reliability, material usage efficiency, and embodied carbon. The case study reveals that a piled foundation localises geotechnical uncertainty, enhances constructability and procurement certainty, reduces material use, and significantly lowers embodied carbon compared to a raft foundation with probing and grouting. Overall, these findings suggest that treating SDGs as outcomes of geotechnical risk management, rather than as fixed design

targets, offers a practical and reproducible approach to sustainability reporting in ground engineering. Future research should apply this method across different geological contexts and foundation types and include region-specific environmental product declarations to reduce uncertainties in carbon data. In addition, it can investigate how construction-stage monitoring and digital tools can further align risk management with sustainable development objectives.

References

BSI (2013) BS EN 1997-1:2004+A1:2013 Eurocode 7 – Geotechnical design –General rules. London: British Standards Institution.

BSI (2023) PAS 2080: Carbon management in buildings and infrastructure. London: British Standards Institution.

EFFC and DFI (2013) Methodological and User Guide on EFFC DFI Carbon Calculator. Available at:https://www.effc.org/content/uploads/2020/10/EFFC-DFI-methodological-and-user-guide-v2.2.pdf, last accessed 30/05/2026.

Hassanain Mohammad A, Al-Harogi Mohammed, Sanni-Anibire Muizz O (2022)Design for safety in the construction industry: a study of architectureand engineering firms in KSA. Facilities, 40(13/14), pp. 895–911.

HSE (2015) Managing health and safety in construction: Construction (Design and Management) Regulations 2015. London: Health and SafetyExecutive. Available at: www.hse.gov.uk/pubns/books/l153.htm, last accessed 30/05/2026.

ISO (2018a) ISO 31000:2018 Risk management — Guidelines. Geneva: ISO.

ISO (2018b) ISO 14689:2018 Geotechnical investigation and testing — Identification, description and classification of rock. Geneva: ISO.

Mahmoud MH, and Deab MA (2021) How to reduce carbon dioxide emissions oninfrastructure projects in the Middle East. Proceedings of theInstitution of Civil Engineers – Civil Engineering. doi: https://doi.org/10.1680/jcien.20.00051.

Mansour HA, Al-Aidaros A and Zaidi FK (2024) Geological and HydrochemicalProcesses Driving Karst Development in Southeastern Riyadh, Central SaudiArabia. Water. doi: https://doi.org/10.3390/w16141937.

MoF (2019) Saudi Tenders and Procurement Law. Riyadh: Ministry of Finance, Kingdom of Saudi Arabia.

Nawaz B, Spyropoulos E and Al-Saafin A (2020) Risk Assessment for KarstHazards at a Facility in Saudi Arabia—A Case Study. Journal of Geoscienceand Environment Protection, 8, pp. 277–312. doi: https://doi.org/10.4236/gep.2020.85018.

Pantelidou H, Nicholson D, Gaba G et al. (2012) Sustainable geotechnics. In ICE Manual of Geotechnical Engineering. ICE Publishing, London, UK,vol. 1, pp. 125–136.

Rasha SM, Taher SA and Shalaby SM (2022) Climate change adaptation and mitigation in the Middle East: A review of challenges and opportunities. Renewable and Sustainable Energy Reviews 160: 112129.

RIBA (2020) RIBA Plan of Work. Available at:https://www.architecture.com/knowledge-and-resources/resources-landing-page/riba-plan-of-work, last accessed 2026/05/30.

SAVE International (2007) Value Standard and Body of Knowledge (VSBOK). Mount Royal, NJ: SAVE International.

Saudi Vision (2023) Saudi Vision 2030 and the Circular Carbon Economy. Saudi Vision 2030, Riyadh, Saudi Arabia. See https://www.vision2030.gov.sa/en/progress/environment-nature/ (accessed 30/05/2026).

SBCNC (Saudi Building Code National Committee) (2018) Saudi Building Code– Structural: Soil and Foundations (SBC 303). Riyadh, Kingdom of Saudi Arabia.

SGS (1991) Geologic Map of the Ar Riyad Quadrangle, Sheet 24, Kingdom of KSA, 1:250,000. Jeddah: Saudi Geological Survey.

UNDESA (United Nations Department of Economic and Social Affairs) (2015) The 17 Goals. UNDESA, New York, NY, USA. See https://sdgs.un.org/goals, last accessed 30/05/2026.

UNFCCC (2023) UN Climate Change Annual Report 2022. Available at: https://unfccc.int/sites/default/files/resource/UNClimateChange_AnnualReport_2022.pdf, last accessed 30/05/2026.

Waltham TB (2005) Sinkholes and Subsidence: Karst and Cavernous Rocks inEngineering and Construction. Berlin: Springer.

Wagener F. and Von M. (1984) Foundation design in karst areas. In: Proceedings of the First Multidisciplinary Conference on Sinkholes: TheirGeology, Engineering and Environmental Impact, Orlando, Florida, 15–17October 1984. Rotterdam: A.A. Balkema.

Disaster Risk Assessment for the City of Pirot: Potential Hazards of Rockfalls, Landslides and Erosion

N. Romić, E. Zlatanović, Z. Bonić, N. Marinković, B. Stanković
University of Niš, Faculty of Civil Engineering and Architecture, Niš, Serbia
nikola.romic@gaf.ni.ac.rs
0000-0002-1075-2738, 0000-0001-6783-1325, 0000-0002-7452-6756, 0000-0001-5834-7910

Abstract

Disaster risk assessment represents a key component of spatial development planning and population protection, particularly in areas prone to intense geodynamic processes. The city of Pirot (southeast part of the Republic of Serbia), characterized by complex geological and geomorphological conditions, is exposed to rockfalls, landslides, and various forms of erosion. The aim of this paper is to conduct a comprehensive assessment of natural hazards related to terrain instability and to identify the most vulnerable zones within the urban and suburban areas. Through the analysis of field investigations, available geological maps, climate data, and historical records, the study defines the main factors influencing mass movement initiation and erosion intensity. The analysis carried out includes two case studies with different amounts of precipitation, given that the aforementioned processes result from increased terrain saturation. The results indicate that several locations in and around Pirot are exposed to elevated risk, especially areas with steep slopes, poorly consolidated soil masses, and pronounced anthropogenic impact. Based on the identified hazards, the paper proposes measures for prevention and mitigation, including terrain monitoring, technical stabilization of critical points, and planned land management.

Keywords

Risk assessment, Rockfalls, Landslides, Erosion, Slope stability, Hazard management, Natural disasters.

1 Introduction

Risk assessment of natural disasters is one of the key instruments of modern spatial management, especially in areas characterized by pronounced geodynamic processes and complex engineering-geological conditions. The intensification of climate change, the increasing frequency of extreme precipitation, and growing anthropogenic pressure on natural systems contribute to an increase in the frequency and scale of phenomena such as landslides, rockfalls, and various forms of erosion. In this context, the systematic identification and analysis of terrain instability factors forms the basis for reducing the vulnerability of the population and infrastructure.

According to the United Nations Report published on the occasion of the International Day for Disaster Risk Reduction(UNDRR & CRED, 2020), 7,348 disasters occurred globally between 2000 and 2020, claiming 1.23 million lives. In the preceding period from 1980 to 2000, almost half as many disasters (4,212) occurred in the same observed area. Consistent with this global trend, a significant increase in natural disasters has been recorded in Serbia over the last 20 years.

The Law on Disaster Risk Reduction and Emergency Management (Sl. glasnik RS 87/2018) recognizes three core documents that local self-government units, as the fundamental elements of the protection and rescue system, are obligated to adopt. The Disaster Risk Assessment and the Protection and Rescue Plan were recognized as such by the Law on Emergency Situations. The territory of the city of Pirot (southeast part of the Republic of Serbia) is characterized by a complex geological structure, diverse lithological composition, and marked relief contrasts, making it highly susceptible to gravitational mass movements. Steep slopes, the presence of poorly consolidated sediments, tectonic fragmentation, and a variable hydrological regime create predispositions for terrain destabilization, particularly under conditions of elevated moisture. Additionally, anthropogenic influences, such as unplanned urbanization, slope cutting, and alterations to the surface runoff regime, act as triggers for instability.

The risk of natural disasters in this context does not arise exclusively from the presence of unfavorable natural conditions, but from their interaction with spatial development and infrastructure systems. Therefore, it is necessary to apply an integrated approach that includes the analysis of geological, geomorphological, climatic, and anthropogenic factors, as well as their interrelationships. It is particularly critical to consider the influence of precipitation as the dominant triggering factor for landslide and erosion processes, since increased water infiltration reduces the effective stress and shear strength of the soil and rock mass.

The aim of this paper is to assess the risk of natural disasters caused by terrain instability in the territory of the city of Pirot, with special emphasis on identifying the most vulnerable zones in the urban and suburban areas. The research is based on the analysis of field data, available geological documentation, climatic parameters, and historical records of landslides and rockfalls, accompanied by a comparative analysis of periods with different precipitation regimes.

2 Research Methodology and Data

The research methodology is based on an integrated approach to the assessment of disaster risks caused by terrain instability, which includes the analysis of natural and anthropogenic factors, spatial data processing, and the comparative evaluation of climatic conditions. The applied methodology was designed to enable the identification of predispositions for mass movements, assessment of the hazard level, and spatial differentiation of risk zones in the Pirot area.

2.1 Data collection and Analysis

The research was conducted utilizing a combination of primary and secondary data sources. Primary data encompasses field observations and the mapping of instability phenomena, including active and potential landslides, rockfalls, and pronounced erosional processes. During fieldwork, morphological indicators of instability (tension cracks, uneven terrain, slope angles, traces of surface wash) were analyzed alongside the influence of anthropogenic interventions.

The fundamental methodology applied in this study relies on a qualitative heuristic approach based on comprehensive field mapping. This was systematically integrated with the spatial analysis of critical

predisposing factors—specifically terrain slope, lithological composition, and historical precipitation thresholds—to evaluate slope stability conditions.

Secondary data includes relevant geological and engineering-geological maps of the study area, geomorphological data regarding slope inclinations and aspects, climatic data regarding precipitation volume and intensity, and historical records of registered landslides and rockfalls. Climatic data were used to analyze seasonal and extreme precipitation values, focusing on prolonged periods of heavy rainfall capable of initiating destabilization processes.

2.2 Analysis of Instability Factors

The identification of risk factors was conducted through qualitative and quantitative analysis of parameters including lithological composition, degree of terrain consolidation, slope morphology, hydrogeological conditions, water infiltration, climate regimes (specifically rainfall intensity), and anthropogenic influences.

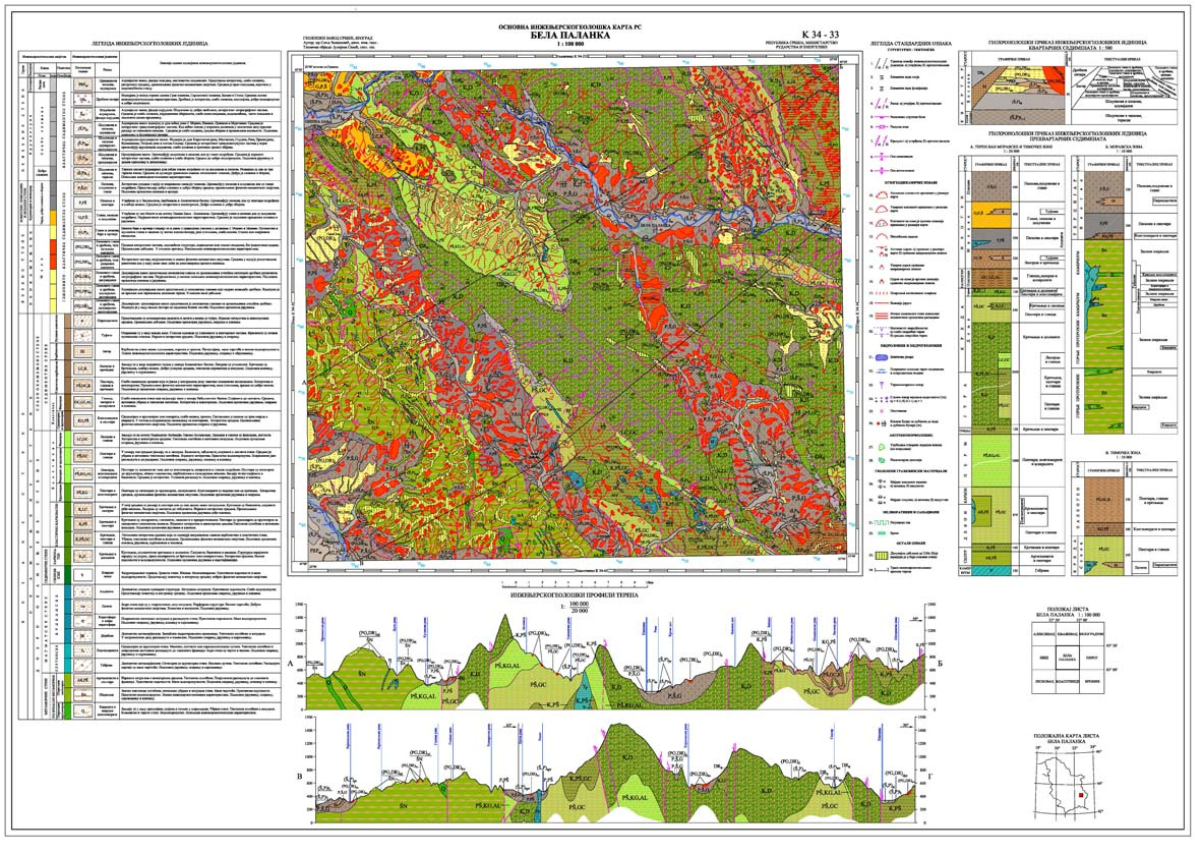


Fig. 1 Basic engineering-geological map of the territory of Bela Palanka (Pirot district) (Đokanović S. 2023).

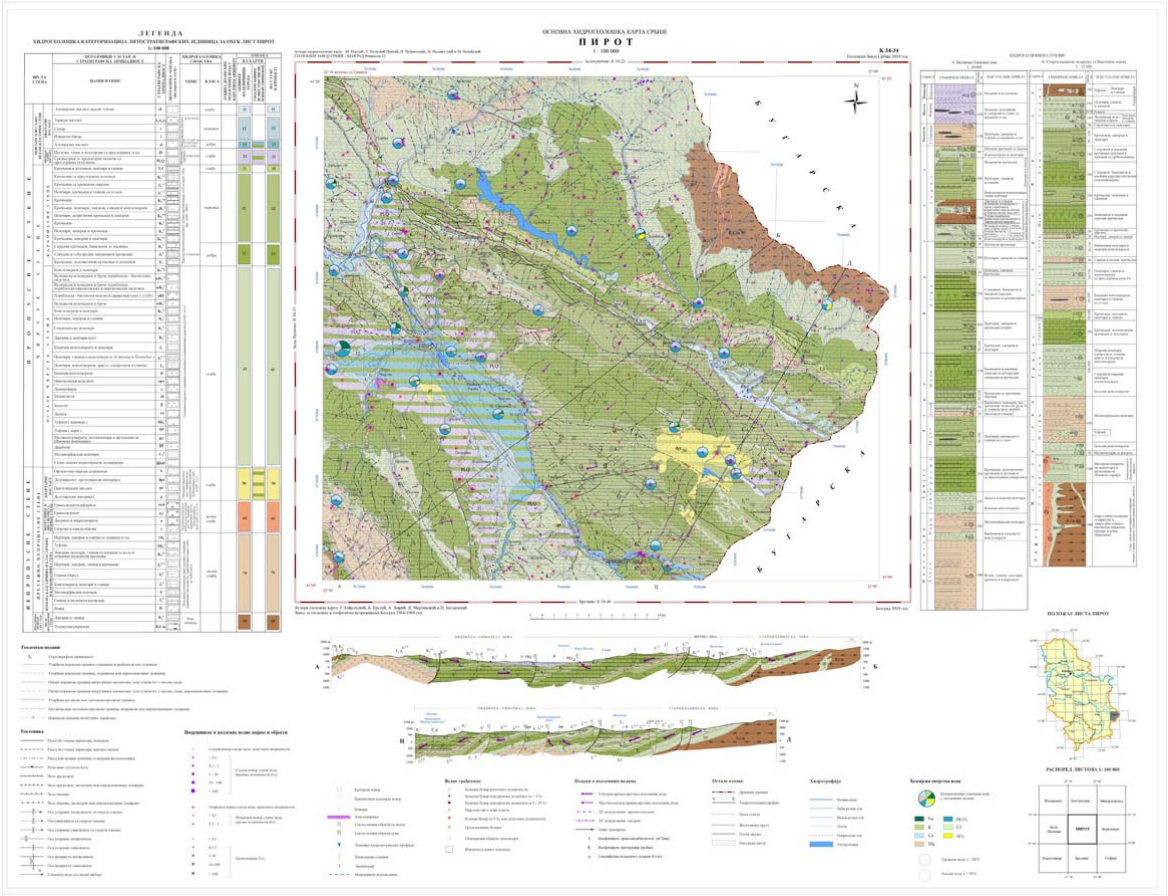


Fig. 2 Basic hydrogeological map of the territory of Pirot.

Special attention was directed toward the interaction between precipitation and the geological substratum (see Fig. 1 and Fig. 2), given that increased water saturation reduces the shear strength of the material and elevates pore water pressures, thereby satisfying the conditions for mass movement.

2.3 Case Studies and Comparative Analysis

To assess the influence of climatic factors, a comparative analysis of two case studies featuring different rainfall regimes was conducted. The first study encompasses a period with average precipitation, while the second examines a period characterized by high-intensity and high-accumulation precipitation. The correlation between precipitation volume and the activation of landslide and erosion processes was evaluated through a comparative analysis of instability occurrences registered in both periods.

Based on the integration of all collected data, a risk assessment was performed using the territory zoning method according to hazard levels. The assessment combines the terrain's inherent predisposition to instability with the intensity of potential destabilizing factors.

Three risk categories were defined: low risk (stable zones lacking pronounced instability indicators), moderate risk (zones with predispositions for mass movements), and high risk (zones with active phenomena or severe destabilizing factors).

The assessment results are presented through thematic spatial interpretation, enabling the identification of priority locations for monitoring and preventive interventions. This applied methodology facilitates a comprehensive analysis of the spatial distribution of risk, providing a reliable foundation for future protection planning and sustainable spatial management.

3 Results and Analysis of Risk Factors

The occurrence of landslides and erosion presents a high probability of damaging water, sewage, and electrical networks, leading to the disruption of infrastructure and temporary loss of essential energy

supplies. Landslides and rockfalls also jeopardize road networks and inflict severe damage on residential and commercial structures. Furthermore, these events carry compounding secondary risks, including floods and fires.

To predict potential outcomes, two adverse impact scenarios were analyzed according to ISO 31000:2018 (2018).

Case 1: In this highly probable adverse scenario, long-term and heavy rainfall (over 30 liters/m²) triggers landslides at three specific locations: the Gnjilan settlement, the Radin Do settlement, and the village of Bazovik. Under this scenario, landslide sliding surfaces range from 30 to 200 m². In Gnjilan, the potential landslide measures 10 x 14 m; in Radin Do, it measures 10 x 5 m; while the projected sliding area in Bazovik is approximately 200 m², featuring a main scarp up to 2 meters deep.

In Radin Do, the proximity of the sliding surface to the transport infrastructure immediately threatens the roadway, resulting in partial, and subsequently complete, traffic suspension. In Gnjilan, the landslide envelops and threatens a residential building, causing structural wall deformations. Consequently, a four-member family would require evacuation to facilitate structural rehabilitation. This landslide also threatens the electrical power grid, causing supply interruptions in parts of the settlement. In Bazovik, the failure surface threatens approximately 15 meters of an adjacent macadam road, obstructing access to agricultural zones. Normal operations are disrupted for up to 10 days, while geotechnical rehabilitation of the active landslides requires 5 to 8 days. The consequences recorded during this simulation impact human life, the economy and ecology (rehabilitation costs), and critical infrastructure (power and transport networks). No damage to institutions or buildings of critical social importance was recorded.

Based on these reference incidents, a frequency approach was utilized. The frequency of negative effects for the most likely adverse event in Pirot is 1 event every 1 to 2 years. However, based on the scenario analysis and risk assessment, the severity level of these landslides, rockfalls, and erosion is classified as *low*, indicating that the overall risk is *acceptable*.

Table 1. The Probability Table.

Probability or frequency				
Category	Qualitatively	Probability	Frequency	Selected
1	Negligible	<1%	1 event in 100 years or less	
2	Small	1-5%	1 event in 20 to 100 years	
3	Medium	6-50%	1 event in 2 to 20 years	
4	Great	51-98%	1 event in 1 to 2 years	X
5	Extremely large	>98%	1 event per year or more often	

Table 2. Table for showing consequences for social stability (total material damage).

Consequences for social stability (material damage)			
Category	The magnitude of the consequences	Criterion	Selected
1	Minimum	< 1% of budget	X
2	Small	1% - 3% of budget	
3	Moderate	3% - 5% of budget	
4	Serious	5% - 10% of the budget	
5	Catastrophic	>10% of budget	

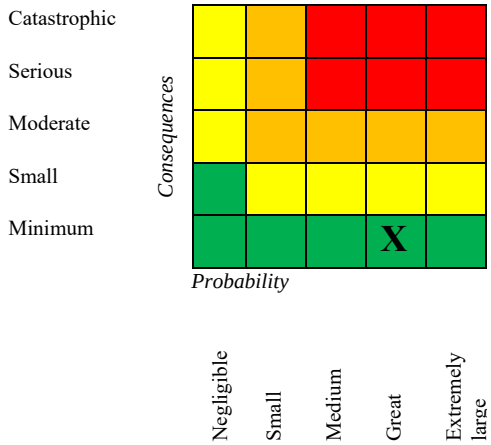
Table 3. Table for showing the consequences for the economy and ecology.

Consequences for economy and ecology			
Category	The magnitude of the consequences	Criterion	Selected
1	Minimum	the amount of which exceeds 1% of the budget	X
2	Small	the amount of which exceeds 3% of the budget	
3	Moderate	the amount of which exceeds 5% of the budget	
4	Serious	whose amount exceeds 10% of the budget	
5	Catastrophic	whose amount exceeds 15% of the budget	

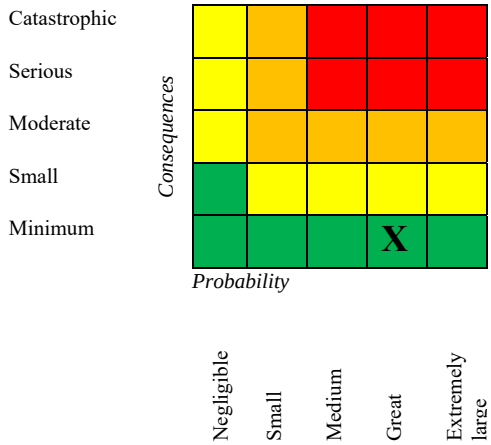
Table 4. Table for showing consequences for life and health.

Consequences for human life and health			
Category	The magnitude of the consequences	Criterion	Selected
1	Minimum	<50	X
2	Small	50-200	
3	Moderate	201-500	
4	Serious	501-1500	
5	Catastrophic	>1500	

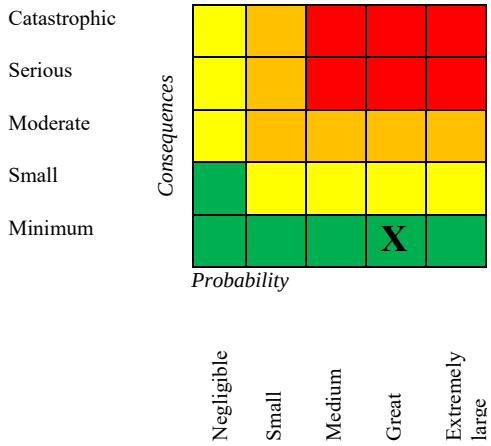
Matrix 1. Risk to human life and health



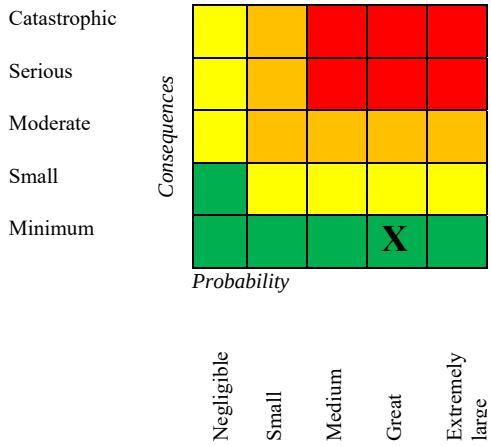
Matrix 2. Risk to the economy/ecology



Matrix 3. Risk to social stability (material damage to infrastructure)



Matrix 4. Total risk



Case 2: The primary triggering mechanism is intense, multi-day rainfall exceeding 70 liters/m². Landslides and rockfalls occur in areas with pronounced slopes, as well as zones subjected to recent rural road rehabilitation. Mass movements activate across multiple locations in Pirot: Trpezica-Mrtvački most, Bazovik village, the stretch between Temska and Rudinje, the road to Sopot, the villages of Crvenčevo, Cerova, Veliki Suvodol, Temska, and the settlements of Radin Do and Gnjilan.

During this activation period, severe threats are posed to residential and auxiliary buildings, transport corridors, electrical grids, telecommunications infrastructure, water supplies, and agricultural land. The estimated number of endangered structures exceeds 15. A 110-meter road failure cuts off the villages of Topli Do and Zaskovci (see Fig. 3), entirely severing their connection to the city. The isolated population in these villages approaches 100 individuals; populations in Crvenčevo, Cerova, and Radin Do are additionally at risk. The total number of people affected by this scenario exceeds 500. Serious damage is recorded across the economic and ecological sectors (population evacuation, project documentation preparation, geotechnical testing, massive rehabilitation works, road clearing) and critical infrastructure.



Fig. 3 Location of villages in Pirot district (Ljubenov G, Roter-Blagojević Mirjana, 2016).

For this maximum-severity unwanted event, the occurrence frequency is estimated at 1 event every 2 to 20 years. Based on the scenario analysis, the risk level is determined to be *very high*, categorizing the risk as *unacceptable*.

An unacceptable level of risk requires risk treatment. In order to reduce the level of risk of negative consequences of the identified potential danger, measures are taken in the field of prevention and response.

Table 5. The Probability Table.

Probability or frequency				
Category	Qualitatively	Probability	Frequency	Selected
1	Negligible	<1%	1 event in 100 years or less	
2	Small	1-5%	1 event in 20 to 100 years	
3	Medium	6-50%	1 event in 2 to 20 years	X
4	Great	51-98%	1 event in 1 to 2 years	
5	Extremely large	>98%	1 event per year or more often	

Table 6.Table for showing consequences for social stability (total material damage).

Consequences for social stability (material damage)			
Category	The magnitude of the consequences	Criterion	Selected
1	Minimum	<1% of budget	
2	Small	1% - 3% of budget	
3	Moderate	3% - 5% of budget	
4	Serious	5% - 10% of the budget	X
5	Catastrophic	>10% of budget	

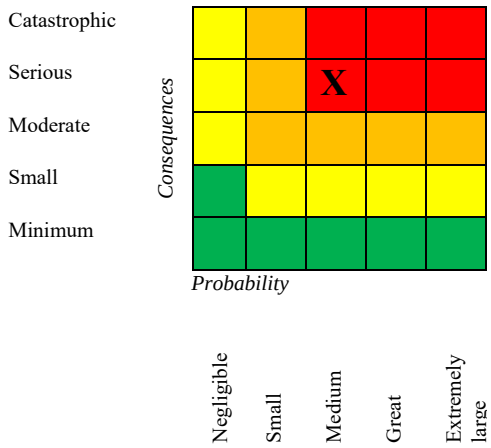
Table 7. Table for showing the consequences for the economy and ecology.

Consequences for economy and ecology			
Category	The magnitude of the consequences	Criterion	Selected
1	Minimum	the amount of which exceeds 1% of the budget	
2	Small	the amount of which exceeds 3% of the budget	
3	Moderate	the amount of which exceeds 5% of the budget	
4	Serious	whose amount exceeds 10% of the budget	
5	Catastrophic	whose amount exceeds 15% of the budget	X

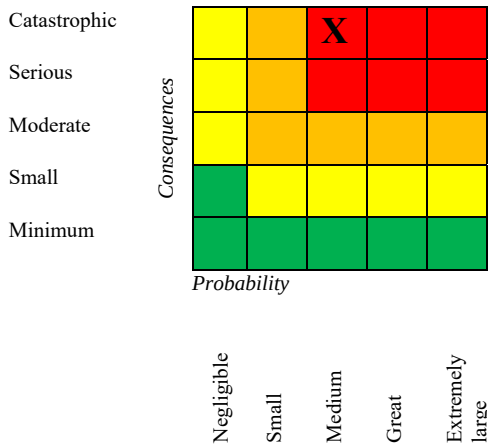
Table 8. Table for showing consequences for life and health.

Consequences for human life and health			
Category	The magnitude of the consequences	Criterion	Selected
1	Minimum	<50	
2	Small	50-200	
3	Moderate	201-500	
4	Serious	501-1500	
5	Catastrophic	>1500	X

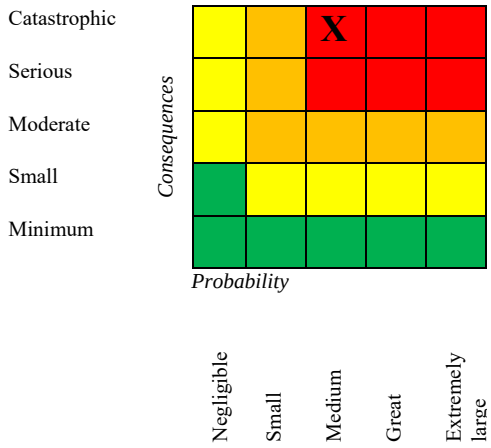
Matrix 1. Risk to human life and health



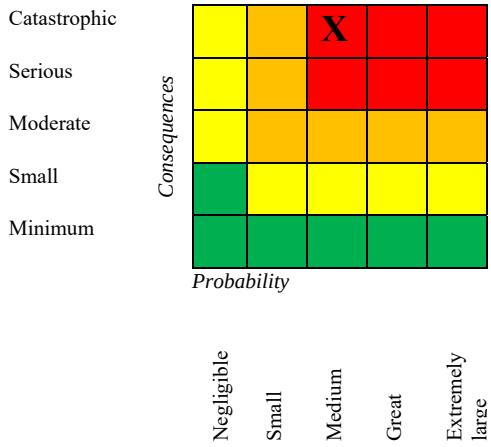
Matrix 2. Risk to the economy/ecology



Matrix 3. Risk to social stability (material damage to infrastructure)



Matrix 4. Total risk



Within the strategic, normative, and planning frameworks for the city of Pirot, a strict prohibition on building construction in areas susceptible to mass wasting and erosion is mandated. Spatial use restrictions have been introduced, including a ban on deforestation on steep terrain. The city administration oversees these activities, while competent inspection services control implementation. Establishing an early warning system and ground monitoring protocol is paramount. This entails the competent services forming a continuous monitoring and recording system for landslides, rockfalls, and erosion. The City Emergency Management Headquarters is responsible for this implementation, with an estimated operational timeline of one year following the Vulnerability Assessment. Regular field reporting will result from these activities.

Furthermore, improved institutional cooperation is planned—primarily with the Seismological Survey of Serbia and the Republic Hydrometeorological Service of Serbia—to ensure the timely gathering of hazard warnings. Regarding spatial planning and building legalization, technical protection measures will be implemented. These include constructing retaining walls, driving piles along endangered roadways, building drainage systems, and regulating stormwater channels. These activities are

executed by the city administration in cooperation with urban planning, housing, communal services, and construction inspection departments. Implementing these measures creates the foundation for highly effective geodynamic risk management, securing the population, infrastructure, and the environment.

4 Conclusion

Based on the conducted analyses, it is concluded that the territory of Pirot faces significant risk from various geodynamic processes, primarily landslides, rockfalls, and erosion triggered by heavy precipitation. The results of the case studies-derived from field visits, specific geotechnical testing, existing documentation, climate data, and historical records-confirm the existence of several critical hazard zones within Pirot's urban and suburban limits. Areas characterized by steep slopes, poorly consolidated terrain, and severe anthropogenic modification are critically endangered. The comparative scenario analysis confirms that elevated soil moisture remains the primary catalyst for mass movement activation. The data strictly emphasizes the necessity for continuous terrain monitoring and the early identification of high-risk locations.

To mitigate risk and protect human life and infrastructure, rigorous preventive and remedial engineering measures are mandatory. These must encompass the systematic monitoring of unstable slopes, structural stabilization of critical failure points, meticulously planned spatial management, and strict control over construction activities. By integrating these measures directly into spatial planning legislation, it is possible to drastically improve territorial safety and mitigate the destructive consequences of natural hazards in the city of Pirot. Future mitigation and early warning strategies must encompass systematic visual site inspections integrated with advanced terrain monitoring technologies, such as terrestrial LiDAR scanning, microseismic sensors, and automated radar-based rockfall detection systems (Bonić, Z. Protić, M.2018).

Acknowledgement. This research was supported by the Ministry of Science, Technological Development and Innovation of the Republic of Serbia, under the Agreement on Financing the Scientific Research Work of Teaching Staff at the Faculty of Civil Engineering and Architecture, University of Niš - Registration number: 451-03-34/2026-03/200095 dated 05/02/2026. (*Sustainable Development Goals: 9. Industry, Innovation, and Infrastructure; 11. Sustainable Cities and Communities*).

References

UNDRR & CRED (2020) The Non-COVID Year in Disasters. Brussels: CRED; 2021. This document is available at: https://emdat.be/sites/default/files/adsr_2020.pdf (Issue 2020)

Ljubenov G, Roter-Blagojević Mirjana (2016) DISAPPEARANCE OF THE TRADITIONAL ARCHITECTURE – THE KEY STUDY OF STARA PLANINA VILLAGES. Serbian Architectural Journal, 8, 43-58, COBISS.SR-ID 227453452.

Đokanović S. (2023) Realizacija projekta Osnovne inženjerskogeološke karte Srbije 1:100 000. TEHNIKA – RUDARSTVO, GEOLOGIJA I METALURGIJA 74 (2023) (6): 673-678. DOI:10.5937/tehnika2306673D.

ISO 31000:2018 (2018) Risk management — Guidelines. The International Organization for Standardization.

Sl. glasnik RS (87/2018) Zakon o smanjenju rizika od katastrofa i upravljanju vanrednim situacijama

Bonić, Z., Protić, M. (2018) EARLY WARNING AND HAZARD ANALYSIS SYSTEM IN REPUBLIC OF SERBIA. 9th GRACM International Congress on Computational Mechanics, Chania, Greece, 181-188.

Rock properties, testing methods and site characterization (incl. planetary rock mechanics)

Numerical investigation of fluid flow in intersecting fractures based on photogrammetry

M. Torkan, S. L. Vidanage, L. Uotinen, M. Janiszewski & M. Rinne
Department of Civil Engineering, School of Engineering, Aalto University, Espoo, Finland
masoud.torkan@aalto.fi
0000-0002-2102-0946

Abstract

Fluid flow through fractured rock networks is controlled by several factors, including hydraulic pressure gradients, fracture density, roughness, aperture, connectivity, and intersections. Characterizing hydraulic behaviour at fracture intersections is essential for understanding flow in rough fractured rock masses, especially for nuclear waste disposal.

In this study, a block of Finnish Kuru granite (10 cm × 10 cm × 10 cm) was prepared with two perpendicular and intersecting fractures. Photogrammetry was applied to reconstruct three-dimensional (3D) point clouds of the sample. To scale 3D models obtained by photogrammetry, markers with predefined distances were used, and accuracy was assessed by using Root Mean Squared Error (RMSE).Subsequently, roughness and physical aperture of fractures were quantified. The 3D point clouds were converted into a mesh domain in MeshInspector and imported into COMSOL Multiphysics, where fluid flow was simulated by solving the Navier–Stokes equations. Simulations were conducted under hydraulic pressure gradients ranging from 10 to 180 kPa/m, in increments of 10 kPa/m. The influence of intersections on flow for two inlets and two outlets was investigated. The Forchheimer equation was used to analyze the numerical results.

The photogrammetric reconstruction accuracy yielded an RMSE of 15 µm. Physical apertures for the two inlets were 190 and 192 µm, while for Outlets 1 and 2, they were 177 and 192 µm, respectively. 3D Roughness values were similar, ranging from 8.7 to 9.3. Numerical results showed nonlinear flow behavior at the outlets. The Forchheimer fitting was used to calculate hydraulic apertures and nonlinear parameters. A higher flow rate with a larger physical aperture, demonstrating the role of geometry in flow distribution.

This research shows that fracture intersections influence fluid flow behavior, leading to discharge changes based on geometrical properties, such as physical aperture. These factors must be considered in fracture network flow analysis.

Keywords

Intersecting fracture, Roughness, Photogrammetry, Numerical modelling, Fluid flow.

1 Introduction

The study of rock masses is essential because they serve as the foundation for critical infrastructure projects, including dams, tunnels, slopes, and nuclear waste disposal sites. A rock mass consists of intact rock and discontinuities, the latter of which govern both structural stability and fluid flow behaviour. In low-porosity rocks like granite, discontinuities, specifically faults and fractures, act as the primary pathways for fluid flow. Consequently, studying and characterizing discontinuities is vital for assessing the hydraulic properties of the rock mass. Fluid flow through fractures is controlled by several factors: at the micro-scale, by geometrical properties such as roughness, physical aperture, and contact area; and at the macro-scale, by fracture distribution, intensity, persistence, and density (Wyllie 1999).

The assessment of hydraulic properties has been conducted at various scales, from single fractures (Torkan et al. 2026) and intersecting fractures (Wang et al. 2025) to fracture networks (Baghbanan and Jing 2007). In single fractures, flow is primarily controlled by roughness and physical aperture, both of which are influenced by normal and shear stress distributions. Conversely, flow through intersecting fractures is further influenced by the angle of intersection (Xiong et al. 2020) and the number of inlets and outlets (Liu et al. 2025). Fluid flow in these systems is typically described by the Cubic Law or by nonlinear behaviour. The transition from the Cubic Law to nonlinear flow is rooted in the hydraulic gradient and in detailed geometrical properties (roughness, aperture, and contact points) of single fractures, as well as in intersection angles and fracture connectivity in intersecting systems.

Characterization of these features is achieved through various high-resolution methods, such as 3D laser scanning and photogrammetry. These methods allow for a realistic simulation of rock mass geometry. Laser scanning is a widely used tool for measuring roughness, physical aperture, and displacements, as well as for extracting fracture networks and simulating fluid flow. Similarly, photogrammetry has emerged as a low-cost, highly accurate alternative for measuring these same parameters. High-detail 3D models obtained via photogrammetry provide a cost-effective basis for simulating fluid flow. Previous studies have employed software such as ANSYS code (Xiong et al. 2020) and COMSOL (Liu et al. 2025; Wang et al. 2025) to investigate flow behaviour under various conditions of intersecting fractures with varying angles and inlet/outlet configurations.

Despite these advancements, the measurement of the actual geometrical properties of intersecting fractures and the use of that data as initial input for fluid flow simulations remains an area requiring further clarity. This study aims to demonstrate the use of photogrammetry to measure the geometrical properties of two nearly perpendicular intersecting fractures for use in COMSOL to simulate fluid flow. The Forchheimer equation was employed to characterize the numerical results regarding flow rates at two outlets versus hydraulic pressure gradients.

2 Methodology

2.1 Sample preparation

To investigate fluid flow behaviour in intersecting fractures, a Finnish Kuru grey granite block was first split from the centre using the feather-and-plug technique. The resulting separated block was cut into a 10 cm × 10 cm × 10 cm cube. Subsequently, a normal loading instrument was used to propagate an orthogonal fracture nearly perpendicular to the initial split (Fig. 1 (a)). This process resulted in a sample composed of four blocks (B1 to B4) separated by two nearly perpendicular fractures (Fig. 1 (c to f)).

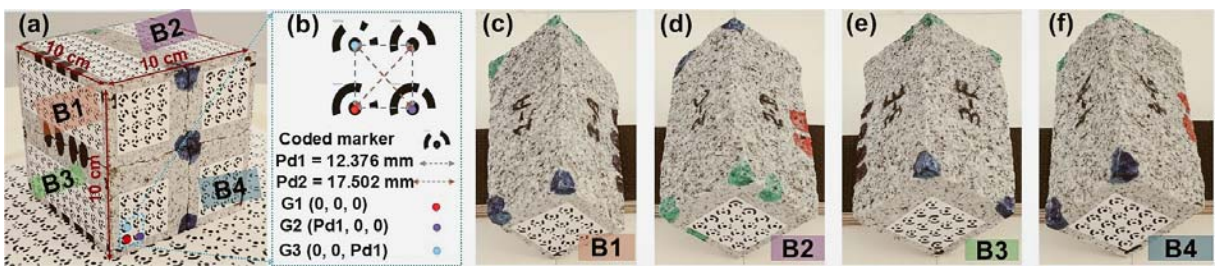


Fig. 1(a) The Kuru granite sample with dimensions of 10 cm × 10 cm × 10 cm, (b) markers with predefined distances and the defined local coordinate system; (c) Block B1; (d) Block B2; (e) Block B3; and (f) BlockB4.

2.2 Photogrammetry

2.2.1 Principle of photogrammetry

A Structure-from-Motion and Multi-View Stereo (SfM-MVS) photogrammetry approach was employed for 3D scanning. Photogrammetry is a technique that utilizes multiple overlapping photographs to reconstruct a 3D model by identifying and aligning matching points across images. This process generates a sparse 3D point cloud, which is then used to calculate depth maps to generate a high-resolution dense 3D point cloud. Specialized patterns, such as coded markers, are used to facilitate alignment and provide accurate scaling. By defining the distances and coordinates between these markers, the 3D model can be scaled and oriented within a specific coordinate system. In this research, RealityCapture software v1.5.1 was used for 3D modelling, utilizing self-calibration based on the Brown3 Tangential 2 distortion model. The final 3D models were exported as point clouds and analysed using CloudCompare software v2.14.

2.2.2 Sample preparation for photogrammetry

First, one-ring-20-bit-coded markers were generated via software, and the distances between them were measured digitally using AutoCAD. These markers were printed at 1200 dpi resolution and attached to the sample (Fig. 1 (a and b). Then the markers covering the fractures' outcrops were removed. The predefined horizontal and vertical distances between markers (Pd1) were 12.376 mm, while the diagonal distance (Pd2) was 17.502 mm.

2.2.3 Photography setup

The sample was placed at the centre of a rotary table (Fig. 2 (a)), with a sheet containing predefined alignment patterns (not used for scaling) placed beneath it. Illumination was maintained at a constant 4000 Lux. The rotary table was rotated in 9° increments over a full 360°, resulting in 40 photos per rotation. A Canon DSLR camera, equipped with a 35 mm lens, was mounted on a tripod at a fixed shooting distance of 50 cm. The camera specifications included a pixel size of 4.17 µm, a sensor size of 36 × 24 mm, and an image resolution of 8688 × 5792 pixels. The acquisition settings were an aperture of f/11 and a shutter speed of 1/8 s. This configuration yielded a Ground Sample Distance (GSD) of 59 µm, ensuring that each pixel represents 59 µm in the real world. The lens was manually focused on the fixed shooting distance, and the focus ring was secured with tape to prevent accidental shifts during photographing. The accuracy was further refined by the photogrammetry software, achieving sub-pixel precision ranging from one-fifth to one-twentieth of a pixel.

2.2.4 Photography workflow

To accurately measure the physical aperture of the intersecting fractures, the sample was photographed in a well-matched position (Fig. 2 (a)). To ensure sufficient image overlap and geometric coverage, photographs were taken at three different pitch angles: 0°, 30°, and 60°, using varying focus points. To increase the number of matching points across different images, an A4 sheet containing coded markers with predefined distances was placed beneath the sample. Each of the four blocks was then photographed separately using the two pitch angles, 30°and 60°, with two focus points per position to ensure depth of field and sharpness across the fracture surfaces (Fig. 2 (b)).Each block was subsequently flipped upside down, and the entire photography process was repeated (Fig. 2 (c)). For this stage, the marker sheet under the sample was not used.

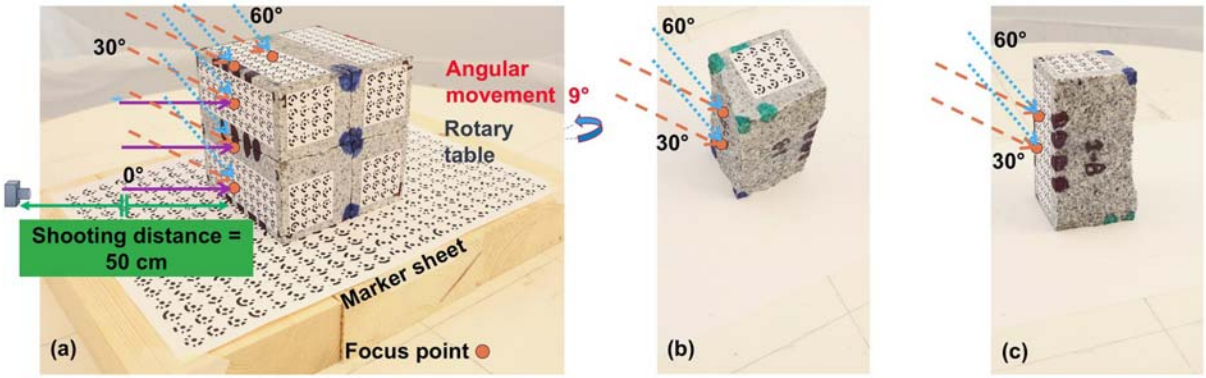


Fig. 2 Photography setup with a 50 cm fixed shooting distance and a rotary table with 9° angular movements. (a) The sample in the well-matched position showing the five different focus points photographed at pitch angles of 0°, 30°, and 60°. (b) and (c) illustrate the focus points on the blocks and the photography pitch angles before and after flipping the sample upside down. For example, (b) shows B1 photographed at 60°, and (c) shows B1 photographed upside down at 30°.

2.2.5 3D model reconstruction

The photograph set of the well-matched sample was imported into RealityCapture and grouped to ensure a consistent calibration across all images. After the software detected the markers, an initial alignment was performed. This well-matched 3D model served as a reference to establish the local coordinate system and to scale the model using the markets with the predefined distances (Fig. 1 (a)). To orient the model within a precise 3D space, the bottom corner of "Side One" was redefined from a tie point to a Ground Control Point (GCP) with coordinates G1 (0, 0, 0). Subsequently, the nearest horizontal and vertical markers were assigned GCP status with coordinates G2 (Pd1, 0, 0) and G3 (0, 0, Pd1), respectively. The 1133 predefined distances between these markers were used as scale bars (800) and check bars (333) to ensure dimensional accuracy. The model was then re-aligned to finalize the scaling and orientation within this desired coordinate system. Then, the coordinates of all detected markers on the sample were extracted. These coordinates acted as the references to put each block into the same coordinate system as the original well-matched sample. The same workflow was applied to each block. However, for these separate components, the 3D models were reconstructed with high detail and texturizing to measure physical aperture and roughness analysis.

2.2.6 Accuracy assessment

Root Mean Square Error (RMSE) (Eq. 1) was employed to assess the accuracy of the photogrammetry model. The obtained photogrammetric values for 800 scale bars and 333 check bars were compared with their real physical values after scaling.

$$RMSE = \sqrt{\sum_{i=1}^{n} \frac{(Predefined\ distance_i - digital\ distance_i)^2}{n}} \quad (1)$$

Here, i = the index of each predefined distance and n = the total number of predefined distances employed for scaling or checking.

2.3 Roughness and physical aperture

To measure roughness (R_{3D}), the two rough surfaces of each block were separated from the edge where the two rough surfaces reached each other. The 3D point cloud was rasterized at a resolution of 0.5 mm × 0.5 mm in the X and Y directions, converted to a mesh, and analyzed by the Surface Roughness Calculator (SRC) (Magsipoc et al. 2020). To measure physical apertures, the distances between two opposite surfaces were calculated in CloudCompare, and the averages of the distances were reported as physical apertures.

2.4 Numerical modelling and theoretical background

To simulate fluid flow through intersecting fractures with two inlets and two outlets, COMSOL Multiphysics v6.4 was employed to solve the Navier–Stokes equations. To create a domain for the simulation, the rough surfaces of the blocks were imported into MeshInspector software, converted into a 3D mesh domain, and subsequently imported into COMSOL. To analyze flow simulations, the surfaces were hypothetically segmented into four distinct pairs of opposing surfaces (Fig. 3 (a and b)). The boundary conditions are illustrated in Fig. 3 (b). The final model contained approximately 2 million elements, including boundary elements Fig. 3 (c).

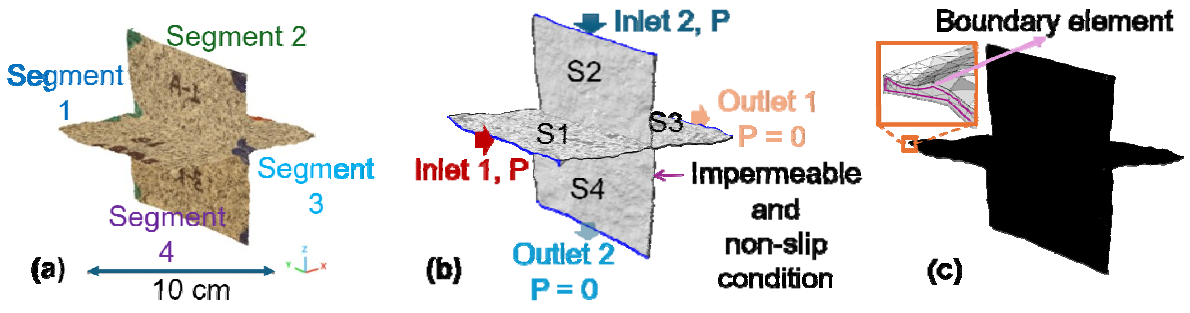


Fig. 3 (a) Segmentation of surfaces, (b) definition of boundary conditions in COMSOL, and (c) the final mesh model.

To analyze the relationship between the flow rate at the outlets and the hydraulic pressure gradients between the inlets and outlets, the Forchheimer equations (Eqs. 2-5) were used.

$$-\nabla P = AQ + BQ^2 \quad (2)$$

$$-\nabla P = \frac{\Delta P}{L} \tag{3}$$

$$A = \frac{12\mu}{we_h^3} \tag{4}$$

$$B = \frac{\beta\rho}{w^2 e_h^2} \tag{5}$$

Here, $-\nabla P$ (Pa/m) denotes the pressure drop (ΔP) over a length (L), and the terms AQ and BQ^2 represent linear and nonlinear flow rates, respectively. In this equation, Q (m^3/s) indicates flow rate, μ (8.9×10^{-4}Pa.s) signifies fluid viscosity, w (m) is fracture width perpendicular to flow, e_h is hydraulic aperture, β (m^{-1}) implies the non-Darcy coefficient related to fracture geometry, and ρ ($997kg/m^3$) is fluid density.

3 Results and discussion

3.1 Accuracy assessment, roughness, and physical aperture

The accuracy assessment of the 800 scale bars and 333 check bars yielded RMSEs of 14 μm and 15 μm, respectively. The aperture fields for each segment are illustrated in Fig. 4 (a to d). Additionally, the calculated R_{3D} and average physical apertures are reported within the same figures. Variations in R_{3D}were found to be negligible, ranging from 8.708 to 9.339. Notably, Segment 3 exhibited the highest roughness (9.339), while Segment 4 was the lowest (8.708). The physical apertures for the two inlets (Segments 1 and 2) were very similar, measuring 190 μm and 192 μm. However, the values for the outlets (Segments 3 and 4) showed a more significant difference of 18 μm, measuring 177 μm and 195 μm, respectively. It can be concluded that Segment 3 is rougher and tighter than Segment 4.

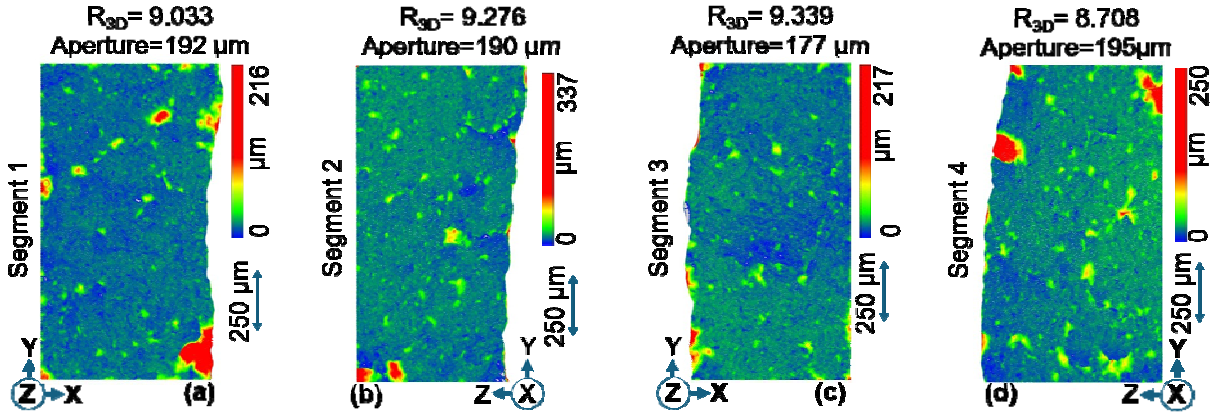


Fig. 4 (a) Physical aperture fields of (a) Segment 1, (b) Segment 2, (c) Segment 3, and (d) Segment 4. Roughness and physical apertures are provided for each segment.

3.2 Numerical modelling results

Fig. 5 (a) illustrates the Forchheimer equation fitted to the numerical results, showing the nonlinear relationship between the flow rate at the outlets and the hydraulic pressure gradient. The calculated hydraulic apertures (e_h) for Outlet 1 and Outlet 2 are 162μm and 175 μm, respectively. These results are consistent with the physical aperture measurements for these segments, where a higher physical aperture directly (Segment 4) corresponds to a higher hydraulic aperture.

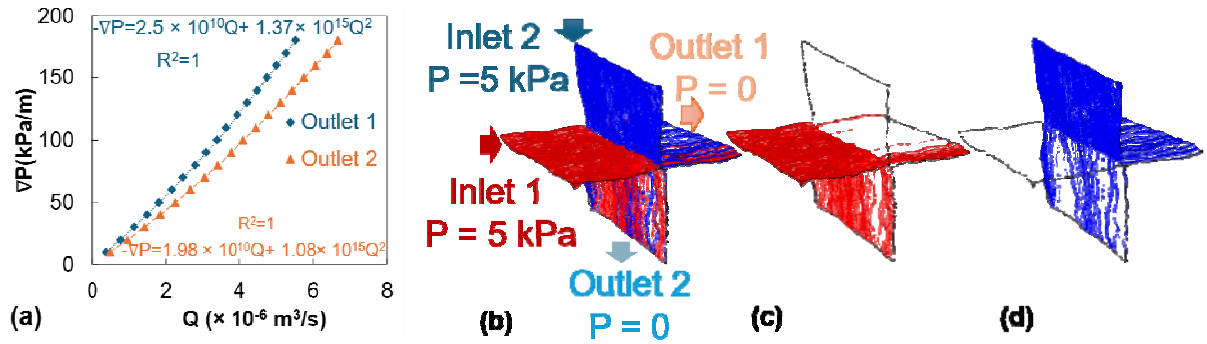


Fig. 5 (a) Nonlinear relationship between flow rate and hydraulic pressure gradient fitted by the Forchheimer equation; (b) streamline distributions of the two inlets at P = 5 kPa; (c) streamline distribution of Inlet 1; and (d) streamline distribution of Inlet 2.

The non-Darcy coefficients (β) were calculated as362 m^{-1} and 333 m^{-1}. This variation can be attributed to the differences in R_{3D}s and physical aperture sizes between Segments 3 and 4; specifically, Segment 3 is rougher and tighter than Segment 4. Fig. 5 (b) shows the streamline distribution originating from the two inlets. As observed, the streamlines from Inlet 1 primarily flow through Outlet 2 (Fig. 5(c)), while those from Inlet 2 exited through Outlet 1(Fig. 5(d)). Some mixing occurred within both Segments 3 and 4, which could be attributed to the intersection geometry and the configuration of the outlet segments. It seems mixing flow in Fig. 5(c) is lower than that in Fig. 5(d). This may be explained by the fact that Segment 4 (leading to Outlet 2) is wider and less rough than Segment 3 (leading to Outlet 1). Overall, it is evident that geometrical properties significantly influence the flow distribution. These intersecting fracture characteristics are critical for accurately analyzing fluid flow behavior within fracture networks.

4 Conclusion

In this study, photogrammetry was employed to reconstruct a 3D model of two intersecting fractures within a 10 cm × 10 cm × 10 cm domain. The accuracy assessment yielded an RMSE of 15 μm, demonstrating the capability of photogrammetry to reconstruct a highly accurate 3D model of a complex fracture intersection. This led to measuring physical apertures (177-195 μm) and surface roughness (R_{3D}, 8.708-9.339). Then, 36 fluid flow simulations were conducted using the 3D model in COMSOL across two inlets and two outlets using 18 different hydraulic pressure gradients (10 to 180 kPa/m).The results exhibited a nonlinear relationship between the hydraulic pressure gradients and the flow rates at the outlets. Fitting the Forchheimer equation to the numerical results showed that the tighter, rougher fracture segment resulted in lower e_h and higher β. Furthermore, the findings revealed mixing behaviour of fluid flow, indicating that fluid flow preferentially migrated toward the fracture segment with a higher physical aperture. These results emphasize that the intersection geometry and surface characteristics are critical factors in governing the flow distribution within fracture networks.

Acknowledgment

This work was funded by the Ministry of Economic Affairs and Employment of Finland as a part of the National Nuclear Safety and Waste Management Research programme (SAFER) in the research projects MIRKA I (funding number SAFER 23/2025) and MIRKA II (funding number SAFER 32/2026). During the preparation of this work, the authors used Gemini to check the language and improve readability. After using Gemini, the authors reviewed and edited the content as needed and take full responsibility for the content of the publication.

References

Baghbanan A, Jing L (2007) Hydraulic properties of fractured rock masses with correlated fracture length and aperture. International Journal of Rock Mechanics and Mining Sciences, 44(5): 704-719. https://doi.org/10.1016/j.ijrmms.2006.11.001

Liu J, Li C, Hu J, Luo Y, Liu B, Wang Z, Xie H (2025) Effect of stress-induced void heterogeneity and intersection geometry on heat transfer through 3D intersected rock fractures. Computers and Geotechnics, 186: 107429. https://doi.org/10.1016/j.compgeo.2025.107429

Magsipoc E, Zhao Q, Grasselli G (2020) 2D and 3D roughness characterization. Rock Mechanics and Rock Engineering, 53: 1495-1519. https://doi.org/10.1007/s00603-019-01977-4

Torkan M, Vidanage SL, Uotinen L, Janiszewski M, Rinne M (2026) Study on physical aperture and fluid flow behavior after dislocation of a rough fracture. International Journal of Rock Mechanics and Mining Sciences, 202: 106511. https://doi.org/10.1016/j.ijrmms.2026.106511

Wang XY, Zhong Z, Xie X, Hu Y, Han C, Lu B (2025) A nonlinear flow model and criterion for 3D natural fracture intersections: Effects of surface roughness and mechanical aperture. International Journal of Rock Mechanics and Mining Sciences, 193: 106169. https://doi.org/10.1016/j.ijrmms.2025.106169

Wyllie DC (1999) Foundations on Rock: Engineering Practice. London, CRC Press. https://doi.org/10.1201/9781482295009.

Xiong F, Wei W, Xu C, Jiang Q (2020) Experimental and numerical investigation on nonlinear flow behaviour through three dimensional fracture intersections and fracture networks. Computers and Geotechnics, 121: 103446. https://doi.org/10.1016/j.compgeo.2020.103446

Updated knowledge of inflatable rock bolts

C. C. Li
Norwegian University of Science and Technology, Trondheim, Norway
charlie.c.li@ntnu.no
0000-0003-2618-3231

Abstract

Inflatable rock bolts can quickly stabilize loosened rock blocks in underground excavations. An inflatable bolt is made of a steel tube that is folded into an omega shape. During installation, high-pressure water is injected into the tube to expand it to the borehole size. A primary contact stress is established on the borehole wall after installation, resulting in frictional resistance that prevents rock blocks from moving. It is recommended in current installation specifications that bolts be installed in boreholes slightly smaller than the original diameter of the steel tube, and small boreholes are generally not preferred. Recent theoretical and experimental studies of inflatable bolts have provided new knowledge, including the optimal borehole size and the relationship between the radial stiffness of the partially unfolded tube and the diameter of the unfolded tube. These studies show that the pullout load is high in both large and small boreholes. In large boreholes, the high pullout load is due to the high radial stiffness of the bolt tube, while in small boreholes it is due to locked contact stress. Middle-sized boreholes should be avoided because the stiffness of the bolt is lowest, and the locked contact stress can also be very low in such boreholes. The high pullout load in small boreholes, which contradicts theoretical predictions, is a new finding. It is attributed to locked contact stress caused by the tight contact of the shoulders of the tongue flanks of the bolt in small boreholes. Therefore, small boreholes can be used for inflatable bolts.

Keywords

Inflatable bolt, Pullout test, Borehole size, Rock bolting, Rrock support.

1 Introduction

Inflatable (or expandable) rock bolts have been used for rock support in mines and civil rock excavation projects for a long time since it was invented in the 1980s.Inflatable bolt is made of a steel tube that is folded into an omega-shape in cross section (Fig. 1). After the bolt installation, contact stresses are established at the interface between the bolt of the borehole wall. The bolt is anchored in the rock mass through the frictional resistance and mechanical interlock at the bolt-rock interface. The bolt installation only takes minutes to finish, and the bolt provides reinforcement function immediately after installation. Infltable bolt cannot be used for permanent rock reinforcement mainly because of its vulnerability to corrosion (Hadjigeorgiou et al. 2019; Villaescusa et al. 2008) and relatively low shear resistance. The bolt is at present mainly used in weak rock masses to provide rapid reinforcement to prevent deterioration of the rock mass quality or in water-abundant environment where grouted rock bolts cannot be cured properly. The field pull tests by Kim et al. (2017) showed that the ultimate

pullout resistance of inflatable rock bolts was not noticeably affected by water leakage in the borehole. However, the pullout resistance of grouted rock bolts was dramatically reduced when the leakage was higher than 1 liter per minute.

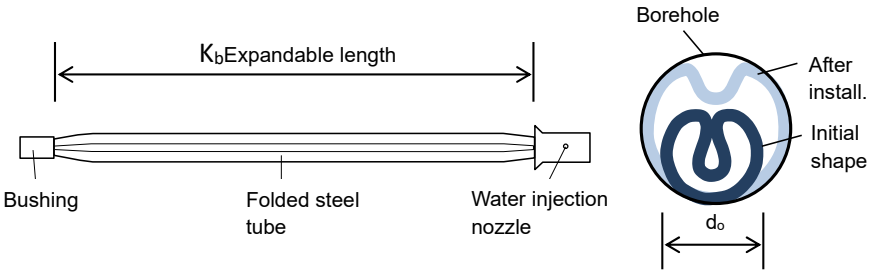


Fig. 1 Sketch illustrating the geometry of an inflatable rock bolt (Li et al. 2023).

It seems that inflatable rock bolt is a satisfactory rock reinforcement element in harsh rock conditions (e.g., Kim et al. 2017; Scolari et al. 2017). However, it was experienced in the practical use of the bolts that the pullout resistance of inflatable bolts varied in a wide range, which brings about confusion and difficulties in the design of rock reinforcement using inflatable bolts. The field pullout tests by Soni (2000) showed that the pullout resistance varied between 20 and 150 kN for the same bolt length and similar resistance values were obtained for different bolt lengths in the range of 0.5 - 3 m. The field tests conducted by Barnard et al. (2016) showed that the pullout resistance of inflatable bolts varied also in a wide range from 5 to 70 kN / m in rock masses of RMR ≈ 30. On the other hand, the pullout resistance remained the same in rock masses with RMR in a wide range from 20 to 80. Gregory (2014) carried out field pullout tests of inflatable bolts from four bolt suppliers, and he found that the pullout resistance of the bolts scattered in a range of 20 – 100 kN. The pullout resistance remained almost unchanged in rock masses of RMR 30 and 60. His tests conducted in Mines 1 and 2 showed that the pullout resistance had nothing to do at all with the rock mass quality.

The inconsistent results of the pullout resistance is certainly associated with the contact status between the bolt and the rock. Essentially the original theory for inflatable rock bolts has a too ideal assumption that the unfolded tube is assumed to be a closed ring, which misleads to an overestimation of the pullout resistance of the bolt. The theory cannot explain the deviations of the pullout results in various rock conditions so that it essentially cannot provide guidance for the design of rock reinforcement using inflatable bolts. Li (1997) and Li and Håkansson (1999) started to test inflatable bolts in artificial weak solid materials in the laboratory in the 1990s. the tests showed that inflatable bolts would become fully unfolded regardless of the borehole diameter, and the contact stress at the bolt-rock interface was relatively high, resulting in a high pullout resistance. After the laboratory tests, Li continued to study the mechanics of the bolt and proposed that the pullout resistance of inflatable bolt is associated with both the primary contact stress induced by the installation water pressure at the bolt-rock interface and a secondary contact stress induced by the borehole roughness that is mobilized when the bolt intends to slide (Li 2016). The primary contact stress is directly influenced by the unfolding degree, or the tongue length, of the bolt. The concepts of the primary and secondary contact stresses, the influence of the borehole roughness and the influence of the installation water pressure were verified afterward by pull tests in the laboratory (Li, Aure and Knox 2023). This laboratory study led to a new finding that high pullout resistance could be achieved in small boreholes which is not recommended in the current bolt installation specifications.

This paper will present an overview over the new knowledge of inflatable rock bolts that has been gained in the recent years, including the influences of the tongue length on the contact stresses, borehole roughness and borehole diameter.

2 Known knowledge

It is assumed that inflatable bolt slides in the borehole when it is mobilized by rock mass movements and the frictional resistant load on the borehole wall prevent the rock mass from disintegration. This mechanical mechanism can be achieved only when the embedment length of the bolt on one side of the opening rock joint is shorter than the critical embedment length of the bolt (Li, Kristjansson &

Høien 2016). Otherwise, the bolt will be locket in the rock mass and the bolt steel elongates until the steel strength is reached. Figure 2 shows the test results of Super Swellex under pull and shear loading, respectively (Stjern 1995; Li et al. 2014). The bolts were installed in two concrete cubes of high strength. The embedment length of the bolt in each block was 0.95 m. The bolt tested under pull sled so that the maximum pull load of 121 kN represented the ultimate frictional resistant load of the 0.95-m bolt segment, corresponding to a pull resistance of 127 kN/m. Under shear loading, the bolt tube became laterally clamped at a shear load of approximately 30 kN. The tube was locked at the joint of the two blocks afterward and the steel was stretched until the ultimate load of the steel was reached at 179 kN. The ultimate shear load is not dependent on the embedment length but on the steel strength.

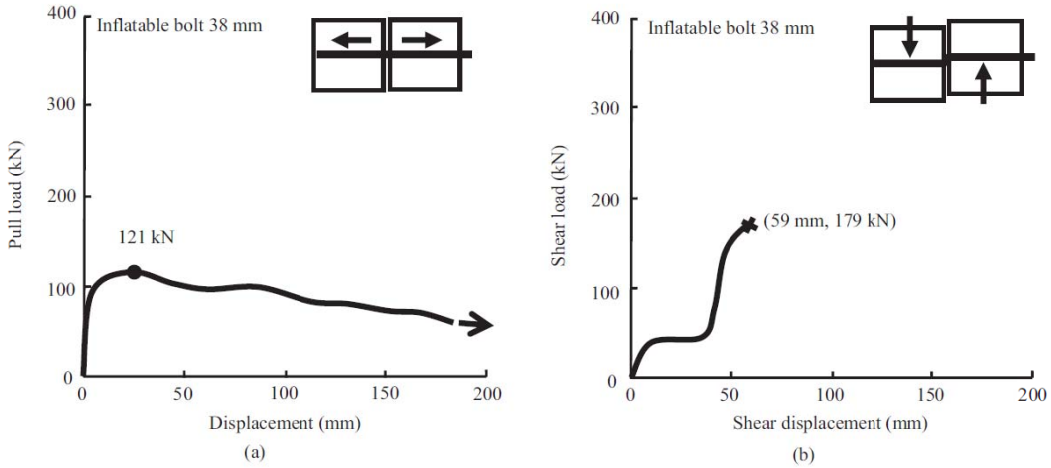


Fig. 2 Load–displacement curves of Super Swellex under pull and shear loading, respectively (Li, Stjern & Myrvang 2014).

The original theory of inflatable bolt was proposed by Wijk and Skogberg B (1982). The theory significantly overestimates the load capacity of the bolt. In practice, theload capacity was determined through pullout tests (Granström et al. 1982). Figure3 shows the pull load capacity versus the borehole size for Standard and Super Swellex bolts, reported by Atlas Copco in the 1990s. The nominal diameter of the steel tube is 42 mm for Standard Sellex and 54 for Super Swellex. The recommended range of borehole diameter is proposed based on the pullout test results. It can be seen in the diagram that the load capacity would be very low in small boreholes. In the current specifications for inflatable bolts, therefore, the recommended borehole diameter is usually in a range smaller than the original tube diameter and greater than the middle diameter between the initial profile diameter of the bolt (i.e., the diameter of the bolt in the folded state) and the original tube diameter (i.e., the diameter of steel tube after full unfolding). Boreholes smaller than the middle diameter are excluded in the recommended diameters. For example, a type of inflatable bolt, which is currently supplied to the market, has an initial profile diameter in 27 mm and an original tube diameter in 41 mm. It is stated that the bolt can be installed in boreholes of 32 – 40 mm, but the recommended borehole diameter is 36 -38 mm, which implies that the best reinforcement would be achieved in a borehole greater than the middle diameter (27 + 41) / 2 = 34 mm. The range of the recommended diameters is small, and the borehole could be drilled oversized, particularly in weak rock masses. The load capacity of inflatable bolt would be dramatically reduced and even drop to zero in extreme cases. In a small borehole, a non-zero resistant load is guaranteed, but it is considered too low, as shown in Fig. 3. The updated knowledge in Section 3 will prove that the load capacity in a small borehole could be as high as that in a large borehole when the bolt is properly installed.

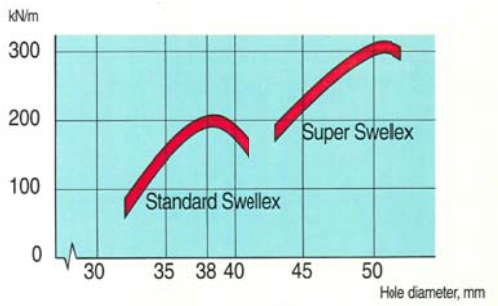


Fig. 3 The pull load capacities of standard and Super Swellex versus the borehole diameter.

3 Updated knowledge

The borehole to receive the bolt has deformed inward for U_0under the in-situ rock stresses before bolt installation (Fig. 4). During bolt installation, the pressured water inside the steel tube presses the

borehole wall to deform outward. The pressure on the borehole wall is p_i when the pre-defined maximum water pressure (24 or 35 MPa) is reached, at which the borehole displacement is U_0. After installation, the water pressure drops to zero and both the borehole wall and the partially unfolded steel tube moves inward toward the borehole centre under the ground pressure. The pressure on the borehole wall decreases with the inward displacement at the same time. The rock moves along the straight green line marked by K_r, while the steel tube moves along the black lines marked by K_b, see Fig. 4. To the end, the primary contact stress $q_1$is established on the borehole wall when the equilibrium is reached. This contact stress is expresses as (Li et al. 203):

$$q_1 = \frac{K_b - \lambda K_r}{K_b + K_r} p_i \qquad (1)$$

where K_b is the radial stiffness of the partially unfolded steel tube, K_r is the stiffness of the rock mass, and λ isa coefficient expressing the recovery of the outward elastic displacement of the steel tube after bolt installation. The coefficient λvaries in the range of 0–1 withλ= 0 for zero recovery (e.g., the elastic displacement is completely locked in),and λ= 1 for complete recovery (e.g., the elastic displacement rebounds completely and the bolt tube recovers to its non-stressing state) (Li 2016). The stiffness of the steel tube is much lower than the stiffness of the rock mass (only a few percentage of K_r). It is seen in Eq. (1) that the contact stress is negative, indicating that the bolt separates from the borehole wall, when the coefficient λis equal to 1 for complete recovery. Therefore, it is required that the outward elastic deformation of the steel tube during bolt installation must be partially locked to achieve a contact stress at the bolt-rock interface. The condition to guarantee a contact stress higher than zero is that the radial stiffness of the steel tube K_r must be greater than λK_r. A rough borehole surface can prohibit the elastic recovery and makes the recovery coefficient λ to be less than 1. That is the reason for the requirement that boreholes for inflatable bolts must be drilled percussively and the borehole surface must be rough.

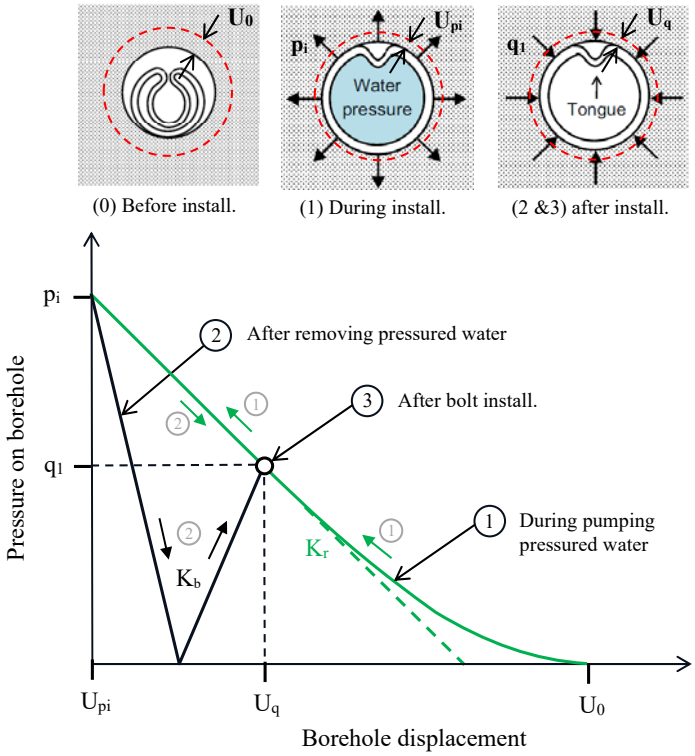


Fig. 4 Sketches illustrating the displacing moments of the borehole during and after bolt installation. Modified after Li (2016)

A secondary contact stress will be induced in a rough borehole when the bolt is stretched by opening rock joints. This contact stress is more important in hard rock masses than in soft rock masses.

The radial stiffness of the steel tube of the inflatable bolt directly determined the primary contact stress, and thus the pull resistant load capacity. Figure 5 shows the curve of the water pressure versus the unfolding degree of an inflatable bolt (the nominal diameter in the diagram) that was expanded outside a borehole. The folded tube started to expand after the water pressure passed the maximum at around point A. the water pressure declined with the opening of the folded tongue (points B and C) until the tube was unfolded to the original diameter of the tube at the middle of the bolt segment when the water pressure dropped to the minimum (before point D). Loading cycles were conducted during the test. The slope of the unloading-reloading line represents the radial stiffness of the partially unfolded tube. The stiffness of each loading of one tested bolt is presented in Fig. 6a versus the nominal diameter of the unfolding bolt tube. The stiffness of the bolt is minimum when the tube unfolded to diameter 32 mm that is slightly smaller than the middle diameter 34 mm.

A number of short inflatable bolt with a expandable segment of 360 mm were pullout tested in boreholes of various sizes drilled in a concrete block of high strength (UCS approximately 110 MPa).

The pullout results are presented in Fig. 6b. The tests confirmed that the pullout load increases with increasing the borehole size, as shown in Fig. 3, in the range above the middle diameter (34 mm in this case) in both the percussively rough boreholes and diamond-drilled smooth boreholes. Surprisingly, the pullout load in small boreholes was as high as in large boreholes, which is contradictory to the current belief that the pullout load is small in small boreholes. An advantage of using small boreholes is that one avoids the risk of oversized boreholes.

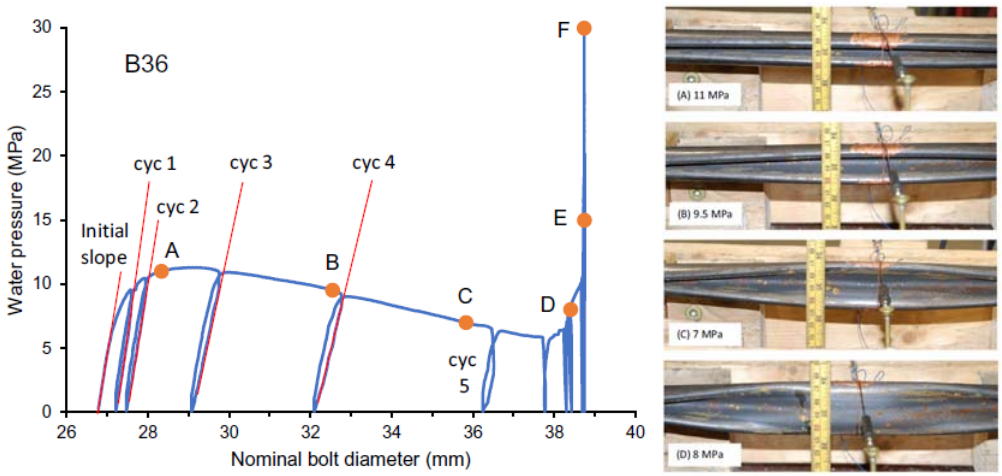


Fig. 5Water pressure versus the nominal diameter of a short inflatable bolt and the unfolding degrees of the folded tube at four moments (Li et al. 2023).

After the pullout tests, the bolts were cut through perpendicularly to the bolt length. The opening status of the folded tongue became visible as shown in Fig. 7. The shoulders of the two flanks of the tongue were not in contact in two larger boreholes (33.5 and 37 mm), see Fig. 7b and 7c. Because of the opening of the tongue shoulders, recovery of the outward elastic deformation of the tube is unavoidable after bolt installation, which leads to the recovery coefficient $\lambda > 0$. In these two boreholes, the pullout load in these two holes is directly associated with the radial stiffness of the bolt. In the small borehole of 31 mm, the tongue shoulders were tightly clamped together (Fig. 7a). The clamping prohibited the recovery of the outward elastic deformation of the steel tube so that the outward elastic deformation might be completely locked after bolt installation, that is, the recovery coefficient $\lambda \approx 0$. In this case, the pullout load would be not only dependent on the radial stiffness of the tube but also on the locked contact stress. This may be the mechanism why a high pullout load was achieved in small boreholes.

The test results in Fig. 6b confirmed that the pullout load is higher in a percussively drilled rough borehole than in a diamond drilled smooth borehole, and when the bolt is installed with a higher pump pressure than with a lower pump pressure.

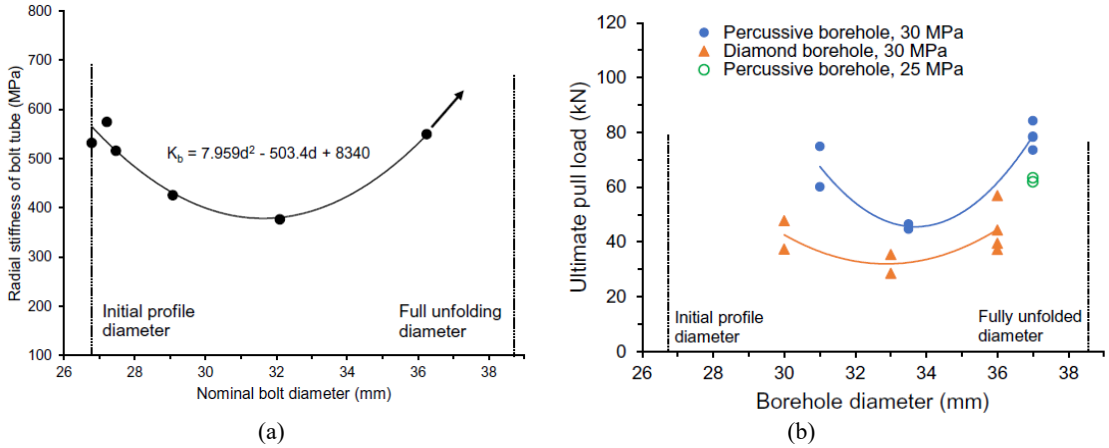


Fig. 6 (a) the radial stiffness of an inflatable bolt versus the nominal diameter of the unfolding bolt, and (b) the pullout loads versus the borehole diameter. (Li et al 2023)

4 Conclusions

The pullout load of inflatable bolt is high in small boreholes due to the tight clamping of the flank shoulders of the bolt tongue which prohibits the recovery of the outward elastic deformation of the steel tube after bolt installation. The quality of bolt installation is more guaranteed in a small borehole than in a large borehole because there is no concern of oversizing in small boreholes.

The radial stiffness of the folded steel tube is lowest in a borehole of around the middle-sized diameter of the bolt. The pullout load is also lowest in this hole.

The pullout load of inflatable bolt is dependent on both the primary and secondary contact stresses. The secondary contact stress is important in hard rock masses, while the primary contact stress is the major factor for the pullout load capacity in weak and soft rock masses.

The surface roughness of the borehole is extremely important in hard rock, but less important in weak and soft rock.



Fig. 7 The cross sections of inflatable bolts installed in boreholes of (a) 31 mm, (b) 33.5 mm and (c) 37 mm. (Li et al 2023)

References

Barnard CK, Kallu R, Warren S, Thareja R (2016).Inflatable Rock Bolt Bond Strength vs. Rock Mass Rating (RMR). 34th International Conference on Ground Control in Mining. 6p.

Granström B, Skogberg B, Wijk G (1982). Swellex test results. 17p

Gregory NA (2014). A Study of Correlations between Rock Bolt Pull-Out Tests and Rock Mass Rating Scores in Underground Mining. Master Thesis, University of Nevada, USA. 44p.

Hadjigeorgiou J, Savguira Y, Thorpe S J (2019). Comparative Susceptibility to Corrosion of Coated Expandable Bolts. Rock Mechanics and Rock Engineering 52:2665–2680.

KimH-J, KimK-H, KimH-M, ShinJ-H (2017). Anchorage Mechanism and Pullout Resistance of Rock Bolt in Water-Bearing Rocks. World Congress on Advanced in Structural Engineering and Materials, 28 Aug. – 1 Sept. 2017, Ilsan, Korea. 16p.

Li C (1997). Swellex rock bolts in weak and soft rocks. Research Report 1997:13, Luleå Univ., Sweden. 86p

Li C, Håkansson U (1999). Performance of the Swellex bolt in hard and softrocks. In: Proceedings of the international conference on rock support and reinforcement practice in mining, Balkema, 103–108.

Li CC(2016). Analysis of inflatable rock bolts. *Rock Mechanics and Rock Engineering* 49: 273–289.

Li CC, Aurea A, Knox G (2023). Experimental study of the effects of borehole size, borehole roughness and installation pressure on the pull load capacity of inflatable rock bolts. Rock Mech Rock Eng. 56:8415–8431.

Li CC, Kristjansson G and Høien AH (2016). Critical embedment length and bond strength of fully encapsulated rebar rock bolts. *Tunnelling and Underground Space Technology* 59: 16-23.

Li CC, Stjern G and Myrvang A (2014). A review on the performance of conventional and energy-absorbing rock bolts. *Journal of Rock Mechanics and Geotechnical Engineering* 6: 315-327.

Stjern G (1995). Practical performance of rock bolts. PhD Thesis, the Norwegian University of Science and Technology, Trondheim, Norway.

Soni A (2000) Analysis of Swellex bolt performance and a standardized rock bolt pull test datasheet and database. Master Thesis, University of Toronto, Canada.

Scolari F, Brandon M, Krekula H (2017). Dynamic inflatable, friction rock bolt for deep mining. Deep Mining 2017, Perth. Australian Centre for Geomechanics. 10p.

Villaescusa E, Hassell R, Thompson AG (2008). Corrosion of rock reinforcement in underground in hard mining excavations. 24p

Wijk G, Skogberg B (1982). The Swellex rock bolting system. 14thCanadian rock mechanics symposium. Canadian Institute ofMining and Metallurgy, 106–115.

A model for estimating the penetration of hard rock tunnel boring machine in practice

S. Yagiz[1,2] & A. Yazitova[1,2]
[1]*School of Mining and Geoscience, Nazarbayev University, Astana 01000 Kazakhstan*
[2]*Rock Excavation and Automation Research Group, Nazarbayev University, Astana 010000 Kazakhstan*
saffet.yagiz@nu.edu.kz

J. Hassanpour
School of Geology, College of Sciences, University of Tehran, Tehran, Iran

Abstract

Assessing the rate of penetration (ROP) of Tunnel Boring Machine (TBM) is one of the most crucial tasks in rock excavation and bore-ability, since the ROP is a main essential input parameter in the scheduling and execution of mechanized tunnelling projects. Despite the advances in tunnelling, a reliable estimate of the ROP is still posing challenges. Hence, this research aims to develop a model to estimate TBM penetration rate in hard rocks based on intact rock, rock mass properties and also machine specifications. In this study, 557 resulting datasets gathered from different tunnelling projects were utilized to predict the ROP using simple linear, linear multiple regression (LMR), and non-linear multiple regression (NLMR) analysis techniques. Firstly, rock fracture index (FI) is introduced as input and then the variety of multiple variable regressions were performed using the statistical software. It is found that the estimation of TBM penetration depend on both intact rock strength and discontinuity properties in rock mass and TBM operational parameters. As a result, nonlinear multiple variable regression equations were developed, and the best-performingmodel, with a correlation coefficient of 0.82, is introduced for TBM tunnelling in practice.

Keywords

Fracture Index, Hard Rock Mass, Penetration Rate, Tunnel Boring Machine, Tunnelling.

1 Introduction

Mechanized excavation refers to the method of rock breakage where the rock is entirely removed from the excavation face by the action of mechanical boring/cutting tools. Mechanized rock excavation is traditionally compared to drill and blast operation. The characteristic advantages of mechanical excavation are increased safety, higher production rate, less labour-intensive operation, higher degree of automation, minimum damage to the walls, better control over the process, uniformity of product size, elimination of blast vibrations, and better ventilation in underground openings. The most common types of mechanized excavators are tunnel boring machines (TBMs), roadheader, raise boring machine (RBM), continuous miner, and longwall drum shear to be used for either civil or mining construction.

One of the important indices or parameters used to evaluate the performance of TBM is the rate of penetration (ROP). The ROP is defined as the ratio of excavation distance to the operating time for the duration of the tunnel construction process. Many parameters are known to influence the ROP during tunnelling which include intact rock properties, rock mass properties and the machine specifications (Rostami and Ozdemir 1993; Bruland 1998; Kim 2004; Alber 2008; Delicia et al. 2013; Hassanpour et al. 2024; Yagiz et al. 2024; Olaiya et al. 2026) as summarized in Table 1.Besides properties of intact rock and rock mass features, in-situ stress distribution around the underground opening is also critical for excavation process, especially unstable ground condition encountered (Adoko et al., 2020).

Table 1.Common parameters influencing the penetration rate of TBM.

Intact rock parameters	**Rock mass parameters**	**Machine parameters**
Uniaxial compressive strength	Rock mass fabric	Total thrust (F_t)
Point load Index	Rock texture	Normal force (F_n)
Brazilian tensile strength	Orientation of discontinuities	Cutter diameter
Rock brittleness, Toughness	Spacing between the fractures	Cutter tip width, RPM
Hardness	Rock Quality Designation	Space between Cutters
Drilling rate index (DRI)	Fissures	Number of Cutters
Thin section analysis	Grain size and minerals	Cutterhead Power

Accurate estimation of TBM penetration is of crucial significance for the successful completion of the mechanized excavation projects. It mainly includes the determination of the rock cutting force and efficiency under different cutter penetration depth and the determination of the optimum rock boring/cutting condition as well as tool consumption; however, this thesis focusses on the aspect of penetration prediction for hard rock tunnel boring machines.

From past to present, many TBM performance estimation models are introduced (Graham and Farmer 1976; Cassinelli et al. 1980; Huges, 1986; Innaurato et al. 1991; Rostami and Ozdemir 1993; Bruland 1998; Barton 2000; Yagiz 2002, 2008; Hassanpour 2011; Goodarzi et al. 2021; Pourhashemi et al. 2021; Yang, et al., 2022; Yazitova et al. 2025). Most commonly used and known models for estimating the TBM penetration is summarized herein. Table 2 provides an overview of various empirical models that have been adopted for practical applications. These models have evolved from simpler to more sophisticated forms. Most complex but accurate models incorporate the key parameters affecting penetration rate, such as intact rock properties, rock mass characteristics, and machine parameters as input. In table 2, the most common empirical models and equations are introduced herein to give an idea for the readers who is familiar with TBM project practice.The purpose of this study is to development of the model for predicting TBM penetration in hard rocks based on intact rock, rock mass properties, and machine specifications, all of which have an influence on TBM tunnelling.

2 Projects

In this study, a database was developed using data from six different tunnel projects, including Queens Water Tunnel in the USA, Manapouri hydropower tunnel in New Zealand, Miryang Dam Tunnel in South Korea, and three Iranian Water Conveyance Tunnels (Karaj, Zagros, and Ghomrood).

The Queens Water Tunnel, 7.5 km long and 7 m in diameter, was excavated in complex geological formations beneath Brooklyn and Queens using a high-power TBM. The tunnel's geology consists of metamorphosed igneous rocks including gneiss to ortho gneiss, pegmatite with shear zones and faults (Queens Tunnel Project Report 2000; Yagiz 2002).

The Manapouri Second Tailrace Tunnel in New Zealand, part of a major hydroelectric project, faced challenging conditions due to the region's complex geology, including hard and abrasive rocks like

met-andesite and gneiss. A 2 km section of the tunnel, 10 m in diameter, was analysed for this study (Manapouri Report 2001; Yagiz et al. 2024a).

The Miryang Dam Tunnel in South Korea, 7.6 km long with a 2.6 m diameter, was constructed using both Drill-Blast and TBM methods. The tunnel faced challenges due to high compressive strength and abrasive granite (Kim 2004; Yagiz et al., 2010).

Data from the Karaj, Zagros, and Ghomrood water conveyance tunnels in Iran, excavated through various geological zones with sedimentary, metamorphic, volcanic, and pyroclastic rocks, were also included in the database (Hassanpour et al. 2024; Yagiz et al. 2024a, b).

Table2. Summary of common empirical models for estimating of the TBM penetration rate.

References	Equations	Outputs
Grahan (1976)	$P_{rev} = 3940 \cdot F_n/\sigma_c$	P_{rev}
Farmer and Glossop (1980)	$P_{rev} = 624 \cdot F_n/\sigma_c$	P_{rev}
Cassinelli et al. (1982)	$ROP = -0.0059RSR + 1.59$	PR
Hughes (1986)	$ROP = 1.667 \cdot (F_n/\sigma_c)^{1.2} \cdot (2/d)^{0.6}$	PR
Innaurato etal. (1991)	$ROP = {\sigma_c}^{-0.437} - 0.047 \cdot RSR + 3.15$	PR
Rostami &Ozdemir (1993)	$ROP = (F_n, \sigma_c, \sigma_t, rpm, s, T, R, \emptyset)$	PR
Yagiz (2002)	$ROP = (F_n, \sigma_c, \sigma_t, rpm, s, T, R, \emptyset, BI, \alpha, DPW)$	PR
Gehring (1995)	$ROP = 4 \cdot \frac{F_n}{\sigma_c}$	P_{rev}
NTNU (Bruland 1998)	$ROP = (f_n, \sigma_c, J_c, RPM, S, d, q, \alpha)$	PR
Q_{TBM} (Barton 1999)	$ROP = 5 \cdot {Q_{TBM}}^{-0.2}$; $Q_{TBM} = 5Q \cdot \gamma \cdot \sqrt[3]{Q \cdot \sigma_c/100/F_n}$	PR
Bieniawski et al. (2007)	$ARA_T = 0.324 \cdot RME - 6.8$ If UCS $\leq$ 45 MPa $ARA_T = 0.839 \cdot RME - 40.8$ If UCS $>$ 45 MPa	AR
Yagiz (2008)	$ROP = 1.039 + 0.028 \cdot BI - 0.003 \cdot \sigma_c + 0.437 \cdot \log(a) - 0.219 \cdot DPW$	PR
Hassanpour et al. (2011)	$FPI = Exp(0.008 \cdot UCS + 0.015 \cdot RQD + 1.384)$	FPI
Goodarzi et.al. (2021)	$ROP = \exp(0.006F_n - 0.016\sigma_c + 1.833)$	PR
Pourhashemi et al. (2021)	$P_{rev} = 1.98 + 0.035F_n - 0.03\sigma_c - 0.011GSI$	P_{rev}
Xu etal. (2021)	$P_{rev} = 16.888 - 0.025\sigma_c - 108243K_v$	P_{rev}
Yazitova et al. (2025)	$ROP = \frac{F_n^{0.308} \cdot WFI^{0.136} \cdot RPM^{-0.027} \cdot CHD^{2.875}}{8.211 \cdot UCS^{0.101} \cdot e^{0.583 \cdot CHD}}$	ROP

Note: ROP, penetration rate (m/h); Prev, penetration per revolution (mm/rev); RPM, cutterhead rotation speed (rev/min); Fn, cutter normal force (kN/c); σ_c, uniaxial compressive strength (MPa); σt, Brazilian tensile strength (MPa); BI, brittleness index; D, tunnel diameter (m); d, cutter radius or diameter (m); s, cutter spacing (m); q, quartz content; RQD, rock quality designation; RSR, rock structure rating; QTBM, rock mass quality rating for TBM driven tunnels; GSI, geological strength index; α, the angle between the tunnel axis and the joint plane; Jc, RMR joint condition partial rating; Jv, volumetric joint count; DPW, distance between the plane of weakness; q, quartz content; Kv, the intactness index of rock mass.

3 Datasets

The dataset includes intact rock properties (such as uniaxial compressive strength), rock mass properties like frequency of fracture spacing, machine specifications (e.g., disc cutter load), and TBM performance data (penetration rate) compiled from six different projects having different operational

parameters. Each input variable, such as rock strength, discontinuities, and machine output, was carefully examined and quantified to create a comprehensive database with 557 datapoints. The statistical range and data distribution were analysed using histograms to ensure the dataset's suitability for developing and testing empirical models as given in Table 3.

Table 3.Statistical description of the dataset in the database.

Parameters	**# of data**	**Minimum**	**Maximum**	**Mean**	**Std. dev**
UCS (MPa)	557	20.0	300.0	155.8	61.6
WFI	557	0.1	189.9	17.05	33.0
F_n (kN)	557	61.4	294.6	193.6	65.5
CHD (m)	557	2.6	10.1	6.4	2.3
RPM (mm/rev)	557	5.1	10.7	7.9	1.7
ROP (m/h)	557	0.2	4.8	1.8	0.8

Note: UCS, uniaxial compressive strength of rock (MPa); WFI, weighted fracture index; Fn, cutter load; CHD, cutter head diameter (m); RPM, rotational speed.

4 Model Development

In data science and engineering, a key step before developing predictive models is data partitioning. Typically, 80% of the data is used for training and 20% for testing, which provides a balance between a large training set for the model and a sufficient testing set to evaluate its performance. Consequently, developed dataset with 557 data point is divided into 445 training and 112 testing data. After examining the relationship between input variables using simple relations, linear multiple regression and non-linear multiple regression models are developed.

In order to find the best model, numerous linear multiple regression (LMR) and non-linear multiple regression (NLMR) were developed with different alternative input parameters including intact rock, rock mass properties as well as machine specification. Based on developed models utilizing variety of regression model techniques, the most accurate output is obtained and given in Equation 1 as follow:

$$\mathrm{ROP} = \frac{F_n^{0.308} \cdot \mathrm{WFI}^{0.136} \cdot \mathrm{RPM}^{-0.027} \cdot \mathrm{CHD}^{2.875}}{8.211 \cdot \mathrm{UCS}^{0.101} \cdot e^{0.583 \cdot \mathrm{CHD}}}, \qquad r = 0.82 \qquad (1)$$

It is found that the NLMR is superior to LMR in terms of correlation coefficients. It is also known that the nature and rock mass conditions inthe field are not homogeneous or isotropic; therefore, the relationships between the input variables and the ROP are not simple. As a result, the relationship between actual and predicted ROP is presented in Figure 1.To check the accuracy of the model, several statistical indices, such as coefficient of determination, root mean square error, mean absolute deviation, and variance account for (R^2, RMSE, MAD, VAF respectively) were obtained. Then, total ranking score method is used to find the best one among them to be introduced herein. Furthermore, the amount of error between measured and estimated ROP for each data point is presented in Figure 2 to show the variation of error along the excavation stations. The more information and model development process in this research could be found in Yazitova et al. (2025).

5 Conclusions

In this study, numerous LMR and NLMR models were developed using the established dataset. Accuracy of the models were checked using several alternative statistical indices, such as correlation coefficient, mean square error, root mean square error, and mean absolute percentage error. It was found that introduced nonlinear equation (Eq.1) is the most accurate among them, due to the quality

and number of input variables in the equation, as well as its performance based on statistical indices, particularly the correlation coefficient. Also, it is concluded that the NLMR is superior to LMR in terms of both input representation and output performance. As a result, the NLMR model equation introduced herein can be used, with caution, to estimate the ROP for scheduling purposes under similar rock and geological conditions. However, the application of the equation is limited to the range of dataset and the types of rocks considered in this study.

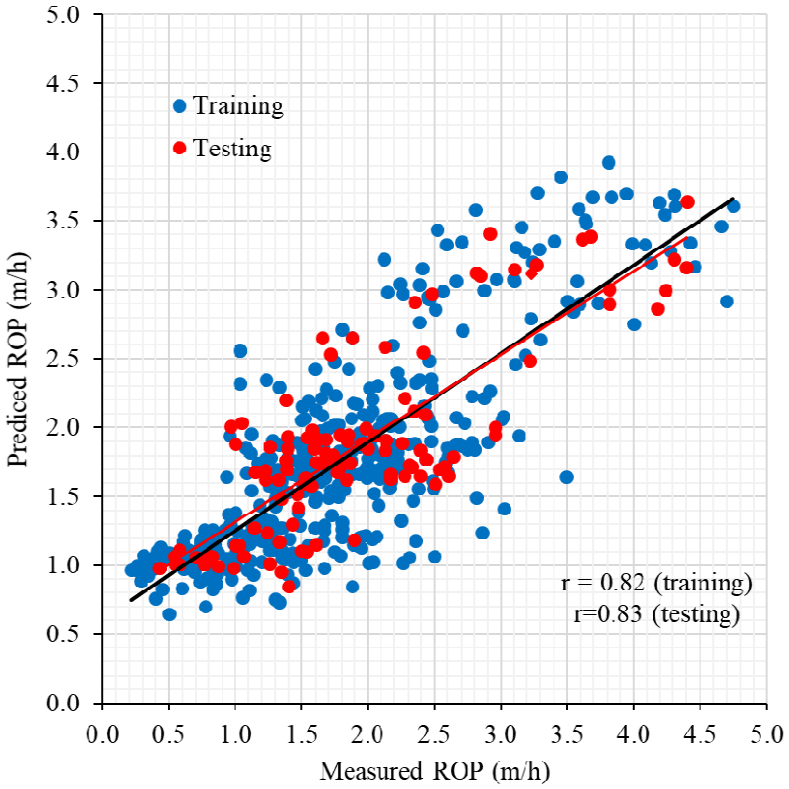


Fig.1 Relations of actual ROP with predicted ROP for both training and testing data.

Acknowledgement

This study was funded by the faculty development competitive research grant program of Nazarbayev University, Kazakhstan, under Grant Agreement Number 201223FD8837

References

Adoko, A. C., Vallejos, J., &Trueman, R. (2020). Stability assessment of underground mine stopes subjected to stress relaxation. Mining Technology: Trans., of the Institute of Mining and Metallurgy, 129(1), 30-39.

Barton, N. (1999) TBM performance estimation in rock using Q_{TBM}. Tunnels, Tunnelling & Inter., 31, 30–34.

Benato, A., Oreste, P. (2015) Prediction of penetration per revolution in TBM tunneling as a function of intact rock and rock mass characteristics. Int. J. Rock Mech. Min. Sci. 74, 119–127

Bruland, A. (1998). Hard rock tunnel boring. PhD Thesis, Norwegian University of Science and Technology, Trondheim

Cassinelli, F., Cina, S., Innaurato, N., Mancini, R., Sampaolo, A. (1982) Power consumption and metal wear in tunnel-boring machines: analysis of tunnel-boring operation in hard rock. Tunneling 82, London. Inst. Min. Metall., pp. 73–81.

Delisio, A., Zhao, J., Einstein, H.H. (2013) Analysis and prediction of TBM performance in blocky rock conditions at the Lotschberg Base Tunnel. Tunnelling Underground Space Technology, 33, 131-142

Farmer, I.W., Glossop, N.H. (1980) Mechanics of disc cutter penetration. Tunnels. Tunnels & Int. 12 (6), 22–25

Farrokh, E., Rostami, J., Laughton, C. (2012) Study of various models for estimation of penetration rate of hard rock TBMs. Tunn. Undergr. Space Technol. 30,110–123.

Graham, P.C. (1976) Rock exploration for machine manufacturers. Exploration of Rock Eng. 173–180.

Goodarzi, S., Hassanpour, J., Yagiz, S., Rostami, J. (2021) Predicting TBM performance in soft sedimentary rocks, case study of Zagros mountains water tunnel projects. Tunnel.Undergr. Space Tech., 109, 103705

Hughes, HM. (1986) The relative cuttability of coal-measures stone. Min. Sci. Technol. 3 (2), 95–109.

Hassanpour, J., Kazemi, C., Rostami, J. (2024) Introduction of a modified QTBM model for predicting TBM penetration rate in rock, based on data from mechanized tunneling project in Iran. Bull. Eng. Geol. Environ. 83,165

Hassanpour, J., Rostami, J., Zhao, J. (2011) A new hard rock TBM performance prediction model for project planning. Tunnelling Underground Space Technology, 26, 595–603

Innaurato, N., Mancini, A., Rondena, E., Zaninetti, A. (1991) Forecasting and Effective TBM Performances in a Rapid Excavation of a Tunnel in Italy. 7th International ISRM Congress.

Kim, T. (2004) Development of a fuzzy logic-based utilization predictor model for hard rock tunnel boring machines. PhD Thesis. Colorado School of Mines, Golden, USA

Macias, F.J., Jakobsen, P.D., Seo, Y., Bruland, A. (2014) Influence of rock mass fracturing on the net penetration rates of hard rock TBMs. Tunn. Undergr. Sp. Technol. 44,108-120

Manapouri Project Report. (2001) Evaluation of geologic condition and boreability. Reach 1, Manapouri Second Tailrace Tunnel No.2.Rocky Mountain Cons., Co, USA

Olaiya TD, Yagiz S, Adoko AC, (2026) TBM penetration rate estimation using Rock Mass Rating (RMR) and machine specifications. *Rock Mechanics Bulletin*, 100328https://doi.org/10.1016/j.rockmb.2026.100328

Pourhashemi, S.M., Ahangari, K., Hassanpour, J., Eftekhari, S.M. (2021) Evaluating the in- fluence of engineering geological parameters on TBM performance during grinding process in limestone strata. Bull. Eng. Geol. Environ. 80, 3023–3040

Queens Project Report. (2000) Rock properties and TBM performance evaluation reports. Vol.1-2, Earth Mechanics Institute of Colorado School of Mines, Co USA

Rostami, J., Ozdemir, L. (1993) A new model for performance prediction of hard rock TBM. In: Bowerman, L.D. et al. (Eds.), Proceedings of Rapid Excavation and Tunnelling Congress, Baston, MA, pp.793–809.

Xu, H.Y., Gong, Q.M., Lu, J.W., Yin, L.J., Yang, F.W. (2021) Setting up simple estimating equations of TBM penetration rate using rock mass classification parameters. Tunnel. Undergr. Space Tech.115, 104065

Yazitova, A., Adoko, A.C., Hassanpour, J., Yagiz, S. (2025) Empirical models for estimating penetration rate of tunnel boring machines in rock mass. *Bull EngGeol Environ* 84;55.

Yagiz, S. (2002) Development of rock fracture and brittleness indices to quantify the effects of rock mass features and toughness in the CSM Model basic penetration for hard rock tunneling machines. PhD Thesis. Colorado School of Mines, Colorado, USA.

Yagiz, S. (2008) Utilizing rock mass properties for predicting TBM performance in hard rock condition. Tunnelling Underground Space Technology, 23 (3), 326–339

Yagiz, S., Merguerian, C., Kim, T. (2010) Geological controls on the breakthrough of tunnel boring machines in hard rock crystalline terrains. ISRM International Symposium-Eurock-2010, Switzerland, June 2010 5p

Yagiz, S., Hassanpour, J., Rostami, J. (2024a) Introducing the concept of fracture index for performance prediction of hard rock TBMs.Eurock2024-New challenges in rock mech andeng.1513-1520.Spain

Yagiz, S., Yazitova, A., Smirnov, G.,Thyagarajan, Vinayak, M., Hassanpour, J. (2024b) Appraisal of boreability characteristics of rocks to estimate the TBM advancement. 58th U.S. Rock Mechanics/Geomechanics Symposium, Golden, Colorado, USA, June 2024.Paper Number: ARMA-2024-0982

Yang, J., Yagiz, S., Liu, Y.-J., Laouafa, F. (2022) Comprehensive evaluation of machine learning algorithms applied to TBM performance prediction. *Underground Space* (China), 7 (1), pp. 37 – 49. DOI: 10.1016/j.undsp.2021.04.003. Article

Using Blanco Mera granite as standard reference and benchmark material

M. A. González-Fernández & M. Muñiz-Menéndez
Laboratorio de Geotecnia, CEDEX, Madrid, Spain
manuel.gonzalez@cedex.es
0000-0001-8495-7990 0000-0001-5202-0044

I. Pérez-Rey
CINTECX, Universidade de Vigo, GESSMin Group, Vigo, Spain
0000-0003-0883-7211

Abstract

In geotechnical engineering, researchers frequently rely on well-known reference soils such as Toyoura sand, Ottawa sand, or London clay. These materials are widely used because of two essential characteristics: reproducibility and comparability. Reproducibility ensures that experiments can be repeated under nearly identical conditions, yielding results consistent across time and location. Comparability makes it possible to benchmark results between testing methods, laboratories, and equipment. Together, these attributes allow such soils to serve as reliable materials for validating numerical models, constitutive laws, and experimental techniques.

In contrast, rocks present a more complex situation. Unlike soils, commonly treated as homogeneous and isotropic materials, rocks are intrinsically heterogeneous and anisotropic, which strongly influence their behaviour. Consequently, establishing typical or reference rocks is less straightforward. Nevertheless, several candidates have gained recognition in the literature, including Lac du Bonnet granite, Berea sandstone, and Westerly granite. These rocks have been extensively tested and are frequently used in studies of fracture mechanics, hydraulic conductivity, and strength characterization. A key challenge is defining the threshold at which a rock can be considered a standard reference material, given the variability observed even within a single quarry.

Based on an extensive experimental campaign on Blanco Mera granite, this study examines the criteria for defining a benchmark rock. More than twenty tests per property were performed, including uniaxial compressive strength (112.71 MPa), tensile strength (9.32 MPa and 5.64 MPa). Results show low standard errors, indicating good repeatability. These findings support considering Blanco Mera granite as a potential reference rock and establish requirements for standardization in geotechnical research. Additional analysis also highlights consistent wave velocity measurements, supporting the mechanical stability of the material across different test conditions and reinforcing its suitability as a reference material for laboratory comparisons and model validation purposes in future applications.

Keywords

Testing, Reference Rock, Benchmark.

1 Introduction

Although soils can often exhibit complex behaviour, they can frequently be described as CHILE-type material, meaning they are *Continuous, Homogeneous, Isotropic, Linear-Elastic*.These properties make them relatively easier to characterize and allow results to be extrapolated in a way that is easier than on rocks. This facilitates the identification of patterns or what we might call "reference soils." Such soils are highly useful in geotechnical engineering because they are employed to calibrate and compare results among testing machines or laboratories, helping to meet rigorous international testing standards.

Rocks, on the other hand, rarely display this behaviour and are almost always better described as DIANE-type solids, meaning they are *Discontinuous, Inhomogeneous, Anisotropic, Non-linear-Elastic*. which, in practical terms, implies that even when using the same rock extracted from different locations within the same quarry, there can be significant differences that affect their mechanical properties

Unlike soils, only a few rocks can be considered "standard" due to their specific applications. For example, Lac du Bonnet granite has been widely studied in laboratories for its thermo-mechanical and mechanical properties (Annor and Jackson, 1986). Another example is a rock extensively analysed for permeability and hydraulic fracturing, the Berea sandstone, primarily in the petroleum industry (Oak et al., 1990). Lastly, Westerly Granite has been widely used in permeability studies under varying temperatures (Summers et al., 1978). These examples illustrate that only a limited number of rocks could be considered as standards. Therefore, in rock mechanics, it is important to establish a framework for defining and using standard reference rocks in specific fields, where the lack of such references makes it difficult to obtain reliable test results and, ultimately, to interpret them within a consistent rock mechanics context.

Through this document, we aim to try to open a debate in this issue by using a type of rock widely employed in different laboratories to propose a tentative framework—or at least to try to define minimum characteristics required—to classify a rock as a standard reference material.

2 Framework of characteristics

In this section we will try to establish a tentative framework in which we can define minimum requirements in order to establish a rock type, based on four different parameters, that means focus on number of tests, fields of studies, laboratories which has performed the studies, and lastly the types of tests.

2.1 Number of tests

In this case, we can establish a minimum number of tests, ensuring that each individual test represents less than 1% of the total dataset. Based on this criterion, at least 100 tests should be performed to adequately characterize the rock. This approach guarantees that the collected data provides a robust representation of its mechanical behaviour, including strength and fundamental elastic properties such as the Elastic Limit and Poisson's ratio. By increasing the number of tests, we reduce the influence of any single measurement and improve the reliability of the overall characterization, which is essential for assessing a rock to be considered as Rock type.

2.2 Number of studies

In this case, at least two independent studies should be available, even if they adopt different methodological approaches, provided that they include the same type of tests. This requirement ensures that meaningful comparisons can be made to determine whether the studies can be considered part of the same group. Furthermore, to strengthen the reliability of the conclusions, it is recommended to include at least three distinct studies, each based on different datasets but containing comparable types of data. This approach enhances the robustness of the analysis and reduces the risk of bias associated with relying on a single source.

2.3 Laboratories

To classify a rock type, it is essential to establish repeatability in the tests performed. This is particularly important because each laboratory, even when following the same procedures or standards, may use different equipment and testing conditions. Such variations can introduce

discrepancies in the results. Therefore, to ensure that a rock can be considered a standard reference material, at least two independent sets of tests should be conducted—either in different laboratories or using different testing machines within the same laboratory. This requirement helps confirm that the results are consistent and belong to the same group, even when obtained under varying conditions. By validating repeatability across different setups, we strengthen the reliability of the characterization and minimize the influence of equipment-specific biases.

2.4 Test type

Regarding the types of tests that should be performed, although the minimum requirements depend on the ultimate purpose for which the rock characterization will be used, the most relevant parameters are typically those related to the rock's strength and elastic properties, as well as the characteristics of its joints. These parameters are essential for accurately establishing the mechanical behaviour of the rock under different loading conditions. Therefore, in order to define a rock type, priority should be given to tests that provide data on these aspects.

3 A Spanish example of

The rock presented here is the Blanco Mera Granite. Blanco Mera is a bright white granite characterized by a mineral composition of 35% plagioclase feldspar, 27% alkali feldspar, and 20% quartz. Accessory minerals include muscovite (7%) and biotite (5%), with trace amounts (under 5%) of chlorite and sericite. As illustrated in Fig. 1, the grain distribution is somewhat irregular, with quartz crystal sizes ranging from 1 to 6 mm and feldspar crystals ranging from 1 to 3 mm along with various mica minerals.This rock is mainly used for ornamental purposes, such as kitchen countertops and as large blocks for fencing plots of land.

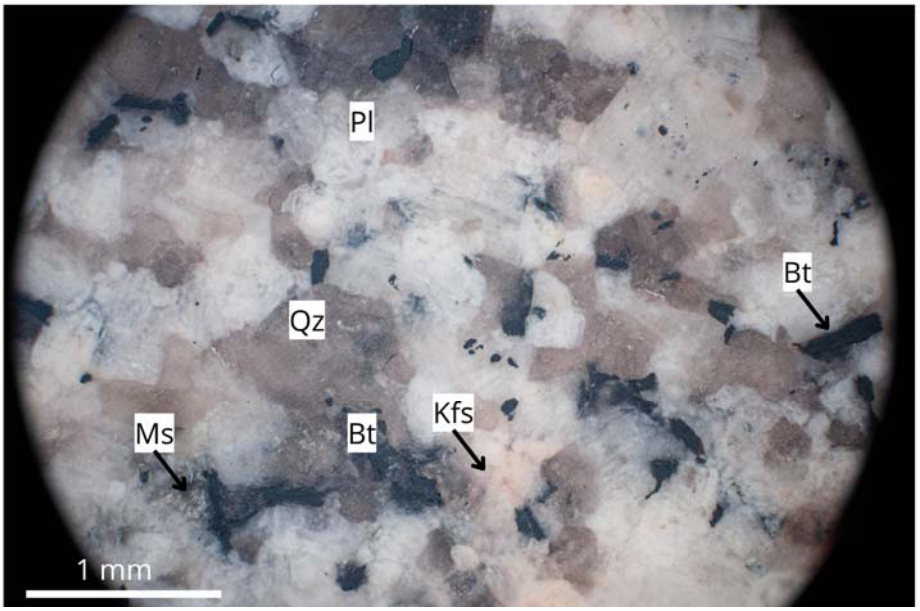


Fig. 1 Details of a surface of Blanco Mera Granite, where the different minerals are observed. Qz refers to Quartz, Kfs Alkali feldspar, Pl Plagioclase feldspar, MS Muscovite and Bt Biotite.

3.1 Available data

During various studies, a database was compiled on Blanco Mera described on the previous section. Although more than 25 studies have been published on this rock in different areas—such as scale effects, jointed rocks, fracture toughness, and permeability—we present here results of the main properties derived from those studies, performed through compressive tests, and its posterior analysis (Alejano et al., 2017 and 2021; González-Fernández et al.,2023, 2024a and 2024b, Quiñones et al, 2017), as well as direct and indirect tensile strength tests (Pérez-Rey et al., 2023 and 2024). Readers can refer to the extended database provided in these studies, which contains more than 100 UCS and triaxial tests performed on NX diameter, having these studies a total of near 400 tests, along with approximately 40 direct tensile tests.

To analyse the data, we will apply different strategies. First, all data of the same type will be grouped, and basic statistical parameters such as the mean, standard error will be calculated. These metrics will

serve as indicators of strength consistency and variability within each dataset. By examining these values, we can obtain an initial assessment of the quality and reliability of the experimental results, providing a solid foundation for subsequent interpretation and deeper statistical analysis.

Finally, we will generate Hoek–Brown failure envelopes along with confidence bounds to compare all strength data from the three studies. This approach will allow us to visualize variability and establish a more robust interpretation of the mechanical behaviour of the rock.

Results of the principal parameters derived from data collected from compressive and tensile tests are presented on Table1.It should be noted that only Nx diameter tests were used for this brief study, although different sizes and types of samples are presented on the studies, and deformability data are available, due to the limit extension of the document we decided to use only NX data.

Table 1. Values of the basic parameters collected through different studies. Alejano et al (2017, 2021), González et al (2023, 2024a, 2024b), Quiñones et al (2017) Perez-Rey (2023, 2024).

Test type	**Average Value**	**Standard Error**	**Number of test**
UCS [MPa]	112.71	3.15	23
DTS [MPa]	5.64	0.21	24
ITS [MPa]	9.32	0.19	10
K_{IC}^{pCT} [MPa m$^{1/2}$]	1.02	0.03	5
E_{UCS} [GPa]	52.72	2.35	5
E_{DTS} [GPa]	23.36	1.34	24
ν_{UCS} [-]	0.26	< 0.01	5
ν_{DTS} t [-]	0.11	< 0.01	17
V_p[km s^{-1}]	5.28	0.02	22
V_s [km s^{-1}]	2.89	0.05	22
γ [kN m^{-3}]	25.63	< 0.01	22
k_n[GPa m^{-1}]	1734.58	189.70	7

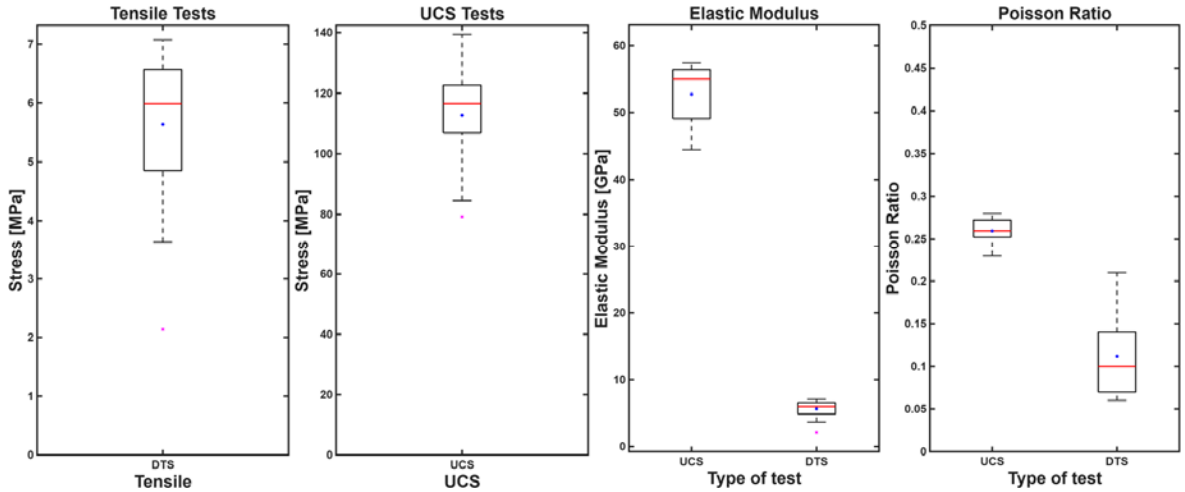


Fig. 2 Box plots of all data used to compute basic statistical data. Left , for tensile tests, middle for UCS tests and right for triaxial compressive tests.

The remaining compressive strength values demonstrate a high degree of agreement across the different confining pressure levels, reflected in their low or assumable dispersity displayed on boxplots of Figure 2. Such low dispersity indicate a strong level of consistency and reliability in the experimental results, suggesting that the material behaviour is stable and that the testing procedures were carried out under well-controlled conditions. In practical terms, this implies that the measured strength values cluster closely around the mean, reducing the likelihood of significant outliers and supporting the statistical robustness of the dataset.

The fitted curves and the corresponding plotted datasets presented on Figure 3 and Table 2 reveal a clear and consistent alignment across all test conditions. The close similarity in both the shape of the curves and the estimated fitting parameters demonstrates strong agreement between the experimental

measurements and the selected fitting models. This concordance indicates that the chosen fit adequately captures the underlying mechanical response of the material over the tested range.

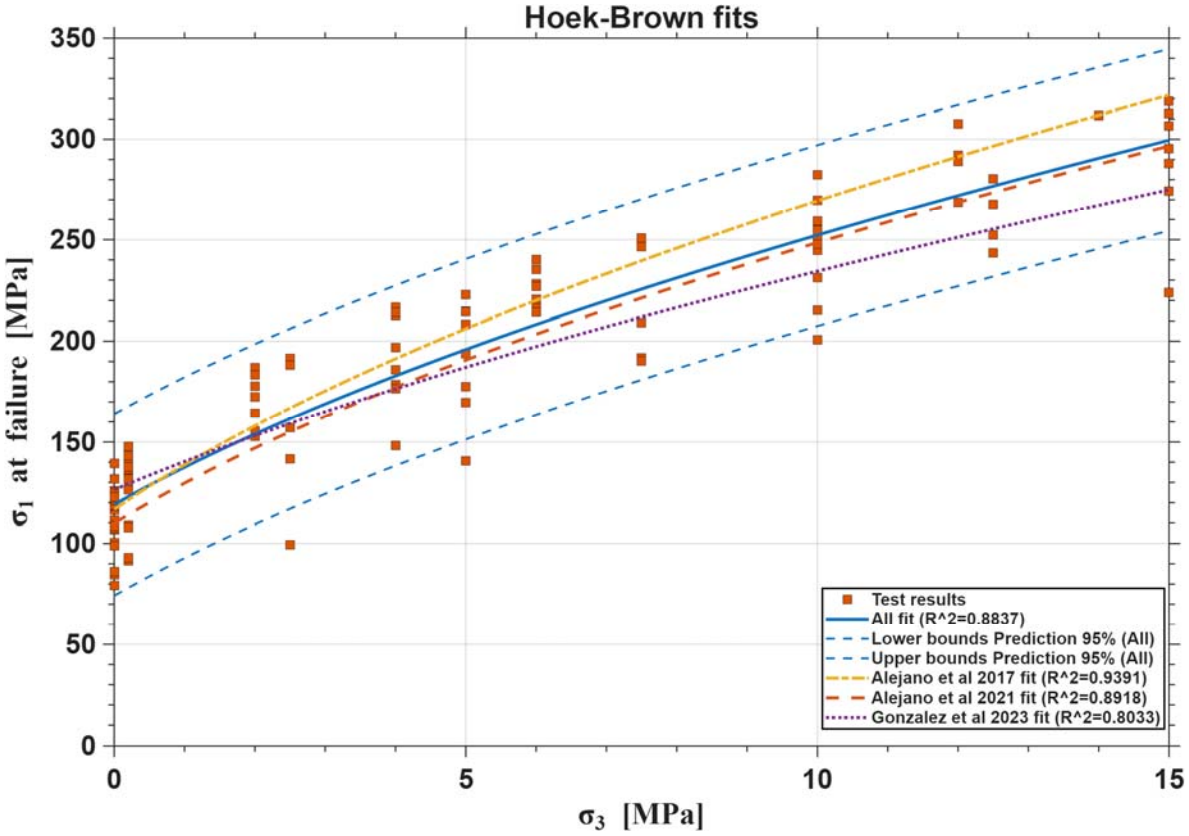


Fig. 3 Hoek-Brown fits for, indiviual studies and all data together.

Such consistency is further reinforced by the overlapping trends observed across the different tests, suggesting that the datasets exhibit comparable statistical and mechanical characteristics. This uniform behaviour supports the interpretation that the results originate from the same material group, or at least from specimens with sufficiently similar properties to justify their joint analysis. The coherence across fits is therefore an important indicator of data reliability, as it reduces the likelihood that the observed patterns are caused by sample-specific anomalies or uncontrolled testing conditions.Although some results, particularly those reported by Gonzalez et al. (2023), show a lower correlation coefficient compared to the others, the authors attribute this to the natural variability of the rock. Even when obtained from the same quarry, the samples may exhibit inherent variability.

Table 2. Values of the Hoek-Brown parameters obtained through different sets of studies.

Study	**Tests**	**H-B parameter**		**Coefficient of correlation R^2**
		m_i [-]	**σ_{ci} [MPa]**	
Alejano (2017)	59	46.02	116.66	0.94
Alejano (2021)	22	40.83	109.84	0.89
Gonzalez-Fernandez (2024)	24	27.20	126.39	0.80
All data	111	37.38	119.06	0.88

4 Conclusions

This document aims to establish a framework for defining when a rock can be considered a standard. Within this framework, it is essential to set a minimum number of tests to ensure statistical robustness and reliability of the results. A sufficient sample size reduces variability and increases confidence in the characterization. Additionally, at least two independent studies should be available, analyzing the same parameters but conducted in different laboratories or using different testing equipment. This requirement guarantees that, after performing statistical analyses, the results are consistent and reproducible across different conditions. Furthermore, the minimum set of parameters to be studied must include those related to strength and elastic properties, as these are fundamental for understanding the mechanical behavior of the rock.

In order to establish a framework for defining a typical rock, we present Blanco Mera Granite as a possible candidate for 'standard rock'. Although the primary dataset includes approximately 150 tests performed exclusively on intact specimens with a diameter of 54 mm, the overall number of tests exceeds 600. These additional tests encompass a wide range of investigations, including scale effects, fissured specimens, tensile strength, fracture toughness, and permeability, among others. Beyond providing fundamental parameters such as strength and elasticity, these tests also deliver specific data relevant to each specialized study. Importantly, the experiments were conducted in different laboratories or, when performed in the same facility, using different machines. This diversity enhances the robustness of the dataset and ensures repeatability and comparability across varying conditions. Therefore, given that the proposed framework is satisfied, we can reasonably conclude that Blanco Mera rock meets the criteria to be considered a standard rock type.

Acknowledgements

The first author acknowledges the Spanish Ministry of Science, Innovation & Universities for financing his research through a grant contract PTA2024-025163-I.

References

Annor A, Jackson J (1986) Mechanical and Thermomechanical Behaviour of Lac Du Bonnet Granite: Some Laboratory Observations. Proceedings of the Canadian Nuclear Society 2nd International Conference on Radioactive Waste Management. Winnipeg, Ontario, Canada, September 1986.

Oak MJ, Baker LE, Thomas DC (1990) Three-Phase Relative Permeability of Berea Sandstone.J Pet Technol42 pages 1054–1061. https://doi.org/10.2118/17370-PA

Summers R., Winkler K., Byerlee J (1978) Permeability changes during the flow of water through westerly granite at temperatures of 100°–400°C. J. Geophys. Res., 83, 339–344, https://doi.org/10.1029/jb083ib01p00339.

Alejano LR, Arzua J, Bozorgzadeh N, Harrison JP (2017) Triaxial strength and deformability of intact and increasingly jointed granite samples. Int J of Rock Mech and Min Sci, 95, 87–103. https://doi.org/10.1016/j.ijrmms.2017.03.009

Alejano LR, Estévez-Ventosa X, González-Fernández MA, Walton G, West IG, González-Molano NA, Alvarellos J (2021) A Method to Correct Indirect Strain Measurements in Laboratory Uniaxial and Triaxial Compressive Strength Tests. Rock Mech Rock Eng 54, 2643–2670 https://doi.org/10.1007/s00603-021-02392-4

González-Fernández MA, Estévez-VentosaX, Alejano LR, Masoumi H (2023). Size-Dependent Behaviour of Hard Rock Under Triaxial Loading.Rock Mech Rock Eng56, 6009–6025. https://doi.org/10.1007/s00603-023-03367-3

González-Fernández MA, Estévez-Ventosa X, Pérez-Rey I, Alejano LR, Masoumi H (2024a). Size effects on strength and deformability of artificially jointed hard rock. Int J of Rock Mech and Min Sci, 176, 105696, https://doi.org/10.1016/j.ijrmms.2024.105696.

González-Fernández MA, Alejano LR, West IG, Walton G, (2024b). Strain analysis and joint stiffness estimation based on jointed granite specimens submitted to triaxial tests. New Challenges in Rock Mechanics and Rock Engineering, Eurock 2024, Alicante, Spain, July 2024. https://doi.org/10.1201/9781003429234-103

Quiñones J, Arzúa J, Alejano LR, García-Bastante F, Mas Ivars D, Walton G (2017) Analysis of size effects on the geomechanical parameters of intact granite samples under unconfined conditions. Acta Geotechnica, 12 (6), 1229 – 1242. https://doi.org/10.1007/s11440-017-0531-7

Pérez-Rey I, Muñoz-Ibáñez A, González-Fernández MA, Muñiz-Menéndez, M, HerbónPenabad M, Estévez-Ventosa X, Delgado J, Alejano LR (2023) Size effects on the tensile strength and fracture toughness of granitic rock in different tests, J of Rock Mech and Geotech Eng 15(9) 2179-2192. https://doi.org/10.1016/j.jrmge.2022.11.005.

Pérez-Rey I, Muñiz-Menéndez M, Frühwirt T, Konietzky H, Jacobsson L, Perras MA, Atefi-Monfared K, Mas Ivars D, Sánchez Juncal A, Alejano L.R (2024) Assessment of Direct Tensile Strength Tests in Rock Through a Multi-laboratory Benchmark Experiment.Rock Mec Rock Eng, 57 (5), 3617 – 3634. https://doi.org/10.1007/s00603-023-03751-z

An adaptive data sampling strategy for in-situ stress characterization

A. Hamidi & J. P. Harrison
University of Toronto, Toronto, Canada
asieh.hamidi@utoronto.ca

D. Mas Ivars
Swedish Nuclear Fuel and Waste Management Company (SKB), Solna, Sweden
Royal Institute of Technology (KTH), Stockholm, Sweden

H. A. Kasani
Nuclear Waste Management Organization (NWMO), Toronto, Canada

A. Sánchez Juncal
Swedish Nuclear Fuel and Waste Management Company (SKB), Solna, Sweden

Abstract

Deep geological repositories (DGRs) for nuclear waste require reliable in-situ stress characterization to ensure appropriate safety during the phases of construction, operation, and post-closure. However, determining optimal data requirements and sampling strategies is challenging due to geological heterogeneity, measurement costs, and varying uncertainty tolerances across these phases. This study introduces a novel adaptive framework that integrates change point detection (e.g., due to regional stress field variations, geological complexities, etc.) and Bayesian hierarchical modeling to optimize stress characterization strategies. The framework applies a multi-tiered methodology, and provides explicit decision criteria for method selection, quantifies data adequacy through statistical power analysis, and identifies optimal measurement campaigns for different repository design phases, from preliminary site characterization (minimum viable datasets) to detailed design (high-confidence predictions). This methodology helps address the fundamental question "how much data are enough?" by providing quantitative, site-specific guidance for stress characterization programs, ultimately enabling more efficient resource allocation and improved confidence for performance assessments in a nuclear waste repository site.

Keywords

In-situ stress data, Deep geological repository, Bayesian hierarchical model, Data adequacy.

1 Introduction

Deep geological repositories (DGRs) are internationally recognized as the most viable long-term solution for high-level nuclear waste (HLW) disposal (Unokiwedi et al. 2025; Wang et al. 2018). From a rock engineering perspective, reliable in-situ stress characterization within the DGR host rock is a prerequisite for safe design, construction, and long-term performance assessment (Amadei & Stephansson 1997; Hudson & Harrison 2000). Stress measurement campaigns are costly, and geological heterogeneity means that data requirements are neither uniform across depth nor constant

across repository design phases, from preliminary site characterization through detailed design and final safety assessment (IAEA 2011; Zoback 2010).

Despite the recognized importance of stress characterization, the fundamental question, "*how much data are enough?*" lacks a quantitative, adaptive answer in current practice. Existing frameworks often treat the rock mass as statistically homogeneous or rely on predetermined measurement programs that are not explicitly linked to quantitative uncertainty reduction (Baecher & Christian 2005; Phoon & Kulhawy 1999). Bayesian hierarchical approaches offer a principled pathway for uncertainty quantification and information sharing across geological domains (Gelman et al. 2013), yet their application to DGR stress characterization has so far been limited (Bao & Burghardt 2022). This paper outlines an adaptive Bayesian-statistical framework that integrates change-point detection, distributional analysis, and hierarchical Bayesian modeling to optimize stress characterization strategies. The framework is validated using overcoring database from the Forsmark site in Sweden (Sjöberg et al. 2025), and provides phase-specific decision criteria for measurement campaign design.

2 Forsmark Overcoring Database

Forsmark, central Sweden, is the site of a proposed DGR and has been extensively investigated by SKB (Martin 2007; Stephansson & Ångman 1986). The raw overcoring database comprises 119 records from ten boreholes (Sjöberg et al. 2025); one borehole was excluded due to incomplete stress tensor records across all its measurements, a standard data quality filter. The dataset analyzed in this paper comprises 114 complete stress tensor measurements from nine boreholes, spanning depths of 10.4–501.8 m. The maximum principal stress σ_1 ranges from 1.8 to 63.4 MPa, and horizontal stresses σ_{Hmax} and σ_{Hmin} range from 1.8–62.6 MPa and 0–42.6 MPa respectively, with vertical stress σ_V up to 30.2 MPa, indicating substantial depth-dependent and spatial variability.

3 Adaptive Framework

To address the fundamental question of "*how much data are enough?*" for in-situ stress characterization in DGRs, a four-step adaptive Bayesian-statistical framework was developed. The framework is designed to account for geological heterogeneity across depth, varying data availability between segments, and the evolving uncertainty tolerance across repository design phases, conditions that make uniform or predetermined measurement programs statistically unjustified (Table 1).

Step 1 partitions the σ_1 depth profile into statistically homogeneous segments using three complementary change-point algorithms. Breakpoint consensus is when at least 30% of configurations agree within a ±30 m tolerance, with a minimum 20 m segment separation enforced. Each segment is classified as unimodal or multimodal by comparing one- versus two-component Gaussian Mixture Models (GMM) via the Bayesian Information Criterion, with $\Delta_{BIC} > 10$ indicating multimodality. Step 2 fits a Bayesian distributional model within each segment, characterizing the posterior of the segment mean μ and standard deviation ς under weakly informative priors to allow the data to dominate. Model adequacy is assessed by posterior predictive coverage, targeting posterior predictive coverage *PPC* $\geq$0.93.

Step 3 addresses data-sparse segments through hierarchical partial pooling, which borrows statistical strength from data-rich segments in proportion to each segment's data scarcity. The three strategies of no pooling, full pooling and partial pooling were formally compared, with partial pooling being adopted as optimal; a credible interval (CI) reduction metric quantifies the gain. Step 4 derives minimum sample size requirements analytically from the 95% CI half-width criterion for three precision targets, and extends this to a four-phase repository lifecycle framework with pre-defined CI targets at each design stage. A four-tier decision tree then provides an explicit method-selection recommendation per depth domain, ranging from a data-insufficiency flag at Tier 0 through to GMM-based ensemble approaches at Tier 3. The components of step 3 provide the quantitative, site-specific, and phase-adaptive decision criteria needed to optimize stress characterization campaigns at any stage of repository development.

4 Results

4.1 Segmentation and Distributional Signatures

Five consensus breakpoints at 73, 151, 238, 300, and 375 m partition the dataset into six depth segments (Fig.1), each with a statistically distinct stress regime. The ±30 m consensus tolerance

represents the positional uncertainty on each boundary, and this should be interpreted as a transition zone rather than a sharp interface. Mean values of σ_1 increase from 13.1 MPa (Segment 1, 10–72 m) to 51.4 MPa (Segment 6, 377–502 m), with Coefficient of Variation (CoV) ranging from 0.163 to 0.615, near-surface segments carry substantially greater relative uncertainty than deeper ones. All six segments are unimodal ($\Delta_{BIC} \leq 0$for Segments 1, 2, 3, 6; $\Delta_{BIC} \leq 2$ for Segments 4, 5), validating the use of Gaussian distributional models.

Table 1. Adaptive framework.

Steps	Methodology & criteria	Equations & Parameters
Change-point detection & domain segmentation Identify depth-related domains	Three algorithms applied to the σ_1 depth profile: - **PELT**: exact dynamic programming (penalized cost minimization) - **Binary Segmentation**: recursive splitting - **Bottom-Up**: agglomerative segment merging **Consensus**: ≥30% of configurations agree within ±30m; minimum 20 m separation enforced. **Sensitivity confirmed**: 20–50% threshold and ±20–40 m tolerance represents identical breakpoints. Segments classified via GMM BIC comparison (1-component vs 2-component Gaussian Mixture): Δ_{BIC}> 10 is multimodal, otherwise unimodal.	Eq. 1. $\sum_{i=1}^{m+1}[C(y_{s_{i-1}+1:s_i})+\beta]$ C(·) = within-segment sum of squared deviations s_i = change-point positions m = number of change-points β = complexity penalty Eq. 1a. $BIC = -2\cdot\ln(\hat{L})+k\cdot\ln(n)$ k = no. model parameters n = segment sample size Δ_{BIC}> 10 → multimodal
Bayesian Distributional Modeling Statistically characterize stress in all domains	**Goal**: characterize posterior of mean μ and std ς within each statistically uniform segment treated as homogeneous (by ΔBIC ≤ 2) Prior for μ centered on segment sample mean $\bar{x}_s$(weakly informative, allows data to dominate) **Implementation**: PyMC, 4 chains, 1500 draws,700 tuning steps per chain (NUTS sampler) **Model adequacy**: posterior predictive coverage PPC = fraction of observed σ_1 within 95% posterior predictive interval Target PPC ≥ 0.93; wide CI reflects data scarcity.	Priors, Eq. 2. $\mu \sim N(\bar{x}_s, 20)$ $\varsigma \sim HalfNormal(15)$ $\sigma_1^{(i)} \sim N(\mu, \varsigma)$ $\bar{x}_s$ = segment sample mean (weakly informative center) Adequacy check: PPC = $\lvert\{\sigma_1^{(i)} \in 95\%PPD\}\rvert$ / N Target: PPC ≥ 0.93
Hierarchical Bayesian Pooling Share data among segments	Segments with n ≤ 9 → **pooling needed** Three pooling strategies formally compared: **No pooling**: fully independent segment models **Full pooling**: single collapsed model (ignores between-segment differences) **Partial pooling** (optimal): hierarchical; middle ground between no- and full-pooling **Strength-borrowing**: sparse segments are pulled toward the global mean proportional to their data scarcity (automatic regularization) **Hyperpriors**: weakly informative, N(25,20) spans full σ_1 range, HalfNormal(15) ensures σ > 0.	Hyperpriors, Eq. 3. $\mu_{global} \sim N(25, 20)$ $\varsigma_{global} \sim HalfNormal(15)$ Segment means, Eq. 3a. $\mu_s \sim N(\mu_{global}, \varsigma_{global})$ s = 1, … , 6 Likelihood, Eq. 3b. $\varsigma_{within} \sim HalfNormal(15)$ $\sigma_1^{(i)} \sim N(\mu_s, \varsigma_{within})$ CI reduction metric Eq. 3c. 1 − pooled CI½ / unpooled CI½
Statistical Power and Data Adequacy + Decision Tree Confirm validity of sample size predictions	Minimum sample size N_{min} derived from: **95% CI half-width criterion** Three engineering **precision targets**:Δ = ±2 MPa, ±3 MPa, ±5 MPa Decision tree: four-tier method assignment:**Tier 0** (N < 8): insufficient data; **Tier 1** (unimodal,Coefficient of Variation(CoV)< 0.20, N < 25); **Tier 2** (unimodal, 0.20 ≤ CoV < 0.40); **Tier 3** (multimodal or CoV ≥ 0.40). **Output**: method label + data sufficiency flag	Eq. 4. $N_{min} = (z_{\alpha/2}\cdot\hat{\varsigma}/\Delta)^2$ $z_{\alpha/2}$ = 1.96 (95% conf.) $\hat{\varsigma}$= segment observed std Δ = target half-width (±2, ±3, or ±5 MPa) Phase CI targets (MPa): Ph1 ≤ 15 | Ph2 ≤ 10 Ph3 ≤ 7 | Ph4 ≤ 5 Decision tree inputs: {N, CoV, distribution type}

4.2 Bayesian Distributional Model Performance

Posterior predictive coverage ranged from 0.93 to 1.0 across all segments (Table 2), confirming well-calibrated models against the conventional benchmark that ≥ 95% of observed values fall within the 95% posterior predictive interval (Gelman et al. 2013). Coverage of exactly 1.0 in smaller segments (*n*=6–13) reflects wide predictive intervals relative to sparse observations, a consequence of high within-segment variability rather than model mis-specification. CI widths directly reflect data

availability: Segment 2 (n=26, CoV=0.271) achieves 4.25 MPa, while Segment 5 (n=6, CoV=0.487) yields 21.49 MPa, quantitatively identifying where additional measurements are most needed.

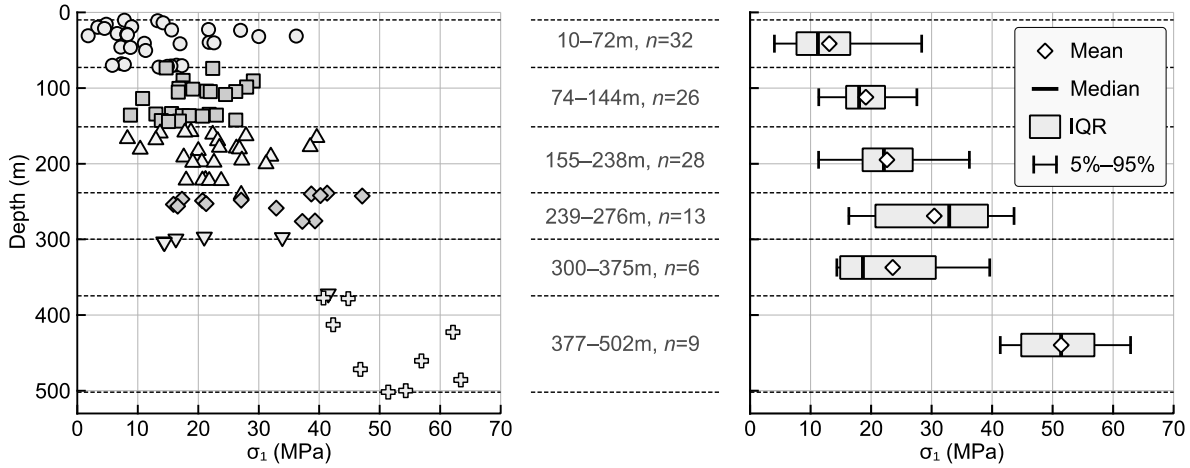


Fig.1 Multi-algorithm change-point detection and final 6-segment depth profile.

Table 2. Bayesian distributional model results.

Seg	N	μ posterior (MPa)	95% CI (MPa)	CI width (MPa)	PPC coverage	Seg	N	μ posterior (MPa)	95% CI (MPa)	CI width (MPa)	PPC coverage
1	32	13.08	(10.23, 15.98)	5.75	0.938	4	13	30.48	(23.38, 37.20)	13.81	1.000
2	26	19.18	(17.03, 21.28)	4.25	1.000	5	6	23.38	(12.21, 33.70)	21.49	1.000
3	28	22.61	(19.77, 25.39)	5.62	0.929	6	9	51.45	(45.07, 58.19)	13.12	1.000

4.3 Hierarchical Strength Borrowing

Partial pooling reduced the 95% CI half-width by 25% for Segment 5 (8.4 to 6.3 MPa) and by 26% for Segment 4 (5.75 to 4.28 MPa), the two most data-limited non-sparse segments (Fig. 2). Segment 2, μ = 19.1 MPa, deviates the most from the global mean (22.4 MPa), and partial pooling slightly increases the CI, a well-understood and expected regularization effect in hierarchical models (Gelman et al. 2013). These results confirm that hierarchical pooling is most beneficial precisely where data are scarce, which is the operationally relevant condition during early repository characterization phases.

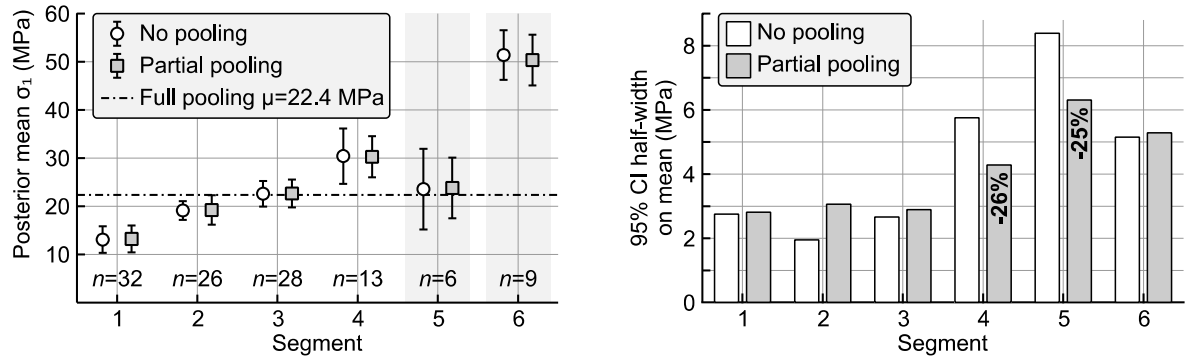


Fig. 2 Hierarchical Bayesian partial pooling: (a) no pooling vs partial pooling; (b) Uncertainty reduction from pooling.

4.4 Sample Size Requirements and Phase Adequacy

Minimum viable sample sizes vary substantially across segments (Table 3), driven entirely by within-segment variability. Segment 2 (ς = 5.18 MPa) requires only 5 measurements for ±5 MPa precision, while Segment 5 (ς = 11.47 MPa) requires 21 for the same tolerance and 57 for the stricter ±3 MPa engineering target.

To evaluate whether the current dataset meets engineering tolerance requirements at each stage of repository development, four characterization phases were defined based on cumulative measurement availability, as shown in Fig. 3 a: Phase 1, Preliminary Site Characterization (n = 17), Phase 2, Advanced Characterization (n = 38), Phase 3, Detailed Design (n = 65), and Phase 4, Final Validation (n = 114). These phases correspond to analytically defined sampling thresholds aligned with repository planning stages, not to specific excavation or in-situ verification events. The CI width achieved at each

phase (Fig. 3 b) is compared against pre-defined engineering tolerance targets (15, 10, 7, and 5 MPa respectively). As Table 3 shows, segment 5 (n = 6) falls below the minimum viable dataset even at the coarsest precision level, quantitatively identifying that future measurement campaigns should prioritize this segment.

Table 3. Minimum sample size requirements and current availability.

Seg.	N available	ς (σ_1 std MPa)	CoV	Min N (±5 MPa)	Min N (±3 MPa)	Min N (±2 MPa)
1	32	8.05	0.615	10	28	62
2	26	5.18	0.271	5	12	26
3	28	7.32	0.324	9	23	52
4	13	11.01	0.362	19	52	117
5	6	11.47	0.487	21	57	127
6	9	8.36	0.163	11	30	67

Extending this analysis to the full repository life-cycle, proportional sampling across all six segments was simulated at four characterization phases, with CI targets calibrated relative to the overall σ_1 standard deviation (12.7 MPa) to reflect realistic engineering tolerances at each stage (IAEA 2011; NEA 2008). All four phases meet their targets, with CI width decreasing progressively from 13.0 MPa at Phase 1 (n = 17, preliminary site characterization) to 4.7 MPa at Phase 4 (n = 114, final validation), answering the question of how much data are enough at each design stage (Fig. 3 a-b).The per-segment minimum sample size curves (Fig. 4) further show that requirements vary from 5 to 57 measurements at ±3 MPa precision, with Segments 4 and 5 remaining below their minimum thresholds at current data levels, confirming where future measurement efforts should be concentrated.

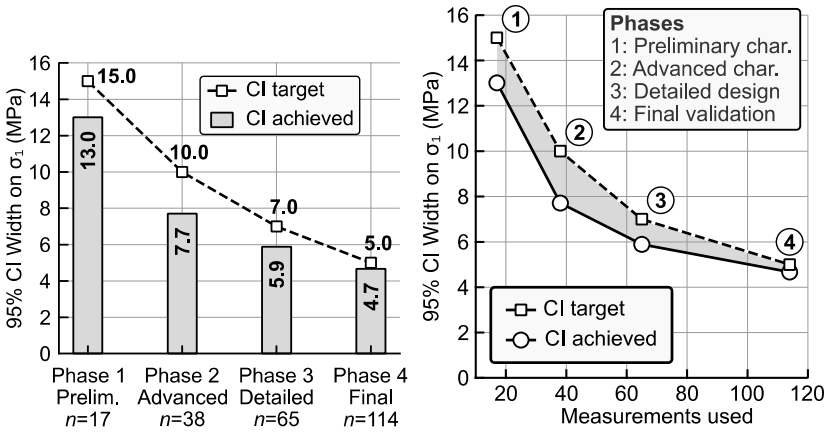


Fig. 3 Data requirements: (a) credible intervals vs. phase; (b) credible intervals vs. number of data.

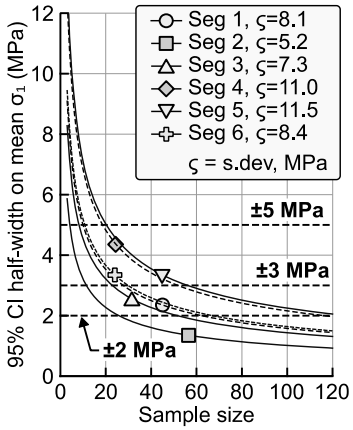


Fig. 4 Data adequacy at different repository life phase CI thresholds.

5 Discussion

The results demonstrate that depth-dependent segmentation is statistically appropriate for the Forsmark dataset, as uniform measurement density across all depths is both statistically unjustified and operationally inefficient given the order-of-magnitude variation in data requirements across segments. Measurement campaigns should therefore prioritize segment coverage before increasing local density.

The decision tree (Fig. 5) synthesizes all preceding results into explicit method-selection criteria per segment, from data-insufficient segments requiring additional measurements to well-sampled segments adequately characterized by single Gaussian models (Gelman et al. 2013). The hierarchical pooling provides an immediate practical tool for data-sparse segments: a 25% CI reduction is achieved for Segment 5 without any new measurements, indicating that this is a valuable interim strategy during early characterization phases. A limitation of this study is that validation is performed at a single site using overcoring data only. The specific breakpoint depths and segment statistics are site-specific; however, the framework itself, change-point detection, distributional modeling, hierarchical pooling, and power-based data adequacy, is site-independent and transferable to any stress measurement dataset.

6 Conclusions

This paper introduces an adaptive Bayesian-statistical framework that integrates change-point detection, distributional analysis, and hierarchical Bayesian modeling to optimize stress characterization strategies, and presents an example application of it using the Forsmark stress database. Multi-algorithm change-point detection identified six statistically justified depth segments, and Bayesian distributional models yielded well-calibrated segment-level posteriors (PPC coverage 0.93–1.0), with CI widths reflecting data scarcity and variability. Hierarchical partial pooling reduces the CI half-width by up to 25% for data-sparse segments, showing that this is an applicable strategy for uncertainty reduction strategy without additional measurements. The minimum sample size requirements were found to vary from 5 to 57 measurements per segment for ±3 MPa precision, demonstrating that uniform sampling strategies are statistically inappropriate and that spatial coverage across all depth segments is more critical than local measurement density. Finally, the framework is seen to be able to provide explicit quantitative decision criteria from preliminary characterization through final validation.

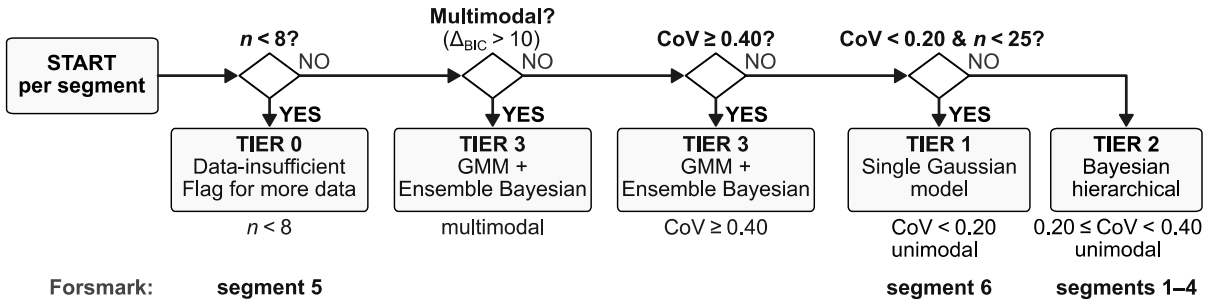


Fig. 5 Decision tree framework.

Acknowledgement

This research was jointly funded by NWMO and SKB. The authors gratefully acknowledge their financial support.

References

Amadei B, Stephansson O (1997) *Rock Stress and Its Measurement*. Chapman & Hall.

Baecher G.B, Christian J.T (2005) *Reliability and statistics in geotechnical engineering*. John Wiley & Sons.

Bao T, Burghardt J (2022) A Bayesian approach for in-situ stress prediction and uncertainty quantification for subsurface engineering. *Rock Mech. Rock Eng.*, *55*(8), 4531-4548.

Gelman A, Carlin J.B, Stern H.S, Dunson D, Vehtari A, Rubin D.B (2013) *Bayesian Data Analysis*. CRC Press.

Hudson J.A, Harrison J.P (2000) *Engineering Rock Mechanics: an introduction to the principles*. Elsevier.

IAEA (2011) *Geological Disposal Facilities for Radioactive Waste*. Intl. Atomic Energy Agency: SSG-14.

Martin C.D (2007) *Quantifying in situ stress magnitudes and orientations for Forsmark* (SKB Report R-07-26). Swedish Nuclear Fuel and Waste Management Company.

NEA OECD (2008) *Moving Forward with Geological Disposal of Radioactive Waste*, A Collective Statement by the NEA Radioactive Waste Management Committee (RWMC). Nuclear Energy Agency: Report 6433.

Phoon K.K, Kulhawy F.H (1999) Characterization of geotechnical variability. *Can. Geotech. J.*, 36, 612–624.

Sjöberg J, Figueiredo B, Hakala M (2025) *Reliability ranking of overcoring stress measurements at Forsmark.* SKB Report R-21-08. ISSN 1402-3091, Svensk Kärnbränslehantering.

Stephansson O, Ångman P (1986) Hydraulic fracturing stress measurements at Forsmark and Stidsvig, Sweden. *Bulletin of the Geological Society of Finland*, *58*(1), 307-333.

Unokiwedi O.P, Gao J, Bethune T, Awolayo A.N (2025) Deep geological repositories—A review of design concepts, near-field evolution, and their implications for nuclear waste containment. *J. Environmental Radioactivity*, *289*, 107750.

Wang J, Chen L, Su R, Zhao X (2018) The Beishan underground research laboratory for geological disposal of high-level radioactive waste in China: planning, site selection, site characterization and in situ tests. *J. Rock Mech. Geotech. Eng.*, *10*(3), 411-435.

Zoback M.D (2010) *Reservoir Geomechanics*. Cambridge University Press.

Examples of cliff failures along the shores of Mediterranean Sea and the role of bioerosion

S. Uğur
Firat University, Faculty of Fisheries, Elazığ, Türkiye
sugur@firat.edu.tr
0000-0001-8367-0920

Ö. Aydan
University of the Ryukyus, Nishihara, Okinawa, Japan

H. Kumsar
Pamukkale University, Departmen of Geological Engineering, Denizli, Türkiye

Abstract

It is known that some organisms can bore holes in rock formations consisting of such as limestone, sandstone, andesite and tuff. The authors investigated several sites along the Mediterranean Sea coasts and found many examples of rocks bored by organisms. The authors carried out some observations on bioerosion state and causes of rocks along sea-shores with cliffs in several locations of this region, particularly, Türkiye (Kuşadası Bay, Ekmeksiz Bay, Antalya, Ayvalık, Bodrum, Ören), Turkish Republic of Cyprus (from Magusa to Yeşilırmak), Croatia (Dubrovnik), Egypt (Alexandria) and Spain (Alicante). Rocks are various depending upon the geology of area surveyed. This study is concerned on the role of several organisms on the toe erosion along sea cliffs and their subsequent collapse. The erosion state and porous structure of some of rocks and their effect on their mechanical strength are assessed. Some available mechanical stability assessment methods are utilized to evaluate stability state of the stable and collapsed cliffs surveyed and their implications and findings are discussed. It is shown that the cliff stability can be assessed with the incorporation of the role of bioerosion.

Keywords

Bioerosion, cliffs, Mediterranean Sea shores, Organism, Rocks.

1 Introduction

It is reported that some organisms can bore holes in rock formations consisting of such as limestone, sandstone, andesite and tuff (e.g., Uğur and Aydan et al, 2023, 2024). The authors investigated some sites in the Ryukyus Islands, Japan and carried out some observations on bioerosion state and causes of rocks along sea-shores with cliffs in several major islands of Ryukyu Archipelago (Uğur and Aydan, 2023, 2024). They now extended their studies to several countries having the shores of Mediterranean Sea. These countries are Türkiye, Turkish Republic of Cyprus (TRC), Egypt, Croatia, Greece and Spain (Figure 1).



Fig. 1 Investigated locations of bioerosion state of rocks in Mediterranean Sea, Aegean Sea and Adriatic Sea.

Rocks are various depending upon the geology of area surveyed and they include limestone, sandstone, andesite and tuff. The erosion state and porous structure of rocks and their effect on their mechanical strength are assessed (Uğur and Aydan, 2023, 2024). Some available mechanical stability assessment methods proposed by Aydan and his colleagues are utilized to assess the stable and collapsed cliffs surveyed with the consideration of the state of rock masses (RMQR) and bio-erosion rates(Aydan, 2020; Aydan and Kawamoto 1992; Aydan et al. 2014; Horiuchi et al. 2019; Tokashiki and Aydan 2010, 2011).The methods involve numerical methods (such as classical finite element method (FEM) and sophisticated discrete finite element method (DFEM) as well as the physical and photo-elasticity model tests under static and dynamic conditions and analytical methods for cliffs as described in the publications of the authors since 1989. In addition, the authors recently initiated multiparameter dynamic monitoring system for cliffs in Miyagi Island of Ryukyu Archipelago (Aydan et al. 2025). The most likely mechanism would be the dissolution of constituents of rocks by the mechanical excavation or enzyme/salvia produced by these organisms and their subsequent discharge of debris from the holes as the UCS of rocks are generally greater than 25MPa. The length of bored holes ranges generally between 5 and 15 cm with a diameter of 1 to 25 mm. The bored rock sites are found to be within the tidal and splash zones.

Besides, the action of sea waves resulting from hurricanes and typhoons imposing some impact type forces, porous structures resulting from bored holes by organisms cause the strength reduction and cyclic degradation, which can be evaluated from the method proposed by the authors (Uğur and Aydan, 2023, 2024) and utilized in this study. Therefore, the cliff stabilityshould be assessed with the incorporation of the role of bioerosion in addition wave induced erosion and other causes. This study is concerned withbioerosion resulting from bivalve and other organisms and its effect on sea cliffs and their subsequent collapses at several sites along the Medirrenean Sea. It is anticipated that this study might be quite unique by bringing different disciplines of science and engineering together to these special kind problems and provide some scientific answers to the problems encountered in nature.

2 Organisms causing bioerosion

Boring bivalves: Some boring bi-valves range in size and they can be up to 80-100 mm in length and they have an ovoid shape shell as seen in Figure 2(a). Borer bivalve species use mechanical or chemical means to bore holes. They have mantle tissue and a foot modified for rapid and effective digging. They use not only their foot for burrowing into sediment but also erodes the substrate by acid secreted from mantle tissue.

Chitons: Chitons have a shell composed of separate shell plates, which overlap slightly at the front and back edges. While the shell structure provides a protection, it allows the chiton to flex upward when they need to over uneven surfaces (Figure 2b). They live on or under rocks, or in rock discontinuities. They eat algae on rock surfaces by scraping with their well-developed radulae resulting in bioerosion.

Limpets: Limpets are categorized as a group of aquatics nails with a conical shell shape and a strong, muscular foot. They live on hard rock surfaces in the intertidal zone and they are capable of moving over the hard surfaces (Figure 2c). They have teeth known as radula, which allows limpets to scrape off algae from rock surfaces, which results in bioerosion.

Crabs: Crabs live in seas, in freshwater, and on land (Figure 2d). They are generally covered with a thick exoskeleton, and have a single pair of pincers, six walking legs and two swimming legs. They often live in nearly all caves and crevices (discontinuities) on rocky sea shores.

Sea Urchins: Sea urchins are found on the seabed of every ocean and live at every depth zone from the intertidal seashore down to 5,000 meters. The shells of sea urchins are of rounded ovoid shape and covered in spines. While the primary diet of sea urchins isalgae, sea urchins may also eat slow-moving animals. The sea-urchins excavate V-shaped holes into rock as seen in Figure 2e. These V-shaped holes can grow in size and depth.

Gastropods: Gastropods are categorized as slugs and snails (Figure 2f). They live in the environment of saltwater, freshwater, and the land. The excretion of gastropods eventually results in ammonia or uric acid as a waste product, which is the main cause of the bioerosion. Furthermore, by the virtue of their radula teeth, they contribute to the overall biological wear process, even though they do not leave wear marks visible to the naked eye.

Polychaetes: Polychaetes are categorized as marine worms and they are segmented with a length generally less than 10cm. They are one of the well-known bioeroders in carbonate rocks. Polychaetes use both chemical secretions and mechanical excavation for dissolving the rocks. They cause long curved holes in rock, which results in a porous structure (Figure 2g).

Sponges: Sponges are prominent bioeroders on coral reefs and excavating sponges are demosponges, which have a siliceous skeleton. Sponge bioerosion involves initially chemical etching of $CaCO_3$ chips and acid regulation, later mechanical removal of the chips from the substrate (Figure 2h).

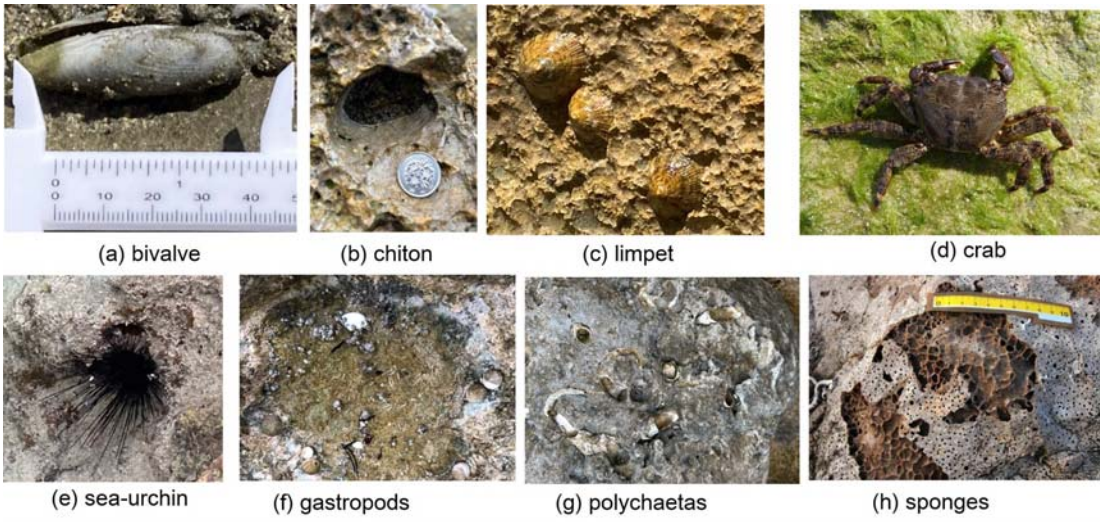


Fig. 2 Views of major organisms causing bioerosion.

3 Observations of the organisms and erosion at some locations along the Mediterranean Sea

The organisms causing bioerosion mentioned in Section 1 are observed at various localities along the shores of Mediterranean Sea investigated by the authors and the localities are marked in Figure 1. The bioerosion processes are fundamentally the same as those observed by the authors as well as others (Uğur and Aydan 2023, 2024; Alwany et al. 2009; Kázmér and Taboroši 2012). The picture of an Onyx vase displayed in a Museum in Alexandria is of great interest and one can easily notice bioerosion on the onyx vase recovered from the seabed along the shore of Mediterranean Sea.

4 The mechanism of bioerosion on cliff failures and some examples

In this section, we discuss how to model the bioerosion due to various organisms. As shown by Uğur and Aydan (2023, 2024), organisms habit within the tidal and splash zonesfor a typical cliff. Organisms such as bivalves, sponges, fishes, sea-urchins and polychaetas impose their bioerosion

actions on rocks below the low-tide level. The bio-rosion action of chitons, limpets and crabs will appear within the intertidal zone. This zone is generally about 2-3 m from the mean sea level. The effect of gastropods may also be observed above the high-tide bioerosion level. Nevertheless, this height might be restricted to the height of the splash zone.

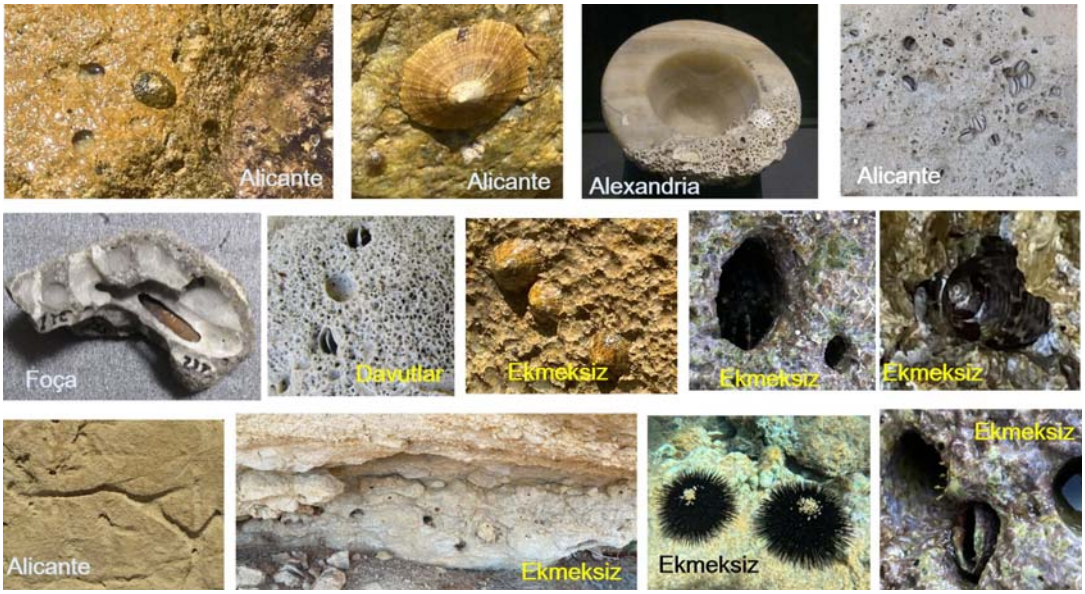


Fig. 3 Views of some organisms causing bioerosion in investigated localities.

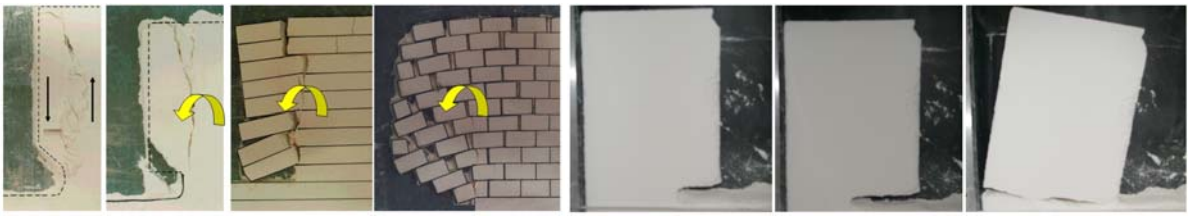
As discussed by Uğur and Aydan (2023, 2024), the bioerosion fundamentally results in a porous zone next to rock surface for a given depth. This rock becomes weaker within this zone due to porous structure, and the impact forces resulting from seawaves. Furthermore, the intrusion and extrusion of seawaters into pores further also weaken the porous zone. As these actions are progressive and cyclic, the weakened rock zone eventually collapses. Besides the mechanical action of winds and seawaves, the bioerosion result in the erosion of the cliff toe. This erosion would cause a cantilever-like rock structure. When the depth of the toe erosion reaches to a certain depth, the cliff fails under gravity and seismic forces. Uğur and Aydan (2023, 2024) proposed a mathematical model in order to consider the effect of bioerosion on the stability of cliffs. This model considered the effect of bioerosion on cliffs to be a linear erosion (l) with time. Thus, this situation is mathematically expressed as:

$$l = \lambda \cdot t \qquad (1)$$

where λ, t are coefficients depending upon rock type and time, respectively. Particularly, the evaluation of erosion rate require long-term observations and this aspect should be investigated in a multi-disciplinary procedure as done in this study.

5 The mechanism of cliff failures and Back-analyses

The cantilever-like cliffs with toe erosion may fail due to bending, shearing or the both as observed on Earth and Mars (Aydan 2020, 2022, 2023; Aydan et al. 1989; Aydan and Tokashiki 2016). Depending upon the distribution and number of discontinuity sets, they fail in several modes as shown in Figure 4a,b. In some cases, vertical discontinuities resulting from stress release may exist and this would result in the toppling of the column (Figure 4b). Figure 5 shows several examples of collapsed cliffs in the investigated localities. As noted, most of collapsed cliffs failed in bending mode.



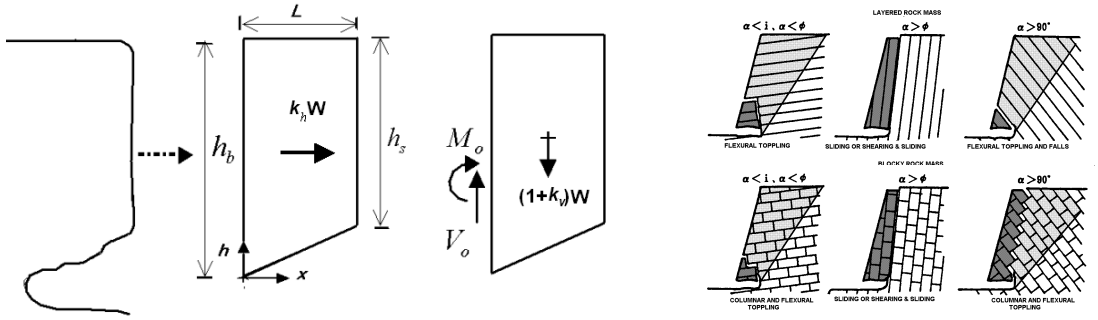
(a) Failure of continuum, layered and jointed cliffs (b) Various stages of a cliff having vertical discontinuity

Fig. 4 Views of model experiments on cliffs with toe erosion.

The mechanical model shown in Figure 6a would be the simplest for analyzing the stable and unstable cliffs with toe erosion. Under gravitational condition with/without seismic force, the limiting erosion depth (L) can be related to the cliff height (H) for bending and shear failure modes and they may be classified as continuum, layered or jointed rock masses (Aydan 2020). However it should be noted that the existence of discontinuities may also results in other forms of failure such as sliding, toppling and/or combined toppling and sliding as illustrated in Figure 6b (e.g., Horiuchi et al. 2019).



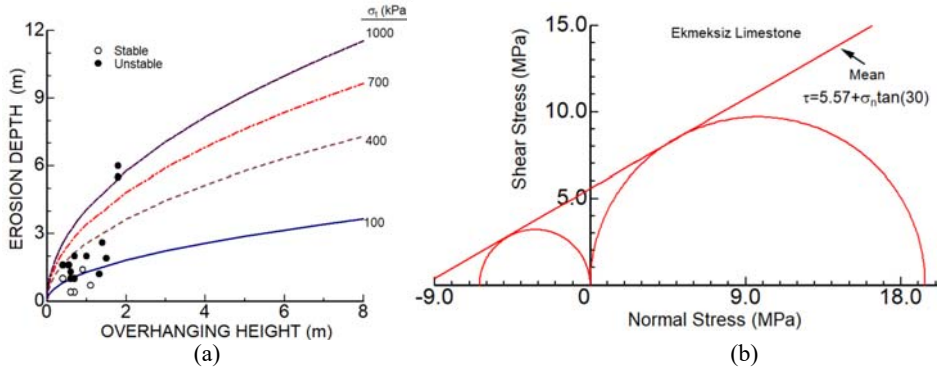
Fig. 5 Examples of cliff failures observed at several investigated localities.



(a) The cantilever model (from Aydan 2020) (b) Failure modes of cliffs with layered and jointed rock mass

Fig. 6 Mechanical models for stability assessment of cliffs and their failure modes with layered and jointed rock mass.

The results of back-analyses for cliffs at Ekmeksiz Bay, Türkiye are shown in Figure 7a. The authors gathered some rockblocks made of limestone from the site and carried out Brazilian and Uniaxial compression tests. The experimental results utilized in the back-analyses. Figure 7b shows the Mohr-Coulomb yield criterion for the limestone outcropping at Ekmeksiz Bay, Türkiye. The back analyses imply that the tensile strength of rock mass is greater than 100 kPa. Despite the tensile strength of the intact limestone was 6.4 MPa, the existence of discontinuities and high porosity resulting from bioerosion as well as from other actions resulted in the great reduction of the mass strength in accordance with the strength estimation from the RMQR rock classification system (see Aydan et al. 2014; Aydan and Tokashiki, 2016; Tokashiki and Aydan 2010 for details).



(a) (b)

Fig. 7 (a) Back-analyses results of stable and unstable cliffs; (b) Mohr-Coulomb yield criterion for intact limestone at Ekmeksiz Bay.

6 Conclusions

The authors carried outsome observations on bioerosion state and causes of rocks along sea-shores with cliffs in several locations along the shores of Mediterranean Sea. Some of conclusions from this study as follows:

Bioerosion occurs due to chemical and mechanical or both erosive activities of the organisms. The effect of bioerosion is mainly observed within the intertidal zone and/or close vicinity. In addition, the toe-erosion is highly affected by impact forces caused by winds and high seawaves.

The reduction of strength of rock mass is related to the porous structure caused by the cyclic bioerosion. The estimated strength reduction was due to bioerosion and the porosity increase due to the bioerosion was between 15-35% from the back-analyses of failed cliffs.

This study is a multi-disciplinary study between the fields of Biology, Rock Mechanics and Rock Engineering. As noted from the material presented, needless to say that there is still a great necessity to investigate the bioerosion rates caused various organisms in various rockformations as well as environmental conditions, quantitatively.

Acknowledgements

The authors sincerely acknowledge Dr. Ali KIRTIK of Ege University for guiding the authors to sites in the vicinity of İzmir and sharing his samples with the authors.

References

Alwany, A. Magdy, A., Ellen Thaler andMichael Stachowitsch (2009). Parrotfishbioerosion on Egyptian Red Seareefs. Journal of Experimental Marine Biologyand Ecology 371, 170–176.

Aydan, Ö. 2020. *Rock Mechanics and Rock Engineering: Applications.* Vol.2, CRC Press, Taylor and Francis Group, 379p, ISBN 978-0-367-42162-5.

Aydan, Ö. (2022). Some thoughts on slope stability issues in Mars, EUROCK2022, Helsinki, Finland, 8p.

Aydan, Ö. (2023). Some Rock Dynamics Issues in Mars. 49th Rock Mechanics Symposium of Japan, 36-41.

Aydan, Ö. and Kawamoto T. 1992. The stability of slopes and underground openings against flexural toppling and their stabilization, Rock Mechanics and Rock Engineering, Vol. 25, Issue 3, pp. 143-165, 1992.

Aydan, Ö., N. Tokashiki (2016). The evaluation of stability of overhanging Ryukyu limestone cliffs utilizing rock mass characteristics inferred from RMQR and intact rock, EUROCK2016, Ürgüp, 601-606.

Aydan, Ö., T. Kyoya, Y. Ichikawa, T. Kawamoto and Y. Shimizu (1989). A model study on failure modes and mechanisms of slopes in discontinuous rock mass. *The 24th Annual meetings of Soil Mechanics and Foundation Eng. of Japan,* Miyazaki, 415, 1089-1093.

Aydan, Ö., Ulusay, R. & Tokashiki, N. 2014. A new rockmass quality rating system:Rock Mass Quality Rating(RMQR) and its application to the estimation ofgeomechanicalcharacteristics of rock masses. *Rock Mech RockEng* 47: 1255–1276.

Aydan, Ö. Tokashiki, N., Ito, T. Shuri, Y. (2025). Multi-parameter response monitoring of a cliff at Miyagi Island of Okinawa Prefecture, Japan and the responses during earthquakes. EUROCK2025, Trondheim, ISBN 978-82-8208-079-8, 8p.

Horiuchi, K,. Ö. Aydan, N. Tokashiki, NZ Nasiry (2019). Some considerations on the causes of cliff failures of Ryukyu Limestone in Ryukyu Archipelago and the analysis of a recent cliff failure. Geotechnical Journal, Japan Society of Civil Engineers, Vol. 75, No. 2, 216-233.

Kázmér, Miklós and Danko Taboroši (2012). Bioerosion on the small scale –examples from the tropical and subtropicallittoral. Monostori Jubilee Volume, Hantkeniana 7, 37-94, Budapest.

Tokashiki, N. Aydan, Ö.2010. The stability assessment of overhanging Ryukyu limestone cliffs with an emphasis on the evaluation of tensile strength of Rock Mass. *Journal of Geotechnical Engineering*, JSCE, 66(2),397-406.

Tokashiki, N. and Aydan, Ö. 2011.A comparative study on the analytical and numerical stability assessment methods for rock cliffs in Ryukyu Islands. *The 13thInternational Conf. of the International Association for Computer Methods and Advances in Geomechanics,* Melbourne, 663-668.

Uğur, S. and Aydan, Ö. 2023. The mechanism of bioerosion and its effect on sea-cliffs (in Turkish). *Yer Mühendisliği*, No. 19, Year 11, June, 38-47.

Uğur, S. and Aydan, Ö. 2024. The possible role of the bioerosion on the stability of sea cliffs in Ryukyu Archipelago. EUROCK2024, Alicante, 716-721.

Integrated Petrographic and Sorption Analysis of Pore Morphology in Sub-bituminous Coals

A. Tripathy
Indian Institute of Technology (ISM) Dhanbad, Dhanbad, Jharkhand, 826004, India
ashutosh@iitism.ac.in
0000-0001-7253-2960

M. Mazumder
Indian Institute of Technology (ISM) Dhanbad, Dhanbad, Jharkhand, 826004, India
0009-0005-6020-3656

T.N. Singh
Indian Institute of Technology, Patna, Bihta, Dayalpur, Bihar, 801106, India
0009-0005-7159-631X

Abstract

The generation and migration of CBM occur in the nanoscale pore found in coals. Nonetheless, the extreme compactness and multifaceted characteristics of nanopores remain poorly understood in terms of their morphology. In this study, coal samples were collected from Jharia coalfield, India. 2D image analysis, geochemical analysis, and low-pressure N_2 adsorption (LPNA) studies were used to examine the morphological parameters of the pore that influence it. According to the petrographic analysis, vitrinite is the dominant group among all macerals in samples (mean 62%), with a notable proportion of liptinite (24%) maceral group, whereas the concentration of inertinite group is the lowest (12.5%). Values of Vitrinite reflectance range from 0.54% to 0.61%, whereas ash content varies between 45.9 and 55.1%, volatile matter ranges from 31.1 to 37.1%, and moisture content varies from 7.1 to 9.2%, indicating that Jharia coal is of sub- bituminous 'B' rank. The primary pore types identified by the microphotographic image observation are the interparticle pores, the intraparticle pores, and the microcracks. Volume of pore ranges from 0.000277 to 0.029754 cm^3 /g, whereas values of SSA range between and m^2/g. From rock-eval pyrolysis result, value of the HI ranges from 201 to 209 mg HC/g TOC, whereas the T_{max} ranges from 423 to 429. HI vs. T_{max} data indicates that samples are thermally mature and type II kerogen in nature. TOC varies from 63.59% to 66.8% wt%. From a rock mechanical standpoint, the heterogeneity in pore morphology and maceral composition indicates variable stress sensitivity and deformation behavior under in-situ conditions. From the above results, it can be shown that total organic carbon is positively and negatively related with pore parameters, indicating that TOC has the greatest influence on pore characteristics and suggesting a significant hydrocarbon potential. Our results strengthen the experimental basis for understanding coal nanopore structure.

Keywords

Coal, Maturity, Coal Bed Methane, Maceral, Organic matter.

1 Introduction

CBM (Coal Bed Methane)gas produced by thermogenic and/or biogenic processes is mostly stored in situ as free gas (found in pores, cracks and fractures) and adsorbed gas (found on organic matter) (Curtis, 2002; Jarvie et al., 2007). Due to the presence of a wide variety of pore sizes with different shapes, types and origins, pore system is usually complex and heterogeneous in coal (Loucks et al., 2009, 2012; Clarkson et al., 2013). On the basis of relationship between pore and mineral particles, coal matrix-related pores can be categorized as interparticle pores between mineral grains and crystals, intraparticle pores within mineral particles, and organic matter pores (Loucks et al., 2012). As it may have negative impact on the CBM exploration in reservoir, it is imperative to precisely characterise the pore development characteristics in various organic materials.

The properties and controlling parameters of pore morphology in reservoir rocks have been determined by several researchers in recent years. For example, Loucks et al. (2009, 2012) noted that thermal maturity primarily regulates the development of organic matter (OM) pores. According to Milliken et al. (2013) and Jarvie et al. (2007), Type I and type II kerogen have a greater capacity to produce hydrocarbons than type III kerogen, which may make them more susceptible to pore generation. According to Yang et al. (2014), Total organic carbon (TOC) regulates specific surface area and methane adsorption ability of coal and coal measure rocks. Recent studies have stated that maceral composition may have an impact on the heterogeneous development of OM pores (Tripathy et al., 2026; Cao et al., 2018; Liu et al., 2017; Ardakani et al., 2018; Wood et al., 2018). The Permian coal reservoir, containing Barakar formation and Raniganj formation in Damodar valley is regarded as a desirable target for CBM exploration (Du et al., 2015; Pan et al., 2015, Mazumder et al., 2024b, 2024c,2026), because of its wide regional extent, shallow burial, large thickness (100–600 m), abundant OM, and moderate maturity. The findings of this investigation have implications for our understanding of pore generation in various OM materials. It is informative for Permian CBM reservoirs and has implications for evaluating gas exploration of the Permian coals and favourable intervals in the Damodar valley (Tripathy et al., 2018a, 2018b, 2019).

2 Methodology

Air-dried, finely crushed (<212 μm) coal samples were used for proximate analysis in accordance with ASTM guidelines. BET isotherms and hysteresis analysis were used to assess the pore size distribution, surface area, and pore morphology using low-pressure N_2 and CO_2 adsorption procedures. The Details of methodological procedure is provided in Tripathy et al., 2018c, Mazumder 2024a. Using the S_1, S_2, S_3, and T_{max} parameters, Rock-Eval pyrolysis was used to assess the amount, kind, and thermal maturity of organic matter. Reflected light microscopy was also used to estimate maceral composition and vitrinite reflectance ($R_{0,max}$), which provided information about coal petrography and maturity.

3 Result

The low-pressure liquid nitrogen adsorption experiment was used to determine the morphological characteristics of pore, including pore volume, specific surface area, and average pore diameter. Based on IUPAC classification, adsorption isotherm curves in Figure 1 (a). shows type B and type D hysteresis (Thommes et al., 2015). Barakar formation coal consists of slit shaped pore, whereas Raniganj formation coal contains bottle-neck pores.

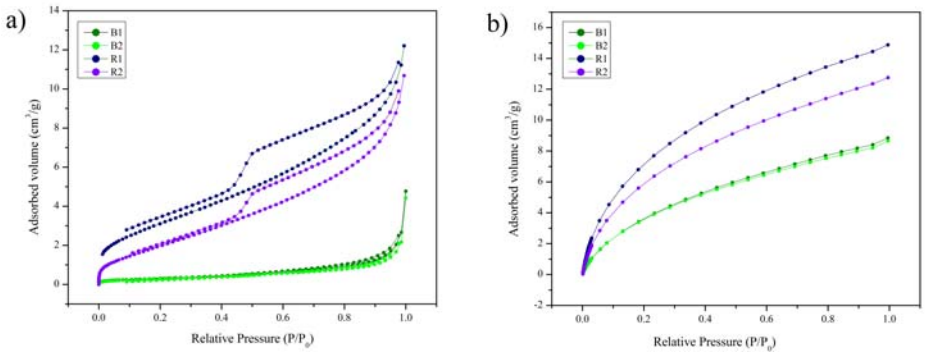


Fig. 1 Isotherm curves from LPGA a) LP-N_2 A isotherm curves. b) LP-CO_2 A isotherm curves.

Important metrics for describing reservoir characteristics and their adsorption capacity are the SSA and PV. SSA of samples ranges from 2.75 to 11.83 m^2/g whereas TPV of samples ranges between 0.003 to 0.02cm^3/g. Values of APD ranges from 6.39 to 24.9 nm. Figure 3 shows that the TPV and SSA have a significant positive correlation, whereas the TPV and SSA decrease as APD rises. This suggests that pores with lower APD create higher TPV and SSA (Chalmers et al., 2012; Yang et al., 2014; Fu et al., 2015; Liu et al., 2015). PSD of samples has been calculated based on BJH model (Xi et al., 2017). Samples from Barakar formation shows multimodal distribution, whereas Raniganj formation samples show bimodal distribution (Fig.2).

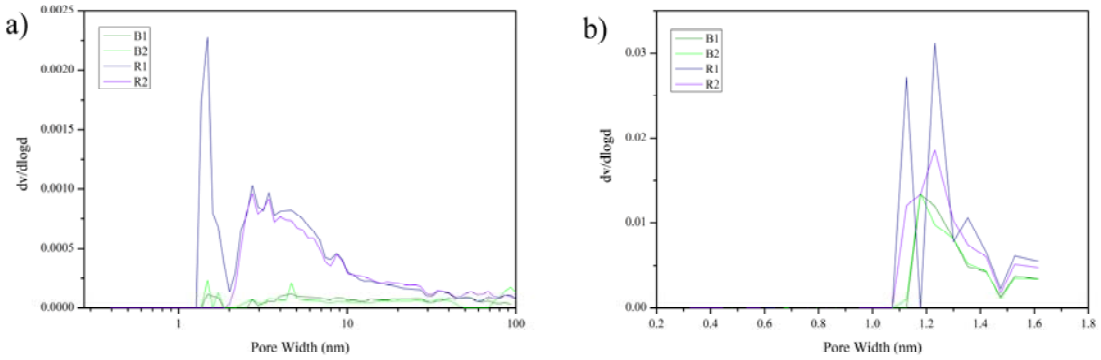


Fig. 2 PSD of coal samples based on LPGA. a) PSD from LP N_2 A. b) PSD from LP CO_2 A.

According to IUPAC, the adsorption curves from LP-CO_2 A in fig 1(b) exhibits the type I isotherm. Based on DFT model, pore characteristics of micropore has been determined. SSA ranges from 18.94 to 39.82 m^2/g and pore volume varies between 0.0089 to 0.0174cm^3/g. PSD of samples shows bimodal distribution.

The most crucial fractal theory parameter, fractal dimension D is computed by computing the various fractal models and is frequently used to quantitatively describe the roughness and structural complexity of pores. The Frenkel-Halsey-Hill (FHH) model is the three most often used fractal model.

Table 1 displays the Rock-eval pyrolysis parameters and TOC content of the samples under study. The average TOC content is with a range of 58.65% to 69.58%. T_{max} and R_0 (%) values of Barakar formation ranges from 462 to 481 °C and 1.14 to 1.24, and Raniganj formation coal varies between 422 and 426 °C and 0.63 to 0.68, indicating that Barakar coals are mature coal and Raniganj coals are immature coal (Pan et al., 2015).

Table 1. Rock eval pyrolysis data of coal.

Sample ID	TOC (wt %)	S1 (mg HC/g rock)	S2 (mg CO_2/g rock)	S3	Tmax (ºC)	HI (mg HC/g TOC)	OI
B1	58.65	1.30	123.89	0.43	481	211	0.78
B2	62.24	2.20	152.59	0.91	462	244	1.48
R1	69.58	0.43	250.23	1.30	422	359	2.98
R2	67.86	0.91	228.48	0	426	337	0.07

The range of vitrinite reflectance (R_0) of studied coal is from 0.66 to 1.2, as seen in Table 2, suggesting that the samples are sub-bituminous coal of middle rank. With a volume ranging from 46.0

to 67.0% (av. 57.5%), vitrinite dominates the coals, surpassing inertinite (15.0–38.0%, av. 25.25%) and liptinite (9.0–15.0%, av. 11.5%), as evidenced by table 2., which displays the maceral groups and elemental composition and fractal characteristics of the coals.

Table 2. Elemental composition, maceral contents and fractal characteristics of coal.

Sample ID	R_0 (%)	Moisture content (%)	Ash content (%)	Volatile matter (%)	Vitrinite (%)	Inertinite (%)	Liptinite (%)	D_{V1}	D_{V2}
B1	1.24	2.45	57.11	16.40	67	15	12	2.39	2.57
B2	1.14	2.29	53.42	19.23	62	17	15	2.3	2.68
R1	0.68	6.45	47.23	31.41	55	31	9	2.41	2.80
R2	0.63	5.35	47.01	35.47	46	38	10	2.21	2.75

4 Discussion

4.1 Effect of Organic Matter on Pore Development

Primary factors affecting the evolution of pore structure in CBM reservoirs during diagenesis are TOC content, kerogen type and degree of thermal maturity (Curtis et al., 2012; Ross and Bustin, 2009). Porosity in coal can be classified into organic and inorganic based on the origin. Secondary pores like OM pore are developed from kerogen during the generation of hydrocarbon. Some researchers suggested positive relationship between TOC and BET SSA, but in our study, TOC is negatively related with SSA. However, in case of samples containing TOC>10%, BET SSA shows a declining trend with increasing TOC. In our study, same thing has been noticed (Fig.3 (a)). Suggesting the contribution of factors other than organic matter in formation of pore.

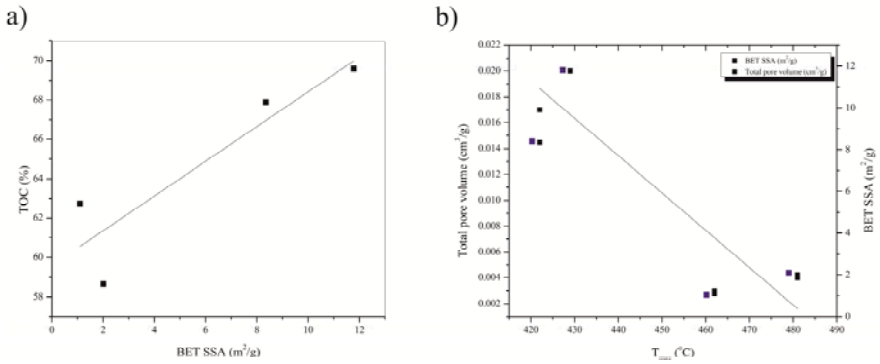


Fig. 3 a) Relationship between organic matter and BET SSA. b) Effect of T_{max} on pore parameters.

4.2 Effect of Thermal Maturity in Evolution of Pore Structure

Pore parameters are significantly affected by degree of thermal maturation. Fig. 3 (b) demonstrates that as Tmax increases, the TPV and SSA of coal's pore decrease. This suggests that as OM maturity rises, the development level of each type of pores decreases as well, leading to a drop in porosity and TPV in the over-mature stage. As graphitization in organic matter reduces the potentiality of hydrocarbon generation, it is responsible for the decrement in the proportion of organic matter.

4.3 Effect of Maceral Composition on pore parameters

Pore parameters can vary in different macerals within same coal. Fig. 4(a) shows inertinite content is positively associated with BJH TPV whereas vitrinite is negative correlated, suggesting that inertinite has greater effect on pore volume than vitrinite. Micropores generally develop in vitrinite, whereas macropores can be found in plant tissues like woody plant cell walls, within inertinite. So, in contrast with inertinite and liptinite, vitrinite has higher amount of micropores. Pore parameters can vary in different macerals within same coal. Fig. 4 (a) shows inertinite content is positively associated with BJH TPV whereas vitrinite is negative correlated, suggesting that inertinite has greater effect on pore volume than vitrinite.

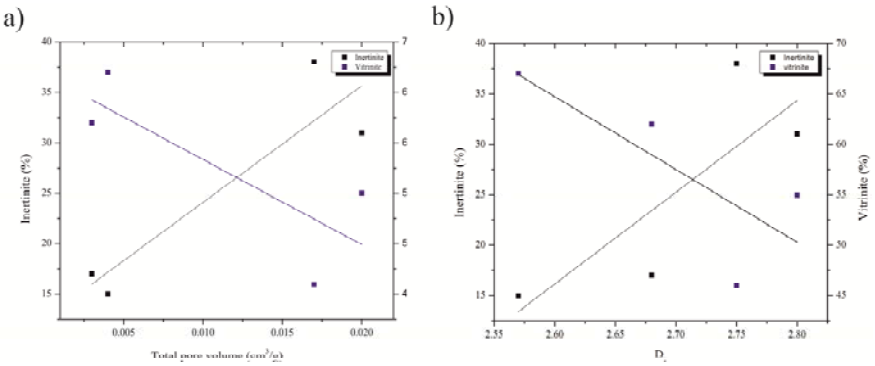


Fig. 4 a) Relationship between maceral contents and pore parameters. b) Relationship between maceral contents and fractal characteristics.

Fig. 4 (b) Coal's fractal dimension provides a thorough representation of its internal structure of pore. It also explains the relationship between complicacy of pore structure differs with different maceral compositions. Value of D_v increases with increasing inertinite content and decreases with increasing vitrinite content suggesting that pore morphology become complex with enrichment of inertinite in coal. However, no relationship has been observed between D_s and maceral composition.

5 Conclusion

- Low pressure N_2 adsorption analysis reveals that the majority of the pores in the coal samples from Raniganj formation are bottle-neck shaped, whereas Barakar formation coal mainly consists of slit shaped pores. The majority of pore volume is contributed by micropores, which make up 65.23% to 70.69%, followed by mesopore and macropore, respectively
- As BET SSA shows a declining trend with increasing TOC, suggesting the contribution of factors other than organic matter in the formation of pores.
- Vitrinite and inertinite have different pore structures with variety of pore size, which suggests a propensity for pore size alter. Inertinite content is positively related with total pore volume, whereas vitrinite is negatively associated with pore volume. Increment in values of D_v suggest that pore complexity gradually increases with increasing inertinite content.
- Outcomes of this study are particularly relevant to the characterization of Permian coalbed methane (CBM) reservoirs and have significant implications for assessing gas exploration potential in Permian coal fields.

References

Ardakani, O. H., Sanei, H., Ghanizadeh, A., Lavoie, D., Chen, Z., & Clarkson, C. R. (2018). Do all fractions of organic matter contribute equally in shale porosity? A case study from Upper Ordovician Utica Shale, southern Quebec, Canada. Marine and Petroleum Geology, 92, 794-808.https://doi.org/10.1016/j.marpetgeo.2017.12.009

Chalmers, G. R., Bustin, R. M., & Power, I. M. (2012). Characterization of gas shale pore systems by porosimetry, pycnometry, surface area, and field emission scanning electron microscopy/transmission electron microscopy image analyses: Examples from the Barnett, Woodford, Haynesville, Marcellus, and Doig units. *AAPG bulletin*, *96*(6), 1099-1119.DOI:10.1306/10171111052

Clarkson, C. R., Solano, N., Bustin, R. M., Bustin, A. M. M., Chalmers, G. R., He, L., ... & Blach, T. P. (2013). Pore structure characterization of North American shale gas reservoirs using USANS/SANS, gas adsorption, and mercury intrusion. Fuel, 103, 606-616.https://doi.org/10.1016/j.fuel.2012.06.119

Curtis, J. B. (2002). Fractured shale-gas systems. AAPG bulletin, 86(11), 1921-1938.

Curtis, M. E., Sondergeld, C. H., Ambrose, R. J., & Rai, C. S. (2012). Microstructural investigation of gas shales in two- and three-dimensions using nanometer-scale resolution imaging. AAPG bulletin, 96(4), 665-677. DOI:10.1306/08151110188

Du, X., Song, X., Zhang, M., Lu, Y., Lu, Y., Chen, P., ... & Yang, S. (2015). Shale gas potential of the Lower Permian Gufeng Formation in the western area of the Lower Yangtze Platform, China. *Marine and Petroleum Geology*, *67*, 526-543.https://doi.org/10.1016/j.marpetgeo.2015.05.031

Fu, H., Wang, X., Zhang, L., Gao, R., Li, Z., Xu, T., ... & Li, Q. (2015). Investigation of the factors that control the development of pore structure in lacustrine shale: a case study of block X in the Ordos Basin, China. *Journal of Natural Gas Science and Engineering*, *26*, 1422-1432.DOI:10.1016/j.jngse.2015.07.025

Jarvie, D. M., Hill, R. J., Ruble, T. E., & Pollastro, R. M. (2007). Unconventional shale-gas systems: The Mississippian Barnett Shale of north-central Texas as one model for thermogenic shale-gas assessment. *AAPG bulletin*, *91*(4), 475-499.DOI:10.1306/12190606068

Liu, B., Schieber, J., & Mastalerz, M. (2017). Combined SEM and reflected light petrography of organic matter in the New Albany Shale (Devonian-Mississippian) in the Illinois Basin: A perspective on organic pore development with thermal maturation. *International Journal of Coal Geology*, *184*, 57-72. DOI:10.1016/j.coal.2017.11.002

Liu, X., Xiong, J., & Liang, L. (2015).Investigation of pore structure and fractal characteristics of organic-rich Yanchang formation shale in central China by nitrogen adsorption/desorption analysis.*Journal of natural gas science and engineering*, *22*, 62-72.10.1016/j.jngse.2014.11.020

Loucks, R. G., Reed, R. M., Ruppel, S. C., & Hammes, U. (2012). Spectrum of pore types and networks in mudrocks and a descriptive classification for matrix-related mudrock pores. *AAPG bulletin*, *96*(6), 1071-1098.DOI:10.1306/08171111061

Loucks, R. G., Reed, R. M., Ruppel, S. C., & Jarvie, D. M. (2009). Morphology, genesis, and distribution of nanometer-scale pores in siliceous mudstones of the Mississippian Barnett Shale. *Journal of sedimentary research*, *79*(12), 848-861.doi.org/10.2110/jsr.2009.092

Mazumder, M., & Tripathy, A. (2024b). Study on the pore morphology and fractal features of coal from Raniganj coalfield, India using gas adsorption and FE-SEM analysis. In *New Challenges in Rock Mechanics and Rock Engineering* (pp. 909-914). CRC Press.

Mazumder, M., Bal, A., Tripathy, A., Liu, S., & Singh, T. N. (2024a). Multiscale Assessment of Transformation in Pore System of Shale during Combustion: An Insight into Poromechanical Response and Sorption Dynamics. *Energy & Fuels*, *38*(18), 17510-17524.doi.org/10.1021/acs.energyfuels.4c02383

Mazumder, M., Tripathy, A., & Singh, T. N. (2024c, January). Quantitative Evaluation of Sub-Bituminous Coal from Jharia Basin, India: Investigation Using Low Pressure N2 and CO2 Adsorption. In *International Conference on Geotechnical Issues in Energy, Infrastructure and Disaster Management* (pp. 649-658). Singapore: Springer Nature Singapore.

Milliken, K. L., Rudnicki, M., Awwiller, D. N., & Zhang, T. (2013). Organic matter–hosted pore system, Marcellus formation (Devonian), Pennsylvania. *AAPG bulletin*, *97*(2), 177-200.

Pan, L., Xiao, X., Tian, H., Zhou, Q., Chen, J., Li, T., & Wei, Q. (2015). A preliminary study on the characterization and controlling factors of porosity and pore structure of the Permian shales in Lower Yangtze region, Eastern China. *International Journal of Coal Geology*, *146*, 68-78.10.1016/j.coal.2015.05.005

Ross, D. J., & Bustin, R. M. (2009). The importance of shale composition and pore structure upon gas storage potential of shale gas reservoirs. *Marine and petroleum Geology*, *26*(6), 916-927.https://doi.org/10.1016/j.marpetgeo.2008.06.004

Thommes, M., Kaneko, K., Neimark, A. V., Olivier, J. P., Rodriguez-Reinoso, F., Rouquerol, J., & Sing, K. S. (2015). Physisorption of gases, with special reference to the evaluation of surface area and pore size distribution (IUPAC Technical Report). *Pure and applied chemistry*, *87*(9-10), 1051-1069.DOI 10.1515/pac-2014-1117

Tripathy, A., Srinivasan, V., & Singh, T. (2018a, April). Pore Size Distribution of shale using Advanced Analytical Techniques. In *EGU General Assembly Conference Abstracts* (p. 1010).

Tripathy, A., Srinivasan, V., & Singh, T. (2018b, June). Pore Characterization of Cambay Shale Using Low-pressure Gas Adsorption and MIP Analysis. In *80th EAGE Conference and Exhibition 2018* (Vol. 2018, No. 1, pp. 1-5). European Association of Geoscientists & Engineers.

Tripathy, A., Srinivasan, V., & Singh, T. N. (2018c). A comparative study on the pore size distribution of different Indian shale gas reservoirs for gas production and potential CO2 sequestration. *Energy & Fuels*, *32*(3), 3322-3334.DOI: 10.1021/acs.energyfuels.7b04137

Tripathy, A., Kumar, A., Srinivasan, V., Singh, K. H., & Singh, T. N. (2019). Fractal analysis and spatial disposition of porosity in major indian gas shales using low-pressure nitrogen adsorption and advanced image segmentation. *Journal of Natural Gas Science and Engineering*, *72*, 103009.10.1016/j.jngse.2019.103009

Wood, J. M., Sanei, H., Haeri-Ardakani, O., Curtis, M. E., Akai, T., & Currie, C. (2018). Solid bitumen in the Montney Formation: Diagnostic petrographic characteristics and significance for hydrocarbon migration. *International Journal of Coal Geology*, *198*, 48-62.

Xi, Z., Tang, S., Zhang, S., & Sun, K. (2017). Pore structure characteristics of marine–continental transitional shale: A case study in the Qinshui Basin, China. *Energy & Fuels*, *31*(8), 7854-7866.DOI: 10.1021/acs.energyfuels.7b0091

Yang, F., Ning, Z., & Liu, H. (2014). Fractal characteristics of shales from a shale gas reservoir in the Sichuan Basin, China. *Fuel*, *115*, 378-384.https://doi.org/10.1016/j.fuel.2013.07.040

Uniaxial compressive strength and durability of sandstones and marls with varying moisture content

S. Dugonjić Jovančević, M. Vivoda Prodan, J. Peranić, I. Ružić
University of Rijeka, Faculty of Civil Engineering, Rijeka, Croatia
sanja.dugonjic@uniri.hr
0000-0002-0242-7409

Abstract

The compressive strength of sedimentary rocks varies significantly with moisture content. In this study, Point Load Tests (PLT) and corresponding Uniaxial Compressive Strength (UCS) correlations were determined for marl and sandstone samples with varying water contents, tested in two pilot areas in the northern Adriatic.

The specimens were collected from the coastal zone where cyclic wetting and drying occurs, influencing the mechanical stability of the rock mass. Samples were tested in their in situ condition, after 24 hours, and after one week of wetting. PLT on irregular samples and Slake Durability Test were performed in the Geotechnical Laboratory at the Faculty of Civil Engineering, University of Rijeka following the standardized procedures.

Marls testing results indicate a clear reduction in UCS with increasing water content, while Slake Durability Tests revealed high resistance to low disintegration of marls under cyclic environmental conditions. On the other hand, sandstone samples have shown varying behaviour, depending on the period of sampling, initial water content and moisture penetration regimes. The results indicate that the mechanical properties of the rock mass are significantly affected by its heterogeneity and the environmental conditions in which it occurs. Furthermore, they emphasize the need to account for additional controlling factors to improve the interpretation of index test results and to validate the mechanical behaviour of surface materials exposed to marine environmental conditions.

Keywords

Uniaxial Compressive Strength, Point Load Test, water content, Slake Durability Testing.

1 Introduction

1.1 Geological context

Research is performed on two pilot areas: Havišće Bay in the Kvarner area (Fig.1B), and Brovinje Bay on the Istrian Peninsula (Fig.1C). According to the geological map of the Republic of Croatia (CGI, 2009), pilot areas are built in Liburnian deposits, foraminiferal limestones and siliciclastic rocks (flysch) of Paleogene age (Vlahović and Velić 2009). Havišće Bay is partly built-in stable limestone rock, and unstable flysch rock mass on the other hand. The cover consists of decomposed marls and more resistant sandstone fragments weakly attached to the slope material or separated underneath the slope. Brovinje Bay is mostly formed of thick layered marls of varying weathering degree (Fig. 2).

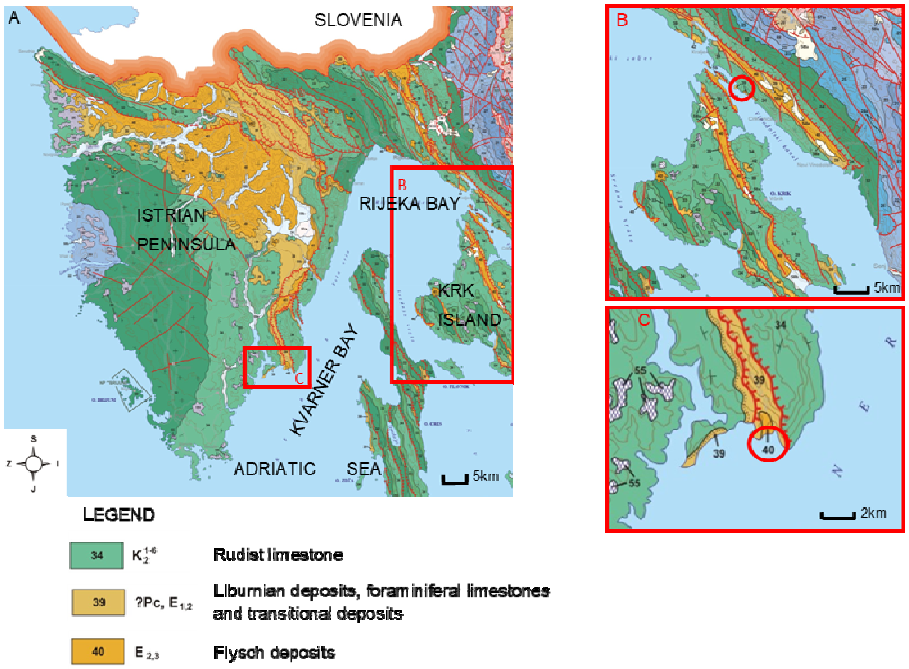


Fig. 1 Pilot area locations on the geological map of the Republic of Croatia Scale 1:300,000 (CGI, 2009).

1.2 Sampling locations

The rock samples were collected at three locations in Havišće Bay, and two locations in Brovinje Bay. All the samples were transported in plastic bags to the laboratory and protected from changing in humidity, kept in laboratory conditions, until the testing. First samples were taken in June: Brovinje marls (L1BJ and L2BJ) and Havišće sandstones (L1HJ, L2HJ, L3HJ). Second sampling of Havišće sandstones was repeated in October (L1HO, L2HO) to study the seasonal effect on the testing properties.

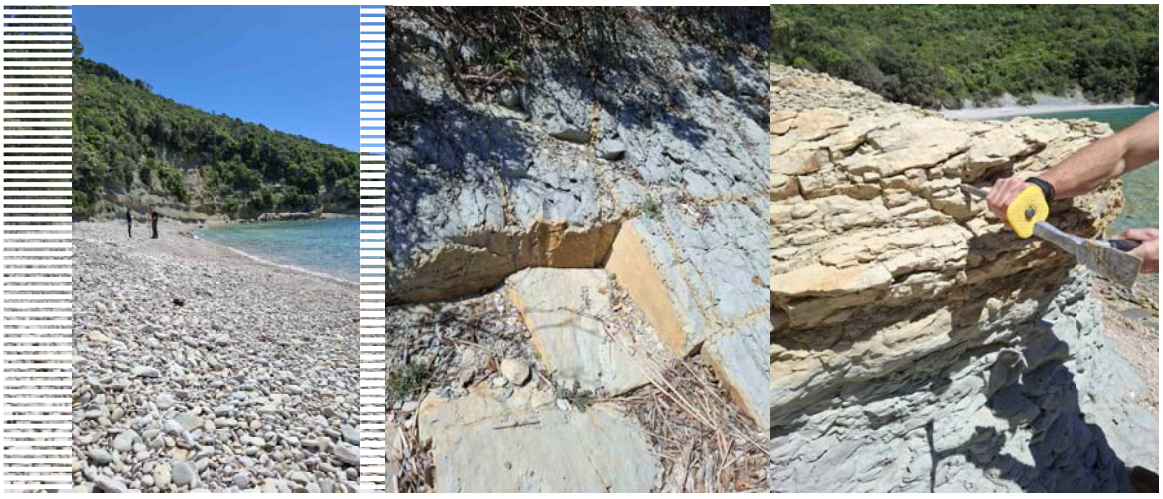


Fig. 2 Brovinje Bay pilot area (left) with visible marls outcrops (middle -L1BJand right photo- L2BJ).

The Brovinje Bay (Fig.2) samples were taken at one sheltered location (L1B) and another location exposed to waves and wind (L2B). Homogeneous marl rock blocks of varying colour were detached using chisel and a hammer (light olive grey to light bluish grey at L1B, and greyish orange to pale

yellowish brown at L2B). Havišće Bay (Fig 3.) samples are mostly homogeneous sandstones, superficially orange to yellowish brown colour, and mostly grey inside. First group of sandstone samples were blocks weakly bound on the unstable and partly collapsed slope (L1HJ/L1HO), another group was collected at the base of the slope (L2HJ/L2HO), and the last one from the weakly bound cover layer (L3HJ). It is important to emphasize that the sandstones samples were highly heterogeneous and that the samples differed from one another in terms of their degree of weathering and mineralogical composition.



Fig. 3 Havišće Bay pilot area (left) with visible sandstone outcrops (middle-L1H and right photo-L2H and L3H).

2 Laboratory and field testing

Uniaxial Compressive Strength was estimated based on a *Point Load Test(PLT)* and ISRM (1985) standardized procedure for irregular sample testing, which corresponds to in situ water content, water content after 24h and 7 days wetting. One part of the samples was also tested after 24 hours of drying. Digital PLT apparatus, from the Geotechnical laboratory, at the Faculty of Civil Engineering in Rijeka was used to perform the testing. The mean value of $I_{s(50)}$ was calculated by deleting the two highest and lowest values from 10 or more valid tests, and calculating the mean of the remaining values. Used index-to-strength conversion factor (β) is 21.4 for marls (Lashkaripour 2002) and 21.9 for sandstones (Singh et al. 2012). Field identification testing of marl rock, was also performed on the Brovinje site using geological and *Schmidt hammer*. At both sampling locations, it was determined that more than one blow of geological hammer was required to fracture the rock, corresponding to strong rock (R4) i.e. uniaxial compressive strength 50-100 MPa (Brown, 1981). L type Schmidt hammer, and the ISRM (1981) suggested procedure were used to calculate the rebound number Rn. The *Slake Durability Test* procedure was carried out in accordance with the ASTM standard (2004) and repeated for the desired number of cycles (n) to determine the durability index I_{dn}. Slake durability index values that are taken after three or more cycles of slaking and drying may be useful for evaluating rock durability so five cycles were applied to each sample from Brovinje site.

3 Results

3.1 Brovinje marls

Obtained mean UCS at Brovinje marls at both testing locations at natural humidity and after 24h wetting is shown in Table 1. PLT testing has shown that the samples were superficially quite soft during the testing, and the cone penetrated into the samples up to over 7mm before cracking. It is visible that moisture penetrated only a small part of the cross-section, mainly at the edges, to a few millimetres (Fig.4.). The natural humidity of the taken samples was 1.5% and 1.57% (at L1BJ, and L2BJ), while the moisture content after 24h of wetting increased to 2,5% and 1,9% correspondingly. It was determined that after a 24h wetting process, the UCS for samples from L1BJ decreased around 2%, and for samples from L2BJ around 3,7%, what confirms that it is necessary to test a larger number of samples to draw precise conclusions. According to the field testing, the average Schmidt rebound number is Rn=27,8, what taking into account the Sight et al. (1983) relation, gave the estimated UCS value of 55.6 MPa.

Table 1. Comparison of strength properties for the marl samples tested at Brovinje site.

Sampling location	**UCS (MPa)- natural humidity**	**UCS (MPa)- 24h wetting**
L1BJ	33,53	32,86
L2BJ	47,05	45,32



Fig. 4 Wet samples after breaking: a) L1BJ; b) L2BJ.

The results of the performed Slake Durability Tests at Brovinje marls are presented in Table 2, The remained samples were not fragmented and appeared to be low degraded after two and five cycles, corresponding to high I_{d2} and I_{d5} values. According to Gamble's classification (1971), the sample from L1BJ can be classified as very high durable, and the rock mass atL2BJas high durable.

Table 2Results of the Slake Durability Testsat two locations samples from Brovinje site.

No. of cycle	**I_d, L1BJ (%)**	**I_d, L2BJ (%)**
1st cycle	99.18	96.45
2nd cycle	*98.57*	*95.71*
3rd cycle	98.27	95.24
4th cycle	97.99	94.87
5th cycle	97.45	94.27

3.2 Havišće sandstones

It can be noticed that some samples, apparently of greater weathering degree, cracked irregularly due to PLT testing, because of barely visible microcracks. More worn brownish areas inside some samples were visible. The cone in the wet samples was significantly indented during testing (up to 30mm), and some samples began spalling near the surface at higher pressures. The natural humidity of the samples at location L1HJ was 0,97%, on the location L2HJit was 0,76%, and on the location L3HJ 0,94%. The moisture content of the samples after 24 h of wetting increased, and was 2,29%, 2,09% and 1,49% correspondingly. The UCS values increased after 24h drying from 75,10MPa to 111,52 MPa (48,5%) at L1HJ, and from 66,21 MPa to 86,34 MPa (30,4%) at L2HJ. The mean UCS value obtained from natural humidity samples at L3HJ is 56.50 MPa. The results of the post-drying testing at L3HJ were not considered as relevant (only 4 samples were tested). After 24h of wetting the results show that the UCS values decreased expectedly (Table 3). Compared to dry samples the strength decreased for 46,4% at the L1HJ, and 42,9% at theL2HJ. The samples from L3HJ after 24h wetting the UCS value was similar as natural water content value (57,37 MPa), but, again, it wasn't considered as relevant because few samples were tested.

Sandstone samples collected in October show mean UCS value of 55MPa at L1HO and 54,13 MPa at the L2HO. The natural humidity of the samples at L1HO was 1,68%, while the natural humidity on the L2HO was 1,41%. The moisture content of the samples after 24h of wetting increased, and was 2,19% for the L1HO and 2,23% for the L2HO. After 7 days of wetting the moisture content increased to 2,64% and 2,70% for locations L1HO and L2HO correspondingly. The sandstone specimens show a clearly defined darker zone, indicating water penetration after wetting. The penetration front is irregular but well delineated, forming a lens-shaped to asymmetric saturated zone. Water ingress is partial, not fully saturating the specimen, which suggests heterogeneous cementation or grain packing and capillary-controlled flow through the intact rock pores (Fig. 5A). Dark brownish zones on the

failure surface indicate on the presence of the mineralogically distinct, iron-oxide–rich or more fine-grained layer in some samples (e.g., Fig. 5B).

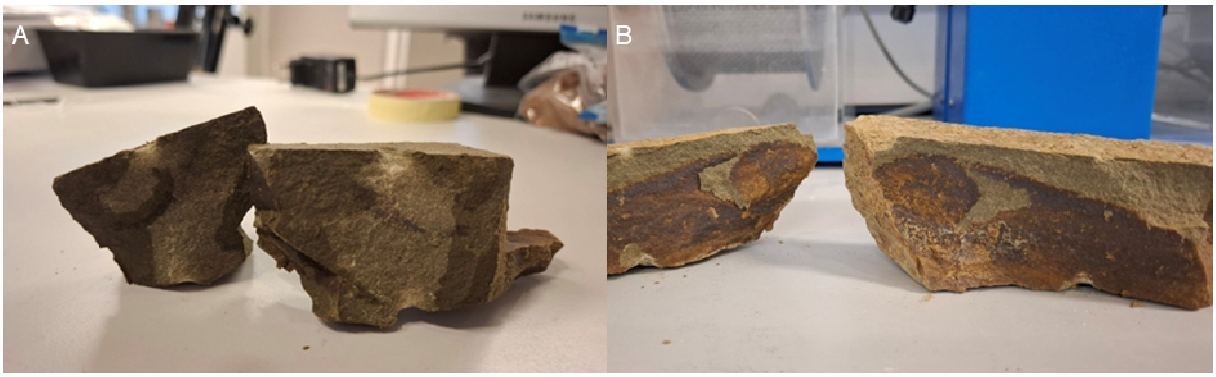


Fig. 5 Sandstone sample after testing: a) different water penetration patterns; b) dark brownish traces on the failure surface.

While it was expected that increased moisture content would result in a reduction of the PLT Index, the results obtained at the L1HO did not confirm these expectations. After 24h wetting, the results show that the UCS values increased to 68,70MPa at location L1HO and to 67,41MPa at the location L2HO (Table 3).

Table 3. Comparison of strength properties for the samples tested in June and October.

Sampling location	**UCS (MPa)-natural w**		**UCS (MPa)-24h wetting**		**UCS (MPa) - 7 days wetting (2 cycles of drying and wetting)**	**UCS (MPa) - 7 days wetting (one cycle of drying and wetting)**
	June	October	June	October	October	October
L1H	75,10	55,00	59,82	68,70	86,61	74,55
L2H	66,21	54,13	49,34	67,41	66,94	54,30

In comparison with the testing performed in June, the natural water content in October at L1H andL2H was around 1% larger than in the case of the specimens tested in the summer period. The samples collected in June show significant change in water content after the 24h wetting, while the samples collected in October show lower water content change after 24h wetting. Since only the group of samples collected in October was exposed for the 7-day wetting, it cannot be compared to sampling in June, and it can be concluded that the water content after 7 days of wetting increased from the natural state for both locations (Table 4).

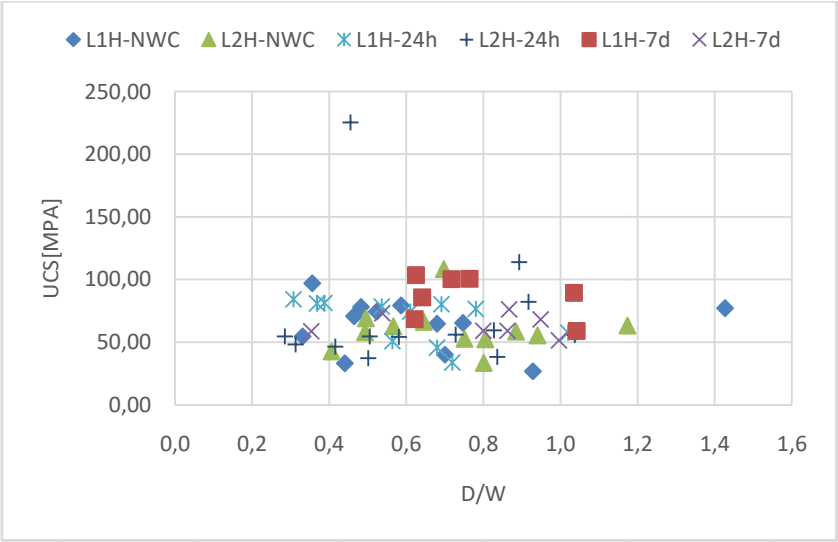


Fig. 6 Sandstone mean UCS values considering different D/W ratio.

Different specimen slenderness (hight/width ratio D/W) for all tested samples in June and October(same location and wetting conditions) wasanalysed (Fig. 6). Ratios lower than 0.3 and greater than 1.0 were not considered (according to the ISRM recommendations). Generally, it can be concluded that the tested group of samples doesn't show dependence of the mean UCS value of the D/W ratio.

Table 4. Changes in water content during different periods and wetting processes.

Sampling location	w (%)-natural		w (%)-24h wetting		w (%)-7 days wetting
	June	October	June	October	October
L1H	0,97	1,68	2,29	2,19	2,64
L2H	0,76	1,41	2,09	2,23	2,70

4 Conclusions

The performed testing indicates on the basic strength and durability properties of marls and sandstones at the pilot areas. The estimated marls UCS decreased with the increase in water content, and the samples were classified as very high to high durable. The sandstones collected and tested in June (L1HJ and L2HJ), have shown increase in UCS values after 24h of drying and expectedly decreased UCS values after short-term wetting (24 h), i.e., classical weakening effect, as predicted in the rock mechanics theory. What was surprising, samples tested in October after 24 h /7 days wetting have shown UCS equal or higher than in the natural condition. The corresponding irregular and mostly surface water penetration may be the cause of the obtained results. The results indicate that the heterogeneity of the investigated samples affected the test outcomes. However, the number of samples is insufficient to draw robust conclusions. It can be seen that the water ingress was partial and did not fully saturate the specimen, suggesting a heterogeneous moisture distribution and a failure surface comprising both wetted and non-wetted areas (Fig 5a). Another influencing factor can be the period of sampling and the corresponding natural water content, since the samples in October were taken after a rainy period, unlike the sampling in June 2025, after a dry and hot period. Other factors, that have not been considered systematically in this analysis, and that might have influence on the PLT results, are mineralogical composition, lamination, grain-size bands and other. It can be concluded that more samples with systematic consideration of all influencing factors should be considered to draw further conclusions and to validate the influence of the marine environment on the mechanical characteristics of the surface materials in parts of the bay more or less exposed to drying and wetting process.

Founded by the European Union-NextGeneration EU-BRAVE-uniri-iz-25-42 and the Interreg project RESONANCE.

References

ASTM (2004) Standard test method for slake durability of shales and similar weak rocks (D4644-87), Philadelphia

Brown ET (1981) Rock Characterization, Testing and Monitoring – ISRM Suggested Methods, Oxford: Pergamon Press, 171-183

Croatian Geological Institute (2009): Geological map of the Republic of Croatia M 1:300,000. – Croatian Geological Institute, Department of Geology, Zagreb

Gamble JC (1971) Durability-plasticity classification of shales and other argillaceous rocks. Ph.D Thesis. University of Illinois

ISRM (1981) Suggested methods for determining hardness and abrasiveness of rocks. In: Brown ET editor. Rock characterization, testing and monitoring: ISRM suggested Methods. Oxford: Pergamon; 1981. p. 95–6.

ISRM (1985) Suggested method for determining Point Load Strength, Int.J.Rock Mech. Min. Sci. &Geomech. Abstr. Vol 22, No 2, pp 51-60, Pergamon press Ltd, Great Britain.

Lashkaripour GR (2002) Predicting mechanical properties of mudrock from index parameters. Bull EngGeol Environ 61:73–77

Singh RN, Hassani FP, Elkington PAS (1983) The application of strength and deformation index testing to the stability assessment of coal measures excavations. Proceedings of 24th US symposium on rock mechanics, Texas A & M Univ, AEG, 599–609

Singh TN, Kainthola A, Venkatesh A (2012) Correlation between point load index and uniaxial compressive strength for different rock types. Rock Mech Rock Eng 45:259–264

Velić and Vlahović (2009) Interpreter of geological maps 1:300,000. – Croatian Geological Institute, Zagreb, 147 pp.

Damage characteristics of thermally treated sandstone using the block punch index test

Sourav Das, Ratan Das & Debasish Mazumder
Rock Mechanics and Rock Engineering Laboratory, Department of Geology,
Cotton University, Guwahati, Assam 781001, India
gly2391001_sourav@cottonuniversity.ac.in
0000-0002-9623-9408

Abstract

The strength characteristics of rock represent an important parameter in geotechnical and engineering applications. While the uniaxial compressive strength (UCS) test is widely utilized, it requires extensive sample preparation and difficulties in evaluating the strength properties of weak, foliated rocks. As an alternative, the Block Punch Index (BPI) test is suitable for thinly bedded rocks; however, the effect of BPI on thermally treated rock remained unexplored.

This research investigates BPI strength variations on calcareous sandstone that have been heated under the range of temperatures upto 800° C, maintained in a muffle furnace for 6 hours, and then cooled to room temperature. The results indicated that with the increase in temperature, the BPI value of the rock decreases, from 15.13 MPa at 25°C to 5.75 MPa at 800 °C. A maximum BPI strength around 22.21 MPa was recorded for the sample treated at 500 °C, as grain expansion fills pores and fissures, making the rock denser and thereby increasing the strength of the specimen. Beyond that, the strength reduction continued till 800° C due to the development of microcracks, as confirmed with linear crack density analysis of the microphotographs. The mechanical degradation of the rock exhibited a non-linear pattern across the entire temperature range tested. Moreover, the porosity of the specimen has increased from 3.16% (room temperature) to 11.76% at 800 °C. In addition, color transitions from grey to rust red were observed, due to iron oxidation. Furthermore, an endothermic peak was observed around ~760-780 °C, which must be due to the decomposition of $CaCO_3$ into CaO.

These findings will provide essential information on the physico-mechanical properties of sandstone, with practical implications for engineering applications such as geothermal energy extraction, nuclear waste disposal, and underground coal gasification.

Keywords

Block punch index test, Thermal treatment, Sandstone, Strength degradation.

1 Introduction

The study of thermal alterations to the physico-mechanical properties of rocks is important in various engineering fields, such as geothermal energy extraction, underground coal gasification (UCG), and nuclear waste disposal (Sirdesai et al. 2017). The study of the physico-mechanical properties of hot dry rock (HDR) is one of the important types of research in the process of geothermal energy development (Li et al. 2024). Therefore, it is important to understand the behavior of rock after thermal treatment. Geothermal energy is a sustainable, clean, and stable energy source that does not affect air quality and, therefore, serves as an alternative source to fossil energy (Xie et al. 2020; Feng et al. 2020; Long et al. 2021). Geothermal energy within the first 10 km of Earth's upper crust is about 1.3 x 10^{27} J, and this could supply global energy for approximately 217 million years (Lu 2018). Han et al. (2019) studied the effects of rapid thermal cycling (RTC) on the physical and mechanical properties of sandstone subjected to temperatures ranging from 100˚C to 800˚C. The results indicate that as temperature increases, both the P-wave velocity and sandstone density decrease, with the P-wave velocity showing a greater reduction than density. Additionally, the uniaxial compressive strength and elastic modulus of sandstone were observed to change in a similar pattern with increasing temperature after RTC treatments.

The generation of heat flux from high-level nuclear waste for an extended period increases the temperature of the surrounding rock. Gautam et al. (2019) investigated the thermal properties of Jalore granite for nuclear waste repository using the transient plane source technique. The result indicated that thermal conductivity, thermal diffusivity, mass loss, and elastic wave velocity of Jalore granite decrease gradually as the temperature increases from 25-250 °C.Hu et al. (2022) studied the effects of thermal shock fatigue on the physico-mechanical properties of limestone. The results show that the p-wave velocity, thermal conductivity, and tensile strength of limestone decrease with increasing temperature at a constant number of thermal cycles. Zhang et al. (2026) developed a new multidimensional rock integrity coefficient system to investigate the potential granite host site for a repository in China. The result tracked over a 100-year period, revealing a progressive degradation of integrity parameters under decaying thermal load, with identifiable inflection points at 10 and 40 years.

The gasification of coal, under site conditions, is conducted at temperatures above 700˚C. The temperature in the cavity may reach temperatures as high as 1500˚C (Sirdesai et al. 2015). Deng et al. (2022) found the influence of the cooling rate on the physical and chemical properties of granite heated at 25-800˚C. It is found that water-cooled specimens exhibit more acoustic emission (AE) signals and larger cracks than natural-cooled specimens, as confirmed by the b-value method. Polarized light microscopy reveals higher crack density and connectivity under water cooling. X-ray diffraction (XRD) analysis shows no significant changes in mineral content or diffraction angle, indicating that mechanical property changes are unrelated to chemical properties. Akdag et al. (2023) investigated the dynamic Mode I fracture toughness tests using a split Hopkinson pressure bar (SHPB) on Cracked Chevron Notched Semicircular Bend (CCNSCB) granite specimens. The results showed that fracture initiation toughness and energy distribution are strongly influenced by loading rate and temperature. Higher loading rates changed the failure modes from axial splitting to pulverization.

Many researchers have utilized different mechanical analyses to evaluate the strength of thermally treated specimens, with Uniaxial compressive strength (UCS) test being the most used approach. However, the UCS test requires extensive specimen preparation, which is difficult for thinly bedded, foliated rocks or those containing fossil fragments. In such cases, obtaining a recommended standard-size specimen becomes challenging. As an alternative, the block punch index (BPI) test provides a practical and efficient method for strength analysis of rocks. Moreover, the studies investigating the behavior of thermally treated specimens using the BPI test remain limited. Hence, this research will fulfill the knowledge gap by examining the mechanical strength of thermally treated calcareous sandstone with the BPI test, along with linear crack density, porosity, and DSC analysis.

2 Materials and methods

Field and laboratory investigations were conducted to attain the research objectives. The present research is illustrated in the methodology flow chart in Fig. 1.

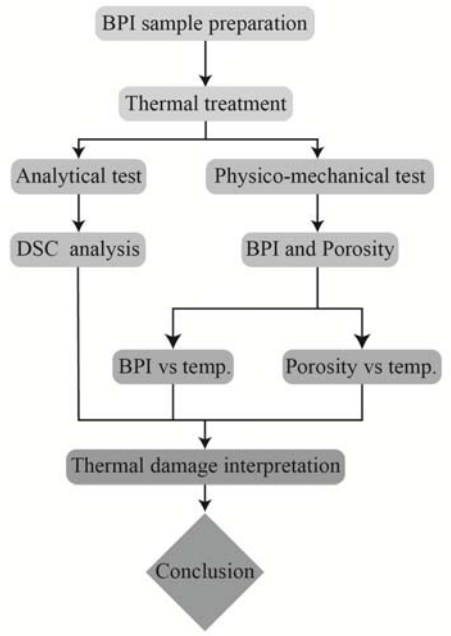


Fig. 1 Methodology flow chart.

2.1 Field visit and sample preparation

Field-collected sandstone samples(from NH-207, Dawki road (22°13′37.11″ N 91°57′44.85″ E) within the East Khasi Hills district of Meghalaya, Northeast India, near Sohlong village (Fig. 2)), have been processed in the laboratory to obtain BPI samples of uniform dimensions for thermal and physico-mechanical testing.

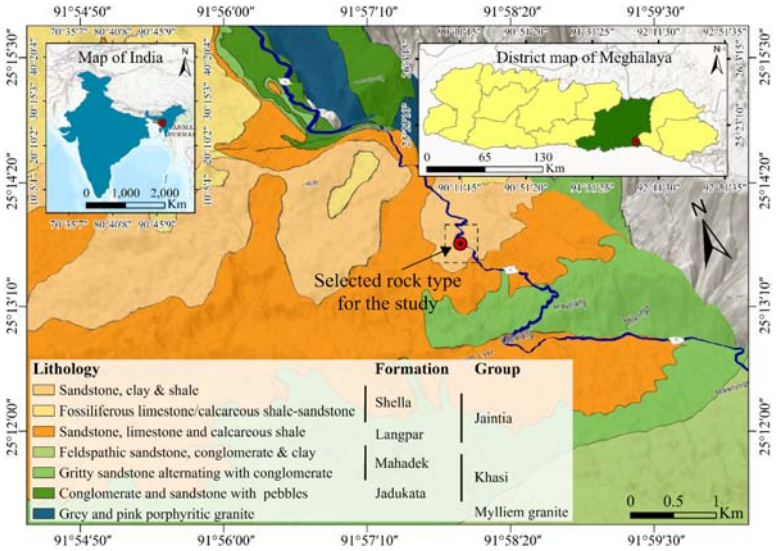


Fig. 2 Map showing the collected source rock lithology (Bhukosh 2025).

2.2 Heat treatment

Calcareous sandstone specimens were utilized to examine the thermal effects on their physico-mechanical properties. Nine specific temperature levels were set: 25° C, 100° C, 200° C, 300° C, 400° C, 500° C, 600° C, 700° C, and 800° C. Two specimens at each temperature were used to investigate the effect of heating on the mechanical properties of sandstone. The thermal treatment was conducted utilizing a muffle furnace (max temperature 1200°C), with a heating rate of 10 °C/min. The specimens were held at a set temperature for 6 hours in the furnace to ensure a consistent temperature distribution across all specimens, and then cooled down to room temperature by the thermal inertia of the furnace (average cooling rate ~4.5°C).

2.2.1 Analytical test

Detailed petrographic studies were conducted using an optical microscope (Leica DM2700 P) to analyze the linear crack density (LCD) of the specimen. Along with petrographic analysis, DSC (NETZSCH STA 449F3) was also utilized to understand the various chemical changes that occurred

due to exposure to high temperatures. The test was carried out at the sophisticated analytical instrument facility (SAIF), IIT Guwahati, India. In this analysis, 13.4 mg sample was heated from room temperature to 1200° C at a constant rate of 10°C/min and has been performed in an inert environment.

2.2.2 Mechanical test

The mechanical behavior of the thermally treated sandstone specimens was evaluated using the BPI test, recommended by Ulusay et al. (2001). The BPI test equipment, along with test specimens, has been shown in Fig. 3.

The uncorrected block punch strength index BPI (in MPa) is calculated from the following equation:

$$BPI = \frac{10^{-3} F_{t,D}}{A} \quad (1)$$

where $F_{t,D}$ is the failure load recorded from the gauge in kN (and converted to MN by the multiplication of 10^{-3}), and A is the area (in m^2) through which the shearing takes place. The formula quoted below is for the area

$$A = 4t(r^2 - 95.1)^{0.5} \times 10^{-6} (m^2) \quad (2)$$

where t and r are the thickness and radius of a disc specimen (in mm), respectively

For each temperature condition, multiple specimens were tested, and the average BPI value was determined to understand the mechanical behavior of the thermally treated calcareous sandstone.

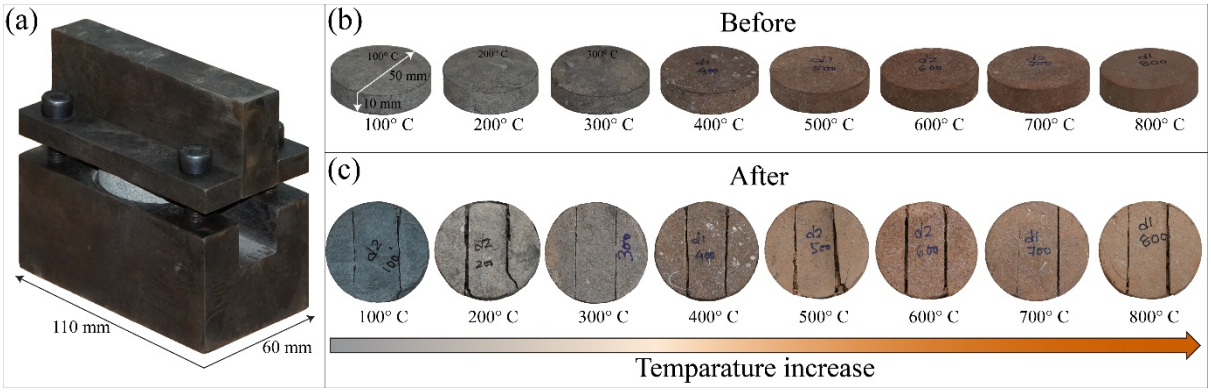


Fig. 3 (a) Block punch index test equipment, (b) and (c) Before and after images of thermally treated specimens.

3 Results and discussion

3.1 Variation of linear crack density in thin sections after thermal treatment

Skeleton analysis in *ImageJ* was used to extract the number of branches and the average branch length of cracks on thermally treated thin sections of calcareous sandstone specimens (Fig. 4). The length of each crack was estimated as the product of the branch number and the average branch length. The total crack length was obtained by totalling the lengths of all cracks. The length of each crack was estimated as the product of the number of branches and the average branch length obtained from Image J.

$$L = N_b \times L_b \quad (1)$$

Where N_b = number of branches of a crack

L_b= average branch length

The total crack length of the microphotograph was then obtained by summing the lengths of all the identified cracks. The linear crack density was defined as the ratio of total crack length to the surface area of the specimen

$$\rho_l = \frac{L_{total}}{A} \quad (2)$$

Where, ρ_l is the linear crack density (mm^{-1}) and

A is the surface area of the specimen (mm^2)

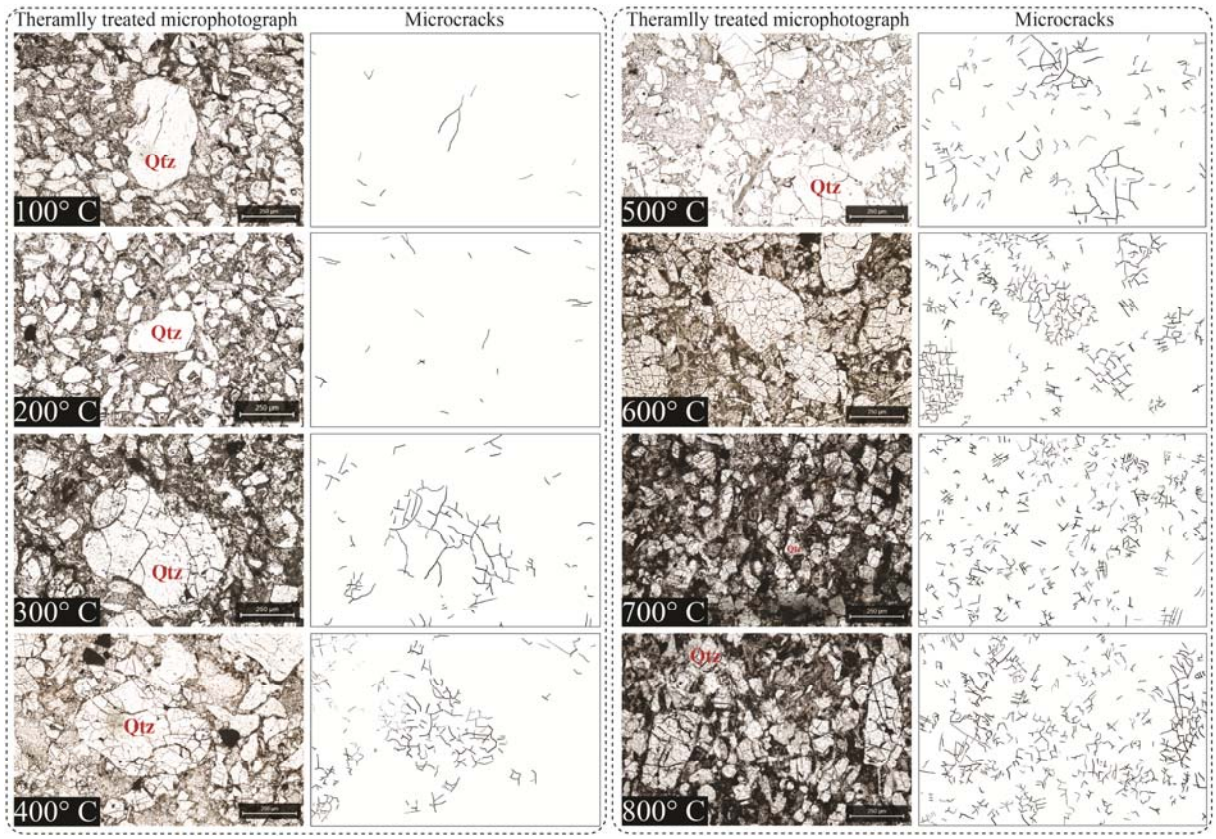


Fig. 4 Variation of microcracks on thermally treated calcareous sandstone microphotographs.

At 100-200 °C, the increase in LCD was less(3.61 mm^{-1} to 4.93 mm^{-1}) (Fig. 5a), due to the evaporation of pore water and the initial thermal expansion of mineral grains.An increase in LCD was observed between 300 °C and 400 °C, where LCD rises to 12.00 mm^{-1} (~3.32 times increase in crack density when compared to 100° C specimen), suggesting enhanced crack initiation and propagation due to differential thermal expansion between quartz grains and surrounding cement.However, beyond 600 °C, the LCD increases sharply, 23.63 mm^{-1} at 800 °C, which is almost 6.54 times the increase in crack density compared to the 100 °C specimen, indicating severe thermal damage and extensive microcrack development caused by high temperature. The linear regression trend ($y = 0.02x + 0.46$; $R^2 = 0.90$) confirms a relationship between temperature and crack density, indicating that an increase in temperature increases microcracks in calcareous sandstone.

3.2 DSC analysis

The DSC analysis has been divided into three temperature ranges. In Stage I, the DSC curve shows an endothermic peak near ~200°C, corresponding to the evaporation of water (free water, adhered water, bound water, and structural water). At~300 °C (Fig. 5b), reduction in heat flow was observed, which is due to the decomposition of amorphous carbonate minerals (Igami et al. 2025) and pre-dihydroxylation of clay minerals(Balek and Murat 1996). Beyond ~300 °C which is stage II, the DSC increases, reaching ~3.7-3.8 mW mg^{-1} near 650-700°C.The enhanced heat absorption by the specimen is due to the differential expansion of mineral grains and the α-β quartz transition at ~573 °C. This transition involves volumetric expansion that generates grain-scale stress, which can induce microcracking in quartz-bearing rock (Johnson et al. 2021). A decrease in heat flow around ~760-780 °C was observed, which may be due to decomposition of $CaCO_3$ ($CaCO_3 \rightarrow CaO + CO_2$).Studies by Igami et al. (2025) also confirms that, peak around 700-800 is attributed to the decomposition of calcite. Furthermore, beyond ~800 °C (Stage III), the decline in DSC intensity indicates the completion of carbonate decomposition, as calcite transforms into CaO with the disappearance of the calcite at high temperatures (Karunadasa et al. 2019).

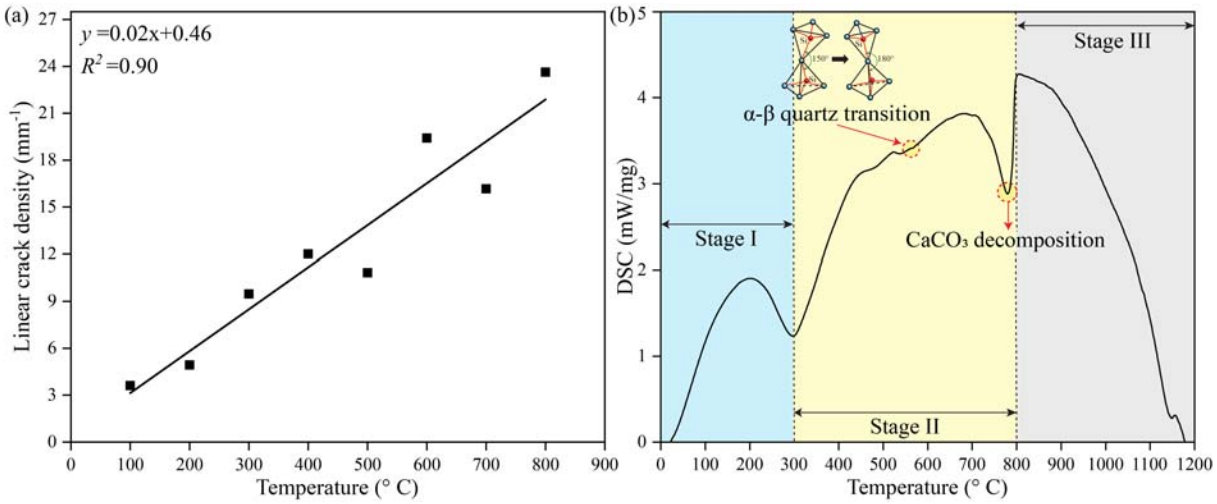


Fig. 5 (a) shows the variation in linear crack density (LCD) of thermally treated thin-section microphotographs of calcareous sandstone specimens, and (b) DSC analyses of calcareous sandstone specimen.

3.3 BPItest analysis

Before the BPI test, a distinct colour transition from grey to rust red was observed on the thermally treated calcareous sandstone, due to iron oxidation (Fig. 3b). The change in colour is a macroscopic indicator of mineralogical and chemical alteration, which may indirectly reflect the thermal damage to the specimen as temperatures increase. Fig. 6 shows the variation of porosity and BPIof calcareous sandstone with temperature.At 25-300° C, the BPI decreases from ~15.13 MPa to ~9.45 MPa (37.5% decrease in strength). It is due to the evaporation of pore-bound water and the formation of initial microcracks.Sirdesai et al. (2017)has also observed a reduction in strength at low temperatures, due to the evaporation of free water from inherent microcracks. However, an increase in strengthwas observed at 500 °C (22.2 MPa), as grain expansion fills pores. Beyond 500 °C, a sharp decline in strength has been observed, decreasing to 14.5 MPa at 600 °C, 10.6 MPa at 700 °C, and ultimately reaching about 5.8 MPa at 800 °C which is overall 61.99% decrease in strength when compared to the room temperature specimen. The strength reduction corresponds to continuous expansion, phase transition of the minerals, and carbonate decomposition at higher temperatures, which leads to the generation of intergranular and intragranular cracks in the specimen. As the grain disintegrates, it loses cohesion, and thus, thermal damage increases with increasing temperature.At lower temperatures (25-300 °C), the BPI decreases from approximately 15.1 MPa to about 9.4 MPa, while porosity shows minor fluctuations (around 3-4%). As the temperature increases to 400-500 °C, the BPI increases, reaching a peak of approximately 22.2 MPa at 500 °C, while porosity remains relatively moderate (4-6%). The temporary increase in strength is due tothe thermal expansion of mineral grains. The volumetricincrease in grain tightens the grains framework, thereby increasingthe strength of the rock(Dong et al. 2022).However, beyond 500 °C, the mechanical behavior changes as porosity increases sharply from approximately 6.8 % at 600 °C to nearly 11-12 % at 800 °C, while the BPI correspondingly decreases from 14.5 MPa to about 5.8 MPa. The increase in porosity is caused by the generation of new microcracks, grain boundary separation, and mineralogical transformations (~573 °C), as well as the decomposition of carbonate cement at higher temperatures. Similar to the present results, in the study of Den'gina et al. (1993) it was observed that at high temperatures, the grains show thermal expansion which leads to the formation of microcracks and subsequently leads to change in porosity. These processes disturb the internal bonding between mineral grains, which leads to formation of interconnected pore networks. Overall, the observed trend indicates that increasing porosity due to thermal damage plays a dominant role in controlling the mechanical deterioration of the sandstone, leading to a significant decline in BPI strength at higher temperatures.

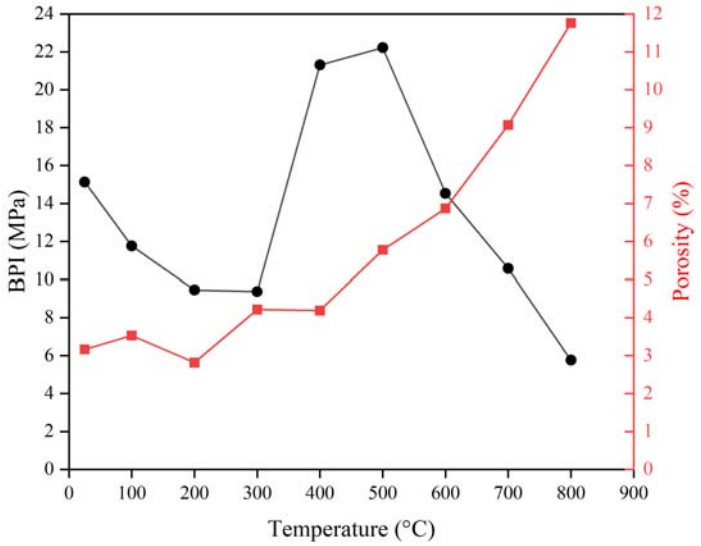


Fig. 6 Variation of BPI and porosity with increasing temperature.

4 Conclusion

- At 100-200 °C, the increase in LCD was less (3.61 mm^{-1} to 4.93 mm^{-1}), due to the evaporation of pore water and the initial thermal expansion of mineral grains. However, beyond 600 °C, the LCD increases sharply at 800 °C (6.54 times increase in crack density compared to the 100 °C specimen), indicating severe thermal damage and extensive microcrack development at high temperature.
- DSC analysis identified dehydration, α-β quartz transition, and calcite decomposition of calcareous sandstone
- A distinct color transition from grey to rust red was observed on the thermally treated calcareous sandstone, due to iron oxidation. Moreover, at 25-300° C, the BPI decreases from ~15.13 MPa to ~9.45 MPa (37.5% decrease in strength), whereas 61.99% decrease in strength was observed at 800° C when compared to the room temperature specimen.
- Overall, these findings will provide essential information about the physico-mechanical properties of sandstone, which has practical implications for engineering applications such as geothermal energy extraction, nuclear waste disposal, and underground coal gasification projects.

Author Contributions

Sourav Das: Writing - original draft, Fieldwork, Software, Data preparation & processing, Formal analysis. **Ratan Das:** Conceptualization, Supervision, Writing - review & editing, Funding acquisition, Resources, Formal analysis, Validation. **Debasish Mazumder**: Fieldwork, Formal analysis.

Funding

No funding was received for the preparation of this manuscript.

Data availability The dataset is included in the manuscript.

Declarations

Conflict of interest

The authors declare that they have no known competing financial interests or personal relationships that could have appeared to influence the work reported in this paper.

Acknowledgement
The research was conducted at the Rock Mechanics and Rock Engineering Laboratory in the Department of Geology at Cotton University, Guwahati, Assam, India. Laboratory testing of rocks was partly supported by the Anusandhan National Research Foundation (formerly known as Science and Engineering Research Board), Government of India, under the start-up Research Grant (SRG) scheme (File Number: ANRF, SRG/2022/000447) funded to RD

References

Akdag S, Karakus M, Nguyen GD, et al (2023) Dynamic response and fracture characteristics of thermally-treated granite under dynamic loading. Int J Rock Mech Min Sci 170:105482. https://doi.org/10.1016/j.ijrmms.2023.105482

Balek V, Murat M (1996) The emanation thermal analysis of kaolinite clay minerals. Thermochim Acta 282–283:385–397. https://doi.org/10.1016/0040-6031(96)02886-9

Bhukosh (2025) Geological Survey of India, Bhukosh. In: Gov. India, Kolkata, India. https://bhukosh.gsi.gov.in/. Accessed 8 Sep 2025

Den'gina NI, Kazak VN, Pristash V V. (1993) Changes in rocks at high temperatures. J Min Sci 29:472–477. https://doi.org/10.1007/BF00733026

Deng L, Li X, Wu Y, et al (2022) Influence of cooling speed on the physical and mechanical properties of granite in geothermal-related engineering. Deep Undergr Sci Eng 1:40–57. https://doi.org/10.1002/dug2.12011

Dong Z, Chen Y, Wang X, et al (2022) Evaluation of Thermophysical and Mechanical Properties of Sandstone Due to High-Temperature. Materials (Basel) 15:8692. https://doi.org/10.3390/ma15238692

Feng G, Wang X, Wang M, Kang Y (2020) Experimental investigation of thermal cycling effect on fracture characteristics of granite in a geothermal-energy reservoir. Eng Fract Mech 235:107180. https://doi.org/10.1016/j.engfracmech.2020.107180

Gautam PK, Verma AK, Singh TN, et al (2019) Experimental investigations on the thermal properties of Jalore granitic rocks for nuclear waste repository. Thermochim Acta 681:178381. https://doi.org/10.1016/j.tca.2019.178381

Han G, Jing H, Su H, et al (2019) Effects of thermal shock due to rapid cooling on the mechanical properties of sandstone. Environ Earth Sci 78:146. https://doi.org/10.1007/s12665-019-8151-1

Hu J, Xie H, Gao M, et al (2022) Damage mechanism and heat transfer characteristics of limestone after thermal shock cycle treatments based on geothermal development. Int J Rock Mech Min Sci 160:105269. https://doi.org/10.1016/j.ijrmms.2022.105269

Igami R, Igarashi G, Aili A, et al (2025) Clinker mineral formation and thermal decomposition of calcium carbonates in carbonated tobermorites: Mechanism of CO2 release in low-temperature ranges. Cem Concr Res 197:107969. https://doi.org/10.1016/j.cemconres.2025.107969

Johnson SE, Song WJ, Cook AC, et al (2021) The quartz α↔β phase transition: Does it drive damage and reaction in continental crust? Earth Planet Sci Lett 553:116622. https://doi.org/10.1016/j.epsl.2020.116622

Karunadasa KSP, Manoratne CH, Pitawala HMTGA, Rajapakse RMG (2019) Thermal decomposition of calcium carbonate (calcite polymorph) as examined by in-situ high-temperature X-ray powder diffraction. J Phys Chem Solids 134:21–28. https://doi.org/10.1016/j.jpcs.2019.05.023

Li P, Zhang H, Wu Y (2024) Study on the evolution of mechanical properties of hot dry rocks after supercritical CO2 injection. Geotherm Energy 12:27. https://doi.org/10.1186/s40517-024-00306-5

Long X, Xie H, Deng X, et al (2021) Geological and Geochemical Characteristics of the Geothermal Resources in Rucheng, China. Lithosphere 2021:. https://doi.org/10.2113/2021/1357568

Lu S-M (2018) A global review of enhanced geothermal system (EGS). Renew Sustain Energy Rev 81:2902–2921. https://doi.org/10.1016/j.rser.2017.06.097

Sirdesai NN, Singh R, Singh TN, Ranjith PG (2015) Numerical and experimental study of strata behavior and land subsidence in an underground coal gasification project. Proc Int Assoc Hydrol Sci 372:455–462. https://doi.org/10.5194/piahs-372-455-2015

Sirdesai NN, Singh TN, Pathegama Gamage R (2017) Thermal alterations in the poro-mechanical characteristic of an Indian sandstone – A comparative study. Eng Geol 226:208–220. https://doi.org/10.1016/j.enggeo.2017.06.010

Ulusay R, Gokceoglu C, Sulukcu S (2001) Draft ISRM suggested method for determining block punch strength index (BPI). Int J Rock Mech Min Sci 38:1113–1119. https://doi.org/10.1016/S1365-1609(01)00078-8

Xie H, Li C, Zhou T, et al (2020) Conceptualization and evaluation of the exploration and utilization of low/medium-temperature geothermal energy: a case study of the Guangdong-Hong Kong-Macao Greater Bay Area. Geomech Geophys Geo-Energy Geo-Resources 6:18. https://doi.org/10.1007/s40948-019-00140-1

Zhang M, Liao F, Yang Y, et al (2026) Impact of Granite Thermo-Mechanical Coupling on the Long-Term Integrity of Engineered Barriers System (EBS) in HLW Repositories. Arab J Sci Eng. https://doi.org/10.1007/s13369-026-11106-3

Exposure Time Dependency of Freeze and Thaw Damage on Hard Rocks

Ayten Ceyda Koseomur & Ahmet GunesYardimci
Middle East Technical University, Mining Engineering Department, Ankara, Türkiye
aceyda@metu.edu.tr

Abstract

Under extreme weather conditions, freeze–thaw (FT) cycles have the potential to compromise the long-term stability of surface and underground rock structures. Pore pressure induced by volumetric expansion of water leads to crack formation through debonding of mineral grains. Although various studies have explored the correlation between the number of cycles and the degradation of mechanical parameters, the influence of FT cycle rate on damage evolution under equivalent exposure durations has received limited attention. This study investigates the short- and long-term effects of slow and fast FT cycles on the mechanical properties of andesite, selected to represent hard rock behavior. Each cycle follows a temperature path between −20 °C and +10 °C, lasting one week under the slow FT regime and 5.5 hours under the fast FT regime. Exposure durations of 2 weeks and 4 weeks were applied under both regimes to enable direct comparison at equivalent total durations. Static deformability tests were conducted for both FT regimes, while triaxial compression and indirect tensile (Brazilian) tests were performed exclusively on slow FT specimens. The results indicate that FT cycle rate plays an important role in stiffness degradation: slow FT specimens exhibit no significant change in Young's modulus, whereas fast FT conditioning induces a progressive reduction of approximately 33% over 4 weeks. These findings highlight the need to consider thermal cycling rate alongside total exposure duration in durability assessments of rock structures in cold-region engineering applications.

Keywords

Freeze and thaw damage, Experimental rock mechanics, Cold-region rock engineering.

1 Introduction

Freeze–thaw (FT) weathering represents a predominant environmental process governing the mechanical degradation of rock masses in cold and alpine climatic conditions. The repeated freezing and thawing of pore water induces volumetric expansion during freezing, generating local stresses within pores and pre-existing microcracks that promote crack initiation and propagation (Chen et al. 2004; Takarli et al. 2008). These microstructural damage mechanisms progressively reduce the stiffness, strength, and durability of rocks, with direct consequences for the long-term performance of slopes, tunnels, shafts, and mine openings in cold-region engineering (Park et al. 2015; Mutlutürk et al. 2004).

Prior experimental studies have documented reductions in uniaxial compressive strength, tensile strength, elastic modulus, and wave velocity across a range of lithologies including sandstone, granite, and andesite (Tan et al. 2011; Khanlari et al. 2015; Momeni et al. 2016; Yavuz 2011). In the majority of these investigations, damage accumulation is correlated with cycle count, while the influence of cycle duration and temperature transition rate on mechanical degradation has received limited systematic attention.

Theoretical models of FT rock fracture identify coupled ice-pressure, moisture redistribution, and crack propagation processes as primary controls on damage (Walder and Hallet 1985), yet the influence of thermal cycle rate on hard volcanic rocks remains poorly constrained.

Andesite is a volcanic rock of particular relevance to cold-region engineering; its low porosity may confer greater resistance to frost-induced damage compared to sedimentary rocks, yet its mechanical response under contrasting FT cycle rates remains poorly characterized (Mal'a et al. 2022; Yavuz 2011). Understanding this response has direct implications for the long-term performance of rock structures in mountainous terrains and underground openings subject to operational thermal cycling.

2 Materials and Methods

2.1 Sample Preparation

Andesite was selected as the test material to represent hard rock behavior under freeze–thaw (FT) conditions. All specimens were prepared from intact, massive rock blocks to minimize material heterogeneity. Specimen preparation and testing were conducted in accordance with the relevant ISRM suggested methods for deformability, triaxial compression, and indirect tensile testing. Cylindrical specimens with a diameter-to-length ratio of 2.5 were prepared for deformability and triaxial compression tests, while disk-shaped specimens were prepared for indirect tensile (Brazilian) tests.

2.2 Freeze–Thaw Cycling Procedure

Two FT conditioning regimes were applied, both following the same temperature range (+10 °C to −20 °C to +10 °C). The slow FT regime consisted of cycles lasting one week (168 hours) each, with 12 temperature steps of 14 hours each. The fast FT regime consisted of cycles lasting 5.5 hours each, with 12 variable-duration steps covering the same range. Slow FT specimens were subjected to 2 and 4 cycles; fast FT conditioning was applied at approximately 30, 60, 90, and 120 cycles, with only the 60-cycle (2-week equivalent) and 120-cycle (4-week equivalent) groups included in the comparative mechanical test program.

Table 1. Summary of freeze–thaw conditioning regimes and specimen distribution across mechanical test types. All regimes follow a temperature range of −20 °C to +10 °C.

FT Regime	Cycle Rate	Exposure Duration	No. of Cycles	Cycle Duration
NC (Unconditioned)	–	–	0	–
Slow FT	Short	2 weeks	2	1 week
Slow FT	Long	4 weeks	4	1 week
Fast FT	Short	2 weeks	60	5.5 h
Fast FT	Long	4 weeks	120	5.5 h

* Fast FT conditioning was also applied at 30 and 90 cycles (1 and 3 weeks); these exposure levels are excluded from the comparative test program.

Each test group comprised 3–4 specimens for static deformability testing; slow FT and unconditioned groups were additionally tested with 3 specimens under triaxial compression and 4 under indirect tension.

3 Results and Analysis

3.1 Variation of Stiffness with Exposure to Different Freeze–Thaw Regimes and Durations

The static deformability test results reveal a pronounced divergence in the mechanical response of andesite between slow and fast FT conditioning regimes (Fig. 1).

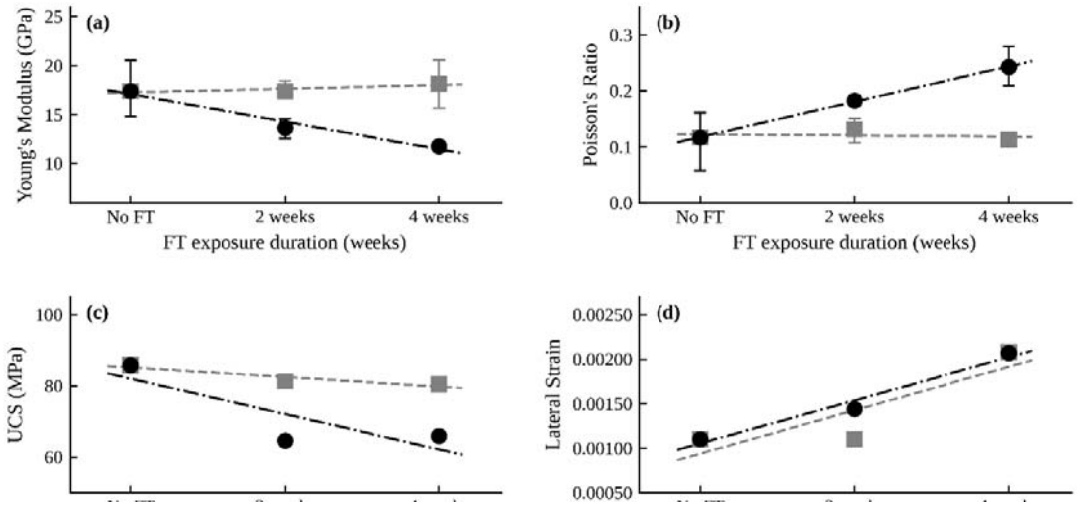


Fig. 1 Static deformability test results for slow and fast FT specimens at equivalent exposure durations: (a) Young's modulus, (b) Poisson's ratio, (c) uniaxial compressive strength (UCS), and (d) lateral strain.

The average Young's modulus of unconditioned specimens is approximately 17.5 GPa. Specimens subjected to slow FT cycles show no significant change with increasing exposure duration, with the modulus remaining approximately 17.5 GPa after 2 weeks and marginally rising to approximately 18.0 GPa after 4 weeks, a variation well within experimental scatter (Fig. 1a). In contrast, fast FT conditioning induces a progressive and substantial reduction in Young's modulus, decreasing to approximately 13.8 GPa after 2 weeks and further to approximately 11.8 GPa after 4 weeks, corresponding to a total reduction of approximately 33% relative to the unconditioned state. The approximately linear trend observed in the fast FT group indicates a consistent, accumulative stiffness loss driven by the higher rate of thermal cycling.

Uniaxial compressive strength (UCS) results follow a pattern consistent with the Young's modulus data (Fig. 1c). Unconditioned and slow FT specimens yield comparable UCS values of approximately 85 MPa, with slow FT exposure producing only a minor reduction to approximately 80 MPa after 4 weeks. Fast FT specimens exhibit a more pronounced decrease from approximately 86 MPa to approximately 65 MPa after 2 weeks, corresponding to a total reduction of approximately 24%, with values remaining similarly reduced at 4 weeks.

Poisson's ratio follows a complementary pattern (Fig. 1b). Slow FT specimens maintain a nearly constant Poisson's ratio throughout exposure (0.11–0.13). Fast FT specimens exhibit a progressive increase from approximately 0.12 to 0.245 over 4 weeks, accompanied by a substantially steeper increase in lateral strain relative to slow FT specimens at equivalent durations (Fig. 1d), confirming a consistent pattern of enhanced transverse deformability in fast FT specimens.

3.2 Variation of Strength under Confinement with Exposure to Different Freeze–Thaw Durations

The triaxial compression test results indicate that freeze–thaw cycling modifies the strength of andesite under confined loading conditions. Failure stresses increase with confining pressure for all specimen groups, confirming a friction-controlled failure mechanism. However, the slope and intercept of the failure envelopes vary systematically with freeze–thaw exposure (Fig. 2).

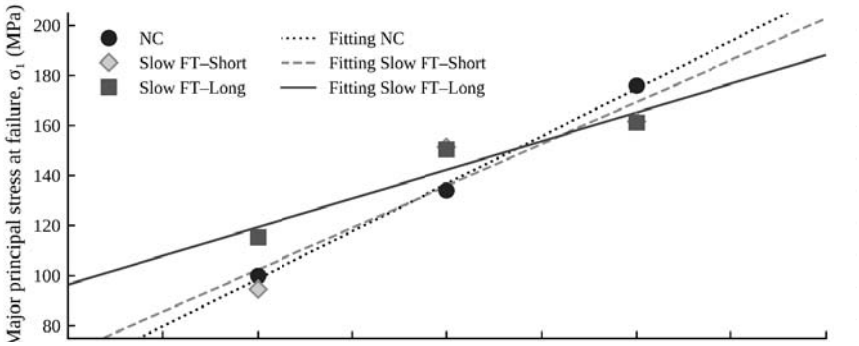


Fig. 2 Triaxial failure envelopes for unconditioned (NC) and slow FT-conditioned andesite specimens tested at confining pressures of 5, 10, and 15 MPa.

For unconditioned specimens, the fitted failure envelope yields a friction angle of approximately 50° and an apparent cohesion of approximately 11 MPa. After short-term slow freeze–thaw exposure, the friction angle decreases to approximately 48°, while apparent cohesion increases to approximately 13 MPa. With long-term exposure, the friction angle further decreases to approximately 40°, accompanied by a marked increase in apparent cohesion to approximately 22 MPa.

The reduction in friction angle suggests progressive degradation of grain interlocking and surface roughness due to freeze–thaw-induced microcracking. In contrast, the increase in apparent cohesion reflects a confinement-dependent response, likely associated with microcrack closure and stress redistribution during triaxial loading rather than intrinsic strengthening of the rock matrix.

3.3 Variation of Tensile Strength with Exposure to Different Freeze–Thaw Durations

The indirect tensile test results demonstrate a sensitivity of tensile strength to freeze–thaw exposure (Fig. 3). The average Brazilian tensile strength of unconditioned specimens is approximately 9.6 MPa. After 2 weeks of slow freeze–thaw cycling, the average tensile strength decreases to approximately 8.9 MPa, corresponding to a reduction of about 7%. Following 4 weeks of exposure, the tensile strength partially recovers to approximately 9.2 MPa, although it remains slightly below the unconditioned level.

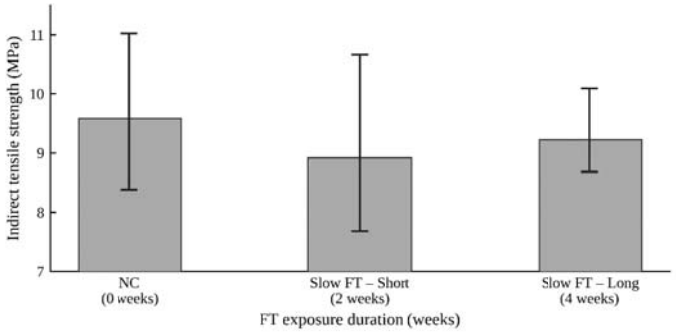


Fig. 3 Indirect tensile (Brazilian) test results for NC and slow FT-conditioned andesite specimens.

4 Discussion

4.1 Interpretation of Freeze–Thaw-Induced Mechanical Degradation

The experimental results indicate that FT cycle rate, in addition to total exposure duration, plays a governing role in andesite stiffness degradation. While slow FT specimens show no clear reduction in Young's modulus at either exposure duration, fast FT conditioning induces a progressive reduction from approximately 17.5 GPa to 11.8 GPa over 4 weeks, corresponding to a loss of approximately 33%. This divergence suggests that the accumulation of thermally induced microstructural damage is controlled not only by cumulative exposure time but also by the frequency of thermal transitions.

The contrasting behavior between the two regimes may be interpreted in terms of time-dependent damage mechanisms operating at the pore and microcrack scale. Under slow FT cycling, the extended duration of each thermal stage may allow partial stress relaxation, moisture redistribution, and limited crack arrest before the subsequent thermal transition. Under fast FT cycling, the rapid succession of

thermal loads may promote repeated crack initiation, propagation, and coalescence within the same exposure period. This interpretation is broadly consistent with the theoretical framework of Walder and Hallet (1985), in which frost-induced crack growth is controlled by coupled ice-growth and water-supply processes at crack tips.

The Poisson's ratio and lateral strain results reinforce this interpretation (Fig. 1b, 1d). Slow FT specimens maintain an approximately constant Poisson's ratio with only modest lateral strain increase, consistent with the absence of stiffness degradation. Fast FT specimens exhibit a monotonic increase to 0.245, with substantially higher lateral strain values, reflecting progressive microcrack development under accelerated thermal cycling (Brace et al. 1966; Jaeger et al. 2007).

The triaxial compression results indicate that slow FT exposure modifies strength parameters even though the static deformability tests did not show a clear reduction in Young's modulus. The reduction in friction angle from approximately 50° to 40° with increasing slow FT duration (Fig. 2) suggests progressive degradation of grain interlocking and frictional resistance along micro-discontinuities, consistent with friction-controlled failure models (Paterson and Wong 2005). The concurrent increase in apparent cohesion from approximately 11 MPa to 22 MPa reflects a confinement-dependent response associated with crack closure under higher confining pressures (Brace et al. 1966; Jaeger et al. 2007) rather than intrinsic material strengthening.

4.2 Implications for Rock Engineering Applications

The indirect tensile test results (Fig. 3) reveal that tensile strength is sensitive to slow FT exposure, with a reduction of approximately 7% observed after short-term conditioning. Following 4 weeks of exposure, the tensile strength partially recovers to approximately 9.2 MPa, although the mechanism remains ambiguous and warrants dedicated microstructural investigation in future work. Compared with compressive behavior, the tensile response is more sensitive to freeze–thaw damage, confirming that crack-controlled failure mechanisms dominate under indirect tensile loading.

These findings are relevant to rock structures exposed to artificial or operational thermal cycling. In such applications, cycle rate may be as consequential as total exposure duration, and design frameworks should account for thermal cycling rate alongside conventional strength-based criteria.

5 Conclusions

This study presents a systematic experimental investigation of the combined effects of FT cycle rate and exposure duration on the mechanical behavior of andesite, through static deformability tests conducted under both slow and fast FT regimes, and triaxial compression and indirect tensile testing conducted under the slow FT regime. Based on the experimental results, the following conclusions are drawn:

1. Slow and fast FT cycling produce markedly different stiffness responses at equivalent exposure durations. Fast FT conditioning induces a progressive ~33% reduction in Young's modulus (17.5 to 11.8 GPa over 4 weeks), a monotonic increase in Poisson's ratio from 0.12 to 0.25, higher lateral strain values, and a ~24% UCS reduction, while slow FT specimens show no significant change in any of these parameters.
2. Slow FT cycling systematically modifies strength parameters under triaxial loading, with the friction angle decreasing from approximately 50° to 40° and the apparent cohesion increasing from approximately 11 MPa to 22 MPa with increasing exposure. The increase in cohesion reflects a confinement-dependent microcrack closure response rather than intrinsic material strengthening, highlighting the importance of stress state in interpreting strength parameters of FT-conditioned rocks.
3. Indirect tensile strength exhibits greater sensitivity to slow FT exposure than compressive behavior, with reductions of approximately 7% observed after short-term conditioning, confirming the dominant role of crack-controlled failure mechanisms under tensile loading. The partial recovery observed at longer durations remains mechanistically unresolved and is identified as a subject for future microstructural investigation.

Overall, the results suggest that FT cycle rate plays an important role in governing stiffness and deformation behavior, while strength and fracture properties respond primarily to cumulative slow FT exposure. This distinction has direct implications for durability assessments in cold-region rock

engineering: cycle count alone is an insufficient proxy for FT damage severity, and thermal cycling rate should be considered alongside total exposure duration.

References

Brace WF, Paulding BW Jr, Scholz CH (1966) Dilatancy in the fracture of crystalline rocks. Journal of Geophysical Research 71(16):3939–3953. https://doi.org/10.1029/JZ071i016p03939

Chen TC, Yeung MR, Mori N (2004) Effect of water saturation on deterioration of welded tuff due to freeze–thaw action. Cold Regions Science and Technology 38(2–3): 127–136. https://doi.org/10.1016/S0165-232X(03)00062-0

Jaeger JC, Cook NGW, Zimmerman RW (2007) Fundamentals of rock mechanics. 4th edn. Blackwell Publishing, Oxford.

Khanlari GR, Sahamieh RZ, Abdilor Y (2015) The effect of freeze–thaw cycles on physical and mechanical properties of Upper Red Formation sandstones, central part of Iran. Arabian Journal of Geosciences 8: 5991–6001. https://doi.org/10.1007/s12517-014-1653-y

Maľa M, Greif V, Ondrášik M (2022) Pore structure evolution in andesite rocks induced by freeze–thaw cycles examined by non-destructive methods. Scientific Reports 12: 8361. https://doi.org/10.1038/s41598-022-12437-5

Momeni A, Abdilor Y, Khanlari GR, Heidari M, Sepahi AA (2016) The effect of freeze–thaw cycles on physical and mechanical properties of granitoid hard rocks. Bulletin of Engineering Geology and the Environment 75(4): 1649–1656. https://doi.org/10.1007/s10064-015-0787-9

Mutlutürk M, Altindag R, Türk G (2004) A decay function model for the integrity loss of rock when subjected to recurrent cycles of freezing–thawing and heating–cooling. International Journal of Rock Mechanics and Mining Sciences 41(2):237–244. https://doi.org/10.1016/S1365-1609(03)00095-9

Park J, Hyun CU, Park HD (2015) Changes in microstructure and physical properties of rocks caused by artificial freeze–thaw action. Bulletin of Engineering Geology and the Environment 74(2): 555–565. https://doi.org/10.1007/s10064-014-0630-8

Paterson MS, Wong T-F (2005) Experimental Rock Deformation: The Brittle Field. 2nd edn. Springer, Berlin

Takarli M, Prince W, Siddique R (2008) Damage in granite under heating/cooling cycles and water freeze–thaw condition. International Journal of Rock Mechanics and Mining Sciences 45(7): 1164–1175. https://doi.org/10.1016/j.ijrmms.2008.01.002

Tan X, Chen W, Yang J, Cao J (2011) Laboratory investigations on the mechanical properties degradation of granite under freeze–thaw cycles. Cold Regions Science and Technology 68(3):130–138. https://doi.org/10.1016/j.coldregions.2011.05.007

Walder J, Hallet B (1985) A theoretical model of the fracture of rock during freezing. Geological Society of America Bulletin 96(3): 336–346.

Yavuz H (2011) Effect of freeze–thaw and thermal shock weathering on the physical and mechanical properties of an andesite stone. Bulletin of Engineering Geology and the Environment 70(1): 187–192. https://doi.org/10.1007/s10064-010-0302-2

Slaking sensitivity of rocks – insights from a multi laboratory parameter study

M. Kaspar & C. Latal
Institute of Applied Geosciences, Graz University of Technology, Graz, Austria
markus.kaspar@tugraz.at
0000-0002-4174-2997

G. Pittino
Chair of Subsurface Engineering, Montanuniversität Leoben, Leoben, Austria

Abstract

The slaking behaviour of rocks is of geotechnical importance, affecting the stability of slopes and excavation pits, for example, as well as influencing the performance of underground excavation works, such as clogging of TBMs. Traditionally, wetting-drying and slake durability tests are performed to assess the degradation behaviour of weak rocks. Depending on their genetic origin, the slaking and disintegration behaviour of these rocks may exhibit different patterns. This study uses the results of widely used slaking tests, combined with the characterisation of disintegrated materials/decay products, to propose a tool for evaluating slaking sensitivity. Combining and extending the evaluation of these tests with mineral composition data and mechanical parameters enables a more detailed evaluation of the slaking behaviour of weak and soft rocks. Sedimentary rocks exhibit strong static slaking, whereas weak rocks derived from crystalline rocks slake under dynamic conditions. These findings have wider implications for estimating rock degradation in different geological settings and offer a quick laboratory method of estimating slaking rates and the potential liberation of fines, for example in the event of extreme precipitation.

Keywords

Rock Slaking, Soft Rocks, Rock Testing, Rock Decay.

1 Introduction

1.1 Background

Rock decay and softening occurs due to the action of external factors acting on the exposed rock, such as mechanical, or chemical weathering. One form of decay is slaking, referring to the formation of cracks and flaking, with associated degradationof rocks in the presence of water (Santi 1998). These processes affect all kinds of rocks, but the severity and intensity at which they act vary strongly. Usually, so-called soft rocks with a UCS <25 MPa (Kanji 2014) or weak rocks that react in the presence of water (Nickmann 2009) are mostly affected by external influences causing them to slake or change their consistency (Morgenstern and Eigenbrod 1974). However also hard rocks (usually grain bound crystalline rocks like igneous or metamorphic rocks) can suffer from slaking if their initial cohesive fabric is disturbed, for example by tectonic stress or advanced stages of weathering. Usually

standardized (laboratory) tests are being performed in order to assess the slaking behaviour and degradation characteristics. The disintegrating patterns after storing rocks for 24 hours in water after EN ISO 14689 areused as an initial classification of rocks into five grades. If the rocks exhibit grade 1 and 2, i.e. little to no reaction in water, the modified wetting-drying test (Nickmann 2009, Nickmann et al. 2025), or slake durability test (ASTM 2016, Herzel 2002) are being employed in order to account for long term changes. The latter imposes a dynamic action on the material by a rotating drum, while the modified wetting-drying test adds two additional cycles of 24 hours water storage and the grain size distribution is determined after the test is finished. In the present study, these widely applied tests and obtained parameters are further being used to compare the slaking behaviour of the rock material. The current study elucidates various aspects of rock disintegration and utilizes the combination of commonly used lab tests to propose a rating system for the slaking sensitivity.

2 Methods

A total of 71 samples were tested: 22 Miocene sedimentary rocks (clay and siltstones) were obtained from the St. Florian Beds in the Pre-Alpine basin region; and 49 samples of soft crystalline rocks and breccias (sericite phyllites, carbonate and sulphate breccias, low-strength micaschists, feldspar schists, tectonized gneiss and cataclasites) were obtained from the Wechsel region, a mountain pass in the Austrian Alps (Kaspar et al. 2025). Initially, on all samples wetting tests were conducted according to the ISO 14689 (ISO 2017) immersing the samples in deionized water for 24 hours at room temperature. Those rocks rated as Grade 1 or 2 were tested further under repeated static conditions in the modified wetting-drying test (WD_{mod}), but also under dynamic conditions in slake durability tests using a second set of sample material. The modified wetting drying test (Nickmann 2009) involves two additional wetting-drying cycles and sieving of the fragments and assignment of six degradation classes (VK classes). The slake durability index (I_d)isobtained from testing the rocks following the procedures described in the ASTM D4644 (ASTM 2016). In accordance with Recommendation No. 20 of the Commission on Rock Testing of the German Geotechnical Society, DGGT (Herzel 2002), resistant rocks are tested for up to six cycles (I_{d6}) or until more than 70% of the material in the drum has been lost. Finally, the bulk mineralogical composition of the material was determined using a PANalyticalX´Pert PRO diffractometer (CoKα radiation). From the clay mineral suspension (<2 µm) textured samples were retrieved. The analysis is performed in a Philips PW 1830 diffractometer (Cu Kα) following the procedure of the ON B 4810 (Austrian Standards International 2024). Uniaxial compressive strength (UCS) was determined on cylindrical specimen with a diameter to length ratio of 2:1 (typically diameter = 50±5mm, length = 100±10mm) using an MTS model 815. The tests are conducted load and/or strain controlled with a minimum duration of 5 minutes following the recommendation No. 1 of the DGGT (Mutschler 2004) and the Austrian standard ON B 3124-9 (Austrian Standards International 1986).

3 Results and Discussion

Selectedrepresentative specimen from the investigated rock types from the WechselSeries were tested for their UCS, showing low to moderate strength (Fig.1a & b). The early diagenetic clastic Miocene sediments from the St. Florian beds were assessed by the ISRM field procedure and estimated to fall into R0 to R2.The specimens were subject to water immersion following the ISO 14689 and graded accordingly (Fig. 2a). Out of the 71 initial samples selected for testing, 49 fell into the ISO 14689 grade 1 and grade 2 after 24 hours of immersion in water indicating no to little decay. Thus, these rocks were additionally tested in the modified wetting drying test and slake durability test. The grade 1 rocks also exhibit a high slaking resistance in the modified wetting drying test where the two additional immersion cycles in water did not substantially degrade the rock, and VK0 rocks comprise only those samples formerly assigned to grade 1. Only one sample from grade 1 rocks disintegrated enough to fall into VK 1. The VK0 class only comprised rocks from the WechselSeries and no Miocene clay-/siltstones. The grade 2 rocks showed a more differentiated behavior and are mostly classified as VK 2 to VK 3 (Fig.2a).After six cycles, none of the grade 1 rocks were found in the highest and lowest slake durability categories *very high* and *very low*, respectively (Fig. 2b). Decay of Grade 2 rocks was more pronounced and they are predominantly present in the lowermost categories. The rate of slaking and disintegration is higher for early diagenetic clay and siltstones compared to the weak, altered crystalline rocks. Especially between the second and the sixth cycle the increase in disintegration is lower for crystalline derived rocks. For example, the tectonized gneiss and clay-siltstone that exhibit a similar I_{d2} of ca. 60%, show a decrease until I_{d6} of 12% and 42%, respectively (Fig. 2c & d).

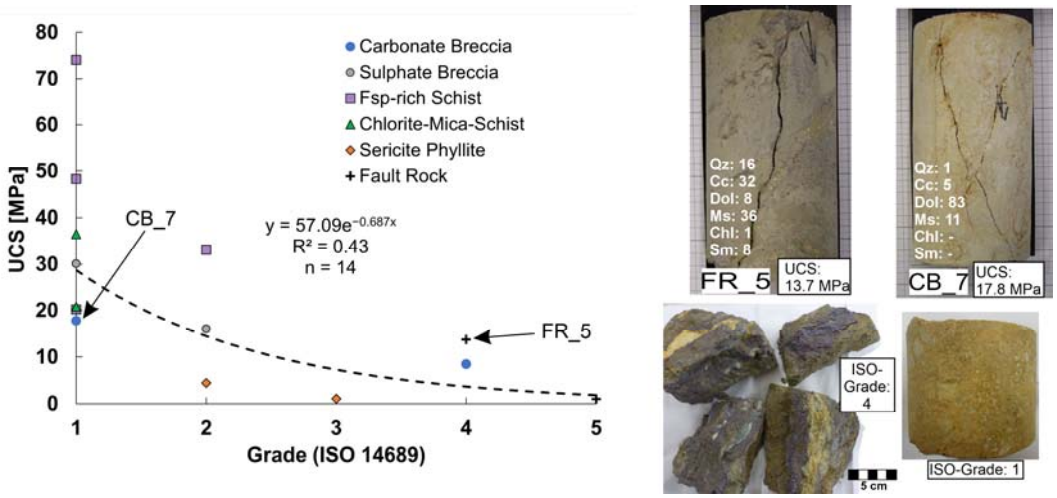


Fig. 1 UCS ranges across ISO grades (after Kaspar et al. 2025). Rocks that degrade stronger in water immersion tend to exhibit slightly lower UCS values. The strength is similar for the two samples shown, however, the slaking behaviour is different. The breccia (CB_7) contains little amounts of sheet silicates and no swelling clays sensitive to water, with a weak carbonate fabric, resulting in a low UCS. The fault rock (FR_5) contains water sensitive smectite leading to slaking, but exhibits a low strength in dry state as shown by UCS.

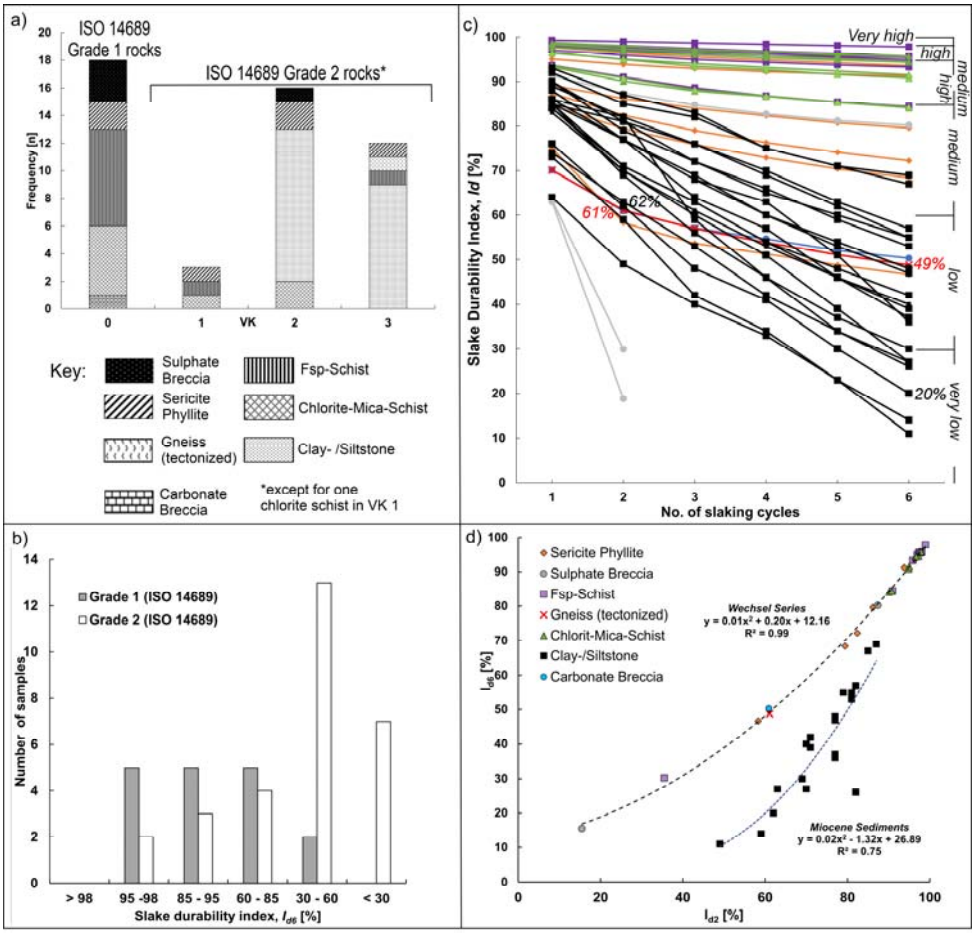


Fig. 2 Plots and diagrams of the wetting-drying and slake durability test results. a) Bar diagram illustrating the distribution of the different rock types according to their slaking classes in the (modified) wetting drying tests. b) Slake durability index classifications after Gamble (1971) within the ISO 14689 grades (from Kaspar et al. 2025). c) Evolution of the I_d over the cycles of the slake durability test; for legend see (d). d) Plot showing the correlation between the I_{d2} and I_{d6}.

The rocks of metamorphic origin with a diagenetic cohesive fabric usually do not exceed an increase of more than 15% between the second and sixth cycle. Exceptions are only sulphate dominated rocks, which did not survive mor than two cycles (i.e. loss >70%). Such rocks containing minerals sensitive to aqueous environments like anhydrite or gypsum are in general difficult or not well suited for slaking tests (Nickmann et al. 2025). However, the nature of disintegration is not obvious from the slake durability index alone (Fig. 3a & b). Therefore, the complementary visual assessment of rock

fragments retained in the drum after ASTM and DGGT is essential. Clay and siltstones exhibiting a strong increase in I_d, may be "2 (rounded)" according to the DGGT, referring to the shape of the pieces, but allow no statement on the fragment size. VK 2 rocks disintegrating in the WD_{mod} may not break apart during the slake durability test, forming downscaled pieces of the original lumps. This was observed for clay and siltstones where "mud balls" remained after the test(Fig. 3c & d). In contrast, rocks that did disintegrate (i.e. DGGT category 3) can still exhibit a relatively high slake durability index. In such cases the rock fragments are still larger than 2mm and thus retained in the drum, resulting in an apparently high slake durability. This was found for the crystalline derived rocks where platy or flaky pieces had formed.

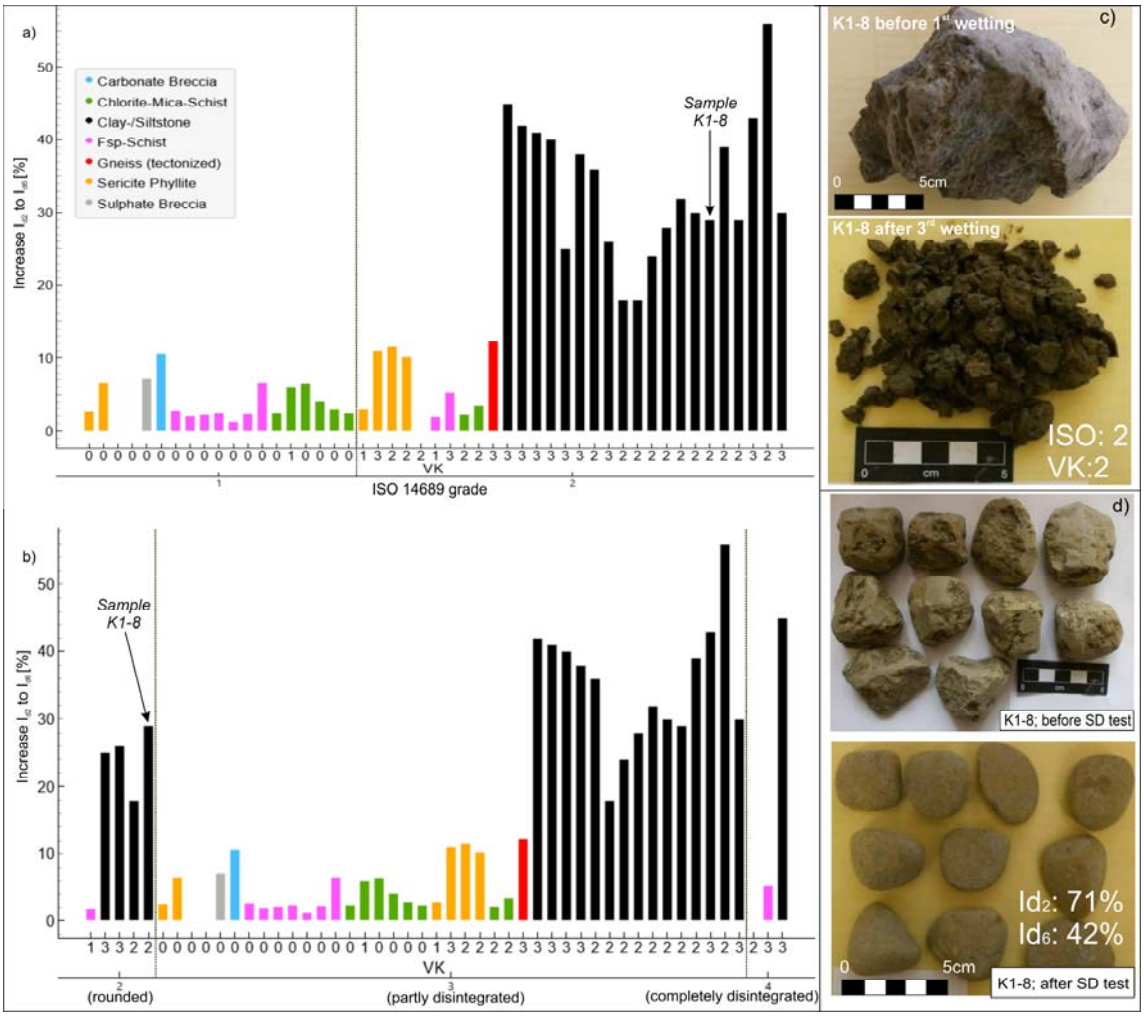


Fig.3 Increase of the slake durability index from the second to sixth cycle for the individual samples of the investigated lithologies (note that missing bars indicate samples that survived only two slake durability test cycles). a) Increase in I_d with respect to the associated ISO grades and VK classes. b) Increase in I_d with respect to the VK classes and DGGT categories. c) Sample K1-8 before and after WD_{mod}.d) Visual documentation of Sample K1-8 before and after slake durability test.

Mineralogically, sheet silicates are one common constituent of all rocks used for correlation. While the WechselSeries rocks contained typically muscovite (Ms) and chlorite (Chl), the clay and siltstones, have higher contents ofsmectite (Sm) and kaolinite (Kaol) (Table 1). The content of sheet silicates showed a negative correlation with the slaking behaviour expressed as the difference of I_{d2} and WD_{mod}(Fig. 4a). A positive or negative excess is determined by linking the $I_d$to the proportion $>2mm_{WDmod}$ (Fig. 4b). The slake durability test provides a simplified sieve analysis, since the material >2mm is retained within the wire mesh drum, expressed as I_d. The slaking sensitivity is the difference between the proportion >2mm from the sieve analysis conducted as part of the WD_{mod} and the I_{d2} or I_{d6}, respectively. If the value is very positive, the rock shows little to no reaction during water storage. However, dynamic slaking sensitivity is high, which is related to low UCS values for crystalline-derived rocks with a pre-damaged fabric, such astectonized gneiss.With higher UCS, crystalline rocks show essentially no slaking regardless of the number/duration of immersion cycles, thus plotting near the origin. If the value is very negative, the material already decayed strongly in the static test compared to the dynamic test as visible from the proportion >2mm of these samples (Fig. 5). The early diagenetic Miocene sediments show high static sensitivity, i.e. negative values, suggesting that the 24

hours of water immersion substantially damage the rock cohesion by water uptake and a change in consistency might occur. During the 10-minute cycles in the slake durability test, the material is capable of maintaining a certain internal cohesion or forms “mud balls” resulting in larger proportions of material >2mm, i.e. higher I_d values. Certainly, material decay progresses with increasing number of test cycles, but the six test cycles allow determining trends, rates and patterns of slakingbased on the amount of degradation occurring between I_{d2} and I_{d6}(Fig. 5). The Miocene sediments with very negative values exhibit low proportions of >2mm after water storage while othersshow delayed slaking under prolonged dynamic action.

Table 1. Ranges of mineralogical composition in percent of the rocks from this study.

Rock type	Quartz	Feldspars	Carbonates	Gypsum	Ms	Chl	Sm	Kaol
Sericite phyllite	9-35	0-11	3-45	0-5	20-36	1-19	0-1	0-1
Chlorite-mica-schist	15-39	0-17	0-16	-	32-83	34-70	-	-
Gneiss (tectonized)	30	32	4	-	32	1	-	-
Fsp-rich schist	24-30	7-22	2-15	0-32	18-70	14-21	0-1	0-1
Carbonate breccia	0-8	-	65-100	-	0-27	3-14	0-4	-
Sulphate breccia	4-39	0-7	0-43	12-32	16-47	0-19	0-2	-
Clay-/siltstone	11-29	0-13	0-30	-	42-66	0-15	1-10	0-7

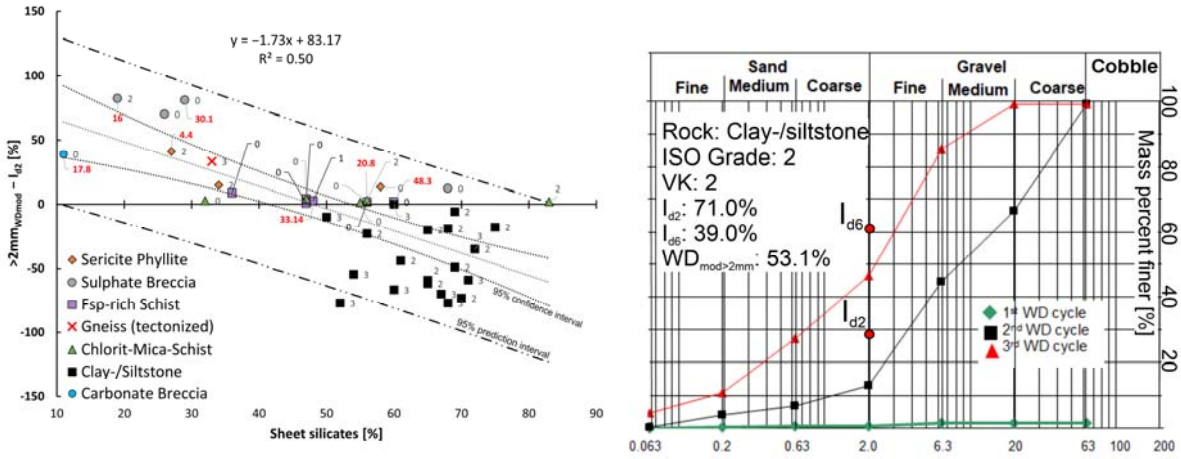


Fig. 4a) Effect of sheet silicate content on slaking type. Labels indicate VK classes. b) Sieve curve illustrating linking the I_d to the sieve curve of the WD_{mod}, i.e. fractions >2mm after the third WD test cycle (from Kaspar et al. 2025).

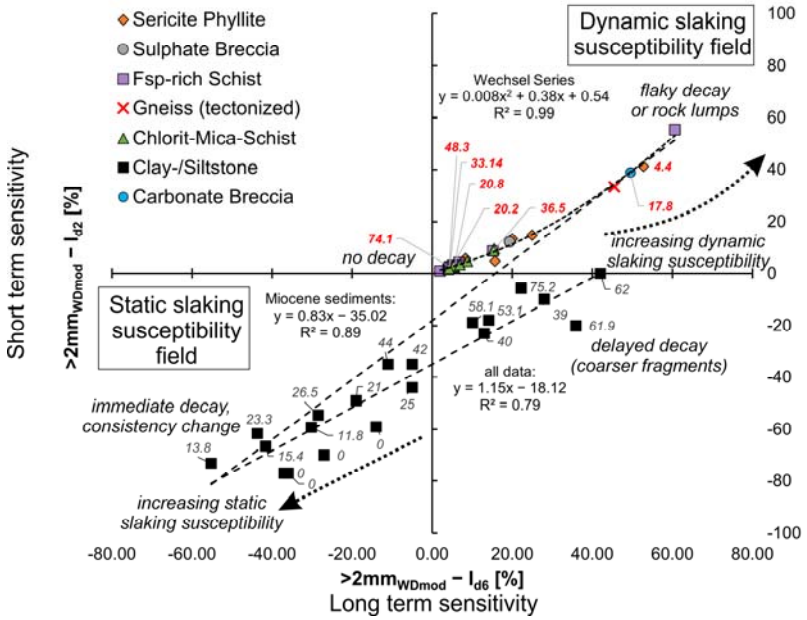


Fig. 5 Slaking sensitivity using modified wetting-drying tests and the slake durability test. (red datapoint labels = UCS; black datapoint labels =proportion>2mmWD_{mod}). The more sensitive the rock, the greater and sooner after immersion is the amount of fines released, i.e. low amount of >2mm and more negative values (adapted from Kaspar et al. 2025).

4 Summary and Conclusion

The combination of established slaking test supplemented by mineralogical analyses and UCS data allows a more differentiated evaluation of the slaking behaviour of rocks from different genetic geologic settings. Early diagenetic, non-lithified rocks slake stronger already under static conditions in aqueous environments, but may show a slaking pattern where the difference in fragmentation between WD_{mod} and slake durability tests is low, pointing to more resistance resulting in a delayed decay. The cohesion of non-lithified rocks can be moderate in a dry state, but water uptake can potentially lead to a change in consistency (e.g. mud balls). Weak rocks derived from lithified protoliths slake little under static conditions and require additional dynamic action to disintegrate substantially. The presence of sheet silicates points to strong mineralogical control on the slaking behaviour, but also the fabric and degree of lithification/ cementation and intergranular cohesionare critical.Other parameters, such as porosity, presumably also play a decisive role as a causative factor in slaking.For lithified rocks, the quality of the grain interlocking and associated UCS affect the slaking resistance in the long term where slaking occurs gradually via surficial flaky spalling rather than decay of the specimen as a whole. The presented diagram for linking grain size and slaking behaviour of the rock can be seen as a proxy for rate, intensity and sensitivity of slaking and used for identifying potential future hot spots or scenarios of intensified rock degradation accompanied by enhanced sediment /debris release. This can be, for example, extreme weather events, or geotechnical settings like soft ground, slurry-supported tunnelling, where liquids and dynamic forces (e.g. cutting wheel) act on the rock, in order to estimate the rates and intensity of potential fine material release. It should serve as an index for site investigations and further validation of its scalability and transferability to field applications will be necessary.

References

ASTM (2016) Standard test method for slake durability of shales and similar weak rocks (D 4644-16). ASTM International, West Conshohocken, PA, USA.

Austrian Standards International (1986) Testing of natural stone; mechanical properties of rock; modulus of elasticity, stress-strain curve and poisson's ratio under uniaxial compressive loading (ON B 3124-9). Austrian Standard International, Vienna, Austria

Gamble JC (1971) Durability-plasticity classification of shales and other argillaceous rocks. Ph.D. Thesis, University of Illinois, Urbana-Champaign, USA

Herzel P (2002) Recommendation No. 20 of the commission on Rock Testing of the Deutsche Gesellschaft für Geotechnike.V. – „slake-durability test“. Bautechnik (79): 101–105. https://doi.org/10.1002/bate.200200620

ISO (2017) Geotechnical investigation and testing — Identification, description and classification of rock (EN ISO 14689). Austrian Standards International, Vienna, Austria.

Kanji MA (2014) Critical issues in soft rocks. J. Rock Mech. Geotech. Eng. (6): 186–195. https://doi.org/10.1016/j.jrmge.2014.04.002

Kaspar M, Latal C, Pittino G, Reinprecht V (2025) Degradation and decay of rocks: linking wetting–drying and slake durability tests for climate-sensitive maintenance. Geotechnics (5):84. https://doi.org/10.3390/geotechnics5040084

Morgenstern NR, Eigenbrod KD (1974) Classification of argillaceous soils and rocks. J. Geotech. Eng. Division(100) 10: 1137–1156. https://doi.org/10.1061/AJGEB6.0000106

Mutschler T (2004) Uniaxial compression tests on rock samples – Recommendation No. 1 (revised) of the Commission on Rock Testing of the German Geotechnical Society. Bautechnik (81): 825–834. https://doi.org/10.1002/bate.200490194

Nickmann M (2009) Abgrenzung und Klassifizierung veränderlich fester Gesteine unter ingenieurgeologischen Aspekten. Münchner Geowissenschaftliche Abhandlungen, Reihe B - Ingenieurgeologie Hydrogeologie Geothermie, Heft 12; Verlag Dr. Friedrich Pfeil: Munich, Germany, 2009.

Nickmann M, Baumgärtel T, Plinninger R (2025) Determination of the slaking potential of rock using the combined method of wetting-drying and crystallization tests - Recommendation No. 27 by Commission 3.3. of the DGGT and Working Group 5.1.5 of the FGSV. geotechnik (48): 126–139. https://doi.org/10.1002/gete.202400039

Santi P (1998) Improving the jar slake, slake index and slake durability tests for shales. Environ. Eng. Geosci. (4): 385–396. https://doi.org/10.2113/gseegeosci.IV.3.385

Estimation of long-term behavior of rock from short-term creep tests

K. Hashiba & K. Fukui
The University of Tokyo, Tokyo, Japan
hashiba@sys.t.u-tokyo.ac.jp

Abstract

Creep tests under constant stress are essential for investigating the time-dependent deformation and failure of rock. At a high stress level, creep strain increases, while the strain rate gradually decreases, reaches a minimum, and increases until failure occurs. Here, the stress level means the ratio of creep stress to short-term strength, and the creep strain is total strain minus elastic strain. That is to say, the creep of rock is composed of decelerating and accelerating portions. In contrast, the strain rate ata low stress level gradually decreases and approaches nearly zero, and hence it is quite difficult to complete the creep test until failure occurs.

To estimate the temporal change in creep strain from the beginning of a test to the final failure at low stress levels, the authors developed a new test method in which axial stress is increased, kept constant for a while at a predetermined stress level, increased again, decreased in the post-peak region, and kept constant at the same stress level until failure occurs. This test method provides both the beginning portion of decelerating creep and the ending portion of accelerating creep.

In this study, this test method was applied to two types of Japanese rocks, tuff and andesite, in uniaxial compression. The relations between creep strain and time in the decelerating portion and between creep strain and residual time in the accelerating portion at low stress levels were in a similar manner to those obtained from conventional creep tests at high stress levels. By interpolating the decelerating and accelerating creep curves, the complete creep curves and hence creep lifetimes were estimated at stress levels of between 20% and 80%.

Keywords

Time-dependent behavior, Creep, Strain rate, Lifetime.

1 Introduction

Understanding the time-dependent behavior of rock is essential for the long-term stability assessment of underground structures, such as tunnels, mines, and high-level radioactive waste repositories (Wagner 2019; Zhang et al. 2025). Creep tests in which time-dependent deformation is observed under constant stress have been widely applied to various rock types (Aydan et al. 2014; Innocente et al. 2021). At a high stress level, creep strain increases, while the strain rate graduallydecreases, reaches a minimum, and increases until failure occurs (Okubo et al. 1991; Bruntut et al. 2014; Imani et al. 2025), as shown in Fig. 1 (a). Here, the stress level means the ratio of creep stress to short-term strength, and the creep strain is total strain minus elastic strain. That is to say, the creep of rock is composed of decelerating and accelerating portions.Figures 1 (b) and 1 (c) are schematic illustrations of the creep strain with the logarithm of time and with the logarithm of residual time (i.e., creep lifetime minus elapsed time), which emphasize the deceleratingand accelerating creeps, respectively (Okubo et al. 1991).

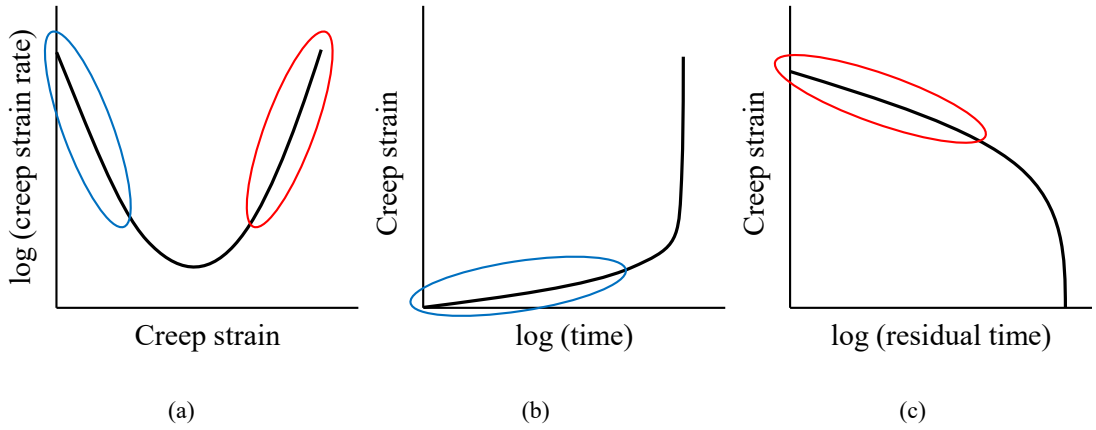


Fig. 1 Schematic illustrations of creep test results ata high stress level. The blue and red ovals indicate the decelerating and accelerating creeps, respectively. (a) log (creep strain rate) versus creep strain, (c) creep strain versus log (time), and (c) creep strain versus log (residual time).

These creep test results can be obtained in a relatively short period of time at high stress levels. In contrast, the strain rate ata low stress level gradually decreases and approaches nearly zero, and hence it is quite difficult to complete the creep test until failure occurs (Itôand Sasajima 1987; Hashiba and Fukui 2020). In previous studies, a multi-stage creep test in which creep stressis increased in stages has been conducted; however, this test method provides decelerating creep in each of the stages and accelerating creep only in the final stage at a high stress level (Bruntut et al. 2013). Hence, there is still little knowledge about the long-term creep behavior at low stress levels. Recently, the authors developed a new test method to estimate the temporal change in creep strain from the beginning of a test to the final failure at low stress levels (Hashiba and Fukui 2025). This paper presents the results of two types of Japanese rocks obtained with the new test method at low stress levels and compares them with short-term creep test results at high stress levels.

2 Test method

Sample rocks are Tage tuff and Sanjome andesite obtained in Japan of which the uniaxial compressive strengths are 22 MPa and 100 MPa, respectively. The specimens are cylindrical with a diameter of 25 mm and a height of 50 mm and were dried in a laboratory for more than two weeks. The tests were conducted in uniaxial compression using a 500 kN servo-controlled testing machine. The axial load and displacement were measured with a strain-gauge-type load cell and a linear variable differential transformer, respectively.

Figure 2 shows a schematic illustration of a stress-strain curve obtained with the test method developed by Hashiba and Fukui (2025). In this test method, a specimen is loaded from O to A, and the stress is kept constant to record the decelerating creep from A to B. The specimen is reloaded from B to C and unloaded from C to D, and the stress is kept constant to record the accelerating creep from D to E at the same stress level as that at A and B. In conventional creep tests, the position of stress and strain moves from A to Evia B and D. In contrast, this test method omits the section between B and D and provides both the beginning portion of decelerating creep and the ending portion of accelerating creep, as the curves enclosed by the blue and red ovals in Fig. 1 (a). By interpolating the separated

decelerating and accelerating creep curves, we can estimate a complete creep curve and hence creep lifetimefrom a single specimen in a short period of time. In this study, the strain rate was set to 10^{-4} /s from O to A, alternated between 10^{-5} /s and 10^{-4} /s at a strain interval of 5×10^{-4} from B to C, and set to -10^{-5} /s from C to D, in a similar way to that in Hashiba and Fukui (2025). Theduration between A and B was set to 1000 seconds. The stress at C was set to 1.1 and 1.15 times higher than that at D for Tage tuff and Sanjome andesite, respectively. This study focused on the creep test results and hence omitted the results about the strain-rate dependence of strength obtained from the strain-rate alternationbetween B and C. The results of Tage tuff obtained by Hashiba and Fukui (2025) were reorganized, and the results of Sanjome andesite were newly obtained in this study.

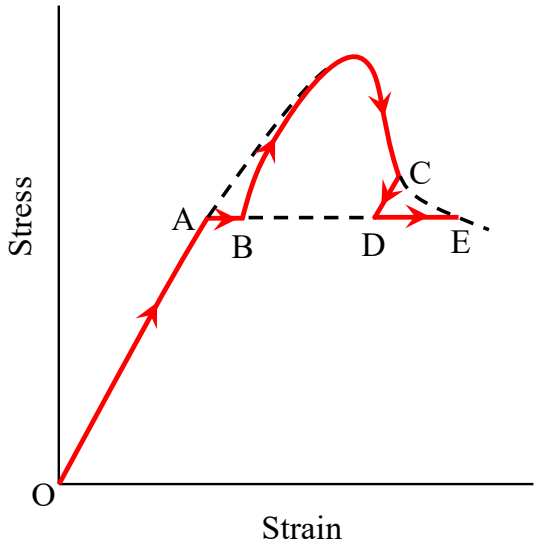


Fig. 2 Schematic illustration of astress-strain curve obtained with the test method developed by Hashiba and Fukui (2025).

3 Test results

Figure 3 shows the relation between creep strain and time obtained for 1000 seconds between A and B in Fig. 2 with the numbers indicating creep stress levels as percentages. The strain at one second after the start of the creep test was set to the origin. The creep strain monotonically increased, and the curves for both rocks are linear or slightly convex downward in a similar manner to the curve enclosed by the blue oval in Fig. 1 (b).

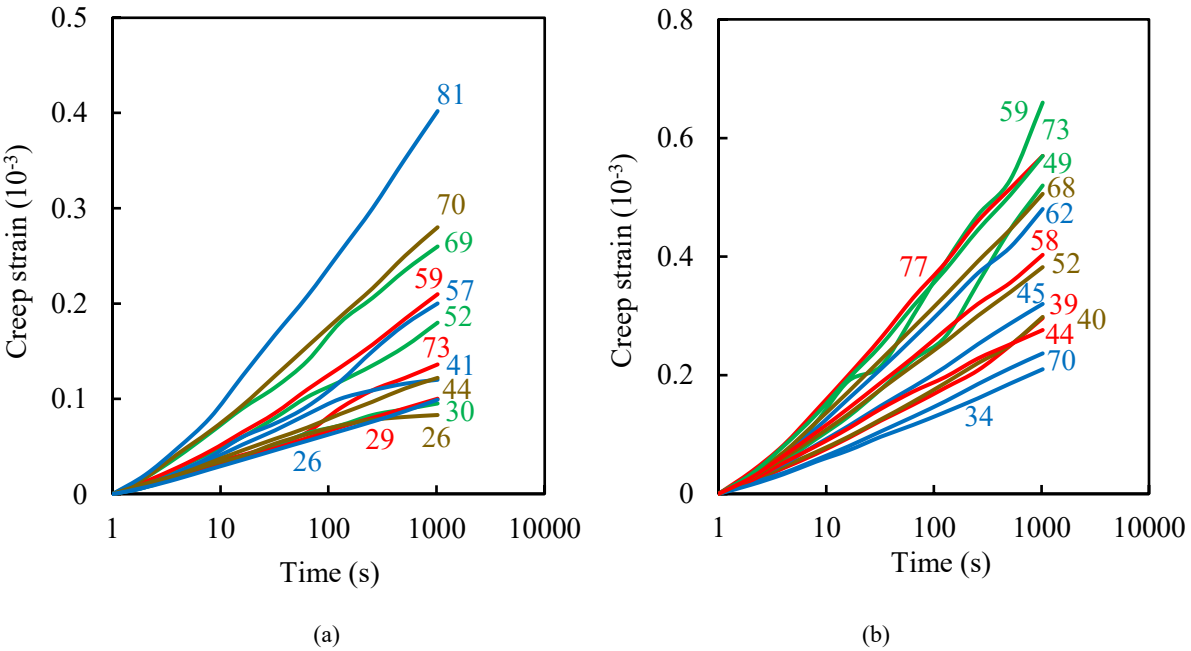


Fig. 3 Relation between creep strain and time in the decelerating creep obtained between A and B in Fig. 2.The numbers indicate creep stress levels. (a) Tage tuff and (b) Sanjome andesite.

Figure 4 shows the relation between creep strain and residual time obtained between D and E in Fig. 2; the time elapsed from right to left in Fig. 4. The curve with the same number and color as that in Fig. 3 was obtained from the same specimen. The curves for both rocks are linear or slightly convex upward in a similar manner to the curve enclosed by the red oval in Fig. 1 (c). The curves are located from bottom to top in an almost descending order of stress levels, and creep failure occurred within a few thousand seconds at not only high but also low stress levels.

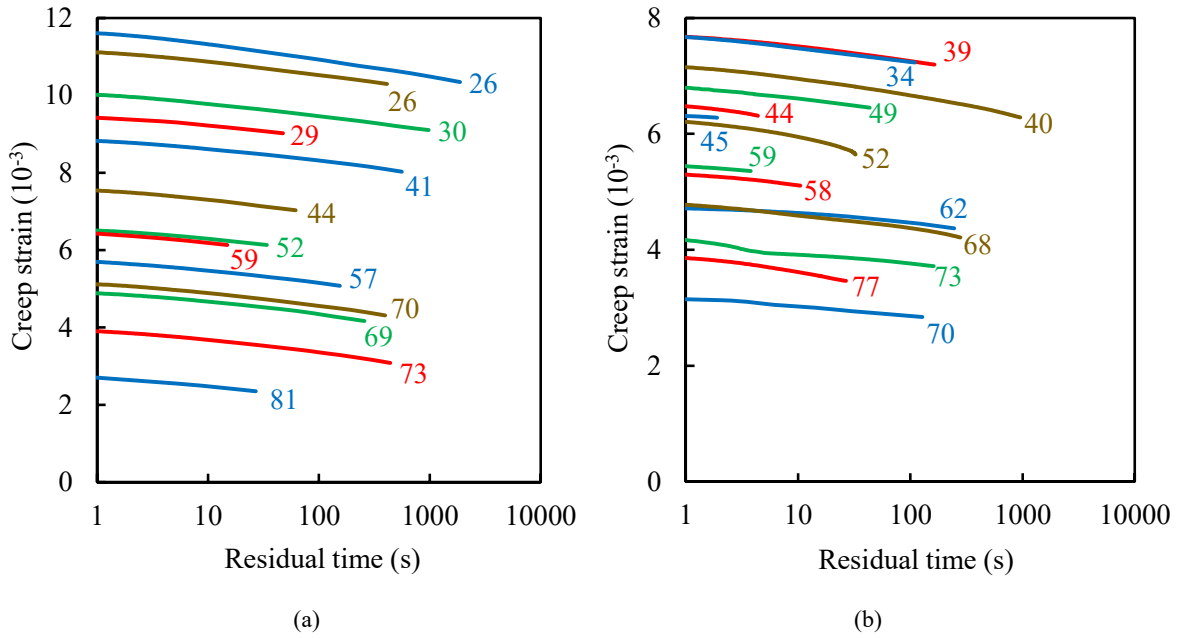


Fig. 4 Relation between creep strain and residual time in the accelerating creep obtained between D and E in Fig. 2. The numbers indicate creep stress levels. (a) Tage tuff and (b) Sanjome andesite.

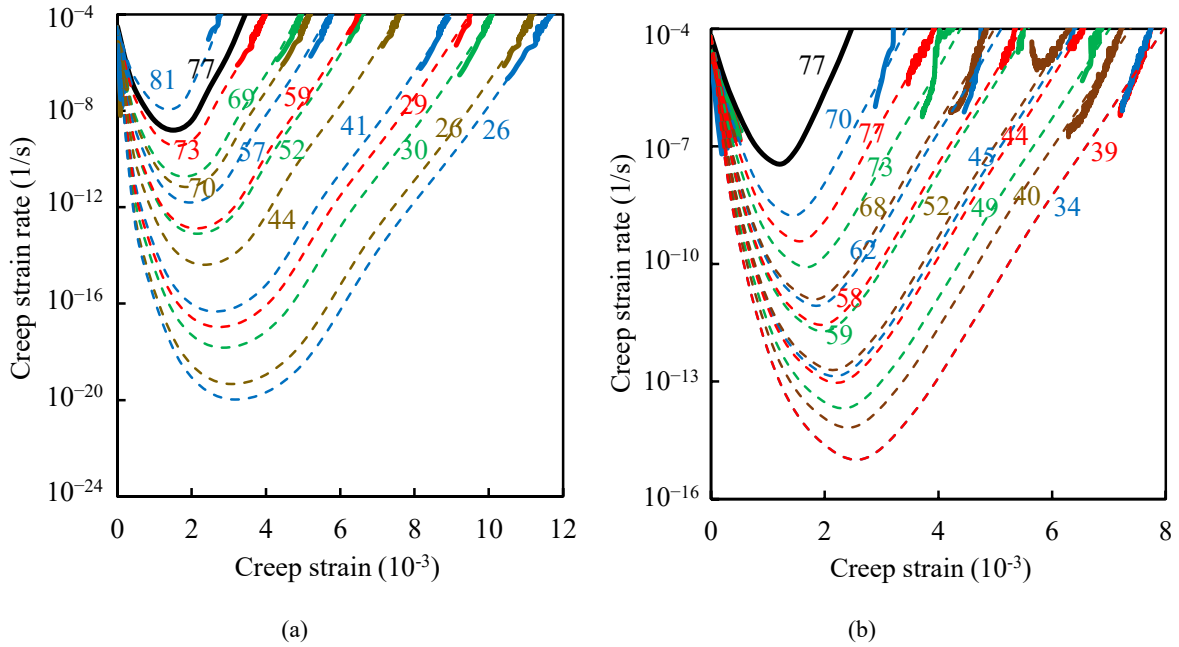


Fig. 5 Relation between creep strain rate and creep strain. The solid lines with colors were obtained in this study. The solidblack lines were obtained by Chu (1995) for Tage tuff and by Fukui (1990) for Sanjome andesite. The dashed lines were calculated from the solid black lines using Eq. (1) and (2). The numbers indicate creep stress levels. (a) Tage tuff and (b) Sanjome andesite.

Figure 5 shows the relation between creep strain rate and creep strain by solid lines with the same colors as those in Figs. 3 and 4. The decelerating and accelerating creep curves are observed at the left and right sides of the figures, respectively, in a similar manner to the curvesenclosed by the blue and red ovals in Fig. 1 (a). The results at high stress levels obtained in previous studies are shown in black, indicating that the strain rate decreases, reaches a minimum, and increases until failure occurs. To interpolate the decelerating and accelerating creep curves atthe low stress levels, the black line for

each rock was enlarged or reduced along both the horizontal and vertical axes using thefollowing equations.

$$\varepsilon_c' = \varepsilon_c \left\{ 1 + (r-1)\frac{\varepsilon_c}{\varepsilon_{cf}} \right\} \tag{1}$$

$$log\frac{d\varepsilon_c'}{dt} = log\frac{d\varepsilon_{c0}}{dt} - r\left(log\frac{d\varepsilon_{c0}}{dt} - log\frac{d\varepsilon_c}{dt} \right) \tag{2}$$

Where r Conversion ratio
ε_c Original creep strain on the black line
ε'_c Converted creep strain
ε_{cf} Final creep strain on the black line
$d\varepsilon_c/dt$ Original creep strain rate on the black line
$d\varepsilon'_c/dt$ Converted creep strain rate
$d\varepsilon_{c0}/dt$ Initial creep strain rate on the black line

Figure 5 shows the relation between the converted creep strain rate and creep strain by dashed lines with the same colors as those of the corresponding solid lines. Here, the conversion ratio r was set such that each of the dashed lines coincides with the decelerating and accelerating creep curves of the same color. This figure shows that the decelerating and accelerating creep curves are appropriately interpolated by the dashed lines and that the strain rate decreases, reaches a minimum, and increases until failure occurs at all the low stress levels.

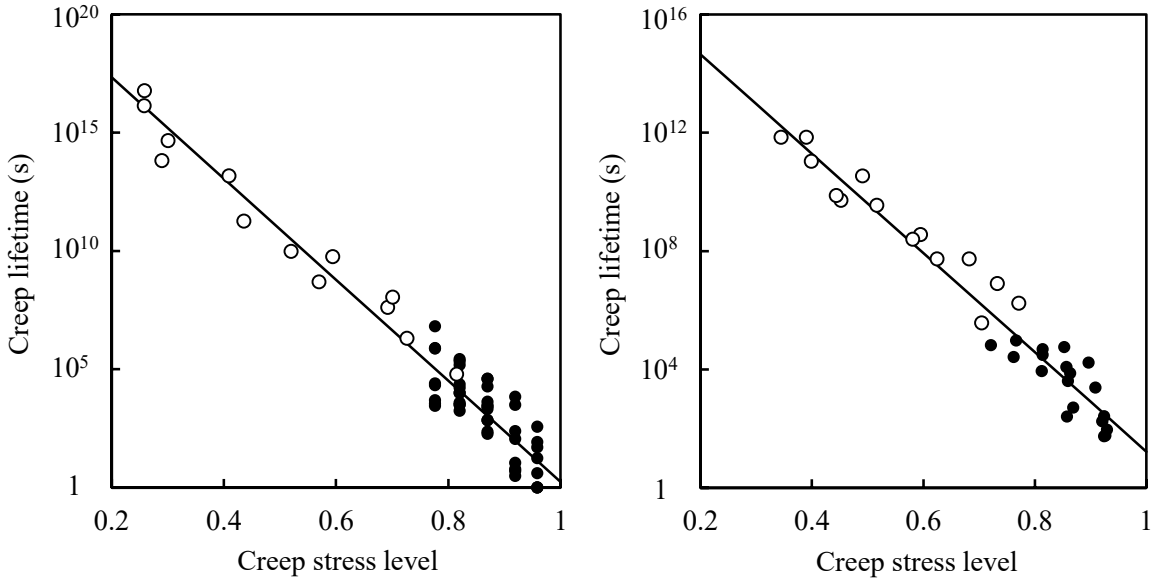


Fig. 6 Relation between creep lifetime and creep stress level. The open symbols were estimated in this study, and the closed symbols were obtained by Chu (1995) for Tage tuff and by Yamaguchi (1980) for Sanjome andesite. The black lines were calculated using Eq. (3). (a) Tage tuff and (b) Sanjome andesite.

The creep lifetime for each specimen was estimated by integrating the reciprocal of creep strain rate with respect to creep strain in Fig. 5 and shown by open symbols in Fig. 6. The closed symbols indicate the results obtained from conventional creep tests at high stress levels in previous studies. The test results at high stress levels as well as the estimated resultsatlow stress levels are located near the straight lines represented by the following equation with a and b of 21 and 22 for Tage tuff and 17 and 18 for Sanjome andesite.

$$\log t_c = -a\sigma_c + b \tag{3}$$

Where a, b Constants
t_c Creep lifetime
σ_c Creep stress level

4 Conclusions

The decelerating and accelerating creep curves were separately obtained for the two Japanese rocks, tuff and andesite, at low stress levels, using the test method in which axial stress is increased, kept constant for a while at a predetermined stress level, increased again, decreased in the post-peak region, and kept constant until failure occurs. The relations between creep strain and time in the decelerating portion and between creep strain and residual time in the accelerating portion were in a similar manner to those obtained from conventional creep tests at high stress levels. By interpolating the decelerating and accelerating creep curves using the results previously obtained at high stress levels, the complete creep curves and hence creep lifetimes were estimated at stress levels of between 20% and 80%. The relation between creep lifetime and creep stress level for the two rocks was found to be almost linear on a single logarithmic chart at not only high but also low stress levels. The applicability of this study to other rocks under various stress states and test environments will be examined in future studies.

The test method to obtain decelerating and accelerating creep curves is promising for investigating the long-term creep behavior of rock at low stress levels. However, the stress history in this test method is much more complicated than that in conventional creep tests, and hence its influence on creep behavior needs to be investigated in future studies.

References

Aydan Ö, Ito T, Özbay U, Kwasniewski M, Shariar K, Okuno T, Özgenoğlu A, Malan DF, Okada T (2014) ISRM suggested methods for determining the creep characteristics of rock. Rock Mech. Rock Eng. (47): 275–290. https://doi.org/10.1007/s00603-013-0520-6

Brantut N, Heap MJ, Meredith PG, Baud P (2013) Time-dependent cracking and brittle creep in crustal rocks: A review. J. Struct. Geol. (52): 17–43. https://doi.org/10.1016/j.jsg.2013.03.007

Brantut N, Heap MJ, Baud P, Meredith PG (2014) Rate- and strain-dependent brittle deformation of rocks. J. Geophys. Res. Solid Earth (119): 1818–1836. https://doi.org/10.1002/2013JB010448

ChuSY (1995) The time dependency of rocks under water-saturated condition. Dissertation at the University of Tokyo

Fukui K (1990) Creep and delayed failure of rocks under various loading conditions. Dissertation at the University of Tokyo

Hashiba K, Fukui K (2020) Twenty-year creep test with tuff under uniaxial compression. Geotech. Test. J. (43): 800–808. https://doi.org/10.1520/GTJ20180358

Hashiba K, Fukui K (2025) Innovative test methods for investigating the time-dependent behavior of rock: Review and new insights. Rock Mech. Rock Eng. (58): 12913–12927. https://doi.org/10.1007/s00603-025-04796-y

Imani M, Hedayat A, Walton G (2025) Critical state of damage at the onset of acceleration creep in Stanstead granite evaluated using 2D-DIC and percolation theory approach. Rock Mech. Rock Eng. https://doi.org/10.1007/s00603-025-05114-2

Innocente JC, Paraskevopoulou C, Diederichs MS (2021) Estimating the long-term strength and time-to-failure of brittle rocks fromlaboratory testing. Int. J. Rock Mech. Min. Sci. (147): 104900. https://doi.org/10.1016/j.ijrmms.2021.104900

ItôH, Sasajima S (1987) A ten year creep experiment on small rock specimens. Int. J. Rock Mech. Min. Sci. &Geomech. Abstr. (24): 113–121. https://doi.org/10.1016/0148-9062(87)91930-9

Okubo S, Nishimatsu Y, Fukui K (1991) Complete creep curves under uniaxial compression. Int. J. Rock Mech. Min. Sci. &Geomech. Abstr. (28): 77–82. https://doi.org/10.1016/0148-9062(91)93235-X

Wagner H (2019) Deep mining: A rock engineering challenge. Rock Mech. Rock Eng. (52): 1417–1446.https://doi.org/10.1007/s00603-019-01799-4

Yamaguchi T (1980) The time-dependent mechanical behavior of rock. Dissertation at the University of Tokyo

Zhang T, Zheng X, Wang S, Yang J, Chen X (2025): Discrimination, mechanical mechanisms, and control technologies for largedeformation in tunnel surrounding rock: A state-of-the-art review. Tunn. Undergr. Space Technol. (163): 106712.https://doi.org/10.1016/j.tust.2025.106712

Research on ambient vibration-based quantitative assessment of tunnel lining defect using laser Doppler vibration measurement

X.P. Zhang
Shandong University of Science and Technology, Qingdao, China
zhangxuepeng0722@126.com

N.B. Li
General Institute of Water Resources and Hydropower Planning and Design, Beijing, China

Y.J. Jiang
Shandong University of Science and Technology, Qingdao, China
Nagasaki University, Nagasaki, Japan

Y. Wang
PowerChina Beijing Engineering Corporation Limited, Beijing, China

G.S. Wei
Shandong University of Science and Technology, Qingdao, China

Abstract

The necessity for automated and information-based inspection methods for the daily maintenance of tunnels is becoming increasingly apparent, given the ongoing increase in the number of tunnels. The paper sets out a method for non-contact detection that uses a laser Doppler vibrometer based on ambient vibration. The approach involves the introduction of a dimensionless quantitative index termed Fundamental Frequency Deterioration Degree (FFDD), which is based on the fundamental frequency itself. To validate this method, laboratory ambient vibration detection tests were conducted on cubic concrete samples which consider strength, cavity, and cracks under compression. The PDV-100 laser Doppler vibrometer was utilized for the purpose of ambient vibration collection. The findings demonstrate a strong correlation between concrete defects and the fundamental frequency. The correlation between FFDD and concrete defects serves to validate its accuracy. The method was applied in situ to detect and assess grouting defects in a newly constructed metro tunnel, thus further validating its use in real-world scenarios.

Keywords

Tunnel lining defect, Quantitative assessment, Ambient vibration, Laser Doppler vibrometer.

1 Introduction

The construction of tunnels has witnessed significant growth globally, particularly in China, over the past few decades. However, such expansion has raised concerns regarding the deterioration and defects that can arise due to natural and man-made factors, as well as the effects of aging on concrete lining structures. Issues such as cracks, cavities, deformations, and leakage have become pressing matters for the daily operation, management, and maintenance of tunnel linings. Inefficient defect detection may eventually lead to structure fracture and even serious safety accidents, leading to immeasurable property losses and casualties (Xu and Qian 2024). Hence, accurate detection and assessment of these damages are crucial initial steps toward effective maintenance and extending the service life of these engineering structures.

Traditional detection methods for tunnel damage, which rely on manual inspection, are time-consuming, subjective, and prone to human error. Additionally, the working environment poses safety risks for personnel (Menendez et al. 2018). Although some non-artificial methods have beenpartially employed in tunnel engineering, the efficiency of drilling cores, acoustic detection, and 3D laser scanning is relatively low. Moreover, geological radar requires contact with the lining surface, making it challenging to meet the requirements of rapid and efficient testing of tunnel linings. Thus, a non-contact and high-efficiency non-destructive detection method is necessary.

Ambient vibration as a continuous, low-amplitude vibrations always present in the surrounding environment is an available tool to characterize the dynamic behavior of the structure itself. Thus, valuable information for structural integrity could be retrieved due to the relationship between the structure stiffness and the dynamic characterization such as fundamental frequency (Du et al. 2024). Currently, ambient vibration measurement technology using patch accelerometers offers advantages such as low cost, good environmental performance, and excellent deviation stability, making it suitable for detecting tunnel lining diseases (Jiang and Zhang 2021). However, it faces challenges in terms of low detection efficiency and contact-based detection. On the other hand, laser Doppler vibrometers (LDVs) technology enables rapid and efficient remote vibration measurement and finds extensive applications in areas such as dangerous rock safety detection and landslide safety and stability evaluation (Du et al. 2017; Du et al. 2022). However, its effectiveness in detecting lining structure defects is not yet clear, and further research is needed to explore its fundamental principles and potential applications.

Thus, this paper quantitatively evaluates tunnel lining defects through the ambient vibration building upon knowledge from damage mechanics and vibration mechanics. On one hand, laboratory experiments are conducted to investigate the material strength level, the presence of an internal cavity, and the occurrence of lining cracks in different concrete specimens by applying the laser Doppler vibrometer. A dimensionless quantitative index called Fundamental Frequency Deterioration Degree (FFDD) based on the fundamental frequency is introduced. Subsequently, the proposed index is employed in situ for detecting and assessing grouting defects in a newly constructed metro tunnel, thereby validating its efficacy.

2 LDVs-based ambient vibration test and assessment methodology

2.1 LDVs-based ambient vibration test methodology

LDVs-based ambient vibration test methodology is a non-invasive technique used to assess the dynamic characteristics of soil and rock layers or structures. It employs the principles of laser Doppler vibrometer to measure ground motion resulting from microtremors or ambient vibrations. By measuring the velocity of ground or structure motion in response to microtremors, the test provides valuable data. During the test, a laser beam is directed toward the surface of the ground or structure, and a sensor detects the reflected light. As the ground or structure vibrates, the frequency of the reflected light undergoes a Doppler shift proportional to the velocity at that point. The acquired velocity data is communicated between the sensor and analysis software in a laptop through the USB data acquisition. The acquired velocity data is then processed to obtain microtremor spectra. These spectra reveal amplitude and phase variations of ground or structure motion at different frequencies. From these spectra, important parameters such as dominant frequency, amplification factor, and resonant frequency can be determined.

Given the knowledge of vibration mechanics and structure mechanics, it is possible to detect damage in an object by observing a decrease in its stiffness, which is indirectly reflected in the natural vibration frequency. Therefore, utilizing ambient vibration for object damage detection proves to be a feasible approach. Its test and assessment flow are as depicted in Fig. 1.

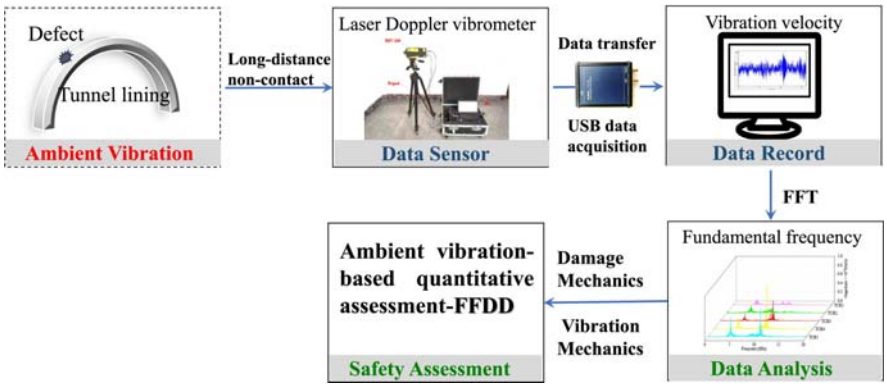


Fig. 1 Flow of the LDVs-based ambient vibration test and assessment methodology.

2.2 Fundamental frequency deterioration degree (FFDD)

Based on the principles of damage mechanics, it is understood that the presence of defects in a material will result in the dissipation of energy within it. This dissipation corresponds to an irreversible change in the material's internal structure. In the case of a one-dimensional linear problem, the extent of deterioration (referred to as DD) can be quantified by examining the change in elastic modulus before and after the occurrence of damage, as outlined below.

$$DD = 1 - \frac{\tilde{E}}{E} \tag{1}$$

where, E is the modulus of elasticity in the healthy state of the material with the unit of *MPa*; $\tilde{E}$ is the material modulus of elasticity in the damaged state with the unit of MPa. Elastic wave propagation velocity of the elastic isotropic body C_p can be obtained through the elastic parameters as shown in Equation (2).

$$C_p = \sqrt{\frac{E}{\rho}\frac{1-v}{(1+v)(1-2v)}} \tag{2}$$

where ρ is density with unit of kg/m^3 and v is the Poisson's ratio. Poisson's ratio remains constant regardless of the defect morphological characteristics of the material (Prassianakis and Prassianakis 2004). Therefore, the propagation velocity $\tilde{C}_p$ of elastic waves in the damaged body can be expressed as follows:

$$\tilde{C}_p = \sqrt{\frac{\tilde{E}}{\tilde{\rho}}\frac{1-v}{(1+v)(1-2v)}} \tag{3}$$

where $\tilde{\rho}$ is the density of the damaged elastic body. Generally, when the structure has only local small damage, the density and wavelength of the structure before and after damage change little (Jiang et al. 2023). According to the quantitative relationship between wavelength λ and wave velocity C_p, Equation (1) can be rewritten considering the natural vibration frequency as follows.

$$DD = 1 - \frac{\tilde{E}}{E} = 1 - \frac{\tilde{\rho}\tilde{\lambda}^2\tilde{\omega}^2}{\rho\lambda^2\omega^2} \tag{4}$$

where, λ and $\tilde{\lambda}$ are the wavelengths in the health and damage state with unit of m, and ω and $\tilde{\omega}$ are the natural frequencies in the health and damage state with unit of Hz. Then Equation (4) can be simplified as:

$$DD \approx 1 - \frac{\tilde{\omega}^2}{\omega^2} = FFDD \tag{5}$$

Equation (5) demonstrates that the quantitative assessment of damage in concrete structures can be achieved by comparing the fundamental frequency values before and after the occurrence of damage. This index is referred to as the fundamental frequency-based deterioration degree (FFDD).

3 Laboratory ambient vibration test for concrete samples

3.1 Specimen preparation and laboratory test procedure

Tunnel lining structures are often subject to material aging, cavities, cracks and other defects and diseases due to various factors. Three indicators including concrete strength deterioration, cavity and crack (through and non-through) were chosen as experimental design factors. Table 1 lists the specific design scheme for the current study.

Table 1. Non-destructive test design scheme for concrete specimen.

Liningdefect	Design factor	Value (Case No.)
Aging	Strength value/MPa	25(D1), 30(D2), 35(D3), 40(D4), 45(D5), 50(D6)
Cavity	Hollow balldiameter/mm	0(CA1), 20(CA2), 30(CA3), 40(CA4), 50(CA5),60(CA6), 70(CA7), 80(CA8), 90(CA9)
Crack	Through crack:length × depth/mm × mm	0 × 0(TCR1), 35 × 150(TCR2), 70 × 150(TCR3), 105 × 150(TCR4), 140 × 150(TCR5)
	Non-throughcrack:length × depth/mm × mm	0 × 0(NTCR1), 35 × 75(NTCR2), 70 × 75(NTCR3), 105 × 75(NTCR4), 140 × 75(NTCR5)

Concrete specimens measuring 150 mm × 150 mm × 150 mm were chosen for the study. Two specimens were prepared for each defect type to achieve the required accuracy for the fundamental frequency. All specimens were kept at a constant temperature of 25°C for approximately 28 days to ensure proper curing.

Regarding the effect of concrete strength, a reference specimen with a uniaxial compression strength (UCS) of 50 MPa was used (refer to asUCS50). Five additional cases were designed with UCS values of 45 MPa, 40 MPa, 35 MPa, 30 MPa, and 25 MPa. For assessing the effect of cavities, hollow plastic balls were inserted at the center of the concrete specimens during the molding process. The diameters of the plastic balls were selected as 20 mm, 30 mm, 40 mm, 50 mm, 60 mm, 70 mm, 80mm, and 90 mm. Since the presence of hollow balls has minimal impact on the strength of the specimens, they were not removed during subsequent testing. To examine the effect of cracks, mortar concrete was embedded with thin iron sheets to create cracks. The iron sheet, half the height of the specimen for through cracks (150 mm), and full height for non-through cracks (75 mm), was placed diagonally across the specimen. After molding, the iron sheets were removed to better simulate the authenticity of specimens with crack defects. The design and physical appearance of the specimens are illustrated in Fig. 2.

An ambient vibration test was conducted on the specimen under uniaxial compression using a laboratory Laser Doppler vibrometer system, as shown in Fig. 3. The applied loads for this test ranged from 0 MPa to 3 MPa, with increments of 0.5 MPa. Each specimen underwent three tests, and the average value was taken for analysis to minimize data dispersion. The velocity-time history data captured by the Laser Doppler vibrometer system was transformed into velocity-frequency data using Fast Fourier Transform (FFT). Subsequently, the first natural frequency (also known as the fundamental frequency) in the frequency domain was used to calculate the fundamental frequency-based deterioration degree (FFDD).

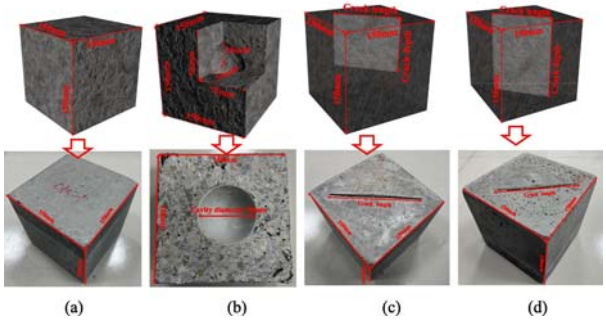


Fig. 2 Design and physical concrete specimen. (a) Specimen with UCS of 30 MPa; (b) Specimen with cavity; (c) Specimen with non-through crack; (d) Specimen with through crack.

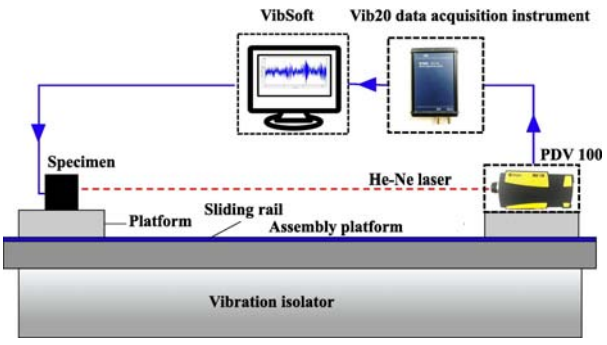


Fig. 3 LDVs-based ambient vibration test for concrete samples in laboratory.

3.2 FFDD-based deterioration assessment

The proposed assessment index for concrete damage, FFDD, is calculated using Equation (5) based on ambient vibration. Fig. 4 displays the FFDD of the concrete specimen about concrete damage under

different compression stresses. Dimensionless quantities are considered: UCS/UCS50 for strength effect, Cavity volume/Specimen volume for cavity effect, Crack length/Specimen diagonal length for crack effect. For the reference specimen, the FFDD is zero according to Equation (5). The FFDD of each specimen shows an exponential relation to the strength with a correlation coefficient of up to 0.75 and quadratic polynomial relations to the defect dimension, with a correlation coefficient of up to 0.93. In cases of strength degradation, the FFDD reaches its maximum value of 14.57% when the UCS/UCS50 of the concrete decreases from 1.0 to 0.5. In cases of internal cavities, the maximum FFDD of 25.11% is observed with a cavity maximum diameter of 90 mm (CV/SV = 0.1885). In cases of cracks, the FFDD reaches its maximum value of 6.63% for non-through cracks and 13.53% for through cracks, with a maximum crack length of 140 mm (CL/SDL = 0.65997). The positive correlations indicate that the proposed ambient vibration-based FFDD can quantitatively assess defects.

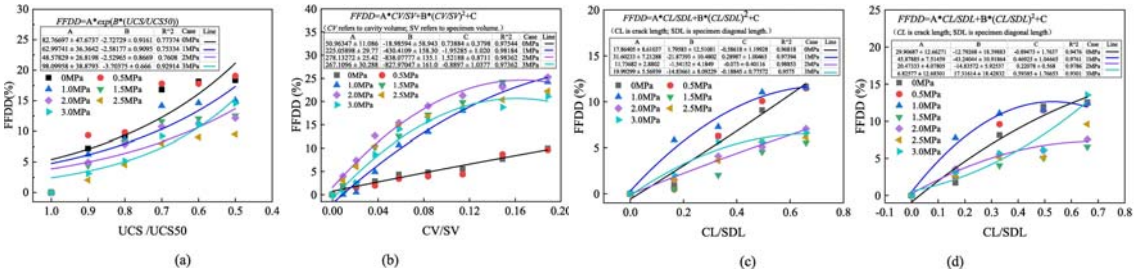


Fig. 4 FFDD of the concrete specimen regarding concrete defect under different compression stresses. (a) Strength effect; (b) Cavity effect; (c) Non-through crack effect; (d) Through crack effect.

4 In-situ application of ambient vibration detection

A newly constructed metro tunnel was detected to check its grouting quality behind shield segments. The same PDV 100 laser Doppler vibrometer is applied for field detection. Detection results were compared to those obtained with Ground Penetrating Radar (GPR) technology. Figure 5 illustrates GPR images indicating the presence of grouting defects in the tunnel segments. Figure 6 presents the fundamental frequency and the corresponding FFDD (calculated using Equation (5)) detected by the PDV-100 laser Doppler vibrometer. When the grouting quality is fine, the fundamental frequency remains constant with a very small floating range. However, when a grouting defect is present, the fundamental frequency decreases.

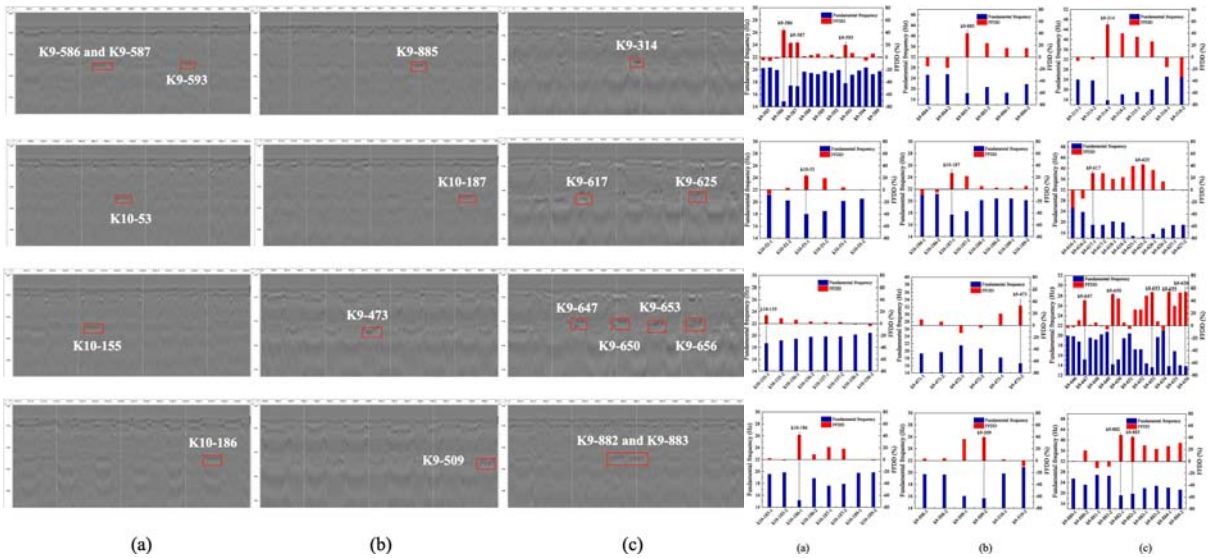


Fig. 5 GPR images with a grouting defect in the newly built metro tunnel. (a) Sidewall; (b) Spandrel; (c) Crown.

Fig. 6 Fundamental frequency and correspondingly calculated FFDD detected by PDV-100 laser doppler vibrometer. (a) Sidewall; (b) Spandrel; (c) Crown.

The correlation between the size of grouting defects and the proposed ambient vibration-based quantitative assessment index FFDD was investigated using GPR images, as depicted in Fig. 7. The analysis reveals a linear relationship between the length of the defect and FFDD, with a correlation coefficient of 0.9584. This linear correlation indicates that the LDVs-based ambient vibration assessment is an effective method for quantitatively evaluating tunnel lining defects, both in laboratory settings and on-site.

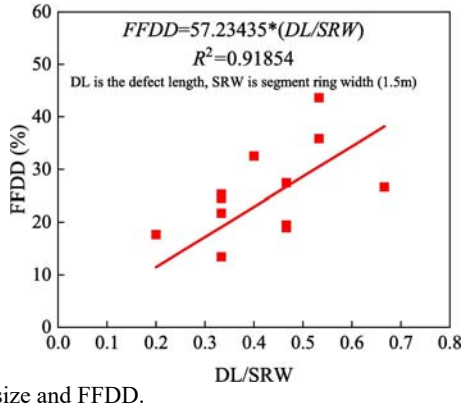


Fig. 7 Correlation between the defect size and FFDD.

5 Conclusions

Investigation of tunnel lining defects using ambient vibration-based quantitative assessment is conducted in this study. A dimensionless quantitative index called Fundamental Frequency Deterioration Degree FFDD is developed for assessing lining defects, based on the knowledge of damage mechanics and vibration mechanics.

Laboratory ambient vibration tests using laser Doppler vibrometer are performed on cubic concrete specimen. The results obtained from laboratory tests indicate strong relationships between the fundamental frequency of the concrete specimen and pre-designed defects. Additionally, the proposed FFDD of each specimen shows a positive correlation with both strength degradation and defect dimensions. These positive correlations demonstrate that the proposed ambient vibration-based FFDD can quantitatively assess concrete deterioration.

The laser Doppler vibrometer is then applied in-situ to detect the grouting quality in a newly-built metro line, in contrast to the SIR-3000 GPR instrument. The proposed FFDD based on the in-situ ambient vibration is calculated quantitatively assess grouting quality. A linear correlation between the grouting defect size and FFDD is observed to confirm the effectiveness of ambient vibration-based quantitative assessment using laser Doppler vibrometer in an in-situ setting.

References

DuY., Huo L.C., Zhang H.D., et al.(2022) Experimental research on remote monitoringand early warning of rock collapse. J. China Uni. Min. Tech. (51): 1201-1208. https://doi.org/10.13247/j.cnki.jcumt.001427.

Du Y., Li H., Chicas S. D., et al. (2024) Mechanical identification method of amplitude warning false alarm points based on dynamical time-frequency domain analysis. Rock Mech. Rock Eng. (57): 5291-5301. https://doi.org/10.1007/s00603-024-03812-x.

Du Y., Xie M.W., Jiang Y.J., et al.(2017) Experimental rock stability assessment using thefrozen-thawing test. Rock Mech. Rock Eng. (50): 1049-1053.https://doi.org/10.1007/s00603-016-1138-2.

Jiang Y.J., Wu F.B., Zhang X.P., et al.(2023) Non-destructive quantitative assessment onthe damage of concrete structure based on laser Doppler vibrometer technology. J. China Uni. Min. Tech. (52): 889-903. https://doi.org/10.13247/j.cnki.jcumt.20230001.

Jiang Y.J., Zhang X.P. (2021) Research on automatic detection and health assessment of tunnel lining. Tunn. Constr. (41):341-348. https://doi.org/10.3973/j.issn.2096-4498.2021.03.001.

Menendez E.,Victores J.G., Montero R., et al. (2018) Tunnel structural inspection andassessment using an autonomous robotic system. Automat. Constr. (87): 117-126. https://doi.org/10.1016/j.autcon.2017.12.001.

Prassianakis N.I., Prassianakis I.N.(2004) Ultrasonic testing of non-metallic materials:concrete and marble. Theo. Appl. Fract. Mec.(42): 191-198, https://doi.org/10.1016/j.tafmec.2004.08.007.

Xu P., Qian T.F. (2024) High-speed rail defect detection using multi-frequency exciting 3DACFM. Measurement (227): 114160. https://doi.org/10.1016/j.measurement.2024.114160.

Numerical modelling of cracking in granite due to Joule heating and piezoelectric actuation

T. Saksala
Tampere University, Tampere, Finland
timo.saksala@tuni.fi

Abstract

Traditional comminution and drilling of hard rock, being based on mechanical breakage, suffers from severe tool wear. This has spurred intensive search for advanced preconditioning methods to facilitate mechanical breakage. One of these method uses high voltage electric pulses to fracture rock. This can happen directly, via Joule heating, whereby a rapid rise of the pressure and temperature in the electric breakdown channel between electrodes break the rock. Alternatively, the quartz phase in quartz-bearing rocks can be actuated by the converse piezoelectric effect.

In the present study, a numerical model to simulate both techniques, the Joule heating and the piezoelectric actuation of the quartz phase, is developed. This task involves developing a rock fracture model and a solution scheme for the underlying coupled piezoelectro-thermo-mechanical problem. As to the rock fracture model, the embedded discontinuity finite elements approach is chosen. In this approach, a crack with the normal parallel to the first principal direction is introduced into a finite element upon violation of the Rankine criterion. Moreover, random clusters of finite elements representing the constituent minerals with their respective mechanical, thermal and electrical properties describe the rock heterogeneity. A staggered approach, with explicit time marching for the mechanical equation of motion, is applied in solving the coupled system of equations at the global level.

In the numerical examples, cracking of a heterogeneous granitic rock specimen under high voltage boundary condition is simulated in axisymmetric conditions. The results demonstrate that at lower voltages cracking is mainly due to Joule heating while at higher level, ~2.5 kV, cracks are induced also by the piezoelectric effect. Such a modelling technique is an asset that facilitates geotechnical project risk management by allowing numerical investigation of different physical and operational factors influencing the electro-pulse based preconditioning of rock mass.

Keywords

Piezoelectric actuation, Joule heating, rock fracture, numerical modelling, finite elements.

1 Introduction

Traditional drilling and mining operations are based on mechanical breakage, e.g. by percussion and rotary drilling methods. However, there techniques incur high costs via tool wear and low penetration in hard, say granitic, formations. These deficiencies have spurred intensive research for non-conventional drilling methods where a non-mechanical agent, such as thermal jet (Rossi et al. 2018) or high-voltage electric pulse (Liu et al. 2023) assists or totally replaces the mechanical breakage action. Despite considerable advances, these methods are still at the research and development stage. The present study attempts to contribute to this research by a numerical study.

The method exploiting high voltage electric pulses is based on the electrical breakdown phenomenon of the material via rapid increase of pressure and temperature in the breakdown (plasma) channel, leading to spalling of the rock surface. When the applied voltage is high enough, cracking may happen in granite via the converse piezoelectric effect in quartz mineral (Saksala et al. 2020). In the present study, these two phenomena are numerically studied. More precisely, a numerical code is developed to simulate these phenomena, i.e. Joule heating and the converse piezoelectric effect in numerical granitic rock. As the present study is of theoretical-speculative nature, no experimental validation is provided at this preliminary stage of research.

2 Rock Fracture Model

Rock fracture is described by the embedded discontinuity finite element approach (Saksala et al. 2015). Accordingly, if the stress in a finite element exceeds the first principal stress, a displacement discontinuity (crack) with the normal parallel to the first principal direction is embedded in that element. Then, for a 3-node triangle element with a discontinuity, the displacement and strain fields are written as

$$\mathbf{u}(\mathbf{x}) = N_i(\mathbf{x})\mathbf{u}_i^e + M_{\Gamma_d}(\mathbf{x})\boldsymbol{\alpha}_d \text{with } M_{\Gamma_d}(\mathbf{x}) = H_{\Gamma_d}(\mathbf{x}) - \varphi(\mathbf{x}) \tag{1}$$

$$\boldsymbol{\varepsilon}(\mathbf{x}) = (\nabla N_i \otimes \mathbf{u}_i^e)^{sym} - (\nabla\varphi(\mathbf{x}) \otimes \boldsymbol{\alpha}_d)^{sym} + \delta_{\Gamma_d}(\mathbf{n} \otimes \boldsymbol{\alpha}_d)^{sym} \tag{2}$$

where N_i and $\mathbf{u}_i^e$ are the standard interpolation functions and nodal displacements (i = 1,2,3 with summation on repeated indices), respectively, and the displacement jump is denoted by $\boldsymbol{\alpha}_d$. Moreover, H_{Γ_d} and δ_{Γ_d} are the Heaviside function and its gradient, the Dirac delta function at a discontinuity. Furthermore, the usual assumption with low order elements that $\nabla\boldsymbol{\alpha}_d \equiv \mathbf{0}$ was made in arriving atEq. (2). This displacement jump is thus elementwise constant, similarly to the ordinary strain for a CST element.

The task of function M_{Γ_d}in (1) is to restrict the effect of $\boldsymbol{\alpha}_d$ inside the corresponding finite element, facilitating the handling of the essential boundary conditions. Function φ appearing in M_{Γ_d} is chosen so that its gradient is as parallel as possible to the crack normal $\mathbf{n}_d$ by the following criterion: $\varphi = \arg\max_{k=1,2}\left|\sum_{i=1}^{k}\nabla N_i \cdot \mathbf{n}_d\right| / \left\|\sum_{i=1}^{k}\nabla N_i\right\|$. The traction vector in the present approach is calculated by the Cauchy expression defining also the stress-strain relation

$$\mathbf{t}_{\Gamma_d} = \boldsymbol{\sigma} \cdot \mathbf{n}_d = \left(\mathbf{C}_\mathrm{e} : (\hat{\boldsymbol{\varepsilon}} - (\nabla\varphi(\mathbf{x}) \otimes \boldsymbol{\alpha}_d)^{sym}) - \boldsymbol{\varepsilon}_\mathrm{pe} - \boldsymbol{\varepsilon}_\theta\right) \cdot \mathbf{n}_d \tag{3}$$

where$\mathbf{C}_\mathrm{e}$ is the elasticity tensor, $\hat{\boldsymbol{\varepsilon}} = (\nabla N_i \otimes \mathbf{u}_i^e)^{sym}$, and $\boldsymbol{\varepsilon}_\mathrm{pe} = \mathbf{d} \cdot \mathbf{E}$ is the piezoelectric strain with $\mathbf{d}$ and $\mathbf{E}$ being, respectively, the piezoelectric constants tensor and the electric field vector. Moreover, $\boldsymbol{\varepsilon}_\theta = \alpha\Delta\theta\mathbf{I}$ is the thermal strain, with $\alpha, \Delta\theta, \mathbf{I}$ being the thermal expansion coefficient, temperature increment and the second order identity tensor, respectively.

Next, a model for solving the crack opening vector and updating the relevant variables as well as the traction vector is needed. For this end, a computational plasticity inspired model presented by Saksala et al. (2015) is employed. The relevant model components, i.e. the loading functions, softening rules and evolution laws are defined as

$$\begin{aligned} \phi_\mathrm{t}\left(\mathbf{t}_{\Gamma_d}, \kappa, \dot{\kappa}\right) &= \mathbf{n}_d \cdot \mathbf{t}_{\Gamma_d} - \left(\sigma_\mathrm{t} + q(\kappa, \dot{\kappa})\right) \\ \phi_\mathrm{s}\left(\mathbf{t}_{\Gamma_d}, \kappa, \dot{\kappa}\right) &= \left|\mathbf{m}_d \cdot \mathbf{t}_{\Gamma_d}\right| - \left(\sigma_\mathrm{s} + \frac{\sigma_\mathrm{s}}{\sigma_\mathrm{t}} q(\kappa, \dot{\kappa})\right) \\ q = h\kappa + s\dot{\kappa}, h &= -g\sigma_\mathrm{t}\exp(-g\kappa), \quad g = \frac{\sigma_\mathrm{t}}{G_\mathrm{Ic}} \end{aligned} \tag{4}$$

$$\dot{\mathbf{t}}_{\Gamma_d} = -\mathbf{C}\colon(\nabla\varphi(\mathbf{x}) \otimes \dot{\boldsymbol{\alpha}}_d)\cdot\mathbf{n}_d$$
$$\dot{\boldsymbol{\alpha}}_d = \dot{\boldsymbol{\alpha}}_{\mathrm{I}} + \dot{\boldsymbol{\alpha}}_{\mathrm{II}} = \dot{\lambda}_{\mathrm{t}}\frac{\partial\phi_{\mathrm{t}}}{\partial\mathbf{t}_{\Gamma_d}} + \dot{\lambda}_{\mathrm{s}}\frac{\partial\phi_{\mathrm{s}}}{\partial\mathbf{t}_{\Gamma_d}},\quad \dot{\kappa} = -\dot{\lambda}_{\mathrm{t}}\frac{\partial\phi_{\mathrm{t}}}{\partial q} - \dot{\lambda}_{\mathrm{s}}\frac{\partial\phi_{\mathrm{s}}}{\partial q}$$
$$\dot{\lambda}_i \geq 0,\ \ \phi_i \leq 0,\ \ \dot{\lambda}_i\phi_i = 0 \quad (i = \mathrm{t},\mathrm{s})$$

where $\mathbf{m}_d$ denotes the unit tangent of a discontinuity,$\kappa, \dot{\kappa}$are the internal variable and its rate related to the softening law for a discontinuity,and σ_{t} and $\sigma_{\mathrm{s}}$are the tensile and shear strength, respectively. Moreover, parameter h is the softening modulus of the exponential softening rule while parameter g controls the initial slope of the softening curve and is calibrated by the mode I fracture energy G_{Ic}. Moreover, the Koiter's rule for bi-surface plasticity is applied in Eq. (4) where the total displacement jump is a sum of the contributions from mode I and mode II increments, while $\dot{\lambda}_{\mathrm{t}}, \dot{\lambda}_{\mathrm{s}}$ are the corresponding crack opening and sliding increments. Furthermore, rate-sensitivity is accommodated by adding a constant viscosity term, with s being the viscosity modulus, to the stress-like internal parameter q. The final equations in Eq. (4) are the consistency conditions.

3 Coupled piezoelectro-thermo-mechanical problem

While the constitutive equation in Eq. (3) couples the mechanical, electrical and temperature fields at the material point level, system (global) level equations are needed to solve for the primary field variables, which are the displacement, $\mathbf{u}$, the electric potential, $\boldsymbol{\phi}$, and the temperature, $\boldsymbol{\theta}$. The finite element discretized version of these equations are

$$\begin{aligned}\mathbf{M}\ddot{\mathbf{u}}_t + \mathbf{f}_t^{\mathrm{int}}(\mathbf{u}_t, \dot{\mathbf{u}}_t, \boldsymbol{\theta}_t, \boldsymbol{\phi}_t) &= \mathbf{0}\\ \mathbf{K}_{\phi\mathrm{u}}\mathbf{u}_t + \mathbf{K}_{\phi}\boldsymbol{\phi}_t &= \mathbf{0}\\ \mathbf{C}_{\theta}\dot{\boldsymbol{\theta}}_t + \mathbf{K}_{\theta}\boldsymbol{\theta}_t &= \mathbf{f}_t^{\theta}\end{aligned} \tag{5}$$

where

$$\begin{aligned}\mathbf{f}_t^{\mathrm{int}} &= \mathbf{A}_{\mathrm{e}=1}^{\mathrm{N_e}}\int_{V_{\mathrm{e}}}\mathbf{B}_{\mathrm{u}}^{\mathrm{e,T}}\boldsymbol{\sigma}_{\mathrm{e}}(\mathbf{u}_t, \dot{\mathbf{u}}_t, \boldsymbol{\theta}_t, \boldsymbol{\phi}_t)\mathrm{d}V,\quad \mathbf{M} = \mathbf{A}_{\mathrm{e}=1}^{\mathrm{N_e}}\int_{V_{\mathrm{e}}}\rho\mathbf{N}_{\mathrm{e}}{}^{\mathrm{T}}\mathbf{N}_{\mathrm{e}}\,\mathrm{d}V\\ \mathbf{C}_{\theta} &= \mathbf{A}_{\mathrm{e}=1}^{\mathrm{N_e}}\int_{V_{\mathrm{e}}}\rho c\mathbf{N}_{\theta}^{\mathrm{e,T}}\mathbf{N}_{\theta}^{\mathrm{e}}\mathrm{d}V,\quad \mathbf{K}_{\theta} = \mathbf{A}_{\mathrm{e}=1}^{\mathrm{N_e}}\int_{V_{\mathrm{e}}}k\mathbf{B}_{\theta}^{\mathrm{e,T}}\mathbf{B}_{\theta}^{\mathrm{e}}\mathrm{d}V\\ \mathbf{K}_{\mathrm{u}\phi} &= \mathbf{A}_{\mathrm{e}=1}^{\mathrm{N_e}}\int_{V_{\mathrm{e}}}\mathbf{B}_{\mathrm{u}}^{\mathrm{e,T}}\mathbf{e}\mathbf{B}_{\phi}^{\mathrm{e}}\mathrm{d}V,\qquad \mathbf{K}_{\phi\mathrm{u}} = \mathbf{K}_{\mathrm{u}\phi}{}^{\mathrm{T}},\qquad \mathbf{K}_{\phi} = \mathbf{A}_{\mathrm{e}=1}^{\mathrm{N_{el}}}\int_{V_{\mathrm{e}}}\mathbf{B}_{\phi}^{\mathrm{e,T}}\boldsymbol{\varepsilon}\mathbf{B}_{\phi}^{\mathrm{e}}\mathrm{d}V\\ \mathbf{f}_{\theta} &= \mathbf{A}_{\mathrm{e}=1}^{\mathrm{N_e}}\int_{V_{\mathrm{e}}}Q_j\mathbf{N}_{\theta}^{\mathrm{e,T}}\,\mathrm{d}V\end{aligned} \tag{6}$$

where the notations are: $\mathbf{A}$ is the finite element assembly operator; $\mathbf{B}_{\phi}^{\mathrm{e}}$ ($\mathbf{B}_{\theta}^{\mathrm{e}} = \mathbf{B}_{\phi}^{\mathrm{e}}, \mathbf{E} = \mathbf{B}_{\phi}^{\mathrm{e}}\boldsymbol{\phi}_e, \boldsymbol{\theta} = \mathbf{B}_{\theta}^{\mathrm{e}}\boldsymbol{\theta}_e$) is the gradient of the electric potential interpolation matrix $\mathbf{N}_{\phi}^{\mathrm{e}}$ ($\mathbf{N}_{\theta}^{\mathrm{e}} = \mathbf{N}_{\phi}^{\mathrm{e}}$), (analogously to $\mathbf{B}_{\mathrm{u}}^{\mathrm{e}}$ which is the gradient of displacement interpolation matrix $\mathbf{N}_{\mathrm{u}}^{\mathrm{e}}$); $\mathbf{M}$ is the mass matrix with ρ being the density;$\boldsymbol{\varepsilon}$ is the dielectric constant matrix; $\mathbf{e} = \mathbf{d}\mathbf{C}_{\mathrm{e}}$ is the piezoelectric coupling matrix; $\mathbf{C}_{\theta}$ is capacitance matrix with c being the heat capacity; $\mathbf{K}_{\theta}$ is the conductivity matrix with k being the thermal conductivity; $\mathbf{f}_{\mathrm{int}}$ is the internal force vector; $\mathbf{f}_{\theta}$ is the vector of thermal loading; $Q_j = \sigma_i\|\mathbf{E}\|^2$is the Joule (Ohmic) heating source (flux) with σ_i being the electric conductivity for each phase in rock.Equation system in Eq. (5) is solved in a staggered manner so that, first, the temperature field, $\boldsymbol{\theta}$, is solved by the explicit (forward) Euler scheme. Then, the mechanical response Eq. $(5)_1$ is explicitly advanced in time (also with the Euler scheme), and, finally, the electric potential, $\boldsymbol{\phi}$, is solved from the electrostatic balance equation Eq. $(5)_2$. Cracking affects the electrical properties so that the piezoelectric coupling term approaches zero as a crack in the quartz (being the only piezoelectric phase) opens, while the isotropic permittivity of all mineral phases approaches that of vacuum. Mathematically this is achieved by

$$\mathbf{e} = \exp(-g\|\boldsymbol{\alpha}_d\|)\mathbf{d}\mathbf{C}_{\mathrm{e}},\ \ \boldsymbol{\varepsilon} = \varepsilon_0(1 + \exp(-g\|\boldsymbol{\alpha}_d\|)(\varepsilon_r - 1))\mathbf{I} \tag{7}$$

whereε_r is the relative permittivity of the mineral, while g is as in Eq. (1), and $\|\boldsymbol{\alpha}_d\|$ is the norm of the crack opening vector.

It should be noted that material properties depend on temperature and deteriorate when the material undergoes damage by microcracking. However, these effects are ignored in this preliminary study, save the key property, i.e. the electric conductivity. As for the dielectric constant of granite as a bulk, it

is almost constant from room temperature to 1000 °C at 2450 MHz (Hartlieb et al. 2016). The electric conductivity for each (granitic) rock forming mineral is defined as (Walsh and Vogler 2020)

$$\sigma_{is} = A\exp(-B/k_b\theta) \tag{8}$$

where A and B are experimental constants, and k_b is the Boltzmann's constant (8.618E-5 eV/K).

When temperature is low, the rock conductivity is dominated by pore fluids. Here also, the work by Walsh and Vogler (2020) is followed by writing the Arps law for pores fluid conductivity under 150 °C as

$$\sigma_{if} = \sigma_{iref}\frac{\theta - 251.65}{\theta_{ref} - 251.65} \tag{9}$$

where σ_{iref} is the reference electrical conductivity at the reference temperature $\theta_{ref} = 150$ °C. At higher temperatures, the pore fluid conductivity is modelled by (Walsh and Vogler 2020)

$$\begin{aligned}\log_{10}\sigma_{if} &= -1.706 - 93.78/\theta + 0.8075\log_{10}c_{sw} + 3.0781\log_{10}\rho + \log_{10}\lambda_0 \\ \lambda_0 &= 1573 - 1212\rho + 537062/\theta - 208122721/\theta^2\end{aligned} \tag{10}$$

where $c_{sw} = 3$ wt% is the effective salinity of the pore water, and λ_0 is the molar conductivity of the brine. Finaly, the effect of pore fluid on the bulk conductivity is calculated by the Archie's law for two-component mixtures (Walsh and Vogler 2020):

$$\begin{aligned}\sigma_{ibulk} &= \sigma_{is}\left(1-\phi_f\right)^p + \sigma_{if}\phi_f^m \\ p &= \log_{10}(1-\phi_f^m)/\log_{10}(1-\phi_f)\end{aligned} \tag{11}$$

where ϕ_f is the fluid volume fraction within a mineral phase, and m= 1.5 is the Archie's exponent.

4 Numerical examples

4.1 Numerical rock model

Granite rock is modelled as an aggregate of random finite element clusters, which represent the rock forming mineral phases. The fraction of elements comprising each phase corresponds to the real mineral content in the rock. The feldspars plagioclase and K-feldspar are merged to a single feldspar phase. The finite element mesh and the spatially random mineral mesotructure with the potential (voltage) boundary condition are shown in Fig.1. The configuration with the cylindrical electrodes placed on the rock surface simulates drilling like conditions.

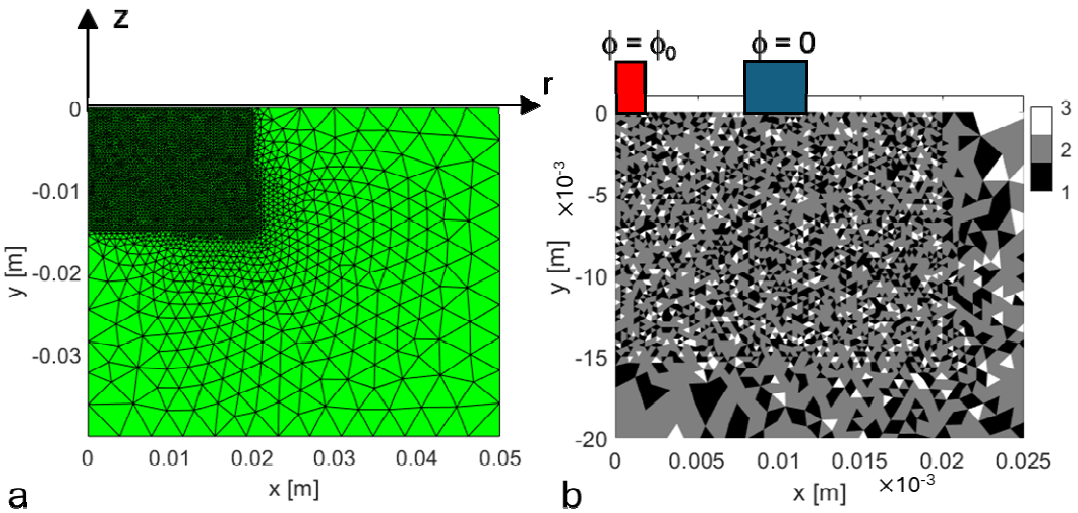


Fig. 1 Finite element mesh (6460 linear triangle elements) for axisymmetric simulations (a), and mineral mesostructure of the numerical rock with the voltage boundary conditions, i.e. the ground and positive electrodes (color code: 1 = quartz, 2 = feldspar, 3 = biotite) (b).

The material and model properties are given in Table 1 and 2.

Table 1.Material and model parameters for simulations I (Saksala et al. 2020, Hartlieb et al. 2016).

Mineral	f [%]	ρ[kg/m^3]	E [GPa]	ν	s [MPas/m]	σ_t [MPa]	σ_s [MPa]	G_{Ic} [J/m^2]	ε [F/m]
Quartz	30	2650	90	0.17	0.005	10	25	40	$4.5\varepsilon_0$
Feldspars	65	2620	60	0.29	0.005	8	25	40	$6.3\varepsilon_0$
Biotite	5	3050	60	0.20	0.005	7	25	28	$7.75\varepsilon_0$

ε_0= 8.854E-12F/m

Table 2 Material and model parameters for simulations II (Saksala et al. 2020, Hartlieb et al. 2016, Walsh and Vogler 2020).

Mineral	α [1/K]	c[J/kg·K]	k[W/m·K]	A [S/m]	B [eV]	ϕ_f [%]	d_r[m/V]	d_z [m/V]	d_{rz} [m/V]
Quartz	1.6E-5	730	4.94	544.57	0.82	0.9	–2.3E-12	2.3E-12	4.6E-12
Feldspars	0.75E-5	730	2.34	1.078	0.85	1.35	0	0	0
Biotite	1.21E-5	770	3.14	1.016E-6	0	0.9	0	0	0

The piezoelectric constants for quartz, i.e. d_r, d_z, d_{rz}, are given in local cylindrical coordinates. Thereby, the matrix including these coefficients in Eq. (3) needs to be rotated to the global coordinates. It is assumed that the quartz phase does not show any texture, i.e. systematic alignment of quartz crystal axes. Hence, the local constants are rotated to global ones by random Euler angles. In this case, the piezoelectric effect of a rock sample with quartz phase is at its weakest (Saksala 2021).

4.2 Rock sample under high voltage electric pulse

The problem described in Fig. 1 is now simulated setting the voltage $\phi_0 = 250$ kV. Fig. 2 and Fig. 3 show, respectively, the simulation results without and with the piezoelectric effect at t = 1 ms. In order to keep the computations stable, the electric conductivity (σ_{ibulk}) of an element is set to zero when the average temperature of the nodes of the element exceeds 1000 °C.

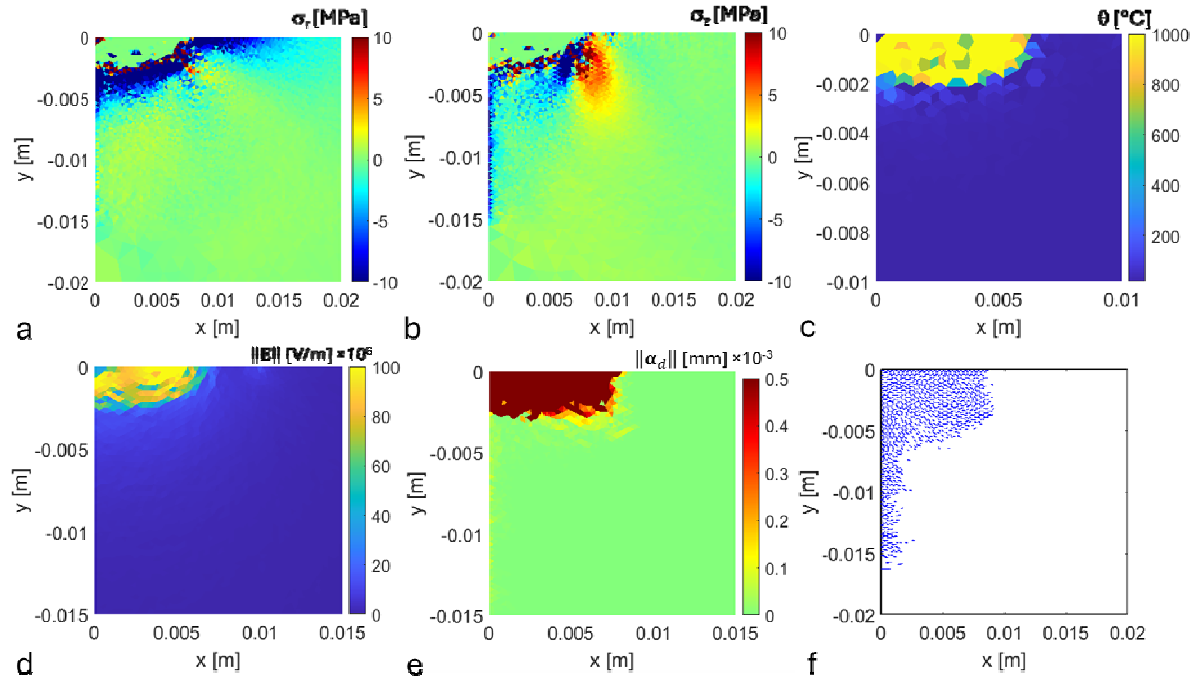


Fig. 2 Simulation results without piezoelectric effect: Radial stress (a); Stress in z-direction (b); Temperature field (c); Magnitude of electric field (d); Crack opening (e); Orientation of cracks (f).

Joule heating caused by the applied DC voltage results in significant temperature rise and consequent thermal stresses and cracking of the rock material, as attested in the results in Fig. 2. The excessive temperature rise, exceeding 1000 °C at which point the Joule heating source was set to zero, in the area between the electrodes, and the resulting crack opening, can be interpreted as crater formation. The stresses in this area are zero. The relevant simulation results with the piezoelectric effect are shown in Fig. 3.

The converse piezoelectric effect has a notable but not crucial influence on the high voltage induced cracking of granite rock. The shape of the cracked area differs from that produced when

piezoelectricity is disabled. However, the volume where crack opening is substantial is similar in both cases. Therefore, it seems the piezoelectricity can be ignored in modelling this problem.

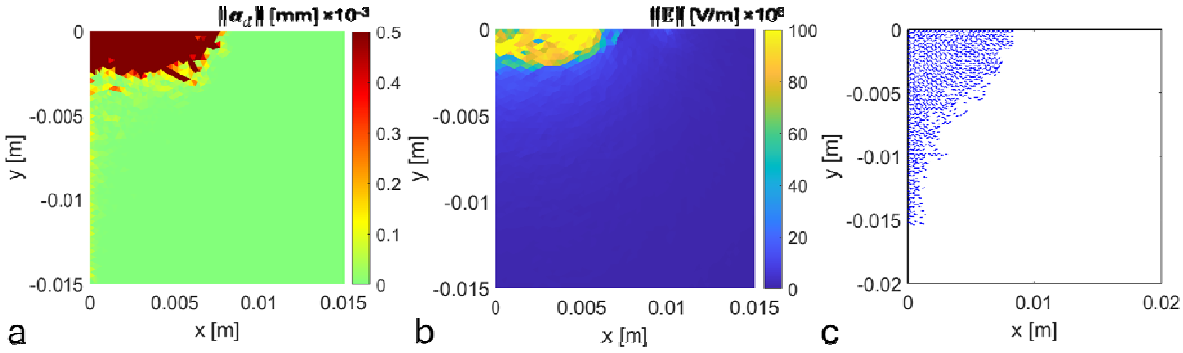


Fig. 3 Simulation results with piezoelectric effect: Crack opening(a); Magnitude of electric field (b); Orientation of cracks (c).

5 Conclusions

A finite element based computational procedure was developed to simulate cracking in granite rock due to high voltage direct current. The present model accounts for Joule heating and converse piezoelectric effect in the quartz phase. As the cracking is modelled explicitly with the embedded discontinuity finite element technology, the present method enables to study the crack orientation and opening magnitude. The numerical simulation mimicking drilling like boundary conditions revealed that the piezoelectric effect can be neglected and the Joule heating is the key phenomenon causing in cracking. In any case, the method predicts crater formation similar to that observed in experiments on electropulse drilling. It can be concluded that the present method could be used in research for the advanced drilling and comminution technologies based on preconditioning of rock before mechanical breakage. However, a full-blown 3D version should be developed for this end.

References

Rossi E, Kant MA, Borkeloh O, Saar MO, von Rohr PR (2018) Experiments on Rock-Bit Interaction during a Combined Thermo-Mechanical Drilling Method. PROCEEDINGS, 43rd Workshop on Geothermal Reservoir Engineering Stanford University, Stanford, California, February 12-14, 2018.

Liu W, Hu H, Zhu H (2023) The rock breaking mechanism of a combined high-voltage electric impulse-PDC bit drilling technology. Geothermics, 111:102723. https://doi.org/10.1016/j.geothermics.2023.102723

Saksala T, Moreno-Navarro P, Ibrahimbegovic A, Kane P-A (2020)Cracking of granite by actuation of piezoelectric properties of quartz by a high voltage electric charge: a numerical study. EUROCK2020, Trondheim, Norway, ISRM-EUROCK-2020-042 (Physical event not held due to COVID19 but the article is published at https://www.onepetro.org/conference-paper/ISRM-EUROCK-2020-042)

Saksala T, Brancherie B, Harari I, Ibrahimbegovic A (2015) Combined continuum damage-embedded discontinuity model for explicit dynamic fracture analyses of quasi-brittle materials. International Journalfor Numerical Methodsin Engineering, 101, 230–250.https://doi.org/10.1002/nme.4814

Walsh SDC, Vogler D (2020) Simulating electropulse fracture of granitic rock,International Journal of Rock Mechanics and Mining Sciences,128,104238. https://doi.org/10.1016/j.ijrmms.2020.104238.

Hartlieb P, Toifl M, Kuchar F, Meisels R, Antretter T (2016) Thermo-physical properties of selected hard rocks and their relation to microwave-assisted comminution. Minerals Engineering,91,34-41,https://doi.org/10.1016/j.mineng.2015.11.008.

Saksala T (2021) Cracking of granitic rock by high frequency-high voltage-alternating current actuation of piezoelectric properties of quartz mineral: 3D numerical study. International Journal of Rock Mechanics and Mining Sciences. 147, 104891. https://doi.org/10.1016/j.ijrmms.2021.104891.

Physical Modeling of Rockfill Material for Construction of Specific Waste Disposals Using a Large-Scale Direct Shear Apparatus

T. Jovanovska & J. Br. Papic
University Ss. Cyril and Methodius, Skopje, Macedonia
tamarajovr@gmail.com
0000-0002-9703-2206

E. Altınc ı & B. Başdemirci
GeoDestek, Ankara, Turkiye

Abstract

Characterization of bimrocks remains a major challenge in rock mechanics due to the complex interaction between strong core blocks and weaker matrix material. Although several empirical approaches exist to estimate their shear strength, large-scale experimental validation is limited and no widely accepted predictive framework has emerged. In particular, the influence of block proportion, block size distribution, matrix properties, and interface conditions on shear behavior at engineering scale is still not sufficiently quantified.

This paper presents the preparation and testing of a physical model for large-scale direct shear testing of rockfill material using a shear box with dimensions of 1.0 × 1.0 × 0.6 m. The material, sourced from the Borov Dol mine pit, represents excess rockfill generated during excavation and intended for the mine's waste dump area.

The applied normal stress is generated by four vertical hydraulic presses with a total capacity of 1 MPa, while the horizontal shear load is applied using two inclined hydraulic presses positioned at an angle of approximately 11° relative to the horizontal plane. The lower frame of the apparatus is static, and the upper frame moves during shearing.

Mixtures of fresh and altered andesitic rock, as well as their combinations, were tested. Results show that higher proportions of large blocks increase the internal friction angle. The influence of fine particles, intact rock strength, and surface roughness on shear behavior was also examined. The obtained data were compared with the Hoek–Brown and Barton strength criteria to support the development of a simplified approach for rapid extrapolation of large-scale test results.

Keywords

Direct shear apparatus, Rockfill mixtures, Physical modeling, Shear strength, Time of failure.

1 Introduction

The disposal of mining waste is an important issue both globally and in Macedonia due to its technical and environmental implications. Large quantities of waste are generated during ore extraction and must be disposed ofin accordance with strict engineering principles to minimize environmental impacts and maintain dump stability. This paper presents a case study of the waste dump at the Borov Dol mine, based on the results of investigations made in the period of 2025/26.

The Borov Dol mine, located in R. Macedonia, comprises an active open pit and a waste. The dump consists of excavated waste rock of different fractions and geological compositions and serves for the disposal of non-economic material produced during mining. Mining production began in 2020, with copper, gold, and silver as the main products, and is expected to prolong the operating life of the Bučim mine until 2030. The planned volume of mine waste is estimated at 50 million m³, while the required disposal space is estimated at 75–80 million m³.

The shear strength of rocky mine waste (overburden) is a key parameter in assessing dump stability. Such material commonly consists of coarse blocks embedded in a finer-grained matrix and may be classified as block-in-matrix (BIM) material or rockfill.

Several empirical approaches have been proposed to estimate the strength of such materials.However, a unified method is still not widely accepted in rock mechanics (1). The mechanical behavior of cohesionless bimrocks depends on the interaction between blocks and matrix (1;2). Studies by Lindquist (1994) (3) and Lindquist & Goodman (1994) (4) show that increasing volumetric block proportion (VBP) leads to higher friction angle (φ) but lower cohesion (c) and UCS, while Yu-Chen et al. (2019) (5) identify volumetric fraction (Vf) as a key parameter. Coli et al. (2009) (6) reported large-scale direct shear tests, though not fully consistent with ISRM recommendations. Based on these findings and the extensive practical experience of the Faculty of Civil Engineering, large-scale direct shear tests (1.0 × 1.0 × 0.6 m) were conducted on modeled cohesionless materials for engineering characterization.

2 Overview of the methods used for determining the shear strength

The determination of the shear strength of dumped mine rock is a key issue in mine dump stability analysis. Because these materials are coarse-grained and heterogeneous, their characterization often requires non-standard approaches, including large-scale direct shear testing.

In addition to direct testing, empirical approaches were considered for comparative interpretation. Barton and Kjaersli (1981) (7) proposed a modification of the Barton failure criterion for overburden rock and rockfill contacts, in which the governing parameters depend on the type of contact considered. The method also incorporates field tilt tests for estimation of roughness-related parameters. Depending on the material structure, different sets of parameters are considered. For joint-controlled behavior, the relevant parameters follow the Barton and Choubey (8) failure criterion and include JCS (or σp), JRC, and the friction angles φr or φb for weathered and fresh rock, respectively. For granular-type behavior, the governing parameters are the intact rock strength S, grain roughness R, and the basic friction angle φb. In cases combining block interaction and joint effects, the key parameters include the intact rock strength S, JRC, and the residual friction angle φr.

A comparative assessment was also made using the Hoek–Brown (9) failure criterion. In this approach, the material constants are expressed as functions of the Geological Strength Index (GSI), the intact rock parameter m_i, and the disturbance factor D. For the highly disturbed dumped material considered in this study, low GSI values were assumed, while the compressive strength input was based on available test results.

3 Description of the apparatus and method of testing

All tests were performed in the accredited Geotechnics Laboratory of the Faculty of Civil Engineering in Skopje using a large-scale direct shear apparatus for coarse-grained rockfill-type materials (Figure 1). The apparatus, originally constructed by the “Jaroslav Černi” Institute, was modified from 1.5 × 1.5 × 0.6 m to 1.0 × 1.0 × 0.6 m to allow normal stresses up to 1.2 MPa. It consists of upper and lower frames, each 0.30 m high, separated by a predefined horizontal shear plane. Normal load is applied by

four vertical hydraulic jacks (total capacity 1000 kN), and shear load by two jacks inclined at 11° to the horizontal. The lower frame is fixed, while the upper frame moves on rollers to reduce resistance.

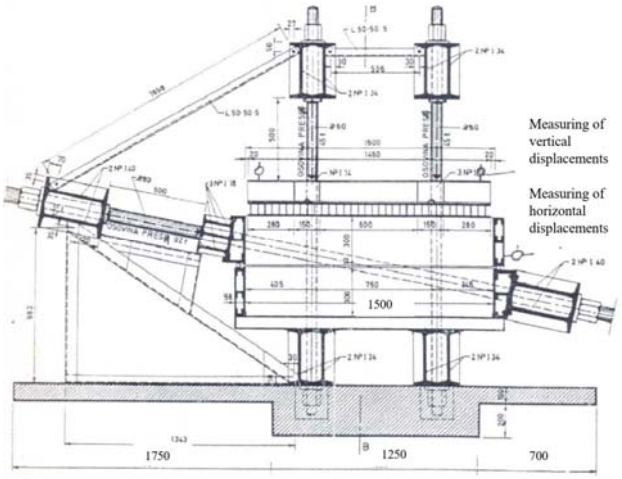


Fig.1 Large scale direct shear box with size 1,0x1,0x0,6 m applied during the testing.

4 Testing

The waste dump material is deposited in situ without controlled compaction. In the initial phase of the investigation, the unit weight, point load strength index (I_{s50}), and uniaxial compressive strength of intact rock fragments were determined. The measured compressive strength of the blocks ranged from 86 to 119 MPa, while the unit weight varied between 17.3 and 18.1 kN/m³.

In the second phase, the investigation program included 16 grain-size analyses (8 before and 8 after shearing) and 8 large-scale direct shear tests. The tested material was predominantly coarse-grained, with coarse fractions accounting for 89–95%, sand-sized particles about 5%, and silt fractions less than 1%.

The water content ranged from 5 to 6%. During the large shear test, the material generally consisted of block fragments 40–80 mm in size embedded in a fine-grained matrix, giving it the characteristics of a block-in-matrix soil (10). Some of the tested samples are given in Figure 2.



Fig. 2 Materials from the Borov Dol Waste Dump used for testing.

After specimen preparation, vertical loading was applied to generate normal stresses on the shear plane in the range of 200–1000 kPa. The load was introduced in three stages, each maintained until vertical displacement stabilized, with the maximum normal stress held constant for 24 h. After consolidation, shear loading was applied incrementally, with each step maintained until horizontal displacement ceased. Horizontal and vertical displacements were recorded continuously throughout the tests to monitor shear response and volumetric change.

As expected, and consistent with previous findings reported in the literature, the friction angle increases with increasing coarse fraction content. For specimens composed predominantly of fresh andesite, the friction angle ranges from 40.3° to 42.2°. In tuff-dominated specimens, it ranges from

29.3° in the more weathered material to 36.2°. For andesite–tuff mixtures, the friction angle varies between 30.2° and 37.1°, depending on the proportion of andesite in the mixture.

The results from the large shear test for specimen no. 3 are presented in figure 3.

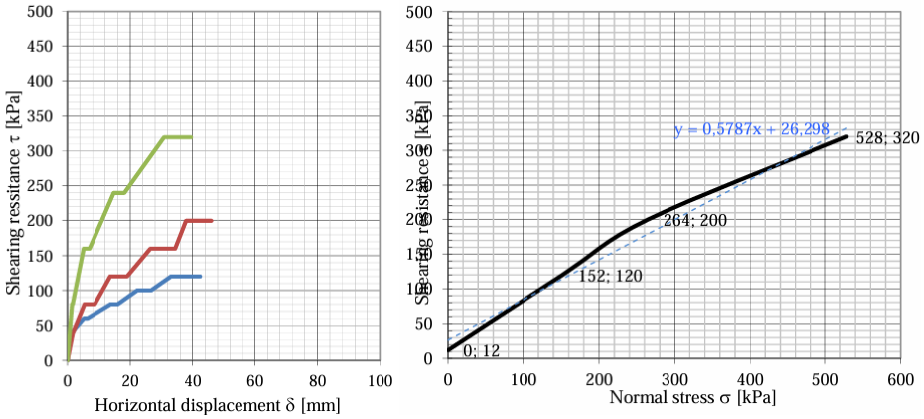


Fig.3 Results from the large-scale direct shear test for specimen no. 3 (10).

5 Comparative analysis of different failure criteria

To evaluate the applicability of the commonly used failure criteria, simulations were conducted using a comparative approach based on the Barton and Hoek–Brown methods. For the Barton method, the input parameter φr was varied within the range of 30° to 35° (30°, 32°, and 35°). The diagrams illustrating the adopted input parameters for both approaches are presented in Table 1, while the result for φr=32° is given in Figure 4.

Table 1. Input parameters for comparative analysis

Input Parameters Barton	**Input Parameters Barton Hoek-Brown**
JRC = 12	σci = 80MPa
JCS = 80	GSI =15
fr = 30, 32, 35	mi=25
	D=0
	Ei=32000
	Unit Weight= 0.022 MN/m3
	Slope Height =50m
	Mohr-Coulomb Fit
	c =0.303746MPa
	f= 49.8717
	Erm =1166.37MPa

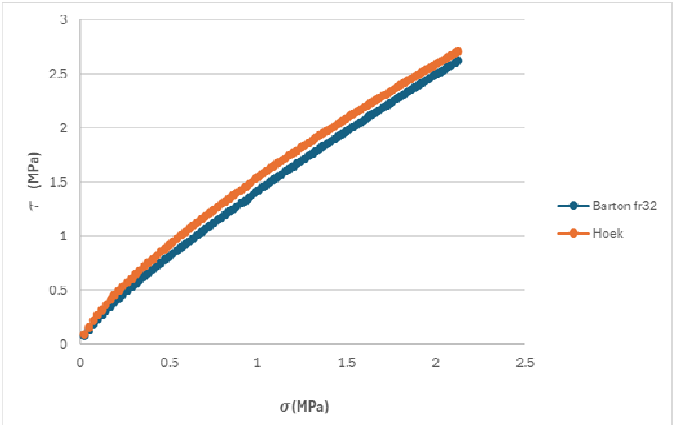


Fig. 4 Comparison of the results from the Barton and Hoek and Brown empirical methods.

Analysis of the results indicates that, for the adopted input parameters, a very good agreement between the curves is achieved. The difference is approximately 15% for φr = 30°, about 8% for φr = 32°, and reduces to approximately 3% for φr = 35° between the two methods.

In the next step, the empirical methods were compared against the results obtained from laboratory testing. Gray andesite was selected as a representative material, as it demonstrated the highest physico-mechanical properties among the tested samples.For the Barton criterion, φr = 30° was adopted, while the Hoek–Brown input parameters were taken as defined in Table 1.The corresponding curves are presented in Figure 5.

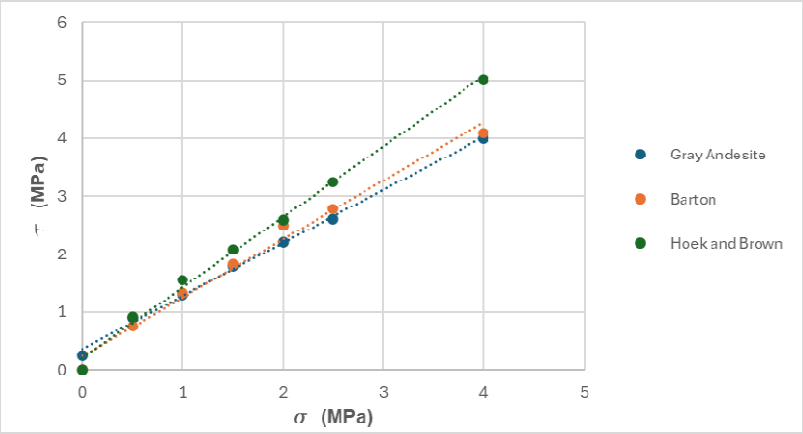


Fig.5 Comparison of the results from the Barton, Hoek and Brown empirical methodswith the laboratory results.

From the presented curves, it can be observed that the results obtained using the Barton method show excellent agreement with the laboratory results from large-scale direct shear tests. The Hoek–Brown results are approximately 20% higher.Considering that the Barton method is specifically developed for fill material, while the Hoek–Brown criterion is intended for intact rock, the observed differences are expected and reasonable. In a subsequent phase, the input parameters for the Hoek–Brown criterion may be further calibrated in order to achieve a better agreement with the other two curves. The use of empirical methods is of significant importance and can be applied in future stages for the interpolation of results at stress levels that cannot be achieved in laboratory testing due to equipment limitations.

6 Conclusion

The stability assessment of mining waste dumps remains a critical issue due to its technical and environmental implications, as demonstrated through the case study of the Borov Dol mine. The performed investigations highlight that the shear strength of rocky mine waste is strongly influenced by material composition, particularly the proportion and condition of andesite and tuff fragments within a block-in-matrix structure.

Large-scale direct shear testing proved to be an effective method for characterizing such heterogeneous materials. The tested specimens exhibited high coarse-grained content, with friction angles ranging from approximately 29° to 42°, depending on lithology and degree of weathering. Fresh andesite materials showed the highest shear strength, while tuff-dominated materials exhibited lower values, with mixed compositions yielding intermediate behavior.

Comparison with empirical approaches indicates that the Barton method provides very good agreement with laboratory results, confirming its suitability for this type of material. In contrast, the Hoek–Brown criterion tends to overestimate shear strength by approximately 20%, which is consistent with its formulation for intact rock rather than block-in-matrix materials. Further calibration of Hoek–Brown input parameters may improve its applicability.

The study confirms the importance of combining laboratory testing with empirical methods, particularly for extrapolating shear strength behavior to stress levels beyond laboratory capabilities. For future work, the same methodology should be extended to a broader dataset of samples to improve the reliability and general applicability of the results.

References

Sonmez H, Kasapoglu KE, Coskun A, Tunusluoglu C, Medley EW, Zimmerman RW (2009) A conceptual empirical approach for the overall strength of unwelded bimrocks. EUROCK 2009, Dubrovnik, Croatia

Sonmez H, Gökçeoğlu C, Medley EW, Tuncay E, Nefeslioglu HA (2006) Estimating the uniaxial compressive strength of a volcanic bimrock. International Journal of Rock Mechanics and Mining Sciences 43: 554–561

Lindquist ES (1994) The strength and deformation properties of mélange. Dissertation at University of California, Berkeley

Lindquist ES, Goodman RE (1994) The strength and deformation properties of a physical model mélange. 1st North American Rock Mechanics Symposium, Austin, Texas

Yu-Chen L, Yong-Ming T, Charng HJ, Jeen-Shang L (2019) Uncertainty of volume fraction in bimrock using the scan-line method and its application in the estimation of deformability parameters. Bulletin of Engineering Geology and the Environment. https://doi.org/10.1007/s10064-019-0

Coli N, Berry P, Boldini D, Bruno R (2009) Investigation of block geometrical properties of the Shale-Limestone Chaotic Complex bimrock of the Santa Barbara open pit mine (Italy). RockEng09, 3rd Canada-US Rock Mechanics Symposium, Toronto, Canada, 9–14 May

Barton N, Kjaernsli B (1981) Shear strength of rockfill. Journal of the Geotechnical Engineering Division 107(GT7)

Barton N, Choubey V (1977) The shear strength of rock joints in theory and practice. Rock Mechanics 10: 1–65. https://doi.org/10.1007/BF01261801

Hoek E, Carranza-Torres CT, Corkum B (2002) Hoek–Brown Failure Criterion—2002 edition. 5th North American Rock Mechanics Symposium, Toronto, 7–10 July

Faculty of Civil Engineering Skopje (2026) Report on geomechanical laboratory testing of samples from Borov Dol mine. Faculty of Civil Engineering, Skopje

Scale effects or statistical misinterpretation: a critical assessment of UCS data

R. Kiuru
Rock Physics Finland Ltd, Vantaa, Finland
Aalto University, Espoo, Finland
risto.kiuru@rockphysics.fi

I. Pérez-Rey
CINTECX, Universidade de Vigo,GESSMin Group, Vigo, Spain

M. Muñiz-Menéndez
Laboratorio de Geotecnia - CEDEX, Madrid, Spain

J. Woodman
Geo-Design Consulting Engineers Ltd, Ringwood, UK

Abstract

Despite significant improvements made on measurement techniques, testing capabilities, computer performance, and data acquisition systems, many rock engineering challenges still fall under the designation of “data-limited problems”. This means that, often, the number of tests is limited, which compromises statistical representativeness and interpretation. In contrast to other engineering disciplines, where materials can be selected based on the desired mechanical properties, in rock engineering, it is the design that adapts to the material. Consequently, the mechanical characterisation of rocks and rock masses represents a key step for successful rock engineering design.

In addition to the inherent heterogeneity associated with natural genesis, the mechanical behaviour of rock masses is scale- or size-dependent. As uniaxial compressive strength is a primary design parameter in rock engineering, its scale effect has been extensively studied, and several empirical correlations and size-effect laws have been proposed. However, many of these studies seem to suffer from the same pitfalls, specifically, a systematic reduction in the number of specimens with increasing physical specimen size, confounding the physical size effect with the effect of the statistical sample size, and the use of unsuitable statistical tests. It appears that in many cases, the data would allow multiple interpretations, and the presented correlations should be used with caution.

Keywords

UCS, Uniaxial compressive strength, Scale effect, Size effect, Review.

1 Introduction

Rock engineering design is inherently constrained by limited data availability, and engineering solutions must adapt to naturally occurring geological variability. Consequently, reliable characterisation and parameterisation remain fundamental requirements for rock engineering design. Despite advances in measurement techniques, laboratory testing and data acquisition systems, many rock engineering problems continue to be characterised by small datasets and significant uncertainty.

The mechanical behaviour of rock masses is widely recognised as scale-dependent, and numerous studies have investigated the influence of specimen size on the mechanical properties of intact rock. Among these, uniaxial compressive strength (UCS) has received particular attention due to its central role in empirical classification systems and design methods. A variety of empirical correlations and size-effect laws have been proposed (e.g., Mogi 1962; Lundborg 1967; Hoek and Brown 1980; Yoshinaka et al. 2008; Masoumi et al. 2016). A comprehensive review on the topic has been presented by Zhang et al. (2011).

However, interpretation of the size effect remains ambiguous. Often, increasing physical specimen size is accompanied by a systematic reduction in the number of tests conducted, primarily due to practical limitations with sampling, preparation and testing of large specimens. As a result, observed strength trends may reflect not only physical size effects but also variations in statistical confidence. This issue is of practical importance as while design parameters derived from large specimens often carry greater uncertainty, they also exert a stronger influence on engineering decisions, as they are considered more representative of block scale behaviour. Misinterpretation of statistical variability as a physical scale effect may lead to biased empirical correlations and inconsistent design practice. Furthermore, many proposed empirical correlations are based on inappropriate statistical tests that often overestimate the significance of the relationship. This study attempts to address these problems through a comprehensive statistical examination of published UCS datasets.

2 Review of existing data

This study presents the compiled results and statistical analysis of the results of 22 publications for a total of 2727 unique UCS results from 198 specimen groups, ranging from 1.5 mm to 1520 mm in lateral dimension, and representing 43 different igneous, sedimentary and metamorphic lithologies. Number of specimens in each group (grouped by lithology and size) range from 1 to 80. Various geometries are represented: mostly right circular cylinders, but also cubes, square rectangular prisms and even equilateral triangular prisms. Beyond physical size (lateral dimension), the effects of specimen shape and statistical sample size Nare studied.

2.1 Igneous rocks

This section presents the compiled results of 16 publications for a total of 913 UCS results from 91 size groups ranging from 1.5 mm to 294 mm (lateral dimension) and representing 23 different igneous lithologies. Table 1 shows the reviewed data sources, rock types, specimen shapes, as well as the average lateral dimension, number of specimens and the average UCS values by size group.

Table 1. Reviewed data sources for igneous rocks with the lateral dimension, number of specimens and average UCS value for each size group. Shapes: R = right circular cylinder, C = cube and T = equilateral triangular prism.

Reference	**Rock type**	**Shape**	**Lateral dimension (Number of specimens) Average UCS** [mm]/[-]/[MPa]			
Lundborg (1967)	Granite	R	19 (5) 215	28 (5) 208	38 (5) 173	58 (5) 171
Hoskins & Horino (1969)	Granite	R	25.4 (45) 337	50.8 (30) 327	76.2 (30) 302	
Nishimatsu et al. (1969)	Andesite A	R	24 (11) 108	35 (14) 112	50 (11) 99.4	56 (10) 99.7
			70 (11) 94.9			
	Andesite B	R	13 (12) 228	18 (16) 243	24 (12) 253	30 (12) 260
			70 (8) 213			
	Granite	R	13 (15) 179	18 (16) 188	24 (12) 175	30 (10) 196
			70 (7) 146			
Pratt et al. (1972)	Diorite	R/T	54 (6) 30.8	76 (3) 26.6	203 (4) 24.3	
	Granodiorite	R/T	54 (6) 193	76 (3) 189	203 (6) 74.5	
Bieniawski (1975)	Norite A	R	21.5 (20) 255	42 (20) 257	54 (45) 250	
	Norite B	R	21.5 (20) 318	42 (20) 313	54 (40) 312	

Table 1. continued Reviewed data sources for igneous rocks with the lateral dimension, number of specimens and average UCS value for each size group. Shapes: R = right circular cylinder, C = cube and T = equilateral triangular prism.

Abou-Sayed et al. (1976)	Quartz diorite	R	25 (11) 41.7	38 (8) 33.3	63 (2) 34.1	102 (7) 28.9
			146 (4) 27.4			
Jackson & Lau (1990)	Granite	R	33 (13) 195	45 (12) 171	63 (10) 199	100 (5) 190
			141 (8) 171	194 (4) 156	294 (4) 166	45 (39) 193
Panek & Fannon (1992)	Basalt	R	21 (27) 191	70 (9) 171	145 (8) 161	
da Silva & Hennies (1993)	Basalt	C	1.5 (20) 278	5 (15) 279	10 (5) 205	15 (10) 198
Thuro et al. (2001)	Granite	R	52 (4) 130	70 (4) 134	80 (4) 125	112 (4) 128
Masoumi (2013)	Granite A	R	19 (3) 183	25 (4) 208	38 (4) 233	50 (5) 218
	Granite B	R	19 (4) 203	25 (2) 183	38 (5) 255	50 (4) 251
			65 (5) 253	96 (2) 267		
Quiñones (2017)	Granite	R	13.9 (10) 62.4	29.3 (10) 84	53.6 (6) 122	98.6 (2) 112
Walton (2018)	Granite	R	43 (4) 142	63 (4) 131	75 (4) 131	
Grenow(2018)	Granite A	R	25.2 (5) 65.3	36.9 (5) 70.1	54.9 (5) 126	
	Granite B	R	25.5 (5) 144	37.1 (5) 168	54.1 (5) 154	
Durmekova et al. (2022)	Andesite	R	20 (10) 172	35 (7) 194	50 (6) 181	
	Granodiorite	R	20 (10) 112	35 (10) 113	50 (10) 115	
Kong et al. (2023)	Granite	C	10 (5) 288	15 (5) 260	20 (5) 234	25 (5) 188

2.2 Sedimentary rocks

This section presents the compiled results of 10 publications for a total of 1189 UCS results from 81 size groups ranging from 10 mm to 1520 mm (lateral dimension) and representing 15 different sedimentary lithologies and tuffs. Due to their similar mechanism of origin, tuffs are included with sedimentary lithologies rather than igneous. Table 2 shows the reviewed data sources, rock types, specimen shapes, as well as the average lateral dimension, number of specimens and the average UCS values by size group.

Table 2. Reviewed data sources for sedimentary rocks and tuffs with the lateral dimension, number of specimens and average UCS value for each size group. Shapes: R = right circular cylinder, C = cube.

Reference	**Rock type**	**Shape**	**Lateral dimension (Number of specimens) Average UCS** [mm]/[-]/[MPa]			
Bieniawski(1968)	Coal	C	19.1 (10) 29.4	25.4 (10) 32.8	50.8 (8) 33.6	68.6 (5) 31.5
			76.2 (6) 28.1	152 (7) 12.8	305 (4) 8	457 (2) 6.3
			610 (1) 5.5	711 (1) 5.3	914 (2) 4.9	1220 (2) 4.5
			1520 (2) 4.4			
Hoskins & Horino (1969)	Limestone	R	25.4 (80) 170	50.8 (70) 172	76.2 (40) 171	102 (25) 171
	Sandstone	R	25.4 (69) 48.4	50.8 (75) 50.3	76.2 (70) 52.4	102 (60) 51.4
			152 (30) 49.5	203 (10) 49.3		
Nishimatsu et al. (1969)	Tuff*	R	17 (13) 65.7	20 (10) 67	25 (13) 70.4	29 (12) 68.8
			35 (10) 72.7	40 (12) 70.1	70 (7) 57.5	
	Sandy tuff*	R	13 (37) 42.7	18 (43) 41.6	24 (32) 38.9	30 (25) 44
			70 (29) 41.6			
Dhir & Sangha (1973)	Sandstone	R	25 (6) 70	50 (6) 72	75 (6) 72	100 (6) 71
Yuki et al. (1995)	Welded tuff* ∥	R	30 (13) 3.7	50 (15) 8.0	150 (12) 9.1	160 (12) 9.3
	Welded tuff* ⊥	R	30 (15) 6.9	50 (15) 8.8	100 (12) 8.9	150 (12) 9.4
	Rhyolitic welded tuff* ∥	C	30 (12) 7.8	50 (12) 6.8	100 (12) 8.0	150 (12) 8.5
			300 (3) 9.7	400 (3) 9.9		
Thuro et al. (2001)	Limestone	R	45 (4) 186	51 (4) 201	55 (4) 203	63 (4) 188
			70 (4) 206	80 (4) 196		
Pells (2004)	Sandstone	R	18 (14) 25.1	45 (9) 25.4	51 (6) 27.7	144 (6) 31.3
Masoumi (2013)	Sandstone	R	19 (6) 34.6	25 (4) 33.1	31 (6) 42.3	50 (3) 54.6
			65 (7) 58.8	96 (2) 56	118 (4) 54.7	145 (2) 54.2
Durmekova et al. (2022)	Limestone	R	20 (10) 98.5	35 (10) 91.9	50 (10) 106	
	Sandstone	R	20 (10) 136	35 (10) 160	50 (10) 138	
Kong et al. (2023)	Sandstone	C	10 (5) 82.7	15 (5) 85.6	20 (5) 87.6	25 (5) 92.5

*Grouped with sedimentary rather than igneous rocks due to the mechanism of origin

2.3 Metamorphic rocks

This section presents the compiled results of 5 publications for a total of 625 UCS results from 26 size groups ranging from roughly 14 mm to 146 mm (lateral dimension) and representing 5 different metamorphic lithologies. Table 3 shows the reviewed data sources, rock types, specimen shapes, as well as the average lateral dimension, number of specimens and the average UCS values by size group.

Table 3. Reviewed data sources for metamorphic rocks with the lateral dimension, number of specimens and average UCS value for each size group. Shapes: R = right circular cylinder, S = square rectangular prism.

Reference	Rock type	Shape	Lateral dimension (Number of specimens) Average UCS [mm]/[-]/[MPa]			
Mogi (1962)	Marble	S	20 (32) 88.3	30 (54) 87.3	40 (34) 81.1	60 (35) 78.7
			100 (22) 79.9			
Hoskins & Horino (1969)	Marble	R	25.4 (60) 107	50.8 (80) 108	76.2 (51) 105	102 (40) 106
			146 (30) 101			
Panek & Fannon (1992)	Metadiabase	R	28 (14) 239	51 (18) 185	145 (8) 128	
Masoumi (2013)	Marble	R	25 (4) 69.5	38 (8) 74.5	50 (7) 72.2	65 (5) 78.3
			96 (5) 81	118 (4) 69.9		
Alejano et al. (2018)	Migmatite	R	13.9 (38) 40.7	22.2 (35) 59.7	29.6 (8) 54.8	42.6 (19) 62
			49.9 (8) 81.2	60.2 (4) 72.5	101 (2) 69.8	

2.4 Statistical analysis

Statistical analysis of the compiled dataset was performed in the R statistics environment (R Core Team 2025). The data were evaluated using cumulative plots, cross-plots descriptive statistics (including specimen shape, dimensions, volume, mean UCS value and standard deviation of the UCS values) and statistical tests, namely the Spearman rank correlation coefficient and Partial Spearman. As most publications did not report individual specimen data, analyses were conducted using the average values reported for each lithological/size group.

The analysis revealed two principal data limitations. First, a systematic decrease in statistical sample size with increasing physical specimen size was observed (Figure 1), resulting in wide confidence intervals that permit multiple empirical models to appear consistent with the data. Most data correspond to specimens with lateral dimensions between 25 and 60 mm, whereas specimens smaller than 14 mm or larger than 146 mm in the lateral dimension are rare.

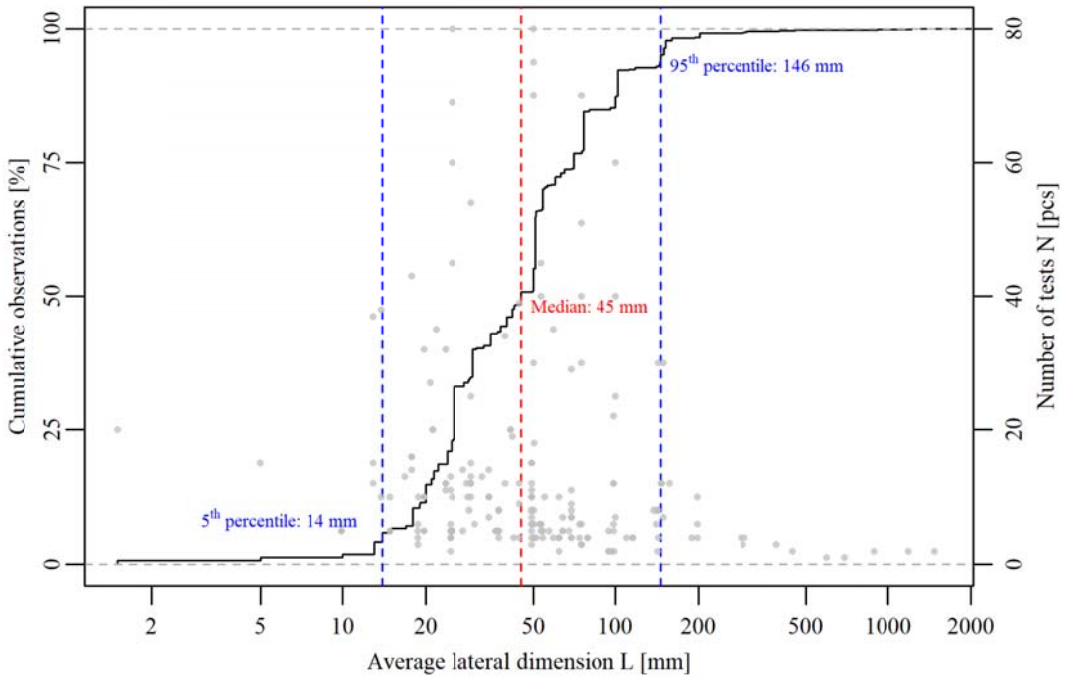


Fig. 1 Cumulative distribution of the total number of observations with respect to physical specimen size (black line), and the number of tests in each specimen group with respect to the average lateral dimension of the group (grey dots). Compiled from the sources listed in Tables 1–3.

The second principal issue concerns the misuse of the Pearson correlation coefficient and insufficient consideration of the assumptions underlying statistical inference. Spearman's rank correlation coefficients between average UCS, average lateral dimension L and number of tests N were calculated for each lithological group and the combined dataset, with significance evaluated using the false discovery rate adjusted p-values. Further, partial Spearman's rho values for the relationship between average UCS and L were calculated controlled for N, thereby isolating the relationship UCS and L independent of N. Figure 2 shows the compiled data and Table 4 shows the results of the statistical tests.

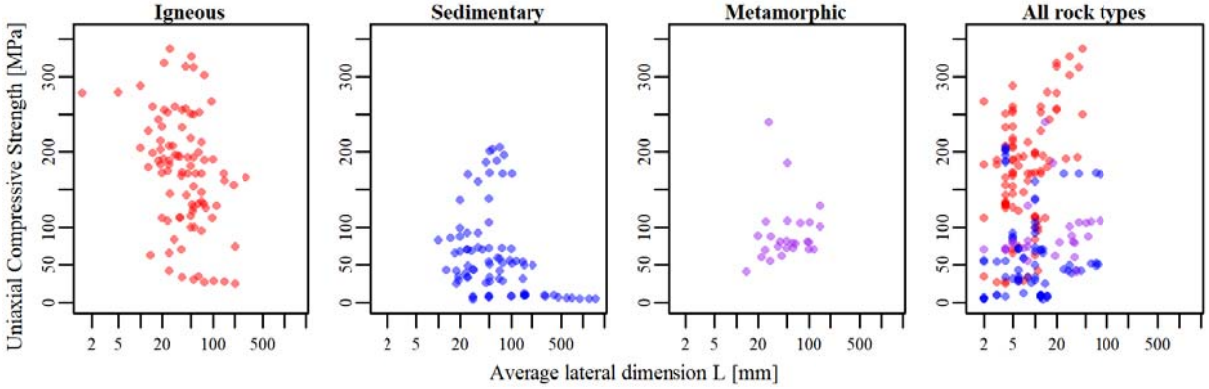


Fig. 2. Uniaxial compressive strength (UCS) vs specimen lateral dimension for igneous, sedimentary and metamorphic rocks, as well as all observations combined. Compiled from the sources listed in Tables 1–3.

For igneous rocks, statistically significant associations were identified between average UCS value and both L and N. However, even after controlling for N, the relationship remains significant. For sedimentary rocks, no significant relationship between N and UCS was observed. There is a statistically significant relationship between UCS and L, which remains relatively stable after controlling for N. For metamorphic rocks, no significant relationship between UCS and L or N was initially observed. However, after controlling for N, a borderline statistically significant relationship between UCS and L is revealed.

Table 4. Results of the statistical tests. UCS is the average UCS value, L is the average lateral dimension, rho is the value of the Spearman rho, Partial rho is the value of the Spearman rho controlled for R and p-FDR is the false discovery rate adjusted p-value for the corresponding test. Shown for igneous, sedimentary and metamorphic separately, and for all together.

	UCS vs L				**UCS vs N**	
	rho	p-FDR	Partial rho	p-FDR	rho	p-FDR
Igneous	-0.363	0.002	-0.279	0.010	0.328	0.003
Sedimentary	-0.357	0.003	-0.368	0.002	0.036	0.750
Metamorphic	0.255	0.250	0.411	0.041	0.396	0.068
All	-0.313	8.5E-5	-0.312	3.3E-5	0.055	0.485

3 Discussion and concluding remarks

Analysis of the compiled data indicates that existing empirical size-effect relationships are affected by two recurring issues: a systematic reduction in statistical sample size with increasing physical specimen size, and insufficient rigour in the selection and use of statistical tests. Both factors can distort the apparent significance of relationships between UCS and specimen size. Substantial variability was also observed in the specimen dimensions and slenderness ratios within individual groups. Consequently, multiple interpretations are possible, and the presented correlations should be used with caution.

Studies investing scale-effect should be designed with statistical considerations in mind. Specifically, the statistical sample size should be kept constant across physical specimen size groups, appropriate statistical tests should be selected, and their assumptions routinely evaluated against the dataset. In the combined dataset, negative associations were revealed for igneous and sedimentary rocks, whereas a positive association was observed for metamorphic rocks. These findings do not imply the existence of a universal relationship between UCS and specimen size, nor that such a relationship can be reliably represented by a numerical formula. The database spans numerous locations, rock types, grain sizes, laboratories and seven decades of testing, resulting in pronounced heterogeneity. Such variability, both within and between groups limits the ability to isolate and interpret scale-effects and highlights the importance of incorporating statistical considerations at the experimental design stage.

References

Abou-Sayed AS, Brechtel CE (1976) Experimental investigation of the effects of size on the uniaxial compressive strength of cedar city quartz diorite. Proceedings of the 17th U.S. Symposium on Rock Mechanics, USA.

Alejano LR, Arzúa J, Castro-Filgueira U, Kiuru R (2018) Scale effect of intact Olkiluoto gneissic rocks through uniaxial compressive testing and geophysical measurements. Posiva Oy, Working Report 2018-13.

Bieniawski ZT (1968) The effect of specimen size on compressive strength of coal. International Journal of Rock Mechanics and Mining Sciences 5: 325–335.

Bieniawski ZT (1975) The point load test in geotechnical practice. Engineering Geology 9: 1–11.

Da Silva LAA, Hennies WT (1993) A methodology for rock mass compressive strength characterization from laboratory tests. Proceedings of Scale Effects in Rock Mass, Lisbon, Portugal. Balkema, pp 217–224.

Dhir RK, Sangha CM (1973) Relationships between size, deformation and strength for cylindrical specimens loaded in uniaxial compression. International Journal of Rock Mechanics and Mining Sciences 10: 699–712.

Durmekova T, Bednarik M, Dikejoba P, Adamcova R (2022) Influence of specimen size and shape on the uniaxial compressive strength values of selected Western Carpathians rocks. Environmental Earth Sciences 81:247.

Grenow M (2018) The importance of specimen size for the uniaxial compressive strength test. MSc Thesis, School of Earth and Environment, University of Leeds.

Hoek E, Brown ET (1980) Underground Excavations in Rock. Institution of Mining and Metallurgy, London.

Hoskins JR, Horino FG (1969) Influence of spherical head size and specimen diameters on the uniaxial compressive strength of rocks. Bureau of Mines Report of Investigations, Washington, USA.

Jackson R, Lau JSO (1990) The effect of specimen size on the laboratory mechanical properties of Lac du Bonnet grey granite. In: Cunha P (ed) Proceedings of Scale Effects in Rock Masses. Balkema, Rotterdam.

Kong L, Wu J, Wang H, Shi X, Gao L, Zhuo X, Chen S (2023) Size effect of mechanical characteristics of sandstone and granite under uniaxial compression. Frontiers in Energy Research.

Lundborg N (1967) The strength-size relation of granite. International Journal of Rock Mechanics and Mining Sciences 4: 269–272.

Masoumi H (2013) Investigation into the mechanical behaviour of intact rock at different sizes. PhD Thesis, University of New South Wales, Sydney, Australia.

Masoumi H, Saydam S, Hagan PC (2016) Unified size-effect law for intact rock. International Journal of Geomechanics. 16 (2), 04015059. https://doi.org/10.1061/(ASCE)GM.1943-5622.0000543

Mogi K (1962) The influence of dimensions of specimens on the fracture strength of rocks. Bulletin of the Earthquake Research Institute 40: 175–185.

Nishimatsu Y, Yamagushi U, Motosugi K, Morita M (1969) The size effect and experimental error of the strength of rocks. Journal of Mining and Material Process Institute of Japan 18: 1019–1025.

Panek LA, Fannon TA (1992) Size and shape effects in point load tests of irregular rock fragments. Rock Mechanics and Rock Engineering 25: 109–140.

Pells P (2004) On the absence of size effects for substance strength of Hawkesbury sandstone. Australian Geomechanics 39(1): 79–83.

Pratt HR, Black AD, Brown WS, Brace WF (1972) The effect of specimen size on the mechanical properties of unjointed diorite. Int. J. Rock Mech. Min. Sci. 9, 513-529.

Quinones J, Arzua J, Alejano LR, Garcia-Bastante F, Mas Ivars D, Walton G (2017) Analysis of size effects on the geomechanical parameters of intact granite samples under unconfined conditions. Acta Geotechnica 12: 1229–1242.

R Core Team (2025) R: A Language and Environment for Statistical Computing. R Foundation for Statistical Computing, Vienna, Austria.

Thuro K, Plinninger RJ, Zah S, Schutz S (2001) Scale effects in rock strength properties. Part 1: Unconfined compressive test and Brazilian test. ISRM Regional Symposium EUROCK 2001, Rock Mechanics – A Challenge for Society.

Walton G (2018) Scale effects observed in compression testing of Stanstead Granite including post-peak strength and dilatancy. Geotechnical and Geological Engineering 36: 1091–1111.

Yoshinaka, R., Osada, M., Park, H., Sasaki, T. and Sasaki, K. (2008) Practical determination of mechanical design parameters of intact rock considering scale effect. Engineering Geology 96, 173-186.

Yuki N, Aoto S, Yoshinaka R, Ogata Y, Terada M (1995) The scale and creep effects on strength of welded tuff. Proceedings of Rock Foundation. Balkema, Rotterdam.

Zhang, Q., Zhu, H., Zhang, L. and Ding, X. (2011) Study of scale effect on intact rock strength using particle flow modeling. International Journal of Rock Mechanics and Mining Sciences 48, pp. 1320-1328.

The correlation between the compressive strength and dielectric constant for granites

S. Kahraman
Hacettepe University, Mining Engineering Department, Ankara, Türkiye
sairkahraman@yahoo.com
0000-0001-7903-143X

Ö. Y. Harman
Hacettepe University, Graduate School of Science and Engineering, Ankara, Türkiye

S. Helhel
Akdeniz University, Department of Electrical and Electronics Engineering, Antalya, Türkiye

Abstract

One of the intact rock properties, the uniaxial compressive strength (UCS), is frequently utilized in mining, oil and gas, and civil engineering projects. Samples for a typical UCS experiment must be smooth and precisely sized. It takes a lot of effort and time to complete the UCS test. Additionally, very weak or heavily jointed rocks cannot be used to create samples of the appropriate size. In these situations, the intrinsic rock properties are replaced with estimates of the rock properties derived from indirect tests, which are practical and simple to perform. In particular, measuring the dielectric constant requires very small samples and is very simple.In this study, the UCS and dielectric constant measurements were performed on different types of granite to investigate the relationship between these two parameters. The evaluation of the results showed that for the granites examined there was no correlation the UCS and dielectric constant. However, a reliable equation has been developed for predicting the compressive force by means of a multiple regression analysis including the parameters dielectric constant and quartz content for analysis. The lack of correlation between uniaxial compressive strength and dielectric constant in a simple regression analysis is most likely due to the fact that the values of the dielectric constant of the granites tested varied within a narrow range. Concluding remark is that the UCS of granites can be estimated by a multiple regression analysis equation.

Keywords

The uniaxial compressive strength, Dielectric constant, Granites, Regression analysis.

1 Introduction

The uniaxial compressive strength (UCS) of rock is widely used in mining and construction projects. The standard UCS test is difficult and labor-intensive and requires samples of specific size and uniformity. Furthermore, the required sample sizes cannot be prepared from highly fractured or very weak rock. In addition, in the feasibility studies, indirect estimates of rock properties are often used. For these reasons, the value of UCS should be estimated using indirect methods. Measuring the dielectric constant is much simpler than testing of compressive strength and requires especially very small samples. Ground Penetration Radar (GPR) measurements taken during geological surveys may also be used for the calculation of the dielectric constant of the rock mass. The dielectric constant of the intact rock may be estimated from the rock mass dielectric constant by the Time Propagation Mixing Model (Complex Refractive Index Model - CRIM) (Feng and Sen 1985). The dielectric constant of the intact rock estimated from GPR measurements may be used to estimate the UCS if a strong correlation is established between the two parameters.

Some researchers have studied the relationship between the dielectric constant and certain rock features. Most studies looked at the relationship between the dielectric constant and density and porosity (Olhoeff and Strangway 1975; Ulaby et al. 1988 and 1990; Russell and Stasiuk 1997; Rust et al. 1999; Heggy et al. (2001). Only two studies (ElShafie and Heggy 2012 and 2013) examined the relationship between the dielectric constant and the Schmidt hammer value. There are no studies in the literature on the relationship between the dielectric constant and the UCS of rock. This paper studies the relationship between the dielectric constant and the UCS of granites.

2 Rock types tested

Stone processing plants around Ankara city were visited and the large block samples of granite were obtained. The block samples were transported the laboratory for testing. Table 1 lists the locations of the six different granite types that were sampled.

Table 1. Rock samples used in the study.

Code	Rock type	Location
1	Granite (Kaman rosa)	Kaman/Kırşehir/Türkiye
2	Granite (Kozak)	Kozak/Balıkesir/Türkiye
3	Granite (Beypazarı)	Ankara/Türkiye
4	Granite (Baltic Brown)	Finland
5	Granite (Krasnaya rosa)	Russia
6	Granite (Orange pearl)	India

3 Mineralogical studies

Mineralogical analysis was carried out on the prepared thin sections of each rock type. Mineral compositions were determined by means of a polarizing microscope. The percentage of each mineral was determined by using a point counting device. The types and percentages of each mineral found in the samples are displayed in Table 2.

Table 2. Mineral constitutes and percentages of the samples.

Code	Mineral constitutes and percentages (%)							
	Quartz	Orthoclase	Plagioclase	Biotite	Amphibole	Muscovite	Chlorite	Opaque min.
1	28	41	18	9	-	-	4	-
2	12	25	32	16	13	-	2	-
3	25	23	37	2	10	-	-	3
4	14	56	12	13	4	-	-	1
5	29	62	4	3	-	1	-	1
6	24	61	11	3	-	-	-	1

4 Experimental studies

4.1 Sample preparation

NQ (47.6 mm) size core samples were taken from the granite blocks and sawn to specific sizes for the laboratory studies. The height of the cylindrical samples was 95 mm, whereas the disc-shaped samples had a thickness of about 22 mm.Some of the prepared samples are shown in Fig. 1.



Fig. 1 Core sample examples.

4.2 Uniaxial compressive strength tests

Data on the uniaxial compressive test (UCS) were taken from our previous study (Kahraman, 2025). The UCS tests were performed in accordance with the ISRM (2007) suggested methods. The stress level has been set at 0.5-1.0 MPa/s. For each type of rock, the tests were repeated at least five times and the mean value was recorded as UCS. The results of the tests are shown in Table 3.

4.3 Dielectric measurement tests

The complex relative permittivity of the samples was characterised using the cavity perturbation technique at a microwave frequency of 915 MHz. The measurement system comprised a high-Q cylindrical resonant cavity coupled to a vector network analyzer (Fig. 2). To ensure high precision and mitigate systematic errors, the system was calibrated using a Polyamide (Nylon 66) reference sample with a known dielectric constant.



Fig. 2 Dielectric measurement system.

Since the dielectric measurement on cylindrical specimens is difficult, disc specimens were used for the dielectric measurement tests. Eachspecimen was placed in the cavity's maximum electric-field region, and the resulting shift in resonant frequency and change in quality factor (Q) were recorded. The real part of the permittivity values, representing the energy storage capacity were calculated using the Bethe-Schwinger perturbation equations. The dielectric constants (ε_r) of the samples are listed in Table 3.

Table 3. Uniaxial compressive strength and dielectric constant values.

Code	UCS (MPa)	ε_r
1	159.9	5.41
2	132.6	5.54
3	136.0	5.66
4	89.9	5.81
5	155.6	5.87
6	137.1	5.56

5 Results and discussions

The correlation between the UCS and $\varepsilon_r$was examined using the data in Table 3, and as Figure 3 illustrates, no correlation was found between the two parameters. The literature contains no research examining the relationship between the two parameters. Nonetheless, some research (ElShafie and Heggy 2012 and 2013) has discovered a correlation between the dielectric constant and the Schmidt hammer value for pyroclastic and basalt rocks. A correlation between the UCS and ε_r is also anticipated since a correlation between the UCS and the Schmidt hammer value is known to exist. Nevertheless, there is no correlation between the Schmidt hammer value and the dielectric constant in the data from these investigations when basalt and pyroclastic rocks are assessed independently. The fact that the tested granites' ε_r values fall within a small range is probably the reason for the lack of correlation between UCS and e_r.

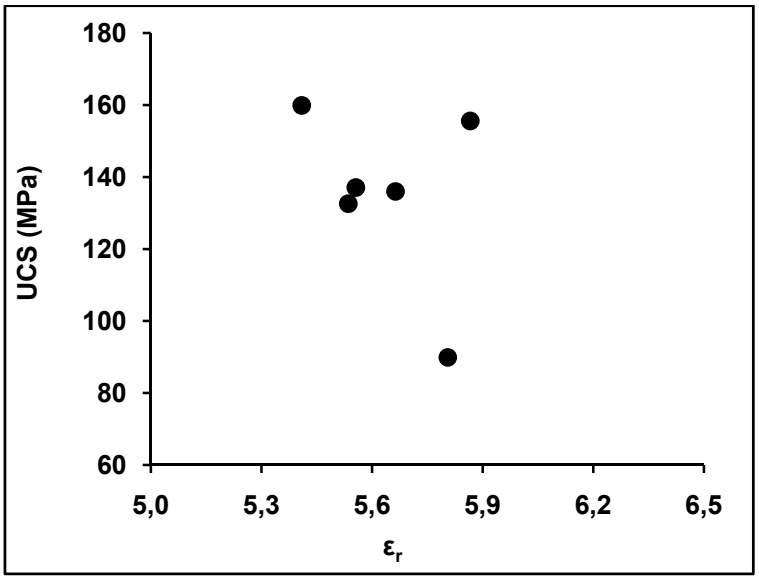


Fig. 3 Correlation between uniaxial compressive strength and dielectric constant.

A rock's dielectric constant is significantly influenced by the minerals that comprise it. The quartz mineral has a ε_r value of about 4.5, which is much lower than the ε_r values of the other minerals (6-7) that comprise granite. It is believed that granites' ε_r value is significantly impacted by their quartz content. Therefore, quartz content was added to the analysis along with the ε_r value in order to create an equation to estimate the UCS value using multiple regression analysis. The resulting equation with high correlation coefficient (r = 0.85) is:

$$UCS = -54.03\varepsilon_r + 2.56Q + 383.35 \quad (1)$$

Where UCS Uniaxial compressive strength (MPa)
ε_r Dielectric constant
Q Quartz content (%)

The 3D surface graph is shown in Figure 4 for Eq. 1. It can be seen in Figure 4 how the fitted response values relate to two continuous variables based on Eq. 1.

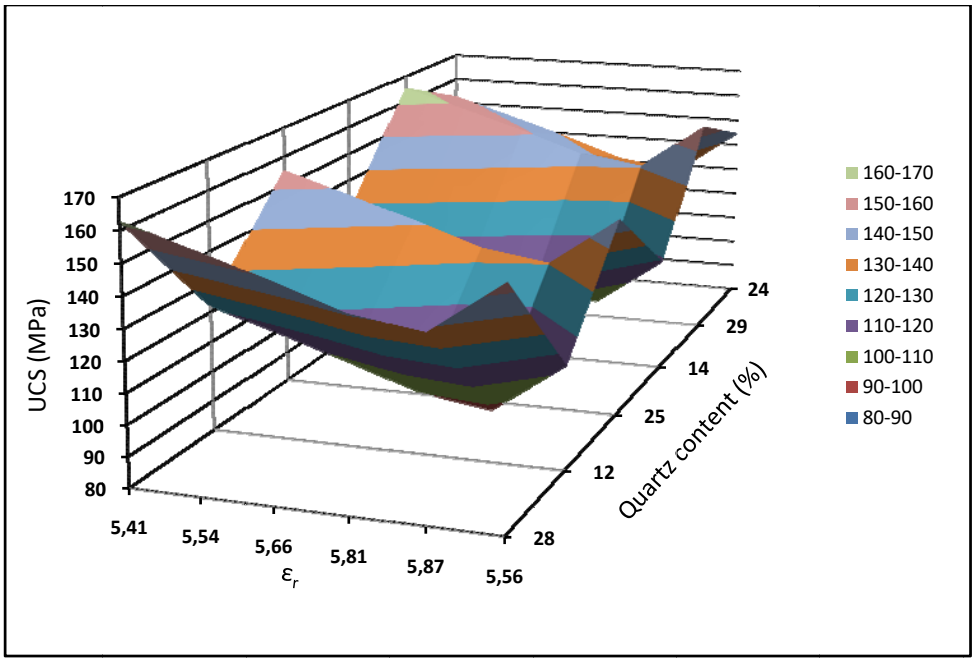


Fig. 4 The 3D surface graph 4 for Eq. 1.

6 Conclusions

Compressive strength, dielectric constant, and mineralogical data were assessed in order to create an equation for estimating the uniaxial compressive strength from the dielectric constant for granites. The analysis of the findings could lead to the following conclusions.

For the granites under test, no relationship was revealed between the dielectric constant and uniaxial compressive strength. Using multiple regression analysis, a reliable equation that considered the quartz content and dielectric constant was developed to predict compressive strength. The dielectric constant values of the tested granites most likely varied within a small range, which is why there was no correlation between uniaxial compressive strength and dielectric constant in the simple regression analysis. It was determined that the UCS of granites could be estimated using the multiple regression analysis equation. Granites with different mineralogy and dielectric constants or other rocks should be included in the analysis for future research.

Acknowledgement

We would like to thank the Hacettepe University-Scientific Research Projects Coordination Unit for funding (Project no. FUK-2025-21804).

References

ElShafie A, Heggy E (2012). Dielectric Properties of Volcanic Material and Their Role for Assessing Rock Hardness in The Martian Subsurface. 43rd Lunar and Planetary Science Conference, Texas (USA), March 19–23, 2012.

ElShafie A, Heggy E (2013) Dielectric and hardness measurements of planetary analog rocks in support of in-situ subsurface sampling. Planetary and Space Science 86: 150–154. https://doi.org/10.1016/j.pss.2013.02.003

Feng S, Sen PN (1985) Geometrical Model of Conductive and Dielectric Properties of Partially Saturated Rocks. Journal of Applied Physics58: 3236–3243.

Heggy E, Paillou P, Ruffie G, Malezieux JM, Costard F, Grandjean G (2001) On Water Detection in The Martian Subsurface using Sounding Radar. Icarus154: 244–257. https://doi.org/10.1006/icar.2001.6717

ISRM 2007 The complete ISRM suggested methods for rock characterization, testing and monitoring: 1974–2006. Suggested Methods Prepared by the Commission on Testing Methods, International Society for Rock Mechanics, R. Ulusay and J.A. Hudson (eds.), Compilation Arranged by the ISRM Turkish National Group, KozanOfset,. Ankara, Türkiye.

Kahraman S (2025). Investigation of the Drillability of Magmatic Rocks with Diamond-Impregnated Drill Bits. Research Project (FHD-2024-21169), Hacettepe University (in Turkish).

Olhoeft GR, Strangway DW (1975) Dielectric Properties of the First 100 Meters of The Moon. Earth and Planetary Science Letters24: 394-404. https://doi.org/10.1016/0012-821X(75)90146-6

Russell J K, Stasiuk M V (1997) Characterization of volcanic deposits with ground-penetrating radar. Bulletin of Volcanology 58(7): 515–527. https://doi.org/10.1007/s004450050159

Rust AC, Russell JK, Knight RJ (1999) Dielectric constant as a predictor of porosity in dry volcanic rocks. Journal of Volcanology and Geothermal Research 91: 79–96. https://doi.org/10.1016/S0377-0273(99)00055-4

Ulaby FT, Bengal TH, East JR, Dobson MC, Garvin JB, Evans DL (1988). Microwave dielectric spectrum of rocks. Radiation Lab. Tech. Report. No. 023817-1-T. Dept. of Elect. Eng. and Computer Sci., Univ. of Michigan, Ann Arbor.

Ulaby FT, Bengal TH, Dobson MC, East JR, Garvin JB, Evans DL (1990) Microwave Dielectric Properties of Dry Rocks. IEEE Transactions on Geoscience and Remote Sensing 28 (3): 325-336. https://doi.org/10.1109/36.54359

Full-scale impact test on a reinforced earth embankment with advanced monitoring for rockfall protection

S. Vigna & M. Nadalini & F. Demonte
INCOFIL TECH SRL, Cirè (TN), Via degli Artigiani 52, 38057, Italy
s.vigna@incofil.com

M. Marchelli & V. De Biagi & S. Saltarin & D. Peila
Politecnico di Torino, Corso Duca Degli Abruzzi 20, 10129, Torino, Italy

A. Grimod
France Maccaferri, 8 Rue Pierre Mechain, 26000 Valence, France

Abstract

Reinforced earth embankments represent a robust solution for rockfall mitigation, yet their dynamic response under high-energy impacts remains poorly documented. This study presents a unique full-scale impact test performed on a 6.54 m-high RPE composed of nine layers of granular material reinforced with Green Terramesh units by Maccaferri, developed in the framework of PERSEIDI project (contributo Legge 6/99 Provincia Autonoma Trento - CUP:C39J21046780001). The test involved a standardized block (EAD 340059-00-0106:2018) impacting below the first reinforcement layer with an energy of approximately 10 MJ, simulating an extreme rockfall event. The novelty of this work lies in the advanced multi-sensor monitoring system integrated into the embankment and in the block. The embankment was instrumented with tri-axial and mono-axial accelerometers positioned across different layers, both at the impact centre and laterally to the impact zone, to capture the propagation of dynamic loads and the volume of disturbed material. A custom-designed network of strain gauges was embedded within the reinforcement layers to monitor tensile forces, while load cells at the foundation recorded stress transmission during the impact. Additionally, the impacting block was equipped with a gyroscope and accelerometer to track its kinematics. High-speed cameras captured the impact sequence, enabling correlation between visual observations and sensor data. Preliminary results reveal the extent of the volume of the embankment disturbed by the impact. The combined dataset provides unprecedented insight into energy dissipation mechanisms and deformation patterns in reinforced earth structures under extreme impacts. This experiment establishes a benchmark for validating numerical models and improving design guidelines for embankments used asrockfall protection systems. The integrated monitoring approach offers a powerful tool for understanding structural resilience and optimizing reinforcement strategies under high-energy impact scenarios.

Keywords

Rockfall protection embankment, Impact test, Monitoring.

1 Introduction

Rockfall events are natural phenomena that can expose infrastructure and human life to significant risk if not adequately protected. Among protective measures, rockfall protection embankments (RPEs) built using reinforced earth (RE-RPEs) represent a suitable solution (Marchelli and Deangeli 2022), especially in cases of high energy levels, where other types of structures (e.g. rockfall barriers) cannot withstand the impact, or, due to their low maintenance requirements, in areas subject to frequent events.

Unfortunately, the structural response of these works under impact loading has not yet been completely investigated or fully understood, mainly due to the limited number of full-scale tests available in the literature. Peila et al. (2007) and, subsequently, Mongiovì et al. (2014) tested RE-RPEs reinforced with HDPE geogrid systems at energy levels of 4200 kJ and 6600 kJ, respectively.However, nowadays these energy levels are typically addressed by rockfall barriers, while RE-RPEs are generally employed for impact energies greater than 10000 kJ.

In this work, an innovative impact test, developed within the framework of the PERSEIDI project, was carried out on an RE-RPE, reaching an impact energy of approximately 10 MJ, representing the highest-energy test performed worldwide on this type of structure. The RE-RPE was built using the Green Terramesh reinforcing units (Fig. 1a) described in Section 1.1with a trapezoidal cross-section, a height of 6.54 m, a crest width of 2.0 m, and faces angles of 67° (Fig. 1b). A cableway system was used to reproduce the impact, and the details of the test setup are reported in Section 2.The innovations of the test consist on the energy level and anadvanced multi-sensor monitoring system, which included a standalone device to record acceleration and angular velocity within the impacting block, together with a 32-channel data acquisition system used to record accelerations at several points of the embankment, dynamic forces at selected points of the foundation, and strain state in the reinforcements. Further details are reported in Section 2.

The test results highlight the resisting mechanisms of the Green Terramesh reinforcing units, together with the capability to record significant physical quantities that are fundamental for understanding the behaviour under impacts of RE-RPEs and to be used as benchmark data in numerical model validation.

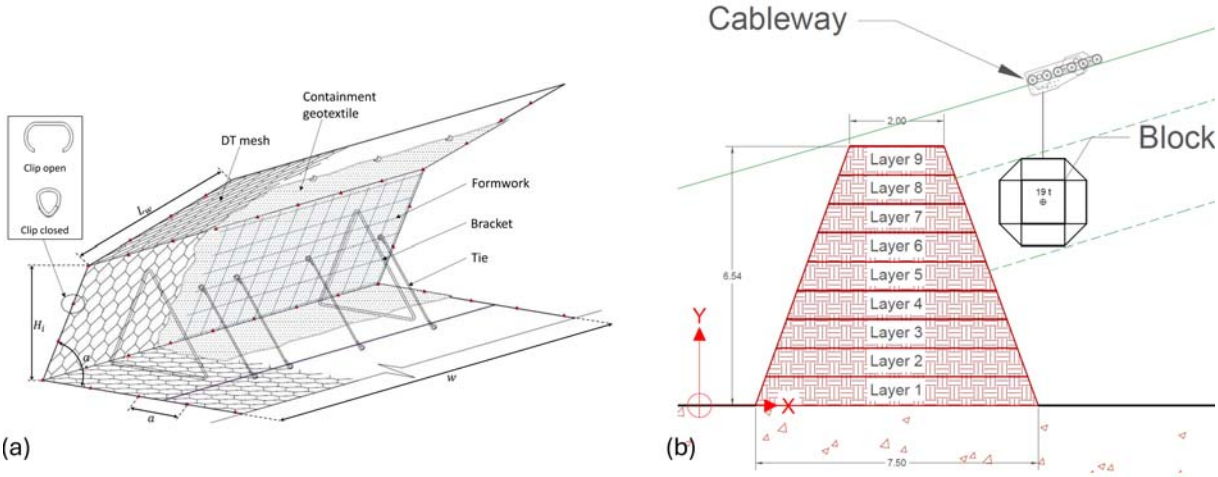


Fig. 1 (a) Terramesh system; (b) RE-RPE cross section of the test and test set-up.

1.1 Green Terramesh reinforcing units

The Green Terramesh Light is a preassembled modular system used to build reinforced soil structures with an inclined vegetative face; the units are manufactured from a continuous element of double twisted (DT) wire mesh, mesh type 8x10, with a polymer (Polimac) coated steel wire having a diameter of 2.20/3.20 mm. All the Green Terramesh Light units adopted for the RE-RPE are 3 m long (Fig. 1a). According to ETA No. 16/0758 (2020), the mesh has a tensile resistance of $F_{max} = 40 \pm 5\ kN/m$ at the strain of $\varepsilon = 10\%$, as reported by thetechnical datasheet. Rectangular electro-welded steel meshes (15×15 cm, Ø8 mm, B450C) are installed on the RE-RPE side banks as formwork purposes and are coupled with the DT reinforcing element through steel clips. The clips, according to EAD 200086-00-0602, have a characteristic strength of 2 kN and are also installed along the boundaries between adjacent Green Terramesh Light elements, acting as joints, with a spacing of 20 cm.

2 Test and monitoring system

The RE-RPE was built according to the typical construction procedure adopted for reinforced-earth works. The compaction method was calibrated on the first layer to achieve a minimum dry soil density equal to 95% of the Proctor value. The soil employed was a local material consisting of 65% gravel, 25% sand, and approximately 10% silt, and its mechanical properties were assessed through large-scale direct shear tests. In particular, the tested samples included a maximum grain size of 30 mm, resulting in cohesion of 36 kPa and a friction angle of 40°. Consequently, the material used during construction was sieved at 30 mm to ensure consistency between the laboratory-derived mechanical parameters and the in-situ material properties.

Plate load tests, performed in accordance with CNR BU No. 146 (1992), were carried out during construction to assess the stiffness parameters of the RE-RPE. The first deformation modulus values obtained were as follows: two tests on the foundation yielded values of 52 MPa and 50 MPa; for the overlying layers, Layer 1 showed 18 MPa, Layer 2 showed 19 MPa, Layer 3 showed 18 MPa, Layer 5 showed 26 MPa, and Layer 7 showed 15 MPa. Moreover, during construction, the sensor network described in Section 2.1 was installed.

The test consisted of launching a standard polyhedric block, in accordance with EAD 340059-00-0106:2018, against the upstream side bank of the embankment. The block had a mass of 18822 kg and an external size of 2.08 m, resulting in an average computed density of 2952 kg/m³. The block was launched leaving the upper layer (Layer 9) unaffected by the impact, as typically assumed in RE-RPE design under impact conditions, with an impacted height measured from the foundation to the centre of the impacted area of approximately 4.72 m. The impact energy was achieved by imposing a difference in elevation along the cableway and launching the block suspended from a trolley; before impact, the block was released to allow free parabolic motion.

The RE-RPE was designed to approach near-collapse conditions under an impact energy of 10 MJ, consistently with the collapse-based design approach under impact conditions proposed in recent literature (Vigna, 2025; Vigna et al., 2025). The design was carried out using a numerical approach based on Abaqus/Explicit, following the modelling strategy described in Vigna (2025), which resulted in the cross-section shown in Fig. 1b. The numerical model was fundamental for estimating the expected magnitude of the physical quantities to be measured and, consequently, for selecting appropriate sensors, thereby avoiding issues related to signal saturation or insufficient measurement resolution.

2.1 Monitoring system design

The physical quantities considered fundamental for a proper understanding of the behaviour of the RE-RPE subjected to impacts werethe forces acting on the foundation, the accelerations within the soil layers, the strain state of the reinforcements, and the three-dimensional deformed shape. Regarding the impactor, the block deceleration was considered the most important parameter to be measured, as it reflects the global structural response of the system.

A standalone acquisition system was selected to measure the deceleration and angular velocity of the block (Set 1), together with a 32-channel acquisition system used for the sensorswithin the RE-RPE (Set 2). The outputs of the previously mentioned numerical model were used to define the required sensor specifications, which are listed in Table 1. The test was recorded using 3 high-speed cameras, one of which was installed perpendicular to the block trajectory at the impact location in order to measure the impact velocity. In addition, the RE-RPE geometry was surveyed before and after the test using LiDAR techniques, allowing the reconstruction of the complete three-dimensional shape with an accuracy of$\pm 1\ cm$.

2.1.1 Instrumentation set-up

The selected instrumentation chosen on the market is reported in Table 1. The installation of the sensors required a dedicated design in order to prevent damage to the measurement system and issues in signal acquisition. Fig. 2 shows some of the adopted arrangements.

Table 1. List of instruments required for the monitoring network planning and the ones selectedfor measures on the block (Set 1) and those on the RE-RPE (Set 2).

Instrument	**Number**	**Minimum specification**	**Model**
		Set 1: measures on the block	
Triaxial accelerometer	1	$\pm 100g$	ASC 5521MF-200-25A
Triaxial gyroscope	1	$\pm 10 rad/s$	ASC 273-075-6A-9L3
Data recorder	1	1s	DATABRICK3
Acquisitor stand alone	6 channels	10 kHz	
		SET 2: measures on the RE-RPE	
Displacement sensor	2	$\pm 25mm$	PS-C15M
Strain gage	6	$\pm 1\%$	ID/KFGS-1-350-C1-11
Load cell	3	$> 500\ kPa$	FTF01-PTC100kN
Triaxial accelerometer	6	$\pm 100g$	ASC 5521MF-200-25A
Monoaxial accelerometer	3	$\pm 100g$	ASC 4421MF-200-25A
Data recorder	1	5s	CronosFlex2000
Acquisitor	32 channels	40 kHz	

The entire Set 1 was installed in the block by means of a stiff steel box rigidly fixed to the block. This solution ensured an appropriate coupling between the sensor box and the block, allowing accurate recording of block vibrations; additionally, a dedicated design was adopted to minimize noise and unwanted vibration effects (Fig. 2a).

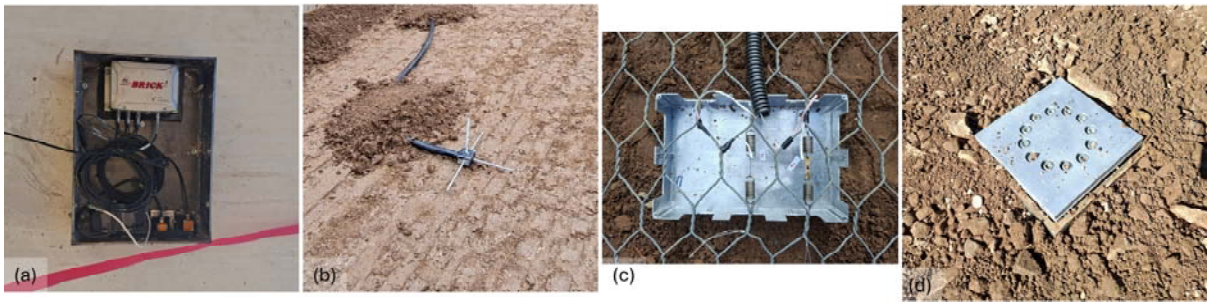


Fig. 2 Some arrangements of the sensors adopted for the impact test: (a) sensors on board of the block (accelerometer, gyroscope and stand-alone acquisitor); (b) accelerometer embedded in a layer of the RE-RPE; (c) device used to measure the strain state on the reinforcement; (d) load cell on the foundation.

The accelerometers of Set 2 were evenly distributed among the embankment layers and were always installed at mid-height of each soil layer. Each accelerometer was protected by a metal box and rigidly connected to the soil through steel bars (Fig. 2b). The strain state of the double-twist mesh was measured using a dedicated device developed and described in Vigna (2025). This device is based on a system of springs connected to the mesh hexagon, which induce deformation in a strain-gauged plate; knowing the relationship between spring displacement and strain, the local strain of the DT mesh can be derived.

Finally, the additional dynamic normal forces acting on the foundation were recorded by three load cells installed at different locations along the foundation. The load cells were housed in steel boxes, with their upper surfaces positioned at the level of the first embankment layer.

A sampling rate of 40 kHz was set for the Set 2 acquisition system. This value was selected considering the spacing between sensors, the wave propagation velocity in the medium, and the required temporal resolution of the measurements.

3 Preliminary test results

The block impacted the structure along its axis of symmetry at a height of approximately 4.72 m, measured from the foundation plane to the centre of the impacted area, leaving a freeboard of about 0.73 m. The high-speed camera located perpendicular to the impact point (frame rate 3000 fps),measured a velocity at the impact of 32.87 m/s, with an inclination angle with respect to the horizontal of 21.18°, resulting in an impact energy of 10168 kJ.

Fig. 3 shows a comparison of the upstream side bank of the RE-RPE before and after the impact. Fig. 3b clearly highlights that the block impacted exactly at the centre of a Green TerrameshLight module, which had been installed in a stacked (i.e. non-staggered) configuration and symmetrically with respect to the side banks.

From a macroscopic point of view, the observed mechanical response consisted of the formation of discontinuities along the boundaries of the Green Terramesh Light modules, extending from the base of the affected layer up to the crest, while the external portions of the embankment appeared to be almost unaffected. This observation is confirmed by the cross-sections obtained from the LiDAR survey and shown in Fig. 4. The cross-section along the symmetry axis of the impact shows a maximum downstream displacement of approximately 1.75 m, associated with an upstream deformation of about 1.0 m. Moving with the sections outwards, in correspondence of the Green Terramesh Light boundaries (Fig. 4b) the displacement field can be considered to remain constant, instead passing in the following section (Fig. 4c) the displacement field drops.

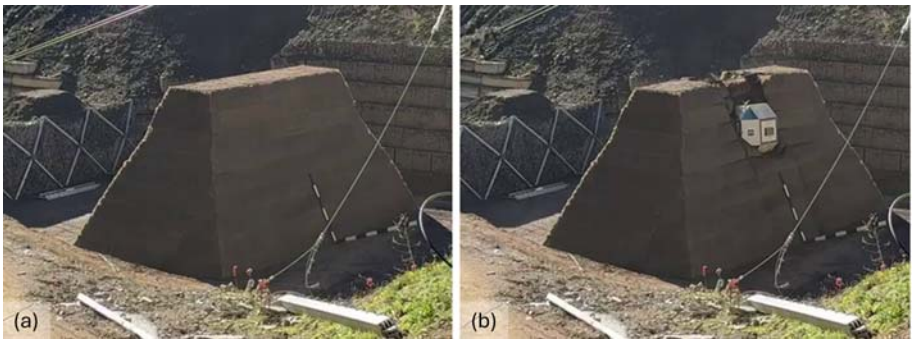


Fig. 3 Upstrem side bank of the tested RE-RPE before the impact (a) and after the impact (b).

The block remained embedded within the embankment, and the structure is self-standing, without reaching global collapse. However, limited soil leakage phenomena were observed on the downstream side bank.

Overall, both monitoring systems successfully recorded the target physical quantities. Only a limited number of accelerometers installed within the RE-RPE showed signal saturation, likely due to their proximity to the impact front. Fig. 5 a reports the acceleration components recorded on the block, showing a proper functioning of the measurement set-up. In particular, the highest acceleration component was recorded along the impact direction (x-direction), with a peak value of approximately 50 g. The maximum computed resultant acceleration was 53.42 g, with an impact duration of about 0.10 s, resulting in an estimated impact force of approximately 11.5 MN.

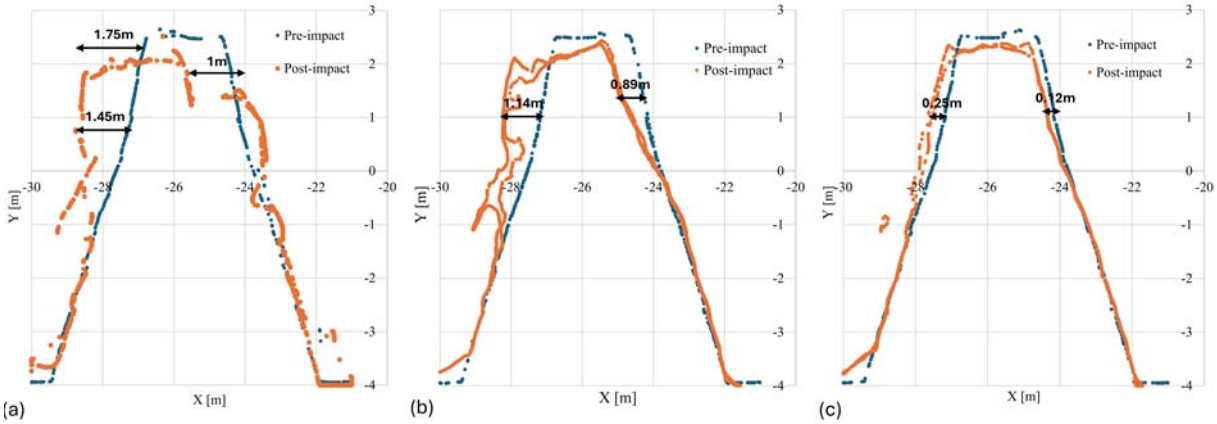


Fig. 4 Comparison of the RE-RPE cross section pre and post impact: (a) along the symmetry axis; (b) 1.5 m from the symmetry axis (in correspondence of the Green Terramesh Light module boundaries); (c) 1.75 m from the symmetry axis.

3.1 Preliminary comparison with FEM modelling

A preliminary comparison between the numerical approach proposed by Vigna (2025) and Vigna et al. (2025) for modelling the RE-RPE under impact conditions and the experimental results was carried out. Fig. 5b shows the downstream side bank predicted by the FEM model, highlighting the capability of the model to capture the large deformations experienced by the structure, as well as the final position of the block embedded within the embankment. Moreover, according to the plastic strain

distribution, the volume involved by the impact appears to be in good agreement with that observed during the experimental test.

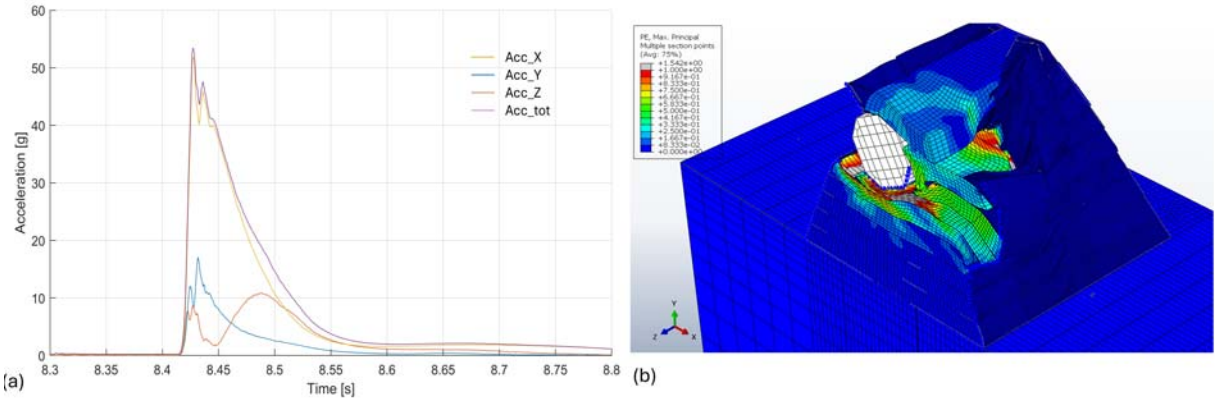


Fig. 5(a) Acceleration recorded on the block (smoothed data); (b) deformed shape obtained with the numerical modelling (PE are the plastic strain magnitude).

4 Conclusions

In this work, an innovative impact test on RE-RPEs was carried out at an impact energy of 10168 kJ, which currently represents the highest energy level investigated in experimental tests on rockfall protection works. Moreover, a key innovation of the study lies in the design and implementation of a multi-sensor monitoring system, which included a standalone device to record acceleration and angular velocity within the impacting block, together with a 32-channel data acquisition system used to record accelerations within the embankment, stresses on the foundation, and local strain fields in the reinforcements.

The monitoring system satisfactorily recorded the target physical quantities; therefore, the results presented in this paper, although only partially discussed, will form the basis for future, more in-depth analyses and interpretations of the observed phenomena. Particularly, they will be used as benchmark data for the validation of robust numerical models.

Finally, the mechanical behaviour observed during the test showed that the affected volume of the RE-RPE was limited and mainly governed by the Green Terramesh Light module length. From a maintenance perspective, this behaviour may represent an advantage for existing embankments subjected to impact events. Nevertheless, additional tests on repaired structures are required to further investigate post-impact performance.

References

Peila, D., Oggeri, C., & Castiglia, C. (2007). Ground reinforced embankments for rockfall protection: design and evaluation of full scale tests. *Landslides*, *4*(3), 255-265.

Marchelli, M., & Deangeli, C. (2022). Towards a codified design procedure for rockfall reinforced earth embankments. *GEAM, Geoingegneria e attività estrattiva*.

L. Mongiovi, M. Bighignoli, A. Danzi, and P. Recalcati (2014). An impact test on areinforced earth embankment. In Proceedings of Interdisciplinary workshop onrockfall protection–Rocexs.

Vigna, S., Marchelli, M., De Biagi, V., Di Pietra, V., Saltarin, S., & Peila, D. (2025). A Method to Compute the Ultimate Displacements in Reinforced Earth Rockfall Protection Embankments: A Perspective for the Design: S. Vigna et al. *Rock Mechanics and Rock Engineering*, 1-27.

Vigna, S. (2025). Innovative Approaches to the Dynamic Behavior of Rockfall Protection Embankments. PhD Thesis, Politecnico di Torino, Torino, Italy.

Officine Maccaferri Italia S.r.l. Terramesh Verde - Manuale di Installazione, rev:05 - itedition, 28-03-2025.

Effect of rock matrix permeability on fluid-injection-induced hydro-mechanical coupled behaviour of rock discontinuities

A. Sainoki
Kumamoto University, Kumamoto, Japan
atsushi_sainoki@kumamoto-u.ac.jp
0000-0003-2754-4801

D. Asahina
The National Institute of Advanced Industrial Science and Technology, Tsukuba, Japan

N. Iwata
Chuden Engineering Consultants Co.,Ltd, Hiroshima, Japan

A. Schwartzkopff
The University of Western Australia, Perth, Australia

Abstract

Fluid injection into rock masses and the associated hydro-mechanical coupled behaviour are of paramount importance in deep underground engineering projects. Although numerous studies have been undertaken to investigate the fluid behaviour in rock discontinuities, most of the studies neglect the possibility of fluid leakage to the surrounding rock matrix, which may lead toan overestimation of the risk for instability leading to shear failure and/or induced seismicity. To evaluate its influence, the present study conducted fluid injection experiment and simulation whilst varying the permeability of the rock matrix surrounding the discontinuity. The experiment employed rectangular parallelepiped rock specimens with a through-going discontinuity inclined at 60°. The experiment indicated the significant effect of the rock matrix permeability on the increase rate and peak value of the pore pressure in the discontinuity as well as the occurrence of slip. Specifically, when fluid is injected at the rate of 0.03 mL/min, slip occurs only for the intact specimen, whilst slip took place for the specimen heated at 500 °C at an injection rate of 0.3 mL/min, implying the existence of a threshold above which the discontinuity stability drastically decreases. This hydro-mechanical coupled behaviour was further confirmed through the numerical simulation, demonstrating the non-linear evolution of the pore pressure and shear displacement. This study provides important insights into the role of the rock matrix in the hydro-mechanical coupled behaviour of rock discontinuities and contributes to the improvement of evaluation methods for the risk of induced seismicity.

Keywords

Induced seismicity, Near-discontinuity rock matrix permeability, Numerical simulation.

1 Introduction

Fluid injection-induced seismicity is associated with various engineering projects including enhanced geothermal system, carbon capture and storage, and hydraulic fracturing for destressing in deep underground mining (Sainoki, 2014; Ge and Saar, 2022). It has been attracting significant global attention due to the increasing depth and scale of these engineering projects. For example, during the 2017 EGS project in Pohang, fluid injection into the stimulated reservoir activated a previously stable fault, triggering a magnitude 5.4 earthquake that caused significant economic damage (Kim et al., 2023). This event became the second-largest recorded earthquake in South Korea, and because the country is generally regarded as a region of low seismic activity, the earthquake attracted considerable attention from both the scientific community and the government. The cause of injection-induced seismicity is primarily the reduction of the effective normal stress acting on discontinuities within a rock mass due to an increase in pore pressure. When the shear stress exceeds the reduced frictional resistance, shear failure occurs along the discontinuity. Such slip behavior can be classified into seismic slip or aseismic slip depending on the stability of the fracture system, the ambient stress state, infilling materials, the stiffness of the surrounding rock mass, and so forth. Furthermore, slip along discontinuities alters the hydraulic properties of fractures (Zhao et al., 2025) and surrounding damage zones, thereby influencing fluid migration and pore pressure distribution within the reservoir. Thus, in-depth investigation of the mechanisms governing the evolution of induced seismicity and its consequences is required for ensuring the sustainable and safe operation in such subsurface engineering projects.

Significant experimental and numerical efforts have been devoted to understanding the influence of fluid injection on the mechanical and hydraulic behaviour of rock discontinuities. These studies have provided valuable insights into various physical phenomena, including the influence of injection rate on slip occurrence (Hutka et al., 2023), slip-induced permeability evolution of rock discontinuities, and the effect of surface asperities (Ji et al., 2023). Some studies indicated the strong influence of microscopic fracture distributions within a rock matrix on the mechanical behaviour of rock discontinuities, especially for rocks with a relatively high matrix permeability (Schwartzkopff et al., 2021). Hence, when fluid injection is performed into such rock discontinuities surrounded by permeable rock matrices, it is essential to evaluate their influence on the evolution of pore pressure along discontinuities and the occurrence of slip. In particular, clarifying and quantifying the relationship among matrix permeability, pore pressure evolution, and discontinuity slip behaviour remains an important research challenge, owing to difficulties in controlling the permeability of the rock matrix surrounding a discontinuity.

To address this issue, in the present study, we performed laboratory-scale fluid injection experiments while varying the permeability of near-discontinuity rock matrix by inducing thermal damage to granite specimens in an oven before the injection experiment. Subsequently, to verify the experiments and quantify the influence of the rock matrix with enhanced porosity, numerical simulations were performed within the framework of the Distinct Element Method (DEM) by performing hydro-mechanical coupled simulation whilst considering the fluid leakage to the surrounding rock matrix. The objective of the present study is to identify key parameters controlling the coupled hydro-mechanical response. The findings obtained from this study are expected to contribute to improving predictive methodologies for fluid injection-induced seismicity and to advancing induced seismicity risk assessment for subsurface engineering applications involving fluid injection into rock masses.

2 Fluid injection experiment

2.1 Specimen preparation

Rectangular prism specimens of Inada granite were used in the experiments. The specimens were cut at an angle of 30° to the longitudinal axis using a rock cutter to create a precut surface, as shown in Fig.1. Subsequently, the precut surface was polished with #400 abrasive paper using a rotary polishing machine. Of the pair of cut specimens, one specimen was drilled with a through-going injection hole (φ = 2 mm) using an ultrasonic drill. This injection hole enabled direct water supply from the syringe pump injection line to the precut surface.

In total, three types of specimens were prepared while varying the degree of microcrack density in the rock matrix, namely I-R, I-300, and I-500. I-R denotes an intact specimen prepared at room temperature without any damage, while the other two specimens (I-300 and I-500) were heated in an oven to generate microcracks, thereby simulating a damage zone with a high permeability. It is known

that the aperture of microcracks in Inada granite increases with increasing maximum thermal history temperature. In this study, specimens were heated at 300°C (I-300) and 500°C (I-500) for 20 minutes.

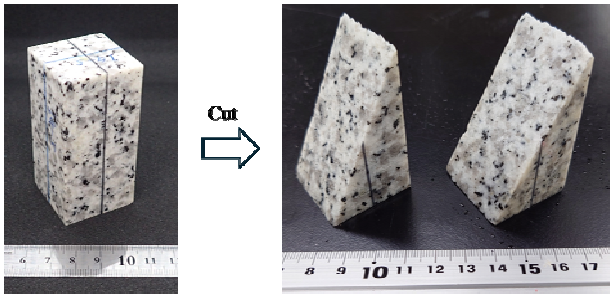


Fig.1 Intact specimens of Inaga granite, with a precut surface, cut at an angle 30° to the longitudinal axis.

2.2 Overview of the experimental apparatus and procedure

The experiments were conducted using a large-scale triaxial testing machine and two syringe pumps. The triaxial testing machine is capable of simulating underground stress conditions by controlling axial loading and confining pressure applied in all directions. In addition, the two syringe pumps enabled control of water flow from both the upstream and downstream sides of the specimen. After being fully saturated, the granite specimen was covered with a transparent silicone jacket and installed in the triaxial testing machine with flow lines connected to the upper and lower end pieces. LDTs were attached in both the longitudinal and lateral directions of the specimen to measure deformation.

The experimental procedure is as follows; (a) The specimen was installed in a pressure vessel, and a confining pressure of 10 MPa was applied uniformly to the entire lateral surface of the specimen; (b) The pore pressure within the specimen was controlled at a constant pressure of 1 MPa; (c) Axial load was applied in the longitudinal direction of the specimen until the stress state reached a critical condition determined by Mohr-Coulomb failure criterion, and then the piston displacement was fixed; (d) While maintaining the downstream side at a constant pressure of 1 MPa, water was injected from the upstream side at a constant flow rate to increase the pore water pressure along the discontinuity (precut surface); (e) The increase in pore water pressure induced slip along the precut surface of the rock specimen;(f) The flow rate was changed, and steps (b)–(e) were repeated.

3 Numerical simulation

3.1 Numerical model

Fig. 2 depicts the numerical model replicating the specimen used for the fluid injection experiment. As shown in Fig. 2(a), the dimensions of the numerical model are 34 mm in width, 34 mm in length, and 66 mm in height, which are consistent with specimens for the experiment. The through-going discontinuity, which is a precut surface in the case of the experiment, dips at 60°. Fig. 2(b) shows a through-going discontinuity simulated in the model, corresponding to the precut surface shown in Fig. 1. The boundary conditions and initial conditions were identical to the fluid injection experiments.

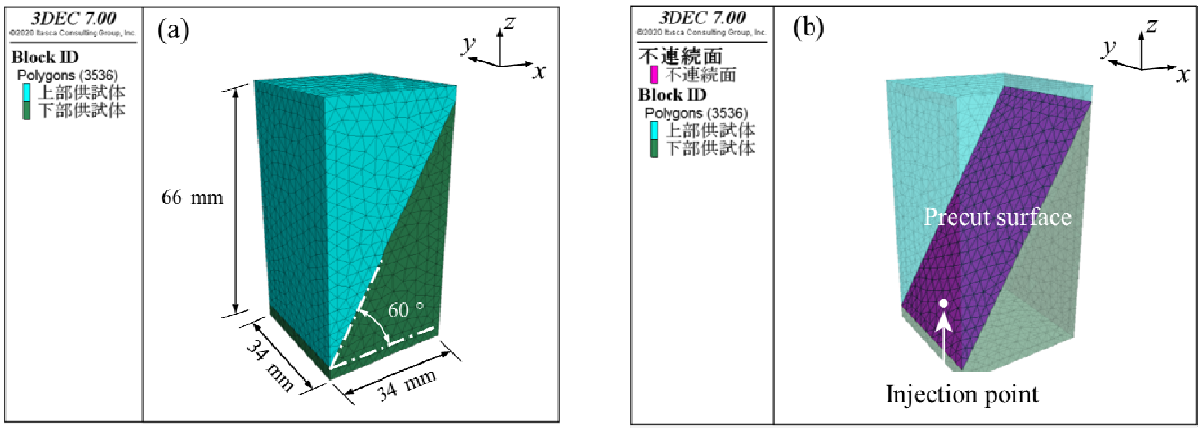


Fig. 2 Numerical model: (a) Isometric view of the numerical model replicating the specimen used for the injection experiment, (b) Perspective view showing a through-going discontinuity in the numerical model and a fluid injection point.

3.2 Input parameters

The elastic modulus of the specimen and Poisson's ratio were assumed to be 60 GPa and 0.2, respectively, considering a reasonable range of elastic parameters for granite. The density was set at 2600 kg/m^3. The hydraulic permeabilities of I-R, I-300, and I-500 were estimated at 1.0×10^{-11} m/s, 3.0×10^{-10} m/s, 1.0×10^{-8} m/s, respectively, by performing permeability tests on specimens that had undergone thermal-induced damage. Regarding the porosity of the specimens, the values were estimated as 0.01, 0.011, and 0.019 for I-R, I-300, and I-500, respectively, from CT scanning and image analysis, as shown in Fig. 3. The CT scanning was performed using a SkyScan2214 system under the conditions of 100 kV, 75 µA, and an exposure time of 7000 ms, which resulted in a scanning time of approximately 21 hours and a spatial resolution of 6 µm.

Regarding the parameters of the discontinuity to which fluid is injected during the simulation, the following parameters were used; the normal and shear stiffnesses were assumed to be 60 GPa/m and 20 GPa/m, respectively; the friction angle was set at 30°, assuming that the value remains unchanged during slip; the cohesion was set at 0° as it is a precut surface; and the hydraulic aperture of the discontinuity was assumed to be 1.5 µm.

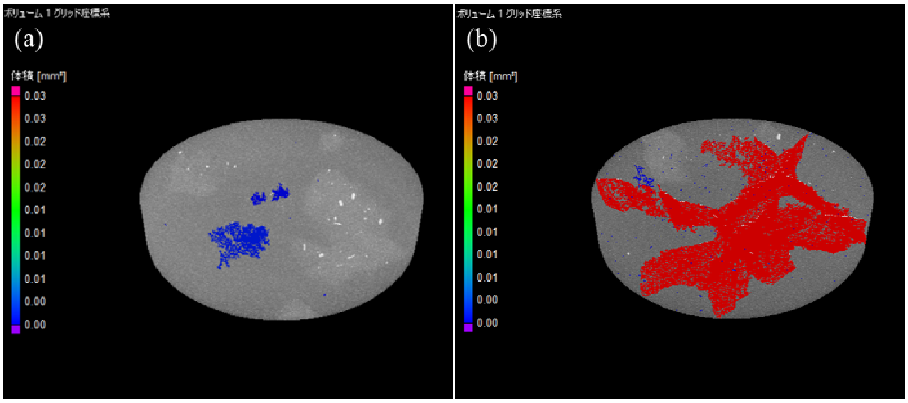


Fig. 3 3D image reconstructed from CT scanning with nano-focused X-ray CT scanner and identification of fracture network based on image analysis: (a) I-300, (b) I-500.

4 Results and discussion

4.1 Experimental results

Fig. 4(a) shows changes in shear stress, lateral displacement, and pore pressure during the injection test at an injection rate of 0.03 mL/min. As explained in the previous section, the axial load is first increased until the stress state reaches almost the critical condition, which is followed by fluid injection at a constant injection rate. As can be seen in Fig. 4(a), after the shear stress reaches the peak value, the fluid injection increases the pore pressure. As the loading plate is fixed during the injection, the shear stress gradually decreases due to relaxation until 500 s. Then, it is to be noted that a sudden reduction of shear stress takes place, as indicated by "slip" in the figure. At the moment, the shear stress suddenly decreases with an increase in the lateral displacement, thus implying the occurrence of slip. The shear stress reduction would be the combined effect of continuously increasing pore pressure and slip-weakening behaviour. Subsequently, the fluid injection is terminated, and the axial load is repeatedly increased so that the stress state acting on the precut surface reaches almost the critical condition. Fig. 4(a) includes results from three injection tests, clearly showing the slip event for each case and thereby demonstrating the reproducibility of the tests. Especially, the most noticeable shear stress reduction took place during the third injection test.

Fig. 4(b) shows results for the three types of specimens, i.e., I-R, I-300, and I-500, when fluid was injected at a constant rate of 0.03 mL/min. As shown in Fig. 4(a), for each specimen, the fluid injection test was repeated. Accordingly, representative results are shown in Fig. 4(b). It is to be noted that as explained previously, the shear stress reduction taking place after fixing the displacement of the loading plate in the axial direction is attributed to relaxation, which is not related to the occurrence of slip. In addition, the timing at which fluid injection was initiated differs among the cases. As the shear stress almost remains stable when the injection was started, the timing does not exert any influence on the result. Given these considerations, the result clearly demonstrates the influence of the rock matrix

permeability in that the shear stress shows a sudden drop during the fluid injection-induced evolution of pore pressure only for I-R. As can be seen, the shear stress starts to decrease 500 s after the onset of the injection test in the case of I-R, whilst the shear stress remains almost the same for the other cases. In addition, the pore pressure evolution history remarkably differs among the specimens. The linear increase in pore pressure in the case of I-R implies that the low-permeable rock matrix hinders the permeation of fluid into the surrounding region. In contrast, in the case of I-300 and I-500, the pore pressure moderately increases, indicating that the microcracks generated when heated in an oven facilitate the filtration of injected fluid into the surrounding rock matrix, so that the increase in pore pressure was controlled. These results provide valuable insights into the role of hydraulic characteristics of rock matrices surrounding rock discontinuities in the occurrence of injection-induced slip behaviour and resultant seismic events.

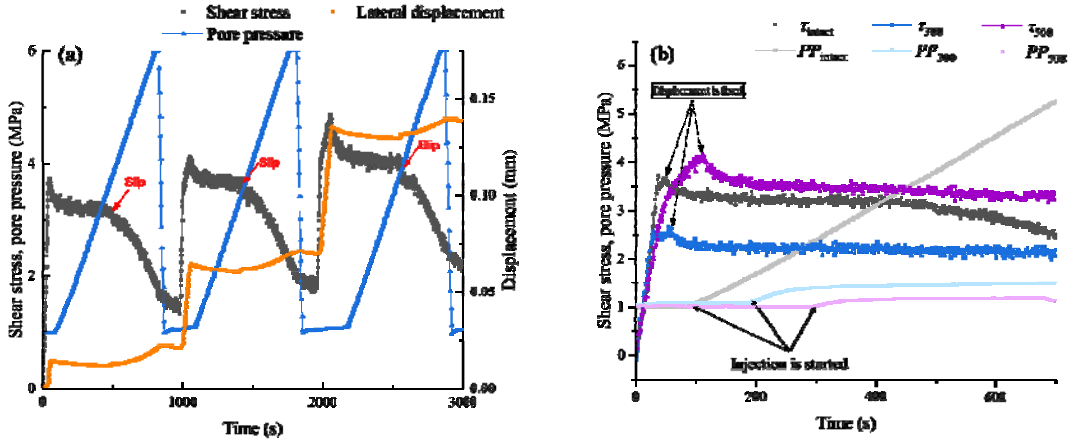


Fig. 4 Experimental results: (a) Results for IR at a fluid injection rate of 0.03ml/min, and (b) Results for I-R, I-300, and I-500 at a fluid injection rate of 0.03 mL/min.

4.2 Numerical simulation results

Fig. 5(a) shows the change in pore pressure over time during fluid injection obtained from the numerical simulation. In terms of pore pressure increment at 300 s after the initiation of fluid injection, the numerical simulation results are comparable to those in Fig. 4(b). For instance, for the experiment, the pore pressure increases by 0.19 MPa in the case of I-500, while the numerical simulation resulted in an increase of approximately 0.20 MPa. Comparable results were also obtained for the other cases, thus verifying the numerical simulation to some extent. However, there is a discrepancy between the experiment and numerical simulation in that the pore pressure gradient differs. It appears that pore pressure increases more rapidly and drastically in the numerical simulation compared to the experiment, irrespective of the degree of thermal-induced damage. It is presumed that this discrepancy is attributed to the location where the pore pressure is measured. In the case of the experiment, pore pressure is measured at the injection tube outside the pressure vessel, whilst the numerical simulation does not consider either the injection tube or the hole drilled in the lower block to inject fluid into the precut surface, and the pore pressure is monitored at the injection point on the discontinuity directly during the simulation. It is thus plausible to assume that the hydro-mechanical coupled behaviour of the hole in the lower block exerted an influence on the pore pressure measured at the tube.

Fig. 5(b) shows pore pressures at 200 s after the initiation of fluid injection for different injection rates. As shown, the response significantly differs among the specimens. More specifically, the intact rock matrix (I-R) results in a higher increase in pore pressure when the injection rate was increased. This result is deemed reasonable because the impermeable rock matrix controls fluid leakage from the discontinuity, yielding a rapid increase in pore pressure on the discontinuity. The contour image shown in Fig. 5(b) corresponds to the pore pressure distribution on a cross-section for I-500 at an injection rate of 0.3 mL/min. As shown, the fluid migrates to the rock matrix surrounding the discontinuity, thereby controlling pressurization at the injection point. The purple colour on the discontinuity corresponds to a slipping region.

These results imply that the permeability of the rock matrix surrounding the discontinuity can play a critical role in the occurrence of instability, i.e., slip can be controlled when an injection rate is properly controlled considering the permeability of the surrounding rock matrix.

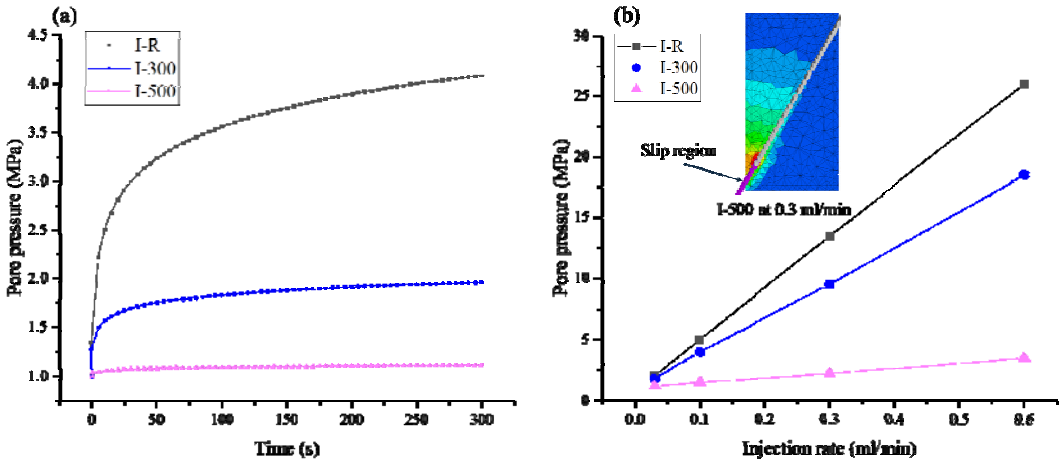


Fig. 5 Pore pressure at the injection point: (a) Pore pressure change during injection, (b) Pore pressure at 200 s for different fluid injection rates.

5 Conclusions

The present study investigated the effect of the discontinuity-surrounding rock matrix permeability on pore pressure evolution and slip occurrence on the discontinuity during fluid injection. To this end, fluid injection experiments were performed by preparing specimens containing a through-going discontinuity. The rock matrix permeability was varied among the specimens by inducing different degrees of thermal damage in an oven prior to the experiment. The thermally induced microfracture network was quantified with nano-focused X-ray CT imaging. Subsequently, fluid injection experiments were carried out, which clearly indicated that when fluid injection rate is 0.03 mL/min, the pore pressure increase rate was sufficiently low to control the occurrence of slip for the specimen that had undergone severe thermal damage, whereas for the intact specimen without thermally induced damage pore pressure rapidly increased, causing slip along the discontinuity. These finding simply show that the rock matrix permeability plays a pivotal role in the pore pressure evolution along the discontinuity and the occurrence of instability. The influence of the fluid leakage to the surrounding rock matrix on the occurrence of slip along the discontinuity was further quantified through numerical simulations after verifying the numerical model. Based on these findings, it can be concluded that fluid injection-induced seismicity can be mitigated by properly controlling fluid injection rate whilst considering the permeability characteristics of the rock matrix surrounding discontinuities.

References

Sainoki, A.,Mitri, H. S. (2014). Dynamic behaviour of mining-induced fault slip. International Journal of Rock Mechanics and Mining Sciences, *66*, 19-29.

Ge, S., Saar, M. O. (2022). Induced seismicity during geoenergy development—A hydromechanical perspective. Journal of Geophysical Research: Solid Earth, 127(3), e2021JB023141.

Kim, T., Park, J. H., Yu, E. (2023). Seismic fragility of low-rise piloti buildings based on 2017 Pohang earthquake damage. Journal of Building Engineering, 76, 107032.

Zhao, W., An, M., Dal Zilio, L., Zhao, L., Zhu, H., Shen, X., Gan, Q., Zhang, F., Elsworth, D. (2025). Coupled evolution of seismicity and permeability in fault zones. Communications Earth & Environment, 6(1), 918.

Hutka, G. A., Cacace, M., Hofmann, H., Zang, A., Wang, L.,Ji, Y. (2023). Numerical investigation of the effect of fluid pressurization rate on laboratory-scale injection-induced fault slip. Scientific Reports, 13(1), 4437.

Ji, Y., Zhang, W., Hofmann, H., Cappa, F., & Zhang, S. (2023). Fracture permeability enhancement during fluid injection modulated by pressurization rate and surface asperities. Geophysical Research Letters, 50(18), e2023GL104662.

Schwartzkopff, A. K., Sainoki, A., Elsworth, D. (2021). Numerical simulation of mixed aseismic/seismic fault-slip induced by fluid injection using coupled X-FEM analysis. International Journal of Rock Mechanics and Mining Sciences, 147, 104871.

Experimental Analysis of Flake Formation Under Roadheader's Pick Impact

D. J. Guerrero-Miguel, M. I. Álvarez-Fernández, M. B. Prendes-Gero & C. González-Nicieza

DinRock Research Group, Universidad de Oviedo, Mieres, Asturias 33600, Spain.
inma@dinrock-uniovi.com

0000-0002-9125-4860
0000-0002-5681-6530
0000-0001-9125-4863
0000-0002-2575-9676

Abstract

The removal of rock material is a fundamental requirement to successful execution of most mining and civil engineering projects. Depending on the properties of the material to be excavated, roadheaders are frequently used as primary excavation tools. These machines employ an array of picks to fragment the rock, producing small portions -flakes. Consequently, the efficiency of this process significantly influences the economic revenue and the viability of such projects.

To gain a deeper understanding into the physical mechanisms underlying flake formation, the phenomenon was replicated at a laboratory mid-scale to examine the influence of most relevant involved variables. Specifically, a previously designed pendulum testing apparatus was used to conduct an experimental campaign in concrete specimens subjected to dynamic impact. The experimental campaign involved variations of the impact angle and the distance from the impact point to the free edge of the specimens. The tests were recorded using a high-speed camera to reveal the strong dependency of flake formation on both the angle of impact and proximity to the free edge. Additionally, the resulting fracture surfaces were characterized using three-dimensional scanning techniques to evaluate the effective damage produced depending on the transmitted energy.

For small angles and elevated distances from the free face, impacts produced minimal surface damage, mainly generating powder without flakes. Conversely, higher angles and closer proximity to the edge favored the formation of distinct flakes, which may also involve internal grain rupture. The fractured surfaces often resembled Gaussian bell shapes, suggesting a potential predictive model for flake volume and propagation based on impact parameters. Some tests exhibited multiple and sequential flake detachments, proving that pick action may be performed in different interactions rather than with a simultaneous failure in the affected area. These insights contribute to a better understanding of dynamic fragmentation in brittle and heterogeneous materials.

Keywords

Dynamic behaviour, Excavation, High-speed video, Rock surface.

1 Introduction

The performance of roadheaders is an essential operating parameter to ensure the execution of ground-related engineering projects within acceptable economic and operational constraints. Many variables influence the excavation process. In this sense, the overall material removal performance results from the interaction between the operational limitations of the machine and the mechanical properties of the excavated material. Hence, a thorough understanding of this interaction between the excavating device and the rock mass is essential to optimize mechanical rock excavation of rock masses and to advance knowledge of the real physical phenomena that arise during the excavation process itself. In the case of roadheaders, material removal is produced by successive impacts of cutting picks against the rock mass. Therefore, conical picks are among the most widely used tools in the field of mechanical rock excavation, with applications ranging from mining to civil engineering works, such as opening underground spaces or the renovation of road surfaces(Cheluszka et al. 2022).

To optimize the excavation process mainly translates as the best manner to increase its efficiency, although this may be achieved through several approaches. In this regard, previous literature pursued to reduce the wear of the conical picks, thus reducing the need for replacements and stops for maintenance operations. While the dominant research directions on pick wear aim to mitigate degradation during excavation (Wang 2024; Youlu et al. 2026), new approaches include the enhancement of pick geometry through topological optimization (Cao et al. 2025) and the incorporation of reinforcing sleeves to improve their performance (Cheluszka et al. 2022). In parallel, and aligned with the increasing automation tendency in mining and civil engineering fields, recent studies addressed the use of real-time sensor data collected during the excavation process to simultaneously optimize the cutting parameters(Kim et al. 2024).

Additionally, it is worth noting that alternative proposals focused on the role of the rock mass were evalauted. These includes disrupting techniques such as pre-slotting of the excavation face (Zhang et al. 2024), the generation of previous cracks in the rock masses to ease the excavation process (Dong et al. 2025)or the application of laser-beams to damage the prior to the impact of the pick (Xu et al. 2025). The results of these studies encourage a promising future when combined with roadheaders, although the available literature regarding these topics is still reduced.

As an initial step towards improving the efficiency, durability and energy consumption during the excavation process, a bespoke impact pendulum was employed to bring the accurate interaction of conical picks with the rock mass during the excavation process to light. The analysis of high-speed imaging data, combined with digital reconstruction of the failure surface, provides valuable insight into the complex mechanisms governing pick-rock interaction and enables to rethink the energy transmission processes between the pick and the material.

2 Methodology

The testing device (Fig. 1) was based on an impact pendulum specifically designed to conduct similar experimental campaigns within the research group (Guerrero-Miguel et al., 2023; Prendes-Gero et al., 2021).



Fig.1Impact pendulum used in the experimental campaign.

In addition to the mechanical setup, a Photron Fastcam Mini AX100 high-speed camera was employed to record the impact tests at frame rates up to 5000 frames per second (fps), which allows a qualitative analysis of the flake formation process. This frame rate was set to optimize both the number of images and their resolution, as due to the limitations of the camera and increase in the acquisition speed will imply lowering image resolution.

To analyse the mechanisms of flake formation as a function of the transmitted energy and the distance to a free boundary within the specimen -its top surface-, commercial concrete blocks were employed (Fig. 2a). Previous mechanical characterization using the Schmidt Hammer test determined that the uniaxial compressive strength (UCS) of this material is 59.0 MPa, with acceptably low variability among specimens. Furthermore, it is worth noting that the heterogeneity of the material used is not only caused by its internal composition but is not only associated with its internal composition, but is also evident in the differing surface quality of the front (Fig. 2b) and back (Fig. 2c) surfaces of the tested specimen.

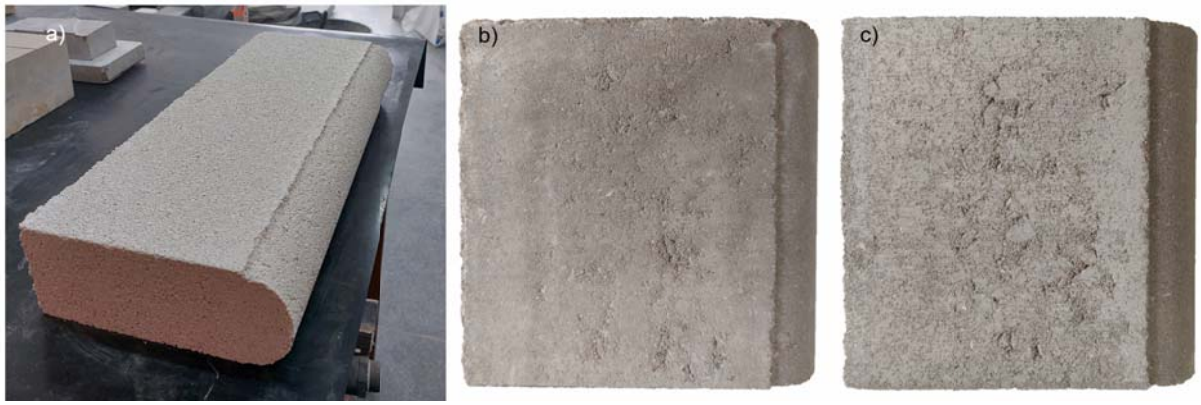


Fig. 2 Figures must be referred to in the text. Try to place the figures close to were they are referred to in the text.

Regarding the basket to place the specimen, it should be observed that the basket was designed to break its motion within predefined angular ranges controlled by a chain transmission connected to two gear. These gears allow the movement of the basket when deviating from the lowest point of the pendulum trajectory but impede its swing towards the pick. Hence, it is guaranteed that all the contact between the pick and the specimen is produced during the impact event and never after several collisions due to swinging movements.

The impact pendulum was instrumented employing an encoder that allows to accurately determined the inclination angle as a function of time. Consequently, the angular position, as well as the corresponding linear and rotational velocities and accelerations, were known throughout the entire pendulum trajectory.

Employing the aforementioned equipment, the experimental campaign consisted of a total of 12 impacts tests in which both the distance to the free surface *h* -defined as distance between the impact point and the top of the specimen- and the initial inclination angle of the pendulum were varied to evaluate their influence on the flake formation mechanism as well as in the overall amount of removed material. Specifically, distances of 5 mm, 10 mm and 15 mm were analysed in combination with angles of 10°, 30°, 50° and 70°. For these inclination angles, the linear speed of the pick is summarized in Table 1, widely covering the spectrum of usual operating speeds, which tend to be around 1.5 to 3.5 m/s.

Table 1. Maximum linear speed for picks under different initial angles.

Pendulum original inclination (°)	**Maximum linear speed of the pick (m/s)**
10°	0.57
30°	1.68
50°	2.75
70°	3.73

After completing the tests for the selected combinations of pendulum inclination and distance to the free surface, the specimens were scanned using a Roland Picza Pix-30 mechanical contact scanner. The scanning needle had semi-spherical head of 80 µm in diameter, enabling highly accurate reproduction of the failure surface. The impact area was scanned by generating a regular grid with a spacing of 0.5 mm between points, allowing the acquisition of the three-dimensional surface coordinates (x, y, z) at the predefined grid nodes. Subsequently, the surface was digitally reconstructed using the Delaunay triangulation technique. Based on this reconstruction, the volume of material removed -thus the volume of the overall flake- for each impact test was determined using a customized code developed ad hoc in the Matlab® environment.

3 Results and discussion

Although a total of 12 different tests were conducted to investigate flake formation, an initial pendulum inclination of 10° did not transmit sufficient energy to generate a flake in any of the considered cases. This behaviour was reproduced for the cases of 30° and 10 mm, as well as for the cases of 30° and 50 ° with a distance of15 mm. These scenarios are therefore excluded from further discussion in the present work, as they are not associated with flake formation. Nevertheless, it should be noted that, in these cases, only fine powder was registered, accompanied by noticeable toolmarks for inclination angles above 30°.

In all tested scenarios that included flake formation, after the pick impacts the surface of the specimen (Fig. 3a), a busrt occurs ejecting material outward of the impact zone. This ejected material generally consists on fine-grained powder and small flakes (Fig. 3b). Despite the fact that that many flakes were detatched at this stage, they were all consistent in size. For higher pendulum inclination angles, however, a secondary flake formation event was observed following the first stage of material detachment (Fig. 3c).

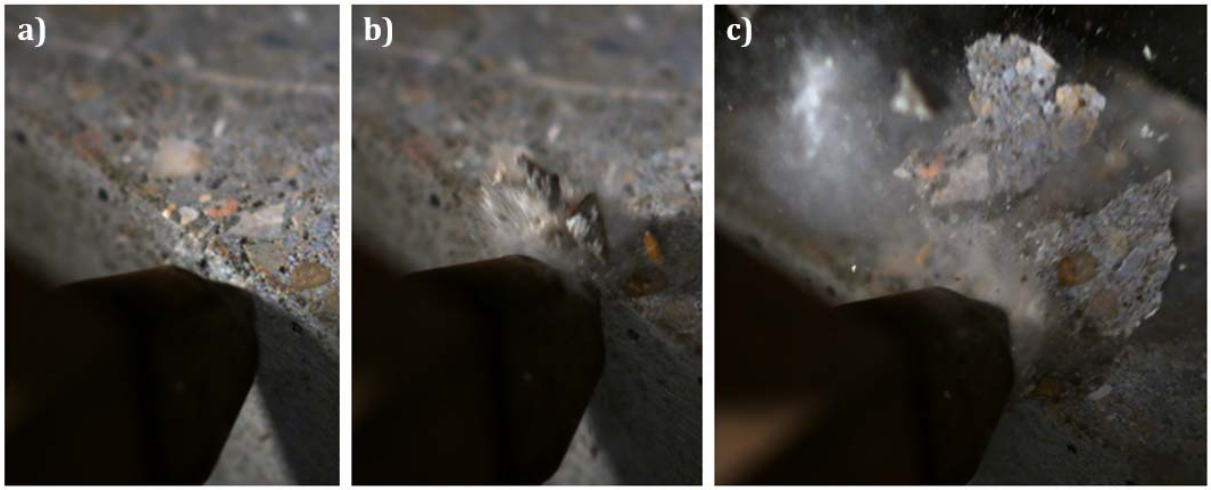


Fig. 3 Stages during the impact of large impact angles: a) initiation of contact, b) first stage of flake formation and c) second stage of flake formation.

This unexpected secondary flake formation mechanism can be successfully explained by a detailed examination of the failure surface generated within the specimen. In Fig. 4, the impact line at which the pick intiated contact with the specimen is indicated by a blue dashed line. This figure reveals that material was removed for distances greater than the predefined 5 mm from the free surface, which may appear contradictory at first glance. However, when the geometry of the pick is simultaneously considered, it becomes clear that although contact was initially established through the rounded tip of the pick, there is a subsequent stage where the frustoconical section reaches the specimen with sufficient speed to induce a larger-scale fracture. This mechanism highlights the existence of two distinct flake formation stages during the impact event.

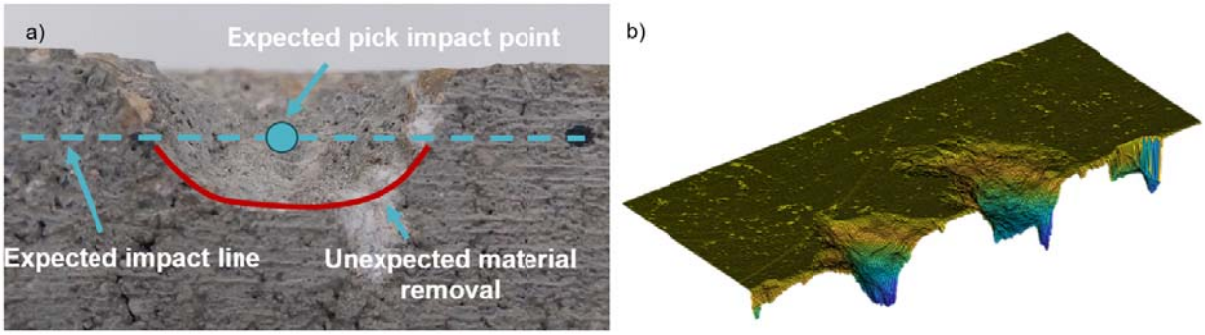


Fig. 4 Detailed analysis of the failure surface for the cases of 5 mm to the free boundary: a) real impact for 70° of inclination angle and b) 3D digital reconstruction of the failure surfaces related to impacts of 50°, 70° and 30°.

Following the quantification of the material removed through flake formation, it can be stated that a linear relationship exists between this value and the original inclination of the pendulum (Fig. 5a). Nevertheless, for larger impact energies the tendency may deviate from this linearity, although, these cases are beyond the scope of this work as they would exceed the regular working conditions of roadheaders. Furthermore Fig. 5a can be schematically interpreted as illustrated in Fig. 5b, where the regression line corresponding to a ditance of 15 mm to the free surface was drawn for explanatory purposes and, as in the case of 10 mm, elongated to determine the intersection points among the different cases. In this schematic representation, the red circles indicate the key points for optimizing the excavation process, as they represent the precise switching moment in which is possible to remove more material for the same amount of transmitted energy, and thus enhacing the efficiency of the excavation proccess. It is worth noting that this evidence suggests potential new approaches in the design of picks for roadheaders. Furthermore, these tentative results encourage the development of a larger experimental campaign, considering more distances to the free face and initial angles, to determine the optimum pick speed for each case.

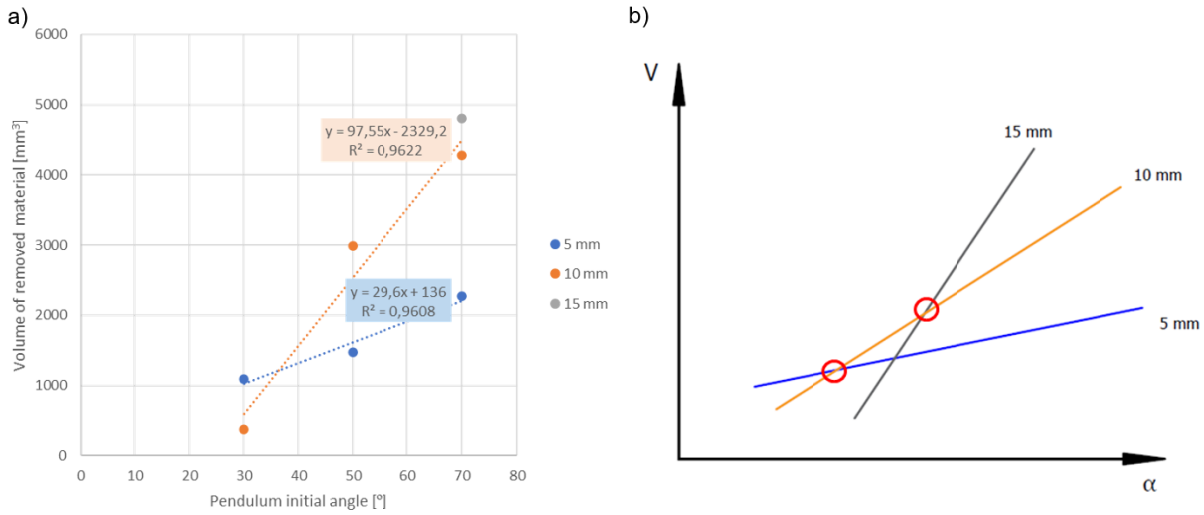


Fig. 5 Volume of removed material versus the pendulum initial angle: a) actual results of the conducted experimental campaign and b) schematic representation with elongated lines to determine the optimum points for increasing removal of material for a certain pendulum initial angle.

4 Conclusions

An experimental campaign was conducted employing a bespoke impact pendulum to evaluate the interaction phenomenon between the rock mass and the picks employed in roadheaders at a laboratory scale. The use of a high-speed camera and the digital recreation of the surface generated after the impact in the specimen allow to conclude that:

- The operational efficiency of the excavation process can be addressed from the combination of the impact energy and the volume of the flakes after identifying the threshold points that allow to remove the maximum amount of material for a given cutting speed.
- The failure surfaces resemble a Gaussian bell shape, which allows to develop predictive mathematical models to estimate the size of the flakes. Nevertheless, this finding should be

regarded as preliminary, and further experimental investigation is required to confirm its general validity and applicability.

- The failure mechanism for high impact speeds consists on a dual-stage fragmentation, transforming the interaction of the pick and the rock mass in a complex scenario with subsequent failures rather than an isolated single event. Hence, the design of conical picks may be tailored depending on their foreseen cutting speed even to the actual operating speeds.

References

CaoY, Zhang Q, Zhang S, Tian Y, Dong X, Song X, & Wang D (2025) Optimization of Rock-Cutting Tools: Improvements in Structural Design and Process Efficiency. In Computation (Vol. 13, Number 7). Multidisciplinary Digital Publishing Institute (MDPI). https://doi.org/10.3390/computation13070152

Cheluszka P, Mikuła (emeritus) S, &Mikuła J (2022). Theoretical consideration of fatigue strengthening of conical picks for rock cutting. Tunnelling and Underground Space Technology (125). https://doi.org/10.1016/j.tust.2022.104481

Cheluszka P, Remiorz E, & Rostami J (2022) The Use of a Roadheader Simulator in Research of Dynamics and Energy-Consumption of Excavating Underground Roadways and Tunnels. Energies 15(18). https://doi.org/10.3390/en15186673

Dong Q, Liu H, & Xu Y (2025) Cutting-Load Characteristics of Excavation Machine Picks in Hydraulic-Precracked Coal–Rock. Applied Sciences 15(22). https://doi.org/10.3390/app152212339

Guerrero-Miguel DJ, Prendes-Gero MB, Conde-Fernández L, Álvarez-Amieva R, Álvarez-Fernández MI, & González-Nicieza C (2023) Design of Customized Impact Pendulums to Address the Fracture of Rock Materials. In F Cavas-Martínez, MDM Granados, RM Buil, & OD De-Cózar-Macías (Eds.), Advances in Design Engineering III. INGEGRAF 2022. Lecture Notes in Mechanical Engineering (pp. 1081–1091). Springer, Cham. https://doi.org/10.1007/978-3-031-20325-1_82

Kim HE, Hwang SP, Yoo WK, Kim WS, Kim CY, & Yoo HK (2024) Laboratory-Scale Limestone Rock Linear Cutting Tests with a Conical Pick: Predicting Optimal Cutting Conditions from Tool Forces. Buildings14(9). https://doi.org/10.3390/buildings14092772

Prendes-Gero MB, González-Nicieza C, Betegón-Biempica C, & Álvarez-Fernández MI (2021) Design of a pendulum prototype for dynamic testing of material removal using picks. Energies 14(20). https://doi.org/10.3390/en14206831

Wang M (2024) Study conical pick cutting performance and fatigue life in breaking rock plate process with numerical simulation. Scientific Reports 14(1). https://doi.org/10.1038/s41598-024-51351-w

Xu B, Huang X, Zhang B, Li B, & Liu T (2025) Experimental study on the performance and mechanism of different combined rock breaking modes of laser-assisted PDC cutter. Geoenergy Science and Engineering 247. https://doi.org/10.1016/j.geoen.2025.213701

Youlu Y, Hongchao W, Yunfei X, Xiangman Z, Lei L, & Yi Z (2026) Wear morphology evolution and rock-cutting performance degradation of conical pick tips under iron ore tunneling conditions. Wear: 584–585. https://doi.org/10.1016/j.wear.2025.206430

Zhang X, Jiang H, Gao K, Gu C,& Li H (2024) Rock cutting using disc tool assisted by the vertical pre-slotting on free-face. International Journal of Rock Mechanics and Mining Sciences 180. https://doi.org/10.1016/j.ijrmms.2024.105811

Application of a Traction Tests Device in Rock Material Specimens

M. I. Álvarez-Fernández, L. Álvarez-Gómez & J. C. Peñas-Espinosa
DinRock Research Group, Universidad de Oviedo, Mieres, Asturias 33600, Spain.
inma@dinrock-uniovi.com
0000-0002-5681-6530

V. Martínez Ibáñez
Polytechnic University of Valencia, Valencia, Spain

Abstract
This work addresses the application of a device designed by the DinRock Research Group from the University of Oviedo (Spain) for performing tensile tests on rock material specimens, with the aim of evaluating its usefulness and versatility under different loading conditions (Nicieza et al., 2020) (Guerrero-Miguel et al., 2021). The research focuses on evaluating the mechanical behaviour of rocks subjected to static and dynamic tensile stresses, in addition to the application of various thermal treatments. Tubular specimens of granite were used as the study materials.
In the static tests, a manual press was used along with strain gauges to register deformations, allowing for the determination of tensile strength and the elastic modulus of the samples.
Dynamic tests were carried out by the controlled drop of calibrated weights from different heights to analyse the material's response to impact loads, reaching velocities between 1 and 50 m/s.
Additionally, complementary tests were performed under different temperature conditions, in both static and dynamic regimes. External heaters were used to maintain a constant temperature throughout the tests. The specimens were tested at temperatures of 200, 300, and 400 ºC, in order to study the influence of thermal treatments on the tensile strength of these materials.
The results obtained demonstrate that the proposed device is an effective tool for characterizing the tensile behaviour of rock materials, providing consistent and reproducible measurements. Furthermore, its adaptability to different loading modes and temperature ranges broadens its potential application in experimental studies and in the analysis of the structural integrity of rocks exposed to extreme conditions.

Keywords
Tensile device, Dynamic, static, Thermal treatment, Rock materials.

1 Introduction

Tensile strength testing in rock-type materials has historically presented challenges in the characterization of their mechanical properties. The Brazilian test is commonly used to determine the tensile strength of brittle materials because it avoids some of the limitations of direct tensile testing, such as premature specimen failure during gripping and the formation of microcracks that may affect the measured strength. In addition, cylindrical specimens are easy to prepare and do not require special fixation systems. Nevertheless, the test provides valid tensile strength values only when fracture initiates at the specimen centre and propagates along the vertical diameter; otherwise, a detailed

analysis of the fracture location and the associated stress state is necessary to correctly estimate the tensile strength.

For this reason, the DinRock research group at the University of Oviedo, has designed a wedge-based device that enables the application of tensile stresses to hollow cylindrical rock specimens through the application of a vertical load to the device (Nicieza et al., 2020;Guerrero-Miguel et al., 2021).Upon vertical compression of the wedge system, the device walls undergo horizontal displacement, thereby inducing tensile stresses across the specimen wall thickness perpendicular to the direction of device motion. A four-component tensile device was developed, consisting of two wedges and two steel walls or semi cylinders as shown in Fig. 1, each featuring inclined internal surfaces that guide the wedges motion during compression of the system. The two wedges have a cylindrical base with a diameter of 52 mm and a height of 8.5 mm. The trapezoidal part of the wedge has 32 mm for the greater base, 12 mm for the smaller base and an angle of 18 º between the z axis and its non-parallel sides. More details appear in Guerrero-Miguel et al. (2021).

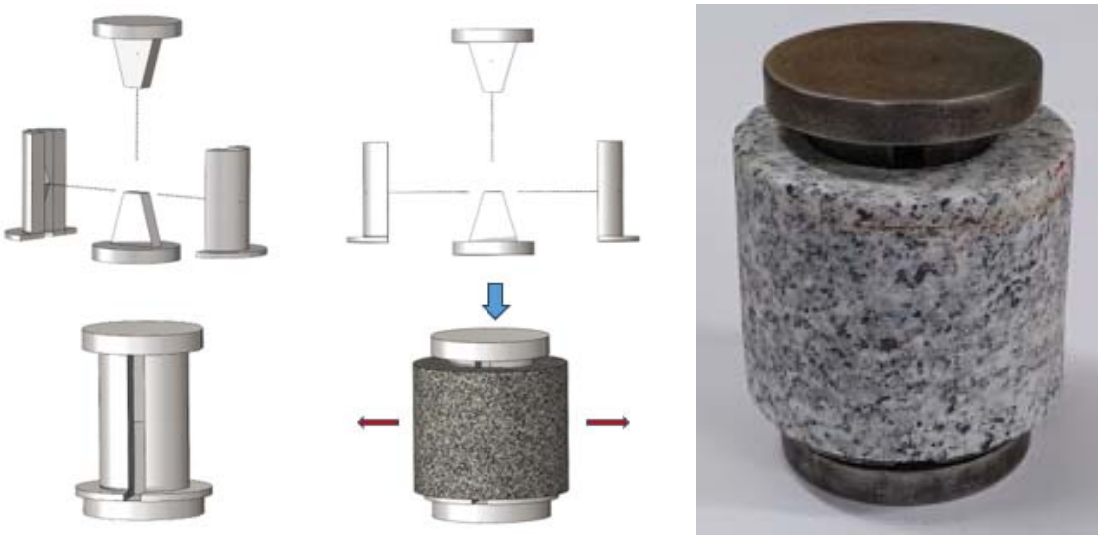


Fig. 1 Traction device parts and assembly example with the test specimen and direction of the loads.

In this case, the aim is to assess the device's versatility by extending its applicability to extreme loading conditions, such as dynamic fracture or the combination of tensile loads and temperature. These conditions are particularly relevant in mining and tunnelling applications (ground subjected to blasting loads) and, in particular, in projects related to the activation or enhancement of geothermal reservoirs.

Although the influence of temperature on the mechanical properties of rock is a field undergoing continuous development, with very recent work such as that by Tomás et al. (2025) or Liu et al. (2023)standing out, the equipment required to carry out tests whilst maintaining the sample temperature is both limited and expensive.

In this regard, the device developed by the DinRock Group provides a simple way of determining the tensile strength of rock at the target temperature.

2 Experimental Procedure

First of all, it was necessary to prepare the samples to test. One natural rock was used, granite, in particular de variety named *Granito Gris Quintana* (from Badajoz, Spain). Their mechanical properties, tested in the Rock Mechanics lab of the Polytechnic University of Valencia, are showed in Table 1.

Table 1. Mechanical properties of rocks tested.

Rock Type	Density [kg/m^3]	Ultrasonic speed [m/s]	UCS [MPa]	Young´s Modulus [GPa]	Poisson´s Coefficient	Indirect Tensile Strength [MPa]
Granite	2,70±0.01	5490±73	162.0±8.0	68.7±8.4	0.29±0.07	9.54±2.21

Starting from 200x200mm blocks, hollow cylindrical test tubes with an outer diameter of 65mm, an inner diameter of 35mm and a variable height between 50 and 60mm were made.

After preparation, the test specimens are divided into two types depending on whether they are limestone or granite. The test specimens used in each test are referenced in the following sections, with one group for static tests, another for dynamic tests, and a third for static tests with thermal treatment.

All test specimens share similar dimensions regardless of their material composition. The length ranges between 50 and 60 mm, the outer diameter between 64.5 and 65.0 mm, and the inner diameter between 35.0 and 35.5 mm. The weight of the specimens falls between 300 and 350 grams.

Each specimen is identified by a name that also conveys additional test information. In the static and dynamic test groups, a letter at the end of each specimen's identification indicates whether the force applied by the wedges is direct or perpendicular to the strain gauges used in those tests. In the thermal treatment group, since strain gauges are not employed, the identifier instead reflects the temperature to which each specimen was subjected. Strain gauges are placed as shown at the next figure

The experimental campaign is divided into three different types of tests:

- Conventional Wedge Tests (CWT): A vertical load is applied to the wedge using a universal press. These results are the “white samples” for the rest of the tests.
- Dynamic Drop Wedge Tests (DDWT): A known weight (24.6 kN) is dropped onto the wedge from a known height (100 or 150 mm) to test the behaviour of the material and the system under dynamic loads. The employed device and sample disposition are showed in Fig.2.In this case, strain gauges were placed in the external surface of the samples.

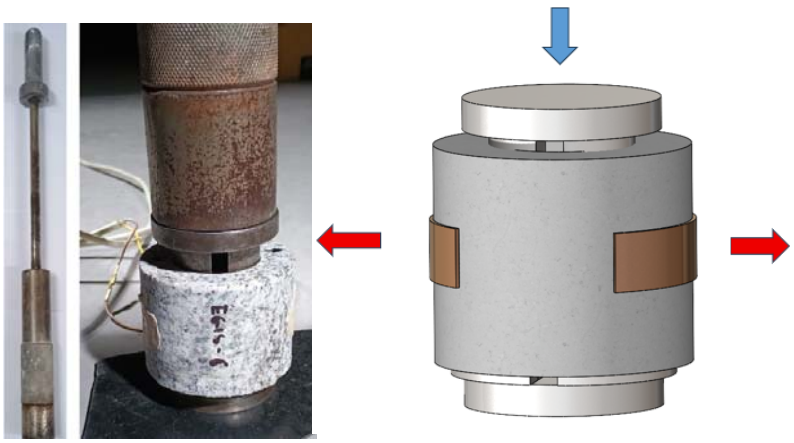


Fig. 2 Disposition for a DDWT and scheme for the strain gauges placement.

- Wedge tests with Temperature (WTT): Using a ceramic ring heater (Fig. 3), the sample rises a target temperature and, simultaneously the mechanical load is applied onto the wedge.Temperatures of 200, 300, and 400°C (±5°C) were selected. A Comet datalogger was used to monitoring the temperature.

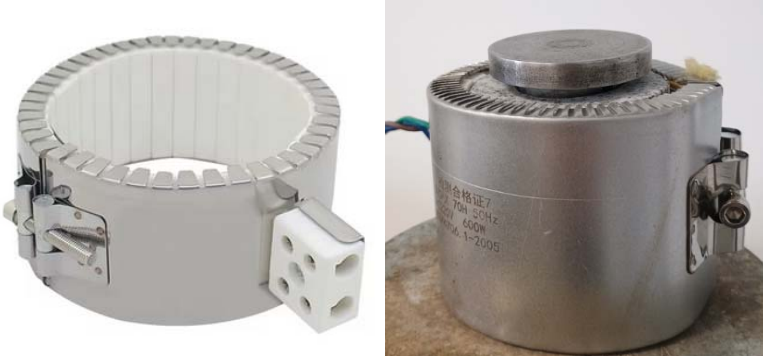


Fig. 3 Heating ring used in test with temperature.

3 Results and discussion

After conducting the various experimental tests, the researchers sought to determine the tensile strength under different temperature conditions and the energy that the materials were capable to absorb during dynamic testing.

The tensile strengths of the specimens were determined using Eq. 1, from (Guerrero-Miguel et al., 2021):

$$\sigma_t = \frac{P_v(-\alpha^4 + 5\alpha^2 + 2)}{1.3RL\alpha(\alpha^2 - 1)^2} \quad (1)$$

Where: σ_t Tensile strength (MPa)
P_v Vertical load applied (N)
α Dimensionless coefficient between the internal radius and the external radius
R External radius of the sample (mm)
L Length of the sample (mm)

3.1 Conventional Wedge Tests (CWT)

Four granite samples (named as CWT1-G, CWT2-G, CWT3-G and CWT4-G) were tested. Results are summarized in Table 2, with a mean value of 8.62 MPa (slowly lower than those obtained with Brazilian tests) and a standard deviation of 1.25 MPa. These values are similar to those found in previous studies (Wang & Hu, 2017), which reported a tensile strength for granite of approximately 8.5 MPa.

Table 2. Summary of tensile strengths obtained through CWT for granite specimens.

Sample	Tensile Strength [MPa]	Mean [MPa]	Standard Deviation [MPa]
CWT1-G	10.15	8.62	1.25
CWT2-G	8.57		
CWT3-G	8.91		
CWT4-G	7.11		

3.2 Dynamic Drop Wedge Tests (DDWT)

In this series of tests, nine samples were tested. Two heights, 100 or 150 mm, were selected to drop the known weight in order to establish the number of impacts needed to break the sample and the energy and velocity of each impact. The observed failure mode was consistent across specimens, corresponding to the expected diametral tensile fracture, in which the rock tubes split into two fragments along the loading axis (see Fig. 4).

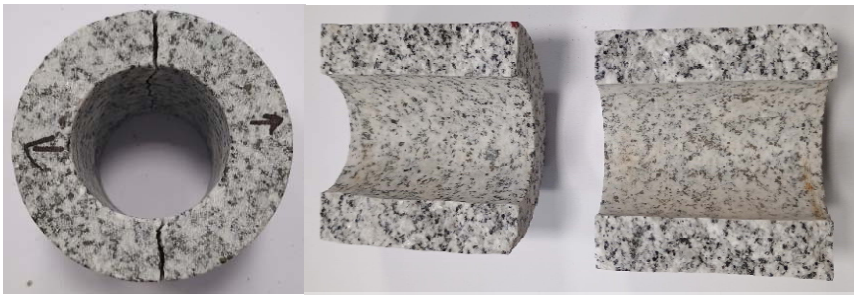


Fig. 4 Fragments obtained during DDWT tests.

The fact that multiple impacts were generally required before fracture occurred suggests that damage accumulates progressively through microcracking until the tensile strength of the material is exceeded. This idea is supported by the strain monitoring during tests. As can be seen in Fig. 5, after each impact, a permanent strain progressive higher, is induced.

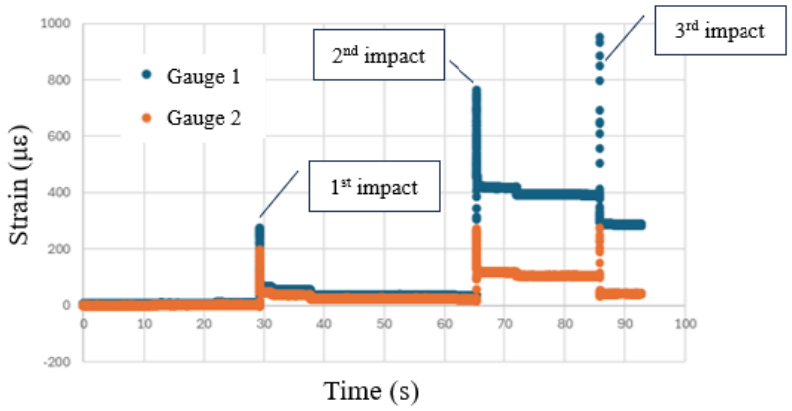


Fig. 5 Strain evolution during a test with three impacts before breakage.

Table 3 summarizes test results. In this case, the term cumulated energy, represents all the energy used to fracture the sample, i.e. the energy of each impact multiplicated for the number of impacts to breakage. As can be seen, in all cases, the number of fragments obtained was two, and the new surfaces generated by fracture was between 1674 and 2497 mm^2. Although, as is usual, there is a variability due the nature of the material, six samples show identical results for cumulated energy (7.39 J). The mean value for all samples is 6.43 J, with a standard deviation of 1.48 J. So, the energy to create new fractures is 0,0032 J/mm^2.

Table 3. Summary of the results from dynamic drop tests.

Sample	Number of Impacts	Height [mm]	Number of Fragments	Impact Speed [m/s]	Cumulated Energy [J]
DDWT1-G	1	150	2	1.72	3.69
DDWT 2-G	2	100	2	1.41	4.93
DDWT 3-G	3	100	2	1.41	7.39
DDWT 4-G	3	100	2	1.41	7.39
DDWT 5-G	3	100	2	1.41	7.39
DDWT 6-G	2	150	2	1.72	7.39
DDWT 7-G	2	150	2	1.72	7.39
DDWT 8-G	3	100	2	1.41	7.39
DDWT 9-G	2	100	2	1.41	4.93

3.3 Wedge tests with Temperature (WTT)

Once the target temperature has been reached using the ceramic heaters, the sample is submitted to a mechanical tensile load through the wedge, maintaining the temperature during the test. Six samples were tested at temperatures of 200, 300 and 400 ºC. Results are provided in Table 4. As can be seen, the two results obtained at 200 °C differ significantly. As with any other experimental test, a larger number of repetitions (typically between three and five) would be required to draw reliable conclusions. In any case, this isolated discrepancy does not undermine the validity of the testing device under heating conditions.

Table 4. Results for wedge tests with temperature.

Sample	Target Temperature (º)	Tensile Strength [MPa]
WTT -1-G	400	11.30
WTT -2-G	400	11.58
WTT -3-G	300	15.29
WTT -4-G	300	12.39
WTT -5-G	200	8.20
WTT-6-G	200	18.01

Fig. 6 shows the representative values alongside the tests carried out at room temperature. It can be seen that there is a slight increase in strength around 300°C, which decreases slightly at 400°C. Although further testing is required to verify this trend, the tensile testing apparatus has been shown to be suitable for use under these conditions.

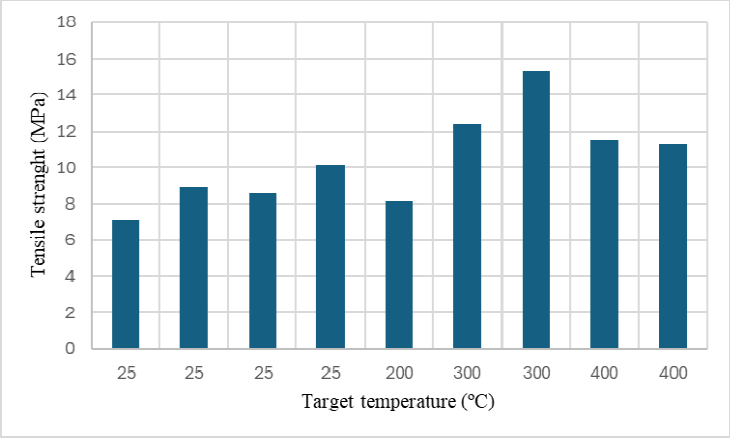


Fig. 6 Tensile strength evolution with the temperature.

4 Conclusions

The wedge-based tensile device developed by the DinRock Research Group has proven to be a viable and adaptable tool for characterizing the tensile behavior of rock materials under static, dynamic, and heated conditions. Across all test types, the device consistently induced tensile failure in hollow cylindrical granite specimens, with fracture patterns largely aligned with theoretical expectations. Cases of anomalous fracture geometry were identified in all test series but were consistently attributed to device misalignment rather than material behavior, underscoring the importance of careful specimen placement in future campaigns. Dynamic tests further confirmed the device's effectiveness under impact loading conditions. Overall, the results support the continued development of this testing approach for applications in the study of rock behavior under extreme conditions.

The tensile device can be easily implemented in a rock mechanics laboratory, requiring only a load cell, a displacement sensor, and, if needed, strain gauges. In addition, it enables the determination of the uniaxial tensile strength without the need to clamp the specimen to the testing machine jaws.

Acknowledgments

This research was funded by the Ministry of Science and Innovation of Spain through Grant MCINN-23-PID2022-142015OB-I00 funded by MCIN/AEI/ 10.13039/501100011033 and by "ERDF A way of making Europe".

References

Gonzalez-Nicieza, C., Alvarez-Fernandez, M. I., Garcia-Fernandez, C. C., & Garcia-Menendez, J. R. (2020). The GIT tensile test: New characterization of the tensile strength in rock materials. *ISRM International Symposium - EUROCK 2020* (Paper No. ISRM-EUROCK-2020-194).

Guerrero-Miguel, D. J., Alvarez-Fernández, M. I., Prendes-Gero, M. B., & González-Nicieza, C. (2021). Determination of uniaxial tensile strength of brittle materials using tubular samples. *IOP Conference Series: Earth and Environmental Science*, *833*(1). https://doi.org/10.1088/1755-1315/833/1/012016

Liu, H., Jing, H., Yin, Q., Zhao, Z., Meng, Y., & Zhang, L. (2023). Study on Mechanical Properties and Fracture Behavior of Granite after Thermal Treatment under Brazilian Splitting Test. *KSCE Journal of Civil Engineering*, *27*(2), 643–656. https://doi.org/10.1007/s12205-022-0296-x

Tomás, R., Benavente, D., Martínez-Ibáñez, V., & Garrido, M. E. (2025). How do high temperatures affect rock properties? A comprehensive review of experimental thermal effects and underlying mechanisms. In *Engineering Geology* (Vol. 357). Elsevier B.V. https://doi.org/10.1016/j.enggeo.2025.108323

Wang, Y., & Hu, X. (2017). Determination of Tensile Strength and Fracture Toughness of Granite Using Notched Three-Point-Bend Samples. *Rock Mechanics and Rock Engineering*, *50*(1), 17–28. https://doi.org/10.1007/s00603-016-1098-6

Advances and Challenges in Multiple Failure State Triaxial Testing of Rocks – 50 years' experience

S. Narimani & B.Vásárhelyi
Dept. Engng. Geol. & Geotechn. Faculty of Civil Engng, Budapest Univ. Techn. and Econ., Budapest, Hungary
vasarhelyi.balazs@emk.bme.hu
0000-0002-7779-9506 & 0000-0002-0568-1031

M. Davarpanah
Institut de Recherche en Mines et en Environnement, Rouyn-Noranda, Canada
0000-0002-8046-5814

Abstract

The "Multiple Failure State" (MFS) triaxial test enables several failure points to be obtained from a single specimen through successive loading under increasing confinement, offering substantial time and material savings over conventional tests. Since its introduction by Kovári and Tisa for 50 years ago, numerous modifications - such as the "Continuous Failure State" (CFS) and strain- or volume-controlled variants - have been developed to enhance test reliability. Despite its efficiency, the method's applicability to brittle rocks remains debated due to cumulative damage and strain localization effects. This paper reviews fifty years of research on MFS testing, summarizing theoretical foundations, experimental progress, and comparisons with single-stage triaxial tests. The review identifies key parameters influencing test validity and provides recommendations for improving measurement accuracy and reproducibility in modern rock mechanics laboratories.

Keywords

Failure envelope, Laboratory tests, Multiple Failure Triaxial Test, Continuously Failure Triaxial test.

1 Introduction

Conventional triaxial tests measure intact rock strength under constant confining pressure but require many specimens, making them time-consuming, costly, and impractical for limited core samples. Multi-stage triaxial testing, originating with de Beer (1950) for one test soil specimen, and later the possibility of "Multiple Failure State" (MFS) Triaxial testing for intact rock samples was raised by Kovári and Tisa (1975) 50 years ago, and since then, measurement technology has undergone numerous changes and modifications. This method is faster, cheaper, reduces the effects of sample heterogeneity, and provides more mechanical insight, but despite proven applicability, it is still not universally accepted by rock engineers.Up to now, this laboratory test method has been widely used for several rock engineering projects around the World.Despite numerous measurements demonstrating the method's applicability, this laboratory test is not accepted in all cases. Many rock engineers and researchers reject its use, such as Hoek and Brown (2019).

This review critically evaluates the conceptual foundations, testing methodologies, and practical applications of the Multiple Failure State (MFS) triaxial test, together with its derivative techniques, including the Continuous Failure State (CFS) and modified radial strain-controlled methods. Although MFS testing has been extensively reported as an efficient means of extracting multiple failure points from a single specimen, its validity and reproducibility remain contested due to damage accumulation, strain localization, and inconsistencies in experimental procedures across laboratories. Accordingly, this review aims to clarify the theoretical assumptions and experimental limitations governing the interpretation of MFS results and to propose a unified framework for its appropriate and reliable application in rock mechanics testing.

2 Summary of Multistage Triaxial Testing Methods for Rock Failure Envelope Determination

Over the past decades, several multistage triaxial testing methods have been developed to determine the rock failure envelope using a single intact specimen. Among these, three principal approaches have gained recognition: the Multiple Failure State (MFS) triaxial test introduced by Kovári and Tisa (1975), the Continuous Failure State (CFS) triaxial test proposed by Kovári et al. (1983), and the Modified Multi-Stage Triaxial Test developed by Crawford and Wylie (1987). These methods were designed to reduce material demand while providing reliable estimates of peak and residual strength under varying confining pressures. The MFS and CFS methods have been formally included in the ISRM Suggested Methods as Type II and Type III tests, respectively (ISRM, 2007) – Type I is the "Single State Triaxial" (SST) test.

Regardless of the specific testing procedure, all multistage triaxial tests require the simultaneous measurement of stress–strain relationships and stress–confining pressure curves. Fig. 1 illustrates the chronological evolution of these testing concepts. The early MFS approach introduced the idea of extracting multiple failure points from a single specimen under strain-controlled conditions. This concept evolved into the CFS method, which aimed to approximate the failure envelope through a continuous stress path using servo-controlled confining pressure. Later, the Modified MFS approach simplified stage termination criteria and improved repeatability, especially for brittle and reservoir rocks (Taheri & Chanda, 2013). Recent developments have further advanced these concepts by integrating automated control systems, radial strain gauge feedback, and acoustic or optical monitoring techniques to enhance objectivity and reduce operator influence.

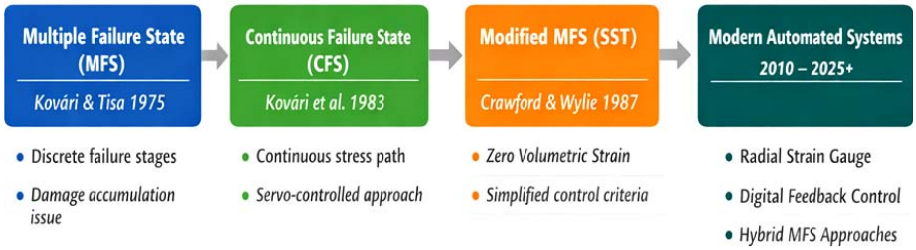


Fig.1 Evolution of multistage triaxial testing methods for rock mechanics.

2.1 Evolution of the Multiple Failure State (MFS) Triaxial Test

The foundation of the MFS concept can be traced back to De Beer (1950), who proposed incremental loading in soil mechanics to generate multiple Mohr circles defining a failure envelope. Building on this idea, Kovári and Tisa conducted systematic rock mechanics experiments at ETH Zürich and formally introduced the "Multiple Failure State" (MFS) triaxial test in 1975. Their method involved applying successive axial loading cycles at increasing confining pressures to a single specimen, as illustrated in Fig. 2.

Kovári and Tisa demonstrated that rock specimens could undergo several distinct strength peaks with negligible variation in peak stress, provided that strain-controlled loading was applied. Experimental results from Buchberg sandstone and Carrara marble showed consistent peak strengths across multiple loading stages, confirming the feasibility of the method for certain rock types. Importantly, the MFS technique was also shown to be suitable for determining residual failure states. The theoretical background of the method was explained using the Prandtl–Reuss hypothesis, which provided a constitutive framework for interpreting the observed stress–strain behaviour.

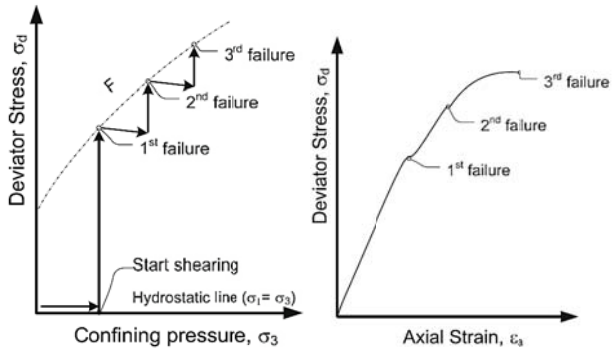


Fig. 2 Multi-stage triaxial test a) stress paths b) stress-strain relation (Youn and Tonon, 2010).

2.2 Continuous Failure State (CFS) Triaxial Test

In the early 1980s, Kovári et al. (1983) proposed the Continuous Failure State triaxial test as a refinement of the MFS concept. In this method, the specimen is initially loaded axially under a fixed confining pressure until signs of failure appear. At this point, the slope of the stress–strain curve, corresponding to Young's modulus, is determined (Fig.3). Subsequently, axial stress continues to increase at a constant strain rate while the confining pressure is simultaneously adjusted to maintain this slope.

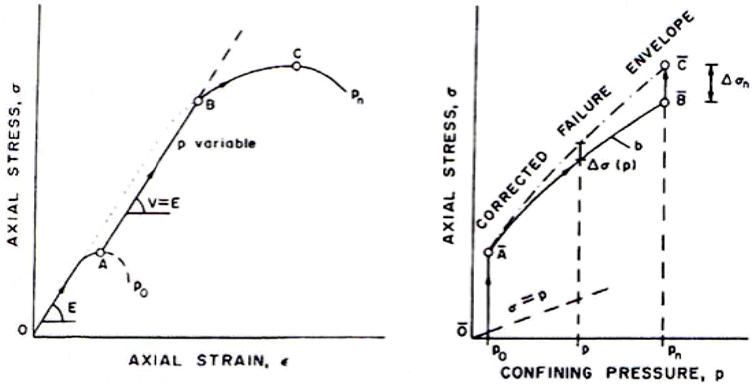


Fig. 3 Concept of the continuous failure state (CFS) triaxial test proposed by Kovári et al (1983). The high slope ratio V/E = 1.0 leading into pre-failure state with reserve of strength $\Delta\sigma n$.

The objective of the CFS method is to preserve a continuous pre-failure state by keeping the stress path tangential to the yield surface until final failure occurs. As a result, the test generates a sequence of closely spaced failure states rather than discrete peak points. The method is based on three key assumptions: the uniqueness of peak strength functions, the reproducibility of stress–strain curves near peak stress, and the independence of material state from the specific stress path followed. According to Kovári's theoretical investigations, these assumptions closely approximate real rock behaviour.

The main innovation of the CFS test lies in its ability to trace a smooth stress trajectory that approximates the true failure envelope more accurately than discrete multistage methods. By minimizing unloading–reloading cycles, the method reduces cumulative damage between stages, which had been a major limitation of the original MFS technique. However, practical implementation of the CFS test is demanding, as it requires highly responsive servo-control systems to maintain the ideal stress ratio. Minor control delays may lead to premature yielding or increased data scatter.

Subsequent studies confirmed the feasibility of the CFS approach using automated feedback control systems, and later research demonstrated its potential for estimating residual failure envelopes in brittle rocks. Nevertheless, the applicability of the method strongly depends on material properties. While it performs well for moderately ductile and homogeneous rocks, its reliability may decrease for highly brittle or heterogeneous specimens due to strain localization and irreversible damage.

2.3 Modified Multi-Stage Triaxial Test

To simplify multistage testing while maintaining reliable failure envelope estimation, Crawford and Wylie (1987) introduced the Modified Multi-Stage Triaxial Test. This approach uses zero volumetric strain as an objective criterion for terminating each loading stage. The procedure, illustrated in Fig.4, involves hydrostatic loading to the desired confining pressure, resetting strain readings, axial loading

until volumetric strain returns to zero, and unloading back to the initial hydrostatic stress. This sequence is repeated at progressively higher confining pressures.

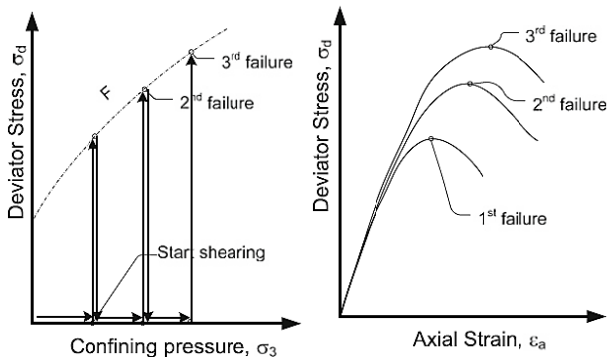


Fig. 4 Modified multi-stage triaxial test a) stress paths b) stress-strain relation (Youn and Tonon, 2010).

Experimental studies on Berea sandstone and Bonnet granite showed that the zero volumetric strain criterion provided reasonable predictions of the failure envelope when compared with conventional triaxial tests. However, for very brittle materials, premature failure sometimes occurred before completion of the planned multistage sequence. To address this issue, the method was later modified by using a volume change ratio relative to a maximum volume change, although this parameter was not clearly defined.

Overall, the Modified MFS approach demonstrated that simplified and objective control criteria could yield reliable failure envelope estimates, particularly for reservoir and moderately brittle rocks. These developments laid the groundwork for modern automated multistage triaxial testing systems, which combine digital control, real-time sensing, and advanced monitoring techniques to improve accuracy, repeatability, and applicability across a wide range of lithologies.

3 Summary of Multi-Stage Triaxial Test

To clarify how the Multiple Failure State (MFS) and Continuous Failure State (CFS) testing concepts have evolved and been applied across different rock types and laboratory conditions, a chronological summary of the principal comparative and methodological studies is presented in Table 1. This structured overview highlights the progressive refinement of the technique, from its conceptual origin in the 1970s to recent implementations using automated radial-strain and volumetric-control systems, and identifies both consistent findings and remaining uncertainties in how MFS/CFS results relate to standard strength parameters.

4 Practical limitations and applicability of MFS/CFS methods

Although MFS and CFS triaxial tests can derive strength parameters from a single specimen, their applicability is limited by damage accumulation, rock type, instrumentation, and data interpretation. Accumulated microcracking can reduce apparent strength in later stages, especially in brittle rocks, while more ductile lithologies remain less affected. Test reliability decreases with increasing brittleness and heterogeneity and depends strongly on precise servo-control and objective failure criteria. Subjective stage-termination and cumulative damage complicate parameter fitting, making non-linear strength models preferable. Overall, MFS/CFS tests are effective when samples are limited and materials are moderately ductile and homogeneous, but single-stage or hybrid approaches are better suited for highly brittle or heterogeneous rocks.

5 Future Perspectives: Automation, Digital Sensing, and Data-Driven MFS Testing

Over the past 50 years, the MFS triaxial test has progressed toward semi-automated systems, with the next major shift driven by automation, advanced sensing, and data-driven analysis. Automated control and objective stage-termination criteria significantly reduce variability and improve reproducibility, while AI-assisted controllers enable adaptive, quasi-static loading. Integrated sensing techniques - such as DIC, acoustic emission, fiber-optic strain sensing, and X-ray CT—allow early detection of damage, reduce subjectivity, and support the development of digital twins. High-density data from automated tests enable machine-learning models to reliably estimate mechanical parameters and classify material behaviour, improving efficiency and standardization compared to conventional

interpretation methods. Unsupervised ML clustering also helps identify brittle–ductile transitions or classify lithologies based on AE signatures and strain energy release patterns (Koosmen et al., 2023). These approaches allow rapid, standardized interpretation of large experimental databases, reducing dependence on manual curve-fitting of Mohr–Coulomb or Hoek–Brown envelopes (Hoek and Brown, 2019; Vásárhelyi et al., 2016). Table 2 summarizes improvement of reliability and efficiency of MFS testing from the point of automation, sensing, and data-driven approaches.

Table 1. Selected major studies on MFS/CFS and short comparison notes.

Reference	MFS/CFS variant/method notes	Main difference vs SST (qualitative)/reported bias
Kovári and Tisa, (1975)	Original Multiple Failure State and Strain-Controlled concepts; theoretical and early lab demonstration	Introduces concept: derive multiple failure points from one specimen; emphasizes instrumentation and stopping rules.
Kovári, et al. (1983)	Continuous failure state / steady stress-path control; theoretical/procedural paper	CFS maintains specimen at failure while changing stress path to trace envelope.
Crawford and Wylie (1987)	Modified MFS variants for reservoir cores — staged confining increases	Used successfully for reservoir cores where sample availability limited; stresses that corrections and careful control required.
Pagoulatos (2004)	MFS variants; volumetric inflection / ΔV/V stopping criteria	Generally close agreement for Berea sandstone with careful stopping rules; differences depend on stopping criterion (authors analyze sensitivity).
Youn&Tonon, (2010)	"Multi-stage triaxial test on brittle rock"; focus on brittle response and post-peak staging	Finds multi-stage can reproduce envelope but brittle instability and localization increase scatter and possible underestimation of peak strength if unloading chosen poorly.
Alsalman, (2015)	Comparison & proposed correction methods to map MST→SST results	Proposes corrections for systematic biases arising from damage accumulation; reports numeric adjustments/improvements.
Kotsanis et al., (2018)	Statistical processing of multistage tests; many stages per specimen	Demonstrates practical efficiency for scarce core material; discusses increased scatter for brittle lithologies.
McKean et al., (2019)	MFS applied to unconventional reservoir cores; demonstrated pre/post-peak characterization	MFS captured pre/post peak behavior for heterogeneous cores; recommended instrumentation improvements.

Table 2. Summary of automation, sensing, and data-driven approaches improving reliability and efficiency of MFS testing.

Technology/ Approach	Function in MFS Testing	Key Advantages	Representative Studies (2020–2025)
Automated closed-loop control	Real-time servo-hydraulic control of σ_1–σ_3; auto stage termination	Removes operator bias; improves reproducibility	Csuhanics & Debreczeni (2013); Jin et al. (2025)
Radial-strain-gradient (RSG) criterion	Objective stage termination	Rock-type independent; high repeatability	Jin et al. (2025)
Digital Image Correlation (DIC)	Surface strain mapping	Captures localization, non-contact	McKean et al. (2019); Youn & Tonon (2010)
Acoustic Emission (AE)	Microcrack activity detection	Detects onset of damage	Choi et al. (2018); Koosmen et al. (2023)
Fiber-optic sensing (FOS)	Distributed strain sensing	High spatial resolution	Gholizadeh et al, (2024)
Machine-learning analysis	Parameter inference from MFS data	Reduces human bias, handles nonlinearity	Trinh et al. (2025)
Digital twin coupling	Real-time model–test feedback	Predictive control, adaptive loading	Minaeian et al. (2020)

6 Conclusion

Over the past five decades, Multiple Failure State (MFS) and Continuous Failure State (CFS) triaxial testing have evolved into established laboratory techniques in rock mechanics. This review demonstrates that the reliability of MFS/CFS methods is strongly dependent on rock type. For ductile to moderately brittle rocks, including shales, weak sandstones, and porous sedimentary formations, multistage tests reproduce single-stage strength envelopes with reasonable accuracy. In contrast, for highly brittle, low-porosity crystalline rocks, conventional MFS methods may underestimate peak strength. Consequently, single-stage triaxial testing remains the reference approach for peak strength determination when sufficient core material is available, whereas MFS/CFS testing offers a reliable and cost-effective alternative when sample availability is limited or residual behaviour is of primary interest.

Acknowledgement

The financial support of the Hungarian-Croatian bilateral project National Research, Development and Innovation Fund, grant no: 2023−1.2.4.-TéT-2023-00044 is acknowledged.

References

Alsalman M (2015) *Comparison and correction of multistage triaxial tests to single stage triaxial test for the rock mechanical testing.* MSC Thesis, Univ. Houston, p. 97.

Choi JH, Dai S, Lin JS, Seol Y (2018) Multistage Triaxial Tests on Laboratory-Formed Methane Hydrate-Bearing Sediments.*J. Geoph. Res.: Solid Earth,* 123(5), 3347–3357. Doi: 10.1029/2018JB015525

Crawford AM, Wylie DA (1987) *A modified multiple failure state triaxial testing method.* In: Proc. 28th US Symp. Rock Mechanics, Tucson; 133–140.

Csuhanics B; Debreczeni Á (2013) Development of automatic control of multi-stage triaxial tests at the University of Miskolc. *Geosciences and Engineering*, 2(3): 37-43.

De Beer IEE (1950) The cell-test. *Géotechnique*, 2(2): 162–172.

Gholizadeh Doonechaly N, Reinicke A, Hertrich M, Plenkers K, Obermann A, Fischli F, Maurer H; Wiemer S (2024) Multiphysics monitoring of cementation operation: Implications for wellbore integrity and hydrogeological characterization. *Env. Earth Sci.,* 83(5), 146.

Hoek E, Brown ET (2019): The Hoek-Brown Failure criterion and GSI – 2018 edition. *J Rock MechGeotechnEngng*11:445-463.

ISRM (2007) *The complete ISRM Suggested Methods for Rock Characterization, Testing and Monitoring: 1974-2006*. Eds: R. Ulusay and J. Hudson, ISRM Turkish Nat. Group & ISRM.

Jin G, Syed SA, González-Pérez HJ, Kwak HT, Yousef AA, al Dhamen AA (2025) New unloading criterion for enhancing multi-stage triaxial tests based on radial strain gradient. *J. Rock Mech. Geotechn. Engng,* 17(8), 4735–4744.

Koosmen K; Serati M; Craig B (2023) *Multistage triaxial testing of intact rock: volumetric strain-based methods applied to rock slope design*. In PM Dight (ed.), SSIM 2023: 3. Int. Slope Stability in Mining Conf. Australian Centre for Geomechanics, Perth, 343-358

Kotsanis D; Nomikos PP; Rozos D; Soffianos AI (2018) Multistage triaxial testing of various rock types: A case study of East Attica Prefecture, Greece. *Procedia Structural Integrity*, 10: 112-119.

Kovári K; Tisa A (1975) Multiple failure state and strain controlled triaxial tests. *Rock Mech* 7:17-33.

Kovári K; Tisa A; Attinger RO (1983)The Concept of "Continuous Failure State" Triaxial Tests. *Rock Mech. Rock Engng*. 16: 117–131.

McKean SH; Priest JA (2019) Multiple failure state triaxial testing of the Montney Formation, *J. Petr. Sci. Engng*, 173, 122-135.

Minaeian V, Dewhurst DN, Rasouli V (2020) Aninvestigation on failure behaviour of a porous sandstone using single-stage and multi-stage true triaxial stress tests. *Rock Mech. Rock Engng,* 53(8), 3543–3562.

Pagoulatos A (2004) *Evaluation of multistage triaxial testing on Berea Sandstone.*MS thesis, Univ. of Oklahoma; p. 130

Taheri A; Chanda E (2013) *New multiple-step loading triaxial test method for brittle rocks*, Proc. 19.NZGS Geotechnical Symp. Ed. CY Chin, Queenstown

Trinh NQ; Grøv E; Vistnes G (2025) A Comparative Study of UCS Results Obtained from Triaxial Tests Under Multiple Failure State Conditions (Test Type II). *ApplSci (Switzerland),* 15(6), 3176.

Vásárhelyi B, Kovács L, Török A (2016) Analysing the modified Hoek–Brown failure criteria using Hungarian granitic rocks. *GeomechGeophys Geo-energ Geo-resour* 2:131–136.

Youn H; Tonon F (2010) Multi-stage triaxial test on brittle rock. *Int. J. Rock Mech. Min. Sci*. 47: 678-984.

Microstructural analysis of granite tested under uniaxial compression

L. C. Witte, M. Duda, A. Chehreh, S. C. Pansa, T. Backers
Ruhr University Bochum, Bochum, Germany
Lucas.witte@ruhr-uni-bochum.de

Abstract

Detailed knowledge of the microstructural damage before, during and after loading is needed for a better understanding of the mechanisms leading to macroscopic failure of crystalline rocks. This is particularly true for granite, which is being discussed (Germany) or has already been selected (Finland, Sweden) as a potential host rock for radioactive waste disposal. Therefore, it is important to evaluate the long-term stability and integrity of such subsurface storage systems in granite. This study examined the microstructure of uniaxially loaded granite up to 40 %, 60 %, 80 %, and almost to and beyond its uniaxial compressive strength. Deformed granite specimens were saturated in coloured epoxy resin before thin sections were prepared from central parts of the cylindrical specimens. The results indicate an increase in number of cracks with increasing maximum axial stress. The resulting crack pattern shows main fractures and fine inter- and intragranular cracks. Both, tensile and shear cracks were identified, while cracks oriented subparallel to the axial stress direction were dominant in most thin sections. Finely ground mineral grains occur in areas of significant damage. These results provide valuable insights into the micromechanical processes of crack initiation and propagation in uniaxially loaded granitic rock samples. They improve the understanding of the mechanical stability of a potential host rock and serve as a basis for further numerical simulations to describe and predict failure mechanisms.

Keywords

Microstructure, Crack analysis, Uniaxial compressive strength, Granite, Nuclear waste disposal.

1 Introduction

The mechanical behaviour of rocks under compressive stress is significantly controlled by the initiation, growth and interaction of microcracks (Brace et al. 1966; Bieniawski 1967). While parameters such as uniaxial compressive strength (UCS) and Young´s modulus are determined according to standards (ISRM 1979; DGGT 2022), the visual correlation between internal damage development and macroscopic failure behaviour is less frequently analysed. While Kranz (1983) discussed the type and distribution of cracks in different rocks, Scholz (1968), Lockner (1993), Heap et al. (2009) and many others investigated the temporal development of microcracks using acoustic emission detection.

The present study provides a detailed examination of crack development in crystalline rock, with a particular focus on the quantitative analysis of microcrack kinetics at different stress levels. Using a combination of mechanical laboratory tests and high-resolution, digitally supported thin section

analysis, the study examines how crack density, orientation and distribution patterns change as a function of axial load. The aim is to get a better understanding of the micromechanical processes leading to the transition from micro- to macroscopic failure.

2 Material and methods

2.1 Sample material

Uniaxial compressive strength tests were carried out on a dense, highly granular granite originating from Padang, China. Its medium-sized grains exhibit very high grain bond strength and appear macroscopically isotropic. The mineralogical composition, derived from X-ray powder diffraction analysis, is dominated by plagioclase, quartz, and feldspar (Fig. 1), which account for 40 ± 5 vol.%, 32 ± 3 vol.%, and 23 ± 3 vol.%, respectively. Minor constituents include biotite with 4 ± 2 vol.% and muscovite/illite with less than 1 vol.%.

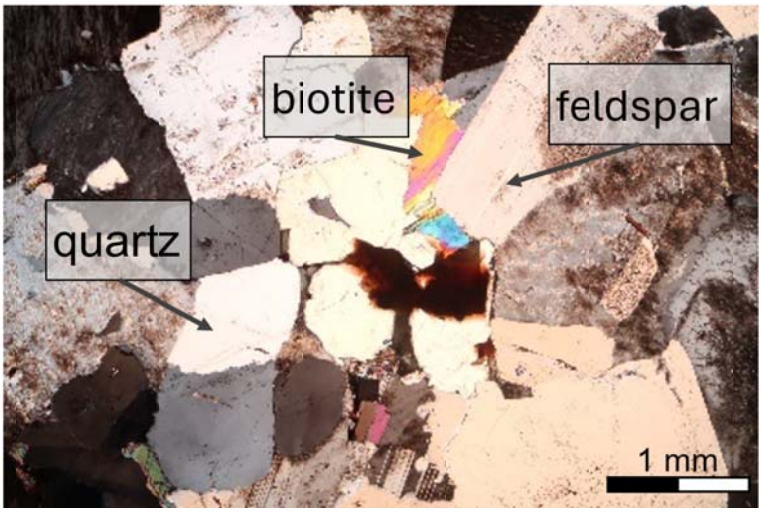


Fig. 1 Optical image in cross-polarized light for thin section orientation of Padang Granite Block 2 in X-Z plane.

2.2 Methods

2.2.1 Uniaxial compressive strength tests

Specimens of 40 mm diameter and 80 mm length were prepared and tested in accordance with DGGT (2022) and ISRM (1979). The specimens were placed in a stiff 4 MN loading frame and centred between a lower and upper spherical seated loading platen. Experiments were performed using graphite powder as lubricant between loading piston and specimen´s end faces to reduce friction. A radial strain chain was placed at the centre of the specimen. Tests were conducted servo-controlled with grade one testing equipment. During testing, axial load was applied to approximately 40 %, 60 %, 80 % of the previously determined reference UCS of 225 MPa. Two further experiments were terminated at maximum strength and after macroscopic failure. Young´s modulus E and Poisson´s ratio υ were determined between 30 % and 40 % of the hypothetical UCS of 225 MPa using axial strains that were calibrated for system characteristics.

2.2.2 Thin section preparation and microstructural analysis

An undeformed reference specimen and uniaxially tested pre- and post-failure granite specimens were saturated in blue epoxy resin after vacuum treatment to preserve microfracture characteristics of the specimen volume (Table 1). The specimen was subsequently cut perpendicular to the main fracture, if visible, and parallel to the axial stress direction. Thin-sections of approximately 30 µm thickness were prepared. In total, 14 thin-sections from seven specimens were investigated.

Thin-section images were recorded with a digital microscope. Images were captured at a magnification of 100 in grid-based mode using a motorised object table and automatically combined to an image showing the complete thin section. A ring light was used for illumination. The brightness was automatically controlled to ensure optimal exposure conditions. To compensate for potential unevenness of the thin section's surface and to ensure a consistently sharp image, automatic height compensation was used in the z-axis. Maximum image sizes of up to 20.000 × 20.000 pixels (≈ 2 µm/px) were achieved, enabling a high-resolution and comprehensive visualisation of the microstructural characteristics.

The microstructure was analysed manually by visually scanning full thin section images. Each microcrack was digitised by two endpoints, converted from pixel-to-µm coordinates using the image scale, and idealised as a straight line. Only epoxy filled cracks were identified, assuming they were coalescing to form the main fracture eventually leading to macroscopic failure, and to avoid confusion with cleavage planes or grain boundaries. Individual tensile and shear cracks were distinguished, primarily based on abrupt orientation changes not attributable to stiffness contrasts. The main fracture was excluded, as the focus is on crack kinetics leading to macroscopic failure through crack coalescence. Dense crack networks were omitted due to identification uncertainty. In complex systems, crack patterns were assessed on a case-by-case study.
Crack statistics were evaluated individually for each specimen using the equations summarised in Table 2. For each specimen, crack datasets from the two separate thin sections were combined. The total number of cracks was counted. Crack length and orientation were calculated from digitised crack endpoints. Mean crack length, crack density, and crack intensity were determined. Crack length histograms were created using 5 µm (reference specimen) or 50 µm (all other specimens) intervals. The most common crack length was estimated by fitting a log-normal distribution. Polar histograms of crack orientations were analysed in 10° intervals. Tensile and shear cracks were evaluated separately. Cracks with an inclination angle of ≤17° to the axial stress direction were classified as tensile cracks, all others as shear cracks. Crack density and intensity maps were derived on a 1 mm × 1 mm grid using crack centre positions.

Table 1. Thin-section photos of specimens deformed uniaxially at 10^{-5} s^{-1} and stopped at different deformation stages.

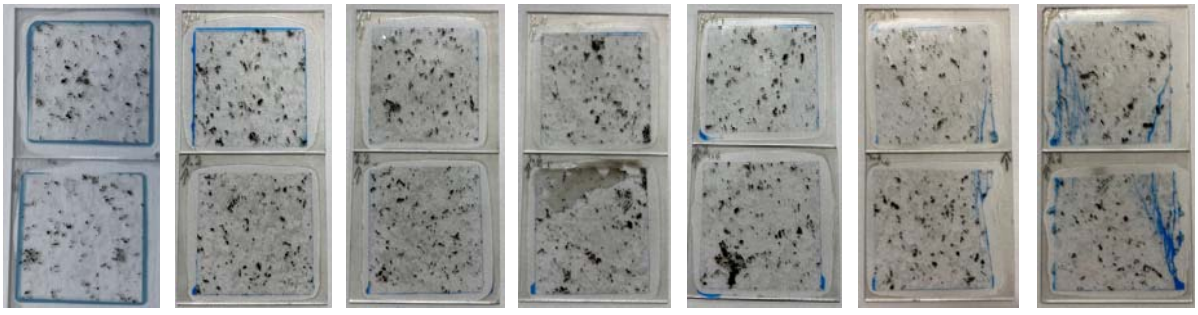
Reference and dry specimens deformed at 10-5 s-1 up to given stages during UCS						
UP0 Reference	UP1-40 40 %	UP2-60 60 %	UP3-80 80 %	UP4-BF Before failure	UP5-AF At failure	UP6 Beyond failure
						

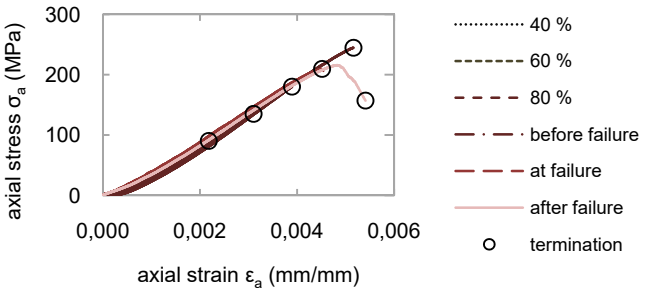
Table 2. Calculation of crack geometry parameters in individual specimens. Individual crack coordinates are represented by their endpoints through $x_{1,i}$, $y_{1,i}$ and $x_{2,i}$, $y_{2,i}$. *Analog calculation for tensile and shear cracks.

parameter	**description**	**calculation**
x_{mode}	Mode of log-normal distribution (PDF) based on its mean $\mu_{\ln}$ and standard deviation $\sigma_{\ln}$	$x_{\mathrm{mode}} = e^{\mu_{\ln} - {\sigma_{\ln}}^2}$
A_{c}	Area covered by cracks	$A_{\mathrm{c}} = [\max(x_i) - \min(x_i)] \cdot [\max(y_i) - \min(y_i)]$
ρ_{c}	Crack density	$\rho_{\mathrm{c}} = \frac{n_{\max}}{A_{\mathrm{c}}}$
I_{c}	Crack intensity	$I_{\mathrm{c}} = \frac{\sum_i^{n_{\max}} L_{c,i}}{A_{\mathrm{c}}}$

3 Results

3.1 Uniaxial compressive strength tests

Young's moduli and Poisson's ratios vary between 51.7 and 54.5 GPa, and 0.18 and 0.35, respectively (Fig. 2). The stress-strain relations show a similar pattern up to the respective stress levels. At the beginning, a slightly curved phase indicates the closure of pre-existing microcracks. With increasing axial strain, the behaviour transitions to a linear section describing a nominally elastic deformation. Shortly before failure, a deviation from linear behaviour can be observed, which is associated with the initiation and growth of new microcracks. Reaching the maximum stress is followed by a significant stress drop, which marks the brittle macroscopic failure of the specimen.



specimen	σ_{max} (MPa)	E (GPa)	υ (-)
UP1-40 %	90.2	54.5	0.21
UP2-60 %	135.1	54.1	0.24
UP3-80 %	180.2	54.5	0.18
UP4-BF	244.7	52.5	0.35
UP5-AF	209.5	52.0	0.22
UP6-afterF	215.6	51.7	0.18

Fig. 2 Results of UCS tests. Left: Stress-strain relations of uniaxial deformation until termination. Right: Maximum axial stress σ_{max}, Youngs´s modulus E, and Poission´s ratioυ of specimens loaded to 40 %, 60 %, 80 % of UCS, immediately before (BF), at (AF) and after failure (after F).

3.2 Microstructural analysis

In the reference specimen, 93 cracks were identified, most of which exhibit a sub-horizontal orientation. Crack lengths vary between 13 µm and 541 µm, with the maximum frequency occurring in the interval from 55 µm to 60 µm (Fig. 3). The mode representing the most frequent crack length after fitting a log-normal distribution is 48 µm. The total number of cracks increases with increasing axial stress (Fig. 4). A significant increase can be seen as the granite approaches its UCS. This applies to both tensile and shear cracks. The ratio of number of tensile to number of shear cracks increases from 0.15 to 1.04 (Fig. 4 b). At 40 % of the UCS, the orientation of the cracks is still largely similar to that of the reference specimen. With increasing maximum axial stress, tensile cracks increasingly dominate (Fig. 4Fig. 5).

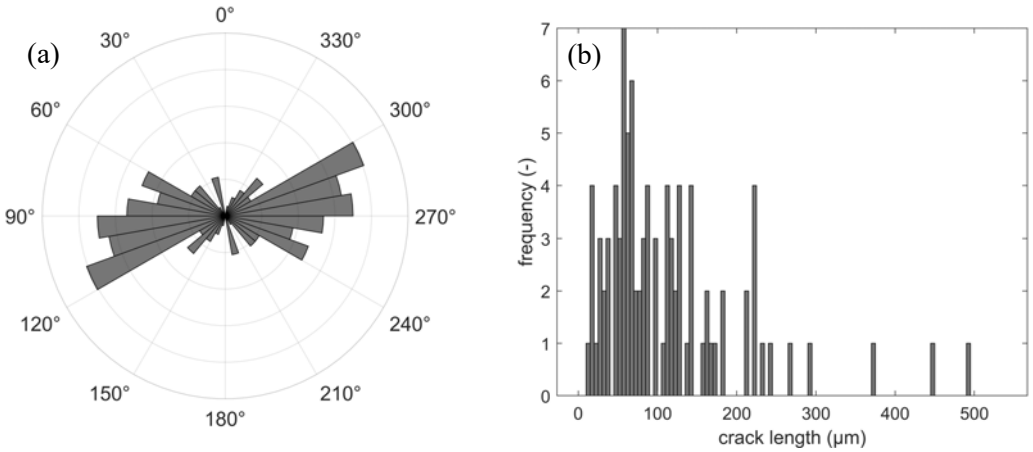


Fig. 3 (a) Frequency distribution of crack orientations in thin section of the Padang granite reference specimen. Radial axes are normalised to total crack number and radial scale ranges from 0 to 0.1. (b) Frequency (number of cracks) distribution of crack lengths (tensile and shear) in intervals of 5 µm.

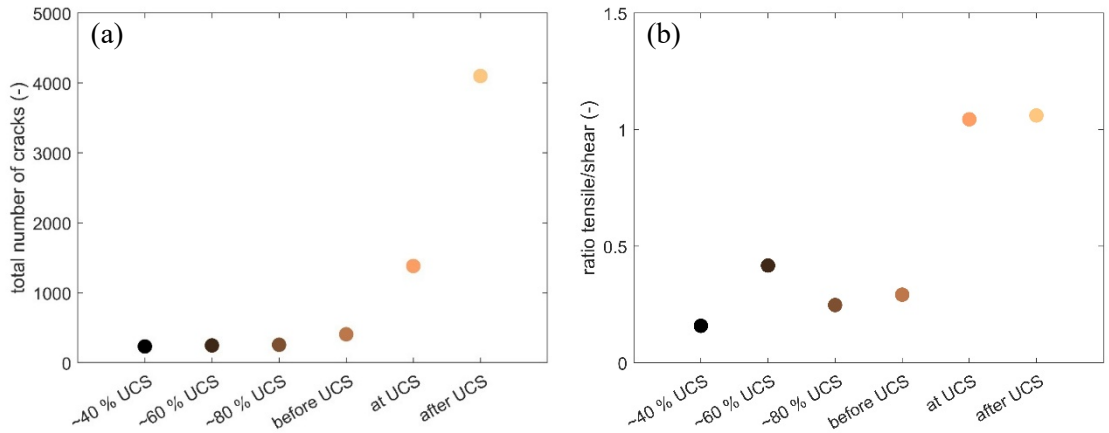


Fig. 4(a) Total number of cracks and (b) ratio of number of tensile to shear cracks in thin sections of Padang granite specimens uniaxially deformed up to different stages.

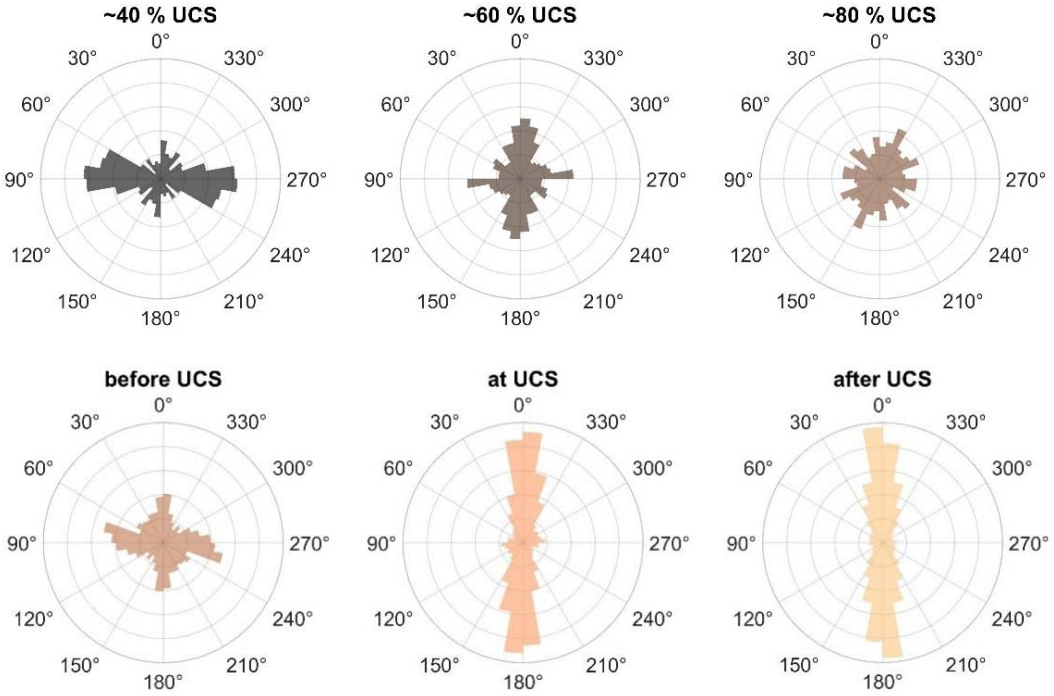


Fig. 5 Frequency distribution of crack orientations in thin sections of Padang granite specimens uniaxially deformed up to different stages. Radial axes are normalised to total crack number in each specimen and radial scale ranges from 0 to 0.1.

Histograms of crack length distributions show a log-normal distribution for all specimens, an increase in the total number of cracks across most length intervals and an increase in maximum crack lengths from 2.0 mm to 5.8 mm (Fig. 6). The mode (most frequent crack length) shows an initial increase with increasing axial stress, which, however, is predominantly attributable to the first 60 % of the axial stress and already approximately twice as large as in the reference specimen at 40 % of the UCS (Fig. 7a). Crack density and crack intensity also increase, in accordance with the increasing number of cracks (Fig. 7b, c).

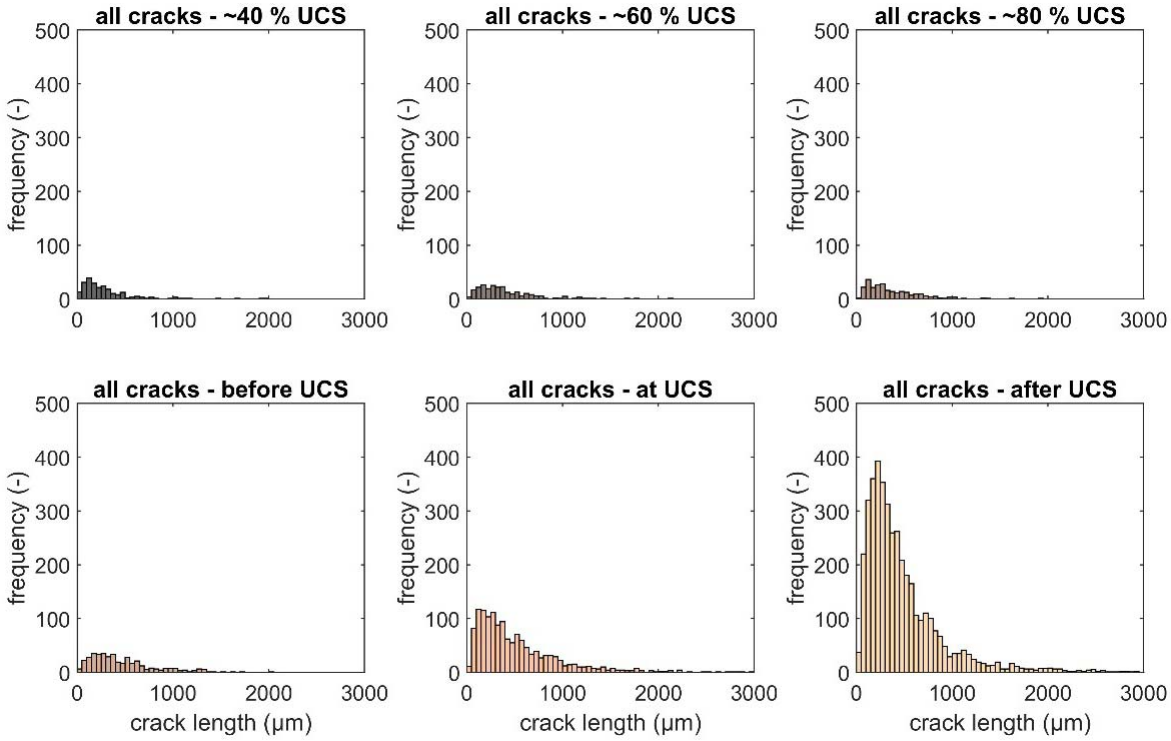


Fig. 6 Frequency distribution of crack lengths (tensile and shear) in intervals of 50 µm in thin sections of Padang granite specimens uniaxially deformed up to different stages.

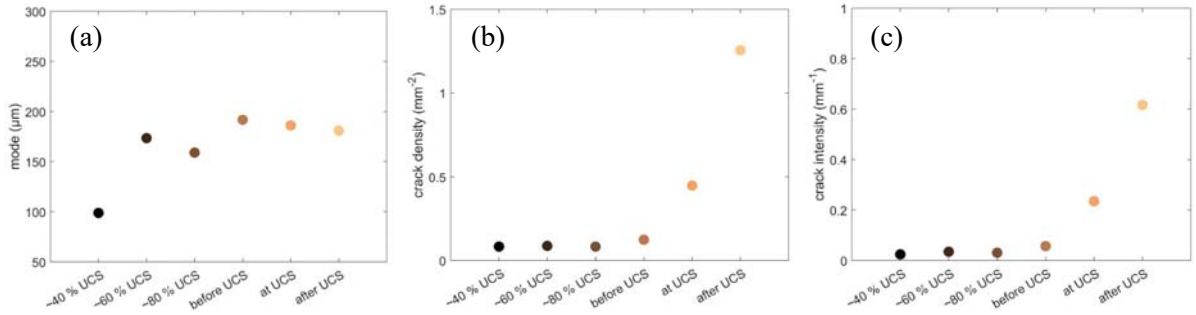


Fig. 7 Mode of log-normal crack length distribution, crack density, and crack intensity in thin sections of Padang granite specimens uniaxially deformed up to different stages.

4 Discussion

The crack inventory of the investigated granite specimens shows a clear correlation between applied maximum axial stress and development of microcracks. As stress increases, the number, density and intensity of the cracks increase. The development in modal crack length with increasing stress indicates that damage is controlled by the growth and coalescence of microcracks. The subsequent flattening of the mode shows that, regardless of a further increase in stress, the dominant microcrack length remains constant, pointing to crack interaction at stresses as low as 60 % of UCS rather than further growth leading to macroscopic failure. For the systematic recording of the crack systems, only cracks filled with blue-coloured epoxy resin were considered and digitised manually using complete thin section images allowing to create a consistent and statistically reliable data basis. To minimise interpretation bias, all cracks were identified by a single person and analysed only after the entire data set had been recorded. The data set clearly shows the relationship between stress and microstructural crack development and offers potential for the calibration of numerical models.

5 Conclusion

This study presents a quantitative microstructural analysis of thin sections prepared from uniaxially tested granite specimens that were subjected to different stress levels. Crack properties were systematically related to increasing maximum axial stress. Total number, length, density and intensity of cracks increased with increasing stress, and a transition from shear- to tensile-dominated crack inventory was observed towards failure. Tensile cracks control the macroscopic failure of granite in uniaxial experiments, whilst dominant crack length does not change significantly beyond 60 % of UCS. A thorough microstructural analysis of the crack inventory is a direct and promising approach to quantify and better understand the mechanisms leading to macroscopic failure.

Aspects of this work were performed within the projects BeNuQuA and MicroBeNuQuA (funded by the Swedish Radiation Safety Authority SSM, Sweden), and AGENS (funded by the German FederalMinistry for Economic Affairs and Energy). We acknowledge the support for our research.

References

Bieniawski, Z. T. (1967). Mechanism of brittle fracture of rock. International Journal of Rock Mechanics and Mining Sciences, 4(4), 395–430. DOI. 10.1016/0148-9062(67)90030-4

Brace, W. F., Paulding, B. W. & Scholz, C. H. (1966). Dilatancy in the fracture of crystalline rocks. Journal of Geophysical Research, 71(16), 3939–3953. DOI. 10.1029/JZ071i016p03939

Heap, M. J., Baud, P., Meredith, P. G., Vinciguerra, S. & Bell, A. F. (2009). Time-dependent brittle deformation of sandstone. Journal of Geophysical Research, 114, B07202. DOI. 10.1029/2008JB006042

Kranz, R. L. (1983). Microcracks in rocks: A review. Tectonophysics, 100(1–3), 449–480. DOI. 10.1016/0040-1951(83)90198-1

Lockner, D. A. (1993). The role of acoustic emission in the study of rock fracture. International Journal of Rock Mechanics and Mining Sciences, 30(7), 883–899. DOI. 10.1016/0148-9062(93)90041-B

Scholz, C. H. (1968). Microfracturing and the inelastic deformation of rock in compression. Journal of Geophysical Research, 73(4), 1417–1432. DOI. 10.1029/JB073i004p01417

Triaxial creep testing on argillaceous weak rock for DSGSD movement prediction

F. Campana, M. Barla & A. Insana
Politecnico di Torino, Torino, Italy
francesco.campana@polito.it
9-0004-3382-1160

Abstract

Deep-Seated Gravitational Slope Deformations (DSGSDs), very slow-moving landslides, are widespread across Italy, from the Alps to the central Apennines. These slow movements, often associated with geological formations exhibiting viscous behaviour, can severely affect infrastructures. A significant example is the interaction between the Sparvo twin-tube motorway tunnel, located in central Italy, and a large DSGSD affecting the area. Such conditions require careful monitoring of the infrastructure and, when possible, the development of tools such as advanced numerical models to study and predict the time evolution of the interaction between the infrastructure and the complex landslide.This can be achieved using time-dependent constitutive models, whose most advanced formulations require the calibration of multiple parameters. The calibration process, in turn, relies on a detailed characterization of the time-dependent behaviour of the geological formations involved.This paper focuses on the characterization of the time-dependent behaviour of Palombini shale formation, anargillaceous weak rockresponsible for the DSGSD movement interacting with the Sparvo tunnel. For this purpose, several triaxial multistage creep tests were carried out on Palombini shales samples. The tests, performed on specimens collected both within the landslide shear band and outside it, revealed a marked tendency of the material to develop time-dependent deformations and allowed the definition of strain–time curves under different stresses. Moreover, the results showed clear behavioural differences between the highly deformed in-situ material sampled from the shear band and the intact material collected outside the shear band, allowing a more comprehensive characterization of the time-dependent behaviour of the argillaceous weak rock.

Keywords

Laboratory testing, soft rocks, time-dependent behaviour, creep, landslides

1 Introduction

Deep-seated gravitational slope deformations (DSGSDs) are large-scale rock mass movements affecting extensive slope sectors, involving depths of up to several hundred metres and exhibiting very slow displacement rates (Chigira 1992). Among the predisposing factors influencing the slow kinematics of these landslides, often associated with creep, is the presence of geological formations at depth exhibiting intrinsic viscous behaviour. Given their exceptional size, these slow-moving landslides may interact with existing infrastructure networks (Vassallo et al. 2019, Barla et al. 2025).

Dedicated studies are therefore required to evaluate the time-dependent evolution of landslide–infrastructure interactions and to ensure the long-term structural integrity and serviceability of the affected assets. On this context, time-dependent infrastructure-landslide interaction requires the development of reliable predictive tools, such as numerical models, and therefore the adoption of appropriate constitutive laws to simulate the landslide creep behaviour. Advanced viscoelastoplastic constitutive models, such as those based on Perzyna's overstress theory (Perzyna, 1966), require the calibration of multiple viscosity-related material parameters. In some cases, these parameters are directly linked to the intrinsic viscous behaviour of the material. To this end, laboratory creep testing (Aydan et al., 2014) provides a means to characterize the time-dependent behaviour of geomaterials involved in landslide movement.

This study presents the investigation and characterization of the Palombini Shale, an argillaceous soft rock responsible for the movement of the large slow-moving Sparvo landslide, in central Italy, which interacts with a recently constructed motorway tunnel. Particular attention is devoted to the results of triaxial creep tests, expressed in terms of strain–time curves, carried out to characterize the time-dependent behaviour of this material, as a prerequisite for more detailed studies on the evolution of tunnel-landslide interaction. The experimental programme included tests performed on both previously deformed material, sampled from the landslide shear zone, and intact material, collected outside the shear zone, in order to identify the main differences in creep behaviour.

2 The Sparvo landslide

In the Italian context, characterised by the widespread presence of slow-moving landslides, particular relevance is given to the interaction between the Sparvo twin-tube motorway tunnel (central Italy) and a large DSGSD affecting the area (Lunardi et al. 2017; Barla 2018).The recently constructed tunnel intersects the deep-seated movement over several hundred metres. Despite its relatively low average displacement rate (approximately 5 mm/year), the DSGSD exerts time-dependent and progressively increasing pressure on the tunnel lining.This long-term interaction led, within the first years following excavation completion, to significant damage to the tunnel lining, necessitating the installation of structural reinforcement measures to ensure its long-term integrity.Furthermore, the need to closely monitor the ongoing interaction between the landslide and the infrastructure required the implementation of a comprehensive monitoring system on the landslide, consisting of a dense network of both continuous and manual inclinometers, piezometers, topographical measurements, and satellite-based radar interferometry. The monitoring network enabled a detailed characterization of the landslide, including its spatial extent, the tunnel section directly affected, and the geological model of the slope, as depicted inFig. 1.

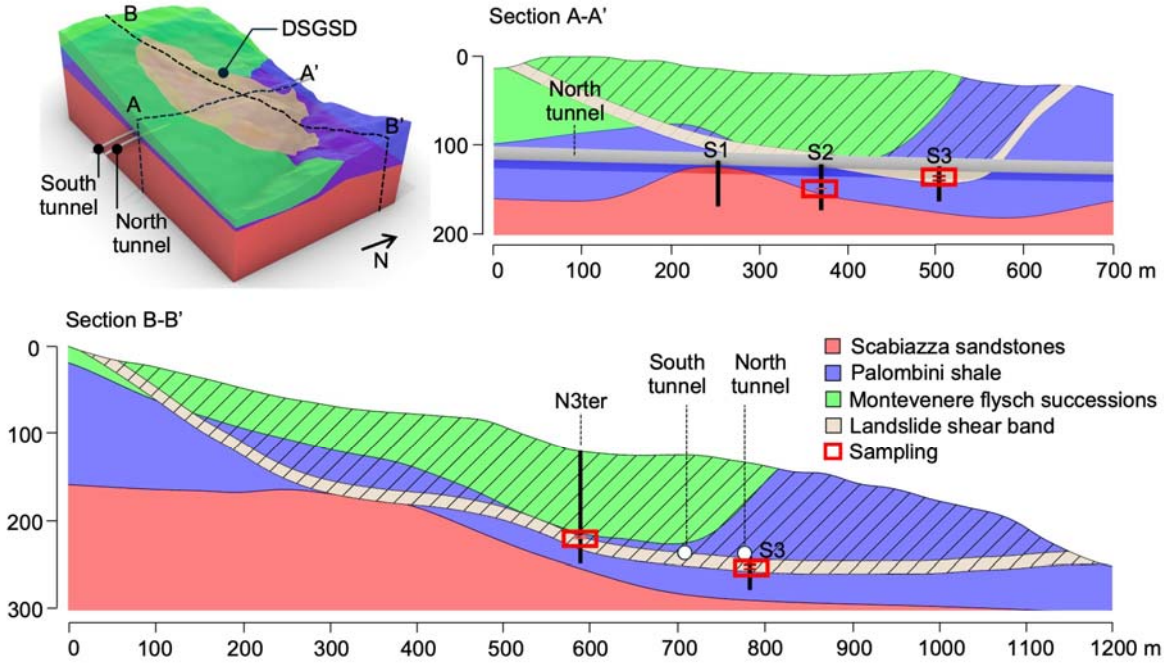


Fig. 1 3D geological model of the slope, spatial extent of the landslide and cross section of the tunnel-landslide interaction.

The landslide extends for approximately 1200 m downslope (Section B–B' in Fig. 1) and, as indicated by the extensive inclinometer network, develops along a shear band.The shear band is predominantly localized within the clayey Palombini Shales formation, composed of dark grey fissile claystones interbedded with calcilutites and tectonized ophiolitic masses.The slow kinematics of the landslide, only marginally affected by seasonal groundwater fluctuations, appear to be primarily governed by the intrinsic tendency of this argillaceous soft rock along the shear band to exhibit viscous deformation.To investigate the time-dependent behaviour of the Palombini Shale involved in the deep-seated landslide, a series of triaxial creep tests was performed on specimens sampled within the shear band (sampled in borehole S3 and N3ter in Fig. 1) and outside it (sampled in borehole S2 in Fig. 1)in order to compare the time-dependent deformational response. In particular, the tests aimed to distinguish between the behaviour of the highly deformed material and that of the intact argillaceous soft rock.

3 Laboratory creep testing on Palombini shale and interpretation

The investigation of the creep behaviour of the Palombini Shales involved triaxial creep tests under undrained conditions (TX-CIU). The tests were performed using the High Pressure Triaxial Apparatus (Barla et al. 2010) at the Geotechnical Laboratory of the Politecnico di Torino. The testing procedure can be summarized in the following stages: 1) specimen saturation, 2)isotropic consolidation of the specimen, 3) undrained shearing phaseto reach the prescribed deviatoric stress *q,* 4) creep phase maintaining constant the deviatoric stress *q*, 5) repetition of stages 3 and 4 until specimen failure.

Five tests were carried out on specimens collected within the landslide shear zone, representing material that has undergone cumulative deformation over time. In contrast, three tests were conducted on the same lithology but outside the shear band, which can therefore be regarded as intact material not previously deformed in situ.Table 1summarizes the main characteristics of the triaxial creep tests. Fig. 2shows, in the p'–q plane, the stress states corresponding to the creep stages compared with the material failure envelope. The failure envelope, derived from standard CID and CIU triaxial tests performed during the tunnel design phase, is defined by afriction angle $\varphi' = 14.9°$ and an effective cohesion $c' = 37.7$ kPa, according to the Mohr–Coulomb failure criterion.

Table 1. Summary of the main characteristics of the triaxial creep tests: consolidation pressures, stress states at the onset of each creep stage and the mobilized shear strengthratio during creep.

			Consolidation		**Creep**				**Failure**
	Test code	**Borehole**	**σ_r [kPa]**	**pp [kPa]**	**Creep stage**	**p'_{creep} [kPa]**	**q_{creep} [kPa]**	**Mobilized Shear Strength Ratio**	**$\varepsilon_{a,failure}$ [%]**
Creep tests on specimens within the shear band	TX - 01	N3ter	1984	800	Creep 1	962	466	0.80	5.49
	TX - 02	N3ter	1984	800	Creep 1	1119	323	0.52	5.47
					Creep 2	1246	514	0.72	
	TX - 03	S3	1984	800	Creep 1	1032	350	0.60	3.54
					Creep 2	1044	481	0.77	
	TX - 04	S3	1984	800	Creep 1	992	329	0.58	6.85
					Creep 2	995	539	0.87	
	TX - 05	S3	1984	800	Creep 1	1043	334	0.57	5.3
					Creep 2	1129	459	0.70	
Creep tests on specimens outside the shear band	TX - 06	S2	2800	1200	Creep 1	1424	706	0.84	9.06
					Creep 2	2016	1010	0.87	
					Creep 3	2562	1417	0.95	
	TX - 07	S2	2800	1200	Creep 1	1437	780	0.90	10.3
					Creep 2	2204	1076	0.85	
					Creep 3	2714	1600	1.00	
	TX - 08	S2	2000	800	Creep 1	1057	345	0.58	Test in progress
					Creep 2	1255	490	0.69	

Fig. 3presents the creep curves in terms of axial strain versus time under constant deviatoric stress, as obtained from the different tests performed. The results highlight a pronounced tendency of the material to develop viscous deformations, with both primary and secondary creep stages clearly identifiable in each loading phase.

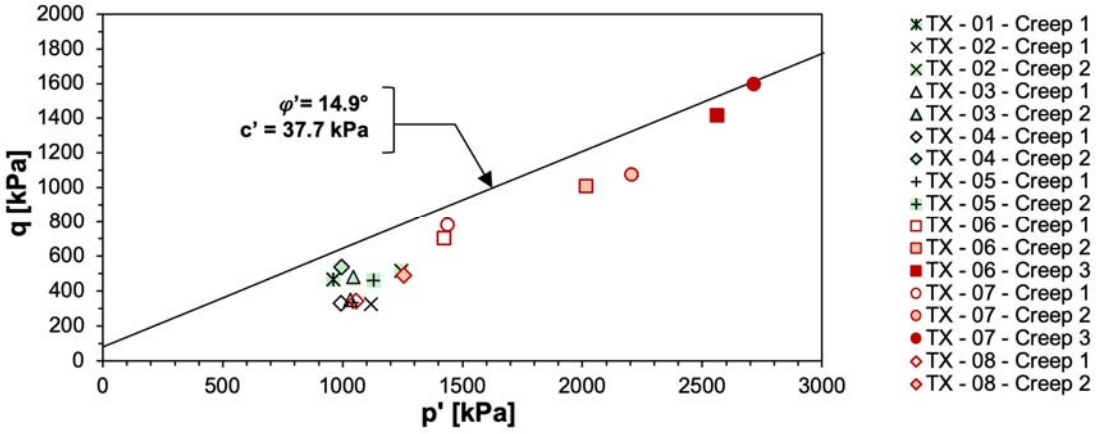


Fig. 2 Stress states corresponding to the creep stages of each test compared with the material failure envelope.

Tertiary creep leading to failure, associated with the localization of a shear surface within the specimen, was observed only in test TX-07, for which the applied stress state corresponded to a mobilized shear strength ratio equal to unity with respect to the theoretical failure envelope.Test TX-06 exhibited a strain rate that increased to such an extent that the response can be considered as approaching failure conditions. However, a distinct tertiary creep stage was not clearly identifiable; rather, a markedly accelerated secondary creep developed. In this case, deformation was more diffuse within the specimen, resulting in a barrel-shaped failure mode.All other tests were brought to failure during subsequent undrained shearing stages following two creep phases, with the exception of test TX-08, which is still ongoing at the time of writing this paper.

Axial strain rates during the secondary creep stage were derived from the creep curves obtained in the various tests. This stage, characterized by an approximately constant strain rate, is considered representative of the behaviour of slow-moving landslides. The observed response is consistent with previous studies (Cristescu and Gioda 1994), indicating that axial strain rate during secondary creep increases with increasing mobilized shear strength, i.e., as the stress state approaches failure.A marked difference in deformational behaviour is, however, evident between the intact argillaceous rock (sampled outside the shear band) and the material collected within the landslide shear zone. Fig. 4 a) illustrates the relationship between axial strain rate and mobilized shear strength at the onset of each creep stage for all tests. At comparable mobilized shear strength levels, the shear band material exhibits systematically higher axial strain rates than the intact material. This behaviour is attributed to the destructuration and cumulative deformation history of the shear zone material, likely associated with a shear-induced reorientation of the microstructure. In contrast, the intact material displays a comparatively stiffer viscous response. The cumulative in situ deformation of the shear band material due to long-term landslide movement also influences the axial strain at failure at the laboratory scale. As shown in Table 1, specimens from the shear zone failed at significantly lower axial strains than those obtained from outside the shear band.The axial strain at failure is higher in the intact material, which must undergo progressive structural degradation to reach the critical state. In contrast, shear band material is already partially destructured, exhibits an oriented shear-induced fabric, and is close to critical state. Consequently, failure occurs at lower axial strains. To further investigate the effect of cumulative in situ deformation within the shear band on the time-dependent behaviour of the Palombini Shales, a “Virtual Time ToFailure” (VTTF) is introduced.This parameter represents the time (in days) required for failure under secondary creep conditions, neglecting tertiary creep acceleration, and is defined as the ratio of axial strain at failure,$\varepsilon_{a,failure}$, to the secondary creep strain rate$\dot{\varepsilon}_a$:

$$VTTF = \frac{\varepsilon_{a,failure}}{\dot{\varepsilon}_{a,secondarycreep}} \tag{1}$$

Fig. 4 b) presents the VTTF values, computed for each creep stage of all tests, as a function of the axial strain rate, with reference to the axial strain at failure measured in each test. The data are well described by a power-law relationship.

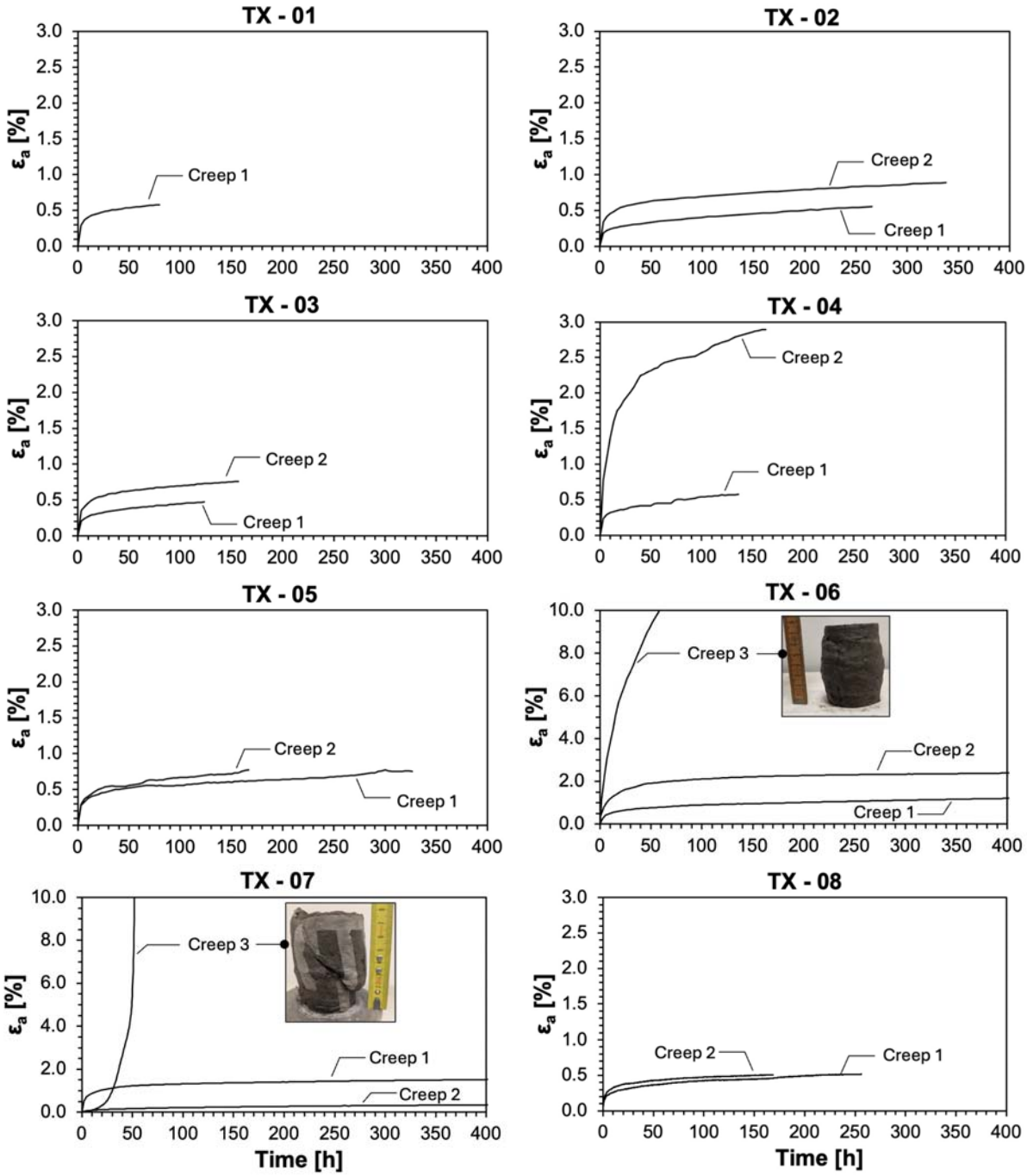


Fig. 3 Time- Axial strain curves of the creep stages of each test.

At the laboratory scale, for a given axial strain rate, the normalized difference between the VTTF of intact material (outside the shear band) and that of deformed material within the shear zone quantifies the degree of damage relative to the initial intact condition. For the Palombini Shales, the shear band material shows a damage level of approximately 46% compared to the intact state, highlighting the significantly shorter creep lifetime of the shear zone material compared to the intact rock.The observations presented herein may contribute to the calibration of numerical predictive models describing the evolution of creep-driven slow-moving landslides.A physically based time-dependent model for such unstable slopes should be capable of capturing not only deformation rate changes driven by variations in the stress state, but also potential failure associated with tertiary creep.This process is controlled not only by the stress conditions within the shear band relative to material strength, but also by the material deformation history, particularly the residual strain at failure. Given that the deformation history of large slow-moving landslides is typically unknown, experimental tests may be used to estimate the current degree of material damage, which can then serve as a starting point for further analysis, accounting the appropriate scale effects between laboratory and field conditions. Consequently, dedicated testing on both intact and in-situ deformed materials is essential in these contexts.

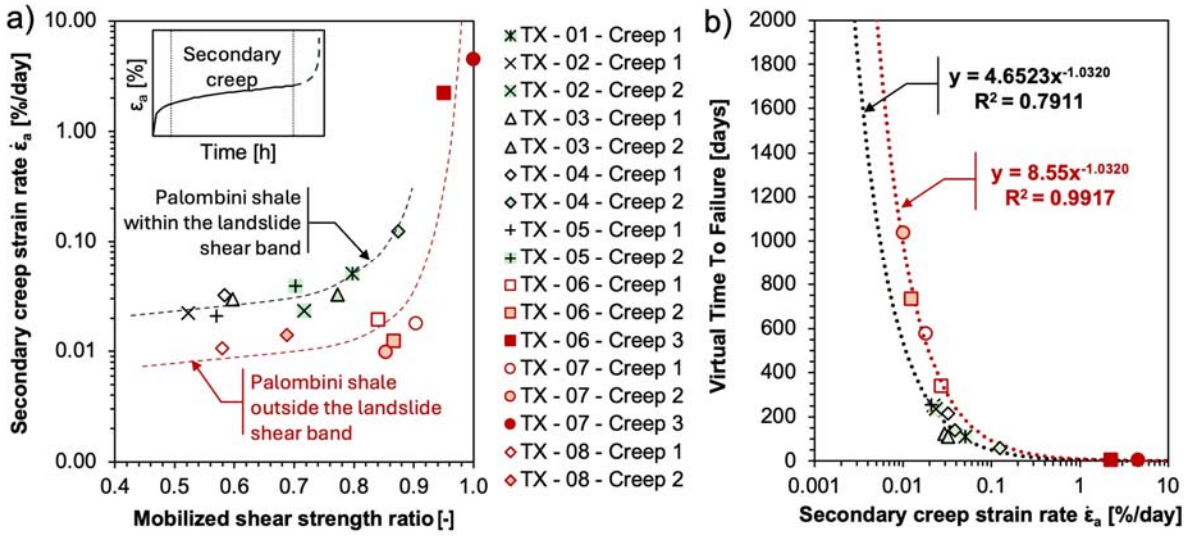


Fig. 4 Relationship between secondary creep strain rate and mobilized shear strength ratio for each creep stage across all tests a) and Virtual time to failure as a function of the secondary creep strain rate b).

4 Conclusions

This study investigates the time-dependent behaviour of the Palombini shale involved in the Sparvo slow-moving landslide through triaxial creep tests on intact and shear band material. The results highlight a pronounced viscous response, with well-defined primary and secondary creep stages and failure occurring only near the strength envelope. A clear difference in behaviour is observed, with shear band material exhibiting higher secondary creep strain rates and lower axial strain at failure due to cumulative deformation and destructuration. The proposed Virtual Time To Failure (VTTF) parameter quantifies this effect, indicating a significantly reduced creep lifetime for the shear zone material. These findings provide experimental support for the calibration of time-dependent constitutive models for creep-driven landslides.

References

Aydan Ö, Ito T, Özbay U, Kwasniewski M, Shariar K, Okuno T, ... & Okada T (2014). ISRM suggested methods for determining the creep characteristics of rock. In The ISRM Suggested Methods for Rock Characterization, Testing and Monitoring: 2007-2014: 115-130. https://doi.org/10.1007/978-3-319-07713-0_9

Barla G, Barla M, Debernardi D (2010) New triaxial apparatus for rocks. Rock mechanics and rock engineering 43(2): 225-230.https://doi.org/10.1007/s00603-009-0076-7

Barla G (2018) Numerical modeling of deep-seated landslides interacting with man-made structures. Journal of Rock Mechanics and Geotechnical Engineering 10(6): 1020-1036.https://doi.org/10.1016/j.jrmge.2018.08.006

Barla M, InsanaA, Campana F, Lopez Ochoa J (2025). Time-Dependent Numerical Modelling of the Effectiveness of a Drainage Intervention on a Large Landslide. International Conference of the International Association for Computer Methods and Advances in Geomechanics, Hong Kong, December 2025.

Chigira M (1992) Long-term gravitational deformation of rocks by mass rock creep. Engineering Geology, 32(3), 157-184.https://doi.org/10.1016/0013-7952(92)90043-X

Cristescu ND, Gioda G (1994) Visco-plastic behaviour of geomaterials (Vol. 350). Springer, Vienna

Lunardi P, Cassani G, Gatti M (2017). Planning of tunnels in landslides situation: the experience in the Italian Apennines. World Tunnel Congress, Norway,2017

Perzyna, P. (1966). Foundamental problems in viscoplasticity. Advances in Applied Mechanics 9: 244–377. https://doi.org/10.1016/S0065-2156(08)70009-7

Vassallo R, Mishra M, Santarsiero G, Masi A (2019) Modeling of landslide–tunnel interaction: the Varco d'Izzo case study. Geotechnical and Geological Engineering 37(6): 5507-5531.https://doi.org/10.1007/s10706-019-01020-x

Physical and analytical modelling of sliding-toppling combined slope failures

S. Yuan, P. Carracelas-Lamela, I. Pérez-Rey & L. R. Alejano
CINTECX, Universidade de Vigo, Grupo GESSMin, 36310, Vigo, Spain
iperez@uvigo.gal
0000-0003-0883-7211

Abstract

Simple failure mechanisms including planar, wedge, toppling and circular failure are typically analysed when studying rock slope stability. However, combined failure mechanisms sometimes take place making rock slopes unstable, so it is convenient to consider their possible occurrence. Despite this, research on combined mechanisms remains limited. Among potential combined failure mechanisms in rock masses reported in the literature, the coupling of sliding in the upper part of the slope and toppling in the front is a possible one. This mechanism has also been observed in masonry retaining walls, where the sliding failure of the backfill induces toppling of the drystone blocks. The main objective of this work is to investigate the stability and failure mechanisms of three different configurations representative of such structures, through an experimental program based on tilt-tests on physical models. The critical tilting angles obtained from the experiments are compared against analytical limit equilibrium estimates, showing good agreement. The slight differences in results observed stem from imperfect granite block cutting, limitations of the testing apparatus and inaccuracies derived from simplifying assumptions. Finally, tentative numerical models are presented, and their results show good agreement with the experimental and analytical ones. While each method has inherent strengths and limitations, their cross-validation offers a more robust analysis of failure mechanisms observed in retaining walls and rock slopes affected by combined failure mechanisms.

Keywords

Rock slope stability, Combined failure mechanisms, Retaining wall, Sliding-toppling instability.

1 Introduction

When assessing rock-slope stability, traditional analyses typically consider four simple failure mechanisms: planar, wedge, circular, and toppling failure (Goodman and Bray 1976). These mechanisms have been widely and successfully applied in slope engineering with excellent results. However, real-world failure cases often involve not a single classic mechanism, but rather the combinations of two or more, where the mechanisms are coupled and interact with each other, resulting in a complex overall behaviour. Although combined failure mechanisms have been identified and studied, research in this area remains limited, and further investigation is deemed to be interesting.

Among potential combined forms, the coupling of sliding (planar or circular) and toppling has been reported in the literature (Alejano et al. 2010; Mohtarami et al. 2014;Wei et al. 2024; Mao et al. 2025).

Fig. 1illustrates various types of mechanisms combining sliding and toppling. In Fig. 1a, b, sliding-toppling cases are depicted, where planar or circular sliding in the upper part drives toppling in the lower part, typically facilitated by a steep joint set dipping against the slope that favours toppling toward the excavation. In Fig. 1c, d, toppling-sliding cases are shown, where toppling occurs in the upper parts of the slope, forcing the lower parts to slide. These mechanisms were proposed as secondary toppling by Goodman and Bray (1976) and Wyllie and Mah (2004) representing instability phenomena triggered by the weakening of the slope toe.

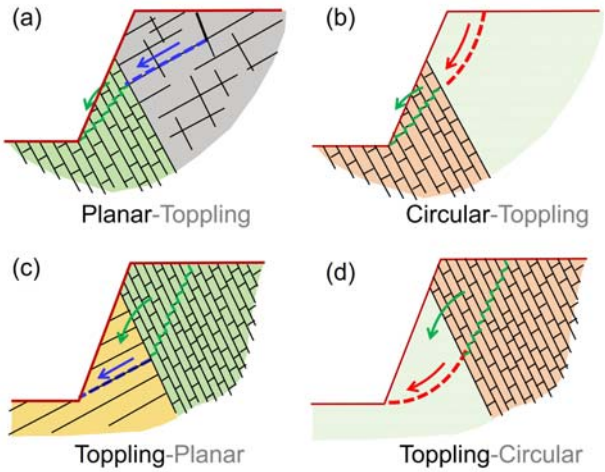


Fig. 1 Schematics of combined failure mechanisms of slope instability: sliding-toppling (planar-toppling (a), and circular-toppling (b)), and toppling-sliding (toppling-planar (c), and toppling-circular (d)).

Simple theoretical methods for computing combined mechanisms are based on limit equilibrium theory, with force transfer between the toppling and sliding parts. The stabilizing force of the upper part of the slope is computed and applied as a load to the lower part, allowing separate stability calculations via traditional methods and overall evaluation based on the stability of the lower part of the slope. For example, Alejano et al. (2010) used this for toppling-sliding. For a sliding-toppling case, applying soil active pressure to the uppermost rock block and analysing toppling is a simple and effective way to assess the mechanism (Mohtarami et al. 2014; Sarfaraz 2020). Physical and numerical methods may validate, supplement, and extend analytical approaches, offering new insights to the study. The sliding-toppling mechanisms herein studied refer to natural rock slopes and engineered structures like dry masonry retaining walls with backfill, where geometry and pressure triggered instability (Alejano et al. 2012; Ding et al. 2025). In these cases, upper backfill slides (following planar or circular surfaces), driving wall toppling and forming a combined failure.

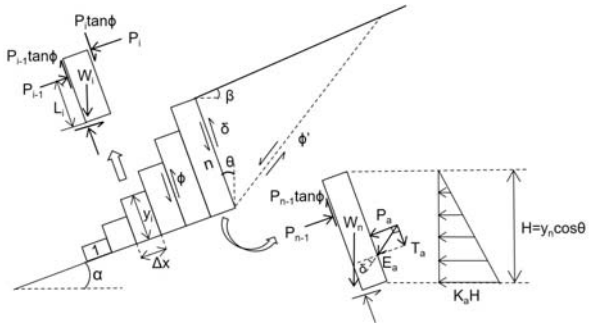


Fig. 2 Schematics and parameters involved in an analytical model of a sliding-toppling combined failure mechanism.

This research seeks to improve safety and economy in wall design and to advance understanding of rock slope stability. This paper proposes a novel analytical model for sliding–toppling failure by integrating classic block toppling theory with Coulomb's earth pressure formulations. Unlike previous studies, this approach captures critical frictional behaviour while significantly simplifying calculations, offering a more practical and efficient framework for engineering applications. Three sets of sliding–toppling lab-scale physical models representing dry masonry retaining walls with granular backfill are designed, prepared and analysed using analytical, physical, and numerical approaches.

2 Theoretical background

Fig. 2 illustrates the elements of the sliding–toppling combined failure mechanism, encompassing a series of blocks and the sliding soil mass behind them. Block toppling is assessed by means of Goodman and Bray (1976) approach. The n^{th} block, with the backfill soil, forms a retaining wall system, and the pressure exerted by the soil is computed according to Coulomb'searth pressure theory.

2.1 Toppling stability

This study adopts the block toppling model proposed by Goodman and Bray (1976), which idealizes the rock mass as a system of 2D rigid, rectangular columns resting on an inclined base. Each block is assumed to rotate about its bottom edge, and toppling stability is evaluated through sequential moment equilibrium analyses of individual blocks. The stabilizing force required for the uppermost block (i = n), is defined by Eq. 1, where active earth pressure is applied as a load on the block.

$$P_{i-1} = \frac{1}{L_i}\left(W_i \sin\alpha \frac{y_i}{2} + E_a \cos\delta \frac{y_i}{3} - W_i \cos\alpha \frac{\Delta x}{2} - E_a \sin\delta\, \Delta x\right) \quad (1)$$

Where P_{i-1} force required to stabilize block i(kN)
L_i lever arm of force P_{i-1}(m)
W_i weight of block i(kN)
α angle of the base plane (tilt or inclination angle)(°)
y_i height of block i(m)
E_a Coulomb active earth pressure(kN)
δ friction angle between the wall and the backfill(°)
Δx width of the block(m)
ϕ friction angle between blocks(°)

The stabilizing forces for the remaining blocks, P_{i-1}, are given by Eq. 2.

$$P_{i-1} = \frac{1}{L_i}\left(W_i \sin\alpha \cdot \frac{y_i}{2} + P_i y_i - W_i \cos\alpha \frac{\Delta x}{2} - P_i \tan\phi\, \Delta x\right) \quad (2)$$

For stability assessment, if the first block (i=1) has P_0>0, indicating instability, the system friction angle is increased until P_0 approaches zero; if P_0<0, it is decreased until the limit state is reached. The friction angle at this condition is defined as the required friction angle, while the material-provided value is the available friction angle. The factor of safety (FoS) is defined by Eq. 3.

$$FoS = \frac{tan(\phi_{available})}{tan(\phi_{required})} \quad (3)$$

2.2 Active earth pressure calculation

For simplified analysis, planar sliding is assumed, and Coulomb's active earth pressure theory is adopted to evaluate the driving force, assuming a cohesionless backfill (c = 0). The active earth pressure acting on the uppermost rock column is given by:

$$E_a = \frac{1}{2} K_a \gamma H^2 \quad (4)$$

Where K_a Coulomb active earth pressure coefficient
γ unit weight of the backfill(kN/m^3)
H vertical height of the wall(m)

The point of application of the earth pressure is at 1/3 of the wall height from the bottom of the wall. Its direction forms an angle δ with the direction perpendicular to the wall. The active earth pressure coefficient K_a is calculated using Coulomb's theory. Its expression is:

$$K_a = \frac{\cos^2(\phi' - \theta)}{\cos\theta + \sin\phi' \sqrt{\frac{(1+\tan\delta/\tan\phi')(1-\tan\beta/\tan\phi')}{(1-\tan\theta\tan\delta)(1+\tan\theta\tan\beta)}}} \quad (5)$$

Where ϕ' friction angle of the backfill(°)
θ inclination angle of the wall(°)
β slope angle of the backfill(°)

2.3 Tilt tests and physical modelling

In analytical methods, the critical inclination angle can be obtained by varying the value of α in the governing equations. In physical modelling, the tilt test provides a simple and effective laboratory approach to determine α and has been widely used to investigate block toppling and wall overturning (Pérez-Rey et al. 2021; Alejano et al. 2015; Gui et al. 2023;Ding et al. 2025), as well as sliding–toppling and toppling–sliding combined failure mechanisms (Amini et al. 2017, 2018). In a tilt test, the inclination of the bearing surface is gradually increased, thereby amplifying the gravity component in the toppling direction until the destabilising moment exceeds the stabilising moment. The corresponding critical inclination angle represents the limit state of system stability and directly reflects the influence of block geometry, centroid position, and interface friction. This method also provides a physical basis for analytical and numerical analyses.

3 Experimental program

3.1 Analytical models

Three analytical models with different number of block rows (n), namely Model I (n=1), Model II (n=2), and Model III (n=3), are developed to investigate the sliding-toppling combined mechanism. When the model is inclined at an angle α, the backfill slope becomes $\beta = \alpha$, and the rock column inclination is $\theta = \alpha$. The process begins by calculating the active earth pressure under inclination α (using the method in Section 2.2) to determine the required force P_{n-1} for the uppermost block (Eq. 1). Eq. 2 is then applied sequentially to compute the required stabilizing forces P_{i-1} for the remaining blocks. By iteratively adjusting α to make P_0= 0, the critical inclination angle is obtained, where the factor of safety equals 1. For non-critical α values, the friction angle is adjusted to set P_0 = 0, and the factor of safety is calculated using Eq. 3.

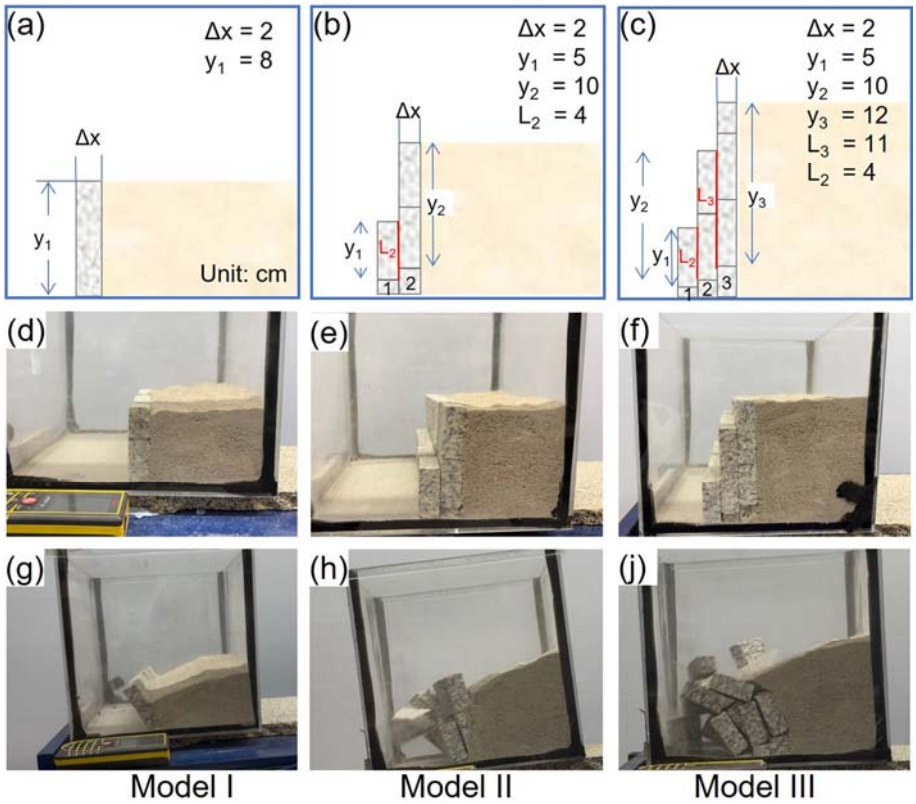


Fig. 3 Experimental results of the analytical models. The schematics in the top row (a-c) depict the analytical models and dimensions, the middle row (d-f) shows the horizontal state at the beginning of the experiment, and the bottom row (g-i) shows the failure moment when reaching the critical inclination angle.

3.2 Physical-modelling experiments and results

Corresponding physical models were constructed based on the analytical setups. The models consist of saw-cut granite blocks with sand backfill and are housed in transparent acrylic boxes mounted on a motor-driven tilting platform rotating at a constant rate of 10°/min. The critical inclination angle at failure onset was recorded, and each experiment was repeated five times. The basic properties of the

granite and sand are listed in Table 1, and the geometric dimensions of the models are shown in the upper part of Fig. 3.

By substituting these geometric parameters along with those from Table 1into the analytical formulas described in Section 2, the critical inclination angles for the models can be determined. Photographs of the experimental process for the physical models are shown in the middle row (horizontal) and the bottom row (tilting failure) of Fig. 3.Each model underwent five repeated tests to obtain the critical inclination angles. The comparison between the analytical, physical and the later obtained numerical values of the critical inclination angle is summarized in Table 2.

Table 1. Parameters of material unit weight and friction angle.

Parameter(unit)	Value
Granite unit weight (kN/m³)	25.31
Sand unit weight γ (kN/m³)	16.02
Sand friction angle ϕ' (°)	30
Sand-granite friction angle δ (°)	28.70
Granite-granite friction angle ϕ (°)	27.72

Table 2. Analytical, experimental, and numerical critical inclination angles for the three models (mean values in parentheses).

Method	Model I (°)	Model II (°)	Model III (°)
Analytical	4.46	3.87	2.95
Physical	3.6–4.6 (4.12)	3.1–4.7 (3.76)	1.9–3.5 (2.36)
Numerical	4.5	3.9	3.0

The results in Table 2 show that the critical inclination angles calculated using the analytical method fall within the range of the physical experimentally measured values. This indicates that the analytical method can effectively capture the sliding-toppling failure mechanism. However, the average experimental values are slightly (0.1 to 0.6º) lower than the analytical predictions. This discrepancy is attributed to block cutting imperfections, such as corner rounding, which affects toppling mechanisms (Alejano et al. 2015).

4 Numerical analyses

Numerical analyses with UDEC 7.0 (Itasca, 2024) were conducted for comparison with results from the other approaches. The wall models were discretized according to their geometry (Fig. 3). In the numerical models, granite is treated as rigid blocks and backfill is a Mohr-Coulomb material with null cohesion, elastic modulus of 10 MPa, and Poisson's ratio of 0.3. The contacts between walls and between walls and backfill are assigned the Coulomb slip criterion, with no cohesion, normal stiffness of 5 GPa/m, and shear stiffness of 1 GPa/m. The friction angles and unit weights of the involved materials are consistent with those in Table 1.

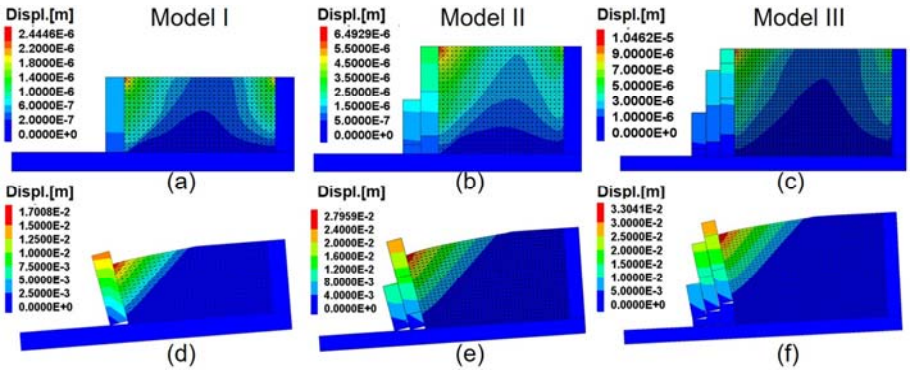


Fig. 4 Total displacement distributions of the three models analysed by UDEC. The upper row (a-c) corresponds to the horizontal condition, and the lower row (d-f) corresponds to the critical inclination angle condition.

The displacement diagrams of the models in the horizontal position and at the critical inclination angle (Table 2) are shown in Fig. 4. From these diagrams, the phenomena of wall toppling and planar sliding of the backfill can be observed, which align with the assumptions and experimentalobservations. Additionally, they capture aspects overlooked by the analytical model. The analytical model simplifies

material deformation and the distribution of contact forces between material interfaces. Therefore, deviations may occur in the safety assessment and critical inclination angle calculations.

5 Concluding remarks

This study investigates the sliding–toppling combined failure mechanism using analytical, physical, and numerical methods. An analytical model evaluates the stability of planar-toppling-prone structures, like dry masonry retaining walls with backfill, by varying the inclination angle. Physical tests successfully reproduce this failure, yielding critical angles that match analytical calculations and are further corroborated by numerical simulations

Discrepancies indicate that physical model failures occur at slightly lower inclination angles than analytical predictions. This behaviour is primarily attributed to geometric imperfections of granite blocks, such as rounded edges, which modify moment arms and centres of gravity. Furthermore, experimental boundary conditions and numerical parameters, particularly contact and elastic properties, significantly influence the results. Due to scaling effects, small laboratory models fail to capture the roughness, joint strength, and corner rounding inherent in large field structures. The impact of these size-dependent features will be addressed in future work.

By cross-validating analytical, physical, and numerical methods, this study provides a comprehensive understanding of the sliding–toppling combined failure mechanism and contributes to improved insight into the stability behaviour of rock slopes.

References

Alejano LR, Carranza-Torres C, Giani GP, Arzúa J (2015) Study of the stability against toppling of rock blocks with rounded edges based on analytical and experimental approaches. Eng Geol 195:172–184. https://doi.org/10.1016/j.enggeo.2015.05.030

Alejano LR, Gómez-Márquez I, Martínez-Alegría R (2010) Analysis of a complex toppling-circular slope failure. Eng Geol 114:93–104. https://doi.org/https://doi.org/10.1016/j.enggeo.2010.03.005

Alejano LR, Veiga M, Taboada J, Díez-Farto M (2012) Stability of granite drystone masonry retaining walls: I. Analytical design. Geotechnique 62:1013–1025. https://doi.org/10.1680/geot.10.P.112

Amini M, Ardestani A, Khosravi MH (2017) Stability analysis of slide-toe-toppling failure. Eng Geol 228:82–96. https://doi.org/https://doi.org/10.1016/j.enggeo.2017.07.008

Amini M, Sarfaraz H, Esmaeili K (2018) Stability analysis of slopes with a potential of slide-head-toppling failure. International Journal of Rock Mechanics and Mining Sciences 112:108–121. https://doi.org/https://doi.org/10.1016/j.ijrmms.2018.09.008

Ding B, Pérez-Rey I, González-Fernández MA, et al (2025) Optimizing shape design in drystone retaining walls: A multi-scope approach focusing on failure mechanisms. Constr Build Mater 489:142116. https://doi.org/https://doi.org/10.1016/j.conbuildmat.2025.142116

Goodman RE, Bray JW (1976) toppling of rock slopes. In: Proceedings of the Specialty Conference on Rock Engineering for Foundation and Slopes ASCE Boulder. Colorado

Gui JY, González-Fernández MA, Estévez-Ventosa X, et al (2023) Toppling susceptibility of a single rock block resting on a regularly rough base. Eng Geol 83:153. https://doi.org/10.1016/j.enggeo.2022.106982

Itasca Consulting Group (2024) UDEC. Universal distinct element code. Itasca, Minneapolis, USA.

Mao Y, Azarafza M, Bonab MH, et al (2025) Innovative stability analysis of complex secondary toppling failures in rock slopes using the block theory. Landslides 22:2037-2054. https://doi.org/10.1007/s10346-025-02464-4

Mohtarami E, Jafari A, Amini M (2014) Stability analysis of slopes against combined circular-toppling failure. International Journal of Rock Mechanics and Mining Sciences 67:43–56. https://doi.org/10.1016/j.ijrmms.2013.12.020

Pérez-Rey I, Muñiz-Menéndez M, González J, et al (2021) Laboratory physical modelling of block toppling instability by means of tilt tests. Eng Geol 282:105994. https://doi.org/10.1016/j.enggeo.2021.105994

Sarfaraz H (2020) A simple theoretical approach for analysis of slide-toe-toppling failure. J Cent South Univ 27:2745–2753. https://doi.org/10.1007/s11771-020-4495-7

Wei T, Chen GQ, Zhu Z, et al (2024) Slope instability mechanism with differential rock mass structure along a fault: a mine landslide from Southwest China. Geomechanics and Geophysics for Geo-Energy and Geo-Resources 10:76. https://doi.org/10.1007/s40948-024-00795-5

Wyllie DC, Mah CW (2004) Rock slope engineering: fourth edition. CRC Press, London

Novel approaches for the evaluation of the roughness of discontinuities and failure surfaces in landslides and rock slopes

O. Chang
XRGeo Technology Inc, Burnaby, Canada
omar.chang@xrgeo.com

D. Stead
Simon Fraser University, Burnaby, Canada

D. Donati
Alma Mater Studiorum – University of Bologna, Bologna, Italy

Abstract

The evaluation of surface roughness has several important applications in the field of engineering geology. Discontinuities, such as joints and faults, control the stability of potentially unstable rock mass volumes at various scales. At the outcrop- and bench-scale, surface asperities contribute to the shear strength of discontinuities, angle of friction and apparent cohesion defining the stability of discontinuity-bounded blocks. At the slope scale, the roughness waviness of basal and lateral release surfaces has a significant impact on both the overall stability and the kinematics of rockslides. On the surface of large landslides, spatial variations in morphological roughness represent subsurface changes in orientation of the basal surface.

The importance of geological surface roughness has long been recognized; however, the methods routinely used for its evaluation still employ fixed orientation, and two-dimensional approaches. Field-based assessments are not fully exploiting high-resolution three-dimensional datasets collected through remote sensing methods. In this work, we demonstrate the application of a suite of innovative digital tools developed to allow the characterization of surface roughness across different spatial scales, using datasets from both internationally renowned landslides and typical rock slopes. The proposed algorithms provide a detailed roughness analysis of discontinuity and topographic surfaces that can be applied both at the outcrop scale and the landslide scale. As numerical modelling and 3D remote sensing become standard in engineering geology, high-resolution characterization of surface roughness at multiple spatial scales will become increasingly important. This work lays the foundation for the enhanced fidelity of complex numerical modelling and improved methodologies for risk assessment and slope stability analysis.

Keywords

Surface roughness, Landslide, Rockfall, Digital reconstruction, Remote sensing.

1 Introduction

In the field of engineering geology, surface roughness represents a key consideration in assessing the stability and evolution of rock slopes at various scales. At the centimetre-scale discontinuities (e.g., single joints), surface roughness controls the shear strength and resistance to sliding of blocks and rock mass volumes and can be quantified using the joint roughness coefficient (JRC). Surface roughness along a rupture surface can spatially vary based on discontinuity set characteristics as well as presence of failed rock bridges (Elmo, 2023). In the field, it can be estimated using profilometers and alloy disks of varied sizes (ISRM, 1978). At larger, meter- or multimeter-scale, overall waviness of the surface can control both shear resistance and landslide kinematics. Landslides moving along bi- or multi-planar sliding surfaces require internal deformation and damage to occur before the unstable volumes are displaced. The resulting damage surface reflects the internal deformation of the landslide body, which in turn is controlled by basal surface morphology and displacement direction (Donati et al., 2021). The introduction of remote sensing methods, such as photogrammetry and laser scanning, for the digital 3D reconstruction of surfaces has enabled more accurate assessment of surface roughness (Tatone and Grasselli, 2013; Zou et al., 2023; Chang et al. 2024). However, methods routinely used for its evaluation still employ statically anchored reference values and restricted two-dimensional resolution approaches. This paper aims at bridging this gap, demonstrating the use of a suite of innovative digital tools that allow surface roughness to be qualitatively and quantitatively measured across different spatial scales, orientations, and conditions, from rockfall scars to the ground surface of major landslides. The tool is tested at two sites in British Columbia (Canada), namely the Stawamus Chief and the Downie Slide.

2 Background information

With the rapid advancement of remote sensing technology, the ability to create digital twins from large scale to small scale applications have become increasingly available (Chang et al, 2024). This rapid advancement has resulted in an influx of high resolution and multi-sensor datasets that are currently being underutilized. For geological analyses aimed at assessing surface roughness, geoscientists can rely on a number of dataset types that can be classified based on the spatial dimension. Two-dimensional datasets (2D) are profiles or imagery which only contain two axes (e.g., photographs or profiles). Two and half dimensional datasets (2.5D) are 2D representations that carries a single value per cell or point (e.g., contours, DEM). Three-dimensional datasets (3D) provide perspective and relativity, allowing observations along different orientations and visualization of complex geometries. The visualization of these datasets in a digital space provides the user the ability to switch between different dimensional domains and datasets. This dimensional fluidity has improved user's capability to visualize complex structures and datasets and allowed the derivation of simplified 2D and 2.5Ddatasets that can be used for quantitative measurements, pattern recognition, and spatial reasoning that remains challenging using fully 3D datasets, inherently characterized by greater complexity. However, the simplification of geospatial data also leads to constraints. Many techniques and methods, such as JRC, were developed for field or laboratory use. The simplification or roughness through the derivation of 2D measurements was due to practical necessity, as acquiring multi-orientation data was largely unfeasible, due to limited surface accessibility and time constraint, resulting in errors due to inhomogeneity caused by orientation and scale (Barton and Choubey, 1977).

Over the past two decades, there have been significant improvements in 3D data collection and numerical capabilities, yet, data collection and interpretation procedures have remained largely unchanged, with standard field protocols being applied to higher resolution, digital datasets. As a result, digital and virtual mapping and numerical modelling procedures are also affected by the same pitfalls and restrictions of field methods, preventing the full exploitation of sophisticated 3D datasets. The growing capability to acquire rich 3D datasets therefore demands a fundamental shift in standardization: rather than adapting 3D data to fit legacy 2D workflows, new robust and systematic standards should be built around 3D representation.

3 Methodology

This study aims at i. demonstrating digital tools used to investigate the role and impact of roughness orientation and scale in geomechanical interpretation and ii. preliminarily testing such tools at two

unstable rockslopes located in British Columbia, Canada, namely the Stawamus Chief and the Downie Slide.

By defining surface profiles through software developed in-house, reference dependency is highlighted. The impacts of location and orientation of the roughness profiles are outlined and discussed by comparing differently oriented profiles from the same location and surface The manner in which the profiles are depicted mirrors the conditions under which standards such as JRC are typically applied, i.e. where orientation is commonly evaluated either down dip or arbitrarily picked, rather than systematically analysed and optimized for the study site. A new procedure is proposed that helps in eliminating orientation bias in profile determination by systematically investigating roughness indifferent directions at each location and allowing roughness orientation sensitivity analysis to be undertaken. The proposed technique can represent the basis for the creation of roughness directionality maps, that can be used to highlight how roughness and asperities vary spatially and directionally across surfaces at various scales.

3.1 Case study 1: The Stawamus Chief

Stawamus Chief, often colloquially referred to as "The Chief" is a granitic monolith located immediately east of the town of Squamish, 30 km north of Vancouver (BC, Canada).The monolith is constituted by a competent, high quality, massive rock mass, with ubiquitous surface-parallel sheeting and exfoliation joints (Coughlan, 2024).The slopes of the Stawamus Chief have been affected, over the last decade, by several rockfall events. In 2021, the most significant recorded rockfall occurred along the "Grand Wall", in the southern sector of the monolith, and involved a volume of 3000 to 3500 m^3 (Ashwood and Manicke, 2021). The Grand Wall is characterized by a prominent, arc-shaped overhang that represents one of the most active rockfall sources of the rock slope. 3D laser scanning data was collected before and after the rockfall allowing a detailed study of the Grand Wall (Chang et al., 2024).

3.2 Case study 2: Downie Slide

The Downie Slide is a 1 billion m^3, slowly moving rockslide located on the western slope of the Revelstoke Reservoir (Columbia River valley, BC, Canada), about 70 km north of Revelstoke dam. The instability extends 3.3 km across and 2.4 km along the slope, between elevation 507 m a.s.l. and 1520 m a.s.l., and has a maximum thickness of 250 m (Kalenchuk et al. 2013). The landslide affects the metamorphic succession of the Monashee Complex, consisting of schist, gneiss, quartzite, and marble of Proterozoic to Lower Paleozoic (Read and Brown, 1981).The landslide surface gently slopes towards the east with an average slope angle of 18°, increasing to 40° in the lower part, near the shore of the Revelstoke Reservoir. The ground surfaceis characterized by lineaments and fractures that are controlled by rock mass discontinuities, displacement trends, and basal surface morphology (Donati et al., 2021) and in turn control morphological roughness (Westin, 2015). Based on the geomorphic characteristics of the landslide ground surface, various domain subdivisions have been proposed for the landslide. In the present study, we consider the subdivision proposed in Donati et al. (2021), in which domains are defined based on intensity and orientation of surface slope damage features.

4 Results

4.1 Case study 1: The Stawamus Chief

Two perpendicular series of 2-m spaced, parallel profiles were traced along a photogrammetric 3D model of the Grand Wall (Fig. 1a), with the objective of detecting topology differences, morphological features and anomalies (Fig. 1). The spacing of the traces and the normal angle between profile sets were arbitrarily defined. Profiles were obtained to the left (PL) and right (PR) of the anchor profile (P-0) and then stacked to visualize topological variations across profiles (Fig. 1c,e). Topological variance was evident based on location and orientation. Variation is indicative of rock mass structures, failure surfaces, changes in rugosity, rock bridges, and inhomogeneity.

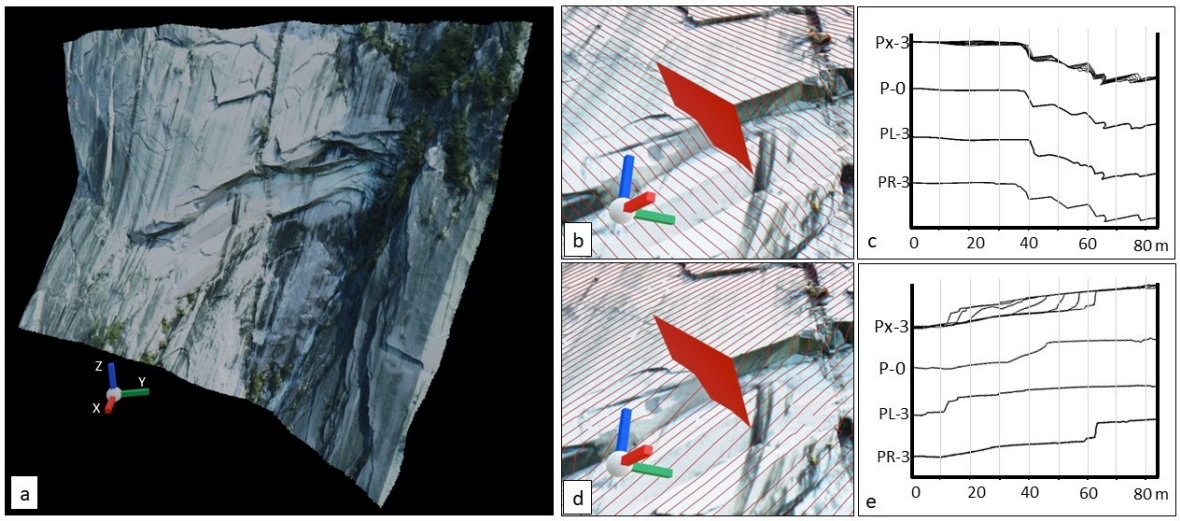


Fig. 1 Profile analysis for the Grand Wall of the Stawamus Chief. (a) Photogrammetric 3D model, with traces of profiles parallel to the reference plane (20 m x 20 m, red plane).Spacing between profile traces is 2m. Traces are constructed (b,c) parallel or (d,e) perpendicular to the reference plane. Derived traces are then stacked (Px -X) where "X" determines the number of stacks in respect to the left (PL) and right (PR) of the reference plane (P-0).Each trace is also examined individually (e.g., PR-3 = Three profiles to the right of P0).

Characterizing orientation dependency and inhomogeneity of the rock mass along the entire surface of the outcrop may not easily allow the identification of spatial variation in surface roughness. A radial sampling approach (referred to as "coral" analysis), in which the mesh is evaluated across a wide range of orientations, is therefore proposed to investigate three-dimensional roughness variability in various parts of the model, at the same time minimizing the orientation bias (Fig. 2). In this sense, choosing appropriate interval angles ensures that no orientation is overlooked, providing a complete geometric envelope for subsequent analysis (Chang et al., 2026).

The radial roughness approach can provide a quantitative depiction of the slope surface roughness in different orientations and locations. A visual analysis of the Grand Wall of the Stawamus Chief shows topological variations controlled by the ubiquitous presence of sheeting and exfoliation joints. Variations in the selected length of the radial profiles can also affect the results, emphasizing the importance of scale on roughness quantification.

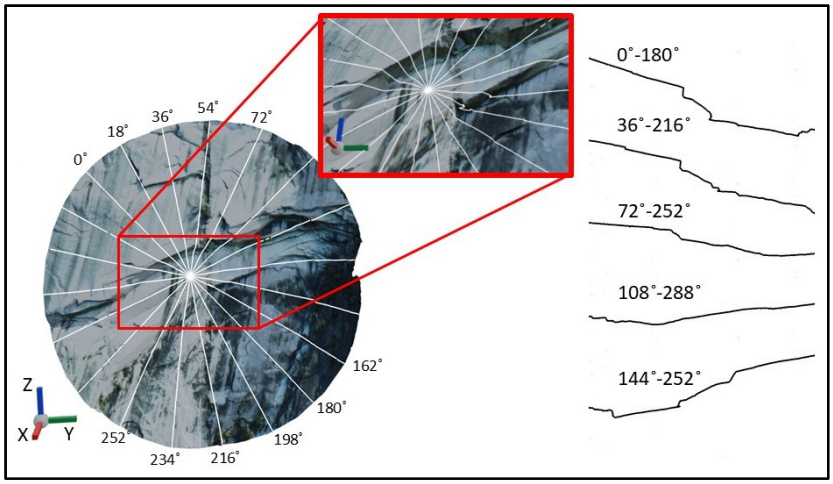


Fig. 2 Overview of the Stawamus Chief analysis, showing a portion of the 3D mesh investigated using a coral approach, and a set of profiles determined in a radial manner to remove orientation bias.

4.2 Case study 2: Downie Slide

The slope damage domains outlined in Donati et al. (2021) are characterized by the presence of morphological features, such as tensile fractures, depressions, scarps, and hummocky regions, the spatial distribution and orientation of which is controlled by the morphology of the basal surface and, in turn, the displacement orientation (Fig. 3). To qualitatively assess the changes in landslide surface roughness and its directionality, a radial set of profiles was traced within each of the identified slope damage domains.

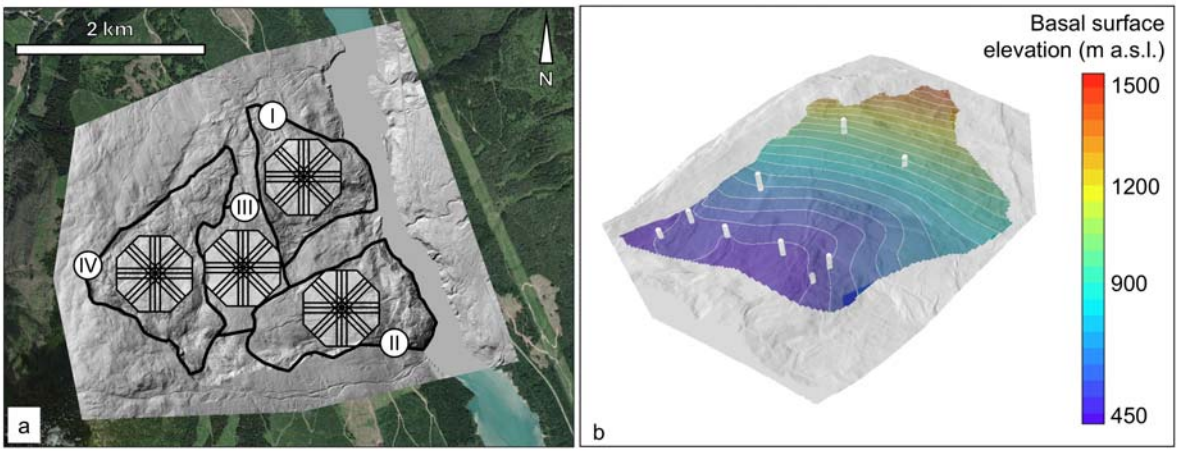


Fig. 3 Downie slide. (a) Hillshade map of the Downie Slide area. The slope damage domains described in Donati et al. (2021) are outlined in black and identified with roman numerals (cfr. fig. 6). Corals used for analyzing each domain are overlaid on the map. (b) 3D view of the basal surface of the Downie Slide, which has been recognized to control the distribution and orientation of surface damage features. The white lines show the depth at which the basal surface was identified within in-hole inclinometers.

For the radial profiles, a length of 400 m was selected, corresponding to the dimension that could fit all domains, to enhance comparison between the different profiles. Four orientations were investigated, with 45° angular offset. For each direction, three parallel profiles, spaced 55m apart, were traced. Therefore, a total of 12 profiles is obtained for each domain. The lowermost part of the basal surface of the Downie Slide is characterized by significant changes in orientation, which control the occurrence of N-S tensile cracking in the central part of the "North knob" (Domain I in Fig. 4), and E-W oriented lineaments and scarps in the "South knob" (Domain II in Fig. 4). The profiles show a marked directionality, with relatively rougher profiles in the N-S (0°-180°) and E-W (90°-270°) directions, respectively. The "Central domain" (domain III in Fig. 4) is characterized by a relatively smooth surface, due to the presence of a locally planar basal surface that allow displacement without little internal deformation and surface damage. Profiles for all directions display such smooth morphology, except for a limited area at the northernmost limit of the domain. The "Upper hummocky region" (domain IV in Fig. 4) progressively formed through block accumulation following landslide head scarp retrogression. Due to its blocky nature, the domain is characterized by the absence of significant directionality in morphological roughness.

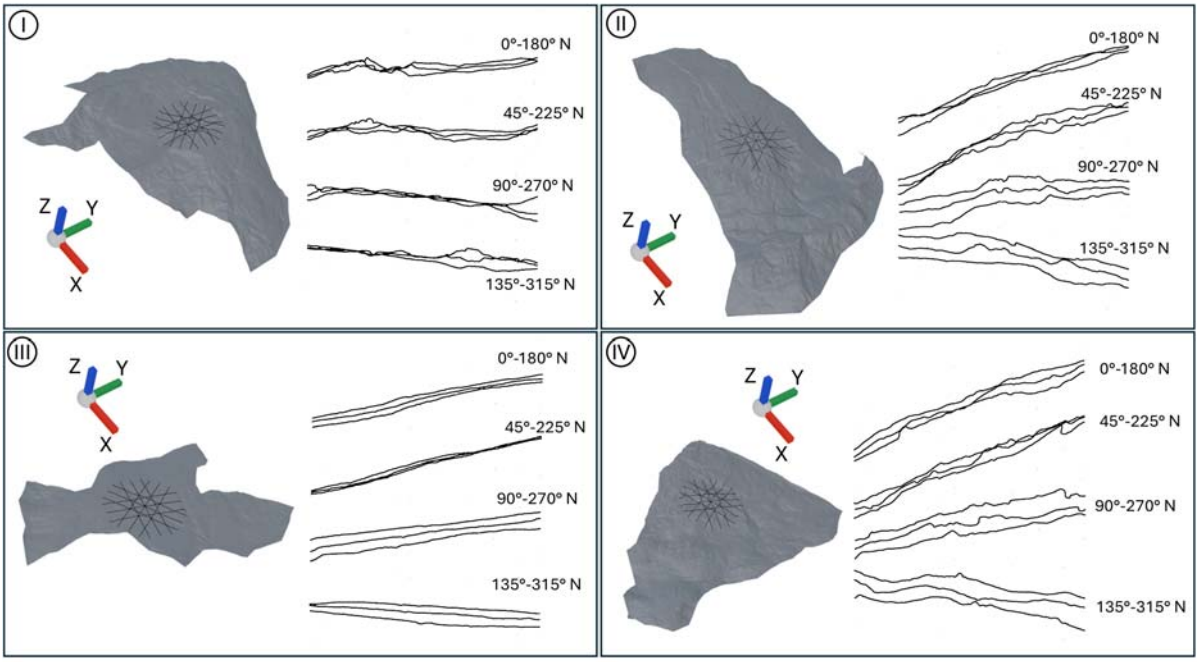


Fig. 4 Overview of the radial profiles traced across the slope damage domains at the Downie Slide. For each domain, a 3D view of the radial profile and the stacked sets of profiled for each direction is shown. The horizontal length of all profile is 400 m. Note the smoothness of profiles in the 90°-270° direction in domain I and in the 0°-180° direction in domain II. See text for additional preliminary interpretation and Figure 3 for the location of domains and radial profiles (corals).

5 Outlook and future development

In this paper, new tools, currently under development, for assessing the spatial variability of surface roughness at various scales were introduced. With more data input and refinement, these tools presented have the potential to significantly reduce orientation bias that has long been embedded in conventional engineering geological practice by relying on a single orientation. The implication of this shift extends across scale and application. Future development will focus on expanding validation datasets, incorporating a broader range of failure mechanisms, geological settings, and data acquisition methods. This represents a standardized orientation sensitivity analysis that is applicable at all scales. Moreover, the use of radial profiles across large surfaces can allow the creation of directional roughness maps that can assist geoscientists and engineers in the identification of geomorphological domains across landslide surfaces and rock slopes.

References

Ashwood, W, Manicke, H (2021) Preliminary Rock Fall Assessment, The Black Dyke - Grand Wall, Stawamus Chief, Squamish, B.C.021-134. Westrek GeotechnicalServices Ltd.

Chang, O, Stead, D, Elmo, D, William-Jones, G (2024) Application of mixed and virtual reality in deep mining, Deep Mining 2024: Proceedings of the 10th International Conference on Deep and High Stress Mining, Australian Centre for Geomechanics, Perth, pp. 867-878, https://doi.org/10.36487/ACG_repo/2465_54

Chang, O, Stead, D, Donati, D (2026). New approaches to the characterisation of discontinuity roughness and landslide failure surfaces.Geohazard9, Edmonton (AB, Canada), 1-3 June 2026 (in press).

Coughlan, BT (2024) Rockfall hazard assessment of the Stawamus Chief using multi-temporal remote sensing analysis. MSc Thesis, Simon Fraser University.

Donati, D, Westin, AM, Stead, D, Clague, JJ, Stewart, TW, Lawrence, MS, Marsh, J (2021) A reinterpretation of the Downie Slide (British Columbia,Canada) based on slope damage characterizationand subsurface data interpretation. Landslides 18:1561–1583. DOI: 10.1007/s10346-020-01601-5

Elmo, 2023. The Bologna Interpretation of Rock Bridges. Geosciences13(2), 33. https://doi.org/10.3390/geosciences13020033

Fofonoff, S, Schlotfeldt, P, Wyllie, D (2015) Preliminary Geotechnical Review,Angels Crest Rock Fall, Stawamus Chief, Squamish, BC. GeoPacific ConsultantsLtd.

ISRM (1978). Suggested methods for the quantitative description of discontinuities in rock masses. International Journal of Rock Mechanics and Mining Sciences & Geomechanics Abstracts 15 (6), 319–368

Kalenchuk KS, Hutchinson DJ, Diederichs MS (2013) Geomechanical interpretation of theDownie Slide considering field data and three-dimensional numerical modelling.Landslides 10:737–756.

Monger,JWH, McNicoll VJ(1993) New U-Pb dates from southwestern coast belt, British Columbia: radiogenic age and isotopic studies: report 7, Geological Survey of Canada Paper 93-2, pp. 119-129.

Piteau DR, Mylrea FH, Blown IG (1978) Downie Slide, Columbia River, British Columbia, Canada. In: Voight B (ed) Rockslides and avalanches, volume 1. Developments in Geotechnical Engineering 14(A):365–392

Read PB, Brown RL (1981) Columbia River fault zone: southeastern margin of the Shuswap and Monashee complexes, southern British Columbia. Canadian Journal of Earth Science 18:1127–1145.https://doi.org/10.1139/e81-108

Tatone, B, and Grasselli, G (2013) An investigation of discontinuity roughness scale dependency using high-resolution surface measurements. Rock Mechanics and Rock Engineering 46, 657–681. https://doi.org/10.1007/s00603-012-0294-2

Zou, C, Li, J, Wu, Y,Yatao, Y, Li, J (2023)2D and 3D evaluation of joint roughness exposed by rock cores. Bulletin of Engineering Geology and the Environment 82, 316. https://doi.org/10.1007/s10064-023-03325-x

Cyclic thermal treatment of a sandstone from the Upper Rhine Graben

K. M. Neumann, M. Duda & T. Backers
Ruhr University Bochum, Bochum, Germany
Katharina.Neumann-j23@ruhr-uni-bochum.de

Abstract

The share of renewable energy in overall electric energy production is continuously increasing. Renewable energy provision is in parts subject to seasonal and daily fluctuations (solar and wind). In 2025, electricity generation in Germany exceeded consumption on 80+ days. Energy storage concepts are required to minimise this energy loss. Thermal energy storage systems are a key element of an effective storage strategy accelerating the energy transition. Subsurface storage systems in rock mass are particularly interesting because of their abundant availability, and the suitable thermophysical properties of the material.
Changes of the mechanical, thermal, and hydraulic properties upon repeated heating and cooling were investigated to evaluate the impact of the maximum temperature and number of loading cycles on the thermal energy storage medium. A sandstone from the Upper Rhine Graben was selected and heated to maximum temperatures of 200 °C to 600 °C. One cycle comprised heating the specimen to the target temperature in a muffle furnace with a rate of ~ 10 to 11.5 °C/min and cooling to 100 °C with an average rate of ~ 0.5 to 1 °C/min. Further specimens were heated between 100 °C and 200 °C for up to 49 cycles. Before and after thermal treatment density, porosity, P-wave velocity, thermal conductivity, permeability, uniaxial compressive strength and triaxial compressive strength were determined.
Repeated heating to 200 °C in 49 cycles did not cause substantial changes in most rock properties; only the P-wave velocity showed a significant decrease in comparison to one cycle and the reference sample before heating. With increasing maximum temperature, density and P-wave velocity decreased, and effective porosity increased. The most drastic differences were determined for the specimen heated to 600 °C, which can presumably be traced back to the α- to β-quartz transition.

Keywords

Thermal energy storage, Sandstone, Cyclic thermal treatment, Experimental investigation.

1 Introduction

The share of renewable energies in the gross electricity generation of Germany was around 59 % in 2025 (Bundesnetzagentur 2025). The target for 2030 is 80% (Sec. 1 (2) Renewable Energy Act - *Erneuerbare-Energien-Gesetz* 2023). Because of the inherent fluctuations of renewable energy availability, e.g., associated with wind and solar, energy production can exceed energy consumption. In 2025, energy overproduction occurred on 84 days in Germany, corresponding to a total of around 6 Mio. MWh (Bundesnetzagentur 2025). To minimise energy loss, integrating energy storage in power grid planning is a central element. Besides pumped storage plants, thermal energy storage is one of the

most common forms to store energy (Tawalbeh et al. 2023). Subsurface storage in rock mass is particularly interesting, because of its abundance and the suitable thermophysical properties of rock (Tiskatine et al. 2016), as well as its limited above-ground space requirements (Fry et al. 2024). Khatod et al. (2022) conclude that sandstone is an excellent thermal energy storage material because of thehigh specific heat capacity and porosity. However, to evaluate a long-term use of thermal storage systems in siliciclastic rock masses, potential changes in geomechanical and thermal properties of sandstone upon repeated heating and cooling must be evaluated.

Previous studies on various sandstones documented that density, P-wave velocity (Fig. 1a), thermal conductivity and diffusivity decreased with increasing temperature (Hao et al. 2022; Li and Liu 2022; Yang et al. 2017; Sun et al. 2016) and number of cycles (Hou et al. 2020; Zhao et al. 2022). Similarly, Young's modulus and uniaxial compressive strength (UCS) decreased with increasing temperature (Li and Liu 2022; Hou et al. 2020; Fig. 1c and d). Porosity (Hao et al. 2022; Jing et al. 2021; Fig. 1b), permeability (Liu et al. 2020; Yang et al. 2017), and specific heat capacity (Tiskatine et al. 2016) increased with increasing temperature. In contrast to UCS, the triaxial compressive strength in some cases increased with increasing temperature (100 °C to 800 °C, Yang et al. 2017; 25 °C to 950 °C, Li et al. 2022).There are exceptions reported for temperatures up to 200 °C (Li et al. 2022), 300 °C (Hao et al. 2022), or 400 °C (Wang et al. 2023; Vidana and Gratchev 2021; Zhao et al. 2022) where P-wave velocity, Young's modulus and UCS increased slightly or did not change with increasing temperature before ultimately decreasing when the temperature exceeded a particular threshold. For similar temperatures porosity did not change or decreased before increasing at higher temperatures (Hao et al. 2022; Fig. 1b).

UCS and Young's modulus gradually decrease with increasing number of thermal cycles (Vidana and Gratchev 2021; Zhao et al. 2022). A higher number of thermal cycles leads to (slightly) higher porosities according to Becattini et al. (2017) and Vidana and Gratchev (2021). The results from Jing et al. (2021) for temperatures up to 600 °C do not indicate a systematic influence of the number of thermal cycles (1 to 5 cycles) on porosity. Thermal cycles have a significant effect on the rock properties (Vidana and Gratchev 2021) and the influence of the number of cycles on the mechanical properties increases with increasing temperature (Hou et al. 2020).

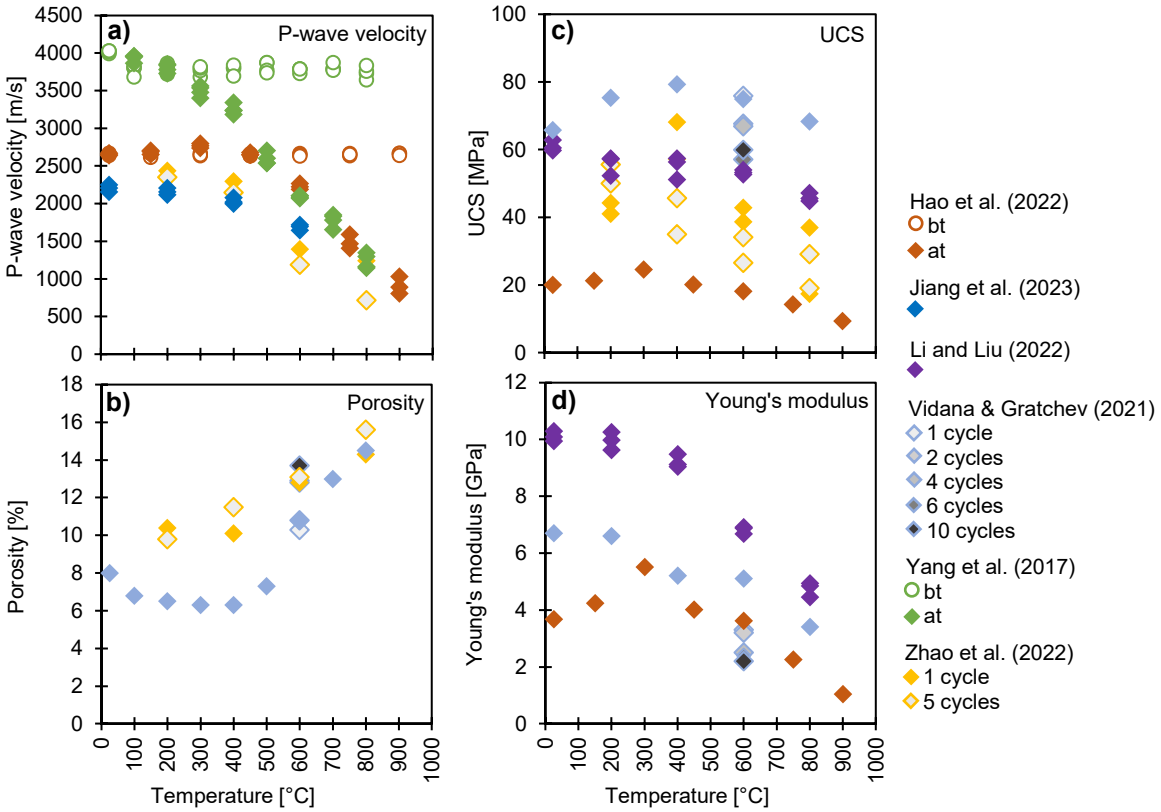


Fig. 1 Comparison of P-wave velocity, UCS, Young's modulus, and porosity after heating sandstone to varying temperatures (and thermal cycles). Sandstone sampling location (mineral composition): Hao et al. (2022) - not specified (21 % qtz., 30 % fsp., 20 % cly., 3 % clc., 16 % o.) , Jiang et al. (2023) - Zigong, China (34 % qtz., 28 % fsp., 28 % cly., 6 % clc., 5 % o.), Li and Liu (2022) - Jiulongpo, China (40 % qtz., 31 % fsp., 14 % cly., 15 % o.), Vidana and Gratchev (2021) - Jimboomba, Australia (39 % qtz., 36 % fsp., 7 % cly., 5 % o.), Yang et al. (2017) - Rizhao, China (mineral composition not specified), Zhao et al. (2022) - Jiangsu, China (qtz., fsp., cly.); Abbreviations: bt - before thermal treatment, at - after thermal treatment, qtz. - quartz, fsp. - feldspar, cly. - clay minerals, clc. - calcite, o. – others.

Due to the high geothermal gradient in the region and the suitable depth and rock properties of the formation, the Buntsandstein (Lower Triassic) in the Upper Rhine Graben (URG) represents a geothermal reservoir of particular interest, which is likely to be increasingly exploited in the future. In this context, potential co-use as thermal energy storage is being examined as part of this study.

2 Material and methods

2.1 Material

A sandstone from a quarry in Neustadt an der Weinstraße, which is located at the western border of the URG between Mannheim and Karlsruhe (Germany), was selected. The rock variety belongs to the Buntsandstein formation (Lower Triassic), has a light beige colour, and contains varying amounts of conglomerates and pores (pore diameters up to ~ 10 mm). The mineralogical composition, determined by X-ray powder diffraction analysis, identified quartz (88 %) and k-feldspar (12 %) as main components, with traces of illite/muscovite and kaolinite (Table 1).

2.2 Methods

Cylindrical cores with a diameter of 42 mm were diamond-drilledperpendicular to beddingand sawed to a length of 84 mm or 21 mm (tensile strength) using water as cooling fluid. The endfaces of the longer cores were ground square to ensure parallelism within 0.02 mm for mechanical testing.Properties of specimens were characterised before and after thermal treatment.

One set of specimens was placed in a muffle furnace and heated to a maximum temperature of 200, 250, 300, 350, 400, 450, 500, 550, or 600 °C with a rate of ~ 10 to 11.5 °C/min, after which the temperature was held for one hour. The specimens were then cooled to 100 °C at an average rate of ~ 0.5 to 1 °C/min, and temperature was again maintained for one hour.

A further set of specimens was heated to an initial temperature of 150 °C (typical in-situ temperature of the Buntsandstein in the URG) with a rate of around 4 to 5 °C/min, which was held for one hour. The specimens were then heated with ~ 2.5 °C/min to a maximum temperature of 200 °C. After holding this temperature for one hour, the specimens were cooled to 100 °C with a rate of ~ 0.5 °C/min, which was again maintained for one hour. For specimens subjected to repeated thermal cycles, the temperature was again raised to 200 °C with about 7 °C/min. Thermal cycles from 100 °C to 200 °C were then repeated up to 49 times. To account for specimen variability, three specimens were tested for each maximum temperature or number of cycles.

Bulk density of oven-dried rock specimens was derived from the ratio of mass and volume. Grain density was determined by milling a representative sample of the sandstone to powder, which was then analysed by pycnometry using distilled water (DIN EN ISO 17892-3).Total porosity of specimens was calculated from the ratio of their bulk density to grain density, and effective porosity was determined from water uptake. P-wave velocity was determined with a standard measurement device (Geotron Elektronik) with two identical P-wave ultrasound sensors in axial and two radial directions with a signal frequency of about 350 kHz emitted from the waveform generator. No coupling medium was used between the sensors and the specimen.

Thermal conductivity and effusivity were determined with a Modified Transient Plane Source (MTPS) sensor using C-Therm's Trident system on cylindrical samples (Harris et al. 2014). A short current pulse is applied to the sensor's spiral heating element, which causes a temperature increase by 1 to 3 °C as the heat diffuses into the specimen in one-dimensional heat flow (ASTM D7984-16). A thermal joint compound (type 120 silicone from Wakefield Thermal) was used as a coupling agent and a 500 g weight was placed on top of the specimens to standardise coupling. Heat capacity was derived from thermal conductivity, effusivity and bulk density of the specimens. Thermal diffusivity was calculated from thermal conductivity, heat capacity and bulk density of the specimens.

UCS, tensile strength (TS) and triaxial compressive strength (TCS) were determined using a stiff 4000 kN loading frame. For UCS, specimens were centered between loading plates and axially loaded ata strain rate of about 10^{-5} s^{-1}. Axial stresses and strains were calculated based on the cross-sectional area and sample length of the specimen before testing. Axial strains were calibrated for system stiffness. UCS was derived from the maximum in the stress-strain-relation. Young's modulus was determined between 40 % and 60 % of UCS. For TS, specimen discs were placed in a steel loading jaw and loaded at a rate of 2.5 µm/s until failure (ISRM 1978). Multi-stage triaxial compressive strength tests were performed using a Hoek cell at confining pressures of 20 MPa, 15 MPa, and 10 MPa. For each pressure stage, the maximum axial stress at failure was determined (ISRM 1978).

3 Results

3.1 Temperature

Specimens that were heated to a maximum temperature of ≥300 °C developed a reddish colour. Yet, mineralogy did not change systematically considering uncertainties of ± 2-5 % (Table 1) and specimen variability. Density decreased by up to 0.8 % with increasing maximum temperature (Fig. 2a), while effective porosity increased by about 4 % (Fig. 2b) compared to before thermal treatment. A significant change in density was observed for specimens heated to ≥350 °C. Effective porosity increased significantly for maximum temperatures of ≥450 °C. P-wave velocities show the most significant change from the untreated state. With increasing maximum temperature, axial and radial P-wave velocities decreased with a maximum decrease of around 45 % for 600 °C (Fig. 2c and d). These results could be reproduced for specimens drilled parallel to bedding. For UCS no systematic relation to maximum temperature can be observed (Fig. 2e), results mainly vary within the range of specimen variability. Young's modulus shows a slightly decreasing trend with increasing temperature (Fig. 2f).

Table 1. XRD-analysis results in volume-% (converting mass-% to volume-% may result in deviations from 100% in the sum of the rounded values), uncertainty +/- 2-5 %, bt - before thermal treatment.

mineral	**bt**	**200 °C 49 cycles**	**300 °C 1 cycle**	**400 °C 1 cycle**	**500 °C 1 cycle**	**600 °C 1 cycle**
quartz	88	87	86	85	85	89
orthoclase	12	11	11	12	13	10
illite/muscovite	traces	2	2	2	2	2
kaolinite	traces		1	1	traces	0

3.2 Cycles

Heating the sandstone specimens to 1 or 49 cycles did not significantly affect colour or mineralogical composition (Table 1), density, porosity, thermal conductivity, Young's modulus, or TS. UCS and TCS also did not show systematic changes when comparing heated to untreated specimens (

Fig. 3a). P-wave velocity, however, decreased significantly

Fig. 3b). A thin section of a heated specimen showed some presumably thermally induced cracks after heating to 200 °C in 49 cycles. Compared to the thin section of an untreated specimen, the number of cracks appears to increase with thermal treatment. A quantitative analysis is pending for future investigations.

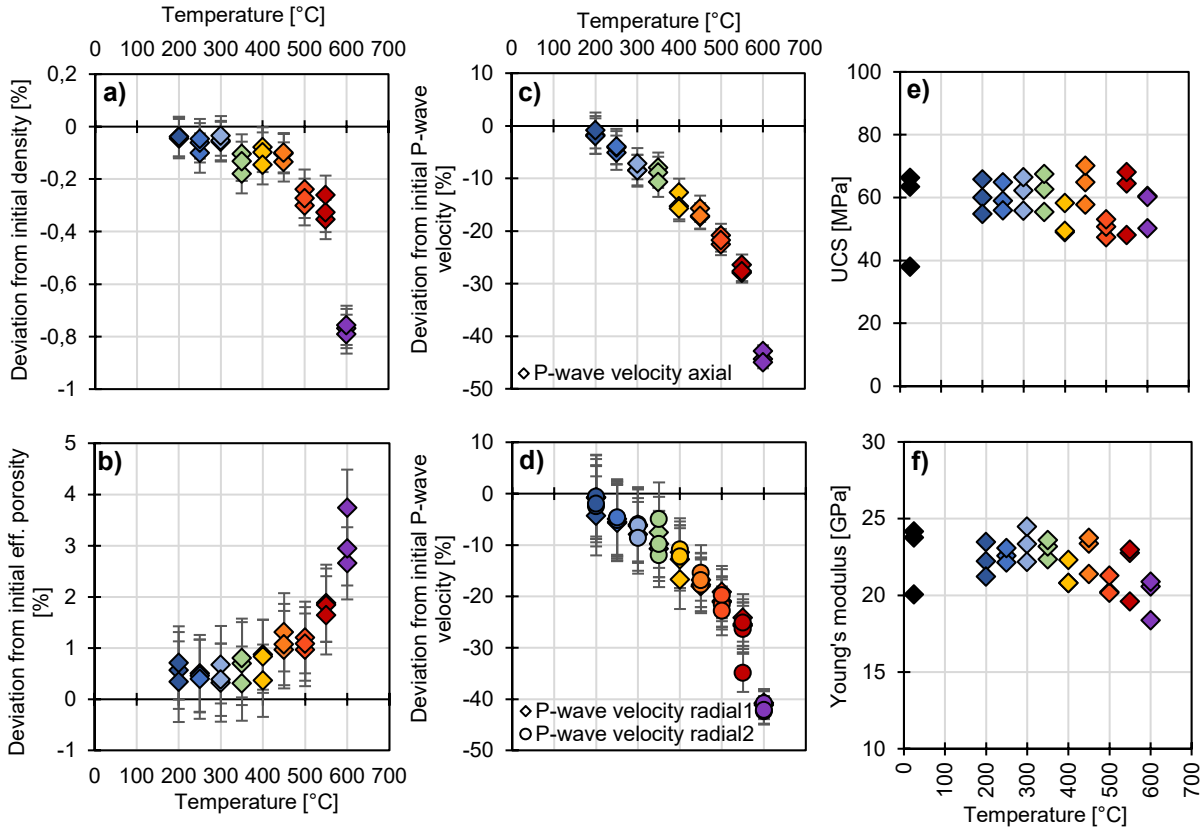


Fig. 2 Results for specimen heated up to 600 °C for 1 thermal cycle, percentage deviation of the results after heating the samples compared to before heating; eff. porosity - effective porosity, P-wave velocity axial/radial - measured in axial/radial direction of the specimen; colours to differentiate temperatures.

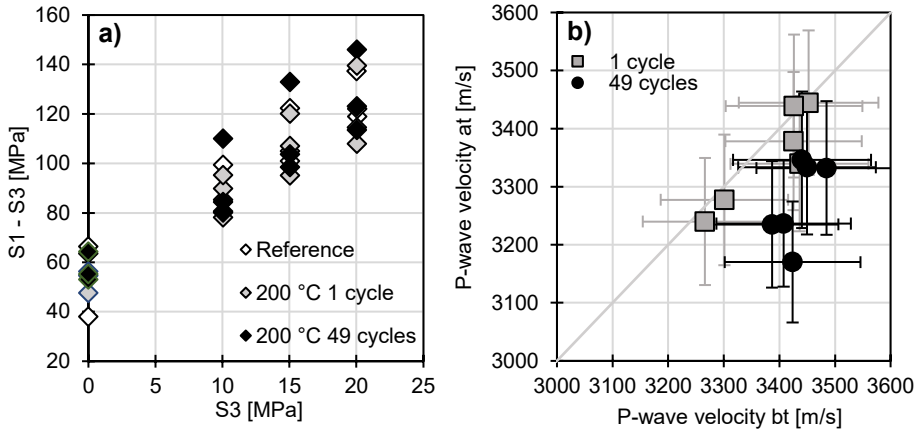


Fig. 3 a) Results from UCS and triaxial compressive strength tests for untreated samples (white), samples heated to max. 200 °C for 1 cycle (grey), and 49 cycles (black), b) P-wave velocity measured in axial direction before thermal treatment (bt, x-axis) and after thermal treatment (at, y-axis) for samples heated to max. 200 °C for 1 cycle (grey) and 49 cycles (black).

4 Discussion

The change of colour, density, porosity, and P-wave velocity of heated specimens compared to their untreated references are consistent with observations reported in other studies (e.g., Hao et al. 2022; Jing et al. 2021; Li and Liu 2022; Vidana and Gratchev 2021; Yang et al. 2017; Zhao et al. 2022). A pronounced increase in porosity after heating sandstone to a maximum of 400 °C can also be found in several other studies (Hao et al. 2022; Jing et al. 2021; Li and Liu 2022; Liu et al. 2020; Vidana and Gratchev 2021; Sun et al. 2016; Zhao et al. 2022). The observed decrease in P-wave velocity with increasing number of cycles was previously reported by Hou et al. (2020), and Zhao et al. (2022). Thermal expansion of the minerals and associated formation of microcracks may explain this observation; thin section analysis supports this interpretation. XRD analyses show no changes beyond analytical uncertainties for heated samples compared to untreated samples (Table 1), but the colour change suggests thermal alterations. Young's modulus shows a decreasing trend comparable to the results of Hao et al. (2022), with a peak at 300 °C (c.f. Fig. 1d &Fig. 2f), which is consistent with the

decreasing P-wave velocity, as a lower P-wave velocity corresponds to a lower Young's modulus. However, contrary to e.g. Li and Liu (2022), Hao et al. (2022) or Hou et al. (2020), the changes in Young's modulus are minor and not related to UCS considering specimen variability. Increasing the number of cycles from 1 to 49 at 200 °C did not result in changes in UCS, Young's modulus (as in Vidana and Gratchev 2021, or Zhao et al. 2022), or triaxial compressive strength, but in P-wave velocity (consistent with Hou et al. 2020, and Zhao et al. 2022; c.f.

Fig. 3b).

5 Conclusion

Repeated heating and cooling of sandstone up to 49 times to a maximum temperature of 200 °C leads to irreversible microstructural changes, resulting in reduced P-wave velocities. Increasing the maximum temperature to 600 °C amplifies the impact on the rock's properties such as density, effective porosity, and P-wave velocity. The potential to induce irreversible changes in the rock mass must be accounted for (e.g. adjusting injection temperatures, depths, etc.), when considering a sandstone reservoir for thermal energy storage.

Aspects of this work have been performed within the projects AGENS (funded by the German Federal Ministry for Economic Affairs and Energy), and LISAGENS (funded by the German Federal Ministry of Research, Technology, and Space). We acknowledge the support for our research.

References

ASTM D7984-16 (2016) Standard test method for measurement of thermal effusivity of fabrics using a modified transient plane source (mtps) instrument

Becattini V, Motmans T, ZapponeA, Madonna C, Haselbacher A, Steinfeld A (2017) Experimental investigation of the thermal and mechanical stability of rocks for high-temperature thermal-energy storage. AppliedEnergy203: 373–389.https://doi.org/10.1016/j.apenergy.2017.06.025.

Bundesnetzagentur (2026) SMARD - Strom- und Gasmarktdaten.https://www.smard.de. Accessed at 11.02.2026

DIN EN ISO 17892-3 (2015) Geotechnische Erkundung und Untersuchung - Laborversuche an Bodenproben - Teil 3: Bestimmung der Korndichte

Erneuerbare-Energien-Gesetz - EEG (2023)

Fry N, Adebayo P, Tian R, Shor R, Mwesigye A (2024) A review of district energy technology with subsurface thermal storage integration. GeothermalEnergy12(1): 29. https://doi.org/10.1186/s40517-024-00308-3.

Hao J, Qiao L, Liu Z, Li Q (2022) Effect of thermal treatment on physical and mechanical properties of sandstone for thermal energy storage: a comprehensive experimental study. ActaGeotechnica,17(9): 3887-3908. https://doi.org/10.1007/s11440-022-01514-8.

Harris A, Kazachenko S, Bateman R, Nickerson J, Emanuel M (2014) Measuring the thermal conductivity of heat transfer fluids via the modified transient plane source (mtps) JournalofThermalAnalysisandCalorimetry116: 1309-1314.

Hou P, Gao L, Xing Y, ZhangZP (2020). Effect of thermal cycling on mechanical properties and energy evolution of sandstone. ThermalScience24(6 Part B): 4001-4009. https://doi.org/10.2298/TSCI2006001H.

ISRM (1978) Suggested methods for determining tensile strength of rock materials part 2: suggested method for determining indirect tensile strength by the brazil test. InternationalJournalofRockMechanicsandMiningSciences15 (3): 99–103

ISRM (1978) Suggested methods for determining the strength of rock materials in triaxial compression. InternationalJournalofRockMechanicsandMiningSciences15 (2): 47-51

ISRM (1979) Suggested methods for determining the uniaxial compressive strength and deformability of rock materials: part 1. suggested method for determining deformability of rock materials in uniaxial compression. InternationalJournalofRockMechanicsandMiningSciences16 (2): 138-140.

Jiang Y, Su H, Zhang L, Yu L, Chen G (2023). Heating-path dependency of fracture behavior of sandstone subjected to thermal treatment. TheoreticalandAppliedFractureMechanics127 104096. https://doi.org/10.1016/j.tafmec.2023.104096.

Jing X, Sun Q, Jia H, Ge Z, Wang T (2021). Influence of high-temperature thermal cycles on the pore structure of red sandstone. BulletinofEngineeringGeologyandtheEnvironment80(10): 7817-7830. https://doi.org/10.1007/s10064-021-02389-x.

Khatod KJ, Katekar VP, Deshmukh SS (2022) An evaluation for the optimal sensible heat storage material for maximizing solar still productivity: A state-of-the-art review. JournalofEnergyStorage50 (104622). https://doi.org/10.1016/j.est.2022.104622.

Li M, and Liu X (2022) Effect of Thermal Treatment on the Physical and Mechanical Properties of Sandstone: Insights from Experiments and Simulations. RockMechanicsandRockEngineering55(6): 3171-3194. https://doi.org/10.1007/s00603-022-02791-1.

Li X, Peng J, Xie Y, Li Q, Zhou T, Wang J, Zheng W (2022) Influence of High-Temperature Treatment on Strength and Failure Behaviors of a Quartz-Rich Sandstone under True Triaxial Condition. Lithosphere2022(Special 10). https://doi.org/10.2113/2022/3086647.

Liu X, Lu W, Li M, Zeng N, Li T (2020) The Thermal Effect on the Physical Properties and Corresponding Permeability Evolution of the Heat-Treated Sandstones. Geofluids 2020: 1-16. https://doi.org/10.1155/2020/8838325.

Sun Q, Lü C, Cao L, Li W, Geng J, Zhang W (2016) Thermal Properties of Sandstone After Treatment at High Temperature. InternationalJournalofRockMechanicsandMiningSciences85: 60-66. https://doi.org/10.1016/j.ijrmms.2016.03.006.

Tawalbeh M, Khan HA, Al-Othman A, Almomani F, Ajith S (2023) A comprehensive review on the recent advances in materials for thermal energy storage applications. InternationalJournalofThermofluids18 (100326). https://doi.org/10.1016/j.ijft.2023.100326.

Tiskatine R, Bougdour N, Idoum A, Bazgaou A, Oaddi R, Ihlal A, Aharoune A (2023) Experimental investigation on rock thermal properties under the influence of temperature. Thermochimica Acta720 179424. https://doi.org/10.1016/j.tca.2022.179424

Vidana Pathiranagei S, and Gratchev I (2021) Engineering properties of sandstone heated to a range of high temperatures. BulletinofEngineeringGeologyandtheEnvironment80(3): 2415-2432. https://doi.org/10.1007/s10064-020-02065-6.

Wang M, Li J, Tan H, Wang J, Shi Z, Li K (2023) Study on fatigue characteristics and thermal damage mechanism of red sandstone under high temperature-cyclic load coupling. InternationalJournalofFatigue,168 (107405). https://doi.org/10.1016/j.ijfatigue.2022.107405.

Yang SQ, Xu P, Li YB, Huang YH (2017) Experimental investigation on triaxial mechanical and permeability behavior of sandstone after exposure to different high temperature treatments. Geothermics69: 93-109. https://doi.org/10.1016/j.geothermics.2017.04.009.

Zhao Y, Du C, Bi J, Li J, Wang C (2022) Influence of multiple porous structure evolution on physical–mechanical properties and damage mechanism of sandstone heated continuously/periodically with the identical heating time. BulletinofEngineeringGeologyandtheEnvironment81(12): 507. https://doi.org/10.1007/s10064-022-03020-3.

Elastic Wave Velocity Response to Saturation in Rocks: Laboratory Characterization

J. L. Figueiredo, D. G. Damaceno & C. Cláuver
Federal University of Viçosa, Viçosa, Brazil
julia.l.figueiredo@ufv.br
0000-0002-7805-9729

B. E. V. F. Souza & I. D. Carvalho
Vale S.A, Belo Horizonte, Brazil

Abstract

The propagation velocity of primary (Vp) and secondary (Vs) elastic waves in rocks are crucial for assessment of rock quality and integrity, as well for the estimation of elastic modulus and Poisson's ratio through empirical correlations. Properties such as porosity, density, and moisture content influence both wave velocities and the geomechanical behavior of rock masses. This variability underscores the need to understand the response of Vp and Vs to varying rock saturation conditions. This study evaluates the influence of saturation and physical properties on the Vp and Vs velocities in three lithotypes including: syenogranite (SG), gneiss (GN), and granitoid (GT). Ultrasonic wave velocity measurements were performed using transducers of 250 kHz and 40 kHz were used for Vp and Vs, respectively, under dry and saturated conditions. Saturation was achieved using a vacuum chamber with water immersion for four hours, while drying was carried out in an oven at 100 °C for 24 hours. Physical index tests (porosity and density) were determined. The results showed that wave velocities increased under saturated conditions across all lithotypes, a behavior attributed to pore filling by water and an increase in rock stiffness. This effect was most pronounced in SG, which exhibited the highest average percentage increases (39% for Vp, 26% for Vs), consistent with its higher porosity. In GN, two samples with higher porosity exhibited more expressive increases and lower overall velocity values compared to the others. In GT, the highest Vp values were recorded in samples with the lowest porosity, while the sample with the lowest density presented the lowest wave velocities, despite having porosity comparable to other samples. The findings confirm an inverse relationship between porosity and velocities, and a direct relationship with bulk density, consistent with previous research. Ultimately, this study demonstrated that Vp is more sensitive than Vs to saturation-induced variations.

Keywords

Porosity, Saturation, Ultrasonic pulse velocity.

1 Introduction

Ultrasonic techniques are non-destructive, indirect methods that are easily applicable in both laboratory and field settings, known for their precision and low operational cost. For these reasons, they are widely employed in geotechnical and geophysical applications for the assessment of the physical properties, composition, and density of rocks (Chawre, 2018; Sabri *et al.*, 2025; Viana and Simas, 2024). Elastic waves in solids can be classified into two main types: primary, or longitudinal and compressional (P) waves and secondary or shear(S) waves. P-waves involve particle motion parallel to the direction of propagation, whereas S-waves propagate through shear deformation, with particle displacements perpendicular to the direction of propagation (Kearey *et al.*, 2002).

The measurement of P-wave (Vp) and S-wave (Vs) velocities enables the estimation of parameters such as Young's modulus and Poisson's ratio, as well as the evaluation of rock quality. However, these velocities are strongly influenced by the intrinsic characteristics and mineralogical composition of rocks, including porosity, density, anisotropy, structure, the size and shape of mineral grains, as well as pore fluid content (Chawre, 2018; Figueiredo *et al.*, 2025; Yagiz, 2011; Yasar and Erdogan, 2004). Understanding the behavior of wave velocities in response to these parameters allows for the correct interpretation of test results and a more realistic assessment of the in situ behavior of rock masses. Therefore, aiming to investigate the influence of saturation, this study evaluates the behavior of primary (Vp) and secondary (Vs) wave velocities in rocks under dry and water-saturated conditions, as well as their relationship with physical properties such as apparent porosity and dry bulk density.

2 Materials and Methods

2.1 Materials

This study investigated the behavior of different lithotypes: syenogranite (SG), gneiss (GN), and granitoid (GT). The samples were obtained from rotary core drilling, preserving the diameters corresponding to the drilling crowns used, namely BX (42 mm) for SG and GT, and NX (54.7 mm) for GN. Five specimens of each lithotype were evaluated, as illustrated in Fig. 1.

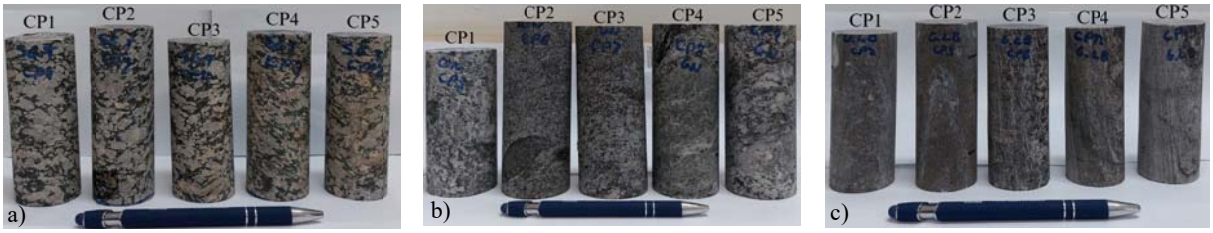


Fig. 1 Samples of SG, GN, and GT. a) Syenogranite (SG); b) Gneiss (GN); c) Granitoid (GT).

2.2 Methods

The physical indices, apparent porosity (η) and dry bulk density (ρ_d), were determined according to the International Society for Rock Mechanics (ISRM, 2007). The elastic wave velocity test, illustrated in Fig. 2, followed the recommendations of theISRM (2014)using 250 kHz transducers for measuring Vp and 40 kHz for Vs. The tests were performed on the specimens under saturated and dry conditions. Saturation was achieved using a vacuum chamber, with the samples immersed in deionized water for 4 hours. The condition was ensured by monitoring the mass of the specimens at hourly intervals until no further variation was observed. Drying was performed in an oven at 100°C for 24 hours.

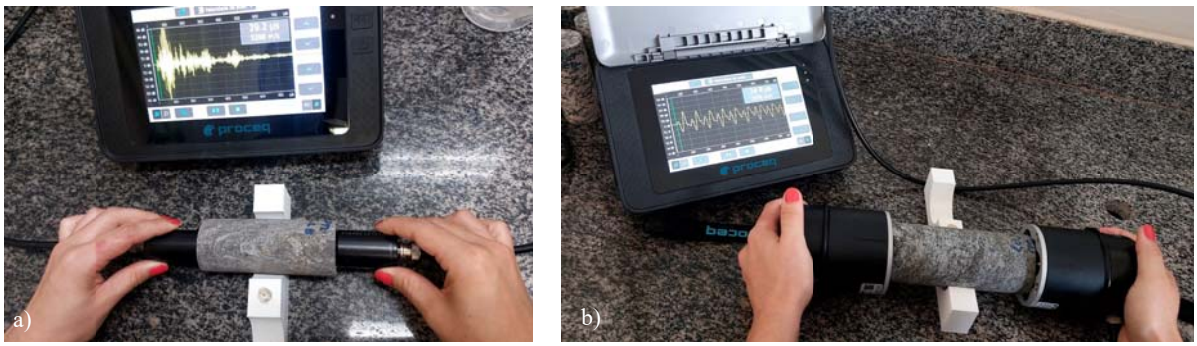


Fig. 2 UPV test. a) Measurement of P-waves. b) Measurement of S-waves.

3 Results and discussion

3.1 Physical Properties

The graph in Fig. 3 illustrates the relationship between porosity and dry bulk density for all specimens.

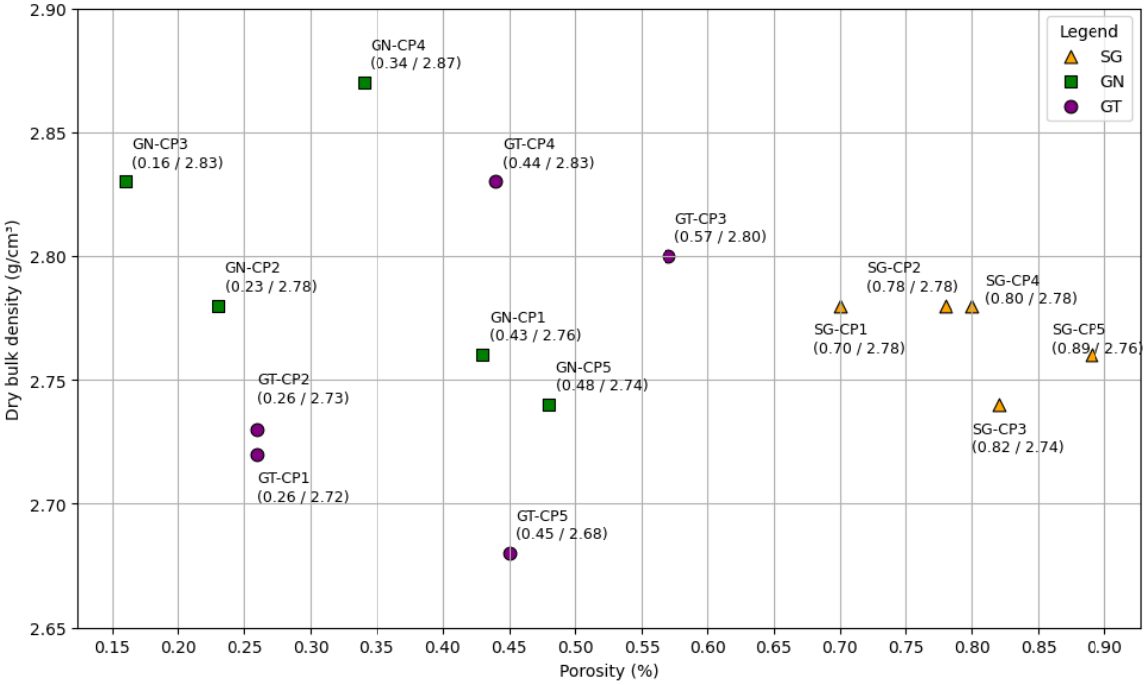


Fig. 3 Results of the physical indices of apparent porosity (η) and dry bulk density (ρ_d).

Based on the analysis of the graph, it is noted that the SG lithotype presented similar physical index results among the samples, indicating that the analyzed specimens tend to exhibit mineralogical and structural homogeneity. In addition, this lithotype stood out for having the highest porosity compared to the others, with an average of 0.80%.

Among the gneiss samples, GN-CP1 and GN-CP5 showed higher η and lower ρ_d values compared with the others, whereas GN-CP2 and GN-CP3 presented the lowest porosities among all samples, of 0.16% and 0.23%, respectively. GN-CP3, in turn, showed an intermediate porosity value but the highest ρ_d among the GN samples. This variability within the lithotype may be associated with the lighter mineralogy observed in GN-CP1 and GN-CP5, while the other samples contain darker minerals (Fig. 1), which results in different physical properties, particularly ρ_d.

Although the granitoid samples exhibit greater dispersion within the dataset, they still show some similarities in their physical indices. Samples GT-CP1 and GT-CP2 presented the lowest porosity values in the group, contrasting with GT-CP3, whose porosity is approximately twice as high. Despite this, GT-CP1 and GT-CP2 presented similar ρ_d values and greater macroscopic similarity. Samples GT-CP4 and GT-CP5 also showed similar η values; however, GT-CP5 stands out for having the lowest ρ_d among all samples. The variability in the physical indices observed in the granitoid may be associated with mineralogical variations between the samples, which presented some visual heterogeneities. These differences, resulting from the presence of distinct minerals or geological contacts, significantly influence the physical characteristics of the material, even though they belong to the same lithotype.

3.2 Elastic wave propagation velocity under different saturation conditions

The graph in Fig. 4presents the Vp and Vs values obtained for all samples under both saturation conditions, as well as the corresponding mean trend lines, which represent the general behavior of these values.

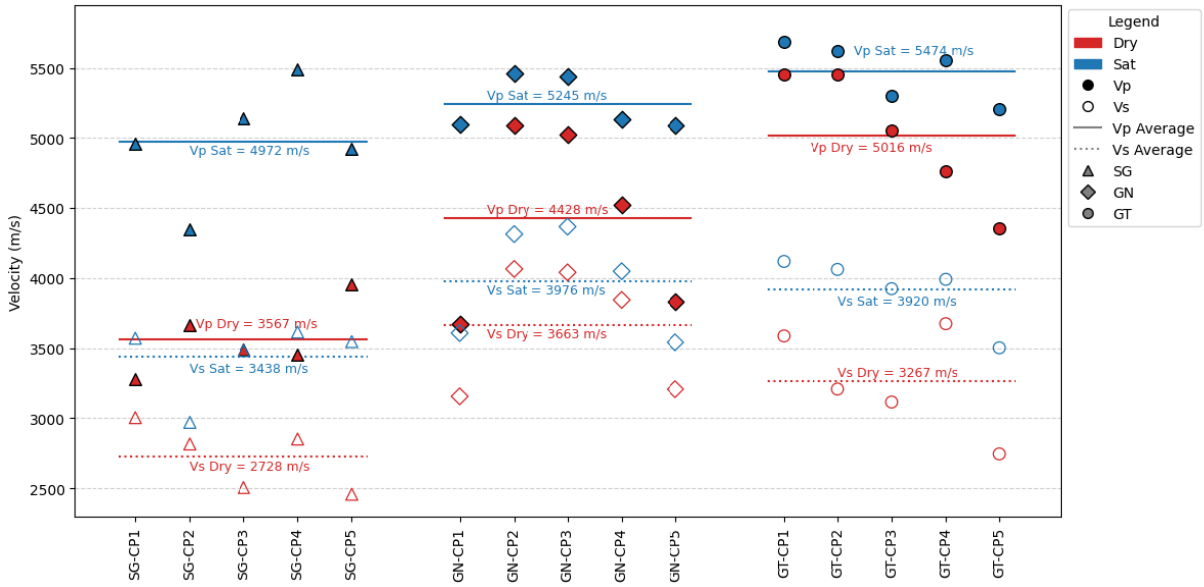


Fig. 4 Results of Vp and Vs under dry and saturated conditions for all samples.

Based on the behavior indicated by the mean value trend lines, a tendency for Vp and Vs to increase with higher saturation levels is observed in all lithotypes. Due to the increase in the rock's compressibility modulus, elastic wave propagation velocity increases as voids become filled with water, especially for primary waves. This behavior has also been reported by Kahraman (2007), Baechle et al. (2009), Uyanık et al. (2019), He et al. (2021), Vukadin, Orešković and Kutasi (2021), Sharo et al. (2022) and Figueiredo et al. (2025).Comparing the mean values under dry and saturated conditions, the percentage increase in Vp from dry to saturated was, in general, greater than that of Vs. The SG lithotype exhibited the highest percentage increases due to saturation, with increases of 39% in Vp and 26% in Vs. The GN lithotype showed an 18% increase in Vp and the smallest variation in Vs, of 9%. The exception was observed in GT, which presented the highest increase in Vs (20%), while its Vp increase was 9%.

In terms of Vs, it is expected that this velocity does not exhibit significant variations with the replacement of pore fluid by water, since fluids do not sustain shear resistance. The effects of saturation on Vs are less frequently reported in the literature when compared to those observed for Vp. Nevertheless, increases in Vs may occur and are commonly attributed to the increase in rock stiffness resulting from the substitution of air by water within the pores, as well as to the characteristics of the pore system, such as pore type, distribution, and connectivity, which may influence elastic wave propagation velocities (Baechle *et al.*, 2009; Uyanık *et al.*, 2019; Vukadin *et al.*, 2021; Yuan *et al.*, 2025).

Regarding the relationship between elastic wave propagation velocity and porosity, an inverse correlation was observed, such that more porous rocks tend to exhibit lower propagation velocities, a trend well established in the literature (Anselmetti and Eberli, 1993; Baechle *et al.*, 2009; Besharatinezhad *et al.*, 2022; Figueiredo *et al.*, 2025; Han *et al.*, 1986; He *et al.*, 2021).This behavior is evident in SG, which presents porosity values approximately twice those of the other samples. In addition to having the lowest average Vp and Vs in both saturation conditions, it was the lithotype that showed the greatest velocity increase with saturation for both Vp and Vs.

With respect to the pairs of samples previously identified as similar in terms of physical indices and macroscopic characteristics, the GN samples demonstrate proximity in velocity values between GN-CP1 and GN-CP5. The Vp values for these samples in the dry condition were close to the Vs values of the other specimens, further reinforcing their distinct behavior. Moreover, this pair presented the greatest increases in Vp and Vs from the dry to saturated states, consistent with the fact that they also had the highest porosities, suggesting the influence of higher pore volumes on wave propagation. Meanwhile, the GN-CP2 and GN-CP3 samples, which had the lowest porosity values, presented similar Vp and Vs in both saturation conditions, and these were the highest values within the lithotype. GN-CP4, with porosity intermediate between the two pairs, presented Vp and Vs values lower than GN-CP2/GN-CP3 and higher than GN-CP1/GN-CP5, reinforcing its intermediate behavior within the lithotype. Additionally, it is observed that the GN-CP1/GN-CP5 pair exhibited the greatest increases

in wave propagation velocity between the dry and saturated conditions. For Vp, this increase was approximately 3.7 times greater than that observed in the other samples, while for Vs the variation was about twice as high.

For the GT lithotype, samples GT-CP1 and GT-CP2, which showed similar physical indices, exhibited comparable Vp values in both saturation conditions, as well as similar Vs under saturated conditions. Furthermore, these samples presented the highest Vp values among all analyzed specimens, even though they did not have the lowest porosities or highest densities. Within this lithotype, GT-CP5 stands out for presenting the largest percentage increase in Vp and Vs from the dry to saturated state. Although its porosity is close to that of GN-CP4 and even lower than that of GT-CP3, its behavior may be associated with its lower bulk density, since this property is directly related to elastic wave propagation velocity, as reported by Anselmetti and Eberli (1993), Uyanık et al. (2019) and Besharatinezhad et al. (2022). Thus, lower density tends to result in lower wave propagation velocities.

It is worth noting that although porosity and bulk density are highly relevant factors influencing elastic wave velocity test results, this method also depends on several other parameters not evaluated in this study, such as mineralogy, pore type, morphology and connectivity, and anisotropy (Anselmetti and Eberli, 1993; Karakul and Ulusay, 2013; Yan and Han, 2016). Therefore, it is not possible to attribute the behavior of the samples in the test solely to the physical properties evaluated here.

4 Conclusion

This study evaluated the influence of saturation on the propagation velocity of elastic waves in fifteen samples of granitic rocks. Additionally, the physical indices of apparent porosity and dry bulk density were determined in order to correlate them with the obtained results. Overall, the results showed an increase in Vp and Vs with saturation for all lithotypes, with this effect being more pronounced for Vp. An inverse relationship between porosity and wave propagation velocity was also observed, as well as the influence of porosity on the increase in velocities from the dry to saturated state, whereas bulk density presented a direct relationship with velocities in specific analyses.

With regard to the lithotypes, syenogranite exhibited a more homogeneous behavior in terms of physical indices, standing out due to its higher average porosity compared with the others. This characteristic was reflected in its lower mean Vp and Vs values, as well as in the highest percentage increases in velocity with saturation. Gneiss, in turn, showed greater internal variability, with samples exhibiting distinct behaviors as a result of differences in physical indices and macroscopic characteristics. The samples with higher porosity presented lower velocities in the dry state and greater increases with saturation, whereas the less porous samples exhibited the highest Vp and Vs values, along with less expressive variations between dry and saturated conditions. The granitoid samples showed greater dispersion in physical indices, indicating less uniform behavior. Although some samples presented high velocities without being associated with the lowest porosities or highest bulk densities, another sample characterized by lower ρ_d exhibited the lowest velocities and the greatest increase with saturation, suggesting that other intrinsic material factors also influence its response.

Therefore, the results demonstrate that porosity and bulk density influence the propagation velocities of elastic waves, particularly in the material's response to variations in the degree of saturation. However, the analysis also indicates that the behavior cannot be explained solely by these physical indices, since other factors such as mineralogy, pore connectivity and morphology, anisotropy, and internal structure are also influential. Thus, the importance of future studies that investigate additional parameters for a more complete interpretation and integration of results is highlighted.

References

Anselmetti, F. and Eberli, G.P. (1993), "Controls on sonic velocity in carbonates", *Pure and Applied Geophysics*, Birkhäuser-Verlag, Vol. 141 No. 2–4, pp. 287–323, doi: 10.1007/BF00998333.

Baechle, G.T., Eberli, G.P., Weger, R.J. and Massaferro, J.L. (2009), "Changes in dynamic shear moduli of carbonate rocks with fluid substitution", *Geophysics*, Society of Exploration Geophysicists, Vol. 74 No. 3, doi: 10.1190/1.3111063.

Besharatinezhad, A., Khodabandeh, M.A., Rozgonyi-Boissinot, N. and Török, Á. (2022), "The Effect of Water Saturation on the Ultrasonic Pulse Velocities of Different Stones", *PeriodicaPolytechnica Civil Engineering*, Budapest University of Technology and Economics, Vol. 66 No. 2, pp. 532–540, doi: 10.3311/PPCI.18701.

Chawre, B. (2018), "Correlations between ultrasonic pulse wave velocities and rock properties of quartz-mica schist", *Journal of Rock Mechanics and Geotechnical Engineering*, Elsevier, Vol. 10 No. 3, pp. 594–602, doi: 10.1016/J.JRMGE.2018.01.006.

Figueiredo, J.L., Damaceno, D.G., Sant'Anna, M.A., Souza, B.E.V.F., Carvalho, I.D. andCláuver, C. (2025), "Análise da Velocidade de Propagação de Ondas Compressivas (Vp) e Cisalhantes (Vs) de Quatro Litotipos em Condições Seca e Saturada", *Congresso Brasileiro de Geologia de Engenharia e Ambiental*, Belo Horizonte, p. 10.

Han, D.H., Nur, A. and Morgan, D. (1986), "Effects of porosity and clay content on wave velocities in sandstones", *GEOPHYSICS*, Society of Exploration Geophysicists, Vol. 51 No. 11, pp. 2093–2107, doi: 10.1190/1.1442062.

He, W., Chen, Z., Shi, H., Liu, C. and Li, S. (2021), "Prediction of acoustic wave velocities by incorporating effects of water saturation and effective pressure", *Engineering Geology*, Elsevier, Vol. 280, p. 105890, doi: 10.1016/J.ENGGEO.2020.105890.

ISRM. (2007), *The Complete ISRM Suggested Methods for Rock Characterization, Testing and Monitoring: 1974-2006*, edited by Ulusay, R. and Hudson, J.

ISRM. (2014), *The ISRM Suggested Methods for Rock Characterization, Testing and Monitoring: 2007-2014*, edited by Ulusay, R.*The ISRM Suggested Methods for Rock Characterization, Testing and Monitoring: 2007-2014*, Springer International Publishing, doi: 10.1007/978-3-319-07713-0/COVER.

Kahraman, S. (2007), "The correlations between the saturated and dry P-wave velocity of rocks", *Ultrasonics*, Elsevier, Vol. 46 No. 4, pp. 341–348, doi: 10.1016/J.ULTRAS.2007.05.003.

Karakul, H. and Ulusay, R. (2013), "Empirical Correlations for Predicting Strength Properties of Rocks from P-Wave Velocity Under Different Degrees of Saturation", *Rock Mechanics and Rock Engineering 2013 46:5*, Springer, Vol. 46 No. 5, pp. 981–999, doi: 10.1007/S00603-012-0353-8.

Kearey, P., Brooks, M. and Hill, I. (2002), *An Introduction to Geophysical Exploration*, edited by Blackwell Science Ltd, Vol. 3, Oxford.

Sabri, M.S., Verma, A.K. and Singh, T.N. (2025), "Direct and indirect methods for uniaxial compressive strength estimation in various geo-environments: A review", *Journal of Rock Mechanics and Geotechnical Engineering*, Elsevier, doi: 10.1016/J.JRMGE.2025.01.050.

Sharo, A.A., Taamneh, M.O., Alawneh, A.S., Nusier, O.K. and Rabab'ah, S.R. (2022), "P-Wave Velocity of Limestone Influenced by Saturation: Experimental Study", *International Review of Civil Engineering*, Praise Worthy Prize S.r.l, Vol. 13 No. 2, pp. 108–117, doi: 10.15866/IRECE.V13I2.20833.

Uyanık, O., Sabbağ, N., Uyanık, N.A. and Öncü, Z. (2019), "Prediction of mechanical and physical properties of some sedimentary rocks from ultrasonic velocities", *Bulletin of Engineering Geology and the Environment 2019 78:8*, Springer, Vol. 78 No. 8, pp. 6003–6016, doi: 10.1007/S10064-019-01501-6.

Viana, J.B.A. and Simas, J. de L. (2024), "ESTUDO E ANÁLISE DE FÍSICA DAS ROCHAS PARA IDENTIFICAÇÃO DE PROPRIEDADES ELÁSTICAS", *Geologia de Engenharia e Ambiental: Análises, Métodos e Técnicas Em Pesquisa*, Editora Científica Digital, pp. 46–56, doi: 10.37885/240316157.

Vukadin, D., Orešković, J. and Kutasi, C. (2021), "Elastic Properties of Pannonian Basin Limestone under Different Saturation Conditions", *Energies 2021, Vol. 14, Page 7291*, Multidisciplinary Digital Publishing Institute, Vol. 14 No. 21, p. 7291, doi: 10.3390/EN14217291.

Yagiz, S. (2011), *P-Wave Velocity Test for Assessment of Geotechnical Properties of Some Rock Materials*, *Bull. Mater. Sci*, Vol. 34.

Yan, F. and Han, D.H. (2016), "Effect of pore geometry on Gassmann fluid substitution", *Geophysical Prospecting*, Blackwell Publishing Ltd, Vol. 64 No. 6, pp. 1575–1587, doi: 10.1111/1365-2478.12348.

Yasar, E. and Erdogan, Y. (2004), "Correlating sound velocity with the density, compressive strength and Young's modulus of carbonate rocks", *International Journal of Rock Mechanics and Mining Sciences*, Elsevier BV, Vol. 41 No. 5, pp. 871–875, doi: 10.1016/j.ijrmms.2004.01.012.

Yuan, H., Zhang, X. and Han, D.H. (2025), "Fluid effect on elastic properties of carbonate and implication for CO2 geologic sequestration monitoring", *Geophysics*, GeoScienceWorld, Vol. 90 No. 1, pp. MR25–MR38, doi: 10.1190/GEO2024-0124.1.

A step forward in the resilience of flexible rockfall protection systems

R. J. Luis-Fonseca[1], W. Gerber[2], R. Dudler[1], H. Lanter[1] & V. Budimir[1]
Geobrugg AG, Romanshorn, Switzerland
Formerly WSL, Birmensdorf, Switzerland
roberto.luis@geobrugg.com
0000-0001-6623-7981

Abstract

Rockfall barriers are widely used worldwide to protect critical infrastructure and must safely dissipate large amounts of energy throughout their lifetime. However, current European approval procedures - followed internationally by default- are based on overly idealized test conditions, involving a single block striking the centre of the middle field at either the service or maximum energy level. This setup represents the most favourable geometric scenario and does not reflect the complexity of real rockfall events, where blocks seldom fall alone or hit the barrier centrally. Instead, actual events involve unpredictable combinations of multiple impacts, block rotation, and fragmentation, leading to highly irregular and dynamic load patterns. Consequently, standard tests fail to capture the true demands placed on barriers. This paper therefore remarks the need for improved experimental approaches, particularly tests at critical areas with eccentric, and simultaneous impacts on border fields to better replicate real field conditions. It also highlights limitations in current guidelines, summarises key insights from research and field experience, and presents new findings from recent investigations.

Keywords

Rockfall barriers, European Technical Assessments, Test in critical areas, Eccentric and simultaneous.

1 Introduction

The use of flexible steel barriers to mitigate rockfall hazards first emerged in the 1950s. Early systems were based on triangular wire rope nets (fig. 1) snow avalanche structures (Spang, 2000). In many cases, repurposed anti torpedo nets from World War II (fig. 2).



Fig. 1 Flexible avalanche structure (1950) (Spang, 2000).



Fig. 2 Mine layer ship collecting an anti-torpedo net Norfolk, Virginia 1945 (public domain).

The first use of steel wire rope nets for rockfall protection happened in 1951 in Schafberg (Switzerland), where nets previously used for blast control, was installed as single field rockfall barrier. Häfeli (ETH, Zurich) later introduced the concept of serial structures and developed design methods for flexible wire rope net snow avalanche barriers. Experience showed that snow control structures could also withstand rock impacts during snow free periods. This led Brugg AG, following Bindschädler's proposal, to adopt wire rope nets for rockfall protection. As a result, the world's first flexible rockfall barrier was installed in Brusio in 1958, protecting power lines with nets mounted on wall. A second installation followed in 1959 in Ardez, also built on a concrete wall.

2 From pragmatism to standardization

Flexible mitigation systems design always begins with analytical and numerical models. Those models are not considered valid -and the systems not considered ready for use- until they are verified through full scale (1:1) field test under real conditions, for decades this philosophy has combined practical engineering with scientific rigor. Over time, full scale testing has proven essential for ensuring system safety and reliability. Field experiments have strongly shaped the development of technical guidelines and standards. Due to testing methods have advanced more quickly than the standards themselves, they need to be treated separately. Current regulations still rely on older results, with the latest findings not yet incorporated.

3 Full-scale test methods

3.1 Historical background

The first systematic tests on protective nets were conducted in 1962 in Brunnen (near Lucerne, Switzerland).About 50 kg rockswere thrown from 45 m high, achieving minimum energies of 22 kJ, marking the beginning of the experimental characterization (fig. 3).



Fig. 3 First trial in Brunnen (1962).



Fig. 4 First vertical droptest in Brugg (1976) .



Fig. 5 Brugg barrier testing for Caltrans (1989).

In 1968, following recommendations from the Swiss Railway Company BLS, tests were conducted in which rocks of up to 1000 kg were released toward a three-field wire rope net barrier. In 1975, Brugg AG (Birr), and Heierli Engineering (Zurich), conducted rockfall experiments to support the development of new protection systems (Spang, 2000). Using a truck mounted crane, concrete blocks of up to 1000 kg were dropped freely from a height of 20 m onto horizontally tensioned wire rope nets (fig. 4). These trials marked the first documented use of braking elements. Around the same period (fig. 5), Caltrans (California Department of Transportation, USA) evaluated wire rope net barriers designed to absorb up to 200 kJ (the barriers were provided by Brugg AG, Switzerland and L'Entreprise Industrielle, France). More than 80 tests were executed with rocks ranging from 136 kg to 5900 kg, rolled down a 34° slope over 76 m (Duffy, 1990). Results showed that the barriers withstood impact energies far above their design values, and damaged components could be quickly replaced using standard equipment. This demonstrated early on that flexible barriers were a reliable and efficient rockfall mitigation option for California roadways. Beginning in 1988, Switzerland launched a new series of full-scale field experiments (more than 350 in total) which led to major advancements in barrier design (Baumann, 2002). One of the first Brugg AG test campaigns took place in Oberbuchsiten, using a procedure like the Caltrans experiments: rocks were released downslope with an excavator. Because the test slope consisted of hard rock, impact energies were significantly higher than in the California trials. Six barriers were tested using more than 100 blocks. Luis Fonseca (1995) later performed full scale tests on two flexible net barrier types at Beckenried.

A cable car launch system generated impact energies up to 250 kJ, and extensive instrumentation (including strain gauges) enabled accurate measurement of dynamic and kinetic responses. This setup offered a decisive advantage: high repeatability and precise control of impact parameters, improving the reliability of system evaluation. Collaboration among researchers and four manufacturers during this period drove rapid improvements in barrier technology, increasing energy absorption capacity from about 250 kJ in 1987 to approximately 2,000 kJ by 1998 (fig. 6).

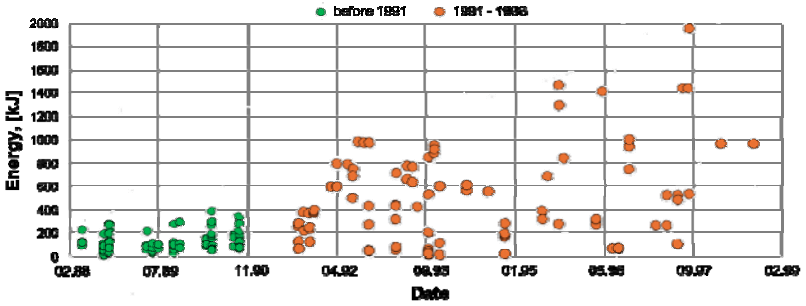


Fig. 6 Rockfall barrier testing in Switzerland from 1988 to 1998 (Gerber, 2025).

Field testing methods also evolved as their limitations became evident. First method (fig. 7.1): rocks were rolled down a natural hard rock slope. However, substantial energy was lost during ground contact, some rocks stopped before reaching the barrier, and impact velocities varied widely (6–24 m/s), resulting in poor repeatability. Second method (fig. 7.2): at Beckenried, a gantry crane with an inclined cable track allowed more controlled rock release. Typical impact velocities ranged from 10 to 22 m/s with realistic translational and rotational components. Nonetheless, impact height and angle still varied, and blocks consistently struck only the middle portion of the barrier. Improved method (fig. 7.3): introduced in 1991, using an inclined cable car system with a guillotine release mechanism. At a predefined point, a secondary rope was cut, allowing the block to travel directly toward the barrier without ground contact. This method achieved velocities of 25–27 m/s in Beckenried and 29–31 m/s in Giswil. In 1998, a similar facility was constructed in Italy (Peila, 1998). Blocks were guided by a cable car system, and an explosive charge severed the lifting rope at the release point to produce a direct impact. The monitoring system was comparable to the one supplied by the University of Cantabria for the Beckenried site (Luis Fonseca, 1995; Ballester et al. 1996). Although this method improved test control, results from some European facilities such as Trento in Italy, were later questioned due to unintended ground contact or unplanned rock braking during impact.Muraishi and Sano (1999) presented a Japanese certification method combining static laboratory tests with full scale slope tests, where a boulder is dropped from a crane onto a barrier on a 35° slope, producing a 55° impact angle. The method uses four test types -basic, cumulative, maximum load, and special component tests- captured with high-speed cameras. They concluded that this free fall approach is the most reliable because it consistently reproduces impact location, angle, and energy, ensuring repeatable performance evaluation. In 2000 the FOEN (Swiss Federal Office for the Environment) initiated the development of a certification procedure for rockfall barriers and introduced a fourth testing method (figs. 7.4 and 8) to overcome the limitations of previous approaches.

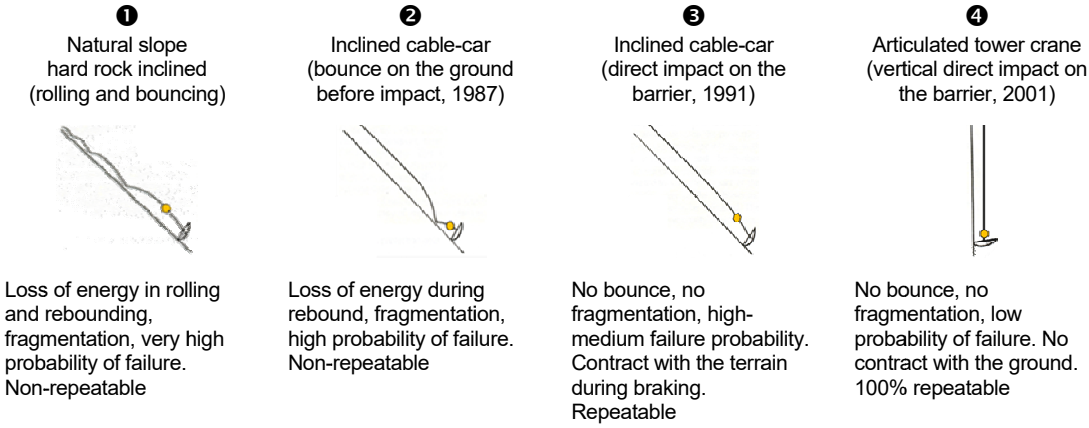


Fig. 7 Classification according to the test method generations (modified from Baumann, 2002).

A permanent test facility in Lochezen (fig. 8) uses a tower crane to drop a controlled concrete block onto a barrier fixed to a vertical rock wall, allowing precise control of impact conditions. The setup

ensures constant impact positions, avoids ground energy losses, and includes video and detailed measurements, improving test reliability and repeatability. The introduction of this evaluation method significantly improved test quality, repeatability, and overall reliability. Between 2001 and 2007, FOEN certified 24 barriers (Gerber, 2025), each tested at both the Maximum Energy Level (MEL) and Service Energy Level (SEL= 50% MEL) and with MEL values ranging from 100 to 5000 kJ.

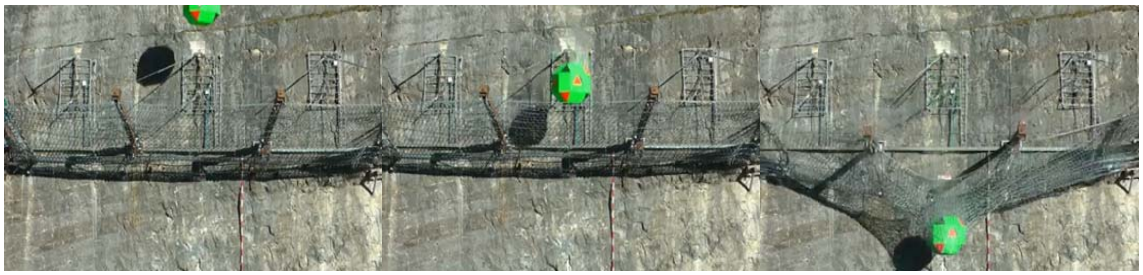


Fig. 8 Vertical test at Walenstadt during April 2025. 12.5MJ barrier (block 25t, v = 32m/s).

In 2018, based on the results of previous experiments, FOEN proposed a more detailed analysis of the braking process and load transmission for both energy levels (SEL and MEL). Figure 9, shows a vertical test on a 2000 kJ barrier (using a 6400 kg boulder impacting at 25 m/s) showed a braking time of 0.4 s, traveling 5 to 7 m within the net elongation path, and a total contact time of 0.56 s. This detailed evaluation highlights the importance of understanding the full braking phase to improve the accuracy of system performance assessments.The variation in braking forces and block deceleration can be measured throughout the contact time with the net, during both the inbound and outbound phases (fig. 10). The measurements show that if maximum deceleration occurs early in the braking phase, the braking distance is short; if it occurs later, braking distance becomes longer.

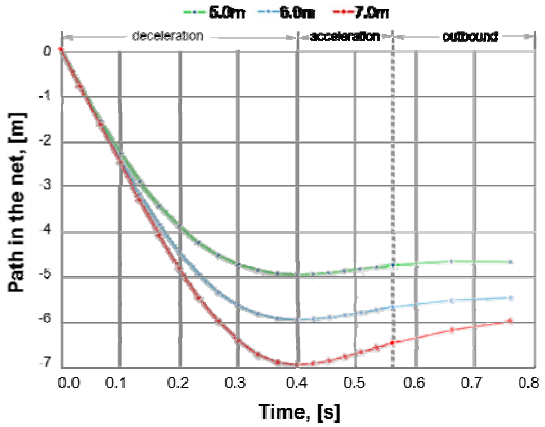


Fig. 9 Braking process in a vertical test 2000kJ of energy (modified from Gerber, 2025).

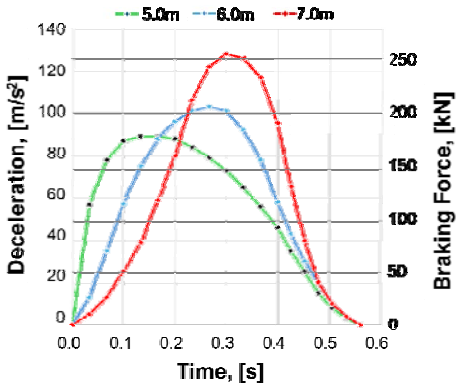


Fig. 10 Deceleration and braking forces at contact time (modified form Gerber, 2025).

3.2 Contrast needed

Natural-slope testing is essential because vertical drop tests (fig 11b), while useful for measuring basic parameters such as impact energy and component performance, many times do not replicate real rockfall behaviour. On a slope, blocks accelerate, bounce, rotate, strike at oblique angles, and often undergo multiple impacts before reaching the barrier, altering their velocity, direction, and impact energy. Natural-slope tests capture ground-barrier interactions and complex dynamics that vertical tests cannot reproduce. They verify the proper activation of energy dissipators and ensure that vertical-test results remain valid under real operating conditions. Between 2019 and 2020, full-scale (1:1) natural-slope tests were conducted at Chant Sura, Flüela Pass, Switzerland (fig. 11a), revealing the real-world effects of eccentric and critical areas impacts.



Fig. 11 Tests on natural slope and vertical drop, equant shaped boulders.

These experiments also demonstrated how block rotation, shape, and size significantly influence random impact energy and load distribution on the system. Thirty experiments were conducted using boulders of different shapes and weights from 320 to 840 kg. After several initial ground contacts, the boulder's behaviour changed significantly once it interacted with the barrier, as the catch membrane's distinct mechanical properties altered the impact angle and rendered ground-based interaction models no longer applicable. The tests showed that oblique impacts increased stresses at the post heads due to added tangential forces, while the blocks' kinetic energy was reduced by up to 67% along their trajectory because of friction, bouncing, and ongoing contact with the ground. Additionally, off-centre impacts led to a more asymmetric load distribution, causing forces in the upslope retaining ropes of the border fields to rise by about 33%. Overall, these findings emphasize the strong influence of impact angle, rotation, and block–terrain interaction on the loading experienced by the barrier (fig. 12).

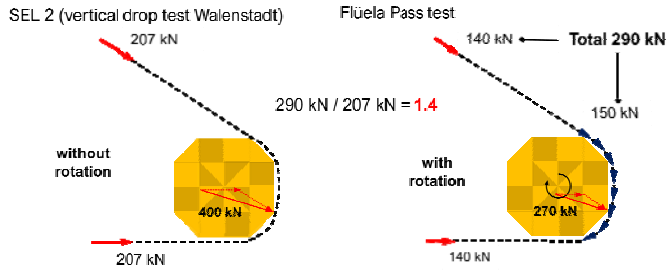


Fig. 12 Comparison vertical drop test (left) with Flüela pass natural slope field test (right). Lower energy in the field testleads to higher forces compared to the vertical test.

3.3 Latest trends at full-scale tests

A series of complementary vertical impact tests were carried out in Walenstadt, Switzerland, following lessons learned from the slope tests at Flüela Pass (Caviezel et al. 2022). These tests aimed to reproduce the barrier loads and deformation observed and to assess how well standardized test setups can simulate real impact conditions. Using the European-prescribed boulder mass and minimum impact velocities, different configurations were examined to determine whether equivalent or substitute loading conditions could reliably represent actual barrier performance and meet user safety expectations. **MEL-E** is a three-field test, with a boulder impacting in a top corner of the centre field (Eccentric), the impact energy also aligns with the 100% MEL value (fig. 13).

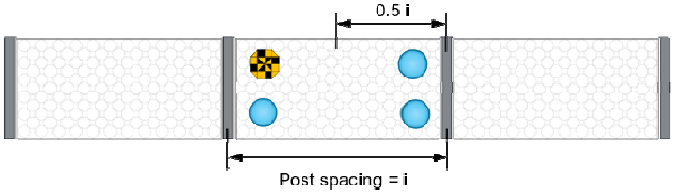


Fig. 13 Eccentric impact at MEL, in the top corner, near the midfield post head of a three-field system.

Tests conducted near the post head, showed increased loads on both the net and the retaining ropes. Because impacts in the upper corner apply greater stress to these components, an asymmetric test configuration is required. The MEL-E test demonstrated 20–30% higher forces in the upslope ropes and a 49% higher braking force compared to the standard MEL test. These results indicate that MEL-E is the most appropriate test to replicate the field-observed behaviour of rotating blocks, which generate asymmetric and high loads. **MEL-S** is a Single field test, where a test boulder impacts centrally within a single field barrier (made up of two posts only). The impact energy aligns with the 100% MEL value (fig. 14).



Fig. 14 Single field impact at MEL, corresponding to an extreme field impact.

Because the MEL-S setup uses a smaller net area and fewer energy-dissipation devices, the barrier must withstand the same impact energy with less components. Tests showed that upslope-rope forces in MEL-S were 26% higher than in the standard MEL, and the remaining U-brakes absorbed 46% more energy. Comparing MEL-S with MEL impacts in the border field revealed similar upslope-rope

forces and no asymmetric energy absorption in the brakes. Overall, MEL-S is the more demanding load case, effectively confirming the proper functionality and robustness of the barrier's border field (fig. 14 right). In addition, internal tests have been conducted per Geobrugg considering two other critical points of the barrier, trying to replicate the impacts seen in the field over the years and the experiences at Flüela, two types of tests are shown in: **rope separation** inside barriers and **direct impacton a post** (Roduner et al. 2023 and TSÜS, 2020).Internal tests on barriers confirm that rope separation area, including brake elements, exhibit high strength, good energy absorption capacity, and controlled deformability. The brake function as main elements in the redistribution and dissipation of impact loads before arriving to the ground anchors or protect the entire length of the barrier by dividing it in sections. The observed deformation modes match with design models. After certifying a 3000 kJ barrier with a MEL and two consecutive SEL impacts, further SEL hits were launched in various locations, trying to replicate impacts observed in the field over the years (Roduner et al. 2023).The **direct impact on post** (free fall test on profile HEA 120) it was done on a 500kJ barrier type GBE that successfully stopped the boulder fell at SEL (m = 580kg, v = 25m/s). Tests results and numerical simulations (Pimpinella, 2025) show that when a post is struck directly, a plastic hinge forms in the steel profile (figure 15). Although this may not compromise the barrier's performance during that specific impact, it weakens the post for any subsequent impacts because the flattened section has reduced bending resistance. Additionally, the permanent deformation of the post lowers the barrier's effective residual height.



(a) (b) (c)

Fig. 15 Steps of the numerical simulation: (a) t = 0.085s (b) t = 0.125s (c) t = 0.450s

Further vertical tests -particularly those examining **rope separation**- are crucial for understanding how flexible components behave under extreme loading and how energy is redistributed when a rope fails. These tests confirm the system's redundancy and ensure that containment performance remains intact. Likewise, direct impact tests on posts are essential to evaluate their structural strength, controlled deformation, and interaction with anchors and ropes. Together, these complementary tests provide key insights for improving barrier design and guaranteeing reliable performance under high-energy rockfall conditions. The **MEL–M** is a three-field test, with two test boulders impacting simultaneously (Multiple Simultaneous Impact) into the centre, and border field (Geobrugg, 2025). The total impact energy of the two impacts shall correspond to 100 % of the MEL energy, with each block carrying 50 % of that energy. Both impacts shall occur simultaneously, within a time difference not exceeding 0.1 s between first and second contact (fig. 16).

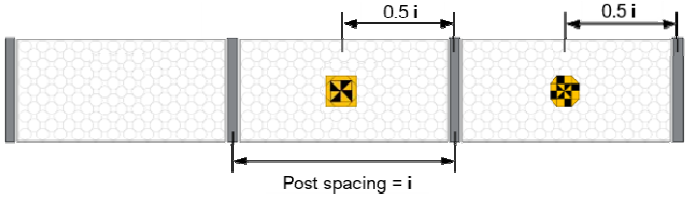


Fig. 16 Two boulders release simultaneously.

A 3000kJ barrier test was performed to validate its behaviour in the multiple impact test, simultaneous fall, and impact (fig. 17) of two boulders of 4800kg mass at 25m/s (using Swiss and European standardised equant shape boulders each with 1500kJ service energy).

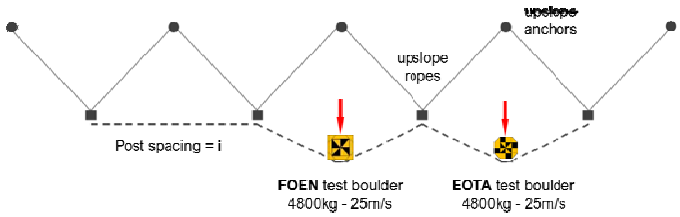


Fig. 17 Scheme of the two boulders released at service level.

Due to the multiple asymmetrical loading of the system of the fields 2 and 3 the post number 3 is subjected to high stress as the support rope is deflected on both sides of the post (like MEL-S test). Further the tension of the ring net on both sides of the post 3 causes the support head and the upslope ropes to experience high loads and no openings of the net occur ad post head (fig. 18). To address fragmentation-related issues, some guidelines recommend reducing a barrier's rated capacity by one-third (MBIE, 2016). However, this simplification is insufficient, as empirical evidence shows barriers can still fail under eccentric impacts at service-energy level.



Fig. 18 Simultaneous impact on two barrier fields (mid-field and extreme field).

Summarising: **MEL-S** as reference for maximum energy absorption for border fields, post stability, and overall structural performance under a symmetric load. In contrast, the **MEL-E** test simulates an eccentric impact in the upper area of the middle field, close to the post head and upper support ropes. This eccentric test simulates the effects of rotating blocks and off-centre impacts, which introduce tangential forces and increase stress at the post head. Using both MEL-S and MEL-E configurations allows assessment of the barrier's energy absorption performance across its full width, covering both symmetric and asymmetric loading conditions. **MEL–M** consider fragmentation and multiple impacts.

4 Regulations. Timeline and status

In the early 2000s, the absence of unified international standards for evaluating rockfall barriers led different countries to establish their own testing approaches. Switzerland introduced a national certification procedure in 2001(Gerber, 2001), later revised in 2006, which became widely adopted internationally, while Italy developed a non-mandatory guideline. Building on the Swiss methodology, European Organisation for Technical Assessment (EOTA) published ETAG 027 in 2008 (ETAG, 2008)to harmonize testing across Europe, later allowing inclined test setups and defining SEL as 33% of MEL before being transformed into European Assessment Document (EAD) 340059-00-0106 in 2018, though its implementation varies among EU countries. Despite these developments, the Swiss approach remains the most stringent and reliable. A key limitation across all standards is that foundation design has never been included in certification, leaving it to contractors based on manufacturer test data. The 2003 AASHTO recommendations emphasized the necessity of full-scale testing due to the limitations of numerical models and compared impact methods, highlighting vertical free-fall tests as the most accurate (Higgins, 2003). Finally, Austria's ONR 24810 (2021) introduced strict requirements to ensure barrier integrity since 2013, including preventing openings, controlling deformation, and enforcing maintenance and inspection to guarantee continuous protection.

4.1 Swiss complementary guidelines 2018 & 2022

Until January 31, 2018, the Swiss "Guideline for the Approval of Rockfall Protection Kits" governed certification, with public funding limited to compliant systems. In 2018, FOEN introduced a complementary guideline to help assess whether commercially available barriers meet project-specific requirements, particularly regarding foundation design, which is not addressed in current European standards. Although ETAG 027 (2008), later converted into an EAD in 2018, established the framework for testing and CE marking-placing responsibility on manufacturers-some regions still require higher safety levels than those defined in EAD 340059-00-0106. Research and full-scale tests by Geobrugg and WSL, supervised by TÜS, demonstrated the need for more realistic testing conditions, including zone-specific impacts and block rotation, presented in Caviezel et al. (2022), significantly improving the evaluation - design of rockfall protection barriers.

4.2 Requirements, according to the complementary guideline of the FOEN 2018

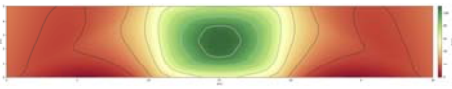
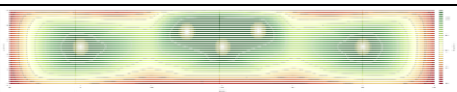
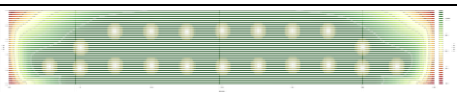
The FOEN (2018) complementary guideline sets stringent criteria to ensure that rockfall protection barriers and their foundations deliver reliable performance in real projects. Only systems meeting all requirements -without weak components such as undersized anchors- are considered sufficiently safe. The evaluation uses the manufacturer's European Technical Assessment (ETA) and technical

documentation to assess key factors including block trajectory, impact energy, deflection, braking distance, anchorage performance, residual height, slope angle, and any intermediate supports. A central requirement is the residual height (h_R), which must remain at least 50% of the nominal height after the MEL test, and 65% for oblique-impact tests. The maximum braking distance (w) is linked to MEL energy and defined through FOEN's logarithmic expression: $w = 1.534 \cdot ln(MEL\ [kJ]\ ) - 3.06$ [m]. Barriers without intermediate brakes must be limited to 60 m in length, and any system failing to meet FOEN requirements should not be used. The FOEN (2018) guideline expands on the ETA and provides a more comprehensive framework to ensure the quality, safety, durability, and real-world suitability of rockfall barriers, with particular focus on anchoring systems and foundation design.

4.3 Additional requirements, according to 2022 supplementary guidance

Since 2020, Geobrugg and WSL have developed extended full-scale test programs to address new market demands and increase the safety factor of rockfall barriers, as emphasized by Caviezel et al. (2022). These programs include specific impact field tests that go beyond FOEN (2018) requirements. Current standards validate impacts only at the centre of the barrier, creating a 'safe zone' of guaranteed performance. However, safety decreases as real impacts deviate from this area. Table 1 highlights the safety levels of existing certified systems and the additional FOEN requirements.

Table 1. Perception versus reality of the current level of security of the barriers.

Outline	Perception versus reality
	barrier resolves 100% of the impacts in its entire catchment area (**perception**)
	current regulations only guarantee the absorption of energy in the centre of the central field, according to all current directives (**reality**)
	the eccentric (MEL-E) and critical areas (MEL-S) trials proposed by Switzerland in 2022, increase the safe zone (**reality**)
	multiple impact tests (MEL-M) and additional tests at critical points, enlarge interception area (**reality close to perception**)

The regulatory process -while essential- evolves more slowly than scientific and technological developments. For this reason, the standard EAD 340059-00-0106 currently in force in all EU member countries, including Norway, Iceland, Liechtenstein and Switzerland it also recognized worldwide as main technical reference. Table 2 provides a summary of the recommended rules, which shall be applied (the last two recommendations could be optional).

Table 2. Design criteria for a safer application of rockfall protection kits.

Criteria	Entity leader
EAD 340059-00-0106. Class A h_R control	EOTA
vertical free-fall testing at both energy levels: SEL and MEL	FOEN, EOTA
maximum elongation control	FOEN
post-impact openings control	ONR
MEL-E eccentric impact test	FOEN
MEL-S single-field or border-field impact test	FOEN
MEL-M multiple-impact	Geobrugg
direct impact on post-test (optional)	Geobrugg
impact on rope separation test (optional)	Geobrugg

5 Conclusions

Current rockfall barrier certification does not reflect real-world rockfall behaviour, as it only evaluates centred, single-block impacts and ignores eccentric loading, block rotation, multiple impacts, and terrain interaction—all of which generate significantly higher forces, especially in posts and border fields. Full-scale slope tests such as those at Flüela Pass reveal critical behaviours missed by standard procedures, including 20–30% higher forces in upslope ropes and increased loads in edge zones. New complementary tests (MEL-E, MEL-S, MEL-M) better reproduce real loading scenarios by assessing eccentric impacts, multiple simultaneous impacts, and stresses on key components like rope partitions and posts. Because the current EAD standard omits foundations, anchoring, eccentric impacts, angular velocity, and multi-block effects, additional requirements from FOEN (2018); Caviezel et al. (2022)

and Geobrugg (2025) are crucial. Combining vertical, eccentric, extreme, multiple, and zone-specific tests greatly expand the barrier's verified safe area, resulting in higher reliability, better-designed components, and improved real-world safety. It is probably time to think about a new EAD release.

References

Ballester, F., Luis-Fonseca, R., and Torres-Villa, J.A., (1996) *Protección contra desprendimientos de rocas, Pantallas dinámicas.* Ministerio de Fomento, Dirección General de Carreteras. Madrid

Baumman, R., (2002) *The worldwide first official approval of rockfall protection nets*. Proceedings Annual Highway Geology Symposium, California State Department of Transportation. San Luis Obispo

Caviezel, A., Munch, J., Bartelt, P. & Lanter, A., (2022) *Rockfall barrier service loads for rock impacts with spin. Theory and experiments*. Report 125. WSL. Birmensdorf

Duffy, J., (1990) *Flexible Wire Rope Rockfall nets. Research Report. Record 1343*. CDT. San Francisco

EOTA (2008) *Guideline for European Technical approval of falling rock protection kits. ETAG 027*. Brussels

EOTA (2018) *EAD-340059-00-0106 Falling Rock Protection Kits*. Brussels

FOEN (2018) *Grundlagen zur Qualitätsbeurteilung von Steinschlagschutznetzen und deren Fundation. Bundesamt für Umwelt* (BAFU). Bern

Geobrugg (2025) *Rockfall protection systems*. https://www.geobrugg.com. Romanshorn

Gerber, W., (2001) (Am. 2006) *Guideline for the approval of rockfall protection kits*. Swiss Agency for the Environment, Forests and Landscape (SAEFL) and the Swiss Federal Research Institute. WSL. Berne

Gerber, W., (2025) *30 Years of Testing Rockfall Nets. Some Results and Findings.* WSL. Birmensdorf

Higgins, J., (2003)*Recommended procedures for the testing of rock-fall barriers*. Colorado School of Mines. AASHTO Standing Committee on Highways. Golden

Luis-Fonseca R., (1995) *Desarrollo de nuevos sistemas de protección de taludes y laderas rocosas. Pantallas dinámicas.* Doctoral Thesis University of Cantabria. Santander

MBIE Guidelines (2016) Rockfall: Design considerations for passive protection structures. Ministry of Business, Innovation & Employment. New Zealand

Muraishi, H., and Sano, S., (1999) *Full-Scale Rockfall Test of Ring Net Barrier and Components Seminar of Rockfall Tests and Standardization.* Davos

ONR 24810 (2021) *Technical protection against rockfall - Terms and definitions, effects of actions, design, monitoring, and maintenance*.Austrian Standards Institute. Vienna

Peila, D., (1998) *Guidelines for the classification and certification of the behaviour of net fences for rock mass protection barriers Guidelines for the Classification and Certification of the Behaviour of Net Fences & Rock Mass Protection Barriers*. Proceedings Annual Symposium, Witten, Germany

Pimpinella, F., (2025)*Mechanical performance of flexible rockfall barriers. Approaches and methods to establish efficientmaintenance procedures*. Polytechnic University of Torino, Italy

Roduner, A., Lanter, H., Eicher M., (2023) *Latest developments to increase the quality of flexible rockfall protection barriers.* ISRM 2023. Salzburg

Spang, R.M., (2000) *Standardisierung von Prüfverfahren für Steinschlagschutzbarrieren – Ziele und aktueller Stand.- Techn*. Akad. Esslingen, 2. Kolloquium Bauen in Boden und Fels

TSÜS (2020) *Technical report 70200042/1 Evaluation and assessment of eccentric, single and support rope separation impact test on Falling Rock Protection Barrier ROCCO-2000*. Bratislava

Development and application of experimental systems for the measurement of thermal properties in rocks using representative-size specimens

M. Herbón-Penabad, Y. Li, A. Muñoz-Ibáñez, J. Delgado-Martín& R. Juncosa-Rivera
Rock Mechanics Laboratory. Universidade da Coruña, Coruña, Spain
jorge.delgado@udc.es
0000-0002-4818-3964

A. Perez-Carreras, E. Ibañez-Martinez, J. M. Segura-Serra, J. Canal-Vila & J. Alvarellos-Iglesias
Repsol Technology Lab, Móstoles, Spain

Abstract

Understanding the thermal behaviour of rocks is essential for the safe and efficient design of geotechnical and energy engineering systems. Applications such as geological storage of CO_2, H_2, CH_4, LN_2 or air, underground heat storage, and the stability assessment of structures subjected to thermal gradients all depend on accurate knowledge of rock thermal properties. Thermal conductivity (λ), specific heat capacity (C_P), and the coefficient of thermal linear expansion (CTLE) must therefore be determined reliably. However, traditional methods often use milligram-scale or miniature samples, which may not adequately represent medium- to coarse-grained lithologies or capture key features such as porosity. This study introduces three experimental devices designed for core-plug size specimens, enabling the characterization of thermal properties in a wide range of conditions of igneous, metamorphic, and sedimentary rocks. The performance of each device was verified against reference materials with well-known thermal behaviour: Thermal conductivity is measured with an enhanced transient heat-flow, divided-bar system that can operate above and below ambient temperature with a maximum thermal gradient of ~520 °C; C_P is determined by drop calorimetry using glycerol as the calorimetric fluid; and CTLE is measured with a high-resolution (~1 µm) push-rod dilatometer. The calorimeter and the dilatometer can operate up to ~800 °C. The results highlight significant impacts derived from mineralogy, density, porosity, and anisotropy on rock thermal properties while confirm the adequacy and reliability of the experimental systems.

Keywords

Thermal properties, Thermal conductivity, Specific heat capacity, Coefficient of thermal linear expansion, Dilatometry, Temperature dependence.

1 Introduction

The thermal behaviour of rocks plays a fundamental role in a wide range of geological, geotechnical and energy engineering applications. Processes such as geothermal energy production, underground thermal energy storage, geological storage of fluids (e.g., CO_2, H_2, CH_4 or compressed air), nuclear waste disposal, or the assessment of the stability of underground structures subjected to thermal gradients strongly depend on the thermophysical properties of the host rock. In these contexts, heat transfer, heat storage capacity and thermally induced deformation can significantly influence both the efficiency and long-term safety of engineered subsurface systems. An accurate knowledge of these parameters is essential for reliable thermo-hydro-mechanical (THM) modelling of geological systems as well as for the safe design of engineering solutions involving thermal loadings.

In the assessment of thermal behavior of rocks, the ISRM Suggested Method (SM) identifies thermal conductivity (λ), thermal diffusivity (a), thermal effusivity (μ) and volumetric heat capacity (C) as key properties although it acknowledges that it is not necessary the measurement of all of them since they are mutually related(Popov *et al*., 2016). Thus, a and μ are defined by the relationship between λ and C according to the following expressions: $a=\lambda/C$ and $\mu=(\lambda \cdot C)^{1/2}$. Likewise, specific heat capacity, C_p is also related with C through rock density, ρ ($C_p=C/\rho$). However, ISRM does not include thermal expansion among the assessed thermal properties and thermal conductivity is only determined in a narrow temperature range close to ambient conditions. Furthermore, based on that work, here we extend the scope of the SM by considering the measurement of thermal conductivity (λ); specific heat capacity (C_p) and the coefficient of linear thermal expansion (CTLE or α) of rocks.

The thermophysical properties of rocks are strongly influenced by different factors such as mineral composition, grain size, density, porosity and other microstructural features such as bedding, foliation or microcracking. For instance, quartz-rich rocks tend to exhibit relatively high λ, whereas increasing porosity generally reduces heat transfer due to the lower λ of pore fluids or air (Zhu et al., 2022). Likewise, many rocks exhibit anisotropic thermal behaviour associated with preferred mineral orientations or stratified structures (Labus and Labus, 2018).

Despite their objective relevance, the experimental determination of rock thermal properties presents several challenges. Rocks are inherently heterogeneous materials, and their thermophysical behaviour may significantly vary even within a single lithology. Conventional laboratory techniques used to determine thermophysical properties, such as differential scanning calorimetry or laser flash analysis, usually require milligram-scale samples or thin specimens. Although these techniques offer high analytical precision, the small size of the tested samples may not adequately capture the heterogeneity of medium- to coarse-grained rocks or the influence of structural features that are relevant at larger scales. Thus, there is a compelling necessity to develop experimental approaches allowing the assessment of thermal properties of rocks using specimens of representative dimensions, such as those typically employed in rock mechanics testing.

In this context, the present work expands the scope of the currently available ISRM SM by describing the development and application of three experimental systems designed to determine these key thermal properties in rocks using plug-size specimens: An enhanced divided-bar apparatus for the determination of λ, a drop calorimeter for the measurement of C_p, and a high-precision, push-rod dilatometer for determiningα. These devices were designed to operate over a wide temperature range and to allow testing of a variety of lithologies representative of common geological materials.

2 Methodology

2.1 Heat capacity

Specific heat capacity, C_p, provides an estimation of the amount of thermal energy that can be stored within a given rock. It can be determined using the drop calorimetry method described in the ASTMD4611 standard. According to it, a rock specimen is heated to a known temperature, dropped into a calorimetric fluid of known thermal properties, and the equilibrium temperature of the mixture observed. Provided that there are not heat leaks, the heat released by the rock during cooling is equal to the heat absorbed by the calorimetric system.

The experimental setup (Fig. 1) is based on two main elements: A high-temperature, vertical tube furnace (which provides the heat source) and a cryogenic Dewar flask (which acts as calorimeter).

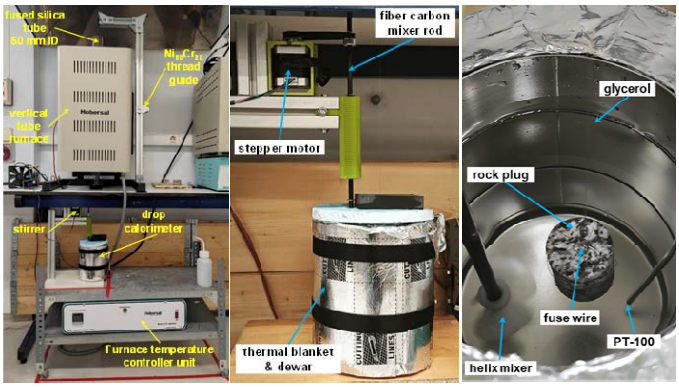


Fig. 1 Tube furnace on top of the calorimeter (left), Dewar flask with a stirring mechanism (center) and rock sample in the calorimetric fluid (right) used to assess constant pressure heat capacity C_P.

The tube furnace (*Hobersal* mod. HTF 116040) is able to operate at a maximum temperature of 1100 °C with a nominal power of 4 kW. According to the manufacturer's specifications, the furnace provides a 100 mm homogeneous heating zone centered along the geometric midpoint of a 400 mm total heated length. The furnace incorporates a fused silica tube (70 mm-OD, 60 mm-ID) where the rock specimen is introduced suspended from a thin nichrome wire (*Parr Inst.* 45C10) to prevent contact with the tube walls and ensure uniform thermal exposure during the heating phase. The calorimeter is based on a *KGW* GSS 1000W Dewar flask, which is a double-walled stainless-steel, thermally-isolated vessel with a nominal capacity of 1000 mL, 100 mm-ID and height of 156 mm that is filled with the calorimetric fluid. To prevent thermal stratification during the experiments in the fluid, the Dewar has been equipped with a simple mechanical stirring system (*i.e.*a stepper motor connected with a belt to a carbon-fiber rod fitted with a polymer propeller at its lower end). This mechanism ensures homogeneous thermal conditions throughout the duration of the thermal transfer. The Dewar flask is further thermally isolated with a thermal blanket and a *Styrofoam*™ lid through which it penetrates the axis of the stirrer as well as a high-precision PT-100 thermal probe connected to a high-resolution (0.001 ºC), high-accuracy (0.015 ºC) data acquisition module (*Pico Technologies* mod. PT-104).

Drop calorimetry provides with the constant-pressure heat capacity of the rock ($C_{P,r}$) and this can be obtained from an energy balance relationship:

$$C_{P,r} = \frac{((m_{fluid} - m_{evap})C_{P,fluid} + mc_p)\,(T_m - T_c)}{m_r(T_d - T_m)} \quad (1)$$

where m_r, m_{fluid}, m_{evap} are the mass of the test specimen, the mass of the calorimetric fluid and the mass of fluid evaporated when the immersion takes place, $C_{p,fluid}$ is the thermal capacity of the fluid, $T_d T_m$,T_c are temperature of the specimen when released from the furnace, the temperature of the mixture and the initial temperature of the fluid and mc_p is the thermal capacity of the system The calorimetric fluid used in the experiments is glycerol ($C_3H_8O_3$), and that was selected due to its low vapour pressure, high boiling point, and well-characterized thermophysical properties (Righetti et al., 1998). The calorimetric system was calibrated using a 99.9%-purity C101 (CW004A) copper sample, and its performance verified using a 99% α-Al_2O_3 ceramic specimen, both with known heat capacity values.

2.2 Thermal expansion

Thermal expansion refers to the increase in volume or length experienced by a rock due to the increase in temperature. In the case of linear expansion, α (or CTLE in engineering practice), this corresponds to the change on length per unit length per degree of temperature (K^{-1}). It determines the magnitude of thermally induced strains which may generate stresses with the potential of modifying the mechanical stability, permeability or fracture behaviour of a rock mass (Schön, 2015). To determine this property in rocks we have developed a simple push-rod dilatometer based on the considerations given in the ASTM E228 standard. In this system, a properly shaped rock plug (ISRM, 1979) is placed inside a

heated chamber where its length variation is transmitted through a fused-silica push-rod to a high-precision linear displacement transducer. Then α is calculated from the following relationship:

$$\alpha = \frac{1}{L_0}\frac{dL}{dT} \tag{2}$$

where $L_0$is the initial length of the specimen and $dL/dT$is the temperature-dependent change in length.

The full system (Fig. 2) consists in a fused-silica tube (60 mm-OD, 55 mm-ID) around which a 1250 W ceramic band heater is installed. The heater is controlled by a PID temperature controller (*OMRON* mod. EC5N) that regulates the temperature of the heated chamber based on the inputprovided by a type-K thermocouple. This sensor is positioned at the midpoint of the tube to ensure an accurate temperature control within the measurement section. A second thermocouple is used to monitor the temperature inside the test space and is located next to the specimen, at its mid-height. This is possible by a retaining ring with set screw that allows the controlled sliding of the thermocouple. Its positioning is further helped by the a centering ceramic plate located on top of the tested sample.

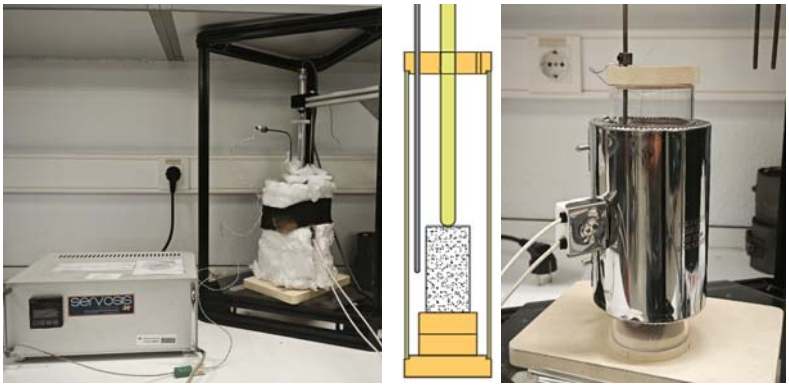


Fig. 2 General view of the push-rod dilatometer (*left*) and detail of the fused quartz tube (*center*) and with the band heater (*right*).

To attenuate external thermal oscillations (specially below 100 °C), the fused-silica tube and heater assembly are wrapped with a heat-resistant thermal-insulation blanket. Additional insulation is provided by two *cordierite* ceramic caps: One at the bottom, without openings, and a second one on top of the fused-silica tube with five perforations which allow the installation of additional temperature monitoring sensors and also provides a passage for the fused-silica push rod. The sample itself is located over a fused-silica pedestal whose height ensures that it is within the bounds of the homogeneous heating volume that is located at the mid-height of the band heater.

The push-rod is made of fused-silica and has 10 mm-diameter and 200 mm-length. The end in contact with the flat top surface of the rock specimen is machined to a hemispherical shape using a diamond grinding wheel to ensure a discrete, point-like contact. The opposite end of the push-rod is milled flat to provide a reliable reference surface for mounting a *Micro-Measurements* HS-10 linear displacement transducer (maximum travel range = 12.7 mm). Temperature measurements are acquired using a 20-bit, 8-channel USB thermocouple data logger (*Pico Technologies* mod. TC-08). When used with type-K thermocouples, this system provides a maximum resolution of 0.025 °C over the temperature range going from −250 °C to 1370 °C. Displacement measurements from the HS-10 transducer is recorded using a 24-bit, 8-channel differential signal-conditioning and acquisition unit (*Pico Technologies* mod. ADC-24).

Since thermal expansion operates over multiple elements of the experimental device (push rod, sample pedestal, test sample, etc.), in order to obtain an accurate and representative α value a number of corrections are required. Thus, to the raw thermal-expansion value (α_{raw}) it must be subtracted the sum of the contributions associated with the expansion of the heat-sensitive system elements (α_{system}). Accordingly, the corrected specimen coefficient is therefore obtained from:

$$\alpha_{sample} = \alpha_{raw} - \alpha_{system} \tag{3}$$

To determine the α_{system}, we have used - fused silica specimens as reference material (α_{sample}= α_{fused_silica}= 0.55 × 10^{-7} K^{-1} between 20 and 320 °C; White, 1973).

2.3 Thermal conductivity

Thermal conductivity governs the rate at which heat propagates through the rock mass according to Fourier's law. In this case, we have developed an enhanced steady state divided-bar apparatus based on the ASTM E1225 standard as well as the ISRM SM (Popov *et al*., 2016).

Figure 3illustrates the experimental device developed. It was designed to accommodate cylindrical rock plugs with diameters up to 54 mm and thicknesses typically ranging from 5 to 30 mm. It consists of a vertical assembly in which a disk-shaped rock specimen is placed between two identical measurement stacks composed of two high-thermal conductivity disk plates (CW614N brass, 50 mm-diameter; 10-mm-thick) and a reference disk of known thermal conductivity (fused-silica, 50 mm-diameter; 9 mm-thick). Radial bores drilled to the center of the brass plates allow the insertion of type-K thermocouples connected to a high-precision temperature acquisition system (*Pico Technologies* mod. TC-08). Heat is supplied from the lower side of the system by means of a 50 mm-diameter Inconel® 600 (UNS N06600) cylindrical platen heated by a 250 W ceramic band heater controlled through a PID controller (*Inkbird* mod. ITC-100VH). This configuration allows operating temperatures of up to ~500 °C. At the opposite end, heat is removed using an aluminium cooling reservoir connected to a recirculating cryothermostat (*J.P. Selecta Frigiterm*, model TFT-30) capable of maintaining the coolant temperature down to −30 °C, thereby establishing a controlled thermal gradient across the specimen–stack assembly. To minimize thermal contact resistance between components, the system incorporates a loading frame composed of threaded bars and a crosshead that applies a small axial seating load. The entire setup is enclosed within a sealed aluminium bell jar connected to a vacuum pump, which suppresses convective heat transfer and reduces external thermal disturbances.

Under steady-state conditions, the temperatures recorded by the thermocouples in the brass plates are used to determine the heat flux through the fused-silica reference disks and the temperature gradient across the specimen, allowing the axial thermal conductivity of the rock to be calculated according to Fourier's law:

$$q = -\lambda \frac{dT}{dx} \tag{4}$$

where q is the heat flux, λ is the thermal conductivity and dT/dx is the temperature gradient across the specimen.

$$\lambda = \frac{\lambda_c}{2(T_6 - T_5)}\left[\frac{(T_4 - T_5)}{L_1} + \left(\frac{(T_6 - T_7)}{L_3}\right)\right] \tag{5}$$

In Eq.(5), λ_c is the known thermal conductivity of the fused-silica reference disks (1.38 W/m·K), temperatures T_4 and T_5 correspond to the sensors located near the hot side, and T_6 and T_7 to those near the cold side. Likewise, L_1 and L_3 denote the axial separation distances between the corresponding pairs of temperature sensors.

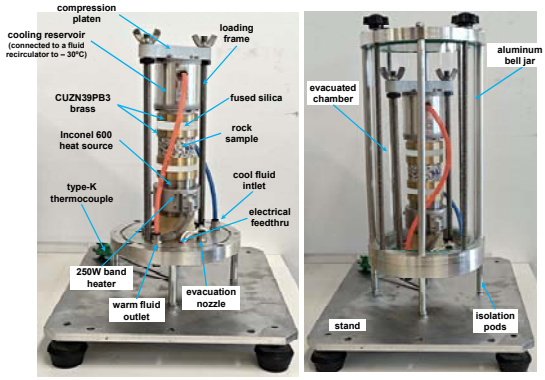


Fig. 3 Split bar thermal conductivity device with the identification of the main elements.

3 Results and discussion

Figure 4illustratesa good fit between the measured and reported heat capacity data of α-Al_2O_3(Furukawa et al., 1956), which was used for verification of the performance of the drop calorimeter. In the same figure we also present the results obtained for up to seven different rock types

which, in addition, have been fitted with the Maier-Kelley function (C_P=A+BT+CT^{-2}; Maier and Kelley, 1932). As expected, we observe that the specific heat of the rocks increases with temperature.

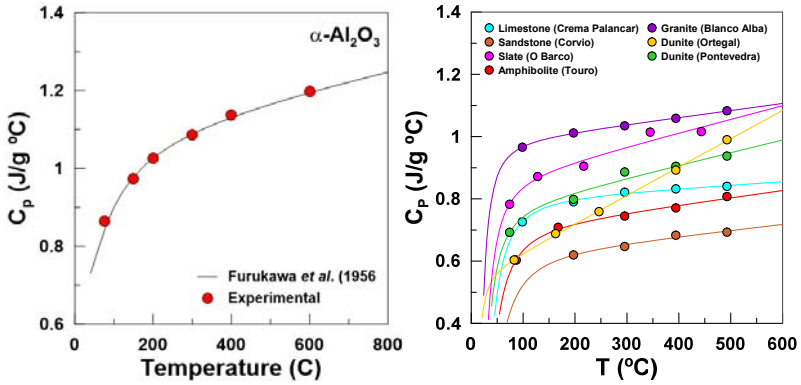


Fig. 4 *Left*: Comparison of specific heat capacity of α-Al_2O_3 measured (dots) and reported by Furukawa *et al*. (1956) (line). *Right*: $C_p$of different rocks (dots) and fitting with the Maier-Kelly function.

The limestone (*Crema Palancar*) shows C_p values between 0.73 and 0.85 J g^{-1} $ºC^{-1}$, aligning closely with the reference interval of 0.71–1.72 J g^{-1} $ºC^{-1}$ given by Schön (2015). The sandstone (*Corvio*) displays C_p values between 0.61 and 0.69 J g^{-1} $ºC^{-1}$, slightly below the wide reference range of 0.75 to3.33 J g^{-1} $ºC^{-1}$ reported by Schön (2015). This is likely due to the significant porosity of this rock (~22%) compared with other sedimentary analogues reported in the literature. In contrast, rocks with significant quartz content (such as the *O Barco* slate and the *Blanco Alba* granite) display C_p values (0.78 to 1.02 J g^{-1} $ºC^{-1}$ and 0.97 to 1.08 J g^{-1} $ºC^{-1}$, respectively) that lay towards the upper bound of their range: 0.88 to1.44 J g^{-1} $ºC^{-1}$ for slate and 0.67 to1.55 J g^{-1} $ºC^{-1}$ for granite (Schön, 2015). This behaviour is consistent with the greater heat capacity of quartz compared with other rock-forming minerals. The amphibolite rock (*Touro*) exhibits C_P values between 0.60 and 0.80 J g^{-1} $ºC^{-1}$, slightly exceeding the single reference value of 0.75 J g^{-1} $ºC^{-1}$ reported by Schön (2015). This deviation may reflect differences in amphibole mineralogy or subtle variations in bulk chemistry, both of which affect the heat capacity of mafic rocks. Finally, the two dunite samples (*Ortegal* and *Pontevedra*) show C_p values between 0.60 and 1.10 J g^{-1} $ºC^{-1}$, fully consistent with published ranges for olivine-rich ultramafic rocks, 0.55 to1.09 J g^{-1} $ºC^{-1}$ (Schön, 2015). The previous comparisons are based on the experimental temperature range (~100 to ~600 ºC) and the reported values at 25 ºC. For all studied samples, the classical Maier–Kelley formulation adequately captures the temperature dependence of heat capacity.

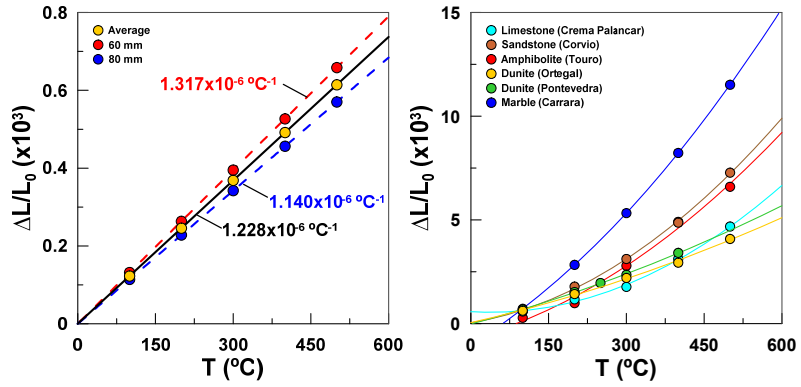


Fig. 5 *Left*: Assessment of the system correction factor for thermal expansion measurements based on two fused-silica rods of 60 and 80 mm-length and their corresponding average. *Right*: Thermal expansion of the different rocks tested.

Figure 5shows assessment of the correction factor applicable to thermal expansion determinations performed with the experimental device based on the observation of two fused-silica rods of different lengths and known α-value (5.5x10^{-7} $ºC^{-1}$). Compared with the actual rock results, we observe that the magnitude of this correction, being relevant, is comparatively small. On the right side of the same figure, the results obtained with the different rocks of interest are also displayed. In general, the data trends can be described well bya third-order polynomial equation (α(T)=A+BT+CT^2), which is considered a sufficient approach to capture the temperature-dependence of Einstein's anharmonicity at moderate temperatures (Blancas et al., 2024).The *Crema Palancar* limestone shows a measured α of 10.1×10^{-6} $ºC^{-1}$, a value close to the lower bound of the reported reference interval (10 to 30×10^{-6} $ºC^{-1}$;

Daoudi, 2025). The *Corvio* sandstone and *Touro* amphibolite exhibit measured α-values of 16.4×10^{-6} ºC^{-1} and 16.5×10^{-6} ºC^{-1}, respectively, both well within their reference ranges (11 to 20×10^{-6} ºC^{-1} (Schön, 2015) and 16 to 32 $\times10^{-6}$ ºC^{-1}(Ma, 2017) respectively. The *Blanco Alba* granite shows a thermal expansion value of 13.9×10^{-6} ºC^{-1}, in line with the reference literature (10 to 16×10^{-6} ºC^{-1}; Schön, 2015) while both dunites (*Ortegal* and *Pontevedra*) display a moderate difference likely due to mineralogical differences or variable serpentinization (with $\alpha= 9.0\times10^{-6}$ ºC^{-1} and 8.4×10^{-6} ºC^{-1} for the *Pontevedra* and *Ortegal* specimens, respectively). In any case, both values fall in the lower bound of the reported range from 8 to 12×10^{-6} ºC^{-1} (Suzuki, 1975). Finally, the *Carrara* marble shows the highest thermal expansion ($\alpha = 27.0\times10^{-6}$ ºC^{-1}) among the tested rocks although closely matching the reference value of ~29×10^{-6} ºC^{-1} (Daoudi, 2025).

The thermal conductivity results obtained with the enhanced divided-bar equipment are presented in Fig.6.On its left-hand side, we present a thermal map of the heating chamber at 300 ºC illustrating the homogeneous temperature distribution in the area of insertion of the specimen. The reported temperatures correspond to those at the mid-height of the combined rock-reference stacks, which is also the location of the mid-height of the tested specimens. It is worth noting that, while for some rocks λ may be represented by a single, constant slope (*e.g.* dunites) for the rest a better fit may be achieved using the Zoth & Haenel (1988) function ($\lambda(T) = A + B(350 + T)$, with T in ºC). For the tested rocks, λ becomes smaller, an aspect already highlighted by other authors (Lee & Deming, 1988).

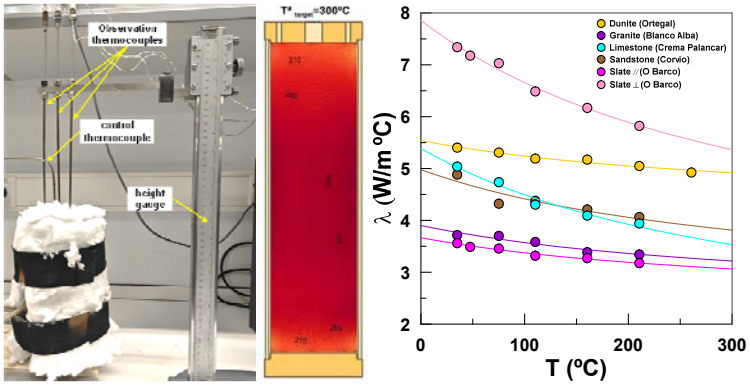


Fig.6 *Left*: Experimental arrangement to obtain temperature maps of the heating chamber; *Center*: Temperature distribution in the heating chamber at 300 ºC; *Right*: Thermal conductivity (λ) results of the studied rocks.

Comparing only 25 ºC data, we see that, for the *Crema Palancar* limestone, thermal conductivity is 13.87 $Wm^{-1}{}^{o}C^{-1}$ while for the *Corvio* sandstone this is 4.93 $Wm^{-1}{}^{o}C^{-1}$, both close to the reference values of 16.2 $Wm^{-1}{}^{o}C^{-1}$and 2.4 to 4.76 $Wm^{-1}{}^{o}C^{-1}$, respectively, reported byRao (2022). The *O Barco* slate reveals a strong thermal anisotropy, with λ- values higher when the specimens are cut parallel to foliation than when perpendicular to it. This behavior has been already documented in the literature (*e.g.* Xiel, 2025). The *Blanco Alba* granite has a thermal conductivity of 3.74 W m^{-1} °C^{-1}, a value consistent with data available in the literature (1.25 to 4.45 W m^{-1} ºC^{-1}; Schön, 2015).Finally, the *Ortegal* dunite exhibits an intermediate conductivity (5.38 W m^{-1} °C^{-1}), also in good agreement with the reference data of 4 to 11.5 W m^{-1} °C^{-1} reported by Zeb (2010). Such value would correspond to an olivine-rich, ultramafic rocks with little serpentinization, as serpentine phases tend to reduce thermal conductivity.

4 Conclusions

The series of experimental devices presented are useful to assess thermal properties of rocks using plug-size specimens at above ambient temperature conditions, expanding and enhancing the limits of the currently available ISRM SM. The results highlight the relevance of mineralogy, porosity, anisotropy, alteration degree, and temperature dependence, demonstrating that these properties cannot be treated as constants. Their determination is therefore essential for engineering applications, as neglecting thermal effects may lead to inaccurate designs, unexpected deformations, or reduced safety, so these tests should be considered mandatory whenever thermal loads are involved.

Acknowledgements

This work has been funded by Repsol S.A. (Near-Wellbore Project). A.M.I. acknowledges support from the European Union's Horizon Europe Research and Innovation programme under the *Marie Skłodowska-Curie* grant agreement No. 101106038. Y.L. gratefully acknowledges the financial support from the *China Scholarship Council* (No. 202206560006).

References

ASTM International (2016) ASTM D4611-16: Standard test method for specific heat of rock and soil. ASTM International, West Conshohocken, PA.

ASTM International (2022) ASTM E228-22: Standard test method for linear thermal expansion of solid materials with a push-rod dilatometer. ASTM International, West Conshohocken, PA

ASTM International (2020) ASTM E1225-20: Standard Test Method for Thermal Conductivity of Solids Using the Guarded-Comparative-Longitudinal Heat Flow Technique. ASTM International, West Conshohocken, PA

Blancas EJ, Lobato Á, Izquierdo-Ruiz F, Márquez AM, Recio JM, Nath P, Plata JJ & Otero-de-la-Roza A (2024). Thermodynamics of solids including anharmonicity through quasiparticle theory. npj Computational Materials 10, 267

Daoudi A, Tadie V, Eslami J, Beaucour AL, Pani C, &Noumowé A (2025) High-temperature performance of limestone-based masonry: Investigations at the material and assembly scales. *Case Studies in Construction Materials* 23, e05361.

Furukawa GT, Douglas TB, McCoske RE & Ginnings DC (1956) Thermal properties of aluminum oxide from 0° to 1,200° K. *Journal of Research of the National Bureau of Standards* 57, 67-82

ISRM (1979) Suggested methods for determining the uniaxial compressive strength and deformability of rock materials. *International Journal of Rock Mechanics and Mining Sciences* 16, 135–140

Labus M, Labus K (2018) Thermal conductivity and diffusivity of fine-grained sedimentary rocks. *Journal of Thermal Analysis and Calorimetry* 132, 1669–1676

Lee Y & Deming D (1998) Evaluation of thermal conductivity temperature corrections applied in terrestrial heat flow studies. *Journal of Geophysical Research* 103, 2447-2454

Ma Z, Tang F, Qi F, & Lian Y (2017) Experimental study on thermal expansion coefficient changing rule of sandstone under high temperature. *Journal of Mining Science and Engineering* 1, 019.

Maier GG, Kelley HK (1932) An equation for the presentation of the high-temperature heat content data. *Journal of the American Chemical Society* 54, 3243–3246

Popov Y, Beardsmore G, Clauser C, &Roy S (2016) ISRM Suggested Methods for determining thermal propertiesof rocks from laboratory tests at atmospheric pressure. *Rock Mechanics and Rock Engineering*49, 4179–4207

Rao SE, Ray L, Khan T, & Ravi G (2022) Thermal conductivity, density and porosity of sedimentary and metamorphic rocks from the Lower and Higher Himalaya, Western Himalaya, India. *Geophysical Journal International* 231, 459-473.

Righetti MC, Salvetti G,& Tombari, E (1998) Heat capacity of glycerol from 298 to 383 K. *Thermochimica Acta* 316, 193-195

Schön JH (2015) Physical Properties of Rocks: Fundamentals and Principles of Petrophysics. 2nd Ed. Elsevier, Amsterdam

Suzuki I (1975) Thermal expansion of periclase and olivine, and their anharmonic properties. *Journal of the Physical Society of Japan - Earth Sciences*, 23, 145-159.

White GK (1973) Thermal expansion of reference materials: copper, silica and silicon. *Journal of Applied Physics D Applied Physics* 6, 2070–2078

Xie L, Yu C, Zhang Y, He B, Wang R, & Liu J (2025) Multiscale and quantitative study of thermal conductivity in shale using TDTR measurements and homogenization techniques. *Applied Clay Science*, 267, 107719.

Zeb A, Firdous T, & Maqsood A (2010) Thermophysical properties of dunite rocks as a function of temperature along with the prediction of effective thermal conductivity. *Natural Science* 2, 626-630.

Zoth G & Haenel R (1988) Thermal Conductivity, in *Handbook of Terrestrial Heat-Flow Density Determination*, R. Haenel, L. Rybach& L. Stegena Eds. p. 449-453, Kluwer Acad., Norwell, Mass

Zhu C, Chen C, Yang Y & Qiu N (2022) Experimental study into the factors influencing rock thermal conductivity. *Petroleum Science Bulletin*7, 321-333

Mode I Fracture Toughness Tests of Limestone under High-Temperature Isothermal Condition

Y. Li, M. Herbón-Penabad, A. Muñoz-Ibáñez, J. Delgado-Martín
Centro de Innovación Tecnolóxica en Edificación e Enxeñería Civil (CITEEC)
Universidade da Coruña, A Coruña, Spain
Yan.li@udc.es
0000-0001-8986-3387

Abstract

Understanding the fracture behavior of rocks at elevated temperatures is essential for evaluating the stability of deep geological engineering systems, such as geothermal reservoirs, deep mining excavations, underground energy storage facilities, and nuclear waste repositories. Although many studies have investigated so farthe thermal effects on rock properties, most of them have been conducted on specimens tested only after cooling to room temperature, while fracture data under isothermal, high-temperature conditions remain limited. In this study, an improved pseudo-compact tension (*p*CT) apparatus is presented to determine the mode I fracture toughness (K_{Ic}) of limestone under controlled thermo-mechanical conditions. Specimens of the so-called Crema Palancar limestone has been tested under two thermal paths: isothermal heating (IT), in which specimens were heated and tested directly at the target temperature, and thermal annealing (TA), in which specimens were heated, naturally cooled to room temperature, and then tested. In both cases, the heating rate was 2°C/min, and the target temperatures ranged from room temperature to 600°C. The results show that the thermal path has a significant influence on the measured K_{Ic} of this limestone. Under IT conditions, K_{Ic} first increases and then decreases with increasing temperature, reaching a maximum at ~ 400°C. Under TA conditions, however, K_{Ic} decreases monotonically with increasing treatment temperature. At the same target temperature, the K_{Ic} values obtained under IT conditions are consistently higher than those measured under TA conditions. These contrasting trends indicate that different thermal stress paths govern the initiation, accumulation, and propagation of microcracks, thereby controlling the fracture resistance of limestone. The results highlight that post-treatment fracture tests do not represent the fracture behavior of rocks at elevated temperatures.

Keywords

Mode I fracture toughness, Pseudo-compact tension (*p*CT) test, Thermo-mechanical conditions, Crack initiation and propagation, High temperature conditions.

1 Introduction

With the expansion of deep mining, geothermal energy extraction, underground energy storage, and nuclear waste disposal, rock masses are increasingly exposed to high-temperature conditions (Guo et al., 2023). Temperature can substantially alter rock properties, including strength, elastic modulus, wave velocity, porosity, and crack development. These changes mainly arise from the heterogeneous thermal responses of mineral constituents, which induce incompatible deformation, thermal stress concentration, grain-boundary debonding, and microcrack initiation. In polycrystalline rocks such as granite, thermal expansion mismatch among quartz, feldspar, and mica is especially critical, making fracture behavior highly temperature-dependent. Because tensile crack initiation and propagation govern rock failure and permeability evolution, mode I fracture toughness (K_{Ic}) is a key parameter for assessing the stability and integrity of thermally affected rock masses.

Although the effects of high temperature on rock properties have been widely studied, most existing work has tested specimens after heating them to a target temperature and then cooling them to room temperature, a thermal path referred to here as thermal annealing (TA) (Guo et al., 2023). Some studies have also examined thermal shock (TS), where heated specimens are rapidly cooled to simulate severe thermal disturbance, such as cold-fluid injection during geothermal stimulation (Wong & Liu, 2025). By contrast, fracture behavior under isothermal heating (IT) remains less explored. In IT tests, specimens are heated to and maintained at the target temperature during fracture loading. Such tests are technically challenging because they require stable high-temperature loading, precise thermal control, and effective protection of the measurement system (Zhou et al., 2024a; Zhu et al., 2018).

TA tests measure the residual fracture toughness after thermal damage and cooling, whereas IT tests measure the fracture resistance of rock at elevated temperature, where thermal expansion, crack closure, and stress redistribution remain active. Thus, TA and IT reflect different thermo-mechanical histories. Although K_{Ic} under TA conditions generally decreases with temperature, IT behavior may be more complex due to the competition between thermal damage and temporary crack closure. Therefore, comparing TA and IT is essential to assess whether cooled specimens can represent the in-situ fracture behavior of hot rock masses.In this study, an improved pseudo-compact tension (*p*CT) apparatus was used to measure the K_{Ic} of limestone under high-temperature IT and TA conditions. Specimens were heated at 2 °C/min to temperatures up to 600°C and tested either at temperature or after natural cooling. The aim is to clarify the effect of thermal path on limestone fracture toughness and support more realistic evaluation of high-temperature rock engineering.

2 Methodologies

2.1 Rock materials and specimen preparations

The *Crema Palancar* limestone was used in this study, and its basic mechanical properties are reported in Li et al. (2026). A total of 28 *p*CT specimens were prepared, including 21 specimens for IT tests and 7 specimens for TA tests. For the IT tests, 3 specimens were tested at each temperature from room temperature (25 °C) to 600 °C, while for the TA tests, one specimen was tested at each temperature over the same range. The *p*CT specimens were cut using a high-pressure water jet system, with average dimensions of D = 50.0 mm, B = 25.0 mm, a = 18.0 mm, and b = 45.0 mm. Thus, the a/b ratio was 0.38. The specimen geometry and notation followed Muñoz-Ibáñez et al. (2020).

2.2 Experimental equipment

To determine the K_{Ic} of rocks under isothermal high-temperature conditions, the original *p*CT test configuration was modified, as shown in Fig. 1.The enhanced *p*CT device employs a stepper motor connected to a small backslash planetary gearhead to drive a precision ballscrew connected to the movable jaw at a constant velocity. That provides stable and controllable load/displacement to the tested specimen. To conduct the experiments at above-ambient temperature conditions, the system incorporates a 130 mm-diameter, 150 mm-length Herge 2500W, ceramic band-heater shielded with two thick refractory plates. The heater is regulated with a universal industrial temperature control unit (CJD-9000P) able to be programmed with temperature ramps and PID control based on a type-K thermocouple. The parts of the bench submitted to high temperatures (push rod and pulling jaws) have been manufactured with *Inconel*® 600 steel alloy (UNS N06600), which offers excellent mechanical performance and thermal resistance at high temperatures (yield strength ~90 – 120 MPa at ~600 ºC). As shown in Fig. 1(a), in order to reduce thermal transmission to sensitive parts of the device (e.g.

load cell, LVDT), the *Inconel*® push rod is sleeved with an external SS316 cooling jacket through which a cooling fluid is continuously recirculated with the aid of a 800 W industrial chiller (CW-5000). This cooling arrangement plays a critical role in ensuring both operational safety and measurement reliability during the high-temperature testing.

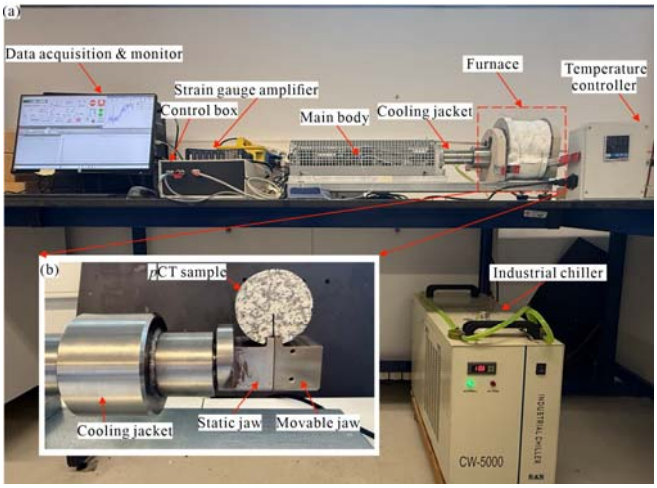


Fig. 1 Photos of the enhanced high-temperature *p*CT testing system: (a) overall view of the apparatus; (b) detailed view of a granite *p*CT specimen and pulling jaws.

Figure 1(b) shows a granite *p*CT specimen positioned inside the furnace. Compared with the original arrangement of the *p*CT test described by Muñoz-Ibáñez et al. (2020), in this enhanced device the sample is self-supported, lying on its weight on top of the pulling jaws. This allows the specimen to self-adjust its position in close groove/pulling jaws contact even when direct visual observation is not possible inside the furnace chamber.

2.3 Experimental procedures

For the IT group, specimens were tested directly in the high-temperature *p*CT apparatus. The furnace temperature was increased at a rate of 2 °C/min to the target temperatures. A separate finite element simulation, based on the specific heat capacity, density, and thermal conductivity of the limestone, showed that under this heating rate the internal and external temperatures of the *p*CT specimen increased synchronously and that the internal temperature field remained relatively uniform. In addition, tests performed at 100 °C, 200 °C, and 400 °C indicated that the holding time (0 – 4 h) at the target temperature did not significantly affect theresults. Even so, each specimen was held at the target temperature for 1 h before fracture testing to ensure thermal homogenization and to allow sufficient time for temperature-induced effects to develop.

For the TA group, specimens were thermally treated in a *Hobersal* muffle furnace with a maximum operating temperature of 1200 °C. The heating rate was the same as that used for the IT group (2 °C/min), but the holding time at the target temperature was extended to 12 h. After thermal treatment, the specimens were removed from the furnace and allowed to cool naturally to room temperature, after which the *p*CT test was carried out under ambient conditions.

For all tests, either IT or TA, the displacement loading rate was maintained at 0.1 mm/min. The applied load P was continuously recorded during the test, and theK_{Ic} was calculated using the expression proposed by Muñoz-Ibáñez et al. (2020) for a 50 mm diameter *p*CT specimen, as shown in Eq. (1) and Eq. (2):

$$K_{Ic} = Y' \frac{P_{\max}}{bB}\sqrt{\pi a} \tag{1}$$

$$Y' = 12.651 - 47.054\left(\frac{a}{b}\right) + 157.72\left(\frac{a}{b}\right)^2 - 247.17\left(\frac{a}{b}\right)^3 + 296.33\left(\frac{a}{b}\right)^4 \tag{2}$$

Where P_{max} Peak value of the applied load during *p*CT test
B Thickness of *p*CT specimen
b Distance from the base of the groove to the bottom of the specimen
a Notch length
Y’ Dimensionless stress intensity factor

3 Results and discussion

Figure 2 presents photographs of the *p*CT specimens after testing at different temperatures for the IT (top) and TA (bottom) groups. In both groups, the apparent color of the specimens changes progressively with increasing temperature, evolving from white at low temperature (25 – 200°C) to grey and then dark grey at higher temperatures (400 – 600°C). A particularly notable feature is observed in the TA specimen treated at 600°C, whose outer surface is partially covered by a whitish layer, while the interior remains dark grey. This surface whitening is likely associated with reactions occurring during cooling and subsequent exposure to ambient moisture, as the whitish layer was not present immediately after the specimen was removed from the furnace. At high temperature, partial decomposition of calcite ($CaCO_3$) may produce lime (CaO), which can subsequently react with moisture in the air during cooling to form portlandite ($Ca(OH)_2$)) (Tomás et al., 2025; Vigroux et al., 2022). This process is accompanied by volume expansion and may promote local surface spalling, thereby exposing the darker interior of the specimen.In addition, the crack pattern observed in the TA specimen treated at 600°C is more complex than that of the corresponding IT specimen, with more pronounced crack branching. This observation suggests that the heating–cooling process generates more severe and heterogeneous damage than isothermal loading.

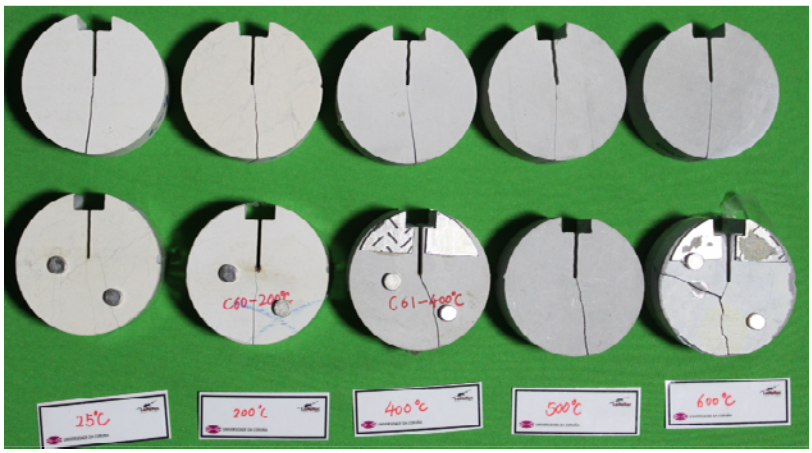


Fig. 2 Photographs of *p*CT specimens after testing under different temperatures for the IT group (top) and TA group (bottom).

The measured K_{Ic} values for limestone under IT and TA conditions are shown in Fig. 3. Although three IT specimens were tested at each temperature, some results are not reported because these tests were considered invalid: failure did not initiate from the tip of the pre-existing notch, and thus no reliable K_{Ic} value could be obtained. Overall, the K_{Ic} values obtained under IT conditions are consistently higher than those measured under TA conditions at the same target temperature. More importantly, the two thermal paths display distinctly different temperature-dependent responses. Under TA conditions, K_{Ic} decreases monotonically with increasing treatment temperature. The decrease before 400°C is relatively mild, whereas a more pronounced reduction occurs between 400 and 600°C.Under IT conditions, in contrast, K_{Ic} first increases and then decreases, reaching a maximum at an intermediate temperature of approximately 400°C. Notably, even at the highest temperature considered (600°C), the K_{Ic} value under IT conditions remains higher than the room-temperature reference value.

The more complex response of K_{Ic} observed under IT conditions can be interpreted as the result of a competition between temporary strengthening and progressive thermal damage while the specimen remains at elevated temperature during loading. Limestone, which is mainly composed of calcite may exhibit anisotropic thermal deformation. During heating, calcite may expand along one crystallographic direction while contracting along another, generating incompatible deformation between adjacent grains and inducing non-uniform thermal stresses within the rock (Rosenholtz & Smith, 1949; Tomás et al., 2025; Wong & Liu, 2025). At relatively low to moderate temperatures (25 –400°C), thermal expansion may partially close pre-existing pores and microcracks, thereby increasing resistance to tensile crack initiation and propagation. This crack-closure effect may explain the initial increase in K_{Ic} under IT conditions. With further increase in temperature (500 – 600°C), however, thermally induced damage becomes progressively more significant (Wang et al., 2025a; Wang et al., 2025b). The anisotropic thermal response of calcite enhances stress concentration around grain boundaries, pores, and cemented contacts, promoting the initiation and growth of new

microcracks. At sufficiently high temperature, partial decomposition of organic components and calcium carbonate may further increase pore development and weaken the internal structure of the rock. Consequently, after reaching a peak value, K_{Ic} decreases because thermal damage gradually outweighs the temporary crack-closure effect.

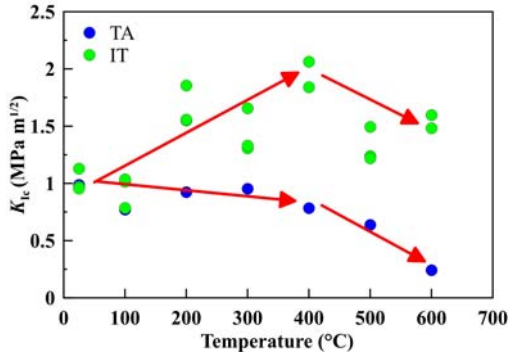


Fig. 3 Measured K_{Ic}values for TA specimens (blue dots) and IT specimens (green dots). The solid lines represent quadratic fitting curves, and the arrows indicate the general trend of each curve.

By contrast, the monotonic decrease in K_{Ic} under TA conditions is mainly associated with the residual thermal damage after cooling. During the heating–cooling process, the anisotropic deformation of calcite persists, and cooling leads to further incompatible shrinkage and stress redistribution. Consequently, microcracks formed during heating may reopen, propagate, or coalesce during cooling, while additional cracks may also develop due to differential contraction between adjacent mineral grains. The fracture toughness measured at room temperature after thermal treatment therefore mainly reflects the cumulative effect of irreversible thermal damage, resulting in a continuous reduction in K_{Ic} with increasing treatment temperature. In contrast, the TA specimens were held in the muffle furnace for 12 h, which is substantially longer than the holding duration used for the IT specimens. This prolonged thermal exposure may also be a contributing factor to the lower K_{Ic} values observed in the TA group, although further investigation is needed to confirm this effect.

Therefore, the difference between the IT and TA results is mainly attributed to their different thermal paths. Direct comparisons between IT and TA conditions remain limited because mechanical testing at elevated temperature is technically challenging. Nevertheless, previous studies support this interpretation. Hu et al. (2023) reported that the K_{Ic} of granite measured at elevated temperature is generally higher than that after thermal annealing, owing to the formation and retention of more irreversible microcracks during cooling. Similarly, Liu et al. (2020) found that sandstone exhibits higher elastic modulus at elevated temperature than after cooling, mainly because pre-existing cracks temporarily close during heating. Although these studies concern different rocks and mechanical parameters, they consistently show that thermal path strongly affects rock mechanical behavior by influencing crack closure, initiation, and accumulation. This agrees with the present limestone results, where K_{Ic} under IT conditions is higher than that under TA conditions at the same target temperature.

4 Conclusions

An enhanced pseudo-compact tension (*p*CT) apparatus has been employed in this study to investigate the mode I fracture toughness (K_{Ic}) of limestone under isothermal, high-temperature conditions and to compare the results with those obtained after thermal annealing treatment. The results show that the thermal stress path has a significant influence on the measured K_{Ic}: At the same target temperature, the K_{Ic} values obtained under TI conditions are consistently higher than those measured under TA conditions. Under TI conditions, K_{Ic} shows a non-monotonic variation with temperature, first increasing and then decreasing, which suggests that the fracture response is controlled by the competition between temporary crack closure and progressive thermal damage. Under TA conditions, however, K_{Ic} decreases monotonically with increasing treatment temperature. This difference is closely associated with the carbonate mineralogy of the limestone, which is dominated by calcite. Owing to its anisotropic thermal deformation, calcite generates non-uniform thermal stresses during both heating and cooling. The cooling stage, in particular, promotes stress redistribution, crack initiation, and crack propagation, thereby explaining the continuous reduction in fracture toughness observed in the TA specimens. At sufficiently high temperatures, possible decomposition of calcium carbonate may further weaken the rock structure. Overall, these results indicate that post-thermal treatment fracture

tests cannot directly represent the fracture behavior of limestone at elevated temperature. The thermal path must therefore be explicitly taken into account when assessing the fracture initiation and propagation of limestone in high-temperature engineering.

Acknowledges

The work has been supported by funds of the project PID2021-126419NB-I00 (FEDER) funded by MCIN/AEI/10.13039/501100011033 and "ERDF A way of making Europe". A.M.I. acknowledges support from the European Union's Horizon Europe Research and Innovation programme under the Marie Skłodowska-Curie grant agreement No. 101106038. Y.L. gratefully acknowledges the financial support from the China Scholar-ship Council (No. 202206560006).

References

Guo P, Bu M, Zhang P, Wang J, Luan Z,He M (2023). Mechanical properties and crack propagation behavior of granite after high temperature treatment based on a thermo-mechanical grain-based model. *Rock Mechanics and Rock Engineering*, *56*(9), 6411–6435. https://doi.org/10.1007/s00603-023-03408-x

Hu Y, Hu Y, Jin P, Zhao G, Zhao Z, Li C (2023). Real-time mode-I fracture toughness and fracture characteristics of granite from 20 °C to 600 °C. *Engineering Fracture Mechanics*, *277*(July 2022), 109001. https://doi.org/10.1016/j.engfracmech.2022.109001

Li Y, Herbón-Penabad M, Muñoz-Ibáñez A, Alejano LR, Alvarellos-Iglesias J, Canal-Vila J,Segura-Serra JM, Delgado-Martín J (2026). Effects of Confining Pressure on Mode I Fracture Toughness Considering Jacketed and Unjacketed Conditions. *Rock Mechanics and Rock Engineering*, *59*(1), 1393–1403. https://doi.org/10.1007/s00603-025-04878-x

Liu W, Zhang L, Luo N (2020). Elastic modulus evolution of rocks under heating-cooling cycles. *Scientific Reports*, *10*(1), 1–9. https://doi.org/10.1038/s41598-020-70920-3

Muñoz-Ibáñez A, Delgado-Martín J, Costas M, Rabuñal-Dopico J, Alvarellos-Iglesias J, Canal-Vila J (2020). Pure mode I fracture toughness determination in rocks using a pseudo-compact tension (*p*CT) test approach. *Rock Mechanics and Rock Engineering*, *53*, 3267–3285. https://doi.org/10.1007/s00603-020-02102-6

Rosenholtz JL, Smith DT (1949). Linear thermal expansion of calcite, var. Iceland spar, and Yule marble. *American Mineralogist: Journal of Earth and Planetary Materials*, *34*(11–12), 846–854.

Tomás R, Benavente D, Martínez-Ibáñez V, Garrido ME (2025). How do high temperatures affect rock properties? A comprehensive review of experimental thermal effects and underlying mechanisms. *Engineering Geology*, *357*(July), 108323. https://doi.org/10.1016/j.enggeo.2025.108323

Vigroux M, Sciarretta F, Eslami J, Beaucour AL, Bourgès A, Noumowé A (2022). High temperature effects on the properties of limestones: post-fire diagnostics and material's durability. *Materials and Structures*, *55*(10), 253. https://doi.org/10.1617/s11527-022-02086-5

Wang C, Zhang Q, He M, Guo S, Jia Y (2025a). Mechanism of fracture process zone development in sandstone and limestone under mode I loading wet-dry cycles and temperature. *Rock Mechanics and Rock Engineering*, *58*(7), 7307–7328. https://doi.org/10.1007/s00603-025-04519-3

Wang C, Meng Q, Lv S, Xiao L, Shen T, Luo L (2025b). Research on the fracture characteristics and thermal-damage mechanisms of coral reef limestone after high-temperature treatment. *Marine Georesources and Geotechnology*, *44*(4), 1–19. https://doi.org/10.1080/1064119X.2025.2550661

Wong LNY, Liu Z (2025). Thermal shock in rocks: A review of mechanisms, impacts, and applications in underground engineering. *Journal of Rock Mechanics and Geotechnical Engineering*, *17*(12), 8172–8197. https://doi.org/10.1016/j.jrmge.2025.01.036

Zhou Q, Zhu Z, Liu W, Lu H, Fan Z, Nie X, Li C, Wang J, Ren L(2024a). Hydraulic fracturing behaviors of shale under coupled stress and temperature conditions simulating different burial depths. *International Journal of Mining Science and Technology*, *34*(6). https://doi.org/10.1016/j.ijmst.2024.06.005

Zhou Q, Zhu Z, Zhang R, Fan Z, Nie X, Gao W, Li C, Wang J, Ren L (2024b). Rock fracture initiation under deep extreme in situ conditions: A review. *Journal of Rock Mechanics and Geotechnical Engineering*, *16*(12), 5297–5324. https://doi.org/10.1016/j.jrmge.2024.02.020

Zhu Z, Tian H, Jiang G, Cheng W (2018). Effects of high temperature on the mechanical properties of chinese marble. *Rock Mechanics and Rock Engineering*, *51*(6), 1937–1942. https://doi.org/10.1007/s00603-018-1426-0

UAV-Based Geostructural Characterization of Discontinuities in a Rock Wall to Support Rockfall Stability Analyses

A. Valletta, S. Khaiiatali & L. C. Mbougoue Mabapgap
Department of Engineering and Architecture - University of Parma, Italy
alessandro.valletta@unipr.it
0000-0001-9126-6717

Abstract

The characterization of discontinuity networks in rock slopes is a fundamental step for assessing block-size distribution and evaluating kinematic feasibility in rockfall modelling. This study focuses on the geostructural analysis of the Groppo Sovrano cliff (Parma, Italy), a sandstone slope located in close proximity Provincial Road SP75 and affected by recurrent block detachments, which hindered the road accessibility and caused its closure. To capture the morphology of the nearly vertical and partially inaccessible rock wall, a high-resolution UAV survey combining photogrammetry and laser scanning was carried out. The integration of these datasets produced a dense, georeferenced 3D point cloud that served as the basis for a detailed structural interpretation. The main families of discontinuities were identified by extracting planar features and subsequent clustering of their orientations by defining virtual scanlines across the point cloud, in order to obtain statistically consistent measurements of discontinuity spacing. The primary objective of the investigation was to quantify block dimensions and provide useful insights for numerical rockfall modelling purposes. With the integration of remote-sensing data, discontinuity mapping, and spacing analysis, the study establishes a coherent framework for the execution of appropriate stability analyses focused on the potential detachment of rock blocks from the cliff, consequently allowing for the identification and planning of mitigation measures to protect the Provincial Road located below the rock wall.

Keywords

Rockfall, Groppo Sovrano, UAV, Discontinuities.

1. Introduction

Rockfalls are commonly defined as a type of landslide that consists of the detachment of a rock block (or several individual rocks) from a vertical or sub-vertical cliff, followed by rapid down-slope motion involving free-falling, bouncing, rolling, and sliding phases (Varnes 1978). Rockfall is the most frequent natural event in mountainous areas, threatening the surrounding environment and generating severe potential for human fatalities within its area of influence (Briones-Bitar et al. 2020). In fact, even though rockfalls have a lower level of economic risk than large-scale landslides, the high velocities associated with these events result in an extremely high risk of injury and loss of life (Ferrari et al. 2016). Therefore, rockfall-related studies, focused on hazard and risk assessment, are of great importance to prevent and reduce critical consequences and to improve disaster mitigation and preparedness capabilities (Ferrero et al. 2016; Scavia et al. 2020), usually supported by advanced monitoring system based on remote sensing and automatic data collection (Valletta et al. 2019; Giacomini et al. 2020; Segalini et al. 2023).

In this context, numerical modelling of rockfall processes represents a fundamental tool for understanding the kinematics and dynamics of falling blocks, as well as for predicting their trajectories, velocities, bounce heights, and runout distances (Li and Lan 2015). Over the last decades, several modelling approaches have been developed to reproduce the complex interaction between falling blocks and the slope surface, allowing a quantitative assessment of rockfall hazard and supporting the design of mitigation measures (Crosta et al. 2015; He et al. 2021). The reliability of these analyses, however, strongly depends on the quality of the input parameters, including slope geometry, block size and shape, and the geostructural features of the rock mass (Umili et al. 2023).

Accurate three-dimensional models of the rock wall are therefore essential for ensuring reliable numerical simulations. A detailed 3D reconstruction enables the precise characterization of discontinuity properties, which control block detachment and the definition of potentially unstable volumes, while simultaneously providing an accurate representation of slope morphology, essential for realistically simulating the phenomenon(Sun et al. 2025).In this framework, remote sensing techniques, particularly those based on Unmanned Aerial Vehicles (UAV), offer significant advantages, enabling the acquisition of high-resolution images and the generation of detailed 3D point clouds and digital surface models (Ferrero et al. 2014; Zhu et al. 2025).

2. Case study description

The Groppo Sovrano rock wall, located in the upper Bratica Valley within the municipality of Monchio delle Corti (Parma, Italy), represents a complex geomorphological setting shaped by long-lasting slope deformation processes. The area extends across elevations between roughly 930 and 1230 m a.s.l., forming a steep rock escarpment on the eastern side of the Sorgroppo ridge (Fig. 1). The present morphology reflects a combination of deep-seated gravitational movements and repeated mass-wasting events that have exposed a significant portion of the local stratigraphic sequence (Vescovi et al. 1998; Chelli and Tellini 2002).

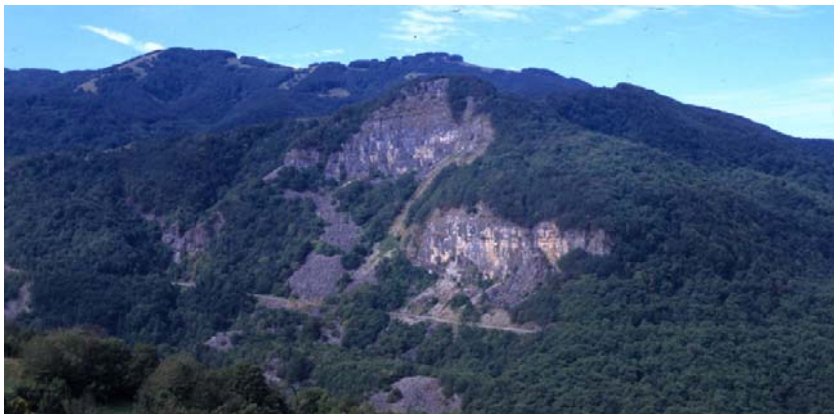


Fig. 1 Frontal view of the Groppo Sovrano rock wall (Source: ER Ambiente website).

At this site, the bedrock mainly consists of the Groppo Sovrano Sandstones, a Lower Eocene turbiditic assemblage belonging to the Ligurian Units. The formation is characterized by very thick and massive

sandstone beds, light grey in color, which alternate irregularly with thin pelitic intercalations ranging from grey to greenish and reddish tones. The sandstone layers commonly exhibit high bioclastic carbonate content, sometimes approaching half of the rock volume, and may include thin microconglomeratic horizons at their basal contacts. Because of these features, the cliff offers a clear and representative exposure of the regional geological framework (Zanzucchi 1980).

The stability of this slope is particularly relevant due to the presence of Provincial Road SP75 at its base. This road, which provides the main connection between the municipalities of Monchio and Corniglio, had to be closed on 10 December 2022 after large blocks detached from the rock wall and reached the roadway. The closure remained in force following technical inspections, as the recurrence of rockfalls makes the definition of mitigation strategies challenging. Furthermore, the upper part of the cliff hosts the only confirmed nesting site of golden eagles in the province, which designates the area as a Special Protection Zone and adds ecological constraints to any engineering intervention.

To analyze the geomechanical conditions of the slope, a detailed remote-sensing campaign was designed. Four complementary surveying techniques were employed in the investigation, each contributing a distinct layer of information to the overall geospatial framework of the study area (Valletta and Segalini 2026). Together, these methods enabled the development of an accurate, high-resolution three-dimensional model of the slope above the SP75 road near Groppo Sovrano, forming the basis for subsequent geomechanical interpretation and rockfall hazard assessment:

- Nadir UAS photogrammetry provided full coverage of the study area, achieving a Ground sampling Distance (GSD) of approximately 1.25 cm/pixel from 100 m altitude. A total of 1,019 images were collected with DJI Zenmuse P1 and DJI Mavic 3 Enterprise sensors, using 80% forward and 70% lateral overlap. Automated flight planning ensured constant altitude above ground and consistent image geometry despite complex topography.
- Oblique UAS photogrammetry complemented the nadir survey by capturing near-vertical rock faces above the SP75 corridor, enabling accurate reconstruction of cliff morphology and identification of key discontinuity sets influencing slope kinematics.
- UAV-based LiDAR scanning was crucial in vegetated areas, providing multi-return data capable of penetrating canopy cover to reconstruct the bare-earth surface. Thirteen overlapping flight lines ensured proper strip alignment, while processed/classified point clouds enabled the creation of a high-quality Digital Terrain Models (DTM).
- High-accuracy GNSS measurements established the geodetic reference frame. These data supported bundle adjustment, improving camera alignment and ensuring geometric consistency between photogrammetric and LiDAR datasets.
-

All aerial acquisitions were completed on 10 July 2023, during midday hours, to ensure optimal illumination of the vertical surfaces and to minimize the presence of shadows that could degrade image interpretability. The integrated approach made it possible to characterize both the morphology of the slope and the structural framework of the rock mass, delivering a three-dimensional model suitable for the geostructural characterization of the area of interest and the subsequent rockfall trajectory modelling.

3. Results and Discussion

3.1. Identification of discontinuity sets

The primary objective of this phase was to identify and characterize the discontinuity planes that condition block detachment mechanisms and govern the overall stability of the cliff. The extraction of structural features was performed directly on the LiDAR-generated point cloud, which provided the desired density and geometric accuracy to detect even small-scale discontinuities across the exposed rock face. Planar segments were identified through clustering and surface fitting procedures, allowing the computation of orientation parameters (i.e., dip and dip direction) for each detected discontinuity. This analysis was carried out using dedicated tools for planar feature extraction and normal vector estimation integrated into the *CloudCompare* software. The selected discontinuity planes were subsequently represented in a stereonet using the *Rocscience DIPS* software, in order to define the discontinuity systems characterizing the rock mass and derive the orientation values for the mean planes. The result of this process is summarized in Fig. 2.

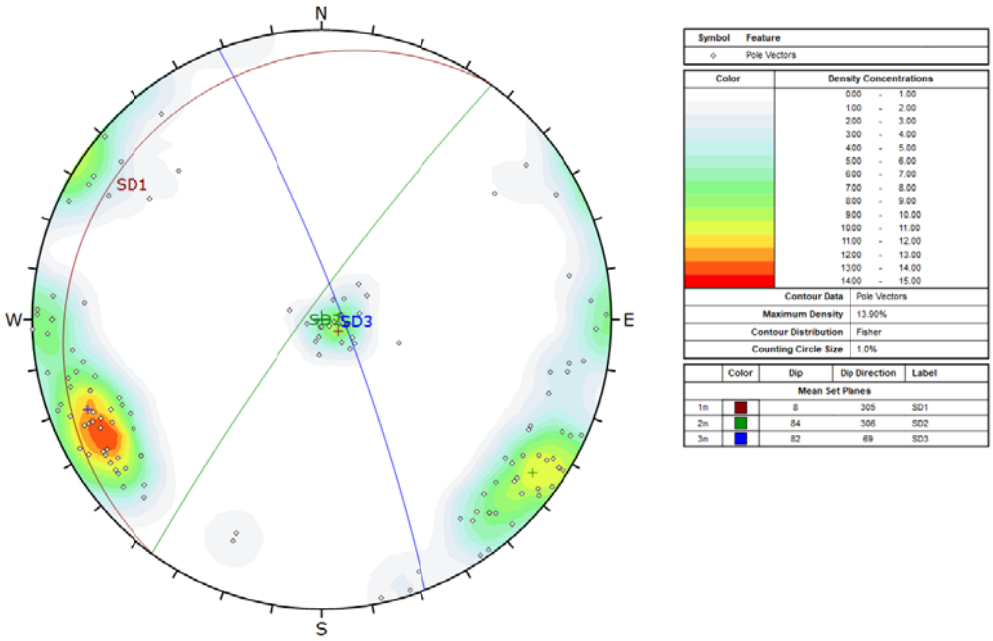


Fig. 2 Stereonet representation of the discontinuities, and related sets, identified on the point cloud.

The dataset reveals one sub-horizontal set (SD1) and two sub-vertical sets (SD2 and SD3), indicating a well-defined structural framework dominated by steeply dipping discontinuities. The combination of near-vertical planes intersecting a horizontal set may facilitate the formation of prismatic or tabular blocks, directly influencing the kinematics and likelihood of rockfall detachment.

3.2. Kinematic analysis

A kinematic analysis was performed to assess the susceptibility of the investigated rock slope to specific failure mechanisms based on the geometrical relationship between discontinuity sets and the slope face. In particular, the Markland test was applied as a rapid and effective method to evaluate the feasibility of failure modes by analyzing the spatial distribution of discontinuity plane intersections in stereographic projection.

For the case study under investigation, the analysis focused on block toppling mechanisms (direct toppling). This approach considers the position of the intersection lines between discontinuity planes with respect to the slope orientation, allowing the identification of three critical kinematic domains that define a zone corresponding to direct toppling (red area) and a zone related to oblique toppling (yellow area), as displayed in Fig. 3. The test was carried out assuming a slope face orientation of 85/127, derived from the point cloud analysis, and an internal friction angle of φ = 38°.

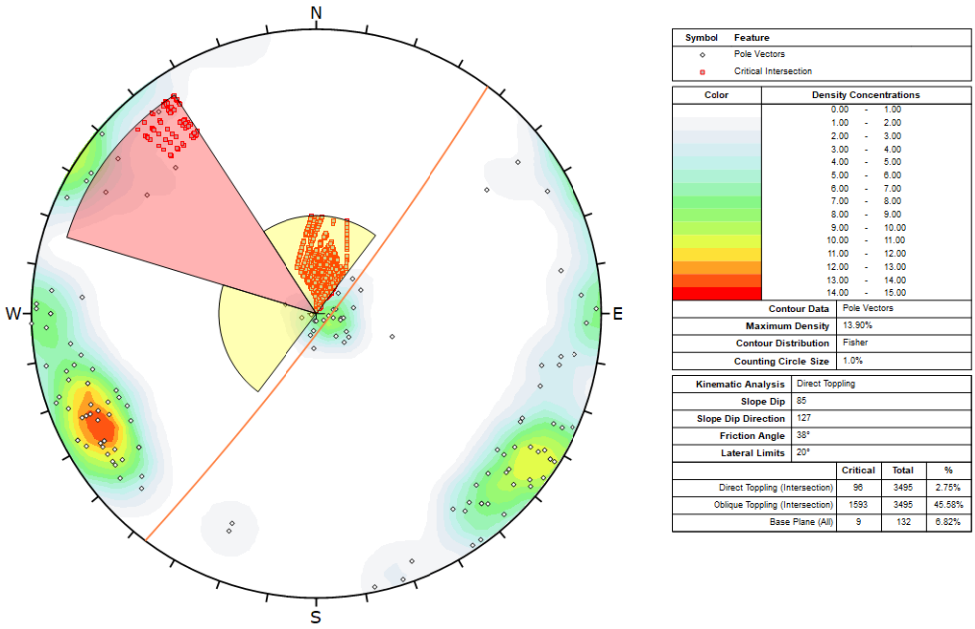


Fig. 3 Result of the kinematic analysis (Markland Test) performed on available data.

The results of the kinematic analysis indicate a significant concentration of discontinuity intersections within the oblique toppling domain, suggesting a pronounced susceptibility of the rock mass to this type of failure mechanism. Additionally, a smaller number of intersections fall within the direct toppling domain, indicating the potential occurrence of complex failure processes involving both mechanisms. The analysis highlights the dominant role of structurally controlled toppling instabilities, with oblique toppling representing the most likely failure mode in the examined slope.

3.3. Discontinuity spacing and block volume evaluation

Subsequently, scanline analyses were performed directly on the point cloud to evaluate discontinuity spacing. A set of virtual measurement transects was defined with orientations perpendicular to each of the three identified discontinuity sets, ensuring the correct assessment of apparent spacing along representative directions. The high resolution of the point cloud allowed the accurate identification of intersection points between the scanlines and the detected discontinuity planes, from which spacing values were derived. The analysis was then carried out in *DIPS* software, where progressive distances along each scanline were assigned and the integrated tools were used to compute statistically representative mean spacing values for each discontinuity set. The results of this analysis are summarized in Table 1.

Table 1 Geometrical features of the discontinuity sets identified on the rock wall.

Name	Dip/Dip direction (°)	Orientation	Mean spacing (m)	Standard deviation (m)
SD1	08/305	Sub-horizontal	1.07	0.65
SD2	84/306	Sub-vertical	1.20	0.51
SD3	82/069	Sub-vertical	1.12	0.45

Moreover, the cumulative frequency distributions of discontinuity spacing (Fig. 4) provide further insight into the variability and statistical distribution of the measured values. All three discontinuity sets show a progressive increase in cumulative frequency, indicating a relatively continuous distribution of spacing without pronounced clustering at specific values. In general, most of the spacing values for all sets fall within the range of approximately 0.5 m to 2.0 m, with cumulative frequencies exceeding 80% within this interval.

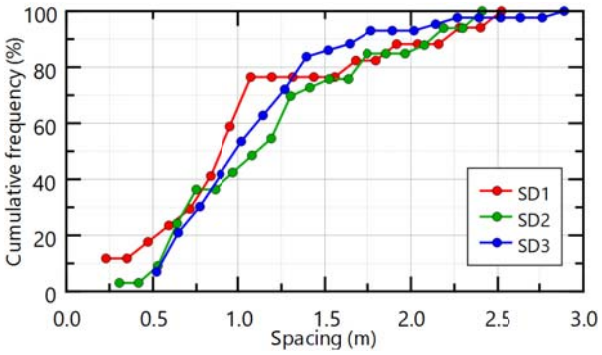


Fig. 4 Cumulative frequency of discontinuity spacing.

Based on the obtained mean spacing values, a preliminary estimation of the representative block size was carried out. Assuming a prismatic block geometry controlled by the three discontinuity sets, the average block dimensions can be obtained from the corresponding spacing values, resulting in a mean block volume of approximately 1.44 m³. In addition to the mean value, an upper-bound block size can be defined using the 90th percentile (P90) of the spacing distribution. The P90 represents the value below which 90% of the observed data fall and can be considered a realistic yet conservative estimate of extreme conditions. In this study, the combined variability of the three discontinuity sets was accounted for by assuming a lognormal distribution of spacing. Under this assumption, the P90 block volume is approximately 2.90 m³. These volumetric values provide a first-order quantitative constraint for subsequent rockfall simulations and energy-based hazard assessments.

4. Conclusions

This study presented an integrated workflow for the geostructural characterization of the Groppo Sovrano rock slope (Parma, Italy) to support rockfall stability analyses, combining UAV-based photogrammetry and point cloud processing. The adopted approach enabled the generation of a high-resolution 3D model of the rock wall, overcoming the limitations of conventional field surveys in

steep and inaccessible areas.The selected case study represents a representative example of a structurally controlled rock slope in a mountainous environment, where rockfall processes pose a significant hazard to the surrounding area, thus providing a meaningful context for testing and validating the proposed methodology.

The extraction of discontinuity planes directly from the point cloud allowed the identification of three main sets, including one sub-horizontal (SD1) and two sub-vertical (SD2 and SD3), defining the structural framework of the rock mass. The kinematic analysis, based on the Markland test, highlighted a marked susceptibility of the slope to structurally controlled instabilities, with failure modes associated with both oblique and direct toppling. Finally, spacing analysis performed through virtual scanlines and processed with appropriate tools provided representative mean values for each set, supporting a preliminary estimation of spacing frequency and block dimensions.

Overall, the results confirm the importance of accurate 3D models for the reliable characterization of discontinuities and slope geometry, which are essential inputs for rockfall simulations. The integration of UAV data with dedicated analysis tools represents an effective and reproducible approach for improving hazard assessment and supporting the development of mitigation strategies.

Acknowledgements
This research was conducted within the framework of the agreement *"Rilievo geomeccanico, analisi di stabilità e valutazione della pericolosità del tratto di strada provinciale prospicente l'abitato di Groppo Sovrano"*, between the University of Parma and the Province of Parma, Italy.

References

Briones-Bitar J, Carrión-Mero P, Montalván-Burbano N, Morante-Carballo F (2020) Rockfall Research: A Bibliometric Analysis and Future Trends. Geosciences 10(10). https://doi.org/10.3390/geosciences10100403

Chelli A, Tellini C (2002) Geomorphological features of the Bratica Valley (Northern Apennines, Italy). Geografia Fisica e Dinamica Quaternaria 25(1):45–60

Crosta GB, Agliardi F, Frattini P, Lari S (2015) Key Issues in Rock Fall Modeling, Hazard and Risk Assessment for Rockfall Protection. In: Lollino G, Giordan D, Crosta GB, Corominas J, Azzam R, Wasowski J, Sciarra N (eds) Engineering Geology for Society and Territory - Volume 2. Springer International Publishing, Cham, pp 43–58

Ferrari F, Giacomini A, Thoeni K (2016) Qualitative Rockfall Hazard Assessment: A Comprehensive Review of Current Practices. Rock Mech Rock Eng 49(7):2865–2922. https://doi.org/10.1007/s00603-016-0918-z

Ferrero AM, Migliazza MR, Pirulli M, Umili G (2016) Some Open Issues on Rockfall Hazard Analysis in Fractured Rock Mass: Problems and Prospects. Rock Mech Rock Eng 49(9):3615–3629. https://doi.org/10.1007/s00603-016-1004-2

Ferrero AM, Migliazza MR, Umili G (2014) Rock Mass Characterization by Means of Advanced Survey Methods. OnePetro

Giacomini A, Thoeni K, Santise M, Diotri F, Booth S, Fityus S, Roncella R (2020) Temporal-Spatial Frequency Rockfall Data from Open-Pit Highwalls Using a Low-Cost Monitoring System. Remote Sensing 12(15). https://doi.org/10.3390/rs12152459

He Y, Nie L, Lv Y, Wang H, Jiang S, Zhao X (2021) The study of rockfall trajectory and kinetic energy distribution based on numerical simulations. Nat Hazards 106(1):213–233. https://doi.org/10.1007/s11069-020-04457-z

Li L, Lan H (2015) Probabilistic modeling of rockfall trajectories: a review. Bull Eng Geol Environ 74(4):1163–1176. https://doi.org/10.1007/s10064-015-0718-9

Scavia C, Barbero M, Castelli M, Marchelli M, Peila D, Torsello G, Vallero G (2020) Evaluating Rockfall Risk: Some Critical Aspects. Geosciences 10(3):98. https://doi.org/10.3390/geosciences10030098

Segalini A, Valletta A, Carri A, Savi R (2023) Impact identification on flexible rockfall barriers: on site test of a wireless monitoring system. IOP Conf Ser: Earth Environ Sci 1124(1):012125. https://doi.org/10.1088/1755-1315/1124/1/012125

Sun J, Zhu S, Sun J, Zhou J, Yao Y, Wang Y, Zhang J, Zhou B, Wang X (2025) A robust deep learning approach for rock discontinuity identification from large scale 3D point clouds. Sci Rep 16(1):1654. https://doi.org/10.1038/s41598-025-31137-4

Umili G, Taboni B, Ferrero AM (2023) Influence of uncertainties: A focus on block volume and shape assessment for rockfall analysis. Journal of Rock Mechanics and Geotechnical Engineering 15(9):2250–2263. https://doi.org/10.1016/j.jrmge.2023.03.016

Valletta A, Carri A, Segalini A (2019) Innovative monitoring instruments as support tools for natural risks management. ROL 48/2019. https://doi.org/10.3301/ROL.2019.44

Valletta A, Segalini A (2026) Risk assessment of the Groppo Sovrano rock wall: interaction between rockfall dynamics and a Provincial Road through 3D analysis. Transportation Research Procedia 93:793–799. https://doi.org/10.1016/j.trpro.2025.12.005

Varnes D (1978) Slope movement types and processes. In: Schuster RL, Krizek RJ (eds) Landslide analysis and control. Transportation Research Board, Special report 176. National Academy Sciences, Washington, DC, pp 11–33

Vescovi P, Villa G, Barbieri G (1998) L'unità tettonica Groppo Sovrano (alta Val Bratica - Provincia di Parma). Atti Ticinensi di Scienze della Terra 40:15–31

Zanzucchi G (1980) I lineamenti geologici dell'Appennino parmense. Note illustrative alla carta e sezioni geologiche della provincia di Parma e zone limitrofe (1:100.000). STEP, Parma, Italy

Zhu R, Xia Y, Zhang S, Wang Y (2025) Stability Assessment of Hazardous Rock Masses and Rockfall Trajectory Prediction Using LiDAR Point Clouds. Applied Sciences 15(12). https://doi.org/10.3390/app15126709

Artificial fracture generation and surface roughness quantification in brittle rocks

T. Nikiema, N. Gonze, JP. Tshibangu & F. Descamps
University of Mons, Faculty of Engineering, Mons, Belgium
tegawende.nikiema@umons.ac.be
0000-0003-2079-2087

Abstract

Understanding the mechanical behaviour of rock masses is essential for the design and stability of infrastructures such as tunnels, slopes, and underground storage facilities. At these scales, discontinuities largely govern the global response of the rock mass. To investigate their behaviour, researchers typically adopt two approaches: working on natural fractures or on artificial ones. Natural fractures provide realistic conditions but pose significant challenges, both in terms of sampling and reproducibility. Artificial fractures, on the other hand, offer better control. They can be either molded from natural fracture surfaces, preserving geometry but losing the original rock nature and behaviour, or generated directly in the laboratory, which risks damaging the specimen. In this study, we focus on producing laboratory-induced fractures under controlled conditions to maintain the integrity of the rock.

Fracture initiation and propagation depend on the loading conditions, the mechanical properties, and the mineralogical composition of the rock. In this work, to produce fractures that preserve the morphology of natural rock splinters, an original methodology is developed to generate tensile fractures in rock samples using a 285 kN compression frame equipped with a blade-jaw system. This setup was tested on prismatic specimens of Soignies Limestone and Vosges Sandstone. These two rocks exhibit brittle behaviour under atmospheric conditions but differ markedly in porosity, stiffness, and strength (high to moderate), leading to distinct fracture patterns.

Optical profilometry is used to accurately characterize the geometry of fracture surfaces. Statistical roughness parameters and the Joint Roughness Coefficient (JRC) were used to quantify and compare the surface roughness of both rocks and assess the variability of laboratory generated fractures.

The methodology will play a key role in future work that will focus on linking joint geometry with the mechanical response of fractured rocks under controlled loading conditions.

Keywords

Laboratory-induced fractures, Soignies Limestone, Vosges Sandstone, Statistical roughness parameters, Joint Roughness Coefficient (JRC).

1 Introduction

Rock mass behaviour is strongly controlled by the presence and geometry of discontinuities such as joints, fractures, and bedding planes. These discontinuities govern the mechanical response, deformation mechanisms, and hydraulic properties of rock masses and therefore play a critical role in the design and stability assessment of underground structures, slopes, and foundations. A key parameter controlling the mechanical behaviour of rock joints is surface roughness, which influences shear strength, dilation, and contact mechanics.

Experimental investigation of joint behaviour requires representative fracture surfaces. In the literature, some have focused on understanding the mechanical behaviour of natural rock fractures (Schneider 1976; Krahn and Morgenstern 1979; Bandis et al. 1983; Huang et al. 1993), but their sampling is often difficult. In addition, natural fractures exhibit significant variability in geometry (roughness, orientation, and dipping), imbrication or opening, overlapping, filling materials, and weathering conditions. These factors make systematic laboratory investigations challenging. To overcome these limitations, artificial fractures are often generated in a laboratory to reproduce joint surfaces under controlled conditions. Several approaches have been used for this purpose, including sawing (Krahn and Morgenstern 1979), molding of natural surfaces (Schneider 1976), controlled splitting (Giwelli et al. 2009), or hydraulic fracturing (Huang et al. 1993). More recently, additive manufacturing techniques have been used to reproduce rock joints (Jaber 2020). While these methods allow the production of discontinuities, they often suffer from limitations such as unrealistic surface morphology, poor reproducibility, or alteration of the rock microstructure.

Establishing reproducible laboratory methods that yield realistic and complementary fracture surfaces remains an open challenge. In this context, the current study investigates a controlled fracturing technique using a blade-jaw system. The method aims to generate complementary fracture surfaces in prismatic rock samples while minimizing material loss and preserving surface morphology, under repetitive conditions. Two lithologies with contrasting mechanical and petrophysical properties were selected to evaluate the robustness of the method: Soignies Limestone and Vosges Sandstone.

The fracture surfaces are then characterized using optical 3D profilometry to quantify surface morphology. Statistical roughness parameters and Joint Roughness Coefficient (JRC) values are derived from surface profiles to evaluate surface characteristics and directional variability.

2 Methods

2.1 Sample description

Two rock types were selected for this study: Soignies Limestone (SL) and Vosges Sandstone (VS), chosen for their availability, relative homogeneity, and contrasting mechanical properties. Soignies Limestone is a compact rock with a porosity of 0.4% and a high compressive strength (UCS typically ranging between 100 and 125 MPa). It consists mainly of $CaCO_3$ (>95%) and displays a micritic texture (Descamps et al. 2011). In contrast, Vosges Sandstone is more porous (≈22%), moderately strong (UCS≈40 MPa), with a granular texture (100 – 150 μm) and a silica content ranging from 70 to 95% (Descamps 2007). Under atmospheric conditions, both rock types exhibit elastic–brittle behaviour (Descamps 2007, Descamps et al. 2011). As sedimentary rocks, both contain bedding planes, but their mechanical behaviour can be considered isotropic.

2.2 Artificial fracture generation

Fracturing was performed using a blade–jaw system (Fig. 1a). The device consists of two tungsten steel blades (10 cm long) forming a loading jaw. The blade tips are V-shaped and fit into pre-machined grooves in the specimen. The upper blade slides along two guiding columns and is connected to a loading platen that applies the load. A ball joint incorporated into the upper platen ensures uniform load distribution along the blade–specimen contact. The lower blade is in contact with a lower platen transmitting the applied load.

The overarching research objectives aim to address the mechanical behaviour of fractures by performing compression and direct shear tests. Particularly for shear tests, ISRM recommendations and ASTM standards provide guidelines for the general sample geometry (Ulusay 2015; ASTM D18 Committee 2017). Coupled with practical constraints of the laboratory, the sample size for the current

study was defined to allow subsequent mechanical testing, with dimensions of 95 × 60 × 60 mm. The fracture surface corresponds to the 95 × 60 mm section.

Lateral grooves (3–4 mm deep) were machined along the edges to initiate and guide fracture propagation, resulting in a slightly reduced effective fracture area. Guiding the fracture in the middle of the block was also necessary to allow further compression and direct shear tests.

Fig. 1b illustrates a fractured surface wall, with a profilometric scan highlighting height variations of the surface.

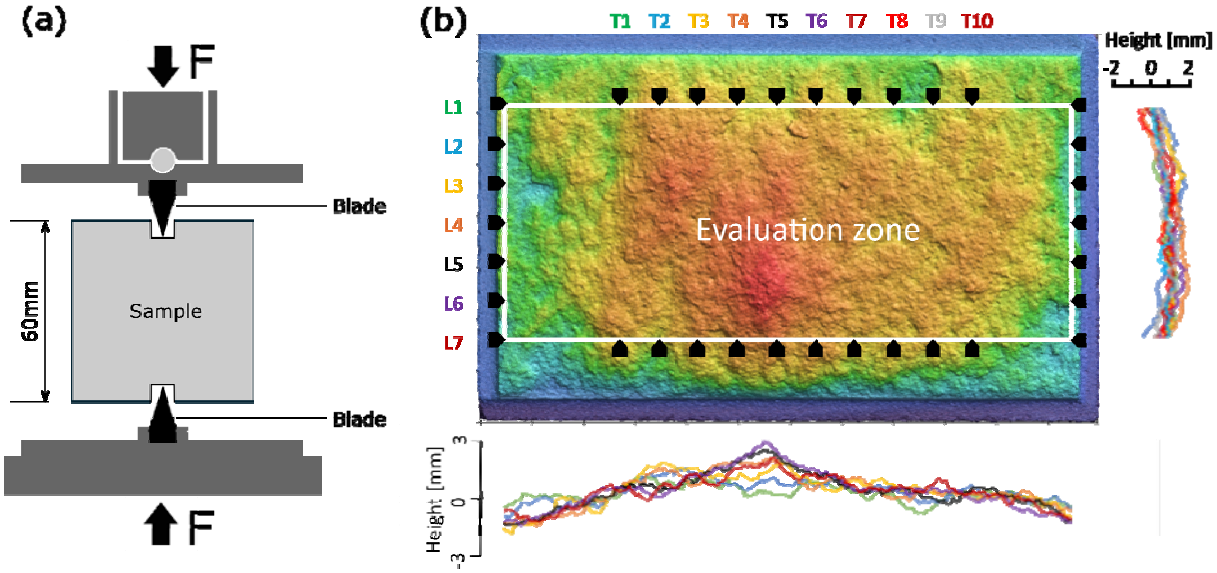


Fig. 1 a) Blade-jaw controlled fracturing system, F is the direction of controlled load application. b) Fracture surface wall with the evaluation area delineated by a white rectangular outline, and the positions of the profiles indicated by black arrows. Roughness profiles are traced in longitudinal and transversal directions.

2.3 Optical profilometric analysis of roughness

Fracture surface roughness was analysed using a Keyence VR-6200 3D optical profilometer, which measures surface topography through structured light projection. The instrument provides a spatial resolution of ±5 µm in the horizontal directions and ±4 µm in the vertical direction.

Each fracture wall was analysed separately. To reduce edge effects caused by the grooves and damage resulting from stress concentration near the blades, an evaluation zone was defined, excluding margins up to11 mm along the longitudinal edges and up to17.5 mm along the transversal edges (Fig. 1b). Within this zone, linear profiles were evenly distributed. Seven longitudinal profiles (L1–L7) with lengths ranging from 80 to 91 mm and ten transversal profiles (T1–T10) with lengths of about 38 mm were extracted. Roughness profiles traced in longitudinal and transversal directions overlap in each direction.

Four common statistical roughness parameters are computed for each profile (Tatone and Grasselli 2010; Nikiema et al. 2024): the absolute roughness (R_z), the arithmetic roughness (R_a), the root mean square slope (Z_2), and the linear roughness (R_L) or roughness profile index (R_p). Z_2 and $R_p$are correlated with Barton's Joint Roughness Coefficient (JRC), the most widely used roughness index in geomechanics for the assessment of rock mass stability. Eq.1 and Eq.2 were proposed by Nikiema et al.(2024):

$$JRC = 65.25Z_2 - 11.21 \qquad R^2 = 0.935 \qquad (1)$$

$$JRC = 238.6R_p - 240.57 \qquad R^2 = 0.924 \qquad (2)$$

3 Results

3.1 Analysis of fracture quality

Fifteen specimens of SL and seven specimens of VS were successfully split without any sample loss. The resulting fractures generally followed the predefined plane, with only minor local deviations, and

no unusable fracture surfaces were produced. Mass measurements performed before and after fracturing indicate a very limited material loss, ranging from 0 to 4 mm³/cm² over the fractured area for both rock types. Moreover, most of the fractured samples show complementary walls that fit closely together, indicating that the fracturing process preserves the morphological correspondence between the two sides of the joint.

As expected, the linear splitting load is higher for SL than for VS, with mean values of 21 N/mm (coefficient of variation (CV): 21.79%) and 9 N/mm (CV: 6.15%), respectively. This difference reflects the contrasting mechanical behaviour.

The fracture morphology varies with rock type. In VS, fracturing appears predominantly intergranular, which is consistent with its granular grain size. In contrast, SL is characterized by a micritic texture and mainly exhibits fracture propagation through the matrix.

3.2 Surface roughness by optical profilometry

Five specimens of each rock were randomly selected for detailed analysis. Three longitudinal and four transversal profiles were extracted per wall to ensure representative coverage. Lower wall roughness values were plotted against upper wall values to evaluate morphological correspondence relative to a 1:1 identity line (Fig. 2). The upper and lower walls were randomly assigned to each specimen.

In the longitudinal direction and for both rocks, amplitude parameters (R_a,R_z) exhibit an excellent fit (R^2: $0.97 - 1.00$), demonstrating strong linear correlation between paired fracture walls. Slope and profile index parameters (Z_2,R_p) show moderate linear correlation (R^2: $0.60 - 0.70$) due to relatively compact clusters around the correlation line. This morphological agreement is validated by Lin's concordance coefficient ($CCC > 0.90\ for\ R_a\ and\ R_z$, except for R_z in SL ($CCC = 0.79$). The relative quadratic error from the 1:1 identity line remains low ($0\,\% - 3\,\%$ for SL ; $1\,\% - 11\,\%$ for VS), confirming that absolute deviations are minor and that roughness variability between corresponding walls is limited.

The transversal direction displays a more pronounced dispersion. For R_a, SL data are asymmetric with most points located in the upper triangular region and scattered ($\mathrm{CCC} = 0.66, \mathrm{error}: 24\,\%$), whereas VS data are more evenly distributed despite a low concordance ($\mathrm{CCC} = 0.17, \mathrm{error}: 66\,\%$). Conversely, R_z maintains high correlation ($R^2 \geq 0.98$) and good concordance ($\mathrm{CCC}: 0.74 - 0.85, \mathrm{error}: 15\,\% - 16\,\%$), indicating that peak-to-valley amplitudes are corresponding between the fracture walls. Although Z_2 and R_p yield very low relative quadratic errors (1 %), they exhibit low concordance (CCC<0.40) due to highly clustered data points, reflecting local slope disparities. Local deviations observed for specimens SL14, VS26, and VS29 are linked to local discrepancies, such as an intact fossil shell in SL14. Furthermore, transversal profiles are much shorter than longitudinal ones. This may amplify the observed differences.

JRC was computed from Z_2 and R_L, using Eq. 1 and 2. For longitudinal profiles, JRC ranges from 6 to 9 for SL (mean: 7, CV: 11 %), and from 10 to 12 for VS. Transversally, JRC ranges from 6 to 15 for SL (mean: 9, CV: 25 %), and from 11 to 15 for VS (mean: 12, CV: 10 %).

To assess the representativeness of the laboratory-induced surfaces, these results were compared with those obtained from eight natural fracture surfaces (Table 1). Most parameters fall within the range measured on laboratory-induced fractures, except R_z, which reaches higher values on natural surfaces, indicating a great amplitude difference in natural surfaces.

Finally, comparing longitudinal and transversal profiles (Fig. 2i and j) shows that the distribution of data points is not correlated between the two measurement directions, indicating directional heterogeneity in fracture surface roughness.

Table 1. Measurements of roughness on natural fractures for both rock types.

Rock type	$\boldsymbol{R_a}[\mu\boldsymbol{m}]$	$\boldsymbol{R_z}\ [\mu\boldsymbol{m}]$	$\boldsymbol{Z_2}\ [-]$	$\boldsymbol{R_p}\ [-]$
Soignies Limestones	1356 ± 227	6341 ± 1437	0.340 ± 0.036	1.051 ± 0.009
Vosges Sandstones	524 ± 125	2588 ± 366	0.293 ± 0.015	1.039 ± 0.003

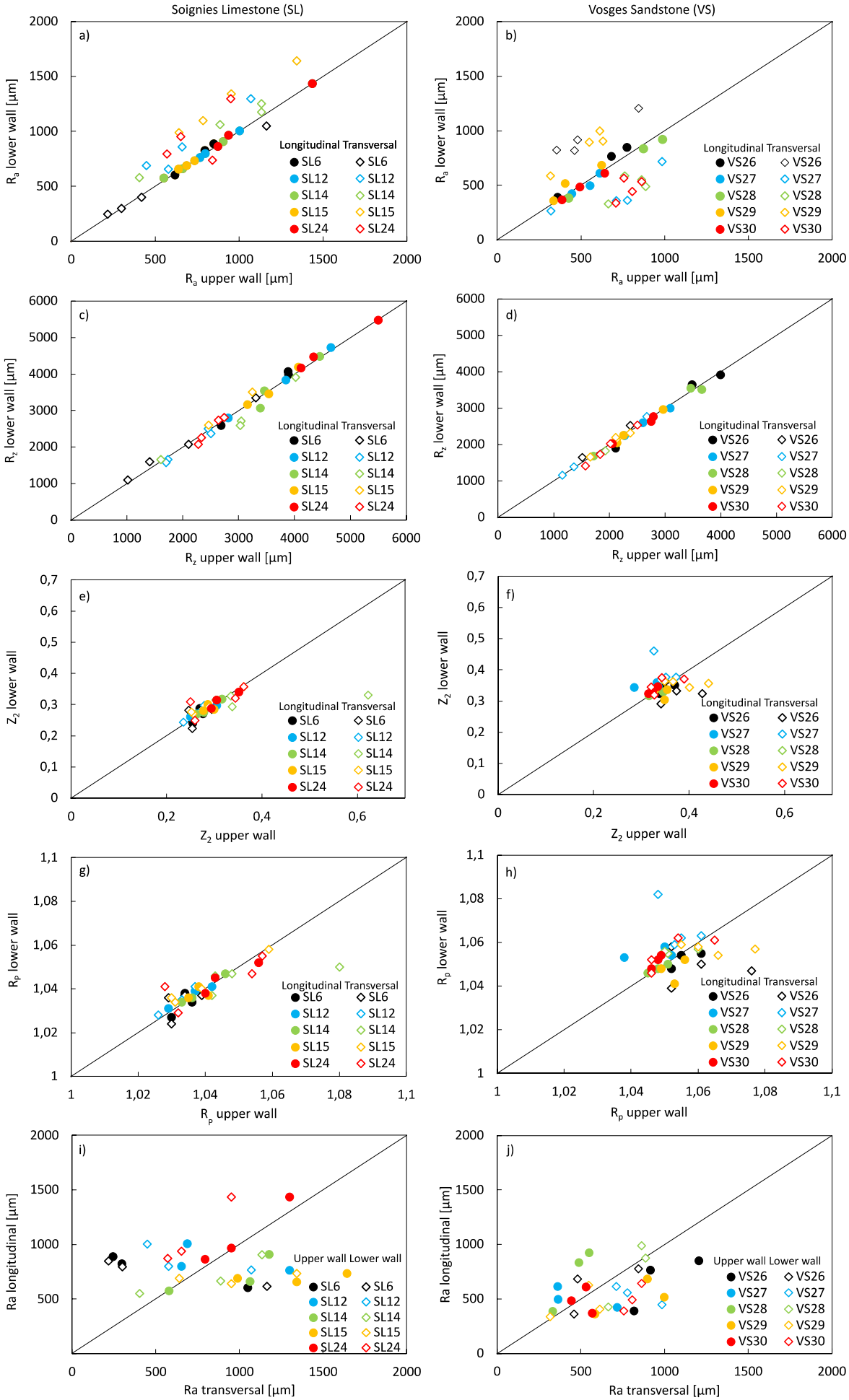


Fig. 2 Relationships between the roughness parameters (R_a, R_z, Z_2, R_p) measured on the two corresponding fracture walls for Soignies Limestone (a, c, e, g,i) and Vosges Sandstone (b, d, f, h, j) in both longitudinal and transversal directions.

4 Conclusion

This study presented an experimental method for generating artificial fractures in rock specimens using a blade-jaw controlled system. Soignies Limestone and Vosges Sandstone, which feature contrasting petrophysical and mechanical properties, were investigated to assess the method's applicability. Surface quality analysis shows that the fracture mostly follows the predefined plane imposed by the grooves, with very limited material loss.

Optical profilometry was used to characterize roughness parameters both on longitudinal and transversal profiles. The results are consistent with roughness parameters measured on natural fractures for the same rocks.

Nevertheless, several limitations remain. The influence of experimental parameters, such as loading rate and groove geometry, has not been thoroughly investigated. Further work should combine the geometric characterization of fracture surfaces with mechanical testing to establish quantitative relationships between roughness parameters and joint mechanical behaviour.

References

ASTM D18 Committee (2017) "D5607 - 16 Test Method for Performing Laboratory Direct Shear Strength Tests of Rock Specimens Under Constant Normal Force." ASTM International. DOI: 1520/D5607-16.

Bandis, S.C., Lumsden, A.C. and Barton, N.R. (1983) "Fundamentals of Rock Joint Deformation," International Journal of Rock Mechanics and Mining Sciences & Geomechanics, Vol 20(No 6), pp. 249–268.

Barton, N. (1973) "Review of a new shear-strength criterion for rock joints," Engineering Geology, 7, pp. 287–332.

Descamps, F.(2007) Étude du comportement des roches poreuses saturées aux conditions de grande profondeur. Thèse de doctorat. Service de Génie Minier - Faculté Polytechnique de Mons - Université de Mons.

Descamps, F.,Tshibangu, JP., Da Silva, M., Schroeder, C., Verbrugge, J.(2011) "Behaviour of carbonated rocks under true triaxial compression," in Y. Zhou (ed.) Harmonising Rock Engineering and the Environment. CRC Press, pp. 597–602. DOI: 10.1201/b11646-105.

Giwelli, A.A., Sakaguchi, K. and Matsuki, K. (2009) "Experimental study of the effect of fracture size on closure behavior of a tensile fracture under normal stress," International Journal of Rock Mechanics and Mining Sciences, 46(3), pp. 462–470. DOI: 10.1016/j.ijrmms.2008.11.008.

Huang, X. et al. (1993) "An investigation of the mechanics of rock joints—Part I. Laboratory investigation," International Journal of Rock Mechanics and Mining Sciences & Geomechanics Abstracts, 30(3), pp. 257–269. DOI: 10.1016/0148-9062(93)92729-A.

Jaber, J. (2020) Application de la fabrication additive à la modélisation physique des joints et des massifs rocheux, par approches expérimentales et numériques. Thèse de doctorat. Université de Lorraine. Available at: https://hal.univ-lorraine.fr/tel-02960385v1 (Accessed: March 25, 2023).

Krahn, J. and Morgenstern, N.R. (1979) "The ultimate frictional resistance of rock discontinuities," International Journal of Rock Mechanics and Mining Sciences & Geomechanics, 16(2), pp. 127–133. DOI: 10.1016/0148-9062(79)91449-9.

Nikiema, T., Gonze, N. and Descamps, F. (2024) "Correlation between Joint Roughness Coefficient (JRC) and statistical roughness parameters," Engineering Geology and Geotechnics: Building for the Future, Proceedings of the Conference EUROENGEO 2024. 4th European Regional Conference of IAEG, University of Zagreb Faculty of Civil Engineering, pp. 135–142. DOI: 10.5592/CO/EUROENGEO.2024.203.

Schneider, H.J. (1976) "The friction and deformation behaviour of rock joints," Rock Mechanics Felsmechanik Mecanique des Roches, 8(3), pp. 169–184. DOI: 10.1007/BF01239813.

Tatone, B.S.A. and Grasselli, G. (2010) "A new 2D discontinuity roughness parameter and its correlation with JRC," *International Journal of Rock Mechanics and Mining Sciences*, 47(8), pp. 1391–1400. DOI: 10.1016/j.ijrmms.2010.06.006.

Ulusay, R. (ed.) (2015) The ISRM Suggested Methods for Rock Characterization, Testing and Monitoring: 2007-2014. Cham: Springer International Publishing. DOI: 10.1007/978-3-319-07713-0.

A robust sampling strategy for UCS using wireline geophysics

A. Shakib1, A. Kepic2, D. T. Kieu2, M. Bunch3, N. J. Cook4, M. Parsajoo2

1 ARC Training Centre for Integrated Operations for Complex Resources, Adelaide University, Adelaide, Australia

2 RoqSense Pty Ltd, Perth, Australia

3 School of Physics, Chemistry and Earth Sciences, Adelaide University, Adelaide, Australia

4 School of Chemical Engineering, Adelaide University, Adelaide, Australia

amirreza.shakib@adelaide.edu.au

0009-0004-8005-2296

Abstract

Determining where to sample a diamond drillcore and estimating how many Unconfined Compression Strength (UCS) samples would be needed to obtain accurate data are tasks largely based on qualitative knowledge. ISRM suggests taking a minimum of five samples per domain. Prior research has shown that due to the natural heterogeneity in rock better insights with statistically based estimations are usually needed. This hypothesis was confirmed in a recent study at the former Brukunga Mine site, South Australia. Our study in a hard/crystalline rock geology revealed a wider variation than initially anticipated. The UCS results showed a minimum value of 22.9 MPa, a maximum value of 320.2 MPa, and a CoV of 59%. Continuous full wave sonic (FWS), and density logs were extracted to calculate dynamic elastic modulus (E_d) along the length of a single borehole. Robust statistical methods were used to create a measure of variation of rock elastic modulus. This measure is called Relative Median of Absolute Deviation (RMAD) over a 5 m-long moving window. Gaussian Mixture Modelling identified a threshold of 3% RMAD that separates the geological record exposed in the borehole into mechanically homogeneous and anomalous zones. A sampling strategy was developed by combination of fuzzy c-means clustering domaining on continuous X-ray fluorescence geochemistry data as well as RMAD zones. The outcome of the study is a sampling strategy guided with RMAD that provides a measurable and quantitative means to take samples, based on the mechanical and geological conditions of the sampled medium.

Keywords

Wireline Logging, Dynamic Elastic Modulus, Mechanical Heterogeneity, RMAD, Sampling Strategy.

1 Introduction

Rock mass shows three-dimensional variability in its mechanical properties. The ever-present question in geotechnical and mining engineering is: what is the reliability and representativeness of the samples we extract from the rock, relative to the bulk volume? Even if we assume that testing procedures involve limited bias, which is itself unrealistic in most cases, two key questions remain: 1- from where should samples be taken, and 2- how many are enough to adequately cover the uncertainty? Working

in such a complex geological and mechanical medium (whether for development, stabilisation, or blasting) requires either the use and development of key diagnostic tools or the acceptance of conservative designs based on large safety margin. Managing risk and optimising costs remains a fundamental aspect of mining operations. An improper or unrealistic mechanical picture of the rock mass can affect multiple aspects of mine engineering. In blasting, it can cause undesirable particle size distribution, dilution, and over or under break which extend to downstream mineral processing, where undesirable particle size distributions increase comminution energy and cost (Jackson and Sellers 2017). In stability and support design, it results in overly conservative support systems. In surface mining it causes unrealistic stripping ratios and low slope angles, while in underground mining it can urges engineers to consider unnecessarily conservative stope designs (Stacey 2015). Growing concerns around the deviation of mine performance from what had been planned during the early phases of study further highlight the need for not only provision of datasets rich in variety (downhole geophysical, seismic tomography, core scanning, optical logging, etc.) but also increase of data reliability and less reliance on untested assumptions. While one may criticise the costs of conducting additional studies or drilling, economically there is no justification for such oversight, given the potentially disastrous consequences of ignoring the reliability and variability of these geotechnical variables (van As 2020). Addressing the issues, authors have criticised the shortcomings of existing characterisation methods and highlighted a need for a paradigm shift in rock engineering (Elmo et al. 2022).

Geophysical methods have strengthened rock mechanics through in characterisation, monitoring, and measurement applications (Hatherly 2013; Kieu et al. 2024; Takahashi et al. 2006). Deere et al. (1966) proposed that wave velocity can provide estimations for Rock Quality Designation (RQD), and Barton (2006) explained the potential of seismic waves for characterising rock mechanics properties. Seismic waves induce small elastic strains in rock and are therefore sensitive to the mechanical properties of the medium(Barton 2006). Apart from prediction, mapping the variability of mechanical properties is also achievable using continuous wireline log data. Wireline tools provide continuous measurements along the entire borehole. Design practice in rock engineering could be improved with a better picture of variation in mechanical properties that wireline log data analysis could provide.

In this study, we present a method for measuring variation in mechanical properties along the length of a diamond borehole using dynamic elastic modulus obtained from full-wave sonic and density logging, and we test whether this indicates UCS level, likely failure mechanism, and finally suggests how it can be combined with geochemical domains to guide sampling strategy.

2 Site, Data, and Methodology

2.1 Site and data collection

As part of a research programme at the Brukunga mine site, north of Adelaide, South Australia, we conducted comprehensive geophysical wireline logging and collected a large number of UCS samples from core acquired at two adjacent boreholes(Each with a depth of 300m and only 5 m apart).They were depth-matched using natural gamma log correlation. Our total dataset contains 162 UCS test results, done based on standards (ASTM 2019, 2023), and various geophysical logs including FWS and density logs, as well as detailed XRF geochemical data came from XRF core scanning (By Veracio) using a proprietary tool (TruScan).

Table 1 represents the statistical results of UCS tests and shows a wide variability in results. Each UCS sample was classified into foliation controlled (FC) and non-foliation controlled (NFC) failure. Failure mode was recorded (Szwedzicki 2007) and the dominant mode of failure in FC was seen to be single shear (SS) while in NFC it was observed to be multiple fracturing (MF).

Table 1. UCS summary statistics.

Group	n	Mean	Std	CoV	Min	Median	Max
All data	162	12.7	74.6	0.59	22.5	99.8	320.2
No foliation Controlled failure	77	184.6	62.6	0.33	29.3	195.4	320.2
Foliation Controlled failure	85	70.4	29.1	0.41	22.5	60.2	168.7

2.2 Dynamic elastic modulus and RMAD

After velocity analysis, intact rock P-wave (V_p) and S-wave (V_s) velocities were extracted from the full-wave sonic logs (By RoqSense). Dynamic Elastic Modulus, E_d, was calculated using elasticity relations (Eq.1). Due to the non-normal distribution of E_d along the borehole, Relative Median Absolute Deviation (RMAD) of E_d over a 5m-sized moving window was adopted as a robust statistical method for quantifying variability (Eq. 2).

$$E_d = \rho V_s^2 \frac{3V_p^2 - 4V_s^2}{V_p^2 - V_s^2} \quad (1)$$

$$RMAD_w(z) = \frac{MAD(E_d\left[z - \frac{w}{2} : z + \frac{w}{2}\right])}{median(E_d\left[z - \frac{w}{2} : z + \frac{w}{2}\right])} \times 100\% \quad (2)$$

Where ρ Density

z Centre value

w Window size

Gaussian Mixture Modelling (GMM) was applied to the full RMAD to identify three mechanical zones (homogeneous, relatively heterogeneous, heterogeneous). It was decided to use the first threshold (3%) as a divider between Homogenous and (relatively or globally) heterogeneous zones (Fig 1):

a) Zone 1(RMAD ≤ 3%) Homogeneous: Representing mechanically uniform rock covering 48.3% of the total borehole length.
b) Zone 2 (RMAD >3%) Heterogeneous: Representing mechanically variable rock covering 51.7% of the total borehole length.

2.3 Geochemical domain

To domain the borehole, continuous XRF data was used, and fuzzy c-means clustering were utilised. Fuzzy c-means (FCM) is an unsupervised soft clustering algorithm in which each data point is assigned a degree of membership to multiple clusters, and cluster centres are iteratively updated by minimising an objective function (Bezdek et al. 1984). 4 main clusters were identified (Fig 1) (Kieu et al. 2024; Shakib et al. 2025). XRF core scanning provides high-resolution geochemical data along boreholes(Harris et al. 2024)and can be used for domaining as the mechanical properties of rock are controlled by bulk composition, mineralogy, and fabric(s) (Barton 2006).

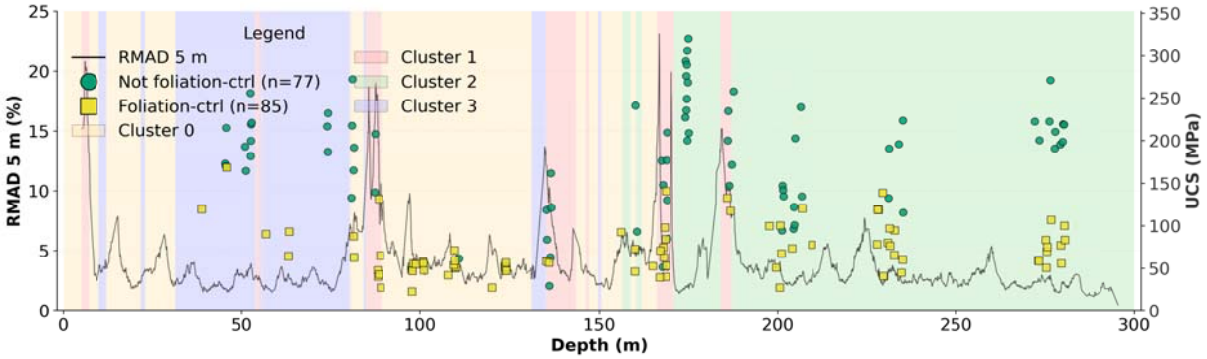


Fig. 1 Borehole profile showing RMAD_5m (upper chart), UCS samples (lower panel), and XRF geochemical domains in background.

3 Results and Hypothesis Testing

According to Table 2, three hypotheses were developed and non-parametric tests were selected to cover the non-normal, multimodal nature of the UCS distributions. The specific test statistic was chosen to match the nature of each hypothesis. Rank-based tests were used to test H1, while contingency-based tests were utilised to test H2 and H3.H1 is supported, as the median UCS in homogeneous zones (169 MPa) is notably higher than in the heterogeneous zone (77 MPa) (Table 2 and Fig 2a). H2 was supported emphasizing that 65.6% of the failures in homogeneous zone were NFC and 64.3% in heterogeneous zone were FC (Table 2 and Fig 2b). Lastly, H3 was supported with

MF occurring 54.7% in the homogeneous zone and SS happening 54.1% in heterogeneous zone (Table 2 and Fig 2c).

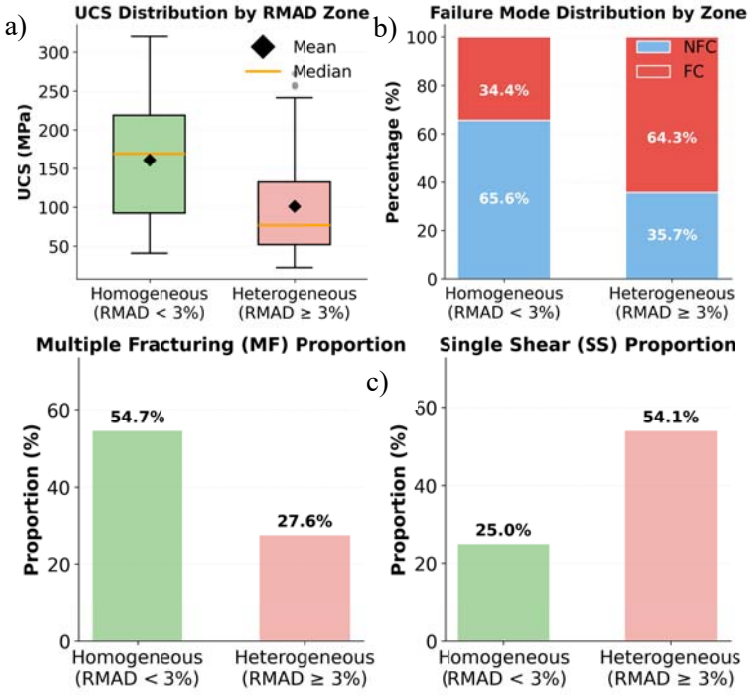


Fig. 2 Distribution by RMAD Zone (a) UCS (b) Failure mode and (c) geometry of failure.

Table 2. Summary of hypothesis testing results.

H	Hypothesis	Test	Statistic	Result	State
H1	The UCS level differs between RMAD zones	Mann–Whitney U	$U = 4621$, $p = 3.7 \times 10^{-7}$	Median: 169 vs 77 MPa [44, 129] at 95% CI	Supported
H2	Foliation-controlled failure is associated with RMAD zone	Chi-squared	$\chi^2 = 12.7$, $p = 3.6 \times 10^{-4}$	FC rate: 34% in homogeneous and 64% heterogeneous zone	Supported
H3	Higher RMAD shows SS failure; lower RMAD shows MF failure	Chi-squared	$\chi^2 = 27.0$, $p < 0.001$	Homogeneous: MF (55%), Heterogenous: SS (54%)	Supported

3.1 Interpretation

Results suggest that RMAD of elastic modulus, as a measure of spatial mechanical heterogeneity, can be indicative of low and high UCS values. However, it must be clearly stated that a direct point-to-point linear relationship between individual UCS values and their corresponding RMAD values cannot be established. There are two principal reasons for this. Firstly, the wireline logging process involved limitations around modifications and adjustments during the campaign and data clipping which affected the resolution of velocity analysis (measurement issue). Secondly, a UCS sample is approximately 15 cm in height, while the RMAD window in our case is 5 m. The RMAD value at a given depth reflects the heterogeneity of a wider section compared to the sample (scale issue).Both issues could be addressed to some extent if we had access to higher-resolution sonic logging (intervals of less than 5 cm and/or slower logging speeds).

The connection between RMAD and failure mechanism provides information regarding heterogeneity of the medium as in our case, the major source of heterogeneity was foliation. On one hand, high RMAD also reflected zones where foliation was controlling the failure mainly through SS failure. On the other hand, Low RMAD values indicated more mechanically uniform rock, where failure occurred through matrix fracturing at higher strengths through multiple fracture failure.

4 Quantitative Sampling Strategy

4.1 Suggested allocation strategy

RMAD-based zonation in conjunction with XRF fuzzy clusters can be used to develop a quantitative sampling strategy for taking UCS samples from drillcore as follow:

1. Acquire full-wave sonic and density logs and compute E_d and RMAD over a desired moving window.
2. Apply the GMM threshold to classify zones.
3. Run Fuzzy C-means clustering on continuous geochemical data.
4. Take at least 3 samples for the smallest cluster and use its length proportion to determine the total required sample (Eq. 3).
5. Allocate UCS samples proportionally to cluster length and RMAD zone fractions as follows:

Allocate n_k samples to cluster k (Eq.3) based on the relative length of each XRF cluster.

$$n_k = round\left(N \times \frac{L_k}{L_{Total}}\right); \sum_{k=0}^{K-1} n_k = N\,; N \geq \frac{3 \times L_{Total}}{L_{k,min}} \tag{3}$$

Within each k cluster, determine the proportional length of the RMAD zones and sample accordingly (Eq.4).

$$n_k^{Heterogeneous} = \max\left(1, round(n_k \times (1 - h_k)\right)$$
$$n_k^{Homogeneous} = n_k - n_k^{Heterogeneous} \tag{4}$$

Where N Total number of samples based on constraints
k XRF clusters (k = 0,1, …, K-1)
L_k Length of cluster k along the borehole
$L_{k,min}$ Length of the shortest XRF cluster
L_{Total} Total logged borehole length
h_k Fraction of cluster k where RMAD ≤ GMM threshold (homogeneous)
$(1-h_k)$ Fraction of cluster k where RMAD >GMM threshold (heterogeneous)

This sampling strategy was tested against UCS data from the Brukunga site. Based on Table 3, the minimum number of samples required by the proposed methodology is 36. According to Fig. 3, at N=36, the probability of exceeding 30% bias in the estimated median UCS (based on 5,000 bootstrapping simulations) is 5% for the proposed methodology versus 19% for the equal-allocation method (taking samples equally across each XRF domain).

Table 3. XRF cluster proportions and RMAD heterogeneous fractions.

Cluster	L_k / L_{Total} (%)	1- h_k
0	30.1	0.24
1	8.5	0.12
2	41.3	0.63
3	20.1	0.7

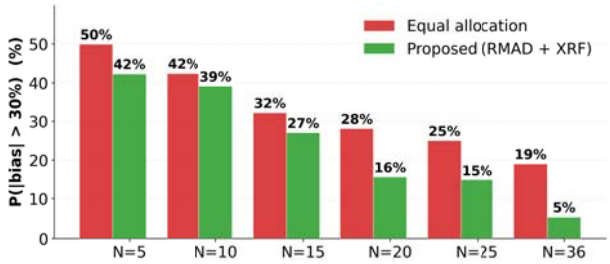


Fig. 3 Probability of more than 30% bias in estimated median UCS vs. sample budget N for equal-allocation and proposed (RMAD + XRF) strategies (10,000 simulations, n=162).

We acknowledge that this framework is presented as a preliminary method. However, the methodology using variability index (RMAD) on continuous geophysical data and using fuzzy c-means clustering on geochemical logs can be useful in formulating a sampling strategy.

5 Discussion

Results of the study shows that RMAD of dynamic elastic modulus, derived from full-wave sonic and density wireline logs, provides a continuous, robust measure of mechanical heterogeneity along the borehole. RMAD can be considered as a spatial heterogeneity indicator. It was shown that a GMM zonation can be considered to separate the borehole into homogeneous and heterogeneous zones.

Based on our statistical observations, homogeneous zones show higher median UCS (169 MPa) and mainly cover NFC and MF failure. Heterogeneous zones exhibit lower median UCS (77MPa) and mainly cover FC and SS failure. RMAD-based zonation when combined with domaining, provides a quantitative approach for informing UCS sampling strategy. Despite the observations presented in this study, careful geophysical data collection, combined with the development of accurate tools, remain as a key topic. There is a need to encourage the mining and rock engineering community to bridge the existing gap between rock mechanics and geophysics at a time when inadequate and/or unreliable data can result in significant economic costs to the client. The paradigm shift that rock engineers strive for may be achieved by the routine integration of geophysical approaches into contemporary rock mechanics frameworks.

Acknowledgements

The authors gratefully acknowledge RoqSense and Veracio for their invaluable support throughout this project. We are also very grateful to the Borehole Wireline Company for their assistance with full-wave sonic logging and ATV imaging. We further thank Advanced Logic Technology Company for providing access to WellCAD software. This research is supported by the Australian Research Council Training Centre for Integrated Operations for Complex Resources (grant IC190100017).

References

ASTM (2019) Standard practices for preparing rock core as cylindrical test specimens and verifying conformance to dimensional and shape tolerances. D4543-19. ASTM International, West Conshohocken, PA.

ASTM (2023) Standard test methods for compressive strength and elastic moduli of intact rock core specimens under varying states of stress and temperatures. D7012-23. ASTM International, West Conshohocken, PA.

Barton N (2006) Rock quality, seismic velocity, attenuation and anisotropy. CRC Press/Taylor & Francis Group, London.

Bezdek JC, Ehrlich R, Full W (1984) FCM: The fuzzy c-means clustering algorithm. Computers & Geosciences 10(2-3): 191-203.

Deere DU, Hendron AJ, Patton FD, Cording EJ (1966) Design of surface and near-surface construction in rock. 8th US Symposium on Rock Mechanics, Minneapolis, USA, 1966.

Elmo D, Mitelman A, Yang B (2022) Examining rock engineering knowledge through a philosophical lens. Geosciences 12(4): 174.

Harris AC, Finn DJ, Maccorquodale FTA, Ravella M, Clarke WJ, Krneta S, Battig E, Maguire S (2024) Empowering geologists in the exploration process - maximizing data use from enabling scanning technologies. SEG Discovery 136: 17-31. doi:10.5382/SEGnews.2024-136.fea-01.

Hatherly P (2013) Overview on the application of geophysics in coal mining. International Journal of Coal Geology 114: 74-84.

Jackson J, Sellers E (2017) Blasting related indices as the key to underground blasting improvements in a challenging rock mass. 13th AusIMM Underground Operators' Conference, Gold Coast, Australia, 2017, pp 23-32.

Kieu D, Parsajoo M, Kepic A (2024) Predicting rock quality designation with geophysical wireline data. NSG 2024 5th Conference on Geophysics for Mineral Exploration and Mining, 2024, pp 1-5.

Shakib A, Kepic A, Kieu D, Bunch M, Cook N (2025) Estimating the confidence in UCS measurements with wireline logging data. NSG 2025 6th Conference on Geophysics for Mineral Exploration and Mining, 2025, pp 1-5.

Stacey T (2015) Rock engineering design - the importance of process, prediction of behaviour, choice of design criteria, review and consideration of risk. Design Methods 2015: International Seminar on Design Methods in Underground Mining, Perth, Australia, 2015, pp 57-76.

Szwedzicki T (2007) A hypothesis on modes of failure of rock samples tested in uniaxial compression. Rock Mechanics and Rock Engineering 40(1): 97-104.

Takahashi T, Takeuchi T, Sassa K (2006) ISRM suggested methods for borehole geophysics in rock engineering. International Journal of Rock Mechanics and Mining Sciences 43(3): 337-368.

van As A (2020) Geotechnical engineering for mass mining. SEG Discovery 120: 22-31. doi:10.5382/Geo-and-Mining-06.

Combined geophysical techniques to predict and map rock mechanics parameters

A. Kepic[1], D.T. Kieu[1], A. Shakib[2], M. Parsajoo[1]

1 RoqSense Pty Ltd, Perth, Australia

2 ARC Training Centre for Integrated Operations for Complex Resources, Adelaide University, Adelaide, Australia

Roqsense@pm.me

0000-0003-2850-7818

Abstract

At the former Brukunga pyrite-sulphur mine site (in South Australia) we investigate the possibility of using cross-borehole seismic travel time tomography with enhanced analysis of borehole wireline data to predict fracture intensity (such as RQD) and rock strength (UCS) as a case history test whether we can predict rock mechanical information and extrapolate to a rock volume. Our proposed methodology provides quantitative and repeatable measurements suitable for physical modelling and offers the opportunity to populate rock block models with engineering data in engineering units.

Engineering of rock mass properties are often interpolated from relatively sparse data spanning tens to hundreds of metres away from diamond-core drilling or interpolated by hand logging and interpretation of rock-core. Geophysical methods should be the natural supporting data for inferring and interpolating information around and between boreholes. Fundamental shared relationships between geophysics measurements and mechanical properties of rock have been noted, tested and studied. However, a well-structured, statistically testable, and economically viable approach of melding geophysical measurement and rock engineering properties does not seem to be regular practice in mining, or in many civil engineering projects. Many issues were rediscovered in our tests and these provide some insights into the practicality of implementing the concept.

Combining borehole and diamond core analysis with imaging with seismic wave propagation produced valuable insights into the structural, mechanical, and dynamic behaviour of rock masse at Brukunga. We were able to use geophysical logging data to find different domains of rock strength, plus characterise the nature of fractures from logging. These developments combined with maps of P- and S-wave velocity in a block model offers vast potential in decision making by allowing informed plans with better safety instead of reactive measures or allowing dilution or waste in mining.

Keywords

UCS, RQD, Geophysics, Petrophysics, Tomography.

1 Introduction

The main issue we try address is that engineers do not have enough volumetric data (Barton, 2006; van As, 2025). Rock classification systems (ASTM STP 984, Kirkaldie, 1988) use various measures, weighting and derating factors and provide guidelines for sampling and measurement. Standards measure such the ASTM standard for Unconfined Rock Strength (UCS; ASTM, 2010) tend to assume representivity and focus upon accuracy and consistency. If the rock mass is very uniform, then a small number of samples and measurements will characterise the rock mass well. In many mining scenarios it is not the case (Jackson, 2019; van As, 2025) as the ore deposit is often associated with complex alterations to pre-existing rocks. Barton (2006) suggests that we should be able to link petrophysics-geophysics and engineering data into rock classification systems, a concept we explore at a test site in Australia.

2 Data and analysis

2.1 Brukunga test area

The Brukunga mine site is 46km east of the city of Adelaide, South Australia and was established in 1950s and closed in 1972 (Skinner, 1958). The Brukunga area is composed of dark pyrite rich siltstones with sandstones and minor calc-silicate interbeds and a massive sandstone unit at its base. The geology is typical of many mineral resource environments in Australia: Cambrian age or olderwith significant metamorphisms, deformation, and intrusions.

The aim was to usea combination of (density, mag-susc, nat gamma, sonic, electrical) petrophysical logging and cross-borehole seismic tomography, with laboratory and core measurements to interpolate important rock mass variables. HQ diameter boreholes, each approximately 300 m deep, and two just 5 m apart (V and G)to verify predictability, were drilled vertically through the same geological units. Samples for rock mechanical testing were taken from different geological units, including adjacent intervals. Core logging and scanning was also involved with calculation of RQD measurements and routine reports. Wireline logging of petrophysics with imaging was also performed. In total, 93 UCS specimens were tested from borehole V, and 60 UCS specimens from borehole G based on ASTM standards (ASTM, 2010).

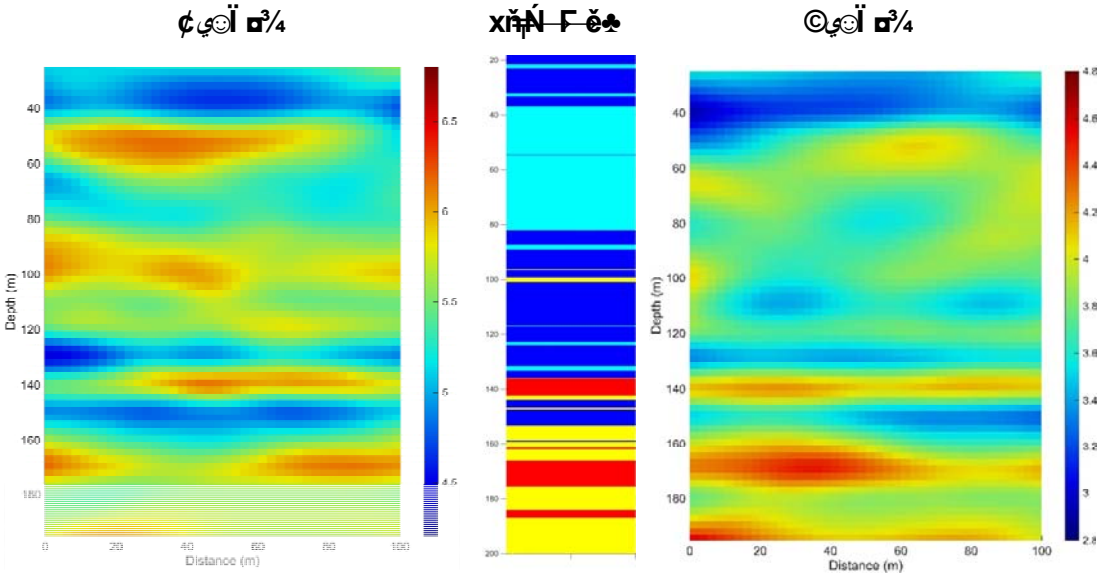


Fig. 1 P- and S-wave velocity tomograms integrated with petrophysically defined lithology for the former Brukunga pyrite mine, near Adelaide, South Australia. The 35–85 m depth interval is characterized by high sulphide mineral content, predominantly pyrite. Thick massive pyrite-rich bands typically correspond to low-velocity zones in both P- and S-wave tomograms, whereas narrow high-velocity zones are interpreted as dolerite sills (shown in red in the clustered lithology). Tomographic inversion was performed using a 2.5 m cell size, yielding an effective vertical resolution of approximately 5 m for resolved layers. (Modified from Kepic et al., 2024).

2.2 Tomography

Seismic while drilling with diamond drill rigs in conjunction with grouted geophone sensor arrays proved feasible in producing tomograms that reflect known geological structures despite relatively low seismic energy (fig 1). The sensor installation and subsequent data acquisition was performed by the drilling crew and supervised by geophysicists from afar. This was done to make tomography more accessible and cost-effective by being compatible with normal geological-engineering assessment processes in hard-crystalline rock. Both P-wave and S-wave tomograms were produced with very high resolution (Kepic, 2024), achieving 5m resolving power, down to at least 150 m depth. S-waves appear to provide slightly higher spatial resolution in the tomograms. The lithology log was produced from Fuzzy Cluster analysis (Bezdek, 1984) from petrophysical logging. These clusters, which match known rock units, were also used in future domaining of the log data to characterise the engineering parameters of various rock units so we could later extrapolate these parameters to the volume with tomography.

2.3 Fractures and Rock Quality Designation

Straightforward use of a previously successful Rock Quality Designation (RQD, Deere and Deere, 1988) prediction methodology (Kieu, 2018) using Full-wave sonic (FWS) wireline logs and seismic data with data domaining was initially unsuccessful in matching the manual RQD logs in our Brukunga test. Initial investigations revealed that FWS tool operating parameters and standard analysis routines were a significant problem. Dedicated FWS analysis algorithms to extract intact rock velocities and separate out fractures by direct attributes produced considerably better results (Kieu, 2024, and fig2). The new FWS analyses methods reliably detected fractures and joints to a resolution of measurement spacing (12-25 cm during logging).

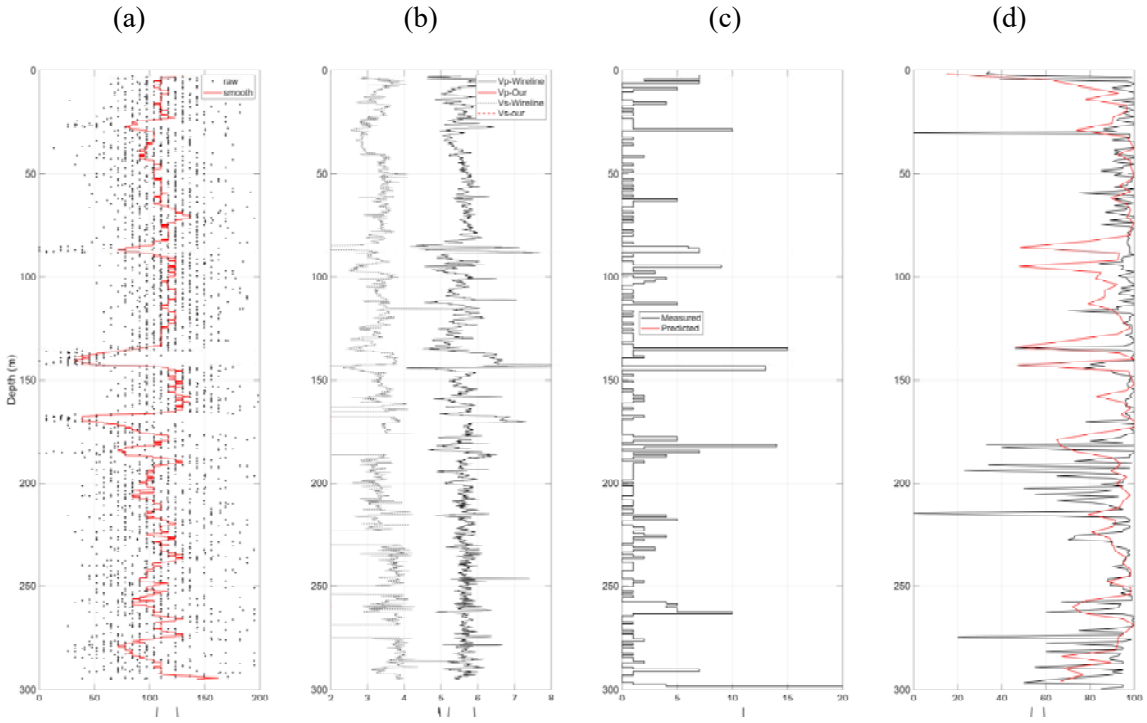


Fig. 2 Borehole data: Natural gamma logs (a); Comparison between P-wave and S-wave computed by WellCAD software and our algorithm from full waveform sonic (FWS) data (b), our results show significant improvement particularly in Vs data. The improvement of Vp and Vs data quality combination with other FWS attributes enabled the prediction of Fracture density (number of fractures per meter, left panel) (c) and RQD (d).

Various cross-comparisons of RQD and fracture measures of two 300m HQ holes only 5m apart with the manual versus FWS analyses demonstrated that RQD and fracture frequency prediction was similar with the various methods (fig 2). Differences in core handing and drilling technique are possible culprits for differences, or geology. Jackson and Sellers (2019) similarly experienced unexpectedly poor matching between adjacent holes at the Olympic Dam mine. FWS analysis and manual acoustic-televiewer (ATV) analysis produced similar results, with both in-situ techniques indicating less fractures that the traditional manual logging of core. A mismatch between the resolution of FWS logs and the minimum intact pieces of 10cm is a possible source of discrepancies.

The more heavily jointed-fractured zones appear to be related to certain cluster-domains, or at certain boundaries. Thus, we feel that the P and S-wave tomographs could be used to extrapolate these zones and provide some measure of volumetric rock mass fracture characteristics. We have not yet performed any significant seismic attribute analysis or anisotropy measures as proposed by Barton (2006), but anticipate these would improve robustness of predictions.

2.4 Unconfined Compressive Strength (UCS)

Various studies show that sonic velocities (Lui. 2022; Parsajoo, 2021) are strongly related to rock strength, with relatively high correlation of R^2=0.95 in the case Parsajoo (2021) by adding density as a factor. Barton also presents much data supporting the sonic-UCS link via elastic properties, but with far less correlation and more caveats. There are also works such as Jauch (2000) where there is much less predictability. Our initial efforts followed the approaches of others, such as Lui (2022) and Parsajoo (2021) where a combination of data domaining and machine-learning was used on a training borehole (V-hole) and then tested on G-hole. Scatter plots of various critical parameters (not shown), such as velocity and density versus UCS did not show clear predictive ability. Using an adaptive domaining-clustering approach with good in-situ measurements of sonic velocity and density to estimate elastic modulus inputs to our prediction ability (fig 3) appears to be quite usable and useful with tomography, but not particularly good.

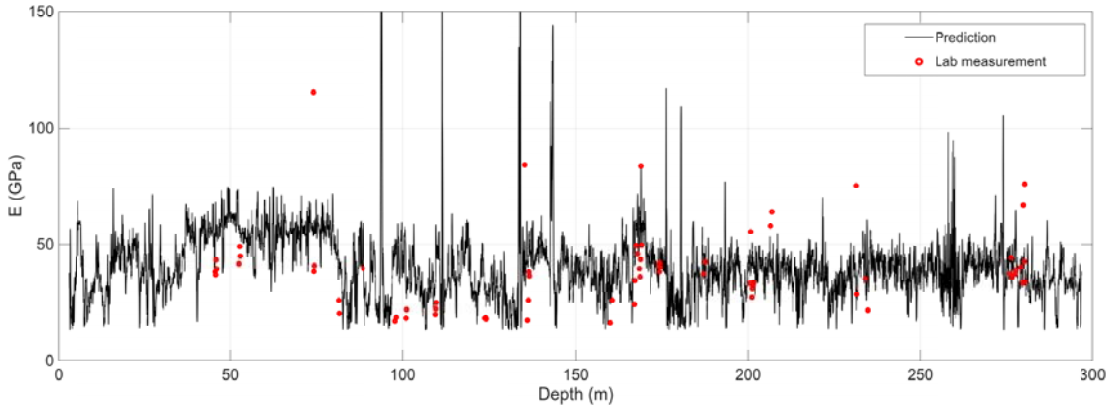


Fig. 3 The comparison between Machine-Learning predicted (black curve – from a nearby hole) of UCS from petrophysics with FCM and lab measurements (Red circles) of sampesfrom borehole G hole(as a blind test).

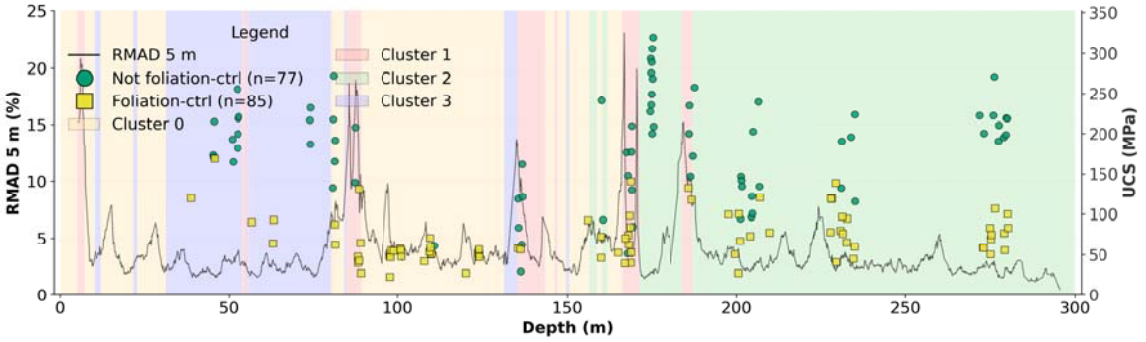


Fig. 4 A comparison between UCS data sorted as Foliated (hetrogeneous – yellow square), Non-Foliated (homogeneous – greed dots) versus a measure of FWS sonic derived elastic propert yvarability (RMAD) with background colour a cluster-domain of rocks with common characteristics (geochemical and pysical).

In gathering the samples for UCS testing it was noted that samples taken within centimetres of each other in similar rock could range between 70 and 250 MPa, rocks in the same cluster-domain. This posed many issues: what is a representative sample to compare to sonic velocities and how should we sample? This is not just a serious issue for our study but poses serious risks for implementing many rock mass rating systems in more complex geological settings.

A measure of sonic variability was introduced by Shakib (2024) (fig 4) to see if we could map these regions of UCS variability. This was partially successful in guiding further sampling but did not seem to detect areas of significant UCS variation. Further samples were collected for UCS testing for in follow up studies and these samples were also tested with ultrasonic pulse transmission between the

sample cylinder faces to measure velocity and other sonic attributes (fig 5).UCS measurements on the first batch of samples from V-hole indicated that at depths >160mhas a bi-modal distribution of values. Furthermore, during the ultrasonic measurements it was note that the received pulse changed shape substantially in some samples, and that these samples had visible heterogenous features. The samples were visually categorised into Foliated and Non-Foliated (fig 4) and similarly with ultrasonic measurements to heterogeneous and homogenous. The homogenous samples tend to be Non-Foliated and provide clean receive pulses. Whereas the Foliated samples had heterogeneous ultrasonic signals, with multi-path/scattering evident in the received signal. Fig 6 shows that the heterogeneous samples clearly are weaker (cluster 3 in Fig 6), and that sonic methods at the sample scale can detect heterogeneity that determines UCS strength.

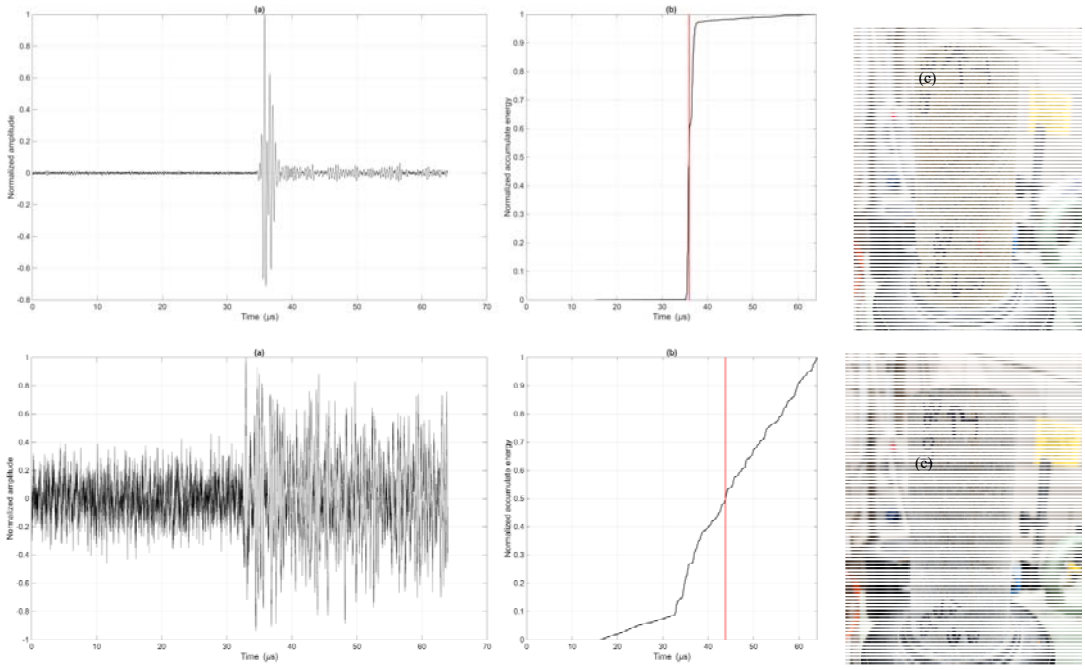


Fig. 5 Laboratory ultrasonic measurements include pulsewaveform (a), accumulated energy (b), and sample photo (c). The red line in Figure (b) indicates the time corresponding to 50% accumulated energy. The later arrival time for Sample 2 compared to Sample 1 suggests that Sample 2 is more heterogeneous. This observation is consistent with the waveform characteristics: Sample 1 exhibits a clear pulse waveform, whereas Sample 2 shows sever multi-path and scattering.

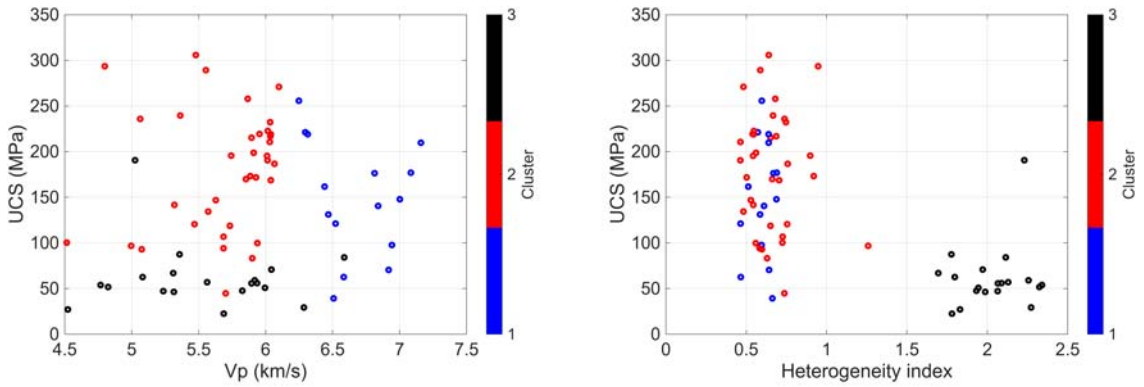


Fig. 6 Cross-plot of Vp and Heterogeneity Index versus UCS. The clusters are results of ultrasonic full-waveform sonic data. Cluster 3 corresponds to the samples exhibiting the highest degree of heterogeneity and lowest UCS.

Rock textures at various scales matter greatly when relating the petrophysical and geophysical domains with engineering parameter domains. The sample ultrasonic measurements demonstrate what could be achieved with sonic logging with higher resolution and precision. The physical variations and macro-textures in rocks influence greatly the rock mass appraisal.

3 Conclusions

Our tests at the Brukunga mine site demonstrated that petrophysical properties and key engineering rock parameters can be estimated as robustly as resampling with conventional methods. Thus, it is possible to extrapolate beyond the borehole with measured data from tomography. Sparse sampling is a barrier to understanding the rock mass properly. Wireline logging with high resolution, especially full-wave sonic, can translate to engineering properties at various scales with a physically plausible methodology. The significant problems of using geophysics for rock mechanical parameter estimation lies mostly with spatial aliasing of the geophysical data and the reference engineering data from samples. Higher resolution physical measurement creates a better understanding of parameter variations and is critical to finding a representative measure of rock parameters for better risk management and optimisation.

Acknowledgements

The authors gratefully acknowledge the significant support from Veracio and the Australian Research Council Training Centre for Integrated Operations for Complex Resources (grant IC190100017).

References

ASTM, A. (2010). Standard test method for compressive strength and elastic moduli of intact rock core specimens under varying states of stress and temperatures.

Barton, N. (2006) Rock quality, seismic velocity, attenuation and anisotropy. CRC press.

Bezdek, J. C., Ehrlich, R., and Full, W., (1984), FCM: The fuzzy c-means clustering algorithm: Computers & Geosciences, v. 10, no. 2-3, p. 191-203.

Deere, D. U. and Deere, D. W., (1988) The rock quality designation (RQD) index in practice. In Rock classification systems for engineering purposes. ASTM STP 984 American Society for Testing and Materials.

Jackson, J. & Sellers, E. (2019) Blasting related indices as the key to underground blasting improvements in a challenging rock mass. The 13th AusIMM underground operators' conference Gold Coast, QLD, Australia. The Australasian Institute of Mining and Metallurgy, AusIMM, 2017. 23-32.

Jauch, F.., (2000) Using borehole geophysics for geotechnical classifications of crystalline rock masses in tunnelling, PhD dissertation., ETH Zurich.

Kieu, D. T. and Kepic, A. (2018). Building 3D Model of Rock Quality Designation Assisted by Co-Operative Inversion of Seismic and Borehole Data. ASEG Extended Abstracts, 2018(1), 1–5.

Kirkaldie, L. (Ed.). (1988). Rock Classification Systems for Engineering Purposes, ASTM STP 984, American Society for Testing and Materials, Philadelphia

Kepic, A., Kieu, D., Crettenden, B. and Zawadzki, R., (2024) Seismic Tomography with Diamond Drilling and Permanent Arrays. In NSG 2024 5th Conference on Geophysics for Mineral Exploration and Mining (Vol. 2024, No. 1, pp. 1-5). European Association of Geoscientists & Engineers.

Kieu, D., Parsajoo, M. and Kepic, A., (2024), September. Predicting rock quality designation with geophysical wireline data. In NSG 2024 5th Conference on Geophysics for Mineral Exploration and Mining (Vol. 2024, No. 1, pp. 1-5). European Association of Geoscientists & Engineers.

Liu, P.H., Wu, J.H. and Lee, D.H., (2022). New rock strength-based UCS-Vp correlation equation for different rock types by statistical regression methods. Geomechanics for Energy and the Environment, 32, p.100403.

Parsajoo, M., Jahed Armaghani, D., Mohammed, A., Khari, M.,and Jahandari, S., S. (2021). Tensile strength prediction of rock material using non-destructive tests: A comparative intelligent study. Transportation Geotechnics. 31.

Shakib, A., Kepic, A., Kieu, D., Bunch, M. & Cook, N. (2025) Estimating the Confidence in UCS Measurements with Wireline Logging Data. NSG 2025: 6th Conference on Geophysics for Mineral Exploration and Mining, 2025. European Association of Geoscientists & Engineers, 1-5.

Skinner, B. J. (1958). The geology and metamorphism of the Nairne pyritic formation, a sedimentary sulfide deposit in South Australia. Economic Geology, 53, 546-562.Kieu (2018) Kevitsa study of RQD

van As, A. (2025). Geotechnical Engineering for Mass Mining. In: Wood Ao, D. & Hedenquist, J. (eds.) Geology and Mining: Evolution of Best Practice. Society of Economic Geologists

Proof-of-concept pipeline for digital rockmass analysis using an inexpensive 360° camera

M. Janiszewski[1], M. Torkan[1], S. L. Vidanage[1], P. Oikkonen[2], A. Riquelme[3], J. Liukko[4] & L. Uotinen[1]
[1] *Aalto University, Finland*
[2] *Normet Group, Finland*
[3] *University of Alicante, Spain*
[4] *YIT, Finland*
mateusz.janiszewski@aalto.fi
0000-0002-7365-2777

Abstract

Rock mass characterisation, specifically characterising fracture distribution, density, and orientation, is crucial for a better understanding of stability and hydraulic properties. There are several methods for characterising fracture networks, such as manual mapping and remote sensing.

This paper presents a proof-of-concept workflow for digital rock-mass analysis using a 360° imaging system photogrammetry combined with a three-dimensional Gaussian Splatting (3DGS). The method was tested ona tunnel drift (Site 1) and a 20-meter wall section (Site 2) in the Underground Research Laboratory of Aalto University (URLA). A compact 360° camera was used to acquire continuous panoramic image sequences of two sites in the tunnel. These images were processed into a 3D representation via photogrammetry combined with 3DGS, providing both accurate surface geometry and highly efficient and hyper-realistic real-time rendering. Fractures and discontinuity sets were extracted from the reconstructed surfaces using established methods such as 3D point cloud processing and semi-automatic clustering of fracture planes, allowing 3D fracture orientation measurements.

The resulting orientations of discontinuity sets measured digitally from the 360° camera-based 3D point cloud differ 3.4° on average compared to previous measurements obtained from laser scanning and photogrammetry data. The 3D point cloud coloured by discontinuity sets was imported into Blender and visualised on the 3DGS. This enabled users to inspect the tunnel digitally, visualise structural features, and review spatial data in high resolution.

The study demonstrates that a functional end-to-end digital rock-mass sensing pipeline can be assembled using an inexpensive 360° camera and existing software tools, offering a practical foundation for advancing automated rock-mass intelligence in future mining and tunnelling applications.

Keywords

Fracture orientation, Photogrammetry, Tunnel, 360 camera, 3D Gaussian Splatting.

1 Introduction

Rock masses are inherently characterised by discontinuities, which influence their mechanical and hydraulic behaviours. Therefore, a thorough and precise mapping of these discontinuities is crucial for evaluating rock mass behaviour in engineering applications, such as tunnelling and mining. Rock mass characterisation utilising digital tools is rapidly becoming a standard across the industry.

Recent years have witnessed significant advancements in geomatic methods for digitising rock mass surfaces into three-dimensional (3D) models, particularly using terrestrial laser scanning (TLS) and Structure-from-Motion Multi-View Stereo (SfM-MVS) photogrammetry. These methods facilitate a semi-automated approach to mapping rock discontinuities, offering numerous benefits including rapid data acquisition, high repeatability, reduced human bias, and the capacity for remote analysis. The deployment of fast, large-scale photogrammetry within underground construction environments is proving highly effective for modern mapping workflows (Evins et al. 2025). Despite their proven advantages, traditional digital mapping methods are not without limitations. Laser scanning, while providing exceptional accuracy, often requires expensive, fragile, and specialised hardware. Conventional photogrammetry offers a more cost-effective alternative, but it necessitates a meticulously planned camera network to ensure sufficient image overlap, which can be challenging and time-consuming in active, underground environments. To address these challenges, previous research explored the use of 360° cameras for rapid SfM-MVS tunnel mapping (Janiszewski et al. 2022). While these studies successfully demonstrated the viability of 360° imaging, the hardware utilised was often expensive, heavy, and difficult to deploy routinely.

Recently, inexpensive and highly compact 360° cameras have become widely available on the market, presenting new opportunities for rapid data collection and enabling easy data collection for new spatial reconstruction methods such as 3D Gaussian Splatting (3DGS). Therefore, the primary goal of this study is to test the feasibility of utilising a small, low-cost 360° camera for SfM reconstruction and structural rock mass characterisation within an underground hard rock tunnel setting. This paper presents a proof-of-concept processing pipeline that integrates 360° panoramic image capture, traditional SfM-MVS point cloud and mesh generation, automated discontinuity set extraction, and 3DGS visualisation, evaluating its potential use for underground rock engineering.

2 Methodology

2.1 Data collection

The data collection for this study was conducted in the Underground Research Laboratory of Aalto University (URLA), Finland. The site is located 10-20 meters below ground. The rock mass is predominantly composed of granite and granodiorite and is characterised as moderately fractured and mostly dry. The fully exposed rock mass makes it an ideal testing ground for photogrammetric mapping. To evaluate the methodology under different spatial constraints, two separate areas within one tunnel were selected. Site 1 was a tunnel drift that was previously used for videogrammetry tests by Janiszewski et al. (2024), though the original control points were no longer present. Site 2 consisted of a larger, continuous 20-meter-long tunnel section near the drift (see Fig. 1).

2.2 360-degree image acquisition

Image data was acquired utilising a compact DJI Osmo 360° camera (see inset in Fig. 1a). The device features two lenses with a 2 mm focal length (8 mm full-frame equivalent). The camera internally stitches the dual-lens output to generate equirectangular images with a resolution of 15520 × 7760 pixels (20 MP) in JPG format.

At Site 1, to minimise shadows and produce even lighting, the drift was illuminated by a single, battery-powered DeWALT DCL074-XJ LED work light, which provided around 5000-lumen luminous flux with 360° coverage (Fig. 1a,c). The 360° camera was mounted on a stationary tripod. To capture the entire geometry, images were taken at three distinct elevations (high, mid, and low) on both sides of the drift, resulting in 17 total camera positions (Fig. 1b). The camera parameters were manually set to ISO 200, an aperture of f/1.9, and a shutter speed of 1/2 s to ensure optimal exposure in the static environment.

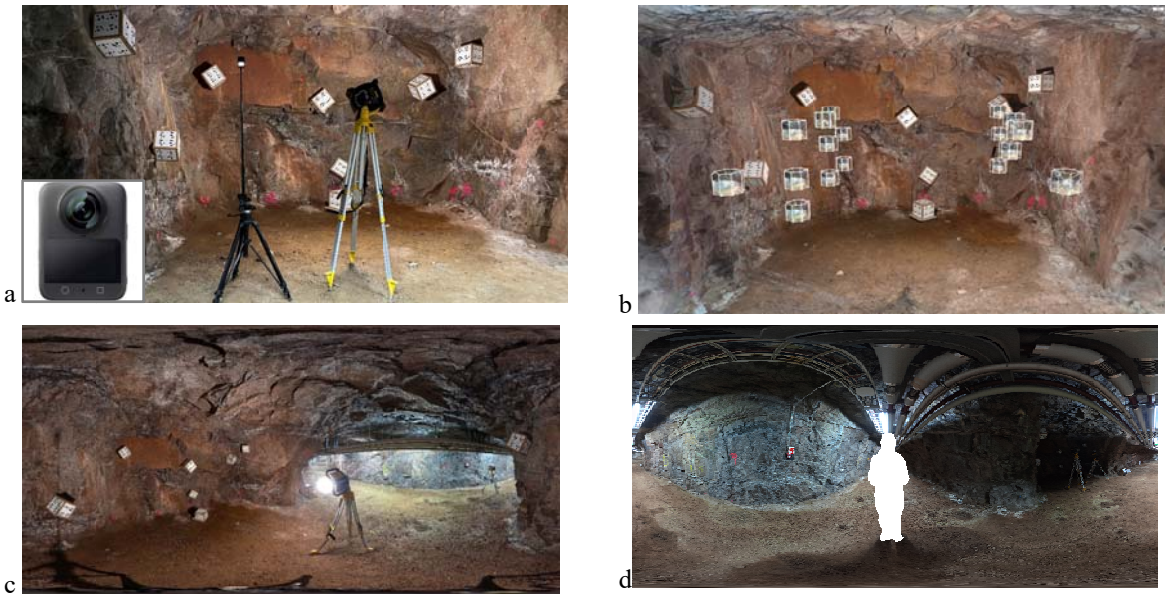


Fig. 1 Data capture set up at Site 1 (a), camera network (b), example panoramic equirectangular image from Site 1 (c), example masked equirectangular image captured handheld from Site 2 (d).

For the extended mapping of Site 2, illumination was provided by the existing fluorescent lights installed along the tunnel roof. To facilitate rapid data collection, the 360° camera was mounted on a dedicated handheld stick. The operator walked along the 20-meter tunnel section, stopping briefly at regular intervals to capture photos. Image sequences were captured at high, mid, and low elevations. To reduce motion blur from the handheld operation, the camera's ISO was increased to 3200, maintaining an aperture of f/1.9, and the shutter speed was increased to 1/60 s. Because the operator was visible in the handheld panoramic shots, a post-processing step was required; Adobe Photoshop was used to manually mask the person out of the images (Fig 1d).

2.3 Data processing – Photogrammetric and 3DGS processing pipeline

Before generating the 3D models, the equirectangular images were converted into standard 2D perspective images using the 360 Image split tool in Meshroom software v.2021.1.0 (Meshroom, 2026). The images were processed into 8 splits with a resolution of 3880 × 3880 pixels. This resulted in a total of 136 images for Site 1 and 448 images for Site 2.

The split images were imported into RealityScan v.2.1 software (RealityScan, 2026). Coded markers mounted on the tunnel walls were automatically detected to establish reference points. The models were scaled and oriented to a local coordinate system using an orientation cube, achieved by setting the top four control points of the cube to the "Ground Control Point" type and assigning their corresponding XYZ coordinates. The images were aligned using default settings, except for 'Image overlap' set to Low, and the 'Max feature reprojection error' was iteratively refined from 2 pixels down to 1 pixel for the final alignment. For Site 1, 136 images were aligned, generating a sparse cloud of 245,848 points with a median reprojection error of 0.41 pixels. For Site 2, all 448 images were aligned, generating a sparse cloud of 1,506,249 points with a median reprojection error of 0.26 pixels.

From the alignment phase, the processing pipeline was divided to serve two parallel visualisation and analysis goals. To enable real-time, hyper-realistic visualisation, the distortion model was set to 'Division', and the alignment data was exported in COLMAP text format for 3D Gaussian Splatting (3DGS) processing within LichtFeld Studio (LichtFeld Studio, 2026). Concurrently, for conventional rock mass analysis, a dense reconstruction was performed in RealityScan on the aligned components. The resulting dense point cloud and mesh were textured, decimated, texture-reprojected, and exported as an .fbx file. The dense point cloud was cropped to the fracture sampling area and exported in .txt format for further processing.

2.4 Data processing – Point cloud analysis and discontinuity extraction

The cropped dense point clouds were imported into CloudCompare v.2.13.2 (CloudCompare, 2026) for pre-processing. To optimise processing, the clouds were subsampled using the spatial method with a minimum spacing of 0.01 m between points. Normal vectors for each point were subsequently computed using the Hough Normals Computation plugin at default settings, and the cleaned data were exported in .ply format.

The semi-automatic extraction of discontinuity orientations was performed using the Discontinuity Set Extractor (DSE) software v.4.00 (Riquelme et al. 2014). The normal vector densities were calculated, and the probability density function (PDF) of the normals' poles was computed using a minimum angle of 30° and 6 bins. A maximum of 5 discontinuity sets was initially allowed (Nmax = 5), which were visually inspected and manually edited. Based on a visual assessment, anomalous sets were subsequently removed. Individual points were classified and assigned to a specific Discontinuity Set (DS) if their normal vector fell within a 30° cone angle of the principal pole. This preliminary classification (XYZ_Js) was exported to CloudCompare for visual validation against the textured mesh. Finally, spatial clustering of each DS was conducted using the DBSCAN algorithm to isolate individual fracture planes. Clusters containing fewer than 100 points were filtered out, and coplanar clusters were merged according to a standard coplanarity test.

Final rendering was done in Blender v.5.0.1 software (Blender, 2026). The clustered point cloud from DSE was imported as .ply, and a shader material was added to display the point cloud coloured by discontinuity sets. The point cloud was overlaid on top of the 3D Gaussian splat (3DGS) imported into Blender using the 3DGS Render by KIRI Engine plugin v. 4.1.5.

3 Results and discussion

3.1 3D reconstruction and visualization

The photogrammetric processing pipeline successfully generated dense point clouds and textured meshes for both test environments, capturing full 360° geometry. For Site 1, the stationary setup yielded a detailed geometric representation of the drift (Fig. 2a). For Site 2, the methodology utilising the handheld 360° camera successfully reconstructed the entire 20-meter tunnel section continuously, proving the viability of the rapid, walking-capture method for larger underground spans (Fig. 2b).

a  b 

Fig. 2 Resulting 3D textured mesh from Site 1 (a) and Site 2 (b).

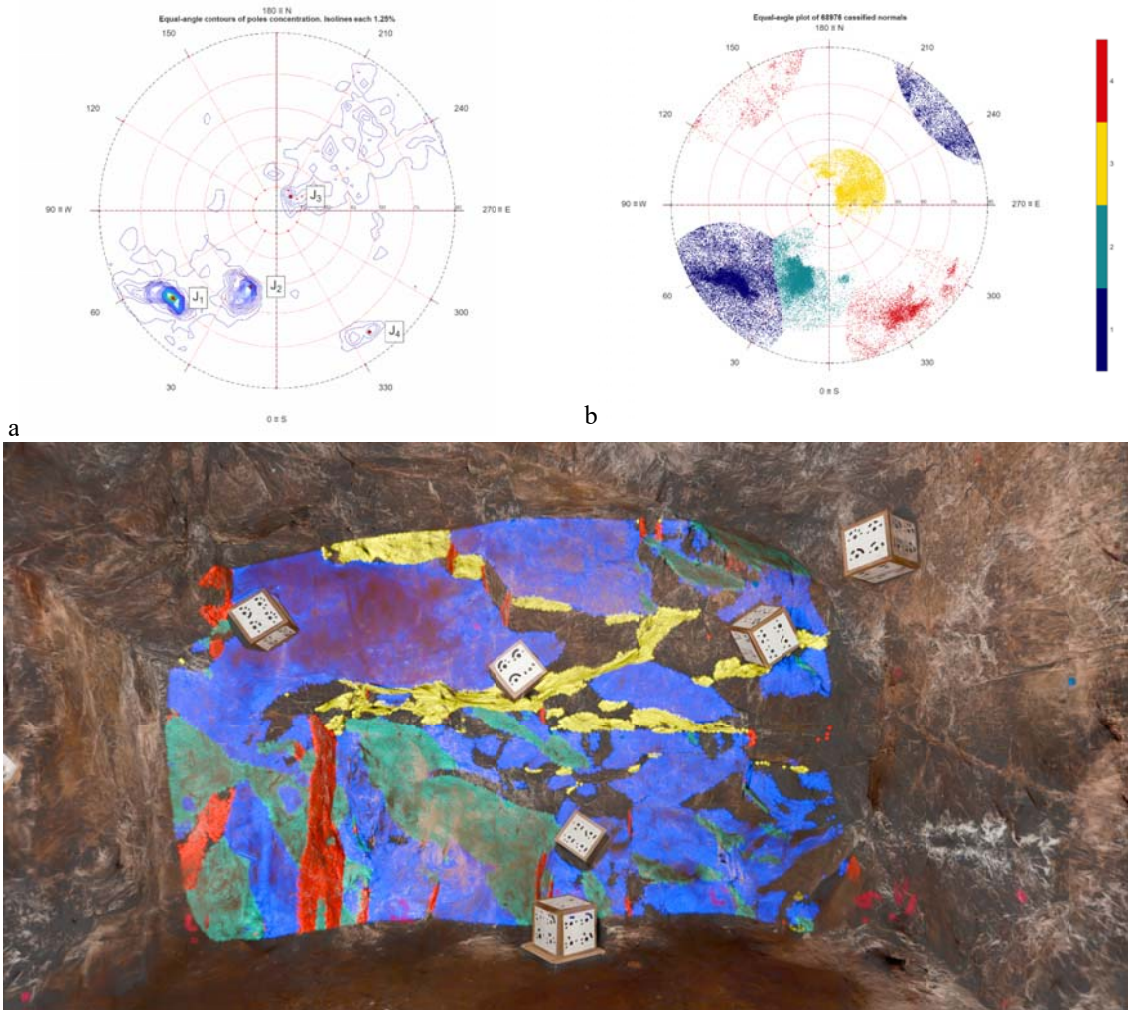
The parallel 3DGS pipeline branch demonstrated the capability for real-time visualisation (Figs. 3–4). Even though 3DGS was only tested for final rendering and not for geometric measurements, as demonstrated by Okutu-Ayiku (2025) for Rock Quality Designation (RQD) measurements, its integration highlights significant potential for future comprehensive digital rock mass characterisation systems. By combining 360° images, 3D point clouds, textured meshes, and 3DGS, a complete multi-data visualisation system can be realised. It has to be noted that the 3DGS from Site 2 suffered from a lack of detail on the floor and roof parallel to the tunnel axis, mainly due to masking of the operator.

3.2 Discontinuity set orientation

At Site 1, four distinct discontinuity sets (DS1–DS4) were extracted from the reconstructed point cloud using the DSE software (Fig. 3). Table 1 compares the mean dip direction (°) and dip (°) values obtained using the compact 360° camera with reference data from previous studies at the same location, which utilised high-resolution Terrestrial Laser Scanning (TLS) and mobile photogrammetry. The orientations derived from the inexpensive 360° camera demonstrate strong alignment with the reference data, particularly for the steeply dipping sets (DS1, DS2, and DS4).

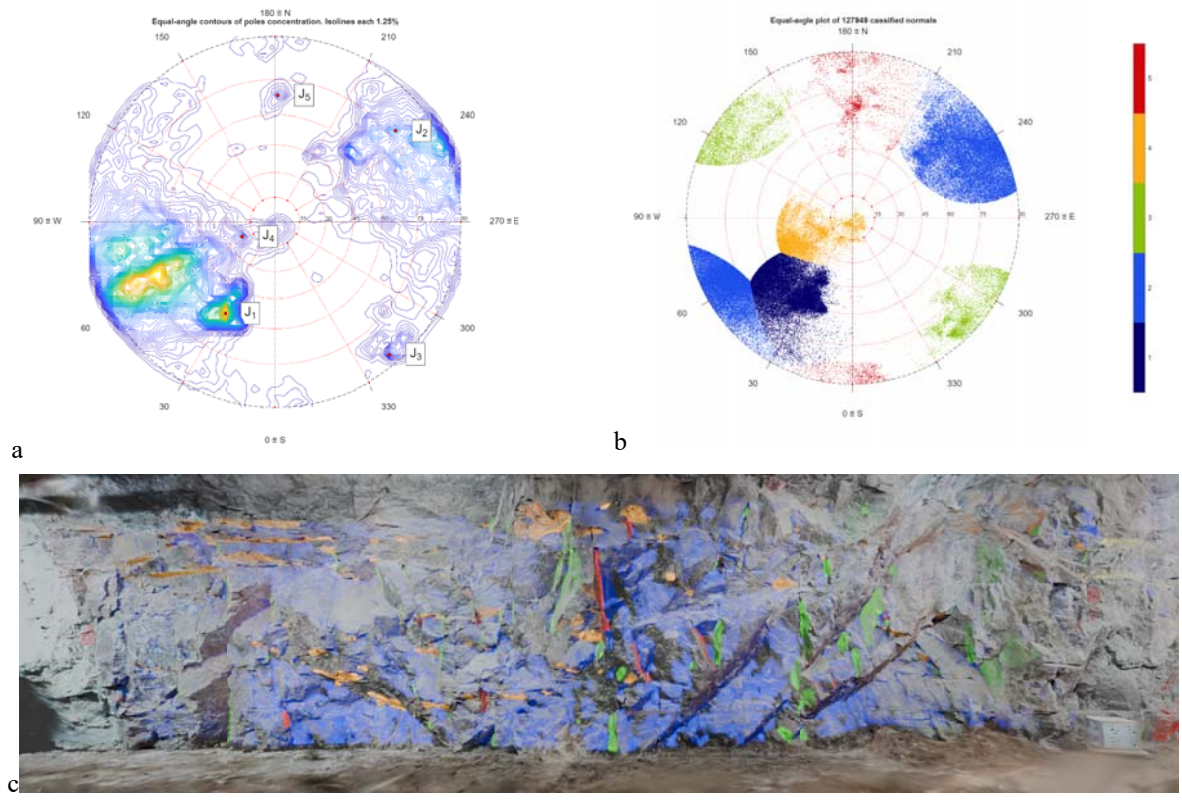
Table 1. Mean discontinuity set orientations (dip direction° / dip°) for Site 1 compared to reference data. The resulting mean and median orientation errors were 3.4° and 2.2°, respectively.

Model	DS1 (Dip dir° / Dip°)	DS2	DS3	DS4
Compact 360° camera (this study)	50.0 / 74.9	18.4 / 48.6	225.0 / 12.8	322.5 / 81.4
TLS reference (Janiszewski et al. 2024)	50.1 / 75.5	20.3 / 51.1	250.0 / 8.7	319.4 / 80.1
Mobile SfM (Janiszewski et al. 2024)	47.5 / 77.6	20.3 / 51.1	224.3 / 11.6	319.4 / 80.0



a b c

Fig. 3 Discontinuity orientation results for Site 1: pole density plot (a), poles with assigned discontinuity set (b), classified discontinuity sets overlaid on the 3DGS of the tunnel face (c).



a b c

Fig. 4 Discontinuity orientation results for Site 2: pole density plot (a), poles with assigned discontinuity set (b), classified discontinuity sets overlaid on the 3DGS of the tunnel wall (c).

Fracture orientation measurements from the compact 360° camera-derived point cloud are comparable to previous studies, but slight deviations exist. This is mainly attributed to the simplified orientation control method employed in the absence of surveyed targets. To resolve this, a permanent control point network with fixed, known coordinates is currently under development at URLA. This will facilitate rigorous benchmarking of the 360° pipeline against standardised TLS data in future tests.

For the extended mapping at Site 2, five discontinuity sets were identified (Fig. 4). Visual assessment confirmed that these sets aligned with previous manual measurements. However, precise values for Site 2 are not reported here. The primary objective for Site 2 was to validate the feasibility of continuous 3D reconstruction over a larger area, which the methodology accomplished.

3.3 Methodological limitations and future work

The utilisation of 360° camera with a smaller sensor inherently results in a reduction of visual quality compared to high-end DSLR cameras. Nevertheless, the geometric quality of the resulting point clouds remains sufficient for extracting reliable rock mass measurements. Lighting strategies present another challenge in underground settings. The use of a stationary 360° work light can cast complex, distinct shadows across the rock face, which may obscure fine structural details. Alternatively, relying on ambient fluorescent lighting by using high ISO settings (as demonstrated at Site 2) proved functional but introduced noise into the source images. Future tests will investigate the effectiveness of dedicated, camera-mounted 360° lighting rigs to provide uniform, shadow-free illumination during mobile capture. Finally, this proof-of-concept was conducted in a controlled underground laboratory, which is largely free of dust and high humidity. For the proposed pipeline to become a robust tool for daily tunnelling and mining operations, future research must validate its performance in active production headings, where dust and humidity may interfere with image capture and the SfM process.

The proposed combined SfM-MVS and 3DGS method provides a framework for visual as-built documentation and for future process automation in underground construction. Integrating this digital pipeline into daily operations could facilitate continuous rock mass classification, driving data-informed decisions for optimised tunnel design and dynamic rock support selection.

4 Conclusions

This study successfully implemented a digital rock-mass analysis pipeline using a lightweight, inexpensive 360° camera in an underground hard rock environment. The workflow reliably produced dense 3D reconstructions and enabled fracture orientation measurements with satisfactory precision. By combining a 360° camera-based photogrammetric model and 3DGS with semi-automatic discontinuity extraction, the proposed method provides an accessible, low-cost framework for rapid rock mass intelligence and visualisation.

References

Blender (2026). Blender (version 5.0.1). https://www.blender.org

CloudCompare (2026). CloudCompare (version 2.13.1) [GPL software]. http://www.cloudcompare.org

Evins P, Hermansson J, Bym T (2025) Systematic photogrammetry integrated into the Contractor's workflow during tunneling: Advantages and lessons learned. Tunnelling into a Sustainable Future – Methods and Technologies 107–114. https://doi.org/10.1201/9781003559047-14

Janiszewski M, Torkan M, Uotinen L, Javed H, Rinne M (2024) Tunnel face videogrammetry for low cost digitization and discontinuity set orientation measurements. New Challenges in Rock Mechanics and Rock Engineering. CRC Press 872–878. http://dx.doi.org/10.1201/9781003429234

Janiszewski M, Torkan M, Uotinen L, Rinne M (2022) Rapid Photogrammetry with a 360-Degree Camera for Tunnel Mapping. Remote Sensing 14(21) 5494. https://doi.org/10.3390/rs14215494

LichtFeldStudio (2026). LichtFeld Studio (version 0.5.1). https://lichtfeld.io/

Meshroom (2026), Meshroom (version 2021.1.9). https://alicevision.org/#meshroom

Okutu-Ayiku S (2025) The use of Gaussian splatting for 3D digitization for rock mass characterization and visualization. Master's thesis. Aalto University.https://urn.fi/URN:NBN:fi:aalto-202512159167

RealityScan (2026). RealityScan (version 2.1.1). https://www.realityscan.com/

Riquelme A, Abellán A, Tomás R, Jaboyedoff M (2014) A new approach for semi-automatic rock mass joints recognition from 3D point clouds. Computers & Geosciences 68(0) 38-52. https://doi.org/http://dx.doi.org/10.1016/j.cageo.2014.03.014

Analysis of the Mechanical Behavior of Callovo-Oxfordian Claystone under Temperature: Contribution of 3D X-Ray Tomography

B. Abou Chakra, D. Grgic & A. Bonnelye
Université de Lorraine, CNRS, GeoRessources, F-54000 Nancy, France
bahaa.abou-chakra@univ-lorraine.fr

C. De Lesquen
Andra, Chatenay Malabry, France

Abstract

The Callovo-Oxfordian claystone (COx), as a host rock for radioactive waste disposal in France (Cigéo Project), will be subjected to coupled THM (Thermo-Hydro-Mechanical) processes, such as stress variations during excavation, changes in saturation, and thermal fluctuations induced by exothermic wastes. To ensure the short- and long-term safety of the disposal and optimize its design, it is essential to analyze the impact of these THM solicitations on the mechanical behavior of the clay host rock.

This study investigates the effect of temperature on the mechanical behavior of the COx claystone through triaxial compression tests conducted under various confining pressures, on samples oriented both parallel and perpendicular to the bedding planes. The tests, performed between 20 and 90 °C with a heating rate of 10 °C/h, revealed a decrease in peak strength with increasing temperature for the perpendicular orientation (from -10 % to -20 %), and no significant effect for the parallel orientation. This is due to the competitive effects of damage induced by pore-fluid overpressure and suction induced by the sample desaturation during heating with the latter being more significant in the parallel orientation.

3D micro-computed tomography was used to analyze the evolution of fractures between the initial state (after core sampling) and the final state (after the mechanical test). This approach highlights the combined influence of anisotropy, confinement and temperature on the fracture mechanisms. For the perpendicular orientation, axial stress generally tends to close pre-existing microcracks; however, at 90 °C, an interconnected fracture network develops, mainly concentrated in the lower part of the specimens. For the parallel orientation, temperature does not induce the development of an additional crack network and the rupture results from the progressive opening of pre-existing cracks, already aligned according to the direction of the bedding plane, without temperature exerting a significant influence on these mechanisms.

Keywords

COx claystone, Triaxial tests, Temperature, Microcracking damage, X-ray tomography.

1 Introduction

The Callovo–Oxfordian (COx) claystone, the host rock selected for the French deep geological repository (Cigéo Project), will be subjected to coupled Thermo-Hydro-Mechanical (THM) processes induced by excavation and heat emitted by radioactive wastes. In recent years, various studies on the thermo-hydro-mechanical (THM) behavior of COx claystone have been conducted, including in situ investigations carried out by the ANDRA (French National Agency for Radioactive Waste Management) and, in parallel, laboratory experiments performed by different research institutions under a range of conditions and experimental methods.

Although numerous laboratory studies have investigated the thermo-mechanical behavior of COx claystone, experimental results remain highly scattered due to differences in testing protocols, limited sample sizes, geological variability, and intrinsic heterogeneity (mineralogy, porosity, microcracking), as well as sample disturbance and saturation conditions(Zhang et al. 2014; Liu et al. 2019; Zhang 2021; Gbewade et al.2023;Wang et al. 2026). Thermal damage is further influenced by stress path, anisotropy, saturation, loading rates, and drainage conditions, highlighting the need for better quantification of these coupled effects.However, few studies combine controlled THM conditions with quantitative 3D fracture analysis.

This study aims to characterize the effect of temperature on the short-term mechanical behavior of COx claystone while reducing experimental dispersion through consistent and reproducible protocols. Triaxial compression tests are performed at different temperatures, confining pressures, and orientations, combined with 3D X-ray tomography to quantify fracture volumetric changes and link macroscopic responses to fracture network evolution.

2 Experimental procedures

The analyzed core samples were extracted from two horizontal boreholes (OHZ8573 and OHZ3011) drilled outside the Excavation Damaged Zone (EDZ) at the main level of the Meuse/Haute-Marne Underground Research Laboratory (~490 m depth). They were stored in T1 cells, concept developed by Andra, in order to preserve their initial degree of saturation and mechanical integrity (Conil et al. 2018). Cylindrical specimens (diameter 20 mm and height 40 mm) were tested parallel and perpendicular to the bedding plane. The mechanical properties of COx claystone being highly sensitive to water saturation (Zhang 2017; Conil etal. 2018; Grgic etal.2023; Gbewade etal. 2023);samples were therefore wrapped and stored under controlled humidity ($Sr > 90$ %).Physical characterization of the cores showed: wet density (ρ_w) ≈ 2.4 g/cm^3, dry density (ρ_d) ≈ 2.23 g/cm^3, grain density (ρ_s) ≈ 2.67 g/cm^3, total porosity (n_t) ≈ 17 %, natural water content (W_{nat}) ≈ 7 %, degree of saturation (S_r) ≈ 95 %, and calcite content ($CaCO_3$) ≈ 18 % (OHZ8573) and ≈ 26 % (OHZ3011).

Before instrumentation, samples were scanned using 2D X-rays to select the least damaged specimens and avoid biases from preexisting microcracks. 3D X-ray scans were performed on some selected samples with the following acquisition parameters: 1440 projections, 3 images per projection, 1000 ms exposure per image, 120 kV voltage, 200 μA current, and a voxel resolution of 20 μm. Data were analyzed using VGStudio MAX software. Strain gauges measured axial and lateral deformations accounting for transverse isotropy (perpendicular orientation: Fig.1a; parallel orientation: Fig.1b. Volumetric strains were calculated from the measured axial and lateral components, with compression taken as positive.After instrumentation, specimens were sealed in a triaxial cell and immersed in a synthetic-oil bath for temperature control (Fig.1 e-f).

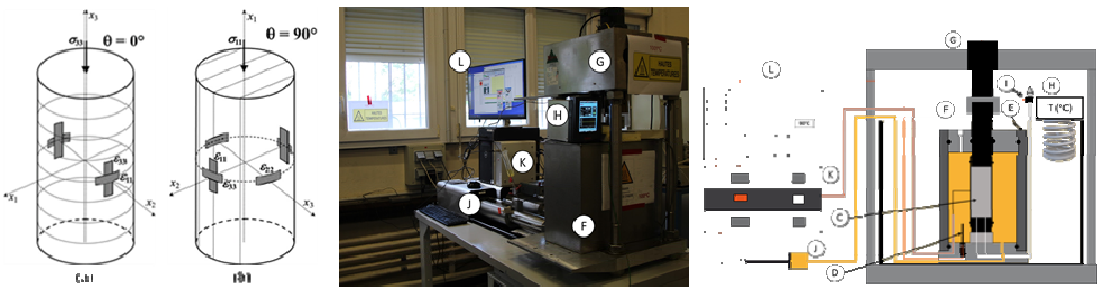


Fig. 1 Strain gauge arrangement and coordinate system for COx claystone specimens in both orientations—(a) perpendicular and (b) parallel to the bedding plane—along with a photo and schematic of the experimental setup: (c) sample, (d). thermocouple, (e) triaxial cell, (f) stainless-steel bath, (g) mechanical press, (h) immersion heater, (i) drainage valve, (j) oil pump, (k) data acquisition system, and (l) press and pump controller.

Four temperatures (20, 45, 70, 90 °C) and four confining pressures (0.5, 4, 8, 12 MPa) were tested on COx claystone in parallel and perpendicular orientations to bedding. Hydrostatic confining pressure was applied at 1×10^{-3} MPa/s and maintained constant (Fig.2). Heating (for T > 20 °C) used a 10 °C/h ramp, generating transient undrained conditions due to the low permeability of the material, followed by 14 - 16 h equilibration to dissipate pore overpressures (Souley et al. 2026). Deviatoric loading was applied at 0.04 μm/s (10^{-6} s^{-1} considering the specimen height) with unloading-reloading cycles each 4 MPa. Before each unloading, a 15 min relaxation phase was applied to dissipate the viscous effects, thus allowing a better determination of elastic parameters.

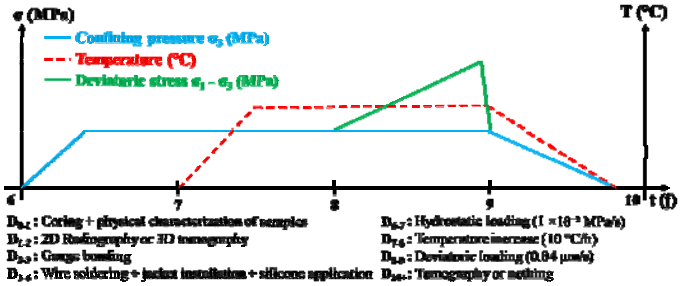


Fig. 2 Stresses and temperature paths during the tests.

After testing, specimens were removed from the Viton membrane, strain gauges were taken off, and samples were protected with plastic and cellophane before a final X-ray tomography scan. Due to the low permeability and short drainage length (38-42 mm), the chosen deformation rate (10^{-6} s^{-1}) ensured quasi-drained conditions (Liu et al. 2019).

3 Influence of temperature on mechanical behavior

A total of 99 triaxial compression tests were conducted under parallel and perpendicular orientations across various confining pressures (0.5, 4, 8, and 12 MPa) and temperatures, with Fig.3 illustrating the peak deviatoric stress versus temperature for both orientations, along with cubic polynomial fits to describe the trends. At least two tests were conducted for each temperature at 4, 8, and 12 MPa, while only one test was performed at 0.5 MPa above 20 °C. First, it is worth noting that peak stress increases with confining pressure, for both parallel and perpendicular orientations. Second, for specimens perpendicular to the bedding plane, peak strength generally decreases with increasing temperature (16-21 % reduction at 90 °C) for confining pressures of 4 - 12 MPa, whereas for parallel orientation the temperature effect remains negligible.

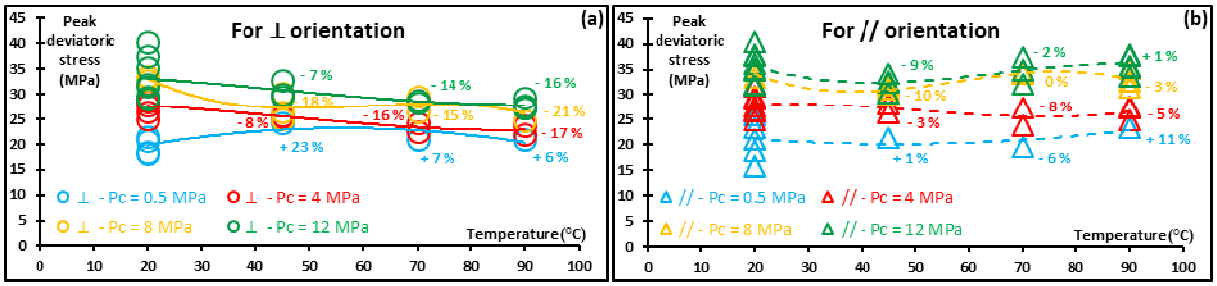


Fig.3 Evolution of peak deviatoric stress as a function of temperature (20, 45, 70, and 90 °C) for different confining pressures (0.5, 4, 8, and 12 MPa) and orientations – (a) Perpendicular; (b) Parallel.

The decrease in strength with increasing temperature for the perpendicular orientation does not follow a linear trend. This behavior has already been reported in the literature (Gbewade et al. 2023 ; Wang et al. 2026). This trend may be related to the limited temperature range studied and the intrinsic heterogeneity of the material, making the interpretation of this behavior challenging. For specimens parallel to the bedding plane, temperature has little effect on peak strength. The suction (capillary attraction forces), which plays a major role due to the small pore size of COx claystone, can explain this different impact of temperature as a function of orientation. Indeed, heating induces desaturation of the samples and therefore the development of suction forces, thus generating an overall confining effect, which partially hides the negative impact of temperature on the peak strength for both orientations. In addition, at mesoscopic scale, suction generates also compaction of bedding planes, as already proposed by Zhang et al. (2012). For this orientation, the failure is mainly due to the opening of bedding planes aligned in parallel to the axial stress. Therefore, the mechanical strength significantly increases due to the action of suction, thus explaining why temperature has almost no negative impact for this orientation.

Heating a low-permeability porous medium such as COx induces pore fluid overpressure, primarily due to the large difference between thermal expansion coefficient of pore water (2.6×10^{-4} °C^{-1} at 25 °C and 5.8×10^{-4} °C^{-1} at 80 °C) and that of the argillite solid skeleton (2.6×10^{-5} °C^{-1} at 25 °C and 11×10^{-5} °C^{-1} at 80 °C) (Mohajerani 2011; Zhang et al. 2017). An initially high heating rate (10 °C/h) was deliberately chosen to simulate in situ undrained conditions, generating significant interstitial water overpressure due to the very low permeability of the argillite. This overpressure was used to analyze microfracture-induced damage, and it likely dissipated during the 14 - 16 h waiting period imposed on each sample before deviatoric loading. Moreover, COx argillite can be regarded as a composite material composed of a clay matrix containing carbonate and quartz inclusions. These constituents exhibit different thermo-mechanical properties, particularly in terms of thermal expansion (Belmokhtar 2017). Mismatches in expansion coefficients - similar for clay and quartz ($\alpha_s = 3.4 \times 10^{-5}$ °C^{-1}) but two to three times lower for calcite and feldspar ($\alpha_s = 1.38 \times 10^{-5}$ °C^{-1}) - may induce localized debonding or shear at mineral interfaces, ultimately degrading the mechanical properties of the rock.

4 Tomographic observations

Fig.4a shows two samples (20 °C and 90 °C) cored perpendicular to the bedding plane and tested under a confining pressure of 12 MPa. Initially, the 20 °C sample exhibits coring-induced cracks mostly parallel to the bedding planes, reflecting the transverse isotropy of COx argillite and the role of bedding as weakness planes. After mechanical loading, a macroscopic shear fracture inclined at about 45° develops in the upper part of the sample, consistent with the expected failure angle under confining pressure. While many initial cracks and bedding planes close under axial stress and confining pressure, some preexisting inclined cracks promote stress concentration and coalescence, leading to final macroscopic failure. Quantitative analysis (Fig.4b, green squares) shows a negligible change in total fracture volume (2.1% to 1.9%), as the reduction of initial crack volume is offset by the formation of the macroscopic fracture.

Initially, the 90 °C sample exhibits very few coring-induced microcracks, representing a negligible volume (0.1%), likely due to a different coring device that generated less initial damage. These cracks do not influence the subsequent test. After heating and loading, a vertical macroscopic fracture (≈90°) develops, accompanied by a marked increase in fracture volume (0.1% to 3.9%)(Fig.4b, red squares), reflecting macroscopic failure. X-ray tomography reveals a dense, interconnected fracture network concentrated in the lower part of the sample, identified as the main deformation and fracture propagation zone, likely enhanced by edge effects and higher thermal gradients in the metallic base plate. The main fracture propagates preferentially through the matrix near inclusion-rich areas, where stress concentrations promote crack initiation and coalescence, consistent with the findings ofShi et al. (2021).

These results indicate that, for the perpendicular orientation, temperature promotes the development of an additional fracture network with specific orientations, which partly explains the moderate but noticeable effect of this parameter on the peak strength observed for this configuration (Fig.3a).

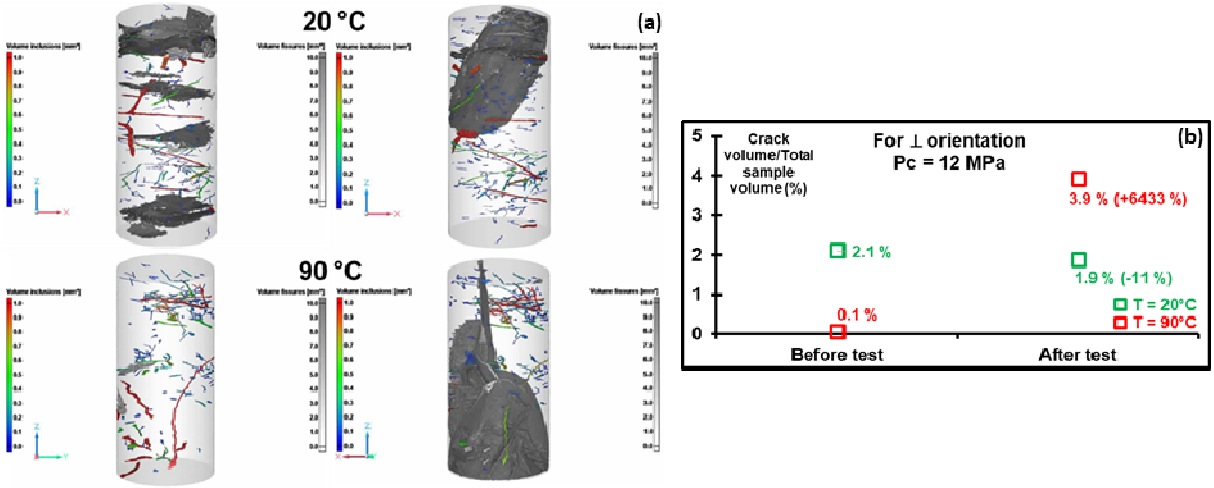


Fig.4 (a) 3D tomography scans of two samples oriented perpendicular to the bedding plane, before testing (left) and after testing (right), under Pc=12 MPa, at T=20 °C (top) and T=90°C (bottom); (b) Comparison of fracture volume before and after testing for samples perpendicular to the bedding plane under Pc=12 MPa at two different temperatures: T=20°C → green; T=90°C → red.

Fig. 5a highlights two samples (20 °C and 90 °C) cored parallel to the bedding plane and tested under a confining pressure of 12 MPa. Initially, the 20 °C sample exhibits coring-induced cracks mainly parallel to the bedding planes. After mechanical loading, a failure fracture inclined at about 60° to the horizontal develops, consistent with expected shear mechanisms under these conditions. Unlike the perpendicular sample tested at room temperature, a significant increase in fracture volume is observed after testing (1.6% to 2.7%) (Fig. 5b, green triangles). This increase results from the progressive opening of preexisting cracks aligned with the bedding plane (parallel here to the major principal stress), combined with the formation of the main macroscopic failure fracture. Preexisting cracks slightly inclined to the bedding likely acted as initiation sites, promoting strain localization and fracture coalescence.

Initially, the 90 °C sample exhibits a higher density of coring-induced microcracks, representing 2.7% of the total volume. After heating and loading, tomography reveals the development of a diagonal macroscopic failure fracture inclined at about 60° to the horizontal, also consistent with the expected shear angle in clayey materials. This failure is accompanied by a significant increase in fracture volume (2.7% to 4.4%)(Fig. 5b, red triangles). Most preexisting cracks keep their original morphology and appear to have had limited influence on the main fracture path, which adopts an inverted "Y" geometry, with part of the initial network remaining isolated while another portion connects to the newly formed shear fracture.

These results indicate that, for the orientation parallel to the bedding plane, and given the 20 μm resolution of the tomographic imaging, increasing the temperature does not generate additional fracture networks within the samples, partly explaining the lack of temperature effect on peak strength for this orientation (Fig.3b).

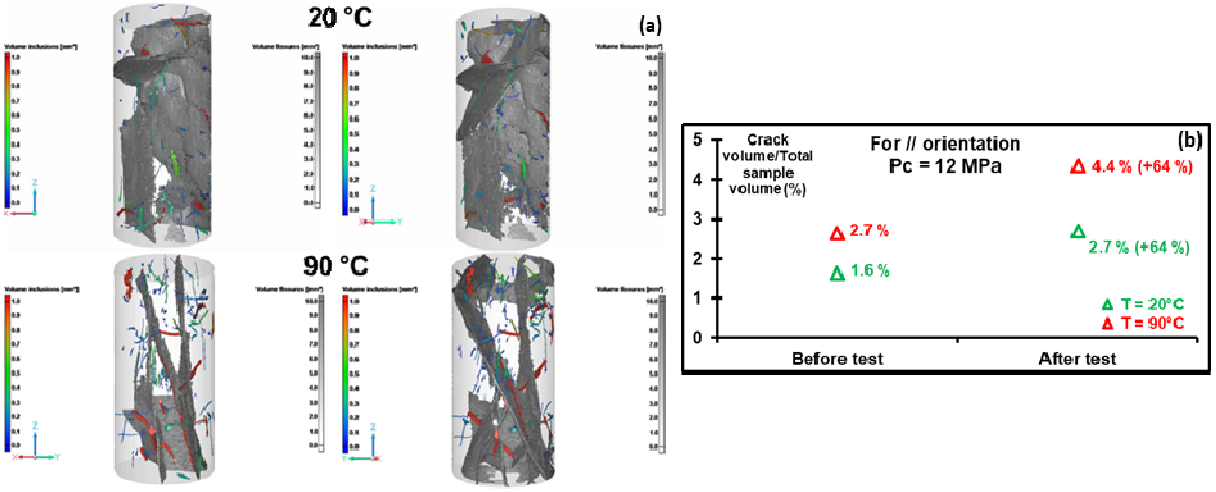


Fig. 5(a) 3D tomography scans of two samples oriented parallel to the bedding plane, before testing (left) and after testing (right), under Pc=12 MPa, at T=20°C (top) and T=90°C (bottom); (b) Comparison of fracture volume before and after testing for samples parallel to the bedding plane under Pc=12 MPa at two temperatures: T=20°C → green and T=90°C → red.

5 Conclusions

The experiments showed that peak strength of the COx argillite decreases with increasing temperature for the perpendicular orientation, while temperature has no effect on the parallel orientation. The initial heating phase induced interstitial water overpressure due to thermal expansion, likely reducing peak strength in the perpendicular orientation due to microcracking damage, with the effect increasing at higher temperatures. For the parallel orientation, suction induced by sample desaturation during heating hides the negative temperature impact on strength due to the compaction of bedding planes. Confining pressure also plays a significant role: higher confinement increases peak strength, confirming that confinement enhances the material's resistance to deformation.

Tomographic results highlight the combined influence of anisotropy, confinement, and temperature on fracturing mechanisms. For the perpendicular orientation, axial stress generally tends to close preexisting cracks aligned along the bedding plane. However, at 90 °C, an interconnected fracture network develops, mainly in the lower part of the samples, linked to edge effects and inclusions. In contrast, for the parallel orientation, temperature does not promote additional fracturing, and failure

occurs through progressive opening of preexisting cracks aligned with the bedding planes. Temperature appears to have little effect on the deformation mechanisms for this orientation.

These results enable the analysis of temperature effects on the mechanical behavior of COx by linking macroscopic responses to fracture network geometry. They also highlight the key role of structural anisotropy (orientation relative to bedding) in controlling thermo-mechanical fracturing and emphasize the importance of carefully controlling experimental conditions to predict the long-term behavior of this host rock. These findings also contribute to improving the design and safety assessment of the Cigéo repository, particularly for optimizing repository layout.

6 Acknowledgements

This study was funded by the French National Agency for Radioactive Waste Management (ANDRA) as part of its mission to develop and implement long-term solutions for radioactive waste management in France. The experiments presented in this study were conducted using the experimental facilities available at the HydroGéoMécanique multi-échelles platform - GeoRessources Laboratory -Université de Lorraine - CNRS.

7 References

Belmokhtar M. (2017) Contributions à l'étude du comportement thermo-hydro-mécanique de l'argilite du Callovo-Oxfordien (France) et de l'argile à Opalinus (Suisse). Thèse de doctorat, Université Paris-Est.https://pastel.hal.science/tel-01630492

Conil N., Talandier J., Djizanne H. N., de La Vaissière R., Righini-Waz C., Auvray C., Morlot C., Armand G. (2018) How Rock Samples Can Be Representative of in Situ Condition: A Case Study of Callovo-Oxfordian Claystones. *Journal of Rock Mechanics and Geotechnical Engineering*. pp. 613-623. https://doi.org/10.1016/j.jrmge.2018.02.004

Gbewade C., Grgic D. Giraud A., Schoumacker L. (2023) Experimental Study of the Effect of Temperature on the Mechanical Properties of the Callovo-Oxfordian Claystone. *Rock Mechanics and Rock Engineering*, pp. 1-22. https://doi.org/10.1007/s00603-023-03630-7

Grgic D., Moumni M., Giraud A., De La Vaissière R., Talandier J. (2023) Water Permeability Measurements by Steady-State and Pulse Decay Methods on the Callovo-Oxfordian Claystone and Impact on Its Mechanical Properties. *Rock Mechanics and Rock Engineering*. https://doi.org/10.1007/s00603-023-03340-0

Liu Z., Shao J., Xie S. Y., Conil N., Talandier, J. (2019) Mechanical Behavior of Claystone in Lateral Decompression Test and Thermal Effect. *Rock Mechanics and Rock Engineering*. https://doi.org/10.1007/s00603-018-1573-3

Mohajerani M. (2011). Etude expérimentale du comportement thermo-hydro-mécanique de l'argilite du Callovo-Oxfordien. Thèse de doctorat, Université Paris-Est. https://pastel.hal.science/pastel-00647890

Shi H. L., Hosdez J., Rougelot T., Xie S. Y., Shao J. F., Talandier J. (2021) Analysis of Local Creep Strain Field and Cracking Process in Claystone by X-Ray Micro-Tomography and Digital Volume Correlation. *Rock Mechanics and Rock Engineering.* pp. 1937-52. https://doi.org/10.1007/s00603-021-02375-5

SouleyM., De Lesquen C., Vu M. N., Armand G. (2026) Advanced Thermo-Hydro-Mechanical Modelling of Callovo-Oxfordian Claystone: Temperature Effects and Multi-Scale Applications for Geological Disposal Safety. *International Journal of Rock Mechanics and Mining Sciences.* Volume 199. https://doi.org/10.1016/j.ijrmms.2026.106397

Wang C., Xie S., Shao J. F., Vu M. N., De Lesquen C. (2026) On the Thermal Effects of Mechanical Behavior in the Callovo-Oxfordian Claystone. *International Journal of Rock Mechanics and Mining Sciences*. https://doi.org/10.1016/j.ijrmms.2025.106367

Zhang C. L. (2017) Examination of Effective Stress in Clay Rock. *Journal of Rock Mechanics and Geotechnical Engineering.* pp. 479-89. https://doi.org/10.1016/j.jrmge.2016.07.008

Zhang C. L., Conil N., Armand, G. (2017). Thermal Effects on Clay Rocks for Deep Disposal of High-Level Radioactive Waste. *Journal of Rock Mechanics and Geotechnical Engineering.* pp. 463-78. https://doi.org/10.1016/j.jrmge.2016.08.006

Zhang F., Hu D. W., Xie S. Y., Shao J. F. (2014) Influences of Temperature and Water Content on Mechanical Property of Argillite. European Journal of Environmental and Civil Engineering. pp. 173-89. https://doi.org/10.1080/19648189.2013.852485

Zhang F., Xie S. Y., Hu D. W., Shao J. F., Gatmiri. B. (2012) Effect of Water Content and Structural Anisotropy on Mechanical Property of Claystone. *Applied Clay Science*. pp. 79-86. https://doi.org/10.1016/j.clay.2012.09.024

Zhang W. (2021) Contribution à l'étude expérimentale du comportement mécanique des argilites du Callovo-Oxfordien : effets du chemin de chargement et de la température. Thèse de doctorat, Université de Lille. https://theses.fr/2021LILUN037

Laboratory Evaluation of Long-Term Behaviour of Different Natural and Cementitious Materials

Goran Baloević*, Goran Vlastelica**, Nikola Grgić***, Mario Filipović*, Saltanat Yesselbayeva****, Gábor Somodi****, Gyula Bögöly**** & Péter Görög****

**University of Split, Faculty of Civil Engineering, Architecture and Geodesy, Department of Materials, Split,Croatia*
baloevic@gradst.hr

***University of Split, Faculty of Civil Engineering, Architecture and Geodesy, Department of Geotechnical Engineering, Split,Croatia*
goran.vlastelica@gradst.hr

****University of Split, Faculty of Civil Engineering, Architecture and Geodesy, Department of Concrete Structures and Bridges, Split,Croatia*
ngrgic@gradst.hr

*****Budapest University of Technology and Economics, Faculty of Civil Engineering, Department of Engineering Geology and Geotechnics, Budapest,Hungary*
gorog.peter@emk.bme.hu

0000-0002-0360-1966

Abstract

The long-term behaviour of brittle materials plays a critical role in understanding time-dependent deformation and failure. For example, it is nowadays essential in the design of a nuclear waste disposal system expected to function for a very long period. It is also crucial when the land above underground quarries that are more than a hundred years old is used as a construction zone. Although brittle materials, such as limestones, dolomites, marls, and concrete, also typically have high stiffness and strength under normal loading conditions, their long-term behaviour, including creep processes, reduces their strength properties over engineering time scales. Creep tests under constant load were performed to investigate this behaviour and to compare the properties of different materials. In brittle rocks, the creep response is commonly divided into three stages: primary (decelerating strain rate), secondary (quasi-steady strain rate), and tertiary (accelerating strain rate). The transition from secondary to tertiary creep is particularly important, as it reflects the onset of unstable crack propagation and provides a basis for predicting long-term failure. Time-dependent deformation is strongly influenced by environmental factors, including moisture, rock composition, and stress level. Samples of drilled rock cores obtained from different locations were examined under long-term uniaxial loading conditions. The normal and long-term behaviour of these materials is evaluated and compared. The results will be used in the second phase of the research to calculate the long-term stability of underground structures and determine the differences between the short-term and long-term behaviour of the cellars, taking into account the effect of surface loads.

Keywords

Brittle materials, Long-term performance, Creep test, Uniaxial loading conditions.

1 Introduction

This study examines the long-term behaviour of various rock and cemented materials, including calcareous marl, porous limestone, while dolomite and concrete will be tested in the second phase of the research. The investigated rocks originated from the Dalmatian area of Croatia and from the Budapest area of Hungary. Firstly, the physical and rock mechanical properties of the investigated materials are introduced. The long-term property tests were conducted at the University of Split. Three types of rocks: Eocene calcareous marl from Dalmatia, Eocene Buda Marl from Budapest area and Miocene porous limestone from Budapest area were tested.

Marl is considered a unique transitional rock in engineering, with a mechanical response between that of stiff soils and soft rocks. Its long-term behaviour is defined by a triad of time-dependent deformation (creep), water sensitivity, and weathering-induced degradation. Understanding these processes is essential for the long-term stability design of civil engineering structures, particularly tunnels and slopes (Görög, 2007). For porous limestone it is also essential to know its creep parameters since they are a host rocks of underground cavities in Budapest (Zenah et al. 2022).

Under sustained loading, marl and soft rocks exhibits significant creep deformation; during this process, long-term strength remains considerably lower than short-term, instantaneous strength (Zivaljevic & Tomanovic, 2021). Laboratory creep tests—which can last from 3 to over 180 days—distinguish three phases of the process: in the primary phase, the closure of microporosity dominates; in the secondary phase, a steady-state deformation rate is established; while in the tertiary phase, micro-pores coalesce into cracks, leading to accelerated deformation and eventual failure. Lateral (horizontal) pressure plays a decisive role in these processes, primarily by influencing the initial and long-term creep rates. Research has also highlighted that marl exhibits "softening" behaviour, especially due to unloading effects during excavation (Tomanovic, 2006; Mánica et al., 2018).

The Eocene flysch formation, which outcrops extensively along the Adriatic coast of Croatia, particularly in the Dalmatian region, represents a thick, geotechnically challenging sedimentary sequence. The backbone of this flysch complex consists of various marly lithotypes, which alternate with siltstones, sandstones, and limestones. Due to the intense tectonic history of the Dinarides, these marly soft rocks are frequently folded, faulted, and heavily jointed, directly defining the geomorphology and engineering geological conditions of the coastal zone. The engineering significance of this marl has expanded drastically in recent decades due to rapid urban development, tourism-driven coastal expansion, and the construction of major transport infrastructure, including highways, deep open cuts, and foundations. These flysch marls occupy a complex transitional spectrum between weak rocks and soils. Consequently, they present severe challenges for slope stability, tunnel support design, and foundational bearing capacity. Engineering hazards associated with the Dalmatian marl are its high vulnerability to rapid environmental degradation. During excavation, moisture fluctuations cause the rock matrix to disintegrate rapidly, leading to a drastic reduction in shear strength and inducing shallow landslides or rockfalls along cut slopes (Vlastelica et al. 2018).

The Eocene Buda Marl is a regional sedimentary formation that outcrops extensively across the Buda Mountains and directly underlies major urban zones of Budapest, Hungary. As a classical transitional lithotype, the Buda Marl occupies a complex geotechnical position between hard rocks and cohesive soils. Its spatial occurrence and variable lithological composition—ranging from clayey marl to highly cemented calcareous marl—have fundamentally influenced both the geomorphological evolution of the capital and its historical urban development (Görög and Török 2026). From an engineering geological perspective, the significance of the Buda Marl is heavily highlighted by its role as the host formation for critical infrastructure, deep foundations, and historic subterranean structures in Budapest. Notable historical structures, such as the underground cellars, tunnels, and foundational retaining walls of the Budapest Castle Hill, are structurally tied to or cut into this formation. Furthermore, due to the expansion of modern metropolitan subway networks and deep multi-story underground parking garages, civil engineering activities routinely interact with this marly sequence. While the highly cemented calcareous marl profiles behave as a stable, medium-to-strong soft rock mass, the lower-carbonate, clay-rich variants often exhibit soil-like plasticity and are highly susceptible to rapid slaking and shear strength degradation upon moisture fluctuations (Görög 2007). The presence of distinct lamination, bedding planes, and tectonic jointing further complicates the in-situ rock mass behaviour, potentially triggering anisotropic failure mechanisms.

The Miocene porous limestone is one of the most significant and historically relevant sedimentary dimension stones in Hungary, particularly within the urban area of Budapest. Due to its favourable workability and availability, this bioclastic and oolitic limestone was extensively quarried for centuries, serving as the primary building material for major historical monuments including the Hungarian Parliament Building, the Citadel, and the Matthias Church (Török et al. 2004). The most intensive surface and subsurface quarrying activities occurred in the Budafok and Kőbánya districts of Budapest. As a direct result of these extensive historic subsurface mining operations, a massive, interconnected network of underground galleries and cellar systems was created. Over time, these shallow underground cavities found secondary use, serving as brewery storage, winery facilities, and mushroom growing. In recent decades, however, the expansion of the urban environment and the critical shortage of greenfield development sites in Budapest have led to intense infrastructural and civil construction directly above these historic quarry zones. Managing the stability of these shallow cavities presents a severe engineering geological challenge. The limestone host rock inherently behaves as a weak, soft rock with extremely high effective macro-porosity (Zenah et al. 2024).Therefore, a precise laboratory and numerical assessment of the long-term behaviour of this porous limestone framework is indispensable.

2 Test methodology

Specimens were obtained from the cellar and tested under laboratory conditions. Several rock physical tests were done according to national standards, such as American Society for Testing and Materials (ASTM) and European Standards (EN): the dry density was calculated according to EN 1936:2006. The uniaxial compressive strength (UCS) test for dry conditions was performed according to ASTM D7012-23.The indirect tensile strength tests (Brazilian tests) were done according to the ASTM D3967-23 descriptions. The rheological test methods are described in the ISRM Suggested Methods (Aydan et al. 2014), and in the code ASTM D7070. In our case, the long-term tests were conducted in accordance with ASTM D7070. Specimens about 100 mm in diameter and about 300 mm in height were cut from the cores of each type of rock. Before the long-term test, the uniaxial compressive strength of each rock type was measured. Drilled specimens were cut with a diamond saw for the compressive strength and creep tests. Specimens were prepared using a diamond-grinding machine to meet the requirements of the standards. Creep tests were conducted in a creep testing machine with a force capacity of 300 kN.

The long-term tests were performed under uniaxial stress conditions, with a constant stress rate applied for a long period. For the long-term test, the 30% of the measured UCS value was applied to each rock type as a long-term load. The load was constant, and the axial displacements of the specimens were measured, allowing the creep characteristics of each specimen to be recorded. For the displacement measurement, a manual displacement indicator with 0.001 precision was used. During the test, strains were measured at the left and right sides of the specimens. Herein, dial gauges and length comparators were used, with an accuracy of 0.001 mm. The strain was measured at the midpoint of the specimens, over a 200 and 220 mm (Fig. 1).



Fig. 1 Calcareous marl from Budapest prepared for the creep test.

The creep load was slowly increased to the test level over about 60 seconds; thereafter, the load was maintained at a constant level until failure. The temperature and humidity were kept constant in the lab during the test (T = 22°C, RH = 55%).A total of six specimens were prepared for the creep test. Four specimens (C1, C2, C3, and C4) were taken from the underground cellar system in the Kőbánya region of Budapest. The material of them is a very soft rock, the porous limestone, with different grain sizes. Specimens C1 and C3 were fine-grained, and specimens C2 and C4 were coarse-grained. Specimen Varosmajor was drilled at the Buda side of Budapest, while specimen GV was drilled at Dalmatia in the Split region. Both samples were calcareous marl with different strengths (Fig. 1).

3 Rock mechanical properties of the investigated materials

3.1 Marl

Marl is a rock that contains clastic material of the clay fraction (<0.002 mm) and carbonate (calcite); therefore, it is defined as a transitional rock between clastic and chemical sedimentary rocks (Pettijohn 1975). The coastal region of Croatia (Dalmatia) lies on the Eocene flysch formations. The most common lithotypes of the flysch formations in Dalmatia are breccias, breccia conglomerates, sandstones, detrital limestones, and marls, with varying $CaCO_3$ content (Šestanović 2000).The Eocene Buda Marl Formation plays an important role in the geology of Hungary. The Buda Marl is mainly associated with Budapest, as its name indicates. It occurs several construction sites in Budapest, construction pits, man-made and natural underground cavities.

The physical and mechanical properties of the Eocene flysch marls from the Dalmatian coastal region (Croatia) are introduced based on an extensive laboratory database according to Duhović et al. (2022). The dry unit weight was measured on 370 specimens; the mean is 22.06 kN/m^3, with a range of 14.14 kN/m^3 to 25.92 kN/m^3. Reflecting its micro-fabric texture dominated by calcitic micrite and varying clay matrix proportions, the mean effective porosity determined from 369 specimens is 15.31% (ranging from a highly compact 0.31% up to a highly porous 45.63%).The Uniaxial Compressive Strength (UCS) dataset, compiled from 400 intact rock specimens, exhibits highly heterogeneous behaviour, with a mean strength of 17.38 MPa. The overall strength spans a broad range from an extremely low 0.04 MPa to a maximum of 89.69 MPa. Notably, approximately 25% of the tested marl samples exhibit a UCS above the traditional soft rock upper limit of 25 MPa, which corresponds directly to the highly cemented, carbonate-rich calcareous marl variants. The tangent Young's modulus measured at 50% of the peak UCS for 192 samples ranged from 0.03 GPa (highly deformable) to 41.46 GPa, with a mean of 6.70GPa.

Among the Hungarian marls, the properties of the Eocene Buda Marl Formation were most extensively investigated due to its widespread distribution around Budapest. As with the marls from the Dalmatian region, the lime content determines their properties (Görög 2007). The physical and mechanical properties of all types of Buda Marl are described by Görög (2007), Duhović et al. (2022), Davarpanah et al. (2022) and Görög and Török (2026). The introduction to its properties in this research focuses on the calcareous type, since the long-term test was conducted on that type of marl.

The following physical and rock mechanical parameters of the calcareous type of Buda Marl ($CaCO_3$ content of 60–80%) are from the research papers mentioned above. Based on 86 tested specimens under air-dry conditions, the intact material has a mean density of 2468 kg/m^3 (median of 2487 kg/m^3 and standard deviation of 83 kg/m^3). Reflecting its highly cemented fabric, the effective porosity measured across 17 specimens yields a low mean value of 2.85% (median of 2.84%, and standard deviation of 0.26%).The uniaxial compressive strength (UCS) data obtained from 90 specimens represent a highly variable distribution due to microstructural heterogeneity, with a mean of 43.41 MPa (median of 38.97 MPa, standard deviation of 21.77 MPa). Under optimal diagenetic cementation, the peak intact compressive strength of the air-dry calcareous marl matrix can reach 100 MPa. The indirect tensile strength determined by Brazilian tests on 89 intact rock samples reveals a mean value of 3.81 MPa (median of 3.68 MPa, standard deviation of 2.04 MPa).The modulus of elasticity, measured from 71 specimens, shows significant scatter due to varying clay-to-carbonate ratios, yielding a mean elastic modulus of 6.87 GPa (median of 5.75GPa, standard deviation of 4.16GPa).

3.2 Porous limestone

The other rock type, which is important and widespread in and around Budapest, is the Miocene Porous Limestone. This oolitic limestone was used as the most important dimension stone in Budapest. The quarrying of this stone resulted in significant areas covered by this rock type being undermined. Investigating it is important for the stability calculations of these areas.

The physical and rock mechanical properties of the Miocene porous limestone were analysed by several researchers, such as Török et al. (2004), Zenah et al (2022), Szabó et al. (2022), Zenah and Görög (2024). The porous limestone is characterised by a highly open, macroporous fabric, which inherently results in lower density and significantly higher effective porosity than the calcareous marl. The laboratory testing of intact air-dry specimens yields a mean density of 1710 kg/m^3 (with values typically spanning a range between 1410 kg/m^3 and 1920 kg/m^3). Due to the bioclastic and oolitic texture of the limestone, the effective porosity is exceptionally high, with a mean value of 32.8% (ranging from 22.0% to 41.2%). Under air-dry conditions, the intact porous limestone behaves as a classic weak rock, exhibiting brittle failure mechanisms during laboratory loading. The UCS is governed heavily by the total porosity of the individual core specimens. The statistical mean UCS under air-dry conditions is 8.12 MPa. The broader laboratory database reveals an experimental range from a very weak 3.22 MPa up to 14.88 MPa for the denser profiles. Brazilian tensile tests performed on the specimen show a mean tensile strength of 1.11 MPa (with an experimental spread between 0.49 MPa and 1.95 MPa). The Young's modulus, reflecting the highly compressible framework of the porous matrix, exhibits a mean value of 2120 MPa (spanning from a flexible 950 MPa up to 3410 MPa in low-porosity core samples).

4 Test results and discussion

Prior to the creep tests, the uniaxial compressive strength of the materials was measured in accordance with ASTM D7012-23. The test results are presented in Table 1, and the UCS values of the materials are in accordance with the descriptions in Chapter 3. The measured UCS of the porous limestone is lower than the average, whereas that of the calcareous marl is higher, especially for the Dalmatian sample.

Table 1. Uniaxial compressive strength of the tested materials.

Specimen	UCS [MPa]
C1	3.69
C2	3.04
C3	4.66
C4	2.85
Varosmajor	52.16
GV	115.71

Since the load was applied at approximately 30% of each material's compressive strength, specimens were divided into groups to apply different axial forces due to the different compressive strengths of the materials. Table 2 shows the dimensions, applied creep load, and creep stress for all specimens.

Table 2. Uniaxial compressive strength of the tested materials.

Specimen	Diameter [mm]	Height [mm]	Base [mm]	Applied creep load [kN]	Applied stress [MPa]
C1	105.1	300	200	6.0	0.7
C2	105.0	300	200	6.0	0.7
C3	105.4	300	200	6.0	0.7
C4	104.9	300	200	6.0	0.7
Varosmajor	101.4	300	220	130.0	16.1
GV	84.8	300	220	190.0	33.6

Immediately after the test began, specimens C2 and C3 failed, therefore the test was stopped. Also, the Varosmajor specimen failed immediately due to a pre-existing crack, leading to material cracking under compressive force (Fig. 2 left side picture). Specimens C1 and C4 maintained load, as well as specimen GV. The successful creep test was performed on two porous limestone specimens (C1 and

C4) and one calcareous marl sample (GV). After 15 days, the specimen C4 began to crush at the top, and several days later, a crack formed in its upper part (Fig. 2, right side), leading to instability of the test system; thus, the measurement of specimen C1 also stopped. The C4 specimen was a coarse-grained porous limestone with the smallest uniaxial compressive strength of 2,8 MPa. Therefore, the prediction was that it would fail first under the long-term constant load.

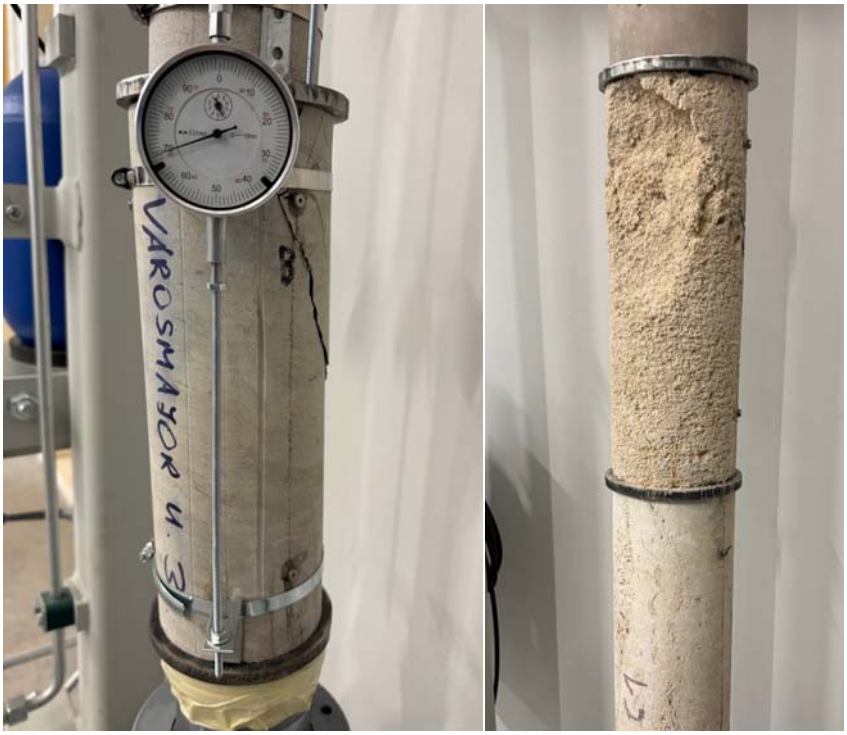


Fig. 2 Failure of the sample Varosmajor (left side) and failure of the sample C4 after 23 days (right side).

Fig. 3 on the left side shows the creep characteristic curve for rocks according to Tarifard at al. (2024). The right side of Fig. 3 shows the measured creep of specimen C4 for the 23-day period. Rock creep deformation is divided into three phases: primary (first or transient), steady-state (secondary), and tertiary (accelerated) creep. The initial stress leads to immediate strain, and the strain rate decreases over time during the transient creep stage, as seen in the measured dataset. In the secondary creep stage, the strain rate remains constant over time, and creep is stable. For the coarse-grained porous limestone (specimen C4), the creep process was rapid, with the transient phase ending after the first day and the secondary stable creep phase beginning. The second phase lasted 17 days according to the measurements, but the first crack appeared on the 15th day. The third phase of creep behaviour is characterised by increased microcracking, which reduces strength and stiffness. After 18 days, the accelerated creep phase was started, and the specimen failed on the 23rd day.

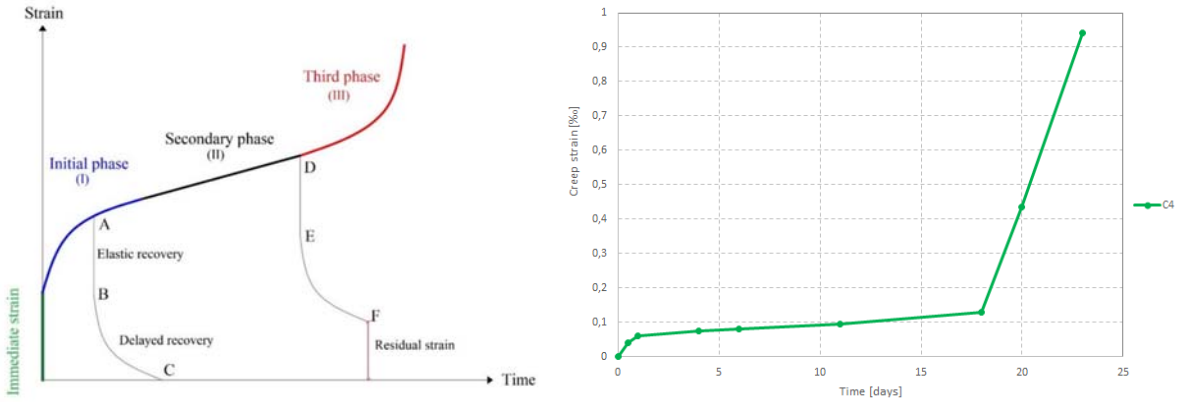


Fig. 3 The three stages of rock creep (left side, Tarifard et al. 2024) and measured creep of sample C4 (right side).

Fig. 4 shows the measured creep for all three specimens without the tertiary creep phase. For the C4 sample, the test ends with sample failure; for the C1 and GV samples, the measurements are only in the secondary phase. The creep measurement for sample GV is still in progress. The first creep stage finished after the first day for all the samples. The creep curve for sample C1 can be compared to C4

since both are porous limestones. C1 is a fine-grained one, while C4 is a coarse-grained one. The creep process, according to the creep curves, is the same, but for the coarse-grained one, the creep strain is almost twice as big as for the fine-grained one. The tangent for the line fitted on the secondary phase creep points 0.004 for sample C4 and 0.0024 for sample C1. Therefore, the slope of the coarse-grained sample is twice as steep as that of the fine-grained sample. It means that the same creep load in the secondary phase produces greater creep strain in the coarse-grained type. While the marl from Dalmatia has an almost horizontal creep curve in the secondary phase.

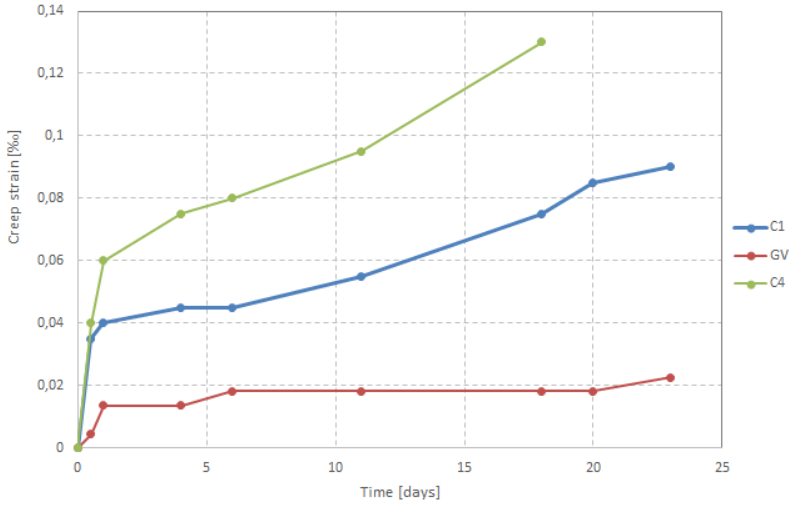


Fig. 4 Measured creep until secondary phase for all three specimens.

5 Conclusions

This study presented a comparative creep analysis for different cementitious rock materials. In this research phase, several materials were planned for testing, but due to limited testing capacity and inhomogeneous samples with microcracks, only three creep tests were performed. One fine-grained, one coarse-grained porous limestone sample originated from cellars from the Budapest area, and one calcareous marl sample from the Dalmatian area. The porous limestone is a very soft rock with high porosity; the calcareous marl behaves like a hard rock. The maximum secondary creep rate was the smallest for the calcareous marl, around 0,02‰. But there were significant differences between the creep of the two different porous limestone types as well. The maximum creep in the secondary creep phase was around 0,09‰ for the fine-grained type and 0,13‰ for the coarse-grained type, but these measurements were taken on different days. For the coarse-grained type, the third, accelerated creep phase was also registered, and after it, the specimen failed.

The creep tests are still in progress, so these results will be completed. The measured data will be used for creep analysis for the underground cellars. The surface above the cellars will be loaded with industrial buildings, and the creep of the unsupported cavities can be significant.

Acknowledgements

The support provided by the Ministry of Culture and Innovation of Hungary from the National Research, Development and Innovation Fund, financed under the TKP2021-NVA funding scheme (project no. TKP-6-6/PALY-2021) The financial support of the Hungarian-Croatian bilateral project, National Research, Development and Innovation Fund, grant no. 2023−1.2.4.-TéT-2023-00044 is also acknowledged.

This paper/research was also partially funded by the European Union (NextGenerationEU) under the Croatian Recovery and Resilience Plan 2021–2026 (NRRP), through the University of Split institutional project “Integrated Approach to the Sustainable Revitalization of the Urban Environment Using Natural Materials (URB-NAT); Ia 1.1.2. URB-NAT”, approved by the Ministry of Science, Education and Youth of the Republic of Croatia.

References

Aydan, Ö., Ito, T., Özbay, U.*et al.* (2014) ISRM Suggested Methods for Determining the Creep Characteristics of Rock. *Rock Mech Rock Eng*47, 275–290. https://doi.org/10.1007/s00603-013-0520-6

Chafia, M. et al. (2010): Analysis of multi-stage creep and swelling oedometric tests on a French marl. EUROCK 2010, Lausanne, pp. 111-114.

Davarpanah SM, Sharghi M, Tarifard A, Török Á, Vásárhelyi B (2022) Studies on the mechanical properties of dry, saturated, and frozen marls using destructive and non-destructive laboratory approaches. Iran J Sci Technol Trans Civ Eng. https://doi.org/10. 1007/s40996-021-00690-z

Duhović, A., Cvitanović, N. Š., Vlastelica, G., Török, Á., & Görög, P. (2022). Marly Soft Rocks: Correlation of Physical and Mechanical Properties—Examples from Dalmatia (Croatia) and Budapest (Hungary).*Symmetry*,*14*(10), 2170. https://doi.org/10.3390/sym14102170

Fei, L. et al. (2025): Multiscale observations of diurnal thermal effects on rock failure and crack dynamics in soft marl layers. Engineering Geology, Vol. 354.

Görög P (2007) Characterization and mechanical properties of Eocene Buda Marl. Cent Eur Geol 50(3):241–258. https://doi.org/10.1556/CEuGeol.50.2007.3.4

Görög, P., Török, Á. (2026) Influence of water on the physical properties of marl, calcareous marl, clayey marl, and limestone: a comparative study.*Bull Eng Geol Environ*85, 115 (2026).https://doi.org/10.1007/s10064-025-04772-4

Mánica, M. et al. (2018): Nonlocal plasticity modelling of strain localisation in stiff clays. Computers and Geotechnics, 103:138-150.

Pettijohn FJ (1975) Sedimentary rocks. Harper & Row, New York, p 628

Šestanović, S. Engineering–geological characteristics of marl from Eocene flysch in the City of Split. In Proceedings of the Second International Symposium on Hard Soils–Soft Rocks: The Geotechnics of Hard Soils–Soft Rocks, Naples, Italy, 12–14 October 1998; Evangelista, A., Picarelli, L., Eds.; Balkema: Rotterdam, The Netherlands, 2000; pp. 311–314.

Szabó, Zs., Zenah, J.; Görög, P. (2022) Effect of surface load on the stability of shallow cavities in Budapest, Hungary. In: Coric, Slobodan; Papic, Jovan; Jovanovski, Milorad; Peshevski, Igor (ed) 5th Symposium of the MAG (Macedonian Association for Geotechnics) an ISRM Specialized Conference, 2nd Conference of regional geotechnical societies : Engineering problems in soft rocks - Tradition of Rock Mechanics in Macedonia, Skopje, Macedonian Association for Geotechnics pp. 282-289.

Tarifard, A., Ákos, T., Görög, P. (2024) Review of the creep constitutive models for rocks and the application of creep analysis in geomechanics. Rock Mechanics and Rock Engineering (2024) 57:7727–7757 https://doi.org/10.1007/s00603-024-03939-x

Tomanovic, Z. (2006) Rheological model of soft rock creep based on the tests on marl. Mechanics of Time-Dependent Materials, 10(2):135-154.

Török Á, Rozgonyi N, Prikryl R, Prikrylová J (2004) Leithakalk: the ornamental and building stone of Central Europe, an overview. Czech Republic, pp 89–93

Vlastelica G, Miščević P, Štambuk Cvitanović N (2018) Durability of soft rocks in eocene flysch formation (Dalmatia, Croatia). Eng Geol 245:207–217. https://doi.org/10.1016/j.enggeo.2018.08.015

Zenah, J, Görög, P. (2024) The Effect of GSI and mi on the Stability of 3D Twin Tunnel in Limestone PERIODICA POLYTECHNICA-CIVIL ENGINEERING 68 : 2 pp. 600-607. 8 p.

Zivaljevic, S. &Tomanovic, Z. (2021): Loading history effect on time-dependent deformations after unloading – reversible creep. Mechanics of Time-Dependent Materials, 26:499–530.

Assessing the uniaxial compressive strength of limestones using indirect testing methods

N. Salčin
Hidrozavod DTD, Belgrade, Serbia
nino.salcin@hidrozavoddtd.rs
0009-0002-3884-616X

M. Marjanović
Faculty of Mining and Geology, Belgrade, Serbia
milos.marjanovic@rgf.bg.ac.rs
0000-0002-9675-1401

Abstract

The uniaxial compressive strength of rocks is a key design parameter, but its reliable determination remains a challenge due to the heterogeneity, cracking, and anisotropy of rock materials. Standard laboratory testing of uniaxial compressive strength gives the most accurate results, but is challenging, expensive, and often limited by sample quality and availability. Therefore, indirect methods are widely used in practice. This paper presents research on limestones from the Belgrade area to determine correlations between compressive strengths obtained using different indirect testing methods. A total of 156 samples were tested, on which needle penetration tests, Schmidt hammer tests, and point load tests were conducted. Numerous existing correlations across different tests and lithologies were considered; a testing procedure combining all three tests was given, and the results can serve as a basis for optimizing future geotechnical investigations of Sarmatian limestones in the Belgrade area.

Keywords

Uniaxial compressive strength, Needle penetration test, Point load test, Schmidt hammer test.

1 Introduction

Uniaxial compressive strength (UCS) is one of the basic parameters in geotechnical design. Although direct laboratory testing is considered the most reliable, it is often expensive, time-consuming, and limited by sample quality. Therefore, indirect methods are widely used in practice, enabling a quick and economical assessment of strength in the field or with minimal sample preparation.
Some methods for the indirect determination of compressive strength include the point load test, the Schmidt hammer test, and the needle penetrometer test. These methods do not directly measure a strength value but instead index parameters that are translated into UCS via empirical correlations. However, the reliability of these correlations depends strongly on rock type, so it is recommended to determine local correlations when possible.

2 Geology and sampling

The samples used in the study were obtained from exploratory boreholes drilled in the Belgrade territory as part of geological investigations for the construction of the metro system. Lithologically, the samples belong to Sarmatian limestones. A significant variability in physico-mechanical properties has been observed, despite the similar lithology. Some samples are characterized by compact, high-strength limestones, Fig 1, while others consist of sandy, more porous limestones with considerably weaker mechanical properties, Fig 2. This heterogeneity significantly impacts test results.



Fig. 1 High-strength limestones.



Fig. 2 Weaker sandy limestones.

3 Methodology

To estimate uniaxial compressive strength, three indirect methods were used: the Point Load Test (PLT), the Schmidt hammer test, and the needle penetration test. The obtained results were interpreted using existing empirical correlations.

The Point Load Test was performed on unprepared core samples with a diameter of 83 mm. The obtained point load strength index was initially corrected to the standard sample diameter of 50 mm, in accordance with the recommendations of the International Society for Rock Mechanics (ISRM 1985), and then multiplied by a correction factor to estimate the uniaxial compressive strength.

Various empirical relationships from the literature were used to estimate UCS, among which the most commonly applied are those proposed by Broch and Franklin (1972) and Bieniawski (1974). See Eq.1.

$$UCS = 24 \times Is_{(50)} \tag{1}$$

Where UCS Unconfined compressive strength
24 Correction factor
$Is_{(50)}$ Corrected point load strength index

Although this correlation is straightforward, numerous authors report significant variability in the coefficients depending on the type of rock being tested (Kahraman, 2001; Tsiambaos and Sabatakakis, 2004), which limits its application without local calibration.

The Schmidt hammer test is a very fast and simple method that measures the rebound, which is then used to indirectly determine uniaxial compressive strength. Despite its simplicity, different correlations are used depending on the rock type. In this study, an L-type hammer was used, which is suitable for testing rocks of lower strength. Empirical correlations proposed by Deere and Miller (1966), Singh et al. (1983), and Kilic and Teymen (2008) were used to estimate UCS. However, as noted by numerous authors, there is no universal correlation applicable to all rock types, since the results are significantly influenced by factors such as surface roughness (Hucka 1965), moisture content (Sumner and Nel 2002), and the degree of rock weathering (Williams and Robinson 1983).

The needle penetration test is a highly practical method that can be easily applied to rocks with weaker physico-mechanical properties, where more complex testing cannot be performed. This method measures the needle's penetration depth under a defined load, yielding the needle penetration index (NPI). The NPI values were then used to estimate UCS through empirical correlations from the literature (Ulusay and Erguler 2012; Aydan and Ulusay 2013; Kahraman et al. 2017). As with the previous methods, it has been observed that correlation coefficients vary significantly with lithology, confirming the need to determine conversion factors specific to the rock type being tested (Aydan 2012).

4 Results and discussion

In total, 156 point load tests, 125 Schmidt hammer tests, and 76 needle penetration tests were performed, providing a representative database for analyzing relationships among different strength-determination methods.
During testing, the most effective sequence was to first perform the Schmidt hammer test. If the rebound value of the L-type Schmidt hammer was below 10 or if surface damage occurred, the use of the needle penetration test was recommended. If the rebound value exceeded 10, it was advisable to skip the needle penetration test to avoid damaging the needle and to perform the Point Load Test instead. This is the reason why not all tests were conducted on every sample. If the needle penetration test is used, it is recommended to perform it on an undamaged, flat surface and on a homogeneous sample without cracks that could lead to excessive needle penetration.

In the point load test, it was observed that different empirical relationships produce a similar trend in strength variation, but the absolute values differ significantly, in some cases by more than 200%. Despite this, the test demonstrates relatively stable behavior and can be considered reliable when an appropriate correction factor is applied for the specific lithology.
The results of the needle penetration test indicate its good applicability to weaker, more porous samples, for which other methods give unreliable results. However, its sensitivity to testing procedure and sample surface quality can lead to significant errors, since the maximum penetration depth is only 10 mm, and even small reading errors can result in large discrepancies.
The Schmidt hammer test shows certain limitations when applied to weaker rocks. In sandy limestones, rebound was often absent due to surface damage, rendering the Schmidt hammer method unusable. For stronger samples, the test results were usable but showed significant dependence on the selected correlation equation.

The results show considerable discrepancies in the UCS values obtained from different correlations across all three methods. Since no direct uniaxial compressive strength tests were performed, it was not possible to determine an exact correlation factor for the tested limestones. Nevertheless, certain relationships between the index parameters obtained from different tests can still be established. Fig 3 shows a linear correlation between the needle penetration index and point load strength, and Fig 4 shows a linear correlation between the Schmidt hammer rebound value and point load strength.

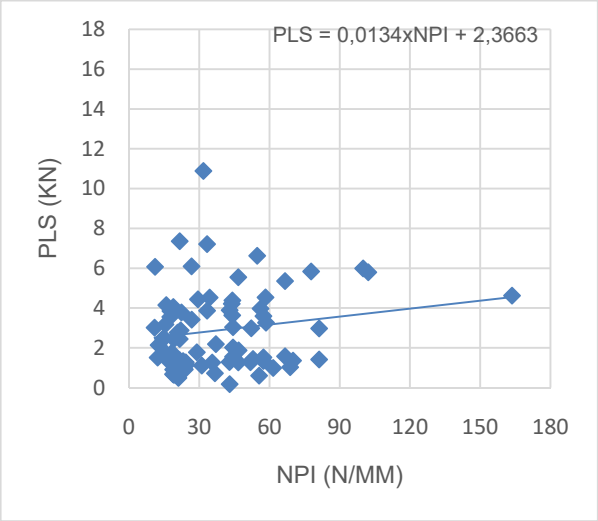


Fig. 1 PLS-NPI correlation in limestones (linear).

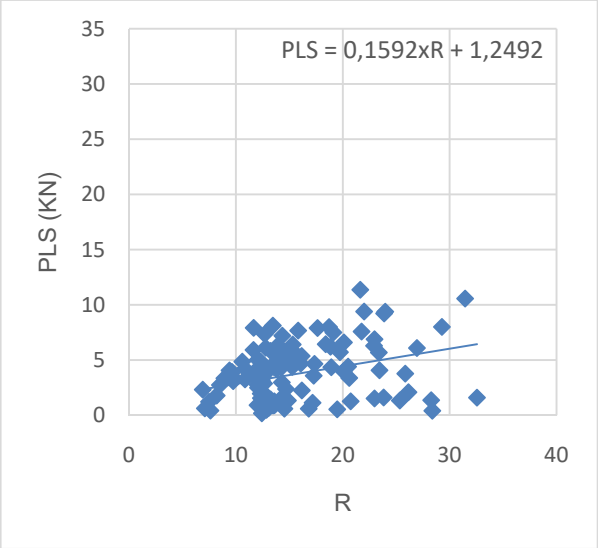


Fig. 2 PLS-R correlation in limestones (linear).

Deriving correlations between UCS and NPI of R via PLS has proven to be imprecise due to large differences in compressive strength if the correction factor is changed. See Eq.1

5 Conclusion

Based on the conducted research, it can be concluded that the selection of a method for estimating uniaxial compressive strength (UCS) largely depends on the rock's physico-mechanical properties.

The Point Load Test proved to be the most universal method; however, it requires careful selection of the appropriate correlation when calculating UCS. The needle penetration test is particularly suitable for weak rocks, where other methods do not yield reliable results. The Schmidt hammer test is a good alternative to the needle penetrometer when dealing with stronger rocks where the needle penetrometer cannot be used effectively. However, as with all indirect methods for determining compressive strength, caution is required when selecting the equations used to estimate UCS.

Based on the results, it can be concluded that a reliable estimate of UCS cannot be based on a single method or correlation. Instead, it is necessary to combine multiple methods and perform local calibration based on direct testing. Additionally, the results obtained can serve as a basis for optimizing future geotechnical investigations of Sarmatian limestones in the Belgrade area.

6 References

Aydan Ö (2012) The inference of physico-mechanical properties of soft rocks and the evaluation of the effect of water content and weathering of their mechanical properties from needle penetrometer tests. American Rock Mechanics Association, Alexandria, VA

Aydan Ö, Ulusay R (2013) Geomechanical evaluation of Derinkuyu antique underground city and its implications in geoengineering. Rock Mechanics and Rock Engineering 46(4): 731–754. https://doi.org/10.1007/s00603-012-0301-7

Bieniawski ZT (1974) Estimating the strength of rock materials. Journal of the Southern African Institute of Mining and Metallurgy 74: 312–320. https://doi.org/10.1016/0148-9062(74)91782-3

Broch E, Franklin JA (1972) The point-load strength test. International Journal of Rock Mechanics and Mining Sciences 9: 669–697. https://doi.org/10.1016/0148-9062(72)90030-7

Deere DU, Miller RP (1966). Engineering classification and index properties for intact rocks. Report AFNL-TR. Air Force Weapons Laboratory, New Mexico

Hucka V (1965) A rapid method of determining the strength of rocks in situ. Scientific Coal Research Institute, Ostrava-Radvanice, Czechoslovakia

ISRM Commission on Testing Methods, Working Group on Revision of the Point Load Test Method (1985). Suggested method for determining point load strength (Coordinator Franklin JA). International Journal of Rock Mechanics and Mining Sciences and Geomechanics Abstracts 22: 51–60. https://doi.org/10.1016/0148-9062(85)92327-7

Kahraman S (2001). Evaluation of simple methods for assessing the uniaxial compressive strength of rock. International Journal of Rock Mechanics and Mining Sciences 38: 981–994. https://doi.org/10.1016/0148-9062(85)92328-9

Kahraman S et al (2017) The needle penetration test for predicting coal strength. Journal of the Southern African Institute of Mining and Metallurgy 117(6): 587–591. https://doi.org/10.17159/2411-9717/2017/v117n6a9

Kilic A, Teymen A (2008) Determination of mechanical properties of rock using simple methods. Bull Eng Geol Environ (2008) 67:237–244 DOI 10.1007/s10064-008-0128-3

Singh RN, Hassani FP, Elkington PAS (1983) The application of strength and deformation index testing to the stability assessment of coal measures excavations. Proceedings of the 24th US Symposium on Rock Mechanics, Texas A&M University, Balkema, Rotterdam, pp 599–609

Sumner P, Nel W (2002) The effect of rock moisture on Schmidt hammer rebound: tests on rock samples from Marion Island and South Africa. Earth Surface Processes and Landforms 27(10):1137 – 1142 DOI:10.1002/esp.402

Tsiambaos G, Sabatakakis N (2004) Considerations on strength of intact sedimentary rock. Engineering Geology 72: 261–273. https://doi.org/10.1016/j.enggeo.2003.10.001

Ulusay R, Erguler ZA (2012) Needle penetration test: evaluation of its performance and possible uses in predicting strength of weak and soft rocks. Engineering Geology 149–150: 47–56. https://doi.org/10.1016/j.enggeo.2012.08.007

Williams RBG, Robinson DA (1983) The effect of surface texture on the determination of the surface hardness of rock using the Schmidt hammer. Earth Surface Processes and Landforms 8: 289–292. https://doi.org/10.1002/esp.3290080311

Assessing rock mass properties for a hydropower projectusing deformability tests

Jigme Tshewang
International Centre of Excellence for Dams (ICED); IIT Roorkee-247667, India
(Druk Green Power Corporation, Thimphu, Bhutan)
jigme_t@iced.iitr.ac.in& jigs.twang88@gmail.com
0009-0006-2069-3644

Mahendra Singh
Department of Civil Engineering, IIT Roorkee, Roorkee-247667, India
mahendra.singh@ce.iitr.ac.in
0000-0003-3775-7026

Abstract

Rocks encountered at hydro power project sites in the Himalayas are generally jointed, anisotropic and show scatter in their engineering response. While the intact rock strength can be obtained easily by testing specimens till failure in laboratory, assessment of the ultimate strength of rock mass by stressing it up to failure is extremely difficult and not feasible. Alternative approaches are therefore preferred to assess the rock mass strength. This article advocates that rock mass strength can be obtained from the deformability of the mass which can be obtained by stressing the rockmass to a very low level of stress. This hypothesis is based on outcome of large number of UCS tests performed on jointed block mass specimens.

The hypothesis is utilised to assess the rock mass properties for a hydro power project located in higher Himalayas. Comprehensive laboratory tests were performed to get the intact rock properties and their probability distributions. Several cyclic plate load tests were performed at the site to get the elastic modulus of the rock mass. These modulus values were then utilised to arrive at a set of UCS values of the rock mass. A non-linear strength criterion was then used to arrive at strength values under confinement. These results were used to simulate instabilities observed in a cut rock slope at the dam site.

It is concluded that deformability of rock mass, which is relatively easy to obtain in the field, along with laboratory test results for intact rock, can be used successfully to arrive at strength of rock mass.

Keywords

Intact rock, Rock mass, Strength, Deformability, Non-linear strength criterion.

1 Background

The Nikachhu Hydroelectric Project located inTrongsa, Bhutan was commissioned in 2024 with an installed capacity of 118 MW. The rocks encountered at the dam site are heavily jointed mica schist intermittently intruded with quartz and garnets.The strength of such a rock mass is not "measured" through direct tests, rather "derived" indirectly. Preliminary estimates of the strength are made through classification techniques (Q, RMR and GSI). However, it was envisaged to improve the estimates by incorporating results from Cyclic Plate Load Tests (CPLTs)for higher reliability. The CPLT does not stress the rock mass to its ultimate failure stress, however, the output the test in the form of deformation modulus, implicitly represents in-situ conditions.It is established in literature (Singh & Rao, 2005)that strength and modulus of rock mass are closely related with those of the parent intact rock. This correlation can be used to arrive at rock mass strength by inputting the field rock mass modulus, and laboratory UCS and modulus of intact rock.

The present study uses an integrated approach for assessing the rock mass strength by incorporating field modulus from CPLTsand UCS test results on intact rock specimens in the laboratory. The main objective has been to derive equivalent material shear strength parameters that better reflect the in-situ rock mass conditions. Initially the hypothesis is discussed and then it is used in assessing the equivalent material strength for a rock mass at a dam site.

2 The Hypothesis

2.1 UCS of Rock Mass

Singh and Rao (2005) suggested an empirical approach to estimate the UCS of jointed rock mass based on the outcome of large number of UCS tests performed on jointedrock mass specimens (Singh, 1997). The test specimens (Singh, 1997)had varying joint configurations exhibiting different levels of interlocking conditions thereby resulting in various failure modes encountered in nature. Typical failure modes observed in the study are shown inFig. 2. The tangent (elastic) modulus and ultimate strength values obtained from the tests were plotted on (Deere & Miller, 1966)classification chart (Fig. 1). It was observed that the jointed rock locations follow a straightlinestarting from point 'I' representing intact rock position on the chart. This empirical line indicates a strong correlation between the modulus and strength values of intact and rock mass. The strength of the rock mass can be obtained as follows:

$$\frac{\sigma_{cj}}{\sigma_{ci}} = \left[\frac{E_j}{E_i}\right]^{0.63} \tag{1}$$

Where $\sigma_{ci}$and σ_{cj}= UCS of intact rock and rock mass; E_i&E_j= Elastic (tangent) modulus of intact rock and rockmass respectively.

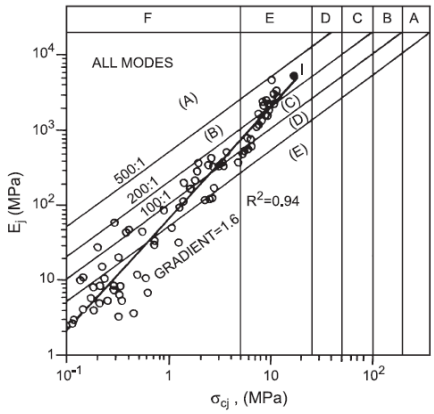


Fig. 1 Strength and tangent modulus of rock mass specimens plotted on DeereMiller classification chart (Singh, 1997)

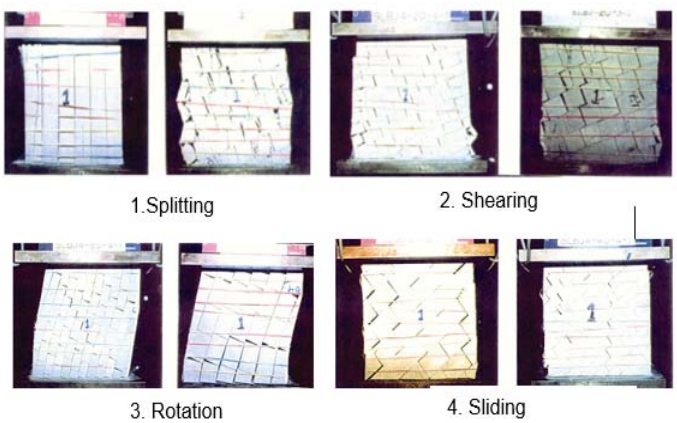


Fig. 2 Rock mass specimens showing various failure modes under uniaxial compression (Singh, 1997)

The Eq. (1) is used to determine the rock mass strength, σ_{cj} for given σ_{ci}, $E_i$and $E_j$values. The present study concerns slope instability of a rock slope at Nikachhu Hydroelectric dam site. The rock mass modulus in the field, $E_j$was obtained by conducting CPLTs. The CPLTs were performed at the base of a drift excavated at the level of the toe of slope. The rockmass under the test plate represents semi-infinite constrained rock mass with restriction on dilation during shear. On the contrary, the rock mass specimens tested by Singh (1997) (Fig. 2)were unconstrained on sides; and the loading platen covered the entire plan area of the rock mass. Consequently, the rock mass was unconstrained and free to dilate. The joint orientations play significant role in case of unconstrained, free to dilate rock mass. To apply the CPLT results to a rock slope problem, a correction needs to be applied to account for the joint orientation. In present study, the correction is applied to the computed rock mass strength by multiplying it with Joint Inclination Parameter 'n'(Ramamurthy & Arora, 1994; Singh et al., 2002) in Eq. (2). The joint inclination parameter accounts for the weakness brought to a jointed rock due to inclination of the joints. The inclination parameter 'n' is presented in Table 1. The corrected UCS of the rock mass is obtained as given below.

$$\sigma_{cj(corrected)} = n \times \sigma_{cj(computed)} \tag{2}$$

Where n = Joint inclination parameter

Table 1. Joint Inclination Parameter (Ramamurthy &Arora, 1994; Singh et al., 2002).

Joint dip	0	10	20	30	40	50	60	70	80	90
n	1.000	0.814	0.634	0.465	0.306	0.071	0.046	0.105	0.460	0.810

2.2 Triaxial Strength of the Rock Mass

Jointed rock masses exhibit large non-linearity in their triaxial strength behaviour. In present study, a non-near failure criterion, Modified Mohr Coulomb Criterion (MMC)(Singh & Singh, 2012)was used to model the non-linear strength response of the rock mass. As per this criterion, the non-linear triaxial strength of a jointedmass is defined as:

$$(\sigma_{1j} - \sigma_{3j}) = \sigma_{cj} + \frac{2sin\phi_{j0}}{1 - sin\phi_{j0}}\sigma_{3j} - \frac{1}{\sigma_{ci}}\frac{2sin\phi_{j0}}{1 - sin\phi_{j0}}{\sigma_{3j}}^2 for\ 0 \leq \sigma_{3j} \leq \sigma_{ci} \tag{3}$$

Where: σ_{cj} = UCS of the rock mass; σ_{3j}&σ_{1j}= minor and major principal stresses at failure for the rock mass; ϕ_{j0} =MMC parameter which represents internal friction angle of the mass at very low confining pressure ($\sigma_3 \rightarrow 0$),obtained as:

$$sin\phi_{j0} = \left\{\left(1 - \frac{\sigma_{cj}}{\sigma_{ci}}\right) + \frac{sin\phi_{i0}}{1 - sin\phi_{i0}}\right\} \Big/ \left\{\left(2 - \frac{\sigma_{cj}}{\sigma_{ci}}\right) + \frac{sin\phi_{i0}}{1 - sin\phi_{i0}}\right\} \tag{4}$$

ϕ_{i0}=MMC parameter for intact rock i.e. friction angle of the intact rock at very low confining pressure ($\sigma_3 \rightarrow 0$) (Singh et al., 2011). Triaxial test data on intact rock is required to computeϕ_{i0}. The following steps are used to compute ϕ_{i0}.

$$A_i = \frac{\sum(\sigma_{1i} - \sigma_{3i} - \sigma_{ci})}{\sum({\sigma_{3i}}^2 - 2\sigma_{ci}\sigma_3)}, \qquad 0 < \sigma_{3i} \leq \sigma_{ci} \tag{5}$$

$$B_i = -2A_i\sigma_{ci} \tag{6}$$

$$sin\phi_{i0} = B_i/\{2 + B_i\} \tag{7}$$

Where: σ_{ci} = UCS of the intact rock; σ_{3i}&σ_{1i}= minor and major principal stresses at failure for the intact rock.

3 Field and Laboratory Investigations

Detailed investigations were conducted in the field and laboratory to characterise the geological materials encountered at the site. A total of seven drill-holes were advanced in the dam area and intact rock cores were tested in laboratory to determine their physical and mechanical properties. The laboratory tests included UCS (20 numbers), triaxialstrength (11 sets) and Brazilian tests (18 tests). In addition, fourteen sets of direct shear testsalong the joint surfaces. In field, six number of cyclic plate load tests (CPLT) were performed in a drift along the dam axis. The intact rock properties were analysed statistically and the cumulative distribution functions of the UCS and the tangent moduli (E_{t50}) of the intact rock were determined. The summary of the results from geotechnical investigations is presented in Table 2.

Table 2 Properties reported for Nikachhu Project(GBR, 2017)

Property	Mean value	Standard deviation	Weibull shape parameter(α)	Weibull scale Parameter (β)
Unit weight, (kN/m^3)	27.00	0.75		
UCS, (MPa) (Saturated)	45	22.01	1.744	52.288
E_{t50}, (GPa) (Saturated)	34.19	13.91	1.763	41.089
P Wave velocity (Km/sec)	3.854	0.941		
Brazilian Tensile Strength (MPa)	7.31	3.20	1.939	8.502
Mohr-Coulomb, c_i (MPa)	2.53	1.14		
Mohr Coulomb ϕ_i(degrees)	42.27	7.79		

4 Rock Mass Properties

The following steps were used to arrive at the rock mass strength:(Fig. 3)

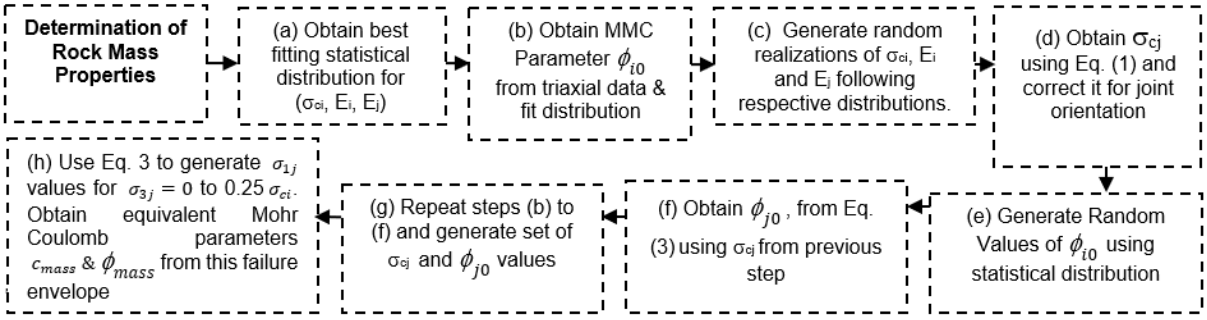


Fig. 3Steps involved in derivation of rock mass parameters

The distributions for equivalent material Mohr-Coulomb shear strength parameters are shown in Fig. 4.

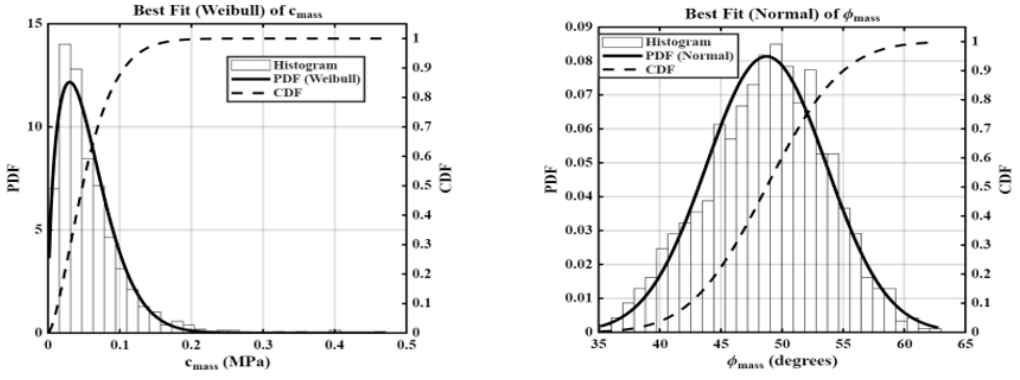


Fig. 4Consolidated distribution plots for Cohesion (MPa) and Friction angle of jointed rock mass

The slope mass at the site is intersected with several joints. The joint planes had low persistence, were not well developed and did not have distinct surfaces. The joint planes having dip direction within

±20° of slope dip direction had an average of dip of55.5°. The influence of these weaker planes wasincorporated through joint inclination parameter ‘n’.

4.1 Slope Stability Analysis

The equivalent material Mohr-Coulomb parameters obtained above are employed to simulate the instabilities observed at the rock slope on left abutment of the dam site.



Fig. 5Slope excavation section and location of instability

The rock slope was to be excavated for constructing the dam as shown in Fig. 5. The excavation was done by making benches of 3 m width 2.5m height respectively. The monsoon had just begun in the month of May 2018. When the excavation reached at El 2300m, tension cracks appeared at El 2309 m andthey propagated further with time. The work was put on hold to arrest the propagation of the tension cracks and infiltration of rainwater by sealing of crack openings with cement grout and installation of additional anchors. However, the slope couldn’t be stabilised, and it failed (Fig. 5). Later, the slope was redesigned, and re-excavation was carried out by shifting it backward. Mitigation measures were applied along with modified support systems.

The stability analysis of the section at the time of instability was done using SLIDE2 (Rocscience 2022) (Fig. 6). It is seen That the FOS is close to one which indicates instability. The mitigations measures were designed and the slope was stabilised.

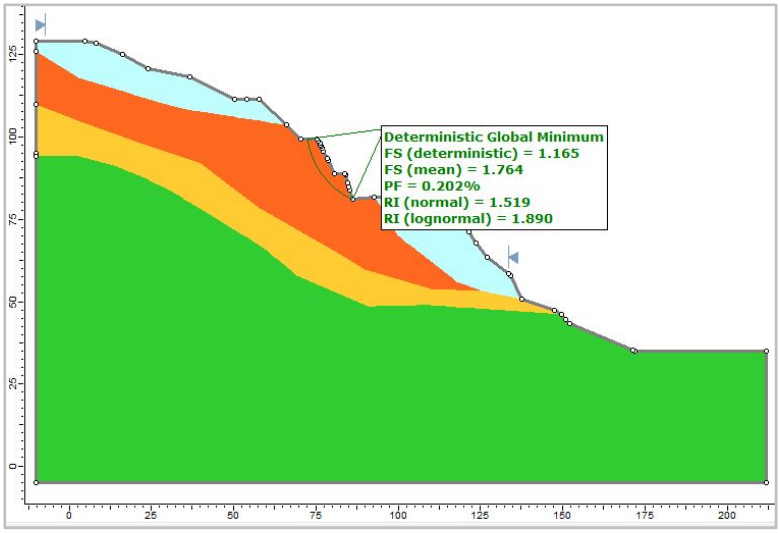


Fig. 6Slope stability analysis using SLIDE 2 (Rocscience, 2022)

5 Concluding Remarks

Shear strength parameters of rock mass are required for analysis and design of structures. The present study has focused on obtaining shear strength parameters for rock slope stability analysis. Orientation of weakness planes have great influence on stability of slopes. For situations where joints are not well developed and have low persistence, an equivalent material may be assumed, and analysis can be done by using equivalent shear strength parameters.

The present study advocates use of field modulus to assess the equivalent shear strength parameters of a rock mass in the field. The approach requires laboratory UCS (σ_{ci}), modulus (E_i) values of intact rock, and rock mass modulus (E_j) from the field which can be obtained through Cyclic Plate load tests. The UCS of the rock mass (σ_{cj}) may be obtained through correlation suggested in the study.

It is envisaged that rock mass modulus from the field will reflect influence of in-situ rock conditions. However, the influence of the joint orientation will not reflect fully as the CPLT is conducted on semi-infinite constrained mass contrary to the unconstrained rock mass in slope which has higher degree of freedom for slip, rotation of blocks and dilation of mass. A correction for joint orientation should be applied to the computed σ_{cj} before using it for slope stability analysis.

The applicability of the suggested approach has been demonstrated by applying it to the left abutment slope of a hydro power project. It is concluded that addition of input from field deformability may be used to enhance the confidence in the shear strength parameters.

Acknowledgements

The first author would like to put on record his sincere thanks to ITEC, India for the scholarship to pursue Master's degree in Dam Safety and Rehabilitation at IIT, Roorkee. He would also like to thank his parent organization Druk Green Power Corporation Limited in granting paid study leave until the course completion. The support extended by the management of Nikachhu Hydroelectric Project, Bhutan is thankfully acknowledged.

References

Deere, D. U., & Miller, R. P. (1966). Engineeeing Classification and Index Properties for Intact Rock. In *Technical Report No. AFWL-TR-65-116* (Vol. 1).

GBR. (2017). *Geological Baseline Report* (Vol. 1, Issue September). Nikachhu Hydroelectric Project 118MW, Trongsa, Bhutan

Ramamurthy, T., & Arora, V. K. (1994). Strength Predictions for Jointed Rocks in Confined and Unconfined States. *International Journal of Rock Mechanics and Mining Sciences*, *31*(I), 9–22. https://doi.org/0148-9062/94

Singh, M. (1997). *Engineering behaviour of jointed model materials*. PhD Thesis, IIT Delhi, New Delhi, India.

Singh, M., & Rao, K. S. (2005). Empirical Methods to Estimate the Strength of Jointed Rock Masses. *Engineering Geology*, *77*(1–2), 127–137. https://doi.org/10.1016/j.enggeo.2004.09.001

Singh, M., Rao, K. S., & Ramamurthy, T. (2002). Strength and Deformational Behaviour of a Jointed Rock Mass. *Rock Mechanics and Rock Engineering*, *35*(1), 45–64.

Singh, M., & Singh, B. (2012). Modified Mohr-Coulomb criterion for non-linear triaxial and polyaxial strength of jointed rocks. *International Journal of Rock Mechanics and Mining Sciences*, *51*, 43–52. https://doi.org/10.1016/j.ijrmms.2011.12.007

Thermal Cycling Effects on Granite Pore Structure at Moderate Temperatures

M. E. Garrido, C. V. Cedeño, V. Martínez-Ibáñez, C. Hidalgo-Signes
Universitat Politècnica de València, València, Spain
egarrido@upv.es
0000-0001-7804-3922

D. J. Guerrero-Miguel
Universidad de Oviedo, Oviedo, Spain

Abstract

Thermally induced microfracturing has emerged as an effective method to enhance permeability of low-porosity crystalline rocks in Enhanced Geothermal Systems (EGS). Most existing studies focus on high-temperature treatments (>500 °C), which limits their applicability under field conditions, where moderate temperatures and controlled thermal shocks are preferred. This study examines the evolution of porosity and pore structure in granite subjected to repeated heating-cooling cycles at relatively low temperatures to assess the feasibility of inducing microfracture development in geothermal reservoir stimulation. Granite samples were heated to 200, 300, and 400 °C and then cooled by immersion in water to generate a steep thermal gradient. Different groups of samples were exposed to 1 to 5 thermal cycles. Total and open porosity, density, and ultrasonic wave velocity were determined to assess progressive thermal damage. In addition, mercury intrusion porosimetry was performed to characterize variations in pore volume, pore size distribution, and pore connectivity. X-ray diffraction (XRD) analysis was conducted to detect potential mineralogical changes resulting from repeated thermal exposure. The results show a progressive decrease in bulk density and ultrasonic velocities with increasing temperature and cycle count, indicating the accumulation of microstructural damage. Open porosity shows a significant increase, particularly at 300 and 400 °C, while total porosity shows more limited changes, suggesting that increasing the cycle count improves pore connectivity. The porosimetry results confirm a shift toward larger pore sizes and improved connectivity after five cycles, especially at higher temperatures, reflecting microcrack coalescence. XRD analyses show no peak displacements or new mineral phases, confirming that the observed changes are not associated with mineralogical transformations. Overall, this study demonstrates that thermal treatment at moderate temperatures effectively improves porosity and microfracture connectivity in these rocks, offering a practical and energy-efficient method for geothermal reservoir stimulation.

Keywords

Granite, Microcracking, Thermal cycling, Porosity, Geothermal reservoir stimulation.

1 Introduction

The increasing demand for low-carbon energy has intensified interest in Enhanced Geothermal Systems (EGS), which enable energy extraction from low-permeability rock formations. Improving permeability is essential to ensure efficient fluid circulation and heat extraction. Among stimulation techniques, thermal treatment has emerged as a promising method to induce microstructural damage and enhance fracture and pore connectivity. Thermal loading generates internal stresses due to differential thermal expansion of minerals, promoting microcrack initiation and propagation, particularly in granite, where mineral heterogeneity leads to stress concentration at grain boundaries (Griffiths et al., 2017).

Previous studies have shown that thermal cycling produces progressive damage in granite, characterized by microcrack development and degradation of elastic properties (Rong et al., 2021; Yin et al., 2021; Zhu et al., 2020). Ultrasonic velocities decrease as microfracture networks evolve, while pore structure changes, including increased connectivity, have been reported (Yu et al., 2021). These processes are critical for geothermal applications, where permeability is mainly controlled by pore and fracture connectivity rather than total porosity. Most experimental studies focus on high temperatures (>500 °C), whereas the effects of moderate temperatures remain less understood. Previous work has shown that treatments between 200 and 400 °C combined with rapid cooling can induce microfracturing without significant mineralogical changes (Tomás et al., 2025). However, the influence of repeated thermal cycles under these conditions is still poorly constrained.

This study investigates the effects of thermal cycling at moderate temperatures on the microstructural evolution of a low-porosity granite from western Spain, with emphasis on pore structure and connectivity. The objective is to improve the understanding of thermally induced damage mechanisms and their implications for permeability enhancement in geothermal systems.

2 Thermal treatment

The thermal treatment was designed to reproduce damage mechanisms relevant to geothermal environments, where temperature variations induce internal stresses and microcrack development. Samples were heated to 200, 300 and 400 °C, representative of moderate geothermal conditions, using a muffle furnace at a rate of 5 °C/min, followed by a 1-hour isothermal stage. Rapid cooling was then applied by immersion in water at 70 °C for 10 minutes to generate a controlled thermal shock.

To evaluate cyclic effects, specimens were grouped according to the number of heating–cooling cycles (1 to 5). Each group included five samples to ensure statistical consistency. Prismatic specimens were used for density and porosity measurements, while cylindrical specimens were prepared for ultrasonic pulse velocity tests. After each cycle, samples were oven-dried at 70 °C to eliminate residual moisture and ensure consistent measurements.

Microstructural characterization was performed using mercury intrusion porosimetry (MIP) and X-ray diffraction (XRD) on selected samples subjected to 1 and 5 cycles at each temperature, as well as on untreated reference samples, allowing evaluation of both initial and cumulative effects of thermal cycling on pore structure and mineralogical stability.

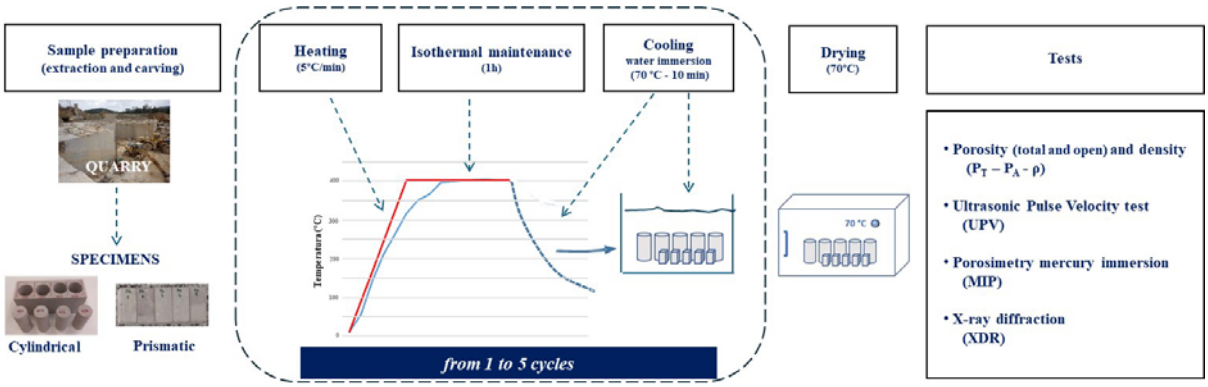


Fig. 1 Diagram of the applied thermal treatment and work methodology.

3 Results

3.1 Density and porosity

Bulk density (ρ_b) shows a slight but consistent decrease with the number of thermal cycles for all tested temperatures (Fig. 2a). This reduction is more pronounced at 400 °C, where the cumulative effect of repeated heating and cooling leads to a progressive loss of density. The observed trend suggests the development of internal microcracking and associated volumetric expansion, even though the absolute changes remain relatively small due to the low initial porosity of the granite. The evolution is not strictly linear, with minor fluctuations at intermediate cycles, which may be related to microstructural rearrangements or closure of pre-existing defects. Nevertheless, the overall decrease in bulk density confirms the progressive nature of thermally induced damage.

Open porosity (OP) exhibits a clear increasing trend with the number of thermal cycles, particularly at 300 and 400 °C (Fig. 2b). The increase becomes more pronounced after the initial cycles, suggesting that thermal loading enhances the opening and interconnection of pre-existing microcracks. Compared to total porosity, the changes in open porosity are more significant, highlighting that the main effect of thermal cycling is the improvement of pore connectivity rather than the generation of new pore volume. At lower temperatures (200 °C), the variations are more limited, suggesting that the induced damage is less intense. The progressive increase in open porosity with cycling confirms the cumulative effect of thermal stresses on the accessible pore network.

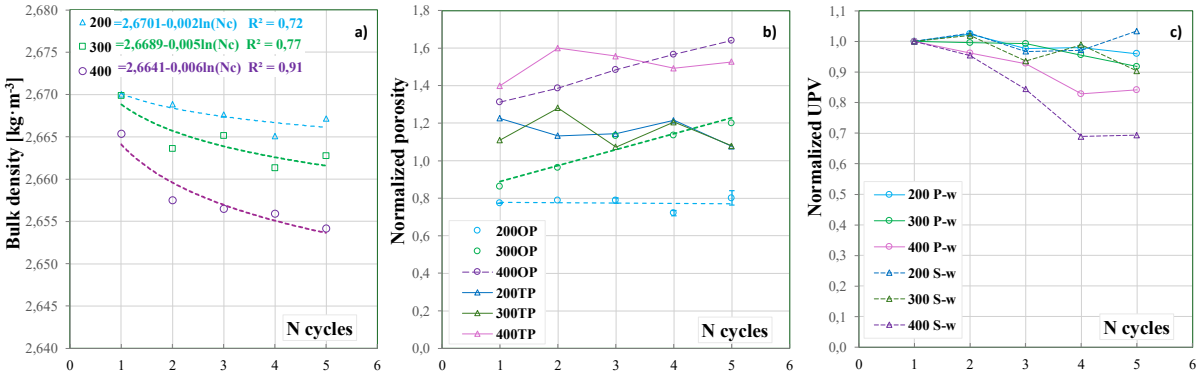


Fig. 2 Tests results: a) bulk density, b) open and total porosity and c) ultrasonic pulse velocity.

Fig. 2b also shows results of total porosity (TP). Its evolution is more moderate and less systematic compared to open porosity. Although a general increasing tendency can be observed with the number of cycles, particularly at higher temperatures, the variations remain relatively small. In some cases, slight decreases or fluctuations are observed at intermediate cycles, which may be attributed to temporary closure or rearrangement of microstructural features during the early stages of thermal loading. The limited increase in total porosity suggests that thermal cycling does not significantly generate new pore volume but rather redistributes the existing pore system. This behaviour is consistent with the low initial porosity of granite and the dominance of microcracking processes.

3.2 Ultrasonic pulse velocity

P-wave and S-wave velocities decrease with increasing number of cycles, reflecting the progressive accumulation of internal damage (Fig. 2c). The reduction is more significant at higher temperature and becomes more pronounced after successive cycles, indicating the cumulative effect of microcrack development. S-wave velocity shows a greater sensitivity to thermal damage than P-wave velocity, exhibiting a more marked decrease, which is consistent with the higher sensitivity of shear waves to discontinuities and crack density. In some cases, slight increases or stabilizations are observed at early cycles, possibly due to microcrack closure or stress redistribution. Overall, the decline in ultrasonic velocities confirms the progressive degradation of the elastic properties of the granite.

3.3 Characterization of the porous system

The results of mercury intrusion porosimetry (MIP) presented in Table 1 show the evolution of the pore system in granite as a function of both thermal cycling and temperature. The untreated samples (C0) are characterized by very low total porosity, with a pore system dominated by micropores and limited connectivity. After one thermal cycle (C1), only slight variations in total pore volume are observed across all temperatures (200, 300 and 400 °C), although changes in pore size distribution indicate the initiation of microcracking and a partial redistribution of the pore network.

The effect of temperature becomes more evident after five cycles (C5), where samples treated at 300 °C and especially 400 °C show a more pronounced increase in accessible pore volume and a clear shift toward larger pore diameters compared to those treated at 200 °C. This behaviour suggests that higher temperatures promote more intense microcrack propagation and coalescence. At 200 °C, the pore system remains relatively stable, with limited development of larger pores, indicating that thermal damage is still incipient. In contrast, at 400 °C, the broader pore size distribution and the presence of larger pores reflect the formation of a more heterogeneous and interconnected pore network.

Table 1. Ranges of MIP-derived parameters for granite samples.

T [°C]	Parameter	C0	C1	C5
25	Total porosity [%]	0.37 – 0.92	-	-
	Interparticle porosity [%]	0.14 – 0.37	-	-
	Intraparticle porosity [%]	0.00 – 0.78	-	-
	Apparent density [kg·m^{-3}]	2560 – 2645	-	-
	Modal diameter [µm]	0.008 – 0.059	-	-
200	Total porosity [%]	-	0.50 – 0.58	0.38 – 1.43
	Interparticle porosity [%]	-	0.16 – 0.40	0.15 – 1.43
	Intraparticle porosity [%]	-	0.10 – 0.42	0.01 – 0.23
	Apparent density [kg·m^{-3}]	-	2589 – 2662	2598 – 2693
	Modal diameter [µm]	-	0.007 – 0.030	0.012 – 0.048
300	Total porosity [%]	-	0.25 – 0.50	0.76 – 2.60
	Interparticle porosity [%]	-	0.20 – 0.28	0.37 – 1.78
	Intraparticle porosity [%]	-	0.05 – 0.21	0.39 – 0.82
	Apparent density [kg·m^{-3}]	-	2601 – 2649	2567 – 2682
	Modal diameter [µm]	-	0.006 – 0.173	0.006 – 0.007
400	Total porosity [%]	-	0.29 – 0.78	0.93 – 1.08
	Interparticle porosity [%]	-	0.06 – 0.29	0.33 – 0.46
	Intraparticle porosity [%]	-	0.00 – 0.71	0.47 – 0.75
	Apparent density [kg·m^{-3}]	-	2645 – 2665	2600 – 2674
	Modal diameter [µm]	-	0.007 – 4.747	0.006 – 0.050

3.4 Mineralogical analysis

XRD analyses reveal no significant mineralogical differences between untreated samples and those subjected to thermal cycling at 200, 300 and 400 °C, even after five cycles. The position of diffraction peaks remains unchanged in all cases, indicating the absence of phase transformations (Fig. 3b). However, slight variations in peak intensities are observed, particularly at higher temperatures and after multiple cycles. These changes are attributed to microstructural effects such as microcrack development, internal stress redistribution and preferred orientation. The results confirm that thermal damage in the studied granite is controlled by physical processes, with temperature and number of cycles enhancing microstructural heterogeneity without affecting mineralogical composition.

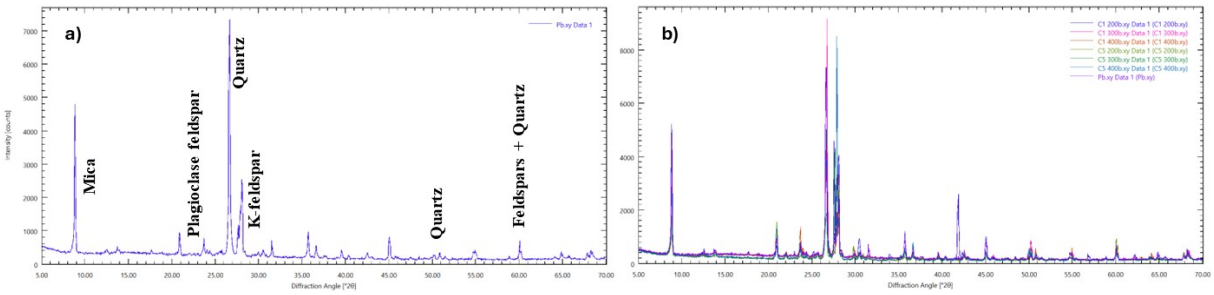


Fig. 3 XRD patterns: a) reference granite highlighting the main mineral phases. b) thermally treated samples.

4 Discussion

The combined analysis of bulk density, porosity, ultrasonic velocities and MIP results provides a consistent interpretation of thermally induced damage in granite. The decrease in bulk density, although limited, reflects volumetric expansion associated with microcrack development, as reported in previous studies (Gautam et al., 2020; Gómez-Heras et al., 2008). The increase in open porosity, more pronounced than total porosity, indicates that thermal cycling enhances pore connectivity rather than generating new pore volume, consistent with previous observations (Yu et al., 2021).

The MIP results further support this interpretation, showing a redistribution of pore sizes and a shift toward larger pores, particularly at higher temperatures and after multiple cycles. This behaviour reflects the progressive coalescence of thermally induced microcracks, as also observed in studies on granite subjected to repeated thermal cycling (Junique et al., 2021). The more pronounced changes observed at 300 °C and especially 400 °C suggest the existence of a thermal threshold above which crack propagation becomes dominant. This threshold behaviour is consistent with previous findings indicating intensified damage beyond approximately 300–400 °C (Tomás et al., 2025).

Ultrasonic pulse velocity results provide additional evidence of damage evolution at the microstructural scale. The reduction in both P-wave and S-wave velocities with increasing number of cycles reflects the progressive degradation of the elastic properties of the granite, as widely documented in the literature (Junique et al., 2021; Rong et al., 2021). The greater sensitivity of S-wave velocity observed in this study is consistent with its stronger dependence on crack density and discontinuities, as reported in previous experimental works (Yin et al., 2021). Minor fluctuations at early cycles may be attributed to crack closure or stress redistribution, a phenomenon also observed in thermally treated rocks (Qin et al., 2020).

The XRD results further support the interpretation that thermal damage in the studied granite is predominantly governed by microstructural processes rather than mineralogical transformations. As observed in the diffractograms (Fig. 3), no significant changes in peak positions are detected between untreated samples and those subjected to thermal cycling at 200, 300 and 400 °C, even after five cycles. This confirms the absence of phase transformations within the investigated temperature range. However, slight variations in peak intensities are observed, particularly at higher temperatures and after five repeated cycles, indicating an increase in microstructural heterogeneity. These changes can be attributed to the development of microcracks, internal stress redistribution and preferred orientation effects, rather than to modifications in crystal structure.

Similar behaviour has been reported in previous studies on thermally treated granites, where physical damage induced by differential thermal expansion occurs without detectable mineralogical alteration (Gómez-Heras et al., 2008; Junique et al., 2021). Furthermore, the absence of differences between C1 and C5 samples in terms of peak position suggests that thermal cycling enhances the degree of damage without triggering new mineral phases, reinforcing the interpretation that the observed evolution in porosity, ultrasonic velocity and pore structure is controlled by progressive microcrack development (Gautam et al., 2020; Zhu et al., 2020).

The influence of temperature is clearly observed across all techniques, with more pronounced changes at 300 °C and 400 °C, indicating that thermal damage intensifies beyond moderate thresholds. At lower temperatures (200 °C), the observed variations are smaller and suggest that microstructural changes are still limited or partially reversible. This behaviour agrees with previous studies indicating that thermal damage at moderate temperatures is initially controlled by microcrack initiation and gradual propagation, without significant mineralogical transformations. Similar observations have been reported in experimental studies on granite, where early-stage thermal damage is dominated by physical processes related to differential thermal expansion (Tomás et al., 2025).

Although the observed mechanisms are consistent with previous studies on thermally treated granites, their magnitude is expected to depend on lithology, mineralogical composition and initial pore structure. Therefore, the present results should be regarded as representative of the investigated low-porosity granite and the tested thermal conditions. Further studies on rocks with contrasting petrophysical properties are required to assess the broader applicability of thermal cycling for geothermal reservoir stimulation.

Overall, the results indicate that thermal cycling at moderate temperatures induces progressive microcrack development, leading to improved pore connectivity and degradation of elastic properties without significant mineralogical alteration. The good agreement between porosity measurements, ultrasonic velocities and MIP data highlights the complementary nature of these techniques for characterizing thermal damage in low-porosity granites. This complementarity has also been emphasized in previous studies, where combined petrophysical and microstructural analyses provide a more comprehensive understanding of damage evolution (Junique et al., 2021; Yu et al., 2021).

5 Conclusion

Thermal cycling at moderate temperatures (200–400 °C) induces progressive microstructural damage in granite through microcrack development and coalescence. Although changes in bulk density and total porosity are limited, open porosity increases significantly, highlighting the dominant role of pore connectivity in the evolution of the pore network.

Ultrasonic velocity results confirm the progressive degradation of elastic properties, with S-wave velocity showing higher sensitivity to damage. MIP analyses indicate a shift toward larger pore sizes and improved connectivity after multiple cycles, particularly at 300 and 400 °C, indicating a thermal threshold beyond which damage becomes more pronounced.

Overall, the strong agreement between petrophysical and microstructural results demonstrates that thermal cycling is an effective method to enhance pore connectivity in low-porosity granites without significant mineralogical alteration, offering a practical and energy-efficient strategy for geothermal reservoir stimulation.

Acknowledgments

The authors would like to thank the Department of Transport and Geotechnical Engineering at the Universitat Politècnica de València and the Department of Mining Exploration and Exploration at the University of Oviedo for their continued support. They also thank the Technical Research Services at the University of Alicante, which carried out the XRD and PIM tests. This research was funded by the Spanish Ministry of Science and Innovation through grant MCINN-23-PID2022-142015OB-I00, funded by MCIN/AEI/10.13039/501100011033 and the ERDF program "A way of making Europe".

References

Gautam, P. K., Dwivedi, R., Kumar, A., Kumar, A., Verma, A. K., Singh, K. H., & Singh, T. N. (2020). Damage Characteristics of Jalore Granitic Rocks After Thermal Cycling Effect for Nuclear Waste Repository. Rock Mechanics and Rock Engineering, (0123456789). https://doi.org/10.1007/s00603-020-02260-7

Gómez-Heras, M., Smith, B. J., & Fort, R. (2008). Influence of surface heterogeneities of building granite on its thermal response and its potential for the generation of thermoclasty. Environmental Geology, 56(3–4), 547–560. https://doi.org/10.1007/s00254-008-1356-3

Griffiths, L., Heap, M. J., Baud, P., &Schmittbuhl, J. (2017). Quantification of microcrack characteristics and implications for stiffness and strength of granite. International Journal of Rock Mechanics and Mining Sciences, 100, 138–150. https://doi.org/10.1016/J.IJRMMS.2017.10.013

Junique, T., Vazquez, P., Benavente, D., Thomachot-Schneider, C., &Géraud, Y. (2021). Experimental investigation of the effect of quenching cycles on the physico-chemical properties of granites. Geothermics, 97. https://doi.org/10.1016/j.geothermics.2021.102235

Qin, Y., Tian, H., Xu, N. X., & Chen, Y. (2020). Physical and Mechanical Properties of Granite After High-Temperature Treatment. Rock Mechanics and Rock Engineering, 53(1), 305–322. https://doi.org/10.1007/s00603-019-01919-0

Rong, G., Sha, S., Li, B., Chen, Z., & Zhang, Z. (2021). Experimental Investigation on Physical and Mechanical Properties of Granite Subjected to Cyclic Heating and Liquid Nitrogen Cooling. Rock Mechanics and Rock Engineering, 54(5), 2383–2403. https://doi.org/10.1007/s00603-021-02390-6

Tomás, R., Benavente, D., Martínez-Ibáñez, V., & Garrido, M. E. (2025). How do high temperatures affect rock properties? A comprehensive review of experimental thermal effects and underlying mechanisms. In Engineering Geology (Vol. 357). Elsevier B.V. https://doi.org/10.1016/j.enggeo.2025.108323

Yin, Q., Wu, J., Zhu, C., Wang, Q., Zhang, Q., Jing, H., &Xie, J. (2021). The role of multiple heating and water cooling cycles on physical and mechanical responses of granite rocks. Geomechanics and Geophysics for Geo-Energy and Geo-Resources, 7(3). https://doi.org/10.1007/s40948-021-00267-0

Yu, L., Peng, H. W., Zhang, Y., & Li, G. wei. (2021). Mechanical test of granite with multiple water–thermal cycles. Geothermal Energy, 9(1). https://doi.org/10.1186/s40517-021-00186-z

Zhu, Z., Tian, H., Mei, G., Jiang, G., & Dou, B. (2020). Experimental investigation on physical and mechanical properties of thermal cycling granite by water cooling. Acta Geotechnica, 15(7), 1881–1893. https://doi.org/10.1007/s11440-019-00898-4

Effect of Biot-Willis Coefficient in Coupled Hydro-Mechanical Hydraulic Fracturing Analysis

K. Kishida, Y. Tatemura & H. Yasuhara
Department of Urban Management, Kyoto University, Kyoto, Japan
kishida.kiyoshi.3r@kyoto-u.ac.jp
0000-0003-1588-4024, 0000-0003-4557-4692

S. Ogata
Osaka University, Suita, Japan

Abstract

Hydraulic fracturing is widely used for in-situ stress measurement and the development of enhanced geothermal systems (EGS), in which fluid is injected to create and propagate fractures. Accurate evaluation of stress state and fracture propagation requires a simulation framework that can reproduce the coupled processes of fluid flow and rock deformation.

This study develops a fully coupled hydro-mechanical simulation model for flow-rate–controlled hydraulic fracturing, implemented within a finite element method (FEM) framework, incorporating pore pressure diffusion and the resulting mechanical response within a porous rock mass. Particular attention is given to the Biot–Willis coefficient α and the initial permeability within the framework of poroelastic theory. The coefficient α governs the contribution of pore pressure to effective stress, whereas the initial permeability controls fluid diffusion and leak-off behavior.

FEM-based numerical simulations are conducted to evaluate the effects of α and permeability on injection pressure during fracture initiation and propagation, as well as on pressure behavior after injection shut-in. The results show that injection pressure decreases with increasing α due to the enhanced contribution of pore pressure to effective stress. However, this effect diminishes as α approaches approximately 0.9, beyond which the influence of α saturates.

In contrast, permeability strongly affects both breakdown pressure and post shut-in pressure decay. Lower permeability results in higher breakdown pressure due to reduced fluid leak-off, whereas higher permeability leads to rapid pressure dissipation after shut-in owing to enhanced fluid diffusion into the surrounding rock matrix.

These results indicate that the Biot–Willis coefficient primarily governs effective stress reduction and fracture initiation, while permeability controls fluid transport and pressure decay. The findings provide useful guidance for parameter identification in coupled hydro-mechanical simulations and contribute to improving the reliability of in-situ stress estimation and geothermal reservoir analysis.

Keywords

Hydraulic fracturing, Fluid–solid interaction, Biot–Willis coefficient, Poroelasticity, Injection pressure.

1 Introduction

Hydraulic fracturing is widely used for in-situ stress measurement and geothermal reservoir stimulation, in which fluid is injected into an isolated borehole interval to create fractures and estimate in-situ stress from the fluid pressure and fracture orientation (Hubbert and Willis, 1957). Accurate evaluation of this process requires a numerical framework capable of reproducing both the stress field and fracture propagation.

Previous studies (Izawa et al., 2020; Ikeda et al., 2024) have mainly employed pressure-controlled conditions, whereas actual operations are often conducted under flow-rate-controlled conditions. To better represent such conditions, this study develops a coupled hydro-mechanical model incorporating flow-rate control. In addition, since pressure behavior after injection shut-in has received limited attention, the model is designed to reproduce the entire process from fracture initiation to stress release.

Within the poroelastic framework based on Biot's theory, particular attention is given to the Biot–Willis coefficient α and the initial permeability. The coefficient α governs the contribution of pore pressure to effective stress, while permeability controls fluid diffusion and leak-off behavior. This study investigates how these parameters influence pressure response, especially after shut-in.

2 Numerical method

2.1 Outline of numerical method

In this study, numerical simulations were performed using an externally coupled framework combining COMSOL Multiphysics (finite element analysis) and MATLAB. A hydro-mechanical coupled analysis is first conducted in COMSOL, after which the damage variable and permeability are updated in MATLAB and fed back into the finite element model. This iterative procedure is repeated throughout the simulation.

2.2 Governing equations

The stress–strain behavior of the rock mass is described using the equilibrium equation and a constitutive relation incorporating pore pressure based on Biot's poroelastic theory (Biot, 1961; Ogata et al., 2020):

$$\boldsymbol{\nabla} \cdot \boldsymbol{\sigma} + \boldsymbol{F}_v = 0 \tag{1}$$

$$\boldsymbol{\sigma} = \boldsymbol{C}\colon \boldsymbol{\varepsilon} + \alpha p \boldsymbol{I}, \tag{2}$$

where σ, ε, C, and p denote the stress tensor, strain tensor, elastic stiffness tensor, and pore pressure, respectively. The Biot–Willis coefficient α represents the contribution of pore pressure to effective stress. Fluid flow is described by Darcy's law.

2.3 Damage theory, permeability and failure criteria

Fracture initiation and propagation are represented using an isotropic damage model. A scalar damage variable $D(0 \le D \le 1)$ is introduced to describe material degradation, and its effect on stiffness and permeability is expressed as:

$$E = (1 - D)E_0 \tag{3}$$

$$k = k_0 \exp(\alpha_k D) \tag{4}$$

Failure is evaluated using a tensile criterion and the Mohr–Coulomb criterion based on principal stresses. Once failure occurs, the damage variable is updated according to the corresponding strain-based evolution law. Damage is assumed to be irreversible, and an upper limit of $D = 0.99$ is imposed for numerical stability.

2.4 Consideration of rock heterogeneity

Rock heterogeneity was represented using a two-parameter Weibull distribution (Zok, 2017):

$$f(u) = \frac{m}{u_0}\left(\frac{u}{u_0}\right)^{m-1} \exp\left\{-\left(\frac{u}{u_0}\right)^{m}\right\}, \tag{5}$$

where u denotes the material property assigned to each element, u_0 is the scale parameter, and m is the shape parameter controlling the degree of variability. In this study, m=4 was adopted based on previous work (Okita et al., 2025). The distribution was applied to the spatial variability of compressive strength, tensile strength, and Young's modulus.

2.5 Analysis conditions

The analysis was conducted using a square domain with a side length of 5 m containing a circular cavity with a diameter of 0.08 m at its center, as shown in Fig. 1. The cavity diameter was selected to represent a typical borehole diameter used in hydraulic fracturing tests (approximately 76–100 mm). The domain was discretized into 28,552 triangular elements. The interior of the cavity was modeled as a fictitious porous region with extremely high porosity and permeability, and it was assumed that Biot's poroelastic theory is also valid within this region.

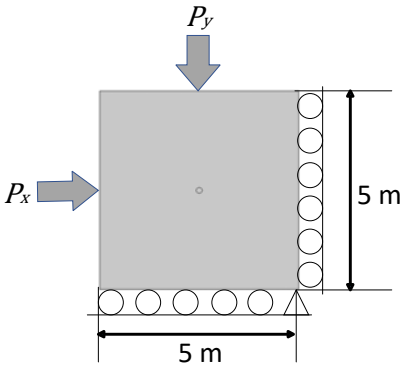


Fig. 1 Numerical model and boundary condition.

Normal stresses p_x and p_y were applied to the top and left boundaries, respectively, while roller boundary conditions were imposed on the bottom and right boundaries. Fluid flow was assumed to follow Darcy's law, and a constant flow rate was injected into the cavity. The fluid was assumed to be incompressible.

The parameters used in the analysis are listed in Table 1. The rock properties were determined assuming andesite, based on previous studies (Heap and Kennedy, 2016; Fujii et al., 2024). The in-situ stress condition corresponds to a depth of 250 m in rock with a unit weight of 25 kN/m³, resulting in an overburden pressure of 6.25 MPa. Lateral stress was applied accordingly. Hydrostatic pressure was imposed as a boundary condition within the cavity and along the outer boundary of the domain.

To consistently simulate the behavior from fracture initiation to post-injection response, fluid injection was stopped 8 s after the start of injection. Stress release was initiated at 11 s, and the analysis was terminated at 17 s. Stress release was achieved by introducing a fluid outlet at the center of the cavity, allowing fluid to be discharged and the pressure to decrease to the hydrostatic level.The analysis was performed for ten cases of the Biot–Willis coefficient and three cases of the initial permeability (Table 2).

Table 1. Parameters for the numerical simulation.

Parameter	**Value**	**Parameter**	**Value**
Young's modulus E [GPa]	20.5	Uniaxial compressive strength f_c [MPa]	25.3
Uniaxial tensile strength f_t [MPa]	3.50	Densityρ [kg/m^3]	2551
Internal friction angle θ [°]	45	Poisson's ratio [-]	0.2
Porosity n [-]	0.042	Damage-permeability coefficient α_k [-]	10
Maximum principal stress p_x [MPa]	7.5	Minimum principal stress p_y [MPa]	5
Hydrostatic pressure p_h [MPa]	2.5	Injection rate Q [mL/s]	0.,25

Table 2. Numerical simulation Cases.

Case	**Biot-Willis coefficient,α**	**Initial permeability [m^2]**	**Case**	**Biot-Willis coefficient,α**	**Initial permeability [m^2]**
Case 1	0.9	1.0×10^{-16}	Case 2	0.8	1.0×10^{-16}
Case 3	1.0		Case 4	0.9	5.0×10^{-17}
Case 5	0.9	2.0×10^{-16}	Case 6	0.6	
Case 7	0.7		Case 8	0.91	1.0×10^{-16}
Case 9	0.92	1.0×10^{-16}	Case 10	0.93	
Case 11	0.94		Case 12	0.95	

3 Results and discussions

In this study, the peak value of the pressure history under flow-rate-controlled conditions is defined as the breakdown pressure.

3.1 Influence of Biot–Willis coefficients α

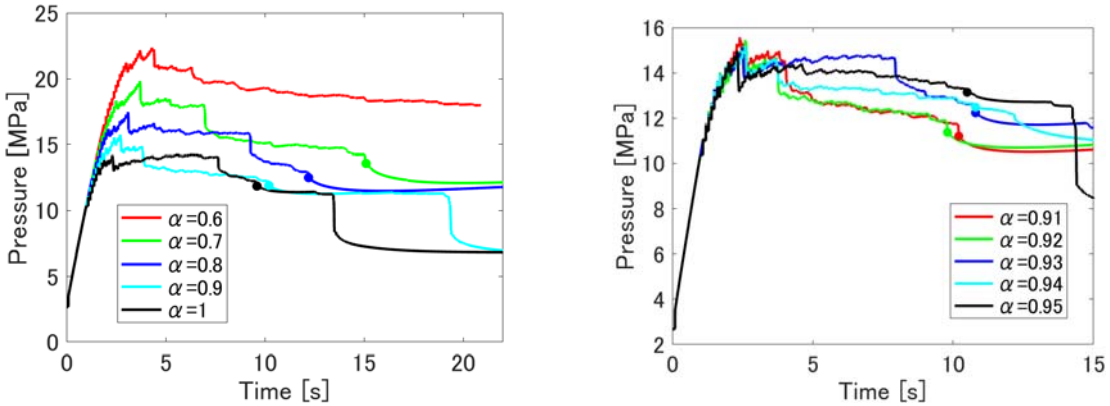
Fig. 2 shows the time histories of injection pressure for different values of the Biot–Willis coefficient α. The markers indicate the time at which the fracture reaches the outer boundary of the computational domain. Once the fracture reaches the boundary, fluid flows out of the domain, causing a rapid pressure drop. Therefore, the discussion focuses on the time period prior to these marker points. It should be noted that, for α = 0.6, the fracture does not reach the boundary even at *t*=20 s.

Fig.3 shows the fracture propagation pattern at *t*=10.2 s for α = 0.9. The fracture propagates along the maximum principal stress direction and reaches the boundary, which is consistent with the imposed stress field.

As shown in Fig. 2(a), the injection pressure decreases with increasing α. However, this decrease becomes less pronounced as α increases, and no significant difference is observed between α = 0.9 and α = 1. This behavior is explained by the effective stress relation $\sigma' = \sigma - \alpha p$, where a larger α enhances the contribution of pore pressure, leading to a greater reduction in effective stress. As α approaches unity, this effect becomes saturated.

Additional simulations for α = 0.91–0.95 (Fig. 2(b)) show no clear monotonic trend, and slight reversals in injection pressure are observed. This indicates that the influence of α saturates around α ≈ 0.9, beyond which other factors such as permeability and fracture propagation behavior become relatively dominant.

From the viewpoint of hydraulic fracturing theory, the pressure immediately before the fracture reaches the boundary can be regarded as slightly higher than the fracture closure pressure. A comparison with the minimum principal stress ($p_y = 5$ MPa) shows that this pressure approaches the theoretical value as α increases. Since the Biot–Willis coefficient varies depending on rock type and geological conditions, it should be identified through inverse analysis in practical applications.



(a) α = 0.6–1.0; (b) α = 0.91–0.95 (zoomed-in range)

Fig. 2 Time histories of injection pressure for different Biot–Willis coefficients α. Markers indicate the time when the fracture reaches the outer boundary of the computational domain.

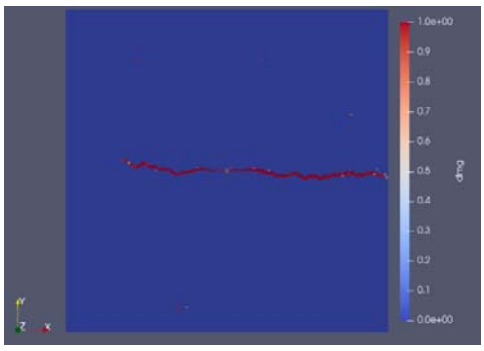


Fig. 3 Fracture propagation pattern at $t = 10.2$s for α = 0.9.The fracture propagates along the maximum principal stress direction and reaches the right boundary.

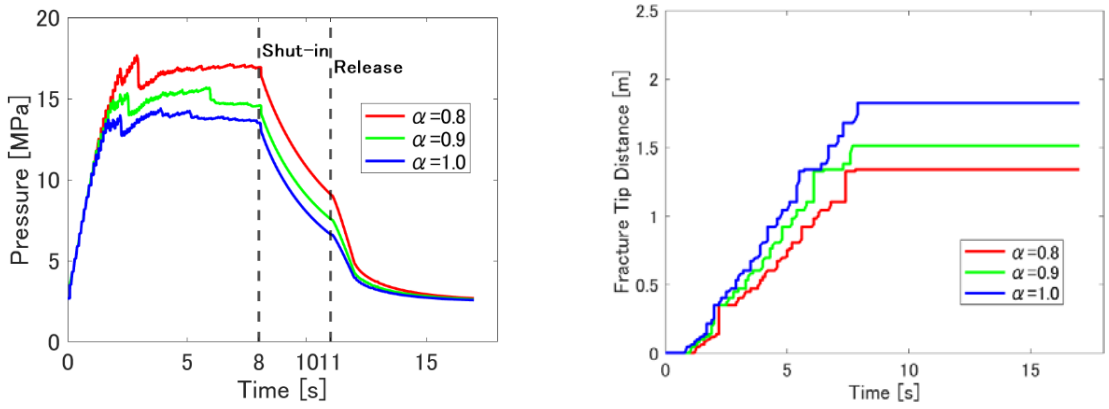
3.2 Pressure response after shut-in

Results for Cases 1–3, in which fluid injection was terminated at $t = 8$s, are shown in Fig. 4. During the pressure buildup phase up to 8 s, lower values of α result in higher injection pressures, and the corresponding breakdown pressure associated with fracture propagation also increases. This trend is consistent with the results shown in Fig. 2(a).

After shut-in, the pressure decay behavior is examined. As shown in Fig. 4(a), the rate of pressure decline is approximately the same for all cases; however, cases with smaller α maintain higher pressure levels during the decay process. This is because the breakdown pressure is higher for smaller α, while the subsequent pressure decline proceeds at a similar rate across the cases.

Fig. 4(b) shows the temporal evolution of fracture tip distance for different values of the Biot–Willis coefficient α. It is observed that fracture propagation is faster at the early stage for larger α. This behavior is attributed to the enhanced contribution of pore pressure to the effective stress, which promotes fracture propagation by reducing the effective stress near the fracture tip.

As a result, under the present simulation conditions where injection is terminated at $t = 8$s, larger values of α lead to longer fracture lengths. Despite the reduction in injection pressure with increasing α, fracture propagation is nevertheless promoted. This trend is consistent with an effective stress–controlled fracture mechanism in hydraulic fracturing.



(a) Injection pressure (b) Fracture tip distance

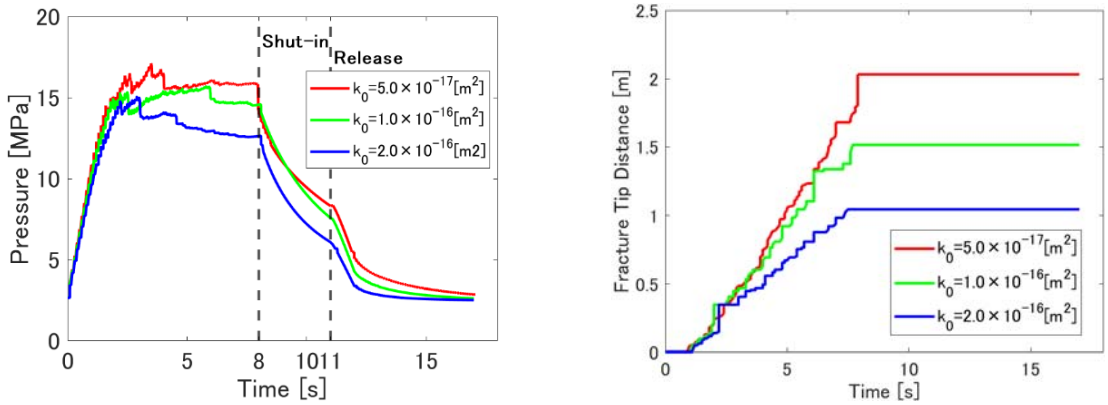
Fig. 4 Time histories of injection pressure and fracture tip distance for Cases 1–3 with injection shut-in at $t = 8$s. Dashed lines indicate the timing of shut-in and pressure release.

3.3 Effect of initial permeability on injection pressure and pressure response

Fig.5(a) shows the pressure histories for three cases with different initial permeabilities (Cases 1, 4, and 5). As observed in the figure, the breakdown pressure increases as the initial permeability decreases. This trend can be attributed to the competition between pressure accumulation within the cavity and fluid leak-off into the surrounding rock mass. In cases with higher permeability, the injected fluid rapidly infiltrates into the surrounding matrix, suppressing pressure buildup and leading to fracture initiation at lower pressures. In contrast, for lower permeability, fluid leak-off is reduced, allowing pressure to accumulate within the cavity and resulting in a higher breakdown pressure.

Focusing on the pressure behavior after shut-in at $t = 8$s, a clear difference in the rate of pressure decline is observed. Higher permeability leads to a more rapid pressure drop, as fluid diffuses more efficiently into the surrounding matrix, making it difficult to sustain the cavity pressure. These results indicate that the initial permeability strongly influences both the breakdown pressure and the pressure decay characteristics after shut-in.

Fig. 5(b) shows the temporal evolution of fracture tip distance for the same cases. Fracture propagation is more pronounced for lower permeability, resulting in longer fractures at $t = 8$s. This behavior is attributed to the suppression of fluid leak-off under low-permeability conditions, which allows fluid pressure to be maintained within the fracture. As a result, pressure is more effectively concentrated near the fracture tip, acting as a driving force for fracture propagation. This tendency is consistent with the pressure histories shown in Fig. 5(a), indicating that lower permeability leads to higher breakdown pressure and consequently promotes further fracture propagation.



(a)Time histories of injection pressure (b)Temporal evolution of fracture tip distance

Fig. 5 Effects of initial permeability on injection pressure and fracture propagation.

4 Conclusion

This study developed a fully coupled hydro-mechanical simulation model for flow-rate–controlled hydraulic fracturing and investigated the effects of the Biot–Willis coefficient α and initial permeability on pressure response and fracture behavior.

The results show that injection pressure decreases with increasing α due to enhanced effective stress reduction, while the influence of α becomes saturated around α ≈ 0.9. In contrast, initial permeability strongly affects both breakdown pressure and post shut-in pressure decay, with lower permeability leading to higher pressure buildup and longer fracture propagation due to suppressed fluid leak-off.

These findings indicate that α primarily governs fracture initiation through effective stress control, whereas permeability controls fluid transport and pressure dissipation. Furthermore, the pressure immediately before fracture boundary arrival approaches the theoretical closure pressure as α increases, suggesting that α plays a key role in the interpretation of hydraulic fracturing tests.

The proposed framework provides useful insights for parameter identification in coupled analyses and contributes to improving the reliability of in-situ stress estimation and geothermal reservoir evaluation.

References

Biot, M. A. (1961) General theory of three-dimensional consolidation, Journal of Applied Physics, Vol.12, No.2, pp.155-164.https://doi.org/10.1063/1.1712886

Fujii, T., Mori, S., Higuchi, Y., Nishida, M., Tokusu, M. and Tsutsui, S. (2024)Design and construction supervision of underground powerhouse cavern of Upper Cisokan pumped storage hydropower plant in Indonesia, Proceedings of the 50th Symposium on Rock Mechanics, JSCE.

Heap, M. J. and Kennedy, B. M.(2016) Exploring the scale-dependent permeability of fractured andesite, *Earth and Planetary Science Letters*, 447, 139-150. https://doi.org/10.1016/j.epsl.2016.05.004

Hubbert and Willis, (1957) Mechanics of Hydraulic Fracturing, *Transaction of AIME*, 210(01), 153 – 169. https://doi.org/10.2118/686-G

Ikeda, S., Ogata, S., Yasuhara, H. and Kishida, K.(2024) Numerical simulation of Hydraulic Fracturing considering Grain Boundary weakness and Fluid-Rock Heat Transfer, *ARMA*2024-0563.https://doi.org/10.56952/ARMA-2024-0563

Izawa, S., Ogata, S., Yasuhara, H., Kinoshita, N., and Kishida, K. (2020) Evaluation of Fracture Evolution of Granite during Brazilian Test by Numerical Analysis of Fracturing Process Considering Mineral Distribution, Journal of the Society of Materials Science, Japan, 69(3), 236 – 247. https://doi.org/10.2472/jsms.69.236

Ogata, S., Yasuhara, H., Kinoshita, N. and Kishida, K. (2020) Coupled thermal–hydraulic–mechanical–chemical modeling for permeability evolution of rocks through fracture generation and subsequent sealing. Computational Geosciences 24, 1845–1864. https://doi.org/10.1007/s10596-020-09948-3

Okita, R., Kishida, K., Yasuhara, H., Ogata, S.,Fujii, T. (2025) Underground cavity excavation analysis introducing damage theory and Weibull distribution, Proceedings of the 16th Japan Symposium on Rock Mechanics, Paper Number 36, pp. 193–198.

Zhu,W. and Tang, C.(2004) Micromechanical Model for Simulating the Fracture Process of Rock, *Rock Mechanics and Rock Engineering*, Vol.37, No.1, pp.25-56.https://doi.org/10.1007/s00603-003-0014-z

Zok, F. W. (2018)On weakest link theory and Weibull statistics, *Journal of the American Ceramic Society*, 100(4), 1265 – 1268.https://doi-org.kyoto-u.idm.oclc.org/10.1111/jace.14665

Tensile fracturing in granite and gneiss investigated by DIC and thin sections

L. Jacobsson & M. Flansbjer
Department of Chemistry and Applied Mechanics, RISE Research Institutes of Sweden, Borås
lars.jacobsson@ri.se
0000-0003-4526-4061

L. Brander
Raw Material Supply, Swerock AB, Göteborg, Sweden

J. Sandström
Surface Ships, Saab Naval, Karlskrona, Sweden

Abstract

The fracture mechanics properties in crystalline rocks depend on the microstructure, and presence of microcracks and pores. The aim was to visualize and quantify tensile fracturing properties during and after experiments. Wedge splitting tests were conducted on two quasi-brittle rock types, a medium- to coarse-grained granite and a finely medium-grained gneiss, to study the fracture processes and to determine fracture mechanics data under tensile loading. The propagating crack was followed during loading by displacement field measurements obtained from digital image correlation analysis. The propagating crack was meandering and branching in the granite, whereas the crack was straighter and smoother with almost no branching in the gneiss. The crack opening displacement was determined from the displacement field in a small band enclosing the crack path and was used to determine fracture process zone data. A fully developed crack, i.e. no cohesive force, was obtained when the crack opening displacement was about 6.5–20 μm in the granite and ≤ 6.5 μm in the gneiss. The length of the process zone was 10 mm initially and increasing to 15 mm when the crack length was 30–40 mm in the granite and 2–3 mm in the gneiss. The results on granite are in line with the few existing results in literature, whereas no previous results on gneiss were found. The onset of crack initiation was determined by the change of the crack mouth opening stiffness and compared with crack opening displacements yielding the same result. The thin section analyses confirmed mentioned observations on the crack path and showed occasionally several parallel crack paths in the granite, but a single crack path in the gneiss with a small amplitude and long wavelength. Intragranular fractures are mainly found in feldspar and large quartz grains. Several of the used methods are novel.

Keywords

Wedge splitting test, Crystalline rock, Mode I fracture mechanics, Fracture process zone (FPZ), Digital image correlation (DIC).

1 Introduction

The fracture mechanics properties in crystalline rocks depend on its mineral composition and microstructure, such as grain size, grain shape, shape and crystallographic orientation, and presence of microcracks and pores. Considering fracturing under tensile loading, many of the cracks pass along grain boundaries. Some pass also through the grains, e.g. feldspars or biotite, if the crystallographic direction is favourable and the grain size large enough (Krantz 1983, Brander et al. 2014). Moreover, occasionally crack branching occurs (Kobayashi and Fourney 1978).

The conceptual model of the progressive tensile fracturing of a rock can be described by three stages visualized by a case when a notched specimen is subjected to a force yielding a tensile stress in the notch (Fig. 1a). Elastic deformations and occasional crack initiation take place in the notch area during stage 1. In stage 2, there will be systematic crack initiation in a zone surrounding the notch when the force is further increased. Finally in stage 3, a fully developed crack has formed and started to propagate with no remaining cohesive force in its tail. By looking at the crack opening displacement (COD) along a crack with length a, there are cohesive forces in the fracture process zone (FPZ) which vanishes when COD reaches COD_{cr} and are zero above this value (Barenblatt 1959). The effect of the cohesive force can be seen if the COD along the crack extension is studied and length of the FPZ (L_{FPZ}) can be determined (Fig. 1b).There are few studies where the FPZ in crystalline rock was studied e.g. Kobayashi and Fourney (1978), Labuz et al. (1985, 1987) and Maji and Wang (1992).

The fracture mechanics properties in a rock are often described by the fracture toughness K_{Ic} using linear elastic fracture mechanics (LEFM) and determined by standard tests. There have been questions raised about the suitability to use LEFM and standard fracture mechanics tests on rock due to the non-linear nature of the response of rocks and small ligament lengths in the standard tests which both violate the foundations in LEFM (e.g. Zhu and Joyce 2012). LEFM is widely used due to its experimental simplicity as compared to using non-linear fracture mechanics.

This paper focusses on the fracture process, i.e. initiation and propagation, in one granite and one gneiss. The aim is to visualize and quantify tensile fracturing properties during and after experiments using different methods. A full description of the study was reported by Jacobsson et al (2025) and Jacobsson and Brander (2025).The figures, some modified, are obtained from these publications.

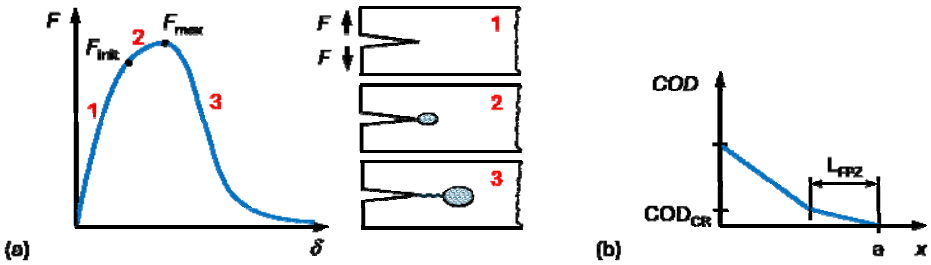


Fig. 1 (a) Example figure showing force versus displacement and stages during tensile fracturing: (1) occasional crack initiation, (2) systematic crack initiation with a partially developed FPZ, and (3) fully developed FPZ and crack propagation; (b) Crack opening displacement along the crack.

2 Experiments

One structurally isotropic medium- to coarse-grained igneous granite and one structurally anisotropic migmatitic and recrystallized orthogneiss were selected for this study. The gneiss consisted of parallel foliation layers of a finely medium-grained mesosome (70%–90% of the rock) and a medium- to coarse-grained leucosome. Petrographic characterizations and uniaxial compression, Brazilian, flexural strength and rupture energy tests were conducted to determine mechanical properties. Wedge Splitting Tests (WST), cf. Brühwiler and Wittmann (1990), were conducted to determine the fracture mechanics properties. The WST specimens are blocks with the dimensions 200 mm × 200 mm × 150 mm (height × width × thickness) manufactured with two types of notch geometries: either a "blunt" notch in shape of a borehole, or a sawn square-shaped notch (Fig. 2a). A constant rate of the crack mouth opening displacement,$CMOD$, of 15 µm/min was applied and the splitting force F_{s} was measured. The granite was tested with a sharp (GR-N) and blunt (GR-H) notch. The gneiss specimens (GN-A, GN-B and GN-C) had a blunt notch and were split in three directions A, B and C to study the effect of anisotropy (Fig 2b). Three specimens of each type were tested, i.e. 15 specimens in total.

The displacement field was measured on one face on the specimen covering the area of the propagating crack using Digital Image Correlation (DIC), cf. Sutton et al. (2009). Two CCD cameras with 2048 × 2048 pixels resolution and 50 mm lens were used to capture the images on the specimen surface. The calibrated measurement volume was ca. 100 mm × 100 mm × 80 mm (Fig. 2a). The COD was measured along the main crack perpendicular to it over a 3 mm wide band surrounding the main crack path. Thin sections were made from the wedge-split blocks after testing, covering the entire length of fractures. The blocks were impregnated by fluorescent epoxy before and during the cutting operations. By this, fractures, microcracks, and other cavities were enhanced.

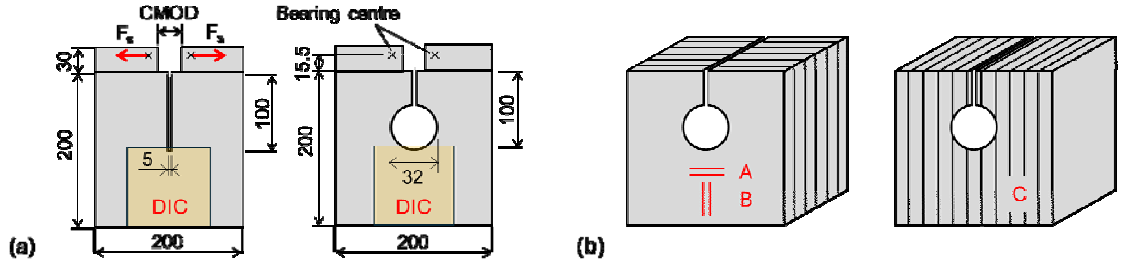


Fig. 2 (a) Specimen dimensions (mm), F_s , $CMOD$ and area for DIC measurements; (b) Black lines show the foliation planes for the gneiss. The red lines with labels A and B show the lineation directions. Label C shows splitting parallel to foliation.

3 Results

The splitting force $F_s$and the crack mouth opening stiffness $K_{\mathrm{CMOD}} = \mathrm{d}F_s/\mathrm{d}CMOD$ are shown in Fig. 3 and 4. A non-linearity at the loading phase and the relative ductility of the granite with a gradual force decrease at the post-peak part of the curve are seen in Fig. 3. The gneiss displays minor non-linearity at the loading part and its brittleness is seen by the rapid transition and load drop at the peak

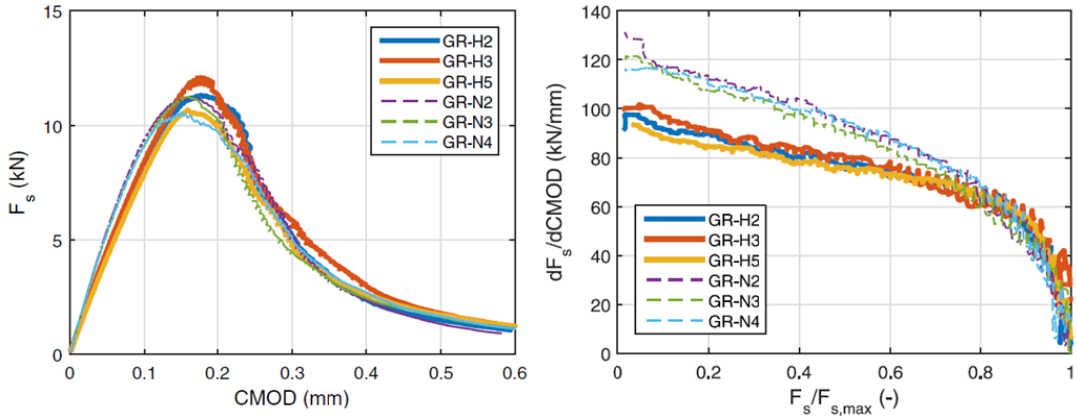


Fig. 3Left: Splitting force versus CMOD on granite specimens; Right: K_{CMOD} versus $F_s/F_{s,\max}$ up to peak load.

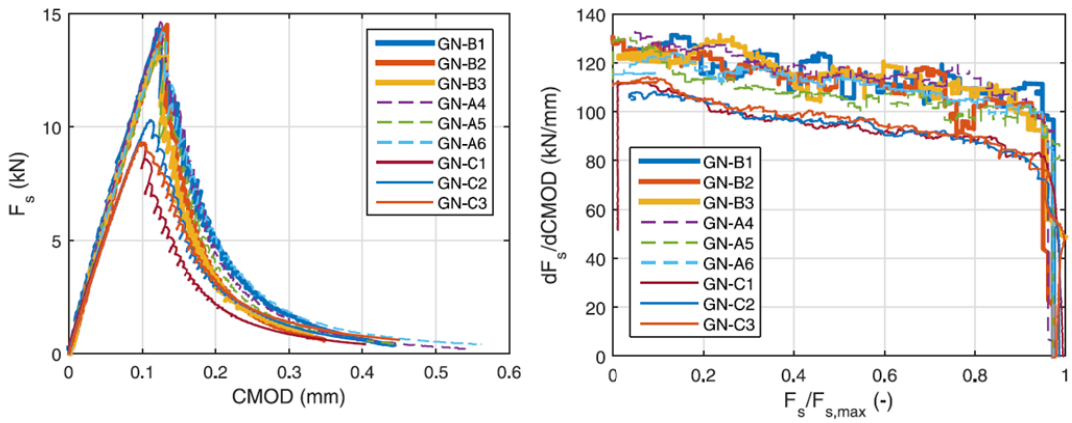


Fig. 4 Left: Splitting force versus CMOD on gneiss specimens; Right: K_{CMOD} versus $F_s/F_{s,\max}$ up to peak load.

load (Fig. 4). The onset of systematic crack initiation (stage 2 in Fig. 1) can be identified when the K_{CMOD}-curves change its slopes. For the granite, it appears to be approximately at $F_s/F_{s,\max}$ equal to 0.78±0.01 for the notched specimens and 0.90±0.02 for the specimens with the blunt notch when all specimens in the respective series are considered. The corresponding numbers for gneiss are 0.92±0.01 (type A and B) and 0.94±0.01 (type C).

The progressive fracturing in three specimens is visualized in Fig. 5–7. The propagating crack is meandering and branching in the granite (Fig. 5), whereas the crack is straighter and smoother with almost no branching in the gneiss (Fig.6 and 7). The onset for crack initiation was determined by the DIC measurements and was equal to the assessment based on changes in K_{CMOD}.

The COD value at full crack initiation,COD_{cr}, is between 10 and 20 µm on GR-H2. The gneiss specimens have a smaller COD_{cr}, ≤ 6.5 µm (GN-B1) and ≤ 4.4 µm (GN-C1).The length of the process zone (L_{FPZ}) was approximately 10 mm initially and increasing to 15 mm when the crack length was 30–40 mm in the granite (concluded by also comparing results on one more granite specimen not shown here) and 2–3 mm in the gneiss.

Looking further at the COD-results, the slope of the COD versus position x from the notch, i.e. the angle between the crack surfaces outside the FPZ begin to increase at a critical crack length (a = 55–60 mm) that was about the same on all specimens. The two observed phases correspond to (1) steady-state propagation without influence from bottom uncracked part of the specimen (ligament) and

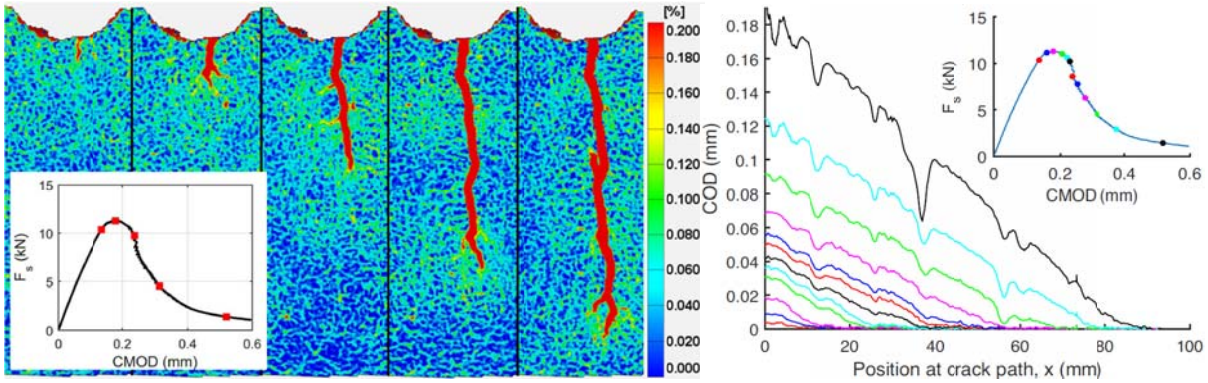


Fig. 5 Specimen GR-H2. Left: Largest principal strain at 5 load stages; Right: COD along the crack path at 12 load stages.

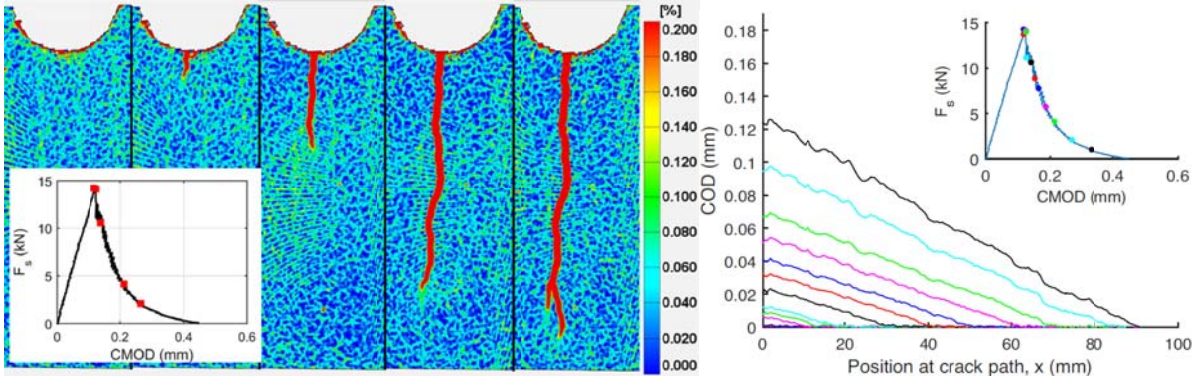


Fig. 6 Specimen GN-B1. Left: Largest principal strain at 5 load stages; Right: COD along the crack path at 12 load stages.

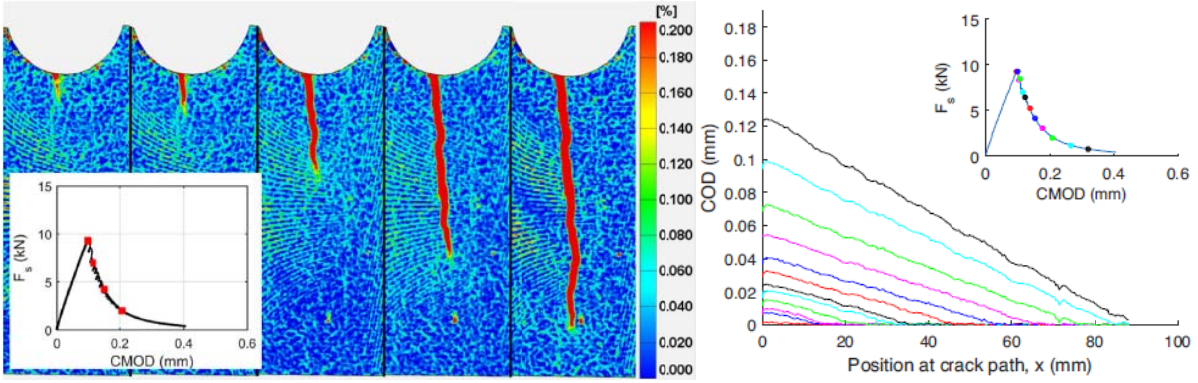


Fig. 7 Specimen GN-C1. Left: Largest principal strain at 5 load stages; Right: COD along the crack path at 12 load stages.

(2) propagation with influence from deformations in the ligament, cf. analogy with plastic hinge (Zhu and Joyce 2012). The deformation gradient becomes successively larger in the remaining part of the specimens that is uncracked with increasing crack length during phase (2). The deformation gradient affects the crack initiation and propagation (Zhu and Joyce 2012).

It is illustrative to study how the crack front advances with increased $CMOD$ to interpret the differences in ductility/brittleness (Fig. 8). There, the long crack initiation phase in the granite (GR-H2) and the instant and unstable propagation during the first 10–15 mm crack propagation in the gneiss (GN-B1 and GN-C1)can be seen. The position of the crack front a was determined at a COD-value of 2 and 4 µm.

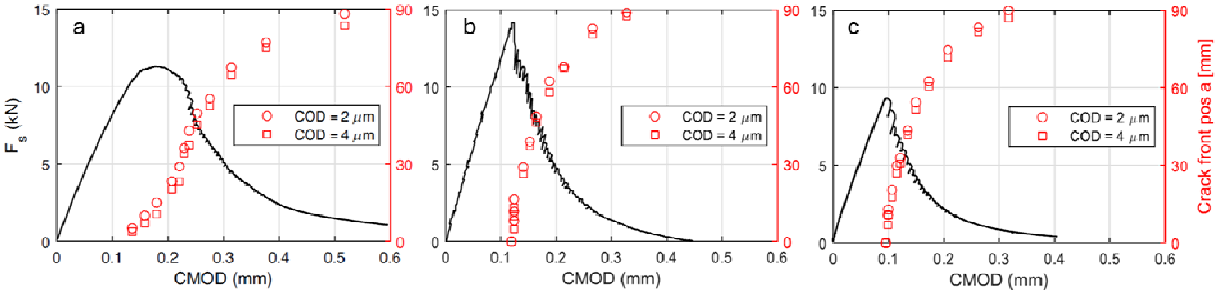


Fig. 8 Crack front position a and splitting force F_S versus $CMOD$ in specimen GR-H2 (a), GN-B1 (b) and GN-C1 (c).

The fracture energy and the strain energy release rate, G_{Ic}, were calculated using the WST-data (Fig. 3 and 4). The results showed that the granite required a much larger fracture energy to split than the gneiss. On the contrary, the maximum splitting force at the WST tests and tensile strength determined from the Brazilian and flexural strength tests were lower for the granite as compared with gneiss when the fractures were inflicted perpendicular to the foliation. This illustrates the difference in strength versus fracturing behaviour. The fracture toughness, K_{Ic}, was calculated from G_{Ic} and elasticity parameters determined from uniaxial compression tests yielding a larger value of K_{Ic} for the granite than for the gneiss. By analysing the test results using LEFM, it yielded consequently lower values of K_{Ic} as compared with values determined using non-linear fracture mechanics based on fracture energy. Moreover, the calculated K_{Ic} based on LEFM was larger in the gneiss when the blocks were split perpendicular to the than foliation, which is contrary to the results obtained from non-linear fracture mechanics. Several of the specimens had a blunt notch which violate the LEFM assumptions, but a relative comparison between the granite and gneiss should still hold.

A thin section image of one of the granite specimens is shown in Fig. 9a and illustrates the crack branching, parallel fractures and a high frequency of intragranular cracks in large grains. Similar branching was repeatedly seen along the main crack paths. A thin section image on one of the gneiss specimens, split perpendicular to the foliation (Fig. 9b), displays no crack branching and fewer intragranular cracks in the more fine-grained microstructure. Almost only grain boundary cracks are seen in Fig. 9c on a gneiss specimen split along the foliation planes.

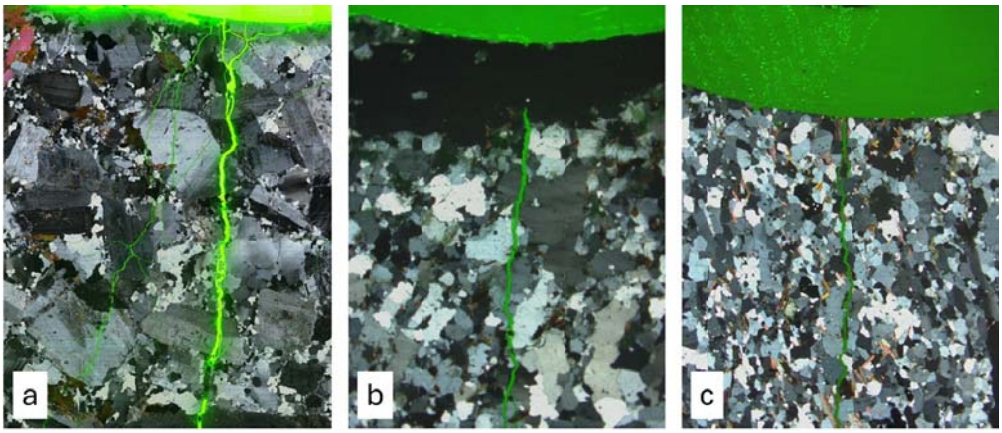


Fig. 9 Thin section images of specimen GR-H3 (a), GN-B1 (b) and GN-C1 (c) in the notch area. Images taken with fluorescent light overlayed on cross polarized light pictures, to enhance the cracks relative the grain structure. Image sizes are 8.4 × 10.8 mm.

4 Discussion and conclusions

The fracture process of one granite and one gneiss was analysed by means of wedge splitting tests and thin sections. The onset of crack initiation was determined based on where stiffness K_{CMOD} versus loading began to deviate from a linear decrease and drop faster during the pre-peak loading phase. The

results complied with determinations done by using strain and displacement fields from DIC measurements. The values of K_{Ic} calculated using non-linear fracture mechanics and LEFM showed a discrepancy. It is noted that the LEFM assumptions are violated e.g. since the rock materials possess a non-linear mechanical behaviour. Moreover, the crack initiation seems to begin before the peak force for the granite. The DIC measurements were further used to visualize the crack propagation, and to quantitatively determine parameters related to the FPZ. The crack branching seen in the granite by the DIC and thin sections is illustrative to understand the more ductile response in the granite and the contrast is large to the gneiss. It was seen that the ligament length was large enough to obtain steady-state crack propagation up to 55–60 mm crack length without influence of the uncracked part (hinge effect). By contrast, often standard LEFM tests are likely not fulfilling this condition which affects the fracture mechanics results which some have pointed out lately. To conclude, some of the used methods are new and some have previously not been fully applied on rock samples and not in a single study. Only a few studies, were the FPZ was examined in rock, were found in the literature. Thin section images confirmed the fracture patterns seen from DIC results and yielded additional detailed results on how the cracks propagated through the microstructures of the two rock types.

5 Acknowledgements

The sampling, sample preparation, experiments and the basic evaluations were carried out within the European project HYDRASPLIT, Grant Agreement No. FP7-SME-2012-1-315530. The advanced evaluations and writing of this paper were partly funded by RISE Research Institutes of Sweden. The use of the figures from other sources complies with the Creative Commons Attribution 4.0 International License.

References

Barenblatt G (1959) The formation of equilibrium cracks during brittle fracture. General ideas and hypotheses. Axially-symmetric cracks. J Appl Math Mech 23(3):622–636. https://doi.org/10.1016/0021-8928(59)90157-1.

Brander L, Flansbjer M, Appelquist K, Casserstedt L, Lindqvist JE(2014) Microtextural fracture study of rock materials subjected to direct tensile tests. CBI Report PX10473, CBI Swedish Cement and Concrete Research Institute, Borås.

Brühwiler E, Wittmann F (1990) The wedge splitting test, a new method of performing stable fracture mechanics tests. Eng Fract Mech 35(1):117–125. https://doi.org/10.1016/0013-7944(90)90189-N.

Jacobsson L, Brander L (2025), Tensile Fracture Initiation and Propagation of Granite and Gneiss at Wedge Splitting Tests: Part 2—Fracturing Studies Based on Digital Image Correlation and Thin Section Analysis. Rock Mech Rock Eng 58, 2031–2054.https://doi.org/10.1007/s00603-024-04257-y.

Jacobsson L, Sandström J, Brander L, Flansbjer M (2025), Tensile fracture initiation and propagation of granite and gneiss at wedge splitting tests: Part—1: Effect of notch type on tensile crack initiation and fracture mechanics results. Int. J. Fracture. https://doi.org/10.1007/s10704-025-00857-z.

Kobayashi T, Fourney WL (1978) Experimental characterization of the development of the micro-crack process zone at a crack tip in rock under load. In: Kim YS (ed) Proc 19th U.S. Symp. Rock Mech., University of Nevada-Reno, May 1978, pp 243–246.

Labuz JF, Shah SP, Dowding CH (1985) Experimental analysis of crack propagation in granite. Int J Rock Mech Min Sci Geomech Abstr 22(2):85–98. https://doi.org/10.1016/0148-9062(85)92330-7.

Labuz JF, Shah SP, Dowding CH (1987) The fracture process zone in granite: evidence and effect. Int J Rock Mech Min Sci Geomech Abstr 24(4):235–246. https://doi.org/10.1016/0148-9062(87)90178-1.

Maji AK, Wang JL (1992) Experimental study of fracture processes in rock. Rock Mech Rock Eng 25(1):25–47. https://doi.org/10.1007/BF01041874.

Sutton MA, Orteu JJ, Schreier H (2009) Image correlation for shape, motion and deformation measurements—basic concepts, theory and applications. Springer. https://doi.org/10.1007/978-0-387-78747-3.

Zhu XK, Joyce JA (2012) Review of fracture toughness (G, K, J, CTOD, CTOA) testing and standardization. Eng Fract Mech 85:1–46. https://doi.org/10.1016/j.engfracmech.2012.02.001.

Comparison of porosity and permeability of sandstones from MIP and laboratory tests

L. Vavro & M. Vavro
The Czech Academy of Sciences, Institute of Geonics, Ostrava, Czech Republic
leona.vavro@ugn.cas.cz
0000-0002-4830-8691

D. Řimnáčová
The Czech Academy of Sciences, Institute of Rock Structure and Mechanics, Praha, Czech Republic

Abstract

The microstructure of pores, defined primarily by their size distribution, shape and mutual connectivity, has a fundamental influence on physical-mechanical and deformation properties of rocks. It also significantly influences fluid transport and storage capacity and co-determines rock resistance to weathering. Precise characterization of pore microstructure and permeability is therefore essential for evaluation of hyrocarbon reservoirs, assessment of the suitability of the rock environment for CO_2 storage and as a geological barrier in deep geological repositories of high-level radioactive waste, or for the protection of stone monuments. In this study, porosity and hydraulic properties of four Czech sandstones (Godula, Mšené, Hořice and Kocbeře) of different microstructure, composition and physical-mechanical properties were investigated using high-pressure mercury intrusion porosimetry (MIP) and direct laboratory measurements of gas permeability and hydraulic conductivity. The most porous sandstones are Mšené (ca 30 %) and Hořice (ca 25 %), followed by the moderately porous Kocbeře sandstone (ca 15 %), while the least porous is the Godula sandstone (ca 5 %). Hydraulic conductivities derived from MIP are in the order of 10^{-9} m·s^{-1} for all sandstones, whereas laboratory tests yield markedly different values: $10^{-5}$to 10^{-7} m·s^{-1} for highly porous sandstones, 10^{-6} to 10^{-8} m·s^{-1} for moderately porous sandstone, and as low as 10^{-12} m·s^{-1} for the least porous sandstone. Similar discrepancies were also found when comparing coefficients of permeability derived from MIP and obtained from laboratory tests. These results highlight differences between porosimetry-based and laboratory-derived hydraulic parameters, reflecting the influence of pore microstructure, pore-throat geometry, tortuosity and connectivity on fluid transport in sandstones, but the different size of the test specimens used in these two methods also plays an undeniable role. The findings confirm that for a reliable evaluation of transport properties of porous rocks, it is necessary to combine MIP results with laboratory tests on larger volumes.

Keywords

Sandstone, Pore microstructure, Fluid permeability, Mercury porosimetry, Permeability measurements.

1 Introduction

Clastic sedimentary rocks, particularly sandstones, are widely utilized both as natural building materials and as reservoirs in hydrogeology and petroleum engineering. In the near future, sandstone formations will also play a crucial role as host rocks for storing greenhouse gases, especially CO_2. Mechanical and deformation behavior of rocks in general, as well as their durability and ability to transport fluids are strongly influenced by pore microstructure and the connectivity of the pore space (Rasiņa et al. 2022; Řimnáčová et al. 2020; Sufian and Russell 2013). Cracks and the pore network therefore determine the overall porosity, permeability and hydraulic conductivity of the rock (Lokajíček et al. 2026; Řimnáčová et al. 2024). Understanding these parameters is essential not only for predicting the long-term stability of sandstones in architectural applications, but also for evaluating their role in groundwater flow and hydrocarbon migration. Many different experimental approaches can be employed to characterize pore systems, such as optical microscopy, scanning electron microscopy, high-pressure mercury intrusion porosimetry (MIP), gas adsorption, X-ray computed micro-tomography, small-angle neutron scattering, nuclear magnetic resonance or laboratory measurements of permeability and hydraulic conductivity (Freire-Lista et al. 2015; Jun and Liang 2024; Košek et al. 2024; Wang et al. 2022; Zeng et al. 2021; Zhao et al. 2024). Among them, MIP, which provides detailed information on pore size distribution and laboratory permeability tests, which directly measure fluid transport properties, are currently among the most widely applied. Comparison of these methods offers valuable insights into how pore geometry translates into effective hydraulic behavior and highlights the importance of integrating multiple techniques when assessing the complex fluid permeability of porous rocks.The aim of this study was to compare commonly used methods for the determination and assessment of porosity and permeability of porous rocks. For this purpose, four types of sandstones with distinct properties were selected, each expected to exhibit different pore space parameters and fluid permeabilities depending on their specific microstructural characteristics.

2 Rock material used for the experiment

The following four types of Czech sandstones, differing in microstructure, composition and physical-mechanical properties were selected for this study: (i) fine- to medium grained glauconitic sandstone from the Řeka quarry, often referred to in literature as Godula sandstone (Vavro et al. 2016), (ii) fine- to medium-grained quartz sandstone from the Kocbeře quarry (Kytýř et al. 2024; Vavrik et al. 2021; Vavro et al. 2026), (iii) fine-grained quartz sandstone from the Podhorní Újezd quarry, commonly referred to as Hořice sandstone (Vavro et al. 2019), and (iv) fine-grained, quartz-rich Mšené sandstone (Koudelka et al. 2020; Kytýř et al. 2024). All of these sandstones are well-known building and sculpture stone materials that have been used in the territory of the present-day Czech Republic for many centuries. In particular, Hořice sandstone has been used in a number of well-known historical monuments, such as St. Vitus Cathedral, Charles Bridge and the National Theatre in Prague.

Physical and mechanical properties of studied rocks are presented in Table 1.

Table 1. Range of values of selected physical-mechanical parameters of rocks used for experiment (according to previous own measurements and data published in above mentioned literature).

Rock property	Godula sandstone	Kocbeře sandstone	Hořice sandstone	Mšené sandstone
Bulk density [kg·m^{-3}]	2440 – 2610	2140 – 2270	1760 – 1960	1850 – 1930
Total porosity [%]	5.4 – 9.4	12.0 – 17.2	27.9 – 28.4	26.3 – 29.7
Open porosity [%]	4.0 – 5.8	9.2 – 17.1	23.8 – 26.3	24.0 – 28.2
Water absorption capacity [%]	0.7 – 3.0	2.2 – 6.1	7.3 – 11.6	10.8 – 13.3
Ultrasonic wave velocity [km·s^{-1}]	3.12 – 4.29	2.74 – 3.48	2.39 – 2.55	2.13 – 2.36
Uniaxial compressive strength [MPa]	103 – 156	56 – 87	26 – 33	21 – 33
Splitting tensile strength [MPa]	4.0 – 10.0	2.6 – 6.1	1.2 – 1.6	1.1 – 1.4

strength properties were tested on dried test specimens, water absorption capacity was determined after 48 hours of soaking

3 Methods, test samples and equipment used in the experiment

Mineral composition and internal texture of sandstones were studied using optical polarization microscopy (OPM) and X-ray powder diffraction (XRPD). OPM for basic petrographic analysis was undertaken in transmitted light on cover-slipped thin sections using a NIKON Eclipse LVDIA-N polarizing microscope (Nikon, Japan), coupled with the NISElements image processing and analysis

software (Laboratory Imaging, Czech Republic). Analysis of mineralogical composition of the sandstone matrix was carried out using XRPD with a Rigaku SmartLab diffractometer (Rigaku Corporation, Japan) with a D/teX Ultra 250 detector. The powder samples were gently ground using agate mortar before analysis and pressed using microscope glass in a rotational sample holder and measured in a reflection mode (Bragg-Brentano geometry). The measured data were evaluated using PDXL 2 software 2.4.2.0 (Rigaku Corporation, Japan) and compared with database PDF-2 (International Centre for Diffraction Data, USA).

The pore space of sandstones and their hydraulic properties were investigated using MIP and direct laboratory measurements of gas permeability and hydraulic conductivity. For MIP measurements, a small piece of rock measuring approximately 0.5 x 0.5 x 0.5 cm and weighing about 1 g was chipped off from the rock using a sharp hammer. This piece was dried in a drying oven at 105 °C before measurement and then weighed. The measurement was performed twice for each rock, with a piece of approximately the same size used for each partial measurement. The MIP measurements of pores in the size range 7 nm – 112 μm were performed using Pascal 140 EVO and Pascal 440 EVO (Thermo Fisher Scientific, USA)mercury porosimeters equipped with SOLID software.The permeability evaluation from MIP data is based on the studies of Scheidegger (1974) and Carniglia (1986).

Hydraulic conductivity measurements were performed in a permeameter from the Infratest Prüftechnik GmbH (Germany) in a triaxial pressure chamber using deaerated pressurized water under the constant hydraulic gradient. For this measurement, cylindrical test specimens with a diameter and length of 48 mm, i.e. with the length-to-diameter(L/D) ratio of 1:1, were prepared. The confining pressure was set at 0.55 MPa during the testing. The calculated hydraulic conductivity coefficient (HCC) at the ambient temperature was subsequently recalculated to the comparative value for HCC k_{10} at 10 °C.Gas permeability of sandstones was measured using a KTK 100 triaxial cell (UNIPRESS, Poland) modified for gas passage. A computer-controlled mechanical press ZWICK 1494 (Zwick/Roell, Germany) served as the source of axial stress, and nitrogen was used as the measuring gas. For the test, cylindrical specimens with 48 mm in diameter and ca 96 mm in length, i.e., with an L/D ratio of 2:1, were used. They were covered with a rubber membrane, then clamped in jaws of the press machine and the confining pressure was set to 3 MPa. Throughout the experiment, the nitrogen pressure was regulated using the control valve and kept at 0.1 MPa. Within the laboratory measurements of gas permeability and hydraulic conductivity, the open (effective) porosity of sandstones was also determined, by calculating it from the measured values of bulk density and water absorption capacity until the sample weight stabilized. Bulk density was calculated from the mass of the specimen and the bulk volume. Water absorption capacity was determined from the weights of dry and water-saturated test specimens. The soaking time until the weight stabilized was approximately 4 to 6 weeks depending on the type of sandstone.

4 Experimental results

Basic petrographic parameters of studied sandstones are presented in Table 2 and in Fig. 1.

Table 2. Mineralogical composition and grain size of studied sandstones obtained using OPM and XRPD.

Sandstone	***Md*of quartz grains [mm]**	**$M_{max}$of quartz grains[mm]**	**Main clastic components**	**Rock matrix and cement**
Godula	0.18 – 0.39	1.35 – 1.55	quartz + quartzite > orthoclase > plagioclase > muscovite > biotite± other rock fragments	ca 10 – 20% of rock volume; clay matrix (illite>illite-smectite mixed-layers>kaolinite) with siliceous and carbonate rock cement and glauconite grains
Kocbeře	0.19 – 0.33	0.95 – 1.45	quartz + quartzite > orthoclase >> muscovite	ca 10 – 15 % of rock volume; clay and siliceous matrix with local limonite, locally intense secondary silicification
Hořice	0.19 – 0.25	0.40 – 1.15	quartz + quartzite > orthoclase + plagioclase >> muscovite	ca 15 – 20 % of rock volume; clay matrix (kaolinite >>illite + smectite) with finely dispersed limonite
Mšené	0.12 – 0.18	0.46 – 0.95	quartz + quartzite >>> orthoclase > plagioclase > muscovite	ca 3 – 5 % of rock volume; clay matrix (kaolinite>>illite) with finely dispersed limonite

Md– average grain size, M_{max}– maximum grain size

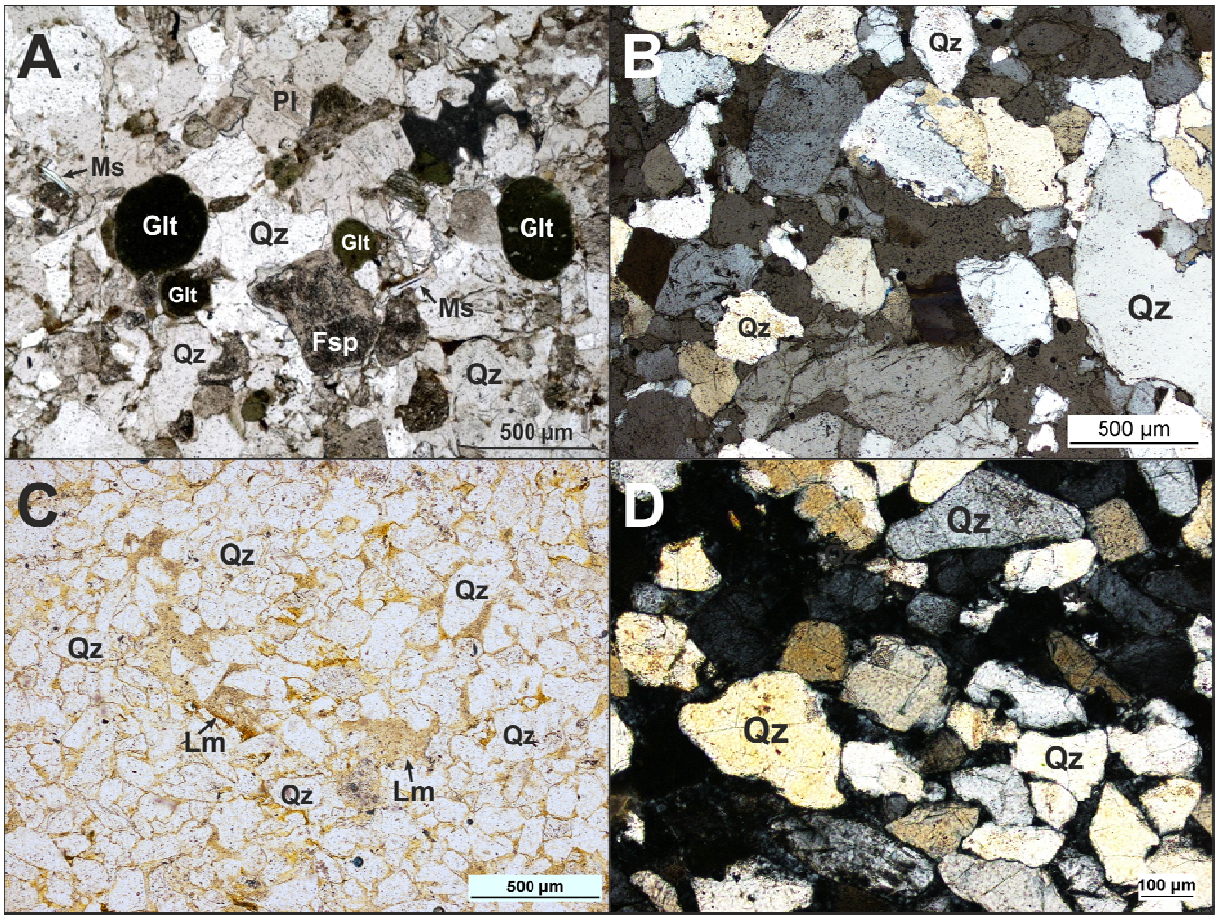


Fig. 1 Micrographs of studied sandstones: Godula (A), Kocbeře (B), Hořice (C) and Mšené (D). Rock-forming mineral abbreviations (in alphabetical order):Fsp – potassium feldspar (orthoclase), Glt – glauconite, Lm – limonite, Ms – muscovite, Pl – plagioclase, Qz– quartz.

From Table 2 and Fig. 1 it is evident that at least the Kocbeře, Hořice and Mšené sandstones are highly similar in the mineralogical composition of clastic framework grains and their size. However, they differ in the rock microstructure, in particular in the type of contacts between quartz grains and therefore the degree of rock compaction, and in the degree of secondary silicification (for details see e.g. Kytýř et al. 2024). These differences consequently affect not only their physical-mechanical properties (Table 1), but also their fluid permeability.

The basic textural parameters, pore size distribution and permeability coefficient (K) and HCC (k) of sandstones derived from MIP measurements are summarized in Fig. 2 and Table 3.

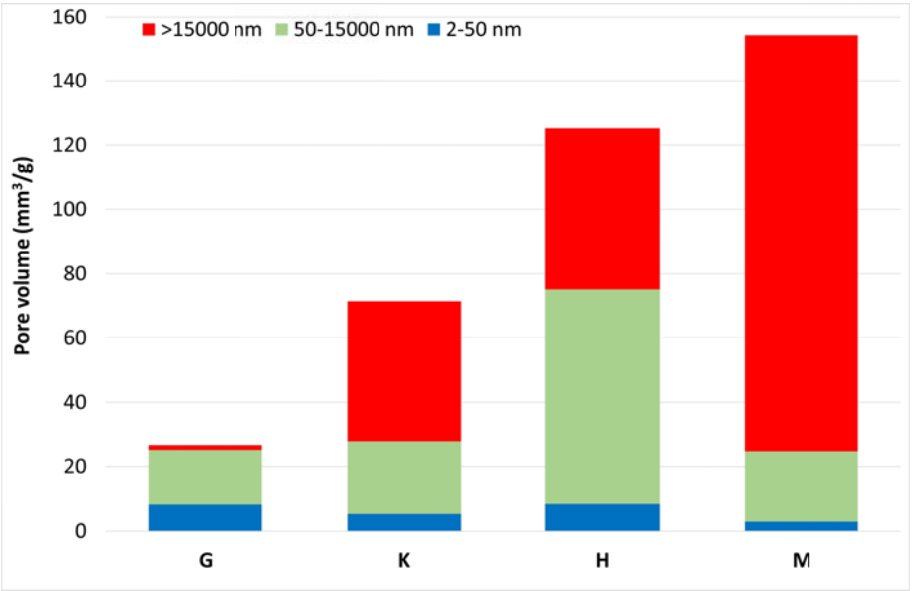


Fig. 2 The volume of pores in selected size classes for individual sandstones (G – Godula, M – Mšené, H – Hořice, K – Kocbeře, 2 – 50 nm = mesopores, 50 – 15000 nm = macropores, > 15000 nm = coarse pores).

Table 3. Average values of textural parameters, open porosity and permeability parameters of tested sandstones based on MIP.

Sandstone	V	S	r	φ	K_{MIP}	k_{MIP10}
	$mm^3 \cdot g^{-1}$	$m^2 \cdot g^{-1}$	nm	%	m^2	$m \cdot s^{-1}$
Godula	26.5	1.7	30.9	6.6	1.6×10^{-16}	1.2×10^{-9}
Kocbeře	71.2	1.6	90.3	15.8	3.8×10^{-16}	2.9×10^{-9}
Hořice	126.8	2.2	116.3	25.3	6.1×10^{-16}	4.6×10^{-9}
Mšené	157.4	1.1	282.2	29.5	7.1×10^{-16}	5.3×10^{-9}

V – total pore volume, S – total pore surface, r – average pore radius, φ – open porosity, K_{MIP} – coefficient of permeability obtained from MIP, k_{MIP10} – coefficient of hydraulic conductivity calculated from MIP for 10 °C

The values of open porosity, coefficient of permeability and HCC, determined based on laboratory tests on cylindrical test specimens, are presented in Table 4.

Table 4. Average values of open porosity and permeability parameters of tested sandstones based on laboratory tests.

Sandstone	BD	WAC	OP	K_{N2}	k_{H2O10}
	$kg \cdot m^{-3}$	%	%	m^2	$m \cdot s^{-1}$
Godula	2530	2.2	5.5	$7.6\times 10^{-18} – 1.5\times 10^{-17}$	$1.4 – 8.0\times 10^{-12}$
Kocbeře	2210	7.0	15.6	$4.9\times 10^{-14} – 6.8\times 10^{-12}$	$3.5\times 10^{-8} – 6.4\times 10^{-6}$
Hořice	1930	12.9	25.0	$8.8\times 10^{-15} – 1.2\times 10^{-14}$	$1.9\times 10^{-7} – 1.1\times 10^{-6}$
Mšené	1850	15.5	28.4	$1.2 – 1.3\times 10^{-14}$	$9.4\times 10^{-6} – 1.3\times 10^{-5}$

BD – bulk density, WAC – water absorption capacityto constant mass,OP – open porosity, K_{N2} – coefficient of permeability obtained from gas permeability measurements, k_{H2O10} – laboratory measured coefficient of hydraulic conductivity for 10 °C

5 Conclusions

The four selected rocks represent a broad spectrum of microstructural, mineralogical, and physical-mechanical characteristics typical of Czech sandstones. Their different degrees of compaction and secondary cementation, reflected in contrasting porosity and other material properties, provide a suitable basis for evaluating how pore space architecture affects fluid transport properties.

The data above clearly illustrate the extent of these differences. The different inner rock texture features lead to variability in bulk density (ca 1800 to 2600 $kg \cdot m^{-3}$), and a wide range of total porosity from ca 5% in the Godula sandstone to nearly 30 % in the Mšené sandstone. These variations are also reflected in mechanical properties, where, for example, uniaxial compressive strength decreases from ca 100 – 150 MPa (Godula sandstone) to only ca 20 – 30 MPa (Hořice and Mšené sandstones).

Fluid transport properties differ by several orders of magnitude. Gas permeability coefficients range from 10^{-17} m² to 10^{-12} m², while HCC spans from 10^{-12} $m \cdot s^{-1}$ to 10^{-5} $m \cdot s^{-1}$. These contrasts highlight how the described differences in pore content and geometry, grain contacts, and secondary silicification lead into major differences in effective fluid movement.

However, significant differences were observed between the hydraulic parameters obtained inthe laboratory and those derived from MIP. HCC derived from MIP are in the order of 10^{-9} $m \cdot s^{-1}$ for all sandstones, whereas laboratory tests provided different values, ranging from $10^{-5}$to 10^{-7} $m \cdot s^{-1}$ for highly porous sandstones to 10^{-12} $m \cdot s^{-1}$ for the least porous sandstone. Similar discrepancies were described by Vavro et al. (2026) when comparing HCC derived from X-ray CT scanning and from direct laboratory tests. Differences were also found in the case of permeability coefficients, where laboratory determined values range from 10^{-17} to 10^{-18} m^2 for Godula sandstone to mainly 10^{-14} m^2 for other sandstones, while the permeability calculated from MIP is in the order of 10^{-16} m^2 for all rocks.

These discrepancies reflect the importance of pore network microstructure such as pore-throat geometry, tortuosity and connectivity in controlling fluid transport. The different specimen sizes in both analyses also play an important role. It is therefore evident that a multi-scale approach combining MIP with testing on larger volumes is required for reliable evaluation of transport properties of porous rocks.

Acknowledgement

Research was financially supported by the projects RVO 68145535 and RVO 67985891.

References

Carniglia SC (1986) Construction of the tortuosity factor from porosimetry. Journal of Catalysis102(2): 401–418. DOI: 10.1016/0021-9517(86)90176-4.

Freire-ListaDM,FortR,Varas-MurielMJ (2015) Freeze–thaw fracturing in building granites. Cold Regions Science and Technology 113: 40–51. DOI: 10.1016/j.coldregions.2015.01.008.

Jun J, Liang W (2024) Investigation of the pore structure characteristics and fluid components of Quaternary mudstone biogas reservoirs: a case study of the Qaidam Basin in China. ScientificReports 14(1): 26512. DOI: 10.1038/s41598-024-78010-4.

Košek F, Dudák J, Tymlová V, Žemlička J, Řimnáčová D, Jehlička J (2024) Evaluation of pore-fracture microstructure of gypsum rock fragments using micro-CT. Micron 181: 103633. DOI: 10.1016/j.micron.2024.103633.

Koudelka P, Fila T, Rada V, Zlamal P, Sleichert J, Vopalensky M, Kumpova I, Benes P, Vavrik D, Vavro L, Vavro M, Drdacky M, Kytyr D (2020) In-situ X-ray differential micro-tomography for investigation of water-weakening in quasi-brittle materials subjected to four-point bending. Materials 13 (6): 1405. DOI: 10.3390/ma13061405.

Kytýř D, Koudelka P, Drozdenko D, Vavro M, Fíla T, Rada V, Vavro L, Máthis K, Souček K (2024) Acoustic emission and 4D X-ray micro-tomography for monitoring crack propagation in rocks. International Journal of Rock Mechanics and Mining Sciences 183: 105917. DOI: 10.1016/j.ijrmms.2024.105917.

Lokajíček T, Přikryl R, Racek M, Řimnáčová D, Petružálek M, Svitek T, Aminzadeh A, Natherová V (2026) Influence of thermal loading on microcrack evolution and elastic anisotropy in Westerly granite. Rock Mechanics and Rock Engineering 59(2): 2667–2691. DOI:10.1007/s00603-025-04939-1.

Rasiņa M, Lūsēns M, Racek M, Přikrylová J, Weishauptová Z, Řimnáčová D, Přikryl R (2022) Distinction between consecutive construction phases by combined microscopic study and quantitative pore space analysis: Case study of Horn's Bastion, Riga Castle (Latvia). Journal of Cultural Heritage 57: 88–96. DOI: 10.1016/j.culher.2022.08.004.

Řimnáčová D, Natherová V, Lokajíček T, Petružálek M, Aminzadeh A, Racek M, Přikryl R (2024) Thermally induced degradation of Westerly granite microstructure documented by dynamic elastic properties and pore space and damage characteristics. Bulletin of Engineering Geology and the Environment 83 (12): 518. DOI: 10.1007/s10064-024-04011-2.

Řimnáčová D, Weishauptová Z, Přibyl O, Sýkorová I, René M (2020) Effect of shale properties on CH_4 and CO_2 sorption capacity in Czech Silurian shales. Journal of Natural Gas Science and Engineering 80: 103377. DOI: 10.1016/j.jngse.2020.103377.

Scheidegger A (1974) The physics of flow through porous media. 3rd edn. University of Toronto Press, Toronto, Canada.

Sufian A, RussellAR (2013) Microstructural pore changes and energy dissipation in Gosford sandstone during pre-failure loading using X-ray CT. International Journal of Rock Mechanics and Mining Sciences 57: 119–131.DOI: 10.1016/j.ijrmms.2012.07.021.

Vavrik D, Benes P, Fila T, Koudelka P, Kumpova I, Kytyr D, Vopalensky M, Vavro M, Vavro L (2021) Local fracture toughness testing of sandstone based on X-ray tomographic reconstruction. International Journal of Rock Mechanics and Mining Sciences 138:104578. DOI: 10.1016/j.ijrmms.2020.104578.

Vavro L, Malíková L, Frantík P, Kubeš P, Keršner Z, Vavro M (2019) An advanced assessment of mechanical fracture parameters of sandstones depending on the internal rock texture features. Acta Geodynamica et Geomaterialia 16(2): 157–168. DOI: 10.13168/AGG.2019.0013.

Vavro M, Souček K, Vavro L, Georgiou L, Mrógala J (2026) Study of the microstructure and permeability of building stone using X-ray micro-tomography. Periodica Polytechnica Civil Engineering 70(1): 11–27. DOI: 10.3311/PPci.42434.

Vavro M, Vavro L, Martinec P, Souček K (2016) Properties, durability and use of glauconitic Godula sandstones: a relatively less known building stone of the Czech Republic and Poland. Environmental Earth Sciences 75(22): 1437. DOI: 10.1007/s12665-016-6248-3.

Wang W, Li W, Xu S (2022) Classifications of the reservoir space of tight sandstone based on pore structure, connectivity, and fractal character: A case study from the Chang 7 member of theTriassic Yanchang Formation in the Ordos Basin, China. ACSOmega 7(12): 10627–10637. DOI: 10.1021/acsomega.2c00252.

Zeng S, Li H, Zhang N, Sun B, Li J, Liu Y (2021) Full-scale pore size distribution features of uranium-bearing sandstone in thenorthwest of Xinjiang, China. Royal Society Open Science 8(5): 202036. DOI: 10.1098/rsos.202036.

Zhao Y, Qin W, Jin A, Wu H, Chen Z (2024) Research and analysis of the impact of the pore structure on the mechanical properties and fracture mechanism of sandstone. Materials Today Communications 38: 107753. DOI: 10.1016/j.mtcomm.2023.107753.

Characterizing Shear Strength of Rock Discontinuities under the Patton Failure Criterion

Mauricio Prudencio
Universidad Católica Boliviana, La Paz, Bolivia
mprudencio@ucb.edu.bo
0000-0002-8411-443X

Abstract

The Patton failure criterion provides a robust framework for characterizing the shear strength of rock discontinuities, including joints and bedding planes. This model defines a bilinear failure envelope governed by the basic friction angle, surface asperity dilatancy, and the effective normal stress.

Integrating experimental evaluation under this criterion with geomechanical rock mass characterization is essential for assessing stability in civil infrastructure and mining operations. This study proposes a methodology to determine the residual friction angle of open rock discontinuities through laboratory-scale direct shear testing based on Patton's model.

Cubic cement mortar specimens with 20-cm sides were prepared, featuring horizontal, 8°-inclined, and 4°-inclined discontinuities to simulate surface waviness. This approach aims to capture the morphological features of the surfaces more realistically (e.g., dilatancy), thereby mitigating scale effects associated with smaller samples. The specimens were prepared following standardized protocols to ensure representative and controlled shear surfaces.

During testing, samples are subjected to varying normal stress levels within a direct shear apparatus. Shear stress, tangential displacement, and normal displacement are continuously monitored until a steady-state condition or failure is reached. The experimental results enable the empirical construction of the failure envelope, highlighting the interaction between sliding friction and dilatant behaviour. These findings validate the non-linear nature of the Patton criterion, particularly under low confinement conditions, and provide critical design parameters such as the friction and dilatancy angles.

Keywords

Direct shear test, Dilatancy, Friction angle, Failure envelope, Patton’s Criterion.

1 Introduction

The characterization of discontinuities is essential in rock engineering because rock mass behaviour depends heavily on planes of weakness.

There are established lines of research dedicated to improving theoretical models for the shear strength of rock joints through rigorous laboratory testing. Patton (1966) proposed a criterion based on residual friction and geometric surface roughness (see Eq. 1). Subsequently, Barton and Choubey (1977) conceptualized an empirical formulation similar to Patton's criterion by incorporating additional physical variables (see Eq. 2); they proposed that the strength, besides depending on residual friction, is also influenced by joint roughness (JRC), joint wall compressive strength (JCS), and intact rock strength. Furthermore, Hencher and Richards (1982, 1989) conducted extensive laboratory investigations where their interpretation of the experimental data successfully isolated the residual friction parameterϕ_r from experimental scatter, aligning with Patton's original theoretical model.

Patton Criterion $$\tau = \sigma_n \tan(\phi_r + \mathrm{i}) \quad (1)$$

Barton Criterion $$\tau = \sigma_n \tan\left(\phi_r + JRC\ log_{10}\frac{JCS}{\sigma_n}\right) \quad (2)$$

Where τ Tangential Shear Strength
σ_n Normal Stress
i Dilatancy
JRC Joint Roughness Coefficient
JCS Joint Coefficient Strength
ϕ_r Residual Friction Angle

Comparing Equations 1 and 2, both authors clearly identify an additional shear strength component; in Patton's model, this component is constant and independent of the contact surface area, whereas in Barton's formulation, it is non-linear. In practice, Patton's criterion can be overly conservative for design purposes; however, it remains highly effective for determining the residual friction angle of a discontinuity at a laboratory scale, as demonstrated by Hencher and Richards. Conversely, while Barton's criterion has proven to be more suitable and comprehensive for design application- provided that the field characterization of the discontinuities is adequate- it may be less practical for isolating the residual friction angle at a laboratory scale.

Based on the criterion established by Patton (1966), Barton and Choubey (1977), and Hencher and Richards (1982, 1989), this study was developed to propose a methodology for determining the residual friction angle of open rock discontinuities through laboratory-scale direct shear testing.

2 Description of the models

The present study experimentally evaluates the behaviour of open joints through laboratory direct shear tests conducted on three pre-existing discontinuities cast with cement mortar, analysing how surface geometry and the direction of the movement influence the overall shear strength.

Fig. 1 shows the layout of specimens tested in the laboratory.

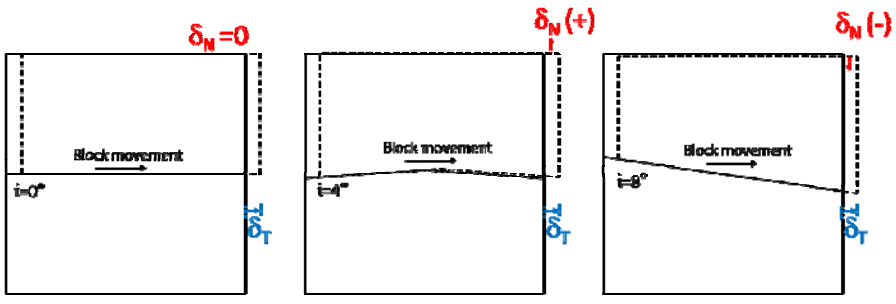


Fig. 1 Layout of the 3 specimens tested in the laboratory.

Through the assessment of the samples it can be defined: a) the residual friction angle of the horizontal smooth contact between cement mortar blocks; b) the effect of a 4° discontinuity inclination and a movement developing positive normal displacement; and c) the effect of an 8° discontinuity inclination and a movement developing negative normal displacement.

3 Laboratory Shear Test

The loading scheme for the laboratory tests was designed to incorporate the parameters described in the Patton failure criterion. To determine dilatancy, horizontal and vertical displacement data were recorded throughout the loading process. Similarly, the application of normal stress, the incremental shear load, and the direction of movement were considered to determine the residual friction angle using the Patton criterion equation rewritten in Equation 3.

$$\text{Patton Criterion} \qquad \phi_r = \text{atan}\left(\frac{T}{N}\right) - \text{i} \tag{3}$$

Where N Normal force
T Tangential Force

Figure 2 presents an example of the experimental setup and the testing procedure for the mortar blocks, illustrating the normal and shear forces along with the normal and tangential displacements recorded for the evaluations.

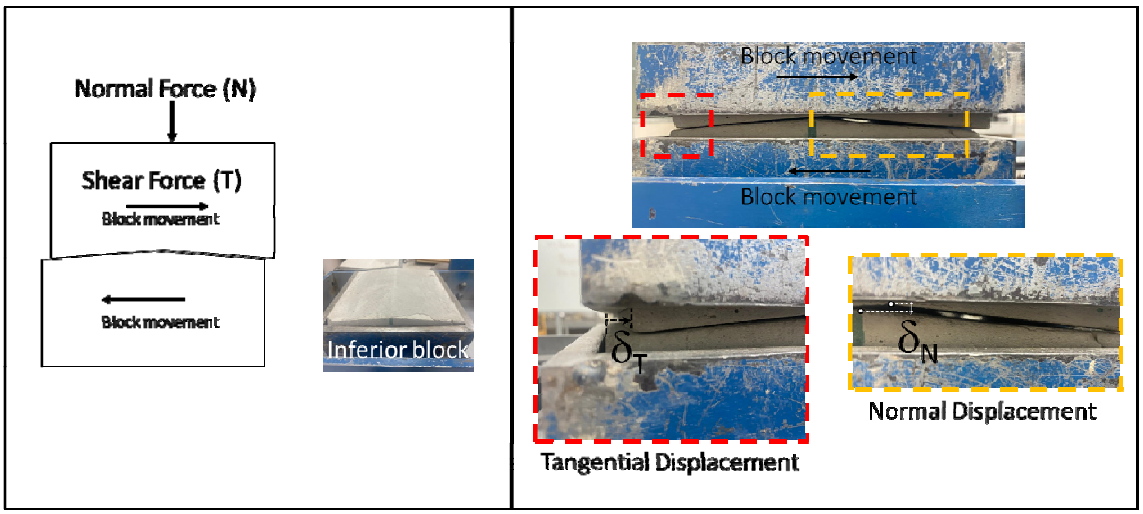


Fig. 2 Example of the testing process and relevant data considered for the evaluation.

The tested specimens were evaluated under the Patton criterion to determine the residual friction angle of open discontinuities. The following loading sequences were applied:

a) For the specimen with the discontinuity orientation aligned with the application of the shear force, a single test was conducted in which the normal load was increased; in the first stage, the normal force reached 0.47 kN, in the second stage it was increased to 0.96 kN, and in a third stage to 1.20 kN.
b) For the specimen with a 4° discontinuity inclination, which simulates an undulating discontinuity, two distinct tests were performed by applying normal forces of 0.47 and 0.96 kN.
c) For the specimen with an 8° discontinuity inclination, three distinct tests were conducted by applying normal forces of 0.47, 0.96, and 1.20 kN.

In all cases, normal and tangential displacement data associated with the applied shear forces were recorded, as recommended by the ISRM Suggested Method for Laboratory Determination of the Shear Strength of Rock Joints.

4 Results

The results from the shear tests on the discontinuities are shown in Figures 3 and 4, which contain the shear force versus tangential displacement curves, the normal displacement versus tangential displacement plots (from which dilatancy is derived), and the mobilized friction angle versus tangential displacement graphs. The mobilized friction angle results were obtained using Equation 3.

Observations show that, in all cases, the mobilized friction angle achieves stabilization after a certain level of tangential displacement and once the shear force reaches its residual state. Figure 3 shows that between tangential displacements of 1 mm and 2.5 mm, the friction angle is approximately 33°;

between 4.8 and 5.8 mm, the friction angle is around 32°, as it is between displacements of 6 to 8 mm. Similarly, under the same approach, Figure 4 shows that the friction angle oscillates between 32° and 34° from 2.5 mm onwards.

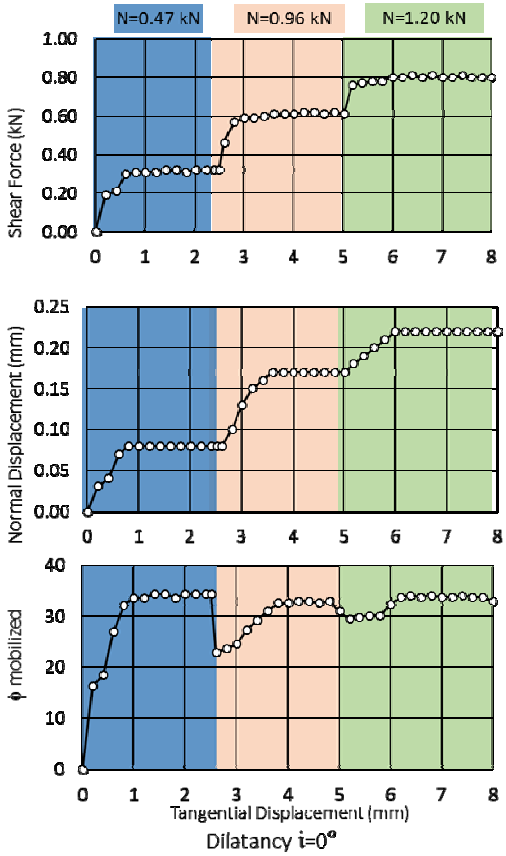


Fig. 3 Results of the shear test applying normal force in 3 stages. Discontinuity inclination 0°.

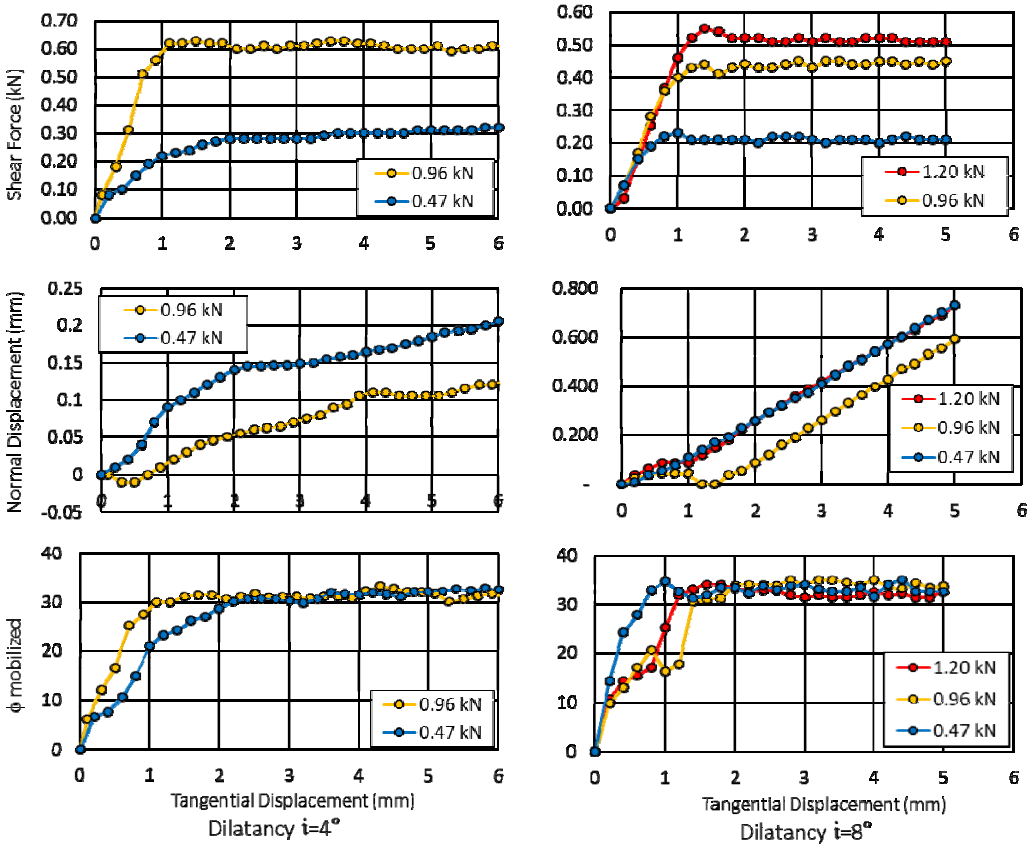


Fig. 4 Results of the shear tests applying normal forces of 0.47 and 0.96 kN for a 4° discontinuity inclination (on a specimen representing an undulating condition), and normal forces of 0.47, 0.96, and 1.20 kN for a continuous 8° discontinuity inclination.

5 Discussion

The experimental results obtained from the direct shear tests on cement mortar specimens provide significant insights into the shear strength components defined by the Patton's criterion. The methodology employed specifically targeted the first linear segment of Patton's bilinear model.

The rewritten Patton Equation 3 helps to demonstrate stabilized values of the mobilized friction angle in Figures 3 and 4, which consistently range between 32° and 34°. Equation 3 is an interesting tool for isolating the residual friction angle as indicated by Hencherand Richards. It is critical to emphasize that Equation 3 is strictly valid for low effective normal stresses.

Some similarity can be shown between Patton dilatancy and Barton's parameters. A basic correlation can be established between the two models by comparing their second terms. In Patton's model, the additional strength beyond basic friction is represented by the constant angle "i". In contrast, Barton represents this as a stress-dependent function $JRC*\log_{10}(JCS/\sigma_n)$.

Considering that the ratio $\log_{10}(JCS/\sigma_n)$ for the present research ranges between 2 and 3, and that the JRC of the tested surface is between 0 and 2, the Patton and Barton criterion achieve a reasonable similarity.

6 Conclusions

This study proposes a methodology to determine the residual friction angle of open rock discontinuities through laboratory-scale direct shear testing based on Patton's criterion. Patton's criterion (Eq. 1) has proven to be simple and practical for evaluating the residual friction angle in the laboratory, effectively isolating factors such as surface asperities or improper specimen installation due to human error.

On the other hand, Barton's criterion (Eq. 2) has proven to be more suitable and comprehensive for design applications, but it is less practical for isolating the residual friction angle at a laboratory scale.

References

Alber M., Schwarz J. (2015). Experiments on low-friction discontinuities from carboniferous strata in the Ruhr Mining District. Proc. EUROCK 2015: Future Development of Rock Mechanics, 531-534.

Barton, N.R. and Choubey, V. (1977). The shear strength of rock joints in theory and practice. Rock Mech. 10(1-2), 1-54.

Hencher, S.R., Richards, L.R. (1982). The basic frictional resistance of sheeting joints in Hong Kong granite. Hong Kong Engineer, 21–25.

Hencher, S.R., Richards, L.R. (1989). Laboratory direct shear testing of rock discontinuities. Ground Engineering. 22 (2), 24–31.

International Society for Rock Mechanics Commission on Standardisation of Laboratory and Field Tests. (1978). Suggested methods for the quantitative description of discontinuities in rock masses. Int. J. Rock Mech. Min. Sci. &Geomech. Abstr.

Muralha, J., Grasselli, G., Tatone, B., Blumel, M., Chryssanthakis, P., Jiang, Y.(2014). ISRM Suggested Method for Laboratory Determination of the Shear Strength of Rock Joints: Revised Version. Rock Mechanics and Rock Engineering. 47, 291–302.

Patton F.D. (1966). Multiple modes of shear failure in rock. Proc. 1st congr. Int. Soc. RockmMech., Lisbon 1, 509-513.

Bonded Contact Calibration in DEM using Nano Indentation Test

M. Yogeshwar
Research Scholar, Department of Civil Engineering, Indian Institute of Technology Madras, Chennai, Tamilnadu, India
yogeshwarmuruga@gmail.com

V. B Maji
Professor, Department of Civil Engineering, Indian Institute of Technology Madras, Chennai, Tamilnadu, India

Abstract

Numerical investigation of crack propagation in rock materials has progressed considerably, with the Discrete Element Method (DEM) providing notable advantages over continuum-based methods in rock mechanics. Particle Flow Code (PFC), an explicit DEM tool, simulates rock behaviour through bonded contact models that describe interactions between rigid particles. Conventionally, calibration of these models relies on a trial-and-error approach, where micro-scale parameters are repeatedly adjusted to reproduce experimentally observed macro-mechanical properties. However, such methods often fail to accurately capture crack initiation from pre-existing flaws and the resulting failure patterns in numerical simulations. The Flat-Jointed Model (FJM) is widely adopted due to its ability to realistically represent the angular and interlocked nature of mineral grains in rock. Nevertheless, calibrating the six required micro-parameters in FJM is complex, time-consuming, and subject to uncertainty. To address this limitation, nano-indentation testing is utilized to directly estimate key micro-mechanical properties, including Young's modulus and stiffness ratio. Using these parameters, crack propagation in flawed synthetic rock specimens under uniaxial loading is simulated in PFC. Validation of the numerical results demonstrates that the proposed calibration approach effectively captures crack growth and reproduces experimentally observed failure patterns with improved accuracy.

Keywords

Particle Flow Code, Rock, Micro-parameters, Nano-indentation, Crack Propagation.

1 Introduction

Numerical modelling of rock using the Distinct Element Method (DEM) has seen significant advancements in recent years. Particle Flow Code 2D (PFC2D) an explicit DEM software has become an important tool for modelling rock. In PFC2D rock is modelled using rigid particles which acts as mineral grains and the bonded contact model (Potyondy 2004) acts as a cementing medium between these mineral grains. By calibrating the bonded contact model, the numerical rock model can replicate the macroscopic mechanical properties of rock.

However, the bonded contact model involves several micro-parameters to be calibrated depending on the type of bonded contact model chosen and the commonly used method of calibration is trial-and-error approach (Itasca 2014). This approach involves matching macro properties (Uniaxial compression strength, Tensile strength, Young's modulus and poisons ratio) of numerical simulated model with laboratory model by varying the micro properties. But the disadvantage of this approach is it is often time-consuming because even though a micro propertycan have a large effect on a specific macro property it can also have a little effect on another macro property. This causes several repeating cycles of varying the micro properties to match the macro properties. To avoid this indirect way of calibrating micro properties a direct way of calibrating micro property involves determining mechanical properties of rock at the micro-scale. Nanoindentation testing enables the measurement of mechanical properties at the Nano-scale.

This paper presents the calibration of micro-parameters using Nano indentation test results. For Validation, crack propagation from a pre-existing flaw is compared between experimental results and numerical models simulated using both the conventional trial-and-error calibration method and the Nano indentation-based calibration approach.

2 Nano indentation test

Nano indentation is an indentation test in which an indent is made on a material to determine its mechanical properties such as hardness and elastic modulus using an indenter with known properties. The applied load is typically in millinewtons, and the displacement is measured in nanometer. A load–indentation depth curve is obtained from the test, from which the elastic modulus (E) and hardness (H) of the material are calculated.

$$E = (1 - \nu^2)(\frac{1}{E_r} - \frac{1-\nu_i{}^2}{E_i})(1)$$

Where E_r Reduced Modulus
E_i Indenter Modulus
ν Poisson's Ratio of Sample
ν_i Poisson's Ratio of indenter

$$H = \frac{P_{max}}{A_c}(2)$$

Where P_{max} Maximum Load Applied
A_c Projected Contact Area

Unlike conventional indentation tests, the contact area (A_c) is calculated depending on the depth of penetration and geometry of the indenter. In our study Berkovich indenter a three-sided pyramidal indenter is used. The projected contact area of Berkovich indenter is given by $24.5\ h_c^2$, where hc is the contact penetration depth.

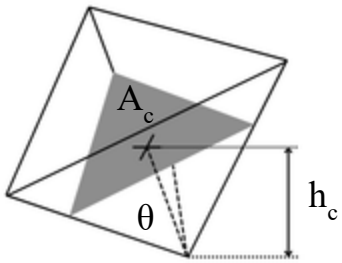
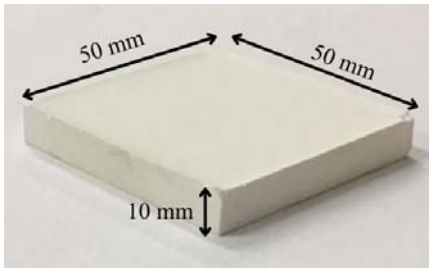


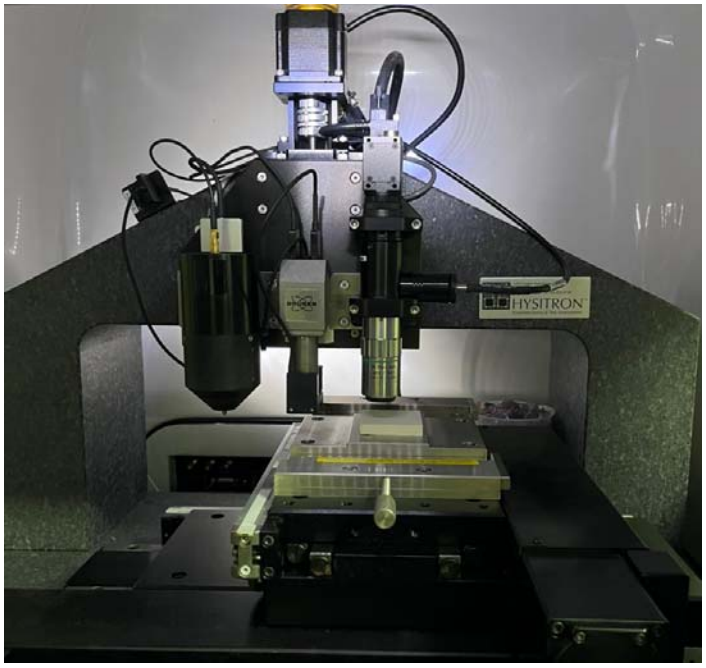
Fig. 1 Berkovich indenter.

2.1 Sample preparation and testing

The present study focuses on homogeneous artificial rock and gypsum was chosen because of its ability to replicate the behaviour of an ideal natural rock (including the presence of secondary crack growth). Additionally, it is easy to prepare in large quantities and specific dimensions.To prepare the gypsum specimen S-35 grade gypsum powder was mixed with 25% water to form a slurry, which was then poured into moulds to produce samples of the required dimensions. A sample of size 50 × 50 × 10 mm was prepared to meet the requirements of the Hysitron TI 950 TriboIndenter as shown in Figure 2. The surface of the specimen is ensured to be smoot has roughness of sample surface can affect the accuracy of results (Yang et al. 2017). Before performing indentation, the indentation locations were selected. The indentation produces a triangular impression on the specimen at the nanoscale, as shown in Figure 3.



(a)



(b)

Fig. 2 a) Sample used for Nano indentation test b) Berkovich indenter c) Hysitron TI 950 Tribo Indenter.

Nano indentation test are performed in three stages. 1) Loading stage - Displacement-controlled mode was selected for testing, and the load was applied until peak load (40,000 µN) is reached. 2) Holding stage - Upon reaching the peak load, a holding stage of 5 seconds was maintained 3) Unloading stage – In this stage the reduced indentation modulus is calculated from the slope of the unloading curve obtained from the load–displacement data, as shown in Figure 4. The Young's modulus of the test sample was then determined using the Young's modulus and Poisson's ratio of the indenter as shown in Eq. 1 and are listed in Table 1.

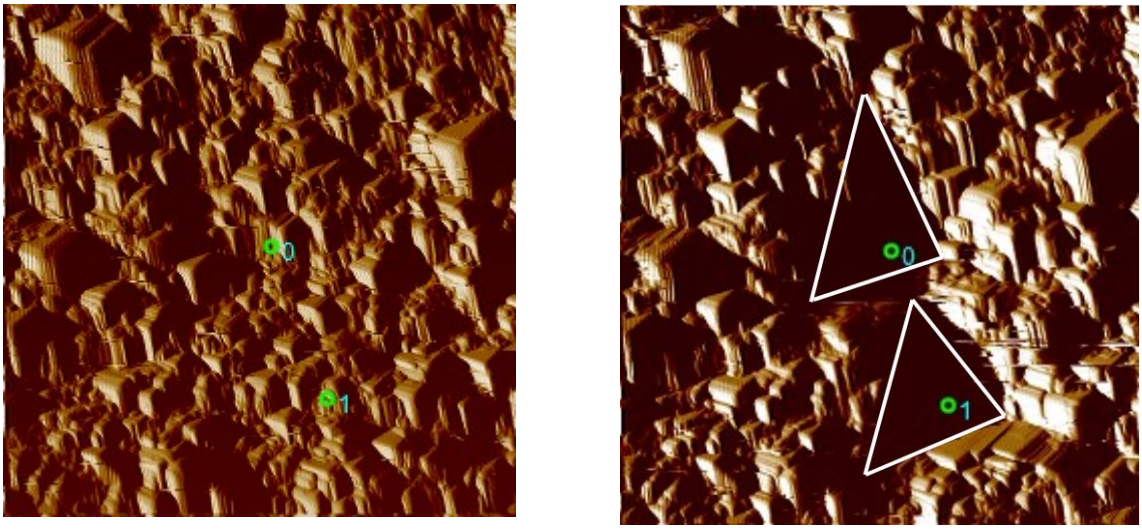


Fig. 3 a) Points marked for Nano indentation (Before Nano indentation) b) After Nano indentation.

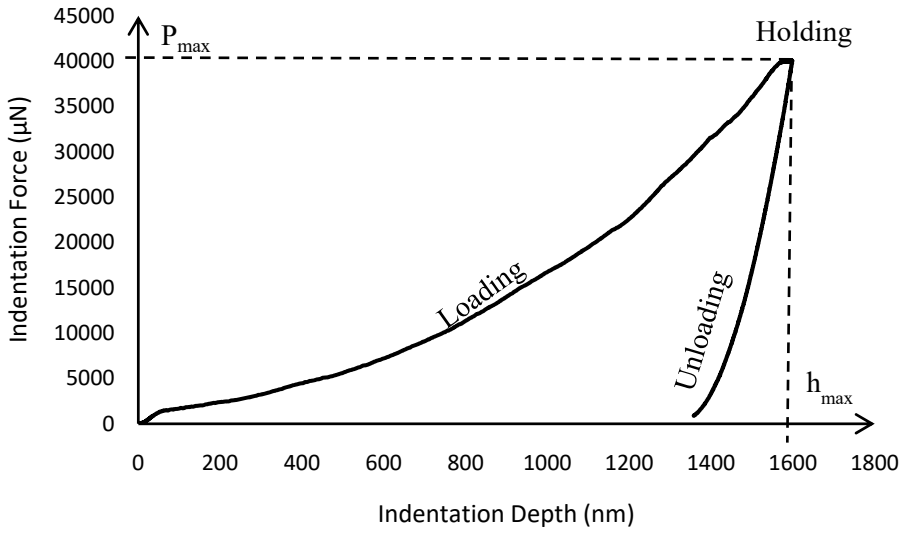


Fig. 4 Load-indentation depth curve of gypsum mineral.

Table 1. Mechanical properties of gypsum determined using Nano indentation.

Nano Indentation Properties	**Value**
Maximum Force, P_{max} (µN)	40031
Maximum Depth, h_{max}(nm)	1598
Reduced Modulus E_r (GPa)	33.97
Young's Modulus E (GPa)	35.72
Hardness (MPa)	733.58

3 Calibration of Micro properties

In Particle Flow Code 2D, Gypsum rock issimulated using 2D rigid particle represents a gypsum mineral grain with voids existing between them and bonded to neighbouring particles using flat-jointed bonded contact model (Potyondy 2012).

To capture the mechanical behaviour of gypsum rock, six microparameters of the flat-jointed model must be calibrated. Previous calibrations proposed by Bahaaddini et al. (2021)were based on a trial-and-error approach in which the microparameters were varied until the macroscopic properties matched the experimental results as shown in Table 2. In the present study, nano indentation testing was used to directly determine two of the six microparameters, while the remaining parameters were calibrated using the trial-and-error method. This approach significantly reduces the complexity of the calibration process.

The Young's modulus of the gypsum mineral obtained from the Nano indentation test was used as input. The stiffness ratio was calculated from Poisson's ratio and is independent of E and G due to the assumed homogeneity of the gypsum material. The particle size distribution was calibrated to match the macroscopic Young's modulus with the known microscopic Young's modulus and stiffness ratio. Finally, the tensile strength, cohesion, and friction angle were calibrated using the trial-and-error method. Table 3 shows the change in micro properties when Nano indentation calibration is adopted. From the micro parameters adopted the calibrated model yields the following macro properties shown in Table 4.

$$k_n = \frac{2E_1E_2}{t(E_1+E_2)} \quad (3)$$

At interior of mineral $E_1 = E_2$

$$k_n = \frac{E}{t} \quad (4)$$

Where E_1,E_2 Young's modulus of mineral on both sides of interface
t Thickness of contact interface
k_nNormal stiffness

$$k_s = \frac{2G_1G_2}{t(G_1+G_2)} \quad (5)$$

At interior of mineral $G_1 = G_2$

$$k_s = \frac{G}{t} \quad (6)$$

Where G_1,G_2 Shear modulus of mineral on both sides of interface
k_s Shear stiffness

Dividing (4) by (5)

$$\frac{k_n}{k_s} = \frac{E}{G} = 2(1+\nu) \quad (7)$$

Where ν Poisson's ratio of the sample

Table 2. Comparison of calibration procedure.

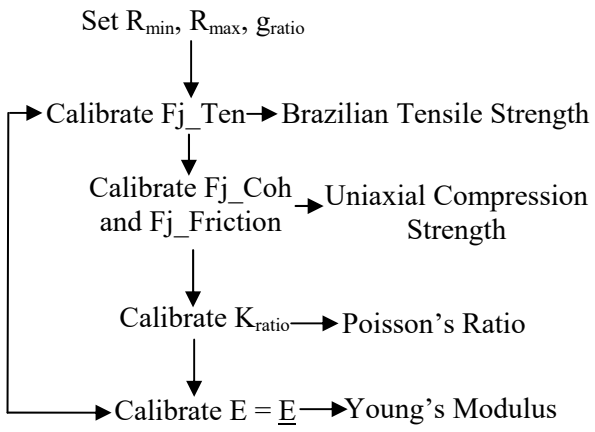
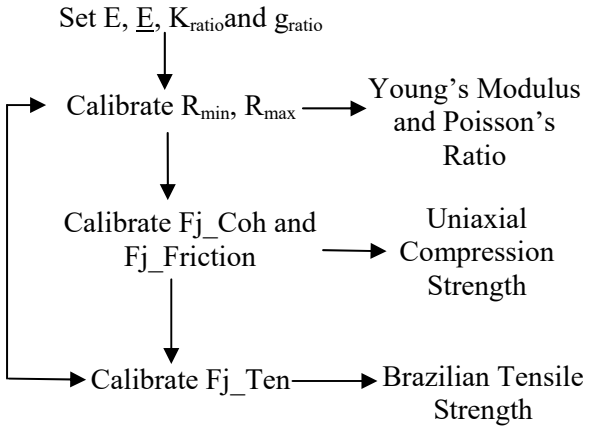
Bahaaddini et al. (2021) Calibration	**Nano Indentation Calibration**
	

Table 3. Comparison of Micro properties.

Micro Properties	**Bahaaddini et al. (2021)**	**Nano indentation**
Elastic modulus, E (GPa)	4.75	32.8
Stiffness ratio, k_n/k_s	1.5	2.7
Tensile Strength (MPa)	12.5	20.25
Cohesion strength (MPa)	22.5	44.5
Friction angle ϕ (°)	10.5	22.0

Table 4. Physico-mechanical properties of experimental and numerical Nano indentation calibrated model.

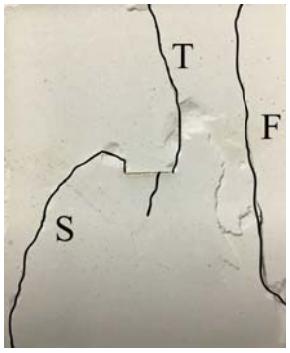
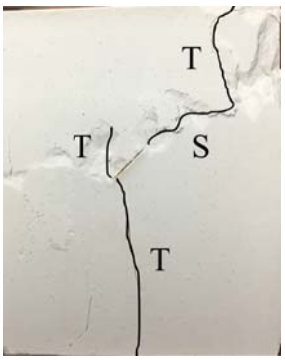
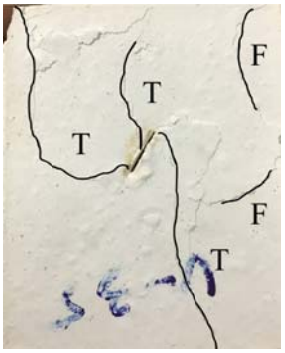
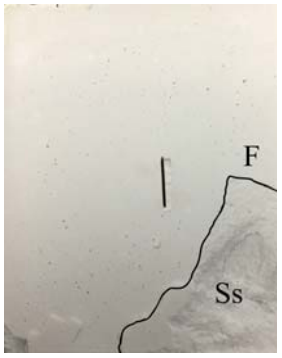
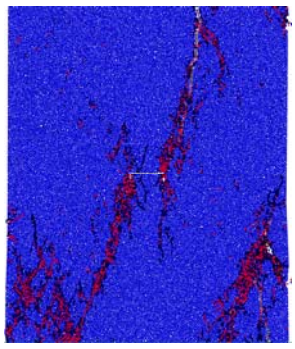
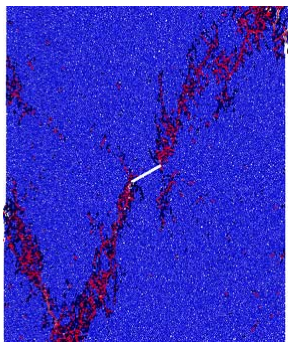
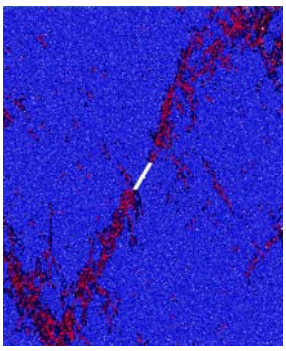
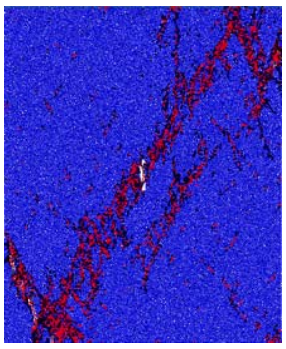
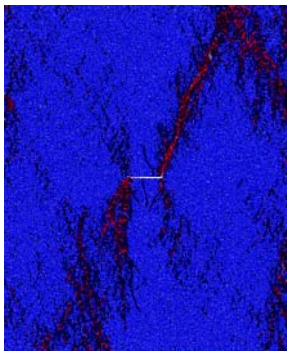
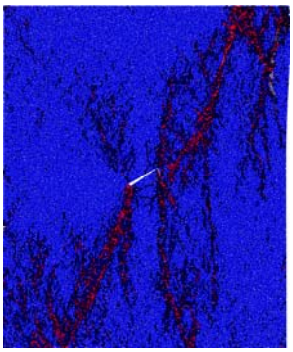
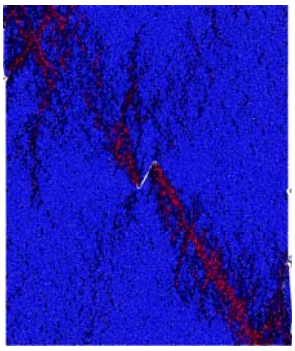
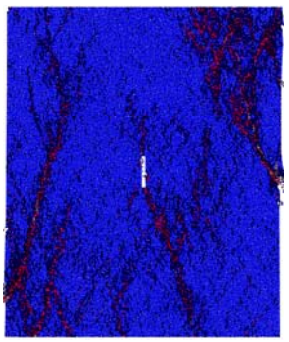
Physico-mechanical properties	**Experimental Results**	**Numerical Results**
Uniaxial Compression Strength (MPa)	42.31	41.71
Young's Modulus (GPa)	2.3385	2.215
Tensile Strength (MPa)	6.25	6.18
Poisson's Ratio	0.35	0.355

Similar calibration approaches have also been applied to multi-mineral rocks such as granite (Liu, Xiu-Yang et al. 2024) and sandstone (Yang et al., 2024), where the particle size in the numerical model is determined based on the mineral grain size (grain-based model). However, this approach is not suitable for the current study. Therefore, an additional calibration step is required to match Young's modulus and Poisson's ratio by employing dual indentation technique namely method developed by Ganneau et al. (2006).

4 Comparison of Results

To evaluate the accuracy of the Nano indentation-calibrated model in capturing crack growth from a pre-existing flaw, a comparison was made between the experimental results and the trial-and-error calibrated model. A specimen of size 52 × 64 × 12 mm was tested under uniaxial loading with a centrally located flaw of length 6mm and thickness 0.6mm inclined at angles ranging from 0° to 90°, in increments of 30°. The differences in the calibrated micro parameters between the two approaches are presented in Table 5.

Table 5. Comparison of crack propagation pattern of experimental and numerical analysis.

0°	30°	60°	90°
Experimental Results			
			
Bahaaddini et al. (2021) Calibration			
			
Nano Indentation Calibration			
			

4.1 0° and 30° flaw orientations

There is no significant difference in the crack propagation patterns between the models, and both agree well with the experimental results. However, the Nano indentation-calibrated model is better able to capture the closure of the pre-existing flaw.

4.2 60° flaw orientation

The final failure pattern shows good agreement with the Nano indentation-calibrated model compared to previous trial and error calibration and a certain degree of flaw closure is observed.

4.3 90° flaw orientation

In the experimental results, the failure pattern is not significantly influenced by the presence of the flaw. This behaviour is not well reflected in the trial and error calibrated model. In contrast the Nano indentation calibrated model limits the influence of the flaw to a greater extent showing better agreement with the experimental observations.

5 Conclusion

In this study, a new calibration method incorporating the Nano indentation technique is proposed. The method is validated by comparing numerical results with experimental observations and it demonstrates improved capability in capturing crack growth from a pre-existing flaw compared to the conventional fully trial-and-error calibration method. The proposed approach also captures the closure of the flaw which subsequently leads to the formation and propagation of tensile anti-wing cracks. The present study focuses on a single homogenous mineral rock (gypsum). Additionally, the current study still involves partial trial-and-error calibration. This limitation can be addressed in future studies by employing the dual-indentation technique, which can help determine the remaining micro-mechanical properties more systematically.

References

Bahaaddini M, Sheikhpourkhani AM, Mansouri H (2021) Flat-joint model to reproduce the mechanical behaviour of intact rocks. European Journal of Environmental and Civil Engineering 25(8): 1427–1448.

Ganneau FP, Constantinides G, Ulm FJ (2006) Dual-indentation technique for the assessment of strength properties of cohesive-frictional materials. International Journal of Solids and Structures 43(6): 1727–1745. DOI.

Itasca Consulting Group Inc (2014) PFC (Particle Flow Code) Version 5.0. Itasca Consulting Group Inc, Minneapolis, United States.

Liu XY, et al. (2024) Study on the micromechanical and crack characteristics of granite based on nano indentation test and discrete element method. Computational Particle Mechanics 11(4): 1547–1563. DOI.

Potyondy DO (2012) A flat-jointed bonded-particle material for hard rock. 46th US Rock Mechanics/Geomechanics Symposium, Chicago, United States, 2012, pp 1510–1519.

Potyondy DO, Cundall PA (2004) A bonded-particle model for rock. International Journal of Rock Mechanics and Mining Sciences 41(8): 1329–1364. DOI.

Yang H, Luo S, Zhang G, Song J (2017) Elasticity of clay shale characterized by nanoindentation. ARMA US Rock Mechanics/Geomechanics Symposium, San Francisco, United States, June 2017.

Yang X, Zhang Y, Li G, Li Z, Feng J, Wang K (2024) Mesoscopic modeling approach and application based on rock thin slices and nanoindentation. Computers and Geotechnics 165: 105875.

Stability Assessment of Block–Flexural Toppling Using Numerical and Deterministic Approaches

H. T. Atmojo
Universitas Pembangunan Nasional Veteran Yogyakarta, Indonesia
hasan.triatmojo@upnyk.ac.id
0000-0003-0621-554X

A. P. Martireni, W. Cakrabuana, & K. Sugianti
Badan Riset dan Inovasi Nasional, Indonesia

Abstract

Block–flexural toppling is a complex failure mechanism commonly observed in jointed rock slopes, resulting from the combined effects of block rotation and flexural deformation. This instability is primarily controlled by geological structures, particularly the orientation, persistence, and mechanical properties of discontinuities. This study presents a stability assessment of block–flexural toppling at Cliff 05, Citatah, West Bandung Regency, West Java, Indonesia, where recurrent rock block detachments have been documented. The slope is dominated by a primary joint set that is nearly perpendicular to the slope face and intersected by a secondary joint set, creating conditions favourable for toppling failure.

To investigate the failure mechanism, stability analyses were conducted using both numerical modelling and the Limit Equilibrium Method (LEM). Numerical simulations were performed using the finite element method within an elastic–plastic framework, while LEM was applied to evaluate the factor of safety under varying geometric and mechanical conditions. Rock mass and discontinuity parameters were derived from field observations and rock mass classification systems, including the Rock Mass Rating (RMR) and Geological Strength Index (GSI). Joint shear strength parameters were estimated using the Barton–Bandiscriterion for both joint sets. The joint network was represented using deterministic and statistical approaches.

Results from numerical modelling indicate total displacements ranging from approximately 9.5 to 19 mm, with plastic zones developing around surface joints and joint intersections. LEM analysis shows a reduction in factor of safety consistent with increasing slope inclination and unfavorable joint orientations. Sensitivity analysis identifies internal friction angle, slope inclination, and slope face angle as the most influential parameters governing block–flexural toppling stability. The comparative results highlight the advantages and limitations of each method in assessing toppling-prone rock slopes.

Keywords

Stability assessment, Block–flexural toppling, Joint fracture network, Numerical Modelling, LEM.

1 Introduction

The stability of rock slopes affected by block–flexural toppling is highly dependent on the geometry and connectivity of discontinuities within the rock mass. Previous numerical studies have often represented toppling mechanisms using simplified joint configurations, such as a single persistent joint set dipping opposite to the slope face or two fully persistent joint sets extending continuously throughout the model. While these idealized models are useful for understanding fundamental toppling behaviour, they may not sufficiently capture the complexity of natural discontinuity systems. In the field, discontinuities are commonly variable and discontinuous, influencing block formation, flexural bending, block interaction, and progressive failure development.

This study assesses the block–flexural toppling mechanism at Cliff 05 Citatah using integrated numerical and deterministic approaches. Field-based scanline mapping is used to characterize joint orientation, spacing, and persistence, which are then incorporated into the stability assessment. Finite element modelling is applied to evaluate stress redistribution, deformation behaviour, and progressive failure, while limit equilibrium analysis provides a deterministic estimation of stability based on block geometry, force equilibrium, and joint shear strength. By comparing both approaches, this study aims to evaluate how simplified deterministic analysis represents the observed toppling mechanism and how numerical modelling can improve the interpretation of failure evolution in discontinuous rock masses.The paper compares FEM and LEM analyses on the same limestone rock slope to evaluate the capability, limitations, and consistency of both methods in assessing block–flexural toppling failure.

2 Research study location

Cliff 05 is a limestone cliff within a quarry site in Citatah village, Cipatat subdistrict, West Bandung regency, West Java, Indonesia. Geomorphologically, the study site is categorized as steep hills (van Zuidam 1986). Geologically, Cliff 05 consists of calcarenite limestone with sand grain size (1/16-2 mm) (Sudjatmiko 1972).Rock mass and discontinuity data of the study site were collected by undertaking engineering geological mapping (Figure 1).

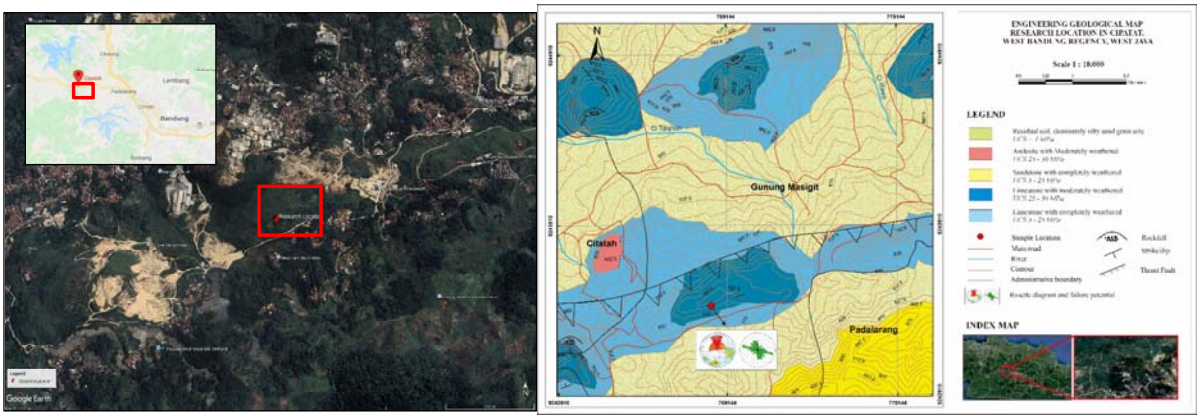


Fig. 1 Engineering geological map of the study location (modified from Atmojo 2021).

The limestone of Cliff 05 Citatah has GSI values ranges between 50 and 60, with a median value of 55 selected for numerical modeling input(Atmojo 2021; Marinos and Hoek 2000).A GSI value of 55 corresponds to a disturbed, interlocked rock mass, consisting of angular blocks formed by the intersection of three discontinuity sets(Hoek and Brown 2018). The surface conditions are rough, slightly weathered, and exhibit oxidation along discontinuity planes (Figure 1 and 2).

The limestone of Cliff 05 is categorized as fair rock mass (Class III) with an RMR value of 60,25 (Atmojo 2021; Bieniawski 1989). From the RMR classification, some material properties can be determined empirically, unit weight of 0.0253 MN/m^3, Poisson's ratio of 0.32, Young's modulus of 5340 MPa, tensile strength of 0.1 MPa, cohesion 0.294 MPa, and friction angle of 51.32°.

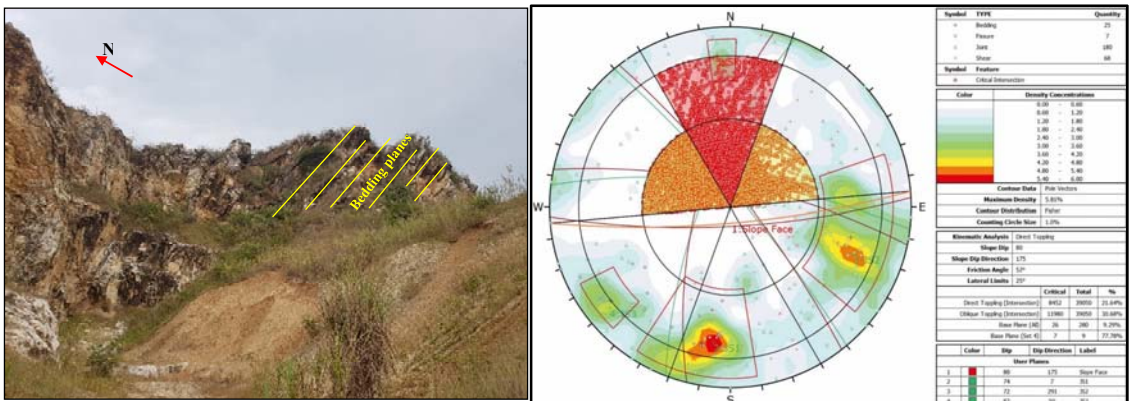


Fig. 2 Outcrop of the cliff shows the discontinuity orientation have dip direction relatively perpendicular to slope face.

The cliff shows a slope geometry with an approximate height of 25 m, a slope length of around 150 m for the area of interest, and a slope face orientation of 80°/N175°E. The discontinuity observed consists of bedding planes, shear fractures, and joints. (Table 1).

Table 1. Discontinuity condition along the slope.

Discontinuity Type	Dip Direction/Dip	Spacing (m)	Persistence (m)	Aperture (mm)	Surface Characteristics	Weathering/ Infill	Seepage Condition
Bedding planes	007°/74°	1.5 m	>10	0.1–10	Very rough; undulating to stepped	Moderately to highly weathered; mainly sandy clay weathered infill, locally calcite	Generally dry, with minor seepage
Shear fractures	050°/82° and 291°/72°	0.8 - 2	1-3	0.1–0.5	Rough; planar to stepped	Slightly weathered; locally sandy weathered infill	Predominantly dry
Joints	177°/65° to 300°/75°	0.45 m	<7	0.1–2.5	Smooth to moderately rough; undulating to stepped	Moderately to highly weathered; sandy weathered infill	Generally moist

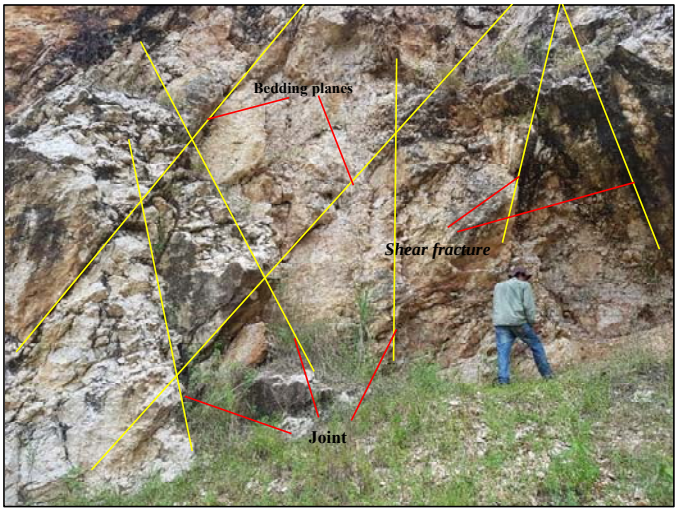


Fig. 3 Discontinuity type in the outcrop contains bedding planes, joint, and shear fracture. The orientation of joint and shear fracture intersects with the bedding planes.

3 Methodology

The discontinuity condition and failure mechanism was determined, contributing discontinuities were picked to be further analyzed. The properties of the contributing discontinuities were then calculated using the formula by (Barton and Bandis 1990) (Equation 1).

$$\tau = \sigma_n \tan\left(\varphi_b + JRC \log_{10}\frac{JCS}{\sigma_n}\right) \quad (1)$$

Where τ Joint shear strength
σ_n Normal stress
φ_b Basic friction angle
JRC Joint roughness coefficient
JCS Joint wall compressive strength

In this study, numerical modeling is a computer programming with the purpose to represent response mechanism of a rock mass that experiences changes in its conditions (Wyllie and Mah 2004). The numerical method utilized in this study is FEM with an elastic-plastic material model. The material model represents the stress-strain relationship, reflecting its behavior. The elastic-plastic model utilizes a strength parameter to limit the acceptable shear stress. The deterministic modeling in this study was conducted by LEM. The method only uses static equilibrium between forces/moments in a slope, and neglecting stress-strain relationship it has (Azizi, 2014). The reliability of LEM depends on the accuracy of slope geometry and the sliding surface. FEM analysis was performed using *RS2* and LEM using *RocTopple*(Rocscience 2021a and Rocscience 2021b).

4 Result and Discussion

4.1 Proposed Model of Block Flexural Toppling

The numerical model was developed using a finite element approach in RS2 with explicitly defined discontinuity elements. Therefore, although the overall analysis is based on FEM, the main discontinuity sets observed in the field were incorporated as discrete interfaces to represent the block–flexural toppling mechanism. The proposed toppling model considers both the type and condition of discontinuities. The main triggering discontinuities for toppling failure are those with an orientation relatively opposite to the slope face, commonly referred to as anti-dip discontinuities. However, under actual field conditions, toppling failure is often also influenced by other discontinuity sets that intersect the anti-dip fractures. Therefore, the proposed slope model represents the discontinuity condition using a joint fracture network, allowing both deterministic and statistical fracture parameters to be incorporated into the numerical model. The proposed slope model is presented below.

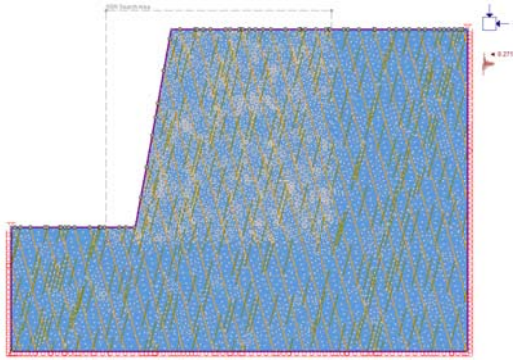


Fig. 4 The slope model of Cliff 05 Citatah. JS1 (yellow), JS2 (green).

In this model, two joint sets are considered, namely Joint Set 1 (JS1) and Joint Set 2 (JS2). JS1 represents the bedding planes, whereas JS2 represents the shear fractures and joints.By using the Barton-Bandis criterion, the properties of JS1 and JS2 were determined. The discontinuity model of JS1 is parallel deterministic, with the average spacing applied, while JS2 is parallel statistical, using a normal distribution of discontinuity. The slope model has a geometry with a slope height of 25 m and a face inclination of 80°.

JS1 has a spacing of 1.5 m and a dip of 74°. Cohesion and friction angle of JS1 are 0.031 MPa and 38.05°. JS2 has a dip of 75, an average spacing of 0.456 m (standard deviation = 0.35), an average length of 4 m (standard deviation = 0.5), and an average persistence of 0.55 (standard deviation = 0.3). Cohesion and friction angle of JS2 are 0.037 MPa and 39.25°. Normal stiffness, shear stiffness, and tensile strength were assumed using the following values for JS1 and JS2, respectively: 100,000 MPa/m, 10,000 MPa/m, and 0.

Groundwater was not incorporated into the FEM model because no groundwater seepage or groundwater level was identified during the field investigation. Therefore, the slope was modelled under dry conditions, and pore-water pressure was assumed to be negligible. The pseudostatic condition in the FEM model was represented by applying a seismic coefficient to simulate earthquake-induced inertial forces acting on the rock slope. The seismic coefficient was defined following SNI 8630:2016. Based on a peak ground acceleration (PGA) of 0.542 g and an amplification factor (FPGA) of 1.0, the horizontal seismic coefficient (Kh) used in the model was 0.271.

4.2 Numerical modeling by FEM

The finite element method analysis effectively describes the deformation patterns associated with toppling failure instability. As illustrated in Figure 5, the deformation mesh highlights the toppling failure mechanism occurring at the intersection of Joint 1 and Joint 2. The maximum total displacement is observed at the crown of the slope, ranging from 9.5 to 19 mm, with the toppling movement oriented away from the slope along the discontinuity plane, following the pattern of Joint 2. Although the displacement values remain relatively low, the deformation pattern of toppling failure is distinctly visible.Furthermore, the analysis reveals the yield elements, as shown in Figure 5, indicating the development of a plastic zone concentrated around the slope surface and the joint intersection. This area corresponds to tensile bending stress, which plays a critical role in the progression of toppling failure.

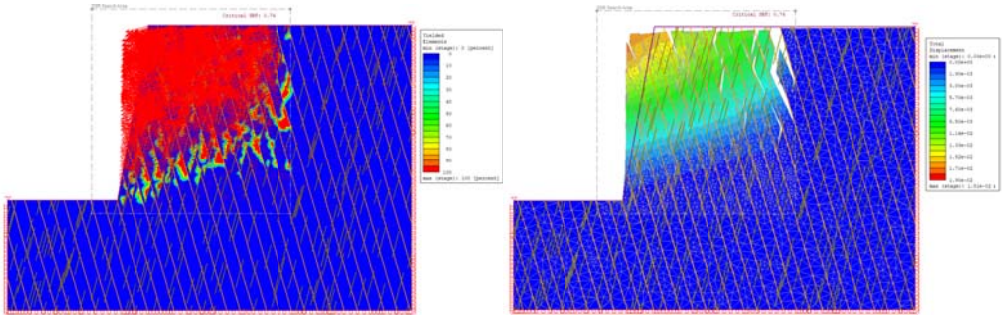


Fig. 5 The deformation model of Cliff 05 Citatah.

4.3 Deterministic modeling by LEM

The deterministic LEM analysis was established to represent the block–flexural toppling mechanism controlled by the anti-dipping discontinuity system observed at the study site. The slope geometry was simplified into a 25 m high rock cliff with a slope angle of 80°, while the basal sliding surface was represented by a block base inclination of 16°. The rock mass was divided into several columnar blocks based on the spacing of the main toppling discontinuity, allowing the interaction between individual blocks to be evaluated. This configuration reflects the field condition, where persistent bedding planes form the main anti-dip discontinuity, while intersecting fractures contribute to block separation and potential flexural deformation. The toppling joint has cohesion of 0.031 MPa and a friction angle of 36.86. The parameters input for the rock mass are cohesion of 0.2 MPa, friction angle of 51^{o}. Based on those inputs, the FoS of the cliff is 0.746, below the stability criteria of SNI 8460:2017. Figure 6 shows several blocks that potentially topple.

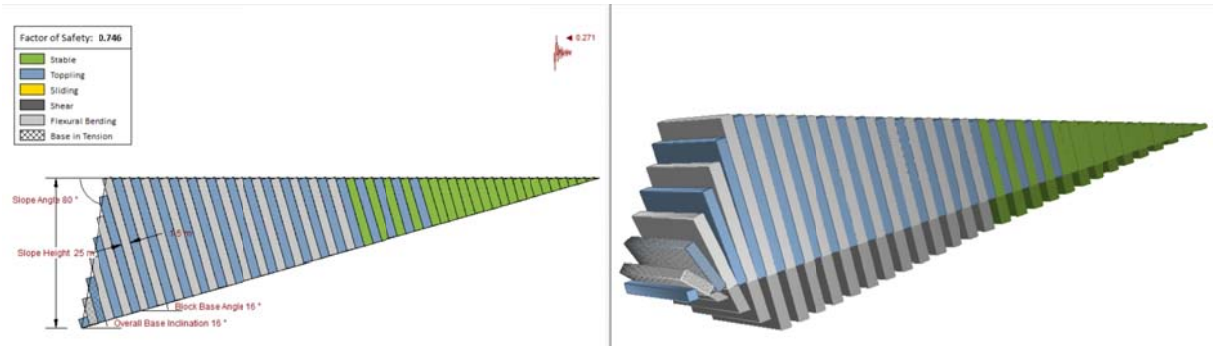


Fig. 6 The block-flexural toppling failure model of the study site.

4.4 Sensitivity analysis

A sensitivity analysis was conducted to evaluate the impact of input parameters on the variation of the factor of safety (FoS) in the numerical model. Both slope and toppling joints parameters were included in the analysis. In this case study, the most influential parameters (curves with the highest gradient) in changing the safety factors are slope angle and toppling joint friction angle (Figure 7). The higher the slope angle, the less safe the slope. The higher the toppling joint friction angle, the safer the slope.

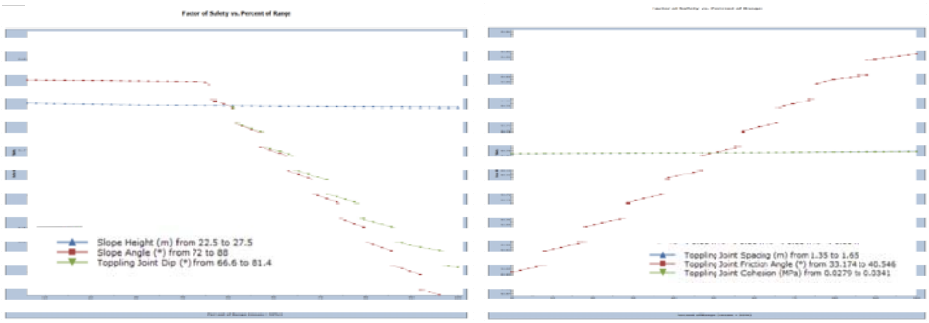


Fig. 7 The sensitivity analysis of the toppling failure parameters.

4.5 Discussion

Both FEM and LEM results indicate that Cliff 05 is in the unstable conditions, with FoS values below the stability criterion of 1.1 based on SNI 8460:2017. FEM produced SRF values of 0.74, while LEM gave a lower FoS of 0.746. The comparison of factor of safety (FoS) values indicates that the FEM and LEM analyses produced relatively similar results, with no substantial difference in the estimated slope stability condition. The difference is mainly caused by the different ways each method represents the slope geometry and discontinuity system. The FEM model provides a more realistic representation of the block–flexural toppling mechanism because both joint sets can be included in the model. JS1 represents the bedding planes as the main anti-dip discontinuity, while JS2 represents shear fractures and joints that cut the bedding planes. The deformation pattern and plastic zone around the slope surface and joint intersections show that the instability is controlled by the interaction between these discontinuities. In contrast, LEM provides a simpler deterministic evaluation by dividing the slope into several columnar blocks. This method is useful for estimating the FoS and identifying the general toppling mechanism. However, LEM cannot fully represent the intersecting discontinuities within the rock mass. Overall, FEM is more suitable for interpreting deformation and progressive failure, whereas LEM is useful as a practical preliminary stability assessment. The sensitivity analysis shows that slope angle and toppling joint friction angle are the most influential parameters. Therefore, accurate field characterization of discontinuity orientation and shear strength is essential for reliable block–flexural toppling assessment.

References

Amini, M., A. Majdi, and M.A. Veshadi. 2012. "Stability Analysis of Rock Slopes Against Block-Flexure Toppling Failure." *Rock Mechanics and Rock Engineering* 45: 519–32. doi:10.1007/s00603-012-0220-7.

Atmojo, H.T. 2021. "Analisis Kestabilan Lereng Batuan Menggunakan Studi Perbandingan Klasifikasi Massa Batuan GSI, RMR, Dan RMi Pada Potensi Longsoran Guling Dan Baji Di Daerah Cipatat, Kabupaten Bandung Barat, Jawa Barat." Institut Teknologi Bandung.

Azizi, M.A. 2014. "Pengembangan Metode Penentuan Reliabilitas Kestabilan Lereng Tambang Terbuka Batubara Di Indonesia." Institut Teknologi Bandung.

Barton, N., and S. Bandis. 1990. "Review of Predictive Capabilities of JRC-JCS Model in Engineering Practice." In *International Symposium on Rock Joints*, Rotterdam, 603–10.

Bieniawski, Z.T. 1989. *Engineering Rock Mass Classifications - A Complete Manual for Engineers and Geologists in Mining, Civil, and Petroleum Engineering*. New York.

Hoek, E., and E.T. Brown. 2018. "The Hoek-Brown Failure Criterion and GSI-2018 Edition." *Journal of Rock Mechanics and Geotechnical Engineering*: 1–19. doi:10.1016/j.jrmge.2018.08.001.

Marinos, P., and E. Hoek. 2000. "A Geologically Friendly Tool for Rock Mass Strength Estimation." In *ISRM International Symposium*, Melbourne: ISRM.

Rocscience. 2021b. "RS2 Tutorials." *RS2 Documentation*. https://www.rocscience.com/help/rs2/tutorials (January 13, 2021).

Standar Nasional Indonesia 2833 (2016): *Perencanaan jembatan terhadap beban gempa*, Badan Standarisasi Nasional, Indonesia, 10 – 60.

Sudjatmiko. 1972. *Peta Geologi Lembar Cianjur*. Bandung: Pusat Penelitian dan Pengembangan Geologi.

Wyllie, D.C., and C.W. Mah. 2004. *Rock Slope Engineering (Civil and Mining)*. 4th ed. London: Spoon Press. doi:10.1201/9781315274980.

van Zuidam, R.A. 1986. *Aerial Photo-Interpretation in Terrain Analysis and Geomorphology Mapping*. Hague: Smiths Publisher.

Study on the Variation of Vibration Characteristics in Rock Tunnels Depending on Ground Conditions and Tunnel Structures Using Ambient Vibration Measurements

K. Kawata, N. Tamura & N. Isago
Tokyo Metropolitan University, Tokyo, Japan
k_kawata@tmu.ac.jp

Abstract

This study investigates the vibration characteristics of rock tunnels using ambient vibration measurements, focusing on the effects of ground conditions and structural configurations. Although ambient vibration techniques have been widely applied to soil deposits, their application to rock tunnels remains limited due to small vibration amplitudes and the complex interaction between ground and structures.

Measurements were conducted in two tunnels in Japan under different geological and structural conditions. One tunnel was excavated but remained without lining and invert structures, while the other included sections with support, lining, and invert, allowing comparison of different construction stages. Fourier spectra and H/V spectral ratios were used to evaluate frequency characteristics.

The results indicate that vibration amplitudes inside the tunnel are significantly smaller than those outside, suggesting limited amplification within tunnels. In the excavated tunnel without structural components, dominant frequency peaks were not clearly identified, and spectral characteristics varied depending on location. In contrast, repeated measurements before and after invert installation indicate that structural conditions primarily affect vibration amplitude and spectral stability, as evidenced by the reduced spectral amplitudes and smoother H/V spectral ratios observed after invert installation.

These findings demonstrate that the predominant frequency is primarily governed by ground stiffness, whereas vibration amplitude and spectral stability are strongly influenced by structural conditions. The results highlight the importance of distinguishing between ground and structural effects when interpreting ambient vibration data in rock tunnels.

Keywords

Ambient vibration, Rock tunnel, Dynamic characteristics, Ground–structure interaction, H/V spectral ratio.

1 Introduction

Mountain tunnels are generally considered to have high seismic resistance due to the confinement effect of the surrounding ground. However, past earthquake events have reported damage in mountain tunnels, particularly in sections with unfavorable geological conditions or structural weaknesses. Therefore, understanding the dynamic characteristics of tunnel–ground systems is essential for rational seismic evaluation and maintenance of underground structures.

Ambient vibration measurement is a non-destructive and efficient technique that enables the evaluation of dynamic characteristics without interrupting tunnel operation. While this method has been widely applied to site characterization in soil deposits, its application to rock tunnels remains limited. This is mainly because vibration amplitudes in rock masses are relatively small and the dynamic response of tunnels involves complex interactions between surrounding ground and tunnel structures.

In addition, previous studies have mainly focused on either ground conditions or structural responses independently, and the combined influence of geological and structural factors on tunnel vibration characteristics has not been sufficiently clarified.

In this study, ambient vibration measurements were conducted in two mountain tunnels in Japan. One tunnel is in a completed state, while the other is under construction with varying structural conditions along the tunnel axis. These different geological and structural conditions provide a useful basis for evaluating their influence on vibration characteristics.

The objective of this study is to investigate the vibration characteristics of rock tunnels using ambient vibration measurements, focusing on the effects of ground conditions and tunnel structures. The dynamic characteristics were evaluated using Fourier spectra and H/V spectral ratios, and the governing factors of vibration behavior were discussed through comparative analysis.

2 Target tunnels and geological conditions

Two mountain tunnels in Japan were selected for this study, hereafter referred to as Tunnel A and Tunnel B.

Tunnel A is located in the southern part of Japan and has already been excavated through, although the lining has not yet been installed. The tunnel is constructed in sedimentary rocks of an accretionary complex of Paleogene age, consisting primarily of interbedded sandstone and mudstone. The surrounding ground is generally classified as soft rock with relatively low stiffness.

Tunnel B is currently under construction and is located in a mountainous area in the central part of Japan. The tunnel is excavated mainly in interbedded sandstone and mudstone formations and tuff breccia–mudstone alternations of Late Miocene age. The surrounding ground is classified as medium-hard to soft rock, showing moderate stiffness with locally heterogeneous features.

Fig.1 and Fig.2 present the geological longitudinal profiles of Tunnel A and Tunnel B, respectively, illustrating the variation of geological conditions along the tunnel axes. The locations of ambient vibration measurements conducted in this study are also shown in these figures.

In Tunnel B, multiple structural conditions are present along the tunnel axis due to the ongoing construction, including sections with only support, sections with lining, and sections where invert structures have been installed. In some sections, invert structures have not yet been installed, although they are planned to be installed along the entire tunnel length in the final design.

These different geological and structural conditions provide a useful basis for evaluating the influence of ground conditions and structural stiffness on the vibration characteristics of rock tunnels. This allows the influence of each factor to be discussed in a systematic manner.

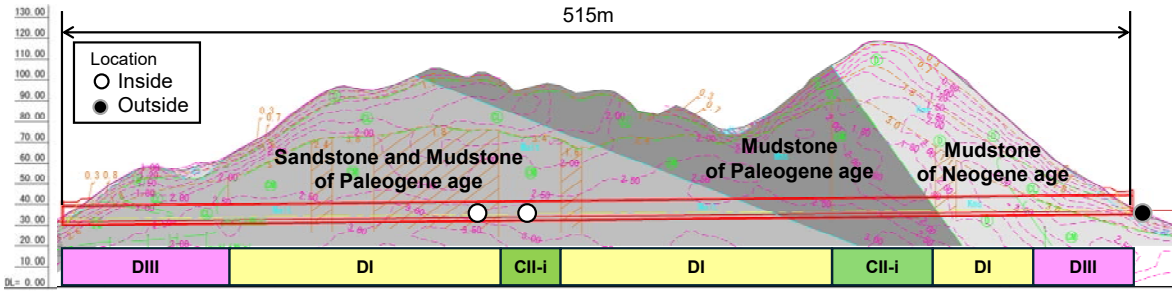


Fig. 1 Geological longitudinal profile of Tunnel A with measurement locations.

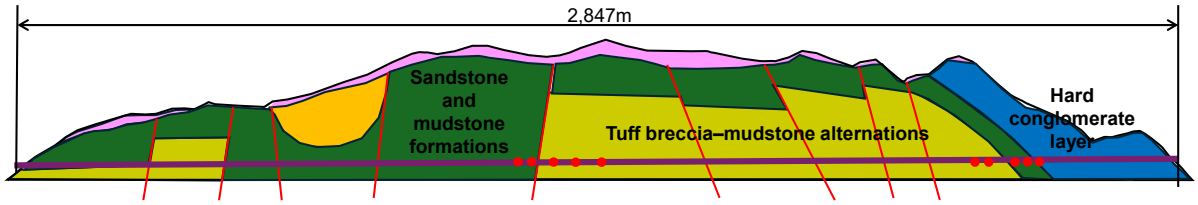


Fig. 2 Geological longitudinal profile of Tunnel B with measurement locations.

3 Measurement and analysis method

3.1 Measurement

Ambient vibration measurements were conducted in Tunnel A and Tunnel B to evaluate their dynamic characteristics. Velocity sensors were installed at representative locations within the tunnel cross-section as illustrated in Fig.3.

Measurements were carried out under ambient conditions without artificial excitation. The sampling frequency was set to 100 Hz for Tunnel A and 500 Hz for Tunnel B, and the duration of each measurement was approximately 10 minutes.

For Tunnel A, the natural frequency of the surrounding rock mass was assumed to be higher than 10 Hz, and the sampling frequency was determined accordingly. In contrast, no clear dominant frequency peak was identified in Tunnel B during preliminary observations. Therefore, a higher sampling frequency of 500Hz was adopted to capture a wider frequency range and to ensure reliable identification of frequency characteristics. This approach is consistent with the Nyquist criterion for frequency analysis.

In Tunnel B, measurements were conducted three times at different stages of construction. At selected measurement points (Support No.1345, No.1364, and No.1492), the first and second measurements were performed before the installation of the invert, whereas the third measurement was conducted after the invert had been installed.

The measurement locations were selected to represent different geological and structural conditions along the tunnel axis, as summarized in Table 1 and Table 2. Examples of the ambient vibration measurements are shown in Fig.3.

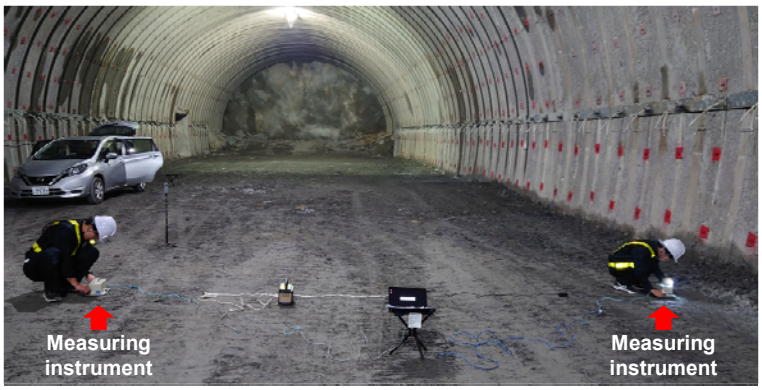


Fig. 3 Overview of ambient vibration measurements (A Tunnel).

Table 1. Summary of Tunnel A conditions and measurement locations.

Locations	Geological condition	Structural condition
Outside	Talus deposit	No
No.250	Sandstone–mudstone alternation	Support
No.300	Sandstone–mudstone alternation	Support

Table 2. Summary of Tunnel B conditions and measurement locations.

Locations	Geological condition	Structural condition
Lining Block 31	Hard conglomerate layer	Lining + Invert
Lining Block 33	Sandstone and mudstone formations	Lining + Invert
Lining Block 36	Sandstone and mudstone formations	Lining + Invert
Lining Block 41	Tuff breccia–mudstonealternations	Lining + Invert
Lining Block 45	Tuff breccia–mudstonealternations	Lining + Invert
Support No.1345	Tuff breccia–mudstonealternations	Support (+ Invert)
Support No.1492	Tuff breccia–mudstonealternations	Support (+ Invert)
Support No.1636	Sandstone and mudstone formations	Support
Support No.1655	Sandstone and mudstone formations	Support

3.2 Analysis

The recorded velocity time histories were processed to evaluate the frequency characteristics of the tunnel–ground system. First, the data were detrended and filtered to remove noise components.

Fourier spectra were calculated to identify dominant frequency components at each measurement location. The predominant frequency was determined based on the peak of the spectral amplitude. In addition, the horizontal-to-vertical (H/V) spectral ratio was computed to evaluate amplification characteristics and to further identify predominant frequencies.

These analyses were used to compare the vibration characteristics among different measurement locations and to examine the influence of geological and structural conditions on the dynamic behavior of the tunnels.

Although ambient vibration measurements were conducted in three directions, namely the transverse (X), longitudinal (Y), and vertical (Z) directions of the tunnels, only the transverse direction (X) is presented in this paper for clarity and consistency, as it is considered to be the most representative direction for evaluating tunnel deformation behavior.

4 Results and Discussion

4.1 Tunnel A

Fig. 4 shows the results of ambient vibration measurements in Tunnel A, including the velocity time histories and H/V spectral ratios.

The velocity time histories indicate that the vibration amplitudes inside the tunnel are significantly smaller than those outside. The maximum vibration velocity outside the tunnel is approximately 0.001–0.002 mm/s, whereas that inside the tunnel is around 0.0001 mm/s, corresponding to roughly one-tenth of the external amplitude. The waveforms are generally random, and no clear dominant periodic motion is observed.

The H/V spectral ratios show that, outside the tunnel, a peak appears at around 15–20 Hz, which is considered to be influenced by artificial sources such as drainage pump operation. In contrast, inside the tunnel, peaks are observed at approximately 1–3 Hz at both the sidewall and the tunnel center.

In the higher frequency range above 10 Hz, the spectral characteristics vary depending on the location. In some sections, random peaks are observed, whereas in others, the spectral ratio tends to be close to unity, particularly in the tunnel center.

These results suggest that the vibration characteristics inside the tunnel are influenced by both the surrounding ground conditions and the structural configuration.

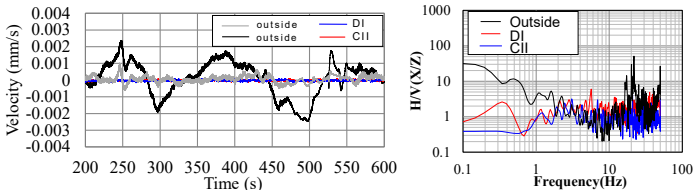


Fig. 4 Overview of ambient vibration measurements (A Tunnel).

4.2 Results of Tunnel B

Fig 5 to Fig 8 shows the results of ambient vibration measurements in Tunnel B, including Fourier spectra and H/V spectral ratios at different construction stages.

The Fourier spectra obtained at the measurement locations indicate that, in the sections with only support, the spectral amplitudes tend to be relatively large and distributed over a wide frequency range. Clear dominant peaks are not consistently observed, and the spectral shapes vary depending on the measurement location. In contrast, in the sections where lining and invert have been installed, the spectral amplitudes generally decrease, and the distribution becomes more stable. Although distinct peaks are still not always observed, the overall variability of the spectra is reduced compared to the support condition.

At specific measurement points (Support No.1345 and No.1492), a comparison of measurements conducted before and after invert installation shows that the vibration amplitude decreases after the installation of the invert. This trend is consistently observed across multiple locations.

The H/V spectral ratios also show differences between construction stages. In the support condition, the spectral ratios tend to fluctuate significantly, whereas in the lining and invert condition, the spectra become relatively smoother and more stable.

These results indicate that the decrease in spectral amplitude observed at Support No.1345 and No.1492 after invert installation reflects improved structural stiffness, whereas its influence on predominant frequency appears limited compared to that of ground conditions.

4.3 Governing factors of vibration characteristics

Based on the results obtained from Tunnel A and Tunnel B, it is evident that both ground conditions and structural configurations influence the vibration characteristics of rock tunnels.

The predominant frequency is mainly controlled by the stiffness of the surrounding ground, whereas the vibration amplitude and spectral stability are strongly affected by the structural condition of the tunnel.This distinction is clearly supported by the observed reduction in vibration amplitude following the installation of invert structures in Tunnel B.

Therefore, when interpreting ambient vibration measurements in rock tunnels, it is essential to distinguish between the effects of ground and structural conditions, particularly because the small amplitudes typically observed in rock tunnels may obscure clear spectral characteristics.

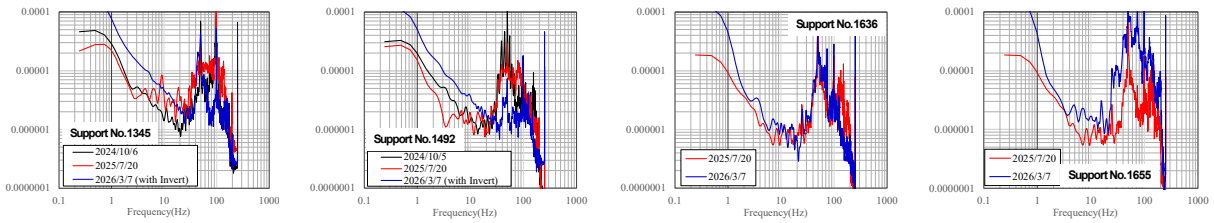


Fig. 5 Fourier spectra of Support(B Tunnel).

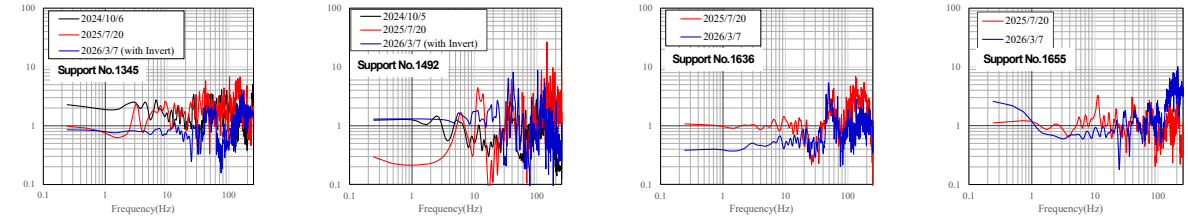


Fig. 6 Fourier spectra of Support(B Tunnel).

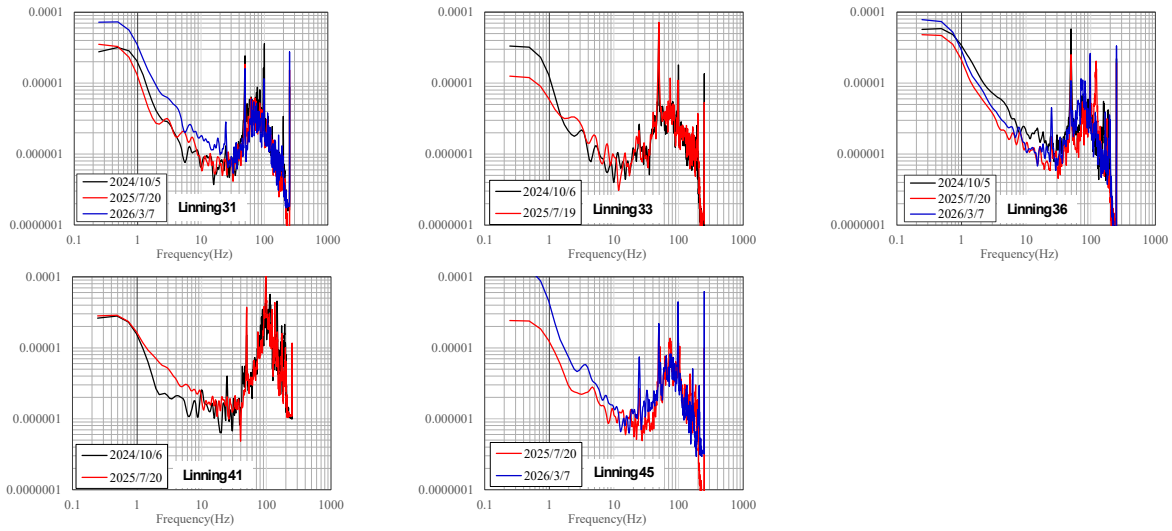


Fig. 7 Fourier spectra of Linig and Invert (B Tunnel).

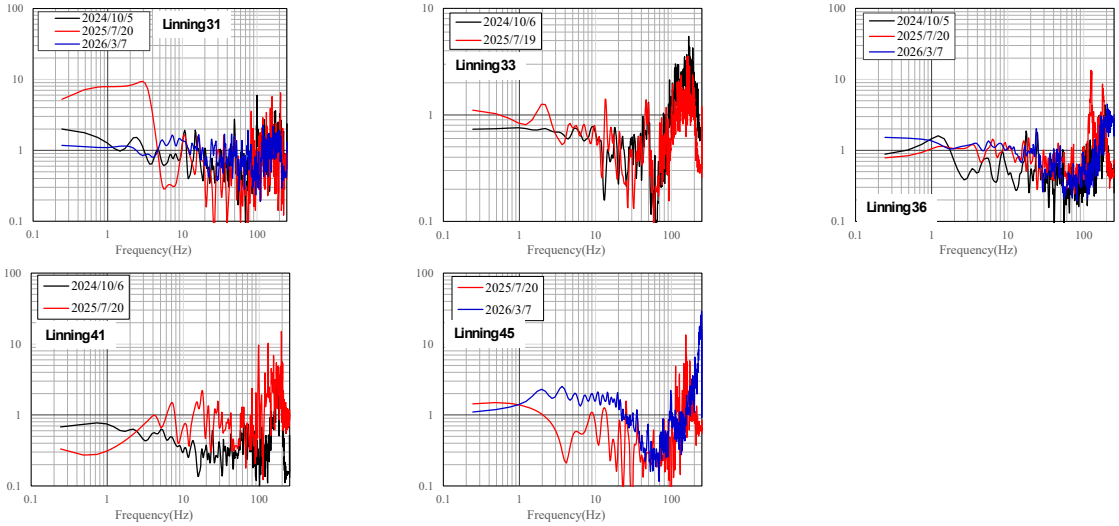


Fig. 8H/V spectral ratios of Linig and Invert (B Tunnel).

5 Conclusions

This study investigated the vibration characteristics of rock tunnels using ambient vibration measurements, focusing on the effects of ground conditions and structural configurations.

The results demonstrated that the vibration amplitudes inside the tunnel are significantly smaller than those outside, indicating that amplification effects within the tunnel are generally limited. Furthermore, the predominant frequency is primarily governed by the stiffness of the surrounding ground, whereas the vibration amplitude and spectral stability are strongly influenced by the structural condition of the tunnel. In particular, repeated measurements at the same locations revealed that the installation of invert structures leads to a reduction in vibration amplitude and a stabilization of spectral characteristics.

These findings highlight the importance of distinguishing between the effects of ground and structural conditions when interpreting ambient vibration data in rock tunnels. The proposed approach is expected to contribute to the rational evaluation of tunnel behavior and its application to seismic assessment and maintenance.

As future work, continuous measurements under different geological and structural conditions are required to improve the reliability of ambient vibration-based evaluations and clarify their influence on tunnel vibration characteristics.

Permeability Estimation Using X-ray CT Based on 3D Digital Rock Core Images

H. J. Je & K. Y. Kim
Korea Maritime & Ocean University, Busan, Republic of Korea
kykim@kmou.ac.kr
0000-0002-4648-7470

Abstract

Fluid flow characteristics in porous media are important in various fields, including reservoir engineering, subsurface hydrology, and geological carbon sequestration, and permeability is a representative hydraulic property used to quantify such flow behavior. In this study, LBM simulations were performed using a CT-based digital core of Bentheimer sandstone, and the causes of permeability overestimation arising from CT resolution limitations and the binarization process were investigated. The uncorrected LBM permeability was 875 mD, about 2.3 times higher than the experimental value of 386 mD. A comparison between CT-based PSD and MIP-based PSD confirmed the presence of micropore regions that could not be directly resolved by CT imaging. To address this limitation, virtual micropores were generated probabilistically and Brinkman resistance was applied to the corresponding regions. As the generated micropore fraction increased, the resistance applied region expanded and the calculated permeability gradually decreased. In particular, the 2.5% virtual micropore case yielded a permeability of 472mD, which was closest to the experimental value. These results suggest that the unresolved resistance effect of microporosity is one of the main causes of permeability overestimation in CT-based LBM simulations, and that virtual micropore–Brinkman correction can be a practical way to improve permeability prediction accuracy.

Keywords

X-ray CT, Digital core, Lattice Boltzmann Method, Permeability, Micropore correction.

1 Introduction

Fluid flow in porous media is important in various fields, including reservoir engineering, subsurface hydrology, and geological carbon sequestration (Bultreys et al. 2016; Soulaine et al. 2016). Permeability is a representative hydraulic property used to quantitatively evaluate how easily fluid can move through porous rock (Gao et al. 2012). However, conventional permeability tests cannot directly capture internal pore structure, connectivity, or dominant flow pathways and repeated experiments may damage samples and increase cost(Blunt 2001; Xiong et al. 2016).

To address these limitations, X-ray CT-based 3D digital core analysis has been widely used because it enables nondestructive reconstruction of pore structure and quantitative flow evaluation(Cnudde and Boone 2013). In addition, CT-based digital core technology offers advantages in terms of rapid analysis, repeatable computation, and multiphysics simulation (Saxena et al. 2017). In particular, the Lattice Boltzmann Method (LBM) is well suited for direct flow simulation in CT-based pore space because binarized voxel images can be directly used as the computational lattice without additional meshing(Rao and Schaefer 2019).

Nevertheless, CT-based digital core analysis still has limitations associated with image resolution and binarization(Ketcham and Carlson, 2001). Low-resolution X-ray CT can capture the porosity of large pores, but may overestimate pore size and connectivity(Jiang et al. 2012; Peng et al. 2012; Yang et al. 2021). As a result, micropores may be omitted or absorbed into adjacent macropores in the CT-based binary structure, leading to flow paths that appear wider and more connected than they actually are. This can cause permeability to be overestimated in LBM simulations (Jivkov et al. 2013; Yi et al. 2017).

In this study, the causes of permeability overestimation in CT-based LBM simulations are analyzed, and a correction method based on virtual micropore generation and Brinkman resistance is proposed. By comparing permeability and flow fields before and after correction, the applicability of the proposed method is evaluated.

2 Materials and methods

2.1 Dataset and image pre-processing

X-ray CT images of Bentheimer sandstone provided by the Digital Porous Media Portal were used in this study. The voxel size of the CT images was 2.25 μm, and the representative computational domain consisted of 400 × 400 × 400 voxels. The porosity and experimental permeability of the sample were 22.4% and 386mD, respectively, and these values were used as reference data for validating the simulation results. The original CT data consisted of multiple two-dimensional grayscale slices, which were stacked in the z-direction to construct a three-dimensional grayscale volume. Otsu thresholding was then applied to distinguish pore and solid phases and a binary digital core was generated (Fig. 1). Otsu's method is a global thresholding technique that automatically selects the threshold that maximizes the difference in gray values between two classes. The resulting binarized pore structure was finally used as the input geometry for the LBM simulations(Otsu 1979).

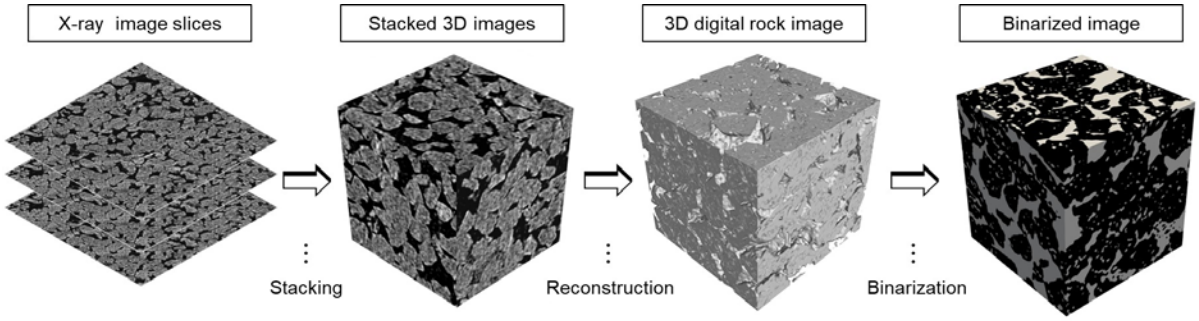


Fig. 1 Workflow for generating the 3D digital core.

2.2 LBM Simulation procedure

LBM simulates fluid flow through the collision and streaming of particle distribution functions on a lattice. In this study, the binarized CT-based digital core was used as the computational domain with each voxel corresponding to one lattice cell. A D3Q19 lattice model and an MRT collision model with an external forcing term were adopted (Xie et al. 2026). The evolution equation of the MRT-based distribution function is given in Eq. (1).

$$f_i(x + e_i\Delta t, t + \Delta t) - f_i(x,t) = -M^{-1}S[m(x,t) - m_i{}^{eq}(x,t)] + F_i (1)$$

In Eq. (1), $f_i(x,t)$ is the density distribution function in the i-th direction at position$x$, and time t, e_i is the D3Q19 discrete velocity vector, M is the transformation matrix, S is the relaxation matrix, $m_i{}^{eq}$ denotes the equilibrium moment,$F_i$represents the external forcing term. In the simulation, a pressure difference was imposed between the inlet and outlet to induce flow in the z-direction, and a bounce-back boundary condition was applied at the solid walls to represent the no-slip condition. The permeability was calculated from the average velocity in the z-direction and the pressure gradient, as shown in Eq. (2).

$$k_{LBM} = \frac{v(u_z)}{\nabla P} (2)$$

where, v is the lattice viscosity, u_z is the average velocity in the z-direction over the entire computational domain, and ∇P is the pressure gradient in the z-direction. The calculated lattice permeability was converted into physical permeability using the voxel size, as given in Eq. (3),

$$k_{phys} = k_{LBM}(\Delta x)^2 (3)$$

where $\Delta x = 2.25 \times 10^{-6} m$. The resulting k_{phys} was then converted into mD and compared with the experimental value.

2.3 Cause of overestimation due to CT resolution limitation

The actual pore network of rock spans a wide range of pore sizes, including many micropores and narrow pore throats smaller than the CT voxel size. However, a CT-based digital core may not fully represent these structures because of the limitations in image resolution and binarization. This limitation can be expressed in two ways. First, when solid and micropores coexist within a single voxel, the averaged gray value may shift toward the solid side, and the voxel is then classified as solid, resulting in the loss of micropore information. Second, if micropores or mixed voxels around macropores are classified as pore, pore boundaries that were originally narrow and discontinuous may be represented as a single continuous large flow channel. In this case, the effective flow path is represented as wider and smoother than it actually is, which leads to permeability overestimation in LBM simulations.

2.4 Virtual micropore generation and Brinkman model

To compensate for the unresolved micropore effect in the CT-based digital core, virtual micropores were additionally defined within the macropore-centered pore structure. Because the exact locations of actual micropores are unknown, virtual micropores were distributed probabilistically within candidate voxels in the computational domain using a random seed (Fig. 2).

Brinkman resistance was then applied to the generated micropore regions. The governing equations of the Brinkman model are given in Eq. (4) and Eq. (5).

$$\nabla \cdot u = 0 (4)$$

$$-\nabla p + \mu_e \nabla^2 u - \frac{\mu}{k_{micro}} u = 0 (5)$$

where u is voxel averaged velocity, p is pressure, μ is the fluid viscosity, μ_e is the effective viscosity, and k_{micro} is the local permeability of the micropore region. The last term represents the resistance

term that suppresses fluid flow in the micropore region. In the LBM implementation, this effect was introduced as an external forcing term, as expressed in Eq. (6).

$$F = -\alpha u (6)$$

In the actual calculation, MRT dynamics with Guo forcing were used, and the force was computed using the pre-force base velocity u_0. As the generated micropore fraction increased, the extent of the Brinkman resistance-applied region also increased, leading to a decrease in the overall permeability of the flow field.

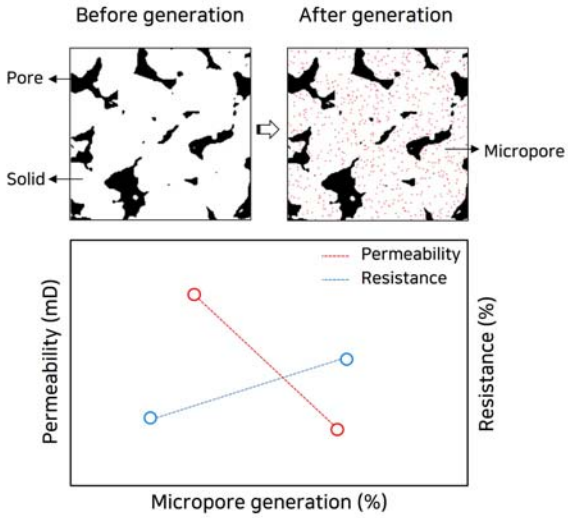


Fig. 2 Visualization of virtual micropore generation.

3 Results

3.1 Uncorrected LBM results and structural limitations of the CT-based digital core

The uncorrected LBM simulation yielded a permeability of 875 mD, which is approximately 2.3 times higher than the experimental value of 386 mD. This suggests that the CT-based binary digital core does not fully represent the actual pore structure. Flow-field visualization also showed that fluid tended to concentrate along a few highly connected large pores rather than passing uniformly through the entire pore network.

To identify the structural cause of this overestimation, the CT-based pore size distribution (PSD) was compared with the mercury intrusion porosimetry (MIP)-based PSD. As shown in Fig. 3, the CT-based PSD is mainly concentrated in the large-pore range of several tens of micrometers, whereas the MIP-based PSD indicates an unresolved micropore region with a significant volumetric contribution in the nanometer range. This provides structural evidence that the CT-based digital core does not sufficiently capture the microporous structure of the actual rock.

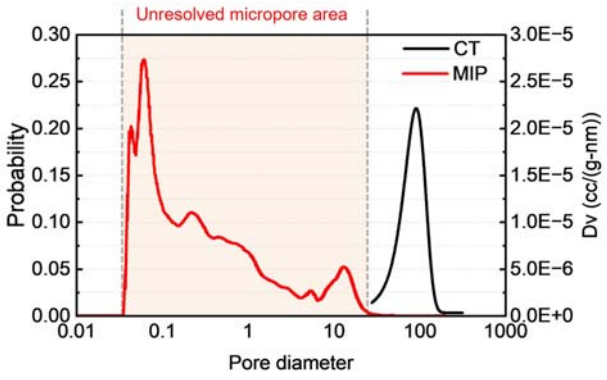


Fig. 3 Comparison between CT-based PSD and MIP-based PSD.

3.2 LBM results and effect of micropore correction

In the LBM simulation using only the CT-based macropore structure, fluid tended to flow preferentially through highly connected large pores, resulting in a simplified flow pathway compared with the actual pore network. To compensate for this limitation, virtual micropores were generated and Brinkman resistance was applied to the corresponding regions, after which the flow field was recalculated. Fig. 4a shows the uncorrected flow field, where the main flow path connecting the inlet and outlet is relatively wide and continuous. In contrast, Fig. 4b shows the corrected case, in which the overall pore geometry is preserved but the dominant flow channel becomes narrower and less continuous. This indicates that the micropore regions acted not as free-flow pore space but as resistive zones that suppressed fluid motion.

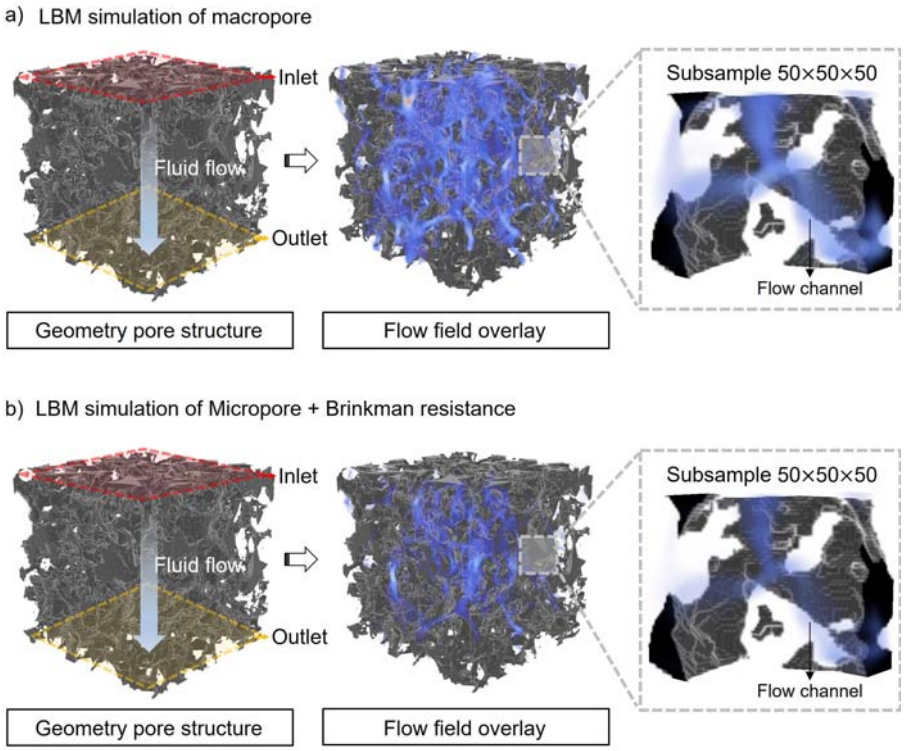


Fig. 4 Comparison of flow fields before and after correction: a)flow field before correction, b)flow field after correction.

Quantitatively, permeability decreased progressively as the generated micropore fraction increased, from 875 mD in the uncorrected case to 792, 713, 628, 537, and 472mD at 0.5%, 1.0%, 1.5%, 2.0%, and 2.5%, respectively (Fig. 5). At the same time, the fraction of the resistance-applied region increased, indicating that a larger portion of the flow domain was subjected to hydraulic resistance. Among the tested cases, the 2.5% virtual micropore condition showed the closest agreement with the experimental value and was therefore considered the most suitable correction condition in this study.

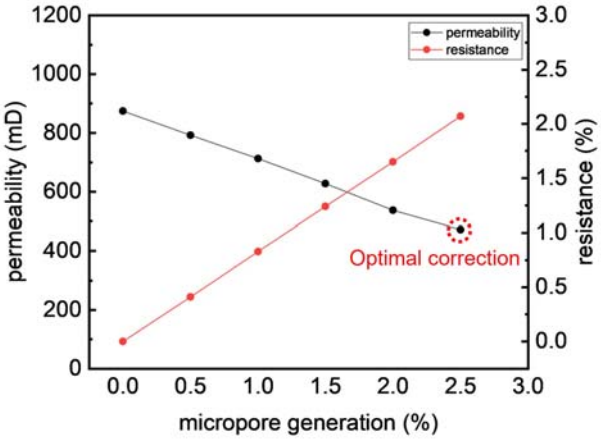


Fig.5 Permeability trend with increasing micropore generation.

3.3 Comparison of experimental, uncorrected and corrected LBM results

The correction effect was evaluated by comparing the experimental permeability, the uncorrected LBM result, and the corrected LBM result. Fig. 6 presents the permeability values for the three cases as a bar chart. The uncorrected LBM result was 875 mD, which is significantly higher than the experimental value of 386 mD, showing that permeability is overestimated when only the CT-based binary digital core is used. In contrast, the corrected LBM result, obtained by introducing virtual micropores and applying Brinkman resistance, decreased to 472mD and showed much closer agreement with the experimental value.

This indicates that micropores below the CT resolution provide additional resistance to fluid flow, and that accounting for this effect can reduce excessively connected flow paths. Therefore, virtual micropore–Brinkman correction is considered an effective method for reducing the overestimation tendency of CT-based LBM simulations. However, because the corrected result does not completely match the experimental value, further calibration of the generated micropore fraction and the Brinkman coefficient is still required.

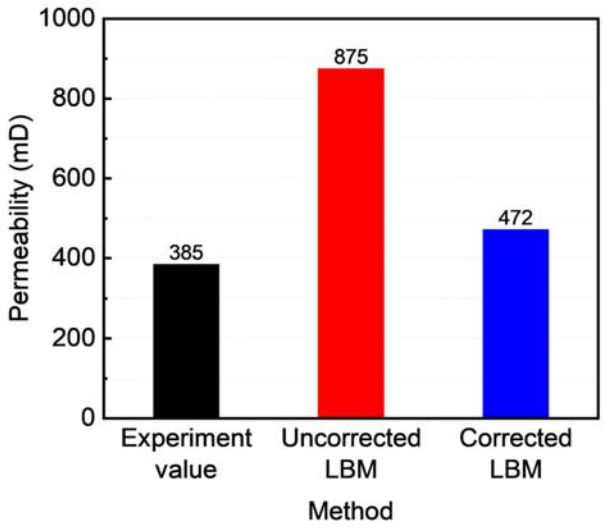


Fig. 6 Comparison of experiment value, uncorrected LBM, and corrected LBM results.

4 Conclusions

In this study, permeability was estimated from a CT-based digital core of Bentheimer sandstone using LBM, and the cause of overestimation associated with CT resolution limitations and binarization was analyzed. The uncorrected LBM result was significantly higher than the experimental value, and the comparison between CT-based PSD and MIP-based PSD confirmed the presence of micropores that could not be directly resolved by CT imaging. To compensate for this limitation, virtual micropores were generated and Brinkman resistance was applied. As the generated micropore fraction increased, the resistance-applied region expanded and the permeability decreased progressively. In particular, the permeability calculated for the 2.5% virtual micropore case showed the closest agreement with the experimental value. These findings suggest that virtual micropore–Brinkman correction is an effective approach for reducing permeability overestimation in CT-based LBM simulations. Future work should focus on improving the physical validity of micropore distribution and systematically calibrating correction parameters for more reliable digital-core-based permeability estimation.

Acknowledgements

This study was supported by the Institute for Korea Spent Nuclear Fuel (iKSNF) (RS-2021-NR056198) and the Busan Metropolitan City grant funded by the Korea government (Ministry of Science and ICT) (A project to support the development of Open-Lab in universities linked to regional industries).

References

Bultreys, T., De Boever, W. and Cnudde, V. (2016) "Imaging and image-based fluid transport modeling at the pore scale in geological materials: A practical introduction to the current state-of-the-art," *Earth-Science Reviews*. Elsevier B.V., pp. 93–128. Available at: https://doi.org/10.1016/j.earscirev.2016.02.001.

Cnudde, V. and Boone, M.N. (2013) "High-resolution X-ray computed tomography in geosciences: A review of the current technology and applications," *Earth-Science Reviews*, pp. 1–17. Available at: https://doi.org/10.1016/j.earscirev.2013.04.003.

Gao, S., Meegoda, J.N. and Hu, L. (2012) "Two methods for pore network of porous media," *International Journal for Numerical and Analytical Methods in Geomechanics*, 36(18), pp. 1954–1970. Available at: https://doi.org/10.1002/nag.1134.

Jiang, Z. *et al.* (2012) "Stochastic Pore Network Generation from 3D Rock Images," *Transport in Porous Media*, 94(2), pp. 571–593. Available at: https://doi.org/10.1007/s11242-011-9792-z.

Jivkov, A.P. *et al.* (2013) "A novel architecture for pore network modelling with applications to permeability of porous media," *Journal of Hydrology*, 486, pp. 246–258. Available at: https://doi.org/10.1016/j.jhydrol.2013.01.045.

Ketcham, R.A. and Carlson, W.D. (2001) "Acquisition, optimization and interpretation of x-ray computed tomographic imagery: Applications to the geosciences," *Computers and Geosciences*, 27(4), pp. 381–400. Available at: https://doi.org/10.1016/S0098-3004(00)00116-3.

Otsu, N. (1979) "A Threshold Selection Method from Gray-Level Histograms," *IEEE Transactions on Systems, Man, and Cybernetics*, SMC-9(1), pp. 62–66.

Peng, S. *et al.* (2012) "Using X-ray computed tomography in pore structure characterization for a Berea sandstone: Resolution effect," *Journal of Hydrology*, 472–473, pp. 254–261. Available at: https://doi.org/10.1016/j.jhydrol.2012.09.034.

Rao, P. and Schaefer, L. (2019) "Lattice Boltzmann models for micro-tomographic pore-spaces," *Computers and Fluids*, 193. Available at: https://doi.org/10.1016/j.compfluid.2019.104294.

Saxena, N. *et al.* (2017) "Effect of image segmentation & voxel size on micro-CT computed effective transport & elastic properties," *Marine and Petroleum Geology*, 86, pp. 972–990. Available at: https://doi.org/10.1016/j.marpetgeo.2017.07.004.

Soulaine, C. *et al.* (2016) "The Impact of Sub-Resolution Porosity of X-ray Microtomography Images on the Permeability," *Transport in Porous Media*, 113(1), pp. 227–243. Available at: https://doi.org/10.1007/s11242-016-0690-2.

Xie, Q. *et al.* (2026) "Pore-Scale Transition Behavior of Digital Carbonate Rock Dissolution During CO2 Geo-Sequestration," *Water Resources Research*, 62(2). Available at: https://doi.org/10.1029/2025WR041604.

Xiong, Q., Baychev, T.G. and Jivkov, A.P. (2016) "Review of pore network modelling of porous media: Experimental characterisations, network constructions and applications to reactive transport," *Journal of Contaminant Hydrology*. Elsevier B.V., pp. 101–117. Available at: https://doi.org/10.1016/j.jconhyd.2016.07.002.

Yang, E., Kang, D.H. and Yun, T.S. (2021) "Ternary segmentation and estimation of permeability for porous rocks based on 3D X-ray computed tomographic images by hidden Markov random field and Brinkman-force lattice Boltzmann model," *Journal of Hydrology*, 599. Available at: https://doi.org/10.1016/j.jhydrol.2021.126377.

Yi, Z. *et al.* (2017) "Pore network extraction from pore space images of various porous media systems," *Water Resources Research*, 53(4), pp. 3424–3445. Available at: https://doi.org/10.1002/2016WR019272.

Safe Footing Distance for an Isolated Footing Adjacent to an Excavation Wall in Jointed Rock Masses

Argha Biswas, Mahendra Singh & Aditya Singh
Department of Civil Engineering, IIT Roorkee, Uttarakhand, India
arghab73@gmail.com
0009-0008-1375-5679

Abstract

Increasing land-use pressure often requires engineers to construct structures in close proximity to a vertical cut and supported by a retaining wall, particularly in hilly regions. In such cases, the distance of a footing from the vertical cut or excavation becomes a critical parameter, as it governs the extent to which excavation-induced effects can be minimized or neglected. Although footings may be placed on either soil or rock, identifying a safe footing location on jointed rock is considerably more complex due to the anisotropic behavior of jointed rock masses compared with the relatively isotropic nature of soils. To investigate this, 2D physical model tests were conducted on an artificial 60°–30° orthogonally jointed rock mass with an isolated footing placed adjacent to an excavation wall. The experimental results indicate that when the footing is positioned beyond a certain safe footing distance, the excavation no longer affects the bearing capacity, regardless of the excavation depth. Complementary finite element modeling analysis was conducted to assess the bending-moment distribution, shear-stress distribution, and load transfer along the excavation wall. The numerical results likewise demonstrate that beyond the safe footing distance, bending moments and shear stresses applied exhibit similar patterns for different excavation depths.

Keywords

Excavation wall, Artificial rock mass, Physical model, Safe footing distance, Finite element modelling.

1 Introduction

Population growth and rapid urbanisation have intensified land-use pressure, particularly in mountainous terrains. This often necessitates the construction of critical infrastructure in geologically unfavourable locations, such as in close proximity to vertical rock cuts or excavations. In such projects, retaining structures are frequently employed to provide lateral support. However, the offset distance between the footing and the excavation face constitutes a critical design parameter, as it controls the extent to which excavation-induced stress redistribution affects the foundation.

Numerous studies have investigated the behaviour of foundations located near vertical cuts in soils. However, the direct applicability of these findings to foundations placed adjacent to vertical excavations in jointed rock masses is limited due to the presence of discontinuities. Because of the isotropic properties of soil, the stress distribution beneath an applied load follows a symmetrical circular pattern. In contrast, the presence of joints imparts anisotropy to rock masses, resulting in a non-uniform, direction-dependent stress distribution that deviates from the conventional circular symmetry (Boussinesq, 1885; Goodman, 1991, Biswas et al 2025b).

A limited number of studies have investigated foundations located near vertical cuts in jointed rock masses. Biswas et al. (2025a, 2025b) performed physical model studies on orthogonally jointed rock masses with a foundation placed adjacent to an excavation wall. Previously, Son and Park (2014) employed both physical model tests and numerical simulations to investigate the earth pressure acting on excavation walls in single-jointed rock at varying excavation depths. Subsequently, Son and Adedokun conducted a series of numerical parametric studies to evaluate earth pressure distributions under diverse conditions, including joint cohesion (2014), layered jointed rock masses (2016), joint inclination (2017a), rock mass quality, ranging from hard to highly weathered (2017b, and wall permeability (2018). However, in these studies by Son and Park (2014) and Son and Adedokun (2014, 2016, 2017a, 2017b, 2018), the foundation was not placed on the jointed rock mass; consequently, the effect of footing distance from the excavation was not examined.

To investigate this, 2D physical model tests were conducted on an artificial 60°–30° orthogonally jointed rock mass with an isolated footing placed adjacent to an excavation wall. Complementary finite element modelling (FEM) was conducted to assess the bending moment distribution, shear stress distribution, and load transfer along the excavation wall for different footing distances.

2 Physical model tests

A series of 2D physical model tests, scaled at 1:20, were performed in the Geotechnical Engineering laboratory at IIT Roorkee to examine the bearing capacity and load-settlement characteristics of isolated footings with varying footing positions and excavation depth. This model rock mass comprised two continuous orthogonal joint sets: one dipping at 60° toward the excavation and the other orthogonal to it, oriented at 30°.

The artificial rock mass was formed using individual blocks (25 mm × 25 mm × 75 mm) cast from a blend of Plaster of Paris, white cement, sand, and water. These blocks were meticulously assembled into a 1.2 m × 0.8 m × 0.15 m configuration to represent the 60°–30° orthogonal joint sets. To represent the excavation boundary, a 0.4 m high acrylic sheet (10 mm thick) was utilised.

As shown in the Fig 1, a rigid foundation was simulated using a 0.15 m square mild steel plate (0.025 m thick) placed on the artificial rock mass upper surface. Vertical loading was applied via a 300 kN capacity hydraulic jack and monitored through a 350 kN proving ring. Foundation settlement was recorded using two dial gauges positioned at the midpoints of opposite edges of the plate. The mechanical properties of the constituent materials and joint interfaces, determined through a comprehensive testing suite (including UCS, triaxial, Brazilian, and direct shear tests), are summarised in Table 1. Further experimental details are documented in Biswas et al. (2025b).

Physical model tests were performed with the footing located at offset distances of 0B, 1B, and 2B from the excavation face, where B is the footing width, 0.15 m. The minimum embedment depth of 0.25h (h representing the wall height) was maintained throughout the experimental program.

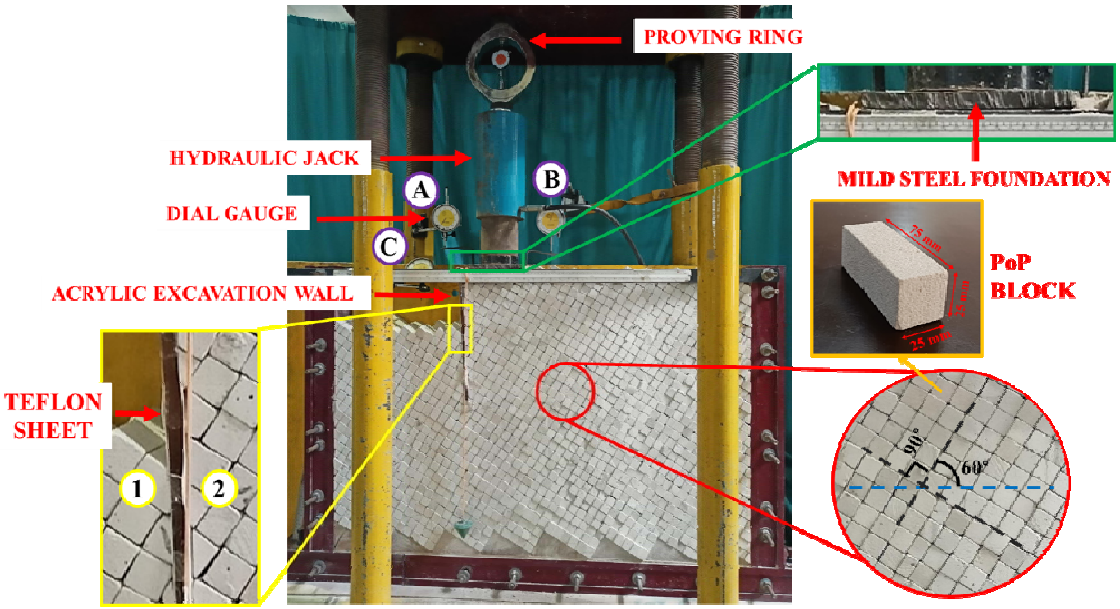


Fig. 1 Experimental setup at the Geotechnical Engineering Laboratory, IIT Roorkee (Biswas et al., 2025b).

Table 1. Material and interface properties.

Material properties		
	Artificial rock	**Excavation wall**
Constitutive model	**Mohr-coulomb plastic**	**Linear elastic**
E (MPa)	2450	3040
γ (kN/m^3)	16.37	11.5
ν	0.3	0.37
c (MPa)	3.2	26
ϕ (°)	31.2	0
Interface properties		
	Rock joint	**Wall and Rock**
Constitutive model	**Coulomb slip**	**Coulomb slip**
K_n(MPa/m)	700	150
K_s (MPa/m)	70	15
c (kPa)	8	0
ϕ (°)	37.6	0

3 Physical model tests results

Figure 2 shows the footing pressure versus vertical settlement of the 60°–30° jointed rock mass for different excavation depths and footing positions. Figure 2(a) shows that for the 0B footing location, the failure stress or bearing capacity decreases rapidly as the excavation depth increases; at a high excavation depth (0.3 m), the rock mass failed under its own weight, so no settlement curve is obtained. Figure 2(b) shows that for the 1B footing, the bearing capacity decreases with increasing excavation depth, but the rate of decrease is less than that of the 0B position. Figure 2(c) shows that for the 2B footing, there is no decrease in the bearing capacity as the excavation height increases. This figure demonstrates that as the footing distance from the excavation wall increases, the excavation effect on the foundation becomes negligible or zero.

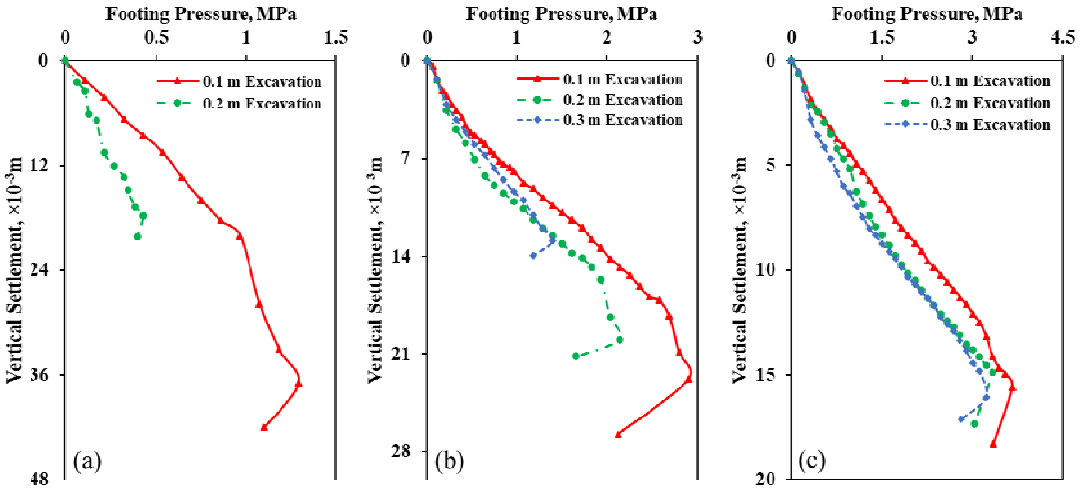


Fig. 2 Footing pressure vs vertical settlement curve for varying excavation depths and footing positions.

4 Numerical modeling and results

In this study a Finite element modelling was created using the Rocscience software (RS2, version 11.026). The numerical model was developed based on the measured physical properties listed in Table 1. To simulate the behavior of the intact rock, Mohr-Coulomb plastic constitutive model was employed, while the flexible excavation wall was modeled using linear elastic properties. Additionally, the Coulomb slip constitutive model was used to simulate the mechanical behavior of the rock joints.

Figures 4 and 5 show the numerical modelling results. Figure 4 shows the bending moment distribution along the excavation wall for different footing positions and excavation depths. In Figures 4(a) and 4(b), when the footing is placed at 0B and 1B distances from the excavation wall, the bending moment distribution varies significantly with the excavation depth. However, when the footing is positioned at a 2B distance, the bending moment distribution exhibits a similar pattern across all depths, as shown in Figure 4(c). For the footing positioned at 2B, the 0.3 m excavation depth results in greater lateral movement of the excavation wall compared to the 0.1 m and 0.2 m depths. Consequently, as shown in Fig. 4(c), while the overall profile of the bending moment distribution remains consistent, the magnitudes are lower than those recorded for the shallower excavation depths.

Figure 5 shows the applied stress distribution along the excavation wall, which exhibits a similar tendency to the bending moment distribution. When the footing is placed at the 0B and 1B positions, the applied stress distribution changes rapidly with variations in excavation depth. However, for the 2B footing distance, the stress distribution shows similar trends and consistent values across all excavation depths.

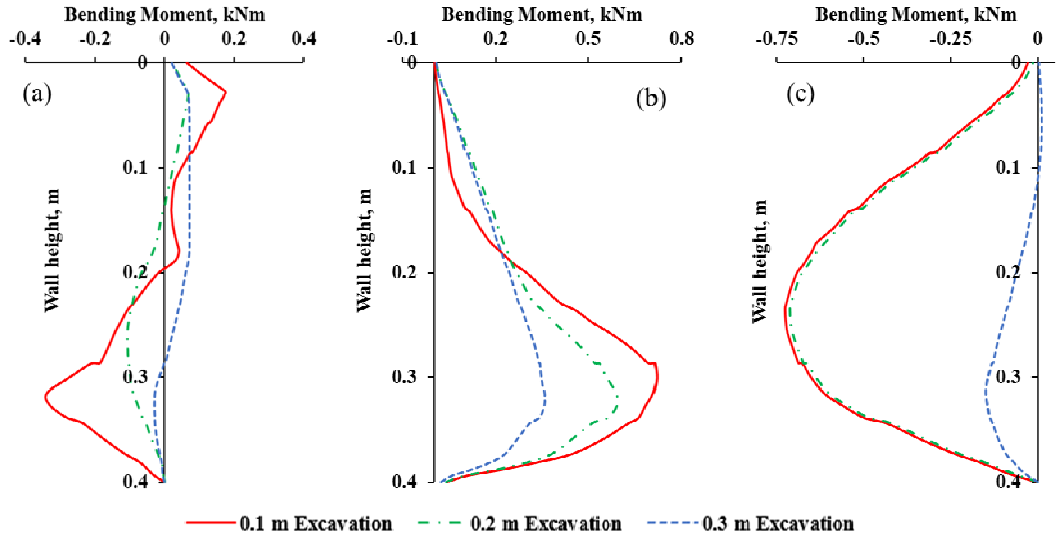


Fig. 3 Bending moment distribution along the excavation wall.

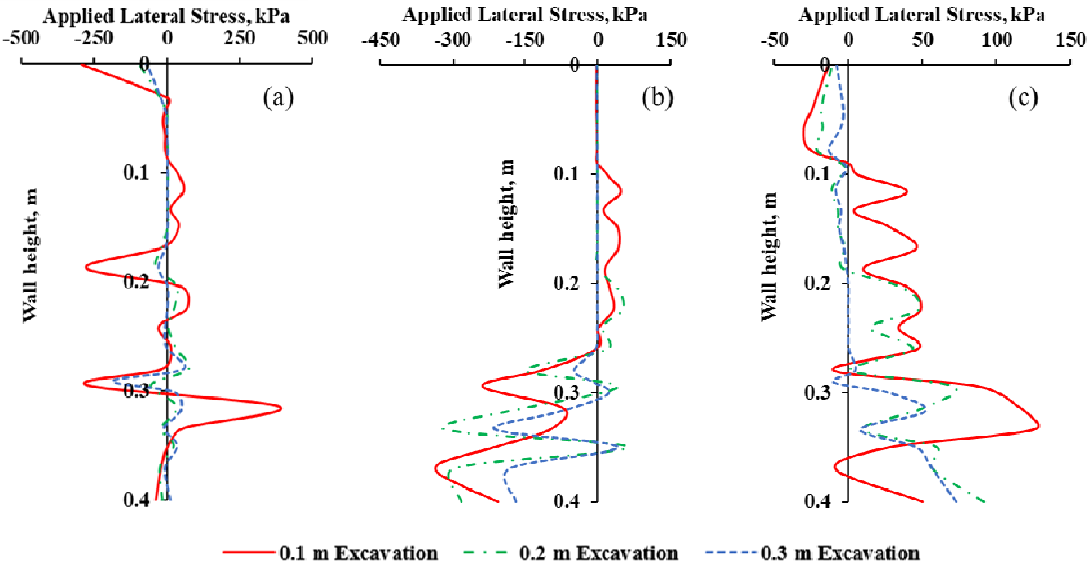


Fig. 4 Applied lateral stress distribution along the excavation wall.

Based on these results, it can be concluded that when a footing is positioned beyond a certain horizontal distance from the excavation wall, the excavation depth no longer influences foundation performance. Beyond this critical distance, the stress distribution generated by the footing does not intersect with the excavation face; instead, the load is fully contained within the rock mass, allowing the system to behave as an unexcavated rock mass (Fig. 5). In the present study, this threshold is defined as the "safe footing distance". For an embedment depth of at least 0.25h, this distance is mathematically expressed as h·cot(θ), where h denotes the height of the excavation wall and θ represents the inclination of the joint set dipping toward the wall (measured from the horizontal).

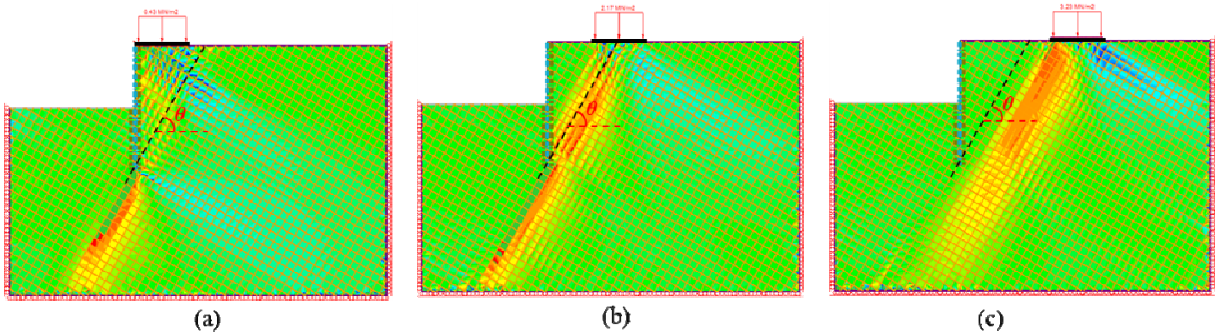


Fig. 5 Total stress distribution for the 60°–30° orthogonally jointed rock mass with an excavation depth of 0.2 m for footing positioned at (a) 0B, (b) 1B, and (c) 2B. The black dashed line indicates the h·cot (θ) horizontal distance for this rock mass (Biswas et al., 2026).

5 Conclusions

Experimental results indicate that for footings located in close proximity to a vertical cut (0B and 1B), the bearing capacity is significantly influenced by excavation depth. In contrast, at a footing offset distance of 2B, the bearing capacity remains nearly constant across all excavation depths, suggesting a negligible influence of excavation depth on the foundation. Finite element analyses further corroborate these findings, showing that at a 2B distance, both the bending moment and stress distribution along the excavation wall exhibit similar patterns regardless of excavation depth, unlike the variations observed for 0B and 1B conditions.

This behaviour can be attributed to the fact that the stress distribution induced by the footing does not intersect the excavation face at this distance; instead, it remains confined within the rock mass, allowing the system to behave comparably to an unexcavated condition. The identified threshold distance, beyond which excavation-induced effects become negligible, is defined as the safe footing distance.

References

Biswas A, Singh A, Singh M (2025) Experimental investigation and a method of calculating bearing capacity for jointed rock masses under excavated and unexcavated conditions. Rock Mechanics and Rock Engineering.

Biswas A, Singh A, Singh M (2025) The effects of staggered and non-staggered joints on the ultimate bearing capacity, load settlement behavior, and failure mechanism with the change of excavation depths. Rock Mechanics Bulletin 4(1): 100154.

Biswas A, Singh A, Singh M (2025) Comprehensive analysis of excavation walls in jointed rock masses: bending moment, applied stress distribution, and empirical load estimation. (Submitted).

Son M, Adedokun S (2014) Effect of joint cohesive strength on the earth pressure against the support system in a jointed rock mass. Journal of the Korean Geotechnical Society 30(7): 41–53.

Son M, Adedokun S (2015) Effect of support characteristics on the earth pressure in a jointed rock mass. Canadian Geotechnical Journal 52(12): 1956–1967.

Son M, Adedokun S (2016) Effect of joint inclination angles on the earth pressure against the support system in a jointed rock mass. KSCE Journal of Civil Engineering 20(4): 1259–1266.

Son M, Adedokun S (2017a) Earth pressure on a retaining structure in layered and jointed rock masses. KSCE Journal of Civil Engineering 21(4): 1147–1153.

Son M, Adedokun S (2017b) Effect of rock mass condition on the earth pressure against an excavation wall in rock mass: numerical investigation. Journal of the Korean Geotechnical Society 33(11): 83–95.

Son M, Adedokun S (2018) Effect of the permeability of excavation wall on the earth pressure in a jointed rock mass. KSCE Journal of Civil Engineering 19(2): 13–21.

Son M, Park J (2014) Physical and numerical tests of the excavation walls in jointed rock masses. Canadian Geotechnical Journal 51(5): 554–569.

The effect of confining pressure on the needle penetration index for three different pyroclastic rocks

S. Kahraman
Hacettepe University, Mining Engineering Department, Ankara, Türkiye
sairkahraman@yahoo.com
0000-0001-7903-143X

Anıl Kaya
Hacettepe University, Mining Engineering Department Undergraduate Program, Ankara, Türkiye

Abstract

The needle penetration test is a non-destructive index test that is applicable in both the field and in the laboratory and requires no special sample preparation. The test has been used for estimating the physical and mechanical properties of soft rock. However, there is no study in the literature about the effect of confining pressure on the needle penetration index. In underground rock engineering applications, the effect of confining pressure on the properties of the rock is of considerable importance.This study investigates the influence of confining pressure on the needle penetration index for pyroclastic rocks. Block samples of pyroclastic rock from three different locations and core samples were taken. Smooth-cut core samples were put into the Hoek Cell and needle penetration index tests were carried out at the different confining stress levels such as 1, 2, 3, and 4 MPa. The uniaxial compressive strength values were also estimated from the needle penetration index. The results were evaluated using regression analysis. It was seen that both the needle penetration index and uniaxial compressive strength values were increased significantly with increasing confining pressure. The increments in both the needle penetration index and uniaxial compressive strength values were about 100 % for the stress level of 4 MPa compared to the unconfined values. It was concluded that the derived equations could be used for the estimation of both the needle penetration index and uniaxial compressive strength values for the different confining stress levels. The findings of the study fill a gap in the literature and they can be used for designing rock engineering projects.

Keywords

Needle penetration index, Confining pressure, Pyroclastic rocks.

1 Introduction

The needle penetration index (NPI) test is a non-destructive method which can be applied both in the field and laboratory and does not require any special sample preparation. The test was originally developed for estimating the uniaxial compressive strength (UCS) of soft rocks. Several researchers have used the NPI to estimate the uniaxial compressive strength of rocks (Okada et al. 1985; Yamaguchi et al. 1997; Takahashi et al. 1988; Uchida et al. 2004; Aydan et al. 2006 and 2008; Aydan 2012; Erguler and Ulusay 2007; Park et al. 2011; Ulusay and Erguler 2012; Kahraman et al. 2017; Rabat et al. 2020). Several investigators have also studied the correlations between the NPI and other rock properties such as tensile strength, Young's modulus and P- and S-wave velocities, density, porosity, cohesion, and friction angle (Aydan, 2012; Aydan and Ulusay, 2013; Aydan et al,. 2014Kahraman and Ince 2023). On the other hand, some researchers (Kahraman et al. 2018; Kahraman et al. 2019; Rostami et al. 2024)have used the NPI to predict the performance of roadheaders used in coal mines. Nevertheless, the impact of confining pressure on the NPI has not been studied in the literature. The impact of confining pressure on the characteristics of rocks is crucial in underground rock engineering applications. This study examines how confining pressure affects the NPI for pyroclastic rocks.

2 Materials and methods

2.1 Samples and sample preparation

Pyroclastic rock blocks from three different regions of Türkiye were collected and transported to the laboratory (Table 1). During sample collection, care was taken to ensure that the rock blocks were unaltered and free of fractures or cracks. NQ-sized (47.6 mm) core samples were taken from the blocks and sawed into 130mm lengths to fit the Hoek Cell membrane (Fig. 1). To ensure homogeneity among samples for each rock type, core samples were taken from a single block. Since the formations in the field were mostly saturated or semi-saturated, the samples were soaked in water for 48 hours to conduct the experiments on saturated samples.

Table 1. The location of samples.

Rock type	Location
Pyroclastic	Bayat/Afyonkarahisar
Pyroclastic	Iscehisar/Afyonkarahisar
Pyroclastic	Bergama/izmir



Fig. 1 Core samples tested.

2.2 Needle penetration index test

The penetrometer's needle is pushed into the rock surface until it reaches 100 N force, at which point the presser's position on the penetration scale is used to determine the penetration depth. The maximum penetration distance of 10 mm can be reached for extremely soft rocks prior to applying the maximum force. In this situation, the test is terminated and the force is read from the force scale. The needle penetration index (NPI) is calculated by the following equation (Ulusay et al., 2014):

$$NPI = \frac{F}{D} \quad (1)$$

Where NPI The needle penetration index (N/mm)
F Penetration force (N)
D Penetration distance (mm).

The samples were put inside the Hoek cell and the NPI tests were carried out according to ISRM (2015) suggested methods (Fig. 2). Hoek Cell was fixed to the wall of the laboratory bench and the tests were carried out by slowly pushing the needle of the penetrometer perpendicularly to the surface of the specimens (Fig. 2a). While one hand held the Hoek Cell still, the other hand inserted the penetrometer needle into the sample (Fig. 2b). To reduce the scattering of the NPI values, the penetrometer was maintained in the same position at all times.

The tests were carried out at various confining pressure levels, e.g. 1, 2, 3, and 4 MPa. A separate sample was used for each stress value, and the experiment was repeated 3-5 times on each sample. The needle penetration point was moved from the prior location by at least 10 mm. Experiments in which cracks formed during penetration were cancelled.



a b
Fig. 2 Hoek Cell with confining pressure apparatus (a), and applying the NPI test (b).

3 Results and evaluation

The NPI test results are given in Table 2 for each rock type, respectively. Estimated uniaxial compressive strength (UCS) values are also presented in Table 2. The UCS values are estimated using the following equation (Ulusay and Erguler 2012):

$$UCS = 0.4NPI^{0.929} \quad (2)$$

Where UCS The uniaxial compressive strength (MPa)
NPI The needle penetration index (N/mm)

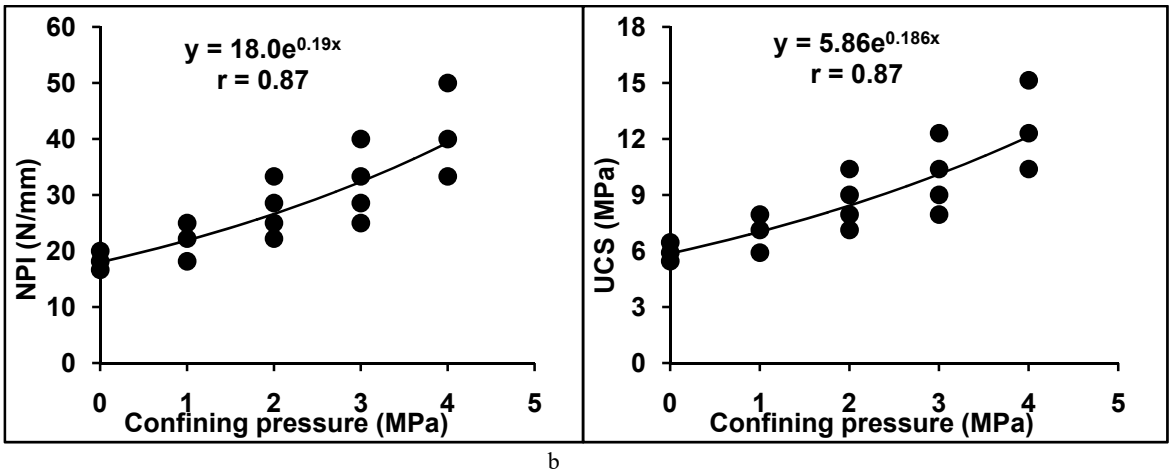
The average NPI values for the Bayat, Bergama, and Iscehisar samples under unconfined conditions are 18.28 N/mm, 27.28 N/mm, and 19.27 N/mm, respectively. The average estimated UCS values for the Bayat, Bergama, and Iscehisar samples under unconfined conditions are 5.95 MPa, 8.62 MPa, and 6.24MPa, respectively. Although the NPI and UCS values of the Bayat and Iscehisar samples are quite close to each other, the values of the Bergama sample are significantly higher than those of the other samples.

Table 2. NPI results and estimated UCS values.

Confining pressure (MPa)	Bayat sample		Bergama sample		Iscehisar sample	
	NPI (N/mm)	UCS (MPa)	NPI (N/mm)	UCS (MPa)	NPI (N/mm)	UCS (MPa)
0	20.00	6.47	25.00	7.96	20.00	6.47
	16.67	5.46	33.33	10.39	22.22	7.13
	18.18	5.92	22.22	7.13	16.67	5.46
	-	-	28.57	9.01	18.18	5.92
1	25.00	7.96	33.33	10.39	22.22	7.13
	22.22	7.13	28.57	9.01	28.57	9.01
	18.18	5.92	25.00	7.96	25.00	7.96
	-	-	28.57	9.01	33.33	10.39
	-	-	-	-	25.00	7.96
2	22.22	7.13	33.33	10.39	25.00	7.96
	33.33	10.39	40.00	12.31	40.00	12.31
	25.00	7.96	28.57	9.01	33.33	10.39
	28.57	9.01	40.00	12.31	40.00	12.31
	-	-	50.00	15.15	28.00	8.84
3	33.33	10.39	40.00	12.31	28.57	9.01
	25.00	7.96	33.33	10.39	33.33	10.39
	28.57	9.01	50.00	15.15	50.00	15.15
	40.00	12.31	50.00	15.15	-	-
4	33.33	10.39	50.00	15.15	50.00	15.15
	40.00	12.31	40.00	12.31	40.00	12.31
	50.00	15.15	66.67	19.79	33.33	10.39
	-	-	-	-	50.00	15.15

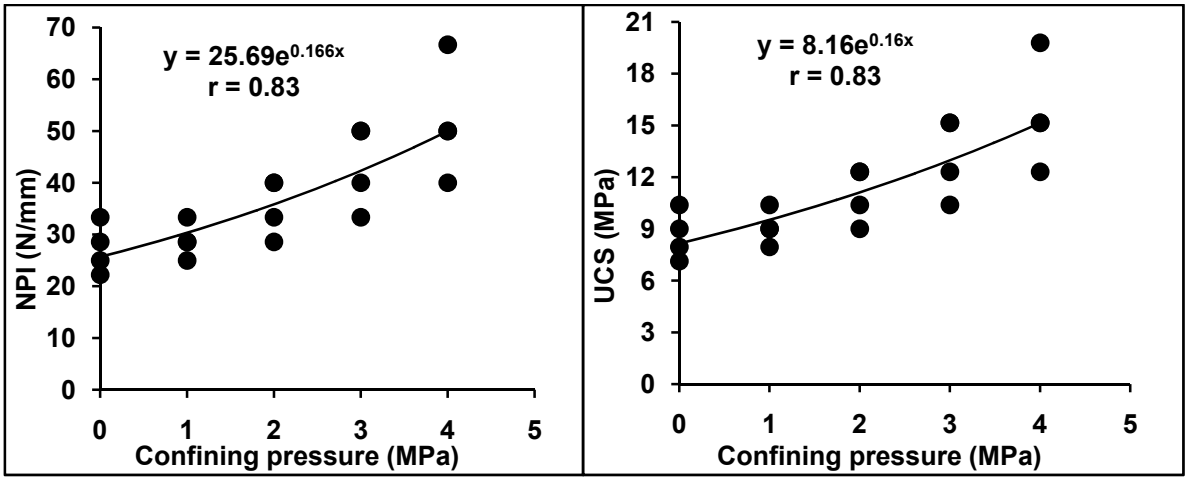
The correlations between confining pressure and both the NPI and UCSvalues are shown in Figs. 3-5 for each rock type. There are exponential correlations between confining pressure and boththe NPI and UCS. The NPI and UCS values increase as confining pressure increases. The trend of the curves is almost identical for all three rock types tested. When compared to the unconfined values, the NPI and UCS values increase by roughly 100% for the stress level of 4 MPa.

The NPI and UCS values of Bergama sample under unconfined conditions are quite scattered, whereas those of Bayat and Iscehisar samples are not. This could be the result of variations in the microstructural properties of the samples. As the confining pressure increases, the data are generally more scattered over all samples. Because the tested rock samples are very weak, microcracks are likely to form in their structure under compression, which may result in the scattering of the data.



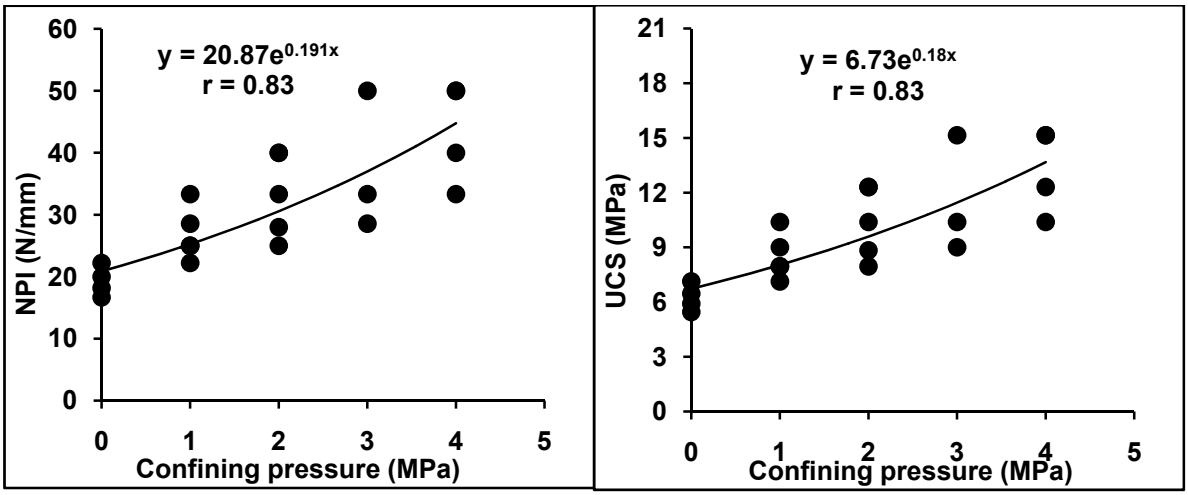
a b

Fig. 3 Correlation between NPI and confining pressure (a), and UCS and confining pressure (b) for Bayat sample.



a b

Fig. 4 Correlation between NPI and confining pressure (a), and UCS and confining pressure (b) for Bergama sample.



a b

Fig. 5 Correlation between NPI and confining pressure (a), and UCS and confining pressure (b) for Iscehisar sample.

It has been clearly shown that the NPI values, and consequently the UCS values, of pyroclastic rocks increase significantly under confining pressure. This point should be taken into consideration when estimating UCS from NPI in any mining or construction project to be carried out in pyroclastic rocks. Otherwise, project planning will be flawed and this will lead to undesirable consequences. For example, when estimating a machine performance in an excavation project, if the increase in strength due to confining pressure is not taken into account, the resulting excavation performance will be much lower than predicted, the project duration will be extended, and costs will increase.

4 Conclusions

The influence of confining pressure on the NPI was investigated for pyroclastic rocks. The confining pressure values were correlated to both the NPI and estimated UCS values. The evaluation of the results revealed that, in comparison to the unconfined values, the increases in the NPI and UCS were roughly 100% for the stress level of 4 MPa. For the various confining pressure levels, the NPI and UCS values could be estimated using the derived correlations or equations. The results of the study fill a literature gap and can be applied to rock engineering project design.

It was concluded that the NPI and UCS values of pyroclastic rocks are significantly affected by confining pressure. This issue should be taken into account when designing underground rock engineering projects.

References

Aydan O (2012) The inference of physico-mechanical properties of soft rocks and the evaluation of the effect of water content and weathering on their mechanical properties from needle penetration tests. Symposium of ARMA, Chicago, Paper No. ARMA12- 639 (on CD).

Aydan O, Ulusay R (2013) Geomechanical evaluation of Derinkuyu antique underground city and its implications in geoengineering. Rock Mech. Rock Eng.46:.731–754. https://doi.org/10.1007/s00603-012-0301-7

Aydan O, Sato A, Yagi M (2014) The inference of geo-mechanical properties of soft rocks and their degradation from needle penetration tests. Rock Mech. Rock Eng. 47: 1867–1890. https://doi.org/10.1007/s00603-013-0477-5

Aydan O, Seiki T, Ito T, Ulusay R, Yuzer E (2006) A comparative study on engineering properties of tuffs from Cappadocia of Turkey and Oya of Japan. Proceedings of the Symposium on Modern Applications of Engineering Geology, Turkish National Group of Engineering Geology, Denizli-Turkey.

Aydan O, Watanabe S, Tokashiki N (2008) The inference of mechanical properties of rocks from penetration tests. Proceedings of the 5th Asian Rock Mechanics Symposium (ARMS5), Tehran-Iran.

Erguler ZA,Ulusay R (2007) Estimation of uniaxial compressive strength of clay-bearing weak rocks using needle penetration response. Proc. 11th Congress on International Society for Rock Mechanics, Lisbon.

ISRM (2015) The ISRM suggested methods for rock characterization, testing and monitoring: 2007-2014. Cham, Switzerland: Springer

Kahraman S, Aloglu AS, Aydın B, Saygın E (2017) The needle penetration test for predicting coal strength. J. South Afr. Inst. Min. Metall.117: 587-591. http://dx.doi.org/ 10.17159/2411-9717/2017/v117n6a9

Kahraman S,Rostami M,Saygın E (2018) The Needle Penetration Index Test to Estimate the Performance of Transverse Type Roadheaders. 4th Int. Symp. on Underground Excavations, 13-14 September, Istanbul.

Kahraman S, Aloglu A S, Aydın B, Saygın E (2019) The needle penetration index to estimate the performance of an axial type roadheader used in a coal mine. Geomech. Geophys. Geo-energ. Geo-resour. 5: 37–45.https://doi.org/10.1007/s40948-018-0097-3

Kahraman S, İnce İ (2023) The needle penetration index for estimating the physico-mechanical properties of pyroclastic rocks. J. South. Afr. Inst. Min. Metall. 123: 463-469. https://doi.org/10.17159/2411-9717/1433/2023

Okada S, Izumiya Y, Iizuka Y, Horiuchi S (1985) The estimation of soft rock strength around a tunnel by needle penetration test. J. Jpn. Soc. Soil Mech. Found. Eng.33(2): 35–38 (in Japanese). https://jglobal.jst.go.jp/en/detail?JGLOBAL_ID= 200902065506608500

Park Y, Obara Y,Kan SS (2011) Estimation of uniaxial compressive strength of weak rocks using needle penetrometer. Proc. 12th ISRM International Congress on Rock Mechanics, Beijing, China.

Rabat Á, Cano M, Tomás, R (2020) Evaluation of Strength and Deformability of Soft Sedimentary Rocks in Dry and Saturated Conditions Through Needle Penetration and Point Load Tests: A Comparative Study. Rock Mech Rock Eng 53: 2707–2726 (2020). https://doi.org/10.1007/s00603-020-02067-6

Rostami M, Kahraman, S, Dibavar B, Fener M (2024) Performance Prediction of Roadheaders Used in Coal Mines from the Needle Penetration Index and the Schmidt hammer value. Geomech. Geophys. Geo-energ. Geo-resour. 10:50.https://doi.org/10.1007/s40948-023-00725-x

Takahashi K, Noto K, Yokokawa I (1988) Strength characteristics of Kobe formation in Akashi Strata (No. 1). Proceedings of 10th Japan National Conf. on Geotech. Eng., The Japanese Geotechnical Society, Japan.

Uchida N, Etoh Y, Ono H, Miura,N (2004) Strength evaluation of deep mixing soil–cement by needle penetration test. J. Jpn. Soc. Soil Mech. Found. Eng. 52(7): 23–25 (in Japanese).https://jglobal.jst.go.jp/en/detail?JGLOBAL_ID=200902252009754068

UlusayR, Erguler ZA (2012) Needle penetration test: evaluation of its performance and possible uses in predicting strength of weak and soft rocks. EngGeol 149–150: 47–56.https://doi.org/10.1016/j.enggeo.2012.08.0

Yamaguchi Y, Ogawa N, Kawasaki M, Nakamura A, (1997). Evaluation of seepage failure response potential of dam foundation with simplified tests. J. Jpn. Soc. Eng. Geol. 38(3): 130–144.https://doi.org/10.5110/jjseg.38.130

Thermal Shock Sensitivity of Limestone Rock Under Rapid CO_2-Induced Cooling

Fawad Sheikh & Ákos Török
Department of Engineering Geology and Geotechnics, Faculty of Civil Engineering, Budapest University ofTechnology and Economics, Budapest, Hungary,
fawad@edu.bme.hu
0009-0009-2553-1821, 0000-0002-5394-4510

Abstract

Carbon dioxide (CO_2) is a major contributor of global warming. Reducing CO_2 emissions remain a major challenge, with several emerging solutions. Carbon capture and storage (CCS) is a viable option for reducing CO_2, either extracted directly from the atmosphere or captured from industrial processes. In CCS, CO_2 is collected from major emission sources and stored securely in deep geological formations such as depleted oil fields, deep coal seams, and saline aquifers. During the injection of CO_2, a transition from gas to liquid phase occurs, which is associated with rapid cooling. This sudden cooling results in internal stress in the rock environment. This process can fracture host rocks, produce induced seismicity and reduce the safety and security of storage sites. This study investigated the impact of cyclic thermal shock on the mechanical properties of limestone rock through laboratory testing. A total 24 limestone specimens were subjected to thermal treatment of up to 12 thermal shocks. Each cycle involved heating the sample for 2 hours in an oven 55°C and then placing this heated sample in a freezer at -17°C for 2 hours to simulate thermal shock associated with CO_2 injection. UCS and BTS tests were conducted at 0, 3, 6, 9, and 12 cycles, along with ultrasonic pulse velocity (UPV) measurements to monitor internal structural changes. The results showed a consistent decrease in tensile strength, with 42% decrease for 12 cycles of thermal shock. Whereas, compressive strength showed a slight decrease, indicating that the tensile strength of limestone is more sensitive to thermal shock cycles than compressive strength. Interestingly, UPV increased despite strength degradation, likely due to micro-pore closure and grain-contact rearrangement. Overall, the results showed that cyclic thermal shocks can weaken the limestone, specifically in tension, and should be considered while designing and monitoring of CO_2 storage in limestone reservoirs.

Keywords

Carbon Capture and Storage (CCS), Limestone, Rapid cooling, Heating.

1 Introduction

Global warming is one of the biggest challenges of the 21st century, and Carbon dioxide (CO_2) is the dominant driver behind it. The CO_2 emissions are a threat to human life and have resulted in the rise of global temperature, an increase in sea level, adverse climate conditions, and many natural disasters such as floods and droughts (Cheng et al., 2024). To mitigate this problem, it is essential to decarbonize the environment and store the CO_2 in long-term safe storage. Considerable research has been done to develop technologies for CO_2 storage. Among these, carbon capture and storage (CCS) is one of the most promising solutions and a practical solution for reducing CO_2 without affecting the industrial productivity (Celia, 2017).

Geological Storage of CO_2 (GSC) is one of the important parts of CCS in which CO_2 captured from major emission sources or the environment is stored securely in deep geological formations such as depleted oil fields, deep coal seams, and deep saline aquifers (Eyitayo et al., 2025). The process mimics the natural trapping mechanism through which oil and gas remain safely stored in underground rock formations for millions of years. Compressed CO_2 under high pressure is injected into the geological formations through injection wells. This process can lead to rapid cooling (Joule Thomson effect) of reservoir rock around the injection well due to expansion of injected CO_2 as it enters from high pressure system to low pressure reservoir (Mok et al., 2026). This rapid cooling causes the development of internal stresses in the rock and significantly affects the mechanical properties of the rock. Therefore, it is essential to investigate the mechanical behaviour of rock corresponding to this cooling.

Previous studies on the thermal response of cap rock and reservoir rock during CO_2 injection mostly relied on numerical modelling, with very few experimental studies. Vilarrasa et al. (2014) studied the effect of cold CO_2 injection on cap rock and reservoir stability over long-term operation using thermo-hydro-mechanical simulations. It was observed that cold CO_2 injection induces thermal stress changes that reduce the reservoir stability; on the other hand, it enhances cap rock stability. Similarly, this numerical study also demonstrated that although thermal stresses from cold CO_2 injection reduces the reservoir stability but enhances the cap rock integrity, and these stresses are unlikely to cause fracture propagation or leakage (Vilarrasa & Laloui, 2015). Using an elastoplastic thermomechanical model, this study simulated the cold CO_2 injection in deep saline aquifers and investigated under what conditions thermal stresses can jeopardize the cap rock integrity. Their results showed that cold injection induces inelasticity in the reservoir, but fractures do not propagate into the cap rock. Moreover, some localized yielding can occur in the lower portion of the cap rock; however, this damage is limited and does not compromise the cap rock's sealing ability (Vilarrasa & Laloui, 2016). In another study, numerical modelling was used to simulate how the temperature difference between the injected CO_2 and the reservoir influences the fracture propagation and damage. The study concluded that fracture growth during CO_2 is dependent on temperature and in-situ horizontal effective stress (Roy et al., 2018). Similarly this study used a thermoelastic 3D model to simulate cold CO_2 injection and its effect on fracture aperture growth in a field-scale reservoir. The findings of the study highlighted that contraction increases the fracture apertures within the reservoir but reduces them in the cap rock. The fracture behaviour is strongly dependent stress condition, orientation and proximity to the injection well. Overall thermal effects significantly influence fracture dynamics and integrity of the reservoir (Salimzadeh et al., 2018). In contrast to previous researches this experimental study evaluated the effect of rapid quenching on the core samples from Salah CO_2 storage site, Krechba field, Algeria. The samples were heated up to various temperatures (50, 150, 250, 350 and 500°C) and then rapidly quenched to room temperature 20°C. Permeability, along with P&S wave were measured before and after the thermal treatment. The study concluded that the effect of thermal shock at the Krechba field is negligible as the expected cooling (~65°C) caused insignificant changes in permeability and seismic velocities (Blake et al., 2022).

In this study, we aim to determine the effect of cyclic thermal shock on the mechanical properties of limestone reservoir rock through controlled laboratory experiments. The rock samples were heated up to 55°C and then rapidly cooled to -20°C to simulate the thermal conditions associated with cold CO_2 injection. The results of this study are expected to provide more comprehensive understanding of how repeated thermal shocks influence the stability and durability of limestone rock and help in the design and maintenance of the carbon storage sites in the long term.

2 Materials and Methods

A total of 30 limestone samples were used in this study. The limestone belongs to the Miocene porous limestone formation of the Budapest region (Hungary). Its micro-fabric is primarily an ooidal grainstone packstone. A total of 15 UCS and 15 BTS samples were prepared; 3 samples from each category were tested before the thermal shock cycles, whereas the remaining 24 samples are illustrated in Figure 1. Prior to thermal treatment, all samples were oven dried at 100°C for 24 hours to remove moisture. After drying the samples were cooled at room temperature before the start of cyclic thermal treatment.



Fig. 1 Porous limestone samples.

Cyclic thermal shock was applied to simulate the rapid cooling around the injection well bore outlet during CO_2 injection in geological formations. Each cycle consisted of two phases: heating and cooling. During the heating phase the samples were placed in an oven with 55°C temperature for 2 hours. After 2 hours, the heated samples were directly transferred to a freezer at -17°C temperature and the samples were cooled for 2 hours to simulate rapid cooling and induce stresses in the rock samples. After cooling, the samples were placed at room temperature for stabilization, and this sequence constituted one cycle. The heating temperature of 55°C was estimated for a representative of GCS site of 1500m depth by applying a typical geothermal gradient 30°C/ Km to a baseline surface temperature of 10°C. Moreover, the cooling temperature of -17°C was used due to laboratory constraints as the refrigerator in the laboratory could achieve only up to -17°C temperature. The duration of 2 hr was selected to ensure a uniform temperature distribution throughout the rock specimens.

The mechanical testing was done on five predefined stages corresponding to 0 (untreated), 3, 6, 9 and 12 thermal cycles. At each stage the ultrasonic pulse velocity along with weight was recorded for each sample. Moreover, at each stage three samples were tested for UCS and other 3 for BTS. The average of three samples was taken as representative strength for each phase. This phased approach was adopted to evaluate the progressive changes in the mechanical properties with increase in thermal shock cycles exposure. Uniaxial compressive strength tests were performed on the cylindrical specimens using a compression testing machine under controlled loading conditions. Load was applied axially at a constant rate until specimen failure, and the peak stress was recorded as the UCS. Brazilian tensile strength tests were conducted by applying diametrical compression to the disc specimens until failure occurred. The tensile strength was calculated from the peak load using standard formulations for the Brazilian test. The experimental results obtained from UCS and BTS were analysed to assess the influence of thermal cycles on the mechanical properties of limestone reservoirs. Variation in strength values across thermal cycles was evaluated to identify the trend of degradation.

3 Results and Discussion

3.1 Brazilian Tensile Strength

The variation of Brazilian tensile strength with thermal shock cycles is presented in Figure 2.The results clearly show a decreasing trend of tensile strength with an increase in thermal shock cycles. The untreated samples (0 cycles) exhibited the highest average strength, approximately 0.96 `. After 3 cycles average strength reduced to 0.88 MPa, which further declined to 0.79 MPa at cycles. A slight

increase in tensile strength is observed at 9 cycles (0.82 MPa). This deviation does not change the overall trend and can be attributed to natural heterogeneity in the limestone rock. After 12 cycles, the strength significantly dropped to 0.56 MPa, representing an overall reduction of 42% tensile strength.

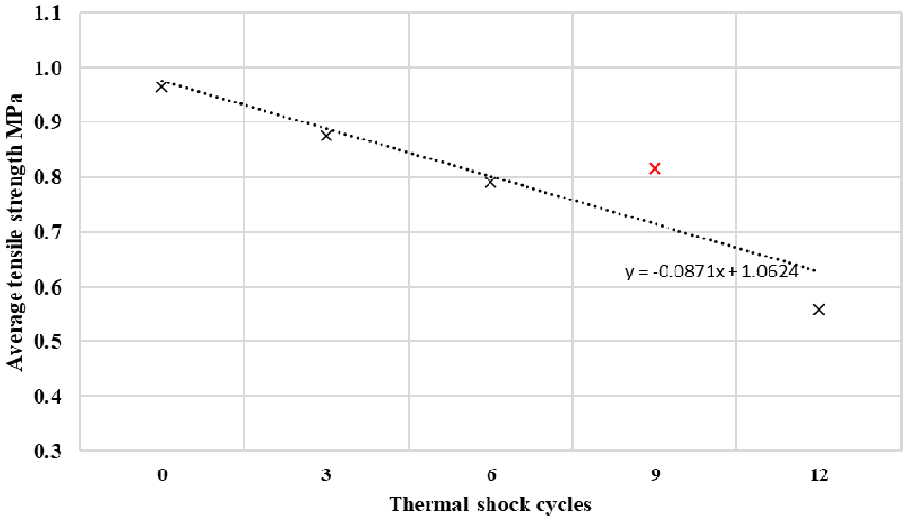


Fig. 2 Variation of tensile strength with thermal shock cycles.

3.2 Unconfined Compression Strength

The variation of compressive strength with thermal cycles is shown in Figure 4. The results overall show a decrease in UCS strength with an increase in thermal shock cycles. The untreated samples exhibited the highest strength of 5.24 MPa, which decreased slightly after the first three cycles to 5.17 MPa. Similarly, the strength again decreased to 4.86 MPa after 6th cycle. However, on 9th cycle significant decrease in strength to 2.99 MPa was observed, and after the 12th cycle, the strength was regained up to 4.25 MPa. The large reduction in strength at the 9th cycle was abnormal to the trend, and possible reason could be some pre-existing defects or cracks in the samples. Overall, the trend shows a gentle decrease in the UCS strength with an increase in thermal shock cycles.

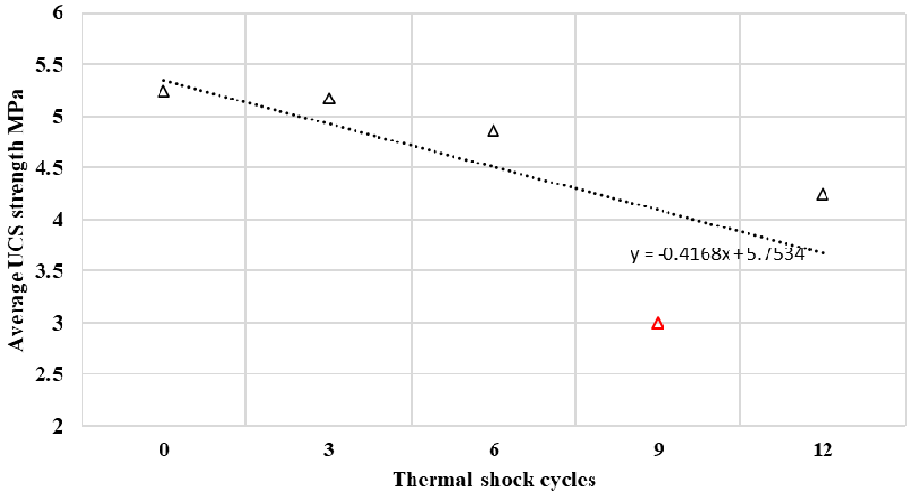


Fig. 3 Variation of UCS strength with thermal shock cycles.

The variation of ultrasonic pulse velocity (UPV) with thermal cycles is presented in Figure 3. The results show a general increase in velocity with an increase in the number of thermal cycles. This trend appears inconsistent to the degradation of strength in BTS and UCS. The possible explanation for it could be that repeated heating and cooling can cause partial closure or rearrangement of micro-pores and grain contacts, improving wave transmission locally even though the overall mechanical strength decreases. Further detailed investigation is required to evaluate this anomaly.

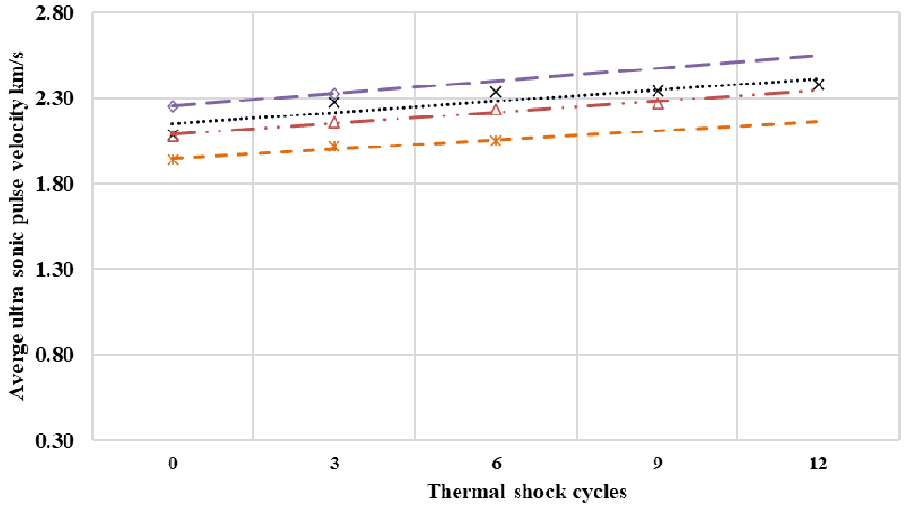


Fig. 4 Variation of ultrasonic pulse velocity with thermal shock cycles.

The failure plane angles after the UCS test showed major variations (Figure 5). It is clearly visible from the Figure that the failure plane progressively shifted towards steeper orientations. Particularly at higher cycles 9 and 12 cycles the failure plane appeared more vertical, indicating a transition towards axial splitting and tensile dominant failure. This change in failure mechanism suggests that cyclic thermal shock cycles induce micro cracks in limestone and reduce its cohesion.

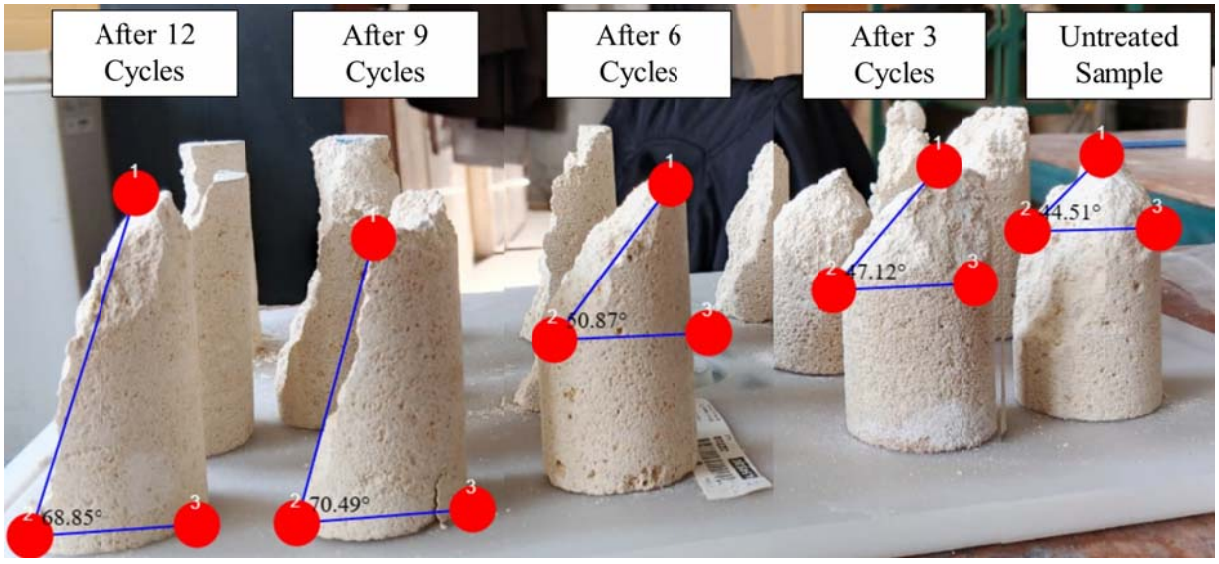


Fig. 5 Fracture patterns and corresponding failure angles observed in limestone specimens after rapid CO_2 cooling.

While the experimental result provides useful insightful into the thermal shock sensitivity of limestone rock. However, it is important to highlight that experiments in this study were conducted in laboratory do not completely represent the in situ thermo-mechanical environment of deep geological storage site. Future studies should investigate the thermomechanical behaviour under in situ stress conditions and field representative temperatures to simulate actual reservoir conditions.

4 Conclusions

This study investigated the effect of thermal cyclic shock associated with CO_2 injection on the mechanical behaviour of limestone rock. Based on experimental results of UCS and BTS along with UPV following conclusions can be drawn:

I. The tensile strength of limestone degrades progressively with the increase in thermal cycles. 42% reduction in tensile strength was observed after 12cycles of thermal shocks. This indicates that even moderate cyclic thermal shocks can weaken the limestone in tension

II. UCS strength also showed a declining trend with an increase in thermal cycles; however, degradation was very less compared to tensile strength. Overall, the compressive strength of limestone is less sensitive to thermal shock cycles.

III. UPV increased slightly with an increase of thermal shock cycles, which is inconsistent with the degradation of UCS and BTS and requires further investigation.
IV. Visual observation of failed UCS specimen indicate that the failure plane shifts from inclined to vertical, showing that the failure mechanism changes from shear to tensile failure with an increase in thermal shock cycles.

Overall, this study highlights that even cyclic thermal shock with moderate temperature can significantly affect the mechanical behaviour of limestones. Therefore, thermal shock effects should be considered in the design and monitoring of CO_2 storage in limestone reservoirs.

References:

Blake, O. O., Faulkner, D. R., Worden, R. H., Armitage, P. J., & Espie, A. A. (2022). Effect of thermal shock on the permeability and seismic wave velocity of the caprock and reservoir during CO2 injection. International Journal of Greenhouse Gas Control, 118, 103691. https://doi.org/10.1016/j.ijggc.2022.103691

Celia, M. A. (2017). Geological storage of captured carbon dioxide as a large-scale carbon mitigation option. Water Resources Research, 53(5), 3527–3533. https://doi.org/10.1002/2017WR020841

Cheng, L., Abraham, J., Trenberth, K. E., Boyer, T., Mann, M. E., Zhu, J., Wang, F., Yu, F., Locarnini, R., Fasullo, J., Zheng, F., Li, Y., Zhang, B., Wan, L., Chen, X., Wang, D., Feng, L., Song, X., Liu, Y., … Lu, Y. (2024). New Record Ocean Temperatures and Related Climate Indicators in 2023. Advances in Atmospheric Sciences, 41(6), 1068–1082. https://doi.org/10.1007/s00376-024-3378-5

Eyitayo, S., Arbad, N., Okere, C., Gamadi, T., & Watson, M. (2025). Advancing geological storage of carbon dioxide (CO2) with emerging technologies for climate change mitigation. International Journal of Environmental Science and Technology, 22(6), 5023–5056. https://doi.org/10.1007/s13762-024-06074-w

Mok, J., Sum, A. K., Kini, R., Teixeira, A., Valim, L. S., & Kane, M. (2026). Differentiating cooling effect for CO2 systems on pressure changes in Joule-Thomson expansion and volume expansion: Implications in CCS. Applied Thermal Engineering, 293, 130509. https://doi.org/10.1016/j.applthermaleng.2026.130509

Roy, P., Morris, J. P., Walsh, S. D. C., Iyer, J., & Carroll, S. (2018). Effect of thermal stress on wellbore integrity during CO2 injection. International Journal of Greenhouse Gas Control, 77, 14–26. https://doi.org/10.1016/j.ijggc.2018.07.012

Salimzadeh, S., Paluszny, A., & Zimmerman, R. W. (2018). Effect of cold CO2 injection on fracture apertures and growth. International Journal of Greenhouse Gas Control, 74, 130–141. https://doi.org/10.1016/j.ijggc.2018.04.013

Vilarrasa, V., & Laloui, L. (2015). Potential fracture propagation into the caprock induced by cold CO 2 injection in normal faulting stress regimes. Geomechanics for Energy and the Environment, 2, 22–31. https://doi.org/10.1016/j.gete.2015.05.001

Vilarrasa, V., & Laloui, L. (2016). Impacts of Thermally Induced Stresses on Fracture Stability During Geological Storage of CO2. Energy Procedia, 86, 411–419. https://doi.org/10.1016/j.egypro.2016.01.042

Vilarrasa, V., Olivella, S., Carrera, J., & Rutqvist, J. (2014). Long term impacts of cold CO2 injection on the caprock integrity. International Journal of Greenhouse Gas Control, 24, 1–13. https://doi.org/10.1016/j.ijggc.2014.02.016

Replica-based experimental framework for characterizing fluid flow in a dislocated fracture

S. L. Vidanage, M. Torkan, M. Janiszewski, M. Rinne & L. Uotinen
Department of Civil Engineering, School of Engineering, Aalto University, Espoo, Finland
sandaru.liyanarathnavidanage@aalto.fi
0009-0002-2790-0589

Abstract

Fractures significantly impact fluid flow in rock masses and comprehending how dislocations influence fracture-controlled flow is important for evaluating fluid movement in geological engineering applications, particularly for the long-term safety of geological nuclear waste disposal sites.

In this method, A 6 cm × 6 cm × 10 cm Kuru granite specimen containing an induced tensile fracture was scanned using photogrammetry. Photogrammetry was used to capture the fracture surfaces and aperture geometries of the perfectly matched state and each dislocation step of the specimen's upper half, using markers with known distances to accurately align and scale the dislocated surfaces.

The 3D models of the upper and lower surfaces of the physical aperture were then modelled for each dislocation step and reproduced using Fused Deposition Modelling (FDM) 3D printing. The printed aperture models incorporated an inlet and outlet to allow fluid flow testing within a fully watertight assembly, enabling precise measurements through accurately replicated apertures. This configuration provided controlled experimental conditions and enhanced the reliability and precision of the flow data. A custom fluid-flow apparatus was developed to measure flow rates through the replicas at varying water pressures, enabling experimental examination of the effects of dislocation on fluid-flow behaviour. Further results were evaluated through the Forchheimer equation for hydraulic aperture calculation.

The fluid flow tests revealed that increasing fracture dislocation results in higher flow rates, following a nonlinear relationship with the pressure gradient and leads to increased hydraulic apertures up to the tested limit of 5 mm dislocation. However, limitations related to the replication of fracture surfaces and physical apertures in 3D printing and photogrammetry must be assessed to ensure the accuracy of the results.

Keywords

Fracture, Dislocation, Fluid flow, Photogrammetry, 3D printing.

1 Introduction

Fractures play a key role in determining the mechanical strength and fluid flow characteristics of rock masses. The behaviour of fluid flow through fractures can be studied either at the scale of single fractures or across a rock mass with many interconnected fractures. Ultimately, the overall conductivity of a rock mass depends on how well the fractures are connected and on the hydraulic properties of each fracture (Hakami 1995). A thorough understanding of single-fracture behaviour is necessary before interpreting the behaviour of fractured rock masses (Hakami and Larsson 1996).Darcy's law, which assumes linear flow, often fails to accurately capture flow behaviour in rock fractures with rough and non-parallel surfaces. This is because natural fractures exhibit complexities such as surface roughness, matedness, variations in physical aperture, and contact areas. These factors lead to deviations from Darcy flow, resulting in nonlinear flow behaviour (Zimmerman et al. 2004).

The Forchheimer lawis widely used to describe the fluid flow through porous media, and it is generally accepted to explain the nonlinear fluid flow behaviour through roughed rock fractures (Zimmerman et al. 2004). Therefore, nonlinear fluid flow through a rock fracture with rough and non-parallel surfaces can be described using the adaptation of Forchheimer's equation (Eq. 1) and is characterised by the term hydraulic aperture (e_h), which is defined as the equivalent aperture between two smooth parallel flat plates that would permit the same flow rate with laminar flow, assuming that the flow follows Darcy's law under an identical pressure gradient.

$$-\nabla P = \left(\frac{12\mu}{we_h^3}\right) Q + \left(\frac{\beta\rho}{w^2 e_h^2}\right) Q^2 \#(1)$$

$$-\nabla P = \frac{\Delta P}{L} \#(2)$$

Here, Q denotes the flow rate (m^3/s), and ∇P is the pressure gradient (Pa/m). The hydraulic aperture is given by e_h (m), while μ is the dynamic viscosity of water (8.90×10^{-4} Pa·s), and w is the fracture width (m). The density of water is represented by ρ (997 kg/m^3), and β denotes the non-Darcy coefficient (1/m). The pressure drop across the fracture length L (m) in the direction of flow is expressed as ΔP.

However, investigating fluid flow using natural rock specimens presents several challenges, especially when fractures have dislocations and complex geometries that are difficult to replicate with precision. Experimental studies are further constrained by specimen size, limitations in testing equipment, and difficulties in controlling fracture geometry. In addition, achieving identical experimental conditions is challenging, which reduces the repeatability of results. To overcome these issues, a method integrating high-resolution photogrammetry, 3D modelling, and 3D printing has been developed in this study. This approach enables the production of accurate fracture replicas with controlled dislocations, allowing fluid flow to be studied under both aligned and dislocated fracture conditions.

Photogrammetry is widely applied to characterise rock fracture geometries and evaluate their hydro-mechanical behaviour (Uotinen et al. 2020). It provides a means to reconstruct individual fracture surfaces in detail, enabling assessment of surface roughness and physical aperture. In addition, this approach has been developed to reconstruct both halves of a fractured rock specimen within a unified coordinate system, ensuring accurate spatial alignment (Torkan et al. 2024). Among 3D printing methods, Fused Deposition Modelling (FDM) is widely used to replicate the joint and fracture features of rock masses with high geometric accuracy. 3D printing in rock mechanics enables controlled and repeatable experiments by producing uniform rock replicas while preserving the original specimens. It also enables the creation of complex geometries, reducing the variability found in natural samples for more controlled experimental studies (Jiang and Zhao 2015).

2 Methodology

2.1 Preparation of the specimen and photogrammetry

A Kuru granite specimen measuring 6 cm × 6 cm × 10 cm was divided into upper and lower halves using the plug-and-feather technique to produce a tensile fracture. The different sides of the specimen, as well as the upper and lower fracture surfaces, were marked with lines for identification. The number of lines indicates the respective side number, ranging from 1 to 4(Fig. 1).



(a) (b) (c)

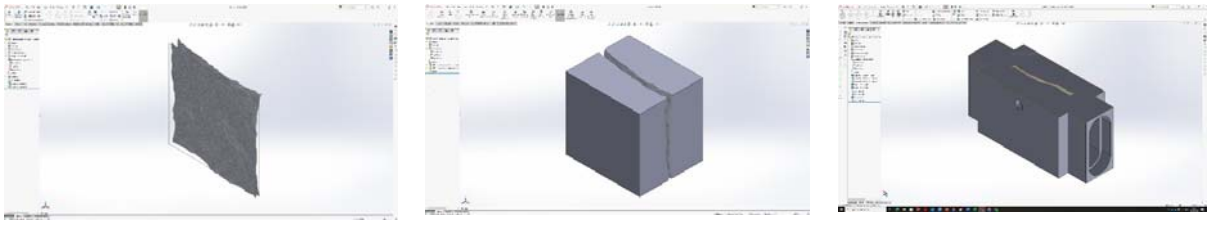
Fig. 1 The Kuru granite specimen with dimensions of 6 cm × 6 cm × 10 cm: (a) in perfectly matched position, (b) the lower half, and (c) the upper half (Torkan *et al.*, 2025).

Photogrammetry was used to generate high-resolution 3D models of the fractured surfaces in both perfectly matched (non-dislocated) and dislocated states. For the dislocated cases, the upper half of the specimen was shifted in the ±X and ±Y directions by 1, 2, 3, 4, and 5 mm (Fig. 4b-c). These displacements were measured using a calliper with a 10 µm resolution. A series of overlapping images was processed in RealityCapture software to produce scaled and properly oriented 3D point clouds for both the matched and dislocated configurations. The accuracy of the models was assessed using root mean square error (RMSE) analysis based on known distances between predefined markers and ceramic calibration blocks of fixed dimensions placed around the specimen. The accuracy assessment yielded RMSEs of 36µm for scale bars and 16-60 µm for ceramic blocks. The detailed description of the photogrammetry workflow, 3D reconstruction process, and accuracy evaluation is provided in a previous study, where the physical aperture of the dislocated fracture in the same specimen was also determined using the same high-resolution photogrammetric method (Torkan et al. 2025).

2.2 3D Modelling of physical aperture of non- and dislocated fracture

After reconstruction and texturing in RealityCapture, the 3D point clouds of the upper and lower halves were exported in *.xyz format and then imported into CloudCompare software. Within CloudCompare, the rough fracture surfaces of each half were trimmed to remove non-essential regions. These cropped surfaces were subsequently used to reconstruct both the dislocated and perfectly matched fracture models in a common coordinate system. For 3D printing of rough surfaces with physical aperture, the point clouds of the upper and lower specimen surfaces, both individually and combined, were meshed using CloudCompare. The resulting surface meshes were then exported in *.ply format for further processing in SOLIDWORKS software.

In SOLIDWORKS, the upper and lower surfaces of the aperture were created as two separate components. First, the imported upper or lower surface of the physical aperture was scaled and re-meshed within the software (Fig. 2a). The mid-surface of the mesh was then used as the reference plane, and the geometry was symmetrically extruded in both directions to form a solid body. After extrusion, the “Cut with Surface” feature was applied to emboss the fracture surface while obtaining the respective halves in the accurate orientation (Fig. 2b). The resulting halves were then assembled, maintaining a 0.4 mm separation between the upper and lower surfaces (Fig. 2c). This spacing was introduced to avoid underestimation of the physical aperture caused by potential nozzle interference during the 3D printing process (Fig. 7a).



(a) (b) (c)

Fig. 2 Modelling of the physical aperture: (a) Imported fracture surfaces after scaling and remeshing; (b) Assembly of the reconstructed upper and lower fracture surfaces; (c) Final assembly of the fracture model, including connector openings.

2.3 3D Printing of physical aperture of non- and dislocated fracture

Each 3D-printed physical aperture model, representing either a perfectly matched or dislocated specimen, was fitted with inlet and outlet connectors for the intended flow direction of the experiment (Fig. 3a). This design was developed to ensure a fully watertight test assembly, enabling accurate fluid flow measurements through a precisely replicated physical aperture of both perfectly matched and dislocated fractures. The aim was to obtain more reliable data under controlled conditions in a simpler

and more accurate testing procedure. The final model, including the connectors, was then exported for 3D printing in *.3mf format using the "Print 3D" function with high-quality settings, ensuring a fully watertight printable object.

Ultimaker Cura 5.7.2 was used as the slicing software for 3D printing, with customised parameters as listed in Table 1. The model was oriented so that one side of the aperture surface was placed directly on the build plate. The printing was performed using an Ultimaker 3 Extended Fused Deposition Modelling (FDM) printer equipped with an AA 0.25 mm nozzle. Polyethylene terephthalate glycol-modified (PET-G) was used as the printing material.

Table 1. 3D printing parameters and settings used.

Parameter	Value	Notes
Layer height	0.050 mm	Quality
Line width	0.25-0.26 mm	Quality
Print speed	55 mm/s	For PET-G
Nozzle temperature	235 ℃	For PET-G
Build plate temperature	85 ℃	For PET-G
Build plate temperature initial layer	90 ℃	For PET-G
Z seam alignment	Random	Walls
Build plate adhesion type	None	-
Remove all holes	Enable	Mesh fixes
Maximum resolution	0.02 mm	Mesh fixes
Enable fluid motion	disable	Mesh fixes
Slicing tolerance	Middle	Experimental

2.4 Fluid flow test

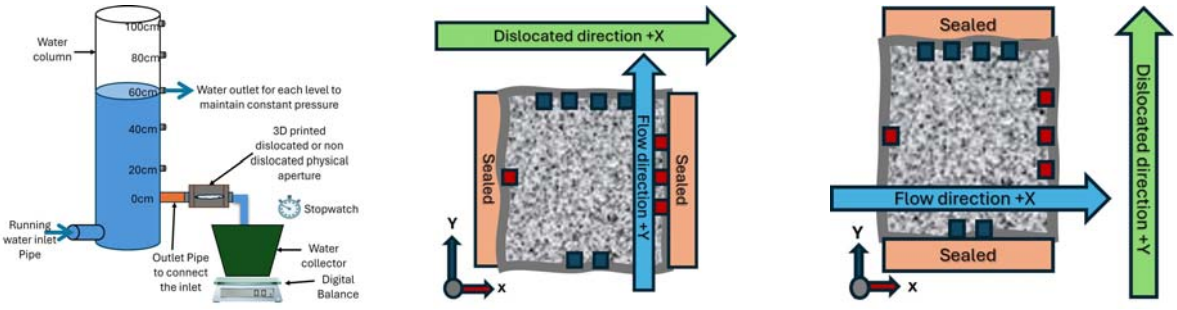
The fluid flow testing setup comprised a water column fitted with a custom-designed outlet pipe (Fig. 3b), which was connected to the inlet connector of the 3D-printed physical aperture model (Fig. 3a). The pipe system was designed to maintain uniform internal dimensions along the entire connection to ensure consistent flow conditions.



(a) (b)

Fig. 3(a) 3D-printed physical aperture model equipped with two connectors; (b) Outlet pipefitted to the water column.

A continuously running tap supplied the water column to ensure a steady and controlled flow of water. A constant pressure was maintained by varying the vertical distance between the water level at the model inlet and the water level in the column (Fig. 4a). For each experimental configuration, this height difference was adjusted in increments of 20 cm during the flow tests. At each 20 cm pressure step, the mass of water discharged from the outlet connector was collected over a fixed time period and measured using a digital balance with a precision of 0.1 g. The 3D-printed physical aperture models were used to conduct fluid flow experiments for different steps of dislocation, applied perpendicular to the flow direction, under varying pressure gradients. (Fig. 4b-c).



(a) (b) (c)

Fig. 4 (a) Schematic diagram of the fluid flow test apparatus and experimental setup; (b) Dislocation of the upper half of the specimen in the +X direction and fluid flow through the fracture in the +Y direction; (c) Dislocation of the upper half of the specimen in the +Y direction and fluid flow through the fracture in the +X direction.

3 Results and discussion

Fig. 5 shows the nonlinear relationship between volumetric flow rate (Q) and hydraulic pressure gradient (∇P) for the 3D-printed aperture models under both perfectly matched and displaced conditions. As anticipated, the flow rate increased with increasing pressure gradient. In addition, higher dislocation levels produced greater flow rates at the same pressure gradient. For further analysis, the data were fitted to the Forchheimer equation (Eq.1), and the hydraulic aperture (e_h) was calculated. These values were then compared with the corresponding physical apertures (e_m) of the rock specimen obtained in the previous study (Torkan et al. 2025). The results show that the hydraulic aperture increases with each increment of dislocation, consistent with the increase in physical aperture. This behaviour can be explained by the fact that increasing dislocation enlarges the physical aperture, which may also increase the hydraulic aperture, leading to enhanced fluid flow through the dislocated rough fracture. The results further indicate anisotropic flow behaviour, as both the measured flow rates and the derived hydraulic apertures depend on the magnitude of the dislocation and the flow direction (Fig. 5 and Fig. 6).

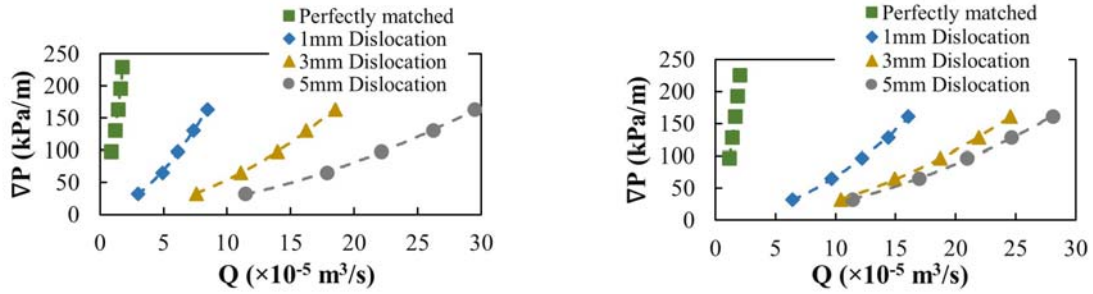


Fig. 5 Nonlinear relationship between flow rate and pressure gradient at dislocation levels:(a) Dislocation in the +X direction and fluid flow in the +Y direction; (b) Dislocation in the +Y direction and fluid flow in the +X direction.

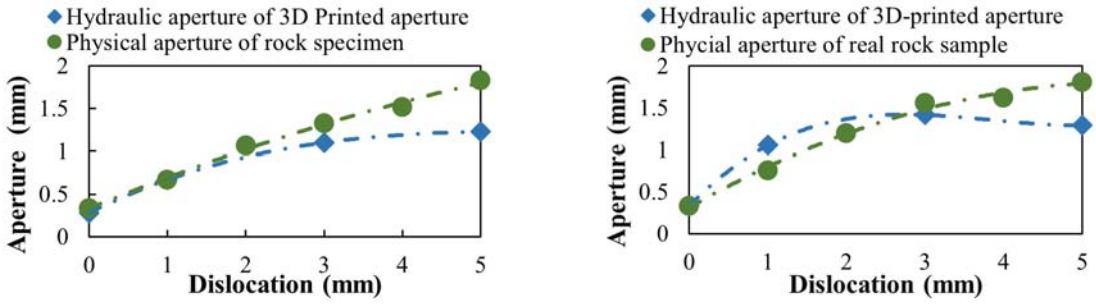


Fig. 6 Comparison between the physical apertures of the rock specimen and the hydraulic apertures of 3D printed apertures for various dislocation configurations:(a) Dislocation in the +X direction and fluid flow in the +Y direction; (b) Dislocation in the +Y direction and fluid flow in the +X direction.

The roughness of 3D-printed replicas may differ from that of real rock specimens due to constraints in 3D printing and photogrammetry. Fine-scale surface details of natural fractures may not be fully captured because of image resolution limits and processing constraints in photogrammetry. Similarly, in FDM 3D printing, additional loss of detail can occur due to the layer height and extrusion width. The resolution of printed surfaces can also vary in the horizontal and vertical directions depending on how the model is oriented on the build plate, while slicing tolerances may further influence the accuracy of the final geometry (Fig. 7b). Collectively, these factors generally result in smoother fracture surfaces compared to natural rock, which can lead to increased flow rates. In addition, introducing a uniform 0.4 mm gap between the fracture surfaces in the 3D-printed aperture may help improve replication accuracy, although the optimal gap size may vary depending on the degree of dislocation (Fig. 7a).

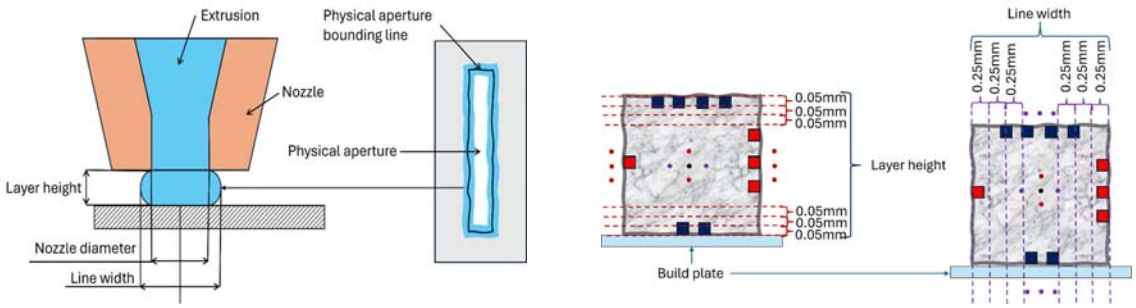


Fig. 7(a) Nozzle interference resulting in an undersized physical aperture; (b) Directional resolution variation in FDM 3D Printing: Influence of nozzle diameter and layer height (Liyanarathana Vidanage 2025).

4 Conclusion

A replica-based methodology integrating photogrammetry, 3D modelling, and FDM 3D printing was developed to investigate fluid flow behaviour in dislocated rock fractures under controlled and repeatable conditions. The experimental findings indicated that increasing fracture dislocation may lead to enlargement of both physical and hydraulic apertures, which in turn produces higher, nonlinear flow rates. Variations in flow behaviour further demonstrated anisotropic flow, influenced by both the extent and orientation of dislocation. Although limitations in photogrammetry and 3D printing resolution tend to smooth fine-scale fracture roughness, and the use of an optimal 0.4 mm gap may contribute to increased flow rates and hydraulic apertures in the replicas, the proposed framework remains effective for quantifying the impact of fracture dislocation on fluid flow. Overall, while photogrammetry-based reconstruction and 3D-printed models successfully reproduce key aperture characteristics and flow trends, challenges still exist in fully capturing the complexity of natural fracture geometries, especially under different dislocation conditions.

Acknowledgment

This work was a part of a master's thesis (Liyanarathana Vidanage 2025) at Aalto University and supported by the National Nuclear Safety and Waste Management Research Programme SAFER2028 (funding numbers SAFER 23/2025 MIRKAI, SAFER 32/2026 MIRKA II and DENSE). During the preparation of this work, the authors used ChatGPT to improve the language and readability. The authors reviewed and edited the content as needed and take full responsibility for the final publication.

References

Hakami E, Larsson E (1996) Aperture measurements and flow experiments on a single natural fracture. International Journal of Rock Mechanics and Mining Sciences & Geomechanics Abstracts 33(4):395-404. https://doi.org/10.1016/0148-9062(95)00070-4

Hakami E (1995) Aperture distribution of rock fractures. Doctoral thesis at Royal Institute of Technology.

Jiang C, Zhao GF (2015) A preliminary study of 3D printing on rock mechanics. Rock Mechanics and Rock Engineering 48(3): 1041–1050. https://doi.org/10.1007/s00603-014-0612-y

Liyanarathana Vidanage S (2025) Fluid flow tests for a non- and dislocated rock fracture of Kuru granite and its replicas. Master's thesis at Aalto University.

Torkan M, Janiszewski M, Uotinen L, Baghbanan A, Rinne M (2024) High-resolution photogrammetry to measure physical aperture of two separated rock fracture surfaces. Journal of Rock Mechanics and Geotechnical Engineering 16(8): 2922–2934. https://doi.org/10.1016/j.jrmge.2023.10.003

Torkan M, Liyanarathna Vidanage S, Aydogmus M, Uotinen L, Anttilainen A, Janiszewski M, Rinne M (2025) Measuring physical aperture of a fracture affected by dislocation using photogrammetry. ISRM International Symposium – EUROCK 2025, Trondheim, Norway.

Uotinen L, Torkan M, Janiszewski M, Baghbanan A, Nieminen V, Rinne M (2020) Characterization of hydro-mechanical properties of rock fractures using steady state flow tests. ISRM International Symposium – EUROCK 2020, Norsk Betongforening.

Zimmerman RW, Al-Yaarubi A, Pain CC, Grattoni CA (2004) Non-linear regimes of fluid flow in rock fractures. International Journal of Rock Mechanics and Mining Sciences 41(1): 163-169.https://doi.org/10.1016/j.ijrmms.2004.03.036

Validating Large-Diameter Bored Pile Design in Danian Limestone via Testing

Anna Wudzka
Ove Arup & Partners Danmark A/S, Copenhagen, Denmark
0009-0003-3540-4507

Adriana Hernandez-Guardado
Aarhus University, Aarhus, Denmark
Ove Arup & Partners Danmark A/S, Copenhagen, Denmark
adriana.hernandez@arup.com
0000-0001-8518-8310

Francesco Petrella
Ove Arup & Partners Danmark A/S, Copenhagen, Denmark
0009-0005-9952-908X

Abstract

This paper presents the case history of preliminary piles tested in Danian limestone as part of the design validation for large-diameter bored piles supporting the Kronprinsesse Marys Bro bridge crossing the Roskilde Fjord in Denmark. The project involved extensive geotechnical investigations and static load tests on two preliminary piles to assess shaft and base resistance in weak, highly variable limestone. The piles, with diameters up to 1.19 m and rock sockets of 5–8 m, were tested using bi-directional O-cell systems, providing direct measurement of load transfer and resistance mobilisation. A statistical analysis of more than 300 UCS tests revealed a significant strength variability, highlighting the importance of site-specific characterisation. The findings demonstrate that bored piles socketed in Danian limestone can achieve higher shaft and base resistances than currently permitted by the Danish National Annex to Eurocode 7. The proposed methodology enables the derivation of representative design parameters, advocating the use of percentile-based UCS values and empirical correlations tailored to local rock conditions. This case history provides valuable insights for practitioners and regulators, supporting the revision of Annex L of the Danish National Annex to Eurocode 7 to incorporate robust methods for estimating shaft and base resistance in soft rock.

Keywords

Danian limestone, Bored piles, Weak rock, Pile load testing, Eurocode 7.

1 Introduction

In Denmark, the resistance of bored, cast-in-place piles is constrained by provisions in the Danish National Annex to Eurocode 7 (DS/EN 1997-1 DK NA), which limit the shaft resistance that may be

adopted relative to comparable driven piles unless project-specific documentation is provided. Although originally introduced to address uncertainties associated with bored pile construction (Knudsen et al., 2019), these provisions often require justification when bored piles are installed in rock formations and may result in conservative foundation designs (Steenfelt, 2017). The increasing use of large-diameter bored piles in Danish projects therefore highlight the need for well-documented case histories demonstrating their performance.

The Kronprinsesse Marys Brobridge is a 1.4 km crossing of Roskilde Fjord, northwest of Copenhagen (Fig. 1a). The offshore piers are founded on large-diameter (1.5-2m) bored piles, approximately 25–50 m long, socketed into Danian limestone (Demeersman and Bauduin, 2019; Petrella and Wudzka, 2021). Owing to the variable strength and induration of the limestone, preliminary pile testing was undertaken during the design phase to validate the correlations adopted for estimating shaft and base resistance. Two preliminary piles were tested using bi-directional static load tests with Osterberg (O-cell) system, allowing direct assessment of load transfer and resistance mobilisation within the rock socket. This paper evaluates UCS-based prediction methods for shaft and base resistance of bored piles socketed in Danian limestone using results from preliminary O-cell tests and a statistically derived rock-strength characterisation. A percentile-based approach is proposed to derive representative design parameters for heterogeneous soft rock.

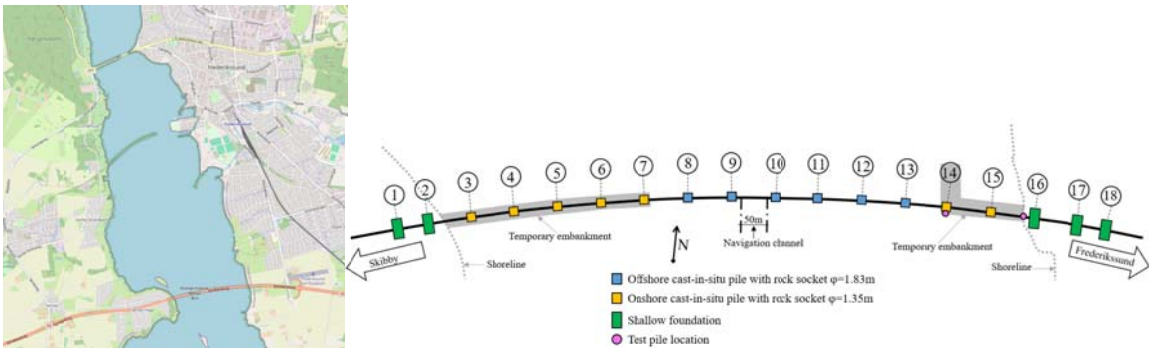


Fig. 1(a) Location of Kronprinsesse Marys Bro crossing Roskilde Fjord and (b) layout of bridge foundations and location of preliminary test piles TP1B and TP2 used for design validation.

2 Rock strength characterisation

The preliminary test piles were installed adjacent to two boreholes considered representative of the geological and geotechnical conditions across the project area. The piles are socketed in Danian limestone, whose strength is influenced by the degree of induration. Limestone cores, recovered from the boreholes with triple barrel core drilling,were described according to the engineering geological classification presented in DGF Bulletin 1 (Larsen et al., 1995), which distinguishes induration categories ranging from unlithified chalk to strongly indurated limestone.

Unconfined compressive strength (UCS) denoted as σ_c,was determined from laboratory testing of limestonecore samples. In total, more than 300 UCS tests were undertaken on specimens selected across all induration categories. The results exhibit significant variability reflecting the heterogeneous nature of the limestone and the occurrence of stronger beds within otherwise weaker material. The distribution of tests across the different induration classes and the corresponding strength ranges are summarised in Table 1. It is noted that no UCS tests were performed on H1 material due to its unlithified nature.

Table 1. Distribution of UCS tests from the D&B Contractor'sground investigation, average adopted by the Designer for each induration and proposed 50th percentile used in this study.

Induration Category	ISRM Rock Category	Description	No. of UCS tests	Range of results, σ_c (MPa)	Average σ_c (MPa)	50th Percentile σ_c (MPa)
H1	R0	Unlithified	-	-	1.3	-
H2	R1	Slightly indurated	59	0.80 – 21.96	6.4	5.7
H3	R2	Indurated	98	0.47 – 44.10	19.5	15.3
H4	R3, R4	Strongly indurated	84	2.90 – 87.00	27.7	29.6
H5	R5, R6	Very strongly indurated	22	1.60 –> 100.00	27.7	35.0

Two approaches for selecting representative UCS values were considered. In the deterministic approach adopted in the original design, representative UCS values were taken as the average strength measured for each induration category. For each pile, these values were assigned to the corresponding induration layers identified in the borehole log, forming a representative UCS profile along the rock socket.

Given the large scatter in the UCS results, a statistical evaluation of the dataset was also performed. The UCS distribution was analysed using both log-normal and kernel density estimators considering the full dataset of 319 test results, as shown in Fig. 2. Unlithified material (H1) and very strongly indurated material (H5) were treated using reference values proposed by Kryger Hansen and Foged (2002), as these materials are rarely tested due to sampling difficulties or testing limitations. The kernel distribution was found to best represent the UCS dataset, and representative UCS values were derived from the corresponding percentiles, with the 50th percentile values adopted for each in duration class (Table 1). These values are broadly comparable to deterministic averages but are less influenced by extreme results and thus provide a more robust representation of rock strength.

For both approaches, the representative UCS profile along the pile was then used for the resistance calculations. A weighted average UCS was calculated over the full length of the rock socket for shaft resistance calculations and over a distance equal to one pile diameter below the toe pile toe for base resistance calculations. The resulting representative values are illustrated in Fig. 3.

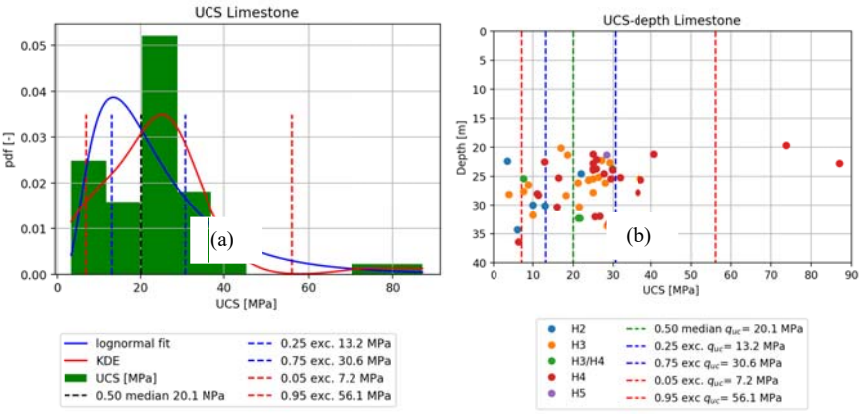


Fig. 2 Kernel/Lognormal density distributions of unconfined compressive strength (UCS, σ_c) Statistical description of the laboratory and borehole log data (a) histogram and (b) scatter data.

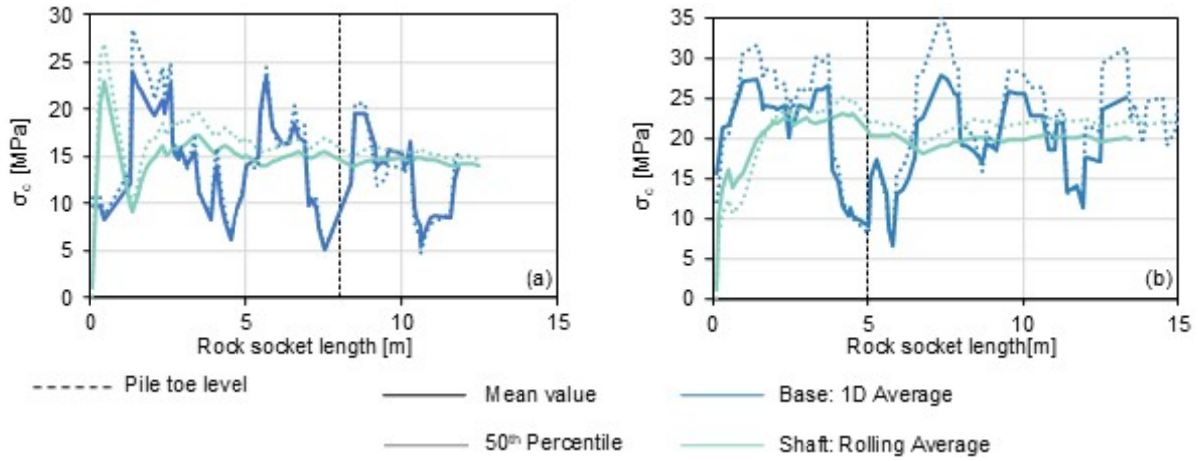


Fig. 3 Average of UCS over entire length (for shaft) and over 1D (for base) (a) TP1B and (b) TP2.

3 Prediction of rock socket resistance

The shaft and base resistance of the preliminary piles were estimated using empirical correlations commonly applied for bored piles socketed in rock. The unit shaft resistance was calculated using the formulation proposed by Zhang (2004), which relates the mobilised side shear resistance to the UCS of the intact rock, as described in Eq. 1.

$$\frac{R_{s;cal}}{A_{si}} = \eta_c \cdot \alpha \cdot {\sigma_c}^{\beta} \quad (1)$$

Where $R_{s;cal}$ Calculated shaft resistance
A_{si} Surfacearea of the pile within the considered layer
η_c Empirical factor, $\eta_c = 0.9$
α Empirical constant,$\alpha = 0.2$
σ_c Unconfined compressive strength of the rock
β Constant in Zhang equation, $\beta = 0.5$

The empirical parameters adopted correspond to values recommended for sockets in weak rock. The base resistance was estimated using the approach proposed by Serrano and Olalla (1994; 2002; 2014), summarized in Eq. 2, which relates the toe resistance to the unconfined compressive strength and rock mass parameters derived from the Hoek–Brown failure criterion.

$$\frac{R_{b;cal}}{A_b} = \frac{m \cdot q_u}{8} \cdot (N_\beta - \zeta) \cdot s \quad (2)$$

Where $R_{b;cal}$ Calculated base resistance
A_b Base surfacearea of the pile
m Parameters of the Hoek and Brown (1980) criterion, $m = 1.3$
N_β Load factor, $N_\beta = 6.7$
ζ Rock mass toughness coefficient, $\zeta = 0.006$
s shape factor, s = 1.5

4 Preliminary pile tests and results

The preliminary piles had diameters of approximately 1.19 m and rock socket lengths of 8.0 m for TP1B and 5.2 m for TP2. While smaller than the contract piles, the use of preliminary piles with different dimensions is permitted under EC7. The geometry of the test piles is summarised in Table 2. The piles were constructed using a rotary drilling rig with temporary casing installed through the soil deposits and soft limestone to the top of the competent limestone (Fig. 4a). The pile bore was filled with water during drilling. The pile base was cleaned using a cleaning bucket and sediments were removed by pumping prior to concreting. The reinforcement cage, incorporating the O-cell assembly and instrumentation, was installed immediately before casting using tremie concrete. Both piles were tested using bi-directional static load tests with O-cell systems installed approximately 1 m above the pile toe (Fig. 4b). The O-cell applies load in two directions, mobilising shaft resistance above the cell and base resistance together with shaft resistance below the cell. The applied loads and corresponding displacements were monitored using displacement transducers and vibrating wire strain gauges installed along the pile (Fig. 4c).

Maximum bi-directional loads of 44.75 MN and 32.7 MN were applied during the tests on TP1B and TP2, respectively. The O-Cell load with respect to displacement curves are shown in Fig. 5. These values are comparable to the predicted resistances of 43.8 MN and 26.8 MN obtained from the design calculations. The load test results were interpreted independently by the Designer and by the testing contractor (Fugro 2017a, 2017b). The interpretations differ slightly due to assumptions regarding pile geometry and stiffness used in the evaluation of the strain gauge measurements. The resulting shaft and base resistances derived from the load tests are compared with the predicted values in the following section.

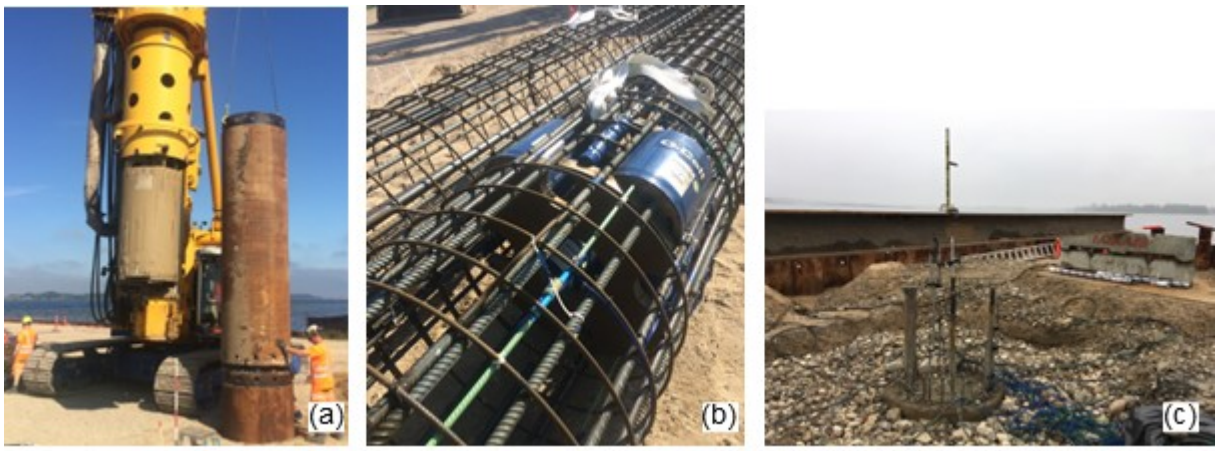


Fig. 4 (a) Drilling bucket used for construction, (b)reinforcement cage with installed O-cells and monitoring instrumentation, and (c) monitoring instrumentation at the top of the pile.

Table 2. Preliminary test piles geometry based on as-built data.

Preliminary pile ID	Platform level [mDVR90]	Pile top level [mDVR90]	Top of limestone [mDVR90]	Pile tip level [mDVR90]	Rock socket length [m]	O-cell base level [mDVR90]	Pile diam. in soil and rock [m]
TP1B	+1.0	+0.5	-19.7	-27.7	8.0	-26.7	1.19
TP2	+1.0	+0.5	-17.7	-22.9	5.2	-21.9	1.19

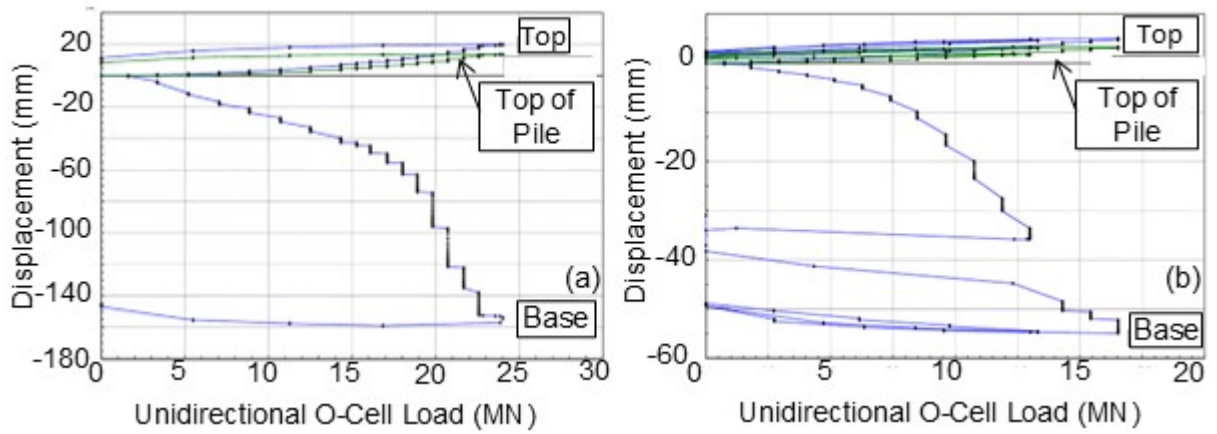


Fig. 5 O-cell load vs. displacement curves at the top and base level of the O-cell and recorded displacement at the top of pile for (a) TP1B and (b) TP2.

5 Comparison between predicted and measured resistances

The Designer evaluated the shaft and base resistances using the maximum upward and downward forces measured during the O-cell tests, assuming equal shaft resistance above and below the O-cell within the limestone. The upward load measured during the test was reduced by the shaft resistance mobilised in the overlying soil layers (5.0 MN for TP1B and 3.6 MN for TP2), which are not considered in the present study. The pile load test results were also interpreted independently by the testing contractor. Differences between the interpretations arise primarily from the assumed pile geometry and stiffness in the analysis. The Designer assumed a constant pile diameter of 1.19 m, whereas the testing contractor considered different diameters within the rock socket and the temporarily cased section in soil and explicitly accounted for pile stiffness in the interpretation.

Error! Reference source not found. compares the predicted unit shaft and base resistances with those derived from the load test interpretations. The predicted base resistance shows reasonable agreement with the values derived from the tests, whereas the measured shaft resistance is significantly higher than that predicted using the empirical correlation with the deterministic representative UCS values.

When representative UCS values derived from the statistical analysis are adopted, the predicted shaft resistance increases slightly. Furthermore, adopting empirical parameters within the range reported by Zhang (2004) for weak rock sockets results in predicted unit shaft resistances of approximately 1.4–1.5 MPa, which are consistent with the values interpreted from the load tests.The comparison indicates that the empirical prediction methods provide a reasonable estimate of the pile capacity when representative rock strength parameters and appropriate empirical factors are used.

For reference, the Danish National Annex L limits the design unit toe resistance of bored piles to 1 MPa, corresponding to a maximum design base resistance of approximately 1.1 MN (or 1.7 MN at characteristic level) for the tested pile diameters, which is lower than both the predicted and measured values.

Table 3. Comparison of UCS-based predictions with measured shaft and base resistances for test piles TP1B and TP2.

	TP1B				TP2			
Resistance	**Mean UCS**	**P50 UCS**	**Contractor**	**Designer**	**Mean UCS**	**P50 UCS**	**Contractor**	**Designer**
Shaft (MPa)	0.70	0.82	1.48	0.66	0.79	0.85	1.45	0.80
Base (MPa)	16.1	13.4	21.9	18.1	7.2	7.8	8.5	12.2

6 Conclusions

This study demonstrates the importance of statistically informed rock strength characterisation when designing bored piles socketed in heterogeneous weak rock. Analysis of a large UCS dataset showed significant variability in Danian limestone, for which percentile-based representative values provide a more robust basis for design than simple deterministic averages. Bi-directional O-cell testing confirmed that both shaft and base resistances mobilised in the limestone exceed conservative design assumptions, and that empirical prediction methods can provide reasonable estimates when appropriately parameterised using representative UCS values. The results highlight that the limitations of the current version of Annex L of the Danish National Annex to Eurocode 7 do not reflect the observed pile behaviour in Danian limestone and that documented testing combined with transparent parameter selection offers a defensible pathway for refining design resistance assumptions for bored piles in soft rock. Future works should include additional testing across a wider range of rock type.

References

Demeersman R, Bauduin Ch (2019) Validation of drilled shafts for a new bridge in Denmark, by means of a holistic approach, CSL testing and pile coring.17th ECSMGE, Reykjavik, 1-6 September 2019.

DS/EN 1997-1 DK NA:2021, National Annex to Eurocode 7: Geotechnical design - Part 1: General rules. 2021.

KrygerHansen H, Foged N (2002) Kalkens bjergmekaniske egenskaber. Dgf-Bulletin 19, dgf, 2002.

Fugro GeoServices Ltd(2017a) Report on bored pile load testing (Osterberg method) – TP1 (Pier 14) – Fjord Link Frederikssund (Roskilde) Bridge Denmark. Project no: FLT20299-2, 11 August 2017.

Fugro GeoServices Ltd(2017b) Report on bored pile load testing (Osterberg method) – TP2 (Pier 16) – Fjord Link Frederikssund (Roskilde) Bridge Denmark. Project no: FLT20299-2, 24July 2017.

Larsen G, Frederiksen J, Villumsen A, Fredericia J, Graversen P, Foged N, Knudsen B, Boumann J (1995) A guide to engineering geological soil description. Dgf-Bulletin 1, May 1995.

Petrella F, Wudzka A (2021) The geotechnical characterisation and foundation design of the Fjord Link Frederikssund bridge in Denmark. Nordic Geotechnical Meeting 2020, virtual conference, 18-19 January 2021

Serrano A, Olalla C (2002) Ultimate bearing capacity at the tip of a pile in rock - part 2 application. International Journal of Rock Mechanics & Mining Sciences (Issue 7), vol. 39: pp. 847-866.

Serrano A, Olalla C (2014) Ultimate bearing capacity at the tip of a pile in rock based on the modified Hoek-Brown criterion. International Journal of Rock Mechanics & Mining Sciences, vol. 71: pp. 83-90.

Serrano A, Olalla C (1994) Ultimate bearing capacity of rockmasses. International Journal of Rock Mechanics andMining Sciences& Geomechanics Abstracts (Issue 2), vol. 31: pp. 93-106.

Zhang L (2204) Drilled shafts in rock: analysis and design. 1st edition. CRC Press, London.

Development of a Rock-Type s Matrix for Using the Combined Compression and Shear Test System (C-CAST) for Design of Inclined Pillars

Doreen Kapiri & Fidelis T Suorineni
Nazarbayev University, Astana, Kazakhstan
fidelis.suorineni@nu.edu.kz

Abstract

The Hoek-Brown criterion is extensively employed in stability evaluations during underground mining, with m and s being the constants for friction and cohesion, respectively. Prior research has indicated that in massive rocks, damage initiation is primarily dependent upon loss of cohesion, which makes the s constant more significant. Although prior research indicated that s may differ from one rock mass type to another, it has been determined based on standard uniaxial compression tests. However, for inclined pillar design in dipping orebodies, the loading condition differs from standard uniaxial compression, and therefore the damage initiation stress cannot be determined from the standard uniaxial compression tests. To address this, this study applies the combined compression and shear test (C-CAST), developed for inclined pillar stability assessment, to determine more appropriate s values for different rock types. The resulting rock type-s values provide a more suitable basis for the design of inclined pillars under combined compression and shear loading conditions.

Keywords

Inclined pillars, s constant, Damage Initiation, Combined compression and shear test.

1 Introduction

1.1 Background

The stability of underground excavations is significantly influenced by the mechanical properties of the surrounding rock masses. One of the key parameters defining the strength of intact rocks is the unconfined compressive strength (UCS) of the rock, usually determined through the standard uniaxial compression tests. While the standard UCS is a key parameter defining rock strength, underground excavations are subjected to complex stress states, that are significantly different from the loading conditions of the standard uniaxial compression strength test loading conditions. The Hoek-Brown failure criterion (Equation (1)) developed by Hoek & Brown (1980) to address the limitations of intact rock and soil failure models is a popular empirical criterion in rock engineering used to determine rock mass strength and failure states. In Equation (1) the constants m and s represent the frictional and cohesive strength components of rock masses.

$$\sigma_1' = \sigma_3' + \sigma_c \sqrt{m\frac{\sigma_3'}{\sigma_c} + s} \quad (1)$$

$\sigma_1^{'}$ and $\sigma_3^{'}$ are the major and minor principal stresses at failure respectively, andσ_c is the uniaxial compressive strength of the intact rock. Previous studies have revealed that rock damage initiation is more significantly influenced by the cohesion component represented by constant s with friction playing little role.

Martin (1993) demonstrated that in massive rock masses with GSI ≥ 75, the friction component represented by constant m plays a limited role in damage initiation, hence m = 0.Thus, Equation (1) simplifies to Equation (2), making the cohesion component the controller of damage initiation in massive rock masses. Field monitoring and laboratory tests by Martin (1993) showed that $\sqrt{s}$ = 1/3 as shown in Equation (2) and (3), which implies the constant s = 0.11.

$$\sigma_1 - \sigma_3 = \sqrt{s}\sigma_c \quad (2)$$

$$\sigma_1 - \sigma_3 = \frac{1}{3}\sigma_c \quad (3)$$

Equation (3) implies that all massive brittle rocks have the same cohesion constant of 0.11. Studies by Suorineni et al., (2009) argued that the application of a single s-value may not accurately portray the behaviour of different rock types since the cohesion of rock depends on the mineralogy, bonding between grains, and rock texture. Therefore, Suorineni et al. (2009) proposed a modified form of the Brittle Hoek-Brown criterion (Equation (4)) in which the constant A is a rock-type-dependent s-value, similar to the rock-type-dependent m_i table in Hoek (2007).

$$\sigma_1 - \sigma_3 = A * \sigma_c \quad (4)$$

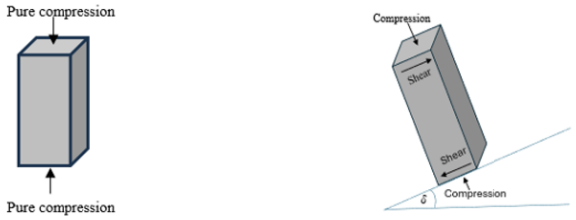
Based on Suorineni et al (2009) there has been an ongoing campaign to determine rock type specific s values for various rock types using the conventional standard uniaxial compression test.

In underground mining, not all pillars are vertical, especially in dipping orebodies where inclined pillars are commonly formed (Suorineni et al., 2011, 2014a). However, most conventional pillar design methods are based on vertical pillars in horizontal orebodies, which may not accurately represent the behaviour of inclined pillars (Suorineni, 2014b). Since inclined pillars are subjected to both normal and shear loading, their strength and stability differ from those predicted by standard uniaxial compressive strength (UCS) tests and conventional pillar strength equations (Ma et al., 2016). The use the standard UCS in the design of inclined pillars has contributed to several pillar failures worldwide, such as the domino pillar failure at Quirke Mine in Canada (Suorineni et al., 2014) and the collapse at Barro Branco coal mine in Brazil (Zingano, 2016), highlighting the need for improved design approaches for inclined underground pillars.

1.2 Vertical and Inclined Pillars

Pillars in underground mines are rock structures left in place to support the surrounding rock mass during mining. The design of pillars depends on several factors, including rock strength, pillar geometry, mining depth, and the in-situ stress field (Brady & Brown, 2006; Hoek, 2007). In horizontal or gently dipping orebodies, pillars are usually aligned with the direction of the vertical stress. These pillars are mainly subjected to compressive stress only, as shown in Fig. 1a, and are commonly

referred to as vertical pillars. The behaviour and strength of such pillars have been widely studied, and their strength is often related to the unconfined compressive strength (UCS) of the rock (Brady & Brown, 2006; Hedley & Grant, 1972). However, in inclined ore bodies, pillars are oriented at an angle to the direction of the vertical principal stress. As a result, these pillars are subjected not only to compressive stress but also to shear stress, as shown in Fig.1b. Such pillars are referred to as inclined pillars. The presence of shear stress can promote earlier crack initiation and reduce the effective strength of the pillar compared to vertical pillars (Suorineni et al., 2011, 2014a). This implies that inclined orebodies pillars behave differently from vertical pillars in horizontal or gently dipping orebodies. The conventional UCS test applies only axial compressive loading. Therefore, it may not fully capture the actual loading condition and failure behaviour of inclined pillars, which experience combined compressive and shear stresses during mining. The empirical pillar strength equations are among the most widely used methods for assessing pillar stability and are generally validated using laboratory testing, numerical analysis, and field experience from existing mines. Most of these equations relate pillar strength to the width-to-height ratio (W/H) of the pillar and the UCS of the intact rock (Hedley et al., 1984). Several such equations have been proposed for hard rock, as summarized in Table 1. The numerical coefficients in these equations represent the stress levels (σ_{ci}) at which crack initiation or damage initiated rather than complete failure (UCS) (Suorineni, 2013). The ratio of these coefficients (σ_{ci}) to UCS is $\sqrt{s}$, which varies for the various rock types. In some of the equations the coefficients are directly equal to $\sqrt{s}$, for example in Lunder and Pakalnis (1997) equation.



a) vertical pillars, b) Oblique loading of inclined pillars

Fig 1. Schematic of pillar orientations (after Potvin, 1985).

Table 1. Summary of empirical pillar strength equations for hard rocks (Suorineni 2013).

Equation	**Uniaxial compressive strength (σ_c MPa)**	**Rock type**	**Reference**	$\frac{\sigma_{ci}}{\sigma_c} = \sqrt{s}$	**Comments**
$133 = [W^{0.5}/H^{0.75}]$	230	Quartzite	Hedley et al. (1984)	0.58	Strength of a unit cube (1 m) from lab testing is taken as 133 MPa
$65[W^{0.46}/H^{0.66}]$	94	Metasediments	Kimmelmann et al. (1984)	0.69	-
$35.4\ [0.778 + 0.222\ (W/H)]$	100	Limestone	Krauland and Soder (1987)	0.35	-
$0.42\sigma_c\ [W/H]$	-	Canadian Shield	Potvin et al. (1989)	0.42	-
$74[0.778 + 0.222\ (W/H)]$	240	Limestone/skarn	Sjöberg (1992)	0.31	-
$\sigma_1 = \sigma_3 + \sqrt{s\sigma_c}$	224	Granite	Martin (1993)	0.33	-
$0.44\sigma_c\ [0.68 + 0.52\kappa]$	-	Hard rocks	Lunder and Pakalnis (1997)	0.44	-

2 Study areas and samples description

The core samples used in this study were obtained from two different mines located in Kazakhstan and Canada. The samples obtained from Kazakhstan are from a mine that features a porphyry copper deposit, characterized by the occurrence of intrusive igneous formations. These formations can be

classified as diorite, andesite, and hydrothermally altered volcanic and intrusive rocks - featuring alteration mineralogy such as sericitization and chloritization. The listed rocks are indicative of a brittle or semi-brittle regime and, thus, can be used to assess the characteristics of failure behaviour. The samples for this study were gabbro and andesite. The other set of samples which were diorite and dolerite were provided by a mine in the Sudbury Basin in Ontario. Sudbury Basin is one of the best-known asteroid impact-related geological formations that exhibit significant mineralisation of nickel-copper sulphides. All cores were selected based on lithological homogeneity and structural integrity, with specimens of through-going natural fissures, extensive weathering, or large veins removed from the test samples.

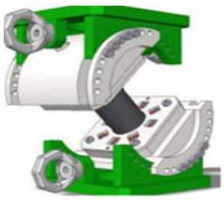
In hand specimen, the andesite is a dark grey porphyritic rock, consisting of large phenocryst of plagioclase feldspar. The gabbro sample is dark grey-to-dark green holocrystalline phaneritic rock with nearly completely sericitized plagioclase. The dolerite is a dark greenish-grey, fine-to-medium grained rock with a dense ophitic texture composed primarily of olivine, plagioclase, and pyroxene, with moderate alteration. Quartz-diorite is a light-to-dark grey, medium-to-coarse grained (phaneritic) rock with an interlocking crystalline fabric made up of plagioclase, hornblende, and quartz, with slight alteration.

3 Methodology

3.1 C-CAST Testing system

Most of the empirical pillar design equations assume vertical loading conditions, where pillars are subjected mainly to axial compressive stress. For dipping orebodies, where pillars are subjected to combined compressive and shear stresses, the failure behavior cannot be accurately estimated using such conventional approaches (Suorineni et al., 2009; Suorineni, 2014). This creates the need for a more suitable testing approach for inclined pillar design. To address this problem, the Combined Compression and Shear Test (C-CAST) (Fig. 2a) system was developed to simulate inclined loading conditions (Suorineni, 2014). C-CAST allows rock samples to be tested under combined compressive and shear stress conditions, making it possible to determine rock damage initiation stress under conditions that are more representative of inclined pillars. Based on this background, this study aims to determine the *s*-values for different rock types using the C-CAST system.

The C-CAST testing system is made up of two major parts, top and bottom adaptors which hold the intact rock samples at various degrees of inclination (2b) and can be used with any standard compression test frame. Acoustic Emission (AE) sensors are also required to measure the damage initiation stress threshold for each sample. The C-CAST used for the study is shown in Fig 2b.



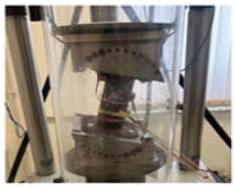


Fig 2. a) Original C-CAST system used b) C-CAST system for this study (Suorineni 2014, 2015).

4 Results, Discussion and Conclusions

This study determined rock-type-specific brittle Hoek-Brown cohesion constants (s) for inclined pillar design using the Combined Compression and Shear Test (C-CAST) system integrated with Acoustic Emission (AE) monitoring. Four rock types, namely andesite, diorite, gabbro, and dolerite were tested to evaluate the influence of inclination angle on damage initiation stress threshold (σ_{ci}), uniaxial compressive strength (UCS), and the brittle Hoek-Brown constant s. There are several ways of determining the σ_{ci}, but the method proposed by Suorineni (2000) was used by plotting the cumulative AE counts against the stress (Fig. 3). The damage is initiation stress threshold is identified where there is rapid rise in the counts as shown in Fig. 3. To determine A and s for the various rock types, Equation (4) was used as shown below.

$$A = \frac{\sigma_{ci}}{\sigma_c} \quad (4)$$

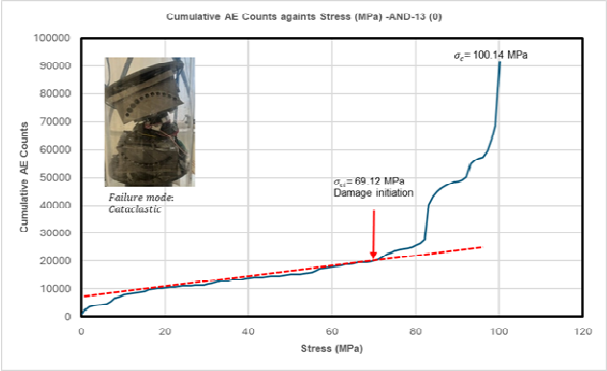


Fig 3. Cumulative acoustic emission (AE) counts versus stress for andesite sample (AND-13) at 0° inclination, showing the onset of damage initiation at σ_{ci}= 69.12 MPa, followed by progressive crack growth and a sharp increase in AE activity approaching peak stress (σ_c= 100.14 MPa).

A summary of the UCS, σ_{ci} and s for the various rock types at varying inclinations are shown in Table 2.

Table 2. Cohesion constant s-Rock type specific matrix.

Rock type	***Inclination (∝°)***	***Failure mode***	***UCS (MPa)***	***σ_{ci} (MPa)***	***s***
Andesite	0	Cataclastic	100.14	69.12	0.48
	5	multiple fracturing	40.02	16.03	0.16
	15	failure along double plane	39.55	18.05	0.21
Diorite	0	shearing along a single plane	146.86	120.9	0.68
	5	shearing along a double plane	116.64	83.67	0.51
	15	shearing along a single plane	116.58	50.59	0.19
	20	Y-shaped failure	93.33	59.3	0.4
Gabbro	0	axial splitting	131.86	107.02	0.66
	5	axial splitting	148.92	116.04	0.61
	10	axial splitting	80.03	51.09	0.41
Dolerite	0	cataclastic	320.99	251.41	0.61
	5	multiple fracturing	275.6	195.52	0.5
	10	multiple fracturing	279.4	211.62	0.57
	15	cataclastic and multiple fracturing	219.44	143.46	0.43
	20	along a single shear	85.63	54.54	0.41

The AE results showed that damage initiation consistently occurred before peak failure, typically between 30-60% of UCS, confirming that brittle failure in hard rocks is governed by early microcrack initiation rather than peak strength. This confirms Martin's (1993) brittle Hoek-Brown damage initiation concept and demonstrates that σ_{ci} is a more reliable design parameter than conventional UCS for brittle rock pillar assessment. The C-CAST results further showed that increasing inclination angle significantly reduced both UCS and σ_{ci} across all rock types, indicating that the addition of shear stress accelerates crack propagation, reduces confinement, and weakens pillar strength under combined compression-shear loading. The calculated s values confirmed that the Hoek-Brown constant s is not a universal value of 0.11, but varies significantly with rock type, mineralogy, alteration, and loading orientation. Dolerite, gabbro, and diorite recorded relatively higher strength and higher s values due to stronger crystal interlocking, lower alteration, and better grain bonding, while andesite showed lower s values associated with higher alteration, microfractures, and weaker mineral bonding. A consistent decrease in s was observed with increasing inclination angle, confirming that inclination strongly influences cohesion loss and brittle response.

The failure mode analysis revealed a transition from axial splitting at low inclination angles to mixed-mode and shear-dominated failure at higher inclinations. This shows that stress orientation controls failure behaviour, hence, using the conventional UCS-based empirical pillar design methods, which assumes dominant vertical loading, overestimate the strength of inclined pillars. The results establish that reliable inclined pillar design must incorporate rock-type-specific *s* values derived under realistic loading conditions. This study therefore provides a practical rock-type specific *s* matrix for inclined pillars design and improves prediction of brittle pillar failure in underground excavations.

Aknowledgements

The study is supported by Nazarbayev University Faculty Development Competitive Research Grant Program number Grant number 201223FD8835.

References

Brady, B. H. G., & Brown, E. T. (2006). *Rock Mechanics For Underground Mining*. ResearchGate. https://www.researchgate.net/publication/49184303_Rock_Mechanics_For_Underground_Mining

Hedley, D. G. F., & Grant, F. (1972). *Stope-and-Pillar Design for the Elliot Lake Uranium Mines*. https://uat-oneminewebsite.azurewebsites.net/documents/stope-and-pillar-design-for-the-elliot-lake-uranium-mines

Hedley, J. W., Roxburgh, S. N., & Muppalaneni, D. G. F. (1984). *A Case History ofRock bursts At Elliot Lake*. OneMine. https://onetunnel.org/documents/a-case-history-of-rockbursts-at-elliot-lake

Hoek, E. (2007). *Hoek, E. (2007). Practical Rock Engineering. Evert Hoek Consulting Engineer, Inc. - References—Scientific Research Publishing*. https://www.scirp.org/(S(351jmbnt-vnsjt1aadkozje))/reference/referencespapers?referenceid=3999391

Hoek, E., & Brown, E. T. (1980). Empirical Strength Criterion for Rock Masses. *Journal of the Geotechnical Engineering Division*, *106*(9), 1013–1035. https://doi.org/10.1061/AJGEB6.0001029

Hoek, E., & Brown, E. T. (2018). The Hoek–Brown failure criterion and GSI – 2018 edition. *Journal of Rock Mechanics and Geotechnical Engineering*, *11*(3), 445–463. https://doi.org/10.1016/j.jrmge.2018.08.001

Hoek, E., C. Carranza-Torres, & B. Corkum. (2002). *Hoek-Brown Failure Criterion—2002 Edition*. Scribd. https://www.scribd.com/document/397217169/hoek-brown-criterion

Ma, T., Wang, L., Suorineni, F., & Tang, C. (2016). Numerical Analysis on Failure Modes and Mechanisms of Mine Pillars under Shear Loading. *Shock and Vibration*, *2016*, 1–14. https://doi.org/10.1155/2016/6195482

Martin, C. D. (1993). *The strength of massive Lac du Bonnet granite around underground openings*. http://hdl.handle.net/1993/9785

Potvin, Y. (1985). *Investigation of underground mine pillar design procedures*. ResearchGate. https://www.researchgate.net/publication/279477820_Investigation_of_underground_mine_pillar_design_procedures

Suorineni, F. T. (2014b). Reflections on Empirical Methods in Geomechanics – The Unmentionables and Hidden Risks. *ResearchGate*. https://www.researchgate.net/publication/269984632_Reflections_on_Empirical_Methods_in_Geomechanics_-_The_Unmentionables_and_Hidden_Risks

Suorineni, F. T., Chinnasane, D. R., & Kaiser, P. K. (2009). A Procedure for Determining Rock-Type Specific Hoek-Brown Brittle Parameter s. *Rock Mechanics and Rock Engineering*, *42*(6), 849–881. https://doi.org/10.1007/s00603-008-0024-y

Suorineni, F. T., Kaiser, P. K., Mgumbwa, J. J., & Thibodeau, D. (2011). Mining of orebodies under shear loading Part 1 – case histories. *Mining Technology*. https://journals.sagepub.com/doi/full/10.1179/1743286311Y.0000000012

Suorineni, F. T., Mgumbwa, J. J., Kaiser, P. K., & Thibodeau, D. (2014a). Mining of orebodies under shear loading Part 2 – failure modes and mechanisms. *Mining Technology*, *123*(4), 240–249. https://doi.org/10.1179/1743286314Y.0000000072

Zingano, A. C. (2016). *Violent coal pillar collapse. 24th World Mining Congress, Rio de Janeiro, Brazil. Pp. 511-521.*

Plastic swelling and hardening mechanisms of in-situ heated Callovo-Oxfordian claystone

J. Ren & P. Braun & S. Ghabezloo
École nationale des ponts et chaussées, Champs-sur-Marne, France
philipp.braun@enpc.fr
0000-0003-3207-5018

C. Plua & M. Vu
Andra, Châtenay-Malabry, France

Abstract

Callovo-Oxfordian (COx) claystone is the candidate host rock for the future French deep geological repository for radioactive waste, designed to experience thermal loads of up to 90°C during operation. In this context, this study characterizes cores extracted after an in-situ heating test where the maximum temperature reached 95°C. A multistep isotropic test was performed on a sample resaturated close to the in-situ stress state. Drained and repeated mechanical unloading-reloading cycles were carried out. Reversible elastic strain and irreversible plastic strain were decomposed from specially designed loading steps to characterize the evolution of plastic yield mechanisms. Results indicate that the sample exhibited plastic swelling during the unloading paths, when the effective mean stress decreased below 8 MPa. The unloading also seemed to have reduced the compression yield limit, since during subsequent reloading, we observed plastic compression at stress levels below the initial state. Furthermore, unloading after loading to high confining pressure revealed that the swelling yield limit increased, exceeding the initial stress level, thereby demonstrating a hardening effect. These observations could be represented by a swelling yield limit at a low effective mean stress, which is strongly coupled with the compression yield limit during the hardening process. The observed swelling during mechanical unloading could be relevant for in-situ stress paths involving decreasing mean effective stress, namely tunnel excavation, fracture self-sealing, thermal pressurization and retrieval of laboratory specimens.

Keywords

Callovo-Oxfordian claystone, In-situ heating, Elasto-plastic behaviour, Plastic swelling, Stress release.

1 Introduction

Callovo-Oxfordian (COx) claystone is the candidate host rock for the future French deep geological repository for radioactive waste, located in the north-east of France. In the design of this repository, COx claystone is expected to experience thermal loads of up to 90 °C during operation. To better understand the response of COx under the complex thermo-hydro-mechanical (THM) loading, various in-situ and laboratory tests have been conducted across different scales (Belmokhtar et al. 2017; Zhang et al. 2019; Braun et al. 2021; Bumbieler et al. 2021; Plúa et al. 2024). It should be noted that before laboratory investigations, the material undergoes complex sequences such as excavation and core extraction, which could induce moisture loss and stress release.

The influence of desaturation on the mechanical performance of clayey rocks has been studied. Ewy (2015) demonstrated that moisture loss during the deconfinement can lead to performance degradation and structural damage. Conil et al. (2018) further emphasized the importance of core extraction and conditioning procedures, leading to the development of special storage cells designed to minimize the effects of desaturation and stress release. Nevertheless, the specific impact of mechanical unloading on the plastic mechanisms of the material is not yet fully understood. Research on similar clay-rich formations, such as the Opalinus claystone, has suggested that the excavation-induced response is not purely linear-elastic (Corkum and Martin 2007). Therefore, investigating the unloading process of COx claystone is important to evaluate the impact of stress release history on its subsequent mechanical properties.

To this end, the present study utilizes a core extracted after an in-situ heating experiment conducted by Andra in the Meuse/Haute-Marne Underground Research Laboratory (MHM URL). One specimen was resaturated and subjected to a series of multi-step isotropic unloading-reloading cycles in the laboratory. By decomposing the total measured strains into reversible elastic and irreversible plastic components, this study quantitatively evaluates the evolution of plastic swelling and hardening mechanisms. The findings aim to understand how the stress history induced by excavation affects the mechanical behaviour, with a particular focus on plastic behaviour.

2 Experimental investigations

2.1 Material and testing device

The MHM URL is located in the Callovo-Oxfordian formation at a depth of approximately 490 m. At this level, a vertical and minor horizontal stress of about12.7 MPa, a major horizontal stress of 16 MPa, and a pore pressure of 4.5 MPa was reported from in-situ experiments (Wileveau et al. 2007). Previous characterisation of the COx claystone at this level reported an average water content of 7.9%, an average porosity of 17.5%, and a clay fraction of about 42% (Conil et al. 2018).

The core used in this study was extracted after the in-situ heating experiment named as CRQ(Plúa et al. 2024), which aims to better understand the thermally-induced hydro-fracturing of the COx claystone. A thermal loading and a corresponding thermal induced pore pressure were applied on the COx to generate tensile stresses higher than the tensile strength. For the core CRQ1733_03 used in this study, it was heated up to 95 °C for 1 month. After cooling down, the core was extracted and embedded in the T1 cell to minimize the mechanical degradation and damage due to the desaturation and microcracking (Ewy 2015; Conil et al. 2018).

Upon opening the packages in laboratory, the cores were immediately wrapped in tape to minimize moisture exchange with the atmosphere. The specimens were cored perpendicular to the bedding planes and machined to a disk with a diameter of 38 mm and a height of approximately 10 mm. Petrophysical characterization was performed using the remaining material. A bulk density of 2.41 g/cm^{3}was determined by hydrostatic weighing in a hydrocarbon, while the dry mass was obtained after oven-drying at 105 °C. Using a solid density of 2.72 g/cm^3 provided by Andra (Gaucher et al. 2004), a water content of 6.8%, a porosity of 17.5% and a degree of saturation of 92.7%were calculated. Additionally, a suction of 24.7 MPa was measured using a chilled-mirror dewpoint tensiometer. These results confirmed high degree of saturation of the specimen, indicating a good conservation of the moisture before laboratory testing. For long-term preservation, the specimen was wrapped in parafilm and aluminium foil and sealed in vacuum bags.

The experiment was performed using a temperature-controlled high-pressure isotropic compression cell (Mohajerani et al. 2012; Belmokhtar et al. 2017; Braun et al. 2021). The apparatus enables independent regulation of confining pressure, pore pressure, and temperature applied on the specimen. Confining pressure and pore pressure were controlled through two pressure–volume controllers. Thermal conditions were regulated by an external heating system surrounding the cell. Axial and radial strains were monitored by strain gauges attached on the specimen, with a reference gauge installed inside the cell to compensate for self-deformation and thermal drift.

2.2 Specimen preparation and loading procedure

The preparation and resaturation protocolis based on the methodology described in Braun et al. (2021) and are presented in Fig. 1a. After mounting, the drainage system was vacuumed to remove entrapped air. The specimen was then brought to an isotropic confinement pressure σ_{conf}=10 MPa and T = 25°C. Upon stabilization, synthetic pore water reproducing the in-situ chemical environment was injected into the specimen. Both σ_{conf} and pore pressure p_f were then increased at the same rate to remain an effective confining pressure σ'_{conf}= σ_{conf}-p_f of 10 MPa, with p_f=3.5 MPa. This resaturation phase, conducted under stress conditions representative of the in-situ state, lasted about ten days until the stabilization of measured swelling strains.

The experimental program on the resaturated specimen followed a multi-step loading procedure where each step comprised two successive phases. In the first phase, a rapid mechanical loading with a rate of ±100 kPa/min was applied. Given the very low permeability of the COx claystone, this rapid loading can be considered under pseudo-undrained, inducing transient pore pressure variation (Braun et al. 2018). In the second phase, the pore pressure inside the specimen returned to its prescribed value through a transient dissipation period. The stabilization of strains indicated hydraulic equilibrium, corresponding to the drained state. This study focuses exclusively on the drained behaviour. This step-by-step technique was utilized within a carefully designed cyclic loading framework to facilitate the analysis of material response. By comparing strain values obtained at identical stress levels during unloading-reloading cycles, the increments and accumulation of plastic strains could be decomposed from the total value and accurately evaluated.

Following this methodology, the test was conducted to investigate the mechanical behaviour after the in-situ thermal cycle and the potential effect raised from the excavation. The loading procedure was conducted through 36 steps and divided into three segments (Fig. 1b): The specimen was first unloaded from the initial stress state (σ'_{conf} =10 MPa) to σ'_{conf} =6 MPa and then reloaded to observe the initial expansion behavior (steps 1-7). This cycle was designed to mimic the stress release during the excavation (Conil et al. 2018). Following the unloading cycle, a loading-unloading cycle (steps 8-23) between 10 and 18 MPa was conducted to investigate the potential effect of previous unloading on the material behaviour during compression. A final cycle was performed between 6 MPa and 14 MPa to investigate the potential influence of the previous stress history on the subsequent development of irreversible strains, as further discussed in Section 3.

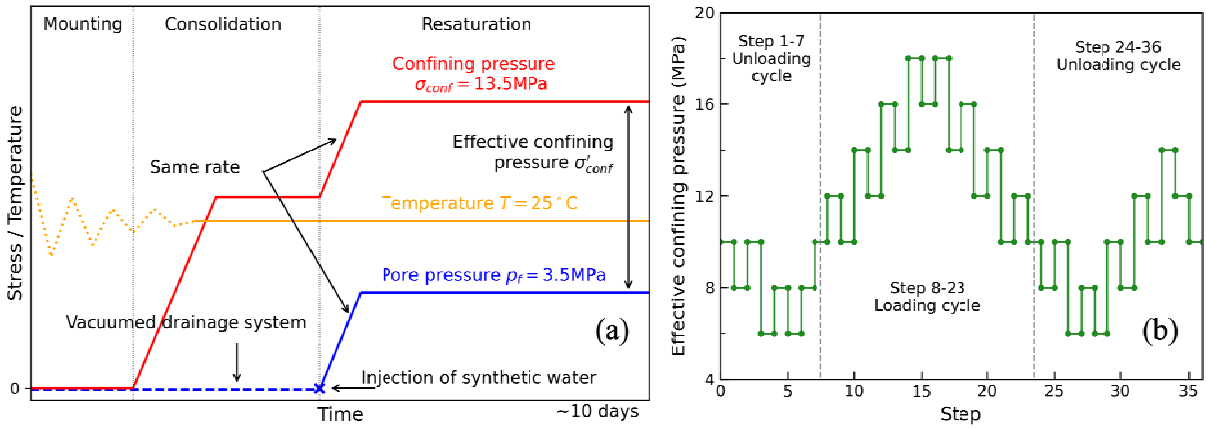


Fig. 1 Preparatory procedures (a) and the cyclic loading programme (b) applied in the isotropic test.(a) Evolution of confining pressure, temperature and pore pressure during mounting, consolidation and resaturation. Synthetic water was injected into the vacuumed drainage conduits after stabilization of confining pressure and temperature, leading to resaturation close to in-situ conditions. (b): Cyclic effective confining pressure applied during the test. The programme consists of three stages: an unloading cycle from 10 to 6 MPa (Steps 1–7), a loading cycle from 10 to 18 MPa (Steps 8–23), and a final cycle between6and 14 MPa (Steps 24–36).

3 Experimental results

The isotropic test was designed to reproduce the stress release and to investigate its impact on the mechanical behaviour of COx claystone. The measured strain under cyclic loading procedure is decomposed into the elastic (reversible) and plastic (irreversible) component, as shown in Fig. 2. The increment of plastic strain is evaluated by comparing the strain value difference, which is the result of the plastic behaviour between two steps. For example, following the path *abcd*, by comparing the states *a* and *d* we can identify the amount of irreversible axial plastic expansion which occurred during the unloading from 8 to 6 MPa.

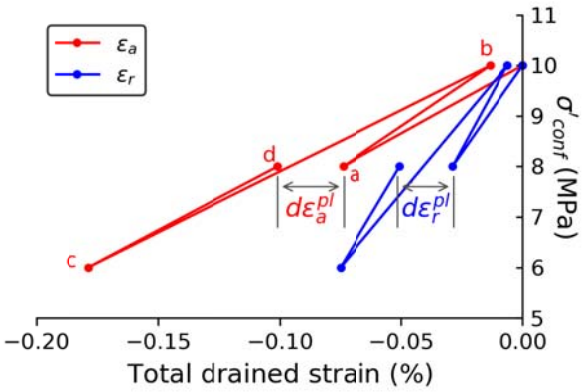


Fig. 2 Schematic diagram of strain analysis. Plastic strain increments $d\varepsilon^{pl}$ are evaluated by comparing total strain at the same stress level. For a given stress-strain path *abcd*, segments *ab* and *cd* are elastic, the strain difference between points *a* and *d* represents the plastic strain increment.

3.1 First unloading cycle: Swelling yield limit

The evolution of total drained strains and the decomposed plastic strains for the first cycle (Steps 1 to 7) are illustrated in Fig. 3a and Fig. 3b, respectively. During the initial unloading from σ'_{conf}= 10 MPa to 8 MPa, the specimen exhibits slight irreversible expansion in both axial and radial directions. This plastic swelling accumulates progressively as the effective confining pressure decreases. At the stress level of 6 MPa, the accumulated plastic strain reaches approximately 0.04% axially and 0.03% radially, accounting for approximately 30% of corresponding total drained strain. Such behavior indicates the activation of swelling yield mechanism at low confining pressure, which triggered the plastic expansion during the applied unloading path.

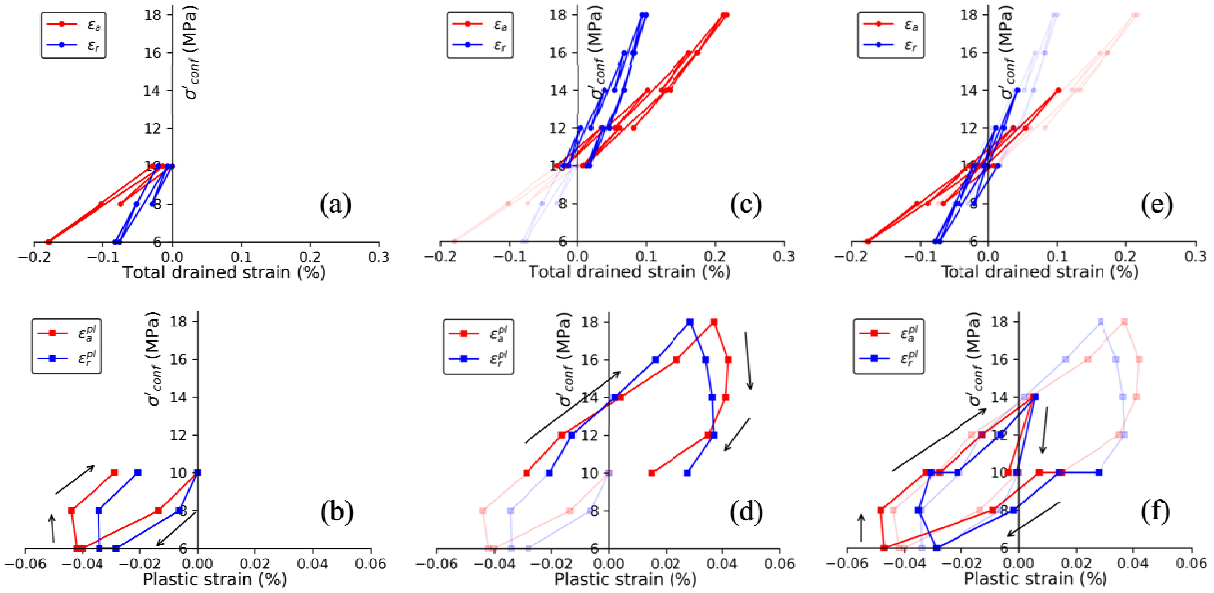


Fig. 3 Evolution of drained strains and corresponding plastic strains. Axial and radial drained strains of each loading or unloading step are shown in subplots (a), (c) and (e), while the corresponding decomposed plastic strains are shown in (b), (d) and (f). Arrows indicate the evolution of plastic strain. (a,b) First unloading cycle between 10 and 6 MPa. (c,d) Second loading cycle between 10 and 18 MPa. (e,f) An additional unloading cycle between 6 and 14 MPa.

During the subsequent reloading phase, the material response is mainly elastic between 6 and 8 MPa, with no significant variation in plastic strain. However, as σ'_{conf} increases above 8 MPa, a plastic

compression in both directions is observed. It is worth noting that this plastic compression initiated at 8 MPa, which is lower than the initial resaturated stress level of 10 MPa. This observation indicates that the previous unloading-induced plastic swelling led to a reduction in the compression yield limit, implying an interaction between the swelling and compression yield limits.

3.2 Second cycle: Compression-induced hardening of swelling yield limit

To further investigate the effect of stress history on the plastic response, a loading-unloading cycle was performed between 10 and 18 MPa (Steps 8 to 23), as shown in Fig. 3c and in Fig. 3d. During the cyclic loading steps, plastic compressive strains develop progressively, reaching approximately 0.037% in axial direction and 0.028% in radial direction. In the subsequent unloading phase, a predominantly elastic response is observed between 18 and 14 MPa, where plastic strains remain relatively stable. However, clear plastic expansion begins to develop in both directions once the effective confining pressure decreases below 12-14 MPa. This variation of the swelling yield limit, compared to the first unloading cycle, indicates an increase in this limit as a result of the previous plastic compression. This observation further implies the 1hardening effect of the compressive loading history on the swelling yield limit.

3.3 Final cycle: Validation of the coupled plastic compression-swelling response

An additional unloading-reloading cycle was conducted between 6 and 14 MPa (Steps 24 to 36) to verify the mutual influence and hardening effect between the two yield limits, as presented in Fig. 3e and Fig. 3f. During unloading from 10 to 6 MPa, plastic swellings continue to develop and reached similar values as the first unloading cycle when σ'_{conf}=6 MPa. During the subsequent reloading, an elastic response was again observed in 6 and 8 MPa, followed by the onset of plastic compression above this stress level. The plastic strains obtained during unloading from 14 to 10MPa show a small expansion in both directions, which can be interpreted as the material being within its elastic range or undergoing a small amount of plastic expansion.

4 Discussion

The mechanical response of the heat-treated COx claystone is governed by its loading history. The strain evolution and plastic behaviour reveal a stress-path dependency, where the yield limits for plastic swelling/compression mechanisms vary according to the stress history. Specifically, the consistent activation of plastic swelling during unloading phases confirms the existence of a swelling yield limit at low confinement. Conversely, subsequent reloading induces plastic compression, which can initiate at stress levels lower than the initial state depending on the previous expansion. These findings also suggest a narrow elastic domain bounded by two yield limits. Furthermore, the interaction between these limits indicates a coupling effect, where the activation of the compression mechanism leads to a hardening and shift of the swelling yield limit.

Such behaviour has been less discussed for COx claystone, but similar responses have been reported in other clayey materials. For instance, Cui et al.(2013), identified the bi-linear unloading/reloading paths in YP Clay, which were interpreted as transitions between mechanical-dominant and physico-chemical-dominant mechanisms. Additionally, loading-unloading cycles applied on Boom clay exhibited stress-strain hysteresis loops attributed to the high clay content (Yu et al. 2021). The plastic swelling phenomenon in such materials can be linked to the increase in the thickness of the adsorbed water layers. Given that the COx claystone in this study has a high clay content of 42%, a similar physico-chemical mechanism is likely responsible for the plastic swelling, and the stress-strain loops observed.

5 Conclusion

To investigate the effect of mechanical unloading on the mechanical response of the Callovo-Oxfordian claystone, a multistep isotropic unloading–reloading test was conducted on a specimen extracted after an in-situ heating experiment. By decomposing total strains into elastic (reversible) and plastic (irreversible) components, the following conclusions can be drawn:

1. During the unloading phase from the initial in-situ stress state, the specimen exhibits significant plastic swelling, suggesting the presence of a swelling yield limit at low confining pressure.

2. The plastic compression and swelling yield mechanisms exhibit a coupled behaviour. Plastic swelling during unloading reduces the compression yield limit, while subsequent compressive loading increases the swelling yield limit, demonstrating a mutual hardening effect controlled by stress history.

These results highlight the path dependency of the mechanical response of COx claystone. The excavation-induced stress release may alter the elastic domain and yield limits of the material prior to laboratory testing. Therefore, the effects of unloading during sampling and excavation should be considered when evaluating the THM performance of COx claystone. Future research focusing on microstructural evidence and advanced constitutive modelling will be useful to quantify these coupled hardening mechanisms.

References

Belmokhtar M, Delage P, Ghabezloo S, et al (2017) Poroelasticity of the Callovo–Oxfordian Claystone. Rock Mech Rock Eng 50:871–889. https://doi.org/10.1007/s00603-016-1137-3

Braun P, Ghabezloo S, Delage P, et al (2021) Transversely Isotropic Poroelastic Behaviour of the Callovo-Oxfordian Claystone: A Set of Stress-Dependent Parameters. Rock Mech Rock Eng 54:377–396. https://doi.org/10.1007/s00603-020-02268-z

Braun P, Ghabezloo S, Delage P, et al (2018) Theoretical Analysis of Pore Pressure Diffusion in Some Basic Rock Mechanics Experiments. Rock Mech Rock Eng 51:1361–1378. https://doi.org/10.1007/s00603-018-1410-8

Bumbieler F, Plúa C, Tourchi S, et al (2021) Feasibility of constructing a full-scale radioactive high-level waste disposal cell and characterization of its thermo-hydro-mechanical behavior. International Journal of Rock Mechanics and Mining Sciences 137:104555. https://doi.org/10.1016/j.ijrmms.2020.104555

Conil N, Talandier J, Djizanne H, et al (2018) How rock samples can be representative of in situ condition: A case study of Callovo-Oxfordian claystones. Journal of Rock Mechanics and Geotechnical Engineering 10:613–623. https://doi.org/10.1016/j.jrmge.2018.02.004

Corkum AG, Martin CD (2007) The mechanical behaviour of weak mudstone (Opalinus Clay) at low stresses. International Journal of Rock Mechanics and Mining Sciences 44:196–209. https://doi.org/10.1016/j.ijrmms.2006.06.004

Cui YJ, Nguyen XP, Tang AM, Li XL (2013) An insight into the unloading/reloading loops on the compression curve of natural stiff clays. Applied Clay Science 83–84:343–348. https://doi.org/10.1016/j.clay.2013.08.003

Ewy RT (2015) Shale/claystone response to air and liquid exposure, and implications for handling, sampling and testing. International Journal of Rock Mechanics and Mining Sciences 80:388–401. https://doi.org/10.1016/j.ijrmms.2015.10.009

Gaucher E, Robelin C, Matray JM, et al (2004) ANDRA underground research laboratory: interpretation of the mineralogical and geochemical data acquired in the Callovian–Oxfordian formation by investigative drilling. Physics and Chemistry of the Earth, Parts A/B/C 29:55–77. https://doi.org/10.1016/j.pce.2003.11.006

Mohajerani M, Delage P, Sulem J, et al (2012) A laboratory investigation of thermally induced pore pressures in the Callovo-Oxfordian claystone. International Journal of Rock Mechanics and Mining Sciences 52:112–121. https://doi.org/10.1016/j.ijrmms.2012.02.012

Plúa C, Vu MN, de La Vaissière R, Armand G (2024) In Situ Thermal Hydrofracturing Behavior of the Callovo-Oxfordian Claystone within the Context of the Deep Geological Disposal of Radioactive Waste in France. Rock Mech Rock Eng 57:4265–4283. https://doi.org/10.1007/s00603-023-03618-3

Wileveau Y, Cornet FH, Desroches J, Blumling P (2007) Complete in situ stress determination in an argillite sedimentary formation. Physics and Chemistry of the Earth, Parts A/B/C 32:866–878. https://doi.org/10.1016/j.pce.2006.03.018

Yu H, Chen W, Gong Z, et al (2021) Loading-unloading behavior of a clayey rock under thermo-hydro-mechanical conditions. International Journal of Rock Mechanics and Mining Sciences 148:104966. https://doi.org/10.1016/j.ijrmms.2021.104966

Zhang C-L, Armand G, Conil N, Laurich B (2019) Investigation on anisotropy of mechanical properties of Callovo-Oxfordian claystone. Engineering Geology 251:128–145. https://doi.org/10.1016/j.enggeo.2019.02.008

Comparison of Empirical Vs30 Modeling and Field Measurements in Kosova Using GIS-Based Spatial Analysis

Latif Hasi
Ss Cyril and Methodius in Skopje, Institute of earthquake engineering and engineering seismology (IZIIS)-Skopje, North Macedonia
latif.hasi@uni-pr.edu
0000-0003-4676-1422

Julijana Bojadjieva, Kemal Edip, Vlatko Sheshov, Irena Gjorgjeska, Toni Kitanovski, Dejan Ivanovski
Ss Cyril and Methodius in Skopje, Institute of earthquake engineering and engineering seismology (IZIIS)-Skopje, North Macedonia

Nazmi Hasi
University of Mitrovica "Isa Boletini", Prishtinë, Kosovë

Abstract
Shear-wave velocity in the upper 30m (Vs30) is a key parameter for seismic site classification and hazard assessment. In regions with limited geophysical data, global empirical models, such as the slope-based approach developed by Allen and Wald (2007), are often used to estimate Vs30. This method relies on the correlation between terrain slope and shear-wave velocity: steep areas generally expose bedrock with higher Vs values, while flat areas typically contain softer materials with lower values. However, this approach does not always fully account for local geological characteristics. This study evaluates the accuracy of the Allen and Wald global model in Kosova by comparing predicted values with locally measured values obtained from field investigations using the MASW method. Model values were extracted at measurement locations using QGIS to analyze spatial deviations. The comparison assesses how well the global model represents local site conditions to identify potential differences. Ultimately, the analysis aims to evaluate the applicability of the slope-based method in Kosova and examine its limitations for detailed seismic site classification. Field measurements play a crucial role in ensuring more accurate seismic site characterization because they provide direct, location-specific data on subsurface conditions, reducing uncertainties associated with global or proxy-based estimation methods.

Keywords
Shear-wave velocity, Seismic site classification, Allen and Wald model, MASW, GIS.

1 Introduction

Seismic site conditions play a critical role in determining the level of ground shaking during earthquakes. Local soil properties can significantly amplify seismic waves, making accurate site characterization essential for earthquake-resistant design and seismic hazard mitigation. One of the most widely used parameters for describing site conditions is Vs30, defined as the average shear-wave velocity in the upper 30 meters of the ground.

Due to the high cost and time required for direct geophysical measurements, many regions lack detailed Vs30 information. To address this limitation, empirical models have been developed to estimate Vs30 from secondary parameters. One of the most influential approaches is the slope-based proxy method proposed by Allen and Wald, which estimates Vs30 using terrain slope derived from digital elevation models. This model is implemented in the global Vs30 map provided by the United States Geological Survey (USGS) and is commonly used in seismic risk models worldwide. Although the slope-based methodology provides consistent global coverage, it does not explicitly account for geological variation, sediment thickness, or subsurface stratigraphy. As a result, its accuracy and reliability vary between regions. Areas with complex geology, significant sedimentary basins, or strong lateral heterogeneity are particularly challenging for slope-based approaches.

Kosova is located in a tectonically active region of Southeast Europe and displays diverse geological and geomorphological conditions. However, publicly available Vs30 data in Kosova remains limited. The objective of this study is to evaluate the accuracy and applicability of the Allen and Wald Vs30 model for Kosova by comparing model predictions with field-measured Vs30 values. This work aims to assess the reliability of the global model under local geological conditions and to identify potential limitations when applying slope-based methods in seismic microzonation studies.

2 Study area

Kosovais located in Southeast Europe on the Balkan Peninsula and covers approximately 10,900 km². The country is characterized by diverse topography, with elevations ranging from 297 m in the DriniiBardhë valley to 2,565 m at Gjeravica, its highest peak. Several mountain ranges surround the territory, including the Kopaonik Mountains in the north, the Mali iSharrit Mountains in the south, and parts of the Alpet Shqiptare in the west. This varied relief reflects the complex geological setting of the region(The Independent Commission for Mines and Minerals, n.d.)

Kosova comprises a complex assemblage of sedimentary, igneous, and metamorphic rocks, resulting in significant lateral variability in subsurface conditions. The country is located within a tectonically active region influenced by the convergence of the Adriatic microplate and the Eurasian plate, where moderate seismicity poses a risk to the built environment. Due to the limited availability of systematic geophysical surveys, no national-scale Vs30 map based entirely on direct measurements currently exists. Consequently, global proxy-based models such as the Allen and Wald Vs30 model are commonly used in preliminary seismic assessments, making Kosova a suitable case study for evaluating their applicability under varied geological and topographic conditions.

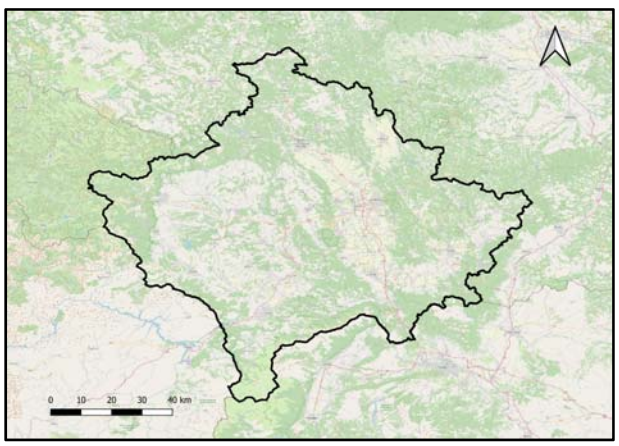


Fig. 1 Study area - Territory of Republic of Kosova.

3 Data and sources

This study uses two primary datasets: (1) the global Vs30 raster developed by Allen and Wald and distributed by the USGS, and (2) field-measured Vs30 values obtained from investigations conducted in Kosova. The USGS raster provides continuous global coverage and serves as the reference dataset for comparison.

Field measurements were collected during several seismic investigations in Kosova. Additional Vs30 data were obtained from the study "Seismic Microzonation: Case Study Ulpiana Settlement in Prishtina – Kosova" (Dojcinovski et al., 2014).

Spatial analysis was performed in QGIS. The USGS Vs30 raster was clipped to the territory of Kosova using a national boundary dataset, producing a localized Vs30 map. A DEM obtained from OpenTopography was also clipped to the study area and used to examine relationships between topography and Vs30 distribution.

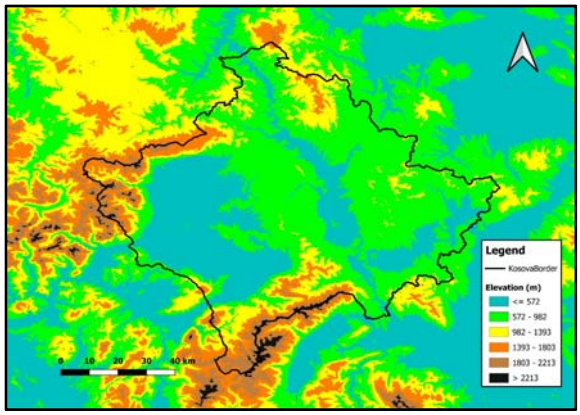


Fig. 2 Elevation map of Kosova extracted from Open topography.

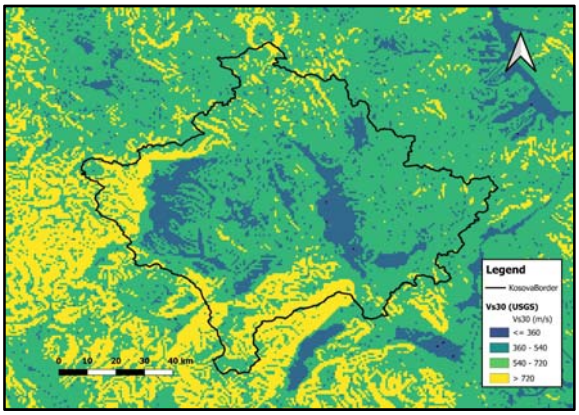


Fig. 3 Vs30 extracted from USGS global dataset.

Figures 2 and 3 show a general relationship between topography and predicted Vs30 values, reflecting the slope-based approach used in the Allen and Wald model. While topographic slope is the primary predictor, the final USGS Vs30 raster also incorporates additional adjustments to account for regional variations in surface conditions. Fig. 4 presents the slope-based Vs30 estimates prior to these adjustments.

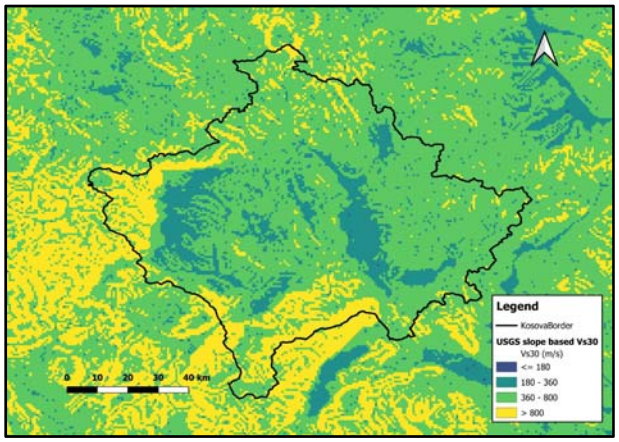


Fig. 4 Predicted values of Vs30 based only on slope.

By comparing Fig 4 and Fig 3, it can clearly be seen that they predict the same overall trend in the whole territory of Kosova indicating that topographic slope plays a dominant role in controlling the large-scale spatial distribution of predicted Vs30 values.

4 Methodology

After acquiring the datasets, spatial analysis was performed in QGIS. The global Allen and Wald Vs30 raster was clipped to the boundary of Kosova to produce a localized Vs30 map (Fig. 3). Field

measurement locations were then overlaid on the raster to compare predicted and measured Vs30 values (Fig. 6).

The Allen and Wald method estimates Vs30 from topographic slope derived from Digital Elevation Models (DEMs), assuming that steeper terrain generally corresponds to higher Vs30 values and flatter areas to lower values. The DEM (Fig. 2) was processed in QGIS to generate a slope map of Kosova (Fig. 5).

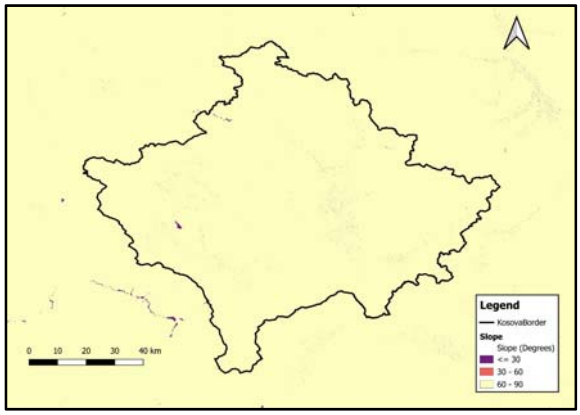


Fig. 5 Slope map of Kosova derived from the Digital Elevation Model (DEM) using the GDAL slope algorithm in QGIS. Slope values are expressed in degrees, illustrating the spatial distribution of terrain steepness.

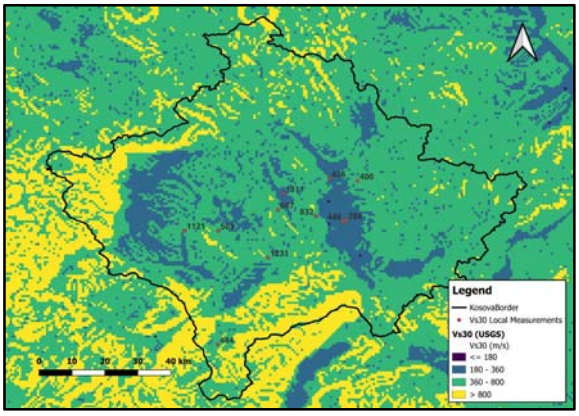


Fig. 6 Field measurement locations were overlaid on the clipped raster.

In Fig 6, the measured values of the shear-wave velocities from the field measurements were overlaid on the USGS raster. Because of the limited number of available measurements, the results should be interpreted cautiously. The differences between the measured values and the predicted values can be further explained using geological maps.

5 Results

Table 1 presents the field-measured and model-predicted Vs30 values for the 11 investigation locations in Kosova. The average absolute difference between measured and predicted values is approximately 345 m/s. While some locations show good agreement, with differences as low as 15 m/s, other sites exhibit substantial discrepancies exceeding 1000 m/s. These results indicate that the Allen and Wald model performs inconsistently across different geological settings within the study area.

Table 1. Comparison of measured and predicted Vs30 values at field investigation locations in Kosova.

ID	Longitude	Latitude	Measured Vs30 (m/s)	Predicted Vs30 (m/s)	Difference (Predicted - Measured) (m/s)
P01	21.1125	42.51833	446	254	-192
P02	20.83333	42.38333	1231	574	-657
P03	20.6478	42.0621	484	469	-15
P04	20.8904	42.621	1311	271	-1041
P05	21.1643	42.6673	400	429	29
P06	20.525	42.4839	1121	499	-622
P07	20.65	42.483	503	597	94
P08	21.061	42.676	436	298	-138
P09	21.1226	42.52134	788	252	-536
P10	21.0106	42.5367	832	436	-396
P11	20.87	42.56	687	615	-73

6 Discussions

The comparison between field-measured and predicted Vs30 values reveals significant discrepancies across the study area. While some locations show good agreement, the Allen and Wald model generally underestimates measured Vs30 values, with an average deviation of approximately 345 m/s. This indicates that the global slope-based model does not fully capture local site conditions in Kosova.

The discrepancies are likely related to geological factors not explicitly considered by the model, including lithology, sediment thickness, weathering, and subsurface stratigraphy. Consequently, reliance solely on slope-based Vs30 estimates may lead to inaccurate site classification and ground-motion assessments, particularly in sedimentary basins. Although the model provides a useful first-order approximation in data-scarce regions, it should not replace site-specific geophysical investigations.

This study is limited by the small number and uneven distribution of available measurements. Future work should expand the dataset and develop hybrid Vs30 models that integrate topographic, geological, and geophysical information.

7 Conclusions

This study assessed the performance of the Allen and Wald global slope-based Vs30 proxy model in the Republic of Kosova by comparing predicted Vs30 values with locally measured Vs30 obtained from MASW investigations. The analysis was conducted using GIS-based spatial methods to evaluate deviations, correlations and spatial patterns across the study area. The comparison revealed that although some locations show good agreement between predicted and measured Vs30 values, significant discrepancies are present at many sites. Predicted Vs30 values generally underestimate measured values, particularly in areas characterized by high Vs30 associated with shallow bedrock or stiff geological formations. The average deviation of approximately 345 m/s indicates that the global slope-based model does not sufficiently capture local site conditions in Kosova when applied without regional calibration.

In the context of seismic hazard assessment and microzonation in Kosova, reliance solely on the global slope-based model may result in inaccurate site classification and ground-motion estimates, particularly in urban areas located within sedimentary basins. A study of seismic hazard assessment and microzonation would benefit from using geological and tectonic maps for the territory of Kosova, as well as more field investigation surveys.

While the Allen and Wald model may serve as a useful first-order approximation in data-scarce regions, it should not replace site-specific geophysical investigations or detailed geological analysis for local seismic applications. Future work should focus on increasing the number and spatial distribution of Vs30 measurements and developing hybrid approaches that integrate terrain, geological and geophysical data. Despite its limitations, this study provides valuable insight into the applicability and limitations of global Vs30 proxies in Kosova and highlights the importance of region-specific calibration for reliable seismic hazard assessment.

References

Allen TI, Wald DJ (2007) Topographic slope as a proxy for seismic site-conditions (VS30) and amplification around the globe. USGS. https://doi.org/10.3133/ofr20071357

Anon (2025) Estimating Vs30 structure from topographic and geological data in the southeast of Spain. Engineering Geology

Cannon EC, Dutta U (2015) Evaluating topographically-derived Vs30 values for seismic site class characterization in Anchorage, Alaska, USA. International Conference on Earthquake Geotechnical Engineering.

Dojcinovski D, Olumceva T, Mustafa S (2014) Seismic microzonation: case study Ulpijana settlement in Prishtina – Kosovo. Second European Conference on Earthquake Engineering and Seismology.

Fang Y et al. (2023) Vs30 prediction models based on measured shear-wave velocities in Tangshan, China. Sustainability. https://doi.org/10.3390/su15043282

The Independent Commission for Mines and Minerals, Kosovo-mining.org. http://kosovo-mining.org

Wald DJ, Allen TI (2007) Topographic slope as a proxy for seismic site conditions and amplifications. Bulletin of the Seismological Society of America 97(5):1379–1395. https://doi.org/10.1785/0120060267

A Large-Scale Shear Apparatus for Rock Discontinuities and Interfaces

C. Gbewade
Cerema Centre-Est, Team GeoCoD, 69500-Bron, France
coffi.gbewade@cerema.fr
0009-0003-3240-8844

Abstract

Characterizing the shear behavior of rock discontinuities, whether natural, reinforced, or associated with engineered interfaces, is a key issue for the design of rock engineering structures. However, conventional laboratory tests are limited by scale effects and simplified loading conditions.

In this context, the large-scale shear apparatus developed by the Cerema enables testing of large specimens with natural roughness and material heterogeneities under controlled stress conditions. The device also allows the investigation of complex configurations, such as reinforced discontinuities and bonded concrete–rock interfaces.

This paper presents the main characteristics of the apparatus, together with selected experimental studies that illustrate its capabilities. These experimental studies include tests on passive rock bolts and instrumented concrete–rock interfaces using optical fiber and acoustic sensors. These studies highlight the value of large-scale testing for improving the understanding of shear and failure mechanisms at a representative scale.

The apparatus thus represents an essential intermediate tool between laboratory testing and in situ observations, opening up important perspectives for improving mechanical models and design practices in rock mechanics.

Keywords

Metric direct shear test, Scale effect, Rock joint.

1 Introduction

Rock slopes and structures interacting with rock masses, such as foundations, dams, retaining structures, and stabilized slopes, are strongly governed by the behavior of rock discontinuities. These discontinuities, whether natural, infilled, open, or associated with engineered interfaces, constitute preferential weakness planes. The mechanical response of these planes, particularly under shear loading, largely controls the stability of structures. However, characterizing this behavior remains challenging due to the inherently heterogeneous, anisotropic, and discontinuous nature of rock masses.

The shear behavior of discontinuities is the result of a combination of several mechanisms, including friction, roughness-induced, interlocking, and, in some cases, adhesion when infilling materials or bonded interfaces are present. This behavior depends on numerous parameters, such as surface morphology, mechanical properties of the materials involved, contact conditions, and the level of normal stress. In the case of reinforced discontinuities, particularly those stabilized by rock bolts, additional load transfer mechanisms are mobilized, further increasing the complexity of the overall response and failure modes.

Despite the importance of these mechanisms for engineering design, they remain challenging to characterize experimentally using conventional laboratory devices. These are generally limited to small-scale specimens and simplified geometries, often less representative of real conditions. Such approaches do not allow accurate reproduction of the geometry of natural discontinuities or the variability of mechanical properties at the rock mass scale. In particular, scale effects represent a significant challenge as parameters measured on small specimens may differ considerably from those mobilized at the scale of engineering structures, leading to uncertainties in design approaches.

In this context, the use of large-scale experimental devices is essential to better capture the actual behavior of rock discontinuities and associated systems. The large-scale shear apparatus developed by the CEREMA addresses this need. It allows testing of large specimens incorporating natural or reconstructed rock surfaces and reproducing loading conditions close to in situ situations. This paper presents the main characteristics of the apparatus together with experimental studies illustrating its capabilities.

2 Large-Scale shear Apparatus

2.1 Description

The shear apparatus was designed to perform direct shear tests on rock discontinuities reinforced with one or several rock bolts. It operates according to the principle of a Casagrande shear box. The devise is presents on Fig.1. The lower box remains fixed, while the upper box, moves horizontally. The upper box is constrained laterally, but free to move in the longitudinal direction through a system of articulated links. This configuration allows rotations and tilting induced by either the discontinuity morphology or by the deformation of the reinforcement elements. The dimensions of the machine enable the testing a joint specimen composed of two blocks with dimension 150 cm in length, 100 cm in width and 62.5 cm in thickness

The tangential displacement is imposed at a controlled rate ranging from 0.1 to 1 mm/min. The maximum horizontal displacement of the upper box is 350 mm. Two horizontal hydraulic jacks apply a tensile to the upper box via a guided shear beam, which is transmitted through articulated links. These jacks are double-acting hydraulic cylinders, each capable of delivering a maximum force of 2.5 MN. The vertical normal load is applied vertically using two hydraulic jacks mounted on a base resting on the upper block. The maximum normal force is 2 MN. These jacks are designed to elevate a loading beam, with its external arms integrated into a cradle system. The connection between the beam and the cradle is articulated, ensuring that the load is always applied normal to the upper surface of the block.

The two half-cradles are connected by two HEB steel sections, which are subjected to compression between the cradle and the underside of the lower box. Contact between these sections and the lower box is ensured by roller pads in order to eliminate parasitic friction during translation.



Fig.1 General view of the large-scale shear apparatus: (1) upper half-box; (2) lower half-box; (3) cradle; (4) hydraulic jack; (5) normal force distribution plate.

2.2 Data Acquisition and Processing

The tangential (horizontal) displacement of the upper box is measured using two magnetostrictive displacement sensors installed on the shear jacks. Due to the large dimensions of the apparatus, the elastic deformation of the upper box is not negligible, particularly under high shear loads. Therefore, an additional LVDT captor is installed at the center of the rear plate of the upper box to provide a displacement measurement independent of the applied shear force.

The normal (vertical) displacement is measured using four LVDTs positioned at the four vertical edges of the upper block. These sensors allow quantification of tilting, rotation, and dilatancy. The tangential force is measured for each shear jack using a load cell placed in compression between the jack head and the distribution plate of the shear beam. Similarly, the normal force is measured for each vertical jack using load cells installed between the actuator heads and the normal loading beam.

2.3 Advantages Compared to Conventional Devices

The Cerema large-scale shear apparatus overcomes several key limitations of conventional laboratory testing devices. Firstly, the dimensions of the specimens allows a better representation of rock discontinuities, thereby preserving natural roughness and heterogeneities. This approach significantly reduces scale effects. In contrast to standard devices, which generally rely on simplified planar surfaces, the apparatus facilitates observation of realistic interlocking mechanisms and shear localization processes.

Secondly, the system allows the application of controlled normal stresses up to approximately 1 MPa. This level of stress can be categorized as moderate to high, depending on the context. It is representative of many near-surface conditions and engineering applications, although it is lower than stresses encountered at greater depths. Nevertheless, it is sufficient to meaningfully investigate the influence of confinement on shear strength and dilatancy.

Another key advantage lies in the instrumentation capabilities. In addition to conventional measurements (forces and displacements), samples can be equipped with advanced monitoring techniques such as:

- Distributed fiber optic sensors for strain measurement,
- Acoustic sensors for damage and microcracking identification.

These tools provide valuable insight into internal processes, particularly during the initiation and propagation of failure. The apparatus is designed to serve as an intermediate experimental scale, bridging the gap between laboratory tests and in situ conditions. It facilitates a more realistic and detailed analysis of the mechanical behavior of rock discontinuities and reinforced systems.

3 Experimental studies

This section presents a selection of experimental studies carried out using the large-scale shear apparatus developed by the Cerema. The present studies address representative issues related to rock mechanics, including reinforced discontinuities and bonded interfaces. Two primary subjects are emphasized: first, the examination of shear tests on plane discontinuities reinforced by rock bolts; and second, the investigation of concrete–rock interfaces, with the objective of characterizing their shear behavior under varying contact and confinement conditions. These examples illustrate the apparatus's capability to reproduce complex configurations and to provide insight into fundamental mechanisms governing shear behavior.

3.1 Rock joints reinforced by fully grouted bolts

Experimental campaigns were carried out to investigate the shear strength of a rock discontinuities reinforced with passive rock bolts. The tests examined the influence of several parameters, including bolt properties such as diameter and inclination, group effects, grout characteristics, and the initial aperture of the discontinuity. The planar discontinuity was modelled using two concrete blocks measuring 150 × 100 × 62.5 cm. The diameter of the bolts that were tested ranged from 25 to 40 mm. A part of this work has been previously reported in other studies, notably by Bidaut et al. (2006)and Maiolino & Pellet (2015; 2018).

Fig.2 show the maximum contribution of sheared bolts in an isolated configuration as a function of diameter and inclination (Maiolino & Pellet 2015). The results show that bolts inclined in the direction of shear displacement, typically 45° to 60°, provide the highest contribution. In this configuration, the bolts are rapidly mobilized in tension from the earliest stages of displacement, leading to efficient load transfer. In contrast, vertical bolts are initially subjected to bending, developing a crank-like mechanism before progressively reorienting at the discontinuity plane and mobilizing tensile resistance. This phenomenon leads to a reduction in the contribution and a significant increase in displacements, which are typically 3 to 4 times higher. The results demonstrate a roughly linear rise in bar contribution with diameter, highlighting the dominant role of the resisting cross-section in load mobilization.

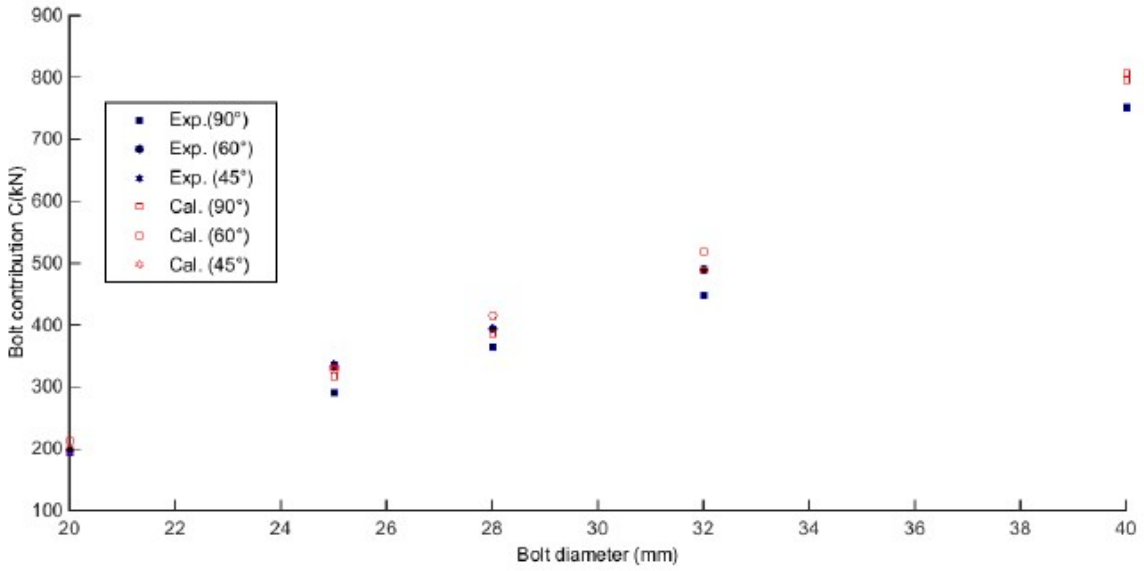


Fig. 2 Ultimate bolt contribution as a function of bolt diameter for different bolt inclinations (Maiolino & Pellet, 2015).

3.2 Study of a Bonded Concrete–Rock Interface

This study focuses on the shear behavior of bonded concrete–granite interfaces at the metric scale, in the context of gravity dam stability assessment. Five direct shear tests were performed on large-scale interfaces with an area of 1.5 m² (Bost et al. 2020).In addition to the standard instrumentation of the machine (force and displacement measurements), the samples were equipped with acoustic sensors and optical fiber (Fig. 3), enabling detailed monitoring of damage processes and strain distribution during shearing.

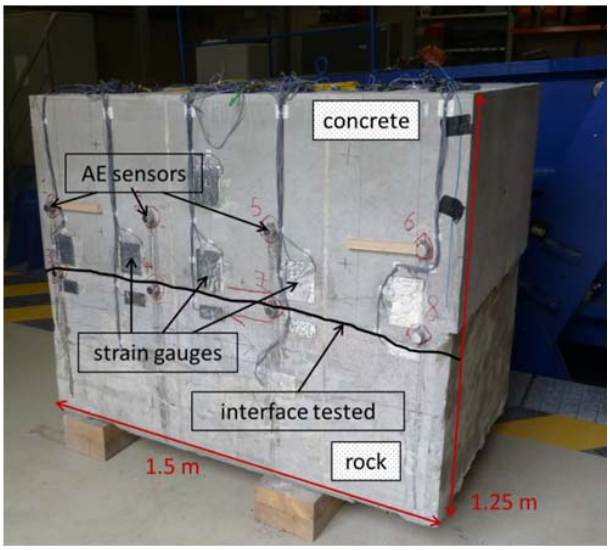


Fig.3 Lateral view of the instrumentation devices set up on a concrete-rock sample (Bost et al 2020).

Fig.4 presents the evolution of shear stress as a function of displacement. In all tests, the shear stress increases progressively up to a peak value, followed by a sharp drop, characteristic of brittle failure. The results show that failure does not occur through shear of the materials (concrete or rock) along the imposed shear plane, but rather through debonding at the concrete–rock interface. This failure mode highlights the critical role of the contact zone, whose properties (adhesion, surface preparation, roughness) directly control the overall shear resistance. These observations underline the value of large-scale testing for capturing realistic failure mechanisms that are difficult to reproduce with conventional laboratory devices.

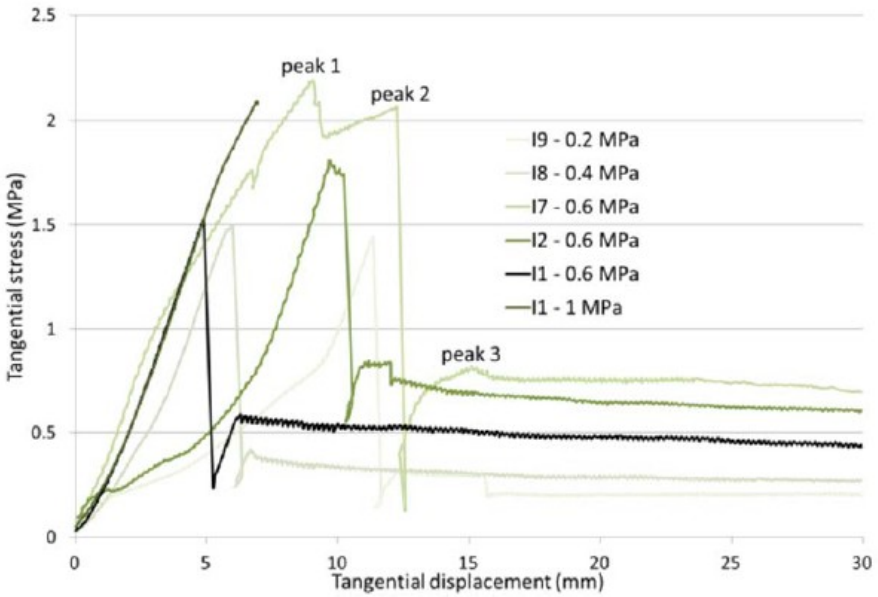


Fig. 4 Shear stress versus tangential displacement for the five direct shear tests (Bost et al 2020).

4 Conclusion

The large-scale shear apparatus developed by the Cerema represents a powerful experimental tool for investigating the shear behavior of rock discontinuities, whether natural, reinforced, or associated with engineered interfaces. The apparatus's dimensions and loading capacity, it enables testing of representative configurations that incorporate real surface roughness, material heterogeneities, and stress conditions close to field situations, while reducing scale effects.

Beyond conventional approaches, the apparatus allows the investigation of complex systems such as reinforced discontinuities, bonded interfaces, and irregular joint geometries, providing detailed insight into deformation and failure mechanisms. The integration of advanced instrumentation, including optical fiber and acoustic monitoring, also opens the way to multi-scale analysis of damage processes.

Consequently, the device constitutes an essential intermediate scale between laboratory testing and in situ conditions, offering strong potential for the development and validation of mechanical models, as well as for improving design methods for rock engineering structures.

References

Bidaut P., Durville J.P., Guillemin P., Richard J. P. &Viktorovitch M. (2006) Essais de cisaillement sur discontinuités rocheuses armées par ancrages passifs : Utilisation d'une boîte de cisaillement de grandes dimensions. Bulletin de Liaison des Ponts et Chaussées, vol. 263-264 : 7-18.

Bost M., Mouzannar H.,Rojat F., Coubard G.&Rajot J. P.(2020) Metric Scale Study of the Bonded Concrete-Rock Interface Shear Behaviour.KSCE Journal of Civil Engineering 24 (2): 390-403. https://doi.org/10.1007/s12205-019-0824-5.

Maiolino S.& Pellet F. L. (2015) Full Scale Lab Testing for the Determination of Rock Bolt Contribution to Reinforced Joint Shear Strength. 13th ISRM International Congress of Rock Mechanics, Montreal, Canada, May 2015.

Maiolino S. & Pellet F. L. (2018) Dimensionnement du boulonnage à la limite élastique : confrontation des formules analytiques avec les essais à l'échelle un ». Journées Nationales de Géotechnique et de Géologie de l'Ingénieur, Champs-sur-Marne, France, June 2018.

Correlation between structural geological and geotechnical properties of the rock mass at the Lukovo Pole dam site

Lj. Kulakov
Faculty of Natural and Technical Sciences, Goce Delcev University, Stip, North Macedonia
ljupcekulakov@gmail.com
0009-0003-9423-9302

G. Petrov & G. Dimov
Faculty of Natural and Technical Sciences, Goce Delcev University, Stip, North Macedonia

Abstract

This paper presents the results from detailed geological investigations carried out at the Lukovo Pole dam site, and makescorrelation between the structural geological and geotechnical properties of the rock mass. This issue is particularly interesting in environments with a rather complex geological structure in which tectonics plays a significant role. By resolving the structural geological properties of the rock mass, we provide a proper way to direct the geotechnical investigations and have better understanding of the physical-mechanical characteristics of the rock.In this context, it is particularly important to know the reason for the formation of the terrain, the type of geological structure, and the nature of the discontinuities. The strike and dip direction of the foliation planes have essential role in defining the drainage character of the rock medium.

The Lukovo Pole Dam is located within the Western Macedonian province, which is distinguished as a separate geotectonic unit in Republic of North Macedonia. It is characterized by its complex lithological and tectonic composition, which is manifested by dominant presence of old paleozoic metamorphic rocks and intense folding. This kind of environment requires large scale of variable research methods and techniques. Therefore, for this purpose, numerous field investigations were carried out, consisting of: detail geological mapping, investigative drilling, water permeability tests, dilatometric tests, determination of joint strength testing with sclerometer, construction of investigative galleries, and geophysical tests. By this, the level of awareness for the lithological composition and tectonic impact of the rock mass was very high. These investigations were concentrated mainly along the axis of the dam, as well as the spillway and the diversion tunnel axis. The dam axis was analyzed as primary zone of interest where total of 14 investigative boreholes were performed. Additionally, side wise two investigative galleries were performed by which direct and detail overview for the geological structure was established.

As special zones of interest in these investigations are considered the sections where diabase intrusions and silification zones appear. What makes this research interesting is the water permeability data in these zones. Despite the high RQD values for both type of rock, water permeability in zones where meta-diabases appear is significantly higher compared to silification zones.

Keywords

Dam, Geology, Geotechnics, Research, Corelation.

1 Introduction

The Lukovo Pole Dam project is part of the Hydro Energetic System “Lukovo Pole” which is an integral partof system “KorabskiVodi”. This project is planned to be implemented in the near future and would complete the entire Korabski Vodi system. The Lukovo Pole dam is situated in the peripheral north-western parts of the Republic of North Macedonia, near the joint point between Kosovo, Albania and North Macedonia. The dam is located on the Crn Kamen River at an altitude of 1520 m on terrain that is part of the Korab mountain. According to the basic design dated from 1989, it has been planned to be arock-fill type of dam with height of 71m which makes the elevation of the dam crown to be 1591m. Maximum elevation of the lake is 1589m, and minimal 1540m. Total volume of water mass in the reservoir is $39x10^6m^3$, out of which life storage is $38x10^6m^3$. Investigations date from the early 70' of the past century and up to 2012 when the last investigations were carried out by the Civil Engineering Institute "Makedonija" J.S.C. - Skopje. During this 40-year time period, a substantial geotechnical documentation has been created that served as the basis for development of the Summary Elaborate for this object.

From a geological perspective, the Lukovo Pole dam is situated within the western Macedonian province, which is distinguished as a separate geotectonic unit in Republic of North Macedonia. Characteristic by its complex lithological and tectonic composition, this zone is manifested by dominant presence of old Paleozoic higly metamorphic rocks and intense folding. Dam site zone is composed of several types of sediments and most of all metamorphic rocks as well as intrusions that are to certain level influenced by metamorphism. Aside from this, the terrain is also characterized by quite distinctive structural-tectonic composition, manifested by fault structure created along the axis of old and eroded anticlinal structure. This complex structural-geological composition of the terrain has considerable influence on the overall engineering-geological characteristics of the terrain. As most significant are considered to be the results from the water permeability tests of the rock in zones where meta-diabase and silicified phyllites appear.

2 Performed terrain investigations

The overall field investigations at the Lukovo Pole dam site consisted ofvarious scope of field research: detailed geological mapping, investigative drilling, water permeability, piezometer installation, dilatometric tests, joint strength testing with Schmidt hummer, investigative galleries, and geophysical tests. For this paper as essential data, results from detail geological mapping, exploratory drilling, geophisical tests and water permeability tests were analyzed.

Geological mapping consisted of engineering - geological and hydro-geological mapping of terrain in the dam zone and the core from the exploration boreholes (Fig 1b). Due to the presence of sediments, the incisions used during the construction of access roads and drilling platforms were used as an auxiliary indirect method for determining the geological structure of the terrain (Fig.1a). By this, detail lithological composition and level of fracturing (RQD) was established on surface and in depth.



a) b)

Fig. 1 Geological mapping a) along an access road b) borehole core.

Drilling consisted of 27 vertical boreholes with total length of 1355m, out of which 14 at the dam axis, spillway tunnel 3, diversion tunnel 5, and river bed 5 boreholes. Their depth variates from 15min the river bed, up to 80m along the dam axis. Geophysical refraction seismic investigations in total length

of 2500m were performed along the diversion tunnel, spillway tunnel and dam axis, as well as perpendicular to the axes. By this sediment thickness and level of fissuring for separate lithological units were established. Water permeability test was performed in 13 boreholes, out of which 9 by "Lügeon" and 4 by "Lefranc" method. Although unusual for examining solid rock masses, the Lefranc method in this case showed quite interesting results for this geological environment.

3. Results and discussion

Based on detailed geological mapping of the terrain and the core from the boreholes, it has been determined that the terrain in the zone of Lukovo Pole dam site is composed of: alluvial and diluvial sediments, and philitic, chlorite-sericitic and meta-diabase as bedrock.

Alluvial sediments are noted within the riverbed and have maximum thickness of around 5m. They are composed predominately of coarse-grained gravel and cobbles with small presence of sand and boulders. In general, they are formed by erosion of the fluvio-glacial sediments situated sidewise in the valley (water accumulation area), and have relatively small transport by water. Diluvial sediments are detected on the right flank where they almost in total cover the metamorphic bedrock. Their thickness and composition are quite variable. Along the dam axis they go from 5m to 10m in thickness, but in some zones on the right flank (approx. 200 north), their thickness is up to 20m. In general, they cover most of the bedrock and make geological interpretation very difficult.

Bedrock formation is detected predominately by drilling and in smaller scale by detection via outcrops. This situation is result of very high fissuring level of the metamorphic rock complex in which the series of phyllites and chlorite-sericitic schist are dominant type of rock. All detected outcrops are presented by meta-diabase, quartz veins or silicified phyllites (Fig 2). These types of rock appear as more compact compared to the phyllites and chlorite-sericitic schist which are dominant in the rock massif. Low compressive strength and high fissuring level along and perpendicular to the foliation plane makes the series of phyllites and chlorite-sericitic schist to be defined as highly weathered. However, the phyllites situated on the right flank appear as most fissured. Their level of weathering is up to form of eluvial debris.

Meta-diabase outcrops are detected on two locations on the left flank of the dam site (Fig 3). They appear as irregular intrusions in the metamorphic complex and are engulfed by low level of metamorphism. Large outcrops of quartz veins are also noted on the left flank (Fig 3). Their formation is related to younger acidic intrusions which is probably younger than the meta-diabases. This conclusion comes by the fact that quartz veins are detected even in the diabase intrusions. However, the possibility for several stages of acidic intrusions is also an option. What makes them distinctive is the fact that they appear generally along the foliation planes of the surrounding complex of phyllites and chlorite-sericitic schist and rarely perpendicular to them.



a) b)

Fig. 2 Detected outcrops a) meta-diabase b) silicified phyllites with quartz veins.

Silicified phyllites are detected generally by exploratory drilling in various zones of the rock massif. Their appearance is related to zones where quartz veins usually appear. Together with meta-databases they present the relatively compact sections of the rock massif.

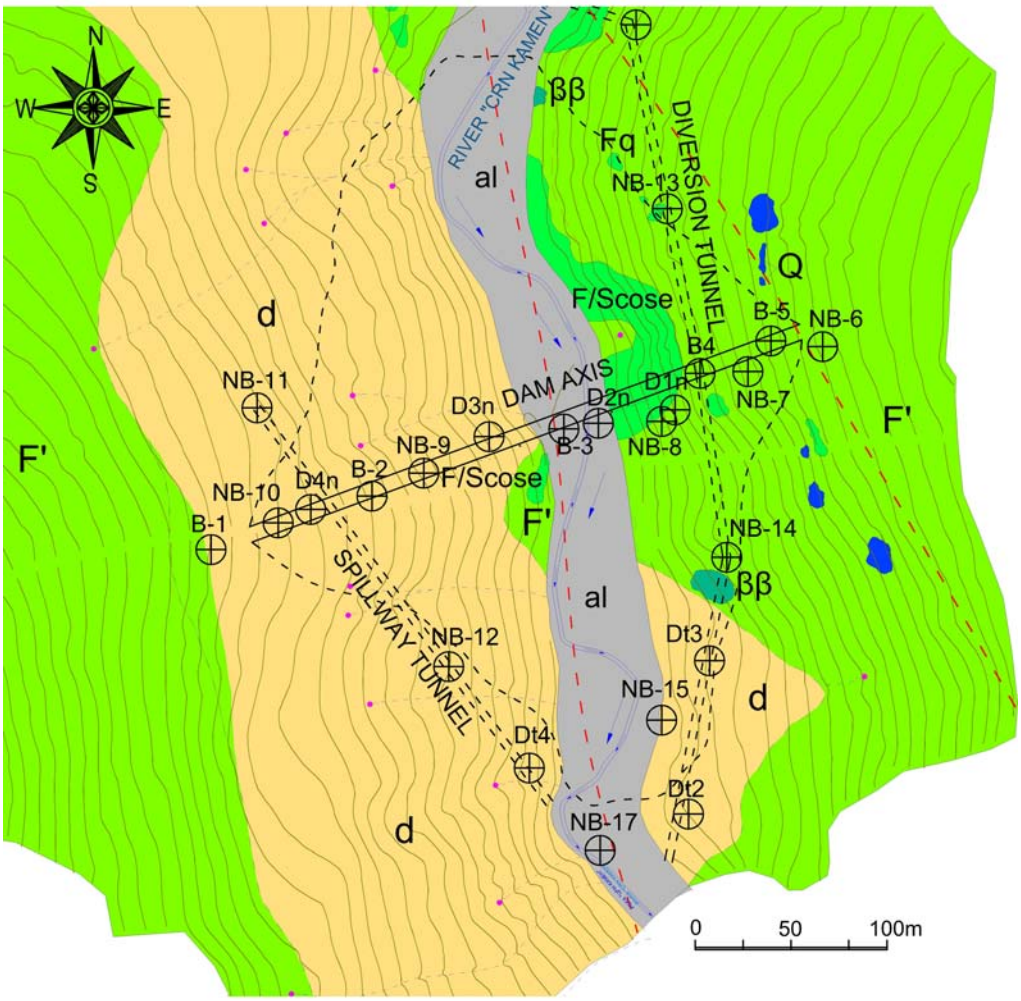
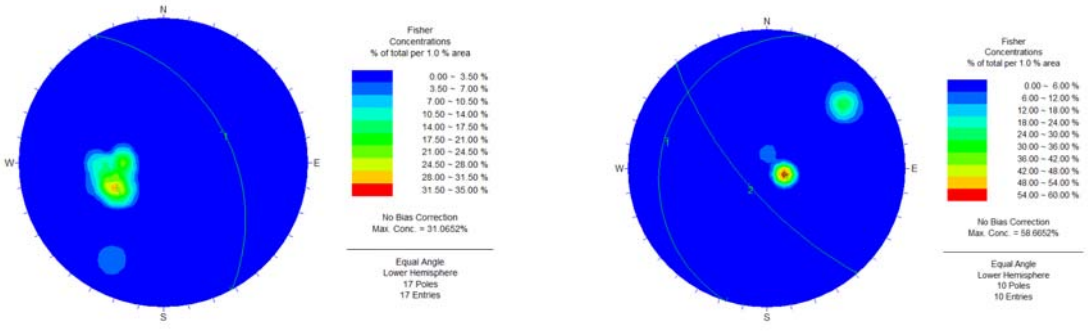


Fig. 3 Engineering-geological map of Lukovo Pole dam site.

Legend:**al**- alluvium, **d** - diluvium, **F'**- phyllites, **F/Scose** - complex of phylitic and chlorite-sericitic schists, **ββ** - meta-diabase, **Q** - quartz veins, B-1⊕ - borehole, _ _ _ _- fault (presumed)

By establishing the structural-geological data of the rock along the access roads, it was concluded that the dip of the foliation planes on both sides of the dam site have opposite dip direction and low to medium dip angle. On the left flank, general dip direction/ dip angle is 62/40°, and on the left flank 287/15° (Fig 4 &6). This situation indicates presence of eroded anticline structure along the axial plane which has perpendicular position towards the dam axis.



a) b)

Fig. 4 Stereo net plot of foliation data a) left flank b) right flank.

Most often in such cases the axial plane also represents a fault surface, i.e. during the formation of the folds, discontinuities appear along the axial plane. In this case, the hinge line represents the direction of the fault (Fig 5). Having in consideration that in our case all of the zone along the predicted hinge line is covered by alluvial sediments, the only logical possibility for defining the discontinuity in this case is as a presumed fault.

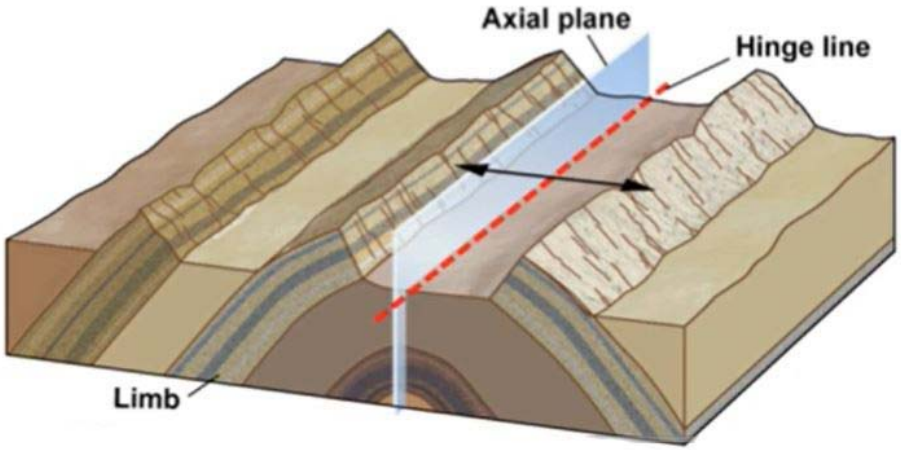


Fig. 5 Theoretical model of how the terrain was formed.

The linear occurrence of large outcrops of quartz veins on the left flank also provides indications of a possible faulting occurrence in that zone. This assumption is based on the fact that the linear sequence of quartz outcrops coincides with the direction of a fault determined north of the dam site (Fig. 3 & 6).

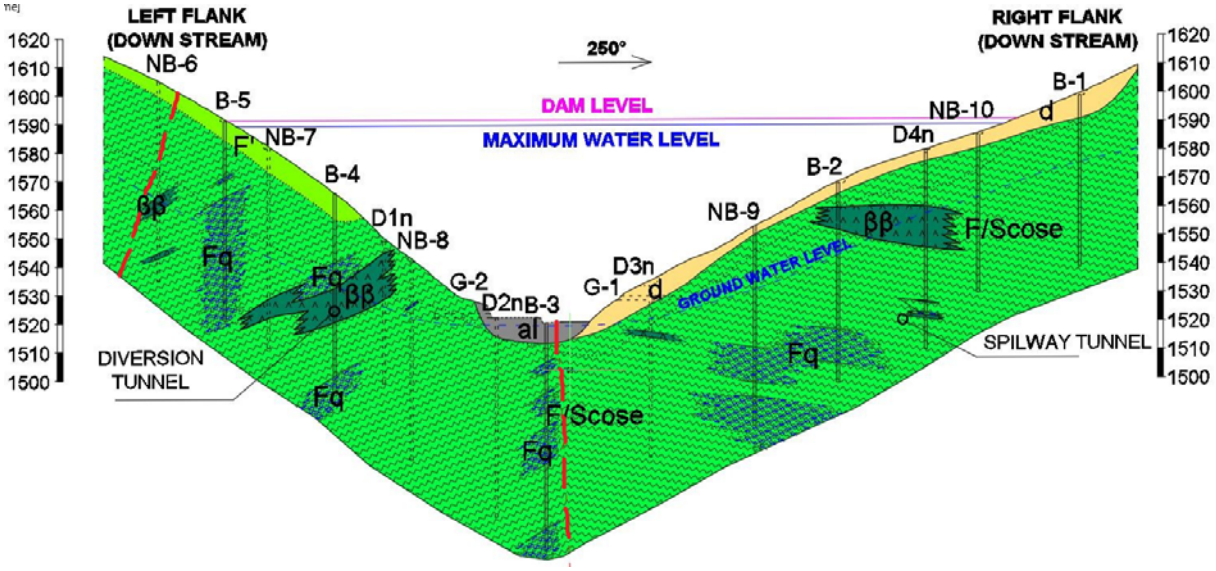


Fig. 6 Engineering-geological profile along the dam axis.

Legend:**al**- alluvium, **d** - diluvium, **F'**- phyllites, **F/Scose** - complex of phylitic and chlorite-sericitic schists, **ββ** - meta-diabase, **Fq** - silicified phyllites (quartz phylites), B-1 - borehole, _ _ _ _- fault (presumed)

In addition to the definition of the characteristics from laboratory examinations, and in combination with data from the field investigation analysis, systematization and classification of the acquired data was performed. Classification of the rock was done in categories (groups) with similar parameters i.e. geotechnical conditions for construction and work usage of the structure. For this purpose, categorization according RMR system of Bieniawski (1989) was performed (Table 1).

Nnecessary parameters were acquired from engineering-geology mapping of the area, mapping of the sampled core form investigation boreholes, as well as from laboratory examinations. Rating points are adopted as for separate parameters in the classification for each rock mass, as well as according the acquired RMR rating, (Table 1). The rating for the condition of joints for types of rock mass is performed according to detail classification of the discontinuities, where the length, opening, roughness, type of fill material and weathering level of the joint walls have been taken into consideration.

The correlation between structural geological properties and GSI and RMR values is based mainly on the genesis of the formation of the individual lithological members. Those that are relatively younger are more compact but with unfilled cracks, while the older phyllite shales are significantly more fractured but mainly filled with silty-clayey filler. This results in relatively higher water permeability mainly in metabasalts, and noticeably lower in phyllite schists.

Table .1 RMR classification of the rock at dam site zone.

P A R A M E T E R	**Rock type and points**		
	phyllite chlorite.-sericitic. schists (F/Scose)	**quartz phyllite (Fq)**	**meta-diabases (ββ)**
Uniaxial compressive strength	2	7	7
Rock Quality Designation (RQD)	3	8	13
Spacing between joints	5 - 8	10	10
Condition of joints	4 – 10	14	18
Underground water	7 - 10	4 - 7	0
Orientation of joints	-5	-5	-5
Rock Mass Rating(RMR)	**16 – 28**	**38 - 41**	**43**
Geology Strength Index (GSI)	24 – 33	49	58
Rock Mass Class	IV →V	IV → III	III

Geological Strength Index (GSI) was calculated as RMR - 5. In this case for RMR calculation 15 points for groundwater and 0 points for joint orientation ware established.

For adequate extrapolation from monolith to massif, the results from the rock mass classification were used for shear strength determination and the deformability of the massif. This extrapolation is done with the empiric non-linear criteria of failure criterion of Hoek & Brown:

$$\sigma_1 = \sigma_3 + \sigma_p \left(m_b \frac{\sigma_3}{\sigma_p} + s \right)^a \; ; \quad m_b = m_i \cdot exp\left(\frac{GSI-100}{28-14D}\right)$$

$$s = exp\left(\frac{GSI-100}{9-3D}\right) \; ; \quad a = \frac{1}{2} + \frac{1}{6}(e^{-GSI/15} - e^{-20/3})$$

σ_1, σ_3 – main perpendicular stress;
σ_p – pressure strength;
GSI – geology strength index according Bieniawski classification;
m_b, s, a – empiric constants deriving from GSI;
D – massif disturbance factor.

The value of the internal friction for the massif (φ_m), the cohesion of the massif (c_m) and the global strength of the rock massif (σ_{cm}) are acquired from the failure criterion of Hoek & Brown (2002), while the deformation modulus of the massif (E_{rm}) is calculated from the empiric formula of Hoek & Diederichs (2006). Results from the calculations are presented in Table 2.

Table 2. Estimated parameters for the shear strength of the rock.

Rock type	**σ_p [MPa]**	**GSI**	**m_i**	**m_b**	**s**	**a**	**γ [kN/m^3]**	**φ_m [°]**	**c_m [MPa]**	**σ_{cm} [MPa]**	**E_{rm} [MPa]**
F/Scose	10	28	6	0.195	1.00×10^{-4}	0.526	25.0	24.28	0.073	0.506	238.74
	10	27	6	0.078	1.57×10^{-5}	0.527	26.0	22.26	0.031	0.308	174.74
	2	24	5	0.134	3.97×10^{-5}	0.533	25.0	17.91	0.016	0.079	34.11
	10	33	7	0.288	1.00×10^{-4}	0.518	26.0	27.04	0.096	0.649	345.76
	8	24	5	0.134	3.97×10^{-5}	0.533	26.0	19.09	0.058	0.315	184.17
Fq	25	49	8	0.209	2.00×10^{-4}	0.506	26.0	33.48	0.129	1.490	1063.0
ββ	35	58	12	0.597	9.00×10^{-4}	0.503	26.0	43.09	0.266	3.625	2265.3
	35	58	10	0.498	9.00×10^{-4}	0.503	26.0	41.44	0.263	3.321	2265.3

Geophysical refraction seismic profiles were performed along and perpendicular to the axis of the dam, spillway and diversion tunnel. According to the obtained velocities of spreading of the elastic waves, three characteristic media were distinguished. Along the axis of the dam site, the first distinguished elastic medium has values of the waves ranging from 400 to 970m/s, and mainly refers to diluvial sediments and rock that is totally weathered and fissured on the surface up to level of diluvial debris. The values of the second zone are between 1580 and 1850m/s and it is a zone that corresponds to a fissured rock mass mainly represented by phyllites. The third zone has the highest values of the elastic waves ranging from 3520 and 3960m/s. This zone corresponds to a relatively less fissured rock mass and is defined as a zone of rock mass of best quality. These investigations did not result in spreading velocity values higher than 4000m/s. This indicates that generally the entire rock mass is significantly fissured.

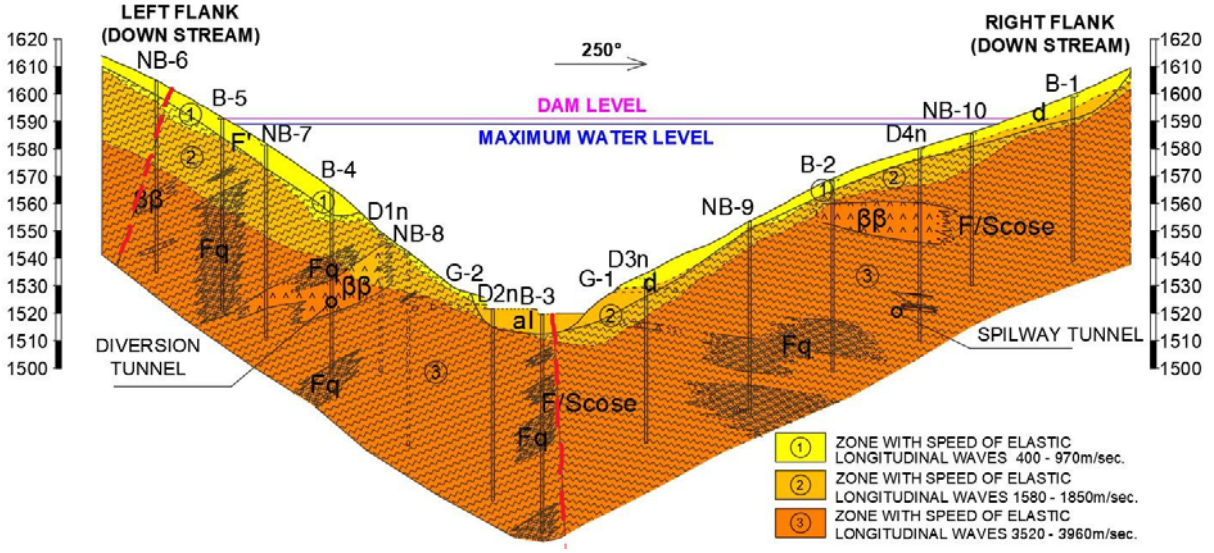


Fig. 7 Engineering-geological model by parameter of seismic waves along dam axis.

Legend:**al**- alluvium, **d** - diluvium, **F'**- phyllites, **F/Scose** - complex of phylitic and chlorite-sericitic schists, **ββ** - meta-diabase, **Fq** - silicified phyllites (quartz phylites), B-1 - borehole, _ _ _ _- fault (presumed)

Water permeability test was performed in 13 boreholes. In 9 boreholes the water permeability test was performed by applying both, the complete and brief Lugeon's method of injecting water under pressure of 0-2-4-6-8-10-8-6-4-2-0 Bar. In 4 boreholes (NB-6, NB-7, NB-8 и NB-9) water permeability was performed by applying the Le Franc method.Highest values (2.84 l/sec.) are registered in borehole NB-9.

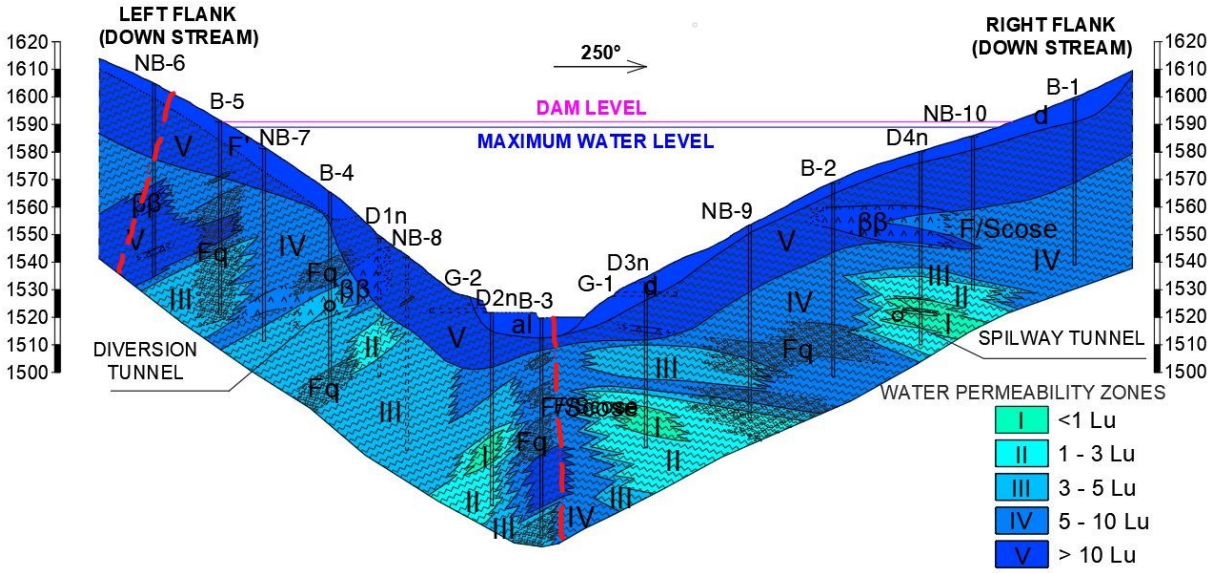


Fig. 8 Engineering-geological model by parameter of water permeability along dam axis.

Legend:**al**- alluvium, **d** - diluvium, **F'**- phyllites, **F/Scose** - complex of phylitic and chlorite-sericitic schists, **ββ** - meta-diabase, **Fq** - silicified phyllites (quartz phylites), B-1 - borehole, _ _ _ _- fault (presumed)

Based on the analyses of the water permeability, it is obvious that in the surface zones with rather degraded rocks and wide joints, there is a high degree of permeability. An interesting data is the water permeability tested in areas of meta-diabases, where there were zones to which it was impossible to reach the designed flow so that it was calculated by the analytic extrapolation per Lugeon, the method of quasi-Lugeon. The reason for occurrence of such high degree of permeability (> 50 Lü at D1n, &> 80 Lü in D2n) is the stiff structure of the meta-diabases i.e. their joints are stiff, hard without filler compared to the phyllitic schists where the joints are filled with clay and silt.

The highest values for water permeability of the rock massif in depth were determined in borehole B-3, which is located in the lowest part of the terrain. This indicates presence of a fault which is positioned along the axial plane of fold.

4 Conclusion

Based on the previously noted data from the field and laboratory research, it can be concluded that the location where the Lukovo Pole dam is designed, represents a complex geological environment with a variable geotechnical parameter of the rock mass.

By analysing the structural data from geological mapping and the water permeability of the rock mass, it can be concluded that the dam is situated on an eroded anticlinal structure along whose axialplane fault structure was formed thru which the erosion process took place. The presence of this fault was indirectly confirmed by water permeability test in B-1 where big values (>5Lu) were detected all the way up to 70m depth. The anticlinal form was established by analyzing the dip amount of foliation planes from both sides of the dam site where approximately symmetrical but opposite dip of the foliation planes was detected.

Special attention is drawn to the occurrence of meta-diabases, where the highest values of water permeability of the rocks have been determined. This situation is a result of the wide openings and unfilled cracks in this type of rock. On the other hand, quartz-phyllites, which also have increased hardness and are even somewhat more fractured than diabases, have significantly lower water permeability values. This stems precisely from the fact that the presence of fine grained (clay/silty) filling in the cracks was determined in borehole core. This is most likely a result of the relatively young age and disorder of the basalt intrusions, as well as the mineralogical-petrographic composition itself, which, in comparison with phyllites, is not of clay origin. What is also characteristic is the planar distribution of water permeability, which, with the exception of the fault zone, is mainly directed along the foliation planes.

Considering the fact that the analyzed structure represents an eroded anticline, it can be concluded that it represents a medium with drainage character. Unfavorable strike and dip direction of the foliation planes on both flanks have crucial role in this case. This actually represents the essential connection between the structural geological form and the geotechnical properties of the rock mass. Relatively younger meta-diabase and quartz intrusions play significant role in formation of more compact and solid sections inside the medium, but also more water permeable. By resolving the structural geological properties of the rock mass in this case, we provided a proper way to direct the geotechnical investigations and have better understanding of the physical-mechanical characteristics of the rock.

Generally speaking, it can be concluded that this is a rather complex geological environment with a specific structural property in which, despite the high level of exploration, it is difficult to precisely distinguish quasi-homogeneous zones with similar geotechnical properties.

References

Kulakov Lj, Velevski A, Angelov D, Kostovski V, (2012) Summary elaborate for performed geotechnical investigations at H.E.S.”Lukovo Pole”, BOOK II - geotechnical investigations of the dam site and dam appurtenances on the dam "Lukovo Pole"(Civil Engineering Institute Macedonia j.s.c. Skopje): 36p.

DumurdzanovN, Petrov G, (2005): Geological mapping. St.Cyril and Methodius University in Skopje, Faculty of Minig and Geology Shtip, 298 p. [in Macedonian].

DIPS v5.0 software (2004) Rocscience Inc. 54 St Patrick St, Toronto, ON M5T 1V1, Canada

Dumurdzanov N, (1999): Structural geology. St.Cyril and Methodius University in Skopje, Faculty of Minig and Geology Shtip, 248 p. [in Macedonian].

Aswar D. S, Ingle G. S, Ambadkar S. D. (2022) Geological characterization of potential dam sites, ISSN PRINT 2319-1775 Online 2320-7876, www.ijfans.org Vol.11, Iss.8, Aug.- 2022 UGC CARE Listed (Group -I) Journal, [11], (8), 3067-3062

Best, E. (1984). Dams, engineering geology . In: Finkl, C. (eds) Applied Geology. Encyclopedia of Earth Sciences Series, vol 3. Springer, Boston, MA. https://doi.org/10.1007/0-387-30842-3_15

Hoek E, (1994): Strengths of rock and rock masses. ISRM News Journal, [2] (2): 4–16

Jovanovski M, Gapkovski N, Pesevski I, Abolomasov B, (2012): Engineering Geology, Faculty of Civil Engineering, 672 p. [in Macedonian]

Paige S, (1950) Application of Geology to Engineering Practice. Berkey Volume, New York: Geological Society of America, 327p

Stapeldon H, (1976) Geological hazards and water storage, Bull. Internat. Assoc. Eng. Geology, (14)249–262

BestE J, (1981) The influence of geology on the location, design and construction of water supply dams in the Canberra area, Bur. Mineral Resources Jour. Australian Geology and Geophysics. [6] (2), 161–179

Hoek, E., Carter, T.G., Diederichs, M.S, (2013): Quantification of the Geological Strength Index Chart. 47th US Rock Mechanics / Geomechanics Symposium held in San Francisco, CA, USA, [4] (1) 1757 - 1764.

Resolution-induced uncertainty in DEM-predicted brittle damage thresholds in sandstone

Jinci Chen[1, 3], Elli-Maria Charalampidou[1], Ali Ozel[2], James Woodman[4] & Audrey Ougier-Simonin[3]

[1] *Institute of GeoEnergy Engineering, School of Energy, Geoscience, Infrastructure and Society, Heriot-Watt University,Edinburgh, UK*
[2] *School of Engineering and Physical Sciences, Heriot-Watt University, Edinburgh, UK*
[3] *British Geological Survey, Keyworth,Nottingham, UK*
[4] *Geo-Design Consulting Engineers Ltd, Ringwood, UK*

jc2138@hw.ac.uk
0009-0002-0920-9778

Abstract

Brittle damage thresholds predicted by discrete element method (DEM) modelling are informative for interpreting rock failure processes and supporting engineering design. Nonetheless, these predictions are constrained by the model particle resolution. This study investigates whether variations in model particle resolution affect the interpretation of damage thresholds in sandstone subjected to uniaxial compression. A recently developed Subspring Network Breakable Voronoi model was used to simulate uniaxial compression at four different particle resolutions. The results show a systematic dependence of the predicted response on model particle solution. With increasing resolution, the predicted uniaxial compressive strength, crack initiation, and crack damage thresholds generally increase, while Young's modulus decreases slightly and Poisson's ratio shows limited sensitivity. Finer resolutions also produce significantly higher crack counts and denser fracture patterns. Despite these variations, the dominant macroscopic failure mode remains tensile dominated; axial splitting is observed across all resolutions. These findings indicate that model particle resolution influences quantitative interpretations of brittle damage more strongly than qualitative identification of failure modes. Consequently, model particlere solution should not be treated merely as a numerical setting but rather as a source of modelling uncertainty in DEM based rock engineering analyses. An intermediate model particle resolution is considered to provide a practical compromise between computational efficiency and representative failure behaviour.

Keywords

Brittle fracture, Model particle resolution, Damage threshold, Rock failure, Modelling uncertainty.

1 Introduction

Rock engineering design and risk assessment are commonly informed by discrete element method (DEM) predictive modelling. Thus, accurate calculations and predictions of brittle damage onset, unstable crack growth, and peak strength appear to be crucial for informed design decisions.

DEM based Bonded-Particle Models (BPMs) have demonstrated sufficient flexibility and capability to accurately reproduce the brittle fracture process in both compact and porous rocks (Potyondy and Cundall 2004; Potyondy 2012; Potyondy et al. 2025). However, the selection of model particle scale can introduce uncertainty, thereby impacting the engineering assessment of rock damage thresholds and strength.

Conclusions drawn from modelling single particle resolution may lead to either overestimation or underestimation of damage initiation and instability thresholds. This uncertainty may affect risk management in rock engineering. Prior research has identified this issue as a particle size sensitivity problem (Peng et al. 2021; Zhang et al. 2022; Li et al. 2024; Sun et al. 2024; Potyondy and Fu 2024), although limited investigations have addressed the influence of discretisation-dependent responses on engineering interpretation.

This paper uses the recently established Subspring Network Breakable Voronoi (SNBV) model (Rasmussen 2021; Potyondy et al. 2025) to study the uniaxial compression of cylindrical specimens of sandstone. Model particle resolution can be expressed through specimen resolution (φ), defined in the current 3D SNBV model as the number of Voronoi particles spanning the specimen diameter. Four different specimen resolutions were examined. By quantifying the influence of φ on key damage and strength thresholds in sandstone, we aim to understand how these results affect engineering interpretation.

2 Computational model configuration

The SNBV model represents rock microstructure using a Voronoi tessellation, where Voronoi particles are bonded by linear elastic subsprings distributed across each particle interface. This model has two main features: first, it explicitly accounts for rock heterogeneity through the application of the Weibull probability distribution; second, it incorporates a grain breakage scheme that supports both inter- and intra-granular crack mechanisms. In this study, the model configuration was defined in terms of specimen geometry, porosity, particle size, and particle-size distribution. To ensure consistency with the laboratory data for Thornhill Rock reported by Woodman (2020) and Woodman et al. (2021), the specimen dimensions were set to 120 mm × 54 mm (height × diameter). A Weibull shape factor of m = 7.6 was adopted, based on values fitted to the indirect tensile strength distribution (Woodman et al. 2021). Additional heterogeneity sensitivity simulations (not shown here) indicate that, for the level of heterogeneity considered (m=7.6), the macroscopic response is only weakly affected. The influence of heterogeneity was therefore not considered further in the present study. Further details of the model formulation and implementation are provided by (Itasca Consulting Group, Inc. 2025).

Table 1. Model particle size configuration in the SNBV model.

Model	Initial seed diameter (mm)	Model particle size (mm)	Specimen resolution (φ)
Analogue 1	3.6	5.4	10
Analogue 2	2.4	3.4	15
Analogue 3	1.8	2.7	20
Analogue 4	1.2	1.8	30

In the present SNBV model, porosity was assumed to be zero due to the dense interlocking Voronoi microstructure. In contrast, Thornhill Rock has a reported grain size range of 63-250 μm and a porosity of approximately 15.5%. Poisson's ratio was implemented through fictitious stress corrections (Rasmussen et al. 2018). The cylindrical model was generated in three steps: (1) generation of non-overlapping spheres as initial seeds with a uniform distribution; (2) application of a Laguerre tessellation using these spheres as seeds, where the seed sizes influence the Voronoi cell size; and (3) trimming of the tessellated particles/blocks to produce a cylindrical specimen. Table 1 summarises the four model particle sizes, defined here as the mean diameter of the Voronoi particles

after trimming. Specimen resolution was calculated as the number of Voronoi particles spanning the cylinder diameter. We considered four initial seed diameters corresponding to four specimen resolution cases (see Table 1).

Compression simulations were performed by moving two rigid walls at the top and bottom towards each other. The frictional coefficient between model specimen and wall is set at 0.02 to reduce end effects. Damping ratio is 0.7, this is for energy dissipation and reduce dynamic effect. The loading rate was chosen to be slow enough to produce a quasi-static response, representative of the strain rate commonly adopted in laboratory rock testing ($10^{-5}$to 10^{-3} s^{-1}; (Paterson and Wong 2005)). It should be noted that, because mechanical timestep scaling was used, model time was not assumed to correspond directly to physical time. Axial strain was calculated from cumulative wall displacements, while axial stress was obtained by dividing the total reaction force acting on the loading walls by its contact area. Lateral strain was determined from radial deformation measurements obtained using circular ring blocks around the specimen diameter. These ring blocks were formed by the outermost Voronoi particles adjacent to the cylindrical specimen boundary, and their average was taken as the overall lateral strain. Simulations were performed using the three-dimensional Particle Flow Code, version 9.3 (Itasca Consulting Group, Inc. 2025).

3 Results

In this section, we discuss how varying specimen resolution (φ) affects macroscopic mechanical response. Each case was repeated three times with different random seed distributions while keeping other input parameters constant and only altering the particle size during model generation. All tests were conducted under consistent physical and boundary conditions throughout the study (e.g., model configuration and loading rate). It should be noted that variations in model particle size may affect the arrangement and interlocking of the grains, thereby affecting the packing fabric; however, these effects are not considered explicitly in the present study.

φ = 15 (blue curve in Fig.1) was adopted as the reference calibration case, as this intermediate resolution was considered representative by Potyondy et al. (2025). Its input parameters were calibrated against the specimens 235 and 207. All specimen resolutions reproduce the main macroscopic features of the experimental response, including crack closure (CC), crack initiation (CI), crack damage (CD) and post-peak stress drop. A clear resolution dependence is observed: as resolution increases, the predicted peak stress progressively increases. In addition, the finer resolution models reach their peak strength at a larger axial strain than their coarser counterparts. The coarsest model underestimates the peak strength, while the finest model tends to overestimate both the peak stress and the strain at peak. These results indicate that φ has a non-negligible impact on themacroscopic mechanical behaviour, which motivates the subsequent analysis of damage thresholds.

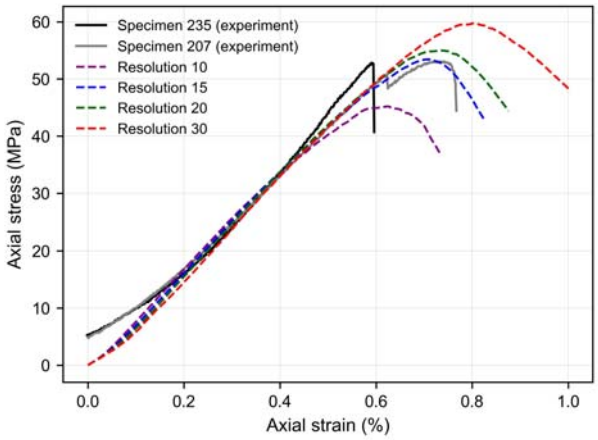


Fig.1 Comparison of axial stress-strain curves from laboratory UCS tests (specimens 235 and 207; Woodman et al. (2021)) and simulations at four specimen resolutions (see Table 1). The experimental curves include a small initial preload used to establish platen-specimen contact.

As the macroscopic stress-strain curves in Fig.1 show a clear dependence on specimen resolution, Fig. 2 quantifies this effect through derived damage thresholds. The CC, CIand CD thresholds were identified from the axial and volumetric strain responses (Nicksiar and Martin 2012). Young's modulus (E) and Poisson's ratio (ν) were determined over the linear interval between CC and CI. The

UCS, CI and CD values show an increasing trend with increasing specimen resolution, indicating that finer model particle size predict higher stress levels for the onset and progression of brittle damage. By contrast, *E* shows a slight decreasing trend, whereas *v* varies only within a narrow range and appears less sensitive to resolution changes. The scatter between repeat simulations remains relatively limited compared with the systematic change in the mean values, suggesting that the observed trend is primarily resolution driven rather than a consequence of random seeds generation alone.

This trend is observed under the specific condition that only the model particle size is varied, while maintaining consistent input parameters across all resolutions. In this study, φ=15 was used as the reference calibration case. Nonetheless, if a different specimen resolution was used as the calibration case, the resulting trend could differ because changes in packing fabric may require adjustments to the input parameters to reproduce the laboratory responses of specimens 235 and 207. In other words, although the model at a given resolution can be calibrated to match the experimental results, it should not be assumed that it will provide same quantitative predictive damage thresholds at other resolutions without any further recalibration. This issue is not confined to the laboratory scale, but also applies to engineering scale interpretation, where differences in discretisation, geometry and loading conditions may similarly affect the parameter set required to reproduce the target response.

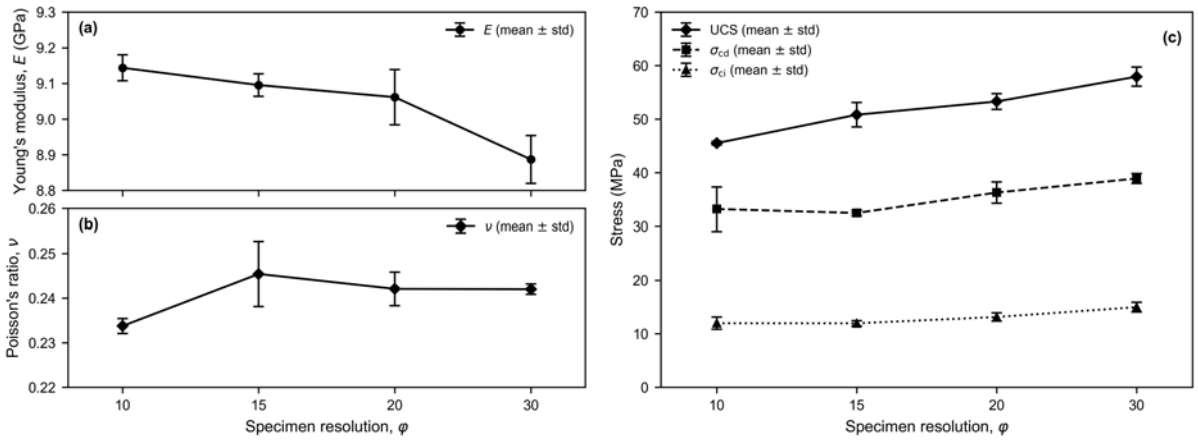


Fig. 2 The dependence of the key mechanical and damage indicators derived from simulations on specimen resolution (φ), including CC, CI, CD, *E*, *v*and UCS. Error bars show the scatter from three repeat runs.

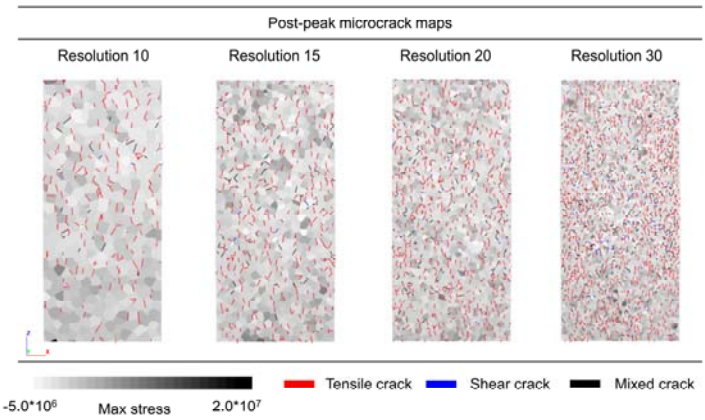


Fig. 3 Fracture traces of tensile, shear and mixed-mode microcracks on the central Z–X cross-section at the post-peak stage for four specimen resolutions.

To visualise damage distribution, Fig. 3 displays crack maps on the central Z–X cross-section of the cylindrical model at the post-peak stage. These maps represent the fracture traces observed on this section. The crack patterns are compared across different specimen resolutions, with Z denoting the specimen height axis and X the radial direction. Fig. 4 summarises the corresponding crack-type proportions and total crack counts. As specimen resolution increases, the total number of recorded crack events rises markedly, producing progressively denser fracture patterns in the finer discretisation. Despite this increase in crack density, the dominant failure pattern remains broadly consistent across the considered resolutions, with tensile cracking prevailing and the specimen exhibiting axial splitting. Fig. 4 further shows that across all resolutions, tensile cracks constitute the largest portion of the crack

population; however, their proportion declines modestly as the fractions of shear and mixed-mode cracks increase.

These results indicate that specimen resolution may alter the extent of crack accumulation but has limited effects on the overall failure mechanism. We speculate that an intermediate specimen resolution may still capture the representative failure mode, even though the predicted crack density and the associated threshold values remain resolution dependent. Based on these results, the trends in Fig. 2Fig. 3Fig. 4 show that specimen resolution influences the quantitative assessment of brittle damage more strongly than the qualitative identification of the failure mechanism. Increasing the resolution introduces more, smaller Voronoi particles and bonded contacts, expanding the number of potential crack paths and promoting more distributed bond breakage. This naturally leads to higher crack counts and shifts the predicted CI, CD and UCS to higher stress levels.

From a rock physics perspective, this distinction is crucial: while a single specimen resolution may still capture the representative failure mode, it may not provide resolution-independent estimates of damage thresholds used to interpret the onset and progression of instability. Since the simulations do not explicitly reproduce the true grain size of the tested sandstone, we adopted a larger but computationally affordable range of model particle size and examined their effect on four different specimen resolutions. The resulting particle size effects, defined by specimen resolution, align with trends reported in experimental studies where finer-grained rock materials typically exhibit higher strengths. In this sense, the behaviour observed in higher resolution simulations resembles that of experimentally tested samples with smaller grain sizes and, in some cases, lower porosity.

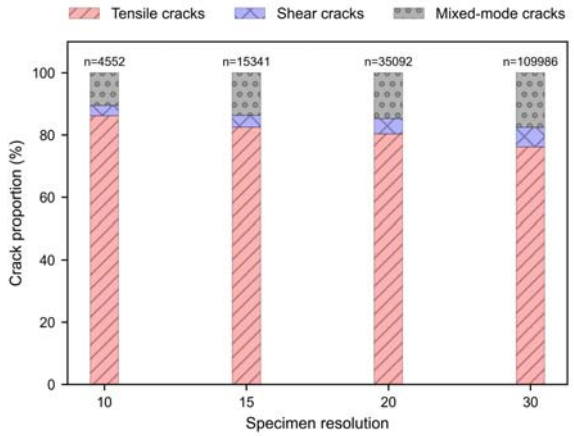


Fig. 4 Proportions of tensile, shear and mixed-mode cracks for different specimen resolutions at the post-peak stage; n above each bar denotes the total crack count.

4 Conclusions

This study investigates the influence of specimen resolution on the mechanical response and damage thresholds of sandstone subjected to uniaxial compression using the SNBV model. The main conclusions are as follows.

(1) Specimen resolution has a systematic effect on the predicted UCS values and associated damage thresholds.
(2) The predicted UCS, CI and CD thresholds generally increase with increasing specimen resolution, whereas Young's modulus shows a slight decrease and Poisson's ratio is comparatively less sensitive.
(3) Although crack density increases markedly at higher specimen resolutions, the dominant failure mode remains tensile dominated as axial splitting is observed across the resolutions considered, indicating that the model can capture well the occurring macroprocesses.

These results suggest that specimen resolution should not be treated merely as a numerical setting but rather as a source of modelling uncertainty that affects the inferred onset and propagation of brittle damage. Using an intermediate specimen resolution still reveals critical damage features while maintaining a practical balance between computational efficiency and representative failure response.

References

Itasca Consulting Group, Inc. (2025) Subspring network model. PFC Documentation. Available at: https://docs.itascacg.com/itasca940/common/contactmodel/rbsn/doc/manual/cmspringnetwork.html?node5092. Accessed 25 May 2026.

Li W, Yu L, Zhang T, Su H, Mi X, Fan D, Jin B (2024) Quantitative analysis of grain size effect on tensile mechanical behavior of granite based on multi-level force chain networks. *Computational Particle Mechanics*, 11(5): 2245–2266.DOI:10.1007/s40571-024-00790-3

Nicksiar M, Martin C (2012)Evaluation of methods for determining crack initiation in compression tests on low-porosity rocks.*Rock Mechanics and Rock Engineering*, 45(4): 607–617.DOI: 10.1007/s00603-012-0221-6

Paterson MS, Wong TF (2005)*Experimental Rock Deformation – The Brittle Field*.2nd edn.Springer,Berlin Heidelberg.

Peng J, Wong LNY, Teh CI (2021) Influence of grain size on strength of polymineralic crystalline rock:Newinsights from DEM grain-based modeling. *Journal of Rock Mechanics and Geotechnical Engineering*, 13(4): 755–766.DOI:10.1016/j.jrmge.2021.01.011

Potyondy DO, Cundall PA (2004) A bonded-particle model for rock. *International Journal of Rock Mechanicsand Mining Sciences,* 41(8): 1329–1364. DOI:10.1016/j.ijrmms.2004.09.011

Potyondy DO (2012)A flat-jointed bonded-particle material for hard rock.*46th US Rock Mechanics/Geomechanics Symposium*,Chicago, Illinois, USA,24–27 June 2012,Paper No. ARMA-2012-501.

Potyondy DO, Fu W (2024)A 3D subspring network breakable Voronoi model for rock: laboratory-scale behavior.*58th US Rock Mechanics/Geomechanics Symposium*,Golden, Colorado, USA,23–26 June 2024,Paper No. D031S029R005.

Potyondy DO, Fu W, Purvance M, Mas Ivars D (2025) A 3D subspring network breakable Voronoi model for rock. *Rock Mechanics and Rock Engineering*. DOI: 10.1007/s00603-025-04655-w

Rasmussen LL (2021) Hybrid lattice/discrete element method for bonded block modeling of rocks. *Computers and Geotechnics*, 130: 103907. DOI:10.1016/j.compgeo.2020.103907

Rasmussen LL, de Farias MM, de Assis AP (2018) Extended Rigid Body Spring Network method for the simulation of brittle rocks. *Computers and Geotechnics*, 99: 31–41.DOI:10.1016/j.compgeo.2018.02.021

Sun Y, Kwok CY, Duan K (2024) Size effects on crystalline rock masses: Insights from grain-based DEM modeling. *Computers and Geotechnics*, 171: 106376. DOI:10.1016/j.compgeo.2024.106376

Woodman J (2020) *Thermo-mechanical loading of intact rock and discontinuities*. PhD thesis, University of Leeds. Available at: https://etheses.whiterose.ac.uk/id/eprint/26306/. Accessed 25 May 2026.

Woodman J, Ougier-Simonin A, Stavrou A, Vazaios I, Murphy W, Thomas ME, Reeves HJ (2021) Laboratory experiments and grain based discrete element numerical simulations investigating the thermo-mechanical behaviour of sandstone. *Geotechnical and Geological Engineering*, 39(7): 4795–4815.DOI:10.1007/s10706-021-01794-z

Zhang T, Yu L, Peng Y, Ju M, Yin Q, Wei J, Jia S (2022) Influence of grain size and basic element size on rock mechanical characteristics: insights from grain-based numerical analysis. *Bulletin of Engineering Geology and the Environment*, 81(9): 347.DOI:10.1007/s10064-022-02856-z

Application of Fiber - Reinforced Concrete in Tunnel Construction: Innovations and Challenges

B. Grujic, Z. Grujic, M. Jaksic
Universtity of Banja Luka, Faculty of Architecture, Civil Engieering and Geodesy, /Department of Civil Engineering/, Banja Luka, Bosnia and Herzegovina
bojana.grujic@aggf.unibl.org
0009-0004-6926-6920
Lj. Markovic
University of Priština, Kosovska Mitrovica, Faculty of Technical Science, /Department of Civil Engineering/, Kosovska Mitrovica, Serbia
S. Zekan
University of Tuzla, Faculty of Mining, Geology and Civil Engineering, Tuzla, Bosnia and Herzegovina
S. Koprivica
University of Union - Nikola Tesla, Faculty of Construction Management, Belgrade, Serbia

Abstract

The introduction of fibers into the testing of concrete mixtures, particularly in the post-elastic zone, induces positive changes ranging from mild to significant, depending on a variety of factors including the strength of the concrete matrix, type of fibers, elasticity modulus of the fibers, fiber strength, surface bonding characteristics of the fiber to the concrete matrix, fiber content, fiber orientation within the matrix, and the effects of aggregate size. The use of concrete combined with steel fibers contributes to the plastic behavior of this type of material, which is especially suitable for applications where traditional reinforcement is difficult to implement, such as in tunnel linings. Modern demands in the field of civil engineering continuously require the introduction of new technologies to achieve higher quality, more durable, and more economical materials. In this context, this paper presents the application of fiber-reinforced concrete for the construction of the primary substructure of tunnel structures. Before being used to create the primary support of the tunnel structure, experimental-theoretical analysis and modeling of the applied fiber-reinforced concrete was conducted. The main scientific contribution of this paper is the use of the obtained laboratory characteristics of cylindrical samples (the working σ-ε diagram of fiber-reinforced concrete) for the calculation of tunnel linings. A review of the research community shows that until now, it has not been possible to apply the working σ-ε diagram of fiber-reinforced concrete in a digital format, thus, from this perspective, the presented paper represents an innovation. Based on the presented analysis and additional analysis of the tunnel structure, it can be safely concluded that the differences between the two compared linings are within the domain of calculation error. The bearing capacities of the linings are close and the savings are reflected in the exclusion of the prefabricated reinforcement position, certainly in the case of economic justification of the use of fiber-reinforced tunnel lining.

Keywords

Tunnel lining, Fiber-reinforced concrete, Nonlinear analysis.

1 Introduction

1.1 Model Description and Input Data

A two-dimensional finite element model was developed to determine the displacement field, stress states, and plastic zones of both unsupported and supported excavation, as well as the effects on the tunnel lining. The model encompasses a sufficiently large portion of the surrounding ground to minimize the influence of boundary conditions on the calculation results within the tunnel zone. In the example presented, fixed boundary conditions are applied on all sides. Three-node finite elements were used for the modeling.

The primary stress state represents the stress conditions in the soil for the undisturbed state prior to tunnel excavation. If no specific measurements of the initial stress state have been conducted and no particular geological conditions exist, the vertical stress can be assumed as the weight of the overlying soil. The horizontal stress is then assumed to be a fraction of the vertical stress for an elastic solution. The ratio of horizontal to vertical stress, when determining the primary stress state, is defined using Poisson's ratio, ν, in the form:

$$\frac{\sigma h}{\sigma v} = \frac{\upsilon}{1-\upsilon} \tag{1}$$

During tunnel excavation, the primary stress state changes. This change is not a fixed value but a function of soil parameters, the stiffness and strength of the lining, and the time of its installation. The excavation is simulated using a step-by-step elimination procedure of finite elements defining the soil (a group of elements from element $m$to element n). The stresses in the eliminated elements are then integrated and applied as external loads.

Stresses in the surrounding materials, caused by stress redistribution during excavation, may exceed the allowable stress limits. In such cases, plastic deformation occurs. The difference between the allowable stress level and the actual stresses causes further redistribution in the surrounding material or the installed lining.

1.2 Model of Tunnel Structure

When selecting the tunnel structure model, the quality of the rock mass, the degree of variability, and the quality along the tunnel are taken into account. Construction technology and the height of the overburden also influence this choice. The cross-section is a complex horseshoe-shaped figure, consisting of a crown with an excavation radius of 5.85 m, a bench 2.00 m high, and a base vault that closes the entire contour. This type of tunnel extends through the geotechnical environment A of the tunnel, with characteristics provided in the following table 1.

Table 1. Characteristics of the Geotechnical Environment.

Physical and Mechanical Properties of the Material	Geotechnical Environment			
	A: Diabase Hornfels Formation – Hornfels	**B:** Diabase Hornfels Formation – Clays	**C:** Deluvial–Eluvial Cover	**D:** Limestones – Zone of Surface Alteration
vp(km/s)	1,80-2,37	3,78	0,60	2,40
vs (km/s)	1 150	1,75		1 300
γ(kN/m3)	25	24		24
μ	0,35	0,34		0,35
Edyn (Mpa)	5 200	22 600		5 800
G (Mpa)	3 300	9 000		3 700
K (Mpa)	9 500	21 000		10 500
Est (Mpa)	1 600 - 2 200	4 800 – 6 300		2 000 - 2 900
D (Mpa)	400 - 700	1 300 – 2 2 0		600 - 1 100

- Coulomb–Mohr Failure Criterion

Model B

For *Coulomb-Mohr*-a:

Geotechnical Data	Diabase Hornfels Formation – Predominantly Hornfels
Class of the Tunnel	Model B
γ (kN/m^3)	25
φ (^{o})	25
E (MPa)	2000
ν (-)	0.28
c (MPa)	0.20
D (MPa)	120

2 Experimental Program and Applied Methodology

2.1 Numerical Models of Excavation Support Using Reinforced Concrete (RC) and Using Fiber-Reinforced Concrete (FRC)

For the numerical investigation comparing the behavior of excavation support, a traffic tunnel model was adopted. The study presents a comparison of the excavation contour support performance during excavation using:

- Conventional concrete of class 25/30 reinforced with a double-layer steel mesh
- Fiber-reinforced concrete of class 30/38.7, reinforced with hooked-end steel fibers with a shape factor of L/D = 50/0.75 and a fiber content of 2% by volume of the total concrete mixture.

The objective of this numerical analysis was to demonstrate the behavior of the rock mass around the excavation in the case of using fiber-reinforced concrete with characteristics L/D = 50/0.75, with emphasis on the significantly increased toughness of this concrete, while all other parameters remain the same for both cases: geotechnical characteristics of the rock mass, loads during staged excavation, and compressive strength of the base reinforced concrete (RC) material. Passive anchors were not installed, as they are not of interest for this study.

The reinforced concrete lining is modeled as a beam element because the reinforcement enables it to carry normal forces, shear forces, and bending moments. The allowable stresses are adopted as follows, according to the current regulations:

- Concrete class C25/30, i.e., 30 MPa
- Allowable bending stress: 12 MPa (safety factor 2.50)
- Allowable tensile stress without cracking: 1.5 MPa (safety factor 20)

The basis for comparing the two linings is the operational principle of the PHASE2 software package for the analysis of tunnel structures. This software requires peak and residual values as input data for both the rock and the RC lining, which is standard when applying the Failure Theory.

Therefore, considering a minimum safety factor of 1.50 for compressive stresses and 10 for tensile stresses for the limit states used to assess and compare the load-bearing capacity of RC and fiber-reinforced concrete (FRC) linings, the following data are adopted for the RC lining:

- Peak compressive stress: 30 MPa
- Residual compressive stress: 5 MPa
- Peak tensile stress: 5 MPa
- Residual tensile stress: 1 MPa

Until now, no software has been capable of accepting defined working σ–ε diagrams of concrete in digital form as input data for further structural behavior analysis. This capability is crucial in the case of fiber-reinforced concrete (FRC) due to its drastically enhanced toughness after reaching peak strength.

One of the significant contributions of this study is the use of a laboratory-derived working σ–ε diagram of fiber-reinforced concrete in digital form for the calculation of tunnel linings. The presented method of modeling FRC is the only way to directly compare conventional reinforced concrete (RC) and FRC models. The comparison between the two proposed linings is made possible by the increased tensile strength of fiber-reinforced concrete, in this case achieved using steel fibers.

Laboratory tests show that the compressive strength of fiber-reinforced concrete increased by approximately 5% compared to standard samples (without fibers), while the tensile strength increased by up to 50%. These laboratory tests apply to a concrete age of 28 days, after which a slight reduction in both compressive and tensile strength is observed.

It should be noted that this study does not address long-term monitoring of changes in compressive and tensile strengths (beyond 28 days), which may be highly relevant in cases such as work

interruptions. This is particularly pertinent to underground works over extended periods due to factors such as financial constraints or abandonment of the project by the contractor for unforeseen reasons.
For the purposes of this study, the following input data for FRC are adopted:

- Peak compressive stress: 38.7 MPa
- Residual compressive stress: 6.5 MPa
- Peak tensile stress: 7.5 MPa
- Residual tensile stress: 1.5 MPa

The RC model and the FRC model share identical geometry, surrounding model mesh, and geotechnical properties of the environment and rock mass, as adopted from the tunnel construction documentation.

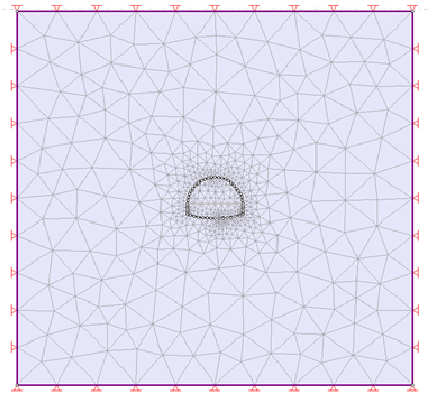
3 Results and Discussion

Graphical representations of the results are generated for both models to allow for comparison.

3.1 Numerical model

The geotechnical characteristics of the surrounding rock mass are:

Material Properties

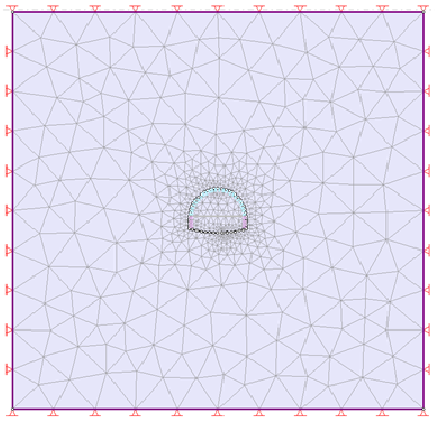


Material: Material 1
Initial element loading field stress & body force
Unit weight 0.025 MN/m3
Elastic type isotropic
Young's modulus 2000 MPa
Poisson's ratio 0.28
Failure criterion Mohr-Coulomb
Tensile strength 0 MPa
Peak friction angle 25 degrees
Peak cohesion 0.2 MPa
Material type Plastic
Dilation Angle 0 degrees
Residual Friction Angle 25 degrees
Residual Cohesion 0.2 MPa
Piezo to use None

Fig. 1 Numerical model.

3.2 Model with Reinforced Concrete (RC)

The numerical model with inserted 25cm thick concrete lining of class C25/30, reinforced with two layers of Q131 reinforcement mesh, is shown in the figure 2. The characteristics of the concrete lining in the model are:



Liner Properties
Liner: Liner 1
Liner Type Standard Beam
Formulation Timoshenko
Thickness 0.25 m
Elastic Properties
Young's modulus 30000 MPa
Poisson's ratio 0.2
Liner: Liner 2
Liner Type Standard Beam
Formulation Timoshenko
Thickness 0.25 m
Elastic Properties
Young's modulus 30000 MPa
Poisson's ratio 0.2

Fig. 2 Model with Reinforced Concrete Lining.

The stress-strain diagram for both phases of tunnel excavation (σ_1, σ_3) is shown in Figures 3 to 8.

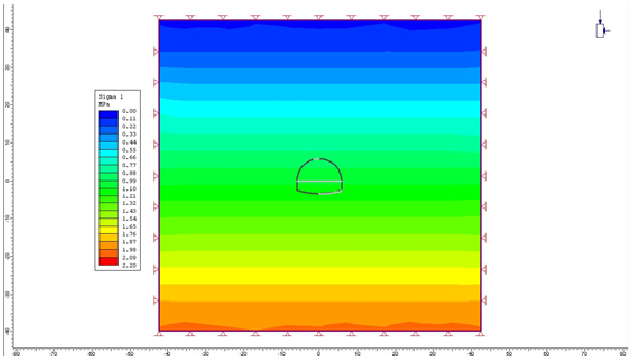


Fig. . σ_1 - Primary state –RC

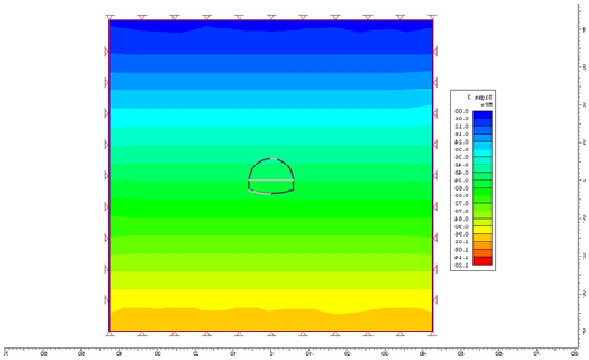


Fig. 4 σ_3 - Primary state – RC.

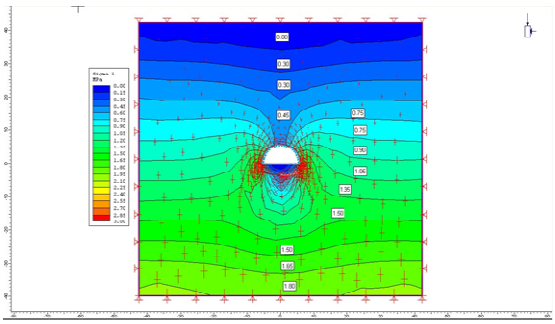


Fig. 5 σ_1-First phase of tunnel excavation- RC.

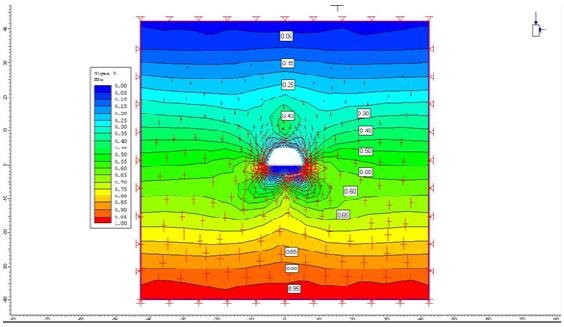


Fig. 6 σ_3 - First phase of tunnel excavation- RC.

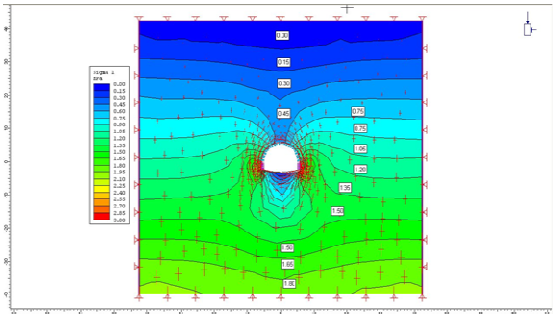


Fig. 7 σ_1 - Excavation of the entire tunnel contour- RC.

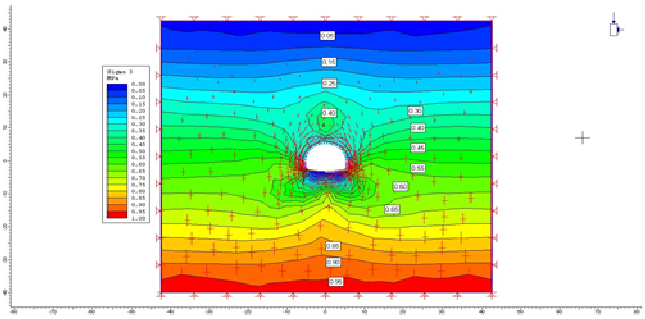


Fig. 8 σ_3 - Excavation of the entire tunnel contour- RC.

3.3 Model with Fiber-Reinforced Concrete Lining (FRC), L/D = 50/0.75, 2% Steel Fibers

Numerical model with inserted 25 cm thick fiber-reinforced concrete lining of class 37.8 MPa as shown in the figure 9.

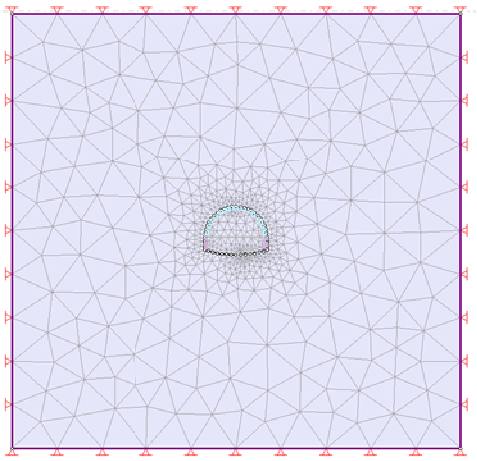


Fig. 9 Model with Fiber-Reinforced Concrete.

The characteristics of the fiber-reinforced concrete lining in the model are as previously stated:

- Peak compressive stress: 38.7 MPa
- Residual compressive stress: 6.5 MPa
- Peak tensile stress: 7.5 MPa
- Residual tensile stress: 1.5 MPa

The stress-strain diagram for both phases of tunnel excavation (σ_1, σ_3) is shown in Figures 10 to 13.

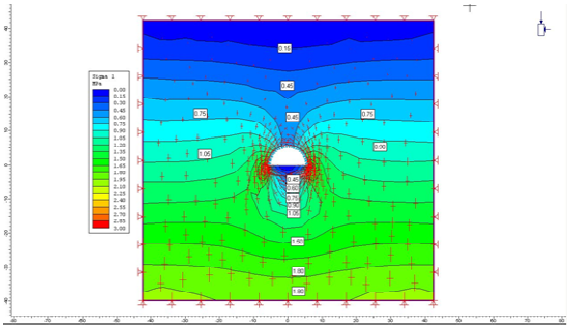


Fig. 10 $\boldsymbol{\sigma_1}$ -First phase of tunnel excavation – FRC.

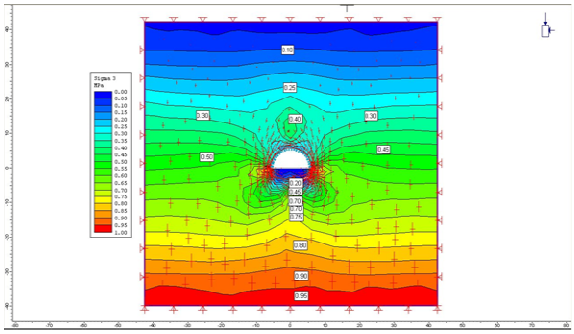


Fig. 11 $\boldsymbol{\sigma_3}$ - First phase of tunnel excavation – FRC.

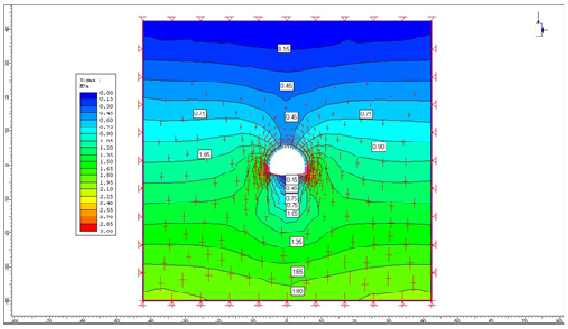


Fig. 1 $\boldsymbol{\sigma_1}$ - Excavation of the entire tunnel contour – FRC.

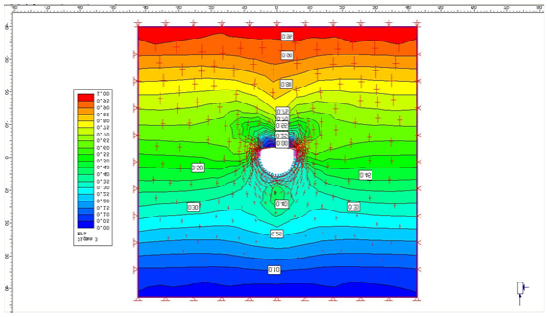


Fig. 13 $\boldsymbol{\sigma_3}$ - Excavation of the entire tunnel contour – FRC.

3.4 Supplementary Analysis

3.4.1 Formation of input files

The input files are the final files for this study, corresponding to the analyzed type of traffic tunnel, which has been cleared of anchors. The same data are provided for the lining for both conventional reinforced concrete (RC) and fiber-reinforced concrete (FRC):

- For the lining without fibers:
  - ❖ Peak compressive stress: 30 MPa
  - ❖ Residual compressive stress: 5 MPa
  - ❖ Peak tensile stress: 5 MPa
  - ❖ Residual tensile stress: 1 MPa
- For the lining with fibers:
  - ❖ Peak compressive stress: 38.7 MPa
  - ❖ Residual compressive stress: 6.5 MPa
  - ❖ Peak tensile stress: 7.5 MPa
  - ❖ Residual tensile stress: 1.5 MPa

The lining thickness varies from 25 cm to 20 cm and 15 cm, depending on the characteristics of the rock mass along the considered section.

In this study, diagrams of U_tot (total displacements) are provided for the two excavation stages. The purpose of this supplementary analysis was to compare displacements for both cases, i.e., conventional reinforced concrete (RC) and fiber-reinforced concrete (FRC), at different excavation stages, and to illustrate the magnitude of displacements for each case. This is supported by the superior mechanical performance of FRC, particularly its pronounced toughness, which allows fiber-reinforced shotcrete to undergo plastic deformation for a longer period.

Input files for PHASE2V6 carry labels:

F B_modelA2_RC_15_PH2v6

B_modelA2_RC_20_PH2v6

B_modelA2_RC_25_PH2v6

or FRC:

B_modelA2_FRC_15_PH2v6

B_modelA2_FRC_20_PH2v6

B_modelA2_FRC_25_PH2v6

Data for max U_tot (maximum displacements) for the models processed in PHASE2v6:

D	maxUtot	
	1. phase	2. phase
RC		
15	0.00661257	0.00607221
20	0.00661257	0.00605811
25	0.00667319	0.00604121
FRC		
15	0.00654235	0.00608391
20	0.00661257	0.00605811
25	0.00667319	0.00604121

Based on the presented analysis and the supplementary analysis of the tunnel structure, it can be confidently concluded that the differences between the two compared linings are within the margin of computational error. The load-bearing capacities of the linings are similar, and the savings are reflected in the elimination of the placement of assembly reinforcement.

4 Conclusion

The use of fiber-reinforced concrete with steel fibers, hooked at the ends, and a shape factor of L/D = 50/0.75, at a dosage of 2% by mass of the concrete, yields excellent results in the structural analysis of the tunnel lining. In this case, the total displacements of the fiber-reinforced tunnel lining coincide with the total displacements of the conventional reinforced concrete lining. This demonstrates the feasibility of using fiber-reinforced concrete in the design of underground structures as a substitute for conventional reinforced concrete linings, with the important caveat that the production technology of fiber-reinforced concrete and the homogeneity of the concrete mixture are key factors for achieving the favorable performance and properties of the tested fiber-reinforced composite.

References

B. Grujic, Z. Grujic, (2025), „Modeling of the physical and mechanical properties of fiber reinforced concrete and its application in tunnel constructions", Geotechnical aspects of civil engineering and earthquake engineering, Vrnjačka Banja, Association of Civil Engineers of Serbia, DOI:10.46793/GEOAG25.457G;

ACI Committee 201.2R-08: (1983),„Guide to Durable Concrete", American Concrete Institute;

Shah, S. P., (1983), "Fiber Reinforced Concretes Handbook of Structural Concrete", edited by F. K. Kong, R. H. Evans, E. Cohen, and F. Roll, McGraw-Hill, London, U.K.;

D.D.Milasinovic,"Geometric non-linear analysis of thin plate structures using the harmonic coupled finite strip method",Thin-Walled Structures, 49/2, pp. 280-290. 2011 doi:10.1016/j.tws.2010.11.005. ISSN: 0263-8231;

J. Šušteršič, A. Zajc, I. Leskovar,(2003), „Surface characteristics of fiber reinforced concrete", Industrieböden Band 1, pp. 255-261;

ACI Committee 210R-93(R2008): (2008) „Erosion of Concrete in Hidraulic Structures", American Concrete Institute;

Physics-informed theory modelling of rock engineering features from TBM operational data

H. Samadi[1] & A. Danzi[2]
[1] *R&D Specialist, R&D Department, SYSTRA S.p.A., Italy*
[2] *Head of IT and R&D Department, SYSTRA S.p.A., Italy*
adanzi@systra.com

Abstract

Accurate determination of rock engineering parameters is important for reliable prediction and optimization of tunnel boring machine (TBM) performance. In this study, TBM performance indicators and operational parameters are used to infer key geomechanical properties, including both intact rock and rock mass characteristics, across several lithological units (e.g. Paragneiss, Amphibolite, and calc- phyllite-schist with low to high grade of metamorphism) encountered along the Brenner Base Tunnel (BBT) alignment that connects the cities of Innsbruck (Austria) and Fortezza (Italy). The dataset, derived from both pre-construction investigations and construction-phase monitoring, is divided into geological zones and lithological units, with representative ranges of considering operational parameters and rock mechanical features defined for each zone.

A framework based on physics-informed theory, engineering mechanics, and stacking ensemble learning model are developed to establish simulation between machine response, mechanical specifications, and ground conditions. The meta-learner stacking logic is implemented using the ridge cross-validation (RidgeCV) and the ensemble is built on three high-performance tree-based algorithms, including extra trees regressor (ET), hist gradient boosting regressor (HGB), and gradient boosting regressor (GB) based on the polynomial interaction technique. They were selected because they handle geological noise and non-linear relationships differently, therefore, providing a balanced prediction of rock mechanical features. The proposed modeling approach shows predictive accuracy, yielding reliable estimates of rock engineering properties and supporting its applicability to future double shield (DS)-TBM operations in metamorphic rock units.

Keywords

Rock engineering, Ground assessment, Tunnel, TBM, Rock-machine interaction.

1 Introduction

Establishing relationships between tunnel boring machine (TBM) parameters and rock mechanical factors under rock ground conditions through forward analysis has been investigated in several studies (Rostami, 1993; Bruland 1998; Barton 2000; Hassanpour et al. 2011; Samadi et al. 2024). However, analyzing rock mechanical factors based on historical TBM performance data through reverse (back) analysis is more complex due to the nonlinear interactions between rock–machine parameters and continuously changing ground conditions. Such analyses require advanced methodologies. To the best of the authors' knowledge, most previous studies have focused on forward analysis, using rock mechanical parameters to predict machine performance, which differs from the scope of this study. This work proposes an approach based on reverse analysis, which has not been adequately addressed in the literature. To overcome these limitations, the present study aims to simulate key rock mass and intact rock parameters from historical TBM performance data from the Brenner Base Tunnel (BBT) project using a coupled physics-informed modelling and stacking ensemble learning model.

2 Project Description

The Brenner Base Tunnel (BBT) is a major railway project that connects Innsbruck in Austria to Fortezza in Italy. It is a joint effort between the two countries, with additional support from the European Union. The tunnel is about 55 km long and runs beneath the Eastern Alps, passing under the Brenner Pass (BBT 1999). Due to its length, the BBT is considered the longest railway tunnel in the world. The tunnel system consists of two main parallel tunnels and an exploratory tunnel. This study focuses on Lot Mules 2–3, specifically the west tunnel (GLON-T2). Excavation in this section was carried out using a TBM (STBM-1071) manufactured by Herrenknecht. The machine has an excavation diameter of 10.7 m and is equipped with 64-disc cutters on the cutterhead. The cutters are spaced at an average of about 90 mm and are designed to apply a thrust force of 176 kN each (cutter load, thrust force per each cutter). More detailed technical specifications of the TBM are provided in Table 1.

Table 1. A detailed description of HR-STBM1071 specifications.

Parameters		**Symbol**	**Value**	**Unit**
Cutterhead	Diameter	D	10710	mm
	Diameter	Ds	10650	mm
Front shield	Length	L	4820	m
	Width	W	80	mm
	Diameter	Ds	10440	mm
Middle shield	Length	L	4150	m
	Width	W	50	mm
	Diameter	Ds	10420	mm
Tail shield	Length	L	2520	m
	Width	W	80	mm
	Number of disc cutters	N_{dc}	64	-
Cutting tools	Disc cutter size	D_{ds}	19	in
	Spacing	S_{ds}	90	mm
Thrust system	Thrust force	TF	112815	kN
Torque	Cutterhead torque	CT	13600*, 27524**	kN.m
Rotation speed	Cutterhead rotation speed	RPM	0-5.11*, 0-2.55**	rpm

Note: Gear I*, Gear II**, nominal values

The Lot Mules 2–3 section (including the GLON tunnel) passes through several different geological formations. One of the most complex areas is the Periadriatic Line, which represents the boundary between the African and European tectonic plates. This zone includes geological intrusions with relatively weak mechanical properties, which makes excavation more difficult. Along this section, the GLON tunnel mainly crosses metamorphic rocks with different levels of metamorphism, from low to high grade. The most common rock types are paragneiss, amphibolite, and calc-phyllite–schist. The geological profile of the studied tunnel section is presented in Fig. 1. Based on laboratory tests and in-situ investigations, the uniaxial compressive strength (UCS) generally ranges from about 33 MPa to 107 MPa, although values up to 140 MPa have been recorded along the entire tunnel alignment. The rock quality designation (RQD) varies from very low values of around 10 up to about 34.

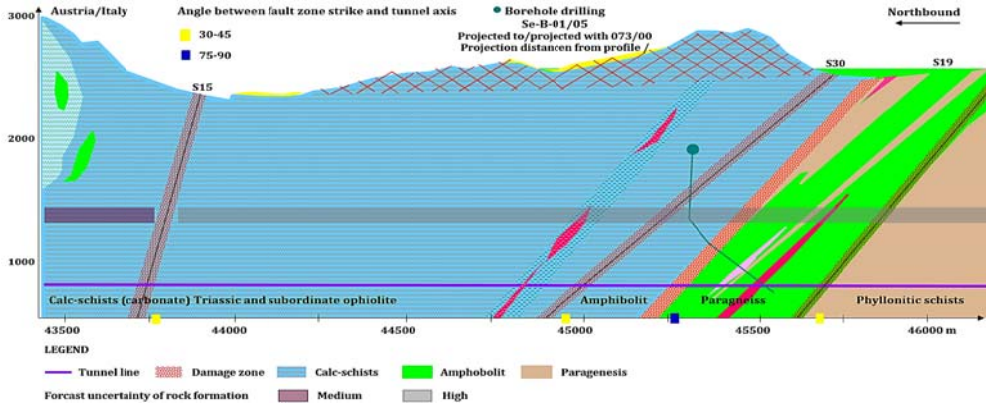


Fig. 1 Geological profile of the GLON tunnel (chainage 43+500 km to 46+000 km).

3 Data Analysis

The dataset used in this study was obtained from the Lot Mules 2–3 (GLON tunnel) project and includes both TBM operational records and rock mass geomechanical data. The TBM-related variables cover cutterhead torque (CT), rotation speed (RPM), penetration per revolution (Pr), cutter load (Fn), cutterhead power (P), and specific energy (SE). In addition, key machine characteristics such as cutterhead diameter and the number of disc cutters were also considered. On the geological side, important rock parameters such as UCS, RQD (Deere 1988), rock mass rating (RMR) (Bieniawski 1989), geological strength index (GSI) (Hoek 1994), and joint volumetric count (Jv) (Palmstrom 1982) were included. After data cleaning and preprocessing and applied principal component analysis (PCA), as well as TBM performance theory and engineering judgement, the final dataset was structured into a 1020 × 11 matrix (reduced from an initial raw dataset of 5500 × 20 variables). This dataset combines both machine performance indicators and rock engineering parameters.

In the modeling framework, rock mechanical properties (including both intact rock and rock mass characteristics) were treated as multi-output targets, while TBM operational variables were used as inputs to capture the interaction between the machine and the surrounding ground conditions. If a dataset for machine learning (ML) analysis is organized by stratigraphic sequence or ring numbers, a model may unintentionally learn the order of the data rather than the true physical relationships between rock parameters and machine performance. To avoid this issue, the data were shuffled so that both the training and testing sets include a well-balanced mix of different geological conditions. This approach helps reduce spatial bias, which can otherwise lead to overly optimistic training results but weak performance when applied to new, unseen data. Moreover, because the chosen models in section 4. Methodology treats each sample independently, the random shuffling adopted to balance geological conditions across the splits fully maintains the integrity of the analysis. The detailed descriptive statistics for each parameter are summarized in Table 2.

Table 2. Statistical descriptive measurement for each parameter used in the database.

Parameter	CT	RPM	Pr	Fn	P	SE	UCS	RQD	Jv	GSI	RMR
Average	2.4	3.1	12.2	221.5	932.3	14537.9	63.4	29.8	25.8	46.5	45.5
Maximum	9.5	5.2	26.5	471.0	1599.1	42042.5	107.0	34.0	31.8	55.0	55.0
Minimum	0.7	0.9	5.7	65.9	40.0	5016.9	33.0	10.0	24.5	33.0	28.0
Std. Dev	0.8	1.0	3.3	51.4	259.0	5259.2	21.8	6.8	2.1	6.6	7.0
Variance	0.7	1.0	10.8	2638.6	67083.9	27659393.4	477.2	46.5	4.3	44.0	49.5
Kurtosis	12.1	-1.3	0.1	0.7	-0.2	3.0	-0.4	2.7	2.6	-1.2	-0.1
Skewness	2.5	0.5	0.5	0.3	-0.3	1.3	0.6	-1.9	1.8	-0.1	-0.7
Median	2.3	2.6	12.4	215.8	960.4	13458.1	55.0	33.0	24.8	45.0	46.0
Count	1020	1020	1020	1020	1020	1020	1020	1020	1020	1020	1020
Type	Inputs						Outputs				
Unit	MN.m	rpm	mm/rev	kN	kW	MJ/m^3	MPa	-	*Joints/*m^3	-	-

4 Methodology

The data were collected from metamorphic rock formations (low to high metamorphism grade). In total, 1020 data samples were available for each geological section and excavation ring, forming a dataset suitable for analysis. The dataset was divided into two parts: 85% of the data (867 samples) were used for model training, while the remaining 15% (153 samples) were reserved for testing. In this study, the meta-learner stacking logic is applied using the ridge cross-validation (RidgeCV) and the

ensemble is built on three high-performance tree-based algorithms, including extra trees regressor (ET), hist gradient boosting regressor (HGB), and gradient boosting regressor (GB) based on the polynomial interaction technique. To reach a valid accuracy rate for 15% test subset of database, several techniques including polynomial interaction mapping (before training the model), standard scaling, multi-output wrapper, and data shuffling were applied. Multi-output wrapper was used because the database predicts five distinct targets (UCS, RQD, Jv, GSI, RMR) simultaneously, and this technique ensures that the stack is optimized for the unique physical distribution of each rock engineering property. Details of the model structures and configurations is provided in Table 3.

Table 3. The structure and configuration to create the stacked model.

Structure	Model	Description
Data pre-processor	Standard scaler and Polynomial features	degree=2, interaction-only=True, include-bias=False
Base expert 1	Extra trees regressor (ET)	n-estimators=1000, max-depth=15, random-state=42
Base expert 2	Gradient boosting (GB)	n-estimators=500, learning-rate=0.05, max-depth=5, random-state=42
Base expert 3	Hist gradient boosting (HGB)	Max-iter=1000, random-state=42
Meta-learner	RidgeCV	Cv = 5, L2-regularized linear regression
Output wrapper	Multi output regressor	Parallelizes the stack to create 5 distinct prediction engines for UCS, RQD, Jv, GSI, and RMR

5 Results and Discussion

The comparison between the model's predictions against the actual observed field values is presented in Fig. 2. Based on the results of evaluation metrics such as A-20 and root mean square error (RMSE), the models appear to perform very well, as the points closely follow the identity line (categorical rather than continuous). The rock mechanical properties along the tunnel route are categorical because they remain constant within each distinct geological unit, changing only when transitioning into a new geological formation, structure, or zone.

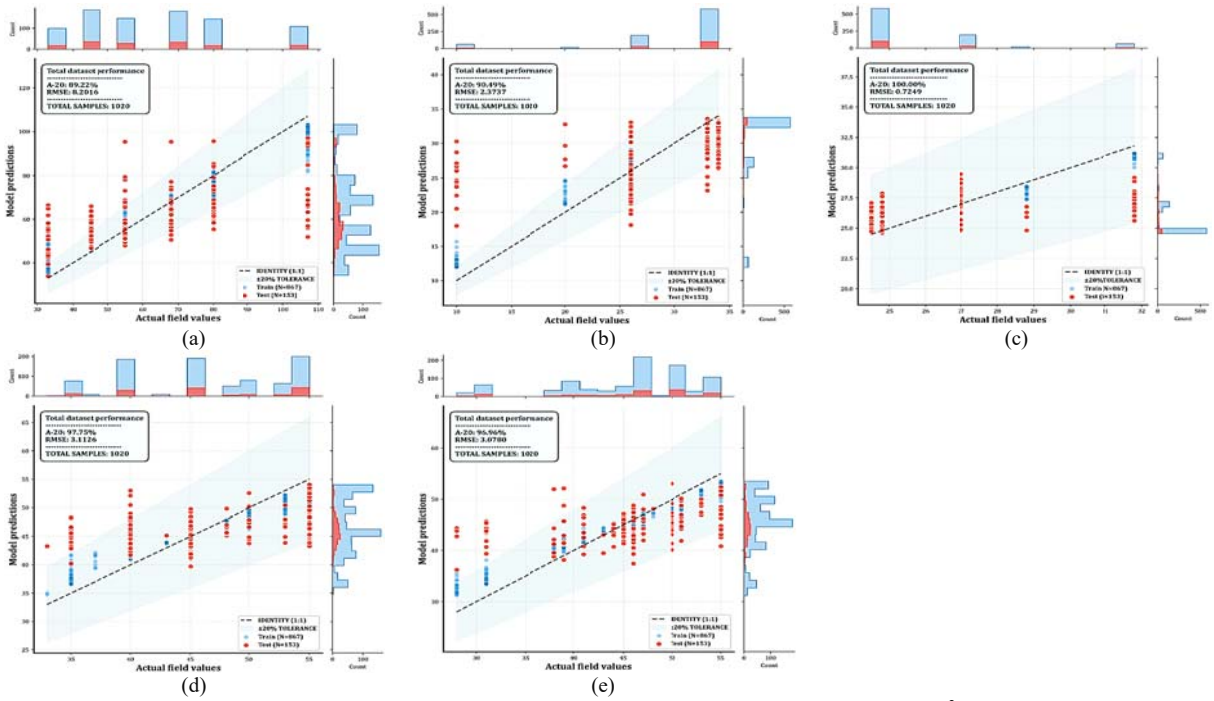


Fig. 2 Comparison between predicted and actual values, (a) UCS (MPa), (b) RQD, (c) Jv (joints/m^3), (d) GSI, (e) RMR.

Additionally, SHapley Additive exPlanations (SHAP) analysis was performed as a tool within explainable AI (XAI). The SHAP results, presented as distribution plots for all outputs, are shown in Fig. 3. These results show how the input features (primarily the first two machine factors) contribute to optimizing the system and provide the control over the outputs in the physics-informed modelling.

Physics-informed modelling (post-hoc interpretability, coupled feature interaction) was applied to all input parameters in the database across all possible scenarios to establish relationships between rock mechanical features and historical TBM performance data. However, due to the page limitations of Eurock 2026, only a representative example of the coupled physics-informed modelling is provided.

Fig. 4 presents the two-dimensional (2D) version, while Fig. 5 shows the three-dimensional (3D) version. The example is based on the two most influential factors identified through the SHAP analysis for each output variable.

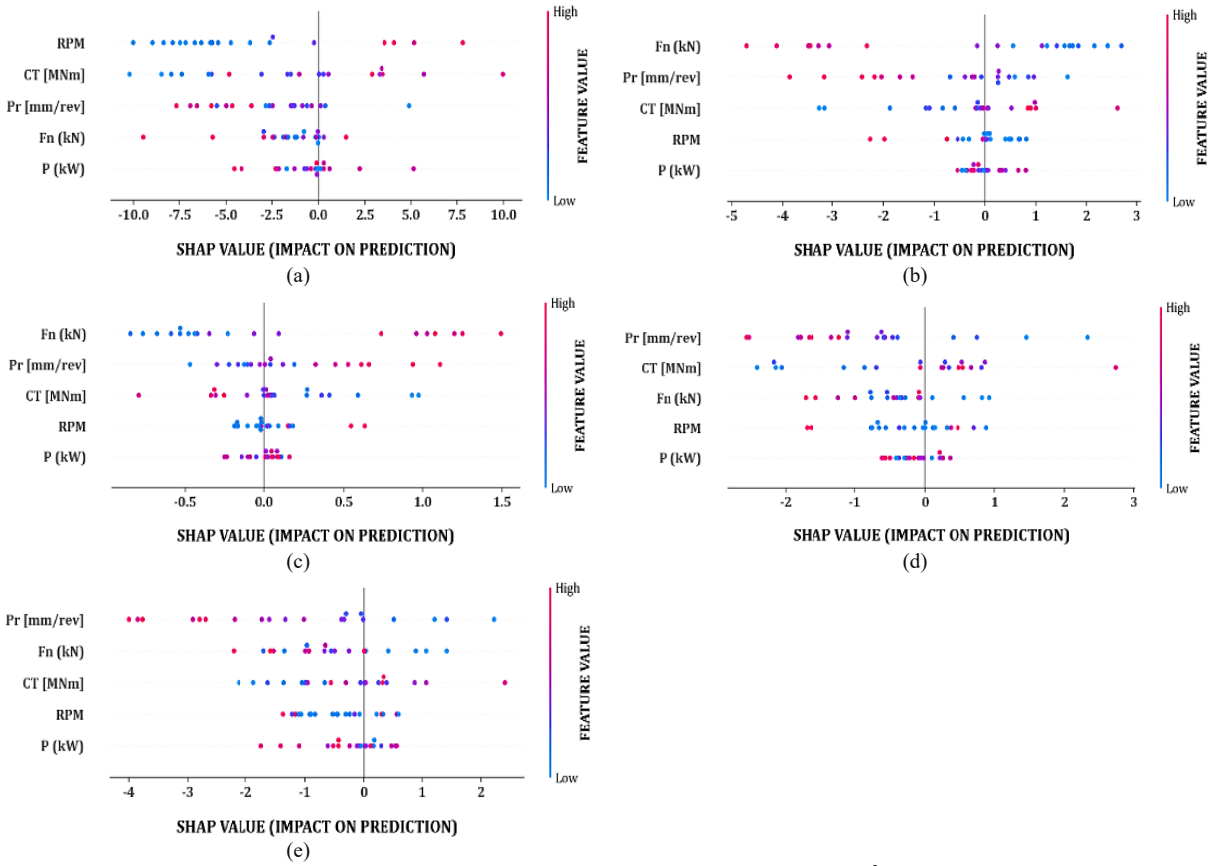


Fig. 3 Results of interpretability SHAP analysis, (a) UCS (MPa), (b) RQD, (c) Jv (joints/m^3), (d) GSI, (e) RMR.

The 3D visualization of the predicted values of all rock mechanical factors for each tunnel segment (1020 installed segments) along the entire tunnel alignment was carried out using four output simulation layouts: resultant force (stress gradient), deformed mesh (wireframe), contour lines (banded), and total difference (projected) (Fig. 6). However, due to the page limitations, only a representative example is presented. The example focuses on RMR, as it considers both intact rock and rock mass properties and serves as a reliable indicator of rock mechanical characteristics.

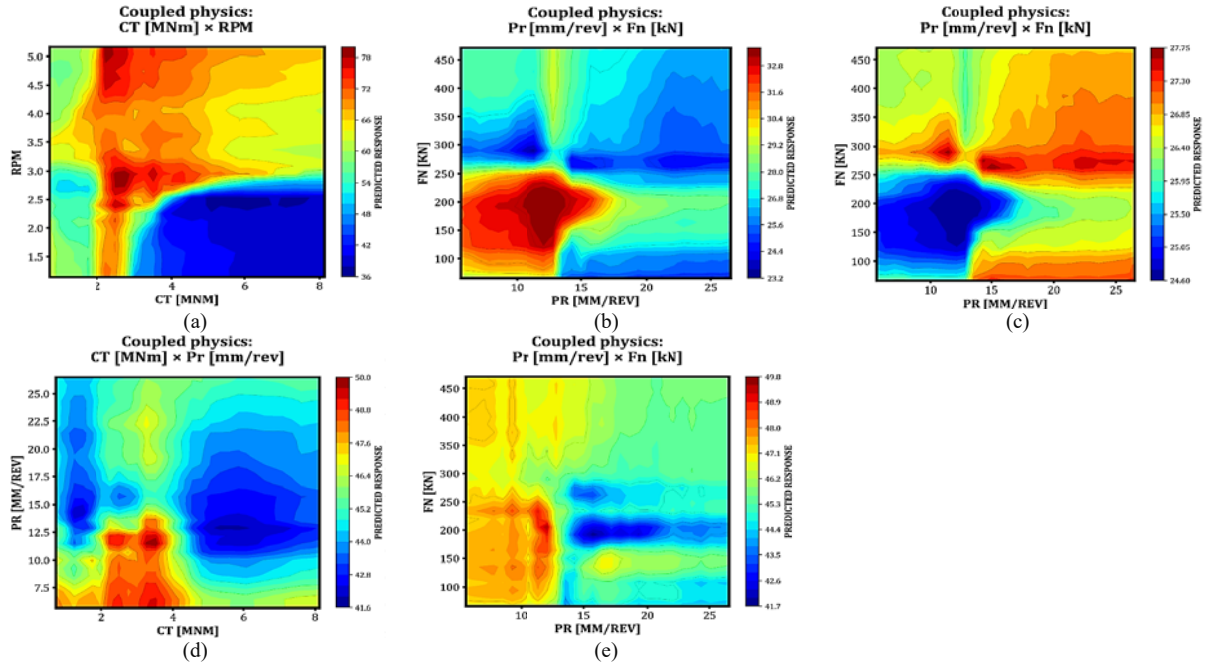


Fig. 4 2D coupled physics-informed modelling (the most important factors in SHAP analysis per each output parameter), (a) UCS (MPa), (b) RQD, (c) Jv (joints/m^3), (d) GSI, (e) RMR.

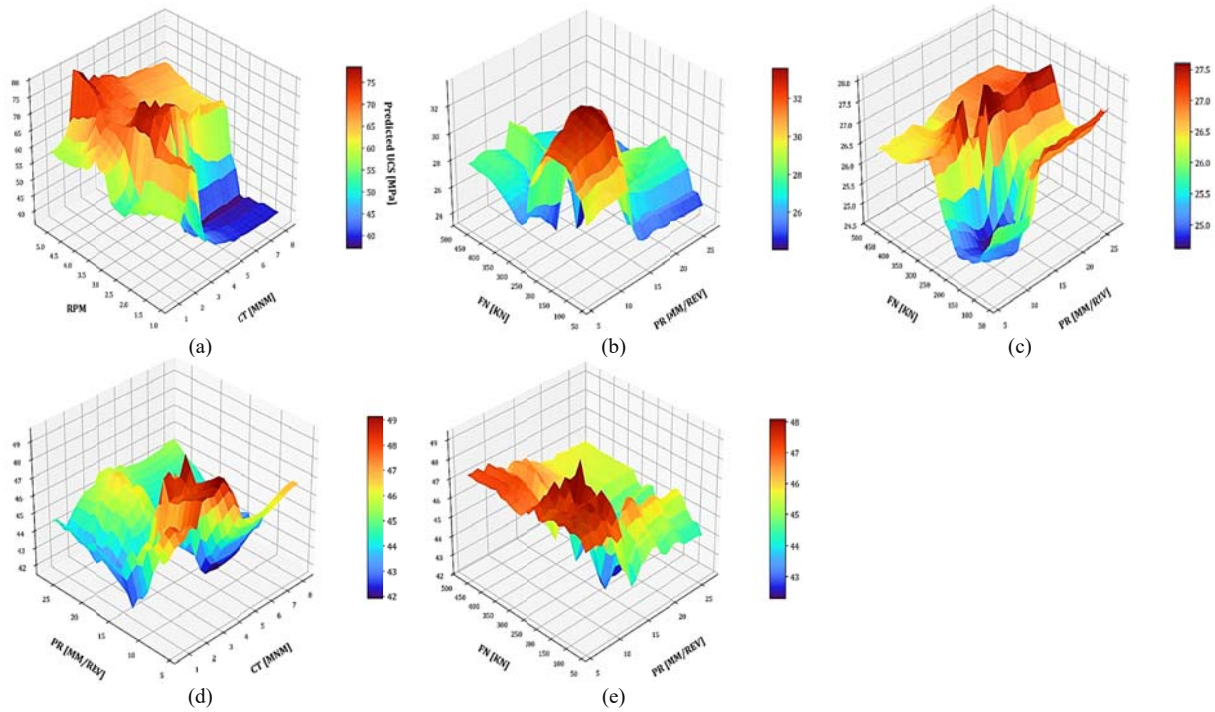


Fig. 5 3D coupled physics-informed modelling (the most important factors in SHAP analysis per each output parameter), (a) UCS (MPa), (b) RQD, (c) Jv (joints/m^3), (d) GSI, (e) RMR.

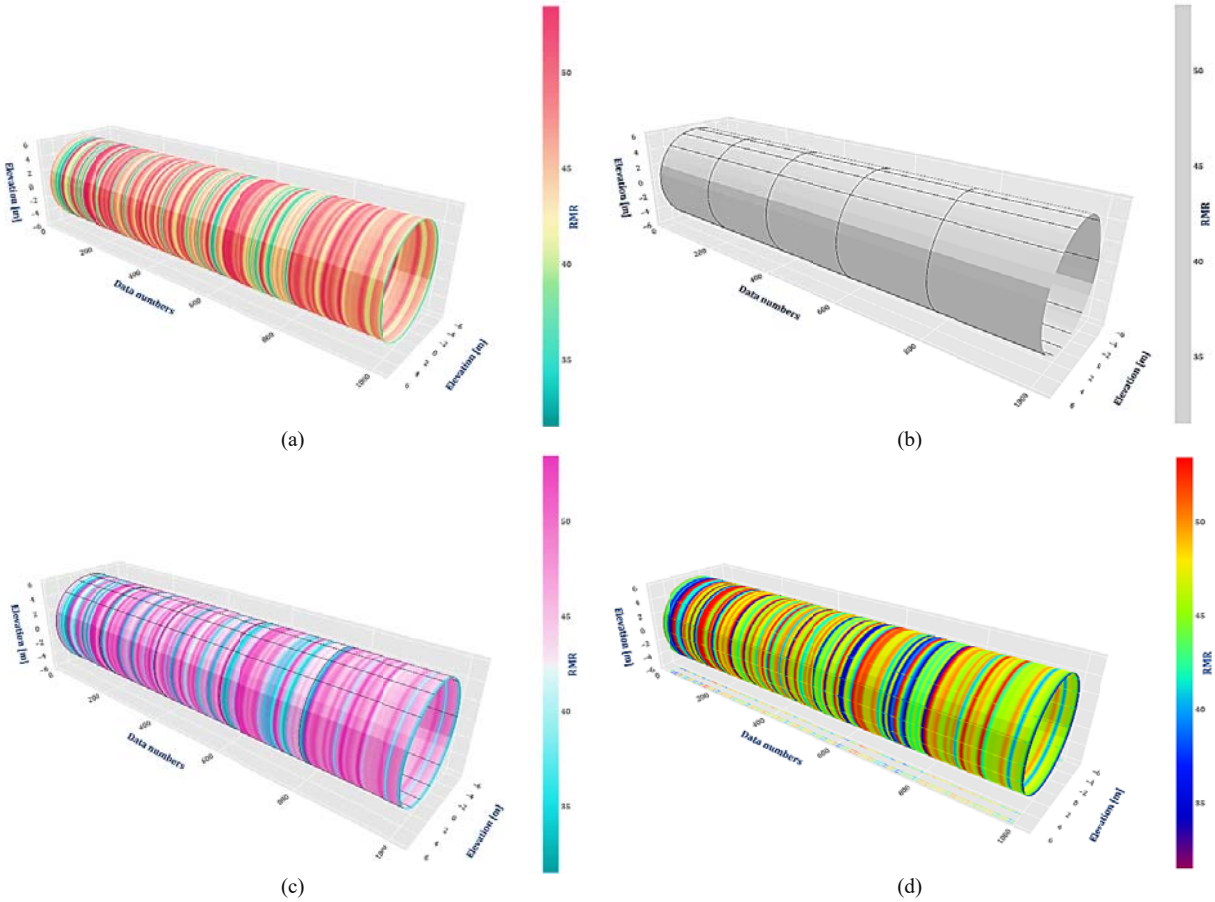


Fig. 6 3D visualization of RMR prediction values per each tunnel segment through the whole tunnel layout, (a) resultant force, (b) deformed mesh, (c) contour lines, (d) total difference.

6 Conclusions

This study presented a framework for the back-analysis of rock engineering parameters using historical TBM performance data. A coupled approach integrating physics-informed modelling with a stacking ensemble learning model was developed to capture the complex, nonlinear interactions between machine behavior and ground conditions. The ensemble model, built on Extra trees, hist

gradient boosting, and gradient boosting regressors with a RidgeCV meta-learner, showed strong predictive capability. Evaluation results, including A-20 and RMSE metrics, confirmed a high level of agreement between predicted and observed values (categorical rather than continuous). Furthermore, XAI using SHAP analysis was done to investigate the impact of each feature on the outputs to make the model more interpretable and explainable. The integration of stacking explainable AI with physics-informed modelling provides deeper insight into rock–machine interaction mechanisms and improves confidence in model perdition.

References

Barton NR (2000) TBM tunnelling in jointed and faulted rock. Balkema, Rotterdam. Crc Press. p.173.

BBT (1999) Project overview. URL: https://www.bbt-se.com/en/tunnel /project- overview/.

Bieniawski ZT (1989) Rock mass classifications: A complete manual for engineers and geologists in mining, civil, and petroleum engineering John Wiley & Sons: Toronto, ON, Canada.

Bruland A (1998) Hard rock tunnel boring. Ph.D. Thesis. Norwegian University of Science and Technology,Trondheim.

Deere D (1988) The rock quality designation (RQD) index in practice. InRock classification systems for engineering purposes: 91-101. ASTM International.

Hassanpour J, Rostami J, Zhao J (2011) A new hard rock TBM performance prediction model for projectplanning. Tunnelling and Underground Space Technology 26(5):595-603. https://doi.org/10.1016/j.tust.2011.04.004

Hoek E (1994) Strength of rock and rock masse. ISRM News Journal 2(2): 4-16.

Palmstrom A (1982) The volumetric joint count—a useful and simple measure of the degree of jointing. In Proceedings of the fourth international congress IAEG V:221-228.

Rostami J (1993) A new model for performance prediction of hard rock TBMs. In Proceedings 1993 rapid excavation and tunnelling conference (RETC).

Samadi H, Karimi H, Khamehchiyan M, Hassanpour J (2024) Prediction of engineering characteristics of rock masses using actual TBM performance data with supervised and unsupervised learning algorithms (a case study in strong to very strong igneous and pyroclastic rocks). Rock Mechanics and Rock Engineering 57(9):7223-7252. https://doi.org/10.1007/s00603-024-03903-9

Status of Rock Slope Characterization Using Remote Sensing Techniques: A Bibliometric Analysis

Raymundo Ruiz Flores[1*],Nelly Lucero Ramírez Serrato[2], Adrián J. Riquelme Guill[3], Fabiola Doracely Yépez Rincón[4], Rodrigo Gutiérrez Navarro[5] & Javier Mancera Alejandrez[5]

[1]*Posgrado en Ciencias de la Tierra, Universidad Nacional Autónoma de México, Mexico City, Mexico.*
[2]*Departamento de Recursos Naturales, Instituto de Geofísica, Universidad Nacional Autónoma de Mexico, Mexico City, México.*
[3]*Departamento de Ingeniera Civil, Universidad de Alicante, Alicante, Spain.*
[4]*Departamento de Geomática, Instituto de Ingeniería Civil, Universidad Autónoma de Nuevo León, Nuevo León, Mexico.*
[5]*División de Ingeniería en Ciencias de la Tierra, Facultad de Ingeniería, Universidad Nacional Autónoma de México, Mexico City, Mexico*
**rayruizflores2@gmail.com*

0009-0000-1843-6177

Abstract

Rock slope characterization is essential for understanding its mechanical stability and its implications for geotechnical engineering projects. Geological conditions play a key role in controlling slope behaviour and are often the primary cause of geotechnical issues. However, traditional field-based characterization methods are frequently limited by site accessibility, safety concerns, and time constraints.

In recent years, remote sensing techniques such as LiDAR and photogrammetry have emerged as powerful tools for acquiring high-resolution three-dimensional data, enabling more efficient and detailed analyses, and avoiding the limitations of traditional fieldwork. This study presents a bibliometric analysis of 1,205 publications from Web of Science database between 2010 and 2025, focusing on the application of remote sensing techniques in rock slope characterization.

Using Bibliometrix and VOSviewer, connections in authors and country co-authorship, keywords, and most cited sources were identified. Results show a significant annual growth rate of 18.31%, with a marked increase in publications after 2021. In terms of scientific production, China leads global research output, followed by European countries, however international and research group collaboration remains limited. Keyword and citation network analyses reveal a strong focus on structural characterization of rock discontinuities, as well as the integration of advanced algorithms and machine learning techniques. The findings highlight the convergence between classical rock mechanics and modern remote sensing technologies, establishing these methods as fundamental tools in contemporary geotechnical research, but also the need to strengthen collaboration between countries and research groups. This study provides a comprehensive overview of the field and future research development.

Keywords

Bibliometric analysis, Rock slopes, Remote sensing, VOSviewer, Web of Science.

1 Introduction

The study of rock slopes is of great importance to understand its mechanical stability to avoid problems during the development of geotechnical engineering works such as rockslides. It is also necessary to know that geology factors are the main causes of geotechnical issues (González de Vallejo et al. 2002).

Therefore, rock slopes undoubtedly require a thorough description of their characteristics during fieldwork; fieldwork groups activities such as identifying the geological structures, lithologies, groundwater conditions and their spatial distribution in the area. (González de Vallejo et al. 2002). Undoubtedly, fieldwork often faces certain limitations, such as long periods of time required, safety concerns for field personnel, and difficulty accessing the study areas (Riquelme et al. 2016; Mancera et al. 2021).

Likewise, in recent years, technological advances have generated numerous improvements in data acquisition and interpretation across a wide range of fields of study. One such advance is undoubtedly the use of remote data acquisition techniques, such as photogrammetry and LIDAR, that allow the acquisition of high-resolution three-dimensional representations of the terrain with high accuracy and high spatial resolution (Riquelme et al.2015).

Many researchers who employ the characterization of rock slopes for geotechnical engineering in their research fields have turned their attention to these techniques since having three-dimensional models of their study areas at their disposal would allow access to a wealth of data and to avoid the limitations that traditional fieldwork.

To understand the current state of publications related to the use of remote data acquisition techniques in studies that aim to characterize rock slopes, it is necessary to conduct a bibliometric study that allows us to track the evolution in the number of related publications over a set period, as well as to identify the main authors, countries, and cited references.

2 Methodology

2.1 Data Collection

The Web of Science (WoS) database was selected as the platform to acquire the data necessary for bibliometric analysis. On February 27, 2026, a search was conducted to obtain information on all papers relating to the application of any remote data acquisition tool in the characterization of rock slopes between 2010 and 2025. This was done using the following query: TS = ((UAV OR UAS OR RPAS OR drone* OR "unmanned aerial vehicle*" OR "unmanned aerial system*" OR "small unmanned aircraft system*" OR LiDAR OR "airborne laser scanning" OR ALS OR "laser scanning" OR "laser scanner*" OR "terrestrial laser scanner*" OR TLS OR "terrestrial laser scanning" OR "ground-based LiDAR" OR "terrestrial LiDAR" OR "digital camera*" OR "digital photograph*") AND ("rock slope*" OR "rock surface*" OR "rock face*" OR "rock wall*" OR "rock cliff*" OR "rock mass*" OR "rock outcrop*" OR "cut slope*" OR highwall OR "open pit slope*" OR "bench slope*" OR "rock joint*" OR "rock discontinuities" OR "fracture characterization" OR "joint mapping" OR "structural mapping")) AND PY = (2010-2025).

2.2 Statistical Analysis and Visualization

A proper metric and statistical analysis allow for the identification of common connections between authors (formed research groups), as well as research trends within the analysed papers. Some software specializing in bibliometric analysis allow for a concise overview of the vast amount of information obtained from scientific databases, displaying intuitive diagrams that reveal the relationships and evolution of a specific topic over the years (Xue et al., 2024). Obtaining this type of data enables detailed observations of the current state of the art in a research field.

For this purpose, the software tools Bibliometrix and VOSviewer were used to obtain data such as the number of works published during the study period, the top ten authors and journals, and to construct bibliometric networks to observe the relationships between authors, countries, keywords, and the most cited works within the publications retrieved from WoS database.

It is important to mention that a previous review of database was conducted to merge synonymous terms for keywords, and to homogenize authors' names since sometimes an author can appear under different abbreviations of its name.

3 Results and Discussion

3.1 Main information analysis

A total of 1205 papers were obtained from the search within Web of Science; their information was initially analysed with the help of Bibliometrix to extract general information from the data, as shown in Table 1. All these articles were published in 338 different journals, and only 23 of them were published by a single author, which means that almost all of them are the result of co-authorship with an average of five authors per document. However, according to the International Co-Authorship Index, only 26.14 % of the articles present international co-authorship; this reflects that although almost every article has co-authorship, most of them reflect collaboration between researchers exclusively from the same country

Table 1. Summary of the main bibliometric indicators of the analysed publications from 2010 to 2025.

Description	Results
Period	2010-2025
Journals	338
Documents	1205
Annual Growth Rate %	18.31
Average Citations per Doc	20.66
References	34850
Authors Key Words (ID)	3301
Keywords Plus (DE)	1775
Authors	3898
Single-Authored Docs	23
Co-authors per Doc	4.99
InternationalCo-Authorships %	26.14%

In the last 15 years, the number of publications has increased considerably, with an annual growth rate of 18.31%. Since 2021 the number of articles published exceeded 100, and according to the data, it is possible to infer that in 2026 it surpassed 200 per year. The highest publication volumes were registered in 2022, 2024 and 2025 accounting nearly 39% of all publications. The distribution of the annual publication output of 1205 articles along with cumulative yearly publication output can be seen in Fig. 1.

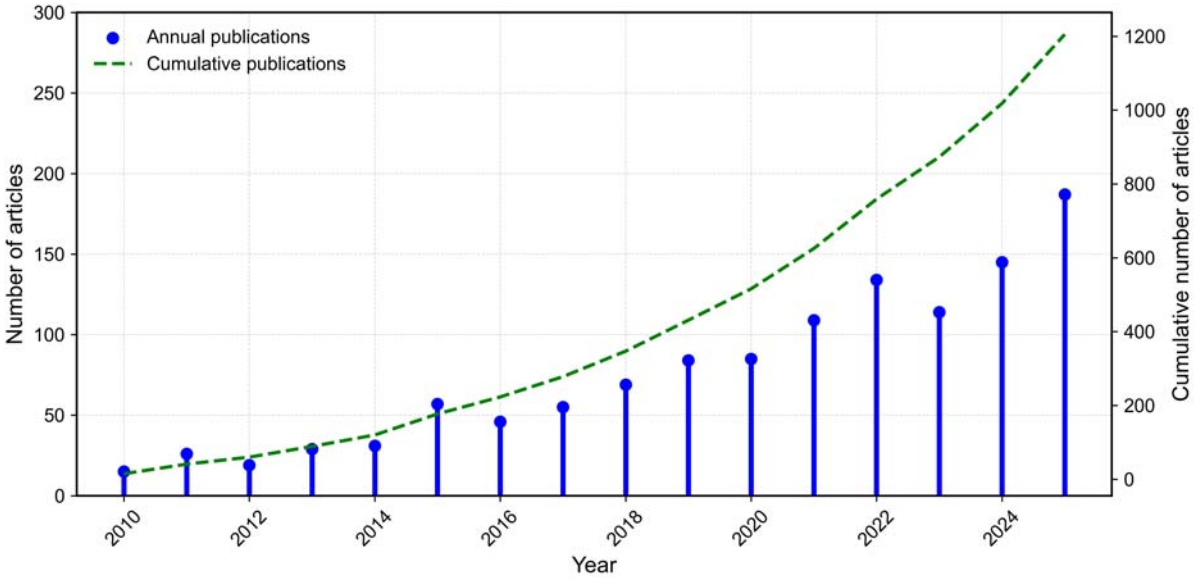


Fig. 1 Evolution of scientific production based on annual publications and cumulative output (2010–2025).

3.2 Bibliometric networks analysis

Four bibliometric networks were obtained from the analysis of the data, focusing on observing the relationship between keywords, principal authors and countries in the field and the most cited references in the papers. These networks can be seen in Fig. 2.

Focusing on the keywords, four principal clusters were obtained from the network (Fig. 2a), keywords that appear in it have at least 15 occurrences. Cluster 1 (red) shows mainly a relationship between geomorphologies and physical processes that can be related to the occurrence of material remotion processes such as landslides. Cluster 2 (green) and 4 (yellow) have some similarities, as they are mainly represented by two famous remote sensing techniques: LiDAR and photogrammetry; cluster 2centres more in the relationship between digital techniques and combination of algorithms and machine learning in identification and structural characterization of rock slopes, cluster 4 centres in the use of low-cost techniques: UAV´s and SfM, to obtain products to evaluate rock slopes and observe its accuracy; Although these clusters shows its differences, they seem to tend to combinate as there is no clear separation between them. Finally, Cluster 3 (blue) clearly shows the characteristics of joints, their behaviour and models, showing that the characterization of these elements in the papers is one of the most important things that are evaluated with remote sensing techniques in rock slopes.

The authors network (Fig. 2b), where all the authors have at least 5 published papers. This network shows principal authors such as Michel Jaboyedoff, Antonio Abellan, Zhang Wen, Doug Sted, etc.It also shows a notable pattern previously identified during the main information analysis. Although there are prominent authors who continually participate in the publication of articles related to the field, it seems that there is no great collaboration between research groups, even the main cluster (red) shows few connections with other clusters. Clusters that surround the principal cluster do not only show that research groups work exclusively between their members but also show that most of its members belong to the same country. This is an important indicator that although there has been good increase in publications, collaboration is still one of the weakest points in this research field.

Additionally, it is important to establish that not all authors appearing in this network are considered primary authors, as the software considers authorship regardless of whether they are primary or secondary authors. Therefore, it is necessary to use the information presented carefully to develop own criteria for which authors to consult when searching for information on these topics.

Fig. 2c shows the country network, where every country has at least 5 published articles. One of the first things that can be seen is that China is the most prominent country in this field of research, with 441 published articles, almost 37% of all the publications analysed in this paper. Even though there are other countries that also have a considerable number of publications, such as Italy, USA, Canada, Switzerland, none of them reach 100 publications and the rest of countries that appear in the network have an average of less than 20 publications.

Following China, it shows some connections mainly with the countries that follow it in publicised articles and most of the seen connections have low link strengths. Moving to other countries, European countries show connections with almost every country in the network; and although the connections seem to have link strengths as in China’s case, it is important to note that European countries seem to tend to collaborate extensively with each other. If we group all the scientific production of the European countries in this field, 595 publications are found. It shows that Europe has reached an important level of research in the field of remote sensing techniques in the characterization of rock slopes.

To know the most important cited references used in the 1205 articles analysed, in Fig. 2d it can be seen the network for this purpose, every cited reference has at least 50 citations. Tree main clusters appear in it. Cluster 3, though it is the smallest, collects important works that are the knowledge basis for the characterization of rock joints, having for example the SM from the ISRM (1978) and Barton and Choubey (1977). Cluster 1 shows important articles that study the use techniques such as photogrammetry, LiDAR, to generate three-dimensional models that could be used to identify and characterise discontinuities (e.g. orientation and spacing) from rock slopes using semi-automated and automated methods. Cluster 2 groups studies related to the analysis and monitoring of instabilities in rock slopes. It includes foundational works on rock slopes classification and landslide types, as well as studies that employ three-dimensional data acquisition technologies such as LIDAR and photogrammetry to detect deformations and monitor failure processes in rock slopes.

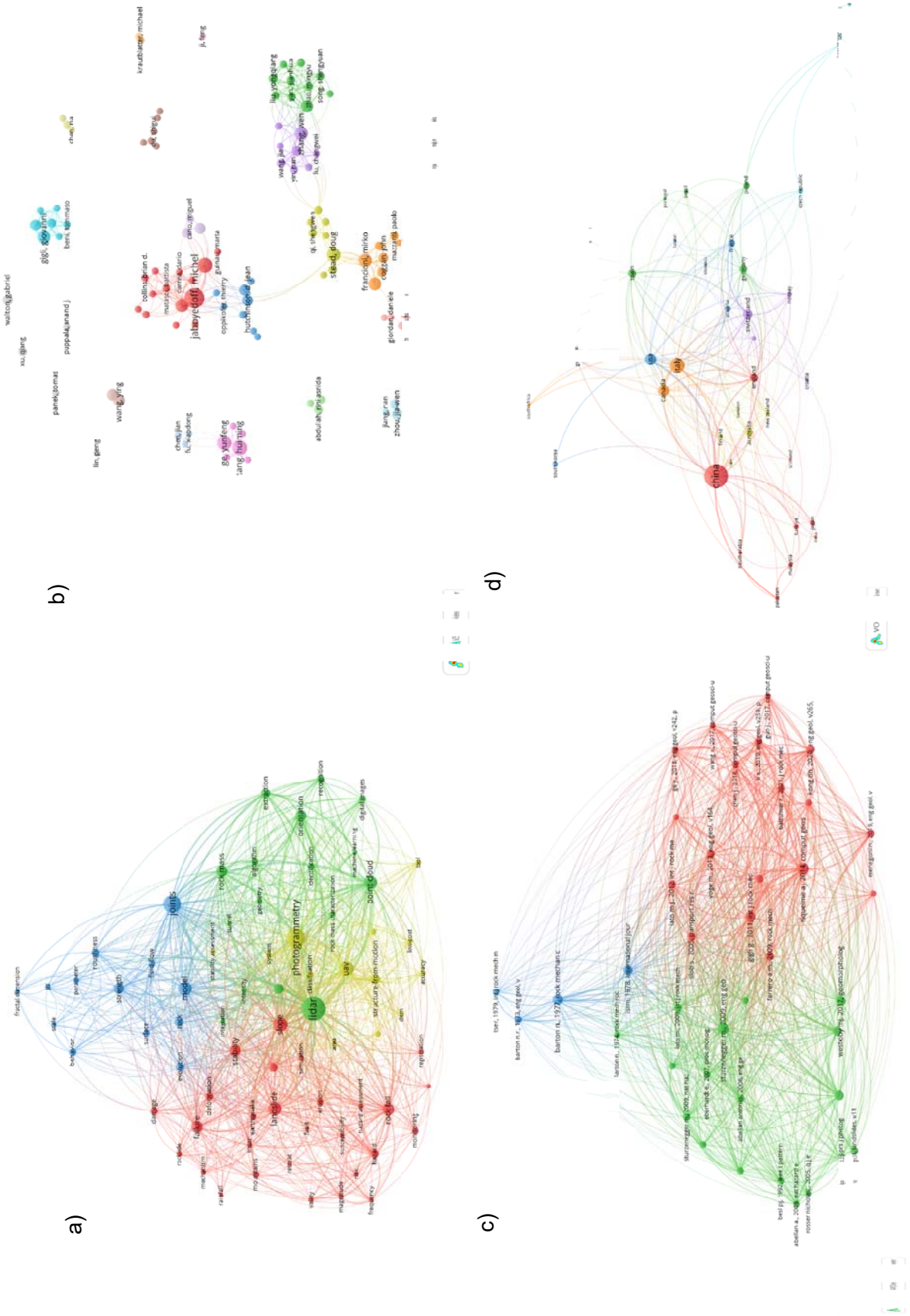


Fig. 2 Bibliometric networks. From left to right and top to botttom: a) keyword co-ocurrence network, b) author co-authorship network, c) country co-authorship network and d) cited references co-citation network.

4 Conclusions

The R-Bibliometrix and VOSviewer softwares were employed to analyze, review and create network maps of the 1205 articles of the application of remote sensing techniques in the characterization of rock slopes from 2010 to 2025 based on the data acquired from WoS database

This analysis shows a sustained and significant growth in paper production during the analyzed period, The use of technologies such as UAV's and techniques as LIDAR and Photogrammetry are some of the essential tools that much of the papers use for its methodologies, not only because of the three-dimensional products that can be obtained but also because it help to overcome the limitations of traditional fieldwork. Bibliometric networks also show the convergence between advanced algorithms in the structural characterization of rock slopes and especially of the joints, because this topic is one of the primary focuses of many papers.

With respect to international production, China emerges as the country that produced most of the papers in the analyzed database, producing almost 37% of them, competing only with European-continent production that reaches almost 39% of the paper production. However, despite this production, both research groups and international collaboration are limited, indicating little collaboration in research works but also showing an important opportunity to strengthen cooperation and foster more integrated research efforts.

Finally, the analysis of the most cited references demonstrates the coexistence of two fundamental pillars in this field: on one hand, the classical knowledge basis of rock mechanics and structural characterization, and on the other, the integration of modern data acquisition and processing technologies. This combination has enabled significant advances in accuracy, efficiency, and scope, establishing remote sensing techniques as indispensable tools in contemporary research. These bibliometric analyses can also offer ideas for future researchers about the state of the art of this field, however more discussion of this analysis is needed, due to the interpretation of the results can be subjective because different researchers may have different perspectives of the same content.

Due to the short extension of this paper, other bibliometric networks and information have been added to an additional document, Appendix 1, to give a broader and more detailed explanation of the database obtained from Web of Science; it is recommended to read this document to have a better idea of the current status of the topics that have been discussed in this paper. This document can be consulted in the next link: https://drive.google.com/drive/folders/1459RonM_gDTvnkZU2OP-4fhKE5oCIzRP?usp=sharing.

References

Barton, N., Choubey, V. The shear strength of rock joints in theory and practice. Rock Mechanics 10, 1–54 (1977). https://doi.org/10.1007/BF01261801

González de Vallejo, L. I., Ferrer, M., Ortuño, L., & Oteo, C. (2002). Ingeniería Geológica. PEARSON EDUCACIÓN.

International Society for Rock Mechanics. (1978). Suggested methods for the quantitative description of discontinuities in rock masses. International Journal of Rock Mechanics and Mining Sciences & Geomechanics Abstracts, 15(6), 319–368. https://doi.org/10.1016/0148-9062(78)91472-9

Mancera-Alejandrez, J., Macias-Medrano, S., Villarreal-Rubio, E., & Solano-Rojas, D. (2021). Spherical data validation of rock discontinuities orientation from Drone-derived 3D Point Clouds. Revista Mexicana de Ciencias Geologicas, 38 (3), p. 152-163.http://dx.doi.org/10.22201/cgeo.20072902e.2021.3.1641

Riquelme, A. J., Abellán, A., & Tomás, R. (2015). Discontinuity spacing analysis in rock masses using 3D point clouds. Engineering Geology, 195, 185–195. https://doi.org/10.1016/j.enggeo.2015.06.009

Riquelme, A. J., Tomás, R., &Abellán, A. (2016). Characterization of rock slopes through slope mass rating using 3D point clouds. International Journal of Rock Mechanics and Mining Sciences, 84, 165–176. https://doi.org/10.1016/j.ijrmms.2015.12.008

Xue, Y., Niu, Z., Zhang, R., Jia, L., & Guo, S. (2024). Current status and future research of groundwater under climate change: A bibliometric analysis. Water, 16(23), 3438. https://doi.org/10.3390/w16233438

Non-destructive Determination of Building Stone Provenance

E. Matoušková & K. Pavelka
Czech Technical University in Prague, Faculty of Civil Engineering, dept. of Geomatics, Prague, Czech Republic
pavelka@fsv.cvut.cz
0000-0003-2743-6296

K. Kovářová
Czech Technical University in Prague, Faculty of Civil Engineering, dept. of Geotechnics, Prague, Czech Republic

Abstract

In professional conservation practice, determining the provenance of building stone used in historic structures represents a frequent and methodologically complex task. Conventional analytical approaches capable of providing reliable answers are predominantly destructive, as they require sampling of the investigated material. Sample extraction is often unacceptable in the case of valuable architectural or artistic elements. For this reason, the present study focuses on the application of reflectance spectroscopy as a promising, efficient, and non-destructive analytical method. The paper introduces the fundamental principles of this technique, discusses its analytical potential, and evaluates its applicability to the study of historic building and decorative stone, including its limitations and the requirements for further methodological development.

Keywords

Non-destructive testing, Reflectance spectroscopy, Spectral characteristics, Spectral library.

1 Introduction

The question of the origin of building stone used in historical structures is frequently encountered in conservation practice, archaeology, and architectural history. Traditionally, its answer has relied on petrographic analysis, archival research, or visual expert assessment performed by experienced geologists. Petrographic analysis remains the most applied method, but it requires physical sampling and is therefore inherently destructive. This limitation becomes critical when the investigated objects are historically or artistically valuable, where any intervention may be restricted or strictly prohibited. Moreover, the interpretation of results depends heavily on the expertise of a trained petrographer whose judgement may vary depending on experience and available comparative materials.

Archival research, although valuable, is often insufficient due to incomplete or missing historical records, which frequently lack information about repairs or later interventions involving different stone types. Similarly, in situ visual assessment is based primarily on expert experience and visual

similarity, which may be significantly distorted by the presence of weathering crusts, surface deposits, or conservation treatments.

The importance of analytical methods for provenance determination has been emphasised, for example, by Dontová (2021), who discussed the use of trace element analysis, typically performed by destructive techniques such as LA-ICP-MS or neutron activation analysis. Přikryl et al. (2015) proposed a methodological framework for determining the origin of limestone and marble using laboratory-based approaches, which are likewise destructive in nature. Hopkinson et al. (2015) demonstrated the effectiveness of combining petrographic and spectroscopic methods to identify potential quarry sources, highlighting the strong potential of modern analytical techniques, but still requiring sampling.

These limitations underline the necessity of developing non-destructive methods based on objective and reproducible data analysis rather than expert judgement alone. Equally important is the possibility of applying such methods directly in situ, without the need for material sampling

2 Reflectance Spectroscopy

The methodology presented in this study assumes that the optical properties of surfaces allow for their identification (Pavelka Jr. et al., 2018). In the case of rocks, these properties are influenced by their mineral composition, internal structure, and conditions of formation, and are therefore characteristic of specific lithological types. Reflectance spectroscopy operates on the principle of the interaction between electromagnetic radiation and matter, measuring the proportion of incident radiation reflected from a material surface as a function of wavelength (Fig. 1). Different materials interact with radiation in distinct ways due to their chemical and structural properties, leading to selective absorption and reflection of specific wavelengths (Clark, 1999; Matoušková, Kovářová, 2021).

The resulting spectral reflectance curve represents a unique “spectral signature” of the investigated material and can be used for identification through comparison with reference datasets. Several factors influence the shape of these curves, including mineralogical composition, grain size and orientation, surface roughness, porosity, moisture content, and the degree of weathering. In the case of near- and mid-infrared measurements, the influence of colour and ambient lighting is significantly reduced due to the use of controlled illumination and contact probes, although proper measurement geometry remains essential for obtaining reliable results.

The identification process is based on comparing measured spectra with reference spectral libraries. Existing databases, such as those maintained by the U.S. Geological Survey (USGS Spectral Library) and NASA (NASA Spectral Library), provide extensive collections of spectral data; however, they are primarily designed for remote sensing applications and often do not include materials typical for specific regions such as Central Europe. For this reason, it is necessary to develop dedicated regional spectral libraries reflecting historically used building stones. Fig. 2 shows the acquisition of spectral data in situ (Matoušková et al., 2021).

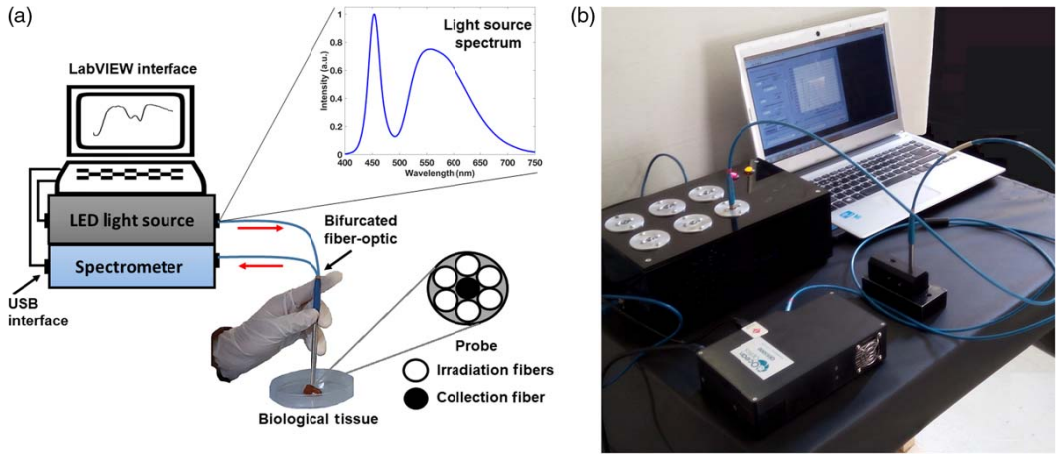


Fig. 1 Right: reflectance spectroscopy device; left: schematic representation of the application (Spie Digital Library).



Fig. 2 Examination of Petr Parléř's tombstone using reflectance spectroscopy, St. Vitus Cathedral in Prague.

The comparison of spectral curves is performed using mathematical algorithms. Among these, the Spectral Angle Mapper (SAM) has proven particularly effective, as it evaluates similarity based on the angle between spectral vectors, with smaller angles indicating higher similarity. Data processing requires averaging multiple measurements and evaluating statistical parameters, which often necessitates custom computational solutions due to the absence of specialised user-friendly software.

3 Results and Discussion

The construction of a comprehensive spectral library is essential for the successful application of reflectance spectroscopy in provenance studies. The present research focuses primarily on sandstones and marlstones, which are common materials in historical architecture in the Czech Republic. Samples were obtained from lithotheques, academic collections, and museum repositories, and measured under controlled laboratory conditions. Each sample was measured repeatedly, and the resulting spectral curve represents an average of multiple measurements to ensure statistical reliability. An example of sandstone CTU spectral library can be seen on Fig. 3, an example of marstone CTU library is shown on Fig. 4.

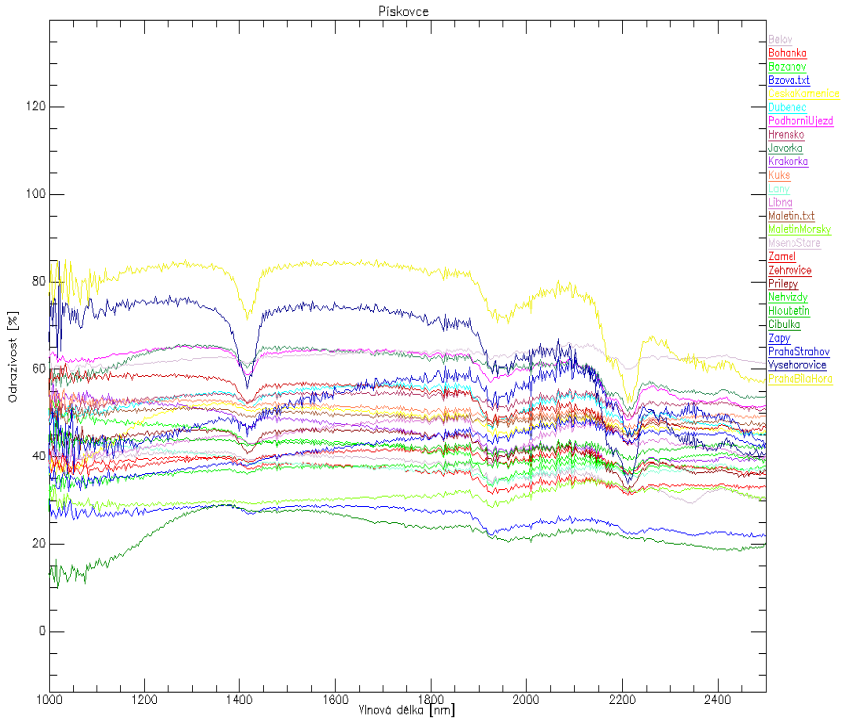


Fig. 3 Spectral reflectance curves of selected Czech sandstones, Spectral Data Library of the Faculty of Civil Engineering, Czech Technical University in Prague.

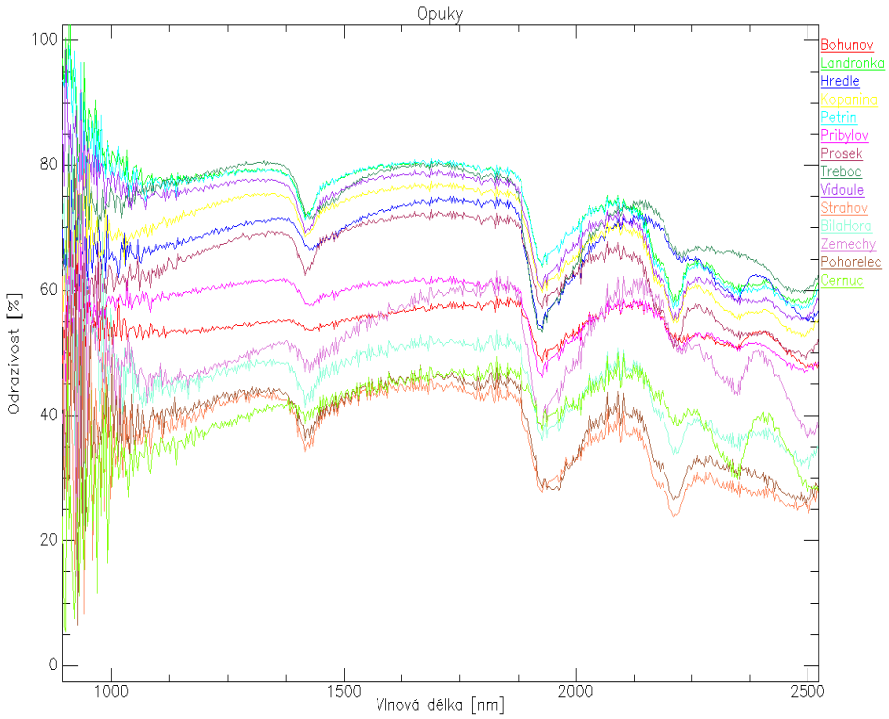


Fig. 4 Spectral reflectance curves of selected Czech marlstones, Spectral Data Library of the Faculty of Civil Engineering, Czech Technical University in Prague.

The practical application of the method can be illustrated by the analysis of a sandstone block from the base of the Wohlmut Gallery (Fig.5), which showed the highest similarity to sandstone from the Kuks locality. This result corresponds well with historical records indicating the use of sandstone from the Dvůr Králové region (Březinová et al., 1996), thereby confirming the validity of the method in this specific case (Kovářová et al., 2025).

Unknown: WK-sokl_prumer.txt:C2		
Library Spectrum	Score	SAM
Kuks.txt:C2	[0.933]:	{0.933}
Bohanka.txt:C2	[0.931]:	{0.931}
Maletin.txt:C2	[0.931]:	{0.931}
Hloubetin.txt:C2	[0.926]:	{0.926}
Hrensko.txt:C2	[0.926]:	{0.926}
Javorka.txt:C2	[0.922]:	{0.922}
Dubenec.txt:C2	[0.921]:	{0.921}
HoriceStare.txt:C2	[0.916]:	{0.916}
Zamel.txt:C2	[0.915]:	{0.915}
Lany.txt:C2	[0.914]:	{0.914}
Zehrovak10mereni.txt	[0.912]:	{0.912}
Bzova1.txt:C2	[0.912]:	{0.912}
MsenoStare.txt:C2	[0.910]:	{0.910}
Prilepy.txt:C2	[0.909]:	{0.909}
Belov.txt:C2	[0.903]:	{0.903}
Libna.txt:C2	[0.901]:	{0.901}
CeskaKamenice.txt:C2	[0.901]:	{0.901}
Bozanov.txt:C2	[0.892]:	{0.892}
Krakorka.txt:C2	[0.885]:	{0.885}
Nehvizdy.txt:C2	[0.880]:	{0.880}
MaletinMorsky.txt:C2	[0.877]:	{0.877}
zapy.txt:C2	[0.824]:	{0.824}
Cibulka.txt:C2	[0.792]:	{0.792}

Fig. 5 Ranking of the visual similarity of the sandstone block forming the base of the Wohlmut pulpit.

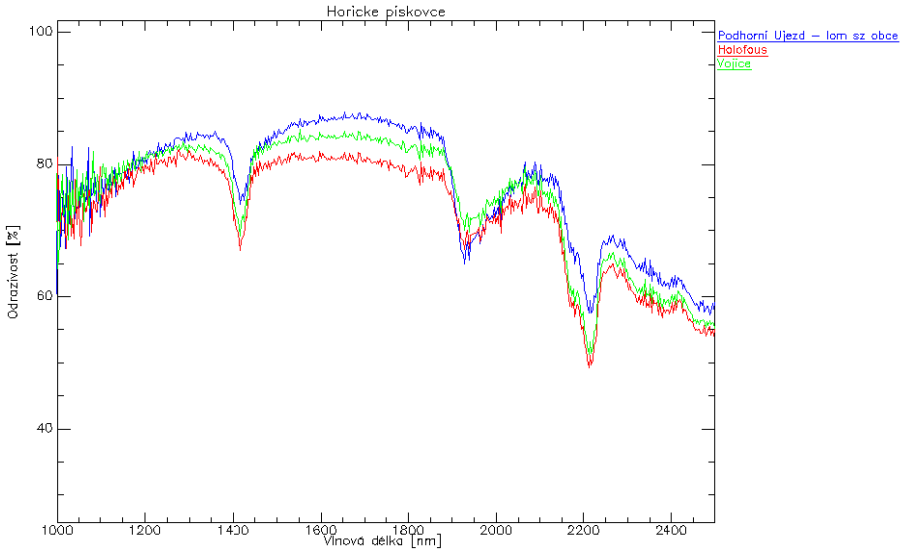


Fig. 6 Spectral reflectance curves of selected Hořice sandstones.

Despite these promising results, several limitations must be considered. One of the main challenges is the high degree of similarity between spectral curves of certain lithological types, such as Hořice sandstones or Prague marlstones, which cannot always be reliably distinguished using the current methodology (Fig.6). Another significant factor is the impact of surface conditions, including weathering processes, contamination, and conservation treatments (Fig.7). These factors can substantially alter the spectral response, often smooth characteristic features and reducing overall reflectance.

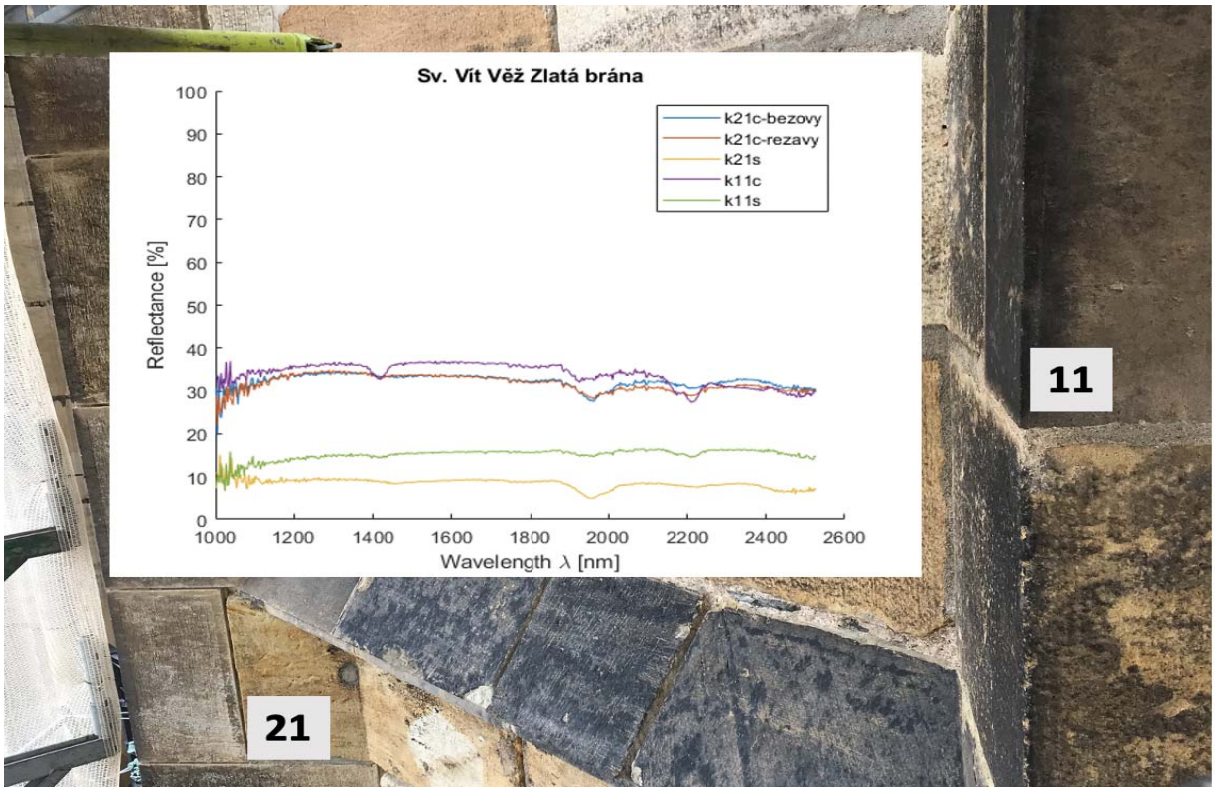


Fig. 7 Spectral reflectance curves for the blocks of the south staircase of St. Vitus Cathedral (samples labeled "c" after the numerical identifier indicate a clean surface; samples labeled "s" after the numerical identifier indicate a soiled surface).

The influence of conservation materials is particularly important. For example, alkoxysilane-based consolidants may result in the formation of silica phases that modify the spectral signature (Xu et al, 2019), while lime-based coatings lead to the formation of calcium carbonate, which also affects reflectance characteristics (Doehne, Price, 2010). These alterations may significantly complicate or even prevent the identification of the original material. In many cases, the complete history of conservation interventions is not known, which further increases uncertainty.

The reliability of the method may be improved by adopting a selective analytical approach, in which measured spectra are compared only with relevant subsets of the spectral library corresponding to specific historical periods. This approach requires independent dating of the studied objects, which may be achieved through archival research or traceological analysis (Cihla et al., 2022). The integration of such methods within a broader multidisciplinary framework significantly enhances the accuracy and interpretability of the results.

4 Conclusion

Reflectance spectroscopy represents a highly promising non-destructive method for determining the provenance of building stone used in historical architecture and artefacts. Its primary advantages include the possibility of in situ application, the absence of sampling, and relatively rapid data acquisition. However, the method also presents several challenges, particularly in terms of data processing, the similarity of spectral characteristics among certain materials, and the sensitivity of measurements to surface conditions and conservation treatments.

At the current stage of development, reflectance spectroscopy should not be considered a standalone tool but rather a complementary method that benefits from integration with other non-destructive analytical approaches. The accuracy of results may be significantly improved through interdisciplinary collaboration involving experts in geology, materials science, conservation, archaeology, and art history.

Future research should focus on expanding spectral libraries to include a wider range of historically used materials, developing more advanced data processing algorithms, and establishing international databases of spectral reflectance data. Such developments would considerably enhance the applicability and reliability of this method in the field of cultural heritage research.

5 Acknowledgement

This paper was supported by the Ministry of Education, Youth and Sport of the Czech Republic in the programme INTER-EXELLENCE II No. LUABA24083 Memory written in stone.

References

Březinová et al. (1996) Praha kamenná, in Czech ("Stone Prague: Natural stones in Prague's buildings and works of art").National Museum in Prague

Cihla et al. (2022). Vzorník stop a rekonstrukce historických kamenických nástrojů, in Czech (Catalogue of Footprints and Reconstructions of Historical Stonemasonry Tools), project "The Topography of Stone, Surfaces and Its Applications in the Restoration of Stone Elements ",2019-2022, Czech Ministry of Culture, https://stonetopography.is.cvut.cz

Clark, R. N. (1999). Spectroscopy of rocks and minerals, and principles of spectroscopy. In A. N. Rencz (Ed.), Manual of Remote Sensing: Volume 3, Remote sensing for the earth sciences (3rd ed., pp. 3–58). John Wiley & Sons.

Doehne, E., Price, C. A. (2010). Stone conservation: An overview of current research (2nd ed.). The Getty Conservation Institute.

Dontová, K. (2015). Methods for determining marble provenance. Bachelor's thesis, Charles University in Prague.

Hopkinson, L. et al. (2015) Sourcing limestone masonry; for restoration of historic buildings, Journal of Cultural Heritage.https://doi.org/10.1016/j.culher.2015.03.007

Kovářová, K., Matoušková, E., Cihla, M. et al. (2025) New methods collection to identify the building and decoration stones provenance. Herit. Sci. 13, 42. https://doi.org/10.1038/s40494-025-01633-x

NASA Spectral Library.https://speclib.jpl.nasa.gov/. Accessed at 2025-12-1

Matoušková, E., Pavelka, K., Ibrahim, S. (2021). Creating a Material Spectral Library for Plaster and Mortar Material Determination, Materials. 13(22), 1-19. ISSN 1996-1944.https://doi.org/10.3390/ma14227030

Matoušková, E.; Kovářová, K. (2021). The Role of the Technical and Natural Sciences in Stone Monument Care. The Civil Engineering Journal. 30(4), 910-919. ISSN 1805-2576.https://doi.org/10.14311/CEJ.2021.04.0070

Pavelka, K., jr., Raeva, P., Hanuš, J.,Gojda, M. (2018). Using of both hyperspectral aerial sensing and RPAS multispectral sensing for potential archaeological sites detectionSPIE2018 Multispectral, Hyperspectral, and Ultraspectral Remote Sensing Technology, Techniques and Applications VII. Bellingham: SPIE-INT SOC OPTICAL ENGINEERING, SPIE. vol. 10780. ISSN 1996-756X. ISBN 9781510621367.https://doi.org/10.1117/12.2324299

Přikryl, R., et al. (2015). Material analysis of natural stone. (Certified methodology). Prague. https://www.nusl.cz.

SPIE Digital Library (reflectance spectroscopy application). https://www.spiedigitallibrary.org/. Accessed at 2025-12-1

USGS Spectral Library. https://www.usgs.gov/labs/spectroscopy-lab/science/spectral-library. Accessed at 2025-12-1

Xu, F., Zeng, W., & Li, D. (2019). Recent advance in alkoxysilane-based consolidants for stone. Progress in Organic Coatings, 127, 45-54 https://doi.org/10.1016/j.porcoat.2018.12.007.

Pre-Peak Nonlinearity of Granodiorite in Mohr–Coulomb and Hoek–Brown Models

A. Z. Ter-Martirosyan & G. O. Anzhelo & L. YU. Ermoshina & V. A. Lunin

MSUCE, Department of Soil Mechanics and Geotechnical Engineering, Moscow, Russia
slava.lunin@bk.ru

0009-0006-9352-332X

Abstract

This paper addresses the use of laboratory-derived deformation parameters of rock specimens for selecting constitutive models in numerical stress–strain analysis. The experimental basis of the study consists of uniaxial compression tests performed on water-saturated cylindrical granodiorite specimens. The tests provided the uniaxial compressive strength, the deformation modulus along the loading branch, the elastic modulus along the unloading branch, the transverse deformation coefficient, and Poisson's ratio.

Analysis of the stress–strain curves shows that the pre-peak behaviour of granodiorite cannot be reduced to a linear elastic response governed by a single constant deformation modulus. A pronounced nonlinear segment is observed at the initial loading stage, which may be associated with the closure of microcracks, pores, and weakened contacts within the rock structure. At the same time, the deformation modulus determined within the standard stress range mainly characterizes the working part of the curve and does not represent the initial deformation stage.

It is shown that the Mohr–Coulomb model and the standard Hoek–Brown model may be used for engineering assessment of limit states and for parametric analysis; however, their application is limited when the objective is to reproduce the complete pre-peak uniaxial compression curve. As a promising direction, the use of models with stiffness evolution is proposed, including modified Hoek–Brown with softening formulations supplemented by a pre-peak deformation modulus evolution law.

Keywords

Granodiorite, Uniaxial compression, Deformation modulus, Mohr–Coulomb, Hoek–Brown.

1 Introduction

Numerical modelling of rock materials requires the selection of a constitutive model capable of describing not only the ultimate strength, but also the deformation behaviour of the material prior to failure. In continuum models of soils and rocks, the stress–strain state is considered as a result of changes in internal variables and material parameters, rather than solely as a function of ultimate strength (Alonso et al. 1990). Therefore, when laboratory-derived parameters are used, it is essential to consider the specific segment of the stress–strain curve from which they were obtained.

For rock materials, one of the most widely used strength relationships is the Hoek–Brown criterion, developed for estimating the strength of intact rocks and jointed rock masses (Hoek and Brown 1980; Hoek and Brown 1997). Its subsequent development through the parameters m_i, GSI, and the disturbance factor D has enabled its broad application in engineering calculations and numerical modelling (Hoek et al. 2002; Hoek and Brown 2019). However, the nonlinear Hoek–Brown strength envelope alone does not ensure reproduction of the complete laboratory stress–strain curve, since the deformational part of standard models is commonly defined by constant values of deformation modulus and Poisson's ratio.

The Mohr–Coulomb model, commonly used as a first-approximation model, is also limited in describing pre-peak nonlinearity, because it assumes a linear elastic response prior to reaching the failure condition. At the same time, the behaviour of rock materials is governed not only by strength, but also by jointing, dilatancy, scale effect, damage accumulation, residual strength, and stiffness evolution during loading (Barton 1976; Barton 1977; Alejano and Alonso 2005; Diederichs 2007; Brown 2008; Cai et al. 2004; Cai et al. 2007; Walton et al. 2019; Brantut and Petit 2022). In this context, Hoek–Brown with softening models are of particular interest, as they allow the degradation of strength parameters and the residual state of the rock mass to be taken into account (Verbilo et al. 2025).

Uniaxial compression tests performed in accordance with modern approaches to determining the strength and deformation moduli of intact rock specimens (ASTM D7012-23 2023) indicate that the calculated deformation modulus often characterizes only a prescribed working stress range. The aim of this study is to assess the applicability of the Mohr–Coulomb and Hoek–Brown models for describing the pre-peak behaviour of water-saturated granodiorite based on laboratory uniaxial compression curves obtained from cylindrical specimens. Particular attention is paid to the relationship between deformation parameters, the shape of the stress–strain curve, and the limitations of models that employ constant elastic stiffness.

2 Experimental Database and Methodology of Analysis

The experimental database includes laboratory tests on water-saturated granodiorite specimens prepared from core samples. Cylindrical specimens of standard geometry were used, and the analysis focused on uniaxial compression curves, which characterize both ultimate strength and stiffness evolution during loading.

The following parameters were determined: uniaxial compressive strength in the water-saturated state $R_{c,ws}$, deformation modulus along the loading branch E_d, elastic modulus along the unloading branch E_y, transverse deformation coefficient ν, and Poisson's ratio μ. The deformation modulus was calculated within the relative stress range $0.05R_c$–$0.5R_c$, which corresponds to the working part of the stress–strain curve but does not include the initial nonlinear deformation stage. This is important when these parameters are used in constitutive models with constant stiffness.

For statistical analysis, a dataset with complete deformation parameters for water-saturated granodiorite was used. For detailed interpretation of curve shape, five representative uniaxial compression curves were selected under comparable conditions in terms of rock type, moisture state, and specimen geometry. In this study, the stress–strain curve is therefore considered not only as a source of input parameters, but also as an independent criterion for assessing the physical suitability of a constitutive model.

3 Correlation Analysis and Deformation Parameters

Correlation analysis was performed to evaluate the relationships between the physical, strength, and deformation characteristics of water-saturated granodiorite. The analysis included complete records with determined deformation parameters. The uniaxial compressive strength in the water-saturated state ranged from 12.54 to 104.24 MPa, the deformation modulus along the loading branch ranged from 3.14 to 38.47 GPa, and the elastic modulus along the unloading branch ranged from 5.82 to 44.11 GPa. This scatter indicates pronounced structural heterogeneity of the granodiorite, even within the same lithological variety.

Table 1. Main correlations between physical and mechanical parameters.

Compared parameters	**Correlation coefficient r**
E_d - E_y	0.959
ν - μ	0.850
τc - $R_{c,ws}$	0.930
$R_{c,w}$s - $R_{c,ad}$	0.618
Depth - $R_{c,ws}$	0.153
ρ - $R_{c,ws}$	-0.121
$R_{c,ws}$ - Ed	0.115

The strongest correlation was observed between the deformation modulus along the loading branch E_d and the elastic modulus along the unloading branch E_y(r=0.959). This confirms a stable relationship between stiffness parameters determined at different stages of testing. However, these parameters are not physically identical: the loading branch includes the effects of microdefect closure and the accumulation of irreversible deformation, whereas the unloading branch mainly reflects the elastic component of the specimen response.

The relationship between uniaxial compressive strength and deformation modulus was weak (r=0.115). This indicates that specimen strength cannot be regarded as a reliable independent predictor of deformation stiffness. Similarly, the weak correlations between density, sampling depth, and strength parameters indicate the limited predictive value of integral physical characteristics.

Thus, the results of the correlation analysis show that selecting a constitutive model based only on individual values of strength, density, or deformation modulus is insufficient. It is necessary to consider the segment of the stress–strain curve from which the deformation parameters were determined. Since Ed is calculated within the range 0.05–0.5Rc, it mainly characterizes the working part of loading and does not describe the initial nonlinear segment.

4 Interpretation of the Curves and Limitations of the Mohr–Coulomb and Hoek–Brown Models

To compare specimens with different strength levels, the normalized stress was used:

$$\eta = \frac{\sigma}{R_c} \tag{1}$$

Where η Relative stress level
σ Current axial stress
R_c Uniaxial compressive strength.

Analysis of the normalized curves shows that the pre-peak behaviour of granodiorite is not strictly linear. At the initial loading stage, a segment with reduced tangent stiffness is observed, after which the curve transitions to a more stable working range. This segment may be associated with the closure of microcracks, pores, and weakened contacts between mineral grains. At this stage, the applied load contributes not only to elastic deformation of the mineral skeleton, but also to rearrangement of the internal structure of the specimen. The normalized curves are shown in Fig. 1.

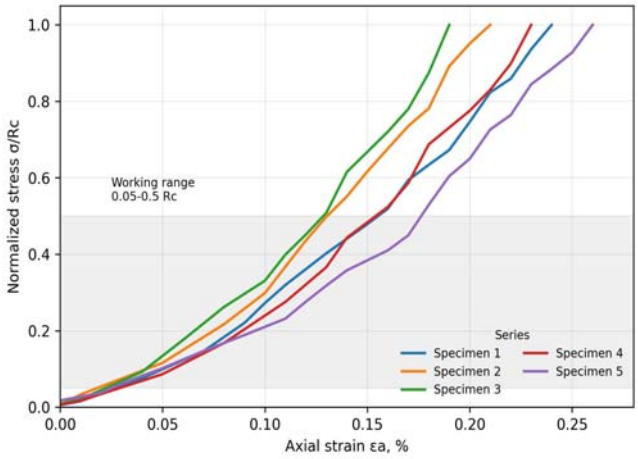


Fig. 1 Normalized uniaxial compression curves of water-saturated granodiorite. The shaded area indicates the initial deformation stage; the range $0.05R_c$–$0.5R_c$ corresponds to the interval used for determining the deformation modulus.

It is important that the deformation modulus E_d, used as a calculation parameter, is not determined over the entire curve, but within the range 0.05–$0.5R_c$. Therefore, it mainly characterizes the working part of loading and does not describe the initial nonlinear segment. If this modulus is directly used in a constitutive model as a constant stiffness parameter, the model will overestimate the stiffness of the specimen at the early loading stage. Conversely, if the modulus is fitted to the initial segment, the calculated stiffness will be underestimated in the main working range.

The Mohr–Coulomb model may be considered a first-approximation model for engineering assessment of rock material behavior. Its advantage lies in the limited number of input parameters and the simplicity of implementation in numerical codes. However, in its classical formulation, the model describes the deformation behavior prior to reaching the limit state using a linear elastic law with constant values of E and ν. For the granodiorite specimens considered in this study, such a formulation cannot reproduce the initial nonlinear segment of the uniaxial compression curve.

The Hoek–Brown model is more consistent with the nature of rock materials in terms of strength description. Its nonlinear strength envelope makes it possible to account for changes in rock resistance at different levels of principal stresses, as well as for the transition from intact rock to rock mass through the parameters m_i, GSI, and D. The generalized version of the Hoek–Brown criterion was specifically intended to facilitate its application in numerical modelling and engineering software; however, the strength envelope itself does not solve the problem of describing the complete laboratory deformation curve. In the standard formulation, the HB model describes strength nonlinearity, but does not introduce an independent law for the evolution of the deformation modulus at the early loading stage.

To account for the initial pre-peak nonlinearity, it is reasonable to introduce a microdefect closure variable χ, varying from 0 to 1 within the initial and working loading ranges:

$$\chi(\eta) = \frac{1 - \exp(-\alpha\eta)}{1 - \exp(-\alpha\eta_w)}, \qquad 0 \le \eta \le \eta_w \tag{2}$$

\Where η_w Upper boundary of the range used to determine the working modulus, η_w=0.5
α Parameter controlling the rate of microdefect closure.
The current deformation modulus can then be expressed as:

$$E(\eta) = E_0 + (E_w - E_0)\chi(\eta) \tag{3}$$

Where E_0 Initial modulus associated with the microdefect closure stage
E_w Working modulus determined in the range 0.05–$0.5R_c$.

The physical meaning of Eq. (3) is that the specimen stiffness is not defined by a single constant value, but gradually increases during the transition from initial structural compaction to the working quasi-elastic segment.

The relationship between stress and axial strain can be written as:

$$\varepsilon_a(\eta) = R_c \int_0^{\eta} \frac{d\xi}{E(\xi)} \tag{4}$$

Eq. (4) makes it possible not only to define a variable modulus, but also to compare the calculated curve with the experimental uniaxial compression curve. In this case, the parameters E_0, E_w, and α can be determined by inverse fitting using the initial and working parts of the laboratory curve. This approach makes the proposed relationship not only a qualitative explanation, but also a potential tool for model calibration.

For the standard Hoek–Brown model, the strength component can be retained in its original form:

$$\sigma_1 = \sigma_3 + \sigma_{ci}(m_b \frac{\sigma_3}{\sigma_{ci}} + s)^a \tag{5}$$

Where σ_1 and σ_3 Principal stresses
σ_{ci} Uniaxial compressive strength of intact rock
m_b, s, a The Hoek–Brown parameters.

Within the proposed approach, Eq. (5) is not replaced, but supplemented by the stiffness evolution law given in Eqs. (2)–(4). This makes it possible to separate two tasks: describing the strength envelope and describing the pre-peak evolution of the deformation modulus.

For Hoek–Brown with softening models, this extension can be formulated using two internal variables: χ, which represents pre-peak microdefect closure, and κ, which represents damage accumulation and post-peak softening. In this case, the strength parameters can be linked to the evolution of GSI:

$$GSI(\kappa) = GSI_r + \big(GSI_p - GSI_r\big)\exp\,(-\beta\kappa) \tag{6}$$

Where GSI_p Initial value of the Geological Strength Index,
GSI_r Residual value
β Degradation rate parameter.

After defining GSI(κ), the parameters m_b, s, and a can be recalculated using the standard Hoek–Brown relationships. This approach is consistent with the general logic of GSI-based rock mass strength assessment, where GSI is used to transition from intact rock to rock mass while accounting for the structure and condition of jointing.

Thus, the proposed extension can be expressed as:

$$E = E(\chi, \kappa), \qquad m_b = m_b(\kappa), \qquad s = s(\kappa), \qquad a = a(\kappa) \tag{7}$$

In this formulation, χ describes the pre-peak stiffness increase associated with microdefect closure, whereas κ represents post-peak degradation caused by damage accumulation. Thus, the proposed scheme separates two physical processes: initial structural compaction and subsequent failure. It should be regarded as a conceptual extension and calibration framework for HB/HBS models rather than a fully verified constitutive model, since the available tests mainly characterize the pre-peak region and do not provide sufficient data for independent calibration of post-peak softening.

5 Conclusions

Laboratory tests on water-saturated cylindrical granodiorite specimens showed that the pre-peak response under uniaxial compression is distinctly nonlinear. The initial loading stage is characterized by reduced tangent stiffness, which may be associated with the closure of microcracks, pores, and weakened contacts within the specimen structure.

The deformation modulus determined along the loading branch within the range 0.05–0.5R_c mainly characterizes the working part of the stress–strain curve and does not capture the initial nonlinear segment. Therefore, using this modulus as a constant stiffness parameter leads to a simplified representation of the deformation behavior of the rock material.

Correlation analysis revealed a strong relationship between the loading deformation modulus and the unloading elastic modulus. However, strength, density, and sampling depth showed weak predictive ability with respect to deformation stiffness, confirming that the shape of the stress–strain curve must be considered in addition to individual parameters.

The Mohr–Coulomb model may be used for preliminary engineering calculations and limit-state assessment, while the Hoek–Brown model provides a more appropriate description of rock strength. Nevertheless, both models are limited in reproducing the complete pre-peak uniaxial compression curve when constant elastic stiffness is assumed.

To improve the physical consistency of the constitutive description, it is proposed to distinguish between pre-peak microdefect closure and post-peak damage accumulation. The former can be described by the variable χ, controlling stiffness evolution, while the latter can be represented by the variable κ, controlling the degradation of GSI, m_b, s, and a within the Hoek–Brown with softening framework.

The proposed scheme does not replace the standard Hoek–Brown criterion, but supplements it with a pre-peak stiffness evolution law. This allows laboratory uniaxial compression curves to be used not only for parameter determination, but also as a basis for selecting and further calibrating constitutive models for rock materials.

References

Alonso EE, Gens A, Josa A (1990) A constitutive model for partially saturated soils. Géotechnique 40(3):405–430. DOI: 10.1680/geot.1990.40.3.405.

Alejano LR, Alonso E (2005) Considerations of the dilatancy angle in rocks and rock masses. International Journal of Rock Mechanics and Mining Sciences 42(4):481–507. DOI: 10.1016/j.ijrmms.2005.01.003.

ASTM D7012-23 (2023) Standard Test Methods for Compressive Strength and Elastic Moduli of Intact Rock Core Specimens under Varying States of Stress and Temperatures. ASTM International.

Barton N (1976) The shear strength of rock and rock joints. International Journal of Rock Mechanics and Mining Sciences & Geomechanics Abstracts 13(9):255–279. DOI: 10.1016/0148-9062(76)90003-6.

Barton N (1977) The shear strength of rock joints in theory and practice. Rock Mechanics 10:1–54. DOI: 10.1007/BF01261801.

Brantut N, Petit L (2022) Micromechanics of rock damage and its recovery in cyclic loading conditions. arXiv preprint arXiv:2206.13407.

Brown ET (2008) Estimating the mechanical properties of rock masses. Proceedings of the 1st Southern Hemisphere International Rock Mechanics Symposium, Perth, pp 3–21.

Cai M, Kaiser PK, Uno H, Tasaka Y, Minami M (2004) Estimation of rock mass deformation modulus and strength of jointed hard rock masses using the GSI system. International Journal of Rock Mechanics and Mining Sciences 41(1):3–19. DOI: 10.1016/S1365-1609(03)00025-X.

Cai M, Kaiser PK, Tasaka Y, Minami M (2007) Determination of residual strength parameters of jointed rock masses using the GSI system. International Journal of Rock Mechanics and Mining Sciences 44(2):247–265. DOI: 10.1016/j.ijrmms.2006.07.005.

Diederichs MS (2007) Mechanistic interpretation and practical application of damage and spalling prediction criteria for deep tunnelling. Canadian Geotechnical Journal 44(9):1082–1116. DOI: 10.1139/T07-033.

Hoek E, Brown ET (1980) Empirical strength criterion for rock masses. Journal of the Geotechnical Engineering Division, ASCE 106(GT9):1013–1035. DOI: 10.1061/AJGEB6.0001029.

Hoek E, Brown ET (1997) Practical estimates of rock mass strength. International Journal of Rock Mechanics and Mining Sciences 34(8):1165–1186. DOI: 10.1016/S1365-1609(97)80069-X.

Hoek E, Carranza-Torres C, Corkum B (2002) Hoek-Brown failure criterion — 2002 edition. Proceedings of NARMS-TAC Conference, Toronto, pp 267–273.

Hoek E, Brown ET (2019) The Hoek–Brown failure criterion and GSI — 2018 edition. Journal of Rock Mechanics and Geotechnical Engineering 11(3):445–463. DOI: 10.1016/j.jrmge.2018.08.001.

Verbilo PE, Iovlev GA, Belyakov NA (2025) Parameter selection for the Hoek–Brown model with softening of rock mass based on laboratory experiments on rock samples and discrete numerical simulations of jointed rock mass. Mining Informational and Analytical Bulletin 2:57–77. DOI: 10.25018/0236_1493_2025_2_0_57.

Walton G, Labrie D, Alejano LR (2019) On the residual strength of rocks and rock masses. Rock Mechanics and Rock Engineering 52:4821–4833. DOI: 10.1007/s00603-019-01879-5.

Application of ARMR for rock slope design

H. Saroglou
NTUA&Geocon, Athens, Greece
saroglou@central.ntua.gr
0000-0002-5253-7972

N. Bar
Gecko Geotechnics, Kingstown, Saint Vincent and the Grenadines

Abstract

The engineering behaviour of rock masses is in many cases anisotropic due to the presence of either bedding, schistosity or joints and fractures. Anisotropic rock mass rating (ARMR) has been developed to assist in rockmass classification and design of structures in anisotropic rockmasses. A modified Hoek & Brown failure criterion, that incorporates ARMR rating, has been developed to calculate the strength of transversely anisotropic rock masses in various orientations with the context of rock engineering design. The paper presents the methodology of applying ARMR and the modified Hoek & Brown criterion to design a slope in an open pit in the Dominican Republic. Slope stability analysisis performed using anisotropic rock mass strength in 2D and 3D. It is demonstrated that the modified Hoek & Brown approach for anisotropic rock mass is slightly higher factor of safety compared to the Generalised Hoek & Brown criterion for isotropic rock masses.

Keywords

ARMR, Anisotropic, Hoek-Brown, Slopes.

1 Introduction

1.1 General

Directional shear strength models allow the application of different shear strengths to different slip surface orientations in numerical analyses. They can be applied in such a way so as to ubiquitously represent weaker bedding planes and foliations upon which shearing is expected to preferentially occur relative to the remainder of the rock mass. In order to apply such models, it is necessary to deter-mine the shear strength of intact rock or rock mass shear strength, the shear strength of the anisotropy plane and define the 'transition' from intact rock or rock mass shear strength to anisotropy plane shear strength (Bar & Weekes, 2017; Saroglou & Bar, 2020).

Linear approximations of non-linear shear strength envelopes derived from Hoek et al. (2002) or Barton& Bandis (1980) failure criteria can be used to predict the behaviour of rock masses and bedding in numerical analyses.

An alternative approach is to determine the strength of anisotropic rock masses for different orientations of the anisotropy plane by using the anisotropic rock mass rating system, ARMR (Saroglou et al., 2019), in conjunction with the Modified Hoek-Brown failure criterion (Saroglou & Tsiambaos, 2008). Using this method, both the shear strength of the intact rock and rock mass strength (in terms of Hoek-Brown or Mohr-Coulomb criteria) can be determined for any orientation of the anisotropy plane, while the least strength of the anisotropic rock mass occurs when the orientation of the anisotropy plane is such that failure takes place along the anisotropy plane, usually at an angle between 30 to 45°.

In this paper, a case study from a slope stability assessment of an open pit mine in the Dominican Republic is presented. The slope is dominated by weak anisotropic rocks and design of future mine slope in this geological environment requires careful consideration of rock mass anisotropy. The slope design is based on a 3D Limit Equilibrium Method (LEM) slope stability analysis using the modified Hoek-Brown criterion and ARMR for the anisotropic rockmass. This assessment is compared with conventional directional shear strength model and recommendations for design are discussed.

2 Anisotropic Rock Mass Rating (ARMR)

2.1 General

The behaviour of anisotropic rock masses is generally dictated by two key aspects – inherent strength anisotropy and structure anisotropy (Saroglou, 2025).Inherent strength anisotropy within the intact rock due to the variation of uniaxial compressive strength (UCS) with respect to the direction of loading relative to the plane of anisotropy (measured in degrees, β). The anisotropy of intact rock can be characterized by the strength anisotropy index (R_c). Structure anisotropy originates from the intensity of anisotropic structure (e.g. foliation, bedding etc.) and the quality or condition of the anisotropy surfaces.

Saroglou et al. (2019) developed the anisotropic rock mass rating (ARMR), specifically developed for anisotropic rock masses to account for the anisotropy of intact rock and rock mass structure anisotropy. Transversely isotropic rock masses, with one or two joint sets in addition to the foliation/bedding can be classified using ARMR, as these joint sets don't influence the persistence of the anisotropic structure. The rating approach of ARMR for each parameter is based on the Rock Mass Rating system (RMR) system by Bieniawski (1989), while the rating scores are modified as two new parameters are added, strength anisotropy index (R_c), and spacing of anisotropy. To account for the effect of confining stress, an adjustment of the rating of anisotropy degree is proposed following the stress classification proposed in Martin et al. (1999).

2.2 ARMR rating

The Anisotropic Rock Mass Rating (ARMR) considers the following parameters:

- Strength anisotropy index, R_c.
- Uniaxial compressive strength of intact rock, σ_c, in which the loading direction is applied perpendicular to the anisotropy planes.
- Degree of structure anisotropy (spacing of anisotropy planes). Scale effects have an influence on the degree of structure anisotropy, so an appropriate scale must be used. For example, when planning a slope excavation of say up to 10 m, an appropriate scale for characterizing the degree of structure anisotropy would be in the order of 2 to 5 m.
- Corrected rock quality designation (RQD_c) whereby the principal anisotropy plane is omitted from calculations. This reduces the direction-dependence of RQD that can arise from sampling bias with 'higher values' when drilled parallel to anisotropy planes or 'lower values' when drilled perpendicular to anisotropy.
- Condition of anisotropy surfaces based on RMR_{89} (Bieniawski, 1989) considering discontinuity length, aperture, roughness, infilling and weathering.

The rating scores of each parameter and the classification to five rock mass quality classes, ranging between isotropic to very highly anisotropic, are presented in Figure 1.

Strength anisotropy degree R_c	≤ 1.1	1.1 - 2.0	2.0 - 3.0		3.0 - 5.0	≥ 5.0	
Description	Isotropic	Low	Moderate		High	Very high	
Rating	**20**	**17**	**13**		**8**	**3**	
UCS (MPa)	>250	100 - 250	50 - 100	25 - 50	5-25	1-5	<1
Point load strength (MPa)	>10	4 - 10	2 - 4	1 - 2	For this low range, uniaxial compressive strength is preferred		
Rating	**15**	**12**	**7**	**4**	**2**	**1**	**0**
Spacing of anisotropic structure	> 1.2 m	0.6 – 1.2 m	200 - 600 mm		40 – 200mm		< 40mm
Rating	**20**	**15**	**10**		**8**		**5**
RQD (%)	90 - 100	75 - 90	50 - 75		25 - 50		< 25
Rating	**15**	**10**	**7**		**4**		**2**
Condition of surfaces	Very rough surfaces, not continuous, no separation, Unweathered wall rock	Rough surfaces, separation <1mm, slightly weathered rock	Slighlty rough surfaces, separation <1mm, highly weathered rock		Slickensided surfaces or gouge < 5mm thick or separation 1 – 5 mm, continuous		Soft gouge > 5mm thick or separation > 5 mm, continuous
Rating	**15**	**10**	**7**		**4**		**0**
Groundwater	Completely dry	Damp	Wet		Dripping		Flowing
Rating	**15**	**10**	**7**		**4**		**0**
Adjustment of total rating based on confining stress range		Low in-situ stress	< 0.15		No change to rating		
		Intermediate in-situ stress	0.15 – 0.4		Move one cell towards left in the anisotropy degree (+5, +4 or +3)		
		High in-situ stress	> 0.4		Move two cells towards left in the anisotropy degree		
ARMR Rating	**100 - 81**	**61 - 80**	**60 - 41**		**40 - 21**		**< 20**
Class number	I	II	III		IV		V
Description	Massive or isotropic rockmass	Slightly anisotropic rockmass	Moderately anisotropic rockmass		Highly Anisotropic rockmass		Very highly anisotropic to sheared rockmass

Fig. 1 Anisotropic rock mass rating (ARMR) classification.

2.3 Modified Hoek & Brown criterion for anisotropic rock mass

The generalized Hoek–Brown criterion (Hoek et al, 2002) is widely used nowadays for the estimation of rock mass strength. The criterion was proposed for isotropic conditions, but in many cases, it has also been applied in anisotropic conditions. The modified Hoek-Brown failure criterion for anisotropic rock (Saroglou et al, 2019) is used to estimate the strength of anisotropic rock masses at different orientations. The modified criterion has been linked with ARMR to derive a criterion for anisotropic rock masses. The total ARMR value is effectively used as a replacement of the GSI in the modified Hoek-Brown failure criterion as described in eq. (1).

$$\sigma_1 = \sigma_3 + \sigma_{ci\beta} \cdot \left(k_\beta \cdot \left(m_{b,an} \left(\frac{\sigma_3}{\sigma_{c\beta}} \right) + s_{an} \right) \right)^{\alpha} \quad (1)$$

Where, $\sigma_{ci,\beta}$ uniaxial compressive strength of intact rock at orientation of anisotropy, β

$m_{b,an}$ reduced value of m_i parameter for anisotropic rock mass

a,s_{an} constants

k_β parameter describing intact rock anisotropy

$$m_{b,an} = m_i \cdot \exp\left(\frac{ARMR - 100}{28 - 14D} \right)$$

$$s_{an} = \exp\left(\frac{ARMR - 100}{9 - 3D} \right)$$

$$\alpha = \frac{1}{2} + \frac{1}{6} \left(e^{-ARMR/15} - e^{-20/3} \right) \quad (2)$$

Based on the modified criterion, rock mass strength at different orientations can be calculated, which may be lower than the strength determined perpendicular to anisotropy planes by the generalized Hoek & Brown criterion.

3 Open pit slope design in anisotropic rock mass

3.1 Geotechnical conditions

An example from a large open pit mine (3 x 2 km) in the Dominican Republic is presented in which the pit slopes are up to 300 m in highly anisotropic and weak carbonaceous sediments (mudstones), overlying various, relatively isotropic volcanic and volcanoclastic rocks (Figure 2). The carbonaceous sediments are in the order of 100 m thick in the upper portion of the slopes and several instabilities were encountered, generally involving sliding on anisotropy planes and intact rock failure. Several of the instabilities within the carbonaceous sediments have been back analysed to derive and calibrate material properties using 3D LEM in Slide3 software (Rocscience Inc), with directional shear strength and 3D finite difference method (FDM) in FLAC3D software (Itasca, 2019) using the ubiquitous joint model considering φ' and c' of bedding and UCS of rock mass (Cancino et al, 2024). 3D LEM models were developed in Slide3 software to assess the stability of each different conceptual inter-ramp slope angle (IRA) design within the carbonaceous sediments (Bar, 2024).

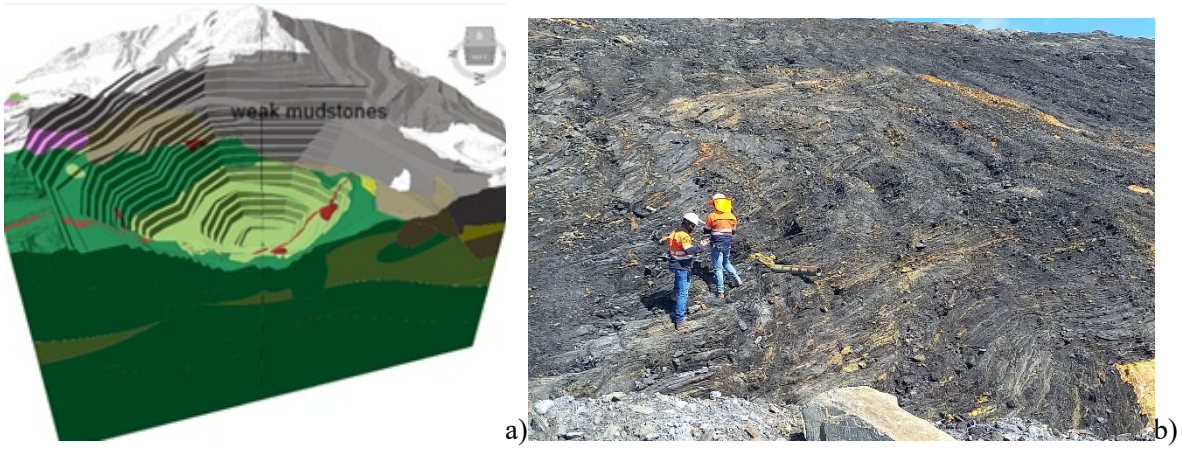


Fig.2 a) Open pit showing area of weak carbonaceous sediments (mudstones), b) exposure of sheared mudstones.

3.2 Slope stability analysis

Two methods of slope stability analysis (using 2D and 3D LEM) were used for future slope design:

a) Conventional anisotropic directional shear strength approach using the generalised isotropic Hoek & Brown criterion for the rock mass and the Mohr-Coulomb criterion with anisotropic linear transition for the bedding planes,
b) Modified Hoek & Brown criterion using ARMR classification with orientation dependent strength rock mass properties. The Hoek & Brown parameters are UCS = 8 MPa, m_i = 8, GSI=35, the bedding strength is c'= 6 kPa and φ'=18^0 (based on back analysis) and the anisotropic linear model transition parameters are A=5^0 and B=30^0. Based on ARMR classification the rock mass is characterized as highly anisotropic (Table 1).

A shear-normal function (non-linear failure envelope) is calculated for different bedding orientations using the modified Hoek & Brown criterion, considering a variation of uniaxial compressive strength and parameter k_β. The failure envelopes for the shear strength of the rock mass using the generalized and modified Hoek & Brown criteria are shown in Figure 3.

Table 1. ARMR classification of mudstone.

Rating parameter	**Description**	**Rating**
Strength anisotropy degree R_c	17/5.3= 3.2	8
Uniaxial compressive strength (MPa)	17	12
Spacing of anisotropic structure (cm)	5 -10	8
R.Q.D. (%)	30 - 50	4
Condition of surfaces	Slickensided, highly weathered	4
Groundwater	Damp	10
Total rating	Highly anisotropic rock mass	36
Stress adjustment	$\sigma_1 / \sigma_c < 0.14$	No

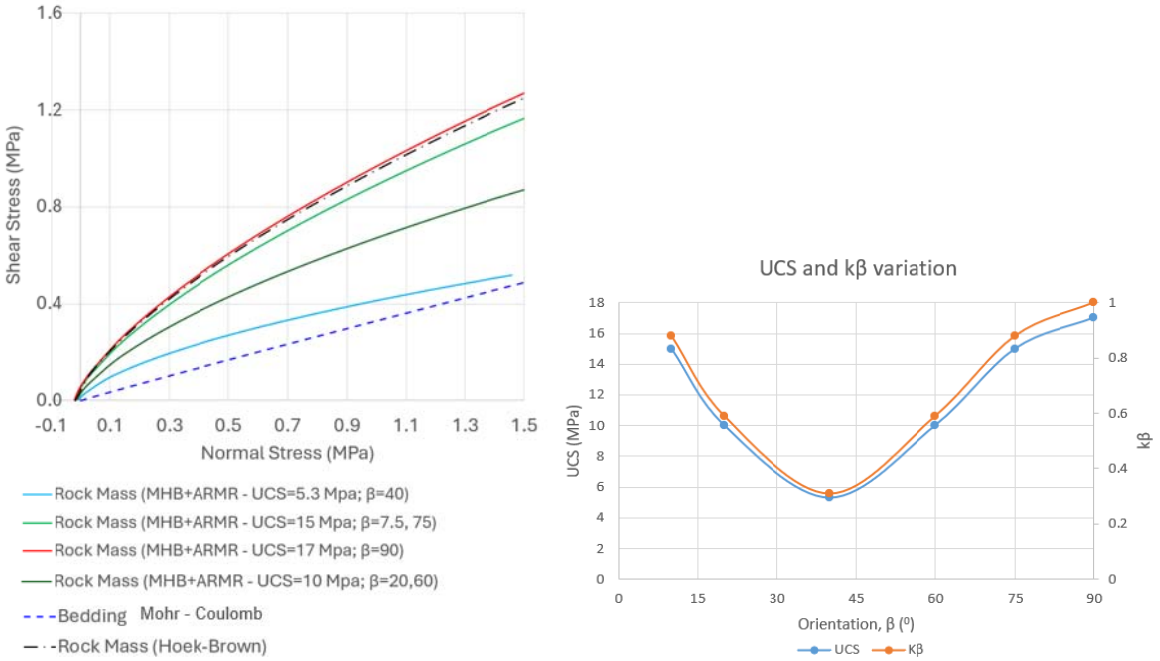


Fig.3 Shear strength of rock mass using generalized and modified Hoek & Brown criteria.

3.3 Slope stability results

The conventional anisotropic directional shear strength approach results to a critical slip surface, that is failing in the carbonaceous mudstones predicting a Factor of Safety (FoS) equal to 0.54 (Figure 4). The stability analysis using the modified Hoek & Brown and ARMR approach resulted in slightly higher FoS equal to 0.77 and the critical slope area is less extensive in relation to that predicted in the previous approach (Figure 5). It is noted that when using the modified Hoek & Brown with ARMR in the 3D LEM model, only anisotropic strength envelopes at minimum ($\beta=40^0$) and maximum ($\beta=90^0$) strength orientations were used due to limitations of Slide3 software.

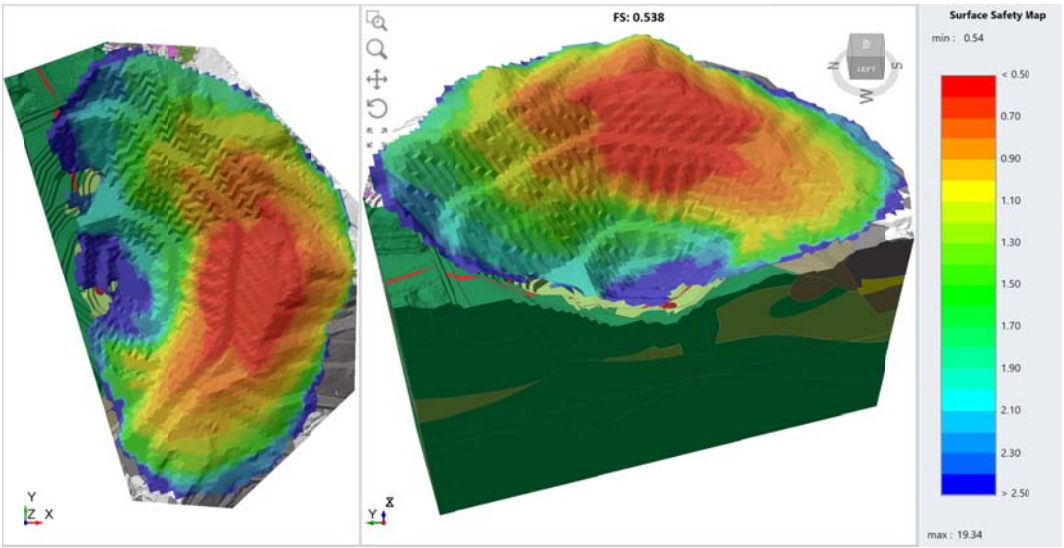


Fig.4 3D slope stability results using anisotropic directional shear strength.

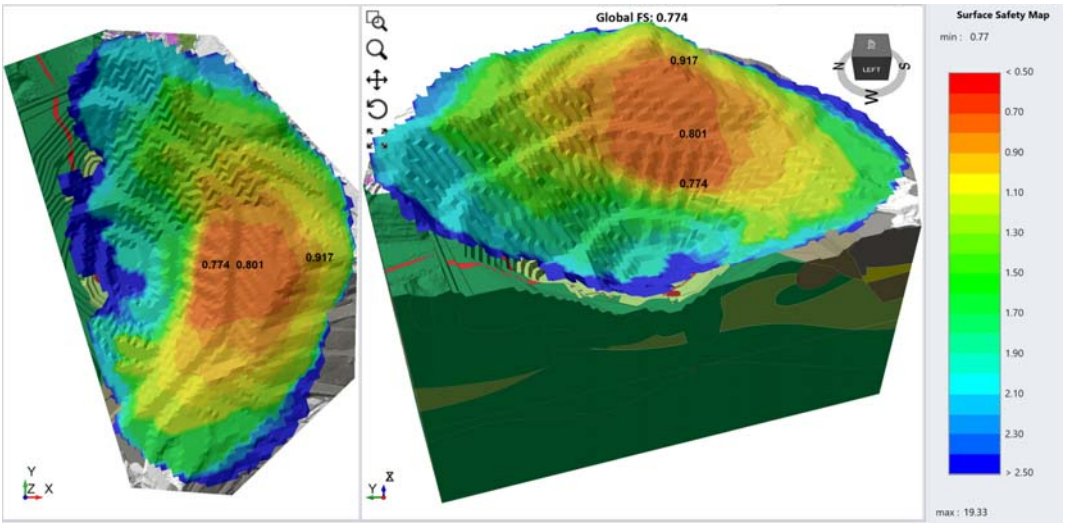


Fig.5 3D slope stability results using the modified Hoek & Brown criterion and ARMR.

4 Conclusions

The advantage of ARMR is that it can be used jointly with the modified Hoek & Brown criterion to determine the rock mass strength in different anisotropy orientations. Based on the results of the 3D slope stability analysis performed in the open pit case study this approach provides a slightly higher factor of safety but generally compares well to the anisotropic directional strength approach. Slope stability of anisotropic rock masses is very sensitive to orientation and strength anisotropy and more analysis is necessary to model the behaviour of anisotropic rock masses. Continued improvement of understanding anisotropic rock masses is key to reliably predicting the stability of slopes.

References

Bar N, Weekes G (2017) Directional shear strength models in 2D and3D limit equilibrium analyses to assess the stability of anisotropicrock slopes in the Pilbara Region of Western Australia", AustralianGeomechanics Journal, 52(4), pp. 91–104.

Bar N (2024) Digital Twin Concept for the Safe and Economic Design and Management of Rock Slopes. Proc. 6thRegional Symp on Landslides in the Adriatic-Balkan Region, ReSyLAB2024. Vol. 6, 11, p. 89–97.

Barton N, Bandis S (1980) Some effects of scale on the shear strengthof joints", International Journal of Rock Mechanics and MiningScience & Geomechanics Abstracts, 17(1), pp. 69–73, 1980.

Bieniawski ZT (1989). Engineering Rock Mass Classification; Wiley: New York, NY, USA.

Cancino C, Lorig L, Bu J, Bar N (2024). Back-analysis for more reliable mine plans at Pueblo Viejo Gold Mine. Proc. Slope Stability 2024.

Hoek E, Carranza-Torres C, Corkum B (2002) The Hoek-Brown failurecriterion – 2002 edition", In: Proc. of the 5th NorthernAmerican Rock Mechanics Symposium and 17th Tunneling Association of Canada Conference (NARMS-TAC), Toronto,Canada, pp. 267–271.

Itasca Consulting Group, Inc. (2019). FLAC3D – Fast Lagrangian Analysis of Continua in Three Dimensions (Version 7.0). Minneapolis: Itasca.

Martin CD, Kaiser PK, McCreath DR (1999). Hoek–Brown parameters for predicting the depth of brittle failure around tunnels. Can. Geotech. J. 36: 136–151.

Saroglou H, Tsiambaos G (2008). A modified Hoek–Brown failure criterion for anisotropic intact rock. Int. Journal of Rock Mechanics & Mining Sciences, 45: 223–234.

Saroglou C, Qi S, Guo S, Wu F (2019). ARMR, a new classification system for the rating of anisotropic rock masses. Bull Eng Geol Env. 78: 3611-3626. https://doi.org/10.1007/s10064-018-1369-4

Saroglou C, Bar N (2020). The ARMR classification system and the modified Hoek-Brown failure criterion compared to directional shear strength models for anisotropic rock masses. Periodica Polytechnica Civil Engineering, 64(1), pp. 14–19.

Saroglou C (2025). The challenge of Rock Mass Classification of anisotropic rockmasses. Rock Mechanics and Rock Engineering https://doi.org/10.1007/s00603-025-04681-8.

Design methods and analysis (incl. EC 7)

A next-generation blast design via seismic intelligence

G. G. U. Aksoy & O. Savaş
Hacettepe University, Mining Engineering Department, Ankara-Turkiye
gulsevaksoy@hacettepe.edu.tr
0000-0002-9328-9899

C. O. Aksoy, H. E. Yaman & V. Özacar
Dokuz Eylul University, Izmir-Turkiye
okayaksoy@deu.edu.tr
0000-0002-4328-4862

Abstract

Blast-induced ground vibration remains one of the most important environmental and geotechnical constraints in open-pit mining. This paper presents a compact Seismic Intelligence framework that integrates pilot-hole seismic monitoring, inverse source-waveform estimation, Q-factor-based attenuation and adaptive electronic-delay optimization. The method uses measured three-component vibration records to reconstruct a representative source signal, propagate it through a frequency-dependent attenuation model and simulate multi-hole wave superposition. A GO-AI optimization routine then adjusts delay intervals under practical constraints, including minimum delay separation, neighbour-based firing and maximum blast duration. Field-scale validation on a blast with more than 300 blastholes showed strong agreement between simulated and measured response, with R^2 approximately 0.94 and practical prediction error below 12%. The optimized delay sequence reduced constructive wave interference, lowered PPV and shifted part of the spectral content toward higher frequencies. The framework also supports hybrid zone-based control, allowing vibration reduction in sensitive sectors while maintaining sufficient seismic energy in waste zones for fragmentation. The results indicate that waveform-based adaptive blast design can improve prediction reliability, environmental compliance and operational control compared with conventional empirical scaled-distance approaches.

Keywords

Seismic Intelligence, Blast optimization, PPV, Delay design, Q-factor.

1 Introduction

Ground vibration induced by production blasting is generally evaluated through peak particle velocity (PPV), frequency content and the response of nearby structures or slopes. Conventional scaled-distance methods remain attractive for preliminary design because they require only charge weight and distance, but they cannot explicitly represent waveform shape, frequency-dependent attenuation or phase interaction between many blastholes (Siskind et al. 1980; Dowding 1996). These limitations become critical in large open-pit blasts where hundreds of holes interact through electronic delay timing and where local geology controls wave transmission.

A modern blast design method should therefore combine field measurements with a physics-informed simulation of wave propagation. The Seismic Intelligence concept developed in this study uses a pilot-hole vibration record as the site-specific source signature and then optimizes the full-blast delay sequence. The aim is to control not only the maximum PPV, but also the temporal and spectral structure of the resulting wavefield. This makes it possible to reduce damaging low-frequency constructive interference while maintaining effective energy release for fragmentation.

2 Methodology

2.1 Workflow

The workflow is summarized in Fig. 1. A pilot hole is first detonated under controlled conditions and recorded at up to five monitoring stations. These measurements are used for source-waveform reconstruction and calibration of attenuation parameters. The calibrated model is then used to simulate the multi-hole response of the full blast, after which the GO-AI optimizer searches for a delay pattern that satisfies operational constraints and reduces the selected vibration objective.

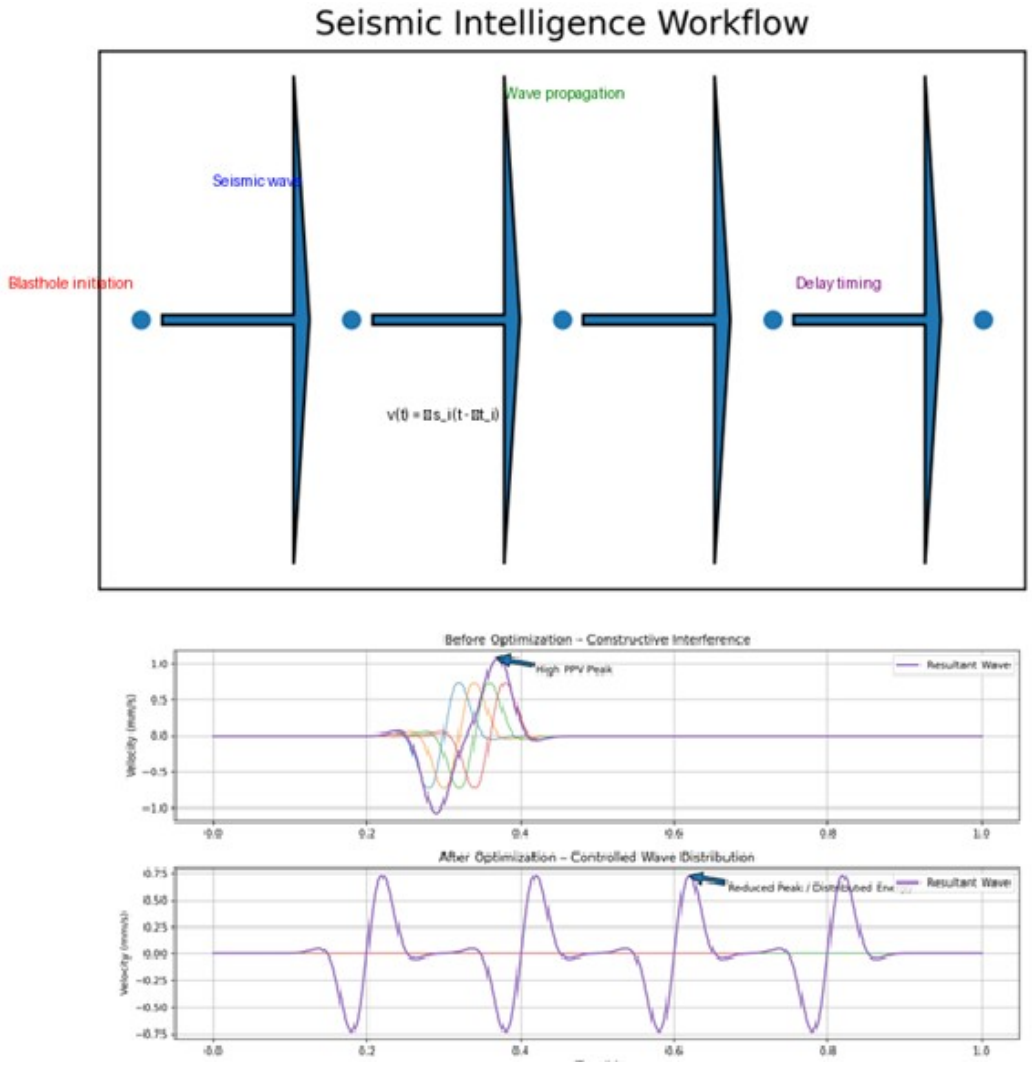


Fig. 1 Seismic Intelligence workflow for pilot-hole measurement, source inversion, attenuation modelling and adaptive delay optimization.

2.2 Signal inversion and attenuation

For the j-th monitoring point, the measured velocity history is written as a source signal multiplied by a propagation function:

$$v_j(t) = G(d_j)s(t) \quad (1)$$

where $v_j(t)$ is the recorded vibration signal, $G(d_j)$ is the propagation function and $s(t)$ is the source signal. The representative source signal is reconstructed by normalizing the measured signals with respect to distance-dependent attenuation:

$$s(t) = (1/N)\ \Sigma_j[v_j(t) / G(d_j)] \quad (2)$$

The attenuation model uses a Q-factor formulation to represent energy dissipation during wave propagation (Kumar et al. 2022; Wang et al. 2023):

$$A(r) = A_0 \exp(-\alpha r), \quad \alpha = \pi f/(Qv) \quad (3)$$

where A(r) is amplitude at distance r, A0 is the reference amplitude, f is frequency, v is wave velocity and Q is the quality factor. This formulation is useful because it accounts for the stronger attenuation of higher-frequency components in fractured rock masses.

2.3 Multi-hole simulation and delay optimization

The vibration response of a group blast is computed by superposing the delayed contribution of individual blastholes:

$$v(t) = \Sigma_i\ s_i(t-\Delta t_i)G(d_i) \quad (4)$$

where $s_i(t)$ is the scaled hole signal, Δt_i is the electronic delay and $G(d_i)$ is the propagation term between the i-th hole and the monitoring point. The optimization problem is expressed as:

$$J = w_1 PPV + w_2(1/E_s) \quad (5)$$

where J is the cost function, E_s is seismic energy, and w_1 and w_2 are weighting factors. The constraints include a minimum delay separation of 8 ms, neighbour-based firing, avoidance of repeated consecutive delay values and a user-defined or default maximum blast duration. For hybrid blasting, the global objective is extended by assigning different weights to vibration-sensitive ore or slope sectors and energy-oriented waste sectors.

3 Results and discussion

3.1 Field-scale validation

The method was evaluated using a large open-pit surface blast containing more than 300 blastholes. Pilot-hole records from multiple monitoring locations were used to calibrate the source signal and attenuation behaviour. The reconstructed waveform preserved the first major peak, dominant frequency and general signal envelope of the measured records. The practical reconstruction error was below 10%, which is sufficient for subsequent waveform-based simulation.

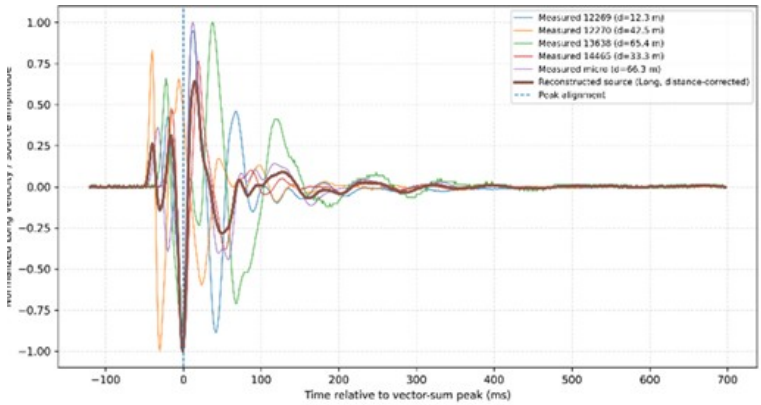


Fig. 2 Example comparison between measured pilot-hole records and the reconstructed source waveform.

The simulated and measured PPV values were then compared across the monitoring points. The agreement was strong, with R^2 approximately 0.94 and most errors within the 10–12% engineering band. This indicates that the combined inversion, attenuation and superposition model captured both the general amplitude decay and the main phase structure of the blast-induced wavefield.

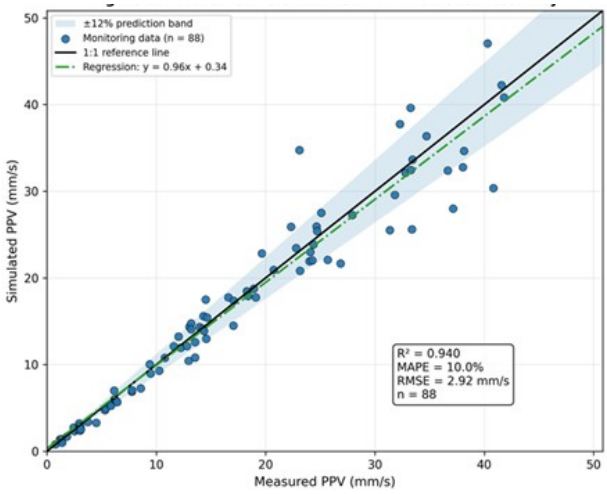


Fig. 3 Simulated versus measured PPV values with a one-to-one reference trend.

Table 1. Summary of model performance and engineering meaning.

Indicator	Result	Engineering meaning
Source reconstruction error	<10%	Pilot record suitable for simulation
PPV prediction	$R^2 \approx 0.94$	Strong measured-simulated agreement
Practical PPV error	<12%	Acceptable controlled-blasting accuracy
Delay optimization	PPV reduction up to about 40%	Reduced constructive interference
Frequency response	Higher-frequency shift	Lower resonance and faster attenuation

3.2 Delay and frequency effects

Before optimization, closely spaced delay intervals caused constructive overlap and relatively high-amplitude peaks. After optimization, the waveforms were redistributed in time, reducing peak amplitude and producing a smoother vibration envelope (Fig. 4). This demonstrates that electronic delay timing is not only a sequencing tool, but also a direct control variable for wave interference.

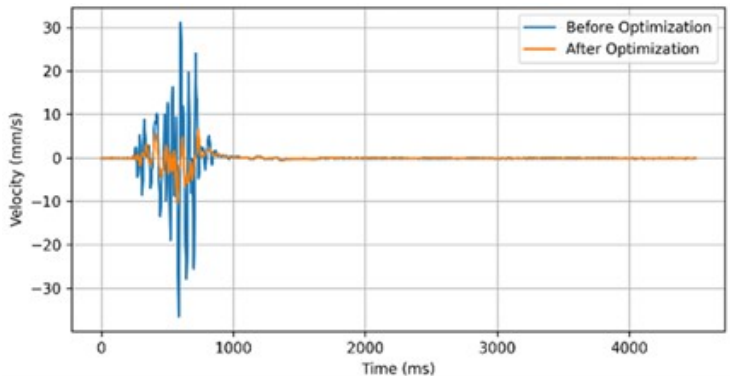


Fig. 4 Comparison of resultant vibration before and after adaptive delay optimization.

Frequency analysis showed a reduction in low-frequency components and a shift of energy toward higher-frequency bands. This is beneficial because low-frequency vibration is more likely to interact with structural resonance, whereas higher-frequency components generally attenuate faster with distance. The frequency-domain result therefore supports the use of waveform-based delay design rather than PPV-only empirical control.

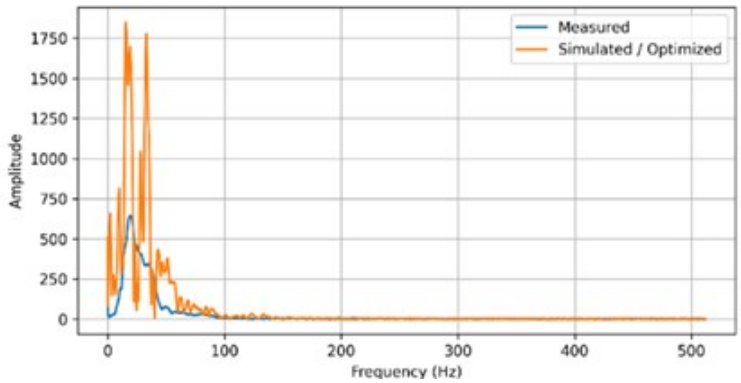


Fig. 5 Frequency-domain comparison showing reduced low-frequency content after optimization.

3.3 Hybrid zone-based control

A practical advantage of the framework is its ability to assign different objectives to different blast zones. In ore or slope-sensitive areas, the optimizer prioritizes lower PPV. In waste sectors, the objective may allow higher seismic energy to support fragmentation. The spatial PPV distribution in Fig. 6 illustrates how a single blast can be managed using different local objectives while preserving a continuous firing pattern.

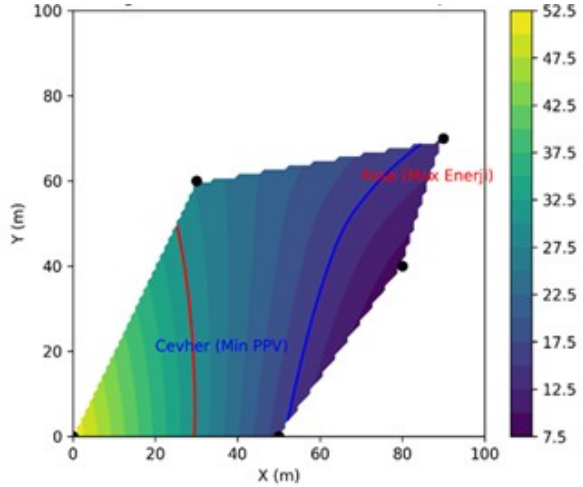


Fig. 6 Spatial PPV distribution used for hybrid zone-based vibration and energy management.

3.4 Residual error and implementation aspects

Residual error analysis was used as a final check on predictive stability. The residuals were concentrated around small values without extreme outliers, indicating that the calibrated model remained stable across different monitoring positions and distances. This is important for practical blast design because a model that performs well only at one station may still be unsafe for regulatory control. The residual pattern shown in Fig. 7 therefore supports the use of the proposed framework as an adaptive design and quality-control tool rather than a single-use prediction equation.

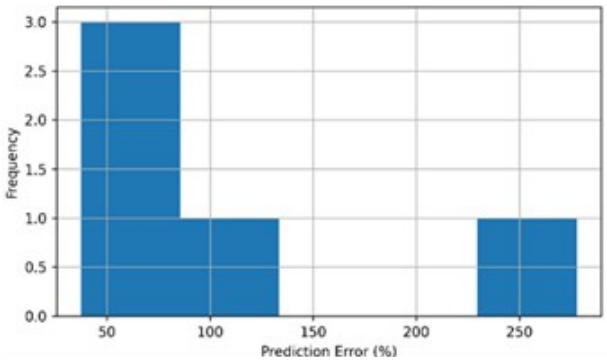


Fig. 7 Residual error distribution used to evaluate stability of the measured-simulated PPV comparison.

For field implementation, the procedure can be embedded into a standard blasting workflow. After the first pilot measurement, the system estimates the source signal and attenuation parameters, calculates trial delay patterns, and produces PPV and frequency checks for the selected monitoring points. After the production blast, measured waveforms are compared with predictions and the error is used to update the next design. This feedback structure is particularly useful in open-pit mines where benches, free faces and geological conditions change continuously.

4 Conclusions

This paper presented a compact Seismic Intelligence framework for controlled blast design in open-pit mining. The method moves beyond empirical scaled-distance prediction by integrating pilot-hole measurements, inverse source reconstruction, Q-factor attenuation, multi-hole superposition and adaptive delay optimization. The following conclusions can be drawn:

– Pilot-hole inversion captured the dominant source waveform with practical error below 10%.

– The Q-factor model provides a physically consistent way to represent frequency-dependent attenuation.

– Multi-hole simulation reproduced field PPV values with R^2 approximately 0.94 and error below 12%.

– Optimized electronic delays reduced constructive interference and shifted vibration energy toward safer higher-frequency ranges.

– Hybrid zone control enables vibration minimization in sensitive sectors while preserving fragmentation energy in waste zones.

Overall, the framework provides a data-driven and physics-informed route for more reliable blast design, environmental compliance and operational control. Future work should focus on real-time monitoring integration, automatic feedback calibration and broader validation under different geological conditions.

References

Ak H, Iphar M, Yavuz M, Konuk A (2009) Evaluation of ground vibration effect of blasting operations in a magnesite mine. Soil Dyn Earthq Eng 29(4):669-676. https://doi.org/10.1016/j.soildyn.2008.07.003

Dowding CH (1996) Construction vibrations. Prentice Hall, Upper Saddle River.

Duvall WI, Fogelson DE (1962) Review of criteria for estimating damage to residences from blasting vibrations. USBM Report of Investigations 5968, United States Bureau of Mines.

Ghasemi E, Sari M, Ataei M (2012) Development of an empirical model for predicting ground vibration in open-pit mines. J Afr Earth Sci 73-74:1-8. https://doi.org/10.1016/j.jafrearsci.2012.07.005

Khandelwal M, Singh TN (2007) Evaluation of blast-induced ground vibration predictors. Soil Dyn Earthq Eng 27(2):116-125. https://doi.org/10.1016/j.soildyn.2006.06.004

Khandelwal M, Singh TN (2009) Prediction of blast-induced ground vibration using artificial neural network. Int J Rock Mech Min Sci 46(7):1214-1222. https://doi.org/10.1016/j.ijrmms.2009.03.004

Kumar R, Choudhury D, Bhargava K (2022) Frequency-dependent attenuation analysis for blast vibration control in rock masses. Bull Eng Geol Environ 81:112.

Kuzu C (2008) The importance of site-specific characters in prediction models for blast-induced ground vibrations. Soil Dyn Earthq Eng 28(5):405-414. https://doi.org/10.1016/j.soildyn.2007.06.008

Li Q, Rybak J (2023) Predictive modelling of blast-induced ground vibrations using empirical and artificial intelligence methods. Applied Sciences 13:2150. https://doi.org/10.3390/app13042150

Monjezi M, Ahmadi M, Sheikhan M, Bahrami A, Salimi AR (2010) Predicting blast-induced ground vibration using various types of neural networks. Soil Dyn Earthq Eng 30(11):1233-1236. https://doi.org/10.1016/j.soildyn.2010.05.005

Nicholls HR, Johnson CF, Duvall WI (1971) Blasting vibrations and their effects on structures. USBM Bulletin 656, United States Bureau of Mines.

Persson PA, Holmberg R, Lee J (1994) Rock blasting and explosives engineering. CRC Press, Boca Raton.

Roy PP (1993) Putting ground vibration predictors into practice. Colliery Guardian 241(1):63-67.

Sari M (2023) Precision timing and destructive wave interference in large-scale blasting. J S Afr Inst Min Metall 123(5):241-252.

Singh PK, Roy MP (2010) Damage to surface structures due to blast-induced ground vibration. Int J Rock Mech Min Sci 47(6):949-961. https://doi.org/10.1016/j.ijrmms.2010.06.010

Siskind DE, Stagg MS, Kopp JW, Dowding CH (1980) Structure response and damage produced by ground vibration from surface mine blasting. USBM Report of Investigations 8507, United States Bureau of Mines.

Torano J, Rodriguez R, Diego I, Rivas JM, Casal MD (2006) FEM models including randomness and its application to blasting vibrations. Comput Geotech 33(1):15-28. https://doi.org/10.1016/j.compgeo.2005.10.001

Wang Z, Zhang Y, Li H (2023) Quantifying seismic attenuation and Q-factor in fractured rock masses. Rock Mech Rock Eng 56:1145-1162.

Yang R, Scovira DS, Patterson NJ (1994) An integrated approach to blast vibration modelling. Fragblast 4:20-32.

Zhang X, Zhou J, Li X (2024) Machine-learning prediction of blast-induced ground vibration in complex geological settings. J Rock Mech Geotech Eng 16(1):88-102.

Zhang ZX (2016) Rock fracture and blasting: theory and applications. Elsevier, Amsterdam.

Zhao Y, Liu C, Wang G (2026) Real-time Q-factor estimation for adaptive blast vibration control. Min Metall Explor 43:12-25.

Integrated Drone-Based Stope Geometry Reconciliation and Stability Assessment at the Dannemora Mine

X. Gwynn[1], S. Wilson[1], M. Meyer[2], C. Carranza-Torres[3]
[1] *SLR Consulting, United Kingdom*
[2] *Grangex AB, Sweden*
3 University of Minnesota, Duluth Campus, USA
xgwynn@slrconsulting.com

Abstract

This paper describes an integrated approach that combines drone-based 3D stope surveys, updated geotechnical data, in-situ stress measurements and numerical modelling to assess stope geometry, stress concentrations and backfill performance at the Dannemora underground iron ore mine. An initial study established a mine-wide geotechnical model; empirical assessments indicated that many existing and planned stopes plot outside the nominally "stable" zone of published stability charts, despite generally favourable historical stope performance. This discrepancy motivated the development of a mine-scale FLAC3D model and acquisition of detailed drone-based 3D stope surveys to test the actual stability of the stopes and to verify backfill behaviour. The drone surveys demonstrate discrepancies between planned and achieved stope geometries, particularly in width and backfill surface elevation and confirm that tailings backfill occupies a substantial portion of the existing voids with little evidence of large-scale caving. These geometries were used to refine the numerical model and check consistency between modelled behaviour and observed stope performance.The integrated dataset shows that, although empirical methods place many stope walls outside nominal stability envelopes, numerical modelling and drone-based reconciliation indicate generally stable behaviour when supported by high rock mass quality, systematic backfilling and appropriate sequencing. The paper outlines implications for stope design and sequencing and how drone surveys can be integrated to provide ongoing stability verification and design refinement.

Keywords

Dannemora Mine, Stope stability, Drone photogrammetry, Backfill, Numerical modelling.

1 Introduction

Dannemora Mine in southern Sweden has operated intermittently since at least 1481 and most recently between 2012 and 2015, with existing stopes extending from surface to ~450 depth and remaining mineralisation modelled and explored to ~750m. The future operation will use open stoping with systematic backfilling in steeply dipping, relatively narrow iron orebodies at depth within a high-quality but stressed rock mass. Figure 1 shows the existing and planned stopes. The analyses form part of a feasibility study update focused on the Botenhäll–Norrnäs and Konstäng mining areas, where existing open stopes, tailings backfill and critical infrastructure interact. Study assessments showed that several planned stopes, including those in the deeper Schaktmalmen, Svea and Diamanten 2 orebodies, do not plot within the empirically "stable" region of commonly used stability charts (Potvin, 1988; Clark and Pakalnis, 1997; Capes and Milne, 2008), even though existing stopes at the

site with similar or larger spans have remained stable. This prompted a more detailed, site-specific stability evaluation. Geotechnical behaviour is critical because, in all but one orebody (Diamanten 2), mining is beneath existing infrastructure in a brownfield footprint where in-situ stresses approach historical levels, and high extraction ratiosand large hydraulic radii raise the potential for dilution, local instabilities and stress-driven pillar damage (Clark and Pakalnis, 1997; Capes and Milne, 2008), with direct implications for safety and project economics. Empirical stability databases (Potvin, 1988; Clark and Pakalnis, 1997; Capes and Milne, 2008) contain relatively few cases combining large hydraulic radii, very good rock mass quality and systematic backfilling, as at Dannemora, and the initial design relied on converted RMR–Q relations and regional stress compilations with limited local verification. Existing stope and backfill geometries in Botenhäll, Norrnäs and Konstäng were only approximately known from conventional survey, limiting model calibration. To address these gaps, the 2024 study combined updated geotechnical logging and laboratory testing, LVDT-based overcoring stress measurements (Stress Measurement Company Oy, 2023) and drone-based 3D photogrammetric stope surveys (AMKVO, 2023) with the mine-scale FLAC3D (Itasca, 2019) model developed during the study.

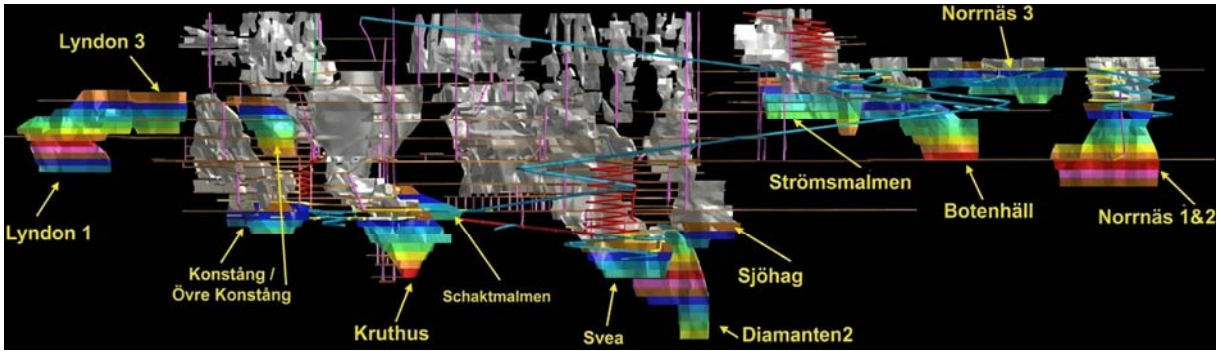


Fig. 1 Long profile view of the Dannemora mine, looking West (grey = existing stopes, multi-colour = planned stopes).

2 Background

2.1 Study Context

The updated rock mechanics assessment defined geotechnical domains and rock mass quality using historical RMR logging, mapping and new logging and testing (Bieniawski, 1973; Barton et al., 1974; NGI, 2015; Schlofeldt and Carter, 2018). Weighted mean RMR89 values generally fall in the "good" to "very good" range, with derived Q values indicating conditions favourable for large open stopes; re-logging and mapping show generally high RQD, with only thinner zones of reduced quality near mapped weakness zones and contacts. On this basis, the rock mass is modelled as a continuum in the mine-scale FLAC3D analyses, while recognising that jointing controls local overbreak and small-scale instabilities. Empirical assessment using the modified Stability Graph and related tools showed many planned and existing stope walls plotting outside the nominally stable region (e.g. Potvin, 1988; Clark and Pakalnis, 1997), suggesting a higher probability of instability than observed in practice at Dannemora. The empirical charts were therefore treated as conservative screening tools rather than hard design limits. A mine-scale FLAC3D model was developed to assess stope and pillar performance and interactions in the Kruthus–Konstäng–Upper Konstäng–Schaktmalmen area, where critical pillars and infrastructure coincide. The main existing stope geometries and qualitative performance classes are summarised conceptually in Table 1.

Table 1. Summary of existing Dannemora stopes (orebody, approximate dimensions, qualitative stability).

Orebody	Max. height (m)	Max. width (m)	Strike length (m)	Performance
Botenhäll	~75	~40	~94	Stable
Diamanten	~243	~60	~241	Stable
Källarmalmen	~196	~64	~189	Stable
Konstäng	~242	~120	~239	Stable; minor local hangingwall failures
Kruthus	~267	~109	~159	Stable
Norrnäs 1 & 2	~105	~36	~168	Stable
Sjöhag	~474	~48	~152	Stable
Strömsmalmen	~170	~39	~302	Stable
Svea	~333	~78	~213	Stable

The study highlighted limitations in the historical geotechnical database, including reliance on converted RMR–Q relationships, sparse large-scale structural data and coarse representation of as-mined stope and backfill geometries. Because many existing stopes plot outside the empirical "stable" zone yet have performed well, additional geotechnical logging, stress measurements and drone surveys were undertaken in Botenhäll, Norrnäs and Konstäng to provide a stronger basis for numerical modelling. This discrepancy led to a programme of additional geotechnical logging and testing, LVDT-based overcoring stress measurements and drone-based 3D surveys of key existing stopes and backfill in Botenhäll, Norrnäs and Konstäng. The resulting dataset provides a stronger basis for numerical modelling and checking whether the apparent empirical "over-span" at Dannemora is consistent with actual stress–strength conditions and observed behaviour.

3 Geotechnical Data and Methods

3.1 Geotechnical inputs overview

The updated dataset combines historical and new geotechnical logging, mapping and laboratory testing to characterise rock mass and intact properties in each orebody and domain. Re-logging using RMR89, Barton's Q-system and GSI corrected biases in historical RMR datasets and provided consistent rock mass inputs for numerical modelling; converted Q values were checked against directly logged Q and found to be consistent, supporting continued use of corrected RMR as the primary classification. Laboratory testing from 2021–2024 campaigns comprised UCS (with deformation), multistage triaxial compression, Brazilian tensile and direct shear tests on ore and waste, with rigorous validation. The combined dataset confirms high intact strengths across most orebodies and broadly appropriate design values. In-situ stresses were characterised using LVDT-based overcoring at levels L145 and L251, and inverse modelling yields stress gradients consistent with regional Fennoscandian data (Stephansson et al., 1986), which have been adopted in the numerical modelling.

3.2 Numerical modelling framework

Stope and pillar stability are evaluated primarily using a mine-scale FLAC3D model that includes all planned and existing stopes and key infrastructure, with refined zoning around Kruthus, Konstäng, Upper Konstäng, Lyndon 1, Lyndon 3 and Schaktmalmen. Because existing open and backfilled stopes, and multiple orebodies interact over large lateral and vertical extents, a single mine-scale model was adopted to capture stress changes, confinement and pillar load sharing, before moving to more detailed orebody-scale analyses. The model employs a Mohr-Coulomb constitutive law fitted to Hoek–Brown rock mass envelopes derived from updated intact strength and GSI (Hoek *et al*., 2002) and represents backfill as an elastic material with moderate stiffness. Mining is simulated in stages following the planned extraction sequence; outputs include plasticity zones and strength–stress ratios around stopes, pillars and infrastructure. Empirical stability charts were used to flag stopes outside nominal stable regions and to identify walls and ore bodies requiring closer scrutiny (Potvin, 1988; Clark and Pakalnis, 1997; Capes and Milne, 2008). In the present work, they provide context for why the detailed FLAC3D analyses and drone surveys were undertaken, namely, to test whether nominally "over-spanned" stopes are in fact stable. In a subsequent phase, local ore body-scale discontinuum models will be developed for selected areas to examine joint-controlled mechanisms and support performance where the mine-scale continuum model stresses are a large proportion of the rock mass or pillar strength.

4 Drone-Based 3D Photogrammetric Stope Survey

4.1 Data acquisition, processing and registration

Drone-based close-range photogrammetry was used to capture high-resolution 3D geometries of selected existing stopes at Botenhäll, Norrnäs and Konstäng. Overlapping image sets from safe vantage points in stopes and connecting drifts were processed using a standard photogrammetric workflow and registered to the mine survey grid, producing dense point clouds and meshes for comparison with historic stope wireframes. For Botenhäll and Norrnäs, cross-sections through stope wireframes and survey meshes show the correspondence between modelled extents, mined voids and backfill surfaces, while at Konstäng, 3D views illustrate the relationship between existing stope voids, fill meshes and planned Upper Konstäng stopes (Fig. 2). These reconciled geometries were used to refine the geotechnical block model and the FLAC3D mesh in the focus area, replacing idealised shapes.

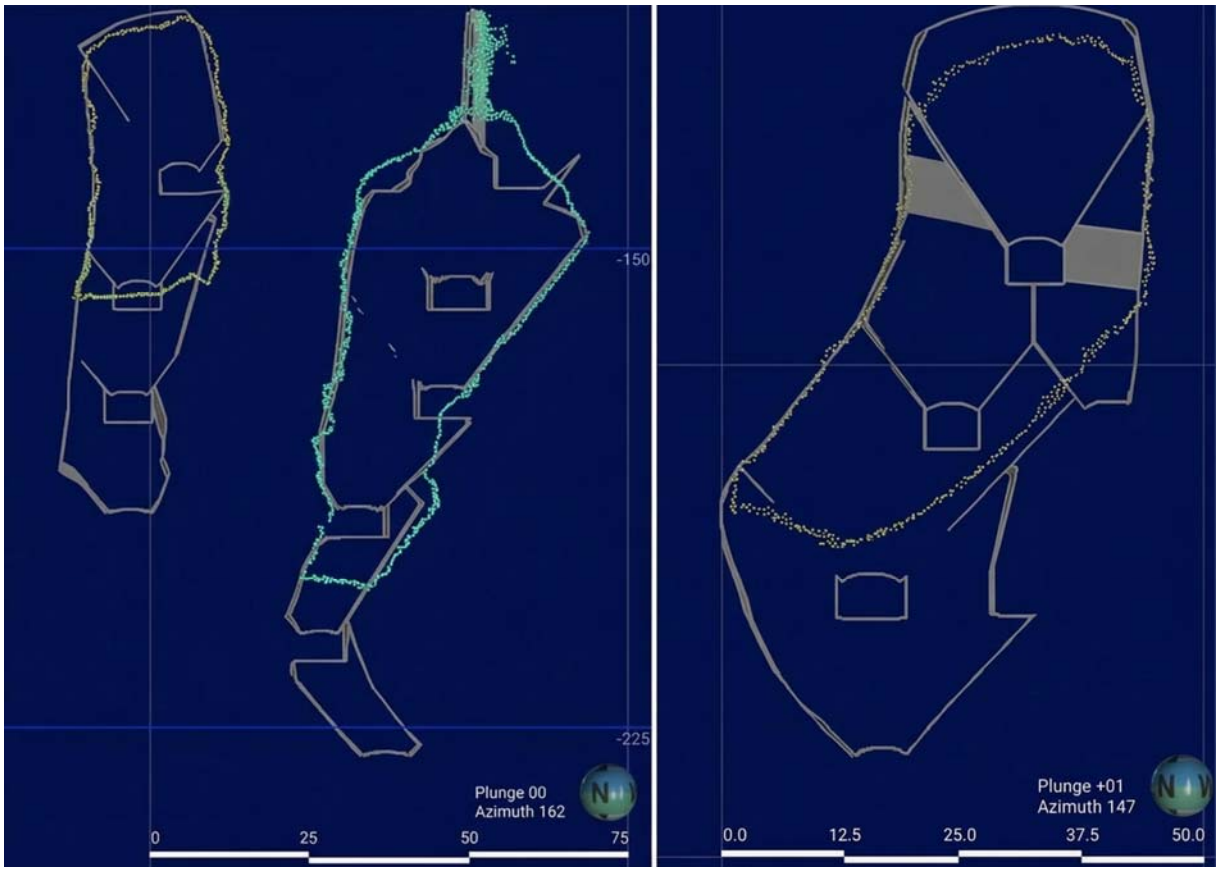


Fig. 2 Cross section through the existing stope wireframes (grey) and recent stope surveys for Norrnäs 1 &2 – Left Image (cyan and dark green) and Botenhäll – Right Image (olive green). The base of the survey point is where the ore bodies have been backfilled.

5 Results: Stope Geometry Reconciliation

5.1 Overbreak, underbreak and geometry differences

In the Botenhäll–Norrnäs area, cross-sections comparing historicalstope wireframes with drone-derived meshes showno evidence of large-scale caving or major backfill collapse.At Konstäng, reconciled stope voids show a poor correlation with the historical stope wireframe, with the surveyed hangingwall located higher than previously interpreted and the overall void significantly larger than depicted in the legacy model (Fig. 3). Tailings placed between 2012 and 2015 infill most of the existing stope, encroaching into the orebody now referred to as Upper Konstäng. The dominant interpretation is that a larger volume of material was mined from Konstäng than indicated by the historical wireframes, and that the current void size primarily reflects production rather than post-mining caving. This is supported by the 2015 tailings surface: the 3D point cloud shows mostly fine-grained tailings and only a few blocks above this horizon, implying the void geometry has been essentially unchanged since backfilling ceased. The lower Konstäng orebody appears to have been undercut and has likely been of approximately its current size since 1982, consistent with historical records of mining of a Konstäng “pillar” down to level −350 m using 37 tonnes of explosives (SSAB, 1982). These findings confirm that both the lower Konstäng and part of Upper Konstäng have long-standing, larger-than-recorded voids, and the updated FLAC3D model therefore incorporates the drone-derived void and fill geometries to better represent actual stress paths and boundary conditions for the critical Konstäng–Upper Konstäng–Kruthus pillar system.

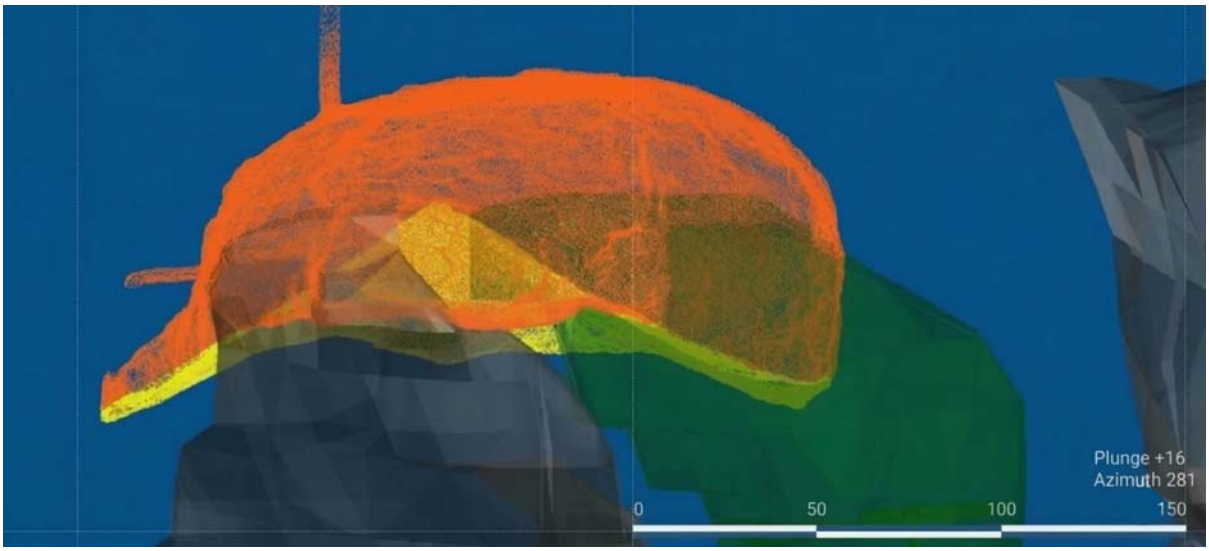


Fig. 3 Example drone-derived stope geometry at Konstäng, showing existing orebody wireframe (grey), surveyed stope void (orange), tailings fill (yellow) and planned Upper Konstäng stopes (green) in mine coordinates.

The surveys delineate backfill extents and surfaces, especially in the Konstäng stopes, where separate meshes for void and fill show that tailings backfill occupies a substantial proportion of the existing stope volume. Backfill surfaces are relatively smooth and gently sloping at stope scale, with no evidence of large, detached blocks or major caving structures, suggesting that long-term behaviour has been dominated by the intact rock mass and stress field rather than progressive backfill collapse, and that blocks observed on the backfill surface most likely detached during drilling or production blasting, rather than reflecting inherent stope instability. In Botenhäll and Norrnäs, the base of the surveyed voids defines the backfill elevations in the examined stopes and constrains fill thicknesses. These observations support representing backfill as an elastic medium in the numerical model and confirm that systematic backfilling has underpinned the favourable stability record of stopes that appear "over-spanned" when judged solely against generic empirical charts.

6 Numerical Stability Assessment with Reconciled Geometries

The mine-scale FLAC3D model, updated to incorporate drone-derived void and backfill, shows inelastic zones confined to a ~2 mshell around excavation boundaries of nominal 40 m diameter and no large-scale failure zones inconsistent with observed stope conditions. Strength–stress ratio plots indicate that critical pillars, including the pillar between Konstäng, Upper Konstäng and Kruthus, show elevated utilisation during Upper Konstäng extraction but retain acceptable factors of safety under the proposed sequencing and backfill strategy. The numerical model provides a direct test of the apparent contradiction between empirical chart positions and observed performance: stopes and pillars outside nominal stability envelopes can be stable when site-specific rock mass properties, in-situ stresses, detailed geometries and presence of backfill are accounted for explicitly. The drone surveys are critical in this respect, as they ensure that modelled spans, stope contacts and backfill extents reflect actual, rather than idealised, conditions. Backfill plays a central role in both the numerical interpretation and the reconciled field evidence: existing stopes marginal on a purely empirical basis have remained intact when systematically backfilled, and model simulations show that backfill reduces stress concentrations. Sensitivity analysis confirms that removing backfill significantly increases plasticity and reduces strength–stress ratios in some pillars, whereas reasonable variations in assumed backfill stiffness do not materially alter qualitative stability conclusions.

7 Discussion

The combined empirical, drone and numerical work at Dannemora shows that reliance on stability charts alone would lead to an unduly conservative view of stope stability, because many existing and planned stopes fall outside the nominal "stable" zone despite demonstrably good performance. Empirical tools are therefore best used as a first-pass screen to identify stopes requiring detailed analysis, not as strict design limits. Numerical modelling constrained by reconciled geometries and updated geotechnical inputs provides a more appropriate basis for assessing stope and pillar stability at Dannemora, particularly in the Kruthus–Konstäng–Schaktmalmen area where extraction is closely

coupled to critical infrastructure. The updated FLAC3D model shows that plasticity is confined to limited zones around excavations and strength–stress ratios in key pillars and infrastructure remain acceptable. The drone surveys are central, confirming that existing "over-spanned" stopes have remained stable and provide the actual void and backfill shapes against which model outputs can be judged. Operationally, integrating drone surveys into mine planning provides an efficient means of monitoring stope geometries and backfill performance, and feeding reconciled data back into numerical assessments to support ongoing stability verification and design.

8 Conclusions

An integrated geotechnical assessment has been developed for the Dannemora underground iron ore mine, combining updated rock mass and intact strength datasets, in-situ stress measurements, drone-based 3D stope surveys and mine-scale FLAC3D modelling. Empirical stability charts indicate that many existing and planned stopes plot outside nominal generic stability limits, but reconciled geometries and numerical modelling show that these stopes and pillars are stable under the site-specific conditions present at Dannemora when supported by systematic backfilling and appropriate sequencing. Drone-derived geometries constrain as-mined stope and backfill shapes, and the updated FLAC3D model indicates generally stable stopes, pillars and critical infrastructure under the proposed mine plan. These findings support the planned stoping strategy and highlight the importance of combining empirical screening with drone-based reconciliation and numerical modelling; integrating these tools into the Ground Control Management Plan will enable ongoing stability verification and effective risk management over the life of mine.

9 References

AMKVO AB (2023) Underground LiDAR and drone inspection services. Uppsala.

Barton, N., Lien, R. and Lunde, J. (1974) 'Engineering classification of rock masses for the design of tunnel support', Rock Mechanics, 6, pp. 189–236.

Bieniawski, Z.T. (1973) 'Engineering classification of jointed rock masses', Transactions of the South African Institution of Civil Engineers, 15, pp. 335–344.

Capes, G. and Milne, D. (2008) 'A compilation of dilution graph data for open stope hangingwall design', in Potvin, Y. et al. (eds) First Southern Hemisphere International Rock Mechanics Symposium. Perth: Australian Centre for Geomechanics.

Clark, L.M. and Pakalnis, R. (1997) 'An empirical approach for estimating unplanned dilution from open stope hangingwalls and footwalls', CIM Bulletin, 90, pp. 57–61.

Holmgren, J. (2015) Induced seismicity in the Dannemora Mine, Sweden. MSc thesis. Uppsala: Uppsala University.

Hoek, E., Carranza-Torres, C. and Corkum, B. (2002) 'Hoek–Brown failure criterion – 2002 edition', in Proceedings of the 5th North American Rock Mechanics Symposium. Toronto: University of Toronto, pp. 267–273.

Itasca Consulting Group (2019) FLAC3D: Fast Lagrangian Analysis of Continua in 3 Dimensions. Version 7.0. Minneapolis, MN: Itasca Consulting Group Inc.

NGI (Norwegian Geotechnical Institute) (2015) Using the Q-System: Rock Mass Classification and Support Design. Oslo: NGI.

Potvin, Y. (1988) Empirical open stope design in Canada. PhD thesis. Vancouver: University of British Columbia.

Schlofeldt, P. and Carter, T.G. (2018) 'Improved estimation of GSI and rock mass strength using volumetric fracture intensity', International Journal of Rock Mechanics and Mining Sciences, 110, pp. 48–67.

SSAB (1982) Mining of Dannemora Mine, Sweden: SSAB.

Stephansson, O., Søråkk, P. and Myrvang, A. (1986) 'State of stress in Fennoscandia', in International Symposium on Rock Stress. Stockholm.

Stress Measurement Company Oy (2023) In-situ stress measurements at Dannemora Iron Mine. Report for Grängesberg Exploration Holding AB.

Vattenfall Power Consultant AB (2009) Rock mass characterisation in the Dannemora Iron Ore Mine. Report for Dannemora Mineral AB.

Sustainability in Rockfall Protection Works: State-of-the-Art and LCA-Based Approaches

L. Turbessi, I. Bianco, G. A. Blengini, AM. Ferrero, G. Umili
University of Turin, Turin, Italy
laura.turbessi@unito.it
0009-0006-6257-970X

Abstract

Starting from the early 2000s, the concept of sustainability has been progressively integrated into the design of civil works, through the reuse of excavation and demolition materials, the reduction of non-renewable resource consumption, the mitigation of landscape impacts, and the improvement of structural durability. Considering the high environmental impact of the construction sector - both in terms of natural resource and energy consumption and in the large volumes of waste generated - it is necessary to orient design practices toward sustainability. Geotechnical engineering can make a significant contribution to sustainable development by promoting environmentally friendly and economically viable solutions.
Despite the widespread research on rockfall, it shows a limited correlation between sustainability and rockfall protection structures. Existing studies mainly focus on block trajectory analysis, fragmentation effects or risk assessment, but they don't systematically address environmental aspects of these structures. At present, no comprehensive environmental evaluations have been conducted to consider the full life cycle of rockfall protection works and to compare alternative design solutions from a sustainability perspective. The only available data come from Environmental Product Declarations (EPD) voluntarily published by some of the leading manufacturers in the sector. In contrast, other areas of geomechanics - such as tunneling - already benefit from a regulatory framework that integrates sustainability criteria throughout project phases.
This paper aims to provide a comprehensive overview of the current state of the art concerning sustainability in rockfall protection works, analyzing existing practices and regulatory guidelines. The analysis seeks to identify the main knowledge gaps and to lay the groundwork for future research focused on environmental assessment and the application of Life Cycle Assessment (LCA) methodologies. The ultimate goal is to develop a sustainable design framework for rockfall protection structures, capable of combining environmental responsibility with the high safety standards required for this type of intervention.

Keywords

Sustainability, Rockfall protection structures, Life Cycle Assessment, Environmental impact.

1 Introduction

1.1 The development of the concept of sustainability

The concept of sustainability emergedin the context of the first international reflections on the environmental impact of human activities. In 1972, the United Nations Conference on the Human Environment, represented the first major global summit dedicated to environmental issues. On that occasion, 113 nations adopted an action plan comprising 109 recommendations and a Declaration containing principles concerning human responsibilities toward the environment (United Nations 1973). This marked the official entrance of environmental concerns into the global political agenda.However, it was the United Nations' Brundtland Commission (Brundtland 1987), that in 1987 released the report "Our Common Future", in which the concept of sustainable development was formally articulated for the first time as:*"Development that meets the needs of the present without compromising the ability of future generations to meet their own needs"*. In the following years, efforts intensified to translate the concept of sustainability,into concrete and actionable plans.

The 1992 United Nations Conference on Environment and Development, held in Rio de Janeiro, consolidated the concept of sustainable development on a global scale. One of the oucomes was the well known Agenda 21 which states:*"Each local authority should enter a dialogue with its citizens, local organizations, and private enterprises and adopt a local Agenda 21 of its own Through consultation and consensus-building, local authorities should learn from and draw on the knowledge of local communities and the private sector to formulate the best strategies"*(United Nations 1992).

Following the Rio de Janeiro Conference, since the early 2000s, sustainability has evolved from a political principle into an operational and technical framework. In this context, the LCAmethodology was developed to monitor and control not only carbon dioxide emissions arising from industrial processes, but also the consumption of raw materials and the energy required for production. This approach enables the systematic and scientifically grounded quantification of the environmental impacts associated with the entire life cycle of a product or structure. The quantification of these parameters has been a crucial step, as it has increased awareness of the environmental impacts associated with production processes and pavedthe way for the development of mitigation strategies. The application of the LCA methodology is now regulated by international standards - UNI EN ISO 14040 and UNI EN ISO 14044 (2006)- which define the principles, requirements, and operational guidelines for conducting such assessments.

The 2030 Agenda for Sustainable Development (United Nations 2015), signed on 25 September 2015 by the Member States of the United Nations, established 17 Goals that today serve as the global reference framework for sustainable development. Among these Goals, Goal 9: '*Develop quality, reliable, sustainable and resilient infrastructure*' plays an overarching role by promoting quality, reliable, sustainable, and resilient infrastructures.

1.2 Sustainability applications in Engineering and Geotechnics

In the field of geomechanics, sustainability generally translates into the reuse of excavated and demolition materials, the reduction of energy consumption, the minimization of ecological impacts, and the design for long-term durability. For instance, in the tunnelling sector, both European and Italian regulations have progressively integrated sustainability criteria throughout all stages of the project life cycle which include the reuse of excavation materials as by-products, comprehensive environmental monitoring, improvements in energy efficiency, and the application of LCA methodologies.

Despite the extensive study of rockfall phenomena in the literature, the aspect of sustainability has not yet been sufficiently addressed in the design of mitigation works. No specific regulations or standards currently address the application of sustainability criteria to rockfall protection structures, either at the European or Italian level. A systematic review of the internationalresearch database confirms this regulatory and scientific gap. Available studies mainly focus on specific technical aspects such as volume and shape quantification of unstable rock masses, risk assessment methodologies, block trajectory modeling or fragmentation effects (Fell et al., 2008; Volkwein et al. 2011; Stavropoulou 2014; Umili et al. 2023, 2024). However, no studies have been identified that apply environmental evaluations to rockfall protection systemsor that attempt to integrate environmental impact quantification with mechanical and design parameters such as energy dissipation capacity, material usage, or structural performance. This gap underscores the need for dedicated studies aimed at developing a sustainable design framework for rockfall protection structures that can balance safety requirements with environmental responsibility. It also represents a significant limitation in a context wherethe achievement of climate neutrality objectives requires the integration of CO_2 emissions

assessments into planning and design processes. The common practice of oversizing protective structures, due to rockfall uncertainty, leads to an unnecessary increase in carbon footprint. Therefore, this approach must be re-evaluated through the lens of sustainability, while still ensuring compliance with the highest safety standards. Companies operating in this sector are showing an increasing awareness of and commitment to sustainability objectives. Leading European manufacturers such as Officine Maccaferri s.p.a., Geobrugg and Trumer Schutzbauten GmbH have published Environmental Product Declarations on a voluntary basis, providing verified data on the environmental performance of their products in accordance with the LCA methodology. These initiatives contribute to enhancing transparency and comparability within the construction sector, supporting the transition towards a circular economy in line with European sustainability policies.
The aim of this paper is to lay the groundwork for future research on environmental assessment, integrating sustainability considerations into all phases of the life cycle of rockfall protection structures.

2 Methodologies

2.1 Some guidelines to assess the sustainability of a rockfall protection project

Assessing the environmental impact of rockfall protection projects requires considering both rockfall dynamics and the production of protective systems. To achieve this, it is necessary to explore a series of key aspects that represent the foundation of the analysis and guide its development:

1) Dimensional optimization of protection works to avoid oversizing and reduce consumption of steel and concrete: Accurate estimation of block volumes is the starting point for reducing the environmental impact associated with rockfalls avoiding oversizing.
2) High-resolution geomorphological analysis to identify potentially unstable areas and preferential propagation paths: A detailed geomorphological analysis enables the identification of preferential block paths, thereby minimizing the need for extensive or unnecessary protective measures (Agliardiand Crosta 2003; Leine et al. 2021; Noël et al. 2023).
3) Barriers'planning based on the natural morphology of the slope, using depressions and ridges as natural elements to divert, slow down, or stop falling rock blocks:Utilizing existing slope features can reduce both the number and extent of required protection systems, thereby limiting landscape and environmental impacts.
4) Evaluation of design alternatives based on energy class, favoring nature-based solutions where feasible: Where possible, nature-based solutions are proposed, such as stabilizing vegetation (rockfallprotection forests), controlled slope re-profiling, and hybrid structures that integrate traditional systems with natural solutions (slope greening).
5) Minimizing earthworks and visual impact by using existing roads for site access during construction to limitlandscape disturbance and land consumption.
6) Selection of recyclable and low-impact materials with preference for locally sourced production.
7) Selective dismantling with recycling of metal components and reuse of structural parts: At the end of their lifecycle, rockfall protection structures become construction and demolition waste (CDW) that can be recovered within a circular economy framework.
8) Application of Life Cycle Assessment (LCA) principles: To quantify the actual reduction in environmental impact achieved through the application of the proposed guidelines for rockfall protection systems, it is essential to determine the carbon footprint of each design alternative and compare it with conventional approaches that do not systematically integrate sustainability into the decision-making process.

The proposed points show that reducing the environmental impact of these structures requires a comprehensive assessment beyond production-related emissions, covering all design phases.

2.2 Life Cycle Assessment of a rockfall protection barrier

While the present study considers multiple aspects of sustainability in rockfall protection, including design strategies, material selection, and end-of-life considerations, a Life Cycle Assessment (LCA) of a rockfall protection barrier is presented here as an illustrative example. This case study provides insights into the potential environmental impacts and demonstrates how the general principles outlined in this work can be applied in practice.The Life Cycle Assessment (LCA) of the product under

investigation was carried out using the SimaPro10.2 software environment, drawing on the Ecoinvent 3.11 and Industry Data 2.0 databases. The selected functional unit consists of a 3 × 10 m^2 module of a rockfall protection barrier with a maximum energy level of 2000 kJ, assembled from the following basic components (with dimensions and masses considered as generic reference values derived from the technical-scientific literature and not referring to any specific commercial product):

- Two H-shaped posts, 3 m in height. Total mass = 269 kg;
- Two base plates measuring 790 × 250 × 32 mm. Total mass = 98 kg;
- One 3 × 10 m^2 steel wire mesh with rope diameter of 9 mm. Total mass = 204 kg;
- Six retaining cables, each 6 m long and 22 mm in diameter. Total mass = 90 kg;
- Two longitudinal cables supporting the mesh, each 10 m long and 22 mm in diameter; Total mass = 50 kg
- 36 stainless steel shackles (spaced at intervals of 0.7 m). Total mass = 5.4 kg

With the exception of the stainless steel shackles, all other components of the analysed barrier are made of galvanized steel. In particular, the posts and plates were manufactured using a hot-dip galvanization process in pieces, while the mesh was produced using a galvanization process in coils. The LCA was conducted following a cradle-to-grave approach, as it also accounts for the end-of-life phase of the product. For this specific case study, the environmental assessment of the structure was limited to the Global Warming Potential (GWP) indicator, which quantifies the impact in terms of kg CO_2 eq. All data used in the analysis are secondary data, obtained from established databases and technical literature. The simulation was performed assuming a representative European context; therefore, European energy mixes and realistic transportation distances were considered. In particular, a transport distance of 300 km by Euro 5 heavy-duty lorry was assumed for all transport stages.In the conducted life cycle assessment, the assembly and disassembly phases of the rockfall protection structure are not considered, as their environmental impact is considered negligible compared to the other life cycle stages, and are therefore excluded from the system boundaries. Fig. 1 presents the flow diagram of the production processes and transportation stages involved in the manufacturing of the investigated rockfall protection barrier.

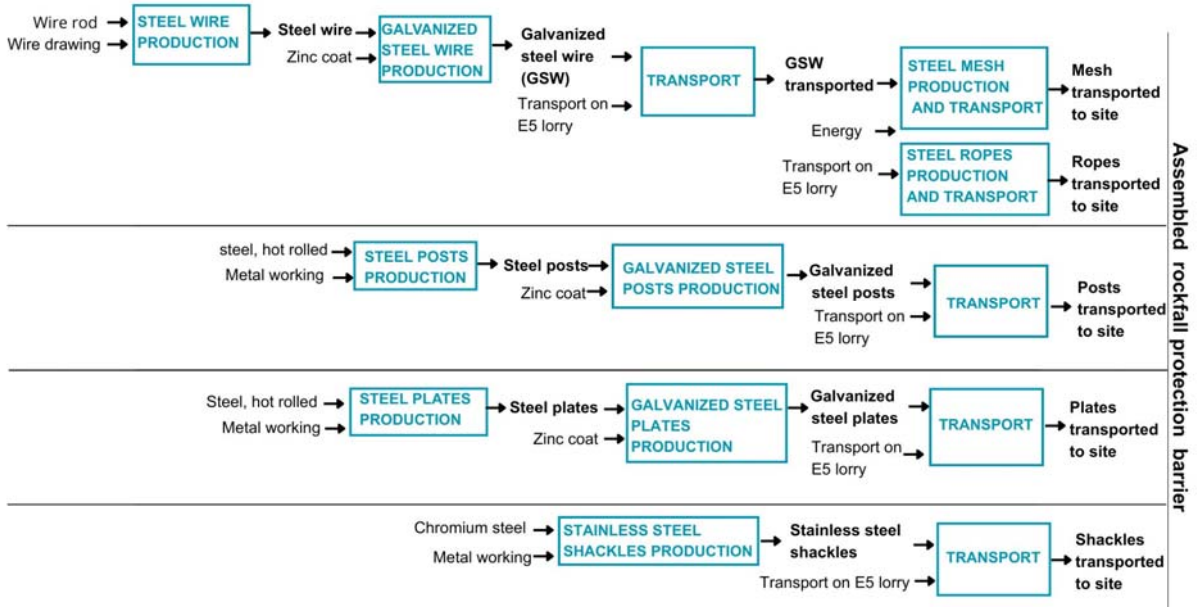


Fig. 1 Flow diagram of the production processes and transportation stages involved in the manufacturing of the investigated rockfall protection barrier.

Once the product was assembled, its end-of-life was modelled through a scenario assuming that the posts and base plates were not damaged during service and could therefore be reused, while the remaining components were recycled. For the recycling treatment, a transport distance of 100 km by Euro 5 heavy-duty lorry was assumed. This distance was estimated as the transportation required to deliver the end-of-life components to recycling facilities.

The ReCiPe 2016 Midpoint (H) method was employed to quantify the impact on climate change indicator associated with the life cycle of the investigated rockfall protection barrier. Rockfall protection structures and their associated components exhibit a highly variable service life, as it depends on the occurrence and frequency of rockfall events.

For this study, two consecutive life cycles of the same structure were modeled. In the first life cycle, all posts and plates are assumed to be reused and therefore enter a second life cycle. At the end of the second life cycle, these components are sent to a recycling facility together with the remaining components of the barrier. As a result, when considering the two life cycles as a whole, an overall reuse rate of 50% is assumed for posts and plates.

3 Results

The life cycle model indicates that the CO_2 eq. emissions associated with the production of the rockfall protection barrier amount to 2.6×10^3 kg CO_2 eq. The majority of these emissions are attributable to the production of the steel from which the structure is entirely composed. Consequently, the implementation of an appropriate end-of-life treatment is crucial for mitigating the overall environmental impact of such structures. Indeed, the end-of-life scenario results in a substantial reduction of total CO_2 emissions, lowering the impact to approximately 1.19×10^3 kg CO_2 eq. (Fig. 2).

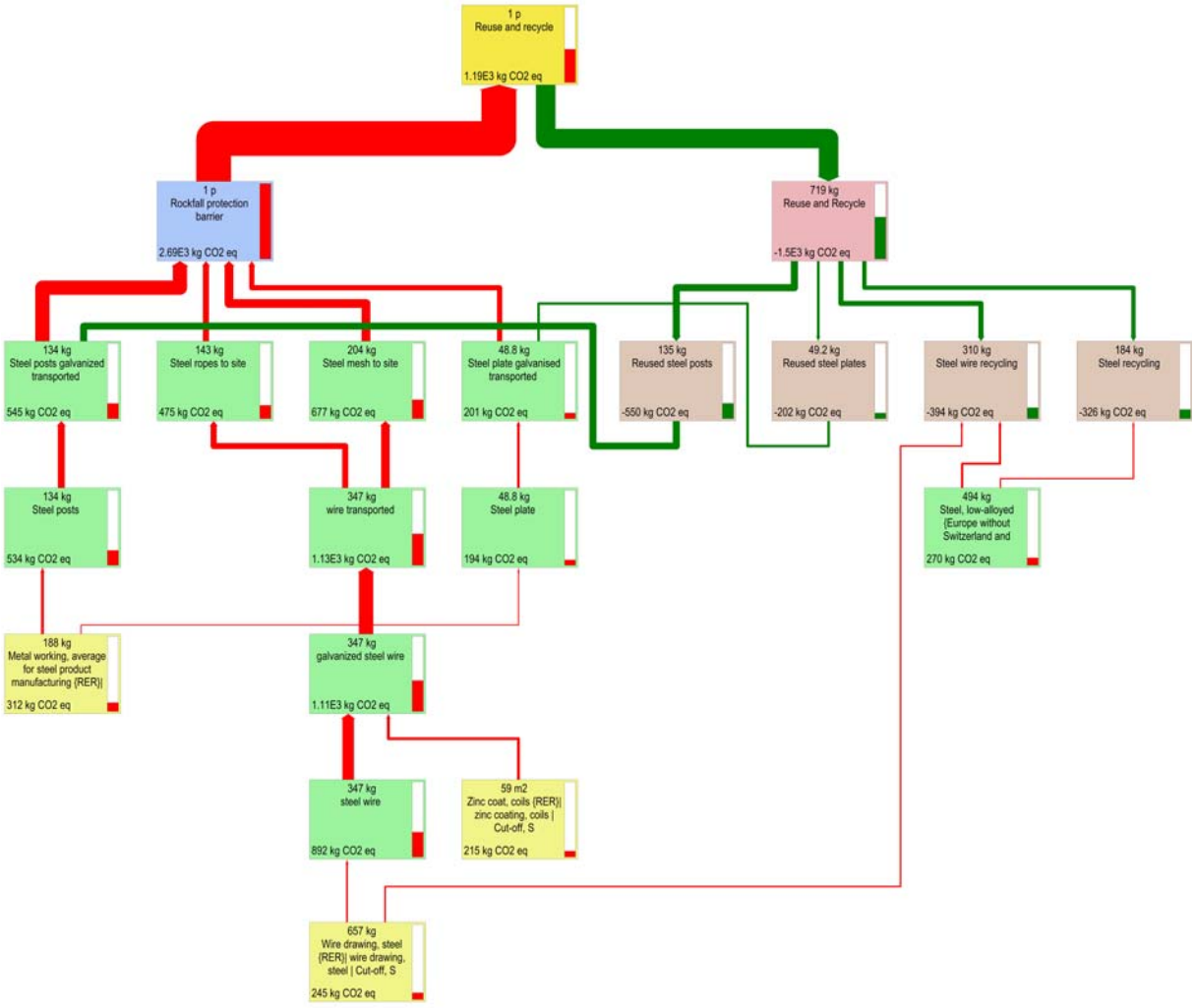


Fig. 2 SimaPro flow diagram of the life cycle of the investigated rockfall protection barrier, including production, transport, and end-of-life processes, with CO_2 emissions quantified in kg CO_2 eq.

The results obtained were compared with the EPDs published by well-known European manufacturers, whose reported total GWP values range from approximately 0.60 to 1.30×10^3 kg CO_2 eq. It should be noted that the consulted EPDs are not always specific to 2000 kJ protection barriers, but generally refer to broader product ranges with energy absorption capacities up to 5000 kJ, which explains the observed variability in the reported results. The outcome of the present study, equal to 1.19×10^3 kg CO_2 eq.,falls well within this range, further supporting the validity of the obtained result.

4 Conclusions

This article provides an overview of the evolution of sustainability concepts in civil engineering and geomechanics from the 1970s to the present, highlighting a regulatory and research gap in the integration of sustainability principles into rockfall protection structures. Furthermore, the paper provides guidance for the integration of sustainability concepts within this sector, highlighting strategies for improving environmental performance in the design of rockfall protection structures. The case study presented here illustrates the application of an LCA to a rockfall protection barrier, demonstrating how CO_2 emissions can be quantified. A logical next step would be to extend the assessment to the structure as a whole, ideally applying LCA to a real case study in which key variables—such as material type, quantity and origin, service life, and end-of-life scenarios—can be evaluated and compared with the variables that ensure the structure has the required safety standards. Moreover, the analysis could be further expanded to include additional impact categories beyond climate change, such as abiotic resource depletion, acidification and ecotoxicity. It should be noted, however, that such barriers represent only one of several mitigation measures available in rockfall-prone areas, and the systematic assessment of their environmental footprint is crucial for understanding and ultimately reducing their impact.

Acknowledgments

This research has been supported by the Italian Ministry of University and Research under PRIN 2022 grant RaRiskD "Rapid landslide risk mitigation: design for sustainability criteria in mountain areas" COD. 2022XLK7ZN

References

United Nations (1973) Action Plan for the Human Environment : programme development and priorities : report of the Executive Director. Stockholm. Available at: https://digitallibrary.un.org/record/508564?v=pdf

Brundtland, G.H. (1987) Our Common Future: Report of the World Commission on Environment and Development. Geneva, UN-DokumentA/42/427.Available at: https://sustainabledevelopment.un.org/content/documents/5987our-common-future.pdf

United Nations (1992) Agenda 21. United Nations Conference on Environment&Development. UN, Rio de Janeiro.Available at :https://www.un.org/esa/dsd/agenda21/Agenda%2021.pdf

ISO (2006) ISO 14040:2006 Environmental management - Life cycle assessment - Principles and framework. Geneva: ISO.

ISO (2006) ISO 14044:2006 Environmental management - Life cycleassessment - Requirements and guidelines. Geneva: ISO.

United Nations(2015). Transforming our world: the 2030 Agenda for Sustainable Development. Resolution adopted by the General Assembly on 25 September 2015 (A/RES/70/1). Available at: https://sdgs.un.org/2030agenda

Fell R., Corominas J., Bonnard C., Cascini L., Leroi E., and Savage W (2008). Guidelines for landslide susceptibility, hazard and risk zoning for land use planning, Eng. Geol. 102, 85–98. https://doi.org/10.1016/J.ENGGEO.2008.03.014

Volkwein A., Schellenberg K., Labiouse V., Agliardi F., Berger F., Bourrier F., Dorren L. K. A., Gerber W. And Jaboyedoff M (2011). Rockfall characterization and structural protection – a review, Nat. Hazards Earth Syst. Sci., 11, 2617–2651, https://doi.org/10.5194/nhess-11-2617-2011.

Stavropoulou M. (2014) Discontinuity frequency and block volume distribution in rock masses. Int. J. Rock Mech. Min. Sci. 65, 62e74. DOI: 10.1016/j.ijrmms.2013.11.003

Umili G., Taboni B., Ferrero A.M (2023). Influence of uncertainties: A focus on block volume and shape assessment for rockfall analysis. Journal of Rock Mechanics and Geotechnical Engineering, 15 (9), 2250-2263. https://doi.org/10.1016/j.jrmge.2023.03.016

Umili G., Carriero M.T., Taboni B., Migliazza M.R., Ferrero A.M.(2024).A New Analytical Solution for Calculating Rock Block Volume. Rock Mechanics and Rock Engineering 57, 3109–3120.https://doi.org/10.1007/s00603-023-03728-y

Agliardi F. and Crosta G.B. (2003) High resolution three-dimensional numerical modelling of rockfalls, International Journal of Rock Mechanics and Mining Sciences,Volume 40, Issue 4, Pages 455-471, ISSN 1365-1609, https://doi.org/10.1016/S1365-1609(03)00021-2.

Leine R.I., Capobianco G., Bartelt P., Christen M. and Caviezel A (2021). Stability of rigid body motion through an extended intermediate axis theorem: application to rockfall simulation. Multibody Syst Dyn 52:431–455. https://doi.org/10.1007/s11044-021-09792-y

Noël F., Nordang S.F., Jaboyedoff M. et al (2023). Highly energetic rockfalls: back analysis of the 2015 event from the Mel de la Niva, Switzerland. Landslides 20, 1561–1582. https://doi.org/10.1007/s10346-023-02054-2.

A new design method for load estimation in yielding tunnel linings

L. Batocchioni & E. Turrini
Sapienza University of Rome, Rome, Italy
lorenzo.batocchioni@uniroma1.it
0000-0003-0706-0826

C. Pandolfi
Polytechnic University of Turin, Turin, Italy

S. Miliziano
Geotechnical Design Group, Rome, Italy

Abstract

Designing yielding tunnel linings in squeezing ground requires an accurate evaluation of axial loads and bending moments from ground–lining interaction. While numerical modeling is computationally heavy and the Convergence-Confinement Method fails to capture internal force evolution, this study proposes a simplified analytical design method providing reliable first-order estimates to complement advanced tools. Based on charts derived from parametric analytical formulations, the method quantifies both the friction-induced axial load increment and the maximum bending moment caused by non-uniform stresses. This physically consistent approach ensures rapid, efficient screening across diverse ground conditions and lining configurations.

Keywords

Design methods, Tunnel lining, Yielding principle, Elasto-plastic elements, Analytical approaches.

1 Introduction

The growing demand for large underground infrastructure emphasizes the need to better understand ground-lining interaction (*GLI*) in deep tunnels, particularly under squeezing conditions (Barla 2001; Hoek 2001). In these cases, the yielding principle (*YP*) (Kovàri 1998) is the most effective design strategy. Implementing the *YP* typically involves adding Elasto-Plastic Elements (*EPEs*) to the temporary lining, allowing controlled circumferential deformation and stress relief through relative ground-lining movements. As projects become more complex, fast and reliable predictive tools are needed to estimate lining forces during preliminary design and to support numerical analyses.

In this context, developing methods to assess internal forces on tunnel support under the specific *GLI* of a yielding temporary lining is essential. When *EPEs* enter the yielding stage, the axial load is limited by the *EPEs*' yielding capacity and remains bounded, unlike in the rigid lining case. However, this comes with a significant bending moment (M_{EPE}), resulting from the support's heterogeneity and the localized concentration of ground normal stresses (σ_n) around the *EPEs*. Furthermore, shear stresses at the ground–lining interface, caused by friction during relative movements, partially increase axial load (ΔN_τ) while reducing the bending moment.

To overcome the limitations of the overly simplified Convergence–Confinement Method (Panet 1995) without relying on complex numerical analyses (Barla et al. 2011; Moritz 2011; Tian et al. 2016; Yang et al. 2023 and Batocchioni et al. 2024), which still require first-approximation input values, intermediate methodologies are needed. Radončić et al. (2009) proposed a semi-analytical formulation to estimate the axial load increment ΔN_τ; however, no method is currently available to evaluate the associated bending moment M_{EPE}. Batocchioni et al. (2026) introduced two semi-analytical approaches to assess (1) the bending moment arising from lining heterogeneities (M_{EPE}) and (2) the axial force increment induced by tangential stresses at the ground–lining interface (ΔN_τ). In the present paper, these methods are reformulated with a more practical focus, leading to two design abaci as the main outcome. Data from two well-documented case histories are finally presented for illustration.

2 Methodology

The proposed design method is based on a simplified analytical framework aimed at capturing the primary mechanics of ground–lining interaction in yielding supports. The formulation conceptualizes the lining as an assembly of rigid structural segments separated by deformable insert elements. The lining heterogeneity caused by the weak *EPEs* embedded in the rigid structural parts makes the *GLI* much more complex, as illustrated in the interaction diagrams in Fig. 1.

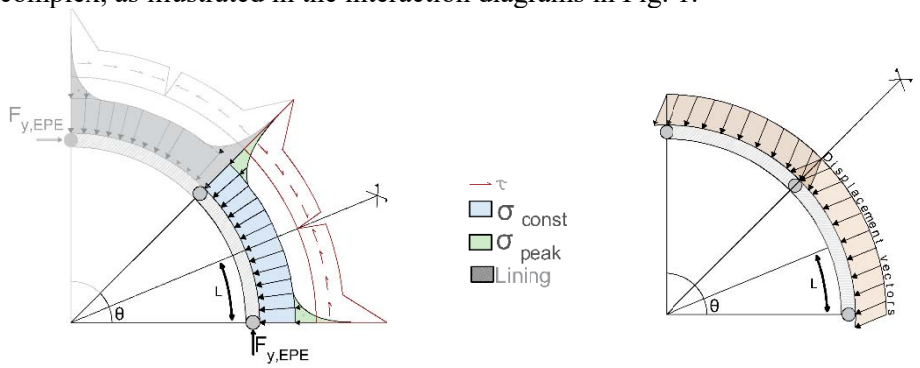


Fig. 1 Diagram of the ground–lining interaction: (left) loads from the ground (normal and shear stresses at the ground–lining interface) and (right) lining displacement vectors. The ground displacement vectors— not explicitly shown—are always radial; therefore, away from the midpoint, relative displacements at the interface are expected (see the shear stress direction).

The analysis focuses on the midpoint between two consecutive *EPEs* and on the adjacent boundaries. Stress concentration near the *EPEs* induces a bending moment at the midpoint (M_{EPE}), while ground–lining relative displacements generate shear stresses that oppose *EPE* closure and produce an axial load increment peaking at the midpoint (ΔN_τ). The proposed approach therefore evaluates internal forces at this critical section-the midpoint between two consecutive *EPEs*-for preliminary structural verification.The following semi-analytical procedures have been developed and validated via sensitivity analyses in (Batocchioni et al. 2026). Here for brevity, only the essential aspects will be reported.

A brief remark is required on the interface friction angle, a key parameter in *GLI* despite its limited physical meaning, as it condenses the complex interaction between steel sets, concrete shell, and ground into a single number. Its use is nevertheless standard in tunnelling and is therefore adopted here. For M_{EPE}, the effect of the interface shear stress (τ) is explicitly considered with a subtractive term, whereas for $\Delta N_\tau$the interface friction angle represents the governing input parameter.

$$M_{EPE} = M_{peak} - M_y = c_r F_y R(\theta sin\theta + cos\,\theta\ - 1) \tag{1}$$

The two semi-analytical equations obtained in Batocchioni et al. (2026) are:

Where c_r fraction of σ_n concentration near the *EPEs*, conservatively value equal to 0.2
F_y *EPEs* yield force
R tunnel radius
θ half of the angle between two consecutive *EPEs* (Fig. 1)

$$\Delta N_\tau = \int_0^{l/2} \tau \, dl = \frac{\mu F_y}{2} \frac{l}{R} \tag{2}$$

Where $\mu = tan(\varphi_{int}) = tan(\varphi - 10)$ interface friction coefficient
$l = \theta R$ half of arc length between two consecutive *EPEs* (Fig. 1) assuming $\sigma_n = const$

Eq. 1 is obtained by subtracting the bending moment induced by the concentrated normal stress at the rigid beam boundaries (M_{peak}, in Fig. 1 the green σ_{peak} are considered as a point load) from the opposing bending moment associated with *EPEs* yielding (M_y, caused by $F_{y,EPE}$). For the design abaci, Eq. 1 is then reformulated to homogenize the expressions. The angular coordinate θ is expressed in terms of the ratio between l and R, and the dependence on the soil friction angle ϕ is explicitly introduced by subtracting from M_{EPE} a second contribution due to interface shear stresses M_τ. Eq. 1, assuming $\sigma_n = const$ (in the new term) and $c_r = 0.2$, thus becomes:

$$M_{EPE} = M_{peak} - M_y - M_\tau = 0.2F_yR\left(\frac{l}{R}sin\frac{l}{R} + cos\frac{l}{R} - 1\right) - \mu F_yR\left(\frac{l}{R} - sin\frac{l}{R}\right) \tag{3}$$

Finally, Eq. 2 and Eq. 3 are used to construct the two design abaci, illustrated through selected tunnel sections from two well-known case histories: the Lyon-Turin Euralpin Tunnel (TELT, Bonini and Barla, 2012) and the Terzo Valicodei Giovi project (Batocchioni 2025).

3 Results

Fig. 2 presents the design abacus for the bending moment M_{EPE} as a function of the soil friction angle ϕ and the ratio l/R, which is conceptually equivalent to half of the angle between two consecutive *EPEs*. The values are generally conservative, as demonstrated in Batocchioni et al. (2026).

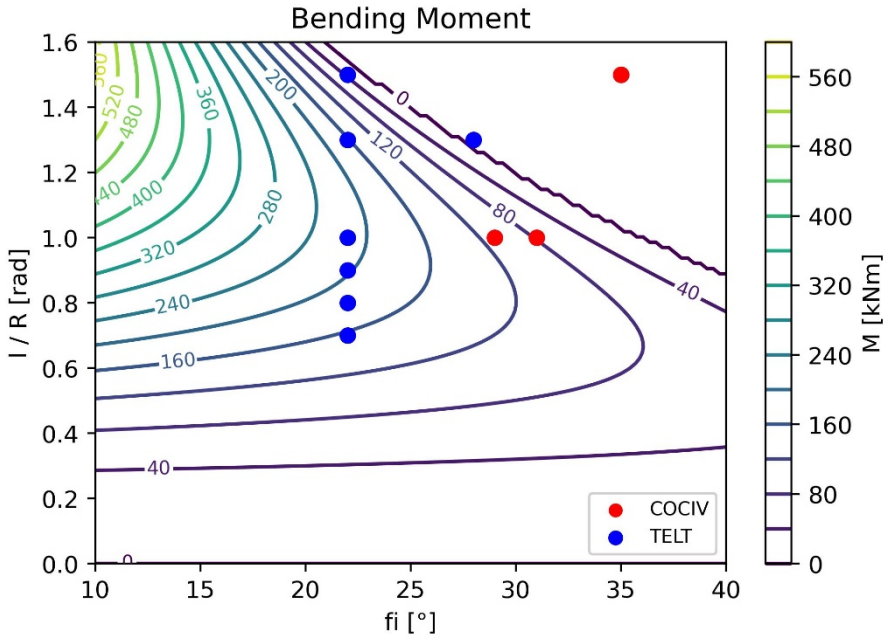


Fig. 2 Abacus for M_{EPE} in the ϕ–l/R domain. The values obtained are generally conservativeexceeding the actual value.

The abacus incorporates the frictional effect through the contribution of interface shear stresses. Neglecting this effect—and thus the subtractive term in Eq. 3—would result in M_{EPE} increasing mostly monotonically with l/R. Conversely, including this opposite contribution introduces a non-monotonic trend. While M_{EPE} generally grows with l/R due to wider *EPEs* spacing, an increase in both l/R and

ϕ simultaneously amplifies the two terms. At high values of l/R and ϕ, this reduction counteracts the growth of the bending moment. Consequently, the highest values of M_{EPE} are reached when large l/R is combined with low ϕ.

The case histories show that, particularly for the TELT project, the expected bending moment can be significant (up to 200 kNm), mainly due to the extensive use of highly spaced EPEs embedded in the lining with a not so frictional ground. Conversely, the points associated with the COCIV project fall in less critical regions of the abacus. Nevertheless, this indicates that, especially in cases such as TELT, simplified approaches should be complemented by more advanced analyses, such as numerical modelling, in order to more accurately assess the magnitude of the bending moment. In practice, when critical bending is anticipated, mitigation strategies involve optimizing the *EPEs* layout by reducing the spacing between consecutive elements-l. This adjustment also enhances the capacity to support ground loads. However, as the margin for further spacing reduction is typically narrow, a rigorous preliminary selection of the *EPEs* arrangement becomes essential.

The second abacus, shown in Fig. 3, presents the design abacus for the normalized axial load increment $\Delta N_\tau/F_y$ in the same ϕ –l/R plane adopted above. Unlike the bending moment, the axial increment increases monotonically with both ϕ and l/R. For a fixed ϕ, larger l/R ratios correspond to longer interaction lengths over which tangential stresses can accumulate, leading to higher axial force increments. Conversely, for a given ll/R, increasing ϕ enhances the shear transfer capacity at the soil–lining interface, resulting in a greater contribution of ΔN_τ. As shown in the abacus, low friction angles combined with short interaction lengths lead to negligible axial increments, whereas higher ϕ values acting over extended lining segments may generate normalized increments approaching 40%.

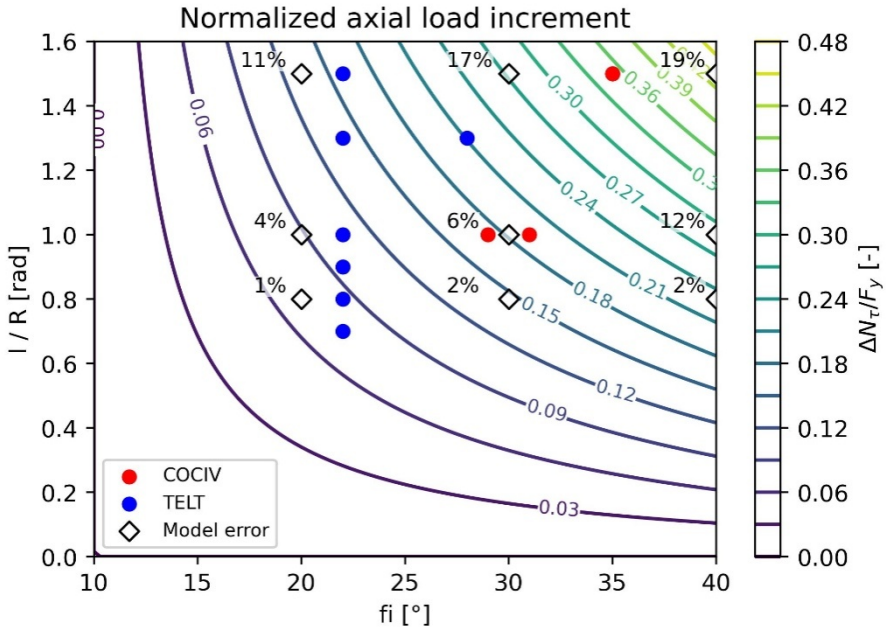


Fig. 3 Abacus for ΔN_τ in the ϕ–l/R domain. The axial load increment is presented as normalized with respect to the yielding resistance of the *EPEs* (F_y).

It should also be noted that the curves are derived using the simplified method proposed by Radončić et al. (2009), which generally underestimate the numerical results. For selected combinations of l/R and ϕ, numerical analyses (Batocchioni 2025) were therefore performed and compared with the analytical predictions to evaluate the corresponding percentage error. As shown in Fig. 3, the error increases with both l/R and ϕ. For the M_{EPE} abacus (Fig. 2), the error evaluation was not included since the simplified formulation was observed to generally overestimate the numerical results.

The case histories highlight distinct behaviours. For the TELT project, characterized by moderate ϕ and relatively high l/R values, the $\Delta N_\tau/F_y$ remains moderate (typically below 0.20), indicating a limited amplification of the structural axial force at yielding. In contrast, the COCIV cases, associated with higher ϕ and comparable l/R ratios, exhibit significantly higher $\Delta N_\tau/F_y$, in some instances exceeding 30% with a 19% of model error, reaching an overall increment values of about 50%.

These results have significant conceptual implications for preliminary design. At this stage, a yielding ratio r_y is typically defined as the ratio between the yielding resistance of the *EPEs* and the axial resistance of the lining. In practice, $r_y \approx 0.5$ is commonly adopted to ensure controlled activation of the *EPEs*. However, at the onset of *EPEs* yielding, the axial force in the lining is $F_y + \Delta N_\tau$, not simply F_y. Therefore, when $\Delta N_\tau / F_y$ assumes high values-such 50%, the axial demand transferred to the lining increases significantly, effectively reducing the admissible value of r_y and restricting the design space. In such cases, the axial increment may be mitigated by reducing the interaction length l (i.e., decreasing *EPEs* spacing) or a lower yielding resistance F_y may be selected for the EPEs, thus reducing the total axial force mobilized in the lining at the activation stage, at the cost of higher tunnel convergence or lining structural demand.

A combined reading of the abaci highlights a clear interaction between the two governing mechanisms. As shown in the "Structural Criticality Regions" map (Fig. 4), it indicates that low ϕproduce a bending-dominated response, while higher ϕ values shift the mechanism toward axial demand. Both actions increase with the l/R ratio: larger spacings between consecutive *EPEs* amplify bending and axial effects, whereas lower l/R values limit the structural demand. For l/R< 0.57, the structural demand remains limited. Conversely, for l/R> 0.57, good conditions are achieved only for specific ϕ. For simplicity, the boundaries of the critical areas are approximated by 3 linear equations.

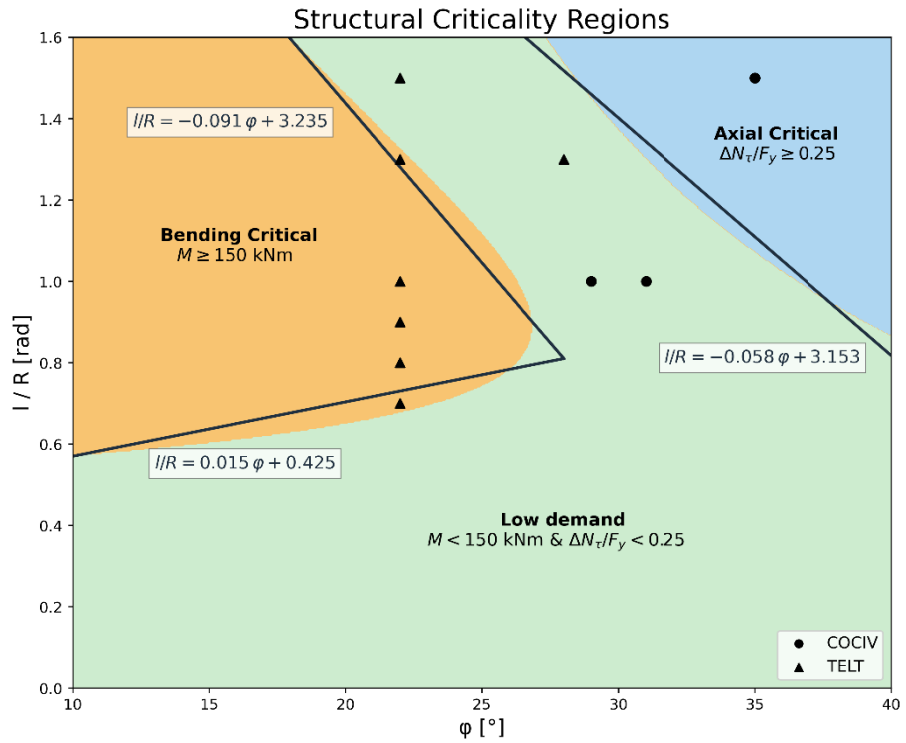


Fig. 4 Structural criticality map in the ϕ–l/R domain, showing bending-dominated, axial-dominated and low-demand regions defined by the adopted threshold. COCIV and TELT are superimposed to illustrate their position in the design space.

The resulting boundaries effectively summarize the application limits of the analytical method. This chart underscores how the optimization of *EPEs* spacing serves as a flexible design tool to safely navigate between bending- and axial-dominated structural risks before proceeding to advanced numerical modeling.

4 Conclusions

This study presents a simplified analytical approach for the preliminary assessment of internal forces in tunnel linings equipped with elasto-plastic elements. The method fills the gap between the Convergence-Confinement Method and numerical modeling by providing reliable first-order estimates of bending moments and normalized axial load increments.

Accordingly, two design abaci were developed to estimate: (i) the maximum bending moment induced by non-uniform ground stresses and (ii) the normalized axial load increment generated by interface shear transfer. The results highlight that while both axial forces and bending moments increase with wider elasto-plastic element spacing, axial demand is amplified by higher friction angles ($\phi > 30°$), whereas bending moments become more significant at lower values ($\phi < 20°$). These abaci serve as practical tools for preliminary design, providing a quick quantification of expected internal forces and a rational reference for subsequent numerical analyses.

Furthermore, a summary chart synthesizes these findings, identifying practical design ranges and the governing structural mechanisms. The analysis indicates that small elasto-plastic elements spacing ensures limited structural demand across all friction angles. Conversely, for larger spacings, acceptable conditions are restricted to intermediate friction angles, as extreme values (low or high) lead to bending- and axial-dominated responses, respectively.

Ultimately, elasto-plastic elements spacing emerges as the primary governing parameter for lining optimization-particularly since the soil friction angle is not a design parameter, but rather an inherent geotechnical property. The proposed method is not intended to replace detailed numerical modeling but to complement it. By providing physically consistent first-order estimates and insight into the governing mechanisms, it enhances design awareness and supports the development of robust lining solutions for tunnels in squeezing ground.

References

Barla G. (2001) Tunnelling under squeezing rock conditions. Rivista Italiana di Geotecnica 35 (4), 38–58.

Barla G., Bonini M., Semeraro M. (2011) Analysis of the behaviour of yield-control support system in squeezing rock. Tunnelling and Underground Space Technology 26 (1), 146–154.

Batocchioni L, González V, Miliziano S. (2024) The effect of a frictional interface in a preliminary yielding support for a deep tunnel. Tunnelling for a Better Life –Proceedings of the ITA-AITES World Tunnel Congress, WTC 2024, 918–931.

Batocchioni L. (2025) Numerical modeling of yielding linings in squeezing conditions. Phd Thesis, Sapienza University of Rome.

Batocchioni L., Turrini E., Pandolfi C., Miliziano S. (2026). An innovative predictive approach for axial force and bending moment estimation in elasto-plastic tunnel linings. Proceedings of CNRIG 2026, L'Aquila, Italy (in press).

Bonini M., Barla G. (2012) The Saint Martin La Porte access adit (Lyon–Turin Base Tunnel) revisited. Tunnelling and underground space technology, 30, 38-54.

Hoek E. (2001) Big tunnels in bad rock. Journal of Geotechnical and Geoenvironmental Engineering 127 (9), 726–740.

Kovàri K. (1998) Tunnelling in squeezing rock. Tunnel 98 (5), 12–31.

Moritz B. (2011) Yielding elements requirements, overview and comparison. Geomechanics and Tunnelling 4 (3), 221–236.

Panet M. (1995) Le calcul des tunnels par la methode convergence-confinement.

Radončić N., Shubert W., Moritz B. (2009) Ductile support design. Geomechanics and Tunnelling, 2(5), 561-577.

Tian H., Chen W., Yang D., Wu G., Tan X. (2016) Numerical analysis on the interaction of shotcrete liner with rock for yielding supports. Tunnelling and Under-ground Space Technology 54, 20–8.

Yang K., Yan Q., Shi Z., Zhang C., Ma S. (2023) Numerical study on the mechanical behavior of shotcrete lining with yielding support in large deformation tunnel. Rock Mechanics and Rock Engineering 56 (2), 1563–1584.

Applicability of the Stability Graph Method for Designing Large Caverns in Rock

C.Torrero, L. Jordá & S. Senent
Universidad Politécnica de Madrid, Madrid, Spain
c.torrero@alumnos.upm.es

Abstract

Rock engineering classification systems have traditionally been widely used in the preliminary design of tunnels, mines and underground caverns excavated in rock. These systems constitute standardized empirical approaches based on field data and accumulated experience, enabling rapid and practical assessment of rock mass conditions. In particular, design charts derived from these classifications — such as the Q-system or the RMR—are commonly applied to estimate the maximum unsupported span and support requirements. In the case of civil engineering caverns, these aspects are especially critical due to the large dimensions of such openings. The stability graph method, introduced by Mathews in 1980, integrates the strengths of the Q classification with the introduction of the hydraulic radius as the design shape factor and the implicit consideration of the critical joint and failure modes. However, the original method was developed for mining stopes under non-entry conditions and short design life spans. This paper examines the applicability of the stability graph method to civil engineering caverns. Aspects such as shape, construction procedure, rock mass conditions or support demands are analysed, evaluating their consistency with the original assumptions and design principles of the method. The shortcomings of the classical mining method applied to civil caverns are exposed such as the requirement for long-term stability in civil caverns versus the short exposure of mining stopes, the different support system typologies, roof geometry, or variations in stress conditions — particularly in shallow and isolated caverns. Despite these limitations, the stability graph method has proven to be a valuable complementary tool for the preliminary design of large-span underground openings.

Keywords

Underground space, Tunnelling, Rock mechanics, Rock engineering classifications.

1 Introduction

Since ancient times the underground space has been used for multiple purposes: transport, good storage, defence, etc. This involves excavating different openings in both soil and rock masses such as tunnels, shafts, or caverns. Hard rock conditions have allowed the excavation of large-section openings. This is the case, for instance, of the powerhouses in hydroelectric projects, railway and metro stations, or the case of the 62 m-span Olympic Ice Hockey Cavern in Gjøvik, Norway (Barton et al. 1994). Nowadays, the green energy sector also calls for the use of underground space inthe form of caverns, for example, for hydrogen storage. The early and feasibility phases of these projects demand preliminary and quick calculations to estimate the geometry of the caverns. Rock engineering classification systems —such as the Q-system (Barton 1974)or the RMR (Bieniawski 1973)—have traditionally been widely used for that purpose. In these preliminary projects, the available geotechnical information is limited, so there are no geomechanical data available to perform more sophisticated calculations. Then, during detail design phase, once the geotechnical investigation has been completed, detailed kinematic analysis and both 2D and 3D numerical models are conducted to analyse the stability of the caverns and to define the different support systems and their implementation along the construction sequence. However, before this, the robustness of the calculation tools in early studies is crucial to make conclusive decisions on the feasibility of these large section projects. Also, during construction, rock engineering classifications are also commonly used to accommodate the predefined excavation and support systems to the real geotechnical conditions encountered as the cavern construction process progresses. Beyond the underground excavations typical of civil and industrial engineering projects, certain mining methods likewise involve the excavation of large-section underground openings, such as the sublevel stoping method, where the ore can be mined by means of non-entry production open stopes. Due to the shape and dimensional similarities between these open stopes and civil engineering caverns, the stability graph method (Mathews, 1980) has occasionally been applied to cavern stability analysis. In this paper the applicability of this method to the preliminary design of caverns is studied, analysing both compatibilities and limitations.

2 The stability graph method

The stability graph method (Mathews et al. 1980; Potvin 1988), developed in Canada to estimate stable spans in sublevel stoping mining, consists of a chart (Fig. 1) in which stable, potentially stable and caving zones are defined. In this chart, the hydraulic radius –defined as the ratio of the exposed surface area to its perimeter and used as shape factor - is determined by introducing the stability number N (Eq. 1).

$$N = Q' \, A \, B \, C \tag{1}$$

Where Q' modified rock mass quality index Q (Barton 1974)
A stress factor (Mathews et al. 1980; Potvin 1988)
B rock defect orientation factor (Mathews et al. 1980; Potvin 1988)
C design surface orientation or gravity factor (Mathews et al. 1980; Potvin 1988)

The parameter Q′ is obtained from the rock mass quality index, assuming both the stress reduction factor (SRF) and the joint water reduction factor (J_w) are equal to 1. Sublevel stops are large openings created in competent rock, comparable in size and shape to caverns in civil engineering projects. Due to the geometrical similarities between both types of openings, some studies have applied the "mining" stability graph method to the stability analysis of permanent caverns, specifically underground hydrocarbon storage caverns (Winn et al. 2018; Xingdong et al. 2020).

3 Applicability of the stability graph method

This section examines the applicability of the stability graph method to the pre-design of civil engineering caverns, emphasizing the method's compatibilities and limitations when applied to this type of permanent opening.

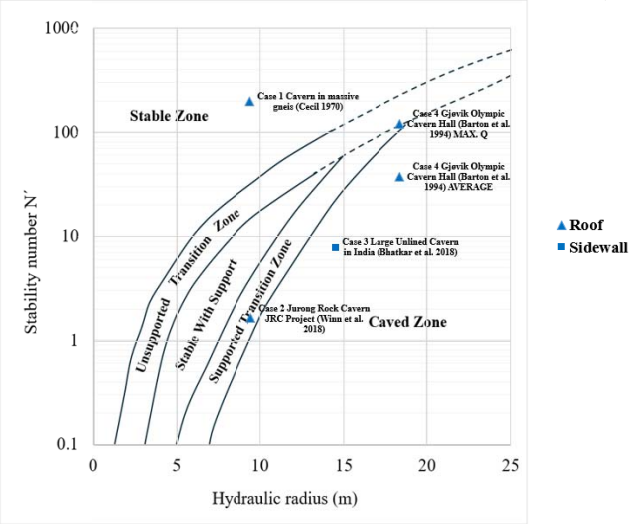


Fig. 1 Chart based on Nickson (1992). Case histories shown in chart are explained in section 3.3.

3.1 Compatibilities and advantages against tunnelling charts

3.1.1 Shape

Tunnel excavation exhibits an inherent three-dimensional stress–strain behaviour due to the tunnel face effect. However, in terms of geometry, due to tunnel width or span is often adopted as per operational criteria, the more relevant parameter to be defined depending on encountered ground conditions is the longitudinal maximum allowable unsupported span. Nevertheless, the caverns are larger section excavations, with significant height and limited length in comparison with a tunnel. Traditional tunnelling stability charts allow determining the maximum allowable cavern roof span or sidewall height. Although excavation and support installation are sequential processes, it is also important to analyse cavern stability as a whole, especially during preliminary design stages. In this context, the hydraulic radius accounts for the two dimensions of the cavern surfaces—roof, sidewalls, and face—in the same way open stopes are analysed when applying the stability graph method. Therefore, this method makes it possible to incorporate the 3D geometry of caverns into the stability analysis, in comparison with the classical geomechanical classifications traditionally used in tunnelling.

3.1.2 Stress environment

In the development of the stability graph method, the parameter SRF of the original rock mass quality index Q was replaced by the stress factor A, due to the SRF is based specifically on tunnelling case histories. This stress factor A, which ranges from 0.1 to 1, depends on the relation in between the induced compressive stress and the uniaxial compressive strength of the intact rock. Potvin highlights the differences between tunnelling and sublevel stoping, noting that in the case of this mining method, the rock mass may be pre-disturbed by adjacent stopes excavated earlier (Potvin 1988). This leads to stress concentrations in the intermediate pillars, in contrast to the virgin stresses generally assessed in tunnelling. However, in civil engineering caverns, it is common to excavate two or more caverns—two in the case of hydroelectric projects, or even more, as in oil storage cavern systems typical in Scandinavia. Additionally, the rock mass is also disturbed by access tunnels and galleries, mucking shafts, and other minor underground excavations around the cavern location. If factor A is assumed to be the inverse of the stress reduction factor (SRF) and corresponds to the inverse of the value ranges given by Barton (1974), it can be observed that for a strength-to-stress ratio greater than 5, the stability method approach aligns with the Q-system range (Fig.2). Conversely, for a strength-to-stress ratio lower than 5, the Q-system penalizes more the rock mass quality than the stability graph method, particularly in the case of the improved version by Potvin (Potvin 1988). The original graph (Mathews 1980) automatically considers failure when the strength-to-stress ratio is below 2. Potvin assumes a minimum A value of 0.1, based on highly stressed cases proven to be stable, although these were characterized by small dimensions. This assumption must be applied with caution in caverns, which are characterized by their large spans. Beyond the stress compatibility issues discussed in this section, limitations related to stress conditions may arise in isolated caverns under virgin stress states, in cases under lower strength-to-stress ratio or in shallow caverns located near the surface. The factor A has been analysed by Barton (Barton 2014), indicating that this factor could not account singular conditions such as shallow depths or faulting and brecciation. Also, despite the geometric similarities

between both openings, differences between caverns and mining stopes arise under singular stress environments. For example, this occurs when stope sidewall inclination is adapted to inclined ore body morphology, in outer stopes in which different rock mass strength conditions occur in between both sidewalls - ore versus host rock –and in secondary stopes which are flanked by previously filled primary stopes using paste backfill. Nevertheless, for most situations involving regular geometries and non-singular stress conditions, the rock stress factor A of the stability graph method can be reasonably applied to the cavern design scenario.

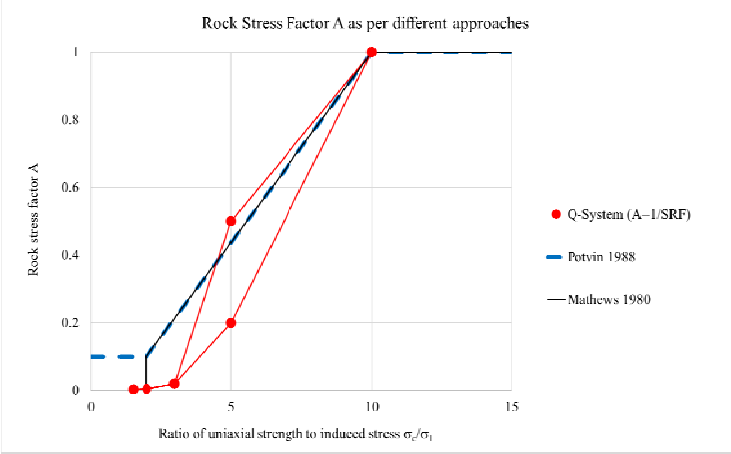


Fig. 2 Stability graph method factorA as per different approaches.

3.1.3 Anisotropy

The relative orientation between the cavern alignment and the joint systems is a critical aspect during the selection of the optimal position of the cavern. Inthe Ricobayo II project (Alonso and Jambrina 1999), the adopted criterium was to align the cavern with the bisector of the angle in between the two main joint system, ensuring that the cavern orientation is not parallel to the main joint directions. However, in tunnelling engineering classifications systems, rock mass anisotropy is not always explicitly implemented. Only the RMR system (Bieniawski 1973) introduces a correction factor that depends on the type of excavation and the relative orientation between the joint systems and the excavation. The stability graph method explicitly accounts for rock mass anisotropy in the design of underground openings by means of the B and the C factors (Potvin 1988). The B factor, which ranges from 0.2 to 1, depends on both the differences in dip and strike between the critical joint and the stope surface. Additionally, the C factor accounts the failure modes derived from the presence of joints and ranges from 2 to 8. Considering that these engineering classifications are widely used in feasibility studies and cost estimations, the stability graph method allows quantify the stability of a cavern more detailing that using the classical tunnelling systems.

3.2 Limitations

3.2.1 Groundwater

The parameter Jw is assumed equal to 1 due in stopes water inflow is negligible (Mathews et al. 1980; Potvin 1988). This could be explained because they are excavated in rock mass with very low primary permeability and the joints are closed at depth bellow 1000 m. However, in tunnelling, Jw may range from 0.1 to 1, depending on the water inflow rate and its evolution, as well as water pressure and associated phenomena such as joint filling outwash. In the particular case of caverns, desirable conditions are as much dry as possible. However, occasionally when excavating in fissured or weathered zones in competent rock masses, significant water inflows associated with higher permeabilities could occur (Geotechnical Engineering Office, 2018). Indeed, in the Honk Kong rock caverns registered up to 1989, Jw ranged from 0.7 to 1 was recorded (Barton 1989). The absence of Jw in the stability graph method has been highlighted (Barton 2014), indicating that the method could not be applied under conditions with Jw values lower than 1. As a conclusion, the fact that the stability graph method does not account the water effect in the stability number, the results in cases where significant water inflows could be expected would lead to optimistic results.

3.2.2 Roof shape

Generally, civil engineering cavern roofs are designed with an arched shape -the natural way to accommodate vertical stress redistribution - and to prevent rock blocks from falling from the

decompressed rock mass above the roof. The standard design usually adopts an arch height of 1/5 of the cavern span. Increasing arch height to improve stability and to reduce support requirements normally does not compensate the increase in excavation costs (Geotechnical Engineering Office, 2018). In open stoping, flat roofs are adopted to facilitate drilling and blasting operations and to prevent dilution, thereby reducing production costs. Moreover, the temporary nature of these openings does not require the stability standards demanded by a permanent cavern. In the case of roof shape, although there is a difference between mining stopes and caverns, the cavern roof surface may be assumed to be planar for the applicability of the stability graph method, resulting in a conservative estimate.

3.2.3 Support

When analysing a cavern using the stability graph method and the result falls within the "stability with support" zone, the support requirements should be evaluated according to the classical Q-system recommendations. This is because, in sublevel stoping mining, support is typically defined by the empirical cable bolt support design chart (Potvin and Milne, 1992), which—as its name suggests—only provides guidance on cable bolt density. Therefore, other support parameters such as bolt spacing and length, as well as shotcrete thickness, must be determined separately, if required.

3.2.4 Entry conditions, operative time and construction sequence

Differences between underground mining and tunnelling have been widely noted by various authors throughout history. The main difference lies in the supported exposure time – distinct from the unsupported exposure time defined the stand-up time concept (Lauffer 1958) - which is related to the distinct purposes of both types of excavations. The stability graph method has been calibrated based on data records on non-entry stopes opened during a relative short time, on the order of several months (Suorineni 2010), in comparison with the design life of civil engineering caverns (50 to 100 years and even >100 years in certain projects). While in stopes small size block falling is allowed, in caverns robust primary supports consisting of unreinforced or reinforced shotcrete and bolting are installed to prevent any size block or wedge falling. Also, is frequent to install a cast concrete secondary lining at the cavern roof. In the case of the Q-system, the parameter ESR - Excavation Support Ratio – accounts the minimum degree of safety and the importance level of an underground excavation allowing to adjust the required support demands and the maximum allowable span. However, this approach is generally regarded as too simplistic to adequately account for the differences that exist between mining applications and civil engineering tunnelling, as for example stated by Potvin 1988. Construction sequence also differs between caverns and stopes. Mining stopes are excavated by means of drilling and blasting from upper drifts, and the blasted ore is recovered from lower adits. In contrast, cavern excavation typically begins from a central gallery along the roof axis, which is then widened through additional galleries until the upper part is completed, while support is installed simultaneously. Afterwards, the cavern is completed vertically by means of successive benches, similar to open-pit blasting. Temporary mucking shafts may be opened to evacuate the muck from lower galleries. The main difference between both construction sequences is that, in the case of a cavern, excavation and support are performed sequentially. Consequently, the disturbance around the excavation—and therefore stress release—is lower than in the case of a stope.

Table 1. Case histories design parameters.

Case	Scenario	Surface	Span or height (m)	Length (m)	Hydraulic radius (m)	Q	Q´	A	B	C	N
1	Self-standing	Roof	20	300	9.4	100	250	0.4[(1)]	1	2	200
2	Supported	Roof	27	340	9.4	5	5	1	0.2	1.7	1.7
3	Collapse	Sidewall	30	840	14.5	10	20	1	0.2	4	8
4	Supported	Roof	62	90	18.4	1-30 (9.4)	1-30 (9.4)	1	1	4	38-120

(1) A value of A=1/SRF in which SRF=2.5 has been taken to account shallow conditions (18 m depth)

4 Example of application

In this section, four cases histories representing three different scenarios - stable without support, supported cavern and collapse - are depicted in the stability graph (Fig.1). Design parameters for each case are shown in Table 1. The grade of conservatism of the Q-system when applied to mining engineering was analysed by Barton (Barton 2014), plotting three self-supporting civil engineering

cases on the stability graph, showing that they were far from the unsupported transition zone, which demonstrates the higher level of conservatism adopted in civil engineering. However, as shown in Fig. 1, the stability method chart generally represents accurately the stability conditions for each case history, with the exception of the record span Gjøvik cavern, which falls within the zones delimited by dashed lines, intended to show uncertainty by its author (Nickson 1992).

5 Conclusions

Geometric similarities and the use the hydraulic radius provide a practical basis for overall stability assessment applying the stability graph method to caverns, offering advantages by explicitly considering rock mass anisotropy and the full geometry of the excavation. However, the approach has limitations, such as not accounting for groundwater effects, which can lead to optimistic results under permeable conditions. For cavern design, specific aspects must be addressed, including the common use of arched roofs for stress redistribution, reliance on the classical Q-system for support design, and careful consideration of the degree of conservatism. While the method is directly applicable to simple cases, more complex scenarios require additional considerations. Despite all these limitations, in cases of simple geometries, hard rock and high in-situ stress conditions, vertical sidewalls, systems of two or more caverns with intermediate pillars, and no water conditions, both types of openings are reasonably similar. Under these circumstances, the stability graph method can be applied to civil engineering caverns to obtain an overall approach to excavation stability conditions.

References

Barton N, By, TL, Chryssanthakis P, Tunbridge L, Kristiansen J, Løset F, Bhasin RK Westerdahl H, Vik, G (1994) Predicted and Measured Performance of the 62 m Span Norwegian Olympic Ice Hockey Cavern at Gjøvik. Int. J. Rock Mech. Min. Sci. &Geomech. Abstr. Vol. 31, No. 6, pp. 617–641.

Barton N, Lien R, Lunde J (1974) Engineering Classification of Rock Masses for the Design of Tunnel Support. Rock Mech (6): 189–236.

Bieniawski ZT (1973) Engineering Classification of Jointed Rock Masses. Civ. Eng. S. Afr. (15): 335–343.

Mathews KE, Hoek E, Wyllie DC, Stewart SBV (1980) Prediction of stable excavation spans formining at depths bellow 1000 m in hard rock. Canada Center for Mineral and Energy Technology. Golder Associates.

Potvin Y (1988) Empirical Open Stope Design in Canada. Dept. Mining and Mineral Processing, University of British Columbia, Canada.

Nickson SD (1992) Cable support guidelines for underground hard rock mine operations. University of British Columbia, Canada.

Winn K, Wong LNI, Alejano, LR (2018)Multi-approach stability analyses of large caverns excavated in low-angled bedded sedimentary rock masses in Singapore.

Xingdong Z, Lei D, Shujing, Z (2020) Stability analysis of underground water-sealed oil storage caverns in China： A case study.

Barton N (2014) Lessons learned using empirical methods applied in mining. 1st. Int. Conf. on Applied Empirical Methods in Mining. Lima, Peru. January 2014.

Geotechnical Engineering Office (2018) Guide to Cavern Engineering. Geoguide 4. Civil Engineering and Development Department. The Government of the Hong Kong. Special Administrative Region.

Barton N (1989) Cavern Design for Honk Kong rocks. Proceedings of the Seminar Rock Cavern, Honk Kong, December 1989.

Alonso A, Jambrina I (1999) Excavación de la caverna de cental del salto hidroeléctrico de Ricobayo II. Aspectos geotécnicos y constructivos. IngeoTúneles 2.

Potvin Y, Milne, D (1992) Empirical cable bolt support design. International Symposium on Rock Mechanics.

Lauffer H (1958) Gebirgsklassifizierung für den Stollenbau. Geologie und Bauwesen. 24 (1): 46–51.

Suorineni T (2010) The stability graph after three decades in use: Experiences and the way forward. Nazarbayev University.

Cecil OS, (1970)Correlations of Rock Bolt - Shotcrete Support and Rock Quality Parameters in Scandinavian Tunnels. Ph.D. Thesis, University of Illinois, Urbana, pp. 1-414.

Bhatkar T, Usmani A, Mandal A, Nanda, A (2018) Wedge failure analysis and remedial measures in large unlined rock cavern: a case study.

Numerical Modelling of Secant Caisson Shoring in High-Stress Shallow Bedrock

Hamzeh AhmadiResketi
AtkinsRéalis Canada Inc., Canada
hamzeh.ahmadiresketi@atkinsrealis.com

Abstract

Large circular shafts excavated into shallow bedrock under high and anisotropic in-situ stress conditions present design challenges that are not adequately captured by conventional earth-pressure-based approaches. In such environments, excavation response is governed by rock mass stress redistribution, stress-path dependence, deformation compatibility, and construction sequencing rather than gravity-driven loading alone.

In the stress regime considered herein, the in-situ stress state within bedrock is dominated by three principal components. The vertical stress component (σ_3) represents pre-existing tectonic and geological loading within the rock mass and is substantially greater than the stress arising from self-weight alone. The horizontal principal stresses (σ_1 and σ_2), oriented along orthogonal horizontal directions, are similarly elevated and anisotropic, resulting in a strongly stress-controlled excavation environment. This stress configuration leads to non-uniform load transfer and directional stress concentration around the shaft perimeter during excavation.

This paper presents a generalized and transferable workflow for the design of secant caisson shoring systems embedded in high-stress shallow bedrock. The methodology integrates staged three-dimensional finite-element ground–structure interaction modelling with sensitivity analysis and complementary rock stability screening. The numerical framework explicitly captures anisotropic in-situ stress conditions, staged soil and rock excavation, partial caisson penetration into bedrock, internal ring activation, and progressive engagement of shotcrete and passive rock anchors in the rock-socketed portion of the excavation.

Results demonstrate that interface stresses and rock mass response are highly non-uniform and directionally controlled by the in-situ stress field and excavation sequence, rather than by classical earth-pressure assumptions. Observed stress redistribution and stress-history effects highlight the importance of deformation-permissive support concepts that allow controlled stress release. Sensitivity analyses are used to bound uncertainty in rock mass properties and stress conditions, supporting a risk-informed, observational design approach applicable to other high-stress shallow bedrock shaft excavations.

Keywords

Numerical modeling, High-anisotropic in-situ stress, Secant caisson wall, Deformation-permissive support, Risk management, Observational approach.

1 Introduction

Large-diameter shafts excavated through overburden soils and into shallow bedrock are increasingly required for underground infrastructure. When excavation extends into bedrock under elevated, anisotropic horizontal in-situ stress, governing mechanisms differ fundamentally from those assumed in conventional earth-pressure-based shoring design. Excavation response becomes controlled by rock mass stress redistribution, deformation compatibility, and construction sequencing rather than by gravitational loading alone.

2 Ground conditions and design constraints

The workflow addresses shafts excavated through overburden soils into competent sedimentary bedrock where horizontal in-situ stresses are high relative to vertical stress. The soil–rock transition is critical because stiffness contrast and stress transfer mechanisms change rapidly with depth, and groundwater may be present in both soil and rock.

For the representative application informing this paper, the excavation comprises a large circular shaft supported by a continuous secant caisson wall socketed into shallow bedrock. Key geometric and construction features include: (i) staged excavation with activation of internal rings, (ii) excavation diameter reduction below the soil–rock interface to provide a rock ledge and shotcrete support, (iii) passive rock anchors below the caisson toe to manage stress release, and (iv) temporary surcharges and construction tolerances considered in design.

The authors were not involved in the original geotechnical exploration program or rock mass characterization; modelling inputs are based on interpreted parameters provided in project geotechnical documentation and are treated with explicit uncertainty through sensitivity analyses.

3 Shoring concept and rock mass design philosophy

The temporary support system consists of a circular secant caisson wall in soil with partial penetration into bedrock, supplemented by internal structural rings to control ovalization and mobilize hoop compression. Below the soil–rock interface, rock excavation is supported by shotcrete and passive anchors.The overall configuration and interaction between the wall, internal rings, and rock support elements are illustrated conceptually in Fig. 1.

A deformation-permissive concept is adopted in the rock portion: shotcrete provides the initial surface stabilization and limits rapid stress release, while passive anchors provide redundancy that engages progressively with increasing deformation. This approach aims to manage stress redistribution in high-stress rock while maintaining stability and limiting long-term load transfer to permanent works.

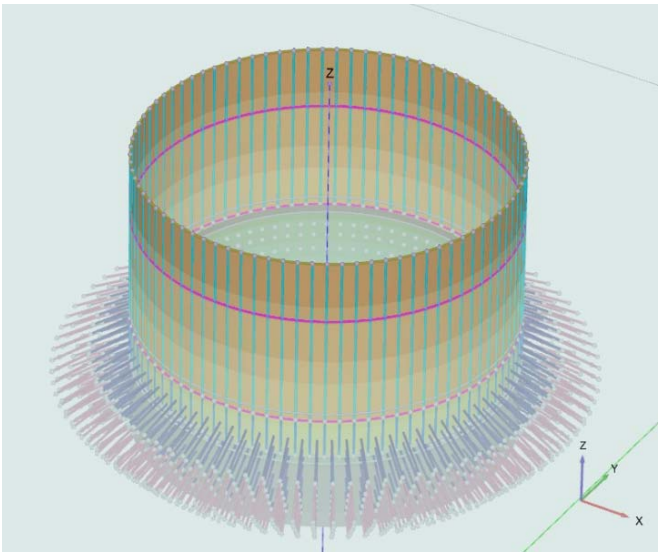


Fig. 1 Conceptual arrangement of the secant caisson wall system with internal rings and rock support elements.

4 Numerical modelling methodology

A three-dimensional finite-element ground–structure interaction model is implemented in PLAXIS 3D to capture stress-path dependence, anisotropic in-situ stress conditions, and the staged excavation and the support installation sequence. The numerical model explicitly represents the soil–rock stratigraphy, secant caisson wall, and supporting elements in three dimensions. Model extents are selected to minimize boundary effects, with local refinement applied in the vicinity of the shaft and the soil–rock transition. The overall model geometry and representative domain extents adopted for the analyses are shown in Fig. 2.

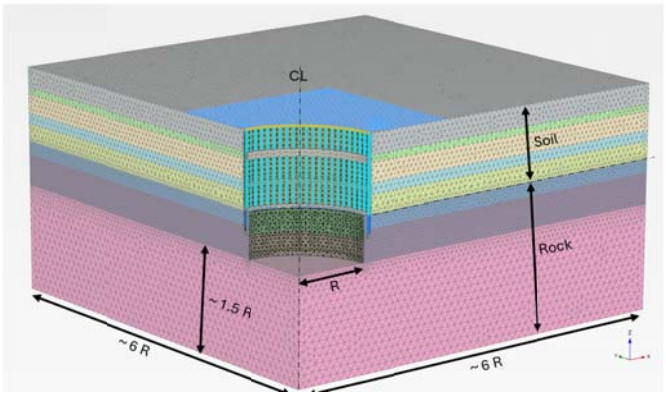


Fig. 2Numerical model geometry and domain extents used in the three-dimensional finite-element analysis.

4.1 Staging and structural representation

Construction is simulated through phases including stress initialization, caisson installation, staged excavation with ring activation, and rock excavation with activation of shotcrete and passive anchors. Structural components are represented using linear-elastic elements to extract deformations and internal forces for subsequent structural checks.

4.2 Constitutive models and parameterization

Soils are represented using a hardening soil model with small-strain stiffness to capture stiffness decay with strain and unloading/reloading response typical of excavation.

Bedrock behaviour is represented using the non-linear Hoek–Brown rock mass failure criterion to capture stress-dependent strength and deformation under elevated horizontal in-situ stress. For large-diameter shafts excavated into shallow bedrock, excavation response is governed primarily by stress redistribution and deformation compatibility rather than by discrete block detachment alone; a continuum representation is therefore appropriate for the numerical modelling scale adopted.

Rock mass parameters are derived from intact properties and GSI-based characterization reported by others and applied using standard Hoek–Brown relationships. Uncertainty associated with these inputs is addressed through sensitivity analysis. The Hoek–Brown continuum model is used to evaluate stress redistribution and deformation demand, while potential discontinuity-controlled mechanisms are addressed separately through complementary stability screening methods.

4.3 In-situ stress field, groundwater, and interfaces

High horizontal stress conditions are initialized as anisotropic principal stresses aligned with the dominant horizontal stress direction. Groundwater is represented using hydrostatic heads consistent with measured/anticipated groundwater levels in soil and bedrock. Concrete–ground interaction is represented using reduced-strength interface elements with gap-closure to avoid non-physical tensile separation.

4.4 Verification and numerical quality checks

Numerical verification checks were performed for both soil and rock components to ensure that predicted responses are governed by material behaviour and excavation sequencing rather than numerical artefacts. For soil, small-strain stiffness implementation was verified through appropriate unloading–reloading response and modulus-reduction behaviour consistent with laboratory observations.

For the rock mass, verification focused on numerical stability and realism of stress redistribution under high horizontal in-situ stress. Mesh density and element formulation near the shaft were assessed to confirm that tangential stress concentrations were not unduly influenced by discretization, and sensitivity checks showed that further mesh refinement did not materially alter stress distribution patterns around the excavation.

Rock deformation response was reviewed to ensure consistency with expected continuum behaviour under the Hoek–Brown representation, avoiding unrealistically brittle failure or excessive localization. Stress paths during staged excavation were examined to confirm that changes in confinement and tangential stress were driven by excavation sequencing and support activation rather than boundary effects or numerical imbalance. Stable equilibrium and convergence were achieved at all stages under anisotropic stress initialization.

These checks provide confidence that the model captures the dominant stress-controlled rock mass response relevant to excavation support behaviour, while recognizing that discontinuity-controlled mechanisms are addressed separately through stability screening.

5 Key modelling outputs and Sensitivity analysis

Sensitivity analyses are performed to bound uncertainty in rock mass stiffness/strength and in-situ stress magnitude and orientation. The analyses assume time-independent rock mass behaviour; time-dependent mechanisms such as creep or swelling are not explicitly modelled over the construction timeframe. However, based on available geotechnical data, creep and/or swelling are not expected to be significant and are unlikely to affect temporary shoring stability.

Key outputs used for design and risk management include: (i) lateral pressure distributions around the shaft, (ii) wall deformations and ovalization response with ring activation, and (iii) tangential stress distributions in bedrock for screening of stress-induced damage potential. These outputs are used to calibrate simplified structural models where required and to define monitoring targets for an observational approach.

Fig. 3 presents the distribution of interface normal stress plotted as a function of circumferential angle relative to the major principal in-situ stress direction. The pronounced directional variation reflects stress-path dependence and redistribution associated with staged excavation under anisotropic in-situ stress conditions, rather than uniform earth-pressure behaviour. The scatter in values at a given circumferential orientation reflects depth-dependent variations in normal stress along the rock–secant wall interface, with different symbols representing stresses extracted at different elevations; the resulting spread illustrates the stress history developed during staged excavation.

Radial deformation of the secant caisson wall extracted from the three-dimensional numerical model is used to support cross-checking of wall response against simplified structural modelling. Fig. 4 illustrates the circumferential distribution of radial deformation at the base of the secant caisson wall, demonstrating directionally dependent deformation consistent with the anisotropic in-situ stress field.

Tangential stress concentrations around the excavation, used for screening of stress-induced damage potential in shallow bedrock, are also shown separately in Fig. 5and are discussed in Section 6 (Stability Screening and Risk Controls).

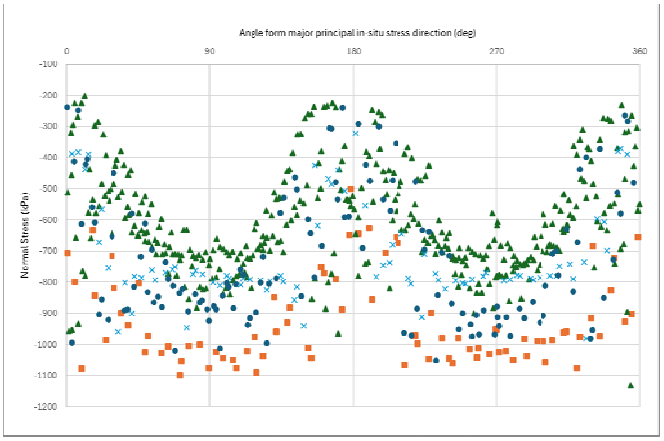


Fig. 3 Normal stress at the rock–secant wall interface plotted versus circumferential angle relative to the major principal in-situ stress direction; different symbols represent stresses extracted at different bedrock elevations. Negative values indicate compressive rock–wall interaction.

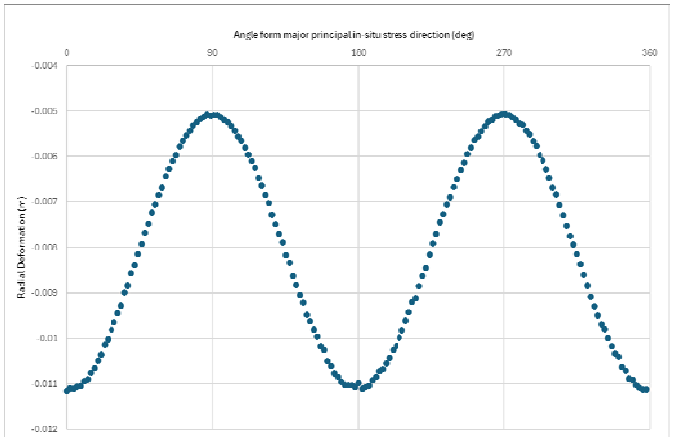


Fig. 4 Radial deformation of the lower portion of the secant caisson wall versus circumferential angle relative to the major principal in-situ stress direction; negative values indicate convergent deformation toward the shaft center.

6 Stability screening and risk controls

Rock stability is evaluated through complementary screening mechanisms addressing both stress-controlled and discontinuity-controlled responses. Stress-induced damage potential is assessed by comparing tangential stresses around the excavation to representative crack-initiation or spalling thresholds expressed as a fraction of intact strength. Discontinuity-controlled instability is screened using representative wedge/block concepts based on bedding-parallel and inferred sub-vertical joint sets.

Global stability is evaluated using a conservative numerical screening approach compatible with the Hoek–Brown rock mass model. As conventional C-φ strength-reduction methods are not directly applicable, adverse conditions are explored by increasing the rock mass disturbance factor to induce instability. Following introduction of shotcrete and passive anchors, the supported excavation exhibits stable deformation without numerical failure, indicating adequate stability under conservative assumptions. The screening results inform risk controls such as groundwater management, staged support timing, exclusion-zone load management, and predefined contingency measures consistent with an observational construction approach.

Tangential stress concentration is evaluated using the σ_{xx} stress component as a representative indicator at locations where the excavation boundary is aligned with the global coordinate system, with zones of elevated stress highlighted in red used to identify potential areas of maximum tangential stress concentration for screening purposes.

Stress-based screening relies on tangential stress indicators such as those shown in Fig. 5, while interface stress redistribution trends inform the risk-control framework as demonstrated in Fig. 3.

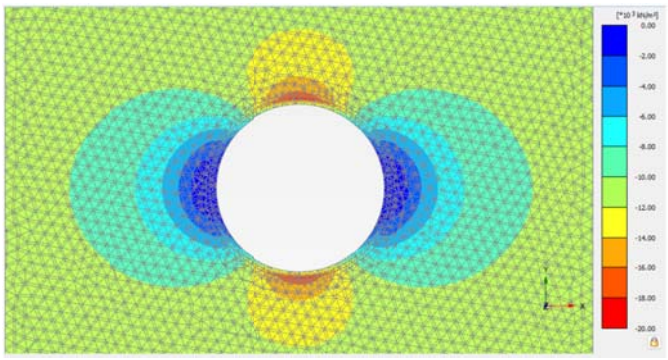


Fig. 5 Contours of σ_{xx} stress component around the excavation at the lower portion of the secant wall, used as a representative indicator of tangential stress concentration for stress-induced damage screening. Red zones indicate locations of elevated tangential stress under anisotropic in-situ stress conditions.

7 Risk management and observational approach

The workflow is intended as a decision-support tool rather than a single deterministic predictor. Risk management is achieved by: (i) identifying governing construction stages; (ii) bounding response with conservative parameter sets; (iii) designing passive, redundant support that engages progressively; and (iv) implementing an observational approach in which field monitoring targets are linked to trigger levels and predefined mitigation actions. This reduces reliance on a single model realization and supports defensible construction decision-making in high-stress rock.

Normalized stress and deformation metrics derived from the numerical analyses provide a practical basis for defining monitoring trigger levels and pre-defined mitigation actions consistent with an observational construction approach.

8 Conclusions

The design of secant caisson shoring embedded in high-stress shallow bedrock is governed primarily by rock mass stress redistribution and deformation compatibility rather than by conventional soil earth-pressure mechanisms. A deformation-permissive support concept using shotcrete and passive anchors below the caisson toe can manage stress release and reduce long-term load transfer to permanent works while maintaining excavation stability.

Three-dimensional staged modelling, combined with sensitivity analysis and stability screening, provides a robust basis for support optimization and risk management.

Interface stress redistribution trends (Fig. 5) reinforce that bedrock response is governed by anisotropic stress history and deformation compatibility rather than uniform pressure assumptions.

9 References

Hoek E, Brown ET (1997) Practical estimates of rock mass strength. International Journal of Rock Mechanics and Mining Sciences 34(8): 1165–1186

Hoek E, Carranza-Torres C, Corkum B (2002) Hoek–Brown failure criterion – 2002 edition. Proceedings of NARMS-TAC 2002

Schanz T, Vermeer PA, Bonnier PG (1999) The Hardening Soil Model: Formulation and Verification. Beyond 2000 in Computational Geotechnics

Martin CD, Christiansson R (2009) Estimating the potential for spalling around a deep repository. International Journal of Rock Mechanics and Mining Sciences 46(2): 219–229

Nicksiar M, Martin CD (2013) Crack initiation stress in low-porosity rocks. EngineeringGeology 154: 64–76

Bentley Systems (2023) PLAXIS 3D Reference Manual. Bentley Systems, Incorporated

Project-specific reports are not cited for confidentiality; only publicly available references are listed

Design of reinforced sprayed concrete arches in rock tunnelling

S. Spasojević
Geo.tunnel.konsult LLC, Belgrade, Serbia
srdjan.s@geotunnelkonsult.com
0009-0004-7280-9930

Abstract

Reinforced sprayed concrete arches are a tunnel support measure commonly used in ground conditions with poor rock mass and low or insufficient rock cover, weaknesses, or fault zones. This is a typical solution for rock excavation support in a single–layer tunnel lining.The initial chapters outline the empirical, analytical, and numerical principles governing the design process. Subsequently, two case histories from Swedish tunnelling practice—the Högdalsdepån and Flemingsbergstunneln projects—are analysed to demonstrate how shotcrete ribs are implemented within single-layer linings to optimise structural stiffness and load-bearing capacity.

Crucial uncertainties remain regarding rock-shotcrete deformation compatibility and interface interaction,the precise load-transfer mechanisms, and design criteria for integrated arch-spile systems.

Keywords Shotcrete arches/ribs, Insufficient cover, Weaknesses, Fault zones, Single–layer tunnel lining, Swedish tunnelling practice.

1 Introduction

Tunnelling mainly involves excavating rock or soil, supporting or lining the tunnel walls, and mucking (removing debris). Depending on the ground conditions, construction methods, and water inflow (pressures), supporting measures can be either permanent or temporary. For rock tunnelling, shotcrete combined with rock bolts has been the dominant support method since the 1980s (Sjölander, 2020).

The traditional approach uses two separate support measures: an initial lining and a final lining. However, the modern trend in rock tunnelling is to design permanent single-shell tunnel linings. In Sweden, this approach has been followed for decades, but these efforts have been strengthened by the European Union (EU) 's ambitious new goal of becoming climate neutral by 2050. The rock support design is often based on a combination of empirical, analytical methods and numerical analysis. In difficult ground conditions, especially where “poor” rock mass prevails, such as thin rock cover and/or poor rock conditions, reinforced sprayed concrete arches are frequently employed.

This paper presents a design approach for reinforced sprayed concrete arches as a permanent single-shell tunnel lining, illustrated by two examples from Sweden. A brief explanation of design principles is provided in the following chapters, followed by case history examples.

2 Design of Reinforced Sprayed Concrete Arches as Permanent Rock Support

The design of reinforced sprayed concrete arches as permanent rock support is conducted as a load-bearing structure with rockinteraction, in accordance with rock-mechanical design principles.

This indicates that empirical, analytical, and numerical approaches are used to link anticipated rock-mass behaviour to appropriate support measures. Additionally, the structural engineering principles are applied to verify the load-bearing capacity of reinforced sprayed concrete arches by calculating their moment and shear capacities in accordance with Eurocode SS-EN 1992-1-1 (Standarder, 2023).

To clarify, the support for the rock tunnel was evaluated through multiple methods: (1) an empirical approach, (2) modelling the rock support as a beam on an elastic foundation, and (3) numerical analysis of the rock and tunnel using the finite element method (FEM). All these design approaches are described in the chapters below.

2.1 Design with an empirical approach

The stability of the rock tunnel and the support measures should primarily rely on a proper understanding of how the rock mass and tunnel structure might behave. To do that, rock mass behaviour andthe design of rock support are initially based on empirical methods using a rock mass classification system.

Recent experience with large tunnelling projects managed by the Swedish Transport Administration generally involves using the Q-method developed by Barton et al. (Barton, Lien , & Lunde, 1974), which has been adopted by the Norwegian Geotechnical Institute (NGI, 2025).

$$Q = \frac{RQD}{J_n} \cdot \frac{J_r}{J_a} \cdot \frac{J_W}{SRF} \tag{1}$$

In the Q-method, the rock mass quality Q is calculated from the three sets of ratios that represent the rock mass structure ($\frac{RQD}{J_n}$), roughness, and joint alternation ($\frac{J_r}{J_a}$), and active ($\frac{J_W}{SRF}$) (Barton, Lien , & Lunde, 1974).To estimate therock mass quality index (Q), 6 parameters are required. The *Q*-value and the equivalent dimension (D_e), which is the ratio of the effective length to the excavation support ratio (*ESR*), are empirically linked to certain support measures. Guidelines for using various supporting elements—such as spiles, arches/ribs, and bolts—in relation to the Q-value and equivalent dimension (D_e) are shown in Fig. 1.

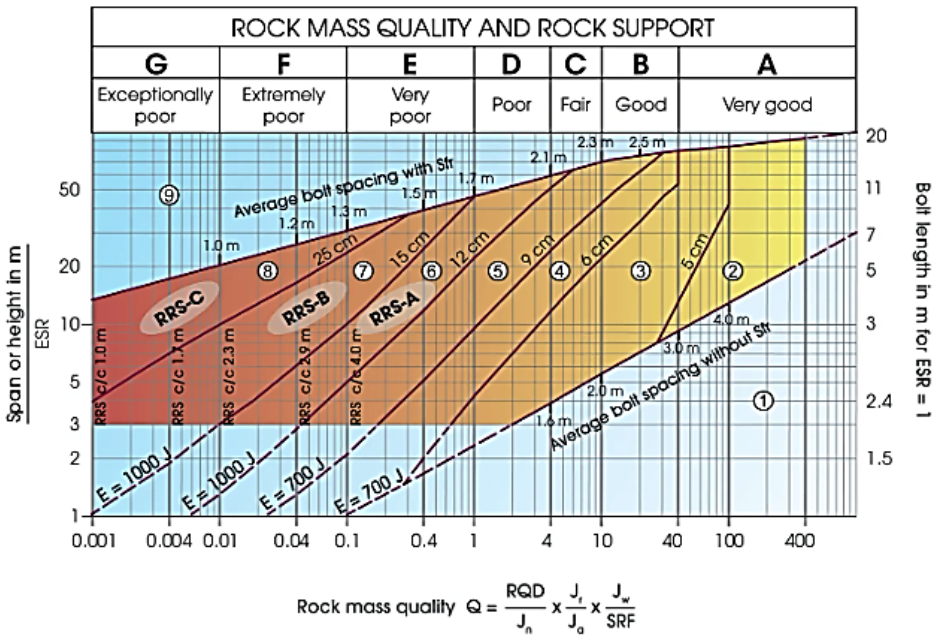


Fig. 1 The latest updated Q-system for design of rock support (NGI, 2025).

This rock mass classification has been significant updated based on recent experience(Grimstad, Kankes, Bhasin, Magnussen, & Kaynia, 2022)in the construction of underground openings in hard rock, using various support methods and excavation techniques.

2.2 Design with a structural design approach

In a structural design approach, moment/thrust interaction is considered, whereby rock support in direct contact with the surrounding rock benefits from rock-structure interactions like natural rock arches and movement restraint. Such a structure can generate moments and thrusts simultaneously, providing a high degree of load-bearing (structural) capacity.

Stable natural rock arching occurs when rock support interacts with the surrounding rock mass. In this phenomenon, the support system and the rock mass act as a composite structure; loads imposed on the support by the rock can be supported by both the lining and the rock, depending on the magnitude of the strain distribution.

Movement restraint refers to rock support placed in direct contact with the rock to prevent the lining from developing large moments.

In the beam-spring method, the rock support is generally modelled as a structural element,a flexible continuous beam. The beam structural elements are modelled as linear elastic, with their stiffness determined by the thickness and elastic modulus of the constituting material. The rock is also assumed to behave as a linear-elastic material, accounting for the stiffness of the surrounding rock. Each segment of the tunnel, from the spring line to the bottom, is supported by springs, whose elasticity represents the ground reaction (K_s); i.e., the rock is modelled as a continuum medium. It is assumed that the ground reaction is generated by the displacement of the rock support (lining) proportional to the rock deformation (Kerr, 1964), (Hetenyi, 1963), (Pasternak, 1954).

$$p(x) = k \cdot \delta(x) \tag{2}$$

$$p(x) = k \cdot \delta(x) - G \cdot \delta''(x) \tag{3}$$

$$p(x) = k \cdot \delta(x) - D \cdot \delta^{IV}(x) \tag{4}$$

where k is the stiffness of the surrounding rock, G is the stiffness of the shear rock layer in the Pasternak model(Pasternak, 1954), and D is the bending stiffness in the Hetényi model (Hetenyi, 1963).

The entire calculation involves defining the geometry with linear elements, modelling rock-structure interaction using elastic springs, determining load size, direction, and nature, analysing load combinations and worst-case scenarios, performing static calculations to find internal forces, moments, and displacements, and finally, moment and shear force capacity verification per Eurocode 2(Standarder, 2023). The final step is to check total displacement, plastic yielding of rock, and stresses at the tunnel boundary and along the bolts and spiles.

2.3 Design with the numerical analysis by using the finite element method

Numerical analysis (FEM) can be employed to identify suitable support measures and to verify if the selected ones are appropriate and sufficient.

The rock support is modelled using a 2D or 3D implicit continuum model that simulates the interaction between the lining structure and the surrounding rock, reproducingactual boundary conditions and all construction phases. 2D models are often used for their computational efficiency, whereas 3D models provide the most realistic representation of the excavation face. Both 2D/3D FEM analysis can predictrock movements, structural forces in the support, and overall stability during construction.

Usually, the rock mass is modelled as an elastic-plastic material, using quadrilateral or triangular continuum elements, while shotcrete or shotcrete arches/ribs are modelled as linear, shell, or solid elastic or elastic-plastic elements. Rock bolts or spiles are modelled as linear or solid elastic or elastic–plastic elements.

FEM results provide spatial insight into the distribution and redistribution of stresses at the tunnel boundary and along bolts, spiles, and other elements; the plastic yielding of rock; internal force distributions; and displacement (settlement) values throughout the entire spatial model.

The stresses in the rock support are calculated from the major and minor principal stresses at the periphery of the tunnels or in other structural elements. These stresses induce the axial thrust, shear

force, and bending moments in the structural elements (shotcrete, bolts, etc.). For shotcrete or shotcrete arches, plots of the thrust-bending moment and thrust-shear force (support capacity diagrams) are constructed to determine whether the rock loads exceed the load-bearing capacity. A similar approach is also adopted for the rock bolt and spile elements. Rock mass movement generates stresses in rock bolts and spiles. These elements are checked to determine whether the loads exceed the bolt or spile capacity or not.

3 Case Study of Reinforced Sprayed Concrete Arches Design

In this chapter, two cases have been reviewed that utilise reinforced sprayed concrete arches as permanent rock support – single-shell tunnel linings.

3.1 Högdalsdepån, service/access tunnel

The Högdalsdepån project began construction in 2020 and is scheduled for completion in 2026. It is a2.5-kilometre-long subway tunnel that will double the capacity of the Högdalen depot. The subway tunnel includes three new tracks: a connecting track and two parking tracks, with the parking tracks located in a separate, large underground storage area. The expanded depot will be able to service trains on both the green and blue metro lines of the Stockholm subway. The total cost is expected to be 800 million Swedish crowns.

As part of the construction of the Högdalsdepån, it is planned to first excavate the access tunnel from the north. The excavation work will be carried out predominantly from this tunnel, without disrupting traffic on other roads. The working tunnel will serve to transport machines and personnel underground and to remove blasted rock. Later, two more working faces will be excavated to the west and east. Once construction is finished, the access tunnel will continue to be used for service and emergency evacuation.

A high-arched tunnel profile with a total cross-sectional area of 38.90 m² has been designed. The tunnel span is 5.4 m, the maximum height along the axis is 6.87 m, and the sidewall height is 5.35 m. The total length of the working tunnel is 342 m.

After construction, the tunnel will serve as a service and emergency evacuation tunnel. Therefore, it includes niches for electrical and technical equipment, service niches, a water supply and sewer station niche, vehicle parking and turning niches, and a fire-protection pressurisation chamber, Fig. 2.

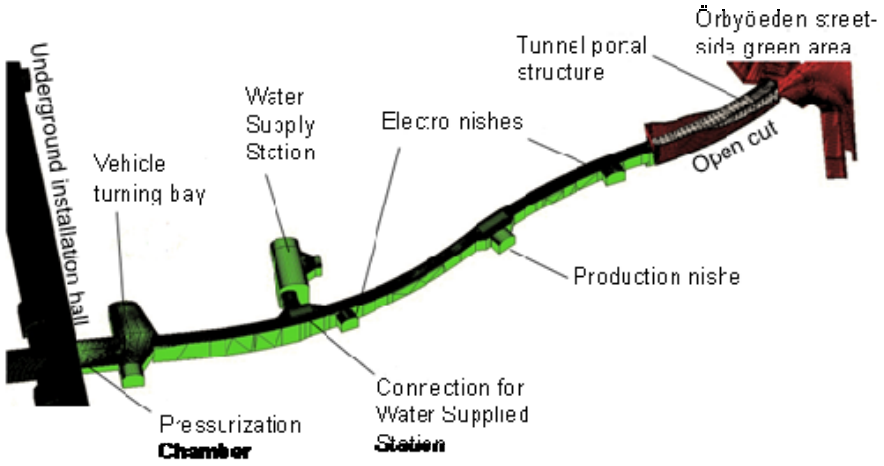


Fig. 2 Overview illustration of the access tunnel with niches for electrical and technical equipment.

The surrounding rock mass consists mainly of well-consolidated fine- to medium-grained orthogneiss, locally intersected by diabase and pegmatite veins, and generally exhibits a blocky structure with occasional weakened or fractured zones.Between km 0+138 and km 0+155, immediately after the first electrical niche, the tunnel passes through a shallow overburden zone with a weakness zone, Fig. 3. The rock cover above the crown ranges from 2.10 to 2.30 m, while the total overburden, including clayey soil, is about 6.60 m. According to the RMR classification, the rock mass in this section is at the boundary between fair and poor rock (RMRbas ≈ 48).

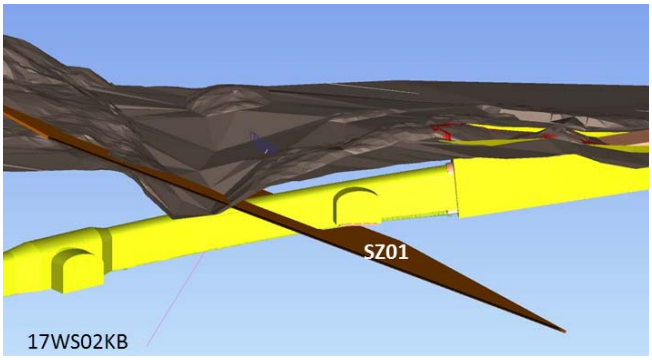


Fig. 3 Location of the low overburden and unfavourably orientedweakness zone relative to the access tunnel.

Due to the low overburden and the unfavourable orientation of the weakness zone relative to the excavation direction, excavation is expected to be difficult.

The initial design of bolts, shotcrete, and reinforced shotcrete arches is performed using the Q-system support chart from Chapter 2.1. The Q-chart indicates the need for reinforced shotcrete arches/ribs (RRS1), with a single layer of 3 rebars, each 16-20 mm in diameter, and covered with 250 mm of shotcrete. The c/c spacing between each arch was determined to be 2.8 m.The Q-chart does not specify requirements for spiling bolts; this decision should be based on experience. Low overburden, the quality of the rock mass, and the unfavourable orientation of the weakness zone restrict the development of a stable natural rock arch above the tunnel roof. This can potentially cause substantial deformation and rapid rock-mass failure during excavation. Spile bolts are designed as a temporary pre-support system to ensure the stability of the tunnel roof perimeter until permanent rock support is installed.

Furthermore, the design with a structural approach: a linear elastic beam on an elastic bed (beam-spring method), assumes that all rock pressures are transmitted from spiles to the rock tunnel support/lining, so the external load on the lining equals the support reaction from the spile system.

The sprayed shotcrete arches are designed to behave like a reinforced concrete T-beam: the 115 mm shotcrete layer acts as the flange, while the remaining 135 mm shotcrete serves as ribs. Both work monolithically due to the high-quality shotcrete. The shotcrete has compressive strength C32/40 and steel fibre reinforcement (MAMB). The influence of steel fibres is taken into account when assessing the shear and bending capacities of shotcrete arches, Fig. 4.

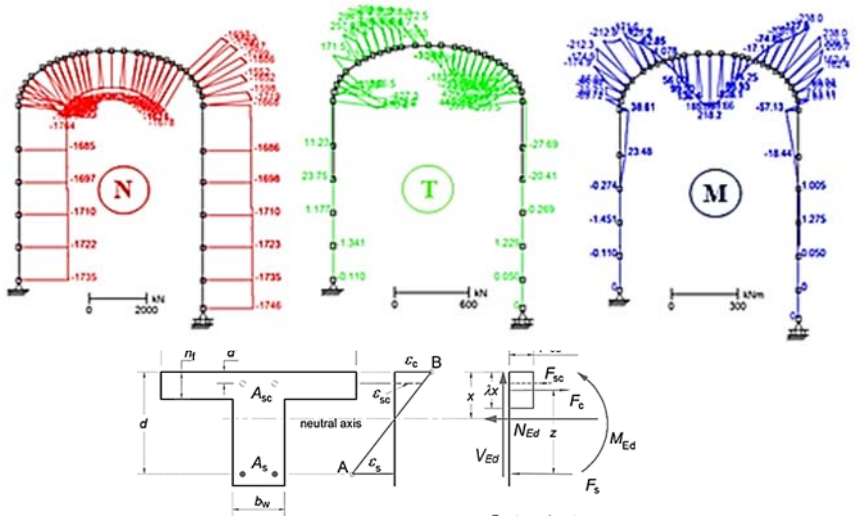


Fig. 4 Distribution of internal forces in a single-shell tunnel lining analysis (beam-spring method) and illustration of sprayed shotcrete T-section in bending and shearing at the ultimate limited state.

A single-layer tunnel lining was analysed using 3D FEM with an implicit continuum model in PLAXIS 3D(Bentley). The model was 61 m long, 46 m wide, and 41 m high, discretised with 10-node tetrahedral elements ranging from 0.02 to 6.40 m. Boundary conditions allowed free movement along the vertical sides, while the bottom boundary was fixed and the top remained free. Shotcrete was

modelled as a linear-elastic material using six-node beam elements with six degrees of freedom per node. The model included both the typical rock support section and a segment reinforced with sprayed-concrete arches (Fig. 5). Bolts and spiles were modelled as linear-elastic materials using three-node beam elements with six degrees of freedom per node.

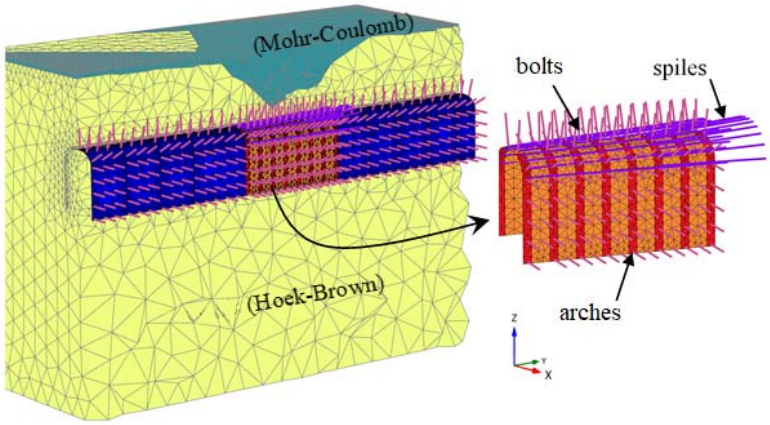


Fig. 5 Location of the low overburden and unfavourably oriented weakness zone relative to the access tunnel.

Excavation and support installation were simulated in 78 construction phases, with advance lengths of 2.0–5.0 m per phase. The rock mass displacements are such that small, limited-height sliding blocks form above the tunnel, allowing the stable rock arch to develop sufficiently (Fig. 6). The largest displacements occur in rock mass depressions, ranging from 0.207 to 0.472 mm.

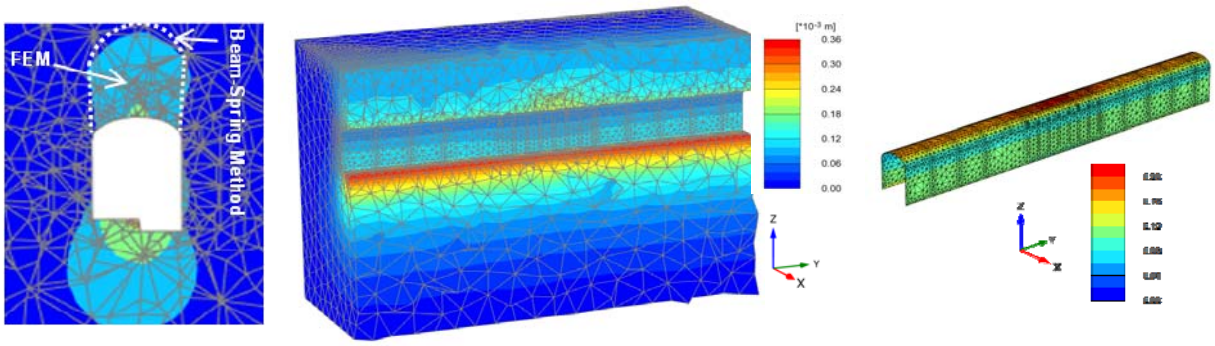


Fig. 6 Contours of the collapse zone are shown by the Finite Element Method (FEM) and Spring-Beam Method on the left. On the right, the displacement of the rock mass and lining after the entire tunnel excavation.

Finally, the self-drilling R51N spiles are designed to be 15 m long, spaced 0.6 m apart.After installation and excavation, sprayed shotcrete arches are constructed to transfer loads from the spiles. First, a 115 mm layer of shotcrete (typical support) is applied, then strengthened with 235 mm shotcrete arches spaced 2.0 m apart, reinforced with 5×RØ25 mm steel bars.In total, seven excavation stages are reinforced with shotcrete arches.

3.2 Flemingsbergstunneln, Tvärförbindelse Södertörn

Flemingsbergstunneln is a 3.1-kilometre tunnel on road 259 Tvärförbindelse Södertörn, between Kungens kurva and the Jordbro interchange in Haninge. The current road 259 is an accident-prone stretch that will now be rebuilt and become a safe road for all road users. The tunnel consists of two tunnel tubes with two lanes in each direction, separated by a 12-meter-wide rock pillar.

The rock mass is mainly made of sedimentary gneiss, with subordinate bands of gneiss-granite, meta-vulcanite, and metabasite. The gneiss has a medium-to-coarse grain size. The rock's structure rangesfrom indistinct to foliated and veined.

The tunnel passes under an existing stormwater tunnel at km 9/693. Road tunnel tubes are trending to the east-south (ES), striking 136° and dipping 2°. The existing stormwater tunnel is trending west-south (WS), i.e., striking 241°. The distance between the designed road tunnel tubes and stormwater tunnel is determined to be 3,00 – 4,30 m. Stormwater tunnel tube has an oval—egg—shaped cross-section, ca 4,50 m wide and ca 4,40-4,70 m high.

The rock class ranges from fair to poor, with $31 \leq RMR_{bas} \leq 45$. Rock mass is with closely spaced discontinuities, which fracture intact rock over small distances.

The designed rock support consists of a typical rock support layer of sprayed concrete (t = 150 mm), located at a specific distance (L = 2.60 m) along the tunnel axis, and additionally strengthened by sprayed concrete arches/ribs (b x h = 600 x 150 mm), Fig. 7. In addition to the arches/ribs, regular rebars are designed to be mounted on brackets and attached to the rock ground using short bolting (L=1.50 m). The short bolts are at a c/c distance of 2,60 m.

Similar to Chapter 2, the rock support is first verified by structural analysis using the beam-spring method and then further investigated by 3D numerical analysis in Plaxis 3D. The full water pressure in the stormwater tunnel is applied in the analysis.

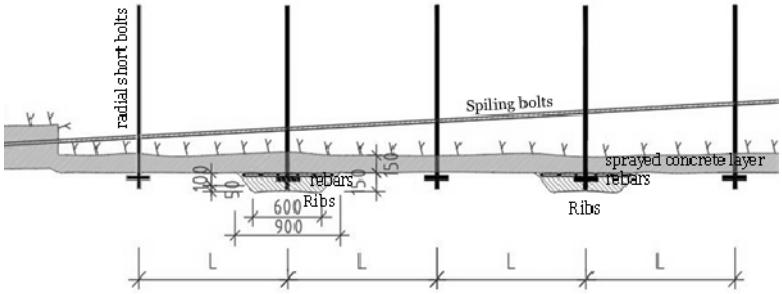


Fig. 7 Sketch of tunnel longitudinal section secured by the spiling bolts, sprayed concrete layer and arches together with short radial bolts.

The Plaxis 3D model measures 86 m × 92 m × 53 m (Fig. 8). The model size is reduced to minimise the likelihood of generating fault-mesh elements and to reduce calculation time.

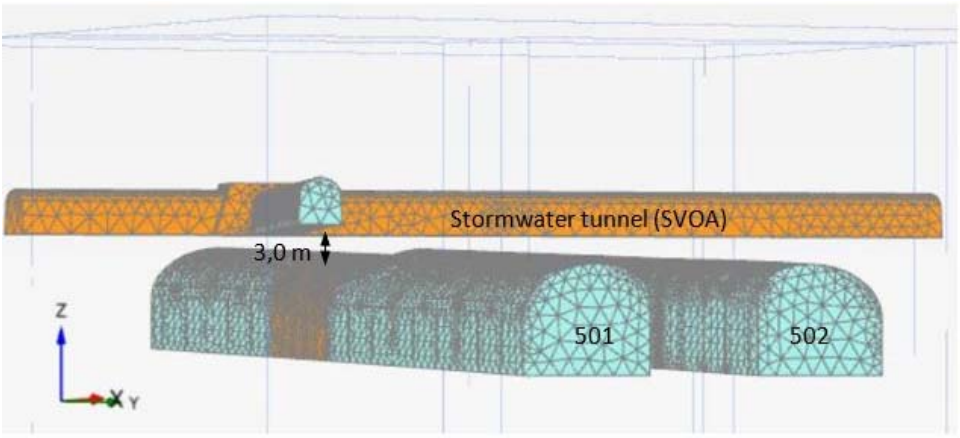


Fig. 8 A 3D finite mesh model for the analysis of the tunnels 501/502 and the existing stormwater tunnel.

The extent of the plastic zone along the periphery of the tunnel walls is limited to the area of 2,0 – 2,42 m. The maximum deformation is observed in tunnel 501, reaching 3,86 mm. Deformations produce critical strains of ε = 0,05 % and are not expected to produce tunnel stability problems.

Bending moments (M), Shear forces (Q), Axial thrusts (N) are maximised at 12,17 kNm, 189,19 kN. and 685,932 kN. A scatter plot of all internal forces on support capacity plots is presented in Fig. 9.

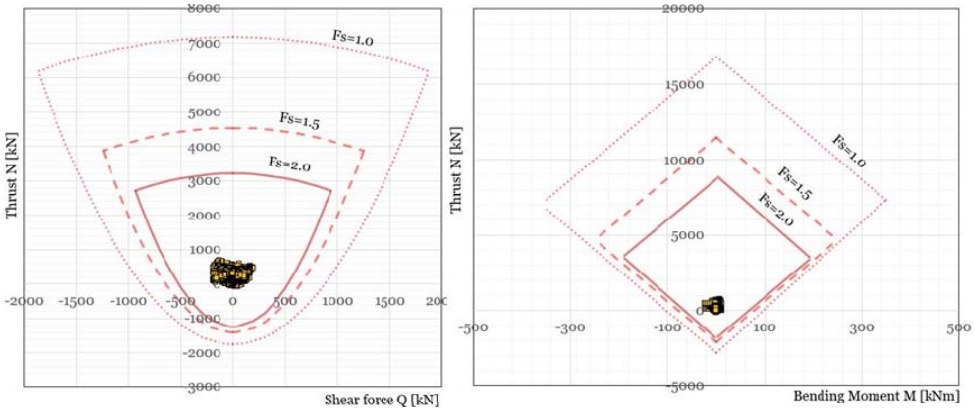


Fig. 9 Support capacity diagrams of shotcrete reinforced ribs.

4 Conclusion

The paper presents case histories from Scandinavian practice on the design of reinforced sprayed concrete arches as a single-layer tunnel lining in complex geotechnical conditions—such as low overburden, poor ground quality, and proximity to objects.

In the above-mentioned practice, it is not clear whether a rock mechanical or a structural engineer should be assigned to the design of shotcrete arches. The author's opinion is that this should be done by personnel with knowledge of both principal structural and rock mechanics. A clear methodology connecting analysis, empirical analysis, and numerical analysis was described, leading to the final design. Reinforced shotcrete arches are designed as load-bearing structures, considering their interaction with the rock mass. There is a critical question about whether shotcrete arches and the rock mass deform in the same way, i.e., whether there is full interaction between the shotcrete arches and the rock mass.

Further work on this topic should examine these questions, as well as the requirements for sprayed concrete arches combined with spiles and the exact mechanism of load transfer.

5 References

Barton, N., Lien , R., & Lunde, J. (1974). Engineering classification of rock masses for the design of tunnel support. . *Rock Mechanics and Rock Engineering 6(4)*, 189-23.

Bentley. (n.d.). *PLAXIS 2025.1 Scientific Manual PLAXIS 3D.*

Grimstad, E., Kankes, K., Bhasin, R., Magnussen, A., & Kaynia, A. (2022). *Rock mass quality Q used in designing reinforced ribs of sprayed concrete and energy absorption. In Proceedings of the 4th International Symposium on Sprayed Concrete.* Davos.

Hetenyi, M. (1963). *Beams on Elastic Foundation: Theory with Applications in the Fields of Civil and Mechanical Engineering.* Michigan: The University of Michigan Press.

Kerr, A. D. (1964). *Elastic and viscoelastic foundation models. J. Appl. Mech. Trans.*

NGI. (2025). *Using the Q-System, Rock Mass Classification and Support Design.* Norwegian Geotechnical Institute .

Pasternak, P. L. (1954). *On a new method of analysis of an elastic foundation by means of two foundation constants.* Moscow: In: Gosudarstvennoe Izdatelstro Liberaturi Po Stroitelstvui Arkhitekture.

Sjölander, A. (2020). *Structural Behaviour of Shotcrete in Hard Rock Tunnels (PhD. Theses).* Stockholm: KTH Royal Institute of Technology.

Standarder, S. I. (2023). *SS-EN 1992-1-1:2023 Eurokod 2 - Dimensionering av betongkonstruktioner - Del 1-1: Allmänna regler och regler för byggnader, broar och anläggningskonstruktioner.*Stockholm.

Optimization of shear strength parameters of deposited clastic sediments via crack shape

D. Božić
Geomatriks, Ljubovija, Serbia
danijelabozic1976@gmail.com
0009-0006-7388-9746

V. Čebašek
University of Belgrade, Faculty of Mining and Geology, Belgrade, Serbia
0000-0002-8667-2339

V. Rupar
University of Belgrade, Faculty of Mining and Geology, Belgrade, Serbia
0000-0002-0296-8467

Abstract
The mechanical behavior of deposited clastic materials at landfills can be analyzed using orthophoto imagery acquired by unmanned aerial vehicles (drones). Tension crack geometry observed on landslide scarp and body along landfill working slopes is used to define a correction parameter for the residual internal friction angle (ψ). This parameter is applied to adjust initial friction angle values and is essential for determining the mobilized friction angle used in slope stability analyses. Slope stability calculations should be based on the mobilized friction angle, as the material consists of loose, unsaturated, mica-rich silty-sandy and weakly clayey deposits. Laboratory results are included to provide an estimate of shear strength parameters in deeper, intact zones not affected by cracking and suction effects, which influence compression and dilatancy behavior. Statistical analysis of crack shape is used to estimate the dilatancy angle (ψ), which is then applied in correcting the residual friction angle for stability assessment. Environmental influences, including wind action (Košava), precipitation, and vibrations, may affect crack development and provide insights into failure mechanisms and sliding surface geometry. These results improve understanding of mechanical degradation in clastic materials and support more reliable parameter selection for landfill slope modelling.

Keywords
Landfill slopes, Clastic materials, Shear strength, Internal friction, Dilatancy.

1 Introduction

The development of modern technology and the use of high-capacity mining equipment have enabled the continuous exploitation of significant quantities of lignite and accompanying sediments in open-pit mines. Excavated geological materials that do not represent an energy resource are deposited in internal and external dumps, where they form large-scale earth structures. These can cover areas exceeding 10 km² and reach heights of over 100 m. The stability of these structures is of key importance for the safety and efficiency of mining operations, as it directly affects production continuity. A particular design challenge is achieving a balance between the intensity of excavation and the dynamics of material disposal.

Research on surface weathering of semi-cohesive rocks remains insufficient worldwide (Jevremović 1999), and these materials form three of the six systems of the observed dump. Reliable data on their mechanical, deformation, and rheological properties, as well as their behavior in dumps, are still limited, further complicating geotechnical slope design. This paper analyzes the deformation behavior of deposited material, presents vertical zoning of the slope, and proposes a new method for estimating the internal friction angle based on orthophoto imagery. The results are part of the author's doctoral research (Božić 2026).

2 Open Pit Mine "Drmno" and Internal Dump Landslide

The "Drmno" open-pit mine is the largest and most important in the Kostolac coal basin. It is located in the eastern part of the Republic of Serbia, near the town of Kostolac. Excavation is carried out using six BBS (bucket-wheel excavator - belt conveyor - spreader) systems and one BBC (bucket-wheel excavator - belt conveyor - crusher) system. Figure 1 shows the layout of the six BBS systems, covering the terrain from the surface down to the lignite roof, with seven excavators engaged (six bucket-wheel excavators and one bucket-chain excavator). The planned mining technology aims to increase the annual excavation capacity to 12 × 10⁶ t of coal, which will significantly increase the dimensions of the dump as well.

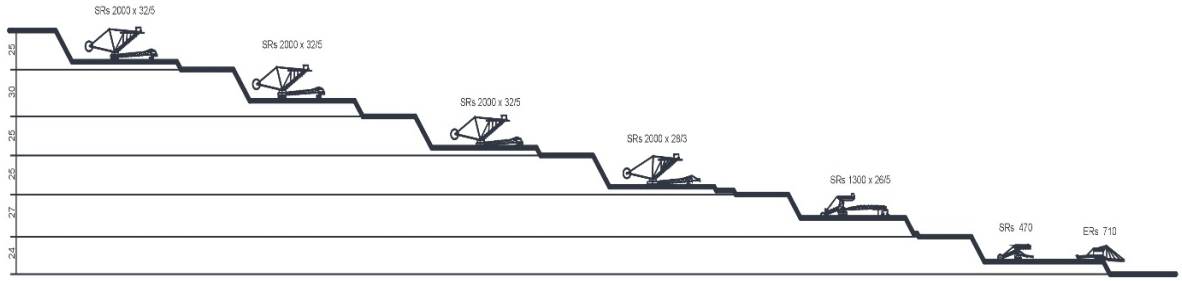


Fig. 1 Drmno Open-Pit Mine Mining Scheme.

2.1 Internal Dump Landslide

At the "Drmno" open-pit mine, 48 million m³ of sediments are excavated and deposited annually. Disposal is carried out at the internal dump located in the southern part of the mine. The structure of the dump consists of the body (deposited soils) and the foundation with a slope of up to 5° (unexcavated, damaged coal of variable thickness and well-bearing, overconsolidated silty-clayey sediments with sand lenses).

With daily expansion toward the northern final slope, in the direction of the Danube River, the stress state changes due to simultaneous dump elevation. As stresses increase, settlements and sliding occur, which are more dangerous for the dump body than for the foundation (Gojković et al. 2008). This is a consequence of the structure and type of soil forming the dump body. The body consists of loose soft rocks (loess-like soils, clays, silts) and cohesionless materials (gravel and sand), with varying permeability, consistency and compressibility.

The most extreme terrain destabilization affects three of the six BBS systems, located at the lowest elevations of the dump, starting from the slope toe. These systems exhibit cracks up to 0.25 m wide (Figure 2a), settlements exceeding 2 m (Figure 2b), and frequent tension cracks longer than 50 m (Figure 2c), along with landslides covering an area of 0.5 km². A solution to this issue is seen in developing a method for optimizing the internal friction angle value, which would enable slope stability analysis of the designed dump height of 200 m and a disposal front 3 km long.

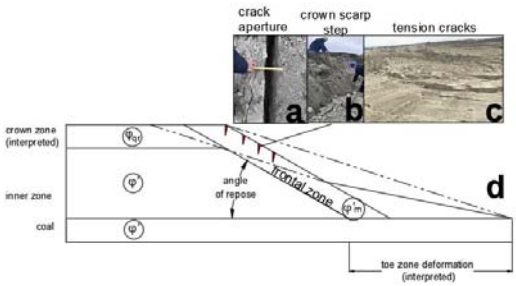


Fig. 2 Basic model of slope.

3 Research Concept of Mechanical Characteristics of Deposited Clastic Materials

The described conditions at the three lowest dump systems limit the movement of personnel and machinery, thereby restricting in situ testing of soil properties. There is also a problem with sampling loose material for laboratory testing. Until 2021, the principle of analogy of physical-mechanical and deformation properties of soil and coal was applied, based on 18,000 samples from 1,600 boreholes across the lignite deposit area (Grupa autora 2011).

However, this concept did not lead to a solution, as all experimental stabilization measures - such as installation of gravel piles, construction of coal retaining structures, drainage channels, diaphragms, and a dense network of wells around the dump perimeter, channels filled with drainage material at the base, as well as buttressing the deformed slope section with a larger mass of excavated soil - proved to be unsuccessful (Božić and Petrović 2021).

At present, there are no established guidelines for preserving the structure of deposited soil or for simulating the slip surface geometry in highly deformed dump segments. Laboratory determination of mechanical properties of clastites is additionally limited by testing conditions. In loose and unsaturated soils, direct shear testing may be affected by specimen disturbance, changes in density, and particle rearrangement during testing. Similarly, conventional triaxial compression tests under constant radial pressure may not adequately reproduce stress conditions in slopes undergoing continuous geometric and loading changes due to ongoing excavation activities (Maksimović 2014).

Literature data indicate that shear strength determination at very low effective stresses may involve significant experimental uncertainty, since measured values can be of the same order as parasitic testing effects (Maksimović 2014). Although originally reported for fine-grained soils, these limitations may also be relevant for loose dump materials in near-surface slope zones.

The initial basis for changing the research concept emerged in 2021 following preliminary UAV surveys using Wingtra and Aibotix drones (Grupa autora 2020b), which enabled the identification of deformation patterns on orthophoto images (Figure 3).

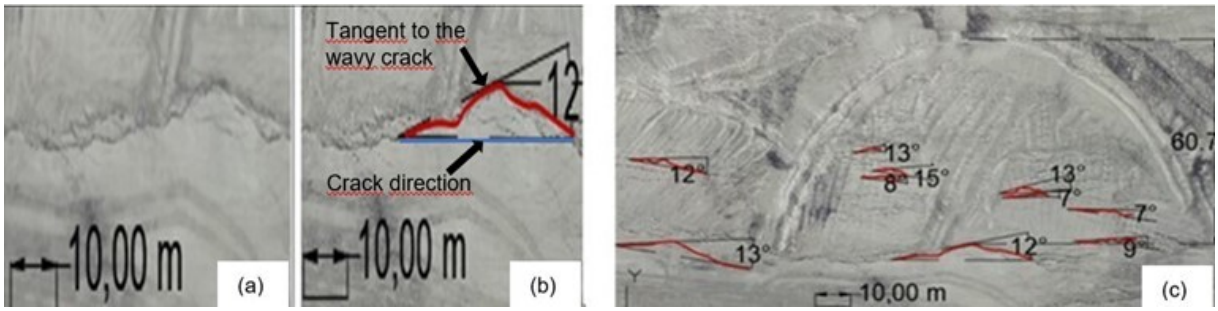


Fig. 3 Display of a crack in the landslide front before (a), after the dilatancy angle reading (b) and examples of readings of dilatancy angles of freely selected tension cracks on landslide (c).

4 Methodology of the Study

Orthophoto images of an inaccessible structure of extreme dimensions enabled a more detailed study of the behavior of different types of deposited materials, as well as the classification of slope deformations. Based on these images, zones with varying risks of deformation and sliding were identified (Božić and Petrović 2021). Through the frequency of tension cracks on the plateau and the slope of the system, criteria were obtained for estimating the depth and shape of the slip surface (Božić and Petrović 2021; Božić 2026), which represent key elements for vertical engineering-geological zoning of the slope.

The main idea is to facilitate the assessment of the distribution of physical, mechanical and deformation properties of deposited micaceous silty-sandy, weakly clayey sediments, with increasing dump height. The conducted zoning made it possible to complement existing classifications of slope deformations, such as the classification by A. M. Demin (Gojković et al. 2008).

For the purposes of this study, describing the phases of slope deformation over one month aims to present the concept of a method for determining shear strength parameters in the frontal, inaccessible zone, as well as to establish criteria for adopting different values of mechanical and physical properties within the same deposited material.

In addition to orthophoto analysis, this research also used data from core logging of four exploratory boreholes with a total length of 120 m (Božić and Petrović 2021; Božić 2026; Grupa autora 2020b), results of laboratory testing of 57 soil samples (Božić and Petrović 2021; Božić 2026; Grupa autora 2020a), and interpretation of 38 standard penetration tests (Božić and Petrović 2021; Božić 2026; Grupa autora 2020a).

4.1 Stages of Deformation of Working Slopes

Based on the research (Božić 2026), four stages of deformation development were defined. The first stage is the formation of the slope with the designed geometry. In the second stage, gravitational tension cracks develop due to initial lateral movements, dividing the slope into vertical blocks with a maximum measured surface scarp height of 2.2 m, corresponding to an estimated slip surface depth of 5 m based on crack density analysis. During this phase, apparent cohesion induced by capillary effects temporarily maintains the stability of these steep, individual blocks, preventing immediate collapse.

The third stage is characterized by cascade settlement of the material. As shear deformations progress, the collapse of the loose soil structure causes a volume reduction (negative dilatancy), forcing the blocks to drop and form a step-like morphology. In the fourth stage, water infiltration destroys the matric suction. Combined with mining vibrations and hydrostatic pressure in the cracks, a drastic reduction in shear resistance occurs, activating the landslide (Božić 2026).

Within one month, simultaneous mass movements can lead to large-scale landslides. Analysis of the orthophoto image confirmed these mechanisms, identifying two subsequent block-type, detrusive landslides: a larger isometric one (0.4 km²) and a smaller frontal one (0.04 km²) (Božić 2026).

4.2 Vertical Zoning of Working Slopes

After analyzing all the research results (Božić 2026), the working slope was divided into the following zones: crown, frontal and inner. A schematic representation of the zoned working bench slope is shown in Figure 2d. The foundation of the dump consists of coal, which, from the perspective of the mechanics of loose rocks, is not the focus of this study. The idea of slope zoning is to explain the vertical distribution of internal friction angle values, using a simplified model as presented in Table 2.

5 Determination of the dilatancy angle and its application

5.1 Determination of the dilatancy angle

The dilatancy angle ψ represents a measure of the volumetric change of soil during shearing and can be defined by the following formula:

$$\tan\psi = \frac{d\varepsilon_v}{d\varepsilon_s} \quad (1)$$

Where ε_v Increment of volumetric strain (-)
ε_s Increment of shear strain (-)

Dilatancy may manifest as either contraction or expansion, depending on the compactness and structure of the soil. In this research, it is used to correct the quasi-residual friction angle φ_{qr} in order to determine the mobilized internal friction angle in the frontal zone φ'_m.

The procedure for determining the dilatancy angle ψ is shown in Figure 3. Figure 3a presents a section of an orthophoto image with a crack, while Figure 3b illustrates the measuring procedure of the angle ψ between the tangent to a wavy crack and its general direction of propagation. Figure 3c shows a set of different measured values of the dilatancy angle ψ, indicating spatial heterogeneity of deformations within the landslide.

Note: Conventionally, the dilatancy angle ψ is defined as the ratio of volumetric strain to shear strain under laboratory conditions. In this study, ψ is estimated from the shape of cracks observed on orthophoto images. This field-based approach provides a practical approximation for soil dilatancy, accounting for local contraction (compression) induced by suction loss, shear deformation, and vibration effects.

The data were randomly sampled from both the front and the body of the landslide to avoid subjectivity in data selection. The analyzed working slope had a total length of 61 m.

Statistical analyses of the data were carried out based on the orthophoto image and the values of angle ψ are presented in Table 1. Further analysis was performed based on obtained values with confidence level of 85% (Božić 2026).

Table 1. Values of dilatancy angles ψ (°) at the front and body of the landslide.

Position	**Dilatancy angle ψ (°)**						
Landslide front	13	12	9				
Landslide body	12	8	15	13	13	7	7

5.2 Frontal zone friction angle

The methodology is based on the analysis of crack geometry in the frontal zone of the slope affected by landslides, aiming to estimate soil shear strength parameters. The quasi-residual internal friction angle φ_{qr} is corrected by the dilatancy angle ψ, thereby obtaining the mobilized internal friction angle φ'_m.

$$\varphi'_m = \varphi_{qr} - \psi \quad (2)$$

Where φ'_m Mobilized internal friction angle in the frontal zone of loose soils (°)
φ_{qr} Quasi-residual internal friction angle from the crown zone of loose soils (°)
ψ Dilatancy angle representing volumetric deformation within the shear band in the frontal zone (°)

In the frontal zone of the slope, loose soil under shear stress, with suction contributing to local compression, undergoes particle rearrangement and local compaction**,** generating the dilatancy angle ψ within narrow localized zones of concentrated deformation. This angle reflects local changes in density and particle arrangement**,** and is used for a more accurate estimation of the mobilized internal friction angle φ'_m.

It should be noted that the dilatancy angle ψ arises solely from local compaction under shear, with suction contributing to additional compression**,** and does not represent a property of the entire material.

Although not directly applied in this study, Maksimović's hyperbolic failure envelope theory could provide a useful extension by modeling the dependence of the mobilized internal friction angle φ'_m on

local compaction, suction effects, and the dilation angle ψ**,** allowing a more accurate assessment of slope stability.

6 Comparison of internal friction angle obtained by different methods

Table 2 presents internal friction angles for the crown, frontal, and inner zones of the working slope, derived from SPT testing (crown), direct shear tests (inner), and orthophoto analysis (frontal) (Božić 2026). The values illustrate the reduction of friction angle in the frontal zone, affected by settlements and landslides, relative to the inner slope mass. For the crown and inner zones, the effective friction angle (φ′) is reported, while for the frontal zone the quasi-residual friction angle (φ_{qr}), mobilized friction angle (φ'_m), and dilation angle (ψ) are given, along with statistical parameters (minimum, maximum, mean, SD) at 85% confidence.

Table 2. Internal friction angles for all slope zones.

Slope zone	index	unit	method	number	Min	Max	mean	Reliability 85%	SD
crown	$\varphi' \approx \varphi_{qr}$	degree	SPT	7	28.60	29.80	29.10	29.00	0.50
frontal	ψ	degree	dilatancy	10	7.00	15.00	10.90	11.00	2.90
frontal	φ'_m	degree	New method*	/	/	/	/	18.00	/
inner	φ'	degree	SPT	31	28.98	33.35	31.00	29.80	1.03
inner	φ'	degree	direct shear	27	32.30	33.70	33.00	32.00	0.60

* - modified friction angle according to new methodology $\varphi_{qr85} - \psi_{85}$

The parameters represent computational values for the working slope model (Figure 2).

7 Conclusion

The proposed method for optimizing the internal friction angle in deposited silty materials represents an initial scientific contribution in the field of slope stability analysis. It indicates the possibility of improving the assessment of sliding length and type of deformation, as well as its application in determining the optimal spacing of working faces and defining operational technology. Furthermore, the proposed method can be used as a supplement to the results of residual strength testing using the ring shear method on processed samples of loose clastites, thereby improving the quality of shear strength parameter determination.

References

Božić D, Petrović M, (2021) Elaborat o izvedenim geotehničkim i hidrogeološkim istraživanjima za izbor metode stabilizacije unutrašnjeg odlagališta PK „Drmno"

Božić D, (2026) Doctoral research (unpublished), University of Belgrade, Faculty of Mining and Geology, Belgrade, Đušina 7

Gojković N, Obradović R, Čebašek V, (2008): Stabilnost kosina odlagališta površinskih kopova, Univerzitet u Beogradu, Rudarsko-geološki fakultet, Beograd, Đušina 7

Grupa autora (2011) Projekat geoloških istraživanja ležišta uglja „Drmno"- Kostolački ugljonosni basen, JP EPS, PD RB „Kolubara" d.o.o., Ogranak „Projekt", Lazarevac, septembar 2011

Grupa autora (2020) Dokumentacioni izveštaj o izvedenim inženjerskogeološkim istražnim radovima na unutrašnjem odlagalištu PO „Drmna", knjiga 1, 2 i 3, 10693, Georad, Drmno

Grupa autora (2020) Ortofoto snimak UO PK „Drmno", Služba za rudarsko-geodetska merenja, Ogranak TE-TO Kostolac, JP EPS, Beograd

Jevremović D, (1999) Uticaj površinskog raspadanja glina i lapora na geotehnička svojstva terena s posebnim osvrtom na područje Beograda, Rudarsko-geološki fakultet, Beograd, Đušina 7

Maksimović M, (2014) Mehanika tla, 5th edn, AGM knjiga, Zemun, 153-242.

Advancing Slope Stability Practice in New Zealand: The NZGS Guidelines and their application in Greywacke

E.Gkeli
New Zealand Geotechnical Society and Stantec, Wellington, New Zealand
eleni.gkeli@stantec.com
0009-0000-0152-8331

N. Peters
Tonkin & Taylor, Wellington, New Zealand

A. Wightman
ENGEO, Wellington, New Zealand

D. Mason
WSP, Wellington, New Zealand

Abstract

The New Zealand Geotechnical Society (NZGS), in collaboration with the New Zealand Natural Hazards Commission (NHC), is developing a modular Slope Stability Guidance series to support consistent and reliable assessment of landslides and slope instability across New Zealand. This paper presents Unit 7C.2 of the guidance series, which addresses slope stability in Torlesse greywacke, New Zealand's most widespread basement rock and a material commonly associated with landslides triggered by rainfall and seismic loading. Torlesse greywacke is characterised by intense deformation, heterogeneous weathering, and closely spaced, variably persistent discontinuities, resulting in complex slope failure mechanisms that challenge conventional rock slope assessment approaches. The paper demonstrates how the guidance was developed, by synthesising recent New Zealand earthquake case histories, published laboratory test data, and practitioner experience. This approach resulted in practical, engineering-focused guidance for characterising greywacke rock masses, interpreting failure mechanisms and selecting appropriate strength parameters for stability analysis. By addressing the challenges associated with typical site investigation constraints especially in urban environments, Unit 7C.2 streamlines slope stability assessments in New Zealand, while it enhances their reliability and consistency. The principles and approaches adopted in the development of the guidance could be applicable to other similar rock conditions and steep landslide prone terrain worldwide.

Keywords

Slope stability, Landslides, Greywacke, Guidance, New Zealand.

1 Introduction

Landslides represent a significant geotechnical hazard in New Zealand, due to the combination of steep topography, complex geology, high rainfall, and high seismicity. To improve consistency of practice for assessing slope instability, the New Zealand Geotechnical Society (NZGS), supported by the Natural Hazards Commission (NHC), is developing a modular Slope Stability Guidance series. This guidance provides a nationally consistent framework for slope instability, including landslide identification, investigation, modelling, and mitigation presented across seven units. The units cover topics from site investigations to specialised assessments for debris flows and region-specific materials and are available to download from the NZGS website (NZGS, 2025a).

This paper focuses on Unit 7C.2 (NZGS, 2025b), which adapts the general principles and processes established in Units 1 to 4 specifically for slopes developed in Torlesse greywacke, New Zealand's most widespread basement rock. The paper demonstrates how Unit 7C.2 integrates recent studies of coseismic landslides in greywacke, laboratory test data, and practitioner experience into practical guidance for the assessment of slope stability in this highly fractured rock mass. This paper also shows how Unit 7C.2 aims to streamline the application of rock-engineering principles for highly fractured greywacke slopes under real cases with investigation and design constraints.

2 General characteristics of Torlesse greywacke rocks

Torlesse greywacke is a Mesozoic age rock complex part of the Torlesse Composite Terrane that forms the basement across extensive areas of both the North and South Islands, including urban areas such as Wellington, the capital of New Zealand (Fig. 1, left). The rocks consist predominantly of fine- to medium-grained sandstone, siltstone, mudstone and argillite, of marginal marine to sub-marine origin, deposited by turbidity currents and mass-flow processes (Suneson, 1993). Although greywacke strictly describes the fine sandstone, it is commonly used as a colloquial term in New Zealand, to describe the rock complex, as a whole. Low-grade metamorphism and a multi-stage deformation history have produced a structurally complex rock mass with great variability in intact rock strength and intensity of fracturing, ranging from closely jointed rock to melange or broken formation.

An example of a typical interbedded Torlesse greywacke outcrop is shown in Fig. 1, right. Bedding orientations and angles can vary, while persistence is interrupted by randomly oriented jointing. Multiple joint sets, typically more than three, exist in the rock mass with one or two dominant with higher persistence. Closely spaced, low-persistence joints are also present, many of which are incipient and do not form continuous failure surfaces until mobilised by loading or seismic shaking (Singeisen, et al., 2022).The rock mass weathering varies and ranges from completely to highly weathered on slope exposures, to moderately to slightly weathered or unweathered on the high hill ranges, or at lower elevations. The strength of the rock material ranges widely, from extremely weak to very strong, depending on the weathering grade and the lithology.

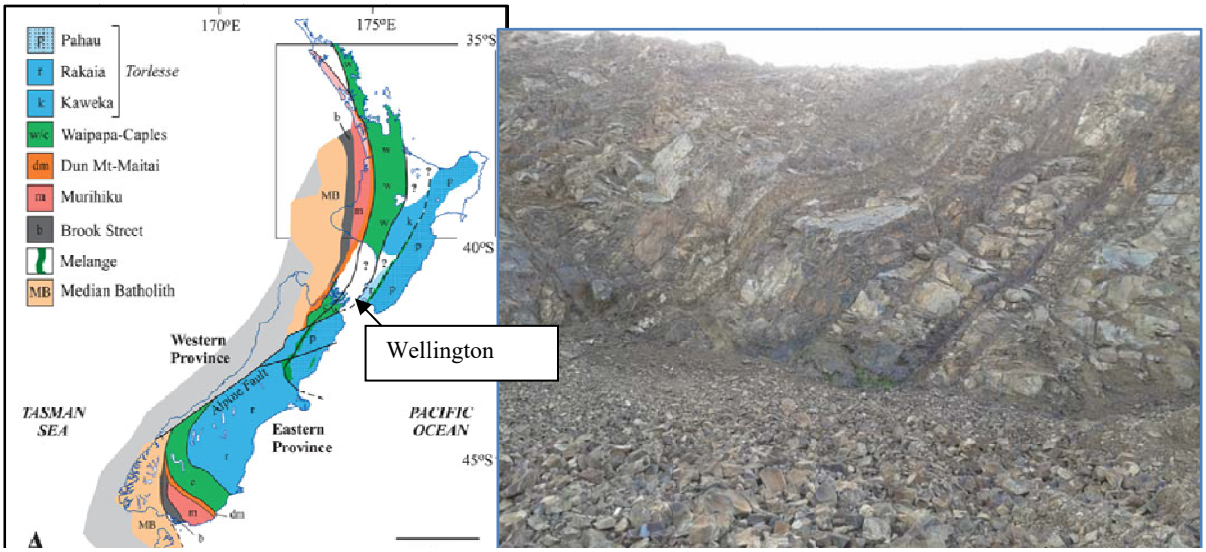


Fig. 1 Left: Extents of greywacke rocks across New Zealand (Price, et al., 2015). The paper covers rocks of the Torlesse terrane. Right: Greywacke rock outcrop – mudstone (dark) and sandstone (light grey) with thin laminated siltstone beds in between (NZGS, 2025b).

3 Modes of slope failure

As a result of the complexity in strength, fracturing, and weathering, greywacke rock slopes can fail by a variety of mechanisms, depending on factors such as the conditions of the rock mass and dominant defects, the geometry of the slope, and the loading conditions. Slope failures in greywacke can be structurally controlled or rock-mass controlled, or a combination of both. Individual slopes may also be affected by more than one failure mode. The modes of failures determined as typical for greywacke slopes in Unit 7C.2 (Table 1) were confirmed in the studies of the landslides triggered by the 2016 Mw 7.8 Kaikoura earthquake (Singeisen, et al., 2022)(Mason & Brabhaharan, 2023).

Table 1. Most common slope failure modes in greywacke rock masses.

Principal Mechanism	**Mode**	**Typical occurrence**	**Typical size and scale (relative to height of slope)**
1. Structurally controlled	Planar, wedge and toppling moderate size failures –	In moderately strong to strong, blocky rock masses with >3 sets of discontinuities.	Small - moderate
	Translational rockslides	In all types of rock masses with at least one persistent discontinuity.	Large
2. Composite (translational and rotational)	Planar with step-path structurally controlled mechanism (en-echelon failures)	In moderately strong to weak, blocky to very blocky rock masses - non-persistent but consistently oriented discontinuities.	Large
	Multi-planar compound slides	In weak rock masses with persistent discontinuity (-ies).	Large
3. Rotational	Circular failure plane	In highly fractured, disintegrated or highly weathered weak to very weak rock mass that can exhibit nearly isotropic behaviour.	Large

4 Assessment of geotechnical parameters

4.1 Intact rock

The intact rock strength of unweathered Torlesse greywacke is generally strong to extremely strong, with reported unconfined compressive strength (UCS) values of up to approximately 350 MPa (Read, et al., 1999). Intact rock strength varies with lithology; sandstone typically exhibits higher UCS values than associated mudstone or siltstone beds. Intact strength decreases markedly with increasing degree of weathering to as low as 1 to 5 MPa. A key difficulty in laboratory determination of intact rock strength in Torlesse greywacke is the frequent presence of hairline or incipient fracturing, which can adversely influence test results and lead to underestimation of true intact strength. Indirect field and laboratory index tests, such as the Schmidt hammer rebound test and Point Load Index test, are useful for estimating intact rock strength and for calibrating laboratory triaxial and UCS test results, particularly where truly fracture-free specimens cannot be obtained.

4.2 Rock mass

Use of the generalised Hoek–Brown failure criterion (Hoek, et al, 2002) for estimating rock mass parameters in slope stability modelling is considered appropriate for very blocky, disintegrated or sheared Torlesse greywacke. As mentioned in Section 4.1, obtaining intact rock specimens for laboratory testing in Torlesse greywacke is inherently challenging. Consequently, best-practice guidance for defining the intact uniaxial compressive strength (σ_{ci}) and the Hoek–Brown material constant (m_i) is provided in Unit 7C.2, based on a combination of published laboratory test data, the authors' experience on New Zealand projects, and available literature. Unit 7C.2 also provides guidance for Geological Strength Index (GSI) assessment, defining typical rock mass classes based on the work of Read et al. (1999). The guidance includes indicative GSI ranges linked to characteristic rock mass appearance on both field exposures and borehole core. Typical rock mass parameters assessed based on the recommendations of NZGS Unit 7C.2 are shown in Table 2. These ranges are provided as starting points and must be validated on a case-by-case basis with appropriate investigation and assessment.

4.3 Discontinuities

The shear strength of discontinuity surfaces is adopted for the assessment of structurally controlled failure modes. For Torlesse greywacke, the Barton–Bandis shear strength criterion (Bandis, 1993) is considered a practical and appropriate approach for estimating discontinuity shear strength,

particularly given the difficulties associated with sampling and laboratory testing in fractured rock mass. To support the calibration of strength parameters derived from the criterion, Unit 7C.2 presents published results from direct shear testing of greywacke joint samples spanning a range of weathering grades. Guidance for recording joint roughness, strength, and weathering discontinuity conditions during engineering geological mapping is provided in NZGS guidance (NZGS, 2005).

Table 2. Typical ranges of rock mass parameters, input to the Hoek-Brown criterion.

Rock mass class	**Rock mass description**	**GSI**	**Unit Weight (kN/m3)**	**m_i**	**σ_{ci} (MPa)**
I	UW or SW – sandstone blocky	50 - 70	26.5 – 27.0	12	100 - 350
II	SW to MW – sandstone very blocky	40 - 60	25.0 – 26.0	12	50 –200 (most common range 50 – 100)
III	MW- HW sheared mudstone, interbedded sandstone / mudstone, blocky disturbed	25 -45	23.0 –25.0	9- 10	5 - 70
IV	CW-HW Interbedded sandstone mudstone, mudstone or very fine sandstone, crushed – disintegrated	15 - 35	22.0 – 24.0	8	3 - 30
V	CW HW Mudstone or fine sandstone (rock material generally sheared) – foliated laminated sheared	10- 20	20.0 – 23.0	8	1 - 10

5 Analysis and Design

Slope stability analysis in greywacke, as in any material, requires a combination of analytical skill, geological understanding, and engineering judgment. Computer modelling using limit equilibrium methods is recommended for slope stability analyses in the guidance. Emphasis is given on the need for a sound engineering geological models to form the basis of these analyses, which are developed by thorough engineering geological mapping of existing outcrops and intrusive investigations where possible, including downhole geophysical investigations.

Observationof existing nearby slopes and evaluation of their past performance are recommended to calibrate the results of computer modelling. Back analysis of failed slopes is recommended for calibrating parameters assumed in the models, recognising its limitations for modelling the exact conditions of failure. Typical slope angles for use in low-risk projects are provided, however the need for review of all designs by experienced geoprofessionals is emphasized. Seismic demand is an important part of most designs that lie within central New Zealand – that area of the country where most greywacke is found. Drawing on past earthquakes, general comments are provided on the expected failure mechanisms in future ones. For greywacke, coseismic landslides typically are disaggregated falls, slides and rock avalanches. As most failures in greywacke are expected to be brittle, and evacuative failure is so common, use of the Newmark sliding block method to estimate seismic displacements of slopes is cautioned against.

6 Unit 7C.2 derived frompractice - Wellington Case History

Landslides of greywacke slopes frequently affect residential properties, transport corridors, and infrastructure in Wellington city. Given the city's steep topography, restricted access, and the close proximity of private property, opportunities for intrusive investigation are often limited. Consequently, slope characterisation is largely dependent on observational methods, supported by experience and engineering judgement. The accumulated experience on successful analysis of slope instabilityin Wellington and elsewhere in New Zealand, underpin the development of the framework presented in Unit 7C.2.

An example of a ~20 m-high slope in a suburb of Wellington city where a landslide occurred is shown in Fig. 2. Engineering geological mapping on the slope aimed to develop the engineering geological model and assist interpreting the failure mechanisms (Fig. 3), a process that is recommended in Unit 7C.2. The mapping identified unfavourably oriented discontinuities and a highly weathered, highly fractured, low-strength rock mass in the upper slope, coincident with the failure zone. The failure took place during very wet conditions, with elevated water content of the slope materials inferred to have

further reduced the strength of both the rock mass and its discontinuities. In this case, the predominant failure mechanism was interpreted to be principal mechanism 2 of Table 1, involving a combination of translational movement along discontinuities and a rotational component through the poor-quality rock mass. Additionally, failure of individual blocks governed by the dip and orientation of discontinuities (principal mechanism 1 of Table 1) was observed at the top of the slope.

The selection of rock-mass and discontinuity parameters followed the methods recommended in Unit 7C.2, employing the generalised Hoek–Brown and Barton–Bandis criteria, and was further refined through back-analysis, a process supported in this case by knowledge of the failure conditions and experience on local slope performance. Stability analysis commenced with the structurally controlled principal mechanism 1, using discontinuity parameters, and the resulting stabilisation measures were then tested and calibrated for the more complex translational failure mechanism 2, modelled using limit equilibrium slice methods and a combination of discontinuity and rock mass parameters. Cases examined include static with normal water pressures, elevated water pressures to simulate high rainfall conditions, and seismic loading. Similar stabilisation strategies as the one followed in this case history, comprising rock anchors, shotcrete facing, and sub-horizontal drainage targeted at the upper slope, are included in the practical, experience-informed methods included in the guidance.

7 Conclusions

The NZGS Slope Stability Guidance series has been developed to address an identified gap in existing guidance for slope stability assessments and analysis in New Zealand. The objective of the guidance series is to transfer accumulated knowledge of experienced local professionals and existing local and international studies to engineering practice, thus ensuring a consistent and structured approach in investigating, analysing and mitigating slope instability, which is a significant geotechnical risk in New Zealand. Unit 7C.2 of the series, provides practical guidance for slopes formed in Torlesse greywacke rock. The recommendations are based on local experience, complemented by published data on failure mechanisms and laboratory testing, and internationally established rock engineering principles. This collective knowledge ensures the guidance remains robust and relevant, offering a consistent and evidence-based approach even in challenging, data-poor settings. By systematically integrating observational methods, engineering geological mapping, back-analysis of failures and modern modelling techniques, the framework supports practitioners in applying consistent methodologies for slope assessment and make informed decisions for remediation strategies tailored to site-specific conditions. The principles of developing the guidance series and their objectives can form a transferable example for developing similar practical and efficient documents worldwide.

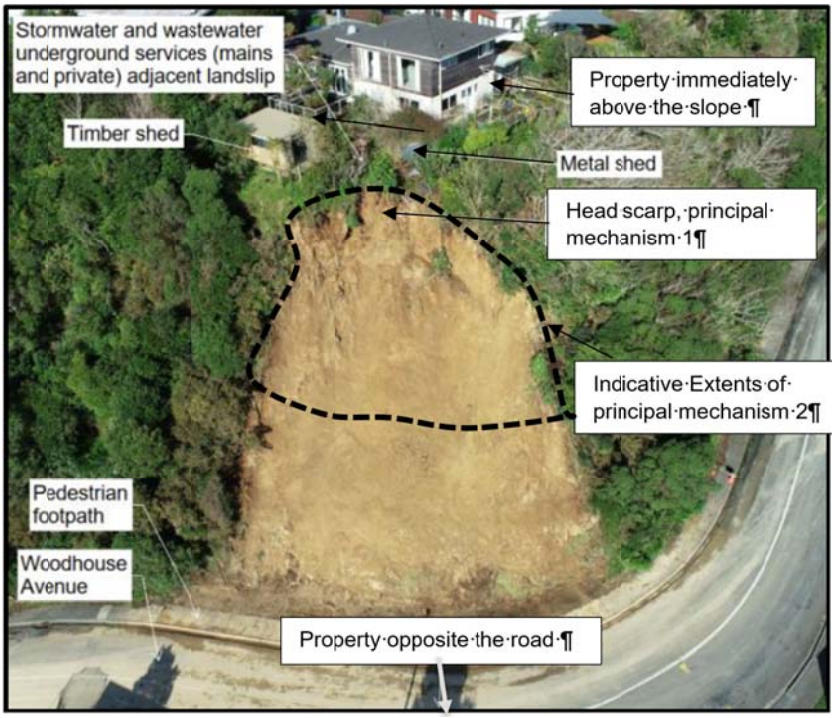


Fig. 2. View of the slope in Wellingtonafter the landslide (Stantec, 2023, modified from Tonkin + Taylor, 2022).

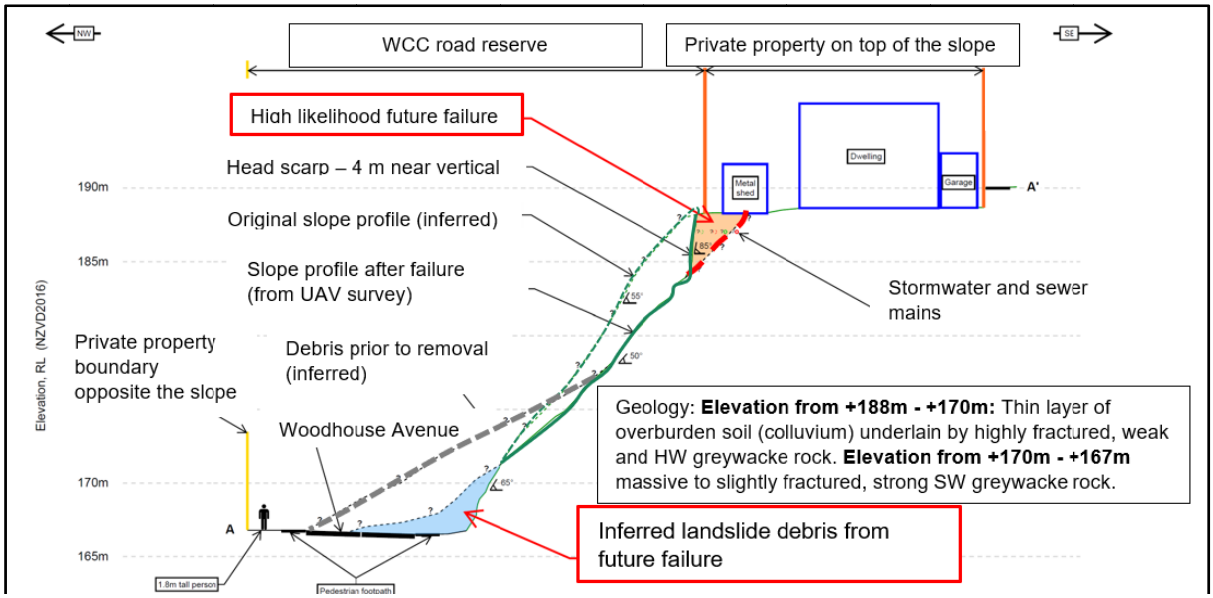


Fig. 3 Engineering geological model and failure mechanisms of the slope (Stantec, 2023, modified from Tonkin + Taylor, 2022).

References

Bandis, S. (1993). Engineering properties and characterization of rock discontinuities. (J. Hudson, Ed.) Comprehensive Rock Engineering: Principles, Practice and Projects, 1, 155-183.Pergamon Press, Oxford.

Begg, J. G., & Mazengarb, C. (1996). Geology of the Wellington area. Scale 1:50,000. Lower Hutt.: Institute of Geological & Nuclear Sciences,Lower Hutt, New Zealand

Hoek, E., Carranza-Torres, C., & Corkum, B. (2002). Hoek-Brown failure criterion-2002 edition. Proceedings of NARMS-Tac, 1(1), pp. 267-273. Toronto, Canada, July 7–10, 2002. University of Toronto Press.

Mason , D., & Brabhaharan, P. (2024). Lessons from the 2016 Kaikōura earthquake for design of cut and fill slopes in New Zealand. Proceedings 8th International Conference on Earthquake Geotechnical Engineering. (8ICEGE), Osaka, JapanMay 7–10, 2024.

NZGS. (2025). NZGS Guidelines - Slope Stability Guidance - Available Units. Retrieved from nzgs.org: https://www.nzgs.org/libraries/slope-stability-guidance-available-units/. Accessed February 2026.

NZGS. (2025). Slope Stability Guidance Unit 7C.2 – Torlesse Greywacke. Retrieved from nzgs.org: https://www.nzgs.org/slope-stability-guidance-unit-7c-2-torlesse-greywacke/. Accessed February 2026

Price, R., Mortimer, N., Smith, I., & Maas, R. (2015). Whole rock geochemical reference data for Torlesse and Waipapa terranes, North Island, New Zealand. New Zealand Journal of Geology and Geophysics, 58(3), 213-228.https://doi.org/10.1080/00288306.2015.1026832

Read, S., Richards, L., & Perrin, N. (1999). Applicability of the Hoek-Brown Failure Criterion to New Zealand Greywacke Rocks. Proceedings of the 9th International Congress on Rock Mechanics, pp. 655–660,Paris France, 25–28 August 1999.

Singeisen, C., Massey, C., Wolter, A., Kellett, R., Bloom, C., Stahl, T., .Jones, K. (2022). Mechanisms of rock slope failures triggered by the 2016 Mw 7.8 Kaikoura earthquake and implications for landslide susceptibility. Geomoprhology(415), 4-17.https://doi.org/10.1016/j.geomorph.2022.108386

Stantec, (2023). 16 – 18 Woodhouse Avenue Landslide – Design Statement. Wellington City Council, Wellington, New Zealand.

Suneson, N. (1993). The geology of the Torlesse complex along the Wellington area coast, North Island, New Zealand. New Zealand Journal of Geology and Geophysics., 36, 369-384.https://doi.org/10.1080/00288306.1993.9514582

Tonkin + Taylor. (2022). Woodhouse Avenue Karori. Initial Inspection Report, Wellington City Council, Wellington.

Analysis of Underground Roadway Stability under Geomechanical Parameters Uncertainty using RS2 Finite Element Modelling

P. Małkowski & M. Kulula
AGH Universityof Krakow, Krakow, Poland
kulula@agh.edu.pl
0000-0003-0870-438X & 0009-0008-0843-7174

Abstract

Underground roadway stability is still often assessed using a single deterministic set of rock mass inputs, which can mask the influence of natural variability in stiffness and strength. This study quantifies the effect of uncertainty in Young's modulus (E) and uniaxial compressive strength (UCS) on roadway performance using RS2 finite-element modelling. Laboratory testing of core specimens from an underground mine provided E and UCS datasets for three lithological units: claystones, siltstones, and sandstones, which were used to define input distributions. UCS was modelled as normally distributed for all lithologies, while E was normal for claystone and siltstone and lognormal for sandstone to reflect observed skewness and non-negativity.

Three complementary scenarios were analysed: (1) a deterministic Base case using laboratory mean E and UCS, (2) an ensemble mean response (μ) from 200 Latin Hypercube realisations per lithology, and (3) a statistical condition ($\mu-0.5\sigma$) reported by RS2 Interpret. Outputs focused on crown vertical displacement and roof strength factor (SF), extracted along a standardised offset query line to ensure consistent comparisons.

Results show that uncertainty effects concentrate in the weakest unit: the claystone-dominated lithology governs convergence demand and stability margin, with crown convergence reaching 28.6 mm and SF_{min} dropping to 0.96 under $\mu-0.5\sigma$. Siltstone and sandstone exhibit lower convergence and generally higher SF, providing consistency checks. Combining μ and $\mu-0.5\sigma$ offers a practical screening basis for separating expected performance from a less favourable statistical condition in variable ground.

Keywords

Underground roadway stability, Geomechanical uncertainty, Latin Hypercube sampling, RS2 modelling, Probabilistic analysis.

1 Introduction

The inherent variability of rock mass parameters creates significant challenges for decision-making in geotechnical engineering (Phoon et al. 2022). This study evaluates roadway stability using three complementary simulation scenarios that progressively move from a deterministic benchmark toward a probabilistic interpretation. The analysis investigates how different deterministic and probabilistic interpretations of laboratory-derived E and UCS affect predicted roadway response while all other parameters are held constant. The three scenarios comprised: (1) a deterministic Base case, (2) an ensemble mean response (μ) derived from Latin Hypercube realisations, and (3) a statistical condition ($\mu - 0.5\sigma$) extracted in RS2 Interpret.

The Base scenario represented the conventional deterministic approach: the use of the laboratory-derived mean values of *UCS* and Young's modulus (*E*) for each lithological unit. Its role is to provide a reference point for interpreting how much the predicted response changes once variability is acknowledged, and to mirror typical design practice where "best-estimate" properties are adopted (Phoon & Kulhawy 1999; Baecher 2003).

In the second scenario, μ represents the ensemble mean response obtained from 200 Latin Hypercube realisations for each rock type. This scenario is most useful for serviceability-type interpretation because it represents the expected model response while filtering out the influence of low-probability but high-consequence combinations within the input space (Zhao et al. 2021).

The third scenario corresponds to the statistical condition ($\mu - 0.5\sigma$) available in RS2 Interpret after the 200 Latin Hypercube realisations were completed. In this study, it is used as a practical lower-bound response indicator for comparing crown displacement and strength factor against the deterministic Base case and the ensemble mean response. In weak or variable ground, such a condition is useful because it highlights how stability margins change when the response shifts away from the central tendency toward a less favourable part of the probabilistic output range (Phoon & Kulhawy 1999; Baecher 2003; Do et al. 2022).

While probabilistic approaches have been applied to tunnel stability, fewer studies examine how parameter uncertainty derived directly from laboratory datasets propagates into numerical roadway stability predictions using practical sampling methods such as Latin Hypercube sampling. Małkowski et al. (2021) showed that the statistical processing of geomechanical input data had a substantial effect on numerical modelling results. Recent reliability analyses of deep tunnels also show that variability in rock mass properties can noticeably change predicted stability, even when deterministic results appear acceptable (Kumar et al. 2024). In this study, UCS and Young's modulus (E) were obtained from laboratory uniaxial compression tests of cylindrical specimens from three lithological units (claystones, siltstones, sandstones), providing the datasets used to define the input distributions and summary statistics. These parameters were then used to populate the three modelling scenarios described above, enabling consistent comparison of roadway stability response across rock types.

2 Geomechanical Input Characterisation

Uniaxial compressive strength (UCS) and Young's modulus (E) were determined from laboratory testing of drill core specimens obtained from an underground mine in Poland, following ISRM suggested methods (Ulusay and Hudson 2007). Core specimens had a nominal diameter of approximately 47 mm and height-to-diameter ratio of 2.5. Load rate was 0.5–1.0 MPa/s. All tests were performed under dry conditions at room temperature. Axial strain was derived from machine displacement measurements. Young's modulus was evaluated as the average modulus, calculated from the linear portion of the stress–axial strain curve. The laboratory dataset comprised 50 claystones, 79 siltstones, and 42 sandstones.

2.1 Young's modulus (*E*) distribution

Claystones and siltstones were represented by normal distributions, whereas sandstones were represented by a lognormal distribution to preserve non-negativity and accommodate observed right-skewness (Table 1).

Table 1. Statistics and probability distributions for Young's modulus, E, used as input into RS2.

Rock type	Number of Samples	Distribution	E mean [GPa]	SD [GPa]	E min [GPa]	E max [GPa]
Claystone	50	Normal	7.64	2.32	1.97	12.10
Siltstone	79	Normal	11.97	1.53	8.17	15.56
Sandstone	42	Lognormal	16.25	2.62	12.07	26.78

2.2 UCS Distribution

Table 2 shows normal distribution modelling for all three rock types. The adopted distributions capture the observed increase in strength level from claystone to sandstones, while preserving comparable scatter across datasets. The paired E–UCS samples define the probabilistic input space used in subsequent RS2 simulations for output statistics of crown displacement and strength factor.

Table 2. Statistics and probability distributions for UCS, used as input into RS2.

Rock type	Number of Samples	Distribution	UCS mean [MPa]	SD [MPa]	UCS min [MPa]	UCS max [MPa]
Claystone	50	Normal	45.07	15.91	11.52	71.37
Siltstone	79	Normal	72.57	14.06	42.80	102.78
Sandstone	42	Normal	106.56	15.30	79.07	139.72

3 Numerical model

Numerical analyses were carried out using the finite element software RS2 (version 11.027) under plane strain conditions. The model represents a horseshoe-shaped underground roadway with a width of 6m and a height of 4m, excavated in a homogeneous rock mass per analysis (each lithology modelled separately). The model size was ca. 60 m ×90 m. All model boundaries were fixed ($u_x = 0$, $u_y = 0$) at sufficient distance from the excavation to minimise boundary influence. Initial in-situ stresses were applied prior to excavation, corresponding to a depth of approximately 700 m (σ_v = 17.5 MPa), in lithological state of stress $\sigma_v = \sigma_H = \sigma_h$.

Rock mass behaviour was modelled using the generalised Hoek–Brown failure criterion with residual strength included ($\sigma_{cr} = 0.1\ \sigma_c$). The adopted RMR values were 40 for claystone, 50 for siltstone, and 60 for sandstone. Elastic–plastic analyses were performed using a staged excavation approach, consisting of an initial intact rock stage followed by instantaneous excavation of the roadway. No support elements were included at this stage, as the analyses were intended to first evaluate inherent ground stability. A graded finite element mesh with triangular elements was adopted. Mesh density was increased near the roadway boundary.

For probabilistic analyses, a sample size of 200 Latin Hypercube realisations was adopted in RS2 to obtain stable statistical estimates while maintaining computational efficiency (Fenton & Griffiths 2008). Only Young's modulus (E) and uniaxial compressive strength (UCS) were treated as random variables, assumed to be statistically independent, while all other parameters were held constant. Model outputs focused on crown vertical displacement and strength factor distributions. For interpretation, RS2 summary outputs were used to extract the Base file values, the ensemble mean response (μ), and the statistical condition ($\mu - 0.5\sigma$) for each lithology. Roof stability was assessed using Strength Factor (SF) extracted along a query line parallel to the crown/shoulder boundary and offset 0.4–1.4m into the rock mass to minimise boundary artefacts and standardise extraction across scenarios (Rocscience 2026).

4 Results and Discussion

4.1 Vertical Displacement

Vertical displacement provides a direct measure of roadway convergence demand and is therefore used here as the primary serviceability indicator (Fig. 1). In the claystone rock mass, the base case yields a peak displacement of 27.0 mm, with deformation concentrated around the excavation boundary (Fig. 1a). The probabilistic ensemble mean shows a similar pattern with a slightly lower peak of 26.9 mm (Fig. 1b), indicating that sampling of UCS–E variability only marginally changes the expected deformation relative to the deterministic benchmark. In contrast, the $\mu - 0.5\sigma$ scenario

amplifies deformation, with peak displacement rising to 28.6 mm, about 5.93% above the base case (Fig. 1c). For the sandstone rock mass, deformation remains much smaller across all scenarios, with peak displacement of 7.81 mm in the base case, 7.89 mm for the ensemble mean, and 8.20 mm under $\mu-0.5\sigma$ (Fig. 1d–f). This indicates that, unlike claystone, sandstone response is comparatively insensitive to the imposed UCS–E variability, with only a modest increase of 4.99% in the adverse case relative to the base case. Overall, the comparison shows that less favourable probabilistic response conditions increase deformation demand mainly in the weaker claystone, whereas the stronger sandstone provides a comparatively stable serviceability response under the same stress conditions.

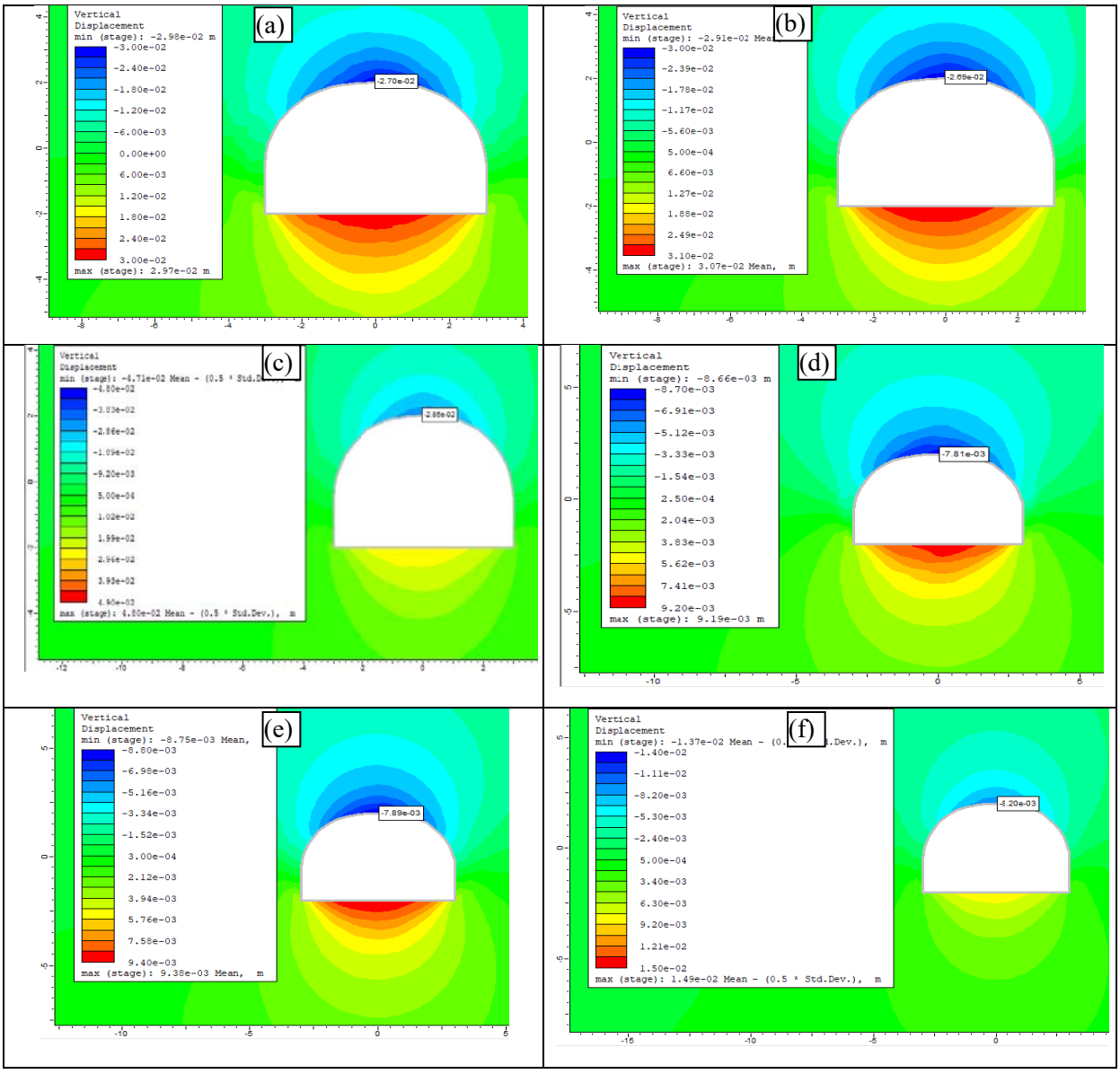


Fig. 1 Vertical displacement contours: for the claystone rock mass(a) base case, (b) ensemble mean, (c) μ−0.5σ, for the sandstone rock mass (d) base case, (e) ensemble mean, (f) μ−0.5σ.

4.2 Strength Factor

For the claystone rock mass, the strength factor (SF) response indicates a near-limit state along the offset roof query line, with scenario selection strongly influencing whether the crown is interpreted as stable or yield-prone (Fig. 2a–c). In the base case, the crown query line spans 1.00–1.25, with a local minimum of 1.00, implying that parts of the roof/shoulder region are at the threshold of yielding (Fig. 2a). The ensemble mean shifts the full query line above unity (1.02–1.38), reducing the apparent risk relative to the deterministic benchmark (Fig. 2b). In contrast, the μ−0.5σ case compresses the crown response tightly around unity (0.96–1.07) and produces three locations with SF < 1.0, indicating an enlarged yield-prone roof zone under the $\mu-0.5\sigma$ statistical condition (Fig. 2c).

For the sandstone rock mass, the SF field is more regular and symmetric, but the crown response also remains close to the SF = 1 threshold (Fig. 2d–f). The minimum SF increases from 1.00 in the base

case to 1.01 for the ensemble mean, before dropping to 0.98 under $\mu-0.5\sigma$. Overall, both lithologies remain sensitive to scenario definition at the crown, with the probabilistic mean slightly increasing the apparent stability margin and the $\mu-0.5\sigma$ case reducing it below 1. Unlike the displacement results, the SF response shows a weaker lithological contrast, indicating that local crown stability remains scenario-sensitive in both rock masses.

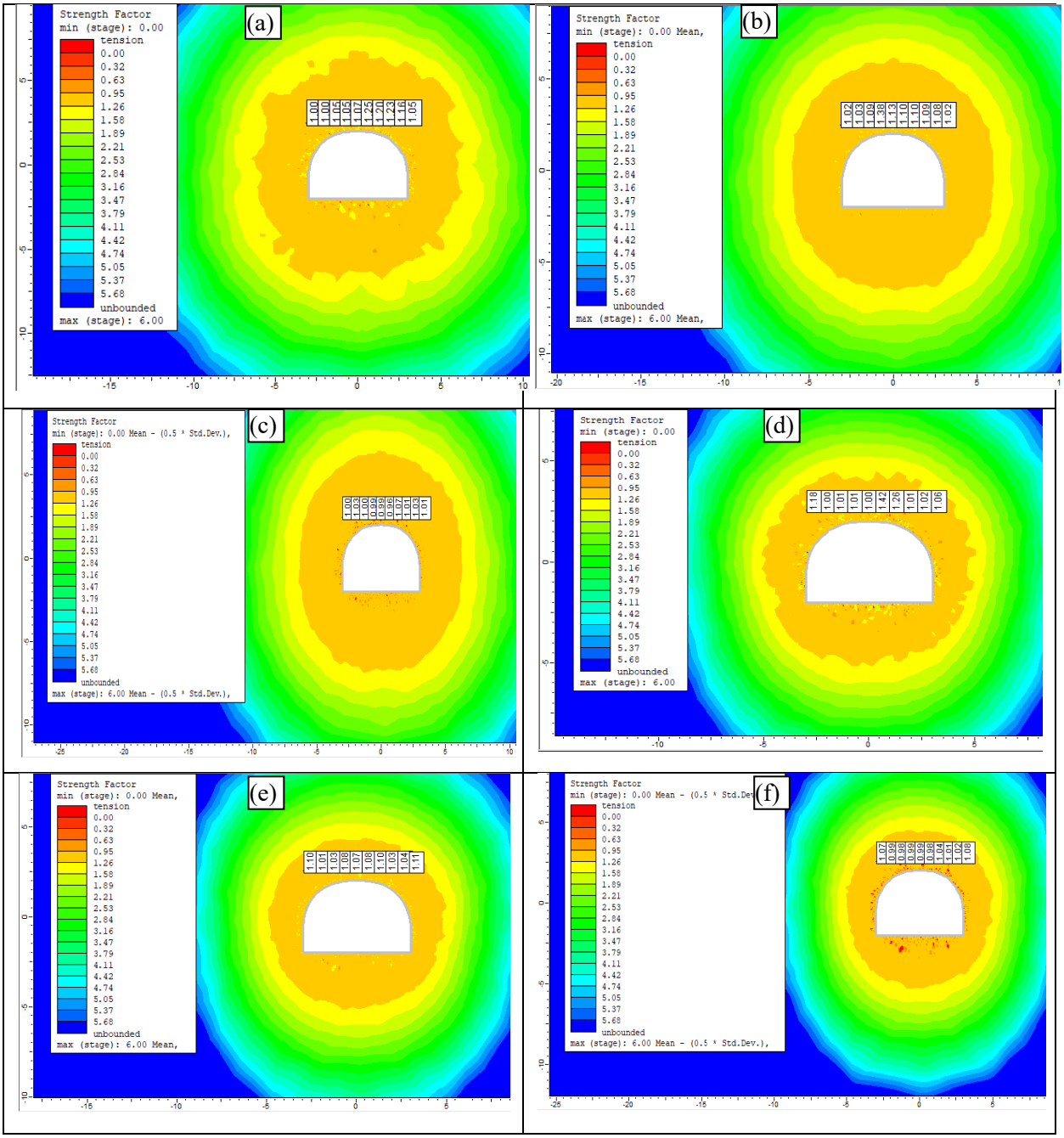


Fig. 2 Strength factor (*SF*) contours for: the claystone rock mass (a) base case, (b) ensemble mean, (c) μ−0.5σ,the sandstone rock mass (d) base case, (e) ensemble mean, (f) μ−0.5σ.

4.3 Cross-lithology analysis

Consistent with reliability-based rock engineering practice (Einstein et al. 2010), the cross-lithology results show that claystone governs both convergence demand and crown stability margin, whereas the stronger rock masses show lower $|u_y|$ and generally higher SF values (Table 3). Siltstone occupies an intermediate position between claystone and sandstone, with crown displacement of 14.30 – 17.90 mm and SFmin ≥1.00 in all scenarios, indicating that uncertainty mainly reduces reserve capacity rather than triggering yield. From a design perspective, μ represents expected serviceability, whereas $\mu-0.5\sigma$ provides a practical lower-bound check on the model response; where it gives SF < 1.00 at the roof or a marked increase in crown displacement, preliminary support decisions should be guided by that less favourable condition unless support and excavation sequence are explicitly modelled (Bjureland 2020; Hoek 2023).

Table 3. Crown displacement and strength factor at the roof for each lithology and scenario.

Rock type	Scenario	$\|u_\gamma\|$ at crown (mm)	SFmin at crown	$\Delta\|u_\gamma\|$ vs Base (%)	ΔSFmin vs Base (%)
Claystone	Base	27.0	1.00	0.00	0.00
	μ	26.9	1.02	-0.37	2.00
	$\mu - 0.5\sigma$	28.6	0.96	5.93	-4.00
Siltstone	Base	15.3	1.00	0.00	0.00
	μ	14.3	1.01	-6.54	1.00
	$\mu - 0.5\sigma$	17.9	1.00	16.99	0.00
Sandstone	Base	7.8	1.00	0.00	0.00
	μ	7.9	1.01	1.02	1.00
	$\mu - 0.5\sigma$	8.2	0.98	4.99	-2.04

5 Conclusion

Probabilistic RS2 simulations using Latin Hypercube sampling show that uncertainty in Young's modulus and UCS affects roadway performance, with the response controlled by the weakest lithology. The claystone rock mass governs behaviour: under the $\mu-0.5\sigma$ statistical condition, crown displacement increases to 28.6 mm and the stability margin reduces to SF_{min} = 0.96, showing that a less favourable probabilistic response can move the system closer to yield. Siltstone and sandstone show lower displacement demand overall, while siltstone maintains $SF_{min} \geq 1.00$ across scenarios. Taken together, μ and $\mu-0.5\sigma$ provide a practical basis for preliminary design screening by separating expected performance from a less favourable statistical condition in variable ground.

References

Baecher GB (2003) Reliability and statistics in geotechnical engineering. John Wiley & Sons, Chichester

Bjureland W (2020) Reliability-based design of rock tunnel support. KTH Royal Institute of Technology, Stockholm.

Do DP, Guo X, Dias D (2022) Probabilistic Stability Analysis of Deep Rock Tunnel Excavated by Mechanized Tunneling Considering Anisotropic Initial Stresses. Applied Sciences 12:7479. https://doi.org/10.3390/app12157479.

Einstein HH, Sousa RL, Karam K, et al (2010) Rock slopes from mechanics to decision making. In: Rock Mechanics in Civil and Environmental Engineering. CRC Press, Lausanne (Switzerland), pp 3-13.

Fenton GA, Griffiths DV (2008) Risk Assessment in Geotechnical Engineering. In: Risk Assessment in Geotechnical Engineering. John Wiley & Sons, Ltd, pp i–xvii.

Hoek E (2023) Practical Rock Engineering. Rocscience, North Vancouver, British Columbia, Canada.

Kumar A, Maurya S, Tiwari G (2024) Reliability analysis of deep tunnels in spatially varying brittle rocks using interval and random field modelling. International Journal of Rock Mechanics and Mining Sciences 181:105836. https://doi.org/10.1016/j.ijrmms.2024.105836.

Małkowski P, Niedbalski Z, Balarabe T (2021) A statistical analysis of geomechanical data and its effect on rock mass numerical modeling: a case study. International Journal of Coal Science and Technology, 8(2), pp. 312–323, https://doi.org/10.1007/s40789-020-00369-2.

Phoon K-K, Cao Z-J, Ji J, et al (2022) Geotechnical uncertainty, modeling, and decision making. Soils and Foundations 62:101189, https://doi.org/10.1016/j.sandf.2022.101189.

Phoon K-K, Kulhawy FH (1999) Characterization of geotechnical variability. Canadian Geotechnical Journal 36:612–624.

Rocscience (2026) RS2 Documentation_Query Boundary. https://www.rocscience.com/help/rs2/documentation/rs2-interpret/material-queries/query-boundary?utm_source=chatgpt.com,accessed 9 Feb 2026.

Ulusay R, Hudson JA (2007) The Complete ISRM Suggested Methods for Rock Characterisation, Testing and Monitoring 1974-2006. ISRM Turkish National Group.

Zhang H, Luo F, Yang S, Wu Y (2023) Probabilistic analysis of crown settlement in high-speed railway tunnel constructed by sequential excavation method considering soil spatial variability. Tunnelling and underground space technology 140:105342,https://doi.org/10.1016/j.tust.2023.105342.

Zhao H, Li S, Zhu C (2021) Uncertainty analysis of rock tunnel based on fractional moment and dimensional reduction method. International Journal of Rock Mechanics and Mining Sciences 139:104656, https://doi.org/10.1016/j.ijrmms.2021.104656.

Transforming Element-Level Testing into Boundary-Value Experiments through Distributed Fibre Optic Sensing

Q. Llabjani & L. Laloui
Laboratory of Soil Mechanics (LMS), Swiss Federal Institute of Technology Lausanne (EPFL), 1015 Lausanne, Switzerland
qaim.llabjani@epfl.ch
0000-0003-1428-1352

A. Ferrari
Laboratory of Soil Mechanics (LMS), Swiss Federal Institute of Technology Lausanne (EPFL), 1015 Lausanne, Switzerland
Engineering Department, Università degli Studi di Palermo, Italy

P. Marschall
Nationale Genossenschaft für die Lagerung radioaktiver Abfälle (Nagra), 5430 Wettingen, Switzerland

Abstract

Gas migration experiments in low-permeability shales are inherently boundary-value and time dependent problems, yet interpretations are often based on boundary pressures/fluxes and point deformation sensors. This work reports a high-pressure triaxial experiment on Opalinus Clay instrumented with distributed fibre optics sensing (DFOS) to measure spatiotemporally resolved surface strains during resaturation, water permeability steps and gas pressurisation under representative stress conditions. After quasi-isochoric resaturation, constant head water permeability tests were performed under isotropic total stress (20 MPa). Gas was then injected from the bottom while maintaining a constant top water backpressure (2 MPa), with bottom gas pressure increased stepwise up to 19.5 MPa and subsequently reduced. DFOS revealed clear spatial and temporal responses, such as end-controlled wetting-induced swelling during resaturation, and during high-pressure fluid injection, an expansion dominated by the injection side coupled to transient outflow that decays during constant high gas pressure. DFOS successfully captured the interplay between porewater displacement and gas migration, and the changes on effective stress and resulting strain. These observations provide spatial and temporal constraints for coupled hydro-mechanical interpretation and model calibration beyond standard boundary measurements.

Keywords

Opalinus Clay, Gas Transport, Hydro-Mechanical Response, Distributed Fibre Optics, Triaxial Testing.

1 Introduction

Gas migration in clay-rich formations is relevant to several subsurface applications, including deep geological disposal of radioactive waste (Nagra 2002), geological CO_2 storage (Busch et al. 2008) and subsurface energy storage and production (Zivar et al. 2021; Passey et al. 2010). In the context of deep repositories, gases generated by corrosion, degradation processes and radiolysis may accumulate in the repository. For instance, while clay host rock presents many advantages thanks to its low permeability, it also limits dissipation of generated gases. This can increase pore pressures, modify effective stresses and influence the modes of gas transport (Levasseur et al. 2020).

Despite extensive experimental work (Romero et al. 2013, Gonzalez-Blanco et al. 2016, 2022, 2025; Minardi 2018; Llabjani et al. 2025a), interpreting and modelling gas injection tests in clay-rich geomaterials remains challenging (Finsterle et al., 2025). A key reason is that gas injection is a boundary-value process: imposed inlet and outlet pressures, together with stress boundary conditions, generate strong and evolving internal gradients in pore pressure and deformation. When interpreted under Representative Element Volume (REV) assumptions, these gradients are implicitly averaged out, removing the spatial information required to resolve the internal processes that govern gas entry, migration, and dissipation. This contributes to divergent interpretations of transient two-phase displacement processes. However, achieving such spatiotemporal characterisation remains challenging. Gas flow experiments at high stress levels require sophisticated setups, yet most still rely on point-based measurements such as linear variable differential transformers (LVDTs) or strain gauges, which cannot capture the distributed nature of the deformation.

Distributed fibre optic sensing (DFOS) provides an untapped opportunity to increase observability in multiphase flow experiments under high stress conditions by measuring strain quasi-continuously along an optical fibre bonded to the specimen surface. When integrated into a triaxial setup, DFOS can resolve where deformation develops during hydro-mechanical testing (Llabjani et al., 2025b). The objective of this contribution is to present a triaxial experiment on Opalinus Clay (OPA) instrumented with DFOS and to highlight the key spatiotemporal deformation pattern that constrain interpretation of the hydro-mechanical response during gas pressurisation.

2 Material and methods

2.1 Material

The tested material is Opalinus Clay, the host rock selected for the Swiss deep geological repository. The specimen was prepared as a cylindrical core suitable for triaxial testing, with dimensions of 43.69 mm in diameter and 39.5 mm in height, and a mass of 147.22 g. Bedding was oriented horizontally, such that axial loading and fluids injection were applied perpendicular to bedding.

The specimen was characterised by a bulk density of 2.486 g/cm^3 and a void ratio of 0.128. Some desaturation was observed, with a water content of 3.1%, a degree of saturation of 67%, and a total suction of 68.9 MPa. These values indicate conditioning effects observed in deep OPA cores (Tuttolomondo et al., 2024) and reflect the partial drying that occurs between drilling and laboratory preparation. This initial state highlights the need for a controlled resaturation phase to restore full saturation before further testing. Mercury intrusion porosimetry (MIP) performed on the same OPA core sample provided a dominant pore size of about 8 nm, and a maximum pore diameter of about 60 nm, corresponding to a gas entry pressure of about 4.8 MPa based on the Young–Laplace equation.

2.2 Test setup

The experiment was performed using a high-pressure triaxial cell allowing control of axial and radial total stresses (Minardi 2018; Kim et al. 2025, Llabjani et al., 2025b). Volume/Pressure Controllers (VPCs)allow independent control of water and gas pressures at the top and bottom specimen surface boundaries(Fig. 1a). Distributed fibre optics measure strain quasi-continuously along the fibre length by tracking changes in the backscattered optical signal. In this study, an optical frequency-domain

reflectometry (OFDR) interrogator was used to obtain strain profiles with sub-millimetric spatial resolution along the bonded fibre. The fibre was deployed on the specimen lateral surface in two configurations (Fig. 1b): (i) 8 axial segments distributed around the circumference, providing axial surface strain along height, (ii) 5 circumferential loops at distinct elevations, providing radial strain under the axisymmetric triaxial conditions and the transverse isotropy of OPA. This configuration offers dense spatiotemporal strain measurements over the surface, with more than 1'500 points.

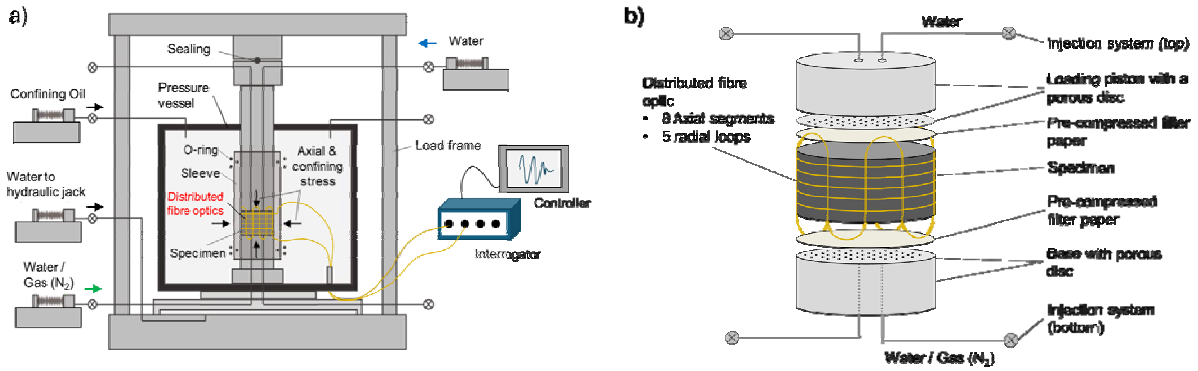


Fig. 1 Experimental set-up: (a) high pressure triaxial cell, and (b) detailed view of the specimen holder including the distributed fibre optics showing the configuration of axial and radial optical fibre segments.

2.3 Test procedure

The test sequence comprised first a resaturation under quasi-isochoric conditions, followed by constant head water permeability steps under constant total stress, and finally, gas (nitrogen) pressurisation.

Resaturation was achieved by placing the specimen in contact with synthetic water at 200 kPa. Axial and radial stresses were initially set to 2 MPa and progressively increased to counteract the swelling induced by wetting, thereby maintaining quasi-isochoric conditions. Once strain and inflow had stabilised, the water pressure and both stresses were raised by 2 MPa to further promote saturation through air dissolution. At the end of this phase, the stresses were reduced to an isotropic level of 20 MPa, which served as the initial condition for the subsequent tests. Intrinsic water permeability was then measured under steady-state flow and constant external stress. Three pressure gradients were applied by setting the bottom water pressure to 2, 5, and 10 MPa, while maintaining the top pressure at 1 MPa. Bottom outflow was monitored and used to calculate permeability following Darcy's law. During the gas phase, the top water pressure was held constant ($u_{w,top}$ = 2 MPa), and gas pressure was applied at the bottom ($u_{g,bot}$) in a sequence of steps up to 19.5 MPa and then reduced to 5 MPa. The applied stress and pressure histories are summarised in Fig. 2.

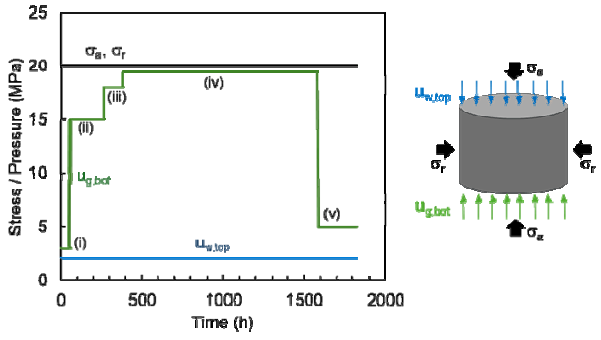


Fig. 2 Applied stress (σ_a, σ_r) and fluid pressure ($u_{g,bot}$, $u_{w,top}$) sequences during the gas injection phase.

3 Results and discussion

The results are presented using the soil mechanics sign convention, where compressive stresses and contractive strains are taken as positive. Given the distributed nature of the measurements, strain data are presented both as time series at five height intervals from top to bottom (H1-H5) (Fig. 3, Fig. 4) and as spatiotemporal fields over the developed lateral surface of the specimen (Fig. 5).To keep the presentation concise, results are reported primarily in terms of radial surface strain from the fibre loops, which provides the most robust deformation observable in this setup.

As OPA permeability is extremely low, boundary flow rates are small (order 0.1-1 mm³/h in this test). Interpretation therefore focuses on flow sign, persistence over long durations and integrated volumes, rather than short-term rate fluctuations.

3.1 Resaturation

During resaturation under quasi-isochoric conditions, average swelling strains remained small (−0.08%), but DFOS showed a pronounced boundary-value response. Swelling initiated at the wetted ends and progressed inward, whereas the specimen centre initially showed contractive strains as axial and radial stresses were increased to maintain quasi-isochoric conditions (Fig. 3). This confirms that the specimen experienced multiple stress–hydraulic paths during resaturation due to the wetting front progression rather than a single representative path.

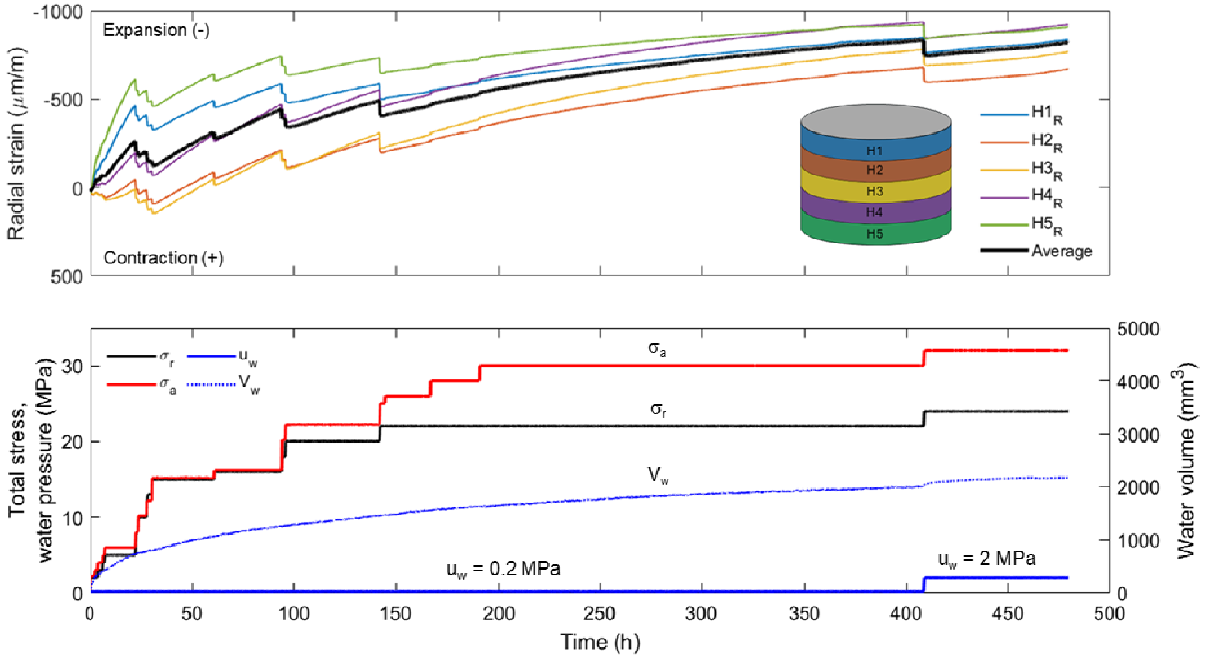


Fig. 3 Water saturation phase: time evolution of radial strains averaged over five height intervals (H1–H5), together with applied axial and radial total stresses(σ_a, σ_r), external water pressure (u_w), and injected water volume (V_w)

3.2 Water permeability

Following resaturation, intrinsic water permeability was assessed by constant head steps under isotropic total stress of 20 MPa. Bottom water pressure was increased sequentially (2, 5, 10 MPa) while top water pressure was maintained at 1 MPa. Because injected volumes were small and sensitive to temperature fluctuations, permeability was quantified from late-time behaviour of the 5 and 10 MPa steps. Mean flow rates were approximately 0.70 mm^2/h (5 MPa step) and 1.12 mm³/h (10 MPa step), resulting in intrinsic permeabilities on the order of1×10^{-21} m^2 for the applied stress state.

3.3 Gas injection

The gas injection phase was performed under isotropic total stress (20 MPa), with water backpressure $u_{w,top}$ = 2 MPa and bottom gas pressure ($u_{g,bot}$) applied in sequences up to 19.5 MPa (remaining bellow total stress).For sequence (i) differential gas-water pressure was below gas entry estimated from MIP. Therefore, both deformation and outflow remained negligible, providing a baseline prior to further pressurisation. When gas pressure was increased to 15 MPa (sequence ii) and then 18 MPa (sequence iii), a coupled response developed: water outflow initiated at the top boundary and expansion concentrated toward the injection side (H5), with peak radial expansions of approximately −0.07% (ii) and −0.10% (iii) (Fig. 4). The strain field exhibited a strong height gradient, with markedly larger strains toward the injection side (Fig. 5). This coupling between boundary drainage and injection-side expansion was consistent with gas access near the injection boundary and associated porewater displacement/pressurisation and effective stress reduction mainly through the connected water phase.

Sequence (iv) ($u_{g,bot}$ = 19.5 MPa, maintained constant) provided a strong time-dependent response. Under fixed boundary pressures ($u_{g,bot}$ held high and $u_{w,top}$ constant), radial expansion reached a peak (−0.12% near H5) and then partially reversed, while boundary outflow decayed over time to near-zero flux. This peak-and-relaxation response under constant boundary conditions is consistent with

transient redistribution during pressurisation followed by dissipation of internal gradients as drainage proceeds (Llabjani et al. 2025).During depressurisation (sequence (v), $u_{g,bot}$ reduced to 5 MPa), water uptake was recorded at the top boundary and radial contraction is observed. This reversal was consistent with re-equilibration during gas depressurization induced by reduced capillary pressure.

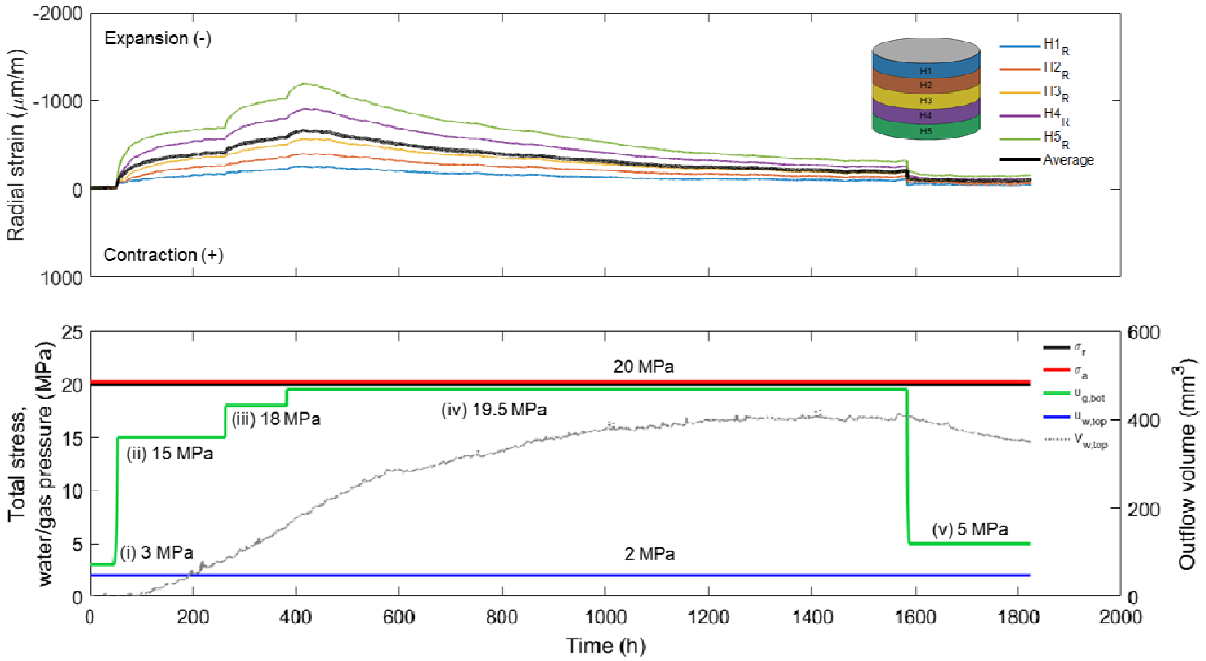


Fig. 4 Gas injection test: time evolution of radial strains averaged over five height intervals (H1–H5), together with applied axial and radial total stresses(σ_a, σ_r), water backpressure ($u_{w,top}$), and gas pressure ($u_{g,bot}$).

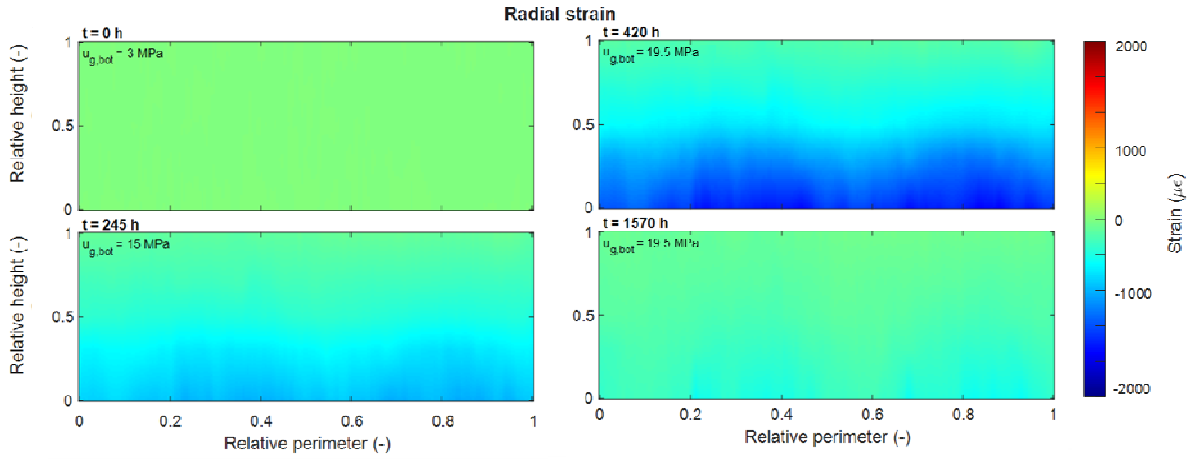


Fig. 5 Two-dimensional visualisation of the radial strain field on the specimen's lateral surface during gas testing. Radial strain measured by the radial loops is mapped onto the specimen lateral surface at selected times (t = 0, 245, 420, and 1570 h). Colours indicate strain magnitude in με (compression positive, extension negative), referenced to t = 0 h.

A key contribution of DFOS in this study is that the strain field provides spatial and temporal constraints on effective stress evolution. In coupled two-phase hydro-mechanical behaviour, deformation reflects effective stress changes driven by porewater and gas pressures, scaled by saturation. For modelling, the dataset constrains multiple coupled components simultaneously by capturing both the spatial and temporal response of the tested specimen. The height-dependent deformation requires reproducing pore-pressure redistribution under bottom gas pressurisation and top drainage. This response depends on flow properties, mechanical properties, and their coupling. The transient response in sequence (iv), where deformation relaxes and outflow decays under constant boundary pressures, adds a time-dependent constraint linking these properties. With more than 1,500 strain measurements per time step, the large dataset enables evaluation against a dense spatiotemporal field rather than a single global variable. This opens element-scale testing to spatial observations, enabling model-support physical understanding and reducing the risk of simulations that reproduce averaged behaviour while misrepresenting internal deformation patterns. This new level of observability in experimental geomechanics enables improvement of the safety and efficiency of complex geosystems.

4 Conclusion

This DFOS-instrumented triaxial experiment on Opalinus Clay provides spatiotemporally resolved deformation information during resaturation, water permeability loading and gas pressurisation under representative stress conditions. DFOS shows that resaturation is spatially heterogeneous with swelling being controlled by water front progression. Furthermore, gas pressurisation generates expansion on the injection side, coupled to time-dependent relaxation under constant high gas pressure. By extending spatial resolution far beyond traditional instrumentation, DFOS transforms geomechanical element testing interpreted under REV assumptions into direct boundary-value observation. This shift provides additional constraints for constitutive, numerical and data-driven model development and offers a step change in experimental geomechanics. The approach improves the interpretation of coupled processes and opens new pathways for the analysis and modelling of complex geomaterials across a wide range of subsurface engineering applications.

References

Nagra (2002) Project Opalinus Clay. Safety Report: Demonstration of disposal feasibility for spent fuel, vitrified high-level waste and long-lived intermediate-level waste. NTB 02-05. Nagra, Wettingen

Busch A, Alles S, Gensterblum Y, Prinz D, Dewhurst DN, Raven MD, Stanjek H, Krooss BM (2008) Carbon dioxide storage potential of shales. International Journal of Greenhouse Gas Control 2 (3): 297–308.https://doi.org/10.1016/j.ijggc.2008.03.003

Zivar D, Kumar S, Foroozesh J (2021) Underground hydrogen storage: A comprehensive review. International Journal of Hydrogen Energy 46 (45): 23436–23462.https://doi.org/10.1016/j.ijhydene.2020.08.138

Passey QR, Bohacs KM, Esch WL, Klimentidis R, Sinha S (2010) From Oil-Prone Source Rock to Gas-Producing Shale Reservoir – Geologic and Petrophysical Characterization of Unconventional Shale-Gas Reservoirs. International Oil and Gas Conference and Exhibition in China, China, 8–10 June 2010. https://doi.org/10.2118/131350-ms

Levasseur S, Collin F, Daniels K, Dymitrowska M, Harrington J, Jacops E, Kolditz O, Marschall P, Norris S, Sillen X, Talandier J, Truche L, Wendling J (2021) Initial state of the art on gas transport in clayey materials. Deliverable D6.1 of HORIZON 2020 project EURAD, Work Package Gas. EURAD, European Commission Grant Agreement No. 847593.

Romero E, Senger R, Marschall P, Gómez R (2013) Air tests on low-permeability claystone formations. Experimental results and simulations. Springer Series in Geomechanics and Geoengineering. Springer, Berlin Heidelberg: 69–83.https://doi.org/10.1007/978-3-642-32492-5_6

Gonzalez-Blanco L, Romero E, Jommi C, Li X, Sillen X (2016) Gas migration in a Cenozoic clay: Experimental results and numerical modelling. Geomechanics for Energy and the Environment 6: 81–100.https://doi.org/10.1016/j.gete.2016.04.002

Gonzalez-Blanco L, Romero E, Marschall P, Levasseur S (2022) Hydro-mechanical response to gas transfer of deep argillaceous host rocks for radioactive waste disposal. Rock Mechanics and Rock Engineering 55 (3): 1159–1177.https://doi.org/10.1007/s00603-021-02717-3

Gonzalez-Blanco L, Llabjani Q, Romero E, Ferrari A, Laloui L, Marschall P (2025) Comparative study of gas testing protocols in clayey rocks for nuclear waste repositories. Environmental Geotechnics: 1–12. https://doi.org/10.1680/jenge.24.00185

Minardi A (2018) Hydro-mechanical characterization of gas shales and Opalinus Clay shale in partially saturated conditions. Dissertation at École Polytechnique Fédérale de Lausanne (EPFL). https://doi.org/10.5075/EPFL-THESIS-8315

Llabjani Q, Ferrari A, Marschall P, Laloui L (2025) Hydro-mechanical insights for radioactive waste disposal from gas injection experiments in shale. International Journal of Rock Mechanics and Mining Sciences 186: 106039.https://doi.org/10.1016/j.ijrmms.2025.106039

Finsterle S, Llabjani Q, Ferrari A, Marschall P (2025) Two-phase analysis of oedometric gas injection tests with simplified representation of geomechanical effects. Computational Geosciences 29 (5).https://doi.org/10.1007/s10596-025-10379-1

Llabjani Q, Ait Oumeziane MA, Ferrari A, Marschall P, Laloui L (2025b) Distributed fibre optic sensing in high-pressure gas injection experiments on shale. Proceedings of the 3rd International Conference on Energy Geotechnics, Paris, France.https://hal.science/hal-05343948

Tuttolomondo A, Ferrari A, Giger SB, Laloui L (2024) Evolution of water content and suction of Opalinus Clay from recovery at the drilling site to handling in the laboratory. International Journal of Rock Mechanics and Mining Sciences 174: 105643.https://doi.org/10.1016/j.ijrmms.2024.105643

Kim J, Ferrari A, Ewy R et al. (2025) Impact of water saturation on the anisotropic elastic moduli of a gas shale. Rock Mechanics and Rock Engineering 58: 4645–4659. https://doi.org/10.1007/s00603-025-04397-9

Application of a nested modelling approach for the analysis of landslide-tunnel systems

P. Festi, D. Donati, A. Ballaera & L. Borgatti
Alma Mater Studiorum – University of Bologna, Bologna, Italy
pietro.festi@unibo.it
0009-0006-3874-7152

A. Ballaera & G. Marcato
Research Institute for Geo-Hydrological Protection (IRPI), Padova, Italy

Abstract

The interaction between landslides and transportation infrastructure represents a critical challenge in mountainous regions worldwide, with significant implications for public safety, regional connectivity, and socio-economic sustainability. Professional geoscientists and engineers often take advantage of numerical simulations to investigate the correlation between landslide movement and structural response. However, one of the main challenges of the analysis of landslide-infrastructure systems (LIS) is related to the difficulty of reliably capturing localized infrastructure damage induced by large-scale landslide processes within computationally feasible frameworks, given the contrasting spatial scales involved.

In this work, we develop a nested numerical modelling approach and explore its capability to investigate a real case study, namely the Passo della Morte LIS. The Passo della Morte landslide is a 30-million-cubic-meter active rock-block slide (moving 2-3 cm/year) crossed by a 2200-meter-long road tunnel. Since its construction, the tunnel began showing evidence of damage and deformation at the intersection with the inferred landslide basal surface. In the developed approach, a landslide-scale model, built using the finite-difference code FLAC3D, is used to capture bulk slope behaviour and stress distributions within the landslide. Custom Python and FISH scripts are then used to extract velocity fields and stress tensors from the landslide-scale model in order to transfer them to a relatively smaller, high-resolution infrastructure-scale model, built using the distinct element code 3DEC. This multi-scale numerical analysis shows that the tunnel model develops deformation patterns consistent with field observations, landslide movement patterns, and monitoring data.

The results of this work demonstrate that numerical simulations can achieve computational efficiency and physical accuracy when nested approaches are used. They also show that multi-scale simulations represent a solid pathway for advancing LIS interaction analysis toward mature frameworks, supporting evidence-based infrastructure management in landslide-prone regions.

Keywords

Nested modelling, Infrastructure-landslide interaction, Passo della Morte, Tunnel, Damage.

1 Introduction

Transport infrastructure constitutes a fundamental component of modern society, as it underpins socio-economic development and territorial connectivity. However, when traversing morphologically complex environments such as mountainous regions, its construction, development and long-term serviceability may be significantly threatened by natural hazards, including landslides. In this context, road tunnels are particularly exposed: structural damage induced by landslide movements can range from minor deformations compromising their functionality to partial or complete collapse. The consequences extend beyond physical damage, as the closure of a critical tunnel can isolate entire communities and impose severe economic costs. The critical importance of such infrastructure, together with the complexity of landslide-structure interaction mechanisms, poses significant challenges for reliable assessment and long-term risk management.

Addressing this challenge through numerical modelling is fundamentally complicated by the inherent multi-scale nature of the problem: landslides deformation may extend over surface areas of hundreds of square meters, whereas infrastructure damage manifests at centimeter-to-meter scales. Simulating both elements simultaneously within a single model at meaningful resolutions is computationally prohibitive and rarely feasible for most real-world scenarios. Existing approaches consistently struggle to achieve adequate resolution for both slope processes and structural response simultaneously (Vassallo et al. 2019). Models focused on the landslide commonly treat infrastructure as simplified boundary conditions, while models focused on the infrastructure prescribe landslide-induced actions as loading assumptions, disconnecting structural damage from actual slope kinematics. To overcome this limitation, this study proposes a nested modelling framework specifically designed to bridge the scale gap. The approach adapts established nested modelling strategies for localized high-resolution analysis within large-scale numerical models (e.g., Ciptokusumo et al. 2009) to the analysis of Landslide–Infrastructure Systems (LIS). A landslide-scale model captures bulk slope behavior and stress distributions, and the results are systematically transferred to a high-resolution infrastructure-scale model through custom data transfer procedures. The approach is applied to the Passo della Morte LIS in Friuli Venezia Giulia (Italy), a well-characterized case study where an active rock-block slide affects a 2200m road tunnel.

2 Case study

The study area is located in the Tagliamento Valley, in the north-eastern Italian region of Friuli-Venezia Giulia, within the municipalities of Forni di Sotto and Ampezzo (Fig. 1).

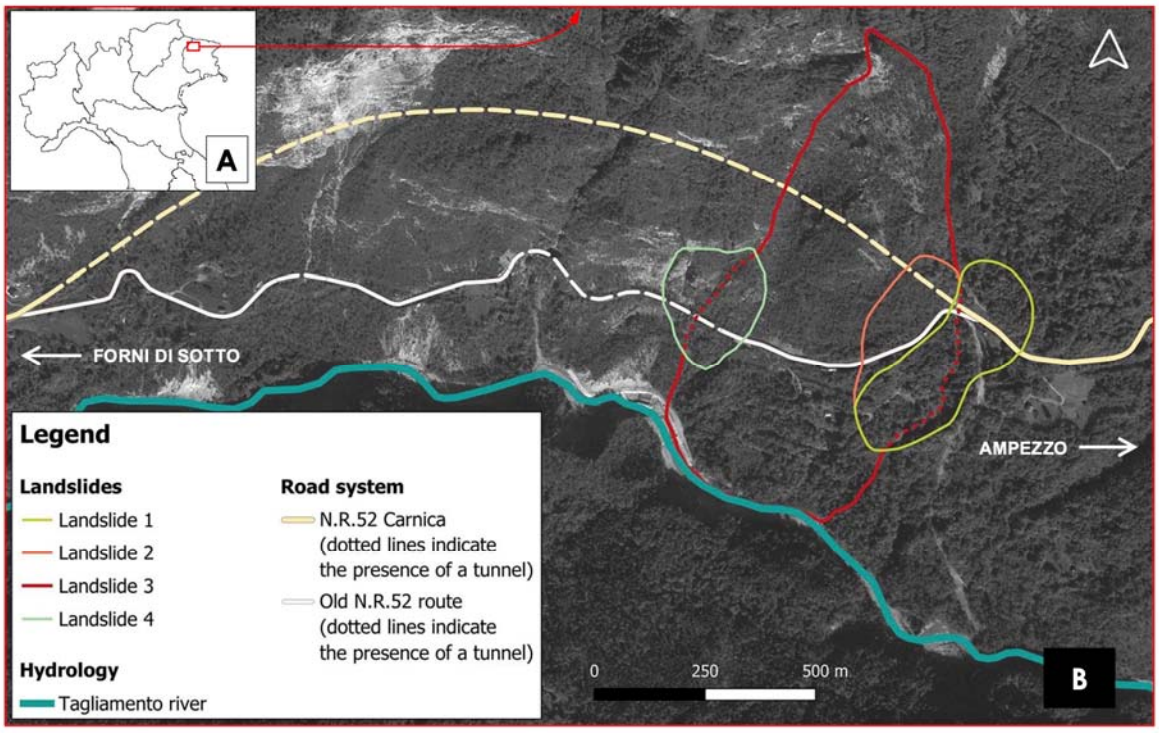


Fig. 1 a) Geographical framework, with study area outlined by the small red rectangle; b) case study area and the four landslides forming the Passo della Morte landslide system (Ballaera et al. 2024).

The area has a history of landslide hazard, as it is affected by a system of four distinct slope instabilities forming part of a larger Deep-seated Gravitational Slope Deformation (DsGSD) (Ballaera et al. 2024).Among these, the largest landslide (indicated as 'Landslide 3' in Fig. 1) commonly referred to as the Passodella Morte landslide, is classified as an active rock-block slide (Hungr et al. 2014). It extends from approximately 970 to 640 m a.s.l., with a surface area of 0.45 km², an estimated average sliding surface depth of approximately 60 m, and a volume of about 30 × 10⁶ m³ (Bossi et al. 2017). The landslide body consists predominately of a highly fractured and permeable dolomitic rock mass overlying plastic, clay-rich units. The contrast in competence between the two plays a key role in controlling slope dynamics: the weight of the fractured dolomite bears on the underlying clay-rich units, triggering slope movement. The landslide reports movements in a south-southwest direction at an average rate of 2–3 cm/year (Marcato 2007).

The study area is crossed by the National Road 52, a critical lifeline for local and regional connectivity. To bypass a section of this road affected by frequent small rockfalls, shallow landslides, and snow avalanches, the San Lorenzo road tunnel was built. It features a horseshoe section, approximately 11.50 m in width, 8.50 m in height, and an excavation area ranging from 85 to 95 m². In 1996, a heavy rainfall event resulted in a partial reactivation of the Passo della Morte landslide, causing widespread structural damage inside the tunnel, including lining cracks and concrete detachments (Fig. 2). Construction works were suspended from 1997 to 2006 while investigations and mitigation measures were carried out. The lining in the damaged portion, approximately the first 400 m from the eastern entrance (on the Ampezzo side), was entirely rebuilt using a succession of 12-m-long independent segments, designed to accommodate ongoing landslide-induced deformation, with a fully reinforced lining. A drainage tunnel was also excavated approximately 40 m below the road tunnel to reduce groundwater pressures. Despite these measures, new damage reappeared after the tunnel opening in 2008, particularly at segments 26–29 (numbered from the Ampezzo entrance), suggesting that the landslide sliding surface intersects the tunnel structure approximately at 360 m from the eastern entrance (Tedesco et al. 2020).

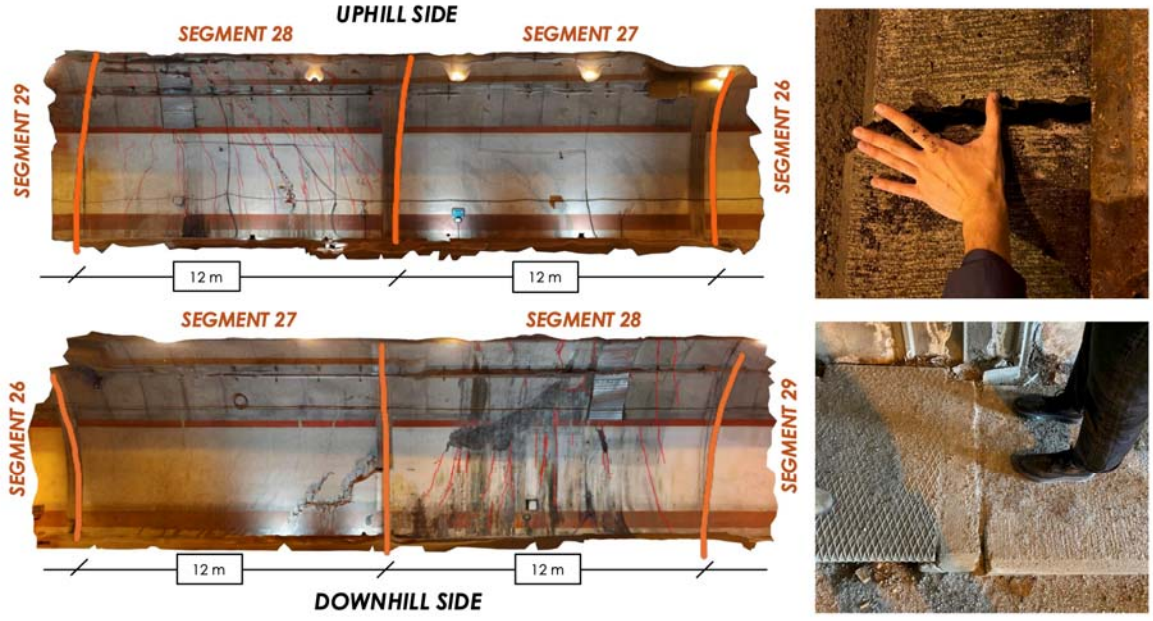


Fig. 2 Cracks pattern in segments 27 and 28, with a close-up of two concrete fractures on sidewalks at inter-segments positions; an opening of 2-3 cm is visible, revealing a discrepancy with landslide displacement rate (2-3 cm/year) and, thus, the indirect nature of landslide-tunnel interaction.

Consequently, a comprehensive monitoring system operated by CNR-IRPI (Italian National Research Council-Research Institute for Geo-Hydrological Protection) has been active since 2012, comprising inclinometers (both in-place and in-hole), piezometers, and a GNSS network to characterize slope kinematics. Since 2014, a dedicated monitoring system was also installed inside the tunnel, consisting of 24 crackmeters and 4 bi-axial clinometers, located at the most damaged segments (i.e., segments 26-29) to document the temporal evolution of structural damage.

3 Methodology

The Passo della Morte case study embodies the multi-scale integration challenges that motivate this research: landslide monitoring system operates at spatial scales of hundreds of meters, whereas tunnel monitoring targets centimeter-scale crack propagation within specific structural elements. This pronounced scale disparity, combined with the availability of comprehensive characterization and monitoring data at both scales, makes this case study suitable as a testbed for the nested framework.

The proposed workflow is structured as a hierarchical numerical strategy: a landslide-scale model captures bulk slope behaviour and provides the boundary conditions required to drive a smaller, high-resolution infrastructure-scale model. The core of the approach lies in the systematic extraction and transfer of velocity fields and stress tensors from the slope model to the tunnel model, concentrating fine-scale resolution only where structural analysis is necessary. This strategy enhances computational efficiency while preserving the mechanical consistency of the loading conditions applied to the infrastructure. Fig. 3 gives an overview of the models' geometry and constituting elements.

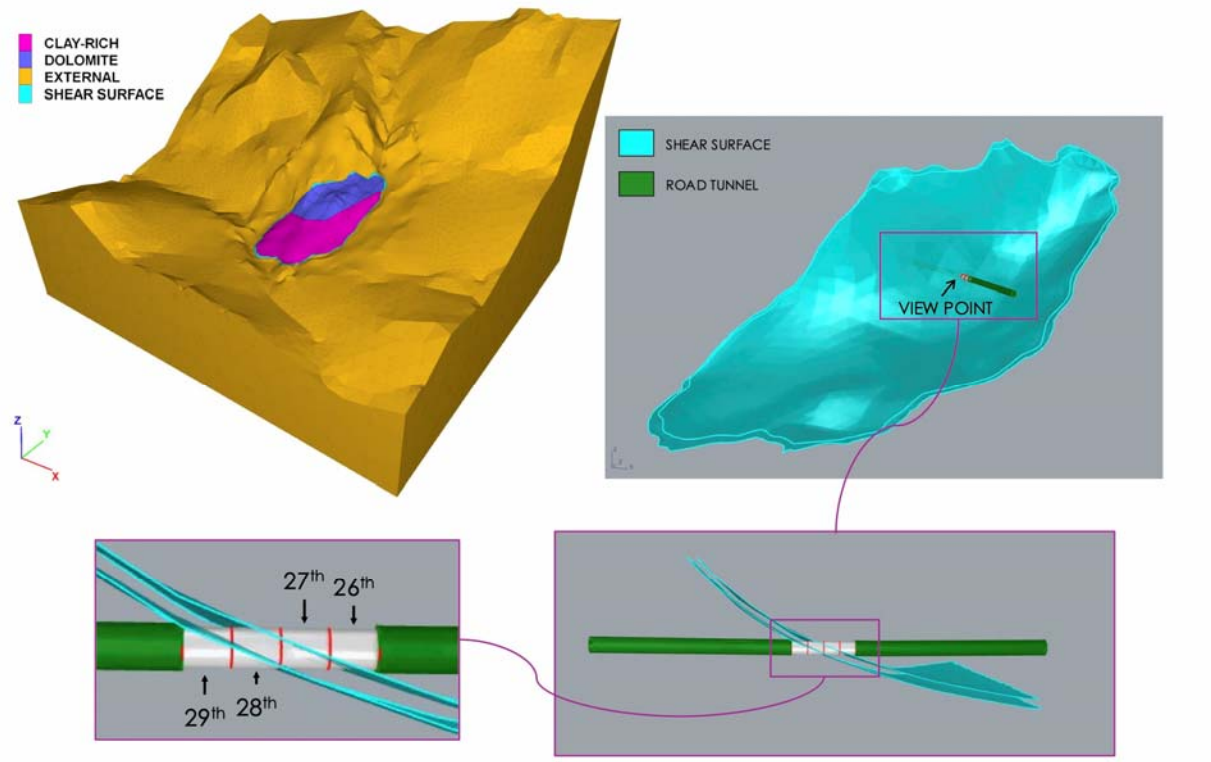


Fig. 3 Modelling elements of both the landslide-scale and the tunnel-scale model; overview of the general relative positioning of the San Lorenzo tunnel and the shear zone (represented as two identical surfaces 6 m apart).

Considering case study characteristics and modelling requirements, FLAC3D (Itasca Consulting Group, Inc. 2023) and 3DEC (Itasca Consulting Group, Inc. 2023) were selected for landslide-scale and infrastructure-scale modelling respectively. The use of two codes from the same developer facilitates the implementation of data transfer procedures, since both packages offer extensive customization capabilities through the FISH programming language and Python integration essential for implementing the multi-scale data transfer. The resulting scripts add flexibility tothe proposed methodology, as they can be readily reproduced for workflows involving different software packages.

The FLAC3D landslide model domain was defined by a bounding box approximately 3 km × 2 km × 2 km encompassing the entire Passo della Morte landslide body and extending sufficiently beyond its volume to avoid boundary effects. This domain was divided in dolomite, clay-rich units, shear zone, and the bedrock material external to the landslide body. A spatially variable mesh refinement strategy was adopted, with the finest discretization applied in a user-defined extraction volume in the immediate tunnel surroundings, ensuring a reduction of computational effort and the accurate representation of stress and deformation gradients for subsequent transfer. Lithological and geomechanical characterization from geological mapping, borehole logging, and laboratory testing data informed the selection of constitutive models and parameters. Particular attention was given to the competence contrast between dolomite and clay-rich units, which has been suggested to control landslide behaviour (Ballaera et al. 2024; Bossi et al. 2017).

Data extraction was performed within the defined volume (108 m × 30 m × 30 m) centered on segment 28, encompassing nine 12-m tunnel segments, providing a sufficient buffer around the tunnel to avoid boundary effects during data transfer. Likewise, an import volume (108 m × 20 m × 20 m) was defined in 3DEC purposely smaller than the extraction volume to ensure complete spatial mapping coverage and avoid assignment of inappropriate boundary parameters near the edges. Custom Python and FISH scripts were developed to extract velocity fields (from gridpoints) and stress tensors (from zone centroids) from the extraction volume. To ensure data integrity, the procedure incorporated redundancy strategies to prevent data loss, proximity-based mapping algorithms to maintain spatial relationships, and a visual validation to confirm that transferred fields reproduce the expected mechanical state.

The 3DEC tunnel model incorporated the San Lorenzo tunnel structure and its immediate surrounding: stable bedrock material, landslide material (entirely composed by the clay-rich units), shear zone, and tunnel lining. The model explicitly represents the independent 12-m tunnel segments as discrete blocks, enabling simulation of relative inter-segment movements. Boundary conditions were derived directly from the transferred velocity and stress fields, replacing the simplified loading assumptions typically used in tunnel analysis. Damage mechanism simulation targeted the reproduction of structural deformation and crack patterns observed in monitoring data, enabling direct validation of the nested multi-scale approach.

4 Results

Model predictions at the landslide scale were validated against field monitoring data. Virtual monitoring points placed at the coordinates of GNSS stations (Ballaera et al. 2024) GNSS2 (upper, dolomitic domain) and GNSS4 (lower, clay-rich domain) reproduce the observed landslide spatial gradient: virtual GNSS4 exhibits greater displacement than virtual GNSS2, consistent with the rock-block slide classification in which the weaker underlying clay-rich units accommodate most of the deformation. Comparison with inclinometer I-16 (Ballaera et al. 2024) confirms good agreement in both displacement magnitude and direction at the shear zone depth.

At the tunnel scale, the 3DEC model show spatial correlation between tensile stress concentrations, principal strain increments, and maximum displacement magnitudes, all focused on the shear zone intersection, consistent with the roto-translational deformation mechanism anticipated for the tunnel as a response to the landslide kinematics. Direct comparison with crackmeter data provides further quantitative validation: on the downhill side of the tunnel, the model predicts closure between segments 29 and 28 and opening between segments 28 and 27, in agreement with monitoring data from inter-segment crackmeters. The spatial correspondence between the oblique tensile stress band in the numerical model and the documented crack distribution in the tunnel (Fig. 4) further confirms that the nested approach reproduces global structural response mechanisms.

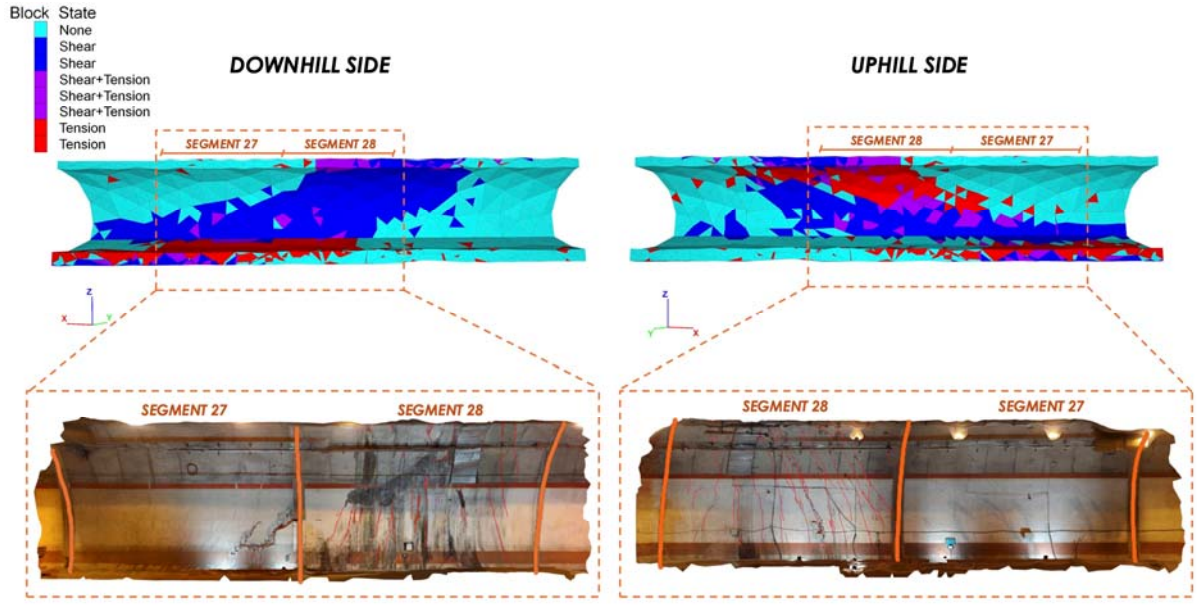


Fig. 4 Comparison between model resulting stress state and actual cracks pattern in the mostly damaged segments.

5 Conclusions

This work demonstrates the feasibility of a nested modelling approach for the analysis of landslide-infrastructure interaction. Applied to the Passo della Morte case study, the workflow successfully reproduced first-order landslide kinematics at the slope scale and structural deformation patterns at the tunnel scale. The qualitative agreement between numerical predictions and crackmeter monitoring logs not only validates the data transfer procedure but also confirms that velocity fields and stress tensors extracted from a landslide-scale model can provide physically meaningful initial state and boundary conditions for an infrastructure-scale model.

The deliberate use of two different numerical methods, FDM at the slope scale and DEM at the tunnel scale, demonstrates that the framework can integrate heterogeneous modelling paradigms, broadening its applicability to scenarios where a single numerical approach would be inadequate to account for the physical or structural characteristics of each system component.

At the same time, the approach is not yet a ready-to-use solution for routine engineering practice. Its successful application demands comprehensive site characterization spanning both scales, interdisciplinary knowledge, and substantial computational resources. The value of this work lies therefore not in providing an immediately deployable tool, but in establishing a viable methodological pathway and identifying the data, tools, and expertise required to advance the understanding of landslide-infrastructure interaction.

References

Ballaera A, Festi P, Borgatti L, Bossi G, and Marcato G (2024). Investigation and Monitoring for Ever-Updating Engineering Geological Models: The Example of the Passo Della Morte Landslide System. *Geosciences* 14 (4): 94. https://doi.org/10.3390/geosciences14040094.

Bossi G, Schenato L, and Marcato G (2017). Structural Health Monitoring of a Road Tunnel Intersecting a Large and Active Landslide. *Applied Sciences* 7 (12): 1271. https://doi.org/10.3390/app7121271.

Ciptokusumo J, Weide-Zaage K, and Aubel O (2009). Investigation of Stress Distribution in via Bottom of Cu-via Structures with Different via Form by Means of Submodeling. *Microelectronics Reliability*, 20th European Symposium on the Reliability of Electron Devices, Failure Physics and Analysis, vol. 49 (9): 1090–95. https://doi.org/10.1016/j.microrel.2009.07.043.

Hungr O, Leroueil S, and Picarelli L (2014). The Varnes Classification of Landslide Types, an Update.*Landslides* 11 (2): 167–94. https://doi.org/10.1007/s10346-013-0436-y.

Itasca Consulting Group, Inc. (2023a). 3DEC 9.0 Software Documentation. https://docs.itascacg.com/itasca900/3dec/docproject/source/3dechome.html?node5845.

Itasca Consulting Group, Inc. (2023b). FLAC3D 9.0 Software Documentation. https://docs.itascacg.com/itasca900/flac3d/docproject/source/flac3dhome.html?node2069.

Marcato G (2007). Valutazione della Pericolosità da Frana in Località Passo della Morte. PhD, University of Modena e Reggio Emilia.

Tedesco G, Marcato G, Bossi G, and Schenato L (2020). Monitoraggio della galleria di San Lorenzo in rapporto ai movimenti franosi esterni nel periodo dal 22 novembre 2018 al 21 novembre 2019. https://iris.cnr.it/handle/20.500.14243/366041.

Vassallo R, Mishra M, Santarsiero G, and Masi A (2019). Modeling of Landslide–Tunnel Interaction: The Varco d'Izzo Case Study. *Geotechnical and Geological Engineering* 37 (6): 5507–31. https://doi.org/10.1007/s10706-019-01020-x.

What are the representative values for the mechanical properties of a rock joint?

J. Spross & F. Johansson
Division of Soil and Rock Mechanics, KTH Royal Institute of Technology, Stockholm, Sweden
johan.spross@byv.kth.se
0000-0001-5372-7519
0000-0002-8152-6092

I. Pérez-Rey
CINTECX, Universidade de Vigo, GESSMin Group, Vigo, Spain
0000-0003-0883-7211

Abstract

The European design standard (code) for geotechnical structures – Eurocode 7 – has been updated in a second generation. The new code has a larger scope than the current code: the new code will also concern the safety of dams and levees, as well as rock engineering structures above ground. For many European countries, this will likely be a considerable change, as neither rock slopes nor dams until now have been designed using a European design code. In this context, there is a need to study how spatial variability in rock mass properties best is managed in the verification of limit states, i.e. determination of their representative values (formerly characteristic values). In this paper, we discuss specifically how representative values can be determined using statistical methods for relevant rock properties, like the friction coefficient of rock joints, for verification of the structural safety regarding sliding stability of dams founded on rock. As a basis for the investigations in the paper, we use data from laboratory direct shear tests on the peak shear strength of rock joints. The result illustrates the importance of having a sufficient number of samples and the need for a thorough understanding of the effect of the sampling location. We hope that this contribution will stimulate a broader discussion in the scientific rock engineering community on limit state verification of rock engineering structures, as there are currently very few studies on this issue.

Keywords

Eurocode 7, Representative value, Dams, Rock joint, Friction angle.

1 Introduction

The second generation of the Eurocodes are being published. For rock engineers the most relevant parts are the general Eurocode EN 1990 (CEN, 2023) and the three parts of EN 1997 (CEN, 2024a; 2024b; 2025), known as Eurocode 7. The second generation aims, among other things, to provide

better applicability to above-ground rock engineering structures, such as rock slopes and rock foundations (Lamas et al, 2023). For the rock engineering community, this means a safety philosophical shift from applying deterministic safety factors to applying limit state design, which is based on a probabilistic view on structural safety (Hansen, 1956; Cornell, 1969). For practising engineers, limit state design implies safety verification using partial factors, which is a simplified, semi-probabilistic verification method.

While the applicability of limit state design to design of rock engineering structures has been questioned on theoretical grounds in some papers (see e.g. Harrison, 2019; Cao and Harrison, 2021), the current literature is largely in the state of inquiry. There are also issues that need to be studied further regarding the practical application of limit state design to rock engineering structures. For example, Spross et al. (2025) noted that there is little to no guidance on how to determine representative values (either as statistically determined *characteristic values* or their subjective counterpart *nominal values*) for common rock engineering properties. There is also no guidance on how to determine and address the uncertainty of geometrical properties such as the orientation of discontinuities.

For verification of rock slope stability, as well as sliding stability of concrete dams, the friction angle of the rock joint is a key parameter. In practice, the determination of the friction angle is often characterised by challenging sampling and consequently small datasets. In this context, there is a need to study how spatial variability in rock mass properties like the friction angle best is managed in the verification of limit states, i.e. the determination of their representative values. In this paper, we discuss specifically how representative values can be determined for friction angles of rock joints, for verification of the structural safety regarding sliding stability of concrete dams founded on rock.

2 Limit state design principles for sliding stability

According to limit state design concepts, structural failure is defined by the ultimate limit state, which can be described by a limit state function $G(\mathbf{X})$, where $\mathbf{X}$ contains uncertain properties which are described as random variables. When $G(\mathbf{X}) < 0$, failure occurs. Thus, the goal of the safety verification is to ensure that the probability $P(G(\mathbf{X}) < 0)$ is less than the acceptable failure probability p_{target}. For sliding stability of a concrete dam founded on rock, the limit state function can be described by $G = N' \tan\varphi - E$, where N' is the effective normal force to the sliding plane, $\tan\varphi$ is the friction coefficient of the rock joint, and E is the driving force (action) along the sliding plane. Cohesion is ignored for simplicity.

Applying partial factors in the safety verification EN 1990 (Eq. 8.1 in CEN, 2023), the design action E_d shall be smaller than the design resistance, R_d. Applying these concepts, we achieve

$$E_\text{d} \leq R_\text{d} \text{ for } E_\text{d} = \gamma_\text{F} F_\text{c} \text{ and } R_\text{d} = \frac{\tau_{dis}}{\gamma_\text{M}} = \frac{N' \tan(\varphi)_\text{rep}}{\gamma_\text{M}} \quad (1)$$

where γ_F and γ_M are partial factors, F_c is the characteristic value for the actions, τ_dis accounts for shear stress of rock-to-rock joint contact at failure, from an appropriate shear strength envelope, and $\tan(\varphi)_\text{rep}$ is the representative friction coefficient of the rock-to-rock joint. The representative value $\tan(\varphi)_\text{rep}$ can be determined either as a statistically evaluated characteristic value, or as a subjectively estimated nominal value. Both alternatives shall in principle yield the same representative value. In this paper, we focus on the determination of the characteristic value, for which Appendix A of EN 1997–1 provides some guidance. Acknowledging that the friction coefficient for the rock joint along which sliding takes place is both spatially varying and associated with epistemic uncertainty, the friction coefficient for the joint can be described as a random variable. Depending on whether the limit state is considered sensitive to spatial variability of the friction coefficient or not, the characteristic value is defined either by the 5$^{\text{th}}$ percentile of the probability distribution or by the average value of the random variable determined with 95% confidence. This distinction is discussed further in section 4.

Ideally, the characteristic value is determined from a large enough sample of laboratory tests of the friction angle from the relevant rock joint, allowing both the average value and the coefficient of variation to be statistically estimated from the data. The average value is estimated by its sample statistics $\overline{\tan\varphi} = \sum[\tan(\varphi)_i]/n$, where n is the number of independent samples. Note that the average of the angles $\bar{\varphi} \neq \text{atan}(\overline{\tan\varphi})$. The coefficient of variation is estimated from a probabilistic

characterisation of the uncertainty associated with the parameter. The total uncertainty expressed as a coefficient of variation, $V_{\tan\varphi}$, has four error components: natural variability, statistical error, measurement error, and transformation model error. The combined effect of these components can be assessed, approximately, as (JRC, 2024)

$$V_{\tan\varphi} \approx \sqrt{\Gamma^2 V_{\text{nat}}^2 + V_{\text{stat}}^2 + V_{\text{meas}}^2 + V_{\text{tr}}^2} \tag{2}$$

where the four squared V denote the respective coefficients of variations of the four error components, as indicated by the subscripts, and Γ is the variance reduction function, which takes value 1 when the limit state is sensitive to spatial variation and 0 when it is not. For the friction coefficient of a rock joint determined from laboratory shear tests, the measurement error and transformation model error are generally negligible; thus, only the natural variability and statistical error need to be accounted for. Depending on how well known the natural variability is, one can assume that $\tan(\varphi)$ is either normally distributed (for an assumed known variability) or Student's-t distributed (for unknown variability in which case the true variability σ^2 is approximated by the sample variance s^2). This gives two alternative equations (Equations 3a and 3b) for the characteristic value:

$$\tan(\varphi)_{c,N} = \overline{\tan(\varphi)}\left(1 - N_{95}\sqrt{\Gamma^2 V_{nat}^2 + V_{stat}^2}\right) = \overline{\tan(\varphi)} - N_{95}\sigma_{\tan(\varphi)}\sqrt{\Gamma^2 + \frac{1}{n}} \tag{3a}$$

$$\tan(\varphi)_{\text{c,Stud t}} = \overline{\tan(\varphi)}\left(1 - t_{95,n-1}\sqrt{\Gamma^2 V_{\text{nat}}^2 + V_{\text{stat}}^2}\right) = \overline{\tan(\varphi)} - t_{95,n-1}s_{\tan(\varphi)}\sqrt{\Gamma^2 + 1/n} \tag{3b}$$

where N_{95}denotes the one-sided 95% quantile of the standard normal distribution (i.e. $\Phi^{-1}(0.95) = 1.645$), and $t_{95,n-1}$denotes the one-sided 95% quantile of the Student's t distribution with$n - 1$ degrees of freedom. Equation 3a is simpler to evaluate than 3b but may underestimate the uncertainty especially when there are few samples. Depending on the testing program set-up, $s_{\tan(\varphi)}$, may also be challenging to determine accurately. If samples are taken from more than one discontinuity, $s_{\tan(\varphi)}$ will represent not only the within-joint variability of an identified governing sliding plane, but also between-joint variability of the averages across comparable joints in the geological domain. This variability is likely to be larger than the within-joint variability.

3 Illustrative example

To illustrate the practical challenges in determining the characteristic value of a friction coefficient, let us assume that the peak friction angle has been determined for 8 rock joint samples under a concrete dam (Figure 1).For this purpose, 8 laboratory shear tests on rock-to-rock contacts of naturally occurring discontinuities in grey coarse-grained granite are used (Table 1), as reported by Ríos-Bayona et al. (2021). The corresponding friction coefficients are presented for the peak friction angle, φ_p (°). Furthermore, we consider that the shear strength of the rock joint in the scale of the governing sliding plane can be represented as the corresponding mean value of a number of smaller laboratory direct shear tests, as shown by Rios Bayona et al. (2022).

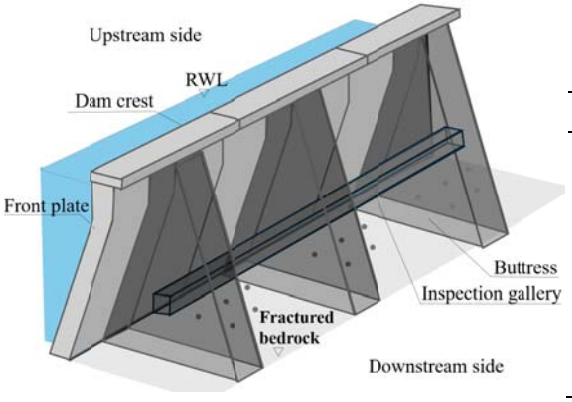


Fig. 1 Buttress dam founded on fractured bedrock.

Table 1. Friction coefficient values from 8 direct shear tests (retrieved from Ríos-Bayona et al. (2021)).

Test	Friction coefficient, $\tan(\varphi_p)$
1	tan(62.1) = 1.889
2	tan(50.5) = 1.213
3	tan(71.8) = 3.042
4	tan(63.1) = 1.971
5	tan(59.9) = 1.725
6	tan(53.5) = 1.351
7	tan(55.3) = 1.444
8	tan(58.1) = 1.607

The 8 determined friction coefficients, tan φ_p, displayed a mean value $\overline{\tan\varphi}$= 1.78, a sample standard deviations $_{\tan(\varphi)}$= 0.57, a maximum value of 3.04, and a minimum value of 1.21. (Subscript p for peak henceforth dropped for convenience). The difficulty in selecting a characteristic value does not lie solely in the statistical treatment of the data, but primarily in the geological representativeness of the samples. In rock engineering, uncertainty is often dominated by whether the tested discontinuities correspond to the actual governing sliding plane. To illustrate this distinction, three conceptual cases are considered, reflecting different assumptions in the probabilistic modelling.

Case 1: All 8 samples are taken from the relevant rock joint (A) where sliding is expected to occur. The $s_{\tan(\varphi)}$ captures the within-joint variability well, which however is of lesser importance as the mean value of the samples governs the limit state; thus Γ = 0.

Case 2: The 8 samples are obtained from 8 different comparable rock joints within the general area surrounding the dam. The specific rock joint forming the critical sliding plane is assumed unknown, which means that this is a prediction problem of sliding along a random joint (Γ = 1). In this case, $s_{\tan(\varphi)}$captures between-joint variability well but says nothing about the within-joint variability. Individual rock joints may exhibit significantly different frictional properties.

Case 3: Only 4 samples are obtained from the governing sliding plane (A), and the other 4 samples from comparable discontinuities in the same geological domain. While this likely is the most realistic sampling scenario, the evaluation of $s_{\tan(\varphi)}$ is less straightforward, as the samples represent a mix of both within-joint and between-joint variabilities. In fact, if plane A is known to be the governing sliding plane (**Case 3a**), it could be argued that the 4 samples from other joints have no effect: the problem reduces to Case 1 but with only n = 4 samples, and since Case 1 is governed by the mean value (Γ = 0), the between-joint variability is not of interest. In that case, the information from the other joints is not at all considered. With only 4 samples, the statistical uncertainty increases.

However, if the governing sliding plane is unknown (**Case 3b**), we again have a prediction problem, but now we get information about both between-joint variability and within-joint variability (albeit only from one joint). In principle, it can be argued that this can be approximated by Case 2, if we assume that $s_{\tan(\varphi)}$ evaluated from all joints now can represent both within-joint and between-joint variabilities. A more accurate assessment of Case 3b could be to set up a more advanced hierarchical model where both within-joint and between-joint variabilities are explicitly estimated, but that would require considerably more samples from all joints to be meaningful. Case 3b is therefore not further addressed in this paper.

Error! Reference source not found. and Figure 2 present representative values for the friction coefficient, determined as statistically evaluated characteristic values from the data in Table 1 for Case 1, 2 and 3a. Case 3a is represented by two results to illustrate the potential effect of random sampling, where (I) shows the result of "sampling" the four highest values of tan(φ) and (II) of "sampling" the four lowest values of tan(φ).

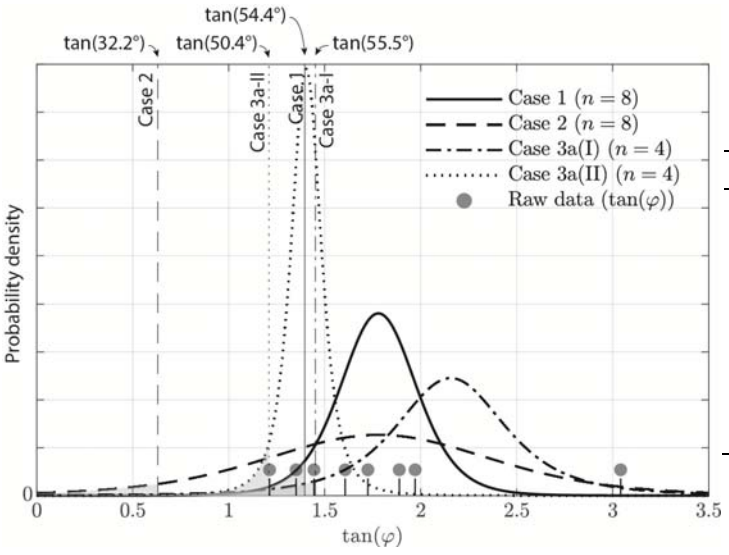


Table 2. Friction coefficients corresponding to the three cases, assuming either a normal or Student's-*t* distribution.

Case	Distribution	$\tan(\varphi)_{rep}$
1	Normal	1.45 = tan(55.4°)
2	Normal	0.782 = tan(38.0°)
3a (I)	Normal	1.66 = tan(59.0°)
3a (II)	Normal	1.27 = tan (51.7°)
1	Student's *t*	1.34 = tan(54.4°)
2	Student's *t*	0.631 = tan(32.2°)
3a (I)	Student's *t*	1.45 = tan(55.5°)
3a (II)	Student's *t*	1.21 = tan(50.4°)

Fig. 2 Estimated Student's-*t* probability distributions and evaluated characteristic values for the three cases.

4 Discussion

It is clear from the results in Figure 2 that the location of the samples and the understanding of the sliding plane governing the failure mode have a considerable effect on the calculated characteristic values. Taking samples from a rock joint that is known to be the governing sliding plane provides a considerably larger characteristic friction coefficient, than if the sliding plane is unknown. Thus, it may be more cost-effective to try to determine the governing sliding plane and take a few samples from that joint, than to try to estimate the between-joint variability by taking samples from many different joints in the area. This effect also seems to be larger than the difference between using a normal distribution and Student's-*t* distribution, at least for this type and amount of data. In this context, there is a note in EN 1997-1, paragraph A.8, saying that it is often "preferable" to use equation 3a with a conservative upper estimate of $\sigma_{\tan(\varphi)}$, than using equation 3b. The code clearly gives room for engineering judgement for handling the small sample problem. As we see in comparing Cases 3a (I) and (II), randomness in sampling can affect $s_{\tan\varphi}$ considerably in small samples. Particularly interesting is the result of Case 3a (II): Even though this case applied the four lowest values of tan(φ), the evaluated representative value is considerably larger than that of Case 2, which considered 8 samples. The reason lies in the relatively small $s_{\tan\varphi}$obtained when the four lowest samples are in a rather narrow range. This illustrates the importance of applying these statistical concepts correctly to the situation at hand, as well as the potential effect of randomness in small samples.

Worth noting is also that Eurocode 7 provides indicative values—table values—of $V_{\tan\varphi}$. For "all soils and rock", $V_{\tan\varphi}$ is in the range of 5–15% (EN1997-1, Table A.1). This indicative value directly gives the standard deviation in equation 3a via$\sigma_{\tan(\varphi)} = V_{\tan\varphi}\ \overline{\tan\varphi}$,as an alternative to determining $s_{\tan(\varphi)}$ from the test results. Using the indicative value might be particularly tempting when there is a lack of data; however, our evaluation of the 8 direct shear tests from Ríos-Bayona et al. (2021) indicates that the variability can be considerably higher than that (we had$V_{\tan\varphi}$= 32.1%), at least for this type of rock joints.

Another important issue is that we assumed that the peak shear strength of a rock joint can be represented by the mean value of a series of tests taken from a single fracture, following the approach of Rios Bayona et al. (2022). They showed that the large-scale peak shear strength is equal to the mean value obtained from small-scale (borehole) samples. However, whether this constitutes an appropriate design strategy remains a matter of debate. Several researchers have reported a negative scale effect, where the shear strength decreases with increasing scale (e.g., Pratt et al. 1974, Barton and Choubey 1977, and Bandis 1980). If such a negative scale effect exists, it means that our assumption may be unconservative. On the other hand, a comprehensive testing program recently carried out by Larsson et al. (2025) found no indication of a scale effect on the peak shear strength of rock joints. Nevertheless, further research is required before the assumption adopted in this paper—that the large-scale peak shear strength is equal to the mean value obtained from small-scale (borehole) samples—can be confidently applied in safety verification of dams.

Another comment is that the representative value of tan(φ) in this study was derived from results obtained from direct shear tests. A common alternative approach to estimate the peak shear strength is to take samples from a discontinuity, measure their general characteristics, and apply that information to a failure criterion. If this approach is adopted, a transformation model error V_{tr} must be considered according to Eq. (2), which will further increase the variability.

5 Conclusions

In this paper, an illustrative example was used to discuss how representative values according to Eurocode can be determined for the friction coefficient of rock joints, when verifying the structural safety of concrete dams against sliding in the rock foundation. The example, which uses the peak friction angle obtained from 8 laboratory direct shear tests as input, clearly illustrates not only the importance of having a sufficient number of samples, but also the need for a thorough understanding of whether the samples are taken from the governing sliding plane or are randomly sampled within the foundation. If this is not known, the design engineer may be forced to adopt a conservative approach, which significantly influence the representative value of the friction angle used in the design. This

highlights the importance of a sound understanding of the site geology, adequate site investigations, and the development of a robust ground model.

The discussed Case 3b provides the most complex collection of samples to evaluate statistically. This illustrates the fine balance between statistical rigour and practical feasibility—we see many potential pitfalls! Providing a reasonable sampling strategy for that situation and recommendation for the evaluation of the test results is an important topic for future studies.

Acknowledgements

The research presented in this paper was funded by the Swedish Hydropower Centre (SVC) (Grant No. VKU32017) and the Swedish Rock Engineering Research Foundation (BeFo) (Grant No. 512). SVC was established by the Swedish Energy Agency, Elforsk and Svenska Kraftnät together with Luleå University, KTH Royal Institute of Technology, Chalmers University of Technology and Uppsala University. http:// www.svc.nu.

References

Bandis S, Lumsden A, Barton N (1981) Experimental studies of scale effects on the shear behaviour of rock joints. *International Journal of Rock Mechanics and Mining Sciences & Geomechanics Abstracts 18*, 1–21. https://doi.org/10.1016/0148-9062(81)90262-X

Barton N, Choubey V (1977) The shear strength of rock joints in theory and practice. *Rock Mechanics 10*,1–54. https://doi.org/10.1007/ BF012 61801

Cao C. Harrison JP (2021). An example of the limitations of partial factor approaches in rock engineering. In: *Proceedings of GeoNiagara*, Niagara Falls, 26-29 September 2021.

CEN (2023). EN 1990:2023 Eurocode – Basis of structural and geotechnical design, Brussels.

CEN (2024a). EN 1997-1:2024 Eurocode 7: Geotechnical design – Part 1: General rules, Brussels.

CEN (2024b). EN 1997-2:2024 Eurocode 7: Geotechnical design – Part 2: Ground properties, Brussels.

CEN (2025). EN 1997-3:2025 Eurocode 7: Geotechnical design – Part 3: Geotechnical structures, Brussels.

Cornell CA (1969). A probability-based structural code. *ACI Journal Proceedings 66*.

Hansen JB (1956). Brudstadieberegningogpartialsikkerhederigeoteknikken [Limit design and safety factors in soil mechanics]. *Ingeniøren 65*, 383-385.

Harrison JP (2019). Challenges in determining rock mass properties for reliability-based design. In: Proceedings of the 7th ISGSR, 11-13 December 2019, Taipei, Taiwan, pp. 11-13, Research Publishing, Singapore.

JRC (2024). Reliability-based verification of limitstates for geotechnical structures: Guidelines for the application of the 2nd generation of Eurocode 7:Geotechnical design. Edited by T. Schweckendiek. JRC139408. Publications Office of the European Union, Luxembourg.

Lamas L, Burbaum U, Estaire J, Harrison J, Nuijten G, Pereira R 2023. Rock engineering design in tomorrow's geotechnical toolbox: Eurocode and the basis of structural and geotechnical design (the second generation of EN 1990 and EN 1997). *Geomechanics and Tunnelling 16*, 469-490.

Larsson J, Flansbjer M, Jacobsson L, Johansson F, Johnson E, Mas Ivars D, Pérez-Rey I (2025). A Three-Factor Experimental Study on the Effect of Specimen Size on the Shear Strength of Rock Joints. *Rock Mechanics and Rock Engineering*, 1-25.https://doi.org/10.1007/s00603-025-04954-2

Ríos-Bayona F, Johansson F, Mas-Ivars D (2021) Prediction of Peak Shear Strength of Natural, Unfilled Rock Joints Accounting for Matedness Based on Measured Aperture. Rock Mechanics and Rock Engineering. 54:1533–1550. https://doi.org/10.1007/s00603-020-02340-8

Ríos-Bayona F, Johansson F, Larsson J, Mas-Ivars D (2022). Peak shear strength of natural, unfilled rock joints in the field based on data from drill cores–a conceptual study based on large laboratory shear tests. *Rock Mechanics and Rock Engineering, 55*(8), 5083-5106. https://doi.org/10.1007/s00603-022-02913-9

Spross J, Ashcroft B, Pereira R, Stille H (2025). On the limit state design of bolted rock slopes: challenges and a way forward.In: Proceedings of the 9th ISGSR, Oslo, Norway, 25–28 August 2025.

Pratt H, Black A, Brace W (1974) Friction and deformation of jointed quartz diorite. In: Proc. 3rd ISRM Congress, Denver, p 306–310

Mobilisation of a fully grouted passive rock bolt along its length

E. Le Guidec
Univ Gustave Eiffel, Univ Lyon, GERS-RRO, Lyon, France
elise.le-guidec@developpement-durable.gouv.fr

C. Gbewade
Cerema, Bron, France
0009-0003-3240-8844

Y. Fargier
Univ Gustave Eiffel, Univ Lyon, GERS-RRO, Lyon, France
0000-0003-1139-6461

M. Bost
Univ Gustave Eiffel, Univ Lyon, GERS-RRO, Lyon, France
Cerema, Bron, France
0000-0003-0452-5931

Abstract

The ageing of hydraulic structures and the reassessment of flood parameters in light of regulatory, technical, and climatic changes are increasing the need for rehabilitation. When the theoretical stability of a structure can no longer be assured, particularly in extreme flood events, one of the reinforcement techniques considered is the use of fully grouted passive rock bolts. Groups of bolts with varying inclination angles could be set in order to withstand the two load directions causing the dam to fail by sliding or tilting. The group effect therefore must be studied through the comparison of the contribution of an isolated bolt with that of a group of bolts, and through the definition of the bolt configurations inducing this effect. This contribution depends on the mobilisation of the rebar and the surrounding environment. It appears relevant to isolate the rebar and analyse its mobilisation in order to subsequently study different configurations.

The aim of this study is therefore to characterise the mobilisation of the rebar along its length.

To achieve this, a large-scale direct shear test is carried out under constant normal stress. The mobilisation all along the rebar is monitored by optical fibre during the test. A finite element model is developed so that rebar mobilisation can be compared considering both numerical and experimental results. The validated numerical model will enable the group effect to be later studied.

Keywords

Untensioned rockbolts, Optical fibre, Finite element model, Dam reinforcement, Shear mobilisation.

1 Introduction

Rock bolting is a widely adopted technique in underground engineering and rock-slope stabilisation, and it is now being considered for the reinforcement of gravity dams (Coubard and Morel 2025), with one or several bolt rows crossing the concrete-rock interface. Configurations involving multiple rows of bolts are particularly complex, as the bolts may not mobilise simultaneously, particularly in the early stages of loading (Ferrero 1997).

For single bolts, analytical models predict that the bolt should exhibit two inflection points symmetrically located around the interface (Panet 1987; Pellet 1993). Previous experimental studies using strain gauges have characterised bolt mobilisation (Ferrero 1995; Mazzoleni and Richard 1998; Grasselli 2005; Jalalifar et al. 2006), but these measurements are limited to discrete points. Distributed optical sensing techniques have been introduced to address this limitation and tested on non-grouted rebars or on double-shear tests (Hyett et al. 2013; Forbes et al. 2017).

To gain insight into the collective behaviour of bolts reinforcing a sheared interface, we propose in this paper an innovative approach to characterise the rebar mobilisation so that it can later be distinguished from the overall response, which also includes changes in the mobilisation of the reinforced interface. This approach combines a dedicated numerical model, a large-scale experimental setup instrumented with innovative optical sensing techniques, and a derivation method to extract force resultants.

First, a large-scale direct shear test is presented evaluating the performance of optical fibre sensing for measuring the mobilisation of a bolt reinforcing a sheared concrete-concrete interface. Then, after presenting the experimental setup and a first finite element model, the bolt mobilisation along its length, as measured by optical fibre and calculated in the model, is discussed through a comparison of numerical and experimental results and through a derivation of force resultants.

2 Experimental Setup

The experiment is carried out using an exceptional device based on the Casagrande shear box concept but of large dimensions (1 m x 1.5 m shear surface) (Bidaut et al. 2006; Mazzoleni and Richard 1998). The upper box moves horizontally relative to the fixed lower box thanks to horizontal cylinders; transverse motion is restrained, while rotation of the upper box is permitted.

The purpose of this first test is to evaluate the instrumentation setup and gain a better understanding of the stress distribution along the length of a rock bolt. The test conditions are for this experiment not dam-specific. The test specimen consisted of prefabricated C40/50 concrete blocks. A 65-mm-diameter grooved steel cylindrical sleeve, inclined at 60° to the shear direction, is incorporated before casting. A 28-mm SAS 500 threaded rebar is subsequently installed inside this sleeve and grouted with a cementitious mortar (compressive strength: 33.4 MPa).

A constant normal load of 994 kN is applied by two hydraulic cylinders attached to a frame that followed the motion of the upper block, thereby maintaining normality of the applied load. Tangential displacement is imposed at a rate of 1 mm/min using horizontal cylinders with a maximum capacity of 5 MN. In order to isolate the influence of the bolt, a preliminary shear test without bolt is conducted before grouting.

The rebar is instrumented using a jacketed optical fibre bonded inside a groove running around the rebar, following a configuration similar to that of Forbes et al. (2017). In order to have only one fibre to interrogate, the fibre loops at the end of the rebar. Distributed strain measurements are obtained every 2.6 mm at an acquisition rate of 50 Hz.

Consequently, in the following analysis, two parallel fibre sections are distinguished (Fig. 1): the first encountered in the shear direction is referred to as the “upstream fibre” and the second as the “downstream fibre”. The lower end of the downstream fibre is assumed to coincide with the lower face of the bottom block, and strain profiles are plotted from the bottom to the top of the rebar. Because the rebar is inclined, the fibre coordinate does not correspond directly to elevation, requiring careful definition of the rebar-interface intersection. The initial fibre state corresponds to the beginning of the shear phase (zero-strain reference). Missing strain data due to signal loss are linearly interpolated when fewer than four consecutive measurement intervals are affected. The strain profiles are then smoothed along the bolt length using a 1-cm moving window.

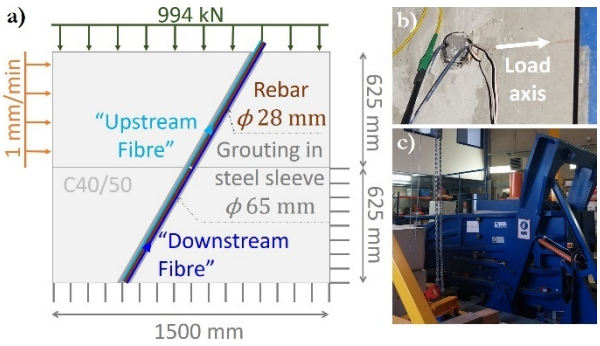


Fig. 1 Experimental setup: (a) Schematic representation of the experimental setup with the optical fibre placement relative to the loading conditions. (b) Photograph of the head of the bolt. (c) Photograph of the apparatus during test preparation.

3 Numerical model

A finite-element model is built in COMSOL v6.4. The rebar, grout, and precast blocks are explicitly modelled, but the cylindrical sleeve around the grout is not included. Interfaces between the rebar and grout, and between the grout and blocks, are assumed fully bonded. The block-to-block interface is modelled as a frictional contact with a friction coefficient of 0.75, corresponding to the measured apparent friction coefficient at 9.7 mm displacement in the preliminary shear test. All materials are treated as linear elastic and isotropic. The blocks and grout share the same concrete material properties, while the rebar is modelled as steel (Table 1). For numerical convergence, the two faces of the lower block normal to the shear direction are constrained against displacement in that direction, and vertical displacement is fixed on the bottom face. Loading is applied in two steps:

- Incremental uniform application of the normal load on the upper surface of the upper block.
- Incremental uniform application of the tangential load on the corresponding face (Fig. 1).

Table 1. Parameters used in the numerical model.

Material	Young's modulus [GPa]	Poisson's ratio [-]	Density [kg/m^3]
Concrete	38	0.2	2400
Steel	200	0.3	7800

4 Bolt mobilisation along its length

4.1 Results

In the experimental test, bolt failure occurred at a tangential displacement of 43 mm. The fibre data at the theoretical interface are presented alongside the force applied by the horizontal cylinders. Only the first 19 mm of displacement are reported here, as the optical fibre broke beyond this point (Fig. 2).

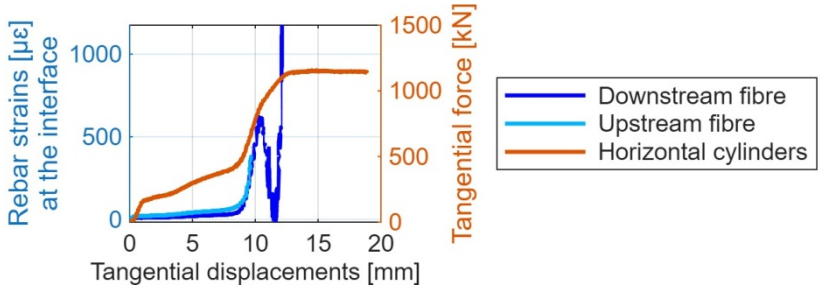


Fig. 2 Rebar strains(cyan / blue) at the theoretical interface, defined as the plane normal to the rebar axis centred at the block interface (white in Fig. 1), and tangential force from the horizontal cylinders (orange) during displacement.

The fibre sections located at the interface undergo the largest strains, which leads to significant signal distortion and early signal loss. Specifically, the upstream fibre signal is first lost at the interface once displacement reaches 9.7 mm, corresponding to a strain of 400 με (Fig. 2). The tangential force curve exhibits three distinct slopes before reaching a plateau of 1.15 MN at approximately 12.5 mm tangential displacement, which persists until bolt failure. Between 1 and 9 mm, the bolt is only lightly mobilised, consistent with the lower slope of the tangential force. After 9 mm of displacement, the bolt becomes more significantly mobilised, and this transition appears to coincide with the change in slope of the tangential force curve (Fig. 2).

Experimental (left) and numerical (right) strain profiles are compared at tangential displacements of 5, 10 and 13 mm (Fig. 3).

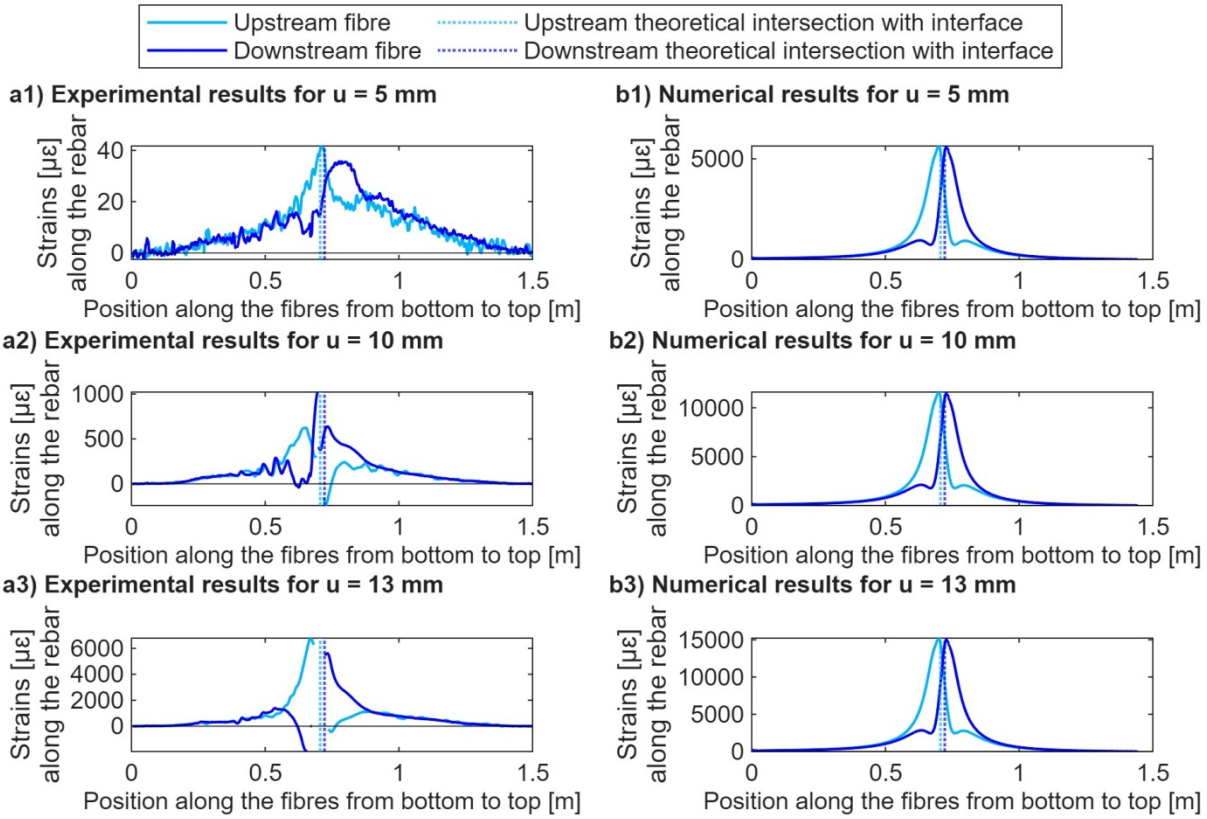


Fig. 3 Upstream (cyan) and downstream (blue) fibre-optic strain experimental (a) and numerical (b) profiles (cf Fig. 1) at 5 mm (1), 10 mm (2), and 13 mm (3) displacements (u tangential displacement of the box).

Experimental strains along the bolt (Fig. 3) increase from a maximum of 40 με at 5 mm of displacement (Fig. 3 – a1) to 8000 με at 13 mm (Fig. 3 – a3). At low levels of mobilisation, each fibre displays a single strain peak (Fig. 3 – a1), near the interface for the upstream fibre and in the upper part of the bolt for the downstream one. Starting at 9-10 mm of displacement (Fig. 3 – a2), isolated narrow peaks develop close to the theoretical intersection between the interface and the upstream fibre, quickly leading to signal loss, while two peaks appear on either side of the theoretical interface. The position of a maximum on one fibre generally corresponds to a local minimum on the other, yet their positions are asymmetric relative to the theoretical interface. With further displacement (Fig. 3 – a3), these peaks increase in amplitude and the signal remains lost in the zone adjacent to the interface.

In the numerical model (Fig. 3 – b1, b2 and b3), the bolt experiences purely tensile loading, with strain magnitudes ranging from 6000 με at 5 mm of displacement to 15000 με at 13 mm. Bolt mobilisation is concentrated within roughly the first 300 mm around the interface. The numerical strain profiles maintain a similar shape throughout shearing, with two peaks located on either side of the interface. The maximum strain on one fibre roughly coincides with a local minimum on the other.

4.2 Discussion

The approximate alignment between strain maxima and minima suggests inflection points on both sides of the interface. Experimental and numerical results show similar features, particularly at 13 mm displacement (Fig. 3 – a3 and b3), although the experimental inflection points appear more widely spaced (from 0.06 to 0.08 m versus 0.03 m in the numerical results), less centred on the theoretical interface, and less symmetric. The numerical model overestimates bolt tension, particularly at the onset of shearing (peak strain ratio of 100at 5 mm displacement, dropping to 2.5 at 13 mm).

Three modelling limitations likely explain these discrepancies. Improved representation of the concrete-concrete interface and the tilting motion of the upper block may help capture the early stages of the test more accurately. Moreover, the effect of the steel sleeve surrounding the grout, which is omitted in the numerical model, on the magnitude of the strains is not known. Nevertheless, it likely causes most of the underestimation of the spacing between inflection points: the spacing between inflection points depends on bolt diameter (Dight 1985), so adding a larger-diameter steel tube likely

increases it. Finally, accounting for grout damage and grout-rebar interaction should improve the shape and concentration of strains; for example, grout failure would promote a more progressive deformation pattern (Azuar 1977).

Assuming a Young's modulus of 200 GPa for the steel rebar, these strain results allow the calculation of stresses along the optical fibres (Fig. 4a). By treating the rebar as a compound bending beam, the normal force and bending moments along the rebar can be computed (Fig. 4b). Assuming an infinitesimal gauge spacing then allows estimation of the shear force along the rebar (Fig. 4c).

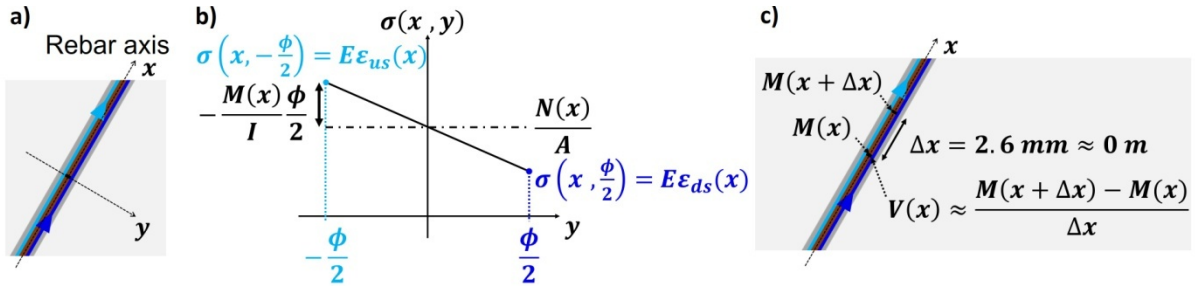


Fig. 4 Assumptions on axial stress $\sigma(x, y)$ (b) and optical fibre gauge spacing Δx(c) for computing normal force$N(x)$, moment$M(x)$, and shear force$V(x)$along the rebar axis x(a) based on strain measurements from the upstream fibre $\varepsilon_{us}(x)$ and downstream fibre $\varepsilon_{ds}(x)$, for a rebar with Young's modulus E, diameter ϕ and moment of inertia I.

The results at the theoretical interface at 9.7 mm displacement, before signal loss in the upstream fibre, show a normal force of 46 kN, a shear force of 17 kN and a bending moment of -24 N.m, near a zero-moment point (Fig. 5). The 53 kN difference between tests with and without the bolt matches the order of magnitude of fibre-optic derived force estimates. However, using this comparison to estimate bolt mobilisation is questionable, especially before the plateau of tangential-force development is reached: the bolt's contribution also depends on the bolt-induced change in interface mobilisation that occurs at the onset of shearing. The effect of the steel sleeve around the grout on mobilisation is also unknown.

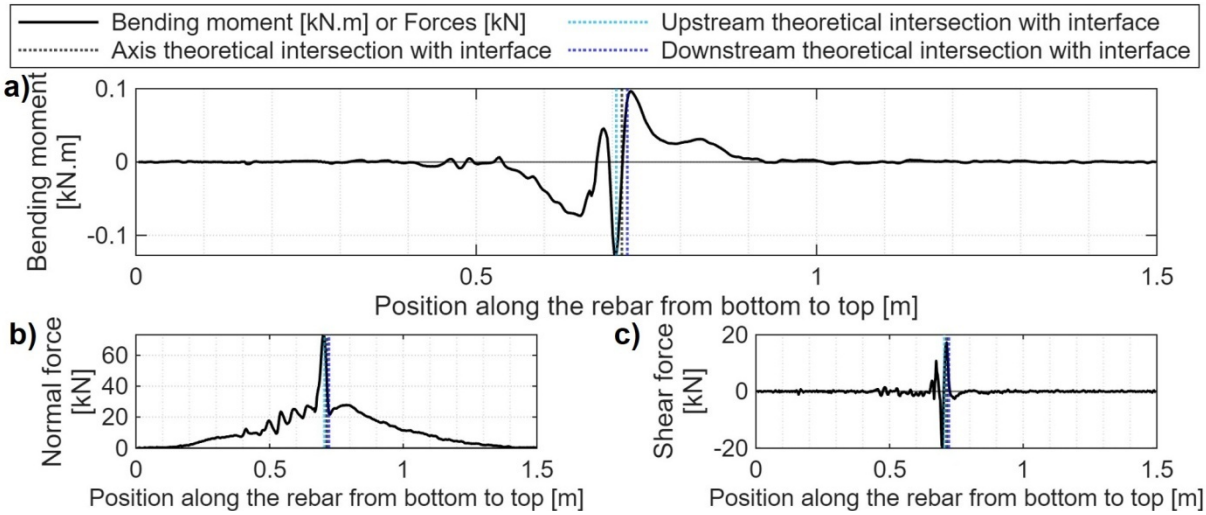


Fig. 5 Bending-moment (a), normal-force (b) and shear-force (c) profiles along the rebar at 9.7 mm displacement.

The alignment of measurement points is critical for computing forces and moments, particularly when strain varies rapidly along the bolt. The uncertainties in the position along the bar, mainly due to the measurement step size, the placement of the fibre during bonding and the end-marking of the fibres, inevitably introduce uncertainties in this alignment. Furthermore, the compound bending-beam model used here is only valid for small rotation gradients. A potential improvement would be to assess the influence of a more accurate representation of shear effects, particularly near the interface and the inflection points.

An effective comparison between these results and the overall contribution of the bolt at the given displacement requires a precise definition of the interface position. This position cannot be reliably determined in post-processing because, unlike the assumptions typically made in analytical models (Panet 1987; Pellet 1993), the point where the computed bending moment becomes zero shifts during the initial stages of loading, and it even crosses zero three times over a very short segment of the rebar for a 9.7 mm displacement (Fig. 5). This issue will be addressed in future experiments. These tests will be performed without the steel sleeve around the grout, which should reduce uncertainties.

5 Conclusion

The mobilisation of an inclined rebar during a shear test is monitored using an optical fibre and compared with numerical simulation of the test.

The optical fibre allowed continuous tracking of rebar mobilisation up to 9.7 mm of displacement, when the signal is partially lost on the upstream side, near the interface. The mobilisation of the remaining portion of the rebar which ultimately failed at 43 mm could still be followed up to 18.8 mm without fibre rupture. Based on the measured strains, axial force, shear force, and bending moment are calculated.

The two inflection points predicted by the analytical framework are clearly identifiable. However, the bending-moment profile reconstructed from the strain data shows more peaks than expected. Improving the localisation of the rebar relative to the interface will be necessary in future experiments to better understand the origin of these variations, especially if they persist in a simpler configuration without the steel sleeve around the bolt reservation.

Even so, this technique appears promising both for quantifying the contribution of bolt mobilisation at the interface during early loading and for locally calibrating numerical models, thereby refining the simplified initial model by improving the representation of the interface and the grouting. It will be applied to later experimental campaigns on group effect under a traction-compression and shear load, as encountered for dam rehabilitation.

References

Azuar JJ (1977) Stabilisation des massifs rocheux fissurés par barres d'acier scellées. Rapport de recherche LCPC n°73. Laboratoire Central des Ponts et Chaussées, Paris, France

Bidaut P, Durville JL,Guillemin P, Richard JC, Viktorovitch M (2006) Essais de cisaillement sur discontinuités rocheuses armées par ancrages passifs : Utilisation d'une boîte de cisaillement de grandes dimensions. Bulletin des Laboratoires des Ponts et Chaussées n°263-264: 7-18.

Coubard G, Morel F (2025) Reinforcement of Existing Dams with Passive Anchors: Thoughts and Proposals from a French Working Group. Twenty-Eighth International Congress on Large Dams, Chengdu, China, 2025-05-23

Dight P (1985) The theoretical behaviour of full contract bolts subject to shear and tension. The Role of Rock Mechanics in Excavations for Mining and Civil Works, International Society for Rock Mechanics, Zacatecas, Mexico, 1985-09-01.

Ferrero AM (1995) The shear strength of reinforced rock joints. International Journal of Rock Mechanics and Mining Sciences & Geomechanics Abstracts 32 (6): 595-605. 10.1016/0148-9062(95)00002-X.

Ferrero AM, Giani GP, Migliazza M, Egger P (1997) Physical and numerical analysis of reinforced rock joint behaviour. RivistaItaliana di Geotechnica 3-4: 63-89.

Forbes B, VlachopoulosN, Hyett AJ, Diederichs MS (2017) A new optical sensing technique for monitoring shear of rock bolts. Tunnelling and Underground Space Technology 66: 34-46. 10.1016/j.tust.2017.03.007.

Grasselli G (2005) 3D Behaviour of bolted rock joints: experimental and numerical study. International Journal of Rock Mechanics and Mining Sciences 42 (1): 13-24. 10.1016/j.ijrmms.2004.06.003.

Hyett A, Forbes B, Spearing S (2013) Enlightening Bolts: Using Distributed Optical Sensing to Measure the Strain Profile along Fully Grouted Rock Bolts. 32nd International Conference on Ground Control in Mining, Morgantown, WV, USA, 2013-07-30

Jalalifar H, Aziz NH, Hadi M (2006) An Assessment of Load Transfer Mechanism Using the Instrumented Bolts. 7th Underground Coal Operators' Conference, Keiraville, Australia, 2006-07-07

Mazzoleni G, Richard JC (1998) Caractéristiques de fonctionnement des ancrages passifs – Campagne d'essais 1997. FAER 2-24-14-7. Centre d'Etudes Techniques de l'Equipement, Laboratoire Régional des Ponts et Chaussée Rhône-Alpes, Bron, France

Panet M (1987) Reinforcement of rock foundations and slopes by active or passive anchors. Sixth International Congress on Rock Mechanics - Theme 2 Rock foundations and slopes, Montreal, Canada, 1987-09-01

Pellet F (1993) Résistance et déformabilité des massifs rocheux stratifiés renforcés par ancrages passifs. PhD Thesis at Ecole Polytechnique Fédérale de Lausanne

Estimation of boundary stresses of high-pressure lined rock caverns using superposition of Inglis solutions

L. Uotinen, M.A. Aydoğmuş & M. Janiszewski
Aalto University, Espoo, Finland
lauri.uotinen@aalto.fi
0000-0001-9646-5029

Abstract

Lined rock caverns (LRCs) are a promising solution for high-pressure hydrogen storage in crystalline bedrock, where early-stage design requires rapid assessment of geometry-dependent boundary stresses. Existing approaches are either analytically rigorous but impractical for scoping, or flexible but computationally expensive.

This study presents a linear-elastic approximation for estimating boundary stresses in ellipsoidal caverns by superimposing classical Inglis solutions and applying a geometric reprojection to approximate three-dimensional effects. Internal pressure is incorporated through FEM calibrated stress intensity factors.

The method is evaluated against three-dimensional finite element models over a wide range of aspect ratios and stress conditions representative of Finnish bedrock. For far-field loading, the approach reproduces numerical results with typical errors of 2-5 MPa. For pressurised cases, the inclusion of stress intensity factors improves agreement, reducing errors to below 1 MPa for roof stresses and 0.5-1 MPa for wall stresses.

The results indicate that far-field stress redistribution can be approximated reasonably using reprojected two-dimensional solutions, whereas pressure-induced stresses require curvature-dependent correction. The proposed method provides a fast tool for early-stage design and parametric screening, while identifying conditions where full numerical modelling remains necessary.

Keywords

Boundary stresses, Kirsch solution, Inglis solution, LRC, Superposition, Hydrogen storage.

1 Introduction

Lined rock caverns (LRCs) are a viable option for large-scale high-pressure (e.g., 20 MPa internal pressure) hydrogen storage in crystalline bedrock, particularly in regions without salt formations such as Finland. At the energy system level, underground storage is required to buffer variability in renewable energy production. A Finnish case study identified LRCs as the most cost-efficient option under such conditions (Pekkinen et al., 2026). Following system-level feasibility, the key question becomes how cavern geometry influences boundary stresses.

Previous studies on LRC mechanics, analytical solutions for elliptical openings, and experimental investigations consistently highlight the strong influence of geometry, loading conditions, and internal pressure on stress distribution and stability (Damasceno et al., 2023; Masoudi et al., 2024; Leong et al., 2025; Patel & Desai, 2020; Zhao et al., 2021).This problem is grounded in classical elasticity. For three-dimensional ellipsoidal openings, Lukić et al. (2009) derived convergent series solutions, while Chiang (2015) demonstrated systematic dependence of stress concentration on shape ratios and the non-trivial link between two- and three-dimensional behaviour. Yin et al. (2022) further showed sensitivity to loading and boundary conditions. Together, these studies confirm that boundary stresses in ellipsoidal openings are strongly geometry-dependent and cannot be reliably inferred from simplified two-dimensional analogies.

At the applied level, numerical studies show that depth, aspect ratio, and internal pressure jointly control whether stresses remain compressive or become tensile. Uotinen and Rinne (2025) showed that unpressurised caverns favour oblate geometries, whereas pressurised caverns shift towards prolate forms, with tensile stresses increasing rapidly at insufficient depth. This highlights a gap between exact three-dimensional solutions, which are rigorous but cumbersome, and numerical modelling, which is flexible but computationally intensive. In early-stage design, this gap limits exploration of large parameter spaces. Analytical approximations, if sufficiently accurate, enable near-instant evaluation and systematic parameter sweeps, offering speedups of 1000x – 10 000x compared to numerical modelling.

Classical solutions such as Kirsch and Inglis provide useful benchmarks but do not extend directly to finite three-dimensional caverns. This study addresses the gap by estimating boundary stresses in ellipsoidal openings through superposition of Inglis-type solutions aligned with the principal axes, with the third stress component obtained from equilibrium with internal pressure. The approximation is exact at the principal-axis intersections and approximate elsewhere, and its accuracy is evaluated against three-dimensional numerical models under stress conditions representative of Finnish crystalline bedrock.

2 Methods

In this paper two analysis methods are used: numerical modelling using the finite element method using Comsol Multiphysics 6.4 software to approximate the boundary stresses around ellipsoid openings and superposition of analytical 2D solutions to construct an approximation of the stress state. For both analysis cases, the shape of the cavern is approximated with an ellipsoid with subradii $r_x$along X-axis, r_y along y-axis, and $r_z$along Z-axis (Fig. 1). The X-axis is oriented along the major in-plane stress σ_H, Y-axis along the minor horizontal stress σ_h, and the Z-axis along the vertical stress σ_V.

The method assumes linear elasticity, homogeneity, and isotropy. The superposition is exact only at principal-axis intersections and approximate elsewhere. The reprojection and pressure correction factors are empirically fitted over a limited height to width aspect ratio range of 1:5 to 5:1. Pressure effects are not derived analytically and are therefore less rigorous than far-field stress estimates.

2.1 Initial data

For the purposes of testing, typical values for material parameters in Finland (Table 1) and a typical coastal stress state (Table 2) at a depth of zmeters from the Olkiluoto island in Finland are used.

Table 1. Material parameters.

Parameter		Value
density [kg/m^3]	ρ	2700
Young's modulus [GPa]	E	40
Poisson's ratio [1]	ν	0.25

Table 2. Stress field.

Parameter		Value
vertical stress [MPa]	σ_V	0.26487 · z
major horizontal stress [MPa]	σ_H	13.0 + 0.031 · z
minor horizontal stress [MPa]	σ_h	8.5 + 0.024 · z

2.2 Classical 2D solutions

Classical linear-elastic solutions provide the baseline for estimating stress concentrations around underground openings. The Kirsch (1898) solution describes stresses around a circular hole in an infinite plate and shows that tangential stress at the boundary varies with angle, reaching a maximum of three times the far-field stress under uniaxial loading. The Inglis (1913) solution extends this to elliptical openings with horizontal subradii r_x and vertical subradii r_z, introducing explicit dependence on aspect ratio (r_z/r_x) and demonstrating that stress concentration increases with elongation,

approaching crack-like behaviour for highly prolate geometries. These solutions establish that boundary stresses are strongly geometry-controlled even under simple loading. Table 3 shows the solutions for the tangential stress in the roof and wall for both formulas as a function of the horizontal stress (σ_h) and the vertical stress (σ_v).

However, both Kirsch and Inglis formulations are inherently two-dimensional and assume an infinite elastic medium with uniform far-field stress. They do not account for variation along the cavern axis, finite length effects, or general three-dimensional stress states, and there is no direct closed-form extension to arbitrary ellipsoidal cavities suitable for design use. Consequently, while these solutions are valuable for benchmarking and rapid scoping, their direct applicability to finite three-dimensional caverns is limited.

Table 3. Boundary stresses for roof and wall using the analytical solutions.

Tangential stress at	Kirsch 1898	Inglis 1913
roof	$\sigma_{roof,K} = 3\sigma_h - \sigma_v$	$\sigma_{roof,I} = \sigma_h\left(1 + 2\frac{r_z}{r_x}\right) - \sigma_v$
wall	$\sigma_{wall,K} = 3\sigma_v - \sigma_h$	$\sigma_{wall,I} = \sigma_v\left(1 + 2\frac{r_x}{r_z}\right) - \sigma_h$

For the tangential stress resulting from the internal pressure, we can use the formulas 1 and 2

roof
$$\sigma_{\vartheta\vartheta} = \sigma_{xx} = -p_{int}\left(2\frac{r_z}{r_x} - 1\right) \quad (1)$$

wall
$$\sigma_{\vartheta\vartheta} = \sigma_{zz} = -p_{int}\left(2\frac{r_x}{r_z} - 1\right) \quad (2)$$

Assuming plane-strain ($\varepsilon_{yy} = 0$), for the change in out-of-plane (Y) stresses we can use the formulas

roof
$$\Delta\sigma_{yy} = \nu[(\sigma_{xx} + \sigma_{zz}) - (\sigma_H + \sigma_V)], \sigma_{zz} = p_{int} \quad (3)$$

wall
$$\Delta\sigma_{yy} = \sigma_H\nu[(\sigma_{xx} + \sigma_{zz}) - (\sigma_H + \sigma_V)], \sigma_{xx} = p_{int} \quad (4)$$

2.3 Geometric conversion from 2D to 3D

A geometric conversion of the stress trajectories must be made to convert from a true cylinder (an ellipse with infinitely long aspect ratio) to a circle (1:1 aspect ratio). The trial function was selected so that at 0 it will result the original stress state (=0) and at infinity it will result in the Kirsch 2D solution (=1). The shape exponent (1.166) was fitted over the aspect ratio range from 1:5 to 5:1 height to width. The approximate formula is then:

$$\omega\left(r_i/r_j\right) = \frac{\left(r_i/r_j\right)^{1.166}}{1 + \left(r_i/r_i\right)^{1.166}} \wedge i, j \in x, y, z \quad (5)$$

2.4 Reprojected Kirsch

A geometric reprojection of the stress trajectories can be made to convert from a true cylinder (an ellipse with infinitely long aspect ratio) to a circle (1:1 aspect ratio). The approximate formulae are:

roof
$$\sigma_{xx} = \sigma_H + 2\sigma_H\omega\left(r_y/r_z\right) - \sigma_V\omega\left(r_y/r_x\right) \quad (6)$$

roof
$$\sigma_{yy} = \sigma_h + 2\sigma_h\omega\left(r_x/r_z\right) - \sigma_V\omega\left(r_y/r_x\right) \quad (7)$$

wall (X)
$$\sigma_{zz} = \sigma_V + 2\sigma_V\omega\left(r_y/r_x\right) - \sigma_H\omega\left(r_y/r_z\right) \quad (8)$$

wall (X)
$$\sigma_{yy} = \sigma_h + 2\sigma_h\omega\left(r_y/r_x\right) - \sigma_H\omega\left(r_y/r_z\right) \quad (9)$$

2.5 Reprojected Inglis

A geometric reprojection of the stress trajectories can be made to convert from a true cylinder (an ellipse with infinitely long aspect ratio) to a circle (1:1 aspect ratio). The approximate formulae are:

roof
$$\sigma_{xx} = \sigma_H + 2\left(r_z/r_x\right)\sigma_H\omega\left(r_y/r_z\right) - \sigma_V\omega\left(r_y/r_x\right) \quad (10)$$

roof
$$\sigma_{yy} = \sigma_h + 2\left(r_z/r_y\right)\sigma_h\omega\left(r_x/r_z\right) - \sigma_V\omega\left(r_y/r_x\right) \quad (11)$$

wall (X) $$\sigma_{zz} = \sigma_V + 2\left({}^{r_x}/_{r_z}\right)\sigma_V\omega\left({}^{r_y}/_{r_x}\right) - \sigma_H\omega\left({}^{r_y}/_{r_z}\right) \quad (12)$$

wall (X) $$\sigma_{yy} = \sigma_h + 2\left({}^{r_y}/_{r_z}\right)\sigma_h\omega\left({}^{r_y}/_{r_x}\right) - \sigma_H\omega\left({}^{r_y}/_{r_z}\right) \quad (13)$$

2.6 Internal pressure stress intensity factor

For the boundary stresses induced by the internal pressure in 3D ellipsoids, no geometrical conversion applies. Instead, a stress intensity factor must be defined as a function of the aspect ratio. The correction factors were fitted over the aspect ratio range from 1:5 to 5:1 height to width:

roof $$\sigma_{\vartheta\vartheta} = \sigma_{xx} = \sigma_{yy} = -\frac{p_{int}}{2}K_{roof}\left({}^{r_i}/_{r_j}\right) \quad (14)$$

wall $$\sigma_{\vartheta\vartheta} = \sigma_{xx} = \sigma_{yy} = -\frac{p_{int}}{2}K_{wall}\left({}^{r_i}/_{r_j}\right) \quad (15)$$

and the stress intensity factor estimates are

roof $$K_{roof}\left({}^{r_i}/_{r_j}\right) = 1 + 1.2626ln\left({}^{r_i}/_{r_j}\right) - 0.07162\left[ln\left({}^{r_i}/_{r_j}\right)\right]^2 - 0.11414\left[ln\left({}^{r_i}/_{r_j}\right)\right]^3 \quad (16)$$

wall $$K_{wall}\left({}^{r_i}/_{r_j}\right) = 1 + 1.8134ln\left({}^{r_i}/_{r_j}\right) - 0.29796\left[ln\left({}^{r_i}/_{r_j}\right)\right]^2 - 0.04647\left[ln\left({}^{r_i}/_{r_j}\right)\right]^3 \quad (17)$$

3 Results

Several tests were conducted to compare the FEM and the superposition approach. The sanity checks were done without internal pressure for an ellipsoid with circular shape in XZ and YZ planes. Later, a series of aspect ratios ranging from 1:5 to 5:1 height-to-width were compared with FEM solutions.

3.1 Verification against 2D solutions

As a baseline, the analytical implementation was first verified against classical Kirsch and Inglis solutions in limiting two-dimensional cases. The results calculated at centroid of ellipsoid at z = -100 m ($\sigma_H = 16.1$ MPa, $\sigma_h = 10.9$ MPa, $\sigma_V = 2.6$ MPa) are for Kirsch and Inglis:

Table 4. In XZ-plane (along major stressσ_H).

Tangential stress at	Kirsch 1898	Inglis 1913	FEM
roof (σ_{xx})	45.7 MPa	45.7 MPa	45.6 MPa
roof (σ_{yy}, Eq. 3)	17.7 MPa (10.9 + 6.8)	17.7 MPa (10.9 + 6.8)	17.6 MPa
wall X (σ_{zz})	-8.3 MPa	-8.3 MPa	-8.3 MPa
wall X (σ_{yy}, Eq. 4)	4.2 MPa (10.9 - 6.7)	4.2 MPa (10.9 - 6.7)	4.2 MPa

Table 5. In YZ-plane (along minor stressσ_h).

Tangential stress at	Kirsch 1898	Inglis 1913	FEM
roof (σ_{yy})	30.1 MPa	30.1 MPa	30.1 MPa
roof (σ_{xx}, Eq. 3)	20.3 MPa (16.1 + 4.2)	20.3 MPa (16.1 + 4.2)	20.2 MPa
wall Y (σ_{zz})	-3.1 MPa	-3.1 MPa	-3.1 MPa
wall Y (σ_{xx}, Eq. 4)	11.9 MPa (16.1 – 4.2)	11.9 MPa (16.1 – 4.2)	12.0 MPa

Table 6. In XZ-plane (along minor stressσ_h), with internal pressure of $p_{int} = 20$ MPa.

Tangential stress at	Kirsch 1898	Inglis 1913	FEM
roof (σ_{xx})	25.7 MPa	25.7 MPa	45.6 MPa
roof (σ_{yy})	17.7 MPa	17.7 MPa	17.6 MPa
wall X (σ_{zz})	-28.3 MPa	-28.3 MPa	-8.3 MPa
wall X (σ_{yy})	4.2 MPa	4.2 MPa	4.2 MPa

3.2 Spherical cavity

For a spherical cavity without internal pressure, the reprojected analytical solution provides a close approximation of the FEM results (Table 7). At the roof, the analytical stresses of 30.9 MPa and 20.5 MPa compare well with FEM values of 31.7 MPa and 21.6 MPa, corresponding to errors of approximately 3-5%. At the wall, the analytical estimates also remain within 10 % of the numerical results. This indicates that the superposition and reprojection approach captures the three-dimensional redistribution of far-field stresses accurately for symmetric geometries.

When internal pressure of 20 MPa is introduced, the agreement remains acceptable for the spherical case. The analytical solution predicts roof stresses of 20.9 MPa and 10.5 MPa compared to FEM values of 21.7 MPa and 11.6 MPa, corresponding to errors of approximately 4-10% (Table 8). At the wall, the agreement is similarly good for the dominant stress component, although deviations increase for the secondary component.

Table 7. Spherical cavity, with internal pressure of $p_{int} = 0$ MPa.

Tangential stress at	Reprojected Kirsch Eqs. 6-9	Reprojected Inglis Eqs. 10-13	FEM
roof (σ_{xx})	30.9 MPa (-3 %)	30.9MPa (-3 %)	31.7 MPa
roof (σ_{yy})	20.5 MPa (-5 %)	20.5 MPa (-5 %)	21.6 MPa
wall X (σ_{zz})	-2.9 MPa (-7 %)	-2.9 MPa (-7 %)	-3.5 MPa
wall X (σ_{yy})	13.8 MPa (+9 %)	13.8 MPa (+9 %)	12.7 MPa

Table 8. Spherical cavity, with internal pressure of $p_{int} = 20$ MPa.

Tangential stress at	Reprojected Kirsch Eqs. 6-9	Reprojected Inglis Eqs. 10-13	FEM
roof (σ_{xx})	20.9 MPa (-4 %)	20.9 MPa (-4 %)	21.7 MPa
roof (σ_{yy})	10.5 MPa (-10 %)	10.5 MPa (-10 %)	11.6 MPa
wall X (σ_{zz})	-12.9 MPa (-4 %)	-12.9 MPa (-4 %)	-13.5 MPa
wall X (σ_{yy})	3.8 MPa (+35 %)	3.8 MPa (+35 %)	2.8 MPa

3.3 Ellipsoid caverns

For no internal pressure ($p_{int} = 0$ MPa, Eqs. 10 & 12), the fits reproduce the overall trend but with a systematic bias. Roof stresses are captured within 2-4 MPa (max. 5 MPa), while wall stresses show 1-3 MPa deviations, with larger relative errors near the zero-crossing due to small magnitudes (Fig. 1).

For internal pressure of $p_{int} = 20$ MPa (Eqs. 10+14& 12+15),the agreement is good. Roof stresses are typically within 1 MPa of the FEM results, and wall stresses within 0.5-1 MPa. Relative errors are generally below 5-10%, except at large aspect ratios where stresses approach zero (Fig. 2).

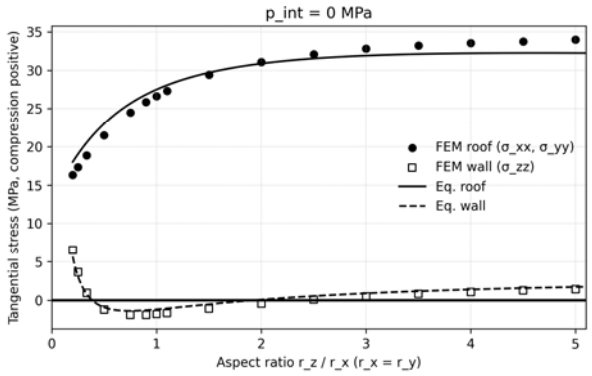


Figure 1. Solutions for unpressurized ellipsoid caverns.

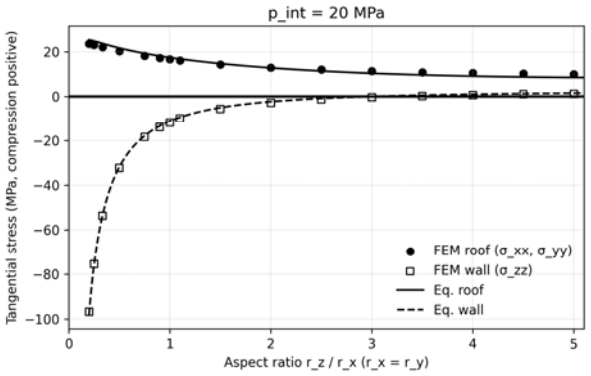


Figure 2. Solutions for ellipsoid caverns with 20 MPa internal pressure.

4 Discussion

The method is suitable for rapid scoping of far-field effects. For pressurised caverns, it captures trends but requires calibrated factors or numerical modelling for design. Superposition of Inglis-type solutions with geometric reprojection provides a consistent approximation for boundary stresses under far-field loading. For spherical and moderately elongated geometries, the method reproduces FEM results with acceptable accuracy, indicating that three-dimensional stress redistribution can be approximated by reweighting two-dimensional solutions.

For internal pressure, the behaviour deviates from this framework. While a simple scaling holds for spherical cavities, it does not extend to ellipsoids. The method overestimates tensile stresses at the roof and underestimates redistribution at the walls, with errors increasing with aspect ratio. This reflects a fundamental difference: far-field stresses redistribute through the rock mass, whereas internal pressure acts as a boundary traction governed by local curvature. As a result, pressure-induced stresses are not captured by superposition alone and require correction using stress intensity factors.

5 Conclusion

Superposition of Inglis-type solutions with geometric reprojection provides a simple and computationally efficient method for estimating boundary stresses in ellipsoidal caverns under far-field loading. The approach yields acceptable accuracy for spherical and moderately elongated geometries and is well suited for rapid scoping and parametric studies. Internal pressure cannot be represented within the same framework, as it is governed by local curvature rather than stress redistribution in the rock mass. Consequently, pressurised cases require calibrated correction factors or numerical modelling for reliable design.

Acknowledgments

This work was inspired by the main outcomes from the HUG (Hydrogen UnderGround research project 2024-2026) and earlier contract research work with a company that wishes to remain unnamed. During the preparation of this work, the authors used ChatGPT to check the language and improve readability. After using AI, the authors reviewed and edited the content as needed and take full responsibility for the content of the publication.

References

Chiang, C.-R. (2015). Stress concentration around a triaxial ellipsoidal cavity in transversely isotropic materials. Archive of Applied Mechanics, 85, 469-479. https://doi.org/10.1007/s00419-014-0923-1

Damasceno, D. R., Spross, J., & Johansson, F. (2023). Rock mass response for lined rock caverns subjected to high internal gas pressure. J. Rock Mech. Geotech. Eng., 15(1), 119–129. https://doi.org/10.1016/j.jrmge.2022.03.006

Inglis, C. E. (1913). Stresses in a plate due to the presence of cracks and sharp corners. *Transactions of the Institution of Naval Architects*, *55*, 219–241.

Kirsch, G. (1898). Die Theorie der Elastizität und die Bedürfnisse der Festigkeitslehre. *Zeitschrift des Vereins Deutscher Ingenieure*, *42*, 797–807.

Leong, C. M., Ghayesh, M. H., Nathan, G. J., Salmachi, A., & Rajabi, M. (2025). A review of the mechanics of lined engineered cavities and their implications on hydrogen storage. Int. J. Hydrogen Energy, 102, 749–766. https://doi.org/10.1016/j.ijhydene.2024.12.467

Lukić, D., Prokić, A., & Anagnosti, P. (2009). Stress-strain field around elliptic cavities in elastic continuum. European Journal of Mechanics - A/Solids, 28(1), 86-93. https://doi.org/10.1016/j.euromechsol.2008.04.005

Masoudi, M., Hassanpouryouzband, A., Hellevang, H., & Haszeldine, R. S. (2024). Lined rock caverns: A hydrogen storage solution. J. Energy Storage, 84, 110927. https://doi.org/10.1016/j.est.2024.110927

Patel, A., & Desai, C. K. (2020). Stress concentration around an elliptical hole in a large rectangular plate subjected to linearly varying in-plane loading on two opposite edges. Theor. Appl. Fract. Mech., 106, 102432. https://doi.org/10.1016/j.tafmec.2019.102432

Pekkinen, S., Muoniovaara, M., Seppälä, E., Pirhonen, P., Rinne, M., & Santasalo-Aarnio, A. (2026). Hydrogen storage model for decarbonization of constant industrial processes. Next Energy, 10, 100484. https://doi.org/10.1016/j.nxener.2025.100484

Uotinen, L., & Rinne, M. (2025). Rock mechanical optimization of the shape and depth for a high-pressure lined rock cavern. In Proceedings of the ISRM International Symposium Eurock 2025 - Expanding the Underground Space, Trondheim, Norway, 16-20 June 2025. https://airdrive.eventsair.com/eventsairwesteuprod/production-atlanticmice-public/5d50a02b6a3643d2a152c555202eb7b5

Yin, J., Liao, H., Kong, L., Cheng, J., Niu, T., Wang, X., & Zhuang, P. (2022). Analytical solution for elastic analysis around an ellipse with displacement-controlled boundary. Mathematical Problems in Engineering, 2022, Article 2148947. https://doi.org/10.1155/2022/2148947

Zhao, H., Sun, H., Zhang, D., & Liu, C. (2021). Mechanical properties and progressive failure characteristics of sandstone containing elliptical and square openings subjected to biaxial stress. PLOS ONE, 16(3), e0246815. https://doi.org/10.1371/journal.pone.0246815

Lessons from Full-and Partial-Face Excavation in Difficult Rock Conditions

G. Bella, M. Falanesca, D. Merlini & F. Gianelli
ARX Group SA, Lugano, Switzerland
gianluca.bella@arx.ing
0000-0002-4745-2974

R. Schuerch & M. Piemontese
ARX Group SA, Zurich, Switzerland

Abstract

The selection between full-face and partial-face excavation methods is a decisive factor in the success and efficiency of conventional tunnelling projects. This choice is shaped by a complex interplay of geological and geotechnical rock mass conditions, environmental and urban constraints, regional design and construction standards, and permissible surface settlement thresholds. Each excavation method imposes distinct implications for project cost, schedule, and safety, highlighting the critical importance of informed decision-making during the early design phase. Over the years, continuous advancements in construction materials, excavation machinery, numerical modelling, and real-time monitoring technologies have significantly enhanced the feasibility of full-face excavation. These advancements enable the safe and efficient construction of tunnels with cross-sectional areas exceeding 150 m², pushing the limits of conventional tunnelling. Nonetheless, partial-face excavation remains an essential and often preferred strategy when staged excavation is required to ensure ground stability, manage deformations, or address specific site constraints. This study presents a comparative analysis of full-face and partial-face excavation methods, drawing on selected complex case histories from one of the major Alpine base tunnels and international projects under low overburden. Critical factors, including rock mass properties, excavation techniques, tunnel geometry, alignment, and construction sequencing, are evaluated to identify their influence on method selection and project outcomes. The case studies provide valuable insights into the practical advantages, limitations, and applicability of each approach, establishing a reference framework for conventional tunnelling practice in challenging geological and urban contexts. The paper highlights key considerations for optimizing excavation strategy, balancing safety, cost, and schedule, and leveraging modern construction technologies, providing engineers with guidance to select the most effective excavation method for complex tunnelling scenarios.

Keywords

Tunnelling, Conventional Tunnelling, Full-Face Excavation, Partial-Face Excavation.

1 Introduction

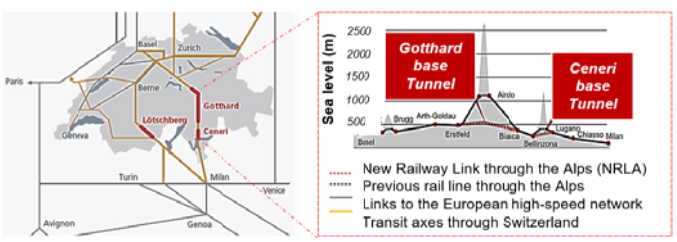
The choice between full-face and partial-face excavation is crucial for tunnel project success, impacting costs, schedule, and safety. This decision depends on geological, geotechnical factors, and environmental and urban constraints. Recent advances in materials, equipment, and monitoring have expanded the use of full-face excavation, even for sections over 150m² in complex ground conditions. According to Gamper (2014), Lunardi et al. (2024), modern full-face tunnelling methods offer significant advantages over traditional partial-face excavation in terms of cost efficiency, safety, and construction performance. By maintaining a continuously reinforced core-face, allowing immediate lining along the entire perimeter, and promoting uniform excavation profiles (i.e., circular or oval geometry), full-face excavation improves face stability and reduces stress concentrations. On the other side, the NATM emphasizes that the rock mass should be maintained in a load-bearing condition to prevent unnecessary loosening and softening. However, static and deformative analyses indicate that total deformation is lower for full-face excavation because of its capacity to improve the face stability by rapid ring closure and pipe arch pre-support systems. Operationally, full-face excavation enables higher levels of industrialization, reduced workforce exposure, and simplified logistics, resulting in improved safety and efficiency, and thus represents a major advancement in conventional tunnelling. Nevertheless, partial-face excavation may still be required in cases constrained by equipment size or tunnel geometry, or in certain geological settings, particularly with highly variable or unstable ground conditions, or where local constraints such as nearby structures require staged excavation. This method allows for better control over ground deformation in complex geologies, though it may involve more intensive support measures and longer construction durations. This paper compares the two methods through complex case histories, offering a framework for assessing the applicability of each one to illustrate the conditions under which each method is appropriate (Tab.1). As the case studies themselves demonstrate well, the method superiority is strongly context-dependent.

Table 1. Main features of the three case studies.

	Minimum Overburden	Unit	Cross section	Constrains	Excavation method
Ceneri BaseTunnel (Switzerland)	5-35m	Gneiss	≅ 80m^2	Historical building / nearby existing tunnels	Partial-face
Road60 Tunnel Project (Israel)	2-8m	Dolomite	≅212m^2	Nearby existing tunnels	Partial-face
Sotra Link Project (Norway)	6-50m	Moraine/Weathered bedrock	≅130m^2	Existing bridge and viaduct	Full-face

2 Ceneri Base Tunnel (Switzerland): partial-face excavation for vibration mitigation at Vezia South Portal

The Ceneri Base Tunnel (CBT) represents the southernmost section of the New Railway Link through the Alps (NRLA), crossing the Swiss Alps from North to South. Connecting the Swiss cities of Lugano and Bellinzona (Fig.1).The CBT lies within the crystalline bedrock of the southern Alps. An extensive geological survey involved boreholes as deep as 700 meters, with a total drilling length almost equivalent to the tunnel itself, allowing the identification and characterization of homogeneous geological units to define geological and geotechnical conditions (Fig.2).



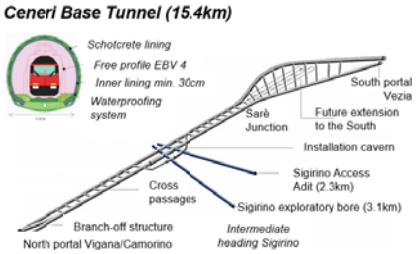


Fig. 1 General overview of the Ceneri Base Tunnel (Merlini et al. 2018).

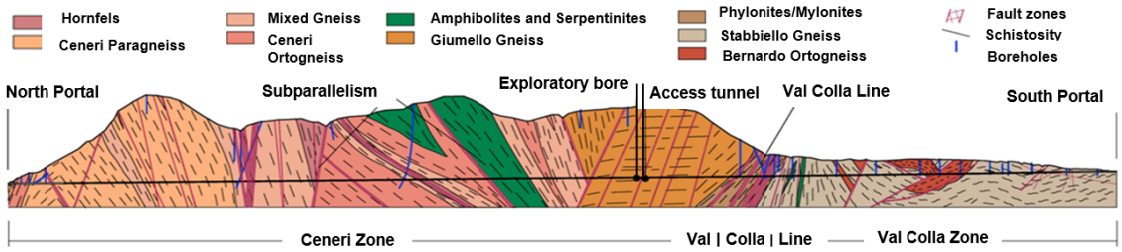


Fig. 2 CBT: geological longitudinal section.

The south portal located within Lot 854 was positioned in a critical urban environment near Vezia, where the minimum overburden was 11 meters, and included the presence of a historical building. It consists of three sub-sectors: 1) two single-line tubes (303m and 340m in length, cross-sectional area of 80m², overburden 5m-35m) excavated with the D&B method, including a 34m long by-pass; 2) two separate cut-and-cover tunnels connecting East and West tubes with the portal (Merlini et al. 2018, Gugelmann 2011); 3) the portal zone, which is the connection of the new section to the rest of the line. The entire site was constrained within a narrow corridor, surrounded by the A2 motorway, the existing Vedeggio-Cassarate road tunnel (distance approx. 4-5m from the Est tube), and the existing federal railway line (Fig.3). The geological formation in the project area, investigated through exploratory boreholes and seismic methods, is composed of Stabiello gneiss. This formation consists of a heterogeneous, jointed sequence of schistose gneisses and sericitic-chloritic schists.

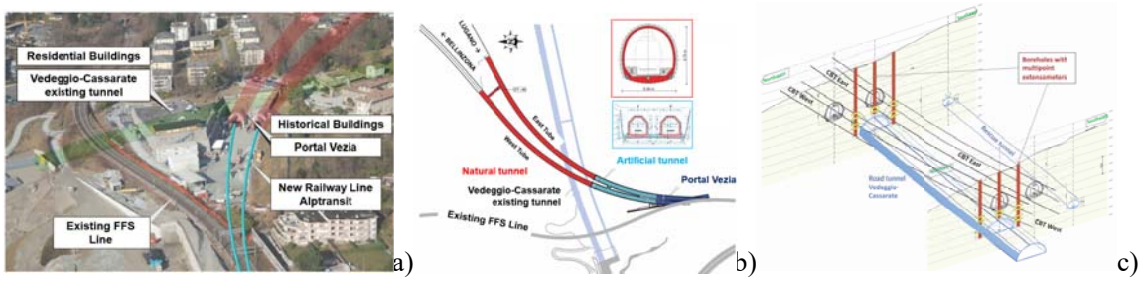


Fig. 3 Overall view of the CBT's southern portal: a) overview; b) plan view; c) axonometric plan of the Vedeggio-Cassarate road tunnel and the CBT south opposed tunnel intersection zone: multipoint extensometers installed in boreholes are able to transmit measurements continuously (Merlini et al. 2018).

A predictive analysis of the behaviour of the interfering structures, along with the implementation of special excavation and support techniques, together with advanced tunnel monitoring systems for subsidence and vibration control, was necessary to evaluate this interference. During the design phase, numerical analyses were performed using the 2D UDEC™ distinct element code, which enabled the prediction of the rock mass's stress-strain response and the surface-level impacts of the excavations (Fig.4).

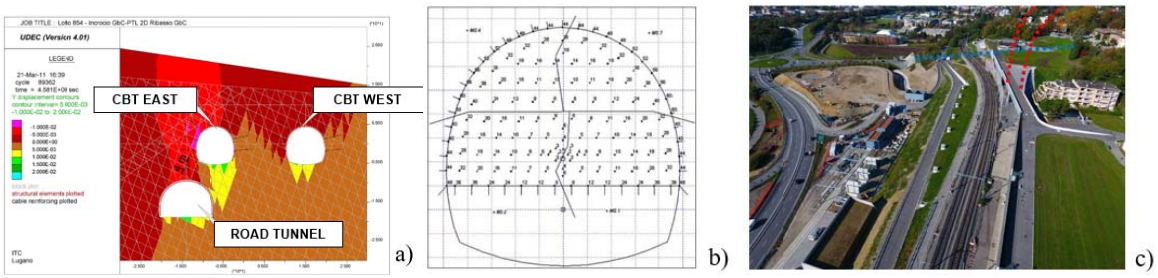


Fig. 4 a) DEM calculations; b) blasting plan for Roof 3A; c) final phase of the CBT's southern portal (Merlini et al. 2018).

To mitigate the risk of blast vibrations, the following measures were implemented: 1) technical restrictions on the D&B process, including: drilling and shot-firing allowed only during specific periods of the day, a general limit on the amount of explosive per initiation stage to less than 0.25 kg·delay^{-1}, subdivision of the excavation cross-section, and a reduction in round length; 2) stricter limits than those specified by Swiss standards (i.e., a minimum value of 6 mm·s^{-1} for frequencies below 30 Hz); 3) a comprehensive monitoring system using geophones, continuously assessed in real-time. The results of the design analyses demonstrated that a full-section excavation would have

exceeded the allowable vibration thresholds. A good agreement between the numerical simulation (5-10mm) and deformations obtained from monitoring (6-7mm) was recorded. The excavation was successfully completed approximately ten months ahead of the scheduled date outlined in the work program, while maintaining both environmental and economic sustainability.

3 Road 60 Tunnel Project (Israel): partial-face excavation to minimize the impact on the adjacent existing tunnel

The Road 60 Tunnels Project (R60TP) is situated along Highway 60 located between the city of Bethlehem and Jerusalem, Israel. R60TP involved the construction of two new road tunnels in addition to the refurbishment of two existing tunnels. The new ones, 870m and 270m in length, respectively, run almost parallel to the existing tunnels. The maximum overburden amounts to 35m and to 70m for the short and long tunnels, respectively, with a minimum of 2m to 8m close to the portal areas. The external width of the new tunnels amounts to about 17m, while their height amounts to about 10 m. Both long and short new tunnels accommodate three traffic lanes and two emergency pedestrian lanes (safety walks). The project also included the construction of four cross passages between the new and existing tunnels, as well as six emergency bays along the road alignment (Schuerch et al. 2025). R60TP provided a challenging case for the application of partial-face excavation. The presence of a highly heterogeneous and weathered "Transition Zone" between the Amminadav and Moza formations (Fig.5), together with the minimal separation between the new and existing tunnels (as low as 3m), imposed severe constraints on the excavation process. The Transition Zone, composed of brecciated dolomite blocks embedded in marl and clay, exhibited rapid variations in mechanical behaviour - from competent rock to cohesionless sandy dolomite or swelling marl - making full-face excavation unsafe and unpredictable. The parameters reported in Table 2 were assigned based on available site investigation data, supported by literature values for comparable rock masses and engineering judgement, with the cohesion values representing equivalent rock mass properties adopted for numerical modelling. To mitigate these geotechnical uncertainties and reduce the risk of damaging the operational existing tunnel - based on the results provided by numerical analyses carried out by the RS2 Finite Element code (Fig.6) - the excavation was performed in multiple partial phases (Sequential Excavation Method).

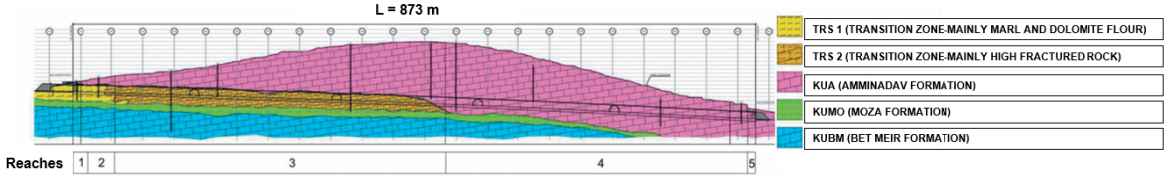


Fig. 5 R60TP: Longitudinal and geological profile of the long tunnels.

Table 2. Geotechnical properties of the soil/rock units.

Unit	**6a**	**4**	**5a, 5b**	**1**	**2**	**3**	**6b**
Geology	**Transition zone 1 (Portal)**	**Transition Zone 2**		**Amminadav Formation**			
Unit volume weight, γ [kN/m^3]	27	27	25	27	27	27	27
Cohesion, c'[kPa]	150	1500	26	6995	5828	3148	1300
Friction angle, φ [°]	30	35	33	40	40	40	35
Young's Modulus, E [GPa]	0.25	2.65	0.15	8	6.5	3.5	0.6

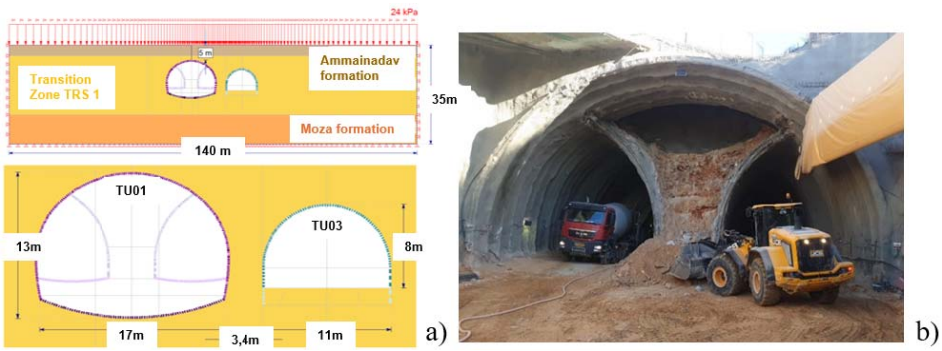


Fig. 6a) RS2 model; b) excavation phase (Schuerch et al. 2025).

The sequence began with a side drift adjacent to the rock pillar separating the two tunnels, followed by one to three additional stages (top heading and benching), the number of which varied according to local ground conditions. This staged approach allowed for progressive assessment of the rock mass and real-time adaptation of support measures. In the most critical sections within the Transition Zone, four excavation stages were implemented to maintain tunnel stability and minimize deformation: two side drifts, top heading, and benching, including invert closure. The use of partial-face excavation offered several advantages: it enabled direct geological mapping of the rock pillar before enlargement, reduced vibration transmission to the existing tunnel, and allowed pre-reinforcement through grouting or transverse bolting when karstic voids or weak zones were encountered. At the peculiar Emergency Bay South section, where the new and existing tunnels intersected under a 55m overburden, partial-face excavation proved essential. The combination of large spans (up to 35m), ongoing traffic in the adjacent tube, and poor ground conditions required controlled excavation stages supported by steel ribs, shotcrete up to 40cm thick, spiling, and fiberglass face bolts. This sequenced construction ensured both safety and service continuity, demonstrating how partial-face excavation within the Sequential Excavation Method can provide a flexible and reliable solution under complex geological and operational constraints. Started in 2019, R60TP was successfully completed in 2024, with the commissioning of the refurbished existing tunnels.

4 Sotra Link Project (Norway): full-face excavation of Drotningsvik Tunnel at the Kipledalen section

The Sotra Link Project (SLP) is one of Norway's priority infrastructure projects. It encompasses the design, financing, construction, and maintenance of a range of surface and underground facilities, connecting the city of Bergen and the Sotra island. The SLP comprises 9km of highway, a 900m-long suspension bridge, 12.5km of tunnels (Kolltveit, Straume, Knarrvika, Drotningsvik), 19 roads and pedestrian underpasses, 3 tunnel portals, 22 bridges and viaducts, and 14km of pedestrian and bicycle paths (Barbieri et al. 2025). Construction works started in March 2023, with ongoing activities across all four main tunnels. The Drotningsvik area, located in the Eastern section, features the most complex underground structure of the project. Excavated near the Kiplevatnet lake, the most complex section of the Drotningsvik tunnel includes both the North tube and the South tubes. This section spans a total length of 30m, with a maximum width of 19m, and a front height reaching up to 9m.The main engineering challenges with this section can be summarized as follow: i) very limited overburden, with a minimum cover of approximately 6m; ii) potential interference with an existing viaduct which pillar load is founded in the ground upon the North tube; iii)interference with the pillar of a planned pedestrian bridge to be built after the tunnel excavation; iv) poor quality of fractured rock mass infillings, which may induce swelling phenomena and consequently affect the long-term performance and durability of the permanent structures (Tab.3). The excavation design solutions for Kipledalen section have been developed to minimize the possible impact of the tunnel construction on the upper viaduct to be maintained fully operative and to avoid draining the lake's water resources.

Bidimensional finite element analyses have been performed by RS2 code, under plane strain conditions, to estimate stresses and displacements on the concrete support during the full-face excavation phases (Fig.7a). An elastic-perfectly plastic Mohr-Coulomb criterion was adopted as the constitutive law. Supports consist of rock bolts (ϕ25, L=4-5m), primary lining (FRC B35 thickness 250mm + steel mesh K335),spiling bolts (73/56 L=8m), fiberglass bolts at tunnel face (ϕ25, L=6m, spacing 1.1x1.1m). Reinforced ribs of shotcrete RRS (spacing 1.50m, shotcrete B35: thickness 600mm, steel bars ϕ20 B500NC) have been adopted as a permanent lining for stabilizing very poor rock mass conditions. The rib-reinforced shotcrete arches provide a superior stiffness if compared to lattice girders, because of an increased adherence with the tunnel perimeter and a systematic bolting of the arches (Fig.7b, Barton and Grimstad 2014). This solution provides a general optimisation if compared to an equivalent primary liner,e.g. in terms of section efficiency and higher capacity to bending moment, under compression. However, a higher load capacity to pure tensile force is given by an equivalent lining, but this represents an infrequent condition in tunnelling.

Table 3. Geotechnical properties of the soil/rock units.

	γ [kN/m^3]	φ [°]	c' [kPa]	E [MPa]	v [-]	Ψ [°]	Q [-]
Rockfill	20	42	10	75	0.25	12	-
Weathered bedrock	29	30	70	1500	0.20	0	0.14
Good rock mass	29	40	4500	6000	0.17	10	290

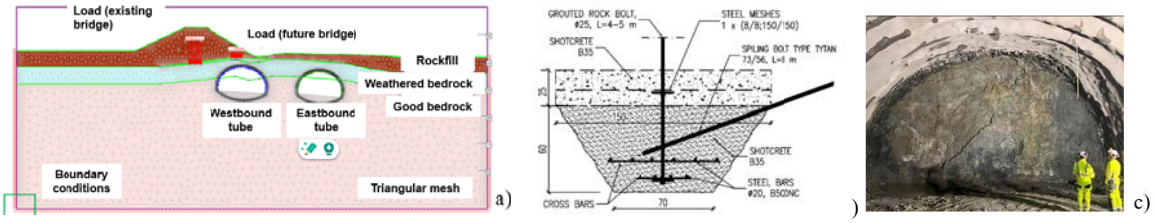


Fig. 7 a) FE model, geometry loads and boundary conditions (km 8+126); b) reinforced ribs of shotcrete detail; c) tunnel face during the excavation of the Kipledalen section (Barbieri et al. 2025).

Monitored displacements during the excavation phase were then considered for the model validation to calibrate the deconfining ratio. The presence of loosened surficial deposits at the tunnel and the lake required grouting of curtains and crowns around and above the excavations to improve the effectiveness of the radial bolting and the waterproofing. Before the tunnel excavation, pre-grouted columns were also executed all along the lake perimeter to avoid water inflow towards the tunnel. The excavation of the Kipledalen section has been completed, and the RRS - as a rigid, permanent lining - has been successfully adopted under critical geotechnical conditions, which do not guarantee complete effectiveness of radial bolting. Under such conditions, traditional tunnelling practice would adopt either a double-shielded support or a trenching methodology, such as cut and cover.

5 Conclusions

The case histories shown in this paper demonstrate that, while full-face excavation enhances efficiency and safety in stable or reinforced ground, partial-face excavation remains indispensable for managing uncertainty, minimizing vibration, or protecting adjacent structures. The integration of observational methods, real-time monitoring, and adaptable support systems is critical in both approaches. The combination of full-face advancement and rapid ring closure has proven especially effective in controlling deformation. The authors would like to highlight the following main conclusions: (1) Full-face excavation offers superior deformation control, safety, and productivity when adequately supported by pre-confinement and reinforcement systems; (2) Partial-face excavation remains essential in complex geological settings or urban areas with strict vibration and deformation constraints; (3) The choice between methods should be based on quantified geomechanical parameters and integrated design tools such as ADECO-RS and NATM; (4) Contract models should encourage early collaboration among designers, contractors, and clients to allow method optimization and risk sharing; (5) Continuous monitoring and data interpretation are vital for real-time decision-making during excavation.

References

Barbieri G, Giani M, Trivellato E, Agrillo A, Bella G, Colo' G, Stadler G, Uthus MJ (2025) Digital tools to enhance design optimization and tunnel construction in the Sotra Link Project. Eurock 2025, Trondheim (Norway) 16/20June.

Barton NR, Grimstad E (2014) Q-system application in NMT and NATM and the consequences of overbreak. Modern Use of Wet Mix Sprayed Concrete for Underground Support. 7th International symposium on sprayed concrete, Sandefjord (Norway) 16-19 June.

Gamper C (2014) Full face versus partial face in NATM tunnelling. Geomechanics and Tunnelling 07(05): 491-502. doi:10.1002/geot.201400050.

Gugelmann B (2011) The challenges of opposed tunnelling Vezia. Swiss Tunnel Congress 2011, Lucerna (Switzerland), 08-10 June.

Lunardi P, Bindi R, Zenti CL (2024) Productivity and safety in conventional tunnel excavation: the added value of full-face advancement. Gallerie e Grandi Opere Sotterranee 04: 41-54.

Merlini D, Stocker D, Falanesca M, Schuerch R (2018) The Ceneri Base Tunnel: Construction Experience with the Southern Portion of the Flat Railway Line Crossing the Swiss Alps. Engineering 04(2): 235-248. doi:10.1016/j.eng.2017.09.004.

Schuerch R, Piemontese M, Perazzelli P, Tzuker D, Grouchko Y (2025) Addressing geological and traffic constraints: Design and construction strategies for the Road 60 Tunnels. World Tunnel Congress WTC 2025, Stockholm (Sweden), 9-15 May.

Assessing Caving Risk Related to Rockmass Bulking

T. G. Carter
TGC-GeoSolutions, Oakville, Ontario, Canada
tcarter@tgcgeosolutions.com
0000-0001-6746-959X

A. van As
University of Queensland / Deep Mining Geoscience Group
a.vanas@uq.edu.au

Abstract

Establishing how much or how little a rockmass bulks during caving is critical to assessing surface subsidence risk for civil tunnel and near-surface mining stope collapses, and to evaluating cave initiation and draw performance in block and panel cave mines. The volumetric expansion that occurs as a rockmass breaks up determines whether the cave back self-chokes or propagates progressively upward. Bulking depends on rockmass characteristics controlling block size and shape, as well as stress conditions, fall height of detached blocks and the fragmented rock debris maturity through comminution and compaction.

The excavation damage/yield zone geometry, fragmentation rates and stress redistribution further influence how the rock mass breaks and ultimately how the cave propagates. Insufficient understanding of these interacting processes has historically caused catastrophic tunnel and crown pillar collapses and major cave propagation difficulties in cave mining.

This paper reviews current modelling empirical method benchmarking methods for evaluating crown collapse risk and caveability, including Carter's Scaled-Span approach and Laubscher's MRMR hydraulic-radius framework. Particular emphasis is placed on the role of bulking in controlling void ratio, stress transfer and cave propagation. Guidelines for assessing bulking are presented, based on precedent case histories, laboratory data and numerical modelling insights.

Keywords

Risk, Caving, Crown Pillars, Bulking, Mining.

1 Introduction

One of the most risk-prone situations in both civil underground works and mining excavations is the potential for adverse surface impacts due to uncertain variabilityin competence of the overlying crown rockmass. Once a crown pillar rockmass fragments, collapse behaviour is commonly assessed using empirical rock mass classifications or span-based stability criteria. However, field evidence from crown pillar failures, filled stope back-break, cave hang-ups and cave subsidence demonstrates that neither span nor rock mass strength alone governs the system response. A critical, but often under-

emphasised, control is the volumetric response of the rock mass during its fragmentation, commonly expressed through bulking or swell factors.

For civil and mining tunnels, stope crown pillars, and cave backs, insufficient bulking of fragmented rock prevents self-choking and facilitates progressive upward migration of failure, potentially leading to breakthrough into overlying mine workings or the surface. In filled stopes, inaccurate swell estimation results in incomplete filling, stress concentration at the crown and progressive back-break. In cave mining the implications are broader and more complex, as bulking governs the void ratio within the broken column; and this void ratio governs stress transfer and arching; and stress transfer governs cave propagation rates, airgap development, cave hang-ups, and breakthrough timing.

Despite its significance, bulking is frequently treated as a constant parameter; often as a single swell factor defined at initiation and assumed constant throughout cave life. Such assumptions neglect the progressive evolution of the fragmented rock mass under increasing confinement, block rearrangement, crushing, fines generation and loading and unloading stress cycles. Bulking is stage-dependent and stress-dependent, varying spatially within the cave column and temporally as propagation conditions change. This paper presents a unified, risk-based framework linking bulking to void ratio, stress transfer and arching, applied to both crown pillar stability assessment and cave propagation.

2 Cave Mechanics and Caveability Assessment

Cave mechanics, and particularly the bulking behaviour of the fragmented rock mass, governs both the collapse processes around the cave back and the material flow behaviour in cave mines. Assessment of crown/cave back breakthrough risk requires an understanding of three primary factors:

1. Rock mass competence of the crown pillar/cave back.
2. Geometry of the crown pillar/cave back (span and void volume).
3. Fragmentation characteristics, and associated bulking behaviour.

For a given crown rock mass quality, caving likelihood is primarily span-controlled. In cave mining, this span is typically represented by the critical hydraulic radius (***HR$_{cr}$***) of the undercut (Laubscher, 1977, 1994, 2000; Fig. 1, right diagram x-axis). Where crowns must remain stable, thickness must also be considered, and the relevant parameter becomes the scaled crown span **(*Cs*)**, accounting for full three-dimensional crown geometry (Golder, 1990; Carter, 1992, 2014; Fig. 1, left diagram, y-axis).

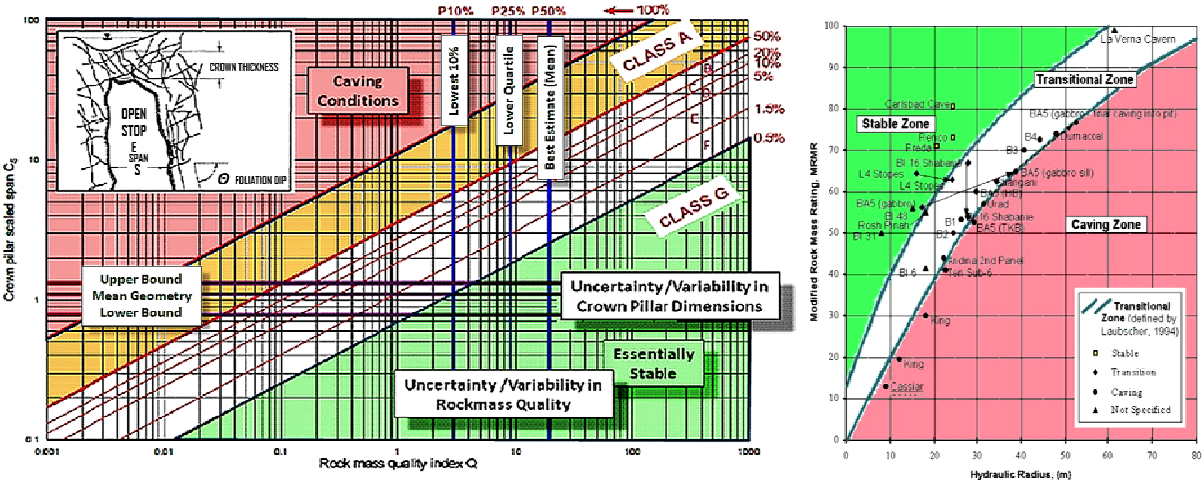


Fig. 1 Empirical Caving Charts: left – Scaled Span Crown Pillar Chart; right – MRMR Caving Chart.

For stoping mines, tunnels, drifts, or cavern assessments, crown breakthrough risk can be assessed by comparing the scaled span *Cs* with the critical span, *Sc* for the controlling rock mass quality (defined by *Q* or GSI/RMR_{76}), with the quotient *Sc/Cs* expressed as Probability of Failure (*PoF*) via the linear logistic regression lines from Carter et al. 2008, or directly from the critical span line $Sc = 3.3\ Q^{0.43}\ xsinh^{0.0016}(Q)$, which it will be noted is slightly non-linear with increasing rock competence. Although the rock quality vs. geometry axes are reversed between the two plots in Fig. 1, colour coding is set approximately equivalent, allowing direct caving comparison.

Critically, crown stability and cave propagation are also governed by the volume balance between available void space and the bulked volume of the fragmented rock. Collapse propagation will only arrest if the fragmented rockmass bulks sufficiently to fill the available void. If bulking is insufficient, progressive upward migration continues until breakthrough. Bulking, therefore, represents a critical parameter, linking fragmentation behaviour with collapse-driven instability.

3 Bulking

3.1 Fragmentation and Bulking Data

Bulking during caving depends not only on rockmass characteristics controlling initial block size and shape distributions, but also on in situ and induced stress conditions, airgap presence, fall height of blocks from the cave back, and fragmentation maturity through comminution and compaction. Supported and unsupported crown/cave back span at any time, and the geometry and depth of the yield/damage zone, also affect fragmentation block size and rate of fragmentation (break up).

Fig. 2 summarises collected bulking data from literature sources, subdivided by rock type. While most of the plotted data originates from evaluation of longwall coal gob collapse behaviour in sedimentary rock types, a significant number derive from hard-rock stope hangingwall failure and civil tunnels. The influence of fabric and rock strength is clear: competent, slabby strong rocks, such as slates break up with the highest Bulking Factors (*Bf%*), while weak, crushable mudstones, siltstones, claystones and schists show the lowest *Bf* values.

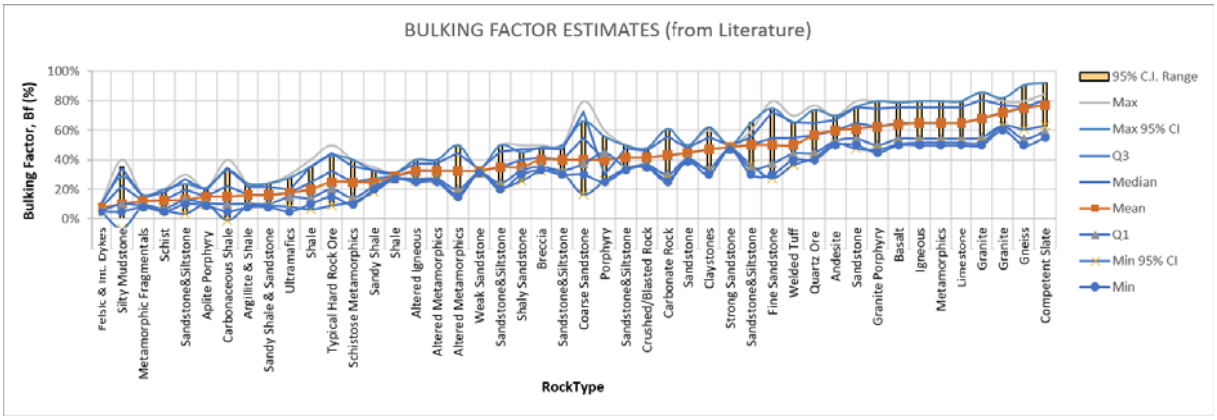


Fig. 2 Summary Box Plot of Bulking Factor (%) values, ranked by mean *Bf%* and rocktype.

Given the Hoek-Brown parameter m_i (Hoek & Brown, 1980) can be utilized as a useful intact rock type competence index, (Marinos & Carter, 2025), and noting that m_b reflects, not just rock type, but also rockmass brokenness (fracture intensity), a correlation to the mean trend of the data in Fig. 2,following earlier longwall coal, square root relationship formulations, can be postulated, suggesting:

$$B_f(\%) \cong 2.1 \cdot \sqrt{m_b \sigma_C},$$

where m_b and σ_C (UCS) need to be rockmass and rock type specific.

3.2 Swell versus Bulking

Swell refers to the initial volumetric increase of a fragmented rockmass relative to its in situ volume immediately following blasting or mechanical breakage, (primary fragmentation). ***Bulking***, by contrast, describes the volumetric state of the mobilized fragmented rock debris under a given stress condition, and thus evolves over time, reflecting block rearrangement, stress-dependent compaction and block breakage (secondary fragmentation).

In cave mining, this distinction is particularly important because the overall bulking factor derived from mass balance calculations evolves over the course of cave life. Initial (primary) fragmentation during undercutting produces *Bf* values of approximately 20–30% for most porphyry copper rock types. As confinement increases within the growing cave column, progressive compaction (secondary fragmentation) commonly reduces effective *Bf*'s to approximately 15–20%. After breakthrough, full column weight further compacts the fragmented mass, leading to long-term *Bf* values of approximately 8–12% (van As& Guest, 2020). Within actively flowing draw zones, shear dilation can produce local *Bf* values approaching 50–60%, while compacted zones outside the draw column may exhibit ≈10%.

This spatial and temporal variability - irrespective of rock type differences, explains much of the scatter in the case history bulking data plotted in Fig. 2, and demonstrates that estimating bulking for cave mining draw control design purposes cannot be adequately represented by a single constant value. For estimating choking balances for crown stability assessment purposes, taking mean values from Fig.2, may however, be considered sufficiently reliable, at least for first cut evaluation requirements.

4 Crown Collapse

4.1 Crown Stability and Caving Risk

Five principal mechanisms drive crown pillar/cave back collapses: plug failure, chimneying, caving, unravelling and delamination (Carter et al, 1989, Carter, 2014). Chimneying and plug failure both occur with little bulking, limiting any likelihood that choking of the void space will arrest collapse. For all other mechanisms, (when high PoFs are indicated from *Sc/Cs* checks), breakthrough likelihood will depend on rock type and on fragmentation-controlled bulking.

Extremely competent crowns (Q> 200, as in natural limestone cave geometries) will remain stable for millennia. More jointed rock masses remain stable for years, if spans are below the critical span, *Sc*, for that rockmass quality. At the other extreme, very poor-quality crowns ($Q \ll 0.1$) disaggregate rapidly, and thus, caving in these rock types frequently leads to surface breakthrough, as bulking is often insufficient to adequately fill and choke-off available void space, almost irrespective of crown thickness.

Weak rock types that fragment readily, and intensely jointed or faulted rock masses (such as shown across the lower row of Fig. 3), can be considered self-caving, and prone to chimney collapse mechanisms. Standup time relative to Q, based on civil and mining tunnel experience, can be estimated from Fig. 4 (Carter & Miller, 1996), and appropriate block size-specific caving rates can also be derived, by comparing that data with the crown pillar dataset. Chimney and plug caving are, however, very difficult to assess, as they can progress rapidly over a very narrow footprint, often with little warning, and frequently, as pointed out by van As & Guest, 2020), also with very low apparent overall *Bf* values (of around 4–5%), reflecting limited total breakage relative to cave volume.

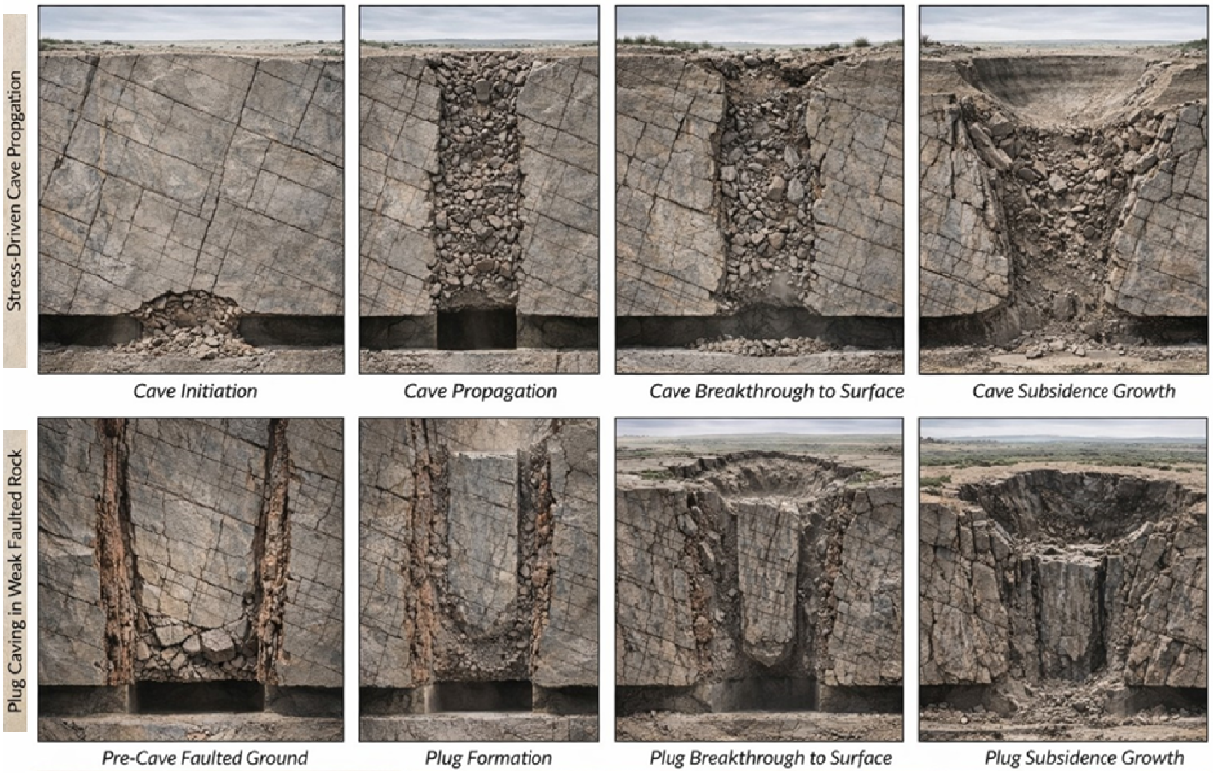


Fig. 3 Comparison– rockmass-controlled caving (top row) with chimney/plug mechanisms in faulted ground (lower row).

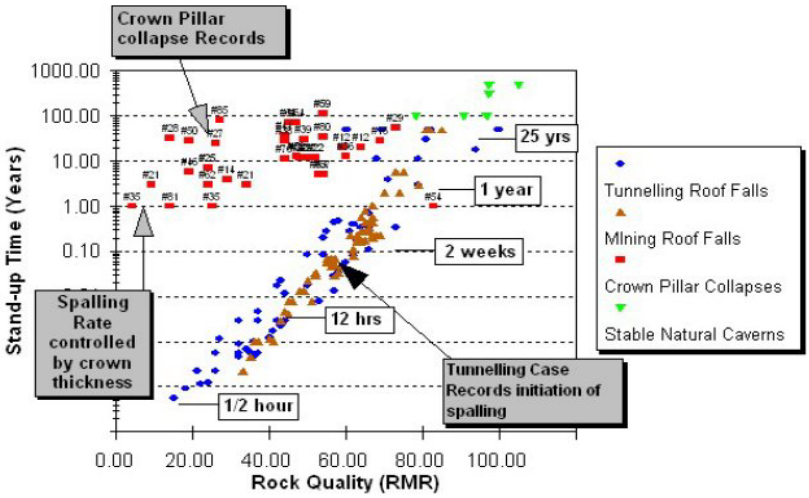


Fig. 4 Longevity for crown pillar collapses vs. stand-up time from tunnel and drift case records (Carter & Miller, 1996).

4.2 Choking Calculations and MRMR Caveability Estimates

Although bulking factors change significantly during cave propagation, advanced numerical modelling (Sainsbury et al., 2011; Sharrock et al., 2012; Cuello & Newcombe, 2014) confirms that, despite spatial variation in bulking/porosity across large cave footprints, a single rock type-specific bulking factor, such as can be extrapolated from Fig. 2, provides a reasonable approximation of overall column fragmentation for choking calculations. This is paralleled by longwall coal experience, where a single *Bf* approximation has proven reliable deeper into the gob, despite local variation near the coal face.

Benchmarking of cave onset from these advanced modelling approaches against the empirical methods outlined earlier suggests that the critical scaled span comparison with *Cs* provides a reliable threshold measure for assessing crown stability and rock mass caving likelihood, while determining the hydraulic radius of the undercut provides a better measure for defining overall caveability onset for thicker crowns where the crown thickness term, *T*, dominates the scaled span algebra. Evaluating the critical hydraulic radius (HR_{cr}) against a known rock mass quality using Laubscher's MRMR chart (Fig. 1, right) provides ready caveability likelihood assessment and allows initial estimates of the minimum undercut geometry dimensions required to initiate caving. It must though be noted that both the MRMR-*HR* and Scaled Span, *Cs* methodologies, although targeted differently, are conceptually analogous: comparing excavation geometry (*HR* or *Cs*) with a rock quality-dependent critical value (*HRcr* or *Sc*). Both methods however define only the initiation threshold for caving; as they implicitly assume that once the critical geometry is exceeded, the rock mass will propagate upward. In practice, post-initiation caving behaviour strongly depends on rock mass-specific levels of bulking. Where fragmentation produces sufficient fine cracking and dilation, stress transfer through the broken column is reduced and upward propagation proceeds readily. Where fragmentation is coarse and bulking is embryonic, efficient stress transfer promotes arching, potentially causing cave stall or hang-ups even when MRMR predictions suggest propagation should occur. Thus, while the critical hydraulic radius appropriately defines the geometric initiation threshold; bulking governs the subsequent mechanical evolution of the cave column.

5 Design Application

Two interrelated caveability design challenges require an in-depth appreciation of bulking: (a) crown pillar collapse risk evaluation, and (b) defining productive caveability for cave mining. Understanding site-specific bulking inter-relationships with rock type (Fig. 2) and stand-up time relationships per rock mass competence (Fig. 4) provides the basis of understanding for both.

5.1 Crown Pillar Surface Breakthrough Collapse Risk Assessment

The original Scaled Span methodology (Golder, 1990, Carter, 1992), which was originally developed from an extensive database of mainly subvertical stoping situations, was found in the late 1990's to be in need of modification for shallow dipping stoping (Carter et al, 2002), resulting in the standard procedures now incorporated in many guidelines, as summarized in Carter, 2014. More recently, with many mines transitioning from underground operations to super pits or, vice versa, going to cave mining from open pits, there has arisen a need to be able to better assess the influence on crown pillar stability of multiple steep orebodies and also complex on-seam and off-seam faulting patterns (Carter, 2019).

Depending on context, a recommended assessment workflow would therefore be as follows:

1. Define Crown Geometry – assess *Cs* (include shallow dip and/or multi-zone corrections).
2. Define Rockmass Quality – assess *Sc* (adjust for on-seam or off-seam faulting, if necessary).
3. Define Rock type controlling likely Caveability/Bulking – assess σ_C, *GSI*, m_i, hence m_b.
4. Assess bulking percentage by rock type – assess likely *Bf%* from σ_C and m_b.
5. Assess potential cave rate (m/year) per assessed most cave-prone rock type.
6. Establish available void space via CMS or similar ultrasonic survey if flooded.
7. Compare potential void volume vs. probable crown collapse volume (as bulked fill).
8. Assess potential breakthrough risk.

5.2 Evaluating Cave Propagation through Bulking Understanding

Cave initiation requires exceeding the critical hydraulic radius or minimum critical span. Sustained propagation and controlled cave growth, however, depends on the evolving bulking behaviour of the cave column. Fragmentation-dominated dilation governs early propagation; stress-dependent compaction governs long-term behaviour. Bulking must therefore be treated as a variable-state parameter, central to cave initiation, propagation, and operational control.

Three cave life-span phases are consistently identified from mass balance data: (1) undercutting phase - *Bf* ~20-30%, fragmentation-controlled; (2) propagation phase (post-*HRcr*) - *Bf* ~15-20%, with increasing confinement promoting partial compaction; and finally (3) steady-state post-breakthrough - *Bf* ~8-12%, full column weight mobilised. Local bulking in active draw zones may reach 50-60%, while surrounding compacted regions may be sub-10%. This spatial heterogeneity in bulking has direct implications for dilution management: the contrast between high-*Bf* draw zones and low-*Bf* compacted regions creates preferential flow paths that can accelerate dilution ingress from overlying waste, while isolated or poorly-drawn zones increase the risk of early mud or waste entry at breakthrough. Draw control strategies must therefore account for evolving void ratio distribution to minimise premature dilution and manage airgap formation. Since bulking is not directly measurable in situ (van As & Van Hout 2008), it must be derived from laboratory characterisation, field back-analysis or calibrated modelling. A suggested workflow, combining laboratory and field-testing methods would be thus:

1. Undertake laboratory testing ("swell" tests[*], confined compression and particle breakage studies) to provide mechanistic insight into initial dilation and stress-dependent compaction, and then calibrate against field behaviour.
2. Undertake calibrated modelling as basis for design, - benchmarked using initial MRMR, Lab data and cave mine operations experience, matching the three life-span phases identified above.
3. Conduct mass balance back-analysis: $Bf = (V_{cave} - V_{in\ situ}) / V_{in\ situ}$, (Brown, 2003,2006), where V_{cave} is obtained from CMS surveys or inferred from propagation height.
4. Carry out field measurements to improve understanding and calibrate modelling:
    - Complete a CMS/laser void scan to provide direct measurement of available void volume; for comparison with expected bulked collapse volume – to underpin calculations for crown breakthrough risk assessment;
    - Monitor drawpoints for block size and bulking (local *Bf*'s within flowing draw zones can reach 50–60% (plug flow) due to shear dilation, while compacted zones outside active flow may be only ~10%).
    - Implement cave marker and propagation tracking systems into the draw columns to help allow independent estimation of cave height vs. tonnage drawn, providing cross-checks on mass balance-derived bulking estimates.
5. Reassess caveability and cave propagation behaviour mechanics, and then update modelling, and if necessary, revise draw control strategies.

6 Conclusions

A combined understanding of cave mechanics, coupled with precedent knowledge of longevity-controlled rockmass degradation-driven crown pillar collapse behaviour, provides unique insight into the mechanisms governing excavation instability and potential surface impacts. For assessing surface impact from crown failure, and assessing propagation and operational control in cave mining, in-depth understanding is needed of rock-type-dependent bulking interrelationships with fragmentation stages.

[*] NB - here "swell" relates to "fragmentation-driven bulking", and should not be confused with "mineralogical swelling"

Empirical methods (scaled span, MRMR-hydraulic radius) define geometric and rockmass quality conditions for determining cave initiation and collapse potential but do not capture the specifics of the volumetric behaviour of fragmented rock that ultimately controls collapse propagation and cave performance. Bulking evolves systematically during cave development, from undercutting through cave propagation, but also continues to change after breakthrough. While bulking factors are strongly block-shape and rock-type controlled, local dilation within active draw zones may temporarily increase *Bf*s to levels significantly higher than baselines.

This evolving behaviour of bulking within a fragmenting rock mass, controls void ratio, stress transfer, arching, cave propagation rate, airgap development, hang-ups and cave material flow. For crown stability assessments, a single, representative early caving *Bf* provides a reasonable approximation for estimating collapse volume relative to available void. For cave mining design, however, bulking must be treated as a stage-dependent and stress-dependent state parameter of the cave column. Incorporating this behaviour into caveability assessment, mass balance analysis and draw control strategies thus provides the most realistic basis for predicting cave propagation and managing subsidence risk.

References

Brown, ET., (2003, 2006) Block Caving Geomechanics. JKMRC, Brisbane.

Carter, TG.,(1989). Design Lessons from Evaluation of OldCrown Pillar Failures. Proc. Int. Conference on Surface CrownPillars for Active and Abandoned Metal Mines, Timmins,Canada. pp.177-187.

Carter, TG.,(1992). A New Approach to Surface Crown PillarDesign. Proc. 16th Canadian Rock Mechanics. Symposium, Sudbury, pp. 75-83.

Carter, TG., Alcott, J. &Castro, LM., (2002). ExtendingApplicability of the Crown Pillar Scaled Span Method toShallow Dipping Stopes, Proc. 5th Nth. American Rock Mech.Symp., pp.1049-1059.

Carter, TG., Cottrell, BE., Carvalho, JL. & Steed, CM., (2008) Logistic Regression Improvements to the Scaled Span Method for dimensioning Surface Crown Pillars over Civil or Mining Openings. Proc. 42nd US Rock Mech. Symp. & 2nd Can-US Rock Symp., San Francisco, Paper 08-282. 13pp.

Carter, TG., (2014) Guidelines for use of the Scaled Span Method for Surface Crown Pillar Stability Assessment. Proc. 1st Int. Conf. Applied Empirical Design Methods in Mining, Lima, Peru, 34pp.

Carter, TG., (2019) Retrospective Assessment of Structurally Controlled Crown Pillar Failures Proc. 53rd N. Amer. Rock Mechanics Symposium. New York. Paper ARMA 19-2163 16pp.

Carter, TG. & Miller, RI., (1996) Some Observations on the Time Dependency of Collapse of Surface Crown Pillars. Proc. 2nd N. American Rock Mech. Symp., Montreal, V.1, pp.285-294.

Cuello, D. & Newcombe, G., (2014) Key geotechnical learnings from cave mining. Proc. 3rd Int. Symp. Block and Sublevel Caving, Santiago.

Golder Associates (1990) (Carter, TG., Yuen., CMK.,Barrett., SLV. & Wong, JS.,)Crown Pillar Stability Back-Analysis. Report to Canada Centre for Mineral and Energy Technology, #23440-8-9074/01-SQ, 90pp.

Hoek E. & Brown ET., (1980) Empirical strength criterion for rockmasses. J Geot.Eng 106,GT9: pp.1013-1035

Laubscher, DH., (1977) Geomechanics Classification of Jointed Rock Masses - Mining Applications. Trans. Inst. Min. Metall. (Sect.A) Vol.86, pp. A1-A8.

Laubscher, DH., (1994) Cave mining - the state of the art. J. S. Afr. Inst. Min. Metall., 94(10): pp.279-293.

Laubscher, DH., (2000) A Practical Manual on Block Caving. Report prepared under auspices of International Caving Study(1997-2000) 525pp.

Marinos, VP. & Carter, TG., (2025) Integrating *GSI* and m_i for Reliable Rockmass Strength Estimation. Proc. 1st International Rock Mass Classification Conference; Oslo, Rock Mechanics & Rock Engineering, Issue 10/2025, vol 58: pp.11216-11260; https://doi.org/10.1007/s00603-025-04792-2

Sainsbury, BL., Pierce, ME. & Mas Ivars, D., (2011) Simulation of rock mass strength anisotropy and scale effects using a Ubiquitous Joint Rock Mass (UJRM) model. Proc. 1st Int. FLAC/DEM Symp., Minneapolis.

Sharrock, GB., Cuello, D. & Rojas, E., (2012) Modelling draw in a sublevel cave mine. Proc. 6th Int. Conf. on Mass Mining, Sudbury.

Van As, A & Van Hout, G.,(2008), Implications of widely spaced drawpoints, in H Schunnesson & E Nordlund (eds), MassMin 2008: Proceedings of the Fifth International Conference and Exhibition on Mass Mining, Luleå University of Technology, Luleå.

van As, A & Guest, A., (2020), 'The design & operating philosophies of Panel vs Block Caving', in R Castro, F Báez & K Suzuki (eds), MassMin 2020: Proceedings of the Eighth International Conference & Exhibition on Mass Mining, University of Chile, Santiago, pp. 207-220,

Geotechnical Challenges and Adaptive Excavation Strategies: The Konovo Tunnel Case Study

B. Volk & E. Muhić
IRGO- Institute for Mining, Geotechnolog and Environement, Ljubljana, Slovenia

V. Jovičić
Faculty of Civil and geodetic Engineering, Ljubljana, Slovenia
vojkan.jovicic@irgo.si

0000-0003-2576-558X

Abstract

The Konovo Tunnel is an approximately 500 m long single-tube road tunnel located on the Third Development Axis expressway in Slovenia, along the section between Velenje and Slovenj Gradec. Excavation was carried out under an overburden of up to 50 m in highly heterogeneous geological conditions, consisting of tectonically intensely fractured dolomite, sandy marl with embedded dolomite blocks, marlstone, claystone, and locally occurring coal seams. Despite its relatively short length, the tunnel construction required the management of several significant geotechnical challenges. One of the key challenges was a continuous section of marlstone and claystone forming a relatively homogeneous geological sequence beneath two residential buildings, with an overburden of approximately 35 m. In this zone, a technologically adapted phased excavation scheme was implemented to ensure adequate control of surface settlements and to maintain the structural safety of the overlying buildings. Additional critical challenges were encountered in the portal areas. The northern portal intersected a 58 m long section located within a slope characterized by very low global stability. To mitigate slope instability risks and ensure a safe transition to underground excavation, a pile-supported cut-and-cover construction method was adopted.At the southern portal, an atypical constraint required the tunnel to be excavated and broken through under extremely shallow overburden due to permitting limitations. The breakthrough was therefore carried out following the excavation of a southern pre-cut, which enabled controlled exposure of the tunnel face.Although relatively short in length, the Konovo Tunnel project encompassed a wide range of geotechnical and construction challenges, which were successfully managed through continuous geological and geotechnical monitoring, as well as adaptive modification of excavation and support measures during construction.

Keywords

Tunnelling, Heterogenous conditions, Low overburden, Ground movement control, Geotechnical supervision.

1 Introduction

1.1 Tunnel and portal layouts

The new road connection from Velenje South to the Slovenj Gradec south interchange has a total length of 17.5 km. One of its key elements is the 1.9 km long section between Konovo and Škale, which comprises a viaduct and the approximately 500 m long Konovo Tunnel. The Konovo Tunnel is designed as a single-tube, bidirectional road tunnel with a design speed of 70 km/h. The tunnel cross-section consists of two traffic lanes, each 3.25 m wide, with a central separation strip 0.50 m wide and two edge strips 0.35 m wide, extending to the service walkway. The overall excavation profile of the tunnels was approximately 100 m2, while the primary support was carried out using the postulates of the NATM method (Rabcevicz, 1964). The overall tunnel structure includes a 425 m long tunnel tube, a 58 m long northern portal structure, and a 14 m long southern portal structure, resulting in a total tunnel length of 497 m.

The northern portal, shown in Fig. 1 is designed as a covered cut-and-cover structure. Due to extremely poor geotechnical conditions, the construction of a sufficiently wide-open excavation for the transition into the tunnel section was not feasible. The ground conditions in this area consist primarily of high plasticity clays containing completely disintegrated dolomite and lenses of organic material, resulting in very low stability of the existing natural slopes. Portal structure was designed as a covered trench gallery (cut and cover structure) using the top-down construction method. Initially, bored piles were installed along the tunnel alignment, followed by the construction of the upper and lower bracing slabs, which together formed the structural frame of the gallery. After completion of the structural elements, backfilling above the top slab was carried out, followed by measures for surface water management, prior to the excavation beneath the top bracing slab.

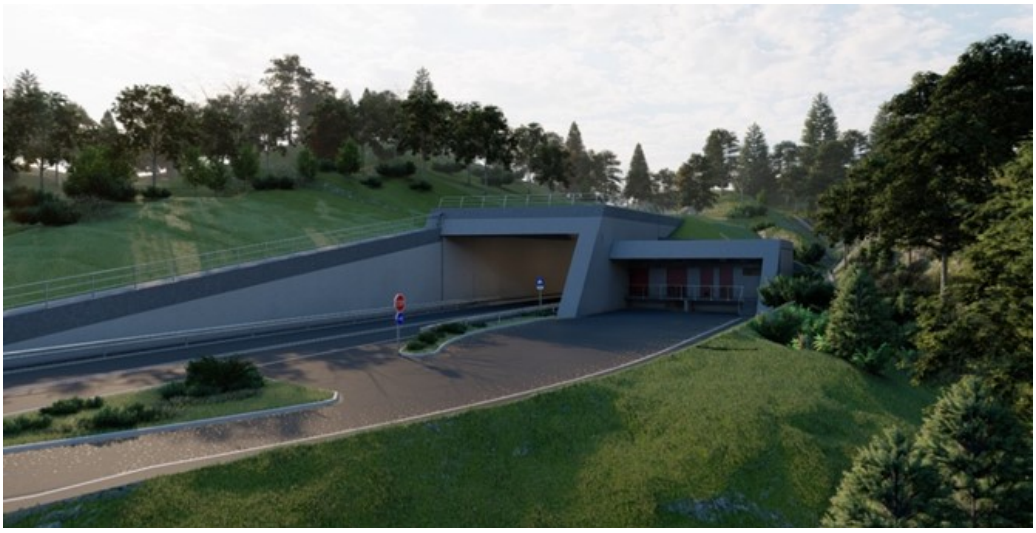


Fig. 1 Render visualization of the final design of the northern portal of the Konovo tunnel.

A specific feature of the southern portal is the transition of the tunnel to a viaduct located on a very steep slope, with the portal positioned relatively high on the hillside. A conventional tunnel portal configuration, combined with reinforced earth embankments combined with a stone masonry retaining structure was executed in limited spatial conditions.

2 Geological and hydrogeological conditions

2.1 Geological and hydrogeological observation during construction

Geotechnical model based on site investigation carried out in 2019 predicted at northern portal a presence of grey to brown high plasticity clays with interlayers of sandy clay, silt, and clayey fine sand. Clays transitioned into organic clays locally with coal lenses reaching thicknesses of several meters. The bedrock along the tunnel alignment was interpreted as Lower Scythian light grey to yellowish dolomite, with interlayers of siltstone and locally marlstone. Siltstone layers occur mostly in frequent alternation with dolomite. At the southern portal, layers of marly limestone and siltstone were also identified. The rock mass was expected to be strongly fractured along the tunnel routewhile

locally tectonically crushed to soil-like material within the tectonic gouge as seen at the northern portal.

During the excavation of the portal cuts and the tunnel, continuous geological and hydrogeological monitoring was carried out. Geological monitoring comprised surface inspections, logging of piles and boreholes, and detailed documentation of the excavation, including face mapping, bench, and invert inspections. Hydrogeological monitoring included the measurement of groundwater inflows within the tunnel, monitoring of piezometric levels at the surface, and the interpretation of the changing hydrogeological conditions during construction.

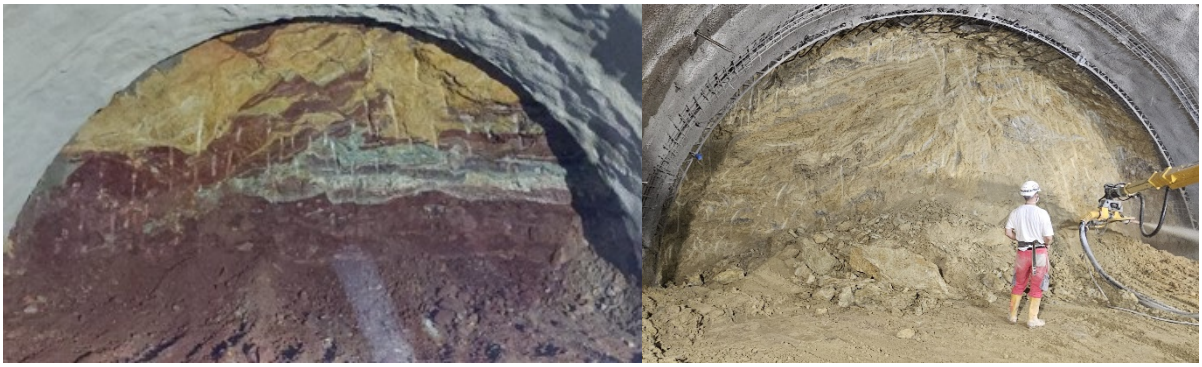


Fig. 2 Comparison of tunnel excavation faces in red and yellow fine-grained marls (left) and in tectonically fractured dolomite with interbedded layers of sandy marl (right).

Comparison between the predicted and observed conditions generally showed that the dolomite unit did not occur as a continuous and homogeneous strata, but in the form of individual blocks tectonically embedded within alternating layers of red, brown, and grey siltstone. In addition, a section of the tunnel was encountered where the excavation consisted almost entirely of red, brown, and grey siltstone layers, shown in Fig. 2, which was reclassified as a separate unit of weak rock. Excavation of the tunnel revealed that this unit dominates in several tunnel sections and typically forms entirely the bench and invert zones. In general, geological mapping repeatedly revealed intense tectonic deformation of the rock mass along the tunnel layout, where lithological conditions change rapidly along fault zones.

Comparison of the predicted and observed hydrogeological conditions showed good agreement with water appearing mainly in the form of seepage, dripping, and minor inflows at the tunnel invert. In the initial section of the tunnel starting from the northern side, the inflows of up 3 l/min per 25 m of tunnel layout were detected. In the mid tunnel section, initial inflows of 30–45 l/min per 10 m of tunnel were recorded during the excavation of the top heading while the steady-state inflows later decreased to approximately 2.5 l/min per 100 m of tunnel. This reduction can be attributed to the effective drainage of groundwater during excavation, which might have induced settlement of the ground surface, as it will be commented later.

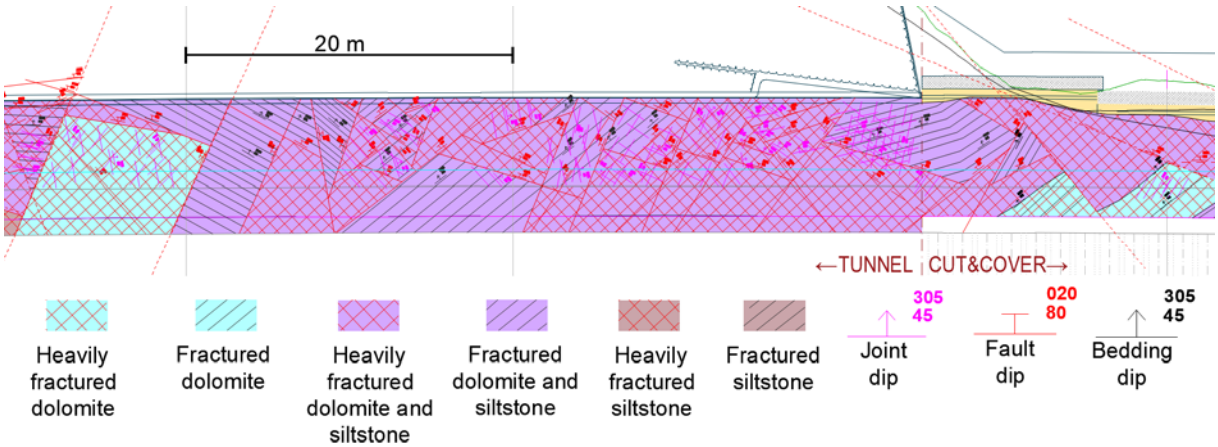


Fig. 3 Longitudinal geological profile of the northern portal area, illustrating tectonic deformation and geological heterogeneity.

3 Challenges encountered during tunnel construction

3.1 Tunnel excavation and support

The transition from the cut and cover structure to the tunnel excavation at the northern side was carried out using a pipe roof support system. This was necessary to address the abrupt transition from the portal structure to the underground excavation, combined with very low overburden, continuous groundwater inflows from nearby torrential gullies, and rapidly varying geological conditions (

Fig. 3).

During the subsequent tunnel excavation, the geological conditions continued to change frequently, requiring permanent adjustment of excavation step lengths and support types. Despite the well-known shortcomings (Kovari, 1994), the flexibility of NATM (Karakus & Fowell, 2004) was found particularly suitable for these geological conditions. As part of the optimisation of the support system the reinforced shotcrete lining was replaced by the steel fibre shotcrete. However, it soon became evident that the wet sandy siltstone base combined with embedded dolomite blocks did not provide suitable conditions for this optimisation. The steel fibre shotcrete exhibited poor adhesion to the substrate, resulting in detachment during application and significant loss of material. After a short trial section, steel fibre shotcrete was abandoned. Following similar conditions experienced in Karavanke tunnel (Jovičić & Volk, 2022), this case also confirmed that wet rock mass substrates with a tendency for disintegration or composed of fine-grained material are not suitable for the application of steel fibre shotcrete based on conventional mix designs.

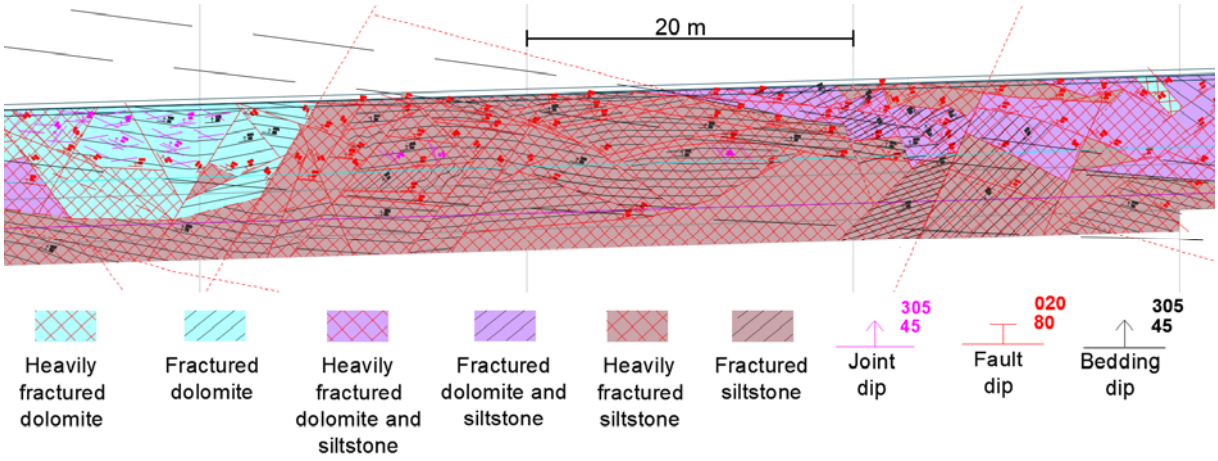


Fig. 4 Geological profile of the tunnel featuring a red shale marl section extending across the entire tunnel cross-section.

3.2 Ground deformation and surface settlements

Beyond initial section, the tunnel entered a relatively homogeneous geological zone (Fig. 4) composed predominantly of red shaly siltstone. From a geotechnical perspective, the ground conditions became significantly less favourable so that the increase in tunnel displacements began to manifest at the ground surface. Two existing residential buildings, which were located directly above the tunnel alignment (Fig. 5) so that a precise levelling monitoring system was established on both structures to measure settlement and structural movements during the tunnel excavation.

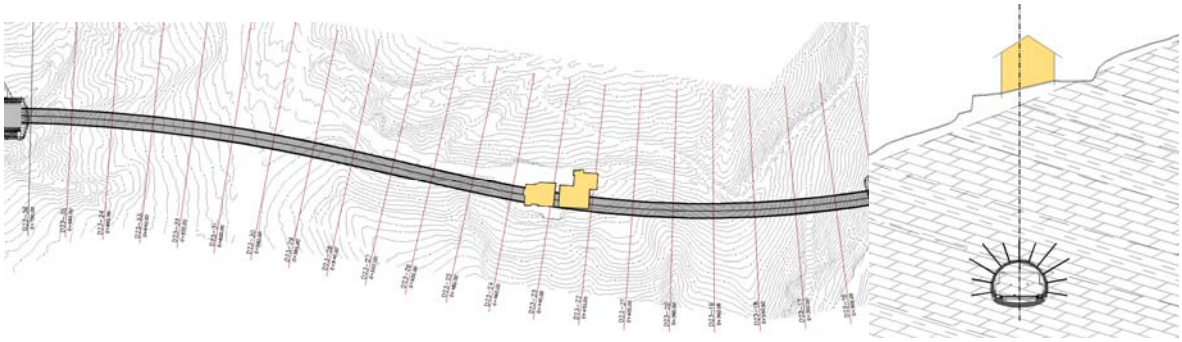


Fig. 5 Location of the 2 residential buildings, situated 35 m directly above the tunnel alignment.

The new support type was introduced in the tunnel approximately 15 m before entering the red siltstone zone within the zone of influence on the settlements of the buildings. The support measures consisted of 20 cm thick shotcrete reinforced with a single layer of Q189 steel mesh, combined with 4 m long SN rock bolts of nominal capacity of 250KN, installed in a 2.0 m grid, with an excavation step length of 1.7 m. Due to increase in settlements recorded on the buildings above the tunnel, the excavation face was temporarily stopped on few occasions, and the invert was closed all the way to the top heading. In continuation, a "stop-and-go" construction procedure was used to limit further deformations.

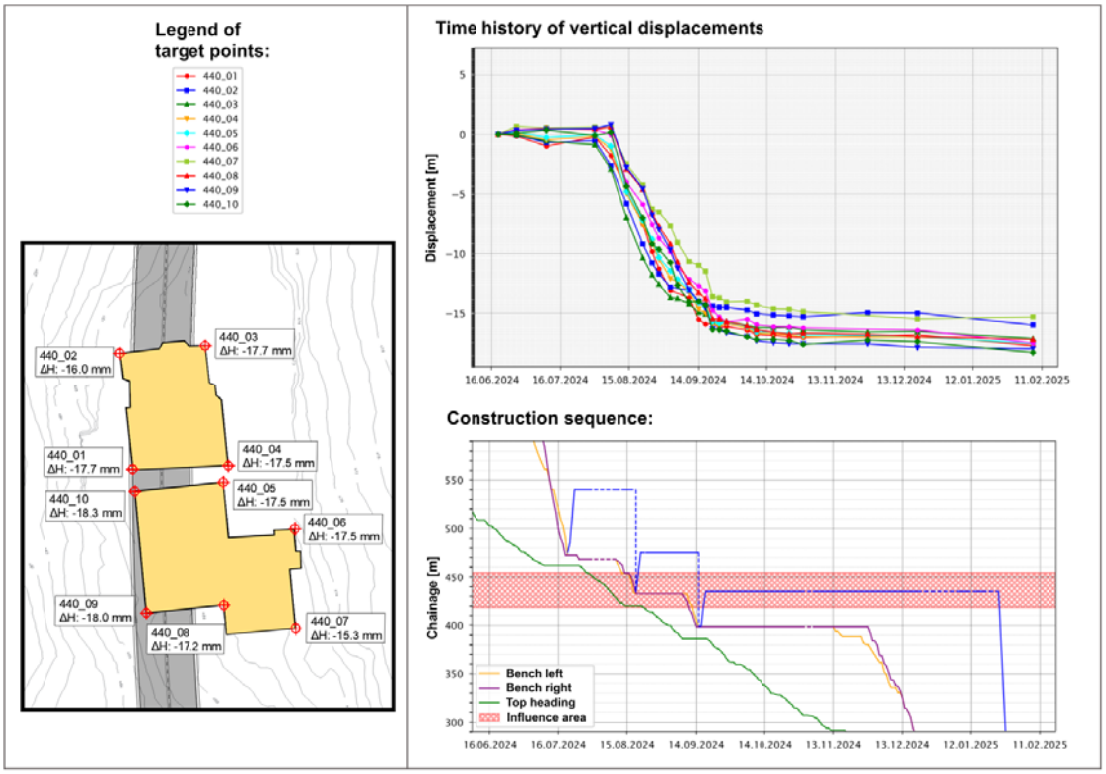


Fig. 6 Presentation of final precise levelling measurements at residential buildings above the tunnel alignment relative to the progress of the tunnel excavation (legend to the left shows the names of different target points at the surface and the buildings).

Mostly vertical tunnel displacements reached approximately a total of 15 cm after completion of the excavation, while surface settlements were up to 18 mm (Fig. 6) where differential settlements on individual structures remained limited to approximately 1.5 mm and no damage to any of the buildings was detected. The absence of differential settlements indicated that lowering of groundwater table may have a significant contribution to this settlement trough.

3.3 Local instabilities at the face of the excavation

The next major challenge encountered during the construction of the Konovo Tunnel was a local instability zone within geological conditions dominated by highly fractured and tectonically disturbed dolomite in the approach to southern portal area. During the excavation, the rock mass proved friable,



Fig. 7 Block failure of dolomite during the excavation of the top heading in the low overburden zone.

while locally larger dolomite blocks detached along unfavourably oriented discontinuities, causing local collapses, as illustrated in Fig. 7. When advancing with an excavation step of 1.3 m, excessive block detachment from the crown occurred, resulting in the formation of larger voids. Considering the low overburden of approximately 6 m above the tunnel axis, and the potential risk to the global stability of the slope caused by ongoing block detachment, a 9 m long pipe umbrella consisting of 26 pipes to mitigate the threat of local instabilities that could potentially have developed into larger-scale collapses or even global tunnel instability at this section. Excavation beneath the pipe roof was carried out with a 1 m excavation step, combined with relatively stiff support measures. These included 25 cm thick shotcrete reinforced with two layers of Q283 steel mesh, together with 6 m long IBO self-drilling anchors installed in a 1.5 m grid. Face stability was ensured using a temporary support core and shotcrete protection. After installation of the primary support, the cavities were filled by pressure grouting to ensure proper contact between the lining and the surrounding ground.

4 Conclusions

Despite its relatively short length of approximately 500m, Konovo tunnel presented a wide range of geotechnical challenges, typical of variable geological conditions and shallow urban tunnelling. One of the key challenges was the construction of the northern portal gallery, which had to be executed as a top-down, cut-and-cover structure due to demanding geological conditions. Another important factor during construction was the strict limitation of ground movements beneath residential buildings, which required continuous adjustment of the excavation sequence and careful implementation of the primary support measures. A particular difficulty occurred during the approach to the southern portal, where detaching blocks of unbound dolomite posed a threat of local instabilities that could potentially have developed into larger-scale collapses or even global tunnel instability. These risks were successfully mitigated through the appropriate selection and timely implementation of additional support measures.

Despite the challenges described, the construction process was efficient and largely consistent with expectations. It should be noted, however, that tunnel construction was constrained by a regulatory restriction prohibiting night-time work in urban areas. Such a limitation is uncommon in modern tunnelling practice, particularly under demanding geotechnical conditions, where continuous operations are often essential. Restricting work to daytime operations significantly reduced excavation progress, since only temporary stabilisation measures could be implemented, thereby negatively affecting tunnel stability and the overall construction schedule.

References

Jovičić, V., & Volk, B. (2022). Impact of water inflow and design solutions for construction of Karavanke tunnel. In S. Ćorić (Ed.), *Inženerski problem vo meki karpi: zbornik na trudovi od Pettiot simpozium na Društvoto za geotehnika na Makedonija, Specijalizirana konferencija na ISRM, Vtora konferencija na regionalnite geotehnički društva, Ohrid, R. S. Makedonija.*(pp. 115–125).

Karakus, M., & Fowell, R. (2004). *An insight into the New Austrian Tunnelling Method (NATM)*. ROCKMEC′2004-VIIth Regional Rock Mechanics Symposium.

Kovari, K. (1994). ERRONEOUS CONCEPTS BEHIND THE NEW AUSTRIAN TUNNELLING METHOD. *Tunnels & Tunnelling International*, *26*(11), 38–42.

Rabcevicz, L. V. (1964). The new Austrian Tunnelling Method (Part 1 and Part 2). *Water Power*, *November 1*, 511–515 and 19–24.

Construction Challenges of the Karavanke Tunnel's Eastern Tube in Water-Bearing Conditions

J. Ratej
IRGO Institute for Mining, Geotechnology and Environment, Ljubljana, Slovenia

B. Volk& S. Galuf
IRGO Consulting d.o.o., Ljubljana, Slovenia

V. Jovičić
Faculty of Civil and Geodetic Engineering, Ljubljana, Slovenia
vojkan.jovicic@irgo.si

0000-0003-2576-558X

Abstract

The construction of the new eastern tube of the Karavanke Tunnel was completed in 2025, while it was opened to traffic in March 2026. Excavation works, accomplished in 2024, were carried out under highly variable geotechnical conditions, including several sections with high-capacity aquifers. The first critical section passed through the Werfen Formation, where the transition from clastic rocks to carbonates was water-bearing. The crossing of an approximately 100 m long fault zone involved significant water inflows, reaching up to 35 litres per second. Another major water-bearing zone was encountered at the transition from the Werfen Formation to the Schlern Dolomite at the Goliški Fault, where tunnel excavation passed through a short fault zone of mylonitic dolomite. The latter section posed almost insurmountable challenges during the construction of the existing western Karavanke tunnel approximately 30 years ago. Caused by the surge of the water inflow of up to 5,000 l/s tunnel a collapse occurred, accompanied by a devastating debris flow of more than 3,000 m³ of material. Following thorough preparations for the excavation of the eastern tube several measures were implemented to ensure effective pre-drainage of the water-bearing sections to prevent high water inflows. These measures enabled the safe continuation of excavation works and provided valuable insights into the hydrogeological conditions of the Karavanke mountain range. The improved understanding was subsequently used to optimize design of the planned underground water collection system, which was constructed to capture and distribute high-quality groundwater for public use.

Keywords

Tunnel Karavanke, Water inflows, Underground water collection system, Anhydrite.

1 Introduction

The 7.9 km long Karavanke Tunnel is located on European Transport Corridor X, connecting Slovenia and Austria, and represents one of the most important north–south transport links in the Alpine region. The existing western tube, constructed between 1986 and 1991, required rehabilitation and, being non-compliant with the European Directive 2004/54/EC (Official Journal reference: 167, 2004) on minimum safety requirements for tunnels posed both traffic and safety risks. Experience gained during the construction of the western tube revealed highly complex geological and hydrogeological conditions and was instrumental in preparation for the excavation of the eastern tube.

One of the most critical sections encountered during the construction of the western tube was the Goliška fault zone. In this zone, extremely high water pressures and a high-capacity aquifer led to one of the most significant water inrush events recorded in tunnel construction, both in terms of energy release and discharge (Petkovšek B, 1990). This event resulted in the collapse of a previously constructed tunnel section in the immediate vicinity of the fault zone, as well as a major failure of the fractured rock mass above the tunnel. Remedial measures required the construction of a bypass tunnel, which enabled the continuation of excavation beyond the Goliška fault zone (Mikoš B., 1991). The bypass tunnel was subsequently repurposed to accommodate a pumping station for the permanent supply of drinking water.

The paper presents key aspects of the construction of the new eastern tube under water-bearing conditions based on invaluable experience gained during the excavation of the existing western tube. Targeted measures were developed and implemented to ensure effective pre-drainage of water-bearing zones, thereby limiting groundwater inflows and reducing the risk of excavation-induced instabilities. In this context, the drainage function of the existing tube was systematically utilised during both the site investigation and construction phases.

2 Construction of the western tube

During the construction of the western tube, significant water inflows were encountered within the Werfen Formation, reaching up to 100 l/s. These inflows were accompanied by local instabilities and the displacement of crushed material by water, which caused major difficulties during excavation due to high water pressures.



Fig. 1 Conditions during excavation through the fault zone in the Werfen Formation in the western tube (Mikoš B., 1991).

The construction of the western tube in the Werfen Formation included regular geological probe drilling and the installation of drainage boreholes. However, due to the low permeability, trapped water in the rock mass exerted pressure on the primary lining, leading to the formation of cracks, followed by yielding and eventual collapse of the primary lining. The tunnel section was temporarily supported with timber beams (Figure 1), additionally anchored, and subsequently reprofiled to the required cross-section.

Excavation of the western tunnel tube later entered the Schlern Dolomite, where, due to the limited extent of deep investigations available at the time, conditions at tunnel level at depth of some 900 m were less well known, particularly between chainages 2.4 km and 3.4 km. As a result, predicting geological and hydrogeological conditions along the tunnel alignment in general, and especially at neo tectonic fault zones within Triassic rocks, such as Goliška fault zone, was not possible. The contractors applied the same approach as in the previously mentioned Werfen Formation, where probe drilling served both for geological investigation of the rock mass ahead of the excavation face and for drainage of fracture-related water inflows. Despite regular probe drilling and drainage, water inflows reached up to 90 l/s and were significantly hampering the excavation progress.

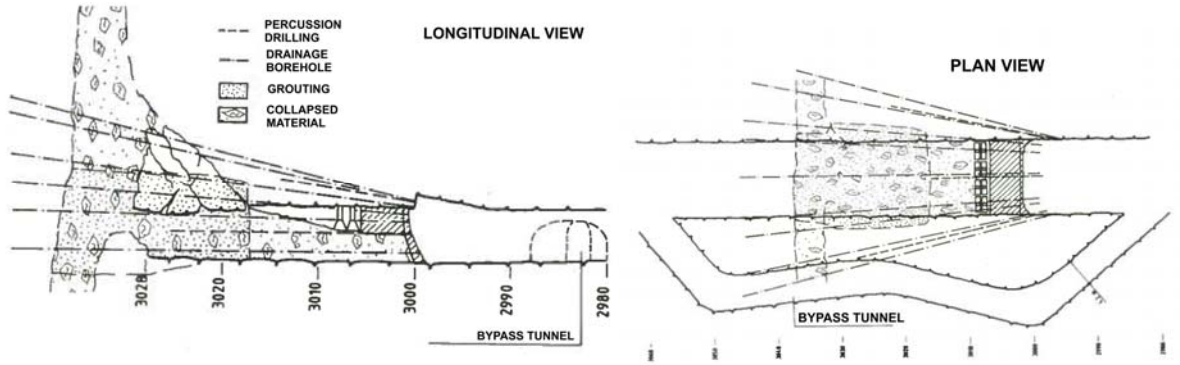


Fig. 2 The longitudinal and plan view show the estimated void space above and in front of the tunnel following the inflow of water and material caused by a hydraulic fracture at the excavation face (Mikoš B., 1991).

At chainage 3,030 m, a Goliška fault zone was identified through probe drilling; however, further excavation proved impossible. During an attempt to advance, in and partly controlled event, a tunnel collapse occurred, accompanied by water inflow of up to 5,000 l/s and a debris flow exceeding 3,000 m³ of material. Fortunately, there were no casualties among the workforce, but significant material damage occurred. Figure 2 presents a schematic longitudinal and cross-section of the collapsed area following the event. Even after 15 days, water inflow remained as high as 385 l/s, stabilizing at approximately 150 l/s after five months. Extensive remediation measures were required, including stabilization of the collapsed tunnel face and grouting of cavities. Concurrently, excavation continued through a smaller bypass tunnel which was later used for a permanent drainage of the groundwater.

3 Construction of the eastern tube in Werfen formation

The design of the eastern tube began in 2016 and was strongly influenced by the conditions encountered during the crossing of the Goliška fault in the western tube, as well as by the associated tunnel collapse. Construction of the eastern tube commenced in 2020 and revealed that, unexpectedly, the Werfen Formation fault zone was more challenging for excavation than the previously confronted Goliška fault zone.

The Werfen Formation is heterogeneous, consisting of marly limestones, dolomites, sandstones, locally also oolitic limestones, and grey micaceous sandstones with gypsum lenses. The rock mass is characterized by intense tectonic fracturing and heterogeneity, resulting in fracture porosity being the dominant mechanism for groundwater flow. Based on experience gained from the western tube, construction of the eastern tube along Werfen Formation was managed in a more systematic manner. Key measures included the timely use of exploratory boreholes for drainage, advance probe drilling ahead of the excavation face, and the installation of sufficient drainage boreholes.

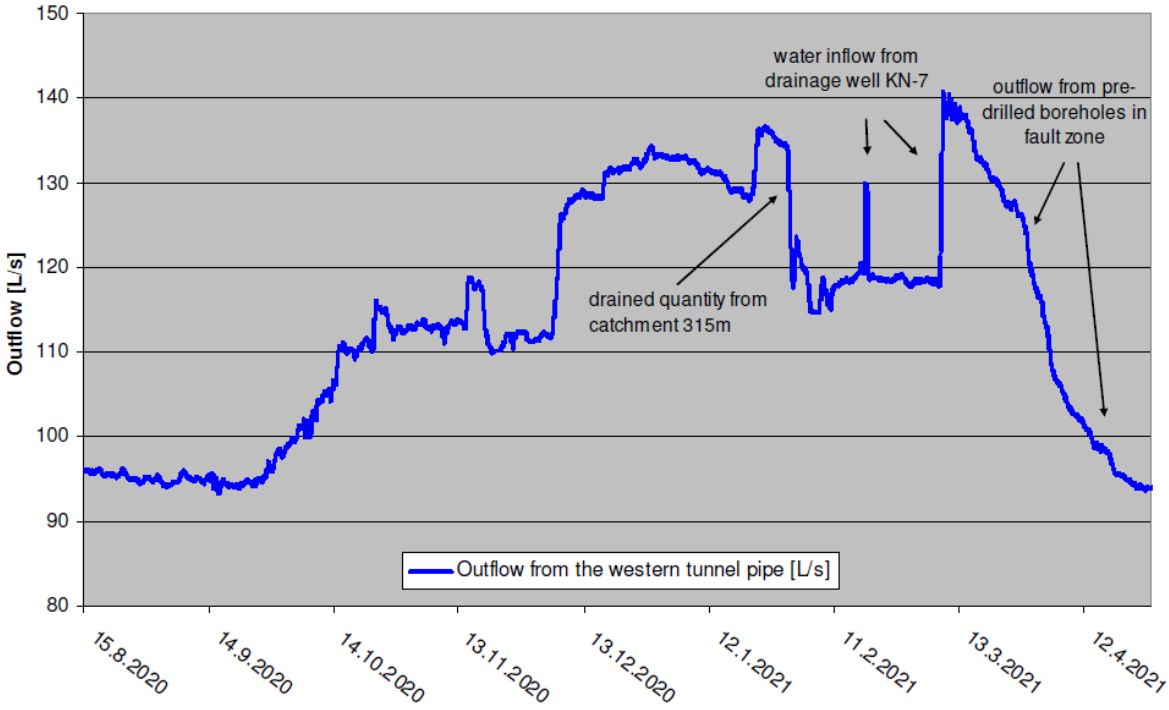


Fig. 3 Total outflow from the west tube, showing the significance of drainage from borehole KN-7 and drainage boreholes at the excavation face (Ratej J, 2024).

Important data were obtained from the exploratory borehole KN-7, drilled from a previously partially constructed cross passage in the western tube, which enabled the monitoring of pressures and inflows for several years before the start of construction of the eastern tube (Ratej J, 2024). With the start of excavation of the eastern tube at the beginning of 2021, measurements showed that pressures were around 5 bar, while inflows at the opening were approximately 30 l/s and occasionally higher. The geological and hydrogeological prognosis indicated that inflows in this area could reach magnitudes of 40 to 90 litres per second. Measured pressure values ranged between 2.5 and 5.5 bar, clearly demonstrating the dynamic response of the system to precipitation and seasonal variations. This confirmed that the aquifer has high permeability within fractured and tectonically deformed zones. To reduce the risk, a controlled release of groundwater pressure was carried out through borehole KN-7 into the drainage system of the western tunnel tube.

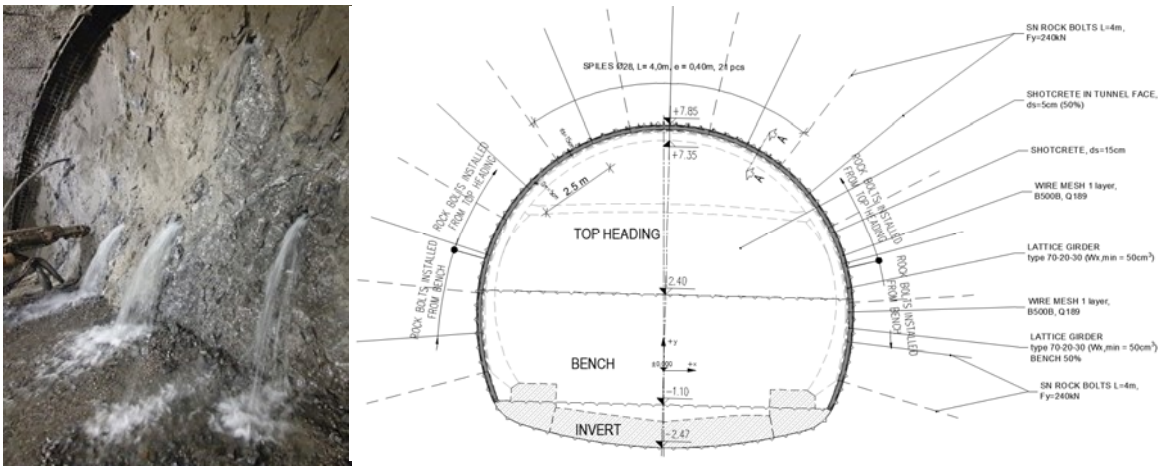


Fig. 4 Water inflow in the area of the Werfen Formation with a representative support type.

Following the start of drainage in March 2021, pressure at borehole KN-7 decreased to 2.6 bar and inflow to approximately 23 l/s. Continuous monitoring of total outflow from the western tube confirmed the effectiveness of the drainage measures (Figure 3). Simultaneously, local inflows in the eastern tube during excavation of the Werfen Formation were linked to drainage from KN-7, confirming a shared aquifer system. This significantly improved excavation conditions by reducing the risk of uncontrolled inflows and erosion. With continued drainage, pressure at KN-7 dropped to 0.22 bar and inflow to 1.6 l/s before crossing the critical zone.

The Werfen Formation exhibits a dual hydrogeological character, combining low-permeability clay layers with highly permeable fractured zones, leading to uneven inflow distribution. These conditions require continuous monitoring and adaptable measures. Long-term observations at KN-7 and in the western tube proved essential for timely and informed geotechnical decision-making.

The key strategy for tunnel construction in the Werfen Formation was systematic probe drilling and installation of 30 m long drainage boreholes with at least 15 m overlap. This enabled effective pressure relief and safe excavation with relatively light support (Figure 4), unlike the extensive remediation required in the western tube (Jovičić & Volk, 2022). Local high inflows (up to 60 l/s) were successfully controlled with additional drainage boreholes. Excavation remained stable, with primary lining deformations limited to a few centimetres, resulting in safer, faster, and more cost-effective progress.

4 Construction of the eastern tube in Goliška fault zone

As previously mentioned, the Goliška fault zone represented the most challenging section of the western tube construction in terms of water-bearing conditions. It is a complex tectonic structure composed of several parallel slices of tectonized dolomite, with highly variable permeability. The inner cores are often mylonitized and act as local hydrogeological barriers, while the marginal zones are strongly fractured and enable rapid groundwater flow. During the investigation phase, exploratory boreholes were drilled from the existing western tube and cross passages, confirming tectonically disturbed dolomite and significant water inflows. The hydrogeological prognosis, based on transferring the permeability field from the western to the eastern tube under reduced hydrodynamic pressures (approximately 3.5 bar), indicated potential inflows of around 100 l/s. The predicted inflows were expected to decrease to 25–50 l/s over the entire Schlern Dolomite section, which was later confirmed during construction.

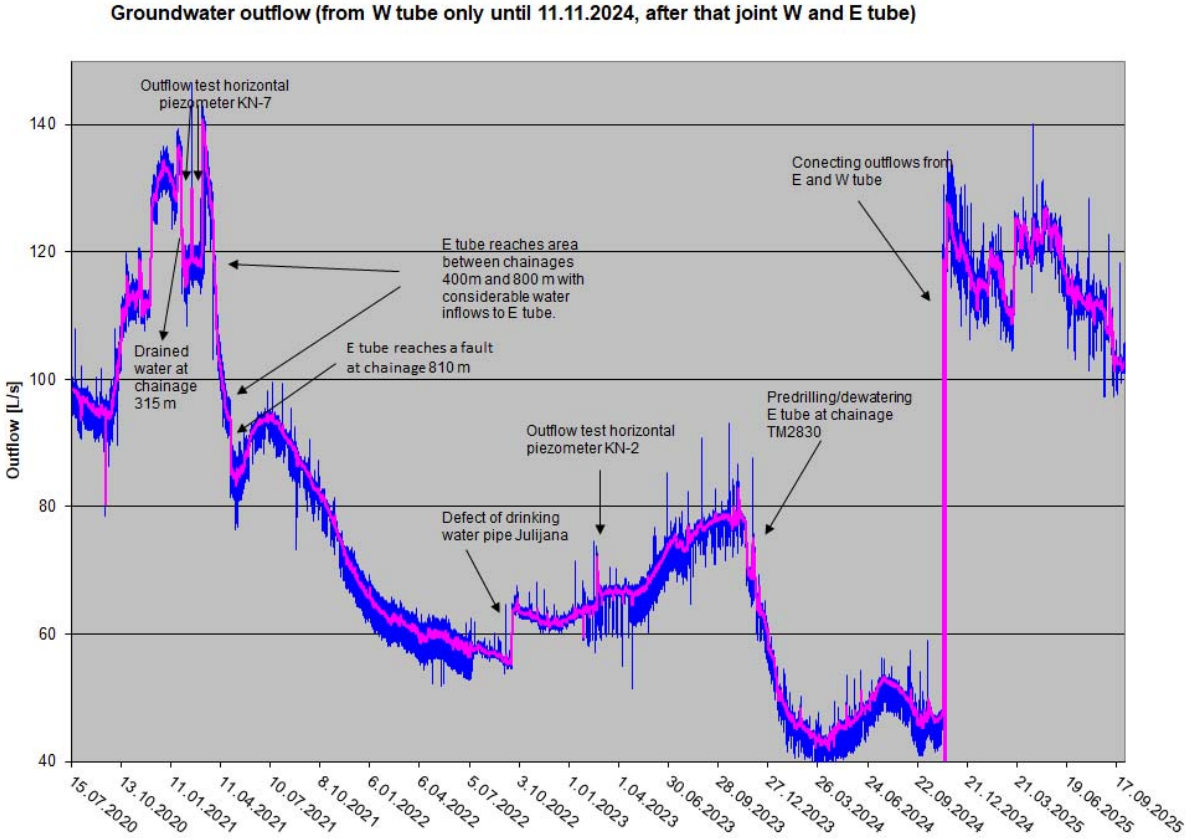


Fig. 5 Water outflows from the western tunnel tube showing the effect of drainage from boreholes KN-2a and KN-2b.

Due to the risk of water inrush, the design included several mitigation scenarios and safety measures, such as a pilot tunnel, pipe umbrella support, and grouting curtains. Additional measures were proposed in the hydrogeological report to facilitate safe excavation through the Schlern Dolomite and the Goliška fault zone. In addition to mandatory pre-drainage by probe drilling, drainage from existing

boreholes (KN-2a and KN-2b) in the western tube was also implemented. During construction of the eastern tube, nearly one year of continuous drainage through exploratory boreholes in cross passage KN-2 significantly reduced hydrodynamic pressures. As a result, the disturbed zone of the Goliška fault was no longer expected to collapse during excavation. Only minor, fracture-related inflows were encountered, and conditions did not deteriorate as the excavation approached the fault zone while no increase in inflow or material washout was observed. After completion of both drainage campaigns, total inflow was reduced to an insignificant 3 l/s.

Long-term drainage from boreholes in the western tube (KN-2a and KN-2b) proved crucial. As shown in Fig. 5, which presents total outflows from the western tube between July 2020 and March 2024, continuous discharge over nine months successfully reduced hydrostatic pressures within the wider fault zone and created a sufficiently deep depression cone, extending below the top heading level. Consequently, excavation took place in largely unsaturated conditions, with only vertically percolating water present, enabling significantly safer progress. As a result, originally planned measures such as grouting and pipe umbrella support were not required, and a standard support system for good rock mass conditions was sufficient.

Since the Goliška fault zone lies within a water protection area, part of the project also included the development of a new freshwater intake. Hydrogeological investigations were conducted to optimize its location. A blind cross passage with a collection basin and a system of wells was constructed, consisting of two wells 60 m long and two wells 100 m long, enabling efficient groundwater capture for drinking water supply.

5 Conclusion

The construction of the eastern tube of the Karavanke Tunnel clearly demonstrates that experience gained during the construction of the western tube, targeted investigations, and, above all, continuous monitoring during construction were crucial for the successful execution of this complex infrastructure project. While the western tube was marked by severe hydrogeological difficulties, water inrushes, and prolonged interruptions due to tunnel collapses, the eastern tube was constructed in a significantly more controlled, safe, and efficient manner. The key factors were a detailed understanding of ground conditions, conservative planning, and continuous monitoring, which enabled timely adjustment of measures.

In both the Werfen Formation and the Goliška fault zone, the main hazards were associated with water inrushes. These risks were effectively managed through systematic drainage. The existing western tube played an important role, as the effectiveness of drainage was verified through continuous pressure and flow monitoring from the boreholes installed during the site investigation campaign for the design of the eastern tube. Additional crucial measure was systematic installation of drainage boreholes throughout construction. These boreholes intercepted groundwater from water-bearing fractures, reducing pressures that could otherwise act on the tunnel walls and primary support system. As a result, water inrushes, and particularly the collapse of weakened and crushed rock were successfully prevented, enabling safe and uninterrupted construction progress.

References

Jovičić, V., & Volk, B. (2022). Impact of water inflow and design solutions for construction of Karavanke tunnel. In S. Ćorić (Ed.), *Inženerski problem vo meki karpi: zbornik na trudovi od Pettiot simpozium na Društvoto za geotehnika na Makedonija, Specijalizirana konferencija na ISRM, Vtora konferencija na regionalnite geotehnički društva ,Ohrid, R. S. Makedonija.* (pp. 115–125).

Mikoš B. (1991). *), Predor Karavanke: geologija in geotehnika, Cestniinženiring, Ljubljana*.

Petkovšek B, D. F. (1990). *Cestnipredor Karavanke Jug, Poročilo o inženirsko geoloških razmerah, Geološki zavod Ljubljana, Inštitut za geologijo, geotehniko in geofiziko, Ljubljana*.

Ratej J. (2024). Poročilo o stanju hidrogeoloških merilnih mest in izvedenih meritvah v vzhodni in zahodni cevi predora Karavanke v marcu 2024.

RMR based tunnel support

F. Deák
Óbuda University, Budapest, Hungary
deak.ferenc@uni-obuda.hu

A. Lowson
Mott MacDonald, Croydon, United Kingdom

Abstract

For professional tunnelling engineers and geologists, particularly in the early stages of a project, this study could be useful as it provides a critical assessment of different solutions works best in the RMR rock mass classification system and how the values derived from it can be translated into the establishment of a practical rock safety system 53 years after its development and extensive accumulated experience.

It addresses three aspects of practical tunnel design: 1) new design tables for determining the required rock support as a function of tunnel span and rock quality; 2) the determination of tunnel cross-section shapes and secondary linings; and 3) an updated RMR grading method for practical applications. The practical solutions presented in this paper are based on the experience accumulated over several decades by Lowson and Bieniawski (2013). After years of validation and application, the authors are glad to observe that the recommendations are genuinely aligned with reality and are effective. Not only the Q method guidelines can be used to establish rock support, but also the RMR. In this paper are presented some updated relations from the original publication (Lowson and Bieniawski 2013).

Keywords

RMR89, RMR14, RQD, Rock support, Rock mass.

1 Introduction

In the form of a table (Bieniawski 1989), the original RMR-based tunnel support standards gave support advice for a tunnel span/diameter of 10 meters. As the technology for steel ribs, shotcrete, and rock bolting has advanced, tunnel designers have been given the responsibility of adapting these standards for different tunnel sizes, which has proven successful. It is now clear after 37 years of usage that practical tunnel designers would benefit from charts and equations that guide the choice of rock support based on the tunnel size and the rock mass quality. Consequently, this is the primary goal of this paper, along with modernizing the methodology for better calculating the RMR values and forecasting the adequate and safe tunnel support (Lowson 2012, Lowson and Bieniawski 2012).

The rock support methods for each rock mass quality are a combination of different support types, as shown in Table 1. The next section discusses how to determine the support needs for particular elements, like rock bolts, shotcrete, and steel ribs, since, for instance, two support approaches are somewhat additive.

Table 1. Original guidelines for support of rock tunnels based on the RMR system (Bieniawski 1989).

Rock Mass Class	**Excavation**	**Support**		
		Rock Bolts (20 mm Dia., Fully Grouted)	**Shotcrete**	**Steel Sets**
Very good rock I RMR: 81-100	Full face 3 m advance	Generally, no support required except spot bolting		
Good rock II RMR: 61-80	Full face 1.0-1.5 m advance	Locally, bolts in crown 3 m long, spaced 2.5 m, with occasional wire mesh	50 mm in crown where required	None
Fair rock III RMR: 41-60	Top heading and bench 1.5-3 m advance in top heading	Systematic bolts 4 m long, spaced 1.5-2 m in crown and walls with wire mesh in crown	50-100 mm in crown and 30 mm in sides	None
Poor rock IV RMR: 21-40	Top heading and bench 1.0-1.5 m advance in top heading. Install support concurrently with excavation 10 m from face	Systematic bolts 4-5 m long, spaced 1-1.5 m in crown and wall with wire mesh	100-150 mm in crown and 100 mm in sides	Light to medium ribs spaced 1.5 m where required
Very poor rock V RMR: <20	Multiple drifts 0.5-1.5 advance in top heading. Install support concurrently with excavation. Shotcrete as soon as possible after blasting	Systematic bolts 5-6 m long, spaced 1-1.5 m in crown and walls with wire mesh. Bolt in invert	150-200 mm in crown, 150 mm, in sides, and 50 mm on face	Medium to heavy ribs spaced 0.75 m with steel lagging and fore-poling if required. Close invert

Before making any recommendations, it is crucial to consider what practicing tunnel designers currently need. Based on the opinion of the authors of this article and earlier publications (Lowson and Bieniawski 2013), when comparing numerical modelling with empirical estimates based on extensive accumulated experience, the use of continuum models often provides unreliable results regarding rock support, especially at shallow depths, although they can be useful in extreme cases where plastic deformation effects are present and the rock mass exhibits high plasticity. The practicing tunnel engineer needs design tables to work efficiently. Accordingly, the practicing tunnel engineer is concerned with design rules for both shotcrete and rock bolts, depending on the tunnel dimensions and rock quality, to assess the final rock support requirements. We believe that the tunnel construction industry takes a pragmatic approach, as it is satisfied with an easily determinable RMR rating, including the orientation of joints as a component.

Following the original 2013 article (Lowson and Bieniawski 2013), an update and revision of the RMR rock mass classification method was published in 2014, launching the modified RMR14 method (Celada et al. 2014).

The RMR14 system has been used in numerous projects in various locations around the world; in contrast, while, the rock mass rating guidelines recommended in 2013 have been used less frequently (Rehman et al. 2018, Kanik et al. 2015, Liu et al. 2021, Zhang et al. 2021).

After a brief introduction to the RMR89 and RMR14 methods, we present in more detail a minor modification of the RMR89 recommended by Bieniawski in 2013, and we present rock mass classification methods based on this system.

The rock mass classification system based on the RMR89 method, developed in 2013, was first applied in Hungary in the geotechnical design and report underpinning the detailed design of the M85 tunnel (Deák 2019).

2 Rock support systems for underground excavations

2.1 Design load

Rock load on a support system is a function of rock mass condition and initial stress state. Where the rock mass is not overstressed and squeezing is not occurring, the design load is taken as (See Eq. 1):

$$\mathrm{P_r}(\mathrm{RMR}, Span) = \frac{100 - \mathrm{RMR}}{100} \cdot 10\mathrm{m} \left(\frac{Span}{10\mathrm{m}}\right)^{\frac{1}{2}} \cdot \mathrm{p_r} \cdot \gamma_r \tag{1}$$

Where γ_r is a partial factor; $\mathrm{p_r}$ is rock density. Assuming a partial factor of 1.5 and a density of 27 kN/m³, this yields the following results, which are shown in Fig. 1.

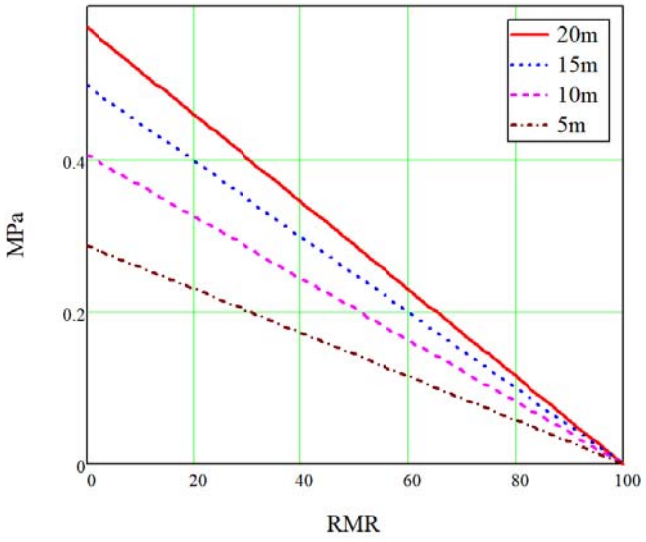


Fig. 1 Rock load versus span.

2.2 Stand up time

Our research in this area is still ongoing; we still need to analyze several historical projects in which we examined underground mined systems. We still aim to classify the rock mass and then examine its stand-up time. For instance, the mined cavity system of the old Roman gold mine Alburnus Major at Rosia Montana - Romania (with varying rock mass quality) has stood unsupported for more than 2,000 years. Based on the original Bieniawski table, several sections of it should have collapsed long ago. We plan to revise this table in the near future.

2.3 Bolt spacing

In our recommendation below, we consider the spacing of the rock bolts solely in terms of the RMR. The spacing must reflect the fracture frequency and ensure that the shotcrete provides adequate support between the bolts at the right end of the scale, where the shotcrete cannot realistically be expected to function as an arch on its own. Experience shows that for RMR ≥ 85, only individually spaced rock anchors are required (Eq. 2-4 and Fig. 2).

if $20 < \mathrm{RMR} \leq 85$

$$S_b = 0.5m + 2.5m \cdot \frac{RMR - 20}{65} \tag{2}$$

if 10 < RMR ≤ 20

$$S_b = 0.25m + \frac{(RMR - 20)^{1.5}}{140} m \tag{3}$$

if RMR ≤10

$$S_b = 0.25m \tag{4}$$

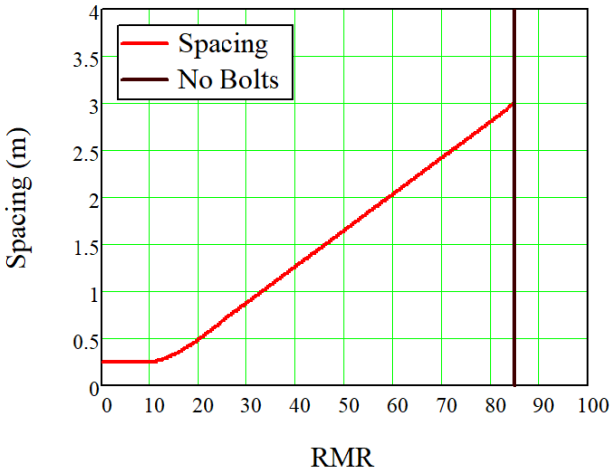


Fig. 2 Rockbolt spacing versus RMR.

2.4 Rock bolt length

Bolt length must vary with span and RMR. Based on empirical guidelines used in mining and the results of numerical modelling studies, the following relationship was obtained (Eq. 5 and Fig. 3):

$$Span = \frac{(L_b + 2.5)^{\frac{RMR+25}{52}}}{3.6} \tag{5}$$

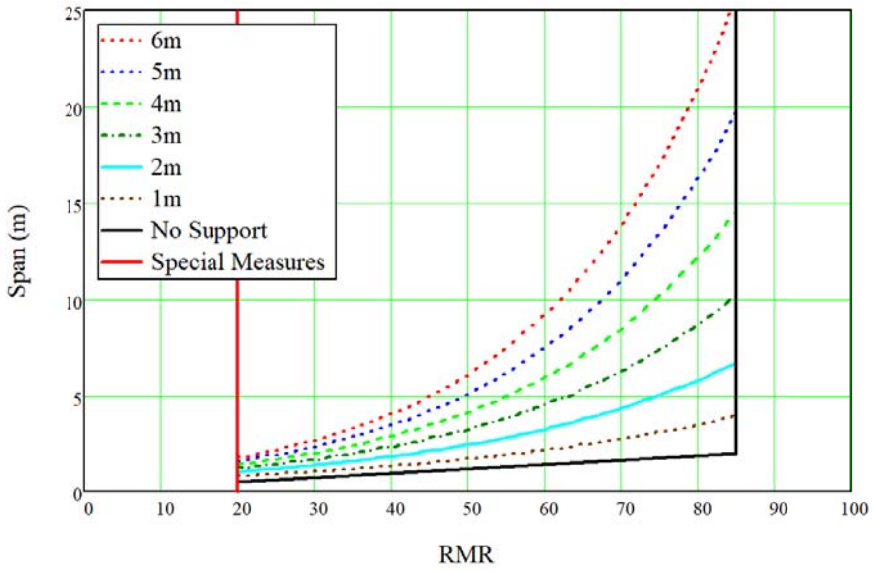


Fig. 3 Rockbolt length chart.

2.5 Rock bolt capacity

The support capacity of pattern rock bolting is considered to be determined by dividing the capacity of each bolt by the area it must support. The capacity of bolts decreases with a lower RMR due to the increasing challenge of achieving an effective bond and the decreasing ability of the bolts to initiate arching action within the rock mass. The resulting relationship is presented below (Eq. 6 and Fig. 4). The graph represents the capacity of a standard 25 mm bolt with an ultimate tensile strength of 25 tons.

$$F_{ub}(RMR) = \frac{F_b}{\gamma_b} \cdot \left(\frac{RMR}{85}\right)^{\frac{40}{RMR}} \tag{6}$$

Where F_b (bolt capacity) = 250 kN, γ_r (bolt partial factor) = 1.5.

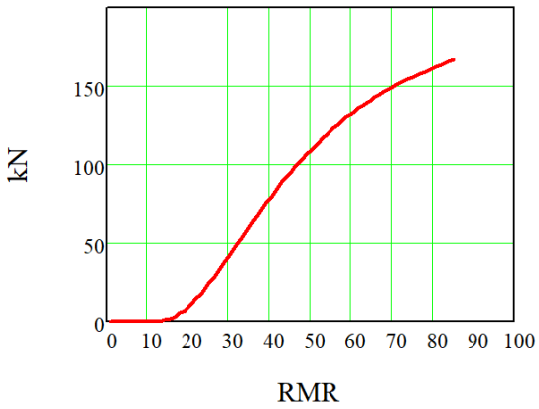


Fig. 4 Design rockbolt capacity versus RMR.

2.6 Shotcrete capacity

If the rock mass has good quality (RMR > 60), only a thin layer of shotcrete is required. Applying a thin layer of shotcrete to an irregular surface in blocky rock results in a layer of shotcrete that is itself irregular, and assuming it behaves as a stand-alone arch is not credible. Where a thin layer is applied to an uneven surface with a texture depth much bigger than shotcrete thickness, the key supporting mechanism is the shotcrete prevents inter-block movement and general loosening, and so mobilises arching in the rock.

For medium quality rock, say RMR = 35 to 60, the shotcrete can more reasonably be thought of as acting as an arch. If large parts of the tunnel are in rock of this quality the tunnel shape will probably be a horseshoe with curved sidewalls, and certainly at the lower end of this scale the shotcrete will have filled a lot of the irregularities in the surface and the inside shape will be curved with few re-entrant areas.

Below RMR values around 35 the excavation would require multiple headings unless the tunnel is very small. This is done to keep the size of the face and therefore the size of any heading collapse to manageable proportions. Analysis of the support system by numerical methods or otherwise finds that the shotcrete is increasingly subjected to flexural and shear forces as well as simple axial compression.

If the axial load values on the Y-Axis are divided by member thickness the result is a Moment / Axial Stress curve. The curve shown below is for 32MPa cylinder strength shotcrete with a thickness of 300mm.

The figure below shows the design strength of 30 MPa (f_{ck}) shotcrete (Fig. 5).

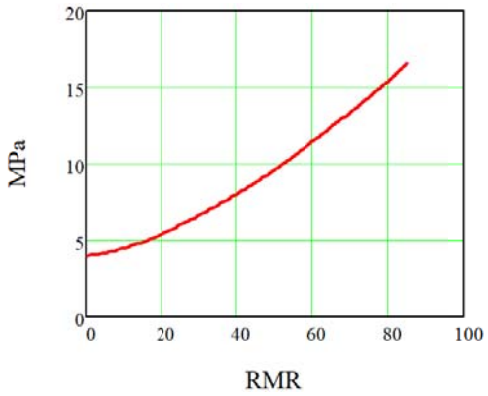


Fig. 5 Design shotcrete strength.

$$f_{cd}(RMR) = \frac{f_{ck}}{\gamma_s} \cdot \left[0.2 + 0.8 \cdot \left(\frac{RMR}{100}\right)^2\right] \tag{7}$$

2.7 Shotcrete support solutions

Based on the above relationships for the capacities of shotcrete and rock bolts a chart relating Span and RMR for a given thickness of shotcrete can be derived. The capacities of the rock bolts and the shotcrete are considered to be additive.

The irregularities in the lines around RMR = 50 to 20 indicate that the rock bolts' ability to provide meaningful support has ended. The middle option in the equation for rockbolt spacing, for RMR between 10 and 20, is used as a transition to create a somewhat seamless curve in the graph below (Fig. 6).

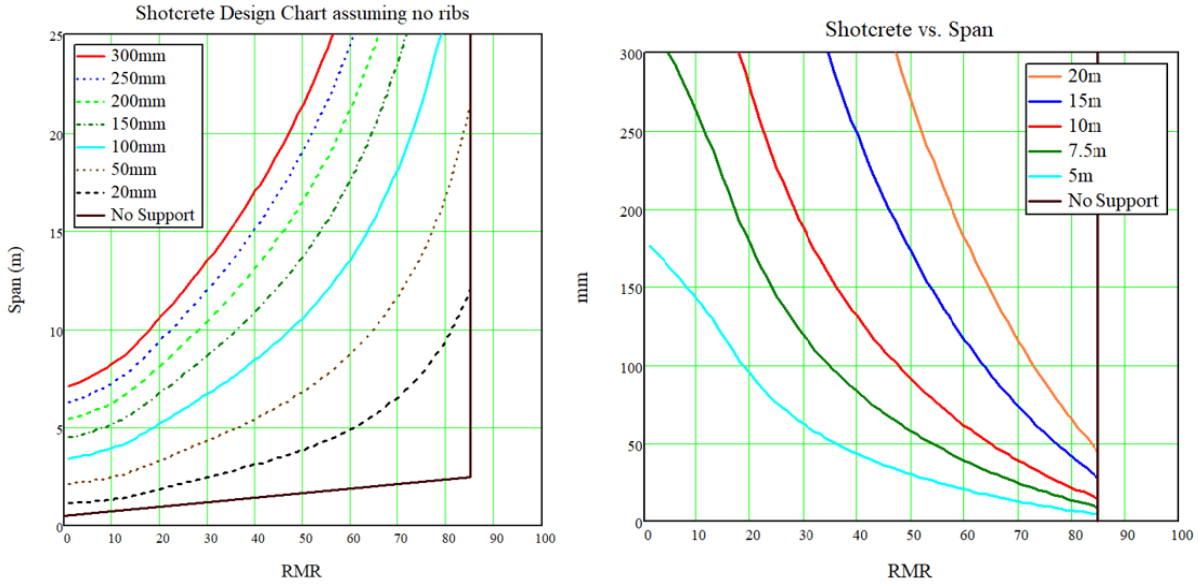


Fig. 6 Shotcrete design charts.

3 Replacement of the RQD during the RMR calculations

This parameter was originally included among the six RMR parameters because all of the case studies collected in 1972 included RQD. Over the years it became apparent that RQD was difficult to determine at the tunnel face, being directed to borehole characterization, and it was subsequently combined with parameter "discontinuity spacing" ("joint" spacing) - and named "spacing density" since the two are interrelated. For the best practical use, this led to the preferred use of "fracture frequency" as an invert of "fracture density" – as depicted in Fig. 7. None of these approaches altered the fundamental assignment of rating values to these parameters.

In this work, we re-examined the schematic summary diagram prepared by Bieniawski in 2013, refined the descriptive equation, and accordingly updated the diagram (Eq. 7 and Fig.7):

$$\text{RQD} + \text{Joint spacing} = -6.6 \cdot \left(\frac{Joints}{m}\right)^{0.46} + 40 \tag{7}$$

Therefore, when conducting engineering-geological descriptions and mapping of tunnels and rock slopes, we recommend continuing to use the JOINT FREQUENCY (number of joints per meter) instead of the distances between RQD (No. 2) and Joint Spacing (No. 3) among the six fundamental factors of the RMR89.

For RMR drill core documentation, we continue to recommend the use of the original RMR89, but for newer core documentation work, it is recommended to include a data column for recording joint frequency as well, so that this information to be available for later correlation studies. At the same time, we would like to point out that for rock material whose intact rock fragments do not exceed a UCS value of 6 MPa, we do not recommend using either the RQD or the RMR to characterize the rock mass and determine rock support systems.

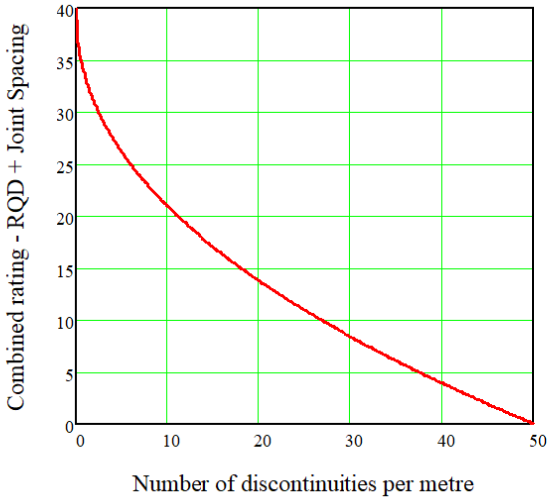


Fig. 7 Combined rating of the discontinuity density parameters: RQD plus discontinuity spacings.

4 Conclusions

The purpose of the brief summary presented here was to provide easy-to-use design charts and equations for the preliminary design of rock mass support based on RMR. The intention was to provide these guidelines in an easily accessible format, with some updates, and, where possible, along with the mathematical relationships, equations, and underlying logical and theoretical background used to construct the diagrams.

It must be emphasized that these charts are intended for preliminary design! This applies to all design diagrams and simplified methods presented here for the design of underground excavations. These are essentially expert systems developed to make design decisions similar to those an expert would make by following a set of rules.

It is also true, however, that while an expert may have deemed the rock support measures reasonable based on the information available before tunnelling begins, it may become apparent during construction that these initial plans need to be checked and modified. This may mean a greater or lesser need for rock support, or it may mean that, depending on the available equipment and the capabilities of the workforce, one type of rock support must be preferred over another. Rock mass conditions are inherently variable, and the stress state of the rock mass can differ dramatically from the "average" values assumed during design. Therefore, every contract must always provide for the ability to modify the preliminary rock support systems to suit the actual-real conditions.

All of the correlations and recommendations presented are based on the original RMR89 method for the analysis of drill cores, while for tunnels they are based on a modified version of RMR89 (omitting the RQD and spacing of discontinuities).

We excluded the use of RMR14 in our work, as decades of experience are available for the original RMR89; however, it should also be noted that, based on current international practice, RMR14 yields higher results than RMR89, so, particularly in the case of rock mass assessment, the balance of safety also leans toward a more conservative rock mass classification.

References

Bieniawski Z.T. (1989) Engineering Rock Mass Classifications. John Wiley & Sons, New York.

Celada B., Tardáguila I., Varona P., Rodríguez A., Bieniawski Z.T. (2014) Innovating Tunnel Design by an Improved Experience-Based RMR System. In Proceedings of the World Tunnel Congress, Foz do Iguaçu, Brazil, p. 9.

Deák F. (2019): Geotechnical Design and Report – M85 Tunnel, in the vicinity of Bécsi Hill, Sopron. Manuscript in Hungarian, 90 p.

Kanik M., Gurocak Z., Alemdag S. (2015) A comparison of support systems obtained from the RMR89 and RMR14 by numerical analyses: Macka Tunnel project, NE Turkey. Journal of African Earth Sciences 109 (2015), pp. 224–238. Doi: j.jafrearsci.2015.05.025

Liu J., Dai G., Gong W. (2021) Joint Frequency in the Rock Mass Rating 2014 ClassificationSystem Based on Field P-wave Propagation Velocity Tests: A New Rating Method. Springer, Geotech Geol Eng, 12 p. Doi: 10.1007/s10706-021-01777-0

Lowson A. R., Bieniawski, Z.T. (2013) Critical assessment of RMR-based tunnel design practices: A practical engineer's approach. In: Proc. RETC 2013. Washington, DC: Society of Mining Engineers, pp.180-198.

Lowson, A.R. (2012) The support capacity of steel sets. Tunnelling Journal, May, 18-20.

Lowson, A.R. and Bieniawski, Z.T. (2012) Validating the Yudhbir-Bieniawski rock mass strength criterion.

Proc. World Tunnel Congress, ITA, Bangkok.

Rehman H., Ali W., Naji A. M., Kim J., Abdullah R. A., Yoo H. (2018): Review of Rock-Mass Rating and Tunneling Quality Index Systems for Tunnel Design: Development, Refinement, Application and Limitation. MDPI Applied Sciences, 27 p.

Zhang Q., Jiang Q., Li Y., Wang N., He L. (2021) Quality Evaluation of Rock Mass Using RMR14 Based on Multi-Source Data Fusion. MDPI Sensors, 20 p.

A hybrid FLAC3D-MPM approach for post-failure slope behaviour

C. Cancino & J. Hazzard
ITASCA, Minneapolis, USA
ccancino@oneitasca.com
0000-0002-9657-3430

C. Coetzee
Stellenbosch University, Stellenbosch, South Africa

Abstract

Simulating large-strain behaviour in rock slopes poses significant challenges for traditional continuum modelling methods, primarily due to mesh distortion leading to numerical instabilities. While mesh remeshing can mitigate this issue, it becomes computationally intensive and technically complex in 3D, especially for irregular geometries. Meshless methods such as the Material Point Method (MPM) and Smoothed Particle Hydrodynamics (SPH) offer an alternative by avoiding mesh distortion entirely; however, they often come with drawbacks including longer run times and difficulty applying boundary conditions.

This paper presents a hybrid modelling approach that combines the efficiency of a finite-volume meshed continuum with the flexibility of MPM for simulating large deformations. The model uses traditional finite-volume zones in regions of low strain, while areas expected to undergo large deformation are handled with material points. The interface between the two domains allows for information transfer through an overlapping region. Material point regions can be defined at the outset or generated dynamically when deformation thresholds are exceeded, enabling a responsive and efficient modelling framework.

To evaluate performance, a rock slope failure with significant runout is simulated using three configurations: fully meshed (FLAC3D), hybrid FLAC3D-MPoint, and fully meshless (MPoint). Displacement patterns and computational times are compared across all cases.

This hybrid formulation is particularly relevant for risk and reliability assessments of rock slopes, where post-failure deformation and runout are critical to consequence estimation. By capturing large displacements without compromising computational efficiency, this approach improves runout predictions and supports risk-informed slope design.

Keywords

Numerical Modelling, Material Point Method, FLAC3D, Slope Stability, Runout Analysis

1 Introduction

Assessment of rock slope stability traditionally focuses on the onset of failure, often quantified through factor of safety or strength reduction methods. However, for high-consequence slopes, prediction of post-failure deformation and runout is equally critical, as it directly governs hazard extent and infrastructure exposure. Conventional continuum methods such as finite difference or finite element approaches are effective in simulating pre-failure stress redistribution and progressive strain localization. Their applicability diminishes once deformation becomes very large, where mesh distortion can lead to numerical instability and artificial resistance.

Meshless methods, including the Material Point Method (MPM), provide an attractive alternative for modelling extreme deformation and flow-like motion. By decoupling material motion from the computational grid, MPM avoids mesh distortion and enables robust simulation of large displacements. However, fully meshless models can be computationally expensive when applied to large three-dimensional domains in which significant portions remain in low-strain conditions.

This paper presents a hybrid numerical framework that combines FLAC3D (Itasca, 2026a) with MPoint (Itasca, 2026b), the commercial implementation of the Material Point Method formerly known as MPAC (Purvance and Coetzee, 2024). The objective is to unify progressive failure modelling and post-failure runout within a single mechanically consistent framework. A benchmark is carried out using a case study of a slope failure in an open pit, in order to compare fully meshed FLAC3D, fully meshless MPoint, and hybrid approaches. The case study allows to demonstrate practical applicability in large-scale engineering problems.

2 Numerical Framework

2.1 Continuum Formulation (FLAC3D)

FLAC3D employs an explicit finite-volume formulation for solving the equations of motion in a Lagrangian framework. It is well suited for modelling stress redistribution, progressive strain localization, and structural control through zone joints or ubiquitous joint formulations. For rock slopes, it enables realistic representation of geological domains, fault geometries, and strain-softening behaviour. The limitation arises when shear localization evolves into large displacement, where element distortion reduced numerical accuracy and may require artificial damping or remeshing when large-strain mode is enabled.

2.2 Material Point Method (MPM)

The Material Point Method represents material as a set of Lagrangian particles carrying state variables such as stress, strain, and density. These material points interact with a background Eulerian grid on which momentum equations are solved. Because the grid is reset each timestep, large deformations do not cause mesh distortion. MPoint provides robust simulation of large strain shear localization, fragmentation-like behaviour, flow-like post-failure motion, etc. However, full-domain MPM simulations can be computationally demanding for large models with extensive low-strain regions.

2.3 Hybrid Coupling Strategy

The hybrid approach combines both formulations within a single model. Regions expected to remain stable are represented by FLAC3D elements (zones), while regions undergoing large deformation are represented by material points. An overlapping transition region allows stress and velocity transfer between the two formulations. The coupling is achieved using the approach of Lian et al. (2012), where “hybrid” points exist at each FLAC3D zone gridpoint within some distance of the material points and these hybrid points act as a bridge passing information between gridpoints and the background MPM grid.

3 Case Study: Open PitStability

3.1 Background

This case study focuses on the stability of the north wall of an open pit mine in Peru. The slope was monitored using ground-based radar, which identified deformation at an inter-ramp scale extending over approximately eight benches above the nearest ramp (Figure 1). Displacement rates increased

significantly, reaching velocities of up to 54 cm/day in August 2019. Subsequently, between November 2019 and April 2020, rainfall events contributed to continued slope movement, resulting in cumulative displacements exceeding 1 m. These observations raised concerns regarding the potential for further acceleration and propagation of the instability under additional precipitation events. As a result, evaluating the potential runout associated with a progressive or fully developed failure became critical to support safe continuation of mining activities at pit bottom.

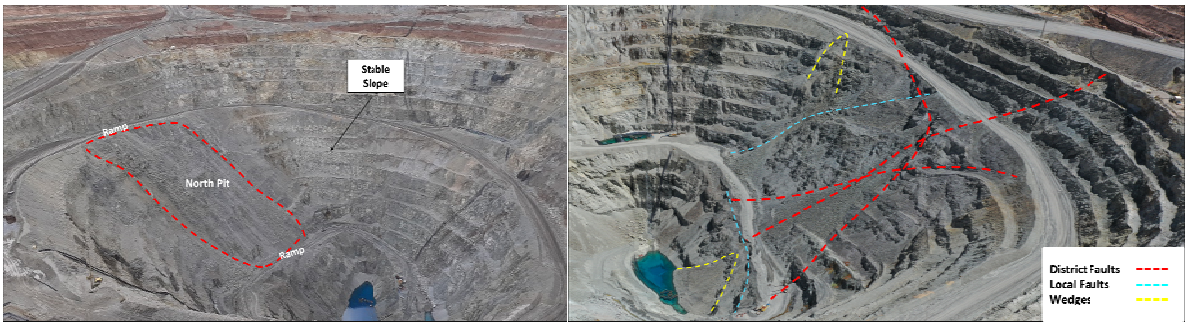


Fig. 1Photos of the North Wall by April 2020, condition after large deformations.

3.2 Model Definition

A three-dimensional FLAC3D model was constructed for this case study, initially calibrated in small-strain conditions and subsequently evaluated in large-strain mode. The element size in the area of interest was 6 m approximately. The rock mass was represented using a Hoek-Brown model with perfectly plastic behaviour. Weaker materials, including damage zones associated with fault halos, were modelled using a Mohr-Coulomb criterion with a cohesion of 10 kPa and a friction angle of 29°. The failure mechanism was interpreted to be strongly controlled by the intersection of major structures forming wedges, combined with elevated pore pressures near the slope face.

Figure 3presents the safety factor (FS) contours obtained from the calibrated small-strain model, compared with an I-site scan of the observed failure. The model captures the location and general extent of the instability, providing a basis for subsequent large-deformation analyses.

Three additional simulations were performed to evaluate post-failure behaviour:

- Fully meshed FLAC3D in large-strain mode
- Fully meshless approach where the entire volume is represented by material points
- Hybrid approach with material points in the region of interest and FLAC3D zones outside of that

The objective of the study was to determine if the runout would reach the bottom of the pit. The three methods above were used for the evaluation. Runout distances and computational efficiencywas compared across the different modelling approaches.

In the following models, the material was weakened by a factor of 1.1 (relative to the model in Figure 2) to promote unstable failure of the volume at marginal condition (FS ~1.1). This potentially represents an extreme rainfall event of another scenario that may further destabilize the slope.

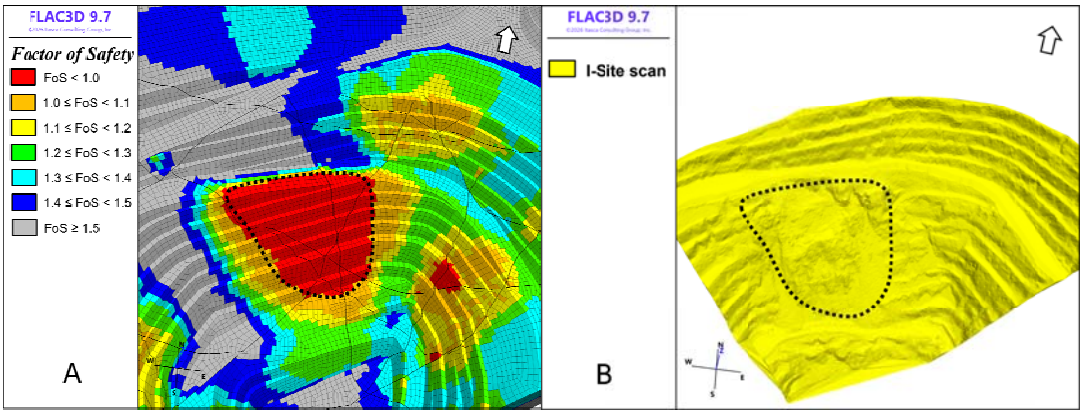


Fig. 2Factor of safety contours from calibrated model in small-strain (A) compared against I-site scan from the failure (B). Dotted black line delineates the area of high deformations identified by radar.

3.3 Methodology

When run in large-strain mode, the finite volume formulation eventually produces zones with highly distorted geometries (illegal geometries), at which point numerical stability is compromised and the calculation cannot continue. To overcome this limitation, the simulation was halted and "rewound" to a stage immediately prior to the onset of mesh degradation.

From this state, two alternative approaches were implemented:

- Meshless method: All zones in the model were converted to material points prior to continued simulation.
- Hybrid method: A predefined volume encompassing the region expected to undergo large deformation was converted from zones to material points prior to continued simulation.

In both approaches, the conversion from zones to material points is performed by directly transferring state variables, including material properties, stresses, and displacements. This allows continuity of the mechanical response during the transition.

3.4 Post-Failure Response

3.4.1 Fully meshed FLAC3D

In the fully meshed FLAC3D model operating in large-strain (Figure 3), numerical stability deteriorated rapidly once displacement exceeded approximately three times the element size (~20 m). Mesh distortion limited reliable prediction of runout extent. This limitation is common in FLAC3D models run in large-strain mode with complex meshes such as open pit geometries.

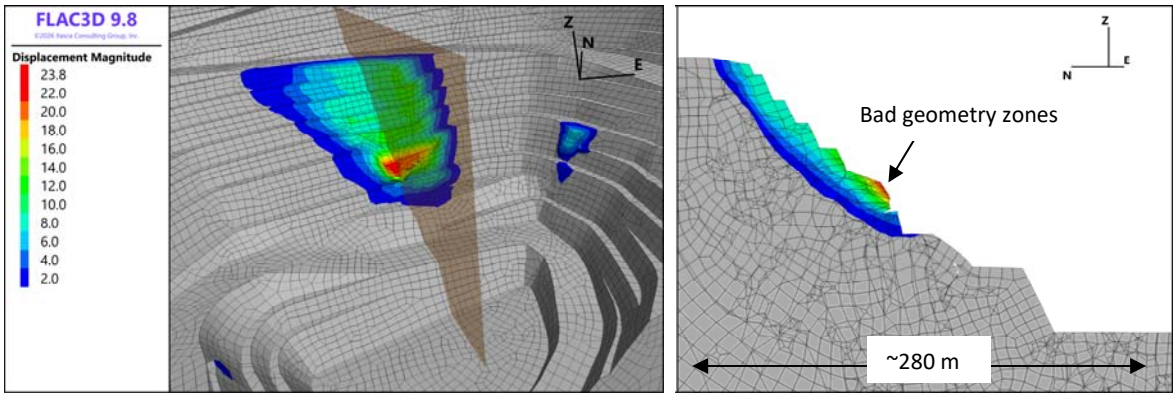


Fig. 3 Fully meshed FLAC3D model results in terms of total displacements (m). The semi-transparent brown rectangle in the left plot shows the location of the cross-section in the right plot.

3.4.2 Fully Meshless Method

The MPoint simulation, in which all zones were replaced by material points, reproduced continuous acceleration, flow, and deposition of the failed rock mass (Figure 4). The results demonstrate that the material point method can simulate large deformations and runout behaviour, which cannot be captured using a purely meshed approach without remeshing.

The model shows that most of the failed material is contained in the ramp below rather than on pit bottom. An interesting observation is the apparent gap between the failing material and the bottom of the pit. There is not a true gap here, there is a specified interaction between the material points that prevents them from interpenetrating. As material points come close together, they are considered part of the same continuum, even though in reality there is probably a sliding contact between the two materials. This problem is addressed in the hybrid model of the next section.

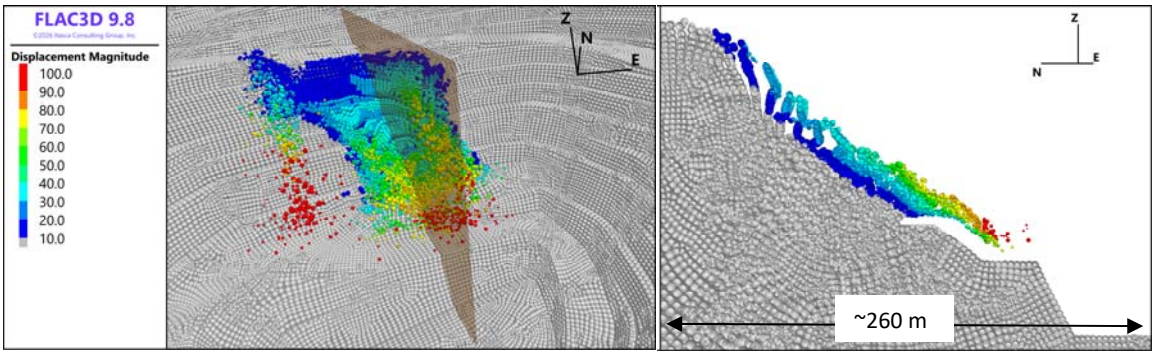


Fig. 4 Fully meshless MPoint model results in terms of total displacements (m).

3.4.3 Hybrid Method

In the hybrid FLAC3D-MPoint simulation, zones within the region of expected large deformation were replaced by material points. Zones adjacent to the material points interact with the material points by using hybrid points as described above. To prevent the unrealistic merging of material in the sliding mass and the bottom of the pit, hybrid points were not added to the zones below the failure region. Instead, a frictional wall was placed on the surfaces of the zones. The wall prevents penetration of the material points into the zones and also offers a frictional surface on which the failing material can slide. The model set up is shown in Figure 5.

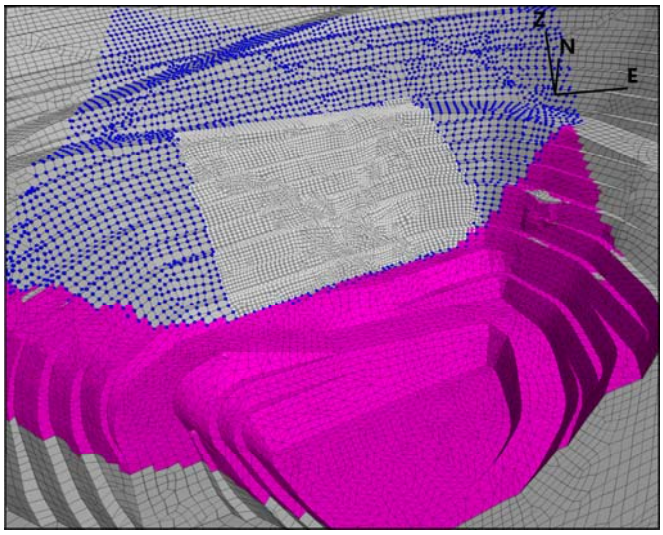


Fig. 5. Hybrid model prior to solving. Blue spheres show the location of hybrid material points used in coupling the FLAC3D zones and the material points. The pink surface represents the frictional wall attached to the zone faces at the bottom of the pit.

Displacement results are shown in Figure 6. In this model, the failure is contained in the ramp below the failure. The advantages of this approach are (a) the spurious "merging" of material at the bottom of the pit can be prevented (b) the calculation is significantly faster (~ 10x).

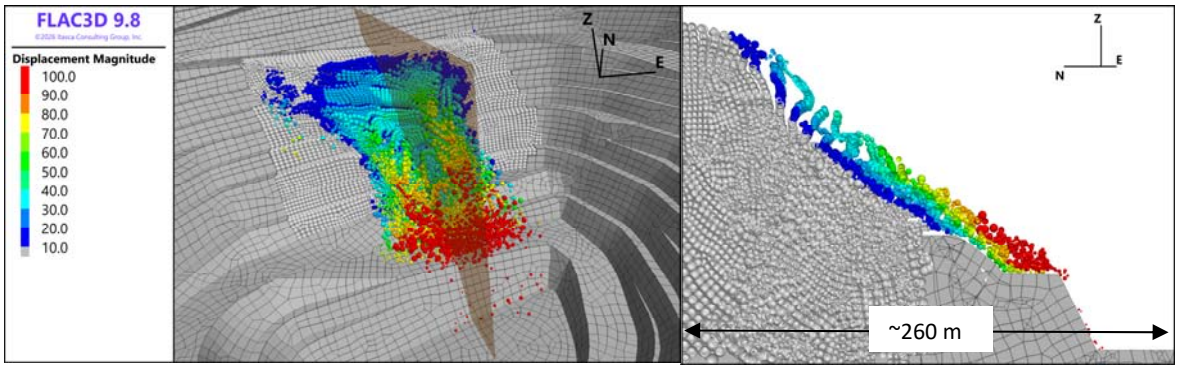


Fig. 6 Hybrid FLAC3D-MPoint model with area of interest replaced by material points. Results in terms of total displacements (m).

4 Discussion and Conclusions

The results demonstrate that the hybrid formulation retains the ability of continuum-based methods to represent progressive failure while enabling simulation of large deformation and post-failure behaviour. The case study shows that this approach can be applied to realistic three-dimensional geometries, including complex open pit configurations. In this case, the MPoint-based simulations indicated that most of the failed material would be contained on the ramp below, with only a limited volume potentially reaching the pit bottom if the failure were to progress during more intense rainfall events.

A key advantage of the FLAC3D-MPoint approach is the use of a consistent numerical framework to assess both slope stability and post-failure response. Conventional workflows typically rely on separate tools for factor of safety calculation and runout analysis, which introduces additional assumptions and potential inconsistencies between the two stages. In addition, modelling the rock mass with finite volume zones away from areas of high deformation and material points only where large strains develop provides significant calculation efficiencies compared with representing the entire domain using material points. The hybrid FLAC3D-MPoint framework allows progressive failure development, velocity evolution, and deposition geometry to be simulated within a single analysis.

The example presented here answers the practical question of whether a slope failure could reach the bottom of the pit. However, more reliable predictions of runout distance, deposition geometry, and failed volume require calibration of the post-peak material behaviour against observed failures whenever such data are available. As with any numerical assessment, calibration remains essential for establishing confidence in the predicted response.

Although the MPoint and hybrid FLAC3D-MPoint approaches successfully extend the analysis beyond the limits of traditional continuum methods, further development and validation are required before the methodology can be routinely applied for quantitative prediction of post-failure behaviour. Future developments should focus on improving numerical robustness and the representation of material separation and deposition processes, enabling more reliable quantitative predictions of final runout extent.

Overall, the methodology provides a practical framework for linking stability analysis with consequence assessment. This capability is particularly relevant for high-consequence slopes, where consistent representation of failure mechanisms and runout behaviour is required to support hazard assessment and risk-informed decision-making.

References

Itasca Consulting Group, Inc.(2026a).*FLAC3D – Fast Lagrangian Analysis of Continua in Three Dimensions* (Version 9.6). Minneapolis: Itasca.

Itasca Consulting Group, Inc.(2026b) MPoint (Version 9.6 Beta). Minneapolis: Itasca.

Lian, Y.P., X. Zhang and Y. Liu. 2012. An adaptive finite element material point method and its application in extremedeformation problems. Computer Methods in Applied Mechanics and Engineering, Vol 241, pp. 275-285.

Purvance M, and Coetzee C (2024). MPAC – Material Point Analysis of Continua, in Applied Numerical Modeling in Geomechanics,–Hazzard, Katsaga, Sanftenberg & Nelson (eds.) Paper: 13-01, Itasca International, Inc., Minneapolis

Integrated Workflow for Bench-Berm Design Optimisation and Reconciliation

F. Sanz
SRK Consulting (UK) Limited, Cardiff, UK
fsanz@srk.co.uk
0009-0003-0254-7325

Abstract

Bench-scale performance represents a critical component of geotechnical risk management in open-pit mining because structurally controlled backbreak and operational overbreak directly influence effective berm retention, rockfall containment capacity, and operational safety. However, uncertainty commonly exists between intended bench geometries and actual as-built conditions due to limitations in structural interpretation, persistence estimation, and blasting disturbance characterization, particularly during early project stages.

This paper presents an integrated and iterative workflow for progressively refining bench-scale engineering interpretation through reconciliation between structural characterization, block formation simulation, and observed operational performance. The workflow was applied across multiple open pit projects and different stages of pit development, ranging from conceptual greenfield studies to operational final wall conditions. The methodology integrates geological interpretation, borehole data, surface structural mapping, laboratory testing, bench-scale block formation simulation, and photogrammetry-based reconciliation of as-built bench performance.

The study demonstrates that representative engineering persistence and operational blasting conditions exert dominant controls on structurally controlled backbreak and effective berm performance. Comparison between simulated and observed bench conditions provided a practical basis for refining engineering assumptions, distinguishing structurally controlled instability from operationally induced overbreak, and progressively reducing uncertainty throughout pit development.

The proposed workflow provides a practical framework for improving confidence in bench-scale design optimisation and supporting risk-informed geotechnical decision-making through continuous operational reconciliation and iterative refinement of engineering interpretation.

Keywords

Integrated workflow, Design optimisation, Bench-scale performance, Operational reconciliation.

1 Introduction

Bench-scale performance is a critical component of geotechnical risk management in open-pit mining because local bench behaviour directly controls effective berm retention, rockfall containment capacity, and operational safety. While slope-scale analyses are commonly used to define overall pit geometries, bench-scale performance is frequently governed by the interaction between structural persistence, blasting disturbance, wall orientation, and operational practices, which together control and balance practical bench–berm configuration and backbreak behaviour (Gibson et al., 2006).

Traditional bench-scale design approaches commonly rely on simplified structural interpretations and limited reconciliation with observed pit performance. Although appropriate during early project stages, these approaches may not adequately capture the variability associated with structurally controlled backbreak and operationally induced overbreak mechanisms. Consequently, uncertainty commonly arises between intended design geometries and actual as-built slope conditions, particularly in structurally complex rock masses.

This paper discusses the application of an integrated and iterative workflow across multiple open pit projects and project stages to progressively refine structural interpretation, improve understanding of bench-scale behaviour, and support risk-informed bench–berm design optimisation. The workflow integrates geological interpretation, borehole data, surface structural mapping, operational observations, laboratory testing, bench-scale block formation simulation, and reconciliation with observed as-built performance.

Fig. 1presents the proposed workflow and its progressive application throughout different stages of pit development, from conceptual greenfield studies to operational final wall conditions. Operational reconciliation represents the central component of the methodology by linking simulated behaviour with observed bench performance to refine engineering assumptions, improve confidence in representative persistence and shear strength interpretation, and progressively reduce uncertainty throughout pit development.

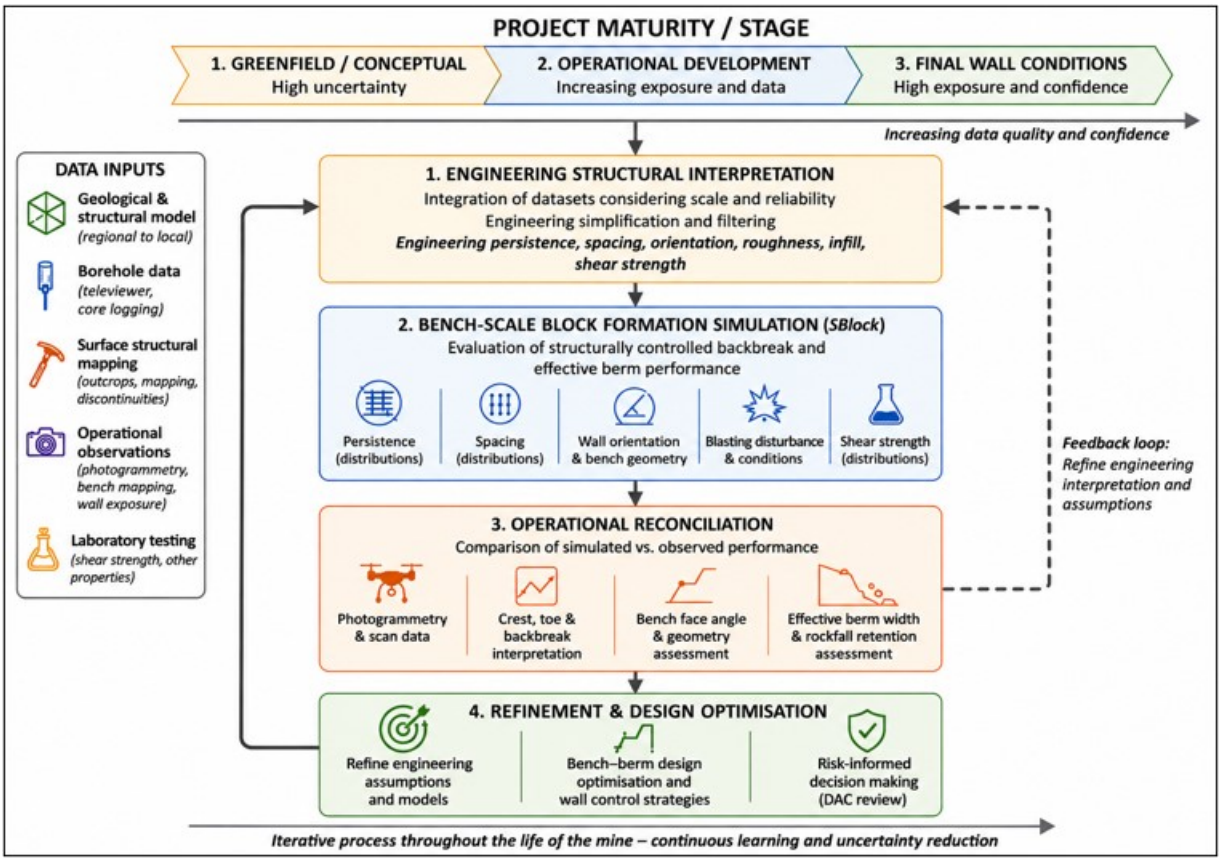


Fig. 1 Integrated workflow for bench-scale modelling, reconciliation, and design optimisation throughout pit development.

2 Structural Interpretation and Engineering Representation

Structural interpretation integrated large-scale geological understanding, borehole-based datasets, surface mapping, laboratory testing, and operational observations to define representative engineering joint sets suitable for bench-scale analysis. The availability and quality of these datasets evolved significantly throughout the project lifecycle, from conceptual greenfield interpretation based primarily on drilling information to operational reconciliation supported by high-resolution photogrammetry and exposed bench mapping.

During early project stages, borehole datasets provided the primary source of information regarding structural orientation, spacing, and geotechnical characteristics. However, persistence remained difficult to constrain reliably using borehole data alone (Shang et al., 2018). As additional operational exposure became available, surface mapping and photogrammetric interpretation provided direct observations of persistence, block formation mechanisms, blasting disturbance, and bench performance (Sturzenegger and Stead, 2009).

Table 1 summarizes the main information and reliability provided by each dataset considered in this work.

Table 1. Summary of information provided by each dataset.

Dataset	Joint Orientation	Joint Persistence	Joint Spacing	Joint Roughness / Infill (other characteristics)	Operational Exposure of Joints
Large-Scale Geological & Structural model	Limited (Interpreted)	Limited (Interpreted)	None	None	None
Televiewer	Excellent	None	Excellent	None/Limited	None
Core Logging	Moderate	None	Excellent	Excellent	None
Surface Mapping	Excellent	Excellent	Moderate	Limited	Excellent
Laboratory Testing	None	None	None	Moderate (Lab-scale strength)	None
Individual Block Back-Analysis	Limited (Local)	Limited (Local)	None	Excellent (Bench-scale strength)	Limited (Local)

A key aspect of the workflow involved distinguishing between geological persistence and engineering persistence, since engineering persistence was intended to reproduce practical block formation mechanisms relevant for bench-scale behaviour rather than actual discontinuity continuity. Consequently, structural simplification and filtering were required to isolate discontinuities capable of generating operationally significant instability mechanisms.

Representative bench-scale shear strength parameters were derived using laboratory testing, engineering judgement, and Barton-Bandis interpretations (Barton, 1973; Barton and Choubey, 1977) adjusted for disturbed operational conditions associated with blasting and excavation.

Table 2 presents a representative example modelling inputs considered for the block simulation.

Table 2: Example summary of engineering joint set characteristics used for block simulation.

Geotechnical Unit 01	Orientation	Geometrical Characteristics: Median [min-max]			Strength (average) Friction Angle (°)	
Joint set	Dip / Dip direction (°)	Spacing (m) [Min-Max]	Persistence (m)			
			Base Case	Sensitivity Case	Base Case	Sensitivity Case
1	75/120	2.8 [0.9 - 8.4]	12.0 [4.0 - 36.0]	18.0 [4.0 – 54.0]	35	30
2	85/245	1.7 [0.6 – 5.1]	8.3 [2.8 – 25.0]	12.5 [2.8 – 37.5]	40	35
3	50/235	2.9 [0.5 – 8.7]	7.2 [2.4 – 22.0]	10.8 [2.4 – 32.4]	40	35
4	45/290	3.4 [0.5 – 10.2]	7.3 [2.4 – 22.0]	11.0 [2.4 – 33.0]	40	35

3 Bench-Scale Modelling and Reconciliation

Representative engineering joint sets were developed using integrated interpretation of structural mapping, borehole datasets, laboratory testing, and operational observations. Block formation analyses were performed using SBlock (Esterhuizen, 2025; Hormazabal 2013) to evaluate structurally controlled backbreak and effective berm performance under varying wall orientations and bench geometries. Modelling assumptions incorporated simplified persistence and spacing distributions, representative friction angles, and disturbed structural conditions associated with blasting and excavation.

Sensitivity analyses demonstrated that persistence exerted the strongest influence on simulated backbreak behaviour, whereas spacing and friction angle generally exhibited comparatively lower influence. Relatively small increases in persistence commonly produced larger backbreak magnitudes and broader distributions of affected wall orientations.

The reconciliation process represented the central component of the workflow because it provided the link between conceptual engineering interpretation and observed operational performance. High-resolution photogrammetry and scan interpretation were used to extract crest lines, toe lines, and backbreak geometries using PointModeller (Maptek, 2025). These interpretations allowed comparison between observed as-built conditions and intended bench geometries, supporting estimation of backbreak magnitude, effective berm width, and bench face angle variability (Pratt et al., 2022).

Fig. 2 presents an example of as-built bench interpretation using photogrammetric scan data and comparison against the intended bench geometry. Crest lines, toe lines, and backbreak geometries were interpreted to estimate effective berm width, bench face angle variability, and structurally controlled backbreak magnitude. In this example, toe flare conditions were observed along sections of the final wall benches, indicating local reduction of catch berm capacity and increased rockfall risk associated with blasting disturbance and bench clean-up practices (Marklund et al., 2007).

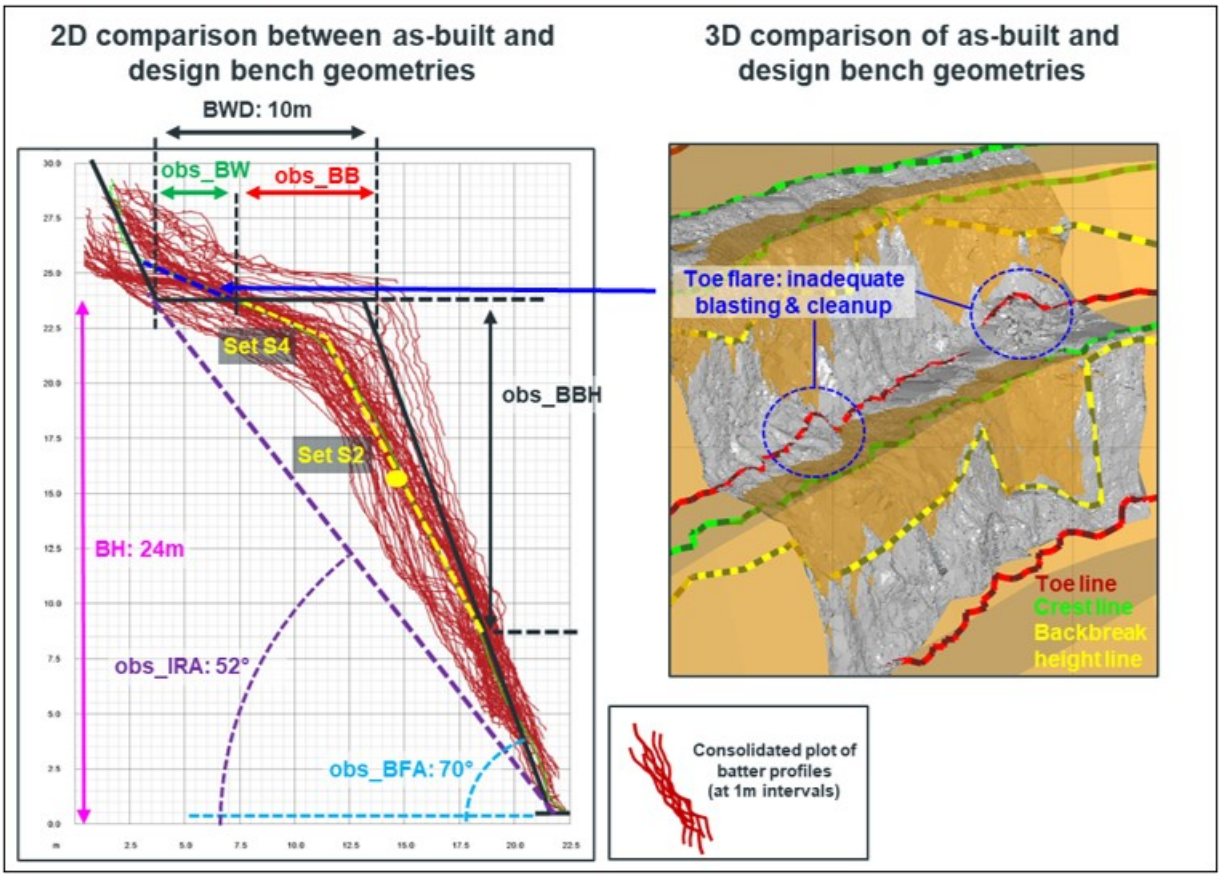


Fig. 2 Integrated reconciliation of bench-scale performance combining field observations, stereographic interpretation, and as-built geometry analysis to quantify structurally controlled backbreak and effective berm performance.

Comparison between simulated and observed bench performance provided a practical basis for refining engineering assumptions and distinguishing between structurally controlled instability and operationally induced overbreak associated with blasting practices.

Fig. 3 presents an example comparison between simulated block formation behaviour and observed as-built performance for an operational final wall condition. The comparison was used to evaluate whether the interpreted structural parameters remained representative under operational conditions and whether refinement of persistence assumptions or blasting practices was required.

Confidence associated with the engineering interpretation increased significantly as operational exposure and reconciliation opportunities became available throughout pit development.

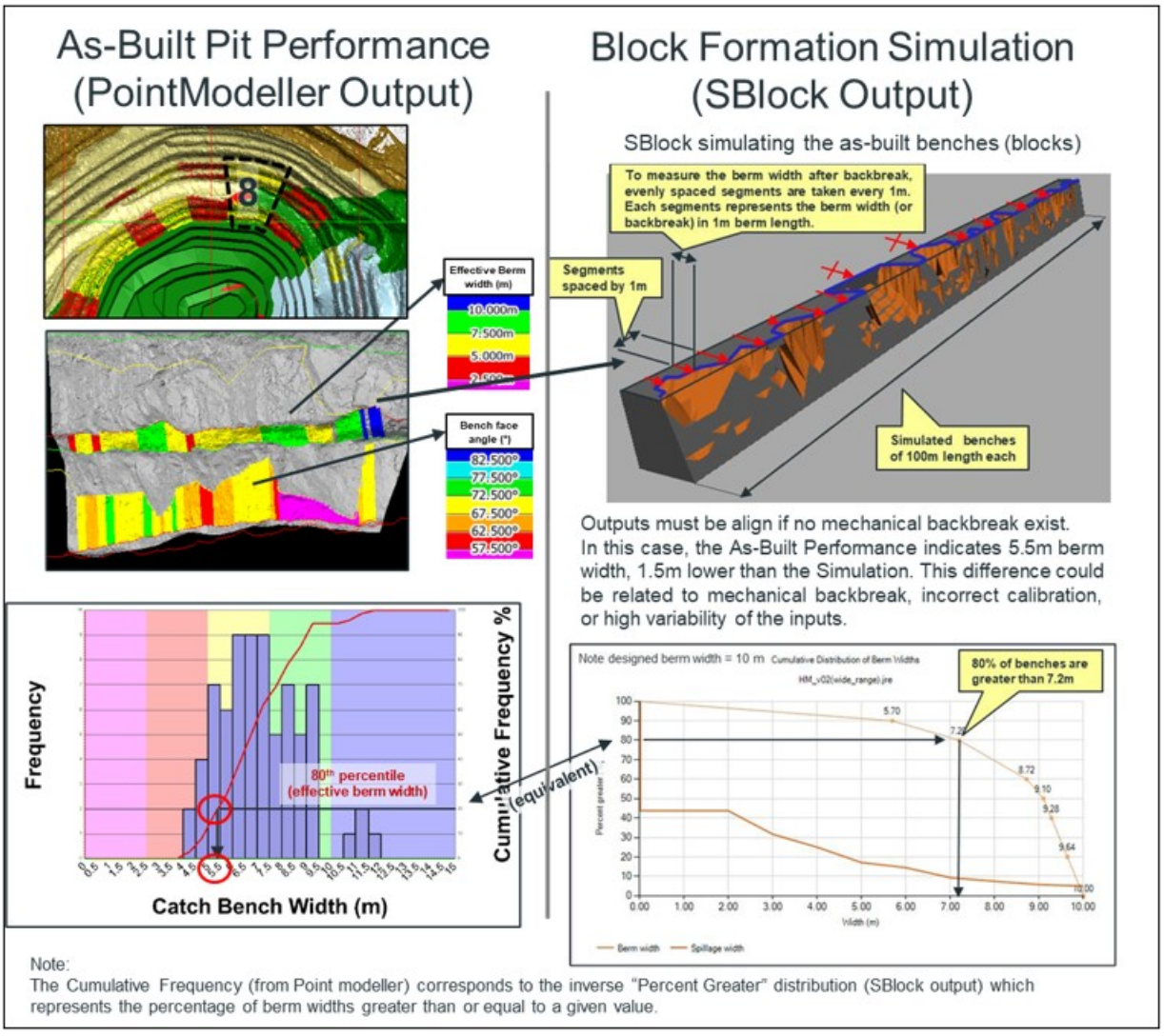


Fig. 3 Example of reconciliation of the bench performance (using PointModeller) and the simulation (in SBlock) for a final pit wall stage.

4 Engineering Implications and Conclusions

Application of the workflow demonstrated generally consistent agreement between simulated and observed bench performance when representative engineering persistence and disturbed structural conditions were incorporated into the modelling process.

The reconciliation process highlighted the importance of distinguishing between structurally controlled backbreak and mechanically induced overbreak associated with blasting practices. In several cases, operational blasting performance exerted a stronger influence on bench performance

than modifications to bench geometry itself, reinforcing the importance of integrating operational observations into bench-scale interpretation and optimisation.

These observations reinforce the need to treat bench-scale design as an iterative process in which excavation control, blasting performance, survey reconciliation, and operational observations are used to update engineering assumptions and manage uncertainty throughout pit development (Simmons, 2013; Graf and Sullivan, 2016).

From a risk management perspective, the workflow supported identification of slope sectors where uncertainty associated with structural persistence, blasting disturbance, or operational practices could significantly influence effective berm performance and rockfall retention capacity. The evaluated projects also demonstrated that acceptable bench performance and Design Acceptance Criteria (DAC) remain inherently project-specific and dependent on operational exposure, mining phase, and operational risk tolerance.

The proposed workflow provides a practical framework for refining structural interpretation, validating modelling assumptions, and improving confidence in bench-scale decision-making throughout pit development through continuous reconciliation with operational performance observations.

References

Barton, N. (1973). Review of a new shear strength criterion for rock joints. Engineering Geology, 7(4), 287–332.

Barton, N., and Choubey, V. (1977). The shear strength of rock joints in theory and practice. Rock Mechanics, 10, 1–54.

Esterhuizen, G. (2025). SBlock v3.01: User guide and reference manual. Computer software/manual.

Gibson, W.H., de Bruyn, I.A., and Walker, D.J.H. (2006). Considerations in the optimisation of bench face angle and berm width geometries for open pit mines. Proceedings of the International Symposium on Stability of Rock Slopes in Open Pit Mining and Civil Engineering, SAIMM, Johannesburg, pp. 557–578.

Graf, C.C., and Sullivan, R. (2016). A journey of wall control improvement at Boddington Gold. APSSIM 2016, Australian Centre for Geomechanics, Perth.

Hormazabal, E. (2013). Bench berm design using probabilistic key block analysis. Slope Stability 2013, Australian Centre for Geomechanics, Perth, pp. 227–236.

Maptek (2025). PointModeller Help Documentation. Maptek Pty Ltd.

Marklund, P-I., Sjöberg, J., Ouchterlony, F., and Nilsson, N. (2007). Improved blasting and bench slope design at the Aitik Mine. Slope Stability 2007, Australian Centre for Geomechanics, Perth.

Pratt, R.W., Conley, M.C., Childs, D.W., McNabb, J.C., and Schmelter, S.C. (2022). Slope auditing for assessment of bench-scale pit slope design utilizing drone photogrammetry.

Shang, J., West, L.J., Hencher, S.R., and Zhao, Z. (2018). Geological discontinuity persistence: Implications and quantification. Engineering Geology, 241, pp. 41–54.

Simmons, J.V. (2013). Excavation control, management of blast damage, and quality control. Slope Stability 2013, Australian Centre for Geomechanics, Perth.

Sturzenegger, M., and Stead, D. (2009). Quantifying discontinuity orientation and persistence on high mountain rock slopes and large landslides using terrestrial remote sensing techniques. Natural Hazards and Earth System Sciences, 9, pp. 267–287.

Verification of underground excavation stability during tunnel construction

H. Antičević
Krešo Geo Ltd., Zagreb, Croatia

J. Peranić & Ž. Arbanas
University of Rijeka, Rijeka, Croatia
zeljko.arbanas@gradri.uniri.hr
0000-0002-2574-6349, 0000-0002-5736-6746

Abstract

Design of tunnels in rock mass according to the New Austrian Method (NATM), using the results of geotechnical field investigations and rock mass classifications (GSI, RMR, Q), is most often carried out in the early design stage. Verification of underground opening stability using observational methods is carried out by measuring the behaviour of the reinforced rock mass during the tunnel construction. This paper will present the verification of underground excavation stability in the Mali Prolog and Šubir tunnels on the A1 Highway Zagreb-Split-Dubrovnik, near the town of Vrgorac, Croatia. During the tunnel excavation, field investigations and observations were carried out to verify the efficiency of the primary tunnel support and the length of the installed rockbolts. During the tunnel construction, investigation drilling at the tunnel face, geophysical seismic measurements, video-prospecting of investigation boreholes, geological mapping of the tunnel face, convergence measurements, and anchor pull-out tests were carried out. The investigations were carried out in the II, III, and IV categories of rock mass (according to the RMR classification), in which excavation by drilling and blasting was envisaged. Multi-layer reinforced shotcrete and rockbolts were used as the primary tunnel support. Based on measurements and observations, it was necessary to confirm the achieved stability of the underground excavation. If the behaviour, or rather the stability of the underground excavation, significantly deviated from the design criteria, the input parameters of the rock mass were corrected, and the analysis was repeated based on test results and back-analyses. Changes in the support system resulted in additional gradual strengthening or, in some cases, reduction of the support elements of the primary support system.

Keywords

Tunnelling, Observational method, Stability verification, Observation, Support system.

1 Introduction

During the construction of numerous roads in Croatia from 2003 to the present, numerous road tunnels have been constructed in the Croatian coastal part of the Dinaric Alps, mostly in carbonate deposits (limestone, dolomites), and less frequently in some other deposits (flysch). Given the large number of tunnels that were built in a relatively short time, common procedures have been developed in exploratory works, design of tunnel excavation and support, and execution of works, and ensuring the stability of the support system based on the New Austrian Tunnelling Method (NATM) (Rabcewicz 1964; Rabcewicz and Golser 1973) and the observational method (Peck 1969; Terzaghi and Peck 1967; Nicholson et al. 1999) with an active design approach. In the initial stages of design, the results of the conducted exploratory works enable the classification of the rock mass using the geotechnical classification (RMR) (Bieniawski 1989), the Geological Strength Index (GSI) (Marinos and Hoek 2000), and, less frequently, the Q-classification (Barton et al. 1974), and the determination of rock mass categories according to the RMR classification and empirical values of strength and deformability of the rock mass. Based on the determined characteristics of the wall mass, the spreading zone, and the span of the underground opening, typical primary support systems were determined for certain estimated rock mass categories (Bieniawski 1989). In the execution phase of the works, verification of the stability of the underground opening was carried out using observational methods, carried out by classifying and measuring the behaviour of the reinforced rock mass during the execution of the works. Measurements were also carried out to reduce the impact of drilling and blasting on the rock mass around the designed underground opening. In fact, the active design phase continued already at the tunnel excavation head, and on the test sections of the tunnel excavation in the II, III, and IV categories of rock mass, the impact of drilling and blasting outside the designed tunnel excavation line on the damage to the rock mass was monitored. Measurements were carried out to identify the depth of damage to the rock mass outside the excavation profile, including geophysical measurements, investigation drilling, RQD, and video-prospecting of investigation boreholes at the tunnel excavation head. Standard geotechnical measurements included: monitoring of deformations (convergence) of the excavation profile, subgrade measurements, and formation of the plasticisation zone through anchor pull-out tests.

This paper will present the verification of the stability of the underground opening and some of the results of measurements and observations on the Mali Prolog and Šubir tunnels on the A1 Zagreb-Split-Ploče Highway, near the town of Vrgorac, Croatia, during their construction from 2007 to 2012.

2 Verification methodology and research implementation

The paper will continue to describe the geological conditions and construction features of the Mali Prolog and Šubir tunnels on the A1 Zagreb-Split-Ploče Highway, near the town of Vrgorac, Croatia. Given the similar geological structure, the height of the tunnel overburden, and the tunnel cross-sections, the experience gained during the construction and verification of the stability of the underground tunnel opening enabled the application of the methods under similar geotechnical conditions.

2.1 Geological setting in the tunnels area

The Mali Prolog Tunnel is a two-tube tunnel, 1,092 m long, with a maximum overburden of 170 m. It is located within a rock massif composed of Eocene foraminiferal limestone (V, $E_{1,2}$) and Upper Cretaceous rudist limestone (V, K_2) (Užarević 2011). Rudist limestone compose the central and northern part, or two-thirds of the rock length of the tunnel, while foraminiferal limestones cover the southern area of the tunnel.

The Šubir Tunnel is a two-tube tunnel, 962 m long with a maximum overburden of 120 m. Šubir is mostly composed of Paleocene–Middle and Upper Eocene foraminiferal limestone (V, Pc-$E_{1,2}$) and Upper Cretaceous rudist limestone (Užarević 2010). In part of the tunnel, there are deposits of Middle and Upper Eocene flysch (F(L); $E_{2,3}$) in which blue-grey marls predominate, which are very fractured in contact with foraminiferal limestone.

Both tunnels have the same horseshoe-shaped cross-section, 10.65 m wide at the bottom and 8.25 m high, with an approximate area of 72.35 m^2, Fig 1a. In both tunnels, the excavation was carried out in the II, III, and IV categories of rock mass according to the RMR classification. For each of the excavation categories, the project defined primary support systems, and the selection of the support

system depended on the mapping of the face, walls, and vault of the excavation and the determination of the category of rock mass in the tunnel.

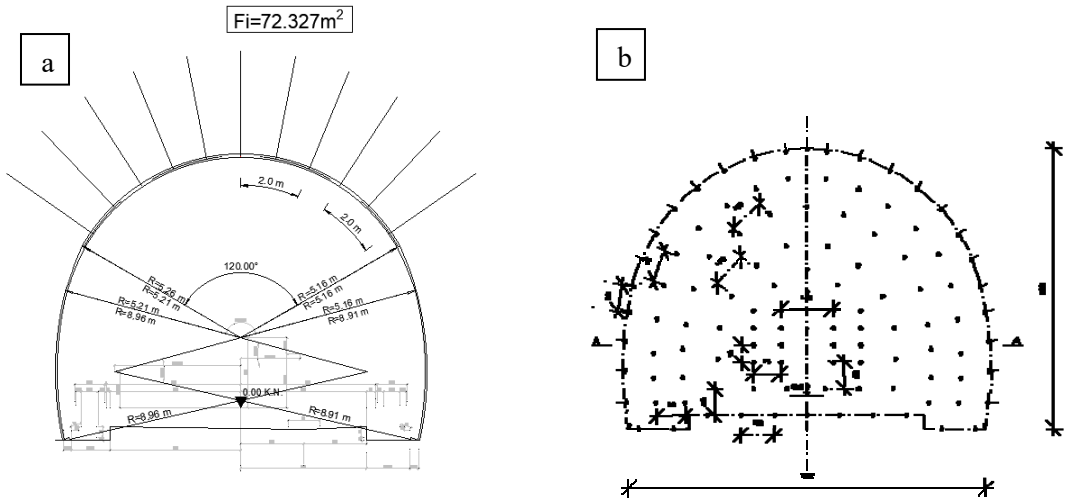


Fig. 1 Cross section of the Šubir and Mali Prolog Tunnels. a) Geometry of the cross section with schematic view of III category primary support system, b) Schematic view of the mining borehole positions at the face of the tunnel.

2.2 Excavation methodology

For the excavation of tunnels in II, III, and IV categories of rock mass, the application of drilling and blasting techniques was envisaged, and the excavation area varied from 71.20–73.46 m^2, and the advancement from 1.0 to 1.5 m (Užarević 2010, 2011). Depending on the category of rock mass, the drilling depth of the mining wells varied, as did the construction of the mining wells, i.e., the mass of explosives per individual ignition stage. For the excavation of each section, the total number of wells at the face was from 106 to 124, with a drilling diameter of 45 mm and a depth of 1.0 to 1.5 m, Fig. 1b.

At the beginning of the tunnel's excavation, test sections were selected for confirmation or possible corrections of the designed drilling and blasting scheme, and at the same time, extended research was carried out on the mentioned sections to verify the stability of the underground excavation.

2.3 Over-profile excavation

Before the start of tunnel excavation, the designed drilling and blasting scheme was tested and confirmed or refined. The drilling of mine boreholes was done by computer and manually. In order to ensure the designed profile of the tunnel, the contour row of mine boreholes is drilled at a minimum angle related to the axis of the tunnel. This angle cannot be smaller than that allowed by the approach of the drilling machine carriage to the already excavated tunnel profile, and this is a technological over profile that cannot be avoided. The drilling machine carriage must be positioned in the over profile of the previous step of blasting so that the drilling angle of the contour row of mine boreholes from the designed excavation contour would be as small as possible, yet sufficient to create an over profile by blasting, that is, space for positioning the drilling machine carriage for the next blasting.

In addition to the technological over profile, excessive over profile due to excessive damage to the rock mass, due to careless drilling and blasting, is a very common occurrence. Sometimes, a certain excessive over profile is a more acceptable cost to the Contractor than a sub profile that must later be mechanically excavated, and mechanical excavation of profile finishing can also cause an over profile excavation. In both cases, unnecessary financial costs and disruption of work dynamics are created.

At the beginning of the tunnel excavation, drilling and blasting were monitored, and the over profile excavation was geodetically recorded to define the technological over profile. The average value of which is usually approximately 25 cm from the designed excavation line. A justified geological over profile is acceptable in the construction costs.

Over profile excavation, apart from its technological significance and cost impact, has a significant impact on the stability of the underground opening. Firstly, it is a real extension of the tunnel span, which is rarely taken into account in stability analyses. Furthermore, it represents additional damage to the rock mass outside the design profile of the tunnel, and can have consequences in reducing stability and increasing deformations in the rock mass.

2.4 Geodetic survey

The part of the verification procedure the stability of the tunnels includes geodetic measurements due to over profile excavation and rock mass damage at the excavation contour, and the need for additional reinforcement of the support lining.

During the excavation of the tunnels, control measurements of the displacements (convergence) were performed at the contour of the tunnel profile. The measuring profiles were installed every 50 to 100 m, and each measuring profile has five measuring points; one in the crown of the tunnel and two on each of the tunnel walls. The frequency of measurements was every day in the first seven days after excavation, and the construction of the primary support. After 7 days, measurements were carried out once a week and after the displacement had subsided, once every six months. The measured values were up to 2 mm, which met the requirements of the Geotechnical Design of the tunnels (Užarević 2010, 2011).

2.5 Engineering geological mapping of the tunnel face

After each blasting in a tunnel, geological mapping and categorization of the rock mass were performed in order to obtain the most detailed picture of the geological structure on the tunnel route. For each tunnel face along a tunnel, the most influential discontinuity systems were measured and plotted. In order to define the quality of the rock mass according to RMR, categorization was performed, and all relevant parameters were determined (rock mass strength, RQD, assessment of the impact of discontinuities, discontinuity spacing, state of discontinuities, mutual influence of discontinuities, groundwater, etc).

Based on results of engineering geological mapping a developed geological profile of the right tunnel tube and geological mapping of the left tunnel tube face of the tunnels were established, on that the rock mass classification were determined. Layering was not identified or is weakly pronounced. According to the RMR classification, the rock mass was classified to adequate tunnelling category.

2.6 Video prospecting of the investigation borehole

At the tunnel face, exploratory boreholes with a diameter of 102 mm were drilled in the side of the profile with a deviation of 200 from the designed excavation contour towards the rock mass Fig. 2a. The boreholes are located at a height of 4.0 - 4.5 m from the vertical alignment, and the length of the boreholes is equal to the length of the mining boreholes drilled in the tunnel face (Antičević 2011). Video prospection was carried out before (Fig. 2b) and after the blasting of the excavation of the tunnel face to detect damage to the rock mass, namely: over-profile excavation, spalling, and expansion of existing cracks, and the formation of new cracks. The imaging data showed the formation of new cracks reaching a depth of 0.61 m, while the spalling and expansion of existing cracks reached a depth of 1.08 m, Fig. 2c.

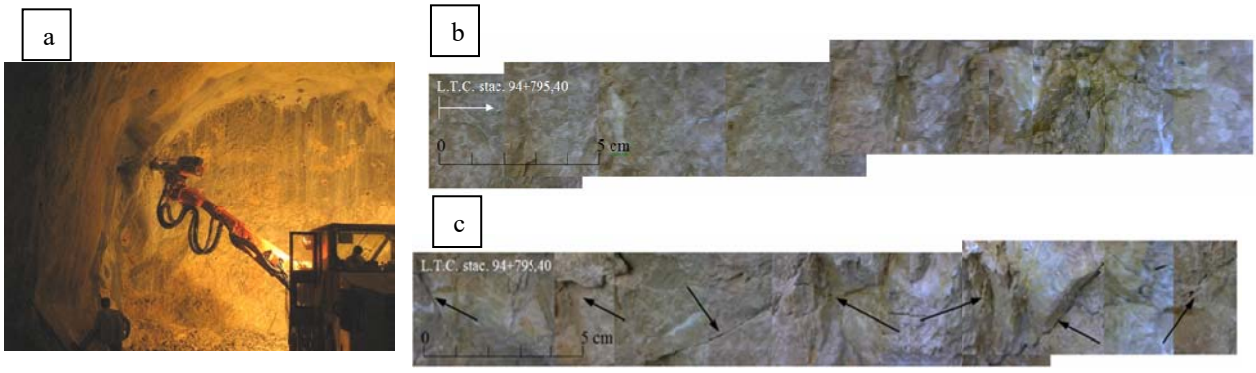


Fig. 2 Video prospecting of the investigation borehole. a) Position of video prospecting borehole, b) Photo of the borehole wall before blasting, c) Photo of the borehole wall after blasting. Black arrows indicate positions with expanded existing cracks or spalling.

2.7 Geophysical measurements in the tunnel

Geophysical measurements included seismic cross-hole tomography in the tunnel side at the location where video prospecting measurements of the exploratory boreholes were performed. Seismic cross-hole tomography measured changes in the velocity of longitudinal (primary) p-waves and transversal (secondary) s-waves propagation from the tunnel excavation contour towards the rock massif. More significant damage in category II of rock mass reaches a depth of 1.6 m, Fig. 3, with a reduction in the velocity of p-waves propagation by 20% compared to the undisturbed rock mass, from3036 m/s

to3753 m/s). In category III rock mass, the damage zone is deeper by 2.5 m, but the reduction in the propagation velocity of p-waves is smaller by 15% from 2700 m/s to 2295 m/s.

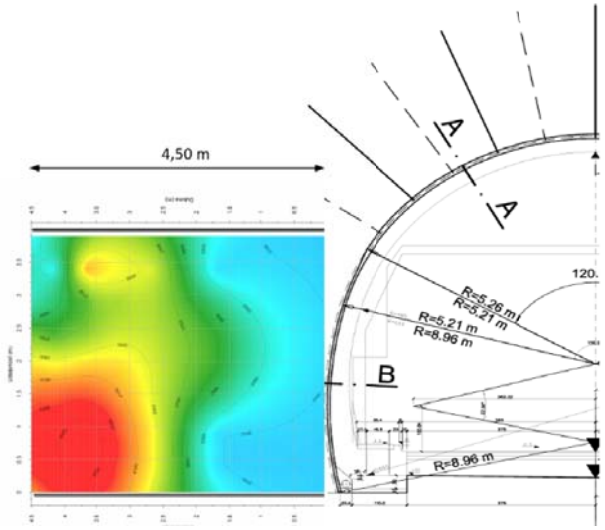


Fig. 3 Results of seismic cross-hole tomography in the wall of the Tunnel Šubir. In blue p-waves from 3.100 to 3.300 m/s: in green p-waves from 3.300 to 3.750 m/s; in yellow p-waves from 3.800 to 3.900 m/s; in orange p-waves from 3.900 to 4.100 m/s; in red more than p-waves from 4.100 m/s.

2.8 Rockbolt pull-out tests

During the excavation of the tunnel, preliminary and control tests of rockbolts are foreseen. The bearing capacity of the anchors was controlled by a pull-out test according to ISRM's Suggested methods for rockbolt testing (ISRM 1974). Preliminary tests or proving the usability of rockbolts include determining the bearing capacity of rockbolts in geological soil conditions similar to those expected during tunnelling. The tests were carried out before the start of the tunnel excavation on the tunnel pre-cut. The rockbolts are installed in the same way as they will be during tunnel construction. Total of 5 rockbolts with a length of 3 m were tested for force until failure (max 150 kN). The time between the installation and testing of the rockbolts was not shorter than 7 days. During the excavation of the tunnel, control tests of rockbolts were carried out, which were tested up to the demanding load capacity of 120 kN. The test frequency was 5 pieces for the first 100 installed rockbolts, and thereafter 5 pieces for every next 200. More than 95% of the tests of the control rockbolts met the required load capacity with deformations within 10 mm, and rarely up to 25 mm.

3 Discussion and conclusion

This paper presents the methods used in the verification of the stability of the underground excavation during the construction of the Mali Prolog and Šubir tunnels on the A1 Zagreb-Split-Ploče Highway, near the town of Vrgorac, Croatia. Given the similar geological settings, the height of the tunnel overburden and the cross-sections of the tunnels, as well as the partially simultaneous construction of both tunnels, the experience gained during the construction and verification of the stability of the underground tunnel opening enabled the verification of the application of the methods to both tunnels constructed in similar geotechnical conditions. During the tunnel construction, investigations were carried out to verify the efficiency of the length of the rockbolts of the primary tunnel support. During the tunnel construction, exploratory drilling, geophysical seismic measurements, video-prospecting of exploratory wells, geological mapping of the tunnel face, geodetic convergence measurements and anchor pull-out tests were carried out in II, III and IV categories of rock mass according to the RMR classification). All measurements taken generally confirmed the values and behaviour of the rock mass according to the requirements of the geotechnical project, with minimal deviations in the rock mass category and therefore changes in the sub-work systems applied in the tunnels. As a method of checking the effect of blasting on the rock mass, the method of video-prospecting of exploratory boreholes in the tunnel face, carried out before and after blasting, was used. The results of the visual prospecting of investigation boreholes showed damage to the rock mass to a depth of 1.08 m from the walls of the tunnel profile (Antičević 2011). Geophysical measurements showed deeper damage, in the II category of rock mass up to 1.6 m, and in III category up to 2.5 m. The reason for this difference between visual and geophysical measurements lies in the fact that there are microcracks that are not

visible, and the propagation and change in the speed of p-waves can detect them. Using the methods of video-prospecting of investigation boreholes at the tunnel head and geophysical seismic measurements at the tunnel side, which are not standard methods within the framework of observational methods, make a significant contribution to determining the damage to the rock mass due to the execution of the works (Antičević 2011). Both methods indicate damage values, which allow a clearer interpretation of the degree of damage to the rock mass in stability analyses, as well as for the purposes of better assessment of technological conditions for reducing over-profile excavation

References

Antičević H (2011): Determination of Blast Induced damage Rock Mass Damaged Zone in Tunnels.Dissertation atUniversity of Zagreb.

Barton NR, Lien R, Lunde, J (1974) Engineering classification of rock masses for the design of tunnel support. Rock Mech 6(4): 189-239.

Bieniawski ZT (1989) Engineering rock mass classification. John Wiley & Sons, New York.

Golser J, Mussger K (1978) The New Austrian Tunnelling Method (NATM) contractual aspects. Tunnelling Under Difficult Conditions, International Tunnel Symposium, Tokyo, Pergamon Press, Oxford, 387-392.

ISRM (1974) Suggested Methods for Rockbolt Testing.

KaićM (2012)TunelŠubir, Engineering geological mapping, Final report. MPsV Ltd., Zagreb.

Marinos P, Hoek E 2000. GSI: A geologically friendly tool for rock mass strength estimation. GeoEng2000 at the international conference on geotechnical and geological engineering, Melbourne, Technomic publishers, Lancaster.

Nicholson D, Tse C-M, Penny C (1999). The Observational Method in ground engineering: principles and applications Report 185. CIRIA, London. Report 185.

Peck RB (1969) Advantages and limitations of the observational method in applied soil mechanics. Geotechnique19 (2) 171-187.

Rabcewicz L (1964) The New Austrian Tunnelling Method, Part one. Water Power, 19-24.

Rabcewicz L, Golser J (1973) Principles of dimensioning the supporting system for theNew Austrian tunnelling method. Water Power, 88-93.

Terzaghi K, PeckRB (1967) Soil mechanics in Engineering Practice. John Wiley, New York.

Užarević D (2010) TunelŠubir, Geotechnial design, Civil Engineering Institute of Croatia, Zagreb.

Užarević D (2011) TunelMali Prolog, Geotechnial design, Civil Engineering Institute of Croatia, Zagreb.

Application of Auxetic reinforced mortar elements for pressurized tunnels

Arsham Moayedi Far
Institute of Subsurface Engineering, Montanuniversität Leoben, Leoben, Austria
arsham.moayedi-far@unileoben.ac.at
0000-0001-9802-9693

Marlene Villeneuve
Chair of Subsurface Engineering, Montanuniversität Leoben, Leoben, Austria

Giuseppe Loporcaro
Department of Civil and Environmental Engineering, University of Canterbury, Christchurch, New Zealand

Abstract

Designing pressurized underground tunnels requires mobilizing confinement from the surrounding rock mass by establishing an effective lining–rock bond; conventionally this is achieved via pressure grouting the annular gap to prestress a stiff steel or concrete lining, but an alternative is a flexible lining that deliberately accommodates larger displacements and develops this bond as internal pressure rises. We investigate this flexible concept using auxetic-reinforced mortar samples, composites that couple mortar infill with 3D-printed auxetic lattices fabricated from nylon filament reinforced with 15% carbon fiber. Auxeticity is the property of materials that have a negative Poisson's ratio, meaning they expand laterally when stretched and contract laterally when compressed. Because direct tensile testing of these composites is challenging, we characterized mechanical performance using splitting tests. Compared with conventional materials, auxetic-reinforced specimens exhibited substantially higher ductility under splitting conditions. Results also show that auxetic geometry and mortar–polymer interfacial strength govern stiffness, post-cracking behaviour, and failure modes. Moreover, the auxetic systems exceed the highest circumferential strain threshold of conventional linings by orders of magnitudes. These findings support a shift from stiff, brittle linings to ductile, auxetic-enabled flexible linings that can deform and expand circumferentially to engage rock confinement in pressurized storage tunnels.

Keywords

Underground pressurized tunnels; Auxetic structures, Flexible linings.

1 Introduction

Under high internal water pressure, tensile stresses can exceed the lining's tensile strength, causing cracking and potential leakage (Dadashi et al. 2017). For high heads in competent rock, prestressed concrete linings are adopted, typically using pressure grouting to induce compressive hoop prestress that counteracts fluid-induced hoop tension (Wang et al. 2020). Steel linings are an alternative for high pressures, yet they are costly, challenging to construct, and susceptible to buckling under high external groundwater pressures, especially during emptying; this necessitates added thickness beyond that required for internal pressure alone (Wang et al. 2020).

These challenges motivate the development of lining materials that combine tensile strength with enhanced ductility (Moayedi Far and Villeneuve 2025) to better mobilize confinement from the surrounding rock mass. Such solutions could complement prestressing, reduce or eliminate grouting, and enhance lining performance. Given demonstrated gains in ductility, toughness, and tension capacity, auxetic concepts are a promising direction.

Auxetic materials exhibit a negative Poisson's ratio, expanding laterally when stretched (Evans et al. 1991). This behaviour underpins superior functional properties versus conventional materials, including improved indentation resistance, higher shear stiffness, enhanced fracture toughness, and greater energy absorption (Carneiro et al. 2013; Evans and Alderson 2000; Alderson et al. 1994). Owing to their rarity in nature, research has focused on auxetic-based composites, typically an auxetic reinforcing framework with a matrix filler, for structural applications requiring combined deformability and strength (Carneiro et al. 2013), including, base isolation, and concrete reinforcement (Zhang and Yang 2016; Gu et al. 2022).

Cementitious materials are economical and strong in compression but brittle in tension, with low energy absorption and limited resistance to impact and vibration; reinforcement strategies using steel, synthetic fibers, and recently auxetic concepts have been explored to overcome these limits (Mukhopadhyay and Khatana 2014; Momoh et al. 2021).Recent studies further substantiate these trends. Xu et al. (2024) developed an auxetic cementitious composite (ACC) by combining 3D-printed Thermoplastic Polyurethane auxetic structures with mortar, achieving strain hardening, recoverable cyclic deformability, and improved energy dissipation over conventional and fiber-reinforced concretes. Chen et al. (2024) examined engineered cementitious composites where the auxetic structure itself is cementitious; their "buckling-induced" auxetic lattices showed higher compressive strength, energy absorption, flexural strength, and toughness than comparable re-entrant and cross-chiral forms. These findings point to auxetic composites as viable solutions for applications requiring toughness, energy absorption, and controlled deformation.

This research aims to investigate the performance of two types of auxetic reinforced mortar samples when subjected to indirect uniaxial tensile testing, providing insights into the applicability of such structures for pressurized tunnels. As specimen geometry, size effects, and equipment differences can strongly influence the results of direct uniaxial tension (Ouyang et al., 2024), the splitting test, an indirect method, has been employed in this investigation. To position these structures relative to conventional options, a comparison based on the induced circumferential strain is also presented. Together, these analyses assess the potential of auxetic reinforced mortar structures for use in pressurized tunnel environments.

2 Lining Design for pressurized tunnels

In pipeline design, the minimum wall thickness is determined by internal pressure, pipe radius, allowable material stress, temperature, and a joint-related coefficient (Antaki 2003). The allowable stress is set at 72% of the material's specified minimum yield strength at the design temperature and is independent of the material's ultimate strength (Antaki 2003). Because yield strength differs among materials (e.g., steel, unreinforced concrete, reinforced concrete), the allowable radial and circumferential strains, and thus the permissible expansion, are material dependent. In pressurized tunnels and underground spaces, this allowable deformation dictates how much the lining can expand to engage the surrounding rock, and any remaining gap is typically filled with pre-stress grouting to ensure contact between the rock mass and the tunnel lining, since conventional linings have limited allowable strain (Fernández 1994).

For pressure tunnels, sections are classified by potential leakage into: (1) sections where hydrojacking or hydrofracturing of the rock mass can occur, and (2) sections where the in-situ stress in the rock mass is high enough to prevent these phenomena (Fernández 1994).

For zones of high hydrojacking and/or hydrofracturing potential, a steel liner must be installed at all locations where the minimum in-situ stress is below 1.3 times the internal tunnel pressure under normal operation (Benson 1986; Brekke and Ripley 1986). In flat areas with marginal in-situ stresses where some leakage can be tolerated, and slope instabilities are unlikely, a heavily reinforced concrete liner can be considered as an alternative to long steel liners.

In areas where in-situ stresses are sufficient, whether a liner is needed primarily depends on the rock mass permeability, the acceptable level of leakage, and the ground pore-water pressures that can be safely induced without triggering instability in the surrounding materials (Fernández 1994). If a liner is required to limit leakage or to reduce excess pore-water pressures outside the tunnel, its effectiveness is governed by the ratio of its permeability with respect to the permeability of the surrounding media (Fernández 1994). Since the permeability of concrete liners is strongly influenced by the circumferential strain developed after pressurization, the magnitude of that strain should be used as a key index for selecting the appropriate liner type (Fernández 1994).

When the rock mass is relatively permeable (rock mass hydraulic conductivity in excess of 1×10^{-5} cm/s), the preferred liner type can be selected based on the circumferential strain induced by the internal tunnel pressure. The following design guidelines are from Fernández (1994):

1. Plain concrete when circumferential strain is less than 1.5×10^{-4}, combined with thorough contact grouting to achieve a relatively "impermeable" barrier.
2. Plain concrete plus consolidation grouting for strain up to 4×10^{-4}; grout hole lengths should be about the tunnel radius or slightly longer, and injection pressures should be at least equal to the internal tunnel pressure.
3. Reinforced concrete for a strain more than 4×10^{-4}.
4. Reinforced concrete with a plastic membrane for strain more than 6×10^{-4}.
5. Concrete liner incorporating a thin steel membrane for strain exceeding 8×10^{-4}.

If the tunnel's internal pressure is high and/or the surrounding ground has relatively low stiffness, the thin steel membrane in option 5 may need to be thickened to avoid buckling under external loads (Fernández 1994). Once the required thickness reaches this point, it is more appropriate to design a conventional steel liner (Fernández 1994).

When the rock mass has low permeability (less than 1×10^{-5} cm/s), installing plain or reinforced concrete liners, whether or not accompanied by consolidation grouting, does little to reduce tunnel leakage or limit induced pore-water pressures in the surrounding ground (Fernández 1994). However, rock with these properties is typically tight and massive, so leakage rates are inherently low. If the rock is nonerodible and not prone to dissolution or deterioration, and the formation is massive and sound, the excavation may be left unlined. The following suggestions are from Fernández (1994):

1. Concrete with nominal reinforcement when the surrounding rock is vulnerable to erosion or deterioration and the liner's circumferential strain is above 6×10^{-4}.
2. Reinforced concrete when the rock is susceptible to dissolution and the circumferential strain exceeds a value of 3×10^{-4}.

If the design requires a stricter control of leakage or pore-water pressures, an embedded impermeable barrier within the concrete liner can be used. Depending on the anticipated circumferential strain in the liner, this barrier may be a plastic membrane or a thin steel sheet (Fernández 1994).

To illustrate this, we consider a tunnel with internal pressure of 10 (MPa), inner radius of 2.5 (m), concrete lining thickness of 0.5 (m), Elastic modulus of 30 (GPa), Poisson ratio of 0.2, and shrinkage strain coefficient of 0.0005 (m/m). Concrete shrinkage causes a radial displacement of -1.5×10^{-3} (m) and hoop strain of -5×10^{-4}. Based on Lame's solution the expansion due to internal pressure would lead to radial displacement of 4.36×10^{-3} (m) and hoop strain of 1.52×10^{-3}. Summing the opposing strains and displacements, the lining would be subjected to expansion with radial displacement of 2.86×10^{-3} (m) and strain of 1.02×10^{-3}.

For the lining to successfully close the gap, the allowable radial expansion would need to be higher than the radial shrinkage of concrete and the lining material would need to be able to handle the induced hoop strain. Even the concrete liner incorporating a thin steel membrane with hoop strain capacity of 8×10^{-4} is unable to provide enough capacity, warranting the exploration of auxetic composites for this function.

3 Materials and methods

3.1 Printing Auxetic Structures

Two auxetic lattice designs, a re-entrant pattern and a missing-rib pattern, were developed and printed for this study. Unit cells were configured to cubic specimens of 40×40×40 mm for splitting tests. All lattices were fabricated using a Prusa i3 MK3S+ with a nylon filament reinforced with 15% carbon fibers, selected for its high strength, toughness, stiffness and resistance to impact, heat, and abrasion.

3.2 Sample preparation

To accommodate the complex auxetic geometries and small specimen sizes, a fine mortar was prepared using quartz sand with particle size<0.5 mm. The mix comprised ordinary Portland cement 865 (kg/m^3), quartz sand (<0.5 mm, 865 kg/m^3), Silica fume (192 kg/m^3), water(218 kg/m^3) and a superplasticizer (38 kg/m^3). Dry constituents (cement, sand, microsilica) were blended for 3–5 minutes. After blending the dry ingredients, approximately 70–80% of the total water was slowly incorporated. The remaining water, pre-mixed with the superplasticizer, was then added, and mixing continued for about five minutes until the mixture became uniform and highly workable. The fresh mortar was cast into molds containing the auxetic lattices, consolidated on a lab vibrator for 1–2 minutes, and stored under humid room conditions. After 24 hours, re-entrant and missing-rib reinforced mortar specimens (MrARC, ReARC) (Fig. 1) were demolded and water cured for 28 days (Moayedi Far et al., 2026).



Fig. 1 Cubic samples; a) MrARC, b) ReARC. (Moayedi Far et al., 2026).

3.3 Laboratory tests

Splitting tests were performed on an MTS 815 servo-hydraulic machine under displacement control to obtain full load–displacement responses. The auxetic-reinforced specimens were tested ata constant rate of 0.35 mm/min. A 2D digital image correlation (DIC) setup was used to obtain full-field surface displacements by correlating reference images with video frames captured during testing. The camera was placed 25 cm from the speckled specimens and aligned parallel to the specimen's surface normal to reduce out-of-plane error.

4 Results and insights

4.1 Splitting tests

Fig. 2 shows force–horizontal strain responses for all specimens in which the strain values were obtained from DIC. The auxetic-reinforced specimens highlight a significant ductility, with both ReARC and MrARC reaching a maximum horizontal strain of about 29%. In terms of peak load, MrARC records the lowest (5.673 kN), whereas ReARC attains the highest mean force (11.577 kN).

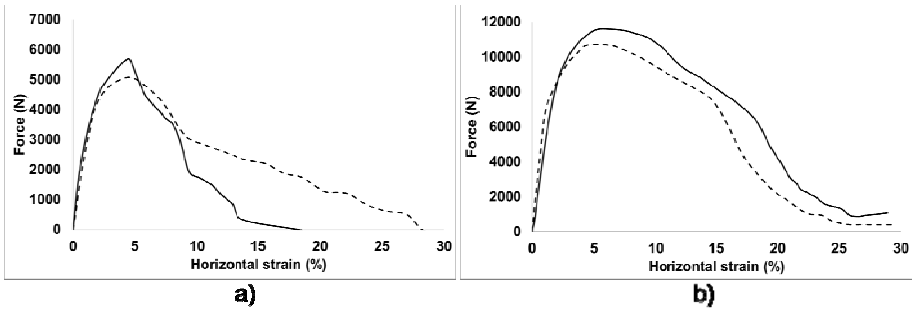


Fig. 2 Force-horizontal strain for a) MrARC and b) ReARC.

Post-failure, for MrARC, the dominant weakness plane forms through coalescence of cracks within the mortar and dilation/offset at the mortar–auxetic interface, which steers the final split(Fig. 3a). In ReARC, auxetic cells near the rollers deform in tension and bending, concentrating damage in the adjacent mortar; the upper mortar is crushed, the lower region near the roller shows fracture growth, and dilation at the mortar–auxetic interface creates the final dominant failure plane (Fig. 3b).



Fig. 3 Final state of a) MrARC and b) ReARC.

4.2 Insights

In splitting tests, the ReARC response is dominated by the auxetic lattice, with the mortar contributing mainly in the regions adjacent to the rollers. A weak mortar–auxetic interface establishes the dominant weakness plane, while the lattice sustains a complex stress state combining tension and shear. ReARC attains higher splitting strength than MrARC, largely because the auxetic members near the rollers are preferentially activated, mobilizing the high tensile capacity of the ePAHT CF lattice; this localized effect elevates the overall load-bearing capacity.

Geometric and interfacial characteristics distinguish MrARC from ReARC. The MrARC pattern (with edges) promotes broader stress transfer and engages more mortar elements, so its capacity depends on the combined performance of mortar and lattice rather than on localized lattice action. In contrast, the simpler ReARC topology makes the global response more sensitive to interface quality; stronger bonding tends to concentrate load transfer through the lattice near the rollers, whereas weaker bonding promotes more independent deformation of the two phases and a larger affected region.

The auxetic-reinforced mortars reached high pre-first-peak tensile strains, MrARC$4.7\times10^{-2}$and ReARC5.3×10^{-2}. Thus, the auxetic systems exceed the concrete liner incorporating a thin steel membrane limit (circumferential strain of 8×10^{-4}) by nearly two orders of magnitude. This increased ductility could close larger gaps and accommodate the induced hoop strainwithout or with minimal additional measures (e.g., grouting).

5 Conclusion

Based on the experimental results, the following conclusions can be drawn:

1. Auxetic-reinforced specimens experience a mixed stress state during splitting tests.
2. Auxetic geometry controls how much of the sample is engaged in tests and how strongly mortar participates.
3. Mortar–lattice bond quality has a significant effect of the level of involvement of accrete cells and failure plane in the samples.
4. Auxetic-reinforced specimens show significant improved ductility.
5. The added ductility could help underground storage linings expand to close the rock–lining gap during pressurization compared to other conventional alternatives.

Acknowledgment

This work was supported by the New Zealand government (MBIE contract UOCX2207) under the Endeavour program "Pūhiko Nukutū: a green hydrogen geostorage battery in Taranaki" and by the Hydrogen Under Ground (HUG) project funded by Business Finland's Co-Research instrument and project partners. An instance of GPT-4 within Academic AI was used for language enhancement; the authors reviewed and edited the content and assume full responsibility. Auxetic samples were printed by Mr. Stephan Schuschnigg, Department of Polymer Engineering and Science, Montanuniversitaet Leoben.

References

Alderson KL, Pickles AP, Neale PJ, Evans KE (1994) Auxetic polyethylene: the effect of a negative Poisson's ratio on hardness. Acta Metallurgica et Materialia 42 (7): 2261–2266. https://doi.org/10.1016/0956-7151(94)90304-2

Antaki GA (2003) Piping and pipeline engineering: design, construction, maintenance, integrity, and repair. 1st edn. CRC Press, Boca Raton

Benson RP (1986) Design of steel lined penstocks and high pressure power tunnels. Proceedings of the 5th Canadian Tunnelling Conference, Niagara Falls, Canada, 1986

Brekke T, Ripley B (1986) Design strategies for pressure tunnels and shafts. Rep. EPRI contract No. RP-1747. Electric Power Research Institute, Palo Alto

Carneiro VH, Meireles J, Puga H (2013) Auxetic materials—A review. Materials Science-Poland 31 (4): 561–571.

Chen M, Fang S, Wang G, Xuan Y, Gao D, Zhang M (2024) Compressive and flexural behaviour of engineered cementitious composites based auxetic structures: An experimental and numerical study. Journal of Building Engineering 86: 108999. https://doi.org/10.1016/j.jobe.2024.108999

Dadashi E, Noorzad A, Shahriar K, Goshtasbi K (2017) Hydro-mechanical interaction analysis of reinforced concrete lining in pressure tunnels. Tunnelling and Underground Space Technology 69: 125–132.

Evans KE, Alderson A (2000) Auxetic materials: functional materials and structures from lateral thinking! Advanced Materials 12 (9): 617–628.

Evans KE, Nkansah MA, Hutchinson IJ, Rogers SC (1991) Molecular network design. Nature 353 (6340): 124–124. http://dx.doi.org/10.1038/353124a0

Fernández G (1994) Behavior of pressure tunnels and guidelines for liner design. Journal of Geotechnical Engineering 120 (10): 1768–1791.

Gu JB, Wang JY, Lu W (2022) An experimental assessment of ultra high performance concrete beam reinforced with negative Poisson's ratio (NPR) steel rebar. Construction and Building Materials 327: 127042.

Moayedi Far A, Villeneuve M (2025) Towards a Safe and Large-scale Solution for Balancing Renewable Energy Supply and Demand. BHM Berg-und Hüttenmännische Monatshefte 170 (12): 766-773.

Momoh EO, Osofero AI, Menshykov O (2021) Bond behaviour of oil palm broom fibres in concrete for eco-friendly construction. Proceedings of the Institution of Civil Engineers – Construction Materials 174 (1): 47–64. https://doi.org/10.1680/jcoma.19.00097

Mukhopadhyay S, Khatana S (2015) A review on the use of fibers in reinforced cementitious concrete. Journal of Industrial Textiles 45 (2): 239–264. https://doi.org/10.1177/1528083714529806

Ouyang X, Huang Y, Hu X, Yin J, Shi C (2024) Evaluation of tensile failure behavior of ultra high performance concrete under double-edge wedge splitting and direct tension loadings. Journal of Building Engineering 90: 109480.

Wang H, Shao J, Zhang W, Yan Z, Huang Z, Liang X (2023) Three-point bending response and energy absorption of novel sandwich beams with combined re-entrant double-arrow auxetic honeycomb cores. Composite Structures 326: 117606. https://doi.org/10.1016/j.compstruct.2023.117606

Wang X, Liu L, Fu R, Sun X (2020) Newly developed pressure adaptable concrete lining for high pressure hydraulic tunnels. Tunnelling and Underground Space Technology 105: 103570.

Xu Y, Meng Z, Bol RJ, Šavija B (2024) Spring-like behavior of cementitious composite enabled by auxetic hyperelastic frame. International Journal of Mechanical Sciences 275: 109364. https://doi.org/10.1016/j.ijmecsci.2024.109364

Zhang XW, Yang DQ (2016) Numerical and experimental studies of a light-weight auxetic cellular vibration isolation base. Shock and Vibration 2016 (1): 4017534. https://doi.org/10.1155/2016/4017534

Moayedi Far, A., Villeneuve, M., Loporcaro, G., & Schuschnigg, S. (2026). Compressive mechanical behavior and energy absorption of auxetic reinforced cementitious elements. Construction and Building Materials, 538, 147278. https://doi.org/10.1016/j.conbuildmat.2026.147278

Computer-Aided Selection of Pillar Geometry in Deep Room-and-Pillar Panels Using Calibrated Large-Scale 3D FEM

K. Fuławka, P. Mertuszka & L. Stolecki
KGHM CUPRUM Ltd. Research & Development Centre, Wrocław, Poland
krzysztof.fulawka@kghmcuprum.com
0000-0002-0534-0712

M. Malesza, R. Wasilewski
KGHM Polska Miedź S.A, „Rudna Mine", Polkowiece, Poland

Abstract

Room-and-pillar mining at great depth must balance two competing targets: keeping the roof–pillar system stable under high in-situ stresses while maintaining high extraction. In panels affected by stress redistribution from nearby mined-out areas, empirical rules and simplified models may miss full-scale interactions and local damage, which can lead to sub-optimal design choices.

To support variant selection, a full-scale 3D finite element model was developed for a high-risk panel in the Rudna copper mine (Poland). The model domain (1.5 × 1.5 × 1.0 km) was implemented in GTS NX and used the Generalized Hoek–Brown failure criterion with GSI-based rock mass reduction. Mining-induced degradation was represented by assigning different parameter sets to key geomechanical zones (intact rock mass, large protective pillars, technological pillars, and mined-out/backfilled areas). The model was iteratively calibrated against in-situ convergence measurements from multiple monitoring locations to obtain a realistic deformation response.

Three room-and-pillar layouts were analysed with staged excavation reflecting mining advance and the liquidation phase with 4×3 m remnant pillars. The tested pillar geometries were 4×4 m, 5×6 m, and 8×8 m. The simulations showed clear differences in stability factor distribution and roof deflection behaviour. The 4×4 m variant produced unstable zones (FS < 1). The 8×8 m variant achieved the highest recovery (~93%), but it also indicated a stiff response and rapid loss of load-bearing capacity during pillar cutting, which may increase the likelihood of dynamic roof behaviour and elevated seismic risk. The 5×6 m variant offered the most balanced outcome, with acceptable stability (FS ≈ 1.1), high recovery (~90%), and a more controlled roof deflection process.

These results show that a calibrated full-scale 3D FEM model can be used as a practical decision tool to compare deep room-and-pillar variants, quantify safety margins, and select layouts that maximise recovery without compromising stability.

Keywords

Deep mining, Room-and-pillar mining, 3D numerical modelling, Finite element method, Hoek–Brown criterion.

1 Introduction

Room-and-pillar mining at great depth must balance roof–pillar stability under high in-situ stress with high extraction and operational efficiency. The challenge extends beyond tributary-area loading to progressive damage, confinement changes, and potential dynamic response linked to mining-induced seismicity (Fuławka et al., 2018). Key design choices—pillar geometry, opening size, sequencing and liquidation—interact in 3D and are influenced by neighbouring mined-out areas and stiffness contrasts (Jing, 2003; Shapka-Fels and Elmo, 2022). Although pillar design has long relied on empirical rules, their reliability decreases when extrapolated to greater depths, different lithologies or modified extraction sequences, where brittle spalling and progressive failure can drive non-linear behaviour (Hedley and Grant, 1972; Rafiei Renani and Martin, 2018). Numerical modelling is therefore increasingly used to capture 3D stress redistribution, excavation sequence effects and yielded zone development (Jing, 2003; Sinha and Walton, 2019). Predicted stability, however, depends on constitutive assumptions and the representation of damage and post-peak behaviour—especially when layouts have similar recovery but different deformation character and hazard potential (Sinha and Walton, 2019; Esterhuizen et al., 2011; Rafiei Renani and Martin, 2018). Reliability is typically improved using rock-mass strength frameworks such as Hoek–Brown and GSI, which support consistent parameter reduction and practical numerical implementation (Hoek et al., 1998; Hoek et al., 2002; Marinos et al., 2005; Benz et al., 2008).

Recent studies from the Lower Silesian Copper Basin confirm the value of staged modelling linked to observations, including frequency-dependent dynamic response analyses and large-scale 3D identification of increased seismic-risk zones validated with monitoring (Fuławka et al., 2022; Fuławka et al., 2024), as well as practical rockburst risk screening based on modelling outputs (Pytel et al., 2023). Against this background, this study presents a computer-aided workflow using a calibrated full-scale 3D FEM model (based on convergence monitoring) to compare feasible room-and-pillar variants for a deep, high-risk panel and support transparent selection by linking stability and deformation indicators with recovery-based economic screening (Esterhuizen et al., 2011; Sinha and Walton, 2019; Theron and Malan, 2024).

2 Geological and Mining Setting

The analysed panel lies at ~1,230 m depth and exploits a thin, stratiform orebody (~1.5 m on average; locally 0.6–2.4 m). The deposit dips gently (2–6°) and the ~380 m mining front makes stress redistribution and roof response sensitive to local geometry and neighbouring mined-out areas. The orebody is hosted in Lower Zechstein carbonates and shales and extends into Rotliegend sandstones. The roof is bedded calcareous dolomite overlain by massive anhydrite, while the floor is mainly quartz sandstone with clay cement underlain by red Rotliegend sandstone (Fig. 1), promoting separation along bedding and interfaces. The panel is weakly tectonised, with a small-throw normal fault (0.1–0.5 m) and preferential NE–SW and NW–SE roof cracking. It is classified as high rockburst risk, consistent with UCS values of ~120 MPa (roof), ~86 MPa (ore) and ~42 MPa (floor) and the seismicity context of deep copper mining.

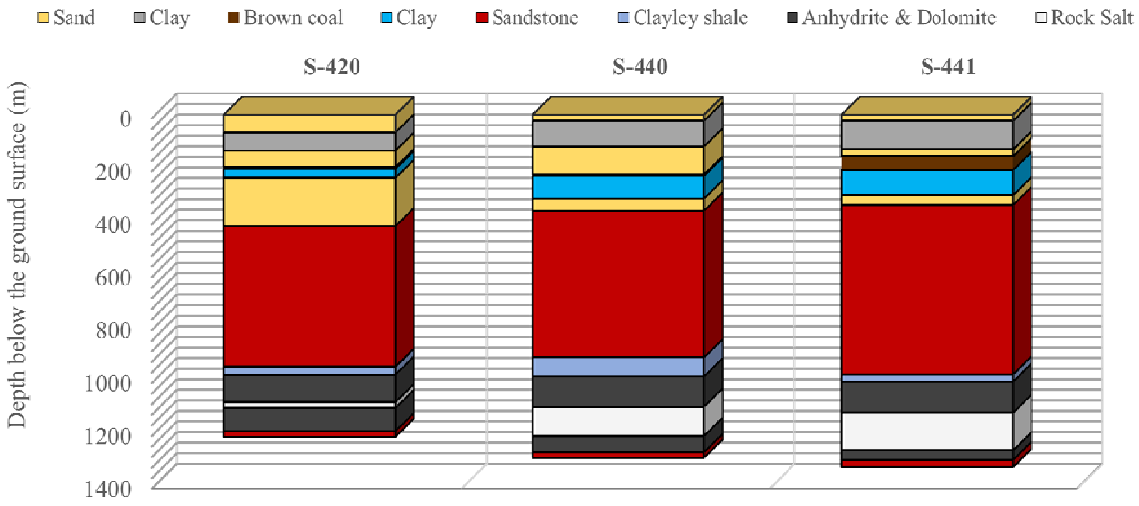


Fig. 1 Data from exploration boreholes in surrounding of analysed mining panel.

3 Material and Methods

The workflow used to compare room-and-pillar variants consisted of four steps: (1) development of a full-scale 3D FEM model representing the panel geometry and main lithological units, (2) iterative calibration using underground convergence measurements, (3) staged simulations of three pillar-size variants under consistent assumptions, and (4) variant ranking based on combined safety indicators and a recovery-based economic screening.

3.1 Numerical Model

A large-scale 3D finite element model was built in GTS NX. The geological framework was prepared from exploration drilling data around the analysed panel, and the model dimensions were 1.5 × 1.5 × 1.0 km to represent the large-scale loading conditions. To balance accuracy and computation time, a hybrid mesh (tetrahedral + hexahedral elements) with element-size gradation was used. The maximum element size at the deposit level was 1.5 m, while in layers far from the mining horizon it increased up to 35 m, since distant layers mainly provide loading and are not the focus of the analysis (Fig. 2).

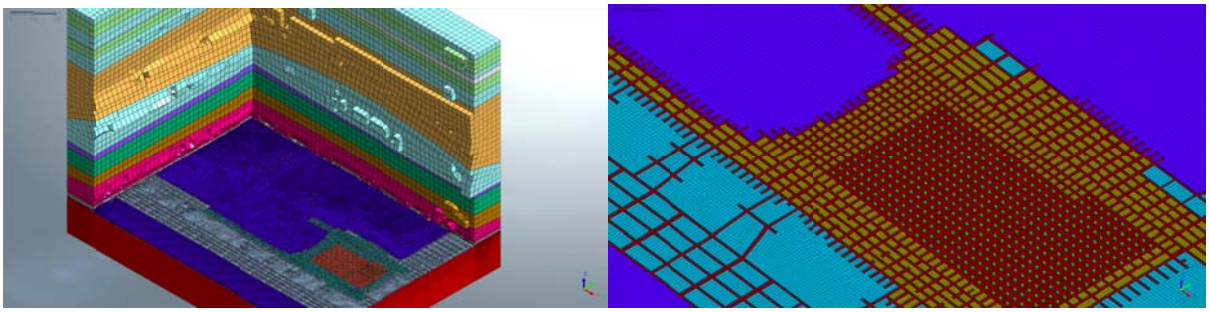


Fig. 2 Discretised 3D numerical model of analysed mining area (left) and view of the dense-mesh area which was base for model calibration (right).

Rock mass behaviour was represented with the Generalized Hoek–Brown (GHB) criterion. Initial parameters at the deposit level served as a baseline (Table 1) and were later reduced during calibration using GSI and disturbance (D) concepts to reflect in-situ degradation.

Table 1. Intact rock data at the excavation level.

Parameter	R_c [MPa]	E_s [GPa]	Cohesion, c [MPa]	Angle of friction, $\emptyset$ [°]	Poisson's ratio, ϑ [-]	Density, ρ [g/cm^3]	m_i [-]
Value	45.0	33.5	20.5	32	0.22	2.28	8

3.2 Calibration

Calibration was performed to ensure that the full-scale model reproduces realistic deformation trends and contrasts between excavation zones. The main dataset consisted of convergence measurements from telescopic convergence indicators installed between the roof and the floor. These measurements typically have low reading frequency (often once per day), so calibration focused on representative convergence levels and spatial patterns rather than short-term fluctuations. The location of convergometers and result of 1-month long convergence measurements are presented in Fig. 3.

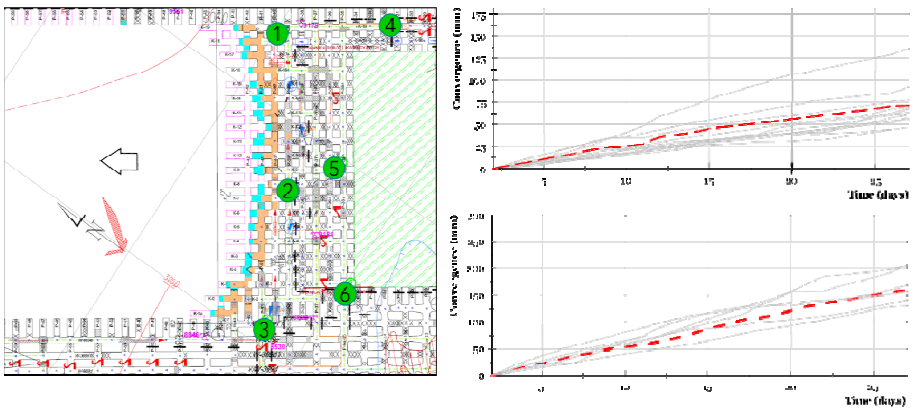


Fig. 3 Location of convergometers (left) and result of convergence measurement (right).

A key mismatch observed in early runs was an underestimation of the difference between the mining front zone and long-life excavations. To address this, rock mass strength reduction was applied separately in four geological-structural zones: technological pillars, backfilled/liquidated zones, intact rock mass, and large protective pillars. Each zone was assigned different GSI and D parameters within the GHB framework to capture varying degrees of mining-induced damage and discontinuity.

3.3 Pillar geometries

After calibration, three pillar geometries were evaluated: 4×4 m, 5×6 m, and 8×8 m. To capture the effect of mining advance, three stages of front progress were simulated for each variant (Fig. 4). In the liquidation phase, remnant pillars were kept identical across all scenarios (4×3 m), ensuring comparability and isolating the influence of technological pillar geometry.

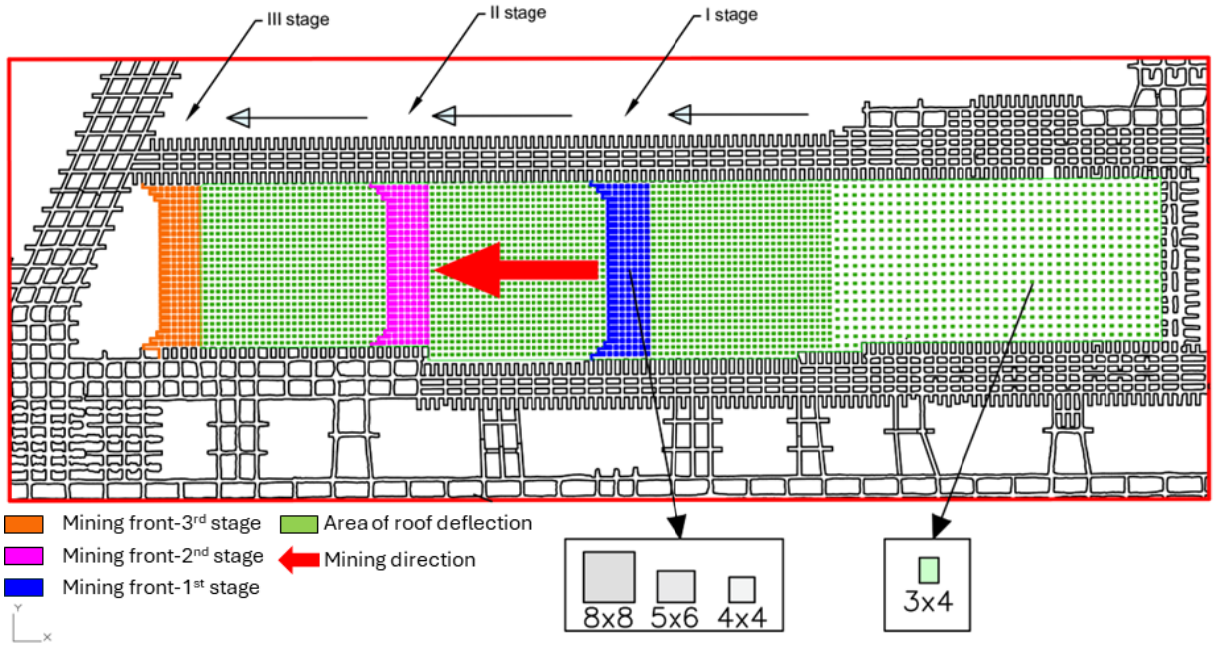


Fig. 4 Considered exploitation scenarios with marked stages of mining front line.

4 Results and discussion

The calibration was performed through iterative updates of the Hoek–Brown rock-mass parameters by adjusting GSI and the disturbance factor D separately in the main model zones, until a satisfactory match of displacement levels was obtained. The goal was achieved after the third iteration for both the active exploitation area and the long-life entries (haulage and ventilation drifts). The exact values of nonlinear GSI parameters are presented in Table 2.

For the purposes of this study, the analysis focused on the distribution of the stability indicator FS at the ore level along a cross-section, covering the transition from undisturbed rock mass, through the active mining front, to the mined-out area behind the front(Fig. 5).After model calibration, three room-and-pillar variants were simulated with staged mining progress (Stages I–III). To ensure direct comparability, the same liquidation approach was applied in all cases, i.e., identical 4×3 m remnant pillars in the liquidation zone.

Table 2. Results of the third iteration of calculations (baseline response before calibration).

Parameter	Intact rock mass	Large pillars	Technological pillars	Goaf's (Liquidation) zone
GSI	100	95	90	60
m_b	8.0000	6.6291	5.4376	1.1909
s	1.0000	0.5629	0.3105	0.0048
D	0.00	0.10	0.15	0.50
a	0.5	0.5001	0.5002	0.5028
E	33.50	31.05	24.15	9.10
c	9.7328	7.5400	5.8959	2.0641
φ	39.84	39.24	38.35	27.67

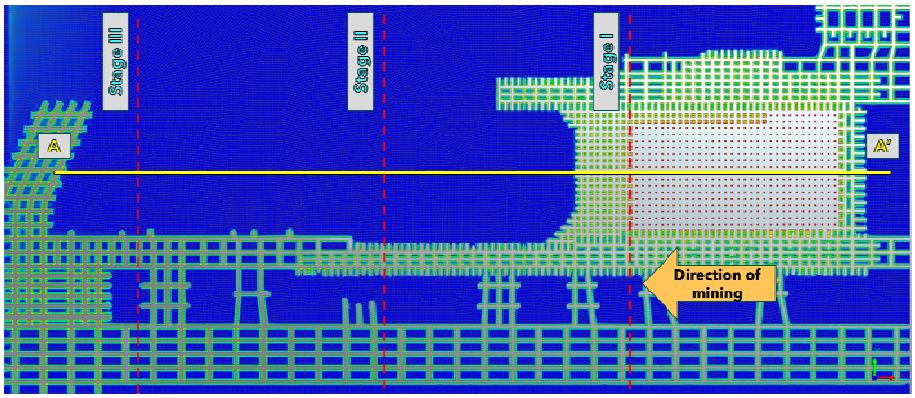


Fig. 5 3D numerical model view showing the location of the assessed cross-section (A-A´)and the three mining-advance stages (Stages I–III) defined by the position of the exploitation front used in the simulations.

All results are synthesised in Fig. 6 which presents the evolution of FS for each variant and stage.

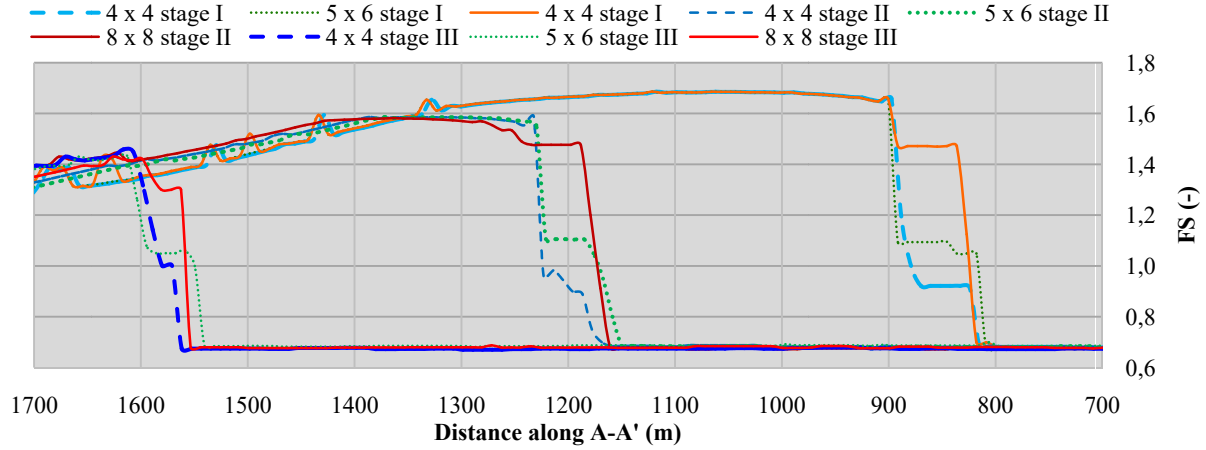


Fig. 6 Safety factor (FS) distribution at the deposit level along the A–A′ cross-section for three room-and-pillar variants (4×4 m, 5×6 m and 8×8 m pillars) in Stages I–III of mining advance.

The 4×4 m variant showed a relatively gentle, distributed roof response but consistently produced sections with FS < 1, indicating insufficient pillar capacity and clear instability risk; it was therefore rejected despite its “calmer” deformation character. By contrast, the 8×8 m variant maintained high FS values (FS≈1.45) at the mining front and between the front and liquidation, confirming strong stability margins during development, but it also introduced excessive stiffness early in the sequence. During liquidation (cutting to 4×3 m remnants), the model indicated a sudden, strongly localised loss of capacity and abrupt roof deflection—unfavourable at great depth because it may trigger dynamic cracking of stiff roof layers and contribute to high-energy seismic events and operational disruptions.
The 5×6 m variant provided the most balanced behaviour, with FS ≈ 1.1 and a more controlled, spatially distributed roof response than the 8×8 m case. Recovery was 93% (8×8 m), 90% (5×6 m) and 87% (4×4 m). Although 8×8 m maximises extraction, the higher likelihood of sudden deformation during liquidation may offset this benefit through downtime and added support costs. Therefore, the 5×6 m layout was identified as the best safety–economics compromise, combining high recovery with stable, predictable response.

5 Conclusions

The calibrated full-scale 3D FEM analyses show that variant selection in deep room-and-pillar mining is controlled not only by recovery but also by how stability and deformation evolve during mining advance and, most importantly, during the transition to liquidation. The 4×4 m variant was rejected due to persistent instability indicators (FS < 1). The 8×8 m variant provided the highest recovery, but the model indicated an unfavourable stiff-to-post-critical response with a sudden, localised loss of load-bearing capacity during pillar cutting, which may increase the likelihood of abrupt roof deflection and higher seismic/dynamic hazard. The 5×6 m layout delivered the best safety–economics compromise, combining acceptable stability margins (FS ~ 1.1) with high recovery (~90%) and a more controlled roof response across the analysed stages.

From a methodological perspective, the key advantage of the proposed workflow is that it converts large-scale 3D modelling into a decision-support tool by combining staged analysis with spatial calibration against field convergence data. Adjusting GSI and disturbance factor D independently in the main geomechanical zones allowed the model to reproduce deformation levels both in the active extraction area and in long-life entries, improving confidence in scenario ranking. This approach is implementable in routine mine planning: once a calibrated "panel-scale" model is established, alternative layouts and liquidation strategies can be screened consistently, safety-critical zones can be identified early, and numerical results can be directly linked to practical design rules (pillar geometry, sequencing, support needs) and recovery-based economic constraints.

References

Benz, T., Schwab, R., Kauther, R.A. and Vermeer, P.A. (2008) A Hoek–Brown criterion with intrinsic material strength factorization. International Journal of Rock Mechanics and Mining Sciences, 45(2): 210–222.

Esterhuizen, G.S., Dolinar, D.R. and Ellenberger, J.L. (2011) Pillar strength in underground stone mines in the United States. International Journal of Rock Mechanics and Mining Sciences, 48(1): 42–50.

Fuławka, K., Pytel, W. and Mertuszka, P. (2018) The effect of selected rockburst prevention measures on seismic activity – Case study from the Rudna copper mine. Journal of Sustainable Mining, 17(1): 1–10.

Fuławka, K., Kwietniak, A., Lay, V. and Jaśkiewicz-Proć, I. (2022) Importance of seismic wave frequency in FEM-based dynamic stress and displacement calculations of the earth slope. Studia Geotechnica et Mechanica, 44(1): 82–96.

Fuławka, K., Kołodziej, R., Stolecki, L. and Jaśkiewicz-Proć, I. (2024) The use of large-scale 3D numerical modelling to identify areas of increased seismic risk in Polish underground copper mines. Proceedings of the 7th International Conference on Geotechnical and Geophysical Site Characterization (ISC'7), Barcelona, Spain, 18–21 June 2024.

Hedley, D.G.F. and Grant, F. (1972) Stope-and-pillar design for the Elliot Lake uranium mines. CIM Bulletin, 65: 37–44.

Hoek, E., Marinos, P. and Benissi, M. (1998) Applicability of the Geological Strength Index (GSI) classification for very weak and sheared rock masses: The case of the Athens Schist Formation. Bulletin of Engineering Geology and the Environment, 57(2): 151–160..

Hoek, E., Carranza-Torres, C. and Corkum, B. (2002) Hoek–Brown failure criterion – 2002 Edition. In: Hammah, R., Bawden, W., Curran, J. and Telesnicki, M. (eds) Proceedings of NARMS–TAC 2002: Mining Innovation and Technology, Toronto, Canada, 10 July 2002, pp. 267–273. University of Toronto, Toronto.

Jing, L. (2003) A review of techniques, advances and outstanding issues in numerical modelling for rock mechanics and rock engineering. International Journal of Rock Mechanics and Mining Sciences, 40(3): 283–353.

Malli, T., Yetkin, M.E., Özfirat, M.K. and Kahraman, B. (2017) Numerical analysis of underground space and pillar design in metalliferous mine. Journal of African Earth Sciences, 134: 365–372.

Marinos, V., Marinos, P. and Hoek, E. (2005) The Geological Strength Index: Applications and limitations. Bulletin of Engineering Geology and the Environment, 64(1): 55–65.

Martin, C.D. and Maybee, W.G. (2000) The strength of hard-rock pillars. International Journal of Rock Mechanics and Mining Sciences, 37(8): 1239–1246.

Pytel, W., Fuławka, K., Pałac-Walko, B. and Mertuszka, P. (2023) Numerical and analytical determination of rockburst characteristics: Case study from Polish deep copper mine. Applied Sciences, 13(21): 11881.

Rafiei Renani, H. and Martin, C.D. (2018) Modeling the progressive failure of hard rock pillars. Tunnelling and Underground Space Technology, 74: 71–81.

Shapka-Fels, T. and Elmo, D. (2022) Numerical modelling challenges in rock engineering with special consideration of open pit to underground mine interaction. Geosciences, 12(5): 199.

Sinha, S. and Walton, G. (2019) Numerical analyses of pillar behavior with variation in yield criterion, dilatancy, rock heterogeneity and length to width ratio. Journal of Rock Mechanics and Geotechnical Engineering, 11(3): 521–536.

Theron, W.J. and Malan, D.F. (2024) Pillar design and the associated mining engineering constraints in hard rock bord-and-pillar mines. Journal of the Southern African Institute of Mining and Metallurgy, 124(11): 631–644.



EUROCK 2026

Risk Management in Rock Engineering

to be updated